

József Karger-Kocsis · Tamás Bárány
Editors

Polypropylene Handbook

Morphology, Blends and Composites

 Springer

Polypropylene Handbook

József Karger-Kocsis (1950–2018)

Tamás Bárány

Editors

Polypropylene Handbook

Morphology, Blends and Composites

 Springer

Editors

József Karger-Kocsis (1950–2018)
Department of Polymer Engineering,
Faculty of Mechanical Engineering
Budapest University of Technology
and Economics
Budapest, Hungary

Tamás Bárány
Department of Polymer Engineering,
Faculty of Mechanical Engineering
Budapest University of Technology
and Economics
Budapest, Hungary

ISBN 978-3-030-12902-6

ISBN 978-3-030-12903-3 (eBook)

<https://doi.org/10.1007/978-3-030-12903-3>

Library of Congress Control Number: 2019931526

© Springer Nature Switzerland AG 2019

This work is subject to copyright. All rights are reserved by the Publisher, whether the whole or part of the material is concerned, specifically the rights of translation, reprinting, reuse of illustrations, recitation, broadcasting, reproduction on microfilms or in any other physical way, and transmission or information storage and retrieval, electronic adaptation, computer software, or by similar or dissimilar methodology now known or hereafter developed.

The use of general descriptive names, registered names, trademarks, service marks, etc. in this publication does not imply, even in the absence of a specific statement, that such names are exempt from the relevant protective laws and regulations and therefore free for general use.

The publisher, the authors and the editors are safe to assume that the advice and information in this book are believed to be true and accurate at the date of publication. Neither the publisher nor the authors or the editors give a warranty, express or implied, with respect to the material contained herein or for any errors or omissions that may have been made. The publisher remains neutral with regard to jurisdictional claims in published maps and institutional affiliations.

This Springer imprint is published by the registered company Springer Nature Switzerland AG
The registered company address is: Gewerbestrasse 11, 6330 Cham, Switzerland

Preface

Polypropylene (PP) has been produced and used in large quantities since 1957. Nowadays, PP is the polymer produced in the second largest quantity worldwide. What is the secret of the unbroken success of this material? It is a versatile polymer and has several properties that justify this popularity. The mechanical properties of PP are between those of commodity plastics and engineering thermoplastics. Other features fascinating both researchers and developers are related to its stereoregularity and polymorphism. A great deal of new knowledge and many inventions are related to these features, including peculiar crystallization, controlled development of beta PP, and the effect of processing conditions on the polymorphic structure. As a consequence, researchers regard PP as an optimum model material to explore different possibilities of further modifications of structure–property relationships. Our intention of this book was to survey the updated knowledge on the structure–property relationship of PP and related systems.

This book consists of ten chapters about the tacticity, regio- and stereoregularity of PP, the solid-state polymorphism of isotactic and syndiotactic PP, the nucleation and crystallization of PP, morphology development and control, polypropylene copolymers, structure and properties of particulate-filled polypropylene, property control by polypropylene blends, PP composites and foams.

In each chapter, existing and established knowledge and rules are summarized but also expanded and completed with the latest research results. All the chapters are prepared by well-known experts, many of whom participated in the former books on polypropylene. This book focuses on processing–structure–property relationships: how can they be manipulated, what can be achieved, and what are the benefits? We are sure that this PP handbook will find its place on the bookshelves of researchers in academia as well as in the industry. We hope it will also be an indispensable handbook for lecturers and students, as well.

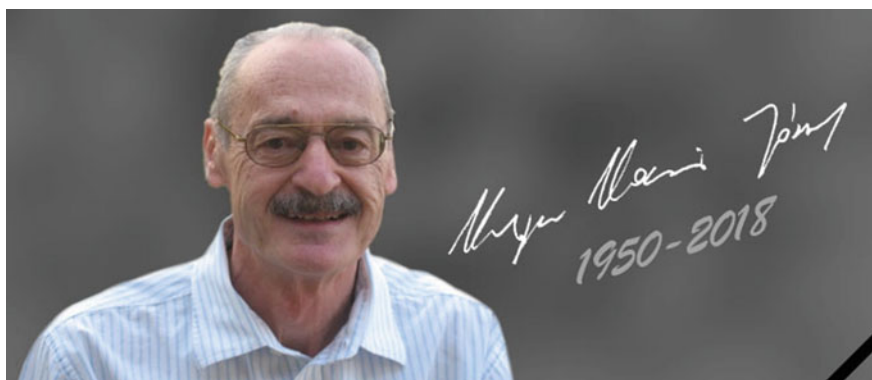
The contributors and editors thank the publishers for granting the copyrights for copyrighted material included in this book. Finally, we would like to dedicate this book to the memory of Prof. József Varga, who taught many of us and was a great scientist and the most important inventor of beta polypropylene.

We expect this handbook to remain an essential first reference book for finding information about PP for the next decade. We hope you will enjoy reading this book and it will help many people to create inventions and come out with new ideas.

Budapest, Hungary
November 2018

József Karger-Kocsis
Tamás Bárány
A.m.D.g.

In Memoriam József Karger-Kocsis



Prof. Dr. h.c. mult. József Karger-Kocsis, Professor of the Department of Polymer Engineering, Faculty of Mechanical Engineering, BME—Honorary Doctor of BME

József Karger-Kocsis, born in 4 March 1950 in Budapest, attended the Benedictine High School of Pannonhalma (Pannonhalmi Bencés Gimnázium), from where he went straight to the Technical University of Budapest, where he graduated as a chemical engineer in 1974. He obtained all levels of doctorate in Hungary between 1977 and 1991. His first job was at the Plastic Industry Research Institute. After this, he became Chief Engineer of the Taurus Rubber Factory. From 1988 to 2009, he worked in Germany, first at the Hamburg University of Technology and then from 1990 at the Technical University of Kaiserslautern. During this period of 20 years, he considered it a very important mission to provide a possibility for Hungarian teachers, researchers, and students to take part in foreign projects and teaching programmes. From 2009, he worked at the Department of Polymer Engineering of the Faculty of Mechanical Engineering at BME and in the MTA–BME Research Group for Composite Science and Technology.

His areas of research included testing; improving the properties and the application of natural and artificial polymers and their composites; developing materials

testing methods; investigating matrix/reinforcement interphase interactions, recycling plastic, and rubber waste; hybrid multifunctional materials and shape-memory and intelligent polymers.

He achieved considerable success in the research of functional or intelligent polymers, investigating shape-memory and self-healing polymers. He developed and patented new kinds of shape-memory polyurethanes. He found that the shape-memory and self-healing functions can be combined if the linear and cross-linked hybrid resins are co-continuous phases, since the thermoplastic (linear) phase is capable of self-healing. He also achieved significant success in making polymers “greener”. In many of his papers, he investigated the curing of functionalized vegetable oils, and the thermal and mechanical properties of the resulting polymer. He pointed out that one obstacle in recycling polymer composites is the difference of the fibre and the matrix, which can be overcome with self-reinforced composites, as these can be recycled with conventional technologies. His team was the first to use fibre Bragg grating optical fibres to measure the curing and the shrinkage of resins used in composites. He successfully improved the toughness of thermoset vinyl ester-based resins. He did pioneering work in investigating the morphology of interpenetrating network thermoset resins.

His work in basic and applied research and innovation was also outstanding, and he was able to unite these areas, which is proved by his 35 patents, his Gábor Dénes Prize awarded in 2014 and the Innovation Prize he received in 2016.

The publication of 4 technical books, 50 chapters, and nearly 500 journal articles and countless invitations as guest lecturer hallmark his career. The quality of his professional work is proved by more than 20,000 citations of his articles, with which he was one of the most cited researchers of Hungary; his h-index is 72. He was Honorary Doctor of several universities, Leader of many international research projects, International Expert, and Member of the editorial team of high-quality journals, who held lectures in English, German, French, Spanish, Italian, and Russian as well. He was an influential and esteemed researcher of his field with many followers in Hungary and abroad. Twenty-three Ph.D. students of him got their Ph.D. degree, and among his students are distinguished professionals, such as company leaders, rectors, deans, and academicians.

József Karger-Kocsis passed away on 13 December 2018. His death is a terrible loss to his family (his wife Mária, his children Anna and Viktor, and his grandchildren and other relatives) and to his friends and academia. His professional heritage is considerable all over the world—we will preserve and continue it.

His students
Prof. Dr. Tibor Czigány, Dean
Dr. Tamás Bárány, Department Head

Contents

1	Tacticity, Regio and Stereoregularity	1
	Giovanni Talarico, Claudio De Rosa and Finizia Auriemma	
2	Solid State Polymorphism of Isotactic and Syndiotactic Polypropylene	37
	Finizia Auriemma, Claudio De Rosa, Anna Malafronte, Miriam Scoti and Rocco Di Girolamo	
3	Polypropylene Nucleation	121
	Flóra Horváth, János Molnár and Alfréd Menyhárd	
4	Crystallization of Polypropylene	185
	Andrzej Pawlak and Andrzej Galeski	
5	Morphology Development and Control	243
	Roberto Pantani, Felice De Santis and Vito Speranza	
6	Polypropylene Copolymers	295
	Markus Gahleitner, Cornelia Tranninger and Petar Doshev	
7	Particulate Filled Polypropylene: Structure and Properties	357
	János Móczó and Béla Pukánszky	
8	Polypropylene Blends: Properties Control by Design	419
	Wen Shyang Chow	
9	Composites	481
	Tatyana Ageyeva, Tamás Bárány and József Karger-Kocsis	
10	Foams	579
	Tobias Standau and Volker Altstädt	

Contributors

Tatyana Ageyeva Department of Polymer Engineering, Faculty of Mechanical Engineering, Budapest University of Technology and Economics, Budapest, Hungary;

Bauman Moscow State Technical University, Moscow, Russia

Volker Altstädt Department of Polymer Engineering, University of Bayreuth, Bayreuth, Germany;

Neue Materialien Bayreuth GmbH, Bayreuth, Germany

Finizia Auriemma Dipartimento di Scienze Chimiche, Università degli Studi di Napoli Federico II, Complesso Monte S'Angelo, Naples, Italy

Tamás Bárány Department of Polymer Engineering, Faculty of Mechanical Engineering, Budapest University of Technology and Economics, Budapest, Hungary

Wen Shyang Chow School of Materials and Mineral Resources Engineering, Universiti Sains Malaysia, Nibong Tebal, Penang, Malaysia

Claudio De Rosa Dipartimento di Scienze Chimiche, Università degli Studi di Napoli Federico II, Complesso Monte S'Angelo, Naples, Italy

Felice De Santis Borealis Polyolefine GmbH, Linz, Austria

Rocco Di Girolamo Dipartimento Di Scienze Chimiche, Università di Napoli Federico II, Complesso Monte Sant'Angelo, Naples, Italy

Petar Doshev Borealis Polyolefine GmbH, Linz, Austria

Markus Gahleitner Borealis Polyolefine GmbH, Linz, Austria

Andrzej Galeski Centre of Molecular and Macromolecular Studies, Polish Academy of Sciences, Lodz, Poland

Flóra Horváth Department of Physical Chemistry and Materials Science, Faculty of Chemical Technology and Biotechnology, Budapest University of Technology and Economics, Budapest, Hungary

József Karger-Kocsis Department of Polymer Engineering, Faculty of Mechanical Engineering, Budapest University of Technology and Economics, Budapest, Hungary

Anna Malafronte Dipartimento Di Scienze Chimiche, Università di Napoli Federico II, Complesso Monte Sant'Angelo, Naples, Italy

Alfréd Menyhárd Department of Physical Chemistry and Materials Science, Faculty of Chemical Technology and Biotechnology, Budapest University of Technology and Economics, Budapest, Hungary

János Móczó Department of Physical Chemistry and Materials Science, Laboratory of Plastics and Rubber Technology, Faculty of Chemical Technology and Biotechnology, Budapest University of Technology and Economics, Budapest, Hungary;
Research Centre for Natural Sciences, Institute of Materials and Environmental Chemistry, Hungarian Academy of Sciences, Budapest, Hungary

János Molnár Department of Physical Chemistry and Materials Science, Faculty of Chemical Technology and Biotechnology, Budapest University of Technology and Economics, Budapest, Hungary

Roberto Pantani Department of Industrial Engineering, University of Salerno, Fisciano, SA, Italy

Andrzej Pawlak Centre of Molecular and Macromolecular Studies, Polish Academy of Sciences, Lodz, Poland

Béla Pukánszky Department of Physical Chemistry and Materials Science, Laboratory of Plastics and Rubber Technology, Faculty of Chemical Technology and Biotechnology, Budapest University of Technology and Economics, Budapest, Hungary;
Research Centre for Natural Sciences, Institute of Materials and Environmental Chemistry, Hungarian Academy of Sciences, Budapest, Hungary

Miriam Scoti Dipartimento Di Scienze Chimiche, Università di Napoli Federico II, Complesso Monte Sant'Angelo, Naples, Italy

Vito Speranza Department of Industrial Engineering, University of Salerno, Fisciano, SA, Italy

Tobias Standau Department of Polymer Engineering, University of Bayreuth, Bayreuth, Germany

Giovanni Talarico Dipartimento di Scienze Chimiche, Università degli Studi di Napoli Federico II, Complesso Monte S'Angelo, Naples, Italy

Cornelia Tranninger Borealis Polyolefine GmbH, Linz, Austria

Chapter 1

Tacticity, Regio and Stereoregularity



Giovanni Talarico, Claudio De Rosa and Finizia Auriemma

Contents

1.1 Introduction.....	1
1.2 Definition and Nomenclature	3
1.3 ¹³ C NMR of Polypropylenes	8
1.4 Steric Defects in PP and Models for Stereocontrol.....	10
1.5 Regio Defects in PP and Models for Regiocontrol.....	17
1.6 Heterogeneous Versus Homogeneous ZN Catalysts	21
1.7 Further Techniques for Polypropylene Tacticity Analysis.....	24
1.8 Polypropylene Microstructures Obtained by Non-metallocene Ligands and by Late Transition Metal.....	26
1.9 Concluding Remarks	28
References	29

Abstract This chapter focus on the polypropylene tacticity. The stereoregularity and regioregularity of the processes catalyzed by heterogeneous and homogeneous Ziegler-Natta catalysts are discussed. The amazing variety of molecular architectures available for polypropylene-based materials are summarized together with the catalytic mechanisms for tacticity control. The main techniques applied for the determination of PP tacticity are reported as well as the outstanding development of new catalyst systems able to achieve unprecedented PP microstructures.

1.1 Introduction

The outstanding performances of polypropylene (PP) market grow continuously and hide the old age of PP which is over sixty. Since the first catalytic synthesis of isotactic polypropylene (iPP) computed in 1954 by using Ziegler catalyst combination

G. Talarico (✉) · C. De Rosa · F. Auriemma
Dipartimento di Scienze Chimiche, Università degli Studi di Napoli Federico II,
Complesso Monte S'Angelo, Via Cintia, 80124 Naples, Italy
e-mail: giovanni.talarico@unina.it

$\text{TiCl}_4/\text{Al}(\text{C}_2\text{H}_5)_3$ and fractionating the resulting polymer to obtain iPP [1, 2], the global demand growth of iPP continues to be led and is expected to increase from 60 million tons in 2015 to 120 million tons by 2030. The Compound Annual Growth rate (CAGR) is estimated of 5.02% for the forecasted period [3], and the PP market is the second largest polymer business in the world (polyethylene, PE, being the first) making up more than 25% of global polymer demand. Several examples have been reported in literature to give the extend of iPP production for the unaware reader: a suggestive comparison has been reported by Severn et al. [4] who estimated that the iPP production for the 2015 corresponds, in volume, to 24 Khufu's great pyramid at Giza, and the estimate for the 2030 correspond to 41 pyramids!

The heterogeneous Ziegler-Natta (ZN) catalysis has been identified as the best catalytic cycle to produce iPP [5] showing ongoing improvements in catalyst performances from first-generation titanium trichloride catalysts used in the manufacturing processes of the late 1960s to the high activity magnesium chloride supported catalysts used today. The latter systems based on MgCl_2 inert support for adsorbing TiCl_4 [6] and modified by internal and external donors (ID and ED, respectively), increased the iPP productivity to more than 100 kg (PP)/g(catalyst) and the isotactic index (I.I., defined as the % in mass of polymer insoluble in boiling heptane) to 98–99% [7]. Despite the catalyst generations, the ZN catalysis maintained the essential feature: a combination of a transition-metal (TM) compound with a coordination vacancy and a base-metal alkyl cocatalyst, (typically an aluminium alkyl) which alkylates the TM, generating a metal-carbon bond.

Although heterogeneous ZN catalysts are synonymous of iPP, it is worth to recall that syndiotactic polypropylene (sPP) was first synthesized by using a TiCl_3 catalyst [8]. However, this sPP was only a small fraction (less than 10%) of crude polymer mixed together with large amounts of isotactic and atactic polymer and showed low crystallinity. The nature of the active sites is not well known and the mechanism of formation of this polymer is still a matter of debate. The sPP was later directly achieved using vanadium triacetylacetonate and aluminum dialkylmonochloride at fixed Al/V ratio and at very low temperatures [9]. Contrarily to the Ti-isospecific systems, these V-catalysts, promote syndiospecific propagation via secondary (2,1-) insertion of the monomer (see next section). The overall stereo- and regioregularity of the polymer is poor, comprising not only syndiotactic blocks resulting from secondary insertions but also short, atactic blocks arising from sequences of primary insertions. An almost complete control of polypropylene microstructure is achieved by using well-defined single-site homogeneous catalysts based on metallocene [10, 11] and non-metallocene [12, 13] complexes. The PP structures going from highly isotactic to highly syndiotactic semicrystalline structures are now available with properties spanning a range from thermoplastic to elastomeric materials.

These amazing results are due to a (very) lucky combination between PP material properties and coordination catalysis based on TM compounds; the tuning of catalyst active sites framework enhances the intrinsic capability of the simple (and low cost) propene prochiral monomer allowing to obtain (all) the desired microstructures. As we are showing in the following sections, this target has been

achieved thanks to a synergistic action of synthetic efforts, detailed mechanistic studies and advanced experimental techniques.

In this chapter we focus on polypropylene tacticity with a special emphasis on the stereoregularity and regioregularity processes; several microstructures will be discussed together with the mechanisms of stereo and regio control and the main techniques used for their determination.

1.2 Definition and Nomenclature

The catalytic cycle of olefin polymerization via the Cossee mechanism [14] is reported in Fig. 1.1 for the simple case of ethene polymerization. The monomer coordination at the available metal coordination site is followed by monomer insertion into the M-C bond via a four-center transition state (TS), possibly stabilized by α -agostic interaction [15–18], leading to the kinetic product. The next ethene insertion is repeating the same path by coordination at the available site previously occupied by the growing polymer chain (chain migratory mechanism). The model is independent of the active specie charge; it can be applied to neutral active species (as the ones postulated on the surface of heterogeneous ZN catalysts, see path a of Fig. 1.1) [19] or the usually cationic metal-alkyl species (as substantiated by discovery of base free cationic 4 metallocene catalysts) [20–22], in equilibrium with the counterion (A^-) (see path b of Fig. 1.1). In the latter case, the counterion reposition at each insertion step is depending on the ion-couple strength [23–26].

The case of ethene polymerization becomes more complicated for a prochiral monomer like propene, that can insert into the M-C bond in four different ways, (see Fig. 1.2). The structures A and B correspond to a 1,2 propene insertion (the incoming propene monomer binds to the metal atom with the C_1 atom and it is often defined as primary insertion) with two different enantiofaces (*re* and *si*, respectively) whereas the structures C and D correspond to a 2,1 propene insertion (or secondary) with the two enantiofaces *re* and *si*, respectively.¹ Considering that the molecular mass of polypropylene of industrial relevance is on the range of 250 kDa (corresponding to roughly 6000 propene insertion) a single macromolecular chain produced without enantioselectivity control (intending both stereoselectivity and regioselectivity) can be formed by 4⁶⁰⁰⁰ diastereoisomers!

Let us focus for a moment on catalytic processes in which the regiochemistry of insertion is 1,2 as in the structures A and B of Fig. 1.2: two propene insertions with the same enantioface (e.g. *re* or *si*) generate a sequence with the same configuration of the stereogenic tertiary carbon atom (marked with * in Fig. 1.3 and R = CH₃), whereas the insertions of alternate enantiofaces (e.g. *re/si*, or *si/re*) shows opposite

¹In this chapter the nomenclature *si*, *re* is used instead of the nomenclature *R*, *S* as suggested in Corradini and Guerra [27].

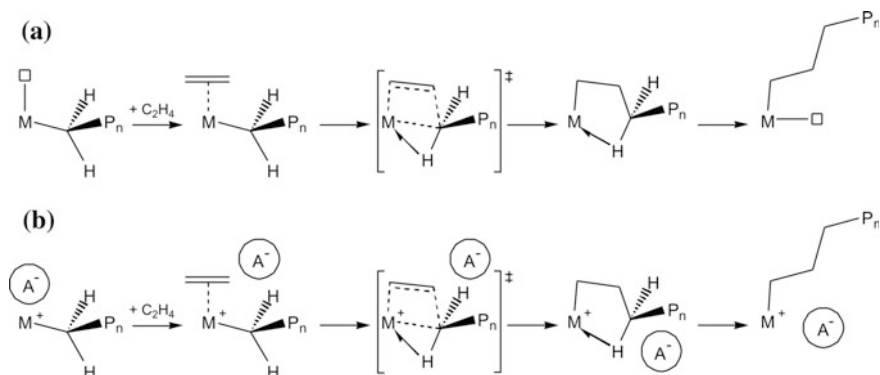


Fig. 1.1 Cossee cycle for **a** neutral and **b** cationic species

Fig. 1.2 Primary or 1,2 (a, b) and secondary or 2,1 (c, d) propene insertions into the M-C bond

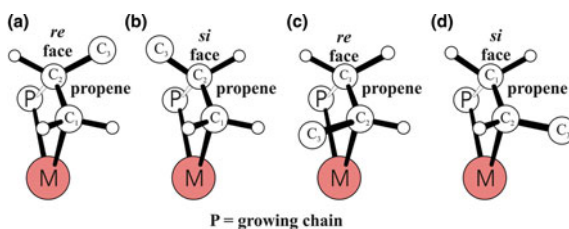
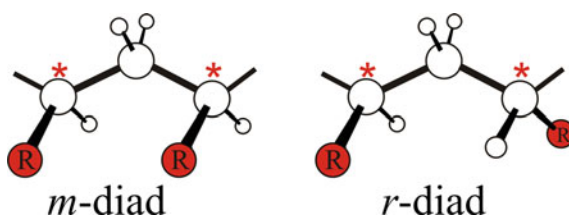


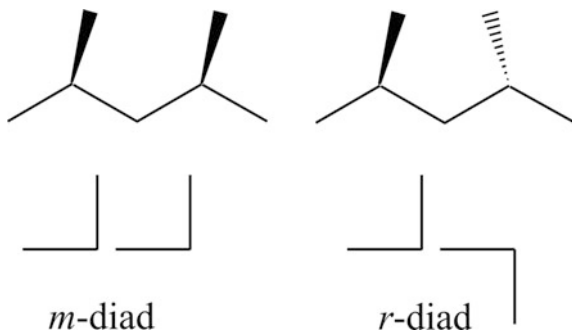
Fig. 1.3 Steric diad formed by propene insertion with the same (*m*-diad) and opposite (*r*-diad) enantioface



configurations (see Fig. 1.3). This is said to constitute a *steric diad* and can be labelled as *meso* (abbreviation, *m*) or *racemo* (abbreviation, *r*), respectively.

The common notation used in the field is a saw-horse representation (see top of Fig. 1.4) or modified Fisher projections (see bottom of Fig. 1.4) using horizontal lines to denote polymer backbone bonds, although this does not give the visual impression of the zigzag chain.

Fig. 1.4 Saw-horse (top) and modified (bottom) Fisher projections for *m* and *r* diads



The polypropylene stereostructures can be described in terms of sequences of steric diads. In fact, the arrangement formed by a succession of *m* diads, is defined as isotactic (see Fig. 1.5a), and a sequence of *r* diads is said to be syndiotactic (Fig. 1.5b). In the iPP, the configurational repeating unit is identical with the configurational base unit whereas in the sPP the configurational repeating unit consists of two configurational base units that are enantiomeric [28]. The lack of configurational order lead to an atactic chain (aPP, see Fig. 1.5c); a partial order formed by even monomeric units with the same configuration and all odd ones having a perfectly random configuration (with a dot line in Fig. 1.5d), is called hemiisotactic (hPP). Hemiisotactic polypropylenes represent a very interesting case in the field of macromolecular stereochemistry. Their typical feature is the coexistence of order and disorder: more precisely, order and disorder alternate along the chain in a well-defined way [29].

The stereosequences reported in Fig. 1.5 correspond to idealized definitions and real polypropylene microstructures are more complicated. The presence of configurational or constitutional defects leads to deviations from ideality and such recommended nomenclature can usefully be applied to the predominant structural features of real polymer molecules. Terms as such as “almost completely isotactic” or “highly syndiotactic”, are commonly used by polymer scientists although such expressions lack the rigor beloved by the purist [28]. The proper “reading” of PP microstructure is a fundamental source of information not only to deduce the structure/properties relationships but also for understanding the polymerization mechanisms of the catalytic species (a sort of a ‘fingerprint’). The typical example is the microstructure achieved with an occasional stereodeflect within the isotactic chain reported in Fig. 1.6.

Following the IUPAC recommendations, we should call both A and B structures of Fig. 1.6 as *predominantly isotactic* being the *m* dyads predominant. The *m* sequences are interrupted by two *r* diads (*rr* = triad) in Fig. 1.6a and by one *r* dyad in Fig. 1.6b. At a glance, these two structures show that the single stereodeflect (reported in red in Fig. 1.6) is originated by two different mechanisms of stereochemical control. The former shows that the insertion error is corrected by another *r* placement immediately after the first *r* dyad, so that the *m* sequences on both sides

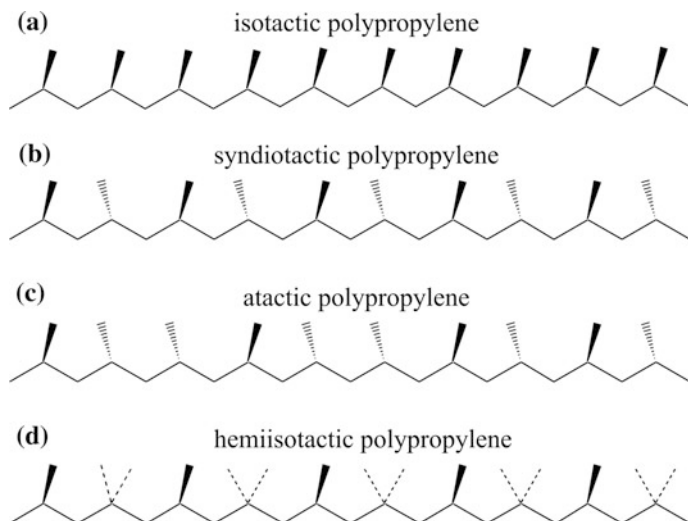


Fig. 1.5 Polypropylene stereostructures available by TM catalysts

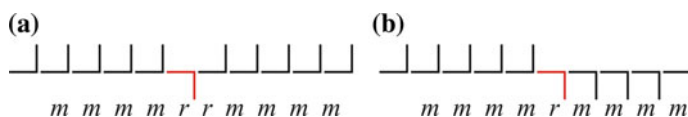


Fig. 1.6 Microstructures of polypropylene synthesized through **a** enantiomorphic site control and **b** chain-end control

of the *rr* placement have the same relative configuration (see Fig. 1.6a). The latter shows that, after a stereochemical insertion, the new configuration is maintained in the propagation until the next insertion error occurs (see Fig. 1.6b).

The first model of stereocontrol is defined as “enantiomorphic site” or chiral site control whereas the second one is defined as “chain-end”, depending on the chirality of the last inserted unit in the polymer chain. Two statistical models based on these mechanisms were developed for the interpretation of the observed stereosequence distributions and are known as enantiomorphic-site model [30] and Bernoullian model [31]. Theoretical explanations for the origin of stereocontrol exerted by these two mechanisms will be reported in Sect. 1.4.

Analogous considerations can be extended to the stereodeflect effect (in red) of predominantly syndiotactic stereosequences reported in Fig. 1.7.

The syndiotactic control is less straightforward than the isotactic one and needs further details (see Sect. 1.4). Nevertheless, we can assume an enantiomorphic-site control for the structure of Fig. 1.7a whereas some cautions need for a clear-cut assumption to the chain-end control for microstructure reported in Fig. 1.7b.

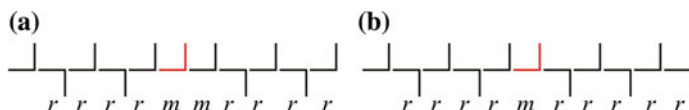


Fig. 1.7 Stereoerror microstructures for propene syndiotactic propagation

The microstructural analysis focused on constitutional defects lead to several microstructures. Heterogeneous ZN catalysts are well known to be highly regioselective in favor of 1,2-insertion of propylene (of the type A and B of Fig. 1.2) and isolated 2,1 enchainment are usually less than 1% [32]. Considering for simplicity an isotactic chain, the isolated 2,1 insertion may produce two different microstructures depending on the inserted enantioface, see Fig. 1.8. We recall that relative configurations at two contiguous carbon atoms in main chains bearing, respectively, substituents a and b ($a \neq b$), are designated by the prefix erythro or threo by analogy with the terminology for carbohydrate systems. The presence of regioinverted unit with vicinal methyls in erythro configuration (see Fig. 1.8) means that the 1,2 and 2,1 propene insertions occur with opposite enantioface (see A and D or B and C structures of Fig. 1.2) whereas the threo configuration indicates that the 1,2 and 2,1 propene insertions occur with the same enantioface, (see A and C or B and D structures of Fig. 1.2), respectively.

As a matter of fact, more complicated microstructures are available from experimental data and further details will be reported in the regiochemistry Sect. 1.5.

Overall, all the microstructures reported in Figs. 1.6, 1.7 and 1.8 can be distinguished by ^{13}C -NMR spectra of polypropylenes because the resonance frequencies observed for chemically equivalent carbon nuclei in the solution ^{13}C NMR spectra of polymers are sensitive to the local conformation of the chain. As the conformation is influenced by the microstructure, the solution ^{13}C NMR resonance frequencies of carbon nuclei in polypropylene are sensitive to the microstructure. The large set of polypropylene microstructures obtained by selecting suitable catalysts (and experimental conditions) is, once again, the powerful demonstration of the microstructural control achieved by coordination catalysis guided by an outstanding knowledge of the catalytic mechanisms.

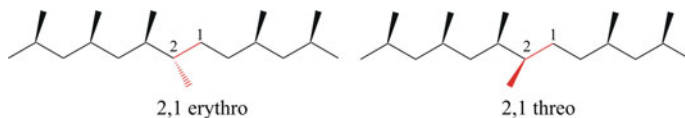


Fig. 1.8 Occasional 2,1 propene insertion in a primary isotactic propagation

1.3 ^{13}C NMR of Polypropylenes

The microstructure of a polymer can best be characterized by nuclear magnetic resonance spectroscopy (NMR) and one-dimensional (1D) proton NMR spectroscopy has made major contributions to the microstructure understanding of synthetic macromolecules. The ^1H NMR spectra of typical iPP and sPP are reported in Fig. 1.9.

However, the elective technique for the tacticity analysis of polypropylene samples is the ^{13}C NMR because of the much greater range of ^{13}C chemical shifts with respect to the ^1H and consequent greater sensitivity to the (local) structural details. The proton NMR spectroscopy is mainly used for the evaluation of chain-end groups [33–35] or for calculating the total branching level of special polypropylenes promoted by late transition metal (LTM) [36].

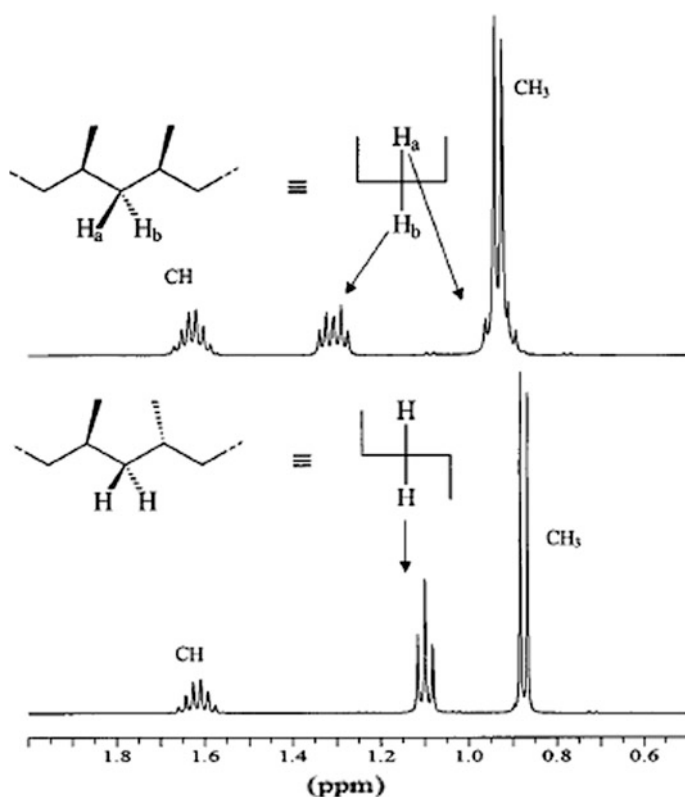


Fig. 1.9 ^1H NMR (400 MHz, $\text{C}_2\text{D}_2\text{Cl}_4$, 120 $^\circ\text{C}$) of iPP (top) and sPP (bottom). Adapted with permission from Ref. [11]. Copyright (2000) American Chemical Society

In Fig. 1.10, the methyl (A), methine (B) and methylene regions of ^{13}C NMR spectra of representative iPP (top), aPP (middle) and sPP (bottom) samples are reported.

The methyl resonance is split in nine major peaks, (see Fig. 1.10a) assigned to these 10 pentads (the *mmrr* and *rmrr* pentads have the same chemical shift) that is: *mmmm*, *mmmr*, *rmnr*, *mmrr*, *mmrm*, *rmrr*, *rmnr*, *rrrr*, *rrrm* and *mrrm* pentads following the numeration of Fig. 1.11.

The nine bands are divided into three distinct regions corresponding to *mm*, *mr* and *rr* centered pentads (see Fig. 1.10a). Sums of the intensities of the three bands in each region correspond to the *mm*, *mr* and *rr* triads and the PP tacticity can be measured by the contents of triads or pentads, such as [*mm*] or [*mmmm*] for iPP and [*rr*] or [*rrrr*] for sPP. The complete assignment of the polypropylene ^{13}C NMR peaks was a difficult task: the successful approach to the assignment was a well-planned synthesis of accurate model compounds and of polymers of known structure or ^{13}C labeled ones [37] combined with the prediction of the chemical shifts by semiempirical [38, 39] and γ -*gauche* effect methods [40–42].

With improvements in sensitivity and resolution of NMR spectrometers, tactic peaks up to heptad/undecad level have been observed in the methyl carbon region of polypropylenes [43, 44]; hexad/decad level for the methylene [44], and pentad/heptad level for the methine resonances [45, 46]. An excellent review on the use of

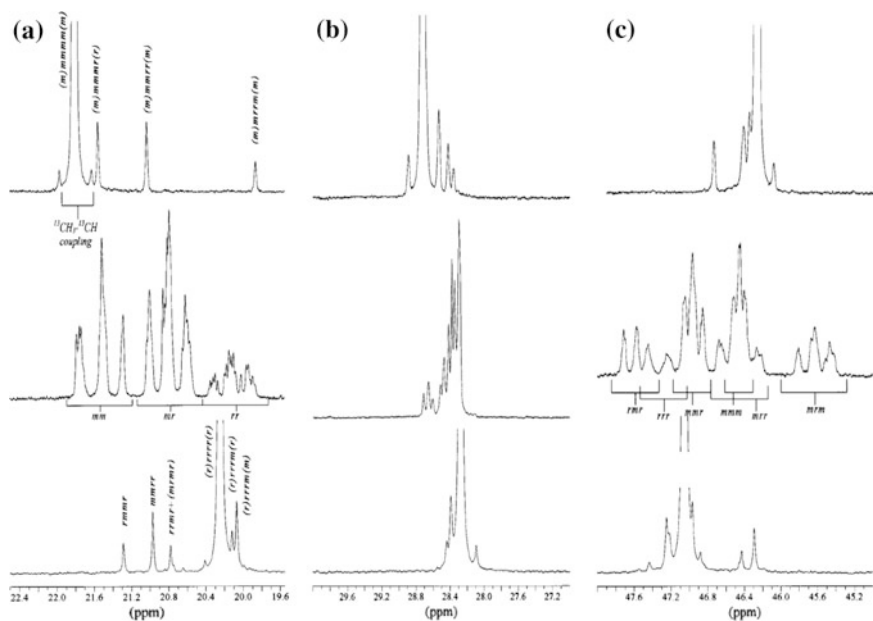


Fig. 1.10 The 100 MHz ^{13}C NMR spectra of iPP (top), aPP (middle), and sPP (bottom) for the methyl (a); methine (b), and methylene (c) regions, respectively. Adapted with permission from Ref. [11]. Copyright (2000) American Chemical Society

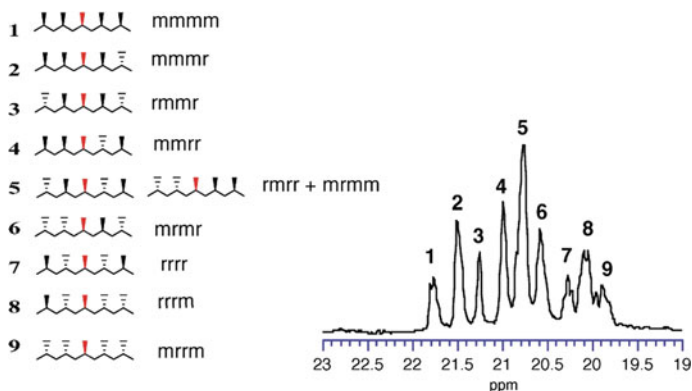


Fig. 1.11 Assignment of the ten pentads available (left) for the methyl region of ^{13}C NMR spectra (right)

high field ^{13}C NMR spectra for the polypropylene microstructure has been published and the reader who is interested in more detail is referred to [47].

In Fig. 1.12 are reported the high-field 150 MHz ^{13}C NMR spectra for the methyl (left) and methylene (right) regions of four model polypropylene samples: two predominantly iPPs (A and B) with a microstructure-type reported in Fig. 1.6 (A and B); one sPP (C) and one hPP (D). The combination of model compounds prepared with suitable homogeneous catalysts and more refined statistical models allowed a full assignment of spectra like those of Fig. 1.12 [44, 46, 48] with the chemical shift of all peaks. The general protocol for the interpretation of high-field ^{13}C NMR polypropylene spectra has been proposed [44] and insights in several complicated mechanisms of stereocontrol have been obtained [49–52] with a special emphasis on the heterogeneous ZN catalysis [53, 54].

1.4 Steric Defects in PP and Models for Stereocontrol

The assignment of methyl resonances in the ^{13}C NMR spectra allowed the identification of predominant...*mmmmrrmmmm*...-type stereodefects (see Fig. 1.6a) in iPP produced by heterogeneous and homogeneous ZN catalysts. The intensity ratio of the peaks [*mmmr*]:[*mmrr*]:[*mrrm*] = 2:2:1 (Fig. 1.13, top), is in agreement with the enantiomorphic-sites model, which is the more effective control to obtain highly isotactic polypropylenes. A lower isotacticity value is reported for the chain-end control (see Fig. 1.6b) obtained with achiral homogeneous systems at very low polymerization temperature and showing a peak ratio [*mmmr*]:[*mmrm*] = 1:1 (Fig. 1.13, bottom) [55].

The origin of enantiomorphic site control which explain the ^{13}C NMR spectra of Fig. 1.13 (top) was firstly rationalized by Corradini and co-workers by considering nonbonded interactions in the TS of propene insertion for a model of heterogeneous

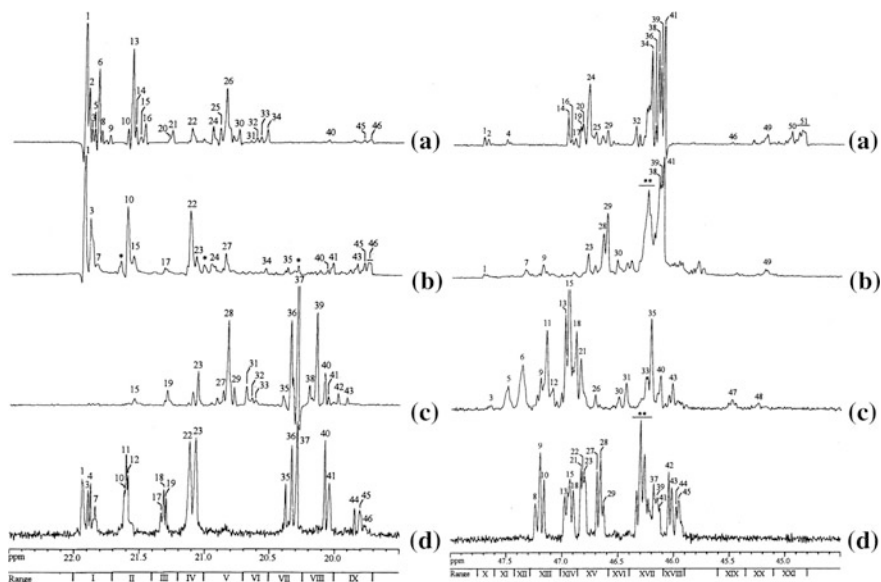
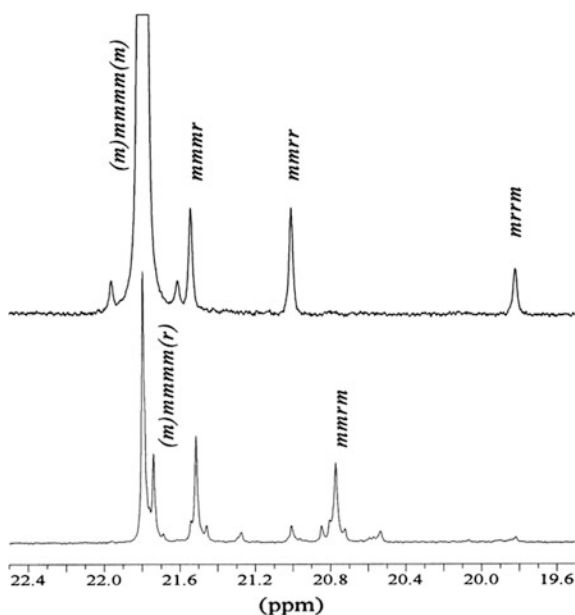


Fig. 1.12 Methyl (left) and methylene (right) regions of the 150 MHz ^{13}C NMR spectra of the four model polypropylene samples **a–d** reported in the text (dissolved in 1,1,2,2-tetrachloroethane- d_2 at 70 °C); δ scale is in ppm downfield of TMS. For peak assignments, see Tables 1–4 reported in Ref. [44]. Adapted with permission from Ref. [44]. Copyright (1997) American Chemical Society

Fig. 1.13 Methyl region of ^{13}C NMR spectra (100 MHz, $\text{C}_2\text{D}_2\text{Cl}_4$, 120 °C, Ref. *mmmm* at 21.8 ppm) of two iPP samples prepared under enantiomorph-site control (top) and chain-end control (bottom). Adapted with permission from Ref. [11]. Copyright (2000) American Chemical Society



ZN active sites [56–58]. The propene enantioface selection (e.g. *re* preferred to *si* in Fig. 1.14a, b) is dictated by the chirality of active site (e.g. Δ site for octahedral specie in Fig. 1.14 top) which induce a chiral orientation of the growing polymer chain (to avoid steric contact with the ligand framework marked with * in Fig. 1.14b). The oriented growing chain selects the propene enantioface with the methyl group in *anti* to the first C_{α} -C of the chain to avoid the steric chain-monomer contacts. The same model well explain the isotactic propagation promoted by C_2 -symmetric *ansa*-metallocene as estimated by computational methods based on the density functional theory (DFT): in fact, looking at the TS geometries for a

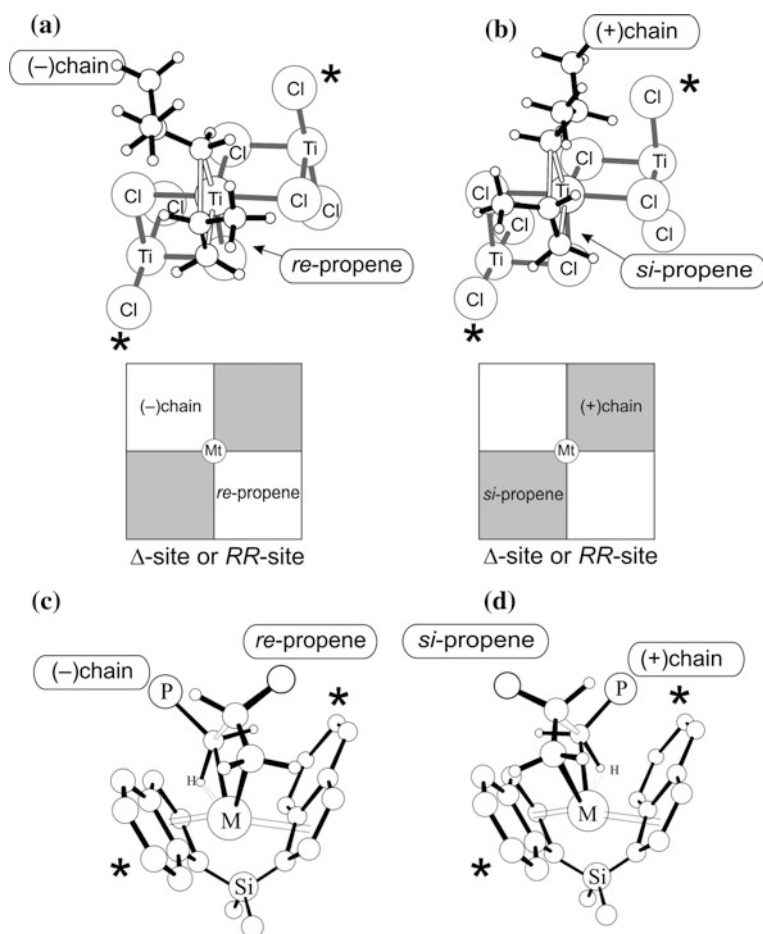


Fig. 1.14 Top: optimized geometries TSs obtained by DFT methods of 1,2 propylene insertion for a C_2 -symmetric octahedral Ti model site with Δ configuration (a) and for stereocenters coming from chain misorientation (b). Bottom: a similar representation is reported for a prototypical C_2 -symmetric *ansa*-metallocene with the *RR* configuration. Middle: the quadrant representation is showing the analogy between these two C_2 -symmetric species

prototypical tetrahedral *ansa*-metallocene (see Fig. 1.14 bottom) the lower energetic TS for the structure C with respect to D (which lead to a stereoerror) is due to the right chiral configuration of the growing polymer chain. The role played by the chlorine atoms on heterogeneous surface and the homogeneous ancillary ligand in orienting the growing polymer chain is substantially similar.

The similar origin of isotactic stereoselectivity promoted by heterogeneous and homogeneous systems emerges clearly by using the appropriate quadrant representation (see Fig. 1.14 middle), where the gray quadrants correspond to relatively crowded zones occupied by Cl atoms on top and indenyl ligands on the bottom.

The quadrant representation is a good tool to rationalize the relationship between complex symmetry and polypropylene tacticity. In fact, homogeneous single-site polymerization catalysts can be divided into five symmetry categories reported in Fig. 1.15. The aPP is usually produced by C_{2v} - or C_s -symmetric catalysts that have mirror planes containing the two diastereotopic coordination sites with the same behavior (deviation from ideal aPP may be generated by a chain-end control mechanisms). The sPP is produced by C_s -symmetric catalysts with a mirror plane reflecting the two enantiotopic coordination sites and iPP is produced by C_2 -symmetric complexes. More complicated PP architectures can be realized with C_1 -asymmetric complexes with diastereotopic coordination sites, ranging from highly to weakly isotactic [59], including isotactic-atactic stereoblock [60] and hemiisotactic [61].

An interesting application of such rules was published by Coates and Waymouth who reported the synthesis of elastomeric PP by using unbridged bis(indenyl) zirconium dichloride bearing bulky phenyl substituents in 2-position of the indenyl moiety. The PP microstructure is formed by isotactic-atactic stereoblocks attributed to changes in the catalyst stereoselectivity during the propagation reaction as schematized in Fig. 1.16.

The syndiospecificity promoted by the typical C_s -symmetric catalyst [62] reported in Fig. 1.17 was indeed the first definitive experimental evidence that Cossee's chain migratory insertion (see Fig. 1.1) was operative. The polymer configurational microstructure is consistent with enantiomorph-site control, with

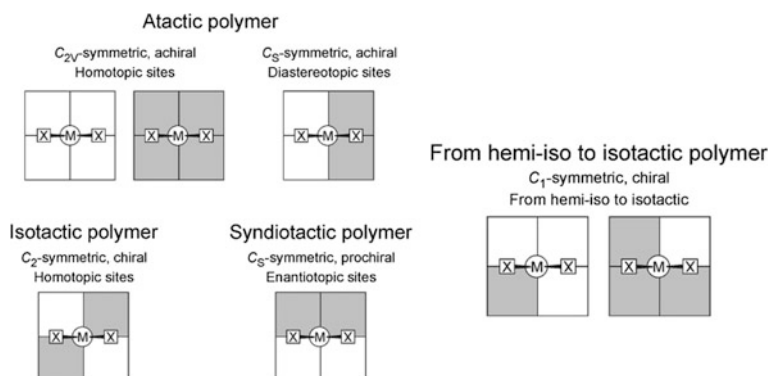


Fig. 1.15 Relationships between catalyst symmetries and polypropylene microstructures achieved

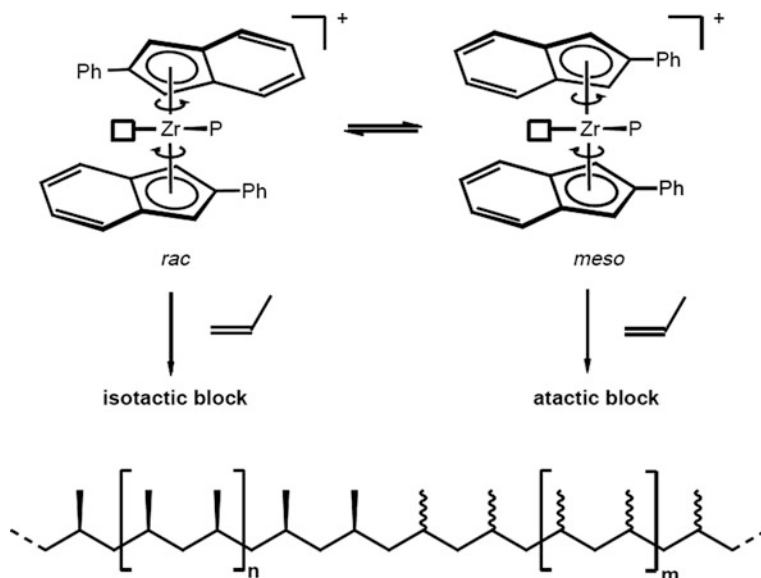


Fig. 1.16 Proposed mechanism for the formation of isotactic-atactic block PP by oscillating catalysts [60]

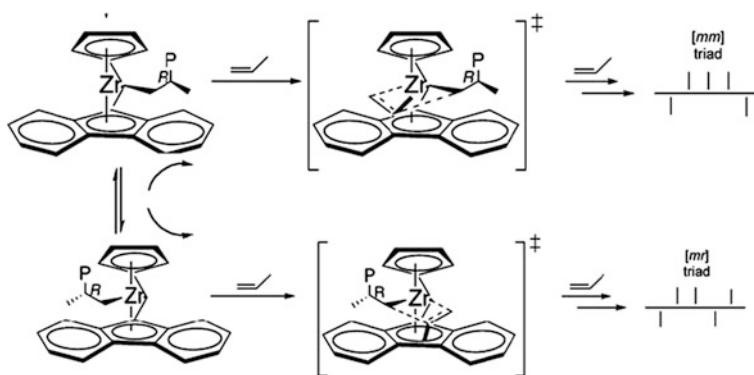


Fig. 1.17 Mechanisms for the formation of stereodefects generated by the entiofacial misinsertion (top) and by the site epimerization (SE) (bottom), and their corresponding signature pentad distributions

the active sites isomerizing at each monomer addition. The entiofacial misinsertion generates the stereodefect with the microstructure of Fig. 1.7a and visualized in Fig. 1.17, top. Occasional skipped insertion of the growing chain before the monomer insertion (often called site epimerization, SE) may also occur, generating instead stereosequences as reported in Fig. 1.17, bottom.

The experimental evidence that the SE error of C_s -ansa metallocene catalyst generates a m -type stereodefects (see Fig. 1.17, bottom) resembling that of a syndiotactic propagation by chain-end control (see Fig. 1.7b) may induce some confusions on the identification of the right polymerization mechanism. In such cases, the way-out is to examine polypropylene samples prepared in the same experimental conditions but at different propene concentrations ($[C_3H_6]$); in fact, the concentration of m defects is expected to increase with decreasing $[C_3H_6]$ under enantiotopic-sites control (see Fig. 1.17, bottom), whereas it is expected to be independent of monomer concentration, in the case of chain-end control.

Finally, remarkable counterion and solvent polarity effects on the stereochemistry of syndiotactic propagation by C_s -ansa metallocene have been probed [63]. The ion pairing selection can strongly modulate the relative rates of syndiotactic enchainment versus $[m]$, with a marginal effect on $[mm]$, which is basically dependent by the catalyst ligand framework. The results are summarized in Fig. 1.18.

As a matter of fact, sPP of high stereoregularity containing only m -type of stereodefects have been prepared also with C_2 -symmetric bis(phenoxyimine)Ti catalysts [64, 65] (see Fig. 1.19).

The formation of sPP by using a C_2 -symmetric catalyst was rather unexpected because of the symmetry rules reported in Fig. 1.15. However, it has been proved by ^{13}C NMR analysis (see Fig. 1.20, top) that these octahedral non-metallocene systems afford highly syndiotactic propagation through 2,1 monomer insertion [66–68] differently from the common 1,2 propagation promoted by C_s -metallocenes (see Fig. 1.20, bottom).

The mechanism for the syndio-selectivity of C_2 -octahedral bis(phenoxyimine)Ti complex is not trivial and resembling the one proposed on homogeneous vanadium-based catalytic systems [69]. The secondary chiral growing chain was pivoted to explain the origin of stereoselectivity by dictating the configuration of the fluxional active sites (Δ and Λ), which, in turn, selects the monomer enantiofaces (see Fig. 1.21, reported from Ref. [70]).

These experimental facts highlighted three conclusions: (a) the regiochemistry is an important aspect in particular for PP microstructures revealed by non-metallocene

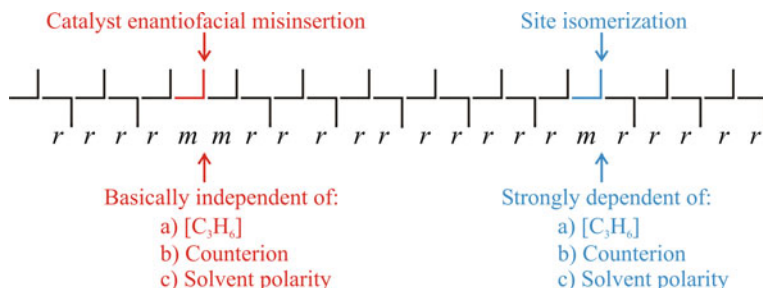


Fig. 1.18 Stereoerrors for syndiotactic propagation due to the enantioface misinsertion and site isomerization

Fig. 1.19 Methyl region of ^{13}C NMR spectra of sPP sample synthesized by C_2 -octahedral bis(phenoxyimine)Ti system shown in the inset at 0°C . Only the *m*-type of stereodeflect is detected [64]

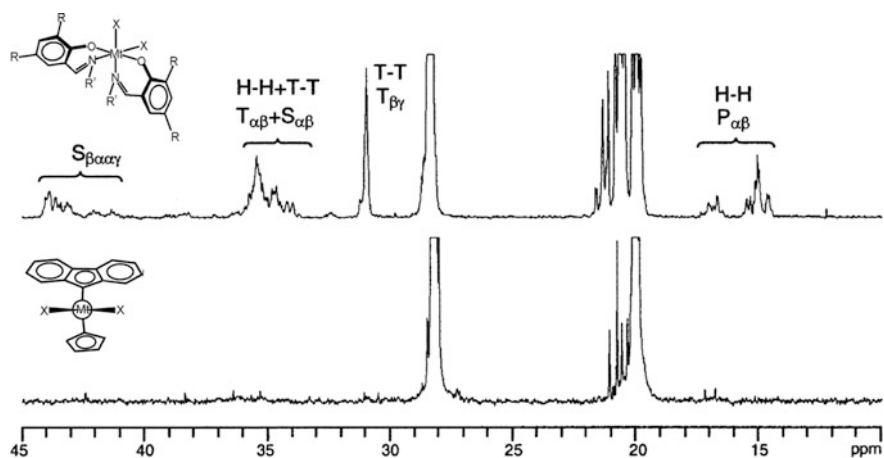
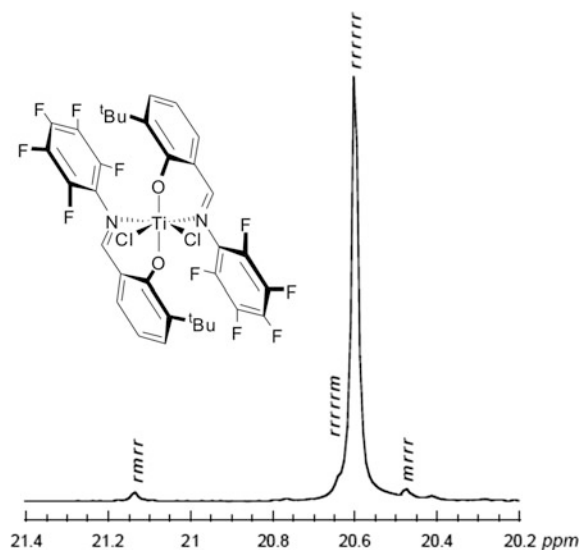
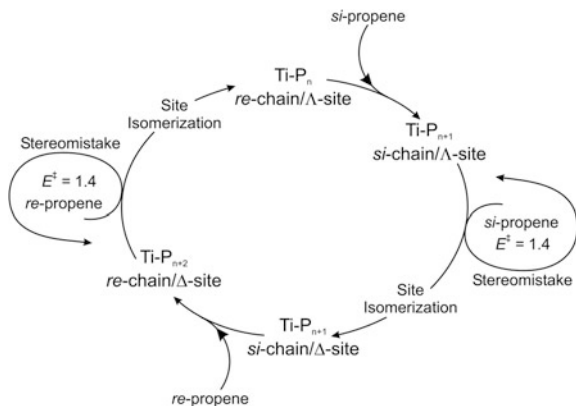


Fig. 1.20 ^{13}C NMR spectra of sPPs obtained by a non-metallocene C_2 -octahedral bis(phenoxyimine)Ti complex (top) and by C_5 -metallocene complex (bottom) [67]. The 13–18 and 30–45 ppm regions are attributable to regioirregular units (H = head = CHCH_3 moiety; T = tail = CH_2 moiety)

Fig. 1.21 Mechanism for syndiotactic propagation of octahedral bis(phenoxymine) Ti complex. Adapted with permission from Ref. [70]. Copyright (2004) American Chemical Society



systems (see Sect. 1.5); (b) the impressive development of homogeneous single-site metallocene-based created a large variety of PP microstructure building a consistent dataset to analyze the microstructure/property relationships; (c) the discovery, after the first half of the 1990s, of new generation of non-metallocene catalysts based on Group 4 and LTM enlarged the database of PP microstructure available [12, 13, 71].

1.5 Regio Defects in PP and Models for Regiocontrol

The regiochemistry of propene insertion at heterogeneous ZN catalyst was considered for a long time a minor topic because of the high 1,2 regioselectivity showed by the catalyst. The amount of occasional 2,1 insertion in the iPP chain was so low that needed of special copolymerization techniques with ethene-1-¹³C/propene to be detected by ¹³C NMR characterization [32, 72]. Isospecific C₂-metallocene catalysts show a generally lower regioselectivity compared to heterogeneous Ziegler-Natta catalysts: indeed, isolated secondary propene units are often detectable in iPP samples (in a typical range of 0.2–1 mol%) combined with (3,1 units), arising from the unimolecular isomerization of the secondary unit (see Fig. 1.22).

Compared to the C₂-symmetric catalysts, the C_s symmetric ones (see Fig. 1.17) are known to be more regioselective because no regioirregular enchainments are normally detected by ¹³C NMR in highly syndiotactic polypropylene samples. Because of the remarkable effects that the regiodeflects have in the lowering crystallinity and melting point of semicrystalline PP and in the mechanical properties [73, 74] we will discuss them briefly.

A secondary propene insertion in the isotactic propagation can, in principle, generate up to four different regiodeflect microstructures (see Fig. 1.23) excluding the isomerization to the 3,1 unit (see Fig. 1.22); two structures come from the (two) enantiofaces of 2,1 inserted unit (see Fig. 1.8) and the other two depend of the absolute configuration of the methyl groups *after* the 2,1 inserted unit (see Fig. 1.23). The conflicting reports in the literature regarding the assignments of the carbon NMR spectrum as well as the stereochemistry of these regio-errors have

Fig. 1.22 Microstructures generated by a propene 2,1 inserted unit

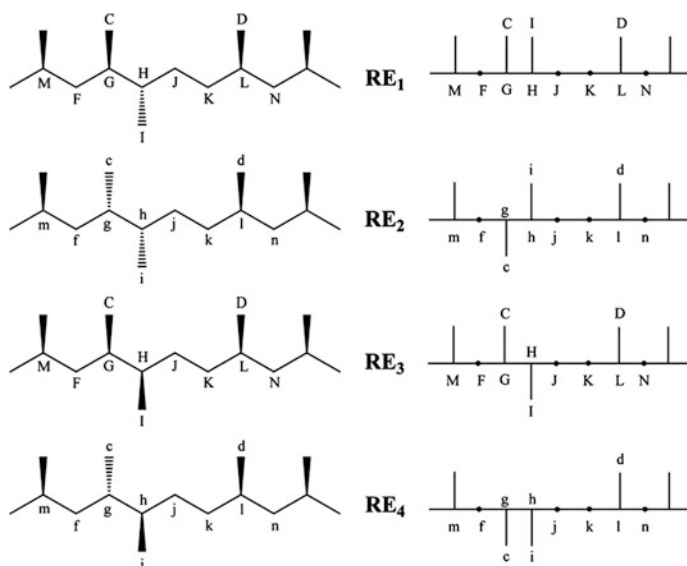
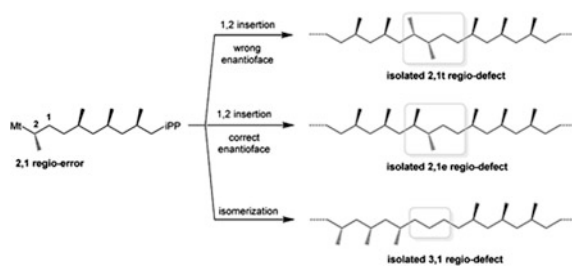


Fig. 1.23 3D structures and Fischer projections of 2,1-insertion regioerrors in iPP. Adapted with permission from Ref. [75]. Copyright (2009) American Chemical Society

been only recently solved by using a high-temperature cryoprobe ¹³C NMR with much better signal/noise and 2D inadequate [75].

Several experimental and theoretical studies focused on the regiochemistry promoted by *ansa*-metallocene catalysts (for all five symmetry categories reported in Fig. 1.15) leading to the conclusion that the 2,1 insertion is highly

enantioselective for C_2 , C_s and C_1 symmetry catalysts (in the last case depending of the catalyst framework), and non-enantioselective for the C_{2v} species. In particular, the 2,1 inserted unit shows the *opposite* enantioface with respect to the 1,2 selected by C_2 and C_1 -isospecific site, and the *same* enantioface by C_s -syndiospecific catalyst, respectively. Finally, the 1,2 following the 2,1 insertion occurs with a lower stereoselectivity.

These finding can be easily visualized in Fig. 1.24 looking the lower energetic TS structures for the preferred 1,2 and 2,1 insertions obtained by DFT calculations for the C_2 and C_s *ansa*-metallocene systems, which confirm the above statements.

DFT calculations explained also that, at the opposite of tetrahedral *ansa*-metallocenes, the non-metallocene systems reported in Fig. 1.19, may be easily targeted by electronic factors in a way to modify the ratio between 1,2 and 2,1 insertion [68, 76] so producing the *blocky* structure as the one reported in Fig. 1.25 and detected by ^{13}C NMR spectra of Fig. 1.20 top.

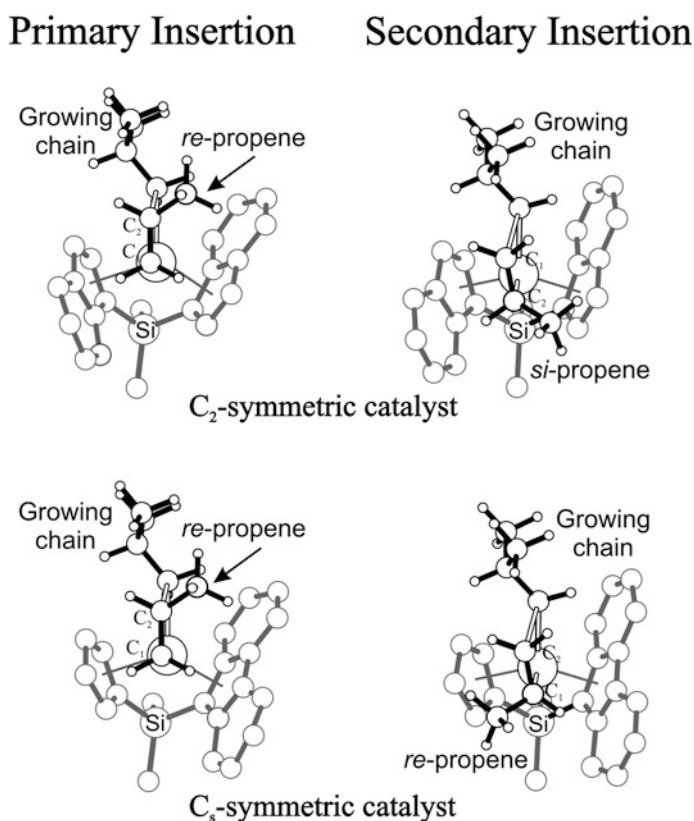


Fig. 1.24 DFT calculated TSs for the preferred 1,2 and 2,1 propene insertions promoted by C_2 (top) and C_s (bottom)-symmetric *ansa*-metallocene species [76]

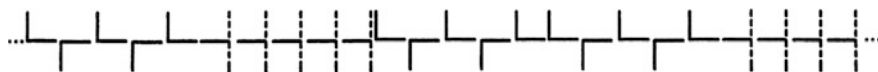


Fig. 1.25 Blocky microstructure of 2,1 and 1,2 propene insertions obtained with non-metallocene systems

The fine tuning of metallocene systems allowed also the synthesis of new complexes able to promote a highly enantioselective 1,2 insertion *after* the regio-error so obtaining the well-defined microstructure reported in Fig. 1.26. In this way iPP samples with a tailored amount of isolated regiodefects coupled to the absence of *mrrm* or any other chain defect have been prepared. This provides an ideal set of samples for structure–property correlations studies on the effect of such regiodefects on iPP properties [77].

At the same time, the development of new class of non-metallocene catalyst based on pyridyl-amino ligands (see Fig. 1.27, top) enlarged the iPP microstructures set and iPPs of very high stereoregularity with detectable amount of selected 2,1 three regiodefects are now available (see Fig. 1.27) [78].

The development of new non-metallocene well illustrates the enormous potential of tuning the catalytic properties of different metal centers by their well-defined ligand environment to obtain new and targeted microstructures often by new mechanisms of stereo and regiocontrol [79, 80].

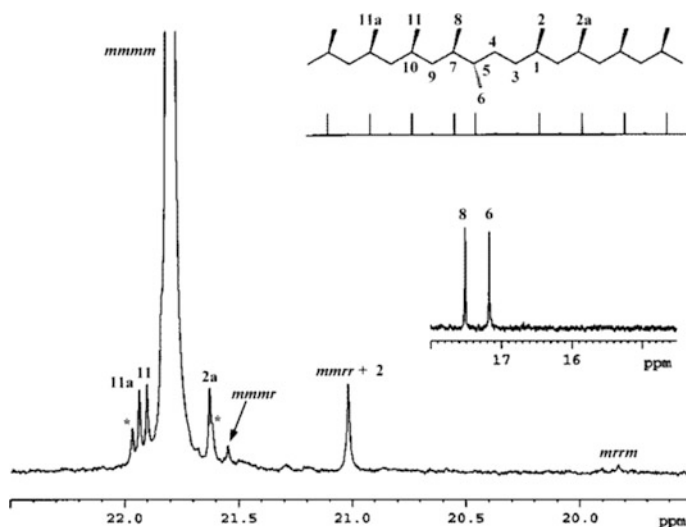


Fig. 1.26 Methyl region of the ^{13}C NMR spectrum of iPP sample produced by a highly stereoselective and not fully regioselective *ansa*-metallocene catalyst, showing the peaks related to 2,1 erythro regiodefects (see Fig. 1.8) and signals corresponding to pentad stereosequences. Adapted with permission from Ref. [73]. Copyright (2005) American Chemical Society

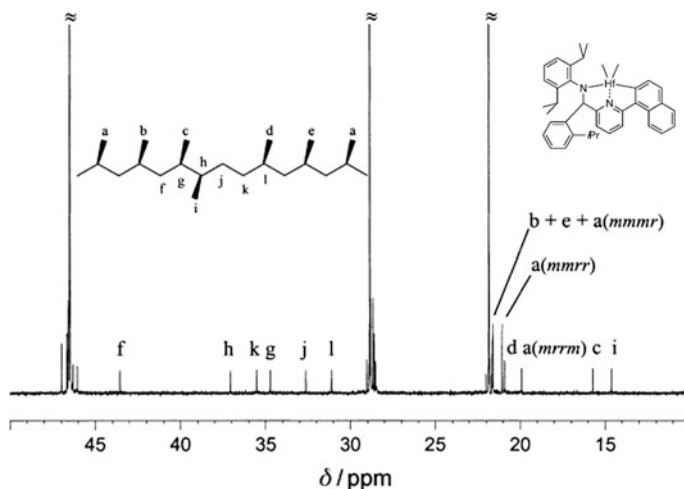


Fig. 1.27 ^{13}C NMR spectrum (100 MHz, $(\text{CDCl}_2)_2$, 120 °C; δ scale relative to tetramethylsilane at $\delta = 0$ ppm) of the polypropylene sample obtained with a non-metallocene catalyst shown in the inset. The main peaks of the iPP are out of scale. Adapted from Ref. [78]

1.6 Heterogeneous Versus Homogeneous ZN Catalysts

The single-site homogeneous catalysts which exhibit more defined microstructures gave a great contribution to the basic understanding of mechanisms and microstructure/property relationship for the PP. However, the large part of industrial iPP production is still demanded to the state-of-art heterogeneous catalysts although it is remarkable the growing market for single-site polyolefins with targeted microstructures and controlled molecular weight distributions, especially in gas-phase and slurry-phase polymerization. The superior performances by iPP of heterogeneous (iPP-ZN) with respect to his homogeneous counterpart (iPP-homo) is certainly due to the increased efficiency of the catalyst and the morphology control of the polymer granule, which reduces the reactor fouling [81]. However, the plot reported in Fig. 1.28 highlights some differences in polymer properties; the melting point achieved by iPP-ZN is usually higher than that of the analogous iPP-homo with the same average degree of isotacticity (measured as *mmmm*%).

Significant advances have been made in understanding the fundamental factors determining the performance of multisite MgCl_2 -supported catalysts. Studies by Busico and co-workers [53, 54, 82] have shown that the chain irregularities in iPP-ZN are not randomly distributed along the chain but are clustered. The chain can therefore contain, in addition to highly isotactic blocks, sequences that can be attributed to less isotactic (isotactoid) and/or to slightly syndiotactic (syndiotactoid) blocks (a schematic example is reported in Fig. 1.29).

It has been suggested that the active site can isomerize very rapidly (during the growth time of a single polymer chain, i.e. in less than a second) between three

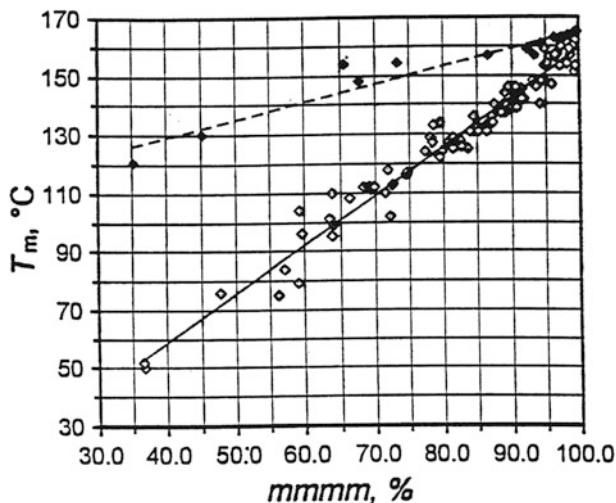


Fig. 1.28 Correlation between % of *mmmm* pentad and DSC melting temperature (T_m ; 2nd heating scan) for (predominantly) isotactic polypropylenes. (open diamond) = samples made with metallocene catalysts (from Ref. [11]); (filled diamond) fractions obtained by temperature rising elution fractionation of samples made with heterogeneous Ziegler-Natta catalysts. Adapted from Ref. [47]. Copyright (2001) with permission of Elsevier

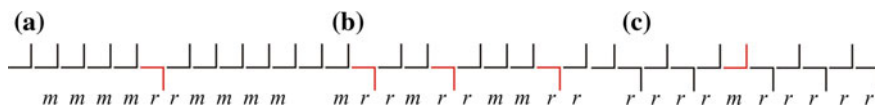


Fig. 1.29 Schematic example of polypropylene microstructure formed by highly isotactic, isotactoid and syndiotactic stereosequences chemically linked

different propagating species. The polymer can therefore be considered to have a stereoblock structure in which highly isotactic sequences alternate with defective isotactoid and/or with syndiotactoid sequences. A mechanistic model (see Fig. 1.30) has been formulated in which the relative contributions of these sequences can be related to site transformations involving the presence or absence of steric hindrance (reported with L1 and L2 in Fig. 1.30) in the vicinity of the active species [53].

Based on these mechanistic assumptions, the various fractions of iPP obtained by fractionation with boiling solvent (e.g. from the diethyl-ether to n-heptane) are characterized by differences in the relative amounts and lengths of these three building blocks. So, the iPP-ZN having *on average* the same % content of steric defects of iPP-homo, will show a higher melting point (see Fig. 1.28) due to longer sequences of chain without defects, as the defects are segregated in the less

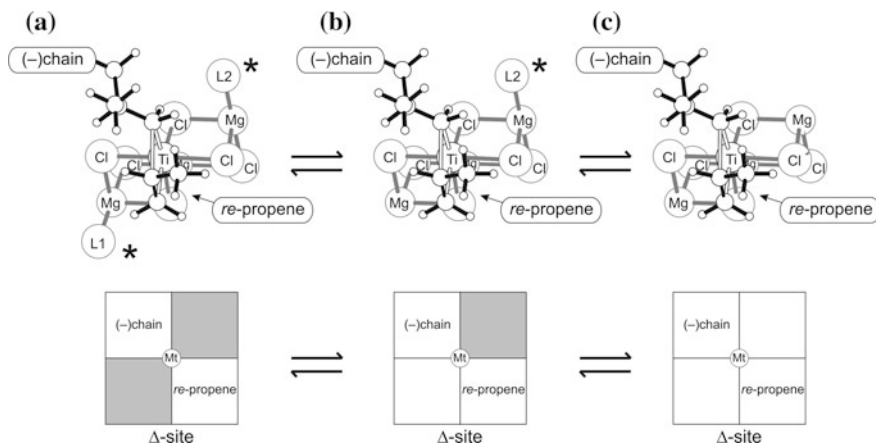


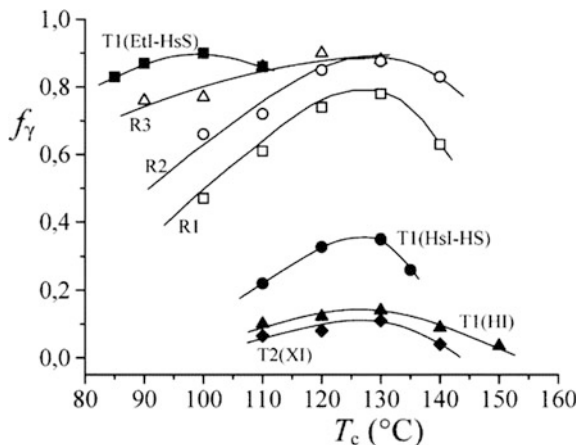
Fig. 1.30 Interconverting three-site model used to explain the stereoblock structures of iPP obtained by ZN heterogeneous catalysts: the site **a** is producing highly isotactic, **b** the isotactoid and **c** the syndiotactic microstructures, respectively. Adapted from Ref. [19]. Copyright (2018) with permission of Elsevier

stereoregular part of the chain. A clear-cut confirmation of these assumptions has been obtained by studying the crystallization behavior of iPPs, because the chain microstructure and the distribution of defects along the polymer strongly influence the polymorphic behavior and, in particular the relative amount of γ form with respect to the α forms (here defined as f_γ). Long regular isotactic sequences of iPP generally crystallize in the α form whereas short isotactic sequences crystallize in the γ form [83, 84]. The amount of γ form developed in the melt-crystallization procedures of model compounds of stereoblock polypropylene samples prepared with the oscillating metallocene catalysts of Fig. 1.16, is much lower than that obtained for iPP-homo samples having the same overall concentration of defects [85]. This suggests that in the stereoblock polypropylene most of the defects are segregated in stereoirregular, noncrystallizable blocks, which alternate to more regular isotactic sequences, long enough to crystallize in the α form. Accordingly, the fact that iPP-ZN largely crystallize in the α form (see Fig. 1.31) as compared to the much higher f_γ value of iPP-homo samples confirms that Ziegler–Natta polypropylenes contain long, almost ideally isotactic sequences along with isotactoid sequences which are practically unable to crystallize [86].

The non-random defects distribution has been verified also on iPP samples produced by heterogeneous systems based on Al_2O_3 -supported tetraalkyl zirconium catalyst and seems to be related to fast equilibria of the active site modifications on heterogeneous surface [87].

A last remark on the iPP-ZN and iPP-homo differences concerns the number average molecular weight (M_n) and the weight average molecular weight (M_w). The ratio M_w/M_n is called the polydispersity index (PDI) and is an indication of the broadness of molecular weight distribution (MWD). As polydispersity index

Fig. 1.31 Comparison between the relative contents of γ form of iPP, f_γ , as a function of the crystallization temperature T_c for metallocene-made iPP samples and Ziegler-Natta samples T1 and T2 fractionated with boiling solvent, isothermally crystallized from the melt. Adapted with permission from Ref. [86]. Copyright (2004) American Chemical Society



increases, MWD broadens and PDI range from 4–8 for iPP-ZN (typical for multi-site catalysts) whereas iPP-homo show PDI of 2–3 indicating a much narrower MWD (typical of a single-site catalyst).

1.7 Further Techniques for Polypropylene Tacticity Analysis

A large part of the PP tacticity discussion of previous sections was based on ^{13}C NMR analysis. As a matter of fact, there are several experimental techniques whose applications (very often in combination with other techniques) furnish important insights particularly on the microstructure/property relationships. The vibrational spectroscopy is one of the most versatile methods of polymer characterization and Infrared (IR) and Raman spectroscopy probe the vibrational spectrum by absorption and inelastic scattering, respectively. In many cases these two techniques are complementary and can be utilized for determining of the configuration, tacticity and conformation of polymer chains [88]. The great advantage of IR and Raman techniques compared with ^{13}C NMR, analysis is that they are much less time consuming and simpler to perform; IR, indeed, was the first techniques to be used for characterizing the crystallinity of iPP together with the fractionation with boiling solvent [1]. These techniques investigate the crystalline bands (associated with the intermolecular forces occurring between atoms and molecules within the crystalline lattice) and the regularity of helical bands (or regularity bands assigned to intramolecular vibrations within a given chain). As a matter of fact, these methods measure parameters relating to the crystallinity or conformational arrangement of the polypropylene macromolecules and not tacticity itself. For a fast application of the absorption bands at polypropylene samples, the ^{13}C NMR has been used as a calibration method.

For iPP, regularity bands are located below 1400 cm^{-1} and are connected to different values of the number n , which describes the minimum number of monomers linked in an isotactic sequence that defines a helical structure. The IR spectral bands at 1168 , 998 , 973 and 841 cm^{-1} are related to the formation of regular isotactic helices. The most widely used bands for calibrating the isotacticity (or crystallinity) are the ones at 998 and 841 cm^{-1} . In literature has been reported that they correspond to sequence lengths of 11–12 and 13–14 consecutive repeat units in crystalline, or mesomorphic regions [88]. The band at 973 cm^{-1} , corresponding to five units, can be attributed to both crystalline and amorphous chains in helical conformations and is often used as an internal reference [89]. The connection between these band absorptions and the temperature/crystallinity has been recently demonstrated [89]. The calculation of the A_{998}/A_{973} ratio from the scanned spectra is straightforward and absorbance ratios A_{998}/A_{973} and A_{841}/A_{973} were used as IR stereoregularity parameters of polypropylene [90, 91]. A similar correlation has been found also for sPP; however, the picture is complicated by the fact that semicrystalline sPP samples shows at least three different regular conformations (structural details for this polymer are deeply discussed in the Chap. 2). These regular conformations are all different from the ones in iPP, which makes easy to distinguish between iPP and sPP by IR spectra. The two most common regular sPP conformations, the 2/1helix ((TTGG) $_n$, where T and G stand for gauche and trans conformation of the backbone torsion angles) and the planar zig-zag, can be identified by characteristic bands at 977 and 962 cm^{-1} , respectively. A band at 867 cm^{-1} exists for both conformations and is often used to assess a syndiotacticity index [92] in various combinations. The stereoregularity effects on syndiotactic polypropylene structure have been reviewed by Sevegney et al. [93]. For the characteristics above summarized, the IR spectroscopy is highly recommended for determining the orientation of polypropylene films.

Together with vibrational spectroscopy, the fractionation techniques share the peculiarity to be the oldest methods to be used for understanding the PP tacticity. In the seminal work on the iPP synthesis by Natta was recognized that semicrystalline iPP was insoluble in organic solvents compared to atactic polymer [1].

The most common fractionation technique for iPP samples is based on Soxhlet apparatus where the polymer sample is extracted by using solvents with different boiling points [94]. The heptane is generally accepted as the solvent of choice leading to the standard definition of I.I. Complementary to the I.I, which is an extraction technique, is the xylene insoluble test (XI) which measure the mass of polymer insoluble in xylene after dissolution of the sample and recrystallization. The PP sample is dissolved in hot xylene ($135\text{ }^\circ\text{C}$), and by cooling slowly the isotactic fraction can be recrystallized, leaving atactic polymer in solution. Although I.I and XI values are often considered similar, the xylene crystallization is a somewhat more accurate measure of atactic polymer than heptane extractables, because the latter also extracts some low molecular mass isotactic polymer. For most iPP samples prepared with last-generation ZN catalysts the isotactic pentad fraction, *mmmm*, measured by ^{13}C NMR spectra has been found to correlate with xylene insoluble values although similar correlations should be taken with caution.

The measurement of polymer MWD is best done by high temperature gel permeation chromatography (GPC) which also provides detailed information on the modality of the molecular weight distribution. GPC separates polymer macromolecules based on a size exclusion principle whereas for the isolation of discrete molecular weight fractions, a related technique is the two-step process called temperature rising elution fractionation (TREF). In the first step polymer dissolved in a hot *o*-xylene solution is slowly precipitated by controlled cooling and in the second step the sample is loaded into a thermostated column eluted with a solvent under a stepwise series of increasing temperature conditions. During this phase, polymer fractions sequentially dissolve and each fraction is isolated by reprecipitation and then characterized by the available techniques [95, 96]. It is worth to recall that TREF does not strictly fractionate polypropylenes according to tacticity but, instead, according to the longest crystallizable sequences of the chain [97]. Further development of techniques based on the chemical distribution analysis (CCD) lead to the “crystallization analysis fractionation” (CRYSTAF) published by Monrabal [98]. CRYSTAF shares with TREF the same fundamentals on separation according to crystallizability, but the whole fractionation process is carried out during crystallization without support by monitoring the polymer solution concentration, through the crystallization process while decreasing temperature [99]. Recently, Monrabal et al. [100] proposed a promising technique, called crystallization elution fractionation (CEF) which combines the separation power of TREF and CRYSTAF and has been shown to provide very fast analysis of the CCD although CEF analysis still requires expensive specific installation. Overall TREF, CRYSTAF and CEF appear to be powerful techniques for PP tacticity distribution although they can hardly provide quick analysis with common instrument, which is one of the main demands of the manufacturing process operating in large-scale production of polyolefin. The research for further development of fast methods for tacticity analysis is still ongoing [101, 102].

1.8 Polypropylene Microstructures Obtained by Non-metallocene Ligands and by Late Transition Metal

Homogeneous *ansa*-metallocene systems contributed enormously to increase the number of PP microstructure available with the great vantages to produce polypropylenes having controlled desired properties not accessible with commercial iPP produced with heterogeneous Ziegler-Natta catalysts. The range spanned for the PP microstructure are visualized in Fig. 1.32 where only representative cases of synthesized catalysts belonging to the “metallocene revolution” are selected. More details on the (huge) ligand variation based on metallocene skeletons can be found in Refs. [11, 103, 104].

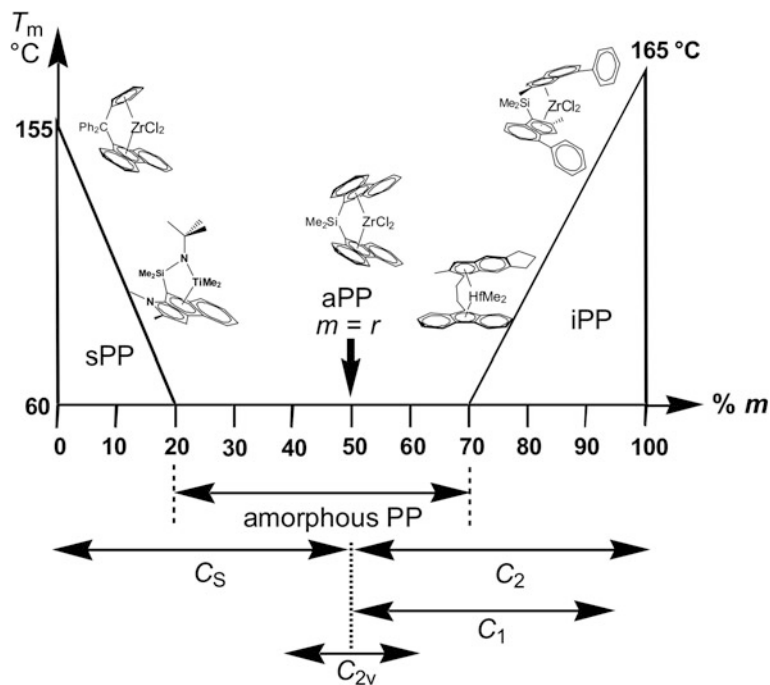


Fig. 1.32 Relationships between catalyst symmetry and PP microstructures available

Research activity in the field of metal-catalyzed olefin polymerization, is still experiencing a significant growth and the number of new catalysts introduced in the last years has provided important developments in the coordination chemistry of transition metals throughout the Periodic Table. The main focus has moved in the achievement of PP microstructures or molecular architectures not available with heterogeneous and homogeneous *ansa*-metallocene systems. Block copolymers (BCP) based on PP are now synthesized by using a living polymerization catalyzed by non-metallocene systems as bis(phenoxy)imine-Ti and pyridylamino-Hf (whose structures are reported in Fig. 1.20, top and Fig. 1.27, respectively) [64, 67, 105–111]. Determining the features that would provide a living system requires further elucidation and works are still in progress [107, 112, 113]; nevertheless, the new molecular architectures reported in Table 1.1 show very interesting and unprecedented properties.

BCPs containing more than one crystallizable block may form nanostructures by microphase separation and self-assembly in lamellar, spherical, and cylindrical microdomains depending on the composition of the BCP [114]. These self-assembled nanostructures with periodicity at the nanoscale level have already shown their potential for fabrication of nanomaterials [115–117]. Very recently a relevant application for multiblock iPP/PE has been disclosed as compatibilizers of iPP and PE blends. The tetrablock copolymers enables morphological control due

Table 1.1 Block copolymer architectures PP-based. With *rir*PP = regioirregular polypropylene

Entry	Block copolymer
1	iPP- <i>block</i> -PE
2	iPP- <i>block</i> -PE
3	iPP- <i>block</i> -poly(E- <i>co</i> -P)
4	sPP- <i>block</i> -poly(E- <i>co</i> -P)
5	sPP- <i>block</i> -poly(E- <i>co</i> -P)- <i>block</i> -sPP
6	sPP- <i>block</i> -aPP
7	PE- <i>block</i> -poly(E- <i>co</i> -P)- <i>block</i> -sPP
8	aPP- <i>block</i> -PE
9	aPP- <i>block</i> -poly(E- <i>co</i> -P)
10	iPP- <i>block</i> - <i>rir</i> PP
11	iPP- <i>block</i> - <i>rir</i> PP- <i>block</i> -iPP
12	iPP- <i>block</i> - <i>rir</i> PP- <i>block</i> -iPP- <i>rir</i> PP- <i>block</i> -iPP

Adapted from Ref. [105]

to the interfacial compatibilization of phase-separated PE and iPP, so transforming brittle materials into mechanically tough blends [118]. This opens interesting perspectives on recycling the two most common polymers.

The living polymerization approach to synthesize the PP-based BCP architectures suffers the fact that metal complexes only form one polymer chain during the polymerization reaction, rendering the displacement of current commodity polyolefins not applied on industrial scale. Significant and highly promising researches are conducted to develop new strategies for obtaining multiple macromolecular chains per catalyst, such as coordinative chain transfer polymerization (CCTP) [119] or chain shuttling polymerization [120]. The latter one has led to promising results to justify a scale-up to industrial process. In this strategy two different catalysts which behave differently in the olefin polymerization are used. A chain shuttling agent transfers the polymer chain from one catalyst to other forming BCPs having segments of different microstructures. In this way BCPs combining different mechanical properties, due to the different microstructures, in one polymer are prepared.

At the same time, successful new classes of highly active non-metallocene catalysts including LTM such as the Ni and Pd diimine catalysts [121], or the Fe bis(imino)pyridyl catalysts are reported [122]. All of them are showing peculiar PP microstructures, mainly because all possible combinations of regio-chemistries and stereo-chemistries have been observed in propylene polymerization.

1.9 Concluding Remarks

The tacticity of polypropylenes has revealed to be always a “hot” topic although more than sixty years are passed from the discovery of its first crystalline form by metal-catalyzed olefin polymerization. The success of the PP is due to for a large part to serendipity of catalyst discoveries and hard empirical works that make the

research activity in this field still attracting for scientists and experiencing a significant growth. In this chapter we tried to summarize the amazing variety of PP microstructures available with TM catalysts. The next important targets for expanding the PP tacticity are already fixed: (a) the functionalization of PP-based materials with polar groups by using catalysts able to promote copolymerization with polar comonomers in good catalytic activity; (b) the synthesis of tuned PP-based BCPs with activity on the scale for industrial applications.

Undoubtedly, the future will witness continued research of organometallic chemistry and polymer science to achieve new PP microstructures for targeted applications. This is, for sure, not the end of the story.

Acknowledgements The author would like to thank the University of Naples Federico II (Ricerca di Ateneo 2017 of University of Naples Federico II, DR_409_2017) for financial support.

References

1. Natta G, Pino P, Corradini P et al (1955) Crystalline high polymers of α -olefins. *J Am Chem Soc* 77:1708–1710. <https://doi.org/10.1021/ja01611a109>
2. Natta G (1955) Une nouvelle classe de polymères d' α -oléfinés ayant une régularité de structure exceptionnelle. *J Polym Sci* 16:143–154. <https://doi.org/10.1002/pol.1955.120168205>
3. (2014) News provided by MarketOptimizer.org. <https://www.prnewswire.com/news-releases/global-polypropylene-market-capacity-to-see-58-cagr-to-2018-says-a-new-research-report-available-with-marketoptimizerorg-268474302.html>
4. Severn JR, Chadwick JC, Duchateau R et al (2006) “Bound but not gagged”—immobilizing single-site α -olefin polymerization catalysts. *Chem Rev* 105:4073–4147. <https://doi.org/10.1021/cr040670d>
5. Moore EP Jr (1996) Polypropylene handbook: polymerization, characterization, properties, processing, applications. Hanser Publishers, Munich
6. Kashiwa N (2004) The discovery and progress of $MgCl_2$ -supported $TiCl_4$ catalysts. *J Polym Sci A Polym Chem* 42:1–8. <https://doi.org/10.1002/pola.10962>
7. Chadwick JC (2009) Polyolefins—catalyst and process innovations and their impact on polymer properties. *Macromol React Eng* 3:428–432. <https://doi.org/10.1002/mren.200900043>
8. Natta G, Pasquon I, Corradini P et al (1961) Alti polimeri lineari del propilene aventi struttura sindiotattica. *Rend Acc Naz Lincei* 28:539–544
9. Natta G, Pasquon I, Zambelli A (1962) Stereospecific catalysts for the head-to-tail polymerization of propylene to a crystalline syndiotactic polymer. *J Am Chem Soc* 84:1488–1490. <https://doi.org/10.1021/ja00867a029>
10. Brintzinger H-H, Fischer D, Mühlaupt R (1995) Stereospecific olefin polymerization with chiral metallocene catalysts. *Angew Chem Int Edit* 34:1143–1170. <https://doi.org/10.1002/anie.199511431>
11. Resconi L, Cavallo L, Fait A (2000) Selectivity in propene polymerization with metallocene catalysts. *Chem Rev* 100:1253–1346. <https://doi.org/10.1021/cr9804691>
12. Gibson VC, Spitzmesser SK (2003) Advances in non-metallocene olefin polymerization catalysis. *Chem Rev* 103:283–315. <https://doi.org/10.1021/cr980461r>
13. Baier MC, Zuideveld MA, Mecking S (2014) Post-metallocenes in the industrial production of polyolefins. *Angew Chem Int Edit* 53:9722–9744. <https://doi.org/10.1002/anie.201400799>

14. Cossee P (1964) Ziegler-Natta catalysis I. Mechanism of polymerization of α -olefins with Ziegler-Natta catalysts. *J Catal* 3:80–88. [https://doi.org/10.1016/0021-9517\(64\)90095-8](https://doi.org/10.1016/0021-9517(64)90095-8)
15. Brookhart M, Green MLH, Wong LL (1988) Carbon-hydrogen-transition metal bonds. *Prog Inorg Chem* 36:1–124 <https://doi.org/10.1002/9780470166376.ch1>
16. Krauledat H, Brintzinger HH (1990) Isotope effects associated with α -olefin insertion in zirconocene-based polymerisation catalysts: evidence for an α -agostic transition state. *Angew Chem Int Edit* 29:1412–1413. <https://doi.org/10.1002/anie.199014121>
17. Grubbs RH, Coates GW (1996) α -agostic interactions and olefin insertion in metallocene polymerization catalysts. *Acc Chem Res* 29:85–93. <https://doi.org/10.1021/ar9501683>
18. Talarico G, Budzelaar PHM (2016) α -agostic interactions and growing chain orientation for olefin polymerization catalysts. *Organometallics* 35:47–54. <https://doi.org/10.1021/acs.organomet.5b00866>
19. Bahri-Laleh N, Hanifpour A, Mirmohammadi SA et al (2018) Computational modeling of heterogeneous Ziegler-Natta catalysts for olefins polymerization. *Prog Polym Sci* 84:89–114. <https://doi.org/10.1016/j.progpolymsci.2018.06.005>
20. Eisch JJ, Piotrowski AM, Brownstein SK et al (1985) Organometallic compounds of group III. Part 41. Direct observation of the initial insertion of an unsaturated hydrocarbon into the titanium-carbon bond of the soluble ziegler polymerization catalyst $Cp_2TiCl_2-MeAlCl_2$. *J Am Chem Soc* 107:7219–7221. <https://doi.org/10.1021/ja00310a100>
21. Jordan RF, Bajgur CS, Willett R et al (1986) Ethylene polymerization by a cationic dicyclopentadienyl zirconium(IV) alkyl complex. *J Am Chem Soc* 108:7410–7411. <https://doi.org/10.1021/ja00283a047>
22. Jordan RF (1991) Chemistry of cationic dicyclopentadienyl group 4 metal-alkyl complexes. In Stone FGA, West R (eds) *Advances in organometallic chemistry*, vol 32. Academic Press, pp 325–387. [https://doi.org/10.1016/S0065-3055\(08\)60482-7](https://doi.org/10.1016/S0065-3055(08)60482-7)
23. Chen EY-X, Marks TJ (2000) Cocatalysts for metal-catalyzed olefin polymerization: activators, activation processes, and structure-activity relationships. *Chem Rev* 100:1391–1434. <https://doi.org/10.1021/cr980462j>
24. Mohammed M, Nele M, Al-Humydi A et al (2003) Counterion effects on propylene polymerization using two-state ansa-metallocene complexes. *J Am Chem Soc* 125:7930–7941. <https://doi.org/10.1021/ja0207706>
25. Correa A, Cavallo L (2006) Dynamic properties of metallocenium ion pairs in solution by atomistic simulations. *J Am Chem Soc* 128:10952–10959. <https://doi.org/10.1021/ja062407v>
26. Rocchigiani L, Ciancaleoni G, Zuccaccia C et al (2011) Low-temperature kinetic NMR studies on the insertion of a single olefin molecule into a Zr-C bond: Assessing the counterion–solvent interplay. *Angew Chem Int Edit* 50:11752–11755. <https://doi.org/10.1002/anie.201105122>
27. Corradini P, Guerra G (1991) Models for the stereospecificity in homogeneous and heterogeneous Ziegler-Natta polymerizations. *Prog Polym Sci* 16:239–257. [https://doi.org/10.1016/0079-6700\(91\)90018-G](https://doi.org/10.1016/0079-6700(91)90018-G)
28. Jones RG, Wilks ES, Val Metanomski W et al (2009) Compendium of polymer terminology and nomenclature: IUPAC recommendations 2008. Royal Society of Chemistry
29. Farina M, Di Silvestro G, Sozzani P (1991) Hemitactic polymers. *Prog Polym Sci* 16:219–238. [https://doi.org/10.1016/0079-6700\(91\)90017-F](https://doi.org/10.1016/0079-6700(91)90017-F)
30. Shelden RA, Fueno T, Tsunetsugu T et al (1965) A one-parameter model for isotactic polymerization based on enantiomeric catalyst sites. *J Polym Sci Pol Lett* 3:23–26. <https://doi.org/10.1002/pol.1965.110030107>
31. Bovey FA, Tiers GVD (1960) Polymer NSR spectroscopy. II. The high resolution spectra of methyl methacrylate polymers prepared with free radical and anionic initiators. *J Polym Sci* 44:173–182. <https://doi.org/10.1002/pol.1960.1204414315>
32. Busico V, Chadwick JC, Cipullo R et al (2004) Propene/ethene-[1-13c] copolymerization as a tool for investigating catalyst regioselectivity. $MgCl_2$ /internal donor/ $TiCl_4$ – external donor/ AlR_3 systems. *Macromolecules* 37:7437–7443. <https://doi.org/10.1021/ma049104a>

33. Leclerc MK, Brintzinger HH (1996) Zr – alkyl isomerization in ansa-zirconocene-catalyzed olefin polymerizations. Contributions to stereoerror formation and chain termination. *J Am Chem Soc* 118:9024–9032. <https://doi.org/10.1021/ja961157n>
34. Resconi L (1999) On the mechanisms of growing-chain-end isomerization and transfer reactions in propylene polymerization with isospecific, C₂-symmetric zirconocene catalysts. *J Mol Catal A-Chem* 146:167–178. [https://doi.org/10.1016/S1381-1169\(99\)00101-6](https://doi.org/10.1016/S1381-1169(99)00101-6)
35. Resconi L, Camurati I, Sudmeijer O (1999) Chain transfer reactions in propylene polymerization with zirconocene catalysts. *Top Catal* 7:145–163. <https://doi.org/10.1023/a:1019115801193>
36. McCord EF, McLain SJ, Nelson LTJ et al (2007) ¹³C NMR analysis of α -olefin enchainment in poly(α -olefins) produced with nickel and palladium α -diimine catalysts. *Macromolecules* 40:410–420. <https://doi.org/10.1021/ma061547m>
37. Zambelli A, Locatelli P, Bajo G et al (1975) Model compounds and ¹³C NMR observation of stereosequences of polypropylene. *Macromolecules* 8:687–689. <https://doi.org/10.1021/ma60047a024>
38. Grant DM, Paul EG (1964) Carbon-13 magnetic resonance. II. Chemical shift data for the alkanes. *J Am Chem Soc* 86:2984–2990. <https://doi.org/10.1021/ja01069a004>
39. Lindeman LP, Adams JQ (1971) Carbon-13 nuclear magnetic resonance spectrometry. Chemical shifts for the paraffins through C₉. *Anal Chem* 43:1245–1252. <https://doi.org/10.1021/ac60304a002>
40. Schilling FC, Tonelli AE (1980) Carbon-13 nuclear magnetic resonance of atactic polypropylene. *Macromolecules* 13:270–275. <https://doi.org/10.1021/ma60074a013>
41. Zambelli A, Locatelli P, Provasoli A et al (1980) Correlation between ¹³C NMR chemical shifts and conformation of polymers. 3. Hexad sequence assignments of methylene spectra of polypropylene. *Macromolecules* 13:267–270. <https://doi.org/10.1021/ma60074a012>
42. Cheng HN, Lee GH (1987) ¹³C NMR assignments of the methylene carbons in polypropylene. *Macromolecules* 20:436–438. <https://doi.org/10.1021/ma00168a038>
43. Hayashi T, Inoue Y, Chūjō R et al (1988) Heptad configurational analysis of ¹³C NMR spectra in highly isotactic polypropylene. *Polymer* 29:138–143. [https://doi.org/10.1016/0032-3861\(88\)90213-3](https://doi.org/10.1016/0032-3861(88)90213-3)
44. Busico V, Cipullo R, Monaco G et al (1997) Full assignment of the ¹³C NMR spectra of regioregular polypropylenes: methyl and methylene region. *Macromolecules* 30:6251–6263. <https://doi.org/10.1021/ma970466a>
45. Miyatake T, Kawai Y, Seki Y et al (1989) ¹³C NMR assignments of the methine carbons in polypropylene using two-dimensional ¹³C-¹³C inadequate NMR spectroscopy. *Polym J* 21:809–814. <https://doi.org/10.1021/polymj.21.809>
46. Busico V, Cipullo R, Monaco G et al (1998) Full assignment of the ¹³C NMR spectra of regioregular polypropylenes: methine region. *Macromolecules* 31:8713–8719. <https://doi.org/10.1021/ma981040e>
47. Busico V, Cipullo R (2001) Microstructure of polypropylene. *Prog Polym Sci* 26:443–533. [https://doi.org/10.1016/S0079-6700\(00\)00046-0](https://doi.org/10.1016/S0079-6700(00)00046-0)
48. Busico V, Cipullo R, Corradini P et al (1995) Advances in the ¹³C NMR microstructural characterization of propene polymers. *Macromolecules* 28:1887–1892. <https://doi.org/10.1021/ma00110a024>
49. Busico V, Van Axel Castelli V, Aprea P et al (2003) “Oscillating” metallocene catalysts: what stops the oscillation? *J Am Chem Soc* 125:5451–5460. <https://doi.org/10.1021/ja0284557>
50. Busico V, Cipullo R, Kretschmer WP et al (2002) “Oscillating” metallocene catalysts: how do they oscillate? *Angew Chem Int Edit* 41:505–508. [https://doi.org/10.1002/1521-3773\(20020201\)41:3%3c505::AID-ANIE505%3e3.0.CO;2-J](https://doi.org/10.1002/1521-3773(20020201)41:3%3c505::AID-ANIE505%3e3.0.CO;2-J)
51. Busico V, Cipullo R, Kretschmer WP et al (2002) The strange case of the “oscillating” catalysts. *Macromol Symp* 189:127–141. <https://doi.org/10.1002/masy.200290002>
52. Busico V, Cipullo R, Cutillo F et al (2003) Syndiotactic poly(propylene) from [me₂si(3,6-di-*tert*-butyl-9-fluorenyl)(*n-tert*-butyl)]TiCl₂-based catalysts: Chain-end or enantiotopic-sites stereocontrol? *Macromol Chem Phys* 204:1269–1274. <https://doi.org/10.1002/macp.200390095>

53. Busico V, Cipullo R, Monaco G et al (1999) High-resolution ^{13}C NMR configurational analysis of polypropylene made with MgCl_2 -supported Ziegler-Natta catalysts. 1. The "model" system $\text{MgCl}_2/\text{TiCl}_4$ -2.6- dimethylpyridine/ $\text{Al}(\text{C}_2\text{H}_5)_3$. *Macromolecules* 32:4173–4182. <https://doi.org/10.1021/ma981941n>
54. Busico V, Cipullo R, Talarico G et al (1997) New evidence on the nature of the active sites in heterogeneous Ziegler – Natta catalysts for propene polymerization. *Macromolecules* 30:4786–4790. <https://doi.org/10.1021/ma9704673>
55. Ewen JA (1984) Mechanisms of stereochemical control in propylene polymerizations with soluble group 4b metallocene/methylalumoxane catalysts. *J Am Chem Soc* 106:6355–6364. <https://doi.org/10.1021/ja00333a041>
56. Corradini P, Barone V, Fusco R et al (1979) Analysis of models for the Ziegler-Natta stereospecific polymerization on the basis of non-bonded interactions at the catalytic site—I. The Cossee model. *Eur Polym J* 15:1133–1141. [https://doi.org/10.1016/0014-3057\(79\)90048-X](https://doi.org/10.1016/0014-3057(79)90048-X)
57. Corradini P, Guerra G, Fusco R et al (1980) Analysis of models for the Ziegler-Natta stereospecific polymerization on the basis of non-bonded interactions at the catalytic site—II: edges, steps and reliefs on the surface of layered modifications of TiCl_3 . *Eur Polym J* 16:835–842. [https://doi.org/10.1016/0014-3057\(80\)90113-5](https://doi.org/10.1016/0014-3057(80)90113-5)
58. Corradini P, Barone V, Fusco R et al (1982) Steric control in Ziegler-Natta catalysts: an analysis of nonbonded interactions at model catalytic sites. *J Catal* 77:32–42. [https://doi.org/10.1016/0021-9517\(82\)90143-9](https://doi.org/10.1016/0021-9517(82)90143-9)
59. Guerra G, Cavallo L, Moscardi G et al (1996) Back-skip of the growing chain at model complexes for the metallocene polymerization catalysis. *Macromolecules* 29:4834–4845. <https://doi.org/10.1021/ma9517431>
60. Coates GW, Waymouth RM (1995) Oscillating stereocontrol: a strategy for the synthesis of thermoplastic elastomeric polypropylene. *Science* 267:217–219. <https://doi.org/10.1126/science.267.5195.217>
61. Farina M, Di Silvestro G, Sozzani P (1993) Hemiisotactic polypropylene: a key point in the elucidation of the polymerization mechanism with metallocene catalysts. *Macromolecules* 26:946–950. <https://doi.org/10.1021/ma00057a010>
62. Ewen JA, Jones RL, Razavi A et al (1988) Syndiospecific propylene polymerizations with Group IVB metallocenes. *J Am Chem Soc* 110:6255–6256. <https://doi.org/10.1021/ja00226a056>
63. Chen M-C, Roberts JAS, Marks TJ (2004) Marked counteranion effects on single-site olefin polymerization processes. Correlations of ion pair structure and dynamics with polymerization activity, chain transfer, and syndioselectivity. *J Am Chem Soc* 126:4605–4625. <https://doi.org/10.1021/ja036288k>
64. Tian J, Hustad PD, Coates GW (2001) A new catalyst for highly syndiospecific living olefin polymerization: homopolymers and block copolymers from ethylene and propylene. *J Am Chem Soc* 123:5134–5135. <https://doi.org/10.1021/ja0157189>
65. Saito J, Mitani M, Mohri J-I et al (2001) Highly syndiospecific living polymerization of propylene using a titanium complex having two phenoxy-imine chelate ligands. *Chem Lett* 30:576–577. <https://doi.org/10.1246/cl.2001.576>
66. Hustad PD, Tian J, Coates GW (2002) Mechanism of propylene insertion using bis(phenoxyimine)-based titanium catalysts: An unusual secondary insertion of propylene in a Group IV catalyst system. *J Am Chem Soc* 124:3614–3621. <https://doi.org/10.1021/ja0122593>
67. Mitani M, Furuyama R, Mohri J-I et al (2003) Syndiospecific living propylene polymerization catalyzed by titanium complexes having fluorine-containing phenoxy – imine chelate ligands. *J Am Chem Soc* 125:4293–4305. <https://doi.org/10.1021/ja029560j>
68. Talarico G, Busico V, Cavallo L (2003) Origin of the regiochemistry of propene insertion at octahedral column 4 polymerization catalysts: design or serendipity? *J Am Chem Soc* 125:7172–7173. <https://doi.org/10.1021/ja029604o>

69. Corradini P, Guerra G, Pucciariello R (1985) New model of the origin of the stereospecificity in the synthesis of syndiotactic polypropylene. *Macromolecules* 18:2030–2034. <https://doi.org/10.1021/ma00152a039>
70. Corradini P, Guerra G, Cavallo L (2004) Do new century catalysts unravel the mechanism of stereocontrol of old Ziegler-Natta catalysts? *Accounts Chem Res* 37:231–241. <https://doi.org/10.1021/ar030165n>
71. Makio H, Terao H, Iwashita A et al (2011) FI catalysts for olefin polymerization—a comprehensive treatment. *Chem Rev* 111:2363–2449. <https://doi.org/10.1021/cr100294r>
72. Busico V, Cipullo R, Polzone C et al (2003) Propene/ethene-[1-13C] copolymerization as a tool for investigating catalyst regioselectivity. 2. The $MgCl_2/TiCl_4 - AlR_3$ system. *Macromolecules* 36:2616–2622. <https://doi.org/10.1021/ma034138o>
73. De Rosa C, Auriemma F, Paolillo M et al (2005) Crystallization behavior and mechanical properties of regiodefective, highly stereoregular isotactic polypropylene: effect of regiodefects versus stereodefects and influence of the molecular mass. *Macromolecules* 38:9143–9154. <https://doi.org/10.1021/ma051004x>
74. De Rosa C, Auriemma F, Di Capua A et al (2004) Structure – property correlations in polypropylene from metallocene catalysts: stereodefective, regioregular isotactic polypropylene. *J Am Chem Soc* 126:17040–17049. <https://doi.org/10.1021/ja045684f>
75. Zhou Z, Stevens JC, Klosin J et al (2009) NMR study of isolated 2,1-inverse insertion in isotactic polypropylene. *Macromolecules* 42:2291–2294. <https://doi.org/10.1021/ma802770f>
76. Correa A, Talarico G, Cavallo L (2007) Regiochemistry of propene insertion with Group 4 polymerization catalysts from a theoretical perspective. *J Organomet Chem* 692:4519–4527. <https://doi.org/10.1016/j.jorganchem.2007.04.015>
77. Reichelt K, Parkinson M, Resconi L (2016) Influence of temperature on the regioselectivity of highly isospecific C_2 -symmetric zirconocenes in propene polymerization. *Macromol Chem Phys* 217:2415–2430. <https://doi.org/10.1002/macp.201600088>
78. Boussie TR, Diamond GM, Goh C et al (2006) Nonconventional catalysts for isotactic propene polymerization in solution developed by using high-throughput-screening technologies. *Angew Chem Int Edit* 45:3278–3283. <https://doi.org/10.1002/anie.200600240>
79. Domski GJ, Eagan JM, De Rosa C et al (2017) Combined experimental and theoretical approach for living and isoselective propylene polymerization. *ACS Catal* 7:6930–6937. <https://doi.org/10.1021/acscatal.7b02107>
80. De Rosa C, Di Girolamo R, Talarico G (2016) Expanding the origin of stereocontrol in propene polymerization catalysis. *ACS Catal* 6:3767–3770. <https://doi.org/10.1021/acscatal.6b00863>
81. Simonazzi T, Cecchin G, Mazzullo S (1991) An outlook on progress in polypropylene-based polymer technology. *Prog Polym Sci* 16:303–329. [https://doi.org/10.1016/0079-6700\(91\)90021-C](https://doi.org/10.1016/0079-6700(91)90021-C)
82. Busico V, Cipullo R, Monaco G et al (1999) New insight in propene polymerization promoted by heterogeneous Ziegler-Natta catalysts. In: Kaminsky W (ed) *Metalorganic catalysts for synthesis and polymerization*. Springer, Berlin, pp 76–88
83. Alamo RG, Kim M-H, Galante MJ et al (1999) Structural and kinetic factors governing the formation of the γ polymorph of isotactic polypropylene. *Macromolecules* 32:4050–4064. <https://doi.org/10.1021/ma981849r>
84. Auriemma F, De Rosa C (2002) Crystallization of metallocene-made isotactic polypropylene: disordered modifications intermediate between the α and γ forms. *Macromolecules* 35:9057–9068. <https://doi.org/10.1021/ma020648r>
85. De Rosa C, Auriemma F, Circelli T et al (2002) Crystallization of the α and γ forms of isotactic polypropylene as a tool to test the degree of segregation of defects in the polymer chains. *Macromolecules* 35:3622–3629. <https://doi.org/10.1021/ma0116248>
86. De Rosa C, Auriemma F, Spera C et al (2004) Comparison between polymorphic behaviors of Ziegler-Natta and metallocene-made isotactic polypropylene: the role of the distribution of defects in the polymer chains. *Macromolecules* 37:1441–1454. <https://doi.org/10.1021/ma035295q>

87. De Rosa C, Auriemma F, Spera C et al (2004) Crystallization properties of elastomeric polypropylene from alumina-supported tetraalkyl zirconium catalysts. *Polymer* 45:5875–5888. <https://doi.org/10.1016/j.polymer.2004.06.037>
88. Sundell T, Fagerholm H, Crozier H (1996) Isotacticity determination of polypropylene using FT-Raman spectroscopy. *Polymer* 37:3227–3231. [https://doi.org/10.1016/0032-3861\(96\)88466-7](https://doi.org/10.1016/0032-3861(96)88466-7)
89. Zhu X, Yan D, Fang Y (2001) In situ FTIR spectroscopic study of the conformational change of isotactic polypropylene during the crystallization process. *J Phys Chem B* 105:12461–12463. <https://doi.org/10.1021/jp012165f>
90. Kissin YV, Tsvetkova VI, Chirkov NM (1972) The stereoregularity of polypropylene from IR and NMR data. *Eur Polym J* 8:529–546. [https://doi.org/10.1016/0014-3057\(72\)90131-0](https://doi.org/10.1016/0014-3057(72)90131-0)
91. Kissin YV, Rishina LA (1976) Regularity bands in the I.R. spectra of C₃H₆-C₃D₆ copolymers. *Eur Polym J* 12:757–759. [https://doi.org/10.1016/0014-3057\(76\)90088-4](https://doi.org/10.1016/0014-3057(76)90088-4)
92. Hsu SL, Hahn T, Suen W et al (2001) An analysis of Raman spectra of syndiotactic polypropylenes. 2. Configurational defects. *Macromolecules* 34:3376–3383. <https://doi.org/10.1021/ma001448n>
93. Sevegney MS, Kannan RM, Siedle AR et al (2006) Vibrational spectroscopic investigation of stereoregularity effects on syndiotactic polypropylene structure and morphology. *Vib Spectrosc* 40:246–256. <https://doi.org/10.1016/j.vibspec.2005.10.003>
94. Pasquini N (2005) Polypropylene handbook. Product, technology, market. Hanser, Munich
95. Xu J, Feng L (2000) Application of temperature rising elution fractionation in polyolefins. *Eur Polym J* 36:867–878. [https://doi.org/10.1016/S0014-3057\(99\)00143-3](https://doi.org/10.1016/S0014-3057(99)00143-3)
96. Amer I, van Reenen A (2009) Fractionation and crystallization of isotactic poly(propylenes) prepared with a heterogeneous transition metal catalysts. *Macromol Symp* 282:33–40. <https://doi.org/10.1002/masy.200950804>
97. Viville P, Daoust D, Jonas AM et al (2001) Characterization of the molecular structure of two highly isotactic polypropylenes. *Polymer* 42:1953–1967. [https://doi.org/10.1016/S0032-3861\(00\)00529-2](https://doi.org/10.1016/S0032-3861(00)00529-2)
98. Monrabal B (1996) Crystaf: crystallization analysis fractionation. A new approach to the composition analysis of semicrystalline polymers. *Macromol Symp* 110:81–86. <https://doi.org/10.1002/masy.19961100107>
99. Monrabal B (2006) Microstructure characterization of polyolefins. Tref and crystaf. In Shiono T, Nomura K, Terano M (eds) *Studies in surface science and catalysis*, vol 161, pp 35–42. Elsevier. [https://doi.org/10.1016/S0167-2991\(06\)80431-3](https://doi.org/10.1016/S0167-2991(06)80431-3)
100. Monrabal B, Sancho-Tello J, Mayo N et al (2007) Crystallization elution fractionation. A new separation process for polyolefin resins. *Macromol Symp* 257:71–79. <https://doi.org/10.1002/masy.200751106>
101. Virkkunen V, Laari P, Pitkänen P et al (2004) Tacticity distribution of isotactic polypropylene prepared with heterogeneous Ziegler–Natta catalyst. 2. Application and analysis of SSA data for polypropylene. *Polymer* 45:4623–4631. <https://doi.org/10.1016/j.polymer.2004.05.027>
102. Kang J, Yang F, Wu T et al (2012) Polymerization control and fast characterization of the stereo-defect distribution of heterogeneous Ziegler–Natta isotactic polypropylene. *Eur Polym J* 48:425–434. <https://doi.org/10.1016/j.eurpolymj.2011.11.023>
103. Alt HG, Köppl A (2000) Effect of the nature of metallocene complexes of group IV metals on their performance in catalytic ethylene and propylene polymerization. *Chem Rev* 100:1205–1222. <https://doi.org/10.1021/cr9804700>
104. Kaminsky W, Funck A, Hähnsen H (2009) New application for metallocene catalysts in olefin polymerization. *Dalton Trans* 8803–8810. <https://doi.org/10.1039/B910542P>
105. Domski GJ, Rose JM, Coates GW et al (2007) Living alkene polymerization: new methods for the precision synthesis of polyolefins. *Prog Polym Sci* 32:30–92. <https://doi.org/10.1016/j.progpolymsci.2006.11.001>

106. Harney MB, Zhang Y, Sita LR (2006) Discrete, multiblock isotactic-atactic stereoblock polypropylene microstructures of differing block architectures through programmable stereomodulated living Ziegler-Natta polymerization. *Angew Chem Int Edit* 45:2400–2404. <https://doi.org/10.1002/anie.200600027>
107. Talarico G, Busico V, Cavallo L (2004) “Living” propene polymerization with bis(phenoxyimine) Group 4 metal catalysts: new strategies and old concepts. *Organometallics* 23:5989–5993. <https://doi.org/10.1021/om049296y>
108. Busico V, Cipullo R, Friederichs N et al (2004) Block copolymers of highly isotactic polypropylene via controlled Ziegler-Natta polymerization. *Macromolecules* 37:8201–8203. <https://doi.org/10.1021/ma048144b>
109. Gottfried AC, Brookhart M (2003) Living and block copolymerization of ethylene and α -olefins using palladium(ii)-*a*-diimine catalysts. *Macromolecules* 36:3085–3100. <https://doi.org/10.1021/ma025902u>
110. Busico V, Cipullo R, Friederichs N et al (2003) The first molecularly characterized isotactic polypropylene-block-polyethylene obtained via “quasi-living” insertion polymerization. *Macromolecules* 36:3806–3808. <https://doi.org/10.1021/ma0342527>
111. Tshuva EY, Goldberg I, Kol M et al (2001) Living polymerization and block copolymerization of α -olefins by an amine bis(phenolate) titanium catalyst. *Chem Commun* 2120–2121. <https://doi.org/10.1039/B105492A>
112. Mitani M, Nakano T, Fujita T (2003) Unprecedented living olefin polymerization derived from an attractive interaction between a ligand and a growing polymer chain. *Chem-Eur J* 9:2396–2403. <https://doi.org/10.1002/chem.200304661>
113. Weberski MP, Chen C, Delferro M et al (2012) Suppression of β -hydride chain transfer in nickel(ii)-catalyzed ethylene polymerization via weak fluorocarbon ligand–product interactions. *Organometallics* 31:3773–3789. <https://doi.org/10.1021/om3002735>
114. Bates FS, Fredrickson GH (1990) Block copolymer thermodynamics: theory and experiment. *Annu Rev Phys Chem* 41:525–557. <https://doi.org/10.1146/annurev.pc.41.100190.002521>
115. Cheng JY, Mayes AM, Ross C (2004) Nanostructure engineering by templated self-assembly of block copolymers. *Nat Mater* 3:823–828. <https://doi.org/10.1038/nmat1211>
116. Stoykovich MP, Müller M, Kim SO et al (2005) Directed assembly of block copolymer blends into nonregular device-oriented structures. *Science* 308:1442–1446. <https://doi.org/10.1126/science.1111041>
117. De Rosa C, Auriemma F, Di Girolamo R et al (2010) Enabling strategies in organic electronics using ordered block copolymer nanostructures. *Adv Mater* 22:5414–5419. <https://doi.org/10.1002/adma.201002649>
118. Eagan JM, Xu J, Di Girolamo R et al (2017) Combining polyethylene and polypropylene: enhanced performance with PE/iPP multiblock polymers. *Science* 355:814–816. <https://doi.org/10.1126/science.aah5744>
119. Valente A, Mortreux A, Visseaux M et al (2013) Coordinative chain transfer polymerization. *Chem Rev* 113:3836–3857. <https://doi.org/10.1021/cr300289z>
120. Arriola DJ, Carnahan EM, Hustad PD et al (2006) Catalytic production of olefin block copolymers via chain shuttling polymerization. *Science* 312:714–719. <https://doi.org/10.1126/science.1125268>
121. Rose JM, Cherian AE, Coates GW (2006) Living polymerization of α -olefins with an α -diimine ni(ii) catalyst: formation of well-defined ethylene-propylene copolymers through controlled chain-walking. *J Am Chem Soc* 128:4186–4187. <https://doi.org/10.1021/ja058183i>
122. Lamberti M, Mazzeo M, Pappalardo D et al (2009) Mechanism of stereospecific polymerization of α -olefins by late-transition metal and octahedral group 4 metal catalysts. *Coord Chem Rev* 253:2082–2097. <https://doi.org/10.1016/j.ccr.2009.02.014>

Chapter 2

Solid State Polymorphism of Isotactic and Syndiotactic Polypropylene



Finizia Auriemma, Claudio De Rosa, Anna Malafronte, Miriam Scoti and Rocco Di Girolamo

Contents

2.1	Introduction.....	38
2.2	Chain Conformation of Isotactic and Syndiotactic Polypropylene in the Crystalline State	40
2.2.1	Isotactic Polypropylene	41
2.2.2	Syndiotactic Polypropylene.....	44
2.3	Crystal Polymorphism of Isotactic Polypropylene	44
2.4	The Crystal Structure of α Form	48
2.4.1	The Crystal Structure of γ Form.....	52
2.4.2	Structural Disorder of γ Form of iPP.....	57
2.4.3	Crystal Structure of β Form.....	59
2.4.4	Mesomorphic Form of iPP.....	61
2.4.5	Crystal Structure of the Trigonal Form of iPP.....	63
2.4.6	The “New Mesomorphic” Form in Copolymers of Isotactic Polypropylene with Branched Comonomers.....	68
2.5	Crystal Polymorphism of Syndiotactic Polypropylene.....	72
2.5.1	Crystal Structure of Form I.....	75
2.5.2	Structural Disorder in Form I.....	79
2.5.3	Crystal Structure of Form II.....	84
2.5.4	Structural Disorder in Form II	88
2.5.5	Crystal Structure of Form III	93
2.5.6	Crystal Structure of Form IV	97
2.5.7	The Trans-planar Mesomorphic Form of sPP	98
2.5.8	Helical Mesophase in Syndiotactic Copolymers of Propylene	105
2.6	Conclusions.....	106
	References	108

F. Auriemma (✉) · C. De Rosa · A. Malafronte · M. Scoti · R. Di Girolamo
Dipartimento Di Scienze Chimiche, Università di Napoli Federico II,
Complesso Monte Sant’Angelo, via Cintia, 80126 Naples, Italy
e-mail: finizia.auriemma@unina.it

C. De Rosa
e-mail: claudio.derosa@unina.it

Abstract The crystal structure and polymorphism of isotactic (iPP) and syndiotactic polypropylene (sPP) are illustrated, highlighting the rich variety of phase behavior of these polymers, the conditions of obtainment of the different polymorphs and the disorder phenomena occurring in the crystals. After description of the concepts of packing and conformational polymorphism occurring in the case of iPP and sPP respectively, the crystal structure of the different polymorphs of iPP and sPP are described. In particular, the main structural features relative to the monoclinic α -, the trigonal β - and the orthorhombic γ -forms, of iPP including the mesomorphic form, and the trigonal form which develops in random isotactic copolymers of propylene with pentene or hexene units, are described at first, the chain conformation in all these polymorphs being the 3/1 helix. Then, the complex polymorphism of sPP and the crystal structure of the orthorhombic helical form I and II, the orthorhombic trans-planar form III, the monoclinic form IV, and the trans-planar and helical mesophases are illustrated. The implications of the crystal structure with the final properties are outlined for these polymers, the great fortune of which was the almost simultaneous discovery of the polymerization catalyst systems and the structural elucidation.

2.1 Introduction

In this Chapter, the polymorphic behavior in the solid state and the crystal structure of isotactic (iPP) and syndiotactic (sPP) polypropylene are reviewed.

The discovery of isotactic polypropylene by Giulio Natta and co-workers in the early '50s [1, 2] marked the beginning of a new extraordinary era, not only from the technological and economical standpoint, but also from the standpoint of basic research in numerous fields, including polymerization catalysis of olefins, polymer crystallography and structural analysis, discovery of new properties and the identification of new classes of materials [3, 4].

In particular, in the field of polyolefins, progress in polymerization catalysis, the development of polymer crystallography, and the identification of new classes of materials proceeded simultaneously. Isotactic and syndiotactic polypropylene (sPP) represents archetypal cases of polymers illustrating the above concept [5, 6]. Indeed, the issues related to the study of polymorphism and crystal structure of iPP and sPP parallel the discovery of the basic rules of polymer crystallography [7], the implementation of new smart methodologies for structural analysis [8–11] and the discovery of new interesting phenomena that control the mode of packing of polymer chains [11–13] and the inclusion of disorder inside the crystals [10, 13, 14]. This entails that the resolution of the crystal structure of each new polymorphic form of iPP and/or sPP represents important milestones that goes beyond the history of structural investigations of polymers [2, 5, 6, 16–22]. Indeed, the crystal structure determination of them constituted a truly breakthrough, a sort of opening out of polymer science toward new frontiers, able to inspire the design of new materials, new synthetic strategies, new properties and new applications [15].

Syndiotactic polypropylene, in particular, represents a case study clearly demonstrating how research efforts in different areas may contribute synergistically toward the progress of knowledge, from the point of view of both basic and—applied science [6]. Indeed, starting from the discovery of stereoselective polymerization of olefins in 1954, sPP has been considered only a scientific curiosity for years. In fact, the samples synthesized by Ziegler-Natta based catalysts showed scarcely interesting physico-chemical properties due to the low stereo- and regio-regularity, and, as a consequence, low crystallinity and melting temperature. For these reasons sPP has never reached the great industrial fortune and commercial diffusion as iPP. A re-birth of sPP was observed in the mid '80s, after the discovery of single-center metallorganic catalysts [22, 23]. Some of these novel catalysts were able to produce highly stereoregular and regioregular sPP and completely new sPP samples, having high crystallinity and melting temperature, were obtained [24]. The new sPP has shown outstanding physical properties, completely different from those of commercial isotactic polypropylene, some of them absolutely unexpected. This has refocused the scientific and industrial interest for sPP. The most important and unique property relies on the fact that sPP is a high modulus thermoplastic elastomer, notwithstanding the high crystallinity and the relatively high glass transition temperature [6].

Isotactic and syndiotactic polypropylene show a complex polymorphism in the solid state, but whereas in the case of iPP the different crystal forms are characterized by chains with identical conformation packed in different unit cells and/or space group symmetries (packing polymorphism) [7, 10–12], sPP shows not only packing isomorphism, but also polymorphism arising from the fact that the chain molecules can assume different stable conformations in the crystalline state (conformational polymorphism) [7, 10–12]. Moreover, this complex polymorphism is complicated by the fact that in polymer crystals in general, and in the case of iPP and sPP in particular, the perfect three-dimensional long-range order is never present and the presence of structural disorder inside crystals is a rule rather than an exception [10–14]. Indeed, small amounts of defects in the regular constitution (constitutional disorder) and configuration (configurational disorder) may be easily tolerated in the crystals, without preventing crystallization. Furthermore, disorder may also arise from local departures of the chain conformation from the regular and periodic one (conformational disorder), due to small distortion of dihedral angles. Finally, even in the case of regular constitution, configuration and conformation, disorder may be present in the crystals, due to the presence of defects in the packing mode of the chains (packing disorder) [1, 10–14]. These defects may influence the crystallization and, besides the decrease of crystallinity, in many cases may drive crystallization towards a polymorphic form by stabilizing that form and destabilizing other polymorphic forms [1, 15].

For this reason, in the description of the crystal structure of the different crystalline forms of iPP and sPP we find convenient adopting the concepts of “*limit ordered*” and “*limit disordered*” model structures [6, 12, 25], that is, ideal fully ordered or fully disordered models. A “*limit ordered model*” is an idealized description of the structure in a given space group, resulting in a fixed position of all

atoms in the crystal with a perfect three-dimensional order. A “*limit disordered model*” is an idealized description in a space group, with statistical occupancy of some or all of the equivalent positions [6, 12, 25].

Structural disorder may arise, while maintaining the same unit cell, whenever a motif (an atom, group of atoms or monomeric units in a chain, polymer chains, or even group of chains) may assume different and equivalent positions in the unit cell, without changing the steric interactions with the neighboring atoms [6]. In any case, such defects do not produce large disturbance of the packing mode, so that the crystallinity and the same lattice geometry are preserved on average. An ideal fully disordered structure characterized by disorder corresponding to the statistical distribution of defects inside the crystals can be described by a “*limit disordered model*”, which actually may describe the relative position of atoms in the long range [6]. A “*limit ordered model*” may be, instead, appropriate for the description of the relative positions of atoms in the short range [6]. The real crystalline forms are, generally, intermediate between limit ordered and limit disordered models, the amount of disorder being dependent on the condition of crystallization and thermal and mechanical treatments of the samples. A condition to have more or less disordered modifications, corresponding to a same unit cell, is the substantial equivalence of steric hindrances in the space regions where a statistical substitution is achieved. Disordered structures belonging to this type arise, for instance, from substitutional isomorphism of different chains or different monomeric units, from conformational isomorphism, from the presence of stacking faults [6].

In the following, after a description of the chain conformation of iPP and sPP in the crystalline state, the polymorphism, the crystal structure and disorder phenomena of the different crystalline forms are described in detail. Illustrating the packing mode of the chains and the implications with polymer crystallography, highlighting how the understanding of material properties at molecular level achieved through the help of crystallography is a fundamental step in the progress of knowledge, toward finding new applications, and in the projecting of new materials with tailored properties.

2.2 Chain Conformation of Isotactic and Syndiotactic Polypropylene in the Crystalline State

The studies of the crystal structure of vinyl polymers produced by Ziegler-Natta heterogeneous catalysts contributed at the development of the basic principles of polymer crystallography, that is the *equivalence postulate* and the *minimum energy principle*, as formulated by Natta and Corradini [7, 26]. Application of these two basic principles allowed rationalizing and predicting the conformation adopted by polymer chains in general, and of iPP and sPP chains in particular, in the crystalline state, and may be enunciated as it follows [6, 7, 26–29].

- (1) **The equivalence principle:** the conformation of a polymer chain in the crystalline state is defined by a succession of equivalent structural units, which occupy geometrically (not necessarily crystallographically) equivalent positions with respect to the chain axis. The chain axis is parallel to a crystallographic axis of the crystal.
- (2) **Principle of minimum internal conformational energy:** The conformation of a polymer chain in a crystal approaches one of the minima of the internal conformational energy, which would be taken by an isolated chain subjected to the restrictions imposed by the equivalence principle.

The necessary geometrical equivalence of structural units along an axis allows defining the possible types of geometrical symmetry that a linear macromolecule may adopt in the crystalline state. Based on that it was possible establishing that the constitution and configuration of iPP and sPP chains are compatible with the identical repetition of a single monomeric unit (structural unit), according to a helical symmetry for iPP and a helical symmetry and/or trans-planar conformation for sPP.

2.2.1 *Isotactic Polypropylene*

In the studies of the crystal structure of polymers, isotactic polypropylene is considered one of the first example of synthetic polymer adopting in the crystals a *helical* conformation, instead of a fully extended one (*trans-planar*) [2]. All the crystalline polymorphic forms of iPP are characterized by the same stable helical conformation including three monomeric units in one turn, with periodicity $c = 6.5 \text{ \AA}$ [2, 5]. If θ_1 and θ_2 are the torsion angles of two successive backbone bonds $\text{CH}_2\text{-CH}$ and CH-CH_2 in two consecutive propene monomeric units (Fig. 2.1A), the three-fold right- and left-handed helices correspond to $(\theta_1 = \text{G}^-, \theta_2 = \text{T})$, and $(\theta_1 = \text{T}, \theta_2 = \text{G}^+)$, respectively, with T and G^\pm standing for trans ($\approx 180^\circ$) and gauche ($\approx \pm 60^\circ$), respectively [30–32] (Fig. 2.2). These are conformations of minimum energy, generally referred as $(\text{G}^-\text{T})_n$ and $(\text{TG}^+)_n$, respectively (Fig. 2.2).

In all the subsequent context, the three-fold helical conformation of iPP in the crystalline state will be addressed according with the notation $M/N = 3/1$ indicating that the integral number M of residues (in our case coinciding with a single monomeric unit) contained in N turns, corresponding to the identity period $c = 6.5 \text{ \AA}$ (in our case $N = 1$), is three.

The $3/1$ helical conformations $(\text{TG}^+)_3$ and $(\text{G}^-\text{T})_3$ found in the crystals of isotactic polypropylene [2, 7] may be easily justified by the application of the principles of equivalence and minimum energy. More precisely, with reference to Fig. 2.1a, the equivalence principle imposes that successive monomeric units take equivalent conformations in the crystalline state and hence couples of bonds adjacent to a methylene carbon atom assume the same values of torsion angles in

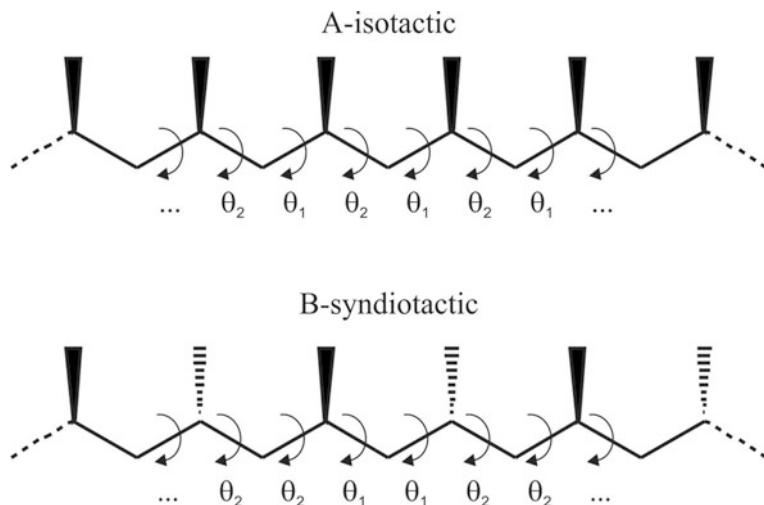


Fig. 2.1 Scheme of isotactic (a) and syndiotactic (b) polypropylene and corresponding sequences of torsion angles θ_1 and θ_2 in the crystalline state. For sPP only the succession of the backbone torsion angles in the helical conformation of lowest energy are indicated. The structural unit coincides with the single monomeric unit in both cases

consecutive monomeric units along the chain, according to the sequence $\dots\theta_2\theta_1\theta_2\theta_1\theta_2\theta_1\dots$ [30–32]. Based on the principle of the staggered bonds, the torsion angles θ_1 and θ_2 tend to be *trans* (T) or *gauche* (G). On the other hand, intramolecular interactions between non-bonded atoms impose some well-established constraints [2, 5, 7, 11]. Moreover, G^+ bonds cannot be followed by G^- bonds, and the pair of torsion angles θ_1 and θ_2 adjacent to a methylene carbon atom cannot be TT for an isotactic polymer. These conditions impose that the only possible conformations for iPP are the right handed $(TG^-)_n$ and left-handed $(G^+T)_n$, helices [2], shown in Fig. 2.2.

The projections of Fig. 2.2 allow to make a further consideration. The helical chains of isotactic polypropylene (and isotactic vinyl polymers in general) of a given chirality (right- or left-handed helix) are directional chains, which may be oriented in two distinguishable, opposite directions along the chain axis [2, 7, 11]. They may be distinguished by the orientation of the bond vectors \mathbf{b} that connect the backbone methine carbon atoms to the first atom of the side group, with respect to the c axis. In a crystal right-handed and left-handed helical chains may be up or down depending on the positive or negative components, respectively, of the bond vectors along the c axis [7, 30–32]. The up and down chains of the right- and left-handed 3/1 helices of iPP are shown in Fig. 2.2. Two equivalent (isomorphous or enantiomorphous) chains in the crystal lattice, having identical component of the bond vectors \mathbf{b} along c , both positive (up) or negative (down), are designed

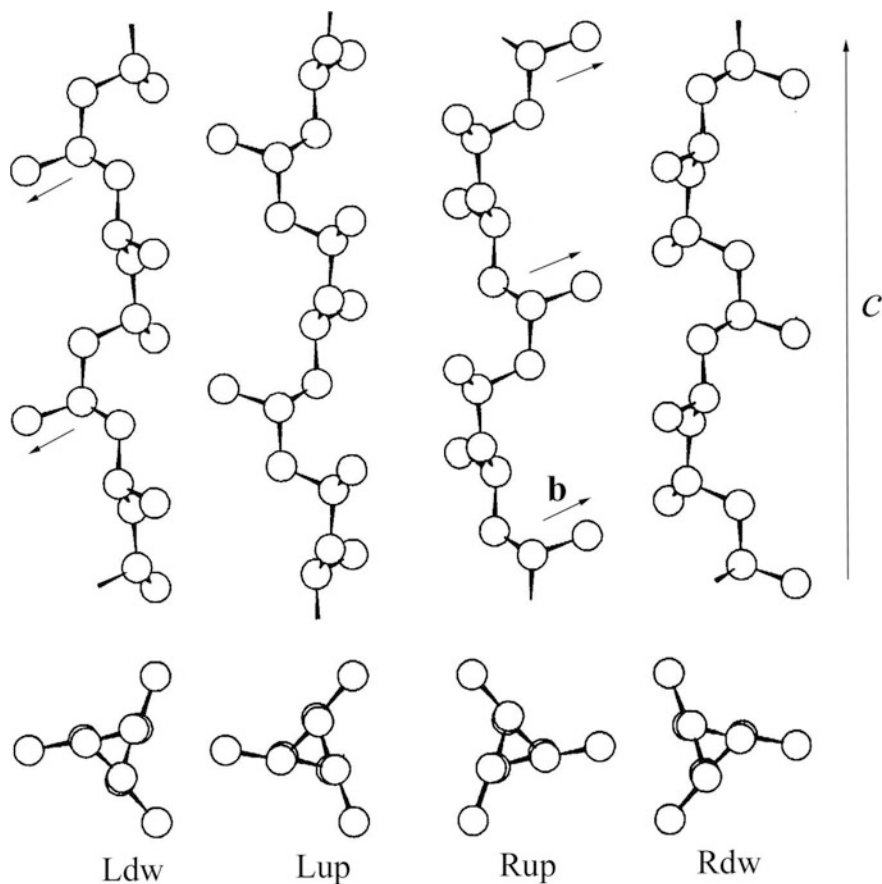


Fig. 2.2 Chains of isotactic polypropylene in three-fold helical conformation, left-handed (L) up and down and right-handed (R) up and down. Reprinted with permission from Ref. [11]. Copyright 2014 by Wiley

isoclined [7, 30–32]; two equivalent chains having both vectors along c of the same magnitude but opposite sign are designed anticlined [7, 30–32]. Isomorphous up and down (anticlined) chains of iPP have a similar external steric hindrance due to the methyl groups. As we shall see, this characteristic has important consequences on the polymorphism of iPP and the possible kind of structural disorder that the crystals may include [2, 7, 11, 33, 34]. Indeed, disorder in the positioning of up and down chains may be present in the crystals because if isomorphous, anticlined helices of iPP substitute each other in the same site of the lattice (up/down substitution type disorder), the same steric interactions with neighboring chains are involved (vide infra) [2, 7, 11].

2.2.2 Syndiotactic Polypropylene

Also in the case of syndiotactic polypropylene (sPP), the chains adopt in the crystalline state conformations of minimum energy, that respect the equivalence principle (Fig. 2.1b). sPP shows both packing and conformational polymorphisms. An easy interpretation of the conformational polymorphism, indeed, is obtained based on energy considerations and the constraints of the equivalence principle by assuming a sequence of the backbone torsion angles $\dots\theta_1, \theta_1, \theta_2, \theta_2\dots$ (Fig. 2.1b), [6, 11, 35].

Accordingly, the conformations of lowest energy are two-fold helical, corresponding either to $\theta_1 = T, \theta_2 = G^-$ or $\theta_1 = G^+, \theta_2 = T$ (Fig. 2.1b). With the restrictions imposed by the presence of a binary axis crossing the methylene groups, the helical conformations found in the crystals of the most stable polymorphic forms of sPP are the right-handed $(TTG^+G^+)_n$ and the left-handed $(G^-G^-TT)_n$ helices [6, 35–37] (Fig. 2.3a) and correspond to the line symmetry $s(2/1)2$ where “s” stands for screw, “2/1” indicates a binary helix and “2” outside the parenthesis indicate binary axes, perpendicular to chain axis, crossing the methylene groups [11, 30–32]. A low energy, but less stable than the two-fold helical conformation is characterized by chains in *trans*-planar conformation with a sequence of torsion angles of the kind $(TTTT)_n$ [11, 35, 38, 39] (Fig. 2.3b). It has also been found that sPP chains may assume in the crystalline state a third different conformation, shown in Fig. 2.3c, characterized by a sequence of torsion angle $T_6G_2T_2G_2$ [40, 41]. This conformation contains both features of helical and *trans*-planar conformations (Fig. 2.3a, b) since it is constituted by rather long sequences of backbone torsion angles in *trans*-planar conformation (T_6) and portions in the two-fold helical TTGG conformation.

It is worth noting that enantiomorphic helices of sPP in the $s(2/1)2$ symmetry have identical external steric hindrance due to the methyl groups. As in the case of iPP in the 3/1 helical conformation, this characteristic has important consequences on the polymorphism of sPP and the possible kind of structural disorder that the crystals may include. In this case disorder in the positioning of right- and left-handed helices may be present in the crystals because if enantiomorphic helices of sPP substitute each other in the same site of the lattice (right/left substitution type disorder), the same steric interactions with neighboring chains are involved [6, 11, 42, 43] (*vide infra*).

2.3 Crystal Polymorphism of Isotactic Polypropylene

The crystallization behavior of iPP is characterized by a complex polymorphism, complicated by the presence of disorder. Three crystalline forms are known, the α , β , and γ forms and a mesomorphic form [2, 16–21, 42–47]. The “building blocks” of these crystalline forms, are chains in a 3/1 $(TG)_n$ helical conformations.

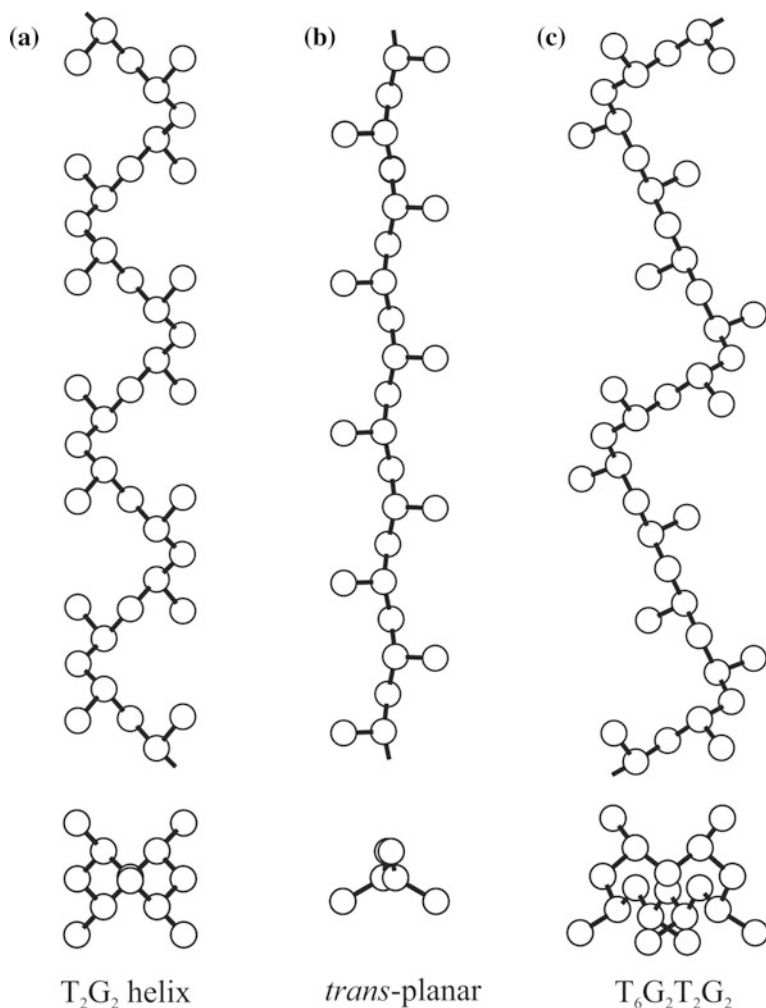
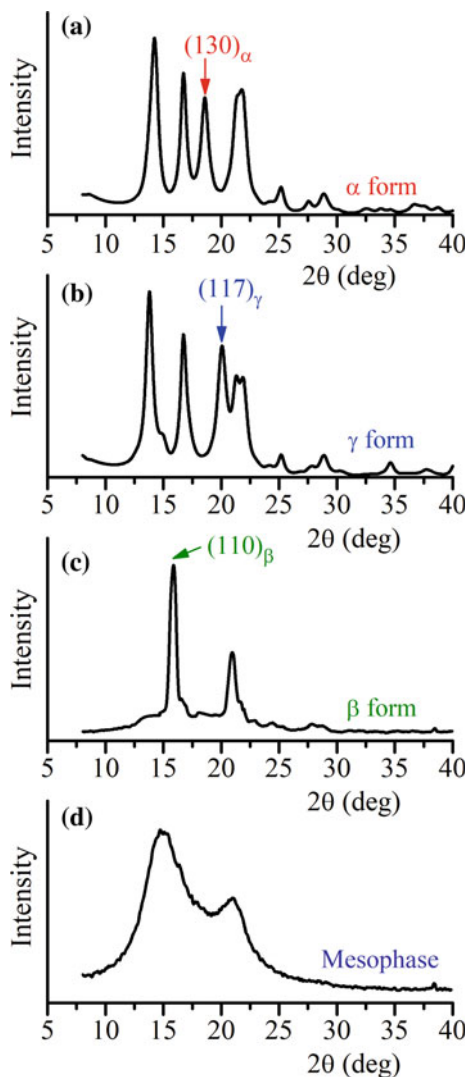


Fig. 2.3 Chains of sPP in helical (TTGG) conformation (a), *trans* planar conformation (b) and $T_6G_2T_2G_2$ helical conformation (c) [6, 36–41] of sPP, respectively. Reprinted with permission from Ref. [11]. Copyright 2014 by Wiley

The X-ray powder diffraction profiles of α , β , and γ forms and of mesophase of iPP are shown in Fig. 2.4, whereas the main reflections of α , β , and γ forms are reported in Table 2.1. The α and γ forms show similar diffraction profiles [2, 5, 16, 17, 44] the major difference consisting in the third reflection of major intensity corresponding to the $(130)_\alpha$ reflection at $d \approx 4.8 \text{ \AA}$ for the α form and $(117)_\gamma$ reflection at $d \approx 4.4 \text{ \AA}$ for the γ form. The β form shows only two strong reflections, the most intense one corresponding to the $(110)_\beta$ at $d \approx 5.5 \text{ \AA}$ [5, 18–21, 44].

Fig. 2.4 X-ray powder diffraction profiles (Ni filtered CuK α radiation) of α , γ and β forms and of mesophase of iPP



Finally, the mesomorphic form of iPP shows only broad signals centered at $d \approx 5.9$ and 4.2 \AA [45–50]. These differences are due to differences in the packing mode of the 3/1 helices.

The different packing scheme of the iPP helical chains which characterizes the various crystalline forms, per se, generates completely different physical properties (melting point, modulus, impact resistance, transparency, etc. [3, 5, 11, 15]). However, the physical properties of iPP are also influenced by the presence of structural disorder inside the crystals [11–14].

Table 2.1 Diffraction angles (2θ), interplanar distances (d) and Miller indices (hkl) of the main Bragg reflections relative to the α , β and γ forms of isotactic polypropylene, observed in the X-ray diffraction profiles (Ni-filtered $\text{CuK}\alpha$ radiation, $\lambda = 1.5418 \text{ \AA}$)

Isotactic polypropylene α form			Isotactic polypropylene γ form			Isotactic polypropylene β form		
$(hkl)_\alpha$	2θ (deg)	d (\AA)	$(hkl)_\gamma$	2θ (deg)	d (\AA)	$(hkl)_\beta$	2θ (deg)	d (\AA)
110	14.2	6.25	111	13.8	6.40	110	16.1	5.51
040	17.1	5.18	113	15.0	5.89	101	16.5	5.37
130	18.6	4.76	008	16.7	5.30	111	21.1	4.21
111	21.1	4.21	115	17.2	5.15	201	23.1	3.85
$\bar{1}31, 041$	21.9	4.06	022	18.3	4.83	210	24.7	3.61
150, 060	25.7	3.46	117	20.0	4.42	300	28.0	3.18
141, 200, 210	27.2	3.28	202	21.2	4.19	211	28.3	3.16
$\bar{1}51$	27.9	3.20	026	21.9	4.06			
220	28.5	3.13	119	23.3	3.81			
			206	24.3	3.66			
			00 12	25.2	3.53			
			11 11	26.9	3.31			
			220	27.5	3.23			
			02 10	27.7	3.23			
			222	27.9	3.20			
			224	28.8	3.10			

The studies of the crystal structure of iPP and related disorder phenomena has evidenced to which extent the inclusion of defects inside the crystals controls the polymorphic behavior of iPP, up to drive the crystallization of the chain in a new crystalline form. This occurs in the case of isotactic copolymers of propene with hexene [51–53] or pentene [54, 55]. At comonomer concentration higher than ≈ 10 mol%, indeed, the inclusion of the comonomeric units in the crystals produces increase of density and the random copolymers crystallize in a new form characterized by a trigonal unit cell where the three-fold helical symmetry of the chains is maintained in the crystal lattice [51–55]. Therefore, even though the trigonal form of isotactic propylene-pentene (iPPE) [54, 55] and propylene-hexene (iPPHe) [51–53] random copolymers is not characteristic of iPP as such, it represents the unique tendency of iPP to accommodate chemical “defects” in the crystals, according to original structural response.

Likewise, random copolymers of iPP with long branched comonomers, as 1-octadecene, crystallize at relatively high branches concentrations (3–4 mol% of 1-octadecene) in a solid mesophase [56, 57] which is completely different from the quenched mesophase of iPP, has a different structure and crystallizes even by slow crystallization of branched iPP copolymers from the polymerization solution or from the melt, without quenching (vide infra).

More recently, a new crystalline form of iPP has been also described, named ε form [58]. This form is elusive, as it is obtained only in the case of a stereodeficient (“an-isotactic”) iPP produced with metallocene catalysts [59], and only in a marginal amount, under peculiar crystallization conditions. The sample, indeed, crystallizes namely in the γ form with small amounts of α form, and the new form is nucleated by a crystal-crystal growth transition on parent α phase crystals. It has been argued that it involves the crystallization of only the most stereodeficient portions of chains of the material. Also in this case the chains are characterized by a 3/1 helical conformation. As the stereo-defects are possibly included in the unit cell, the three-fold helices generate a near-irrational helix projection perpendicular to the chain axis, which are packed in an orthorhombic unit cell with $a = 12.50 \text{ \AA}$, $b = 24.60 \text{ \AA}$, and $c = 6.50 \text{ \AA}$, where the length of b -axis is nearly twice the a -axis length ($b \approx 2a$). This results in a low-density metastable crystal structure characterized by a tetragonal-like packing of the chains, which is quite unusual for three-fold helices [58]. As the ε -form has been obtained only in a marginal amount by very slow cooling of thin films, in a stereodeficient iPP crystallizing mainly in the γ form, the crystal structure of the ε -form will not be further discussed here.

2.4 The Crystal Structure of α Form

The α form is generally obtained from melt-crystallization procedures and in drawn fibers [2, 5, 45, 60, 61]. The crystal structure of α form (Fig. 2.5) was firstly proposed by Natta and Corradini [2]. It can be described in terms of a monoclinic unit cell (b unique axis, c chain axis) with parameters $a = 6.65$, $b = 20.96$, $c = 6.50 \text{ \AA}$, $\beta = 99.3^\circ$ (Fig. 2.5b, c), containing four chains. The structure consists of ac layers of isochiral helical chains (all right-handed, R or left-handed, L) alternating along the b -axis with ac layers of helical chains of opposite hand. Couples of adjacent $a - c$ rows (delimited by the vertical dashed lines in Fig. 2.6) form a bilayer of chains $|LR|$ (or $|RL|$) where the helices face each other along b side by side.

The crystalline modifications of α form obtained in the usual crystallization conditions from melt and/or by drawing procedures in oriented fibers are generally disordered [2, 33, 34, 60, 62–64]. Disorder consists in the random positioning of up and down chains (Fig. 2.2) [2, 60]. Isomorphous up and down (anticlinal) chains have a similar external steric hindrance because the methyl groups may assume the same position (Fig. 2.5a). Disorder arises because if isomorphous and anticlinal helices of iPP substitute each other in a site of the lattice, the same steric interactions with neighboring chains are involved. In the ideal *limit ordered model* (defined α_2 form, [61]) $a - c$ rows of chains within a bilayers are related by a glide plane symmetry c , perpendicular to b , and therefore the helices are all isoclinal. The chains belonging to a given bilayer are anticlinal with respect to those belonging to the adjacent bilayers according to the space group $P2_1/c$ (Fig. 2.5b) [61]. The *limit disordered model* (defined α_1 form) [2] corresponds to a statistical distribution of “up” and “down” isomorphous helices (Fig. 2.5c) according to the

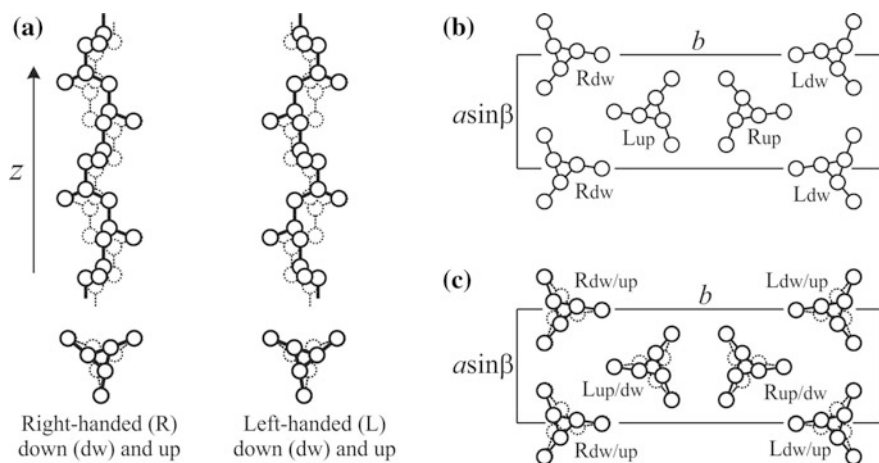


Fig. 2.5 **a** Right-handed (R) and left-handed (L) chains of isotactic polypropylene in 3/1 helical conformation in the down (dw) (continuous lines) and up (dashed lines) orientation. Isomorphous down and up chains (right-handed or left-handed) have the same steric hindrance since the side methyl groups may assume the same positions. **b** Limit-ordered model structure (space group $P2_1/c$) [61] and **c** limit-disordered model structure (space group $C2/c$) [2] of the α form of iPP. (Reprinted with permission from Ref. [13]. Copyright 2006 by the American Chemical Society)

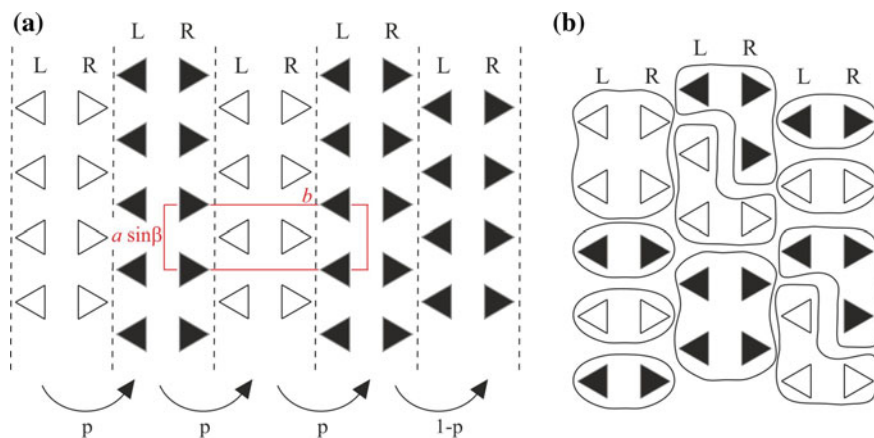


Fig. 2.6 Packing models of right (R) and left (L) handed threefold helices of iPP in modifications of the α form having different degrees of up/down disorder [34]. Up and down chains are indicated with black and white triangles, respectively. **a** Ordered bilayers of chains, composed of enantiomorphous and isoclined chains (all up or all down), succeed along b with a probability p that the chains are anticlined (bilayers of up chains alternate with bilayers of down chains), and with probability $1-p$ that the chains are isoclined. $p = 1$ corresponds to the limit ordered model $P2_1/c$ (α_2 form, Fig. 2.4b). **b** Small clusters of isoclined (all up or down) chains are packed along a and b with equal probability that the neighboring chains are isoclined or anticlined. Reprinted with permission from Ref. [34]. Copyright 2000 by the American Chemical Society

space group symmetry $C2/c$ [2]. Up and down isomorphic chains can substitute each other in each site of the lattice (up/down substitution type disorder).

The real crystalline modifications of α form of iPP may be considered as a continuum of disordered modifications intermediate between the ideal limit disordered α_1 form, corresponding to the space group $C2/c$, and the ideal limit ordered α_2 form, corresponding to the space group $P2_1/c$ [34].

This result emerges from analysis of Bragg reflections and diffuse scattering, found in powder [62–64] and fiber [33, 34, 60] diffraction patterns of iPP samples crystallized and/or annealed in different conditions. The degree of disorder, indeed, depends on the crystallization conditions and the thermal and mechanical history of the samples [34, 62–64] and is indicated by significant variations in the relative intensity of some Bragg reflections in the X-ray diffraction patterns. In particular, well-crystallized [64] or high temperature annealed [62, 63] iPP samples present sharp and narrow hkl reflections with $h + k = 2n + 1$. This indicates that the samples are characterized by a structure close to the limit-ordered form (α_2 form, Fig. 2.5b). For samples crystallized or annealed at low temperatures, such reflections become weak and broad, whereas those with $h + k = 2n$ remain narrow and sharp [62, 63]. When the Bragg hkl reflections with $h + k = 2n + 1$ are completely absent, the structure is close to the limit-disordered (C -centered) form (α_1 form, Fig. 2.5c). Moreover, the diffraction intensity subtending the Bragg reflections (diffuse scattering) increases with increasing degree of disorder and assumes characteristic shapes along the layer lines in oriented samples. The localization of such diffuse scattering on the layer lines is indicative of long-range positional up/down disordering of the chains.

As an example, the X-ray powder diffraction profiles of iPP samples annealed at different temperatures are shown in Fig. 2.7. They show different intensities of hkl reflection with $h + k$ odd [62–64], indicating the presence of variable amount of up/down disorder. The degree of order R has been evaluated from the relative intensities of these specific reflections in the X-ray diffraction pattern (Fig. 2.8) [62, 63], finding that the order parameter R increases with increasing the annealing or melt-crystallization temperature, due to an increase of the order in the up/down positioning of the chains in the lattice position [25, 62–64].

These X-ray diffraction data have suggested a model for the development of the up/down disorder in the crystals of the α form [33, 34]. According to this model, ordered bilayers of threefold helices, composed of enantiomorphous and isoclined chains (all up or all down) follow each other along b with a probability p that the chains are anticlinal (bilayers of up chains alternate with bilayers of down chains), and with probability $1-p$ that the chains are isoclined (Fig. 2.6a). These disordered modifications present up/down disorder, which develops essentially along the b direction [33, 34]. When $p = 1$ there is a regular succession of bilayers with anticlinal chains and the structure corresponds to the limit ordered α_2 form (space group $P2_1/c$, Fig. 2.5b). When $p < 1$ the structure presents defects in the regular alternation along b of anticlinal bilayers (Fig. 2.6a), while the unit cell dimensions and the lattice geometry remain unaltered. For samples crystallized at low temperatures the up/down disorder develops also along the a axis and inside the

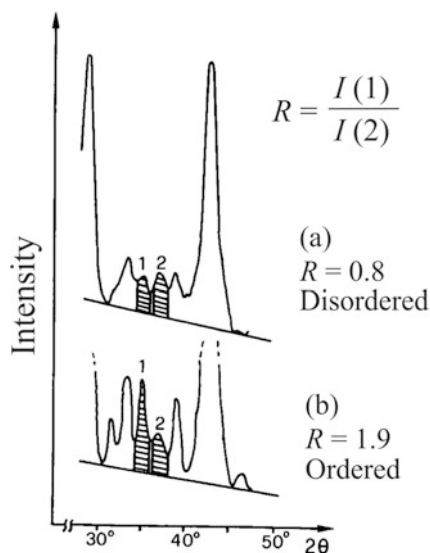


Fig. 2.7 Definition of the up/down order parameter R as the ratio of the intensities of the reflection peaks 1 and 2, present in the X-ray powder diffraction profile of iPP samples at values of 2θ in the range $32\text{--}38^\circ$ [62, 63]. **a** unannealed sample; **b** sample annealed at 167 C . Peak 1 contains mainly the contribution of hkl reflections with $h + k = 2n + 1$, which have low intensities or are extinct for disordered modifications close to the limit disordered model $C2/c$ of Fig. 2.5c, whereas have high intensities for ordered modifications close to the limit ordered model $P2_1/c$ of Fig. 2.5b. Reprinted with permission from Ref. [64]. Copyright 1985 by Elsevier

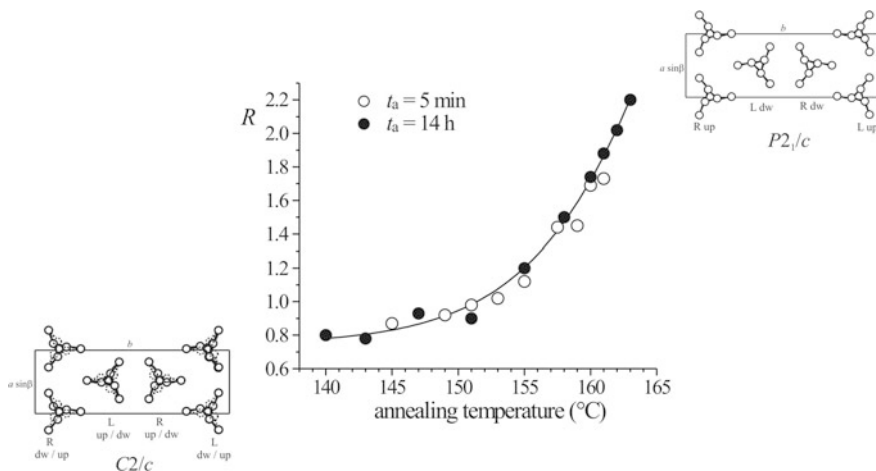


Fig. 2.8 Values of the order parameter R of annealed samples of iPP reported as a function of the annealing temperature for different annealing time t_a [62, 63]. Reprinted with permission from Ref. [11]. Copyright 2014 by Wiley

bilayers, so that only in small clusters of chains the order typical of the bilayers is preserved (Fig. 2.6b) [34].

It is worth noting that the crystal structure of iPP in the α form is an important exception to one of the basic rules of crystallography corresponding to the *entropic principle of conservation of the chain symmetry*. Indeed, the basic rules of crystallography that control the packing mode of chains are the **Principle of Close Packing** and the **Principle of Maximum Entropy** [7, 11]. The **Principle of Close Packing** states that “*macromolecules tend to achieve the closest distance between nonbonded neighboring atoms; this distance is, however, never lower than the sum of their van der Waals radii*”, whereas the **Principle of Maximum Entropy** states that “*a molecule in a crystal tends to maintain part of its symmetry elements, provided that this does not cause a serious loss of density*” [7, 11].

Indeed, since the crystal structure of a molecule must correspond to one of the minima of the free energy surface, the **close packing principle** implies that the *free energy* minima are close to the minima of *internal energy* and, hence, to the minima of the specific volume [7, 11]. Moreover, the **maximum entropy principle** entails that the entropy also determines the mode of packing of molecules, because in a more symmetric position, a molecule has a greater freedom of vibration, that is, the structure corresponds to a wider energy minimum.

Yet, in the case of iPP in the α form, the threefold helical symmetry of the chains is not maintained in the crystal lattice. In fact, the chains, in the 3/1 helical conformation are not packed in trigonal or hexagonal unit cells, maintaining the three-fold symmetry as crystallographic element of symmetry, as instead occurs in the case of isotactic polybutene (iPB) [65] and polystyrene (iPS) [66, 67] in the trigonal forms, because this would produce a crystal lattice with very low density due to the too small side groups (the methyl groups), compared with the ethyl or phenyl groups in iPB or iPS, respectively [7]. The packing of the three-fold helical chains in a monoclinic unit cell, according to the space group $C2/c$ or $P2_1/c$ [7, 60, 61], allows for denser packing (Fig. 2.5, $\rho_c = 0.936 \text{ g/cm}^3$). Therefore, since the local symmetry of the chain conformation is lost in the lattice, the crystal structure of the α form of iPP represents an exception of the *entropic principle of conservation of the chain symmetry* [7, 11].

2.4.1 The Crystal Structure of γ Form

The γ form has been considered a rare crystalline polymorph of iPP for years, until the discovery of metallocene homogeneous catalyst systems for the polymerization of 1-olefins [22, 23]. The iPP samples prepared using heterogeneous Ziegler-Natta catalysts, indeed, under the most common routes, crystallize from the melt in the α form [3–5]. The γ form can be obtained in sufficiently high proportions only under specific conditions. In particular crystallization of pure γ form occurs for high molecular mass Ziegler-Natta iPP only at high pressures (ca. 500 MPa.) [68–72], or at atmospheric pressure in the case of low molecular mass iPP fractions obtained by

pyrolysis or through specific synthesis [73–76], for the stereo-block fractions soluble in low boiling solvents [77] and/or in the case of copolymers containing 5–20 mol% of ethylene or 1-olefins such as 1-butene, 1-octene, etc. [78, 79].

In the case of iPP samples prepared with metallocene catalysts [80], instead, the γ form crystallizes from the melt more easily even at atmospheric pressure and for high molecular weight samples [80–97]. These samples crystallize as mixtures of α and γ form, and the relative amount of γ form increases with increasing the concentration of stereo- and regio-defects introduced along the iPP chains in the polymerization step by each specific catalyst system [81–85, 87–90, 93, 95].

The difference in the polymorphic behavior of iPP samples obtained with heterogeneous and homogeneous catalysts is related to differences in the type and distribution of stereo- and regio-defects, generated by the different kinds of catalytic systems [90]. In fact, the distribution of defects influences the average length of the crystallizable (fully isotactic) sequences. In general, the crystallization of γ form is favored for short isotactic sequences, whereas long regular isotactic sequences generally tend to crystallize in the α form [81–85, 87–90, 93, 95]. For the iPP samples obtained with metallocene catalysts the defects are uniformly distributed along the chains, and the length of fully isotactic sequences is, roughly, inversely proportional to the content of defects. Therefore, even a small concentration of defects reduces the length of the regular isotactic sequences favoring the crystallization of γ form [81–85, 87–90, 93, 95]. For iPP samples prepared with heterogeneous Ziegler-Natta catalysts, instead, the distribution of defects is non-uniform, and large part of the defects is located in a small fraction of poorly crystallizable chains. As a consequence, the fully isotactic sequences are on average much longer, leading to the crystallization of α form even in samples with a relatively high concentration of defects [98–100].

The preferred crystallization in the γ form from short iPP sequences is strictly related to its unique and stunning crystal structure [16, 17]. The crystal structure of the γ form of iPP, indeed, is characterized **by a nonparallel arrangement of the chains** within an orthorhombic unit cell, with axes $a_\gamma = 8.54$ Å, $b_\gamma = 9.93$ Å, $c_\gamma = 42.41$ Å (Fig. 2.9A) [16, 17]. **The nonparallel arrangement of chain axes** in polymer crystals represents a rare example of molecular architecture in the crystals of synthetic polymers [16, 17], and constituted a true breakthrough in polymer crystallography, contradicting one of the main “dogma” **that the chains in a crystal must be parallel** [7, 11].

In the γ form of iPP, the chains, in a 3-fold helical conformation, lie parallel to the diagonals in the a_γ - b_γ plane of the orthorhombic unit cell proposed by Brückner and Meille [16, 17], where the diagonals ($|\mathbf{a}_\gamma + \mathbf{b}_\gamma| = |\mathbf{a}_\gamma - \mathbf{b}_\gamma| = 13.08$ Å) correspond to twice the helical periodicity of ≈ 6.5 Å. The chain axes (along the two diagonals) form an angle of 81.4° , a value which is close to that one formed by chain axes at the interface between branched lamellae of α form (vide infra) [101]. The proposed space group is $Fddd$, in the limit disordered model structure characterized by the random substitution in the same lattice position of coaxial, isomorphous and anticlinal chains, (up/down disorder) and $F2dd$ or $Fd2d$, in the limit ordered model structure, if up/down disorder is absent [16, 17]. The structural

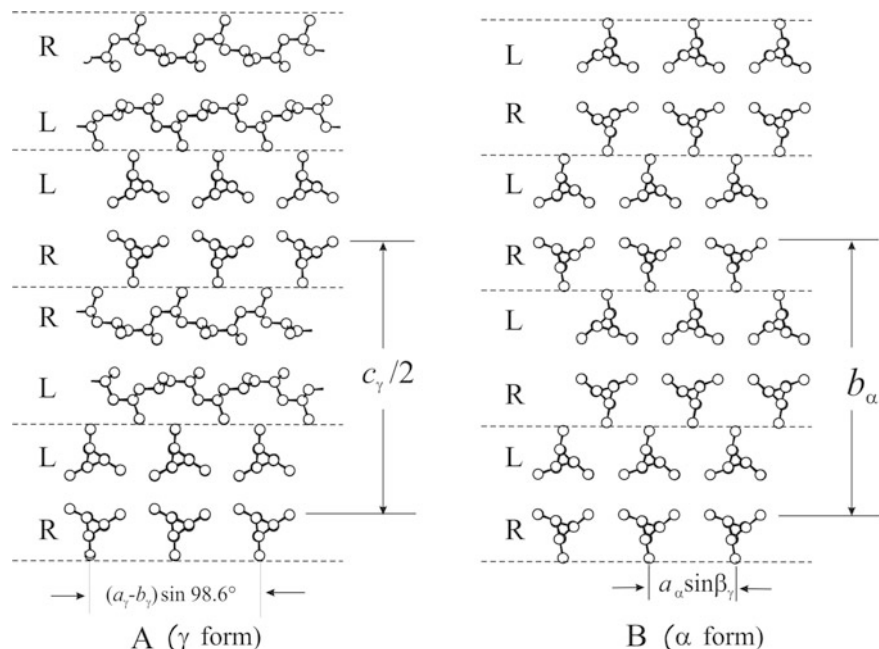


Fig. 2.9 Packing models of threefold helical chains in the γ (A) and α (B) forms of iPP. The dashed lines delimit double layers of chains. The subscripts γ and α identify unit cell parameters of the orthorhombic and monoclinic unit cells of the γ [16, 17] and α forms [2], respectively. R and L identify rows of all right and all left-handed helices, respectively. Coaxial anticlined helices are omitted from the drawing, for clarity. Reprinted with permission from Ref. [87]. Copyright 2002 by the American Chemical Society

model of the γ form of iPP of Fig. 2.9A is drawn in a projection in a plane perpendicular to one diagonal (i.e. $\mathbf{a}_\gamma + \mathbf{b}_\gamma$), to clearly distinguish helices tilted by $\approx 81^\circ$ each other.

The crossing of chain axes in the unit cell of γ form of iPP was confirmed immediately after the structural resolution by Brückner and Meille [16, 17], through electron diffraction analysis of single crystals [18]. It was shown that the electron diffraction patterns obtained by tilting lamellar crystal of iPP in the γ form by $\approx +40^\circ$ or $\approx -40^\circ$, to bring the incident electron beam parallel to the two diagonals of the ab face where the two chain axes are oriented, were identical. This result, not only confirmed the non-parallelism of the chain axes in the γ form of iPP, but also indicated that the chain axes of the stems, instead than parallel, are inclined by $\approx 40^\circ$ to the normal to the lamellar surface (Fig. 2.10) [18].

The packing mode of the helices in the α and γ forms of iPP show several analogies. This is evidenced in Fig. 2.9, where for comparison, the structural model of the α form of iPP is shown (Fig. 2.9B) in a projection in the plane $a_\alpha \sin \beta_\alpha - b_\alpha$ (unit cell parameters $a_\alpha = 6.65 \text{ \AA}$, $b_\alpha = 20.73 \text{ \AA}$, $c_\alpha = 6.50 \text{ \AA}$, $\beta_\alpha = 98.67^\circ$) [86, 87, 96]. In both forms, the chains, in the 3/1 helical conformation (chain

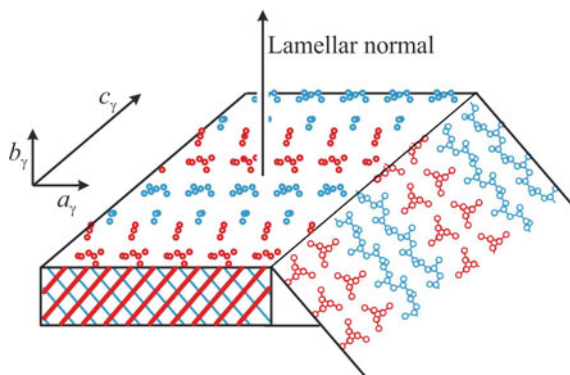


Fig. 2.10 Lamellar crystal of iPP in the γ form showing that the chain axes of the stems (red and blue stripes) instead than parallel are inclined alternatively by $\approx +40^\circ$ and $\approx -40^\circ$ to the normal of basal surface. Reprinted with permission from Ref. [96]. Copyright 2006 by the American Chemical Society

periodicity $\approx 6.5 \text{ \AA}$), are organized to form double layers (delimited by the dashed lines in Fig. 2.9) piled along the b_α axis direction in the α form, along the c_γ axis direction ($c_\gamma \approx 2b_\alpha$) in the γ form. In both crystalline forms, the chains within the bilayers are of opposite chirality, and are related by a glide plane symmetry. Moreover, both forms are characterized by up/down disorder [2, 16, 17, 33, 34, 60],

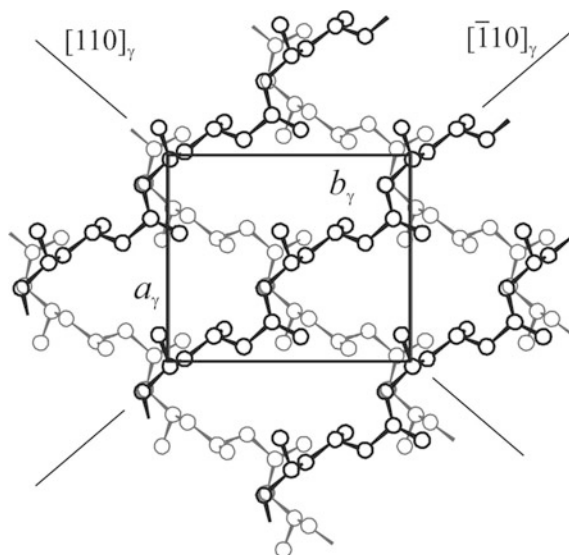


Fig. 2.11 Local arrangement of 3/1 helical chains of iPP in the γ form at the interface between adjacent bilayers entailing a $\approx 80^\circ$ rotation of chain axes between isochiral chains [86]. Reprinted with permission from Ref. [86]. Copyright 2001 by the American Chemical Society

but while in the α form the chains are all parallel to the c_α -axis (Fig. 2.9B) [2], in the γ form the double layers succeed along c_γ with the chain axis tilted by 81° (Fig. 2.9A) [16–18], that is, they are oriented alternatively along the $[110]$ and $[\bar{1}10]$ diagonal directions forming an angle of 98.6° (or 81.4°), which is nearly coincident with β_α of α form (Fig. 2.11). It is worth noting that the $\approx 80^\circ$ tilt between adjacent bilayers is a feature of the regular crystallographic structure of γ form and is also at the basis of the geometrical relationships that governs the homoepitaxy (lamellar branching) of crystals in the α form (Fig. 2.12) [101–103]. In particular, in the γ form, as well as at the interface between the branched lamellae of α form, consecutive bilayers of chains are faced through isomorphous chains. Therefore whereas in the α form consecutive bilayers of chains follow each other with a strict alternation of helical hands according to the sequence $|LR|LR|LR|\dots$ (Fig. 2.8) [2], lamellar branching, with the $\approx 80^\circ$ (or 100°) change in the chain orientation, entails that this alternation is not respected, leading to a succession of consecutive bilayers of the kind $|LR|\mathbf{LR}|\mathbf{RL}|\mathbf{RL}|\mathbf{RL}|\dots$ [101–103]. In the case of γ form, the $\approx 80^\circ$ (or 100°) change in the chain orientation occurs systematically at any bilayer interface, leading to sequences of helical hands of the kind $|LR|\mathbf{RL}|\mathbf{LR}|\mathbf{RL}|\mathbf{LR}|\dots$ [16, 17].

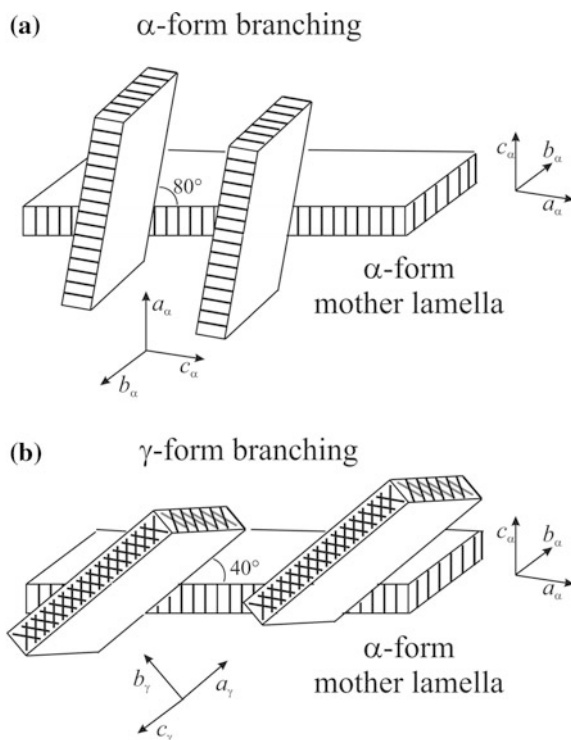


Fig. 2.12 Scheme of branching α lamellae on α lamellae (a) and γ lamellae on α lamellae (b) of iPP. Reprinted with permission from Ref. [96]. Copyright 2006 by the American Chemical Society

The epitaxial relationships of α - α lamellar branching consists in the contact between the $(010)_\alpha$ planes of mother and daughter lamellae and corresponds to a strict parallelism of $(a_\alpha)_1$ and $(c_\alpha)_1$ axes of a mother lamella with the $(c_\alpha)_2$ and $(a_\alpha)_2$ axes, respectively, of the daughter lamella, and common b_α axis (Fig. 2.12a) [101–103]. It is worth noting that the key of the lamellar branching in the α form of iPP lies in the near-identity of the dimensions of a_α and c_α axes, $a_\alpha = 6.65 \text{ \AA}$, $c_\alpha = 6.50 \text{ \AA}$, for which the daughter lamella tends to grow with the c_α axis aligned to the a_α axis of the substrate lamella (Fig. 2.12a) [101–103]. This explains the experimental observation that mother and daughter lamellae are oriented at an angle of $\approx 80^\circ$ to each other, identical to the complement of the angle $\beta_\alpha = 99.67^\circ$ between the a_α and c_α axes of the monoclinic unit cell of the α form of iPP.

The lamellar branching leading to the growth of α lamellae on parent lamellae of α form (α -to- α epitaxy) is not the only case of homoepitaxy in iPP. Due to the structural analogies of α and γ forms of iPP a second kind of homoepitaxy in iPP is the epitaxial growth of γ form on parent lamellae of α form (α - γ epitaxy) [102], illustrated in Fig. 2.12b.

The contact plane for homoepitaxy is the $[010]_\alpha$ plane for lamellae of the α form and the $[001]_\gamma$ plane for lamellae of the γ form [101] (Fig. 2.12b). Therefore, the b_α and c_γ axes of lamellae of α and γ forms, respectively, coincide (Fig. 2.12b). The crystallographic relationships at the contact face between the crystals of α and γ forms corresponds to a parallelism of a_α and c_α axes of lamellae of α form with the diagonals ($\mathbf{a}_\gamma + \mathbf{b}_\gamma$ and $\mathbf{a}_\gamma - \mathbf{b}_\gamma$) of the orthorhombic unit cell of γ form. Therefore, also in this case, the key of α -to- γ lamellar branching is of structural origin [102], and lies in the non-parallel arrangement of chain axes of γ form, running along the diagonal of the orthorhombic unit cell at an angle of $\approx 80^\circ$, identical to the complement of angle β_α of 99.67° of the monoclinic unit cell of iPP in the α form.

2.4.2 Structural Disorder of γ Form of iPP

The large number of studies performed so far on metallocene-made iPP samples, characterized by a truly random distribution of defects have evidenced that the γ form of iPP is thermodynamically more stable than α form in stereodeficient iPP samples and develops mainly by slow crystallizations at high temperatures [83, 87, 90]. As an example, the X-ray diffraction profiles of iPP samples containing different concentrations of a stereo-defects, isothermally crystallized from the melt at different temperatures, are reported in the Fig. 2.13 [90]. They crystallize as mixtures of α and γ forms as indicated by the presence of the $(130)_\alpha$ reflection of the α form at $2\theta = 18.6^\circ$, and of the $(117)_\gamma$ reflection of the γ form at $2\theta = 20.1^\circ$. The relative amount of crystals of γ form increases with increasing the crystallization temperature and concentration of rr stereodeficient. However, the low relative intensities of the $(130)_\alpha$ and $(117)_\gamma$ reflections and in some cases the absence of both reflections, in

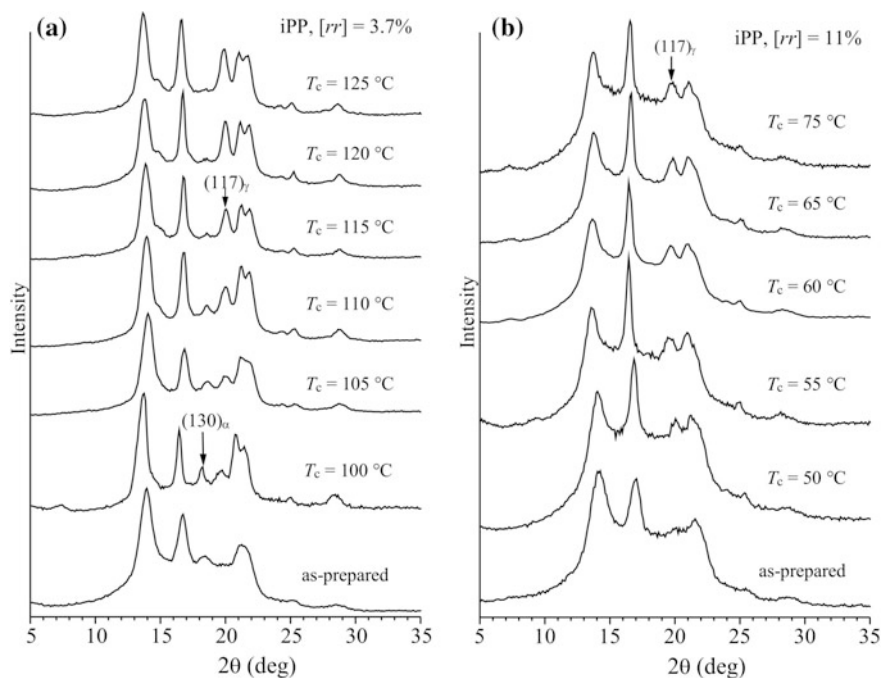


Fig. 2.13 X-ray powder diffraction profiles of samples of iPP prepared with different metallocene catalysts and containing only *rr* stereodefects in concentration of 3.7 (a) and 11 mol% (b), isothermally crystallized from the melt at the indicated temperature (T_c). The “as-prepared” samples correspond to the samples rapidly crystallized from the polymerization solution [90]. Reproduced with permission from Ref. [90]. Copyright 2004 by the American Chemical Society

particular at low crystallization temperatures, and the presence of diffuse haloes, cannot be explained by assuming a simple mixture of crystals of α and γ form of Fig. 2.9. Indeed, the γ form obtained in these samples always present structural disorder [86–90, 95, 96].

These samples, indeed, crystallize from the melt in disordered modifications having structures intermediate between the two ideal limit ordered models of the α and γ forms of Fig. 2.9 [86–90, 95, 96]. The proposed model of disorder is reported in Fig. 2.14 [86–90]. Disorder consists in the statistical succession along the b_α (c_γ) axis direction of double layers of chains with the chain axes either parallel (like in the α form) or nearly perpendicular (like in the γ form). Therefore, inside the same crystalline domain, local arrangements of the double layers of chains, piled along the b_α (c_γ) axis, typical of the α form (with parallel chains) and typical of the γ form (with chains nearly perpendicular) are present [86–90, 95, 96]. The degree of disorder characterizing the structure depends on the concentration of defects and the crystallization temperature [87–90, 95, 96], and for stretched samples, on the draw ratio [86, 91–97].

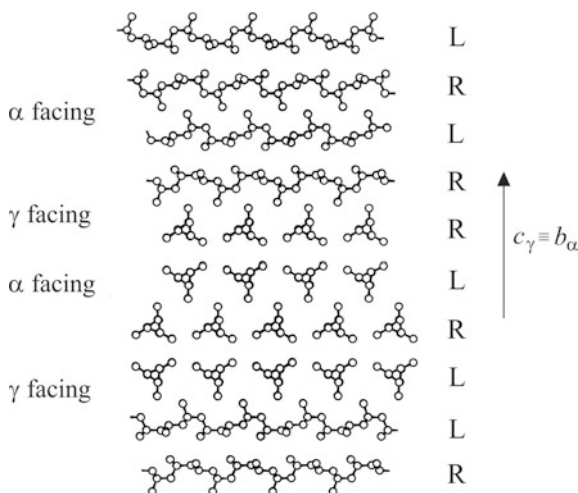


Fig. 2.14 Model of α/γ disorder occurring in the disordered modifications of iPP intermediate between α and γ forms [86, 87]. Consecutive $a_\gamma b_\gamma$ ($a_\alpha c_\alpha$) bilayers of chains are stacked along c_γ (b_α) with the chain axes either parallel or nearly perpendicular. R and L identify rows of all right- and all left-handed helices, respectively. Reprinted with permission from Ref. [87]. Copyright 2002 by the American Chemical Society

It is worth noting that the crystallization of disordered modifications of the γ form of the type of Fig. 2.14 explains the observation that the melting temperature of γ form is always lower than that of the α form [90, 104], even though the packing energy of α and γ form is identical [105].

2.4.3 Crystal Structure of β Form

The β form of iPP can be obtained often in mixture with α form by crystallization in a temperature gradient [106, 107], from sheared [108, 109] or strained melt [110] or in presence of selective β -nucleating agents [111–113] as for instance γ -quinacridone [114], di-sodium orthophthalate [115], pimelic acid/calcium stearate [116] or even polymeric species such as poly(trimethyl allyl silyl) [117, 118]. In general, the β form crystallizes in mixture with α form, and the most convenient and reliable method to obtain iPP with high content of β form is the addition of specific nucleating agents, often in combination with some other route [111–113].

The β form of iPP is less stable and shows a melting temperature (≈ 155 °C) lower than α form (≈ 170 °C) [111–113, 119, 120]. In general, the condition of formation of β form are rather demanding, since spontaneous nucleation occurs more easily for the α than for the β form [101–113]. Indeed, even in presence of nucleating agents, it can be obtained only in a restricted range of temperatures,

corresponding to ≈ 100 – 141 °C interval, that is at temperatures for which the growth rate of β crystals is higher than that of α form [121–125]. Outside this critical temperature range the growth rate of α form is higher than that of β form. This singular behavior of kinetics re-entrance [124] is unique in polymer science, and entails a β to α transition at temperatures lower and higher than the critical values of ≈ 100 and ≈ 141 °C, respectively [109, 112, 125–127]. During the β to α transition, the α form is nucleated at the growth front of the crystals in the β form, leading to spherulites with a core region of β form, surrounded by an overgrowth of crystals in the α form [109, 112, 125–127].

Also the melting behavior of β form is peculiar, as during heating the crystals of β form, tend first to melt and then immediately to recrystallize in the α form [128–130]. It has been demonstrated that the β to α melting/recrystallization process becomes minimal in samples crystallized almost completely into the β form at a temperature intermediate between ≈ 100 and ≈ 141 °C, provided that it is not cooled below the lower critical temperature of ≈ 100 °C [112, 131–133].

The crystal structure of the metastable β form of iPP has been puzzling the polymer science community for years. It was first observed in 1959 [134] but its crystal structure has been solved only in 1994 [18–21], from two independent groups, almost simultaneously, resorting to the analysis of electron diffraction

Fig. 2.15 Electron diffraction pattern of hexagonal single crystals of β form of iPP. The indicated $hk0$ reflections are indexed on the basis of the trigonal unit cell with axes $a = b = 11.03$ Å and $c = 6.5$ Å [21]. Reproduced with permission from Ref. [21]. Copyright 1994 by the American Chemical Society

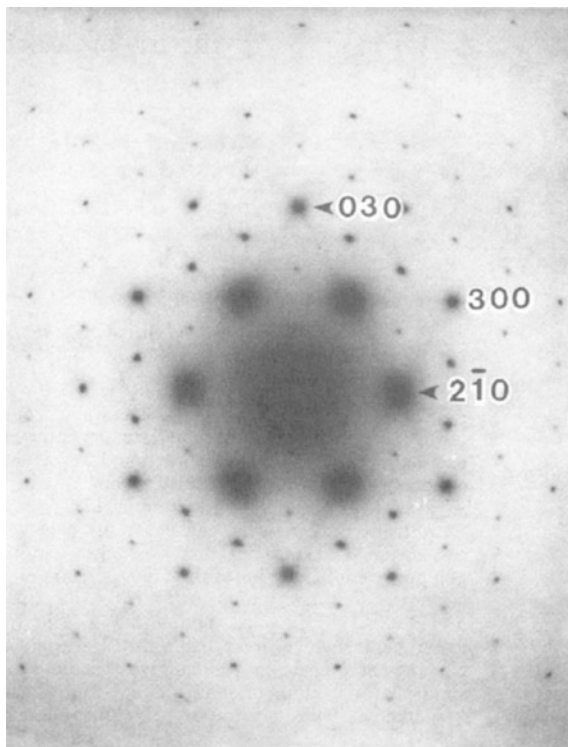
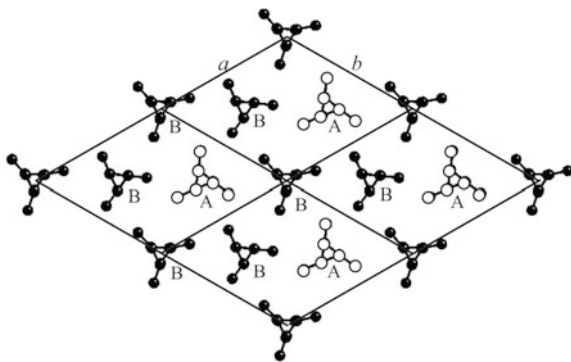


Fig. 2.16 Model of packing of the chains in the β form of iPP [18–21]. Chains B (black balls) have nearly the same orientation around the chain axis, different from that of the chains A (white balls)



patterns from single crystals (Fig. 2.15). Indeed, the β form show X-ray powder diffraction profiles with only few reflections (Fig. 2.4c), and cannot be obtained in oriented fibers, since it is mechanically unstable, and transforms into the α form by effect of stretching [135].

On the basis of electron diffraction analysis the packing model of β form, reported in Fig. 2.16, corresponds to a trigonal unit cell with $a = b = 11.03 \text{ \AA}$ and $c = 6.5 \text{ \AA}$, contains three isochiral threefold chains having different azimuthal settings (and shift along z) and packed according to the space group $P3_1$, if the chains are right-handed, $P3_2$ if they are left-handed. It represents the first example of **frustrated structure** [18–21].

Indeed, as shown in Fig. 2.16, the chains have different azimuthal setting in the unit-cell. Frustration arises because the crystallographic environment of two chains is different from that of the third chain. In particular, it is apparent that the chain A is surrounded by six nearly equivalent chains (chains B), while the other two chains (chains B) are surrounded by three chains having a given azimuthal orientation (chains A) and three other chains having a different orientation (chains B). Therefore, it is possible to consider that two chains experience strong interactions with the neighbors, whereas the third chain interacts weakly with the neighboring chains [18–21]. More precisely, chains B of Fig. 2.16 create a sort of *honeycomb* lattice, as they are involved in favorable helix-helix interactions. This leaves aside the chains A located at the center of each “cell” of the honeycomb (Fig. 2.16), which are *frustrated* since they must adapt to a less favorable environment due to the different azimuthal setting (and/or different shift along the chain axis) [18–20]. This scheme creates the three-chain unit-cell and establishes its frustrated character.

2.4.4 Mesomorphic Form of iPP

The mesomorphic form of iPP may be obtained through fast cooling procedures of the melt in cold water [46, 136–164]. It is a metastable solid mesophase, which transforms into the stable α form by annealing at elevated temperatures

[46, 150–157]. The degree of transformation reaches a saturation level which depends on the annealing temperature and becomes almost complete at 140–150 °C [165, 166]. Furthermore, the saturation requires amounts of time which decreases with increase of the annealing temperature.

In general, the mesophase develops from the melt at temperatures between about 27 °C and the glass transition (T_g) temperature (≈ -23 °C) [138, 141, 148, 149] at cooling rates high enough to prevent the crystallization of the more stable α form, achieved either in ballistic conditions (quench) or using controlled cooling rates. Typical cooling rates must be in the range 100–1000 °C/s. Cooling to a temperature lower than the glass transition faster than 1000 °C/s even inhibits mesophase formation, with formation of amorphous glass [140–142]. The mesophase, however, may be obtained by cold crystallization on subsequent heating of the amorphous glass [140, 142], at a rate not higher than $\approx 10^4$ °C/s. The cooling of the melt at rates higher than 1000 °C/s to temperatures lower than the glass transition, or the heating of the amorphous glass from temperature lower than T_g with rates higher than 10^4 °C/s, prevents all ordering processes, so that neither the α form, nor the mesophase are formed.

X-ray powder diffraction profiles of the mesomorphic form of iPP are shown in Figs. 2.4d and 2.17a. They present strong and broad reflections at $2\theta \approx 15$ and 21° [45–50]. By stretching unoriented films of iPP in the mesomorphic form, oriented fibers are obtained [46, 48–50], showing X-ray fiber diffraction patterns of the kind reported in Fig. 2.17b. It is apparent that the reflections at $2\theta \approx 15$ and 21° become polarized on the equator and on a well-defined layer line, respectively, indicating that the chain periodicity of iPP in the mesomorphic form corresponds to 6.5 Å, as in the crystalline α form [46, 48].

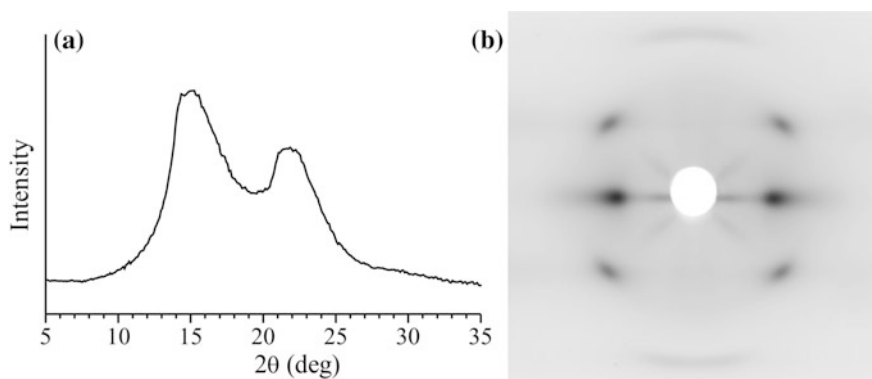


Fig. 2.17 X-ray powder diffraction profile (a) and X-ray fiber diffraction pattern of the mesomorphic form of iPP (b). The powder sample has been obtained by quenching the melt of a iPP sample in cold water, and the fiber specimens have been obtained by stretching at room temperature the unoriented quenched film. Reprinted with permission from Ref. [11]. Copyright 2014 by Wiley

Oriented fiber of iPP in the mesomorphic form can be obtained also by stretching at high deformations samples of iPP crystallized in the α or γ forms [90, 92, 94, 95, 167, 168] or copolymers of iPP with different comonomeric units (as butene, hexene, octene etc.) [52, 56, 169, 170]. It has been suggested that this transformation occurs through the destruction of the lamellar crystalline phase, probably by pulling chains out from crystals and successive re-organization of the chains in the crystalline mesomorphic aggregates [168].

The analysis of diffraction data [48–50, 167] (Fig. 2.17) and of the results obtained using additional techniques such as infrared spectroscopy [46] indicate that the mesophase of iPP is composed of bundles of parallel chains in the ordered three-fold helical conformation, as in the α form [2, 48–50]. In the small mesomorphic aggregates long range order is maintained only along the chain axes because of the ordered chain conformation, whereas large amounts of disorder in the lateral packing of the chains is present [2, 48–50]. In particular, the comparison of the results of Fourier transform calculations performed for various disordered models with the experimental X-ray diffraction patterns, as reported in Refs. [48, 49], suggest that some kind of short range order (SRO) in the relative arrangement of the chains inside the small mesomorphic aggregates is maintained. A possible structural model for bundles of chains in the mesomorphic form of iPP emerging from the analysis of Refs. [48, 49] is shown in Fig. 2.18. SRO consists in the facing of close neighboring enantiomorphic chains similar to that characterizing the crystal structure of the monoclinic α form. However, correlation about the relative position of the atoms is lost at distances higher than 30–40 Å [48]. The metastable disordered quenched crystalline form of iPP is, therefore, *a solid mesophase* characterized by long range periodicity along one direction only, that is along the chain axes, due to the presence of chains in an ordered 3/1 helical conformation, and lateral disorder in the packing of the chains.

2.4.5 Crystal Structure of the Trigonal Form of iPP

As stated in the preceding paragraph, the crystal structure of α form of isotactic polypropylene (iPP) (Fig. 2.5) does not comply with the possible rule of maintaining the threefold helical symmetry of the chains in the crystal lattice (**Principle of Maximum Entropy**) [2]. In fact, chains of iPP assume the stable 3/1 helical conformation but they are not packed in trigonal or hexagonal unit cells, maintaining the three-fold symmetry as crystallographic symmetry, but are instead packed in a monoclinic unit cell [2]. This is because the loss of the local symmetry of the chain conformation in the lattice, allows for denser packing [7]. The crystal structure of the α form of iPP has been considered for long time an exception of the *entropic principle of conservation of the chain symmetry* [7, 11, 12].

Recently, it has been shown [51–55] that random isotactic copolymers of propylene with pentene or hexene crystallize in a new form, characterized by a trigonal unit cell where the comonomeric units are included producing increase of

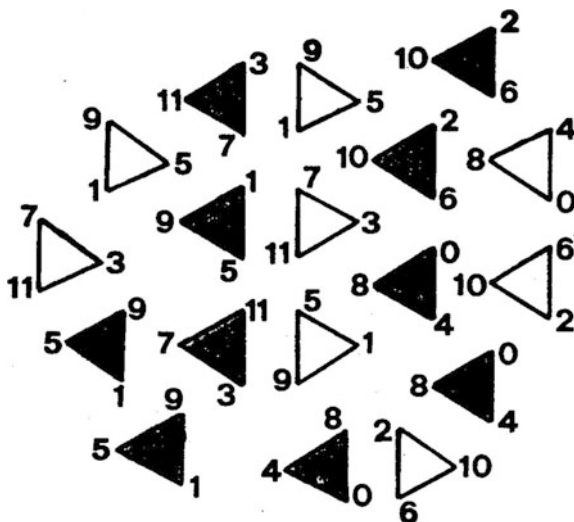


Fig. 2.18 A model of disordered packing of the chains of iPP in the mesomorphic form [48]. The chains in the ordered three-fold helical conformation are arranged in small aggregates characterized by local correlations similar to those of the α form. In the core of the bundles the chains are arranged as in the α form with the typical facing of enantiomorphous 3/1 helical chains. These correlations are lost at distances higher than 30–40 Å [48]. Clear and dark triangles indicate enantiomorphous chains. The height of the methyl groups, which project on the vertices of the triangles, are expressed in $c/12$ units ($c = 6.5$ Å). Reprinted with permission from Ref. [48]. Copyright 1986 by the American Chemical Society

density while maintain the three-fold helical symmetry in the crystal lattice [51, 52, 54, 55]. The structure of isotactic propylene-pentene (iPPe) [54, 55] and propylene-hexene (iPPHe) [51–53, 171] random copolymers are the best examples for the demonstration of the general principle of *density* (or *entropy*)-driven phase formation in polymers [51, 52, 54, 55].

The X-ray powder diffraction profiles of selected samples of iPPe [54, 55] and iPPHe [51, 52] random copolymers prepared using single-site metallocene catalysts are reported in Fig. 2.19. They are compared with those of samples of iPP and iPB homopolymers.

It is apparent that the copolymers crystallize in the α form of iPP up to a concentration of comonomeric units (pentene or hexene) of nearly 10 mol% (profiles a–c of Fig. 2.19a and b, c of Fig. 2.19b). The Bragg distance of 110 and 040 reflections (at $2\theta = 14$ and 16.8° , respectively in the α form of iPP) slightly increase with increasing comonomer concentration, indicating increase of a and b axes of the monoclinic unit cell of the α form (Fig. 2.20a) [52, 54, 55]. This indicates inclusion of pentene or hexene units in the crystals of α form of iPP.

At comonomer concentrations of 9–10 mol% an additional reflection at $2\theta = 10.2^\circ$ appears in the X-ray diffraction profiles (Fig. 2.19) and for higher comonomer contents the X-ray diffraction profile totally changes, the main

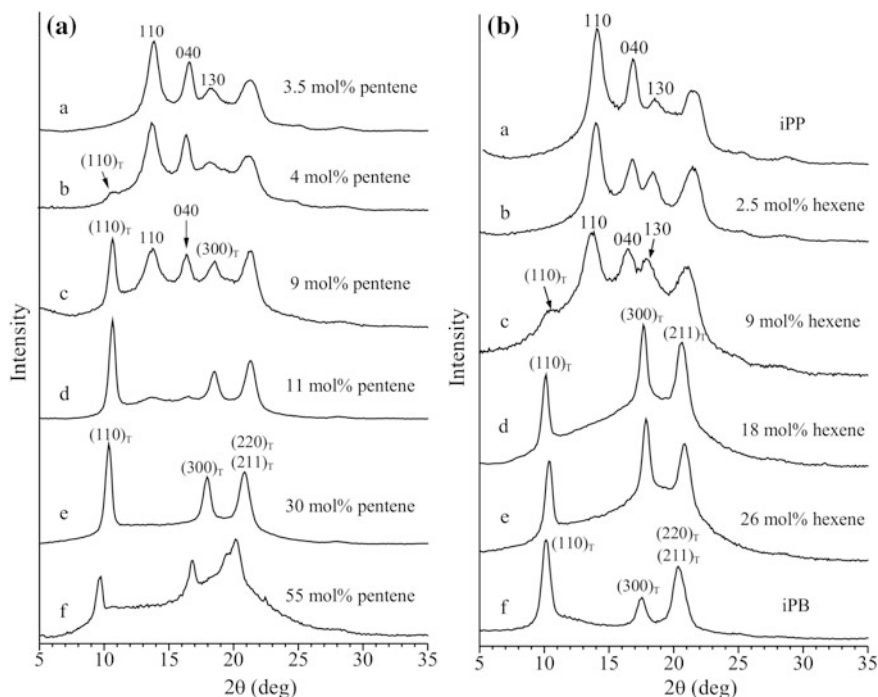
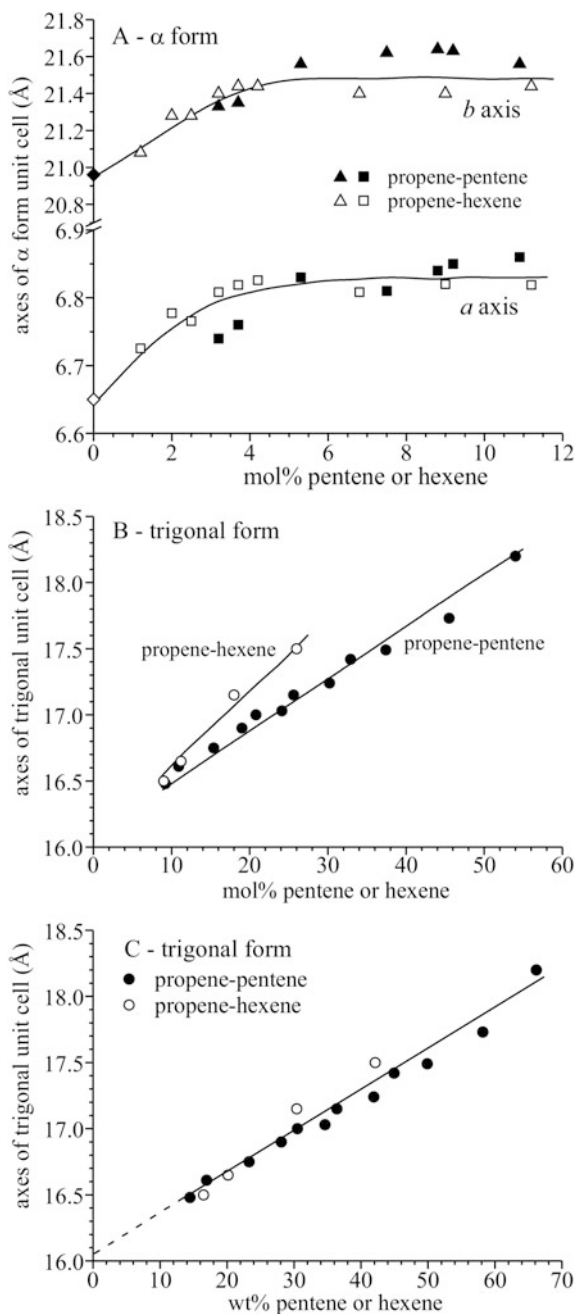


Fig. 2.19 X-ray powder diffraction profiles of samples of isotactic random copolymers of propylene with pentene (a) [55] and hexene (b) [51, 52] having the indicated concentration of comonomeric units, in comparison with those of α form of iPP and form I of iPB. The 110, 040 and 130 reflection of the α form of iPP and the $(110)_T$, $(300)_T$ and $(220 + 211)_T$ reflections of the trigonal form I of iPB are indicated. Reproduced with permission from Ref. [54] (a) and Ref. [51] (b). Copyright 2007 (a) and 2006 (b) by the American Chemical Society

reflections being at $2\theta \approx 10, 17$ and 20° (profiles d–f of Fig. 2.19a and d, e of Fig. 2.19b), and becomes equal to the diffraction profile of form I of iPB (profile f of Fig. 2.19b). This indicates that for these pentene or hexene concentrations the copolymer samples crystallize in a new crystalline form similar to the structure of form I of iPB [51–55]. The modified chains of iPP in 3/1 helical conformation, incorporating pentene or hexene comonomeric units, are packed in a trigonal unit cell according to the space group $R3c$ or $R\bar{3}c$ [51–55], as in the cases of form I of iPB [65]. Pentene and hexene units are included in the crystals of the α form at low concentration and in the crystals of the trigonal form at high concentration (Fig. 2.20A, B) and, in particular, the change of the crystal habit at comonomer contents higher than 10 mol% allows a nearly complete accommodation of pentene and hexene units in the crystal lattice of the trigonal form (Fig. 2.20B). This produces a strong increase of the crystal density that approaches that of crystals of form I of iPB [65].

Fig. 2.20 Values of a (filled square, open square) and b (filled triangle, open triangle) axes of the monoclinic unit cell of the α form of iPP (A) and values of $a = b$ axes (filled circle, open circle) of the unit cell of the trigonal form (B) that crystallizes in as-prepared samples of iPPe (full symbols) and iPPHe (empty symbols) copolymers as a function of mol% (A, B) and wt% (C) of comonomeric units [51, 52, 54, 55]. The values of a and b axes (filled diamond, open diamond) of α form of iPP homopolymer are also reported [2].

(A) Reproduced with permission from Ref. [55]. Copyright 2012 by the American Chemical Society



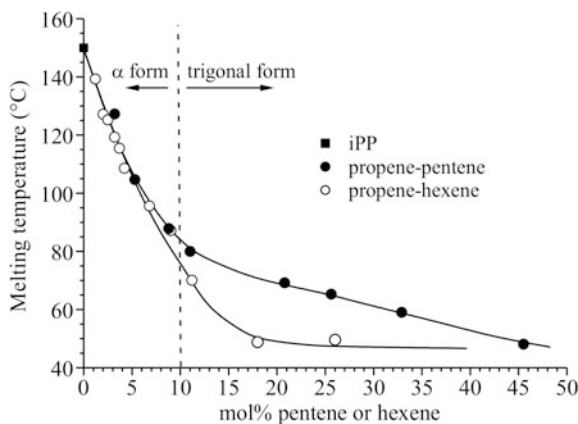


Fig. 2.21 Melting temperature of samples of iPPe (filled circle) and iPPHe (open circle) copolymers as a function of comonomer (pentene or hexene) concentration [51, 52, 54, 55]. The melting temperature of the iPP homopolymer sample prepared with the same catalyst is also reported (filled square). Reproduced with permission from Ref. [55]. Copyright 2012 by the American Chemical Society

This is also confirmed by data of melting temperature and degree of crystallinity of copolymers. The melting temperatures of samples of iPPe and iPPHe copolymers are reported in Fig. 2.21 as a function of comonomer concentration. The decrease of melting temperature (and of crystallinity) with increasing hexene or pentene content is fast up to 8–9 mol%, then becomes slower for higher comonomer concentration. This is in agreement with the hypothesis that hexene and pentene units are partially included in the crystals of α form for low concentrations and act as a lattice defect, producing large disturbance of the crystalline lattice and a consequent decrease of melting temperature, melting enthalpy and crystallinity. For concentrations higher than 9–10 mol%, larger amount of hexene and pentene units are more easily accommodated in the crystalline lattice of the trigonal form producing a lower decrease of crystallinity and melting temperature [55].

The values of a and b axes of the trigonal unit cell depend on the comonomer concentration (Fig. 2.20B), and increase with increasing comonomer content, approaching the values of the axes of the unit cell of form I of iPB ($a = b = 17.7 \text{ \AA}$) [65] for high comonomer concentrations (higher than 50–55 mol% for iPPe copolymers), when the average composition of the copolymers approaches that of iPB [51, 52, 54, 55].

The data of Fig. 2.20B seem to indicate that the extent of lattice expansion depends on the size of the substituent. In fact, at a given molar composition the values of $a = b$ axes of the trigonal unit cell are larger for the iPPHe copolymers than for those of iPPe copolymers (Fig. 2.20B), according with the hypothesis of inclusion of comonomeric units into the crystal lattice. However, the values of unit cell axes of the trigonal form of iPPHe and iPPe copolymers are almost fitted by a single master line if the data are reported as a function of comonomer concentration

expressed as wt% of hexene or pentene units (Fig. 2.20C) [55]. Therefore, at the same mass comonomer composition the dimensions of the trigonal unit cell are the same for pentene or hexene comonomers. This still indicates that the crystallization of the trigonal form and the unit cell dimensions are only driven by the density [51, 52, 54, 55]. When the crystal density is sufficiently high (ca. 0.89 g/cm^3), at around 10 mol% of hexene or pentene, the trigonal form can crystallize.

The extrapolation of the master line to zero comonomer composition (dashed line in Fig. 2.20C) gives the values of the axes of the unit cell of the hypothetical trigonal form of the iPP homopolymer $a = b = 16.05 \text{ \AA}$ [55]. These values would correspond to a theoretical density of crystals of the trigonal form of iPP of 0.865 g/cm^3 that is too low to allow crystallization of the trigonal form for the iPP homopolymer, and is definitely lower than the crystalline density of 0.936 g/cm^3 of the monoclinic crystals of α form [65].

Therefore, when propene and pentene units or propene and hexene units are randomly blended along the same macromolecules and the average overall composition of the two comonomers approaches that of butene ($\approx 50\% \text{C}_3\text{H}_6 + \approx 50\% \text{C}_5\text{H}_{10} = \text{C}_4\text{H}_8$), copolymer chains behave as poly(butene) macromolecules and crystallize into the stable form I of iPB, provided that the distribution of the comonomer is random [51, 52, 54, 55]. Models of the crystal structures of the trigonal form that crystallize in iPPe and iPPHe copolymers, according to the space group $R3c$, are shown in Fig. 2.22. The increase of crystalline density due to the comonomer inclusion into the unit cell allows the crystallization of the three-fold helical chains of iPP in a trigonal unit cell, where the helical symmetry of the chains is maintained in the crystal lattice and coincides with the crystallographic three-fold axes, as predicted by the *entropic principle of conservation of the chain symmetry* [7, 11, 12]. This form does not crystallize and has never been observed so far for the iPP homopolymer because, in the absence of bulky side groups, it would have a too low density [7]. Almost fifty years after the resolution of the crystal structure of α form of iPP and the enunciation of general principles of polymer crystallography [2, 7], it has been shown that iPP is no longer an exception but the structure of propylene-pentene and propylene-hexene copolymers represents the fulfilment of these principles and indicates that the packing of polymer molecules is mainly driven by density and guided by the entropy principle of maintaining the chain symmetry (*principle of density (entropy)-driven phase formation in polymers*) [51, 52, 54, 55].

2.4.6 The “New Mesomorphic” Form in Copolymers of Isotactic Polypropylene with Branched Comonomers

The crystallization of random copolymers of iPP with long branched comonomers such as 1-octadecene (C18), at C18 concentrations of 3–4 mol% in a solid

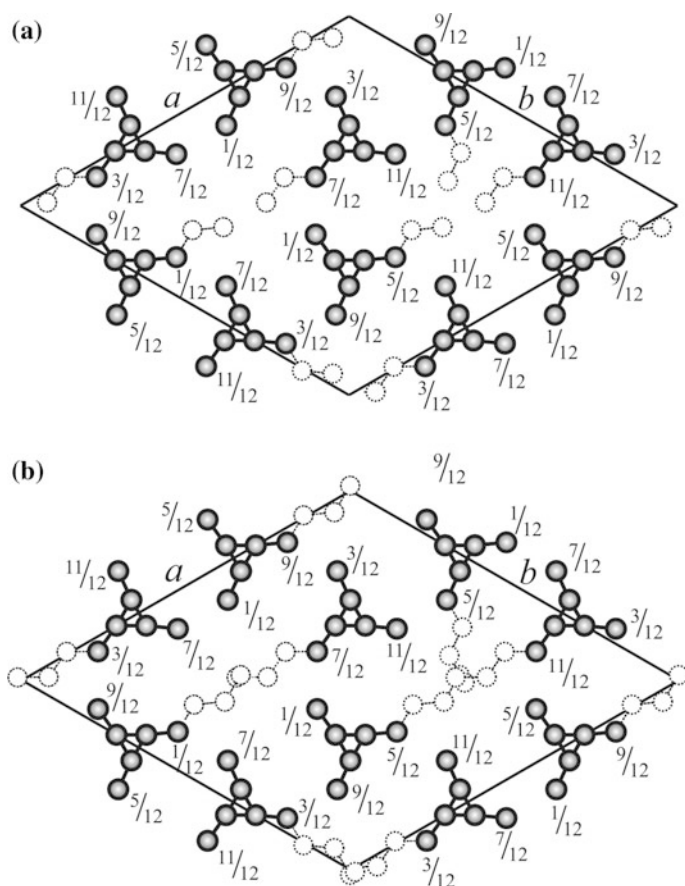
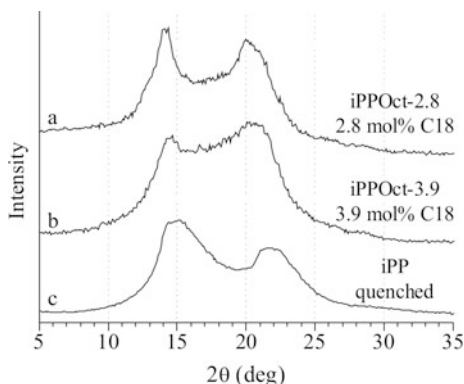


Fig. 2.22 Models of the crystal structures of the trigonal form of iPP in the space groups $R3c$ found in propylene-pentene (a) [54, 55] and propylene-hexene (b) [51, 52] copolymers. The atoms of ethyl and propyl side groups of pentene or hexene comonomeric units, randomly distributed along each iPP chain, are shown as thin dotted lines. Reproduced with permission from Refs. [54] (a) and [51] (b). Copyright 2007 (a) and 2006 (b) by the American Chemical Society

mesophase [56] which is completely different from the quenched mesophase of iPP discussed in the previous section represents a further example of the “resilient” attitude of iPP to adapt the relative arrangement of the $3/1$ helices (the building blocks) up to form a new crystalline polymorph characterized by a high level of inclusion of defects inside the crystals, while maximizing the entropy at minimum cost of internal energy.

The X-ray powder diffraction profiles of as-polymerized samples of propylene-octadecene (iPPOct) copolymers with 2.8 and 3.9 mol% of C18 are reported in Fig. 2.23. For comparison, the diffraction profile of the quenched mesophase of iPP homopolymer is also reported. The diffraction profiles of the

Fig. 2.23 X-ray powder diffraction profiles of as-prepared samples of iPPOct copolymers with the indicated 1-octadecene (C18) concentration compared with the powder diffraction profile of iPP homopolymer sample in the quenched mesomorphic form (profile c) [56]. Adapted with permission from Ref. [56]. Copyright 2010 by the American Chemical Society



iPPOct copolymers with 2.8 and 3.9 mol% of C18 (profiles a and b of Fig. 2.23) show only two broad peaks at $2\theta = 14$ and 20° , indicating that for these octadecene concentrations iPPOct copolymers crystallize in a highly disordered crystalline mesomorphic form [56]. The diffraction profiles of the mesophase of iPPOct copolymers are similar to that of the quenched solid mesophase of iPP (Fig. 2.23c). However, the 2θ positions of the diffraction peaks of the mesophase of the copolymer samples ($2\theta = 14$ and 20°) are different from those of the iPP mesophase ($2\theta = 15$ and 21.3°).

These structural differences are better evidenced by comparing the X-ray fiber diffraction patterns, and the corresponding equatorial diffraction profiles, of the mesophase of iPP (Fig. 2.24a'), obtained by stretching films of iPP homopolymer in the quenched mesomorphic form [48, 50] and of the mesophase of iPPOct copolymers (Fig. 2.24b'), obtained by stretching compression-molded films of the sample iPPOct-3.9 with 3.9 mol% of octadecene [56].

As discussed in the previous section, the two broad reflections observed at $2\theta = 15^\circ$ ($d = 5.88 \text{ \AA}$) and 21.3° ($d = 4.17 \text{ \AA}$) in the powder diffraction profile of the iPP mesophase (Fig. 2.23c) are in the fiber diffraction pattern confined along different layer lines (Fig. 2.24a). The reflection at $2\theta = 15^\circ$ is an equatorial reflection ($l = 0$), whereas the reflection peak at $2\theta = 21.3^\circ$ corresponds to a first layer line reflection (Fig. 2.24a) and is absent in the equatorial profile of Fig. 2.24a' [56]. From the fiber pattern of the mesophase of iPPOct copolymers of Fig. 2.24b it is clear that the two broad peaks at $2\theta = 14$ and 20° observed in the powder diffraction profiles of Fig. 2.23 a, b are both polarized on the equator [56]. While in the mesophase of iPP the reflection at $2\theta = 21.3^\circ$ is a first layer line reflection, in the mesophase of iPPOct copolymers the reflection at $2\theta = 20^\circ$ is both on the equator and on the first layer line. These data indicate that the disordered mesomorphic form that crystallizes in iPPOct copolymers is different from the mesophase of iPP [56].

The value of the c -axis of 6.5–6.6 \AA evaluated from the fiber pattern of Fig. 2.24b, indicates that this mesophase is characterized by chains in the ordered 3/1 helical conformation [56], as in the case of the quenched mesophase of iPP. The

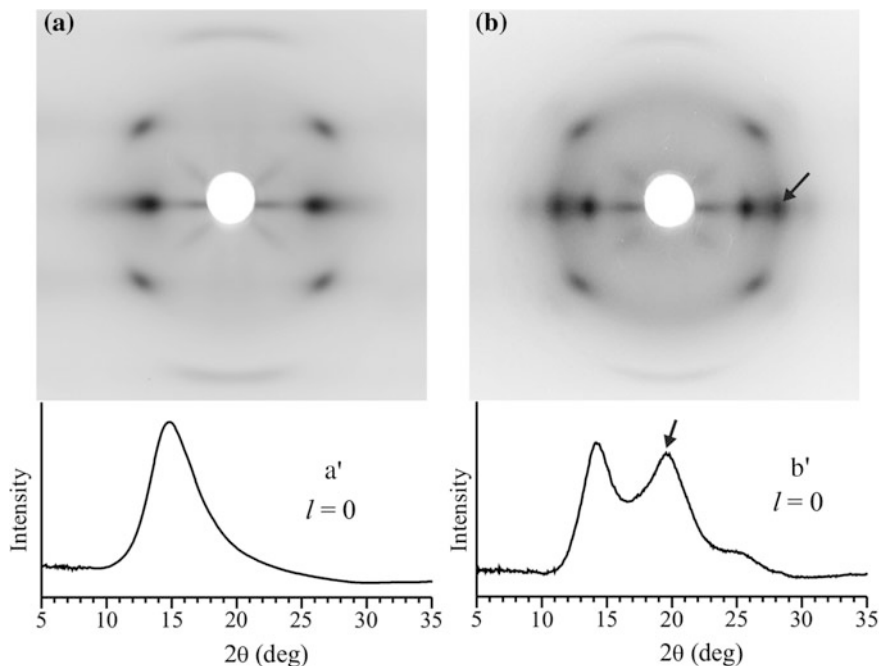


Fig. 2.24 X-ray fiber diffraction patterns (**a**, **b**) and corresponding equatorial diffraction profiles (**a'**, **b'**) of fibers of the mesomorphic form of iPP homopolymer (**a**, **a'**) [48, 50] and of the mesophase of iPPOct copolymers obtained by stretching compression model films of the sample iPPOct-3.9 with 3.9 mol% of octadecene (**b**, **b'**). The arrows in B indicate the equatorial reflection present in the diffraction pattern of the mesophase of the branched copolymer and absent in that of the mesophase of iPP [56]. Reproduced with permission from Ref. [56]. Copyright 2010 by the American Chemical Society

difference with the mesophase of iPP is, therefore, related only to the lateral packing of the 3/1 helical chains.

The crystallization of this new (solid) mesophase in highly branched iPP copolymers is driven by the low compatibility between the long alkyl branches and the chain backbone and the resulting gain of entropy and enthalpy from optimization of the organization of the side groups and the chain backbone [56]. A possible structural model for this new mesophase is shown in Fig. 2.25. The mesomorphic aggregates are characterized by parallel chains in the ordered 3/1 helical conformation with periodicity of nearly 6.5 Å. The side chains are included in the mesomorphic aggregates. As a consequence, the chains are packed at average interchain distance of about 6.3 Å, defined by the self-organization of the flexible disordered side groups placed at average distance of about 4.4 Å [56].

Therefore, the mesophase of branched copolymers is characterized by short-range order in the lateral packing of the chain axes and long-range order in the regular conformation of the 3/1 helices [56] and is a solid mesophase characterized by long range periodicity along one direction only [11].

Fig. 2.25 Schematic model of the organization of chains of iPPOct copolymers in the mesophase. Reprinted with permission from Ref. [56]. Copyright 2010 by the American Chemical Society



It has been argued that the crystallization of long branched iPP copolymers, in the appropriate composition range, in this new mesophase is the result of the intrinsic molecular structure of these copolymers achieved resorting to metallocenic catalytic systems for their synthesis, that is the random placement of long branched comonomers along the chains and the high degree of stereoregularity of the isotactic copolymers. Thanks to this molecular structure, indeed, the regular 3/1 helical conformation can be maintained for long portions of chains. The possibility of maintaining long-range order along the chain axis, and the short-range order that develops thanks to the parallel arrangement of these defective portions of chains, driven by the interactions of the long branches, determine the crystallization of the disordered mesophase [56].

2.5 Crystal Polymorphism of Syndiotactic Polypropylene

Syndiotactic polypropylene presents a complex polymorphic behavior. The studies performed in the early 1960s on regio-irregular and poorly syndiotactic polypropylene samples prepared with the vanadium-based Ziegler-Natta catalysts already showed the presence of polymorphism [36–38, 172, 173]. Two different

crystalline forms, characterized by chains having different conformational, were described at that time, characterized by chains having a two-fold helical conformation, with $s(2/1)2$ symmetry [35, 174–176] (the sequence of torsion angles along the backbone is $(TTGG)_n$), and a *trans*-planar conformation [174] (with a sequence of torsion angles of the kind $(TTTT)_n$). The two-fold helical and *trans*-planar conformations of sPP chains are shown in Fig. 2.3a, b, respectively.

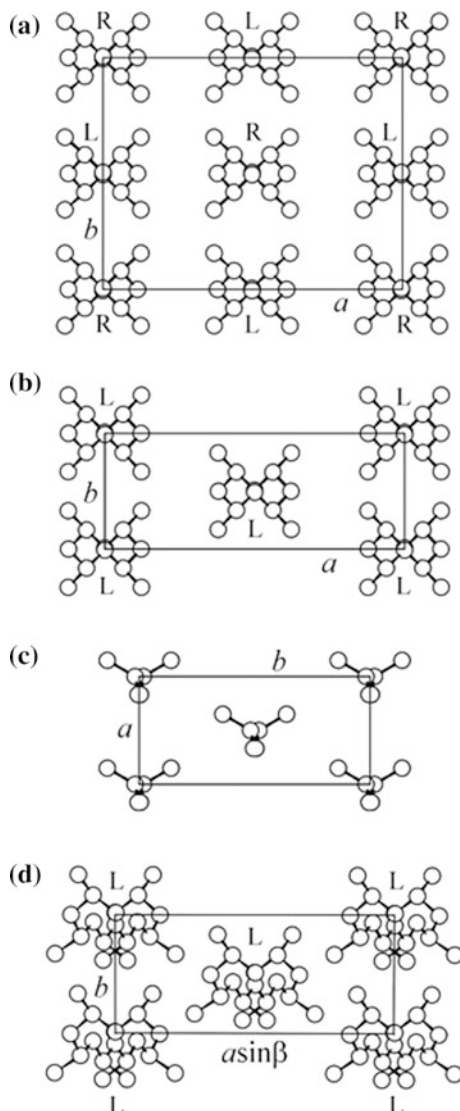
The complete resolution of the crystal structure of the helical form of sPP now defined form II was already carried out by Corradini in the 1960 on a sPP fraction obtained from separation procedures of the isotactic polymers produced with heterogeneous $TiCl_3$ based catalysts, before the discovery of the homogeneous vanadium based catalysts [36]. This crystalline form has been considered for long time the most stable form of sPP. The possible presence of two different stable conformations for the chains of sPP was also predicted by calculations of the conformational energy before the discovery of the *trans*-planar form [172, 173] and confirmed by successive calculations [12, 38, 174].

Only the more recent structural studies, performed on the highly regioregular and stereoregular sPP [39–42, 175–191], prepared with metallocene catalysts [24], have shown that the polymorphic behavior of sPP is more complex [6] for the presence of new crystalline forms and for the presence of different types and amounts of disorder in the crystalline phases, depending on the degree of stereoregularity and the mechanical and thermal histories of the samples [43, 192–195]. Four different polymorphic crystalline forms (Fig. 2.26) and two disordered mesomorphic forms have been found so far [6, 196]. The crystalline forms have been called forms I, II, III and IV regardless of the chronology of their discovery but only considering that form I is the most stable and common form (even though it has been discovered much later than form II) [6, 188], whereas forms III and IV are the less stable forms observed only in oriented fibers [38–40]. This nomenclature [188] is nowadays widely accepted. Form I and form II are characterized by chains in $s(2/1)2$ helical conformation packed in different orthorhombic crystalline lattices (Fig. 2.26a, b), form III presents polymer chains in the *trans*-planar conformation (Fig. 2.26c) and, finally, form IV is characterized by chains in $T_6G_2T_2G_2$ conformation (Fig. 2.26d) [6].

The X-ray powder diffraction profiles of form I and form II are reported in Fig. 2.27, whereas the main reflection peaks are listed in Table 2.2. In Table 2.2 the main reflections of Form III, are also reported. Form I and form II have similar diffraction profiles, the main difference consisting in the second strong reflection at $d \approx 5.3$ and 5.6 Å, corresponding to the 110 and 020 reflections of form II and form I, respectively [42].

It is worth noting that the conformational polymorphism is a characteristic of sPP which manifests not only in the crystalline polymorphs of Fig. 2.26, but appears also in the formation of two different types of solid mesophases obtained by stretching homo and copolymers of sPP [6, 196]. The classic mesophase of sPP is characterized by chains in *trans*-planar conformation (*trans*-planar mesophase)

Fig. 2.26 Limit ordered models of packing of form I (a), form II (b), form III (c) and form IV (d) of sPP. R = right-handed helix, L = left-handed helix



[6, 11], whereas in the case of some copolymers a new mesophase characterized by chains in the $s(2/1)2$ helical conformation (helical mesophase) is obtained [196]. The type of mesophase which develops by effect of stretching depends on type and concentration of comonomers (vide infra) and once again is the result of the random distribution of the comonomeric units along the chains, which allows to enhance the effect of comonomers on the stabilization/destabilization of a given conformation of sPP, up to drive crystallization in a different polymorph or a completely new one.

Fig. 2.27 X-ray powder diffraction profiles of sPP in the helical form I (a) and II (b) (Ni filtered CuK α radiation)

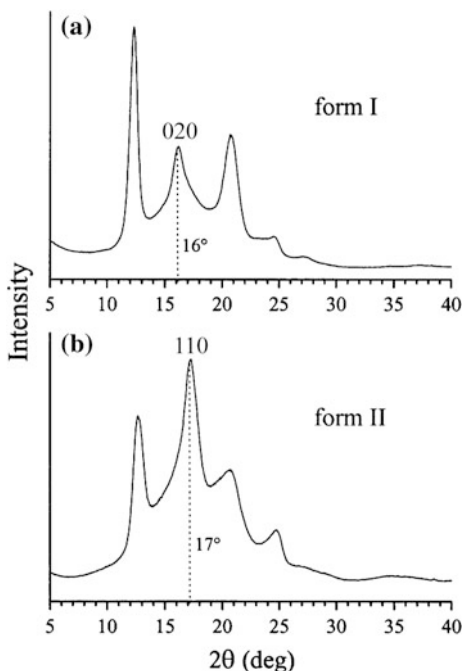


Table 2.2 Diffraction angles (2θ), interplanar distances (d) and Miller indices (hkl) of the main Bragg reflections relative to form I, II and III of syndiotactic polypropylene, observed in the X-ray diffraction profiles (Ni-filtered CuK α radiation, $\lambda = 1.5418 \text{ \AA}$)

Syndiotactic polypropylene form I			Syndiotactic polypropylene form II			Syndiotactic polypropylene form III		
$(hkl)_I$	2θ (deg)	d (\AA)	$(hkl)_{II}$	2θ (deg)	d (\AA)	$(hkl)_{III}$	2θ (deg)	d (\AA)
200	12.2	7.25	200	12.3	7.20	020	16.3	5.45
020	15.9	5.57	110	16.9	5.26	110	18.2	4.88
211	18.9	4.70	201	17.1	5.18	021	23.7	3.75
220, 121	20.6	4.31	111	20.7	4.29	111	25.8	3.45
221	23.5	3.79	002	24.0	3.70			
002, 400	24.5	3.63	400	24.8	3.59			

2.5.1 Crystal Structure of Form I

Form I was identified by Lotz, Lovinger et al. [177–180]. It is the stable form of sPP obtained under the most common conditions of crystallization, including by melt and solution crystallizations in powder samples and as single crystals. Lotz and

Lovinger obtained highly regular single crystals of sPP and performed the first electron diffraction analysis of this form [177–180]. They found the same molecular conformation and basic unit cell dimensions as form II [36, 37], but they found a different packing mode of the two-fold helical chains in the unit cell [177]. This new crystalline form (form I) is the most stable form of sPP, much more stable than the older form form II.

Form I is characterized by chains in $s(2/1)2$ helical conformation packed in an orthorhombic unit cell having axes $a = 14.5 \text{ \AA}$, $b = 11.2 \text{ \AA}$, $c = 7.4 \text{ \AA}$ (Fig. 2.11). The axes of the helical chains are in the positions $(0, 0, z)$ and $(1/2, 0, z)$ of the orthorhombic unit cell and, in the ideal limit ordered structure, helical chains with opposite chirality, right-handed and left-handed, alternate along a and b axes of the unit cell (Fig. 2.23a), according to the space group $Ibca$ [175–178]. Lovinger and Lotz have then demonstrated that form I (Fig. 2.23a) is obtained not only in the case of single crystals in ultrathin films, but also in the case of polycrystalline thick films, for bulk specimens obtained directly from the polymerization, and for oriented thin film [177–180].

The structural model of Form I was inferred based on the electron diffraction analysis of single crystals grown at high temperatures, showing the presence of equatorial 200 and 020 reflections at $d = 7.25$ and 5.6 \AA and the 211 reflection at $d = 4.70 \text{ \AA}$ [177–180] (Fig. 2.28a, b). The presence of these reflection ($2\theta \approx 12^\circ$, 16° and 19° $\text{CuK}\alpha$ radiation, respectively) is common also to the X-ray powder diffraction profiles of samples crystallized from the melt at temperatures higher than $130 \text{ }^\circ\text{C}$ [37, 188, 189] (Fig. 2.28c).

The key feature is the presence of the 020 reflection at $2\theta \approx 16^\circ$, not observed in the X-ray fiber diffraction pattern of form II [36, 37] (Fig. 2.28a), and of the 211 reflection on the first layer line at $2\theta \approx 19^\circ$ (Fig. 2.28b). These observations have indicated that the b axis of the unit cell is doubled ($b = 11.2 \text{ \AA}$) with respect to that in the crystal structure of form II ($b = 5.6 \text{ \AA}$, Fig. 2.26b) [37] and that the axes of the helical chains are in the positions $(0, 0, z)$ and $(1/2, 0, z)$ of the unit cell with alternation of the helical chirality along both a and b axes (Fig. 2.26a) [177–180].

The model of Fig. 2.26a for the form I of sPP, in the space group $Ibca$, [177–180, 186] corresponds to a lattice having the highest symmetry compatible with the symmetry of the sPP chains, because the local two-fold rotation symmetry axes of the $s(2/1)2$ helical chains, perpendicular to the chain axis, are maintained in the lattice as crystallographic elements of symmetry (Fig. 2.29a). However, the electron diffraction pattern of single crystals of sPP grown at very high temperature of Fig. 2.28b shows the presence of the 011 reflection [177–180], which is not permitted by the space group $Ibca$. This indicates that the symmetry of the space group should be lower than $Ibca$ [42, 188].

Additional hints indicating a space group of symmetry lower than $Ibca$ come from solid state ^{13}C NMR CPMAS analysis of annealed samples of sPP in form I, showing that the resonance of the methyl carbon atom is split in a doublet [192, 193]. The doublet indicates that the methyl carbon atoms experience two non-equivalent environment in the unit cell. In the high symmetry model $Ibca$ of Fig. 2.26a, instead, all methyl carbon atoms are equivalent and should give a single

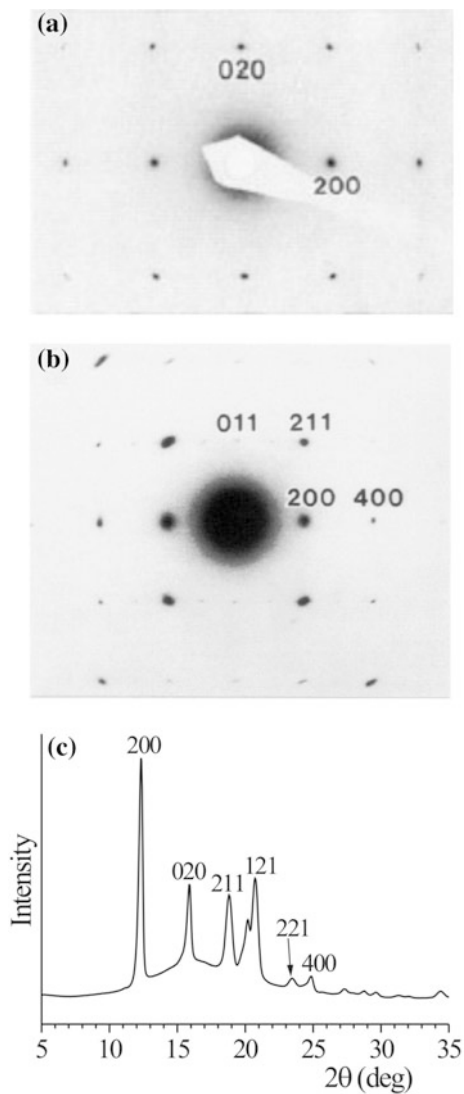


Fig. 2.28 Electron-diffraction patterns of sPP single crystals grown isothermally at 145 °C (a) and at 140 °C after tilting by 57° about the a axis (b). The electron beam is directed along the lattice directions $[001]$, i.e. normal to the lamellar crystals, in (a) and $[0\bar{1}1]$ in (b). Reproduced with permission from Ref. [37]. Copyright 1993 by the American Chemical Society). c X-ray powder diffraction profile of a highly stereoregular sample of sPP crystallized from the melt at 140 °C. Reproduced with permission from Ref. [188]. Copyright 1996 by the American Chemical Society

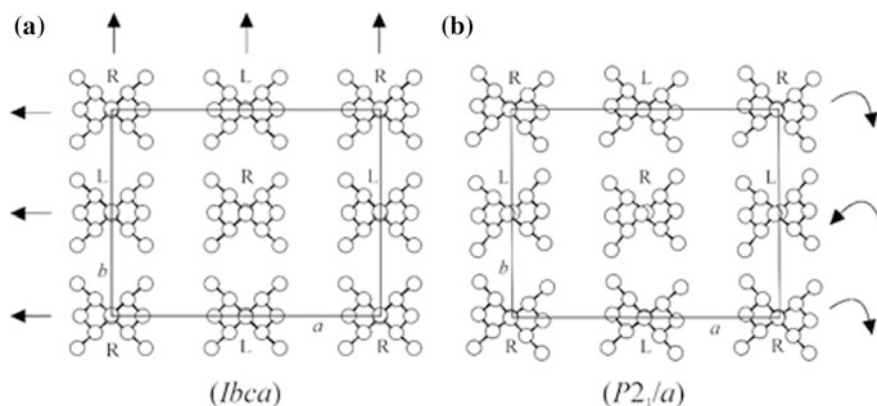


Fig. 2.29 Models of packing of chains in the form I of sPP according to the space groups *Ibca* [177–180] (a) and *P2₁/a* [188] (b). The arrows indicate the crystallographic twofold axes, present in A and lost in B. In the model B the chains are rotated by nearly 5° around the chain axes, according to the direction indicated by the arrows [188]

resonance in the solid state ^{13}C NMR. A lower symmetry arises by removing the local two-fold rotation axes of the chains, perpendicular to the chain axis, in the lattice, and allowing for rotation and translation of chains around and along their chain axis, respectively [188]. The space group is monoclinic *P2₁/a* and two of the four chains included in the unit cell are independent, that is, not related by any element of symmetry (Fig. 2.29b) [188]. The refined structural model corresponds to a monoclinic unit cell with axes $a = 14.31 \text{ \AA}$, $b = 11.15 \text{ \AA}$, $c = 7.5 \text{ \AA}$ and $\gamma = 90.3^\circ$ [188]. Similar to the space group *Ibca*, the strict alternation of right and left handed helical chains along the a and b axes of the unit cell is preserved, and also the positions of the chain axes remain unaltered (Fig. 2.29b). The breaking of the symmetry in the space group *P2₁/a* results from a rotation by $\pm 5^\circ$ of the chains around the chain axes, shifts of consecutive bc layers of chains along the a axis of $0.13c$ along the chain axis c , and a further shift along the chain axis, of consecutive chains along b by $0.034c$ [188]. Compared to the *Ibca* structural model (Fig. 2.29b), in the refined model of Fig. 2.29b consecutive chains along the b axis, are rotated around the chain axis by the same angle $|\omega|$ but in opposite directions and displaced along c by $0.034c$, whereas consecutive chains along a are related by an inversion center and are rotated around the chain axis by the same amount in the same direction and are displaced along c by $\approx 1 \text{ \AA}$ ($0.13c$) [186].

Symmetry breaking entailing structural variations from the high symmetry model *Ibca* have also been confirmed by energetics calculations, that have indicated that the *Ibca* model corresponds to an energy maximum, whereas more stable structures can be obtained permitting c -axis shifts of consecutive bc layers of chains piled along a [194], and/or b -axis shifts [195, 196].

The low symmetry model of Fig. 2.29b accounts for the presence of the 011 reflection in the electron diffraction pattern and the splitting observed in the solid

state NMR spectrum. It describes a local arrangement of the chains, that is, the order at very short distances, which can be detected only by a direct observation of very small area of the diffracting crystals. Owing to possible different setting angles of the chains in adjacent (coherent) crystalline domains, the model with higher symmetry *Ibca* (Fig. 2.29a) may be considered as an average model structure, suitable for the description of the structure at long range distances [197].

The crystal structure of form I of sPP represents **an example of symmetry breaking**, a general principle that has been demonstrated to control the mode of packing of some polymers [12]. According to this principle, when the conformation of polymer chains has a very high symmetry, the global symmetry can be broken in the limit ordered crystalline lattice of polymers. In general, from the electron diffraction data of form I it may be deduced that *the low symmetry of the unit cell may be revealed even for symmetric single crystals, by the asymmetries of the diffraction patterns* [12]. The observation of the lack of the symmetry in the ordered structures of polymers is strictly related to the possibility of the direct observation of the local arrangements of polymer chains by selected area electron diffraction. The study of the crystal structure of polymers, performed with the traditional X-ray diffraction, generally leads to models of packing that describe the order in the long range [12].

2.5.2 Structural Disorder in Form I

The X-ray powder diffraction profiles of melt crystallized sPP samples and the electron diffraction patterns of single crystals of form I generally indicate that the intensities of the reflections change as a function of the condition of crystallization [42, 43, 177–180, 189, 198]. In particular, the electron diffraction patterns reveal the presence of streaks around the 211 reflection at $2\theta \approx 19^\circ$ (Fig. 2.30a), whereas X-ray diffraction patterns show weak or even absence of this reflection (Fig. 2.30b). This indicates the presence of structural disorder. Disorder consists in departures from the perfect alternation of two-fold helical chains of opposite chirality along the *a* and *b* axes of the unit cell of Form I. The model of Fig. 2.29, characterized by the *Ibca* or *P2₁/a* symmetry, should be considered as the limit ordered modification of form I, which can be obtained only when highly stereoregular samples of sPP are crystallized from the melt at high temperatures (e.g. 140 °C) [42, 190, 191] or crystallized in single crystals grown at temperatures higher than 130 °C [177–180]. In particular, the electron diffraction pattern of Fig. 2.30a is relative to a single crystal of sPP grown at low temperature (100 °C) whereas the X-ray powder diffraction profile of Fig. 2.30b is relative to an as-prepared sample of sPP which was rapidly crystallized by precipitation from the polymerization solution and then dried without any other thermal treatment.

The presence of streaks and, in some cases, the absence of the 211 reflection has been explained suggesting that in samples of sPP quickly crystallized at low temperatures a structural disorder is present, due to deviations from the perfect

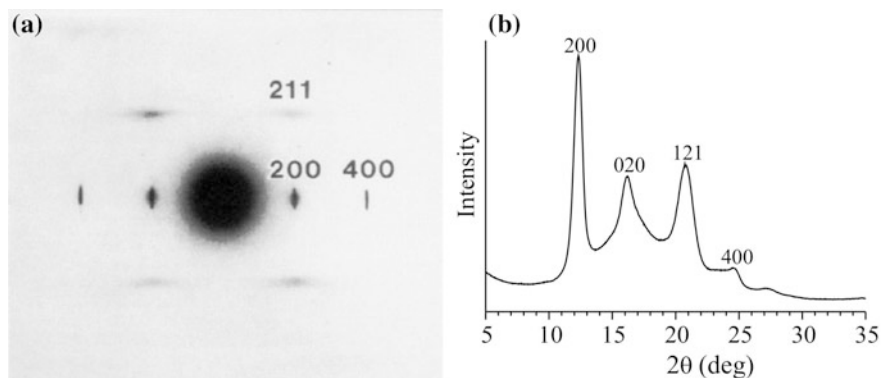


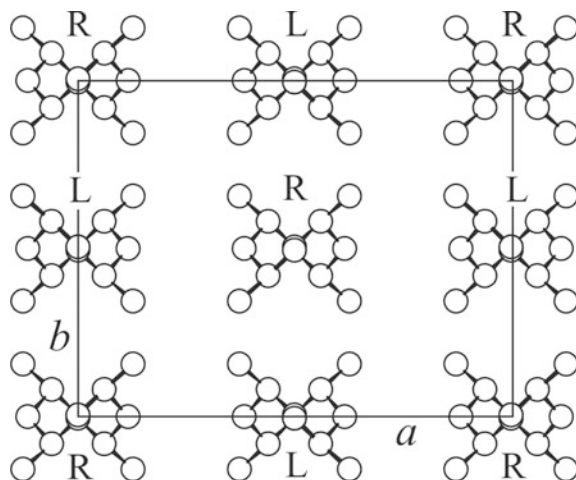
Fig. 2.30 **a** Electron-diffraction pattern of single crystals of sPP crystallized at 100 °C and tilted by 57° about the a axis. The electron beam is directed along $[0 \bar{1} 1]$ to permit the visualization of 211 reflection. Reproduced with permission from Ref. [107]. Copyright 1993 by the American Chemical Society. **b** X-ray powder diffraction profile of an as-prepared sample (quench precipitated from the polymerization solution) of highly stereoregular sPP, having concentration of *rrrr* pentad of 96%. Reproduced with permission from Ref. [42]. Copyright 1993 by The American Chemical Society

alternation of enantiomorphous helices along a and b axes [42]. A limit disordered model, consisting in a random substitution of right- and left-handed chains in each site of the lattice, corresponds to an orthorhombic unit cell with axes $a = 14.5 \text{ \AA}$, $b = 5.60 \text{ \AA}$, $c = 7.4 \text{ \AA}$ and the statistical space group $Bmcm$ [42, 43]. The limit disordered model is shown in Fig. 2.31b in comparison with the fully ordered model (Fig. 2.31a). Right-handed or left-handed helical chains can be found in each site of the orthorhombic unit cell with the same probability, due to their similar steric hindrance and interactions with neighboring chains.

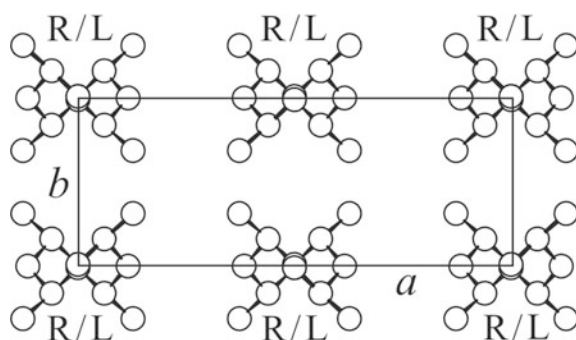
The structures of Fig. 2.31 represent ideal limit ordered (fully ordered, Fig. 2.31A) and limit disordered (statistically, fully disordered, Fig. 2.31B) models. Real modifications are intermediate between the two ideal models of Fig. 2.31 and present different amounts of defects in the perfect alteration of right-handed and left-handed helical chains.

The X-ray powder diffraction profiles of a highly stereoregular sPP sample, crystallized from the melt at different crystallization temperatures are reported in Fig. 2.32 [189]. It is apparent that the intensity of the 211 reflection at $2\theta \approx 19^\circ$ depends on the crystallization temperature and increases with increasing crystallization temperature. At high crystallization temperature, the high intensity of the 211 reflection indicates that the sample crystallizes in modification close to the limit ordered model (Fig. 2.31A), characterized by a perfect alternation of enantiomorphous helices along both axes of the unit cell (Fig. 2.32g–i). At low crystallization temperatures, the low intensities of the 211 reflection (Fig. 2.32b–e) indicates that the sample crystallizes in disordered modification including defects in the regular alternation of left and right handed helices [189].

Fig. 2.31 Limit ordered model (space group $Ibca$ or $P2_1/a$) [186] (A) and limit disordered model (space group $Bmcm$) [42] (B) for the crystal structure of form I of sPP. R = right-handed helix, L = left handed helix



A ($Ibca$ or $P2_1/a$)



B ($Bmcm$)

The degree of right/left substitution disorder present in form I of sPP is evaluated by calculating the ratio R between the intensities of 211 and the 020 reflections at $2\theta \approx 19$ and 16° , respectively, [189]. The order parameter R increases with increasing crystallization temperature (Fig. 2.33) from $R = 0$, corresponding to a completely disordered structure (Fig. 2.31B, space group $Bmcm$), to a value $R = 1$, corresponding to the limit ordered structure (Fig. 2.31A, space group $Ibca$ or $P2_1/a$) [189]. As-prepared samples (Figs. 2.33 and 2.30), or samples crystallized at very low temperatures, showing $R \approx 0$ (the 211 reflection is absent), are crystallized in disordered modifications close to the limit disordered model $Bmcm$, characterized by statistical disorder in the positioning of enantiomorphous helices. However, local correlation about the chirality of neighboring chains may be still preserved. Figure 2.33 indicates that form I of sPP is better described by a continuum of disordered modifications, intermediate between the limit disordered model $Bmcm$ of

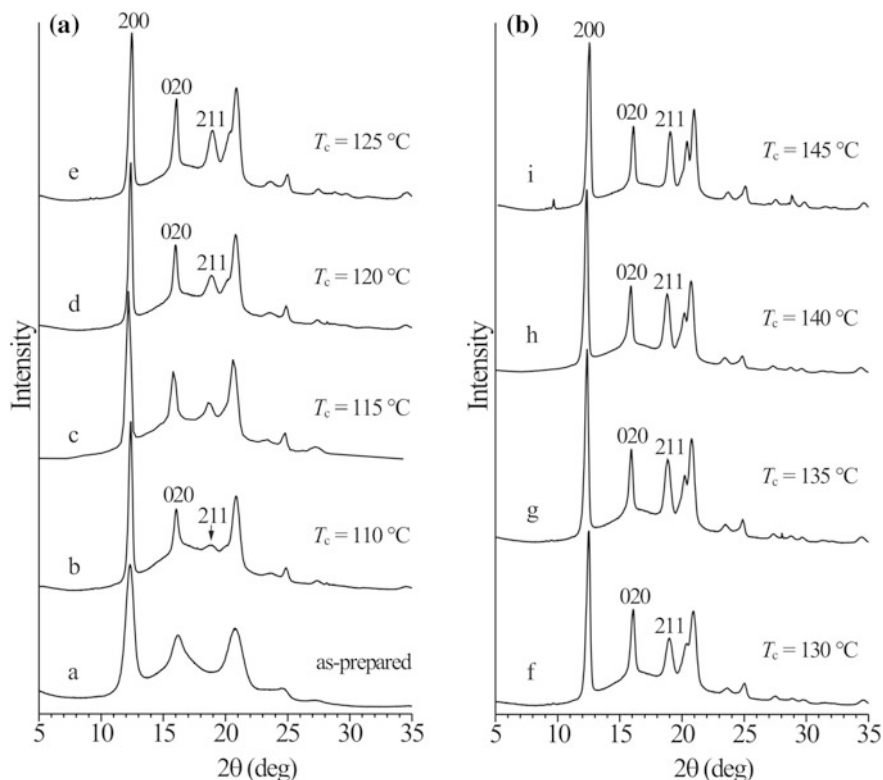


Fig. 2.32 X-ray powder diffraction profiles of samples of a highly stereoregular sPP (concentration of the fully syndiotactic *rrrr* pentad of 96%) isothermally crystallized from the melt at the indicated crystallization temperatures T_c . The as-prepared sample (profile a) corresponds to the sample rapidly crystallized from the polymerization solution. The 200, 020 and 211 reflections at $2\theta \approx 12^\circ$, 16° and 19° of the antichiral helical form I are indicated. Adapted with permission from Ref. [189]. Copyright 1997 by the American Chemical Society

Fig. 2.31B and the limit ordered model $Ibca$ or $P2_1/a$ of Fig. 2.31A, the degree of order being dependent on the crystallization temperature [189].

Therefore, also in the case of sPP crystallized from the melt at high and low temperatures, the concept of limit ordered and limit disordered ideal structures turns out useful for the description of the real structure of form I, in terms of intermediate modifications between the ideal models [12].

The degree of structural order in the alternation of right- and left-handed chains achieved in form I of sPP depends on the stereoregularity of the sample and in particular on the presence of *mm* or *m* stereodefects [43, 189, 191, 198], regiodefects and also constitutional defects [199].

The diffraction data of samples of sPP crystallized in form I in different conditions reveal also another kind of disorder. In particular, Lovinger and Lotz have observed that single crystals of sPP grown at low temperatures show electron

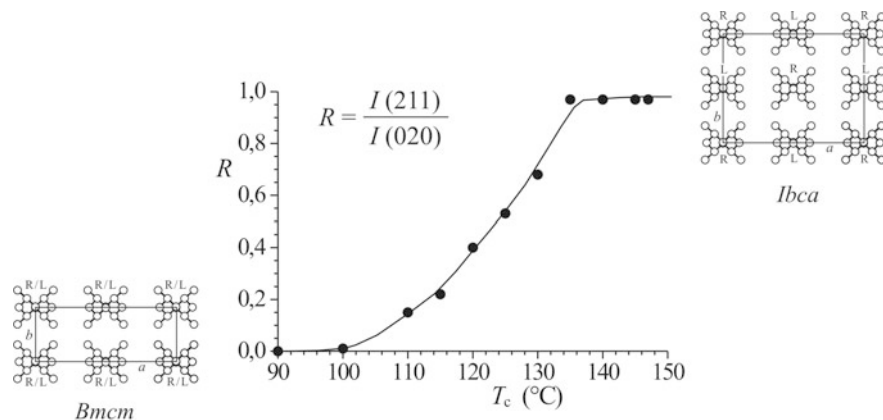


Fig. 2.33 Values of the order parameter R of samples of highly stereoregular sPP, having concentration of *rrrr* pentad of 96%, isothermally crystallized from the melt as a function of the crystallization temperature T_c [12]. Reproduced with permission from Ref. [6]. Copyright 2006 by Elsevier

diffraction patterns (Fig. 2.34c–e) characterized not only by streaks around the 211 reflection along the $h11$ layer line (Fig. 2.30a), but also streaks along the $h20$ layer in the equatorial plane [180, 189]. In particular, single crystals grown at the high temperatures (130–145 °C, Fig. 2.34a, b) show a sharp 020 reflection at $2\theta \approx 16^\circ$, typical of the structure of form I with $b = 11.2$ Å (Fig. 2.26a), and absence of any diffraction around the 120 reflection at $2\theta = 17^\circ$, typical of the structure of the isochiral form II (for the unit cell of form II of Fig. 2.26b with $b = 5.6$ Å this reflection must be indexed as 110). This is in agreement with the fact that at high temperatures crystals in the pure form I with ordered antichiral packing of Fig. 2.26a are obtained. At lower temperatures streaks along $h20$ are observed (Fig. 2.34c–e). At the lowest temperatures the streaks become a continuous diffraction along the $h20$ layer (Fig. 2.34e) with a consequent presence of diffraction in the region of the 120 reflection. This indicates departure from regular antichiral packing along the a axis.

Moreover, the powder diffraction profiles of samples crystallized at low temperatures, or of as-prepared samples (Figs. 2.30b and 2.32a), show a broad diffraction peak at $2\theta \approx 16^\circ$, corresponding to the 020 reflection. In some cases the 020 reflections shows also a shoulder, at values of 2θ of $\approx 17^\circ$, that is in the region of the 120 reflection (110 reflection of form II). The model of disorder emerging from these data consists in defects in the stacking of ordered bc layers of chains along the a axis, implying shifts of $b/4$ between consecutive layers ($b/4$ shift disorder) [180–182]. A model for this kind of disorder is shown in Fig. 2.35. Antichiral packing of first neighboring chains may be still preserved but is lost in the long range because of the shift of layers [42, 43, 180, 181, 189]. These defects produce, locally, occurrence of the C-centered mode of packing of form II (Fig. 2.26b), as a defect in a prevailing antichiral mode of packing of form I

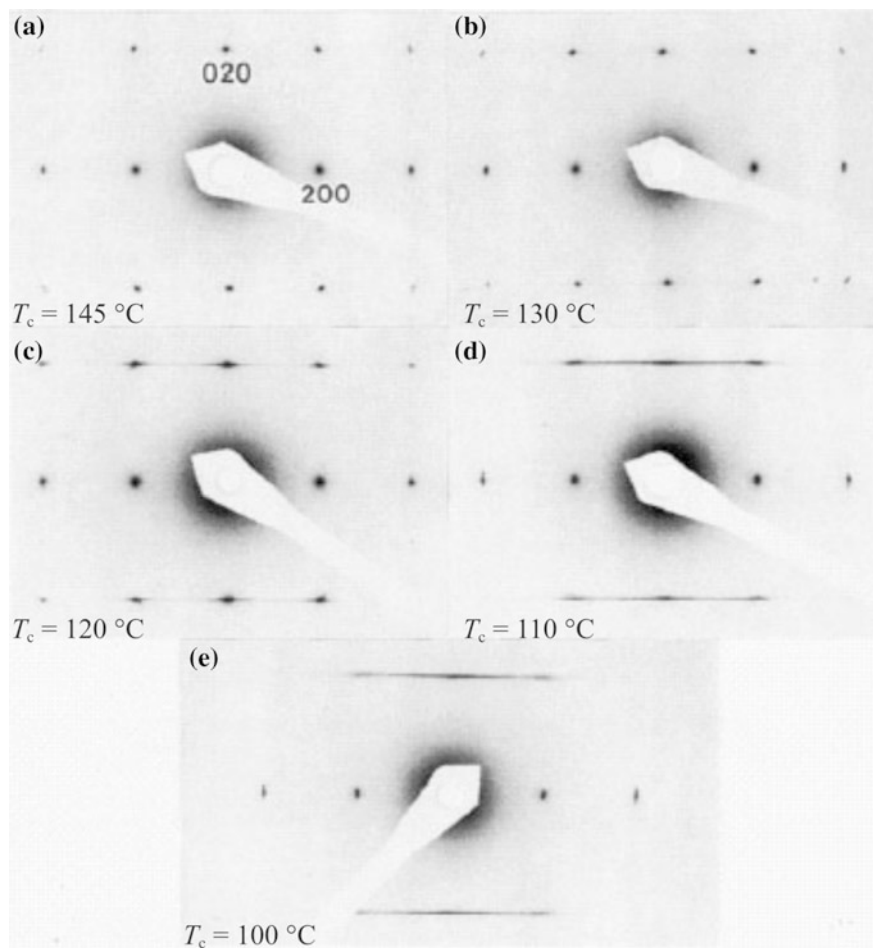


Fig. 2.34 Electron-diffraction patterns of single crystals of sPP grown isothermally at 145 (a), 130 (b), 120 (c), 110 (d) and 100 °C (e). The electron beam is directed normal to the lamellar crystals. Reproduced with permission from Ref. [180]. Copyright 1993 by the American Chemical Society

(Fig. 2.26a) and give rise the weak and broad diffraction in the region of the 110 reflection of form II around $2\theta = 17^\circ$.

2.5.3 Crystal Structure of Form II

Form II is the metastable crystalline form of sPP with chains in helical conformation (Fig. 2.26b). Since the resolution of the crystal structure of form II by

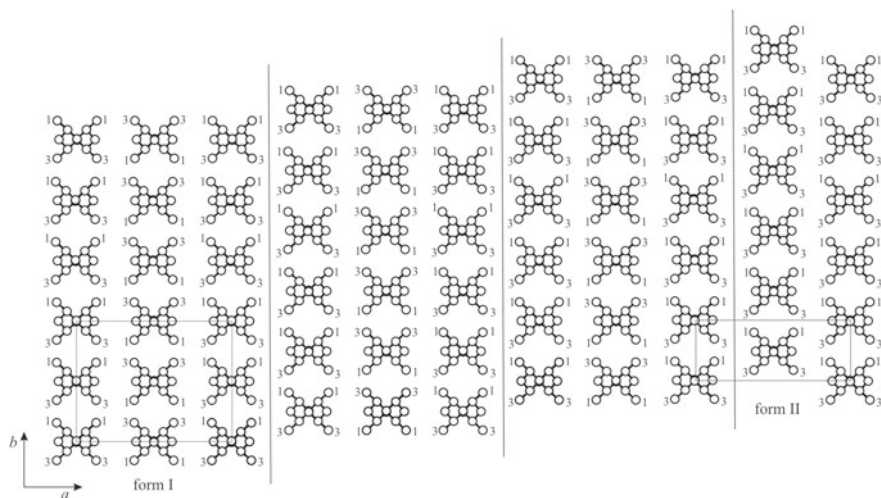


Fig. 2.35 Packing model of chains of sPP in the form I, showing disorder in the stacking of bc layers of chains along the a axis. The numbers indicate the relative heights of the methyl carbon atoms in $c/4$ units. The vertical dashed lines indicate the positions of defects, which correspond to the shift of bc layers of chains of $b/4$ along the b axis. These defects produce, locally, occurrence of the C -centered mode of packing of form II as a defect in a prevailing antichiral mode of packing of form I [12, 43, 180, 189, 197]. The unit cells of form I and form II are shown. Reproduced with permission from Ref. [10]. Copyright 2013 by Wiley

Corradini et al. dating back to 1960 [36], this helical form has been considered for about 30 years, the most stable polymorph of sPP. The structural model was deduced [36, 37] from the X-ray fiber diffraction analysis of oriented fibers of low stereoregular and regioregular sPP samples available in the 1960s, prepared with Ziegler-Natta catalysts [36, 200]. This form is characterized by chains in $s(2/1)2$ helical conformation packed in the C -centered orthorhombic unit cell with axes $a = 14.5 \text{ \AA}$, $b = 5.60 \text{ \AA}$, $c = 7.4 \text{ \AA}$, according to the space group $C222_1$ [36, 37]. Helical chains having the same chirality are included in the unit cell.

Form II can be obtained in oriented fibers, by stretching low stereo- and regioregular sPP samples prepared with vanadium-based Ziegler-Natta catalysts [36, 37, 190] or, in the case of highly stereoregular sPP samples, by removing the tension starting from stretched fibers initially in the *trans*-planar form III [190]. In fact, when highly syndiotactic samples, prepared with homogeneous metallocene catalysts, are stretched at room temperature fibers in the *trans*-planar form III (Fig. 2.26c) are generally obtained [42, 186, 190]. Form III is stable only in the stretched state and transforms into the more stable isochiral helical form II (Fig. 2.26b) by releasing the tension [190, 201–204].

The X-ray diffraction patterns of a fiber of highly stereoregular sPP sample, having *rrrr* pentad content of 93%, stretched at 600% deformation and after removing the tension are reported in Fig. 2.36a, b, respectively. The presence of the equatorial $(020)_t$ and $(110)_t$ reflections at $2\theta = 15.9$ and 18.8° , respectively, and of

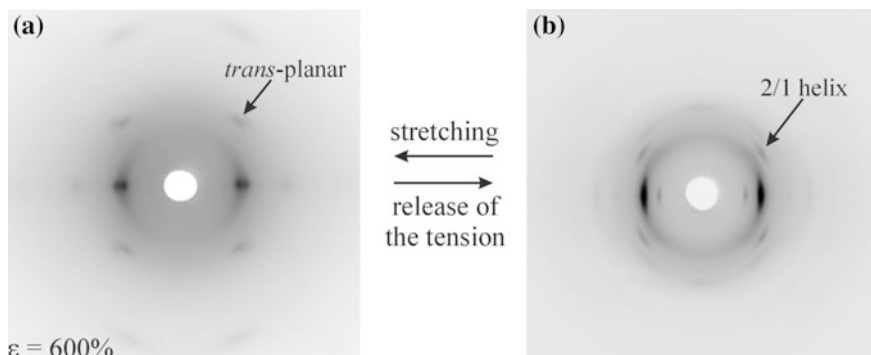


Fig. 2.36 X-ray fiber diffraction patterns of oriented fibers of a highly stereoregular sPP sample, having concentration of *rrrr* pentad of 93%, obtained in stretched compression-molded films up to 600% deformation, kept in tension (a), and after the release of the tension (b). The arrows indicate reflections on the first layer line arising from the diffraction of crystals in the *trans-planar* form III with a periodicity of 5.1 Å and in the helical form II with a periodicity of 7.4 Å. The fiber in (a) is in the pure *trans-planar* form III, whereas the fiber in (b) is basically in the helical form II

reflections on the first layer line corresponding to a *trans-planar* chain axis periodicity of 5.1 Å ($(021)_t$ and $(111)_t$ reflections) [186], indicate that the fiber in Fig. 2.36a is in the *trans-planar* form III (Table 2.2) [42, 190, 200]. The diffraction pattern obtained upon removing the tension (Fig. 2.36b) shows the typical 200 and 110 reflections at $2\theta = 12.2$ and 17° of the isochiral form II, and reflections on the first layer line (201 and 111 reflections at $2\theta = 17.1$ and 20.7° , respectively) corresponding to the helical chain axis periodicity of 7.4 Å (Table 2.2) [190, 200].

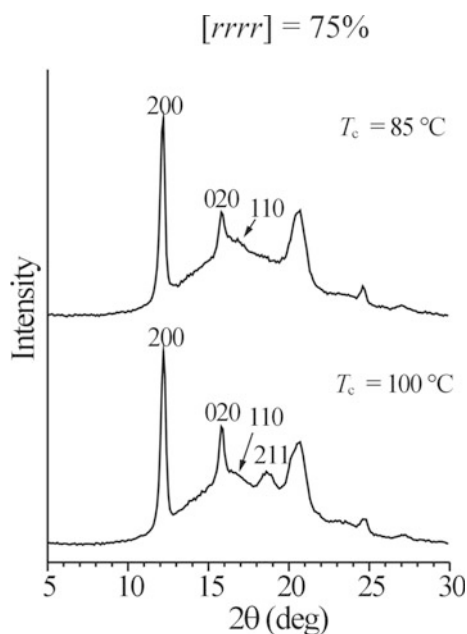
Based on the packing energy calculations the energy of form II is only 0.12 kcal/mol higher than that of the antichiral form I, whereas the energy of the *trans-planar* form III is significantly higher than those of the helical forms I and II [197]. The higher energy of form III is in agreement with the fact that form III transforms spontaneously into the helical form II in stretched fibers by releasing the tension (Fig. 2.36) [190, 201–204]. This transformation is a reversible crystal-to-crystal transition occurring in the solid state and is of first thermodynamic order [201–204]. In fact, the *trans-planar* form III and the isochiral form II transform each other by successive stretching and relaxation of sPP fibers. This transition plays a fundamental role in the mechanical properties of sPP (vide infra) [201–204].

The isochiral form II (Fig. 2.26b) may be also obtained in mixture with the antichiral helical form I (Fig. 2.26a), by annealing oriented fibers of *trans-planar* form III at high temperatures (100–120 °C), while keeping the fiber specimens under tension [42, 190]. The transition of the *trans-planar* form III into the helical forms is generally complete by annealing at 120 °C for highly syndiotactic samples ($[rrrr] > 90\%$ and melting temperature of 150 °C), and at 90–100 °C for less stereoregular samples having lower melting temperatures ($[rrrr] = 85\text{--}90\%$ and $T_m = 120$ °C) [42, 202].

Form II has also been obtained by crystallization from the melt at elevated pressure [205]. In particular, at pressures higher than 2 kbar, crystals of form II are obtained in mixture with a small amount of crystals of disordered form I, by cooling the melt to room temperature. The crystals of form I are formed at low undercoolings at the early stages of crystallization [205]. On cooling from the isotropic melt at pressures below 1.5 kbar, the sample crystallizes mainly in the more ordered antichiral form I. These results indicate that at pressures higher than 1.5 kbar form II becomes thermodynamically stable in powder unoriented samples [205]. Since the densities of form II and form I are similar, density cannot be considered responsible for the thermodynamic stability of the form II at elevated pressures and temperatures. A possible reason for the thermodynamic stability of form II, may be envisaged in the observation that while the antichiral form I deforms on compression, the isochiral form II is much more able withstanding compressive forces [205].

The crystallization of form II at high pressure is the only example of formation of a nearly pure isochiral form II from melt-crystallization. Other examples of crystallization of form II from the melt, but in mixture with a prevalent amount of form I, have also been reported [42, 43]. For instance, in the case of low stereoregular sPP samples (with $[rrrr] = 70\text{--}80\%$) a small amount of crystals of form II can be obtained by melt-crystallization along with higher amount of crystals of disordered modifications of form I [189–191]. The X-ray powder diffraction patterns of two specimens crystallized from the melt at low and high temperatures of a sPP sample having syndiotactic pentad content $[rrrr] = 74.8\%$, are reported in Fig. 2.37 [191].

Fig. 2.37 X-ray powder diffraction profiles of a low stereoregular sPP sample having $rrrr$ pentad content of 75%, isothermally crystallized from the melt at the indicated crystallization temperatures T_c . The 200 reflection of the helical forms at $2\theta \approx 12^\circ$, the 020 and 211 reflections at $2\theta \approx 16$ and 19° of the antichiral helical form I, and the 110 reflection at $2\theta \approx 17^\circ$ of the isochiral helical form II, are indicated. Reproduced from Ref. [191] by permission of American Chemical Society



The presence of a broad 020 reflection at $2\theta \approx 16^\circ$ of form I, with a shoulder or a small peak at $2\theta = 17^\circ$, corresponding to the 110 reflection of form II, and the low intensity, or the absence, of the 211 reflection at $2\theta \approx 19^\circ$, indicate that small amounts of crystals of form II are present and/or a mode of packing of form II occurs as a defect in a prevailing mode of packing of form I, due to the occurrence of the $b/4$ shifts disorder, discussed above (Fig. 2.35) [179, 180].

Another example of crystallization of form II from the melt is provided by syndiotactic propylene-ethylene copolymers prepared with the metallocene catalyst [199]. These samples crystallize from the melt as mixtures of forms I and II. The relative amount of form II increases with increasing crystallization temperature and ethylene content and nearly 70% of form II is obtained for a copolymer sample containing ≈ 14 mol% of ethylene crystallized from the melt at 80°C [199]. This is the first example of crystallization of significant amount of the isochiral helical form II of sPP from the melt at atmospheric pressure.

Finally, form II can be also obtained by epitaxial crystallization from the melt of single crystals in ultrathin films on the surface of crystals of a low molecular weight substance (2-quinoxalinol) [187], due to the favorable correspondence of the surface topographies at the contact faces of crystals of sPP in form II and of the substrate (2-quinoxalinol). In these conditions, form II can be produced only at low crystallization temperatures, even though, during growth away from the substrate, it converts to form I [187].

2.5.4 Structural Disorder in Form II

The isochiral form II of Fig. 2.26b (space group $C222_1$) corresponds to an ideal limit ordered model. In practice, the form II obtained in both oriented fibers and powder samples may present various types of structural disorder [42, 43, 198, 206–208].

In the case of stress-relaxed or annealed fibers, the corresponding X-ray fiber diffraction patterns (Fig. 2.36b) show that the observed intensities of the 201 and 401 reflections on the first layer line, at $2\theta \approx 17^\circ$ and 27° , respectively, are lower than those calculated for the space group $C222_1$ [42]. Moreover, a diffuse scattering along the first layer line surrounding the 201 reflection is generally present. These data have indicated the presence of disorder possibly related to a statistical departure from the regular fully isochiral packing, due, for instance, to a statistical substitution of right- and left-handed helices in the sites of the unit cell [42]. A limit disordered model characterized by random positioning of right- and left-handed helical chains in each site of the unit cell may be described by the statistical space group $Cmcm$ [42]. This ideal fully disordered model implies the systematic absence of the 201 and 401 reflections. The presence of these reflections with low intensities and of the diffuse scattering in the X-ray fiber diffraction patterns around the 201 reflection indicate that in the real crystalline modifications a partial degree of disorder, intermediate between the order of the limit ordered model $C222_1$ and the

statistical disorder of the limit disordered model $Cmcm$, is present [42, 43]. In these intermediate structures the local correlation about the chirality of neighboring chains is preserved in the short range and lost in the long range because of the statistical substitution of enantiomorphous chains.

As in the case of form I, this type of structural disorder in form II depends on the stereoregularity of the sample [42, 43, 190]. In particular, departures from the fully isochiral packing of form II may arise from the presence of inversions of the helical chirality along a single chain, and occur in presence of isolated m diad defects of stereoregularity included in the unit cell in correspondence of sequences of steric diads of the kind $\dots rrrrmrrrrr \dots$ [43].

As discussed above, crystallization of form II in powder unoriented samples is not common and nearly exclusive formation of form II has been observed from the melt only at high pressure [205]. At atmospheric pressure only a limited amount of form II can be obtained, in mixture with prevalent form I, by crystallization from the melt of sPP samples having a relatively low stereoregularity ($[rrrr] = 70\text{--}80\%$) [191]. Kinetically favored crystallization of form II has also been observed in as-prepared samples of sPP having moderately high stereoregularity ($[rrrr] = 86\%$), quench precipitated from the polymerization solution [206–208]. In this case exclusive crystallization of form II has been obtained but the formed crystals of form II are characterized by chains having conformational disorder [206]. In this defective form II of sPP the chains are, therefore, no longer in the ordered two-fold helical conformation with $s(2/1)2$ symmetry.

This particular kind of disorder has been revealed from the parallel analysis of the X-ray powder diffraction profiles and the solid-state ^{13}C NMR spectra (in the cross-polarization, magic angle spinning mode, CPMAS) of the samples [206, 208]. A comparison between the X-ray diffraction profiles and the corresponding solid-state ^{13}C NMR CPMAS spectra of two samples of sPP crystallized in the stable helical form I and in the defective form II, not containing, and containing conformational disorder, respectively, are reported in Fig. 2.38. The sample crystallized in form II is characterized by $rrrr$ pentad content of 86% and has been quench precipitated from the polymerization solution [206].

The X-ray powder diffraction profile of the sample in form I presents the typical 020 reflection at $2\theta \approx 16^\circ$, whereas the 211 reflection at $2\theta \approx 19^\circ$ is absent (Fig. 2.38a), indicating that the sample is crystallized in the disordered form I (Fig. 2.30b). This sample shows a solid-state ^{13}C NMR CPMAS spectrum (Fig. 2.38b), typical of sPP chains having the regular two-fold $(TTGG)_n$ helical conformation [192, 209], characterized by the typical resonances of the methyl carbon atoms at 21.3 ppm, of methine carbon atoms at 26.7 ppm, and of methylene carbon atoms at 40.2 and 49.1 ppm. The last two resonances at 40.2 and 49.1 ppm correspond to two non-equivalent methylene carbon atoms in the two different conformational environments GT.TG and TG.GT, respectively (where the dot identifies the position of the methylene in a given sequence of backbone torsion angles), found along the $s(2/1)2$ helical conformation [192, 209]. The difference of chemical shift between the two methylene resonances is ≈ 10 ppm, which corresponds to the shielding produced by two γ -*gauche* effects. This splitting is due to

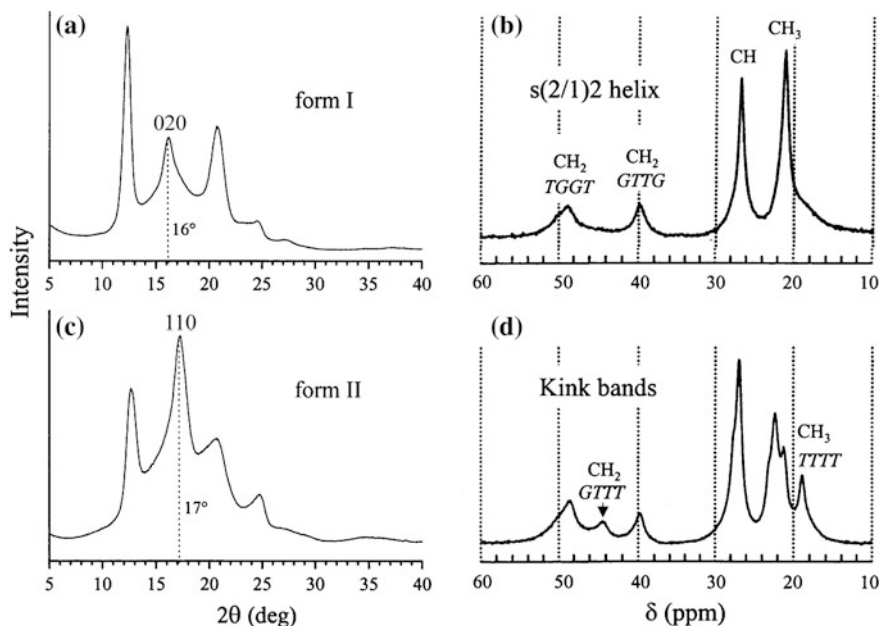


Fig. 2.38 **a** X-ray powder diffraction profile of the as-prepared sample of a highly stereoregular sPP, having content of *rrrr* pentad of 96%, crystallized in the antichiral helical form I, and **b** corresponding solid-state ^{13}C NMR CPMAS spectrum. **c** X-ray powder diffraction profile of a less stereoregular sample of sPP, having content of *rrrr* pentad of 86%, quench-precipitated from solution, crystallized in the isochiral helical form II, and **d** corresponding solid-state ^{13}C NMR CPMAS spectrum [121, 122]. Reproduced with permission from Ref. [6]. Copyright 2006 by Elsevier

the fact that in the $s(2/1)2$ helix, the methylene carbon in the GT.TG environment experiences two γ -gauche shielding effects, since they are in a *gauche* arrangement with both the methine carbons in γ position, giving the resonance at higher field, at 40.2 ppm, whereas the methylene carbons in the TG.GT conformational environments are in *trans* arrangement to both the methine carbons in γ -position and do not experience γ -gauche effects, giving the resonance at 49.1 ppm.

The sample of sPP quench-precipitated from solution presents X-ray powder diffraction profile with the typical 110 reflection at $2\theta = 17^\circ$ of form II (Fig. 2.38c) and shows additional resonances in the region of the methylene and methyl carbon atoms of the solid state ^{13}C NMR CPMAS spectrum (Fig. 2.26d). In fact, besides the main four peaks listed above, additional resonances are present in the spectrum of Fig. 2.38d, in the regions of the methyl groups at 18.9 and 22.4 ppm and in the region of the methylene groups at 44.9 and 50.2 ppm. These additional resonances were explained by assuming the presence of conformational disorder consisting in the presence of portions of chain in *trans* planar conformation ...TTTT... in a chain having a prevailing two-fold helical conformation (TTGG)_n [206, 207]. In particular the resonance at $\delta = 44.9$ ppm was assigned to methylene carbon atoms in TT.

TG or GT.TT conformational environment, which experience one γ -*gauche* effect, whereas the resonances at 18.9 and 50.2 ppm were assigned to methyl and methylene carbon atoms, respectively, in portions of chains in *trans*-planar TTTT conformation [206]. Finally, the resonance at 22.4 ppm were attributed to methyl carbon atoms placed at the interface between the *trans*-planar and the helical portions of chains [206].

A possible model of disorder, which accounts for the X-ray diffraction pattern and the solid-state ^{13}C NMR spectrum of Fig. 2.38c, d is shown in Fig. 2.39. Chains in prevailing $s(2/1)2$ helical conformation present defects represented by long sequences in *trans*-planar conformation [206–208]. In the most probable proposed model this portions of chain are basically T_6 sequences [208]. These conformationally disordered chains are still able to pack in the *C*-centered crystalline lattice of form II, so that the conformational defects do not destroy crystallinity (Fig. 2.38c). In the proposed model of Fig. 2.39 the defective region, characterized by chains in T_6G_2 conformation, is clustered in planes and forms kink bands. Portions of chains in the regular twofold helical conformation, all having the same chirality, are packed according to the limit ordered model of form II (Fig. 2.26b) and are connected by portion of chains in *trans* planar conformation. The most

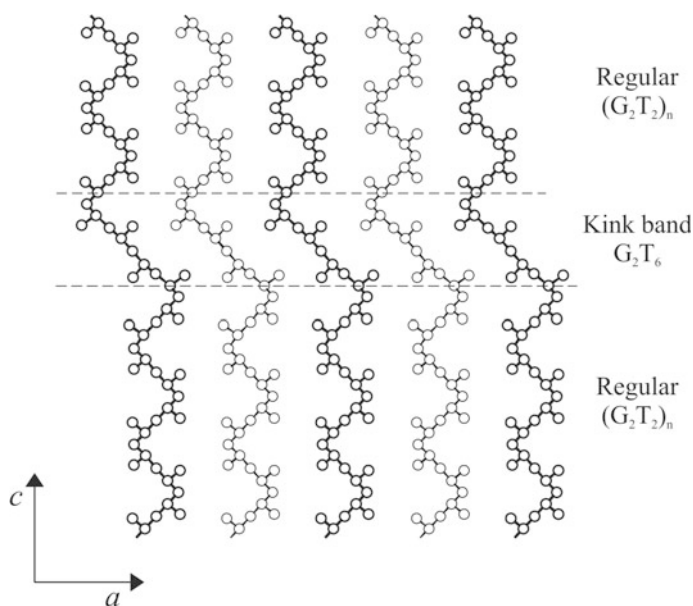


Fig. 2.39 Model of packing of conformationally disordered chains of sPP in disordered modifications of form II presenting kink-bands [206–208]. Chains drawn with thick and thin lines are at 0 and 0.5 along *b*, respectively. In the ordered portions of the crystal the chains are in the regular two-fold $(T_2G_2)_n$ helical conformation, whereas in the defective portion (delimited by the dashed lines) the chains are in G_2T_6 conformation. Reproduced with permission from Ref. [208]. Copyright 1997 by American Chemical Society

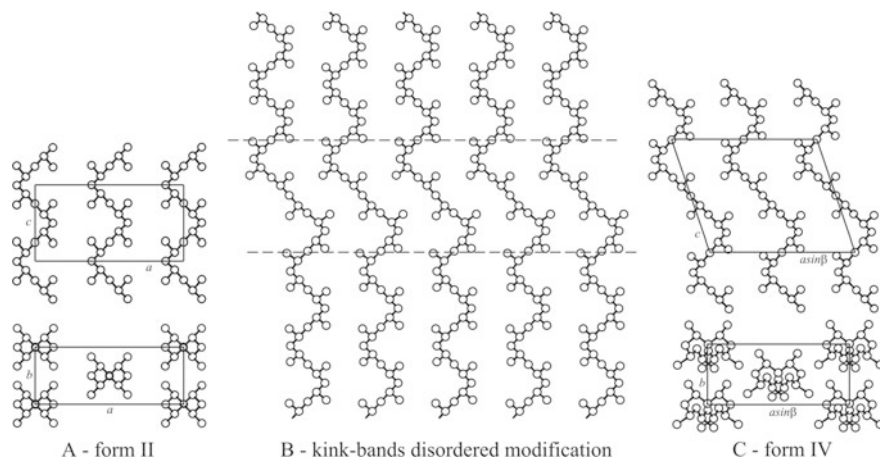


Fig. 2.40 Models of packing in the limit ordered form II (A) and form IV (C) of sPP and model of a conformationally disordered modification, presenting kink-bands (B), intermediate between the limit ordered models of forms II (A) and IV (C). In the defective region of the model B, delimited by the dashed lines, the chains are packed like in the form IV (C), whereas in the ordered regions the chains are packed like in the form II (A). Reproduced with permission from Ref. [208]. Copyright 1997 by American Chemical Society

important feature is that a substantial parallelism among the local chain axes is maintained, so that a good packing of the chains is preserved. These kink bands may be regarded as stacking faults cutting the chain axes, but preserving a substantial parallelism of the chains. The presence of the conformational disorder does not avoid the possibility of crystallization, provided that the parallelism of the chains is preserved.

It is worth noting that in the defective regions the chains are packed like in the form IV of sPP, having chains in the regular $T_6G_2T_2G_2$ conformation (Fig. 2.26d) [40, 41], whereas in the ordered regions the chains are packed like in the form II (Fig. 2.26b). Therefore the model of Fig. 2.39 describes disordered modifications of sPP having structures intermediate between forms II and IV of sPP (Fig. 2.40) [41]. This suggests that, depending on the condition of crystallization, there exists a continuum of conformationally disordered modifications of sPP containing kink bands, intermediate between two limit isochiral structures, the limit ordered form II and the limit ordered form IV.

Conformational disorder and kink bands structures have been found also in random copolymers of syndiotactic propylene-ethylene copolymers [199]. The formation of these disordered modifications is easier in the copolymers than in the case of the sPP because it is kinetically favored by the easier local formation of *trans*-planar sequences in the presence of ethylene units. The inclusion of ethylene comonomeric units in the crystalline regions of copolymers favors, locally, the formation of *trans*-planar sequences, which, in turn, induces the crystallization of the samples in disordered modifications of form II containing kink-bands [199].

2.5.5 Crystal Structure of Form III

The Form III of sPP is characterized by chains in *trans*-planar conformation packed in an orthorhombic unit cell with axes $a = 5.22 \text{ \AA}$, $b = 11.17 \text{ \AA}$, $c = 5.06 \text{ \AA}$ (Fig. 2.26c), according to the space group $P2_1cn$ [39]. It is obtained by stretching at room temperature and at high deformations films of highly stereoregular sPP samples prepared with metallocene catalysts [39, 42, 190].

Crystals of the most stable antichiral helical form I, present in the film prepared, for instance by compression-molding, transform by stretching into the *trans*-planar form III [42] (Fig. 2.41) The degree of this transformation basically depends on the stereoregularity of the sample [190, 201, 204]. For highly syndiotactic samples, with *rrrr* pentad contents higher than 90%, the transition of the helical form into the *trans*-planar form III is complete already at nearly 300–400% deformation, whereas higher values of deformations are necessary to obtain the pure form III in samples of lower stereoregularity ($[rrrr] = 75\text{--}80\%$) [201, 202].

The polymorphic form of sPP with chains in *trans*-planar conformation was first obtained in the 1964 by cold-drawing specimens quenched from the melt of regioirregular and low stereoregular sPP samples prepared with Ziegler-Natta catalysts [38]. Because of the low stereo- and regio-regularity, samples of low crystallinity, including the *trans*-planar form with high degree of disorder were obtained, so that only the *trans*-planar conformation was determined from the value of the chain axis periodicity of 5.1 \AA [38]. The complete crystal structure of form III was determined later by Chatani et al. [39] by using the X-ray fiber diffraction data obtained from fibers of highly syndiotactic and fully regioirregular samples prepared with metallocene catalysts.

As discussed above, form III is stable only in the stretched state and transforms into the helical form II by releasing the tension (Fig. 2.41) [190, 202–204]. Energy calculations support the experimental evidence that form III is metastable since its energy is significantly higher than those of the helical forms I and II [193, 194]. In agreement with the higher energy of form III, indeed, well-formed crystals of form III are found only under the influence of an external stress and the so-obtained form III transforms spontaneously into the helical form II by removing the tension [190, 202–204].

Finally, form III transforms into the most stable helical forms by annealing the stretched fibers at temperatures above $100 \text{ }^\circ\text{C}$ and keeping the fibers under tension [116, 119] obtaining mixtures of crystals of the helical form I and form II [116, 119, 133].

It is worth noting that the polymorphic transition occurring by effect of stretching from the stable helical form I present in the unoriented compression-molded films (Fig. 2.41a), into the *trans*-planar form III obtained in the stretched oriented fibers (Fig. 2.41b) is accomplished by the irreversible transformation of the initial spherulitic morphology into a fiber morphology characterized by a high degree of orientation of the crystals with chain axes parallel to the stretching direction. In the successive step of release of the tension (Fig. 2.41b,

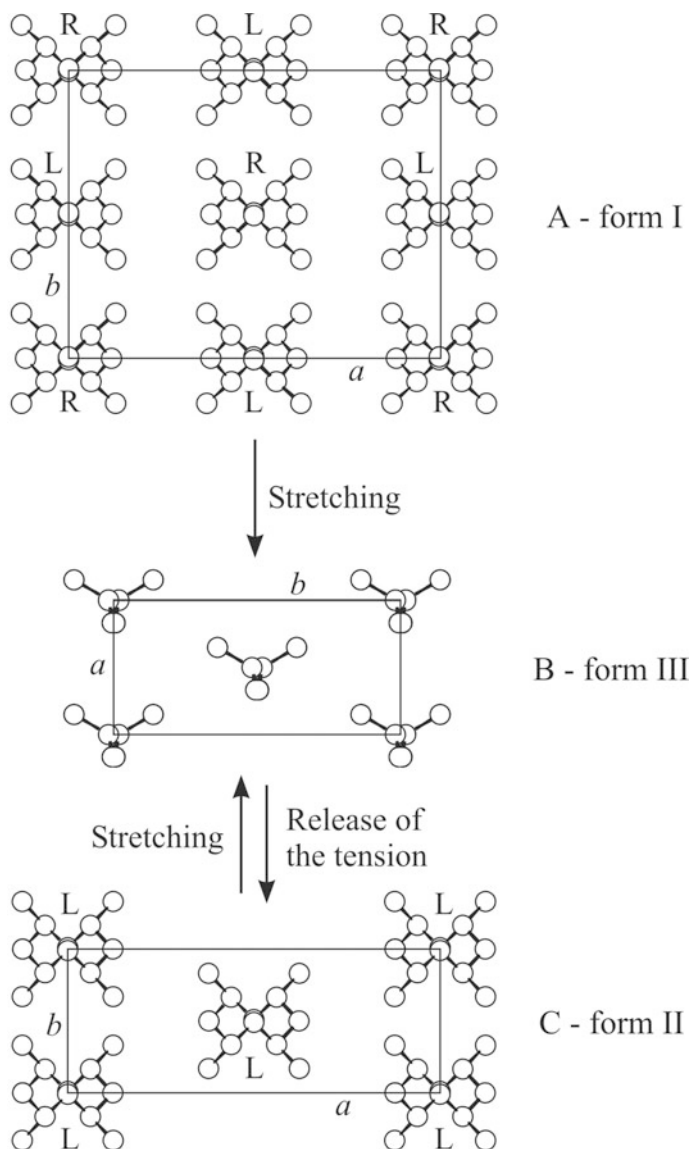


Fig. 2.41 Crystal structures of the antichiral helical form I (A), the *trans*-planar form III (B) and the isochiral helical form II (C) of sPP. The *trans*-planar form III is obtained in oriented fibers by stretching unoriented samples in form I, and transforms into the helical form II by releasing the tension of the stretched fibers. In a successive stretching step of the sample, form II transforms back to form III. From this point on, the form II \rightarrow form III transition is reversible in consecutive step cycles of stretching and releasing the tension, while the sample recovers the initial shape and dimensions

c), the *trans*-planar form III transforms into the helical form II, and the high degree of orientation achieved by the crystals in the oriented fiber is preserved. Due to the irreversible morphological transformations occurring during the first mechanical cycle of stretching and release of the tension of not previously oriented samples, only a partial recovery of the sample dimensions is observed [6, 119, 190].

Concerning transformations occurring at microscopic length scale, during the transition from the two-fold helical form into the *trans*-planar form III by effect of stretching, an increase of the periodicity per structural unit h (which includes two monomeric units) from $h = c/2 = 3.7 \text{ \AA}$ of the two-fold helical form to $h = c = 5.1 \text{ \AA}$ of the *trans*-planar form III, occurs (Fig. 2.42). The crystal dimensions increase by about 38% along c . This increase is completely recovered upon releasing the tension due to the transition of the *trans*-planar form into the helical form II, and, correspondingly, a reduction of the length of the specimen occurs. Therefore, the 38% shrinkage of crystals experiencing the mechanical stress field upon release of the tension contribute to the partial recovery of the macroscopic dimensions of not previously oriented samples [201–204, 210].

Oriented fibers, prepared by stretching compression molded films up to a given deformation and successive release of the tension, show a different mechanical behavior [201–204, 210]. A perfect elastic recovery is observed in successive cycles of stretching and relaxation of fibers. During these mechanical cycles a reversible crystal-crystal polymorphic transition between the helical form II and the *trans*-planar form III occurs [201–204, 210]. The helical form II of the stress-relaxed fibers transforms by stretching into the *trans*-planar form III, which

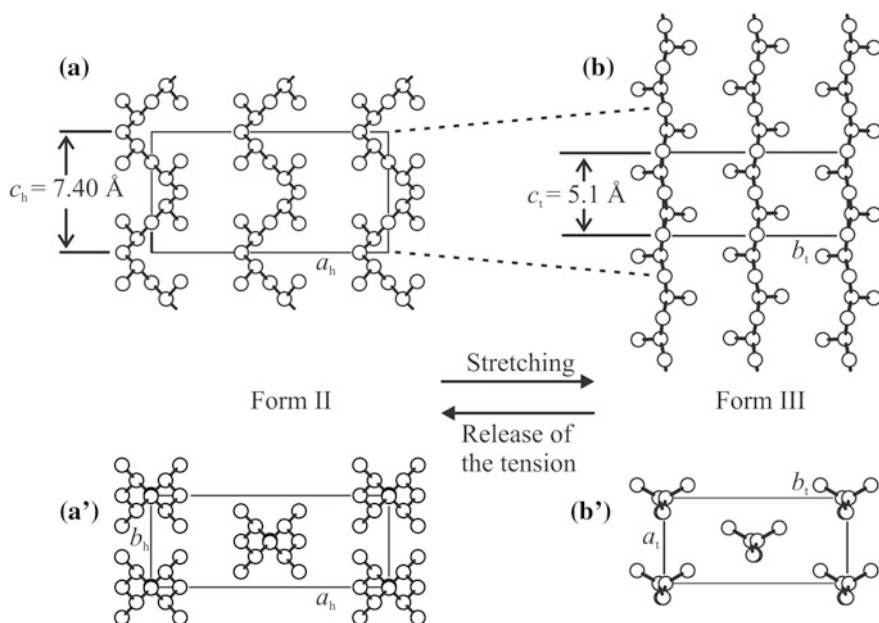


Fig. 2.42 Models of packing of limit ordered forms II (a, a') and III (b, b') of sPP in projections parallel (a, b) and perpendicular (a', b') to the chain axes. Upon stretching, the size of form II crystals increases by 38% ($(2c_t - c_h)/c_h = 0.38$) along the chain axis direction. Upon release of the tension the size of form III crystals shrinks by 38% along the chain axis direction. Adapted with permission from Ref. [210]. Copyright 2007 by Wiley

transforms back into the helical form II by releasing the tension (Figs. 2.41B, C and 2.42). It has been demonstrated that this transition is a fast and direct process occurring on the same time scale as the rate the material is strained and relaxed [202–204, 210]. Since oriented fibers do not experience irreversible plastic deformation during the stretching step, a complete elastic recovery is observed.

It has been suggested that the polymorphic transition of the metastable *trans*-planar form III into the helical form II is in part responsible for the elasticity of sPP due to the enthalpy gain achieved when the fibers are relaxed [201–204, 210]. In sPP, indeed, both the crystalline and amorphous chains play key roles. The small crystalline aggregates actively participate to the elasticity of sPP, locally acting as microscopic engines. The chains in the amorphous regions are possibly well oriented and in more extended conformation in the stretched state, and experience a reversible conformational transition between disordered random-coil and extended conformations when the samples are repeatedly stretched and relaxed. These chains are also highly entangled and connect, as *tie-chains*, different crystals, which undergo the structural transition during the mechanical cycles. During elongation, the chains in the amorphous regions assume extended conformations and tend to orient parallel to the stretching direction. The crystalline aggregates also tend to assume a preferred orientation with the chain axes parallel to the stretching direction; at the same time, when a given crystal experiences a stress higher than a critical value a crystal-crystal phase transition from the helical form II into the *trans*-planar form III occurs and the size of the crystals increases by 38% along the chain axis direction (Fig. 2.42a, b). During the relaxation step, when a given crystal experiences a stress level below a critical value, the *trans*-planar form III becomes unstable and transforms instantaneously into the more stable form II; correspondingly, the crystal shrinks by 38% along the chain axis direction [202–204, 210] (Fig. 2.42a, b). The enthalpy difference associated with the reversible crystal-crystal phase transition between the helical forms II and the *trans*-planar form III, $\Delta H_{(II-III)} = 2.6 \text{ kJ}/(\text{mol of monomeric units})$ has been evaluated from the equilibrium values of the critical stress experienced by the crystals at various temperatures (found by stress-relaxation experiment) [210]. The enthalpy gain achieved upon relaxation when the tensile tension is removed is mainly responsible for the elastic recovery of the sPP fiber samples [202–204, 210].

This crystal transition, in turn, induces an abrupt conformational transition in the chains of the amorphous phase close to the crystals. These amorphous springs assume less extended conformations generating a sort of chain reaction, which rapidly extends to the whole material. The return into entropically favored disordered conformations of amorphous chains produces the entropic factor also involved in the recovery process. Therefore, while the driving force leading the conventional elastomers to recover the initial dimensions is merely entropic, in the case of sPP elasticity is also assisted by the enthalpy gain achieved when the sample is relaxed [202–204, 210]. When the tension is removed, both the enthalpic factor,

due to the structural transition in the crystalline regions, and an entropic factor, due to the conformational transition of the chains in the entangled amorphous phase, contemporarily contributes to the elastic recovery of the sPP fibers [202–204, 210].

2.5.6 Crystal Structure of Form IV

Form IV was obtained by Chatani et al. [40] by exposing stretched fiber of sPP originally in the *trans*-planar form III to organic solvents (e.g. benzene at temperature below 50 °C). The crystal structure of form IV, as reported by Chatani [40], is characterized by chains in the $(T_6G_2T_2G_2)_n$ helical conformation (Fig. 2.43a), packed in a triclinic unit cell with axes $a = 5.72 \text{ \AA}$, $b = 7.64 \text{ \AA}$, $c = 11.60 \text{ \AA}$, $\alpha = 73.1^\circ$, $\beta = 88.8^\circ$ and $\gamma = 112.0^\circ$, according to the space group $P1$ [40]. Form IV has been found only in oriented fibers and never in powder samples. It is metastable and readily transforms into the two-fold helical forms by annealing above 50 °C [40].

Successive studies have shown that the crystal structure of form IV could be described by an analogous model having higher symmetry [41]. In this alternative model the unit cell is monoclinic with parameters $a_m = 14.17 \text{ \AA}$, $b_m = 5.72 \text{ \AA}$, $c_m = 11.60 \text{ \AA}$ and $\beta_m = 108.8^\circ$ and the space group is $C2$ with two chains included in the unit cell [41]. The monoclinic model can be easily obtained from the triclinic structure by small changes of the atomic coordinates and packing arrangement [41].

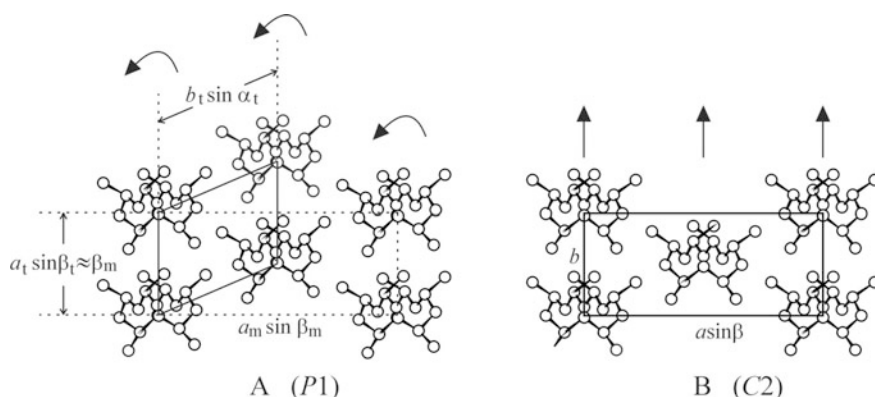


Fig. 2.43 Models of packing of form IV of sPP, according to the triclinic space group $P1$ [40] (A) and monoclinic space group $C2$ [41] (B). The arrows indicate the crystallographic twofold axes, present in model B and lost in A. In the model A the chains are rotated by 6.5° according to the direction of the arrows and the continuous and dashed lines show the triclinic and monoclinic unit cells, respectively. Reproduced from Ref. [6] by permission of Elsevier

The triclinic and monoclinic models are compared in Fig. 2.43. In the monoclinic model (Fig. 2.43B and 2.26d) the local two-fold rotation axes of the chain, perpendicular to the chain axis, are maintained in the lattice as crystallographic symmetry elements (space group $C2$). In the triclinic model (Fig. 2.43A) all the chains are rotated by the same amount (nearly 6.5°) around the chain axis with respect to the monoclinic model. The crystallographic two-fold rotation axes are lost as a consequence of this rotation and the symmetry is broken (space group $P1$). Since starting from the monoclinic structural model, two equivalent triclinic models can be obtained upon rotations of the chains clockwise or counterclockwise by 6.5° around the chain axis, the monoclinic model with higher $C2$ symmetry (Fig. 2.43B) may be considered as an average model for the structure of form IV, which describes the order in the long range. The triclinic model (Fig. 2.43A) describes local situation of order, where the symmetry, locally, is broken. Therefore, the crystal structure of form IV of sPP provides another example of symmetry breaking in the limit ordered structure of polymers [41]. Energy calculations have indicated that the energy of the monoclinic model is 0.01 kcal/mol lower than that of the triclinic model [196], in agreement with the hypothesis of Ref. [41].

The monoclinic description of the crystal structure of form IV has evidenced that the ideal models of the structures proposed for form II and form IV (Figs. 2.26b, d and Fig. 2.40A, C) of sPP present close analogies: (1) both are C -centered; (2) both correspond to an isochiral packing of helices; (3) they are nearly isometric since the a and b axes of the unit cells are very similar. This allows for an understanding of the formation of kink-bands defects in form II (Figs. 2.39 and 2.40) [206–208]. Structural models with kink-bands of Fig. 2.40 can be considered as possible examples of intermediate structures between the limit ordered models of form II and form IV. Indeed, in the model of Fig. 2.40, there are zones with chains in $(TTGG)_n$ conformation packed according to the orthorhombic model of form II, and zones with chains in a long *trans*-planar sequence, packed according to the monoclinic model of form IV. In this view, it has been suggested that there exists a continuum of disordered structures intermediate between the limit ordered models of form II and form IV of sPP [41].

2.5.7 The *Trans-planar Mesomorphic Form of sPP*

Syndiotactic polypropylene (sPP) crystallizes in a solid mesophase by quenching the melt to 0°C and keeping the sample at 0°C for long time (at least 20 h) [211–221]. The X-ray powder diffraction profile of a highly stereoregular sample of sPP in the mesomorphic form is shown in Fig. 2.44a [211, 217]. The X-ray fiber diffraction pattern of fibers of sPP in the mesomorphic form, obtained by stretching the unoriented samples in the mesomorphic form and, then, removing the tension, is shown in Fig. 2.44b. The diffraction patterns are characterized by broad reflections on the equator at $2\theta = 17^\circ$ and on the first layer line at $2\theta = 24^\circ$, indicating disorder in the structure. The layering of the reflection in the X-ray fiber diffraction pattern,

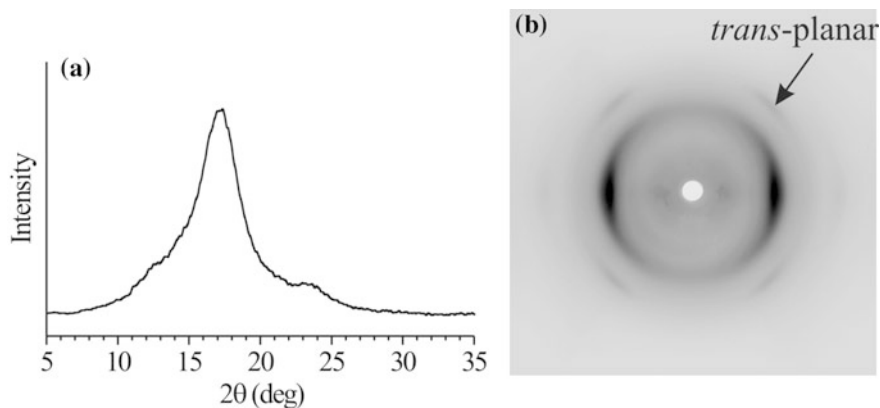


Fig. 2.44 X-ray powder diffraction profile (a) and fiber diffraction pattern (b) of the mesomorphic form of sPP [211, 217, 220]. The unoriented powder sample is obtained by quenching the melt of a highly stereoregular sPP sample at 0 °C and keeping the sample at 0 °C for 16 h [217, 218]. The fiber specimen has been obtained by stretching the unoriented sample in the mesomorphic form and then removing the tension [220]

corresponding to a chain periodicity of 5.1 Å (Fig. 2.44b) indicates that the chains are in the ordered *trans*-planar conformation [211, 217].

The *trans*-planar conformation of sPP chains in the mesomorphic form is confirmed by the solid-state ^{13}C NMR spectra (Fig. 2.45) [217], that shows the characteristic resonance of the methylene carbon atoms at $\delta \approx 50$ ppm in the conformational environment TT.TT typical of the *trans*-planar conformation [222].

The solid mesophase of sPP is characterized by lateral disorder in the packing of *trans*-planar chains associated with a rotational disorder of chains around the chain axes and translational disorder along the chain axes. Because of these types of disorder it was suggested that the *trans*-planar chains of sPP in the mesomorphic aggregates assume locally, on average, a pseudo-hexagonal arrangement.

X-ray diffraction analysis of sPP samples quenched from the melt to 0 °C and kept at 0 °C for different times (Fig. 2.46) indicates that if the samples are

Fig. 2.45 Solid state ^{13}C NMR CP MAS spectrum of a highly stereoregular sPP sample in the mesomorphic form, obtained by quenching the melt to 0 °C and keeping the sample at 0 °C for 2 months [217]. Reproduced with permission from Ref. [217]. Copyright 2000 by the American Chemical Society

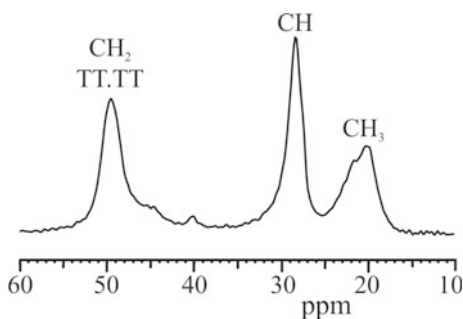
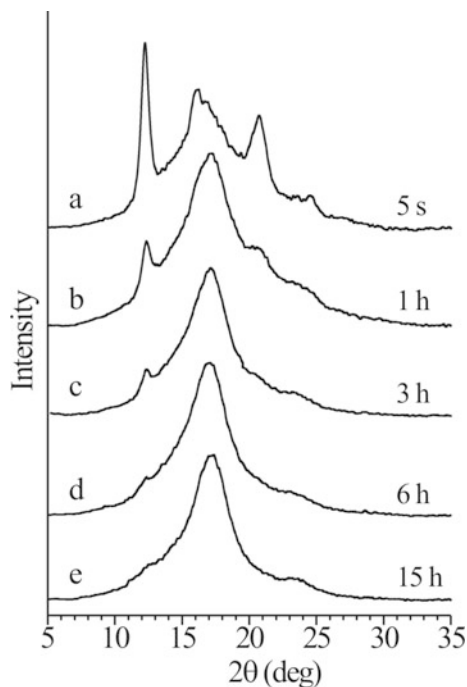


Fig. 2.46 X-ray powder diffraction profiles of a highly stereoregular sPP sample, having concentration of *rrrr* pentad of 96%, quenched from the melt to 0 °C and kept at 0 °C for the indicated amount of time. Reproduced with permission from Ref. [218]. Copyright 2001 by Elsevier Science Ltd.



immediately taken out from the bath at 0 °C, they rapidly crystallize at room temperature in the more stable helical form I (Fig. 2.31a) [211]. Only keeping the sample for long times at 0 °C the crystallization of the sample into the more stable helical form I at room temperature can be inhibited, favoring the formation of *trans*-planar mesomorphic form (Fig. 2.46) [211–217]. Solid state ¹³C NMR spectra recorded at room temperature for films of a highly stereoregular sPP sample, quenched at 0 °C from the melt, indicate that the amount of nuclei in *trans*-planar conformational environment embedded in rigid regions of the samples, increase with increasing the time the sPP films are kept at 0 °C [211, 217]. The formed crystallites are rather small and give rise to diffuse X-ray diffraction pattern, as shown in Fig. 2.44a. Only a low level of crystallinity of about 30% is achieved even for very long permanence time at 0 °C.

The crystallization of the *trans*-planar mesomorphic form of sPP at 0 °C was explained considering that the sample just after quenching to 0 °C is in a non-crystalline state [212]. Portions of sPP chains in the *trans*-planar and two-fold helical conformations are in equilibrium in the amorphous state at 0 °C. If the sample is kept at 0 °C for a time long enough, some mobility of the chains is still present, to allow the *trans*-planar portions of the chains to organize in small mesomorphic aggregates [212, 218]. The formation of such aggregates produces an increase in the fraction of C–C bonds in the *trans*-planar conformation. According to ¹³C NMR results, indeed, the fraction of backbone C–C bonds in the *trans* state,

f_{trans} , measured at 0 °C and keeping the quenched sPP sample at 0 °C for 10 min, corresponds to $\approx 80\%$ and increases with increasing the permanence time of the sample at 0 °C [212]. A high value for f_{trans} is in agreement with the equilibrium fractional amount of C-C bonds in the *trans* state expected at 0 °C for a fully syndiotactic chain of $\approx 67\%$ as predicted by the isomeric rotational state model [223]. Indeed, the formation of stable mesomorphic aggregates with chains in *trans*-planar conformation, probably controlled by diffusion, alters the normal distribution of conformational states typical of an amorphous sample, because the longer *trans*-planar strands of chains results segregated in the more ordered mesomorphic zones. When the permanence time at 0 °C is long enough, the crystalline *trans*-planar mesomorphic bundles are well-formed and stable and prevent the crystallization at room temperature of the stable crystalline helical form I, when the sample is heated from 0 °C to room temperature [210–216, 218].

The mesomorphic form transforms into the stable helical form I of sPP (Fig. 2.26a) by annealing at 90 °C [219]. Moreover, samples in the mesomorphic form transform into the crystalline *trans*-planar form III of sPP by stretching at high deformations [220, 224]. However, oriented fibers of sPP in the *trans*-planar mesomorphic form (Fig. 2.44b) can be obtained by stretching films in the mesomorphic form and, then, removing the tension [220, 224]. The X-ray fiber diffraction patterns of fibers of a sample of sPP, initially in the *trans*-planar mesomorphic form, stretched at room temperature at different deformations (Fig. 2.47) [220] indicate that stretching at low deformations, up to 200–300%, induces orientation of the mesomorphic crystals, as indicated by the presence in the diffraction patterns of Fig. 2.47a of only the reflections at $2\theta = 17^\circ$ on the equator and at $2\theta = 24^\circ$ on the first layer line, typical of the *trans*-planar mesomorphic form. With increasing deformation, the mesomorphic form transforms into the crystalline *trans*-planar form III of sPP, as indicated by the splitting of the diffraction peak at $2\theta = 17^\circ$ into the $(020)_t$ and $(110)_t$ reflections at $2\theta \approx 16$ and 19° , respectively (Fig. 2.47b, b'), typical of the form III of sPP [39]. The transformation into the crystalline form III is also apparent by the diffraction on the first layer line, where the broad peak of the mesomorphic form at $2\theta \approx 24^\circ$ is replaced by two sharp reflections corresponding to the $(021)_t$ and $(111)_t$ reflections of the crystalline form III [219] (Fig. 2.47b). After releasing the tension, the crystalline *trans*-planar form III transforms back into the mesomorphic form (Fig. 2.47c, c'), as indicated by transformation of the two $(020)_t$ and $(110)_t$ reflections at $2\theta \approx 16$ and 19° of form III into the broad peak at $2\theta = 17^\circ$ of the mesomorphic form. The transition between the *trans*-planar form III and the mesomorphic form is reversible upon successive stretching and relaxing of the fiber and indicate a memory effect of the phase transformations induced by tensile deformation and successive relaxation by removing the tension [220].

The crystallization of the *trans*-planar mesomorphic form of sPP depends on the stereoregularity of the polymer sample [218]. The X-ray diffraction profiles recorded at room temperature of sPP samples having different stereoregularities, quenched from the melt to 0 °C and kept at 0 °C for different times, are reported in Fig. 2.48. The higher the degree of stereoregularity of the sample, the shorter the

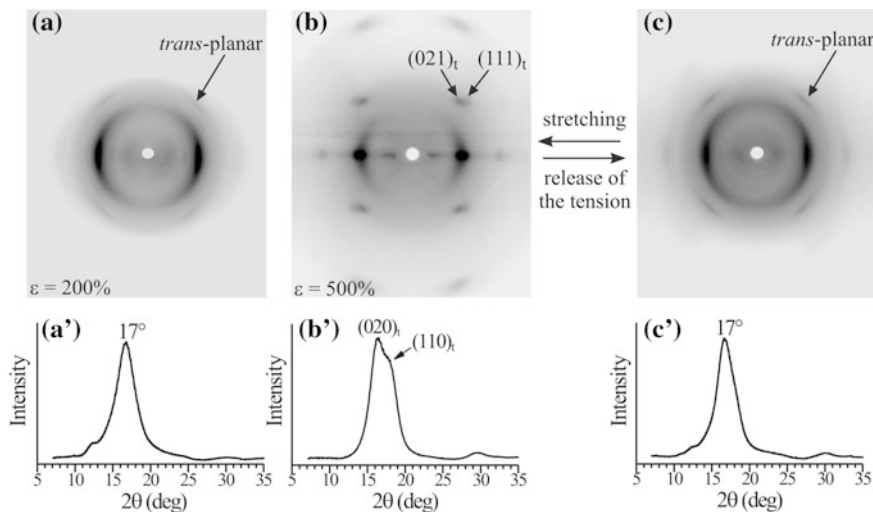


Fig. 2.47 X-ray fiber diffraction patterns (a–c), and corresponding profiles read along the equatorial lines (a'–c'), of fibers obtained by stretching at room temperature and at different deformations ϵ a sample of sPP initially in the mesomorphic form, keeping the fibers under tension (a–b, a'–b') and after removing the tension from deformation of 500% (c, c'). The $(020)_t$ and $(110)_t$ reflections of the *trans*-planar form III and the broad peak at $2\theta = 17^\circ$ of the mesomorphic form are indicated. On the first layer line the reflections arising from the diffraction of crystals of the *trans*-planar forms ($(021)_t$ and $(111)_t$ reflections in the case of the crystalline form III) with chain periodicity of 5.1 Å, are also indicated [220]. Reproduced with permission from Ref. [220]. Copyright 2004 by the American Chemical Society

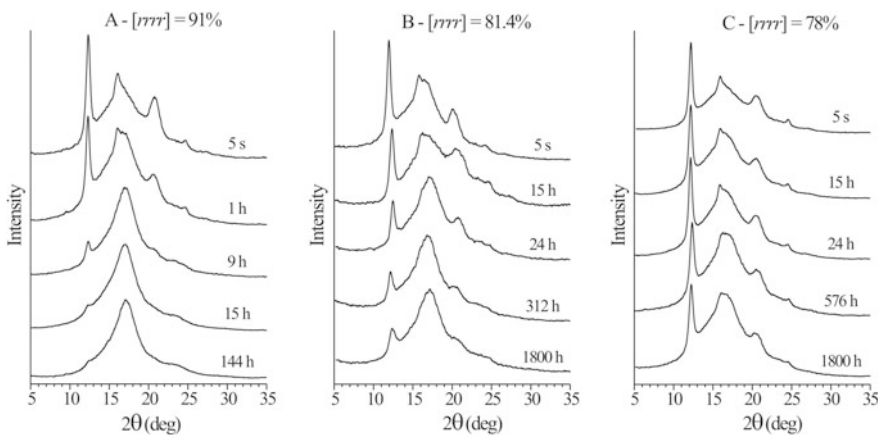


Fig. 2.48 X-ray powder diffraction profiles of sPP samples of different stereoregularity, having concentration of *rrrr* pentad of 91% (A), 81.4% (B) and 78% (C), quenched from the melt to 0 °C and kept at 0 °C for the indicated different permanence times. Reproduced with permission from Ref. [218]. Copyright 2001 by Elsevier Science Ltd.

permanence time at 0 °C necessary to stabilize the *trans*-planar mesomorphic form and inhibit the crystallization of the helical form I at room temperature [218].

For stereoirregular sPP samples the pure *trans*-planar mesomorphic form is never obtained even for long permanence time at 0 °C and the crystallization of the stable helical form is not inhibited (Fig. 2.48C). Therefore, the higher the degree of stereoregularity, the faster the formation of the *trans*-planar mesomorphic form. Moreover, the maximum relative amount of mesomorphic form is 100% of the crystalline phases for the most stereoregular samples, and only 43% for the less stereoregular samples [218].

The formation of the pure *trans*-planar mesomorphic form only for highly stereoregular sPP samples can be explained considering that long sequences in *trans*-planar conformation are less stable in the presence of configurational defects characterized by *mm* triads or isolated *m* diads, typical of sPP samples prepared with syndiospecific C_2 -symmetric metallocene catalysts. These defects, which are randomly distributed along the chains of sPP, are probably more easily tolerated in the two-fold helical conformation than in the *trans*-planar conformation of sPP. In the presence of configurational defects long portions of the sPP chains are able to crystallize only if they assume the helical conformation [218], whereas act as interruption point for chain stretched in *trans*-planar conformation.

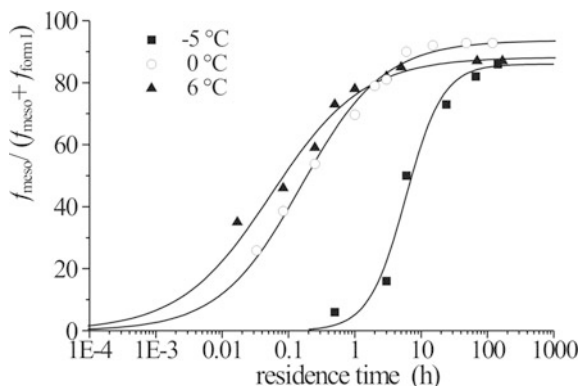
The mesomorphic form of sPP can be obtained also by stretching the stable helical form I in low stereoregular samples [6]. Indeed, in highly syndiotactic samples the helical form I transforms at high deformations into the ordered *trans*-planar form III [6, 39, 42], whereas in low stereoregular samples, prepared with suitable metallorganic catalysts [6, 225], the high concentration of stereodeflects prevents the formation of the crystalline *trans*-planar form III by stretching, and only the disordered mesomorphic form is obtained at high deformations [225–228].

The rate of formation of the mesomorphic form, as well as the maximum amount of the mesomorphic form obtained by quenching, also depend on the quenching temperature [219]. The crystallization from the melt of the *trans*-planar mesomorphic form of sPP has been studied at the quenching temperatures of -5, 0 and 6 °C [219]. At any temperature mixtures of crystals of the *trans*-planar mesomorphic form and helical form I of sPP are obtained, and a total degree of crystallinity of nearly 30% is always achieved. The relative amounts of the two forms depend on the quenching temperature and the residence time of the sample at this temperature (Fig. 2.49). With increasing the quenching temperature, in the examined range between -5 °C and +6 °C, an increase of the rate of formation of the mesomorphic form is observed. However, the maximum amount of mesomorphic form, nearly 100% of the total crystalline phase, is achieved only at 0 °C (Fig. 2.49). In fact, even though the formation of the mesomorphic form is faster at 6 °C, the maximum amount of mesomorphic form is lower [219].

These results can be explained considering that below 0 °C, approaching the glass transition temperature of sPP, portions of chain in *trans*-planar conformation, in equilibrium in the amorphous state with the portions of chain in helical conformation, organize slowly in crystalline aggregates, forming mesomorphic bundles, because of the low mobility of the system. At higher crystallization

Fig. 2.49 Fraction of the *trans*-planar mesomorphic form, with respect to the total crystalline phase, for samples of a highly stereoregular sPP, having content of *rrrr* pentad of 96%, quenched from the melt to $-5\text{ }^{\circ}\text{C}$ (filled square), $0\text{ }^{\circ}\text{C}$ (open circle) and $6\text{ }^{\circ}\text{C}$ (filled triangle), as a function of the residence time at the quenching temperature.

Reproduced with permission from Ref. [219]. Copyright 2003 by Elsevier Science Ltd



temperatures (slightly above $0\text{ }^{\circ}\text{C}$), the higher chain mobility allows a faster formation of the crystalline mesomorphic bundles. However, the mesomorphic aggregates rapidly grown above $0\text{ }^{\circ}\text{C}$, or slowly grown below $0\text{ }^{\circ}\text{C}$, are not big enough to be stable at room temperature, so that the crystallization of the helical form I at room temperature is not completely inhibited. The mesomorphic bundles formed at $0\text{ }^{\circ}\text{C}$ are instead stable enough to prevent the crystallization of form I at room temperature. This could explain the experimental observation that the maximum amounts of mesomorphic form obtained at 6 and $-5\text{ }^{\circ}\text{C}$ are lower than the amount achieved at $0\text{ }^{\circ}\text{C}$ [219].

The crystallization of sPP from the glassy state, after quenching at $0\text{ }^{\circ}\text{C}$, has been studied by Strobl using time- and temperature-dependent simultaneous small- and wide-angle X-ray scattering experiments and dilatometry [229]. This study has indicated that the layer thickness and the long spacing are the same independent of the permanence time at $0\text{ }^{\circ}\text{C}$ and, therefore independent of the inner structure of the lamellae, i.e. mesomorphic form or helical form I. These results have suggested that the crystallization of sPP from the glassy state is mediated by the formation of a mesomorphic intermediate phase [229]. The crystals form only in a second step, subsequent to an initial formation of mesomorphic layers. These observations have been claimed as indicative of a general concept that polymer crystallization is a multistage process with a passage through transient mesomorphic states [226, 230–232].

In conclusion, the metastable disordered quenched crystalline form of sPP is a *solid mesophase* characterized by long range periodicity along one direction only, that is along the chain axes, thanks to the presence of chains in the ordered *trans*-planar conformation, and lateral disorder in the packing of the chains. The disorder in the packing of *trans*-planar chains is probably associated to a rotational disorder

of chains around the chain axes and to translational disorder along the chain axes, which produce departure from the order of the crystalline form III. Because of these types of disorder the *trans*-planar chains of sPP in the mesomorphic aggregates assume locally on average a pseudo-hexagonal arrangement.

2.5.8 Helical Mesophase in Syndiotactic Copolymers of Propylene

The effect of comonomeric unit **in syndiotactic copolymers of propylene** on the crystallization of the mesomorphic form of sPP has been also studied [197, 233–235]. These studies have indicated that the *trans*-planar mesomorphic form of sPP is obtained also in stretched fibers of copolymers of propylene with ethylene. This is in agreement with the fact that the presence of ethylene comonomeric units stabilizes the *trans*-planar forms in fibers of the copolymer samples [233–235]. In the case of syndiotactic copolymers of propylene with 1-hexene, 1-octene and 1-octadecene, instead, a different solid mesophase, characterized by chains in the ordered two-fold helical conformation, has been found in stretched fibers [197].

The different behavior of copolymers characterized by the presence of long branched comonomers is due to the fact that the bulky side groups destabilize the *trans*-planar conformation of sPP chains and, at relatively high concentrations, prevent the crystallization of both the *trans*-planar form III and the *trans*-planar mesophase. Only at (relatively) low hexene or octene concentrations (in the range 2–5 mol%) the stretching produces transformation of the stable helical form I into the *trans*-planar mesophase. For hexene or octene concentrations higher than 4–5 mol%, indeed, the helical form I transforms by stretching into a different mesomorphic form, characterized by chains in the ordered 2/1 helical conformation, and disorder in the lateral packing of the chains [194].

The X-ray fiber diffraction patterns of the *trans*-planar and helical mesophases are compared in Fig. 2.50. The figure shows similar diffraction patterns. Both show a single, broad reflection at $2\theta = 16\text{--}17^\circ$ on the equator, and a first layer line reflection. The difference is in the separation between layer lines, which corresponds to the periodicity of $c = 5.1 \text{ \AA}$ of the *trans*-planar conformation of the chains in the mesophase of sPP (Fig. 2.50a), and to a periodicity $c = 7.4 \text{ \AA}$ relative to the 2/1 helical conformation of the chains in the mesophase of the propylene-hexene and propylene-octene copolymers (Fig. 2.50b).

The metastable disordered mesomorphic form of sPP obtained in stretched fibers of copolymers of sPP with long branched comonomers (1-hexene, 1-octene, 1-octadecene) is a solid mesophase characterized by long range periodicity along one direction only, that is along the chain axes, because of the presence of chains in the ordered s(2/1)2 helical conformation, and lateral disorder in the packing of the chains.

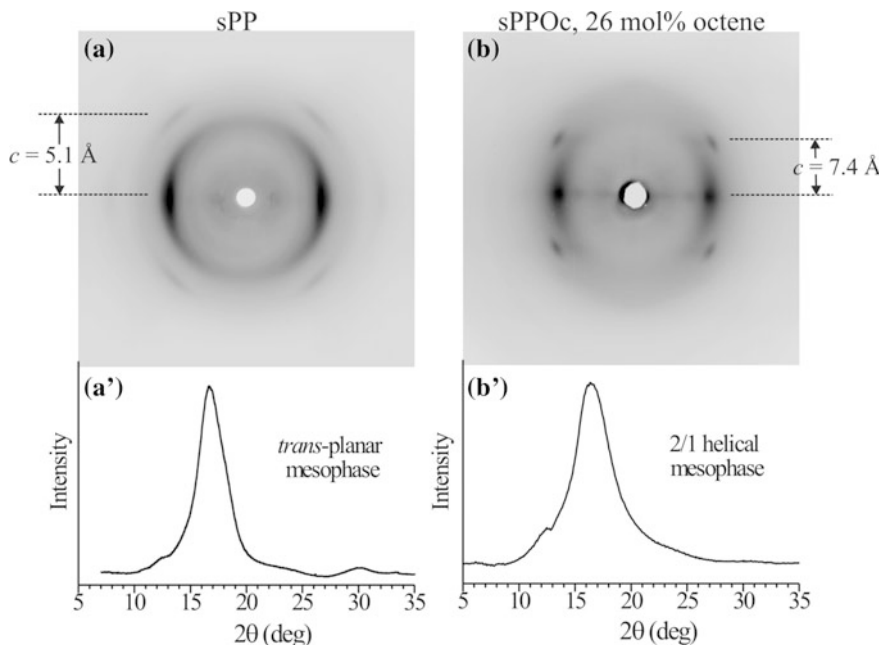


Fig. 2.50 Comparison between the X-ray fiber diffraction patterns (a, b) and the corresponding equatorial diffraction profiles (a', b') of the *trans*-planar mesophase of sPP (a, a'), obtained by stretching the unoriented sample of sPP in the mesomorphic form and then removing the tension [220], and of the 2/1 helical mesophase of sPP (b, b'), obtained in fibers of the propylene-octene copolymer sample with 26 mol% of octene stretched at high values of deformation (750%) [197]. Reproduced with permission from Ref. [197]. Copyright 2010 by the American Chemical Society

2.6 Conclusions

The determination of crystal structure of isotactic and syndiotactic polypropylene and the study of related disorder phenomena illustrated in this chapter represent a superb example highlighting the enormous progress made in the field of structural analysis toward the identification of the basic principles that govern the ordering process of polymer chains in the crystals, the discovery of new phenomena, the breaking of paradigms, the study of disorder, new materials and new properties.

For instance we have shown that the identification of the chain conformation of stereoregular polymers in the crystalline state, and isotactic polypropylene in particular, provided at that time, the first example of synthetic polymers crystallizing with a helical symmetry. From that point on, **the equivalence postulate**, and the **principle of minimum conformational energy** for the isolated chains were build up, and are nowadays at foundations of polymer science.

On the other hand, we have also shown that the packing mode of the 3/1 helical chains of iPP in a monoclinic unit cell instead than trigonal, provides an important

exception to the **Principle of Maximum Entropy**. The packing of the three-fold helical chains of iPP in a monoclinic unit cell, indeed, allows for denser packing than in a more symmetric environment such as trigonal, were the local symmetry of the chains would be preserved.

Moreover, the resolution of the crystal structure of γ form of iPP represented a true breakthrough in polymer crystallography, since **the nonparallel arrangement of chain axes** in the crystals broke the paradigm **that the chains in a polymer crystals must be parallel**.

Also, the crystal structure β form contributed to the discovery of a new concept in crystallography, which resides in the **frustrated** character of the packing mode of chains in the crystals. The **concept of frustration** was demonstrated to be more general than that identified in the β form of iPP and arises whenever two motifs maximize their interactions at the expense of the third motif.

In the case of sPP, we have shown that electron diffraction analysis, coupled with the accurate analysis of data measured with different techniques, such as solid state NMR, allow for identification of symmetry breaking in form I, packing disorder in form I and form II, stacking fault disorder parallel or perpendicular to chain axes (kink band in form II).

Besides, in 20 years, after the discovery of metallocene catalysts, the study of the new iPP and sPP samples with tailored chain architectures, not only have allowed to introduce new materials, with new properties and applications, but have pushed the research toward the development of new methods for the analysis of structural disorder, more sophisticated techniques and/or approaches for the measure of properties.

In general, the determination of the crystal structure of a polymer represents per se an ambitious goal. However, it represents also the starting point in successive studies having fundamental and applicative implication. For instance, we have shown that the studies of the structure and polymorphism of sPP has allowed identifying a new class of polymers with elastomeric properties, the crystalline elastomers, showing elastomeric behavior of enthalpic nature associated with the reversible crystal-crystal phase transition between the helical form II and trans-planar form III.

Another significant example is related to the studies of the structure, polymorphism and disorder phenomena occurring in the case of stereoirregular iPP samples. These studies have allowed identifying a new category of materials having completely different properties from those of Ziegler-Natta iPP. It has been shown, that depending on the kind and concentration of defects along the chains, it is possible controlling independently each other, properties not easily reconcilable in the same material, such as density, melting temperature, ductility, rigidity and mechanical strength.

The study of the crystal structure of polymers using the methods and the language of crystallography, may open new opportunities, allows attaining new concepts, identifying new applications, inspiring the development of new methods for the synthesis of new polymers, and the processing/production of new materials.

References

1. Natta G, Pino P, Corradini P et al (1955) Crystalline high polymers of α -olefins. *J Am Chem Soc* 77:1708–1710. <https://doi.org/10.1021/ja01611a109>
2. Natta G, Corradini P (1960) Structure and properties of isotactic polypropylene. *Il Nuovo Cimento* 15:40–51. <https://doi.org/10.1007/BF02731859>
3. Kaminsky W (ed) (2013) Polyolefins: 50 years after Ziegler and Natta I. Polyethylene and Polypropylene *Adv Polym Sci* 257. <https://doi.org/10.1007/978-3-642-40808-3>
4. Kaminsky W (ed) (2013) Polyolefins: 50 years after Ziegler and Natta II. Polyolefins by metallocenes and other single-site catalysts. *Adv Polym Sci* 258. <https://doi.org/10.1007/978-3-642-40805-2>
5. Brückner S, Meille SV, Petraccone V et al (1991) Polymorphism in isotactic polypropylene. *Prog Polym Sci* 16:361–404. [https://doi.org/10.1016/0079-6700\(91\)90023-E](https://doi.org/10.1016/0079-6700(91)90023-E)
6. De Rosa C, Auriemma F (2006) Structure and physical properties of syndiotactic polypropylene: a highly crystalline thermoplastic elastomer. *Prog Polym Sci* 31:145. <https://doi.org/10.1016/j.progpolymsci.2005.11.002>
7. Corradini P (1968) The stereochemistry of macromolecules. In: Ketley AD (ed) Marcel Dekker Inc., New York, p 1. <https://doi.org/10.1002/9781119044123>
8. Kakudo M, Kasai N (1972) X-ray diffraction by polymers. Elsevier, New York. ISBN 0444410317
9. Tadokoro H (1979) Structure of crystalline polymers. Wiley, New York. ISBN 0894643495
10. De Rosa C, Auriemma F (2013) Crystal structures of polymers. In: Piorowska E, Rutledge GC (eds) Handbook of polymer crystallization. Wiley, Hoboken. <https://doi.org/10.1002/9781118541838.ch2>
11. De Rosa C, Auriemma F (2014) Crystals and crystallinity in polymers. Diffraction analysis of ordered and disordered crystals. Wiley, Hoboken. <https://doi.org/10.1002/9781118690444>
12. De Rosa C (2004) Chain conformation, crystal structures, and structural disorder in stereoregular polymers. *Top Stereochem* 24:71. ISBN: 0471054976
13. Corradini P, Auriemma F, De Rosa C (2006) Crystals and crystallinity in polymeric materials. *Acc Chem Res* 39:314. <https://doi.org/10.1021/ar040288n>
14. Auriemma F, De Rosa C, Corradini P (2005) Solid mesophases in semicrystalline polymers: structural analysis by diffraction techniques. *Adv Polym Sci* 181:1. <https://doi.org/10.1007/b107169>
15. De Rosa C, Auriemma F (2011) Single site metallorganic polymerization catalysis as a method to probe the properties of polyolefins. *Polym Chem* 2:2155. <https://doi.org/10.1039/c1py00129a>
16. Bruckner S, Meille SV (1989) Non-parallel chains in crystalline γ -isotactic polypropylene *Nature* 340:455. <https://doi.org/10.1038/340301a0>
17. Meille SV, Bruckner S, Porzio W (1990) γ -Isotactic polypropylene. A structure with nonparallel chain axes. *Macromolecules* 23:4114. <https://doi.org/10.1021/ma00220a014>
18. Lotz B, Kopp S, Dorset L (1994) Original crystal structure of polymers with ternary helices *C R Acad Sci Paris* 319:187. ISSN: 1251-8069
19. Dorset DL, McCourt MP, Kopp S et al (1998) Isotactic polypropylene, β -phase: a study in frustration. *Polymer* 39:6331–6337. [https://doi.org/10.1016/s0032-3861\(97\)10160-4](https://doi.org/10.1016/s0032-3861(97)10160-4)
20. Stocker W, Schumaker M, Graff S et al (1998) Epitaxial crystallization and AFM investigation of a frustrated polymer structure: isotactic poly(propylene), β phase. *Macromolecules* 31:807. <https://doi.org/10.1021/ma971345d>
21. Meille SV, Ferro DR, Bruckner S et al (1994) Structure of β -isotactic polypropylene: a long-standing structural puzzle. *Macromolecules* 27:2615. <https://doi.org/10.1021/ma00087a034>

22. Ewen JA (1984) Mechanisms of stereochemical control in propylene polymerizations with soluble Group 4B metallocene/methylalumoxane catalysts. *J Am Chem Soc* 106:6355. <https://doi.org/10.1021/ja00333a041>
23. Kaminsky W, Kulper K, Brintzinger HH et al (1985) Polymerization of propene and butene with a chiral zirconocene and methylaluminoxane as cocatalyst. *Angew Chem* 97:507. <https://doi.org/10.1002/anie.198505071>
24. Ewen JA, Jones RL, Razavi A et al (1988) Syndiospecific propylene polymerizations with Group IVB metallocenes. *J Am Chem Soc* 110:6255. <https://doi.org/10.1021/ja00226a056>
25. Corradini P, Guerra G (1992) Polymorphism in polymers. *Adv Polym Sci* 100:182. <https://doi.org/10.1007/BFb0051637>
26. Natta G, Corradini P (1960) Structure of crystalline polyhydrocarbons. *Nuovo Cimento Suppl* 15:9. <https://doi.org/10.1007/BF02731858>
27. Huggins ML (1945) Comparison of the structures of stretched linear polymers. *J Chem Phys* 13:37. <https://doi.org/10.1063/1.1723965>
28. Bunn CW (1942) Molecular structure and rubber-like elasticity I. The crystal structures of β gutta-percha, rubber and polychloroprene. *Proc Roy Soc (London)* A180:67. <https://doi.org/10.1098/rspa.1942.0024>
29. Pauling L, Corey RB, Branson HR (1951) The structure of proteins: two hydrogen-bonded helical configurations of the polypeptide chain. *Proc Natl Acad Sci USA* 37:205. <https://doi.org/10.1073/pnas.37.4.205>
30. IUPAC Commission on Macromolecules Nomenclature (1979) *Pure Appl Chem* 51:1101. <https://doi.org/10.1351/pac198355071101>
31. IUPAC Commission on Macromolecules Nomenclature (1981) *Pure Appl Chem* 53:733. <https://doi.org/10.1351/pac198153030733>
32. Recommendations IUPAC (2011) Definitions of terms relating to crystalline polymers. *Pure Appl Chem* 83:1831–1871. <https://doi.org/10.1351/PAC-REC-10-11-13>
33. Corradini P, Giunchi G, Petraccone V et al (1980) Structural variations in crystalline isotactic polypropylene (α -form) as a function of thermal treatments. *Gazz Chim Ital* 110:413. ISSN:0016-5603
34. Auriemma F, Ruiz de Ballesteros O, De Rosa C et al (2000) Structural disorder in the α form of isotactic polypropylene. *Macromolecules* 33:8764. <https://doi.org/10.1021/ma0002895>
35. Corradini P, De Rosa C, Guerra G et al (1992) On the chain conformation of the syndiotactic vinyl polymers. *Gazz Chim It* 122:305. ISSN:0016-5603
36. Natta G, Pasquon I, Corradini P et al (1960) Propylene linear high polymers with syndiotactic structure. *Rend Fis Acc Lincei* 28:539
37. Corradini P, Natta G, Ganis P et al (1967) Crystal structure of syndiotactic polypropylene. *J Polym Sci Part C* 16:2477. ISSN:0360-8905
38. Natta G, Peraldo M, Allegra G (1964) Crystalline modification of syndiotactic polypropylene having a zig-zag chain conformation. *Makromol Chem* 75:215. <https://doi.org/10.1002/macp.1964.020750120>
39. Chatani Y, Maruyama H, Noguchi K et al (1990) Crystal structure of the planar zigzag form of syndiotactic polypropylene. *J Polym Sci Part C* 28:393. <https://doi.org/10.1002/pol.1990.140281301>
40. Chatani Y, Maruyama H, Asanuma T et al (1991) Structure of a new crystalline phase of syndiotactic polypropylene. *J Polym Sci: Polym Phys Ed* 29:1649. <https://doi.org/10.1002/polb.1991.090291310>
41. Auriemma F, De Rosa C, Ruiz de Ballesteros O et al (1998) On the form IV of syndiotactic polypropylene *J Polym Sci Polym Phys Ed* 36:395. [https://doi.org/10.1002/\(sici\)1099-0488\(199802\)36:3%3c395::aid-polb1%3e3.0.co;2-r](https://doi.org/10.1002/(sici)1099-0488(199802)36:3%3c395::aid-polb1%3e3.0.co;2-r)
42. De Rosa C, Corradini P (1993) Crystal structure of syndiotactic polypropylene. *Macromolecules* 26:5711. <https://doi.org/10.1021/ma00073a028>
43. Auriemma F, De Rosa C, Corradini P (1993) Analysis of the disorder occurring in the crystal structure of syndiotactic polypropylene. *Macromolecules* 26:5719. <https://doi.org/10.1021/ma00073a029>

44. Turner-Jones A, Aizlewood JM, Beckett DR (1964) Crystalline forms of isotactic polypropylene. *Makromol Chem* 75:134. <https://doi.org/10.1002/macp.1964.020750113>
45. Natta G, Corradini P (1955) Crystal structure of a new type of polypropylene. *Atti Accad Naz Lincei-Memorie* 4:73
46. Natta G, Peraldo M, Corradini P (1959) Modificazione mesomorfa smettica del polipropilene isotattico. *Rend Fis Acc Lincei* 26:14
47. Slichter WP, Mandell ER (1958) Molecular motion in polypropylene, isotactic and atactic. *J Appl Phys* 29:1438. <https://doi.org/10.1063/1.1722964>
48. Corradini P, Petraccone V, De Rosa C et al (1986) On the structure of the quenched mesomorphic phase of isotactic polypropylene. *Macromolecules* 19:2699. <https://doi.org/10.1021/ma00165a006>
49. Corradini P, De Rosa C, Guerra G et al (1989) Comments on the possibility that the mesomorphic form of isotactic polypropylene is composed of small crystals of the β crystalline form. *Polymer* 30:281. ISSN: 02636476
50. Guerra G, Petraccone V, De Rosa C et al. (1985) X-ray analysis on unoriented and oriented samples of the quenched form of isotactic polypropylene *Makromol. Chem., Rapid Commun.* 6:573. <https://doi.org/10.1002/marc.1985.030060811>
51. De Rosa C, Auriemma F, Corradini P et al (2006) Crystal structure of the trigonal form of isotactic polypropylene as an example of density-driven polymer structure. *J Am Chem Soc* 128:80–81. <https://doi.org/10.1021/ja0572957>
52. De Rosa C, Dello Iacono S, Auriemma F et al (2006) Crystal structure of isotactic propylene–hexene copolymers: the trigonal form of isotactic polypropylene. *Macromolecules* 39:6098–6109. <https://doi.org/10.1021/ma0606354>
53. Lotz B, Ruan J, Thierry A et al (2006) A structure of copolymers of propene and hexene isomorphous to isotactic poly(1-butene) form I. *Macromolecules* 39:5777. <https://doi.org/10.1021/ma052314i>
54. De Rosa C, Auriemma F, Talarico G et al (2007) Structure of isotactic propylene-pentene copolymers. *Macromolecules* 40:8531–8532. <https://doi.org/10.1021/ma701985m>
55. De Rosa C, Auriemma F, Ruiz de Ballesteros O et al (2012) Crystal structure of the trigonal form of isotactic propylene–pentene copolymers: an example of the principle of entropy–density driven phase formation in polymers. *Macromolecules* 45:2749–2763. <https://doi.org/10.1021/ma201849w>
56. De Rosa C, Auriemma F, Di Girolamo R et al (2010) A new mesophase of isotactic polypropylene in copolymers of propylene with long branched comonomers. *Macromolecules* 43:8559. <https://doi.org/10.1021/ma101543d>
57. Palza H, López-Majada J, Quijada R et al (2005) Metallocenic copolymers of isotactic propylene and 1-octadecene: crystalline structure and mechanical behavior. *Macromol Chem Phys* 206:1221. <https://doi.org/10.1002/macp.200500036>
58. Lotz B (2014) A new ϵ crystal modification found in stereodeficient isotactic polypropylene samples. *Macromolecules* 47:7612–7624. <https://doi.org/10.1021/ma500986f>
59. Rieger B, Mu X, Mallin DT et al (1990) Degree of stereochemical control of racemic ethylenebis(indenyl)zirconium dichloride/methyl aluminoxane catalyst and properties of anisotactic polypropylenes. *Macromolecules* 23:3559–3568. <https://doi.org/10.1021/ma00217a005>
60. Mencik Z (1972) Crystal structure of isotactic polypropylene. *J Macromol Sci Phys* 6:101. <https://doi.org/10.1080/00222347208224792>
61. Hikosaka M, Seto T (1973) Order of the molecular chains in isotactic polypropylene crystals. *Polym J* 5:111. <https://doi.org/10.1295/polymj.5.111>
62. Guerra G, Petraccone V, Corradini P et al (1984) Crystalline order and melting behavior of isotactic polypropylene (α form) *J Polym Sci: Polym Phys* 22:1029. <https://doi.org/10.1002/pol.1984.180220608>
63. De Rosa C, Guerra G, Napolitano R et al (1984) Conditions for the α_1 – α_2 transition in isotactic polypropylene samples. *Eur Polym J* 20:937. [https://doi.org/10.1016/0014-3057\(84\)90073-9](https://doi.org/10.1016/0014-3057(84)90073-9)

64. De Rosa C, Guerra G, Napolitano R et al (1985) Conditions for the α_1 - α_2 transition in isotactic polypropylene samples. *J Therm Anal* 30:1331. ISSN:0368-4466
65. Natta G, Corradini P, Bassi IW (1960) Crystal structure of isotactic poly(1-butene). *Nuovo Cimento. Suppl* 15:52. <https://doi.org/10.1007/BF02731860>
66. Natta G, Corradini P (1955) Crystal structure of isotactic polystyrenes. *Makromol Chem* 16:77. ISSN:0025-116X
67. Natta G, Corradini P, Bassi IW (1960) Crystal structure of isotactic polystyrene. *Nuovo Cimento Suppl* 15:68. <https://doi.org/10.1007/BF02731861>
68. Kardos JL, Christiansen AW, Baer E (1966) Structure of pressure crystallized polypropylene. *J Polym Sci A-2*:777. ISSN:0098-1273
69. Pal KD, Morrow DR, Sauer JA (1966) Interior morphology of bulk polypropylene. *Nature* 211:514. <https://doi.org/10.1038/211514a0>
70. Mezghani K, Phillips PJ (1998) The γ -phase of high molecular weight isotactic polypropylene: III. The equilibrium melting point and the phase diagram. *Polymer* 39:3735-3744. [https://doi.org/10.1016/S0032-3861\(97\)10121-5](https://doi.org/10.1016/S0032-3861(97)10121-5)
71. Mezghani K, Phillips PJ (1997) The γ -phase of high molecular weight isotactic polypropylene. II. The morphology of the γ -form crystallized at 200 MPa. *Polymer* 38:5725-5733. [https://doi.org/10.1016/S0032-3861\(97\)00131-6](https://doi.org/10.1016/S0032-3861(97)00131-6)
72. Brückner S, Phillips PJ, Mezghani K et al (1997) On the crystallization of γ -isotactic polypropylene. A high pressure study. *Macromol Rapid Commun* 18:1-7. <https://doi.org/10.1002/marc.1997.030180101>
73. Lotz B, Graff S, Wittmann JC (1986) Crystal morphology of the γ (triclinic) phase of isotactic polypropylene and its relation to the α phase. *J Polym Sci Polym Phys Ed* 24:2017. <https://doi.org/10.1002/polb.1986.090240909>
74. Kojima M (1967) Solution- γ grown lamellar crystals of thermally decomposed isotactic polypropylene. *J Polym Sci B5*:245. ISSN:0360-6384
75. Kojima M (1968) Morphology of polypropylene crystals. III. Lamellar crystals of thermally decomposed polypropylene. *J Polym Sci A-2*:1255. ISSN:0098-1273
76. Morrow DR, Newman BA (1968) Crystallization of low-molecular-weight polypropylene fractions. *J Appl Phys* 39:4944-50. <https://doi.org/10.1063/1.1655891>
77. Natta G, Mazzanti G, Crespi G et al (1957) Polimeri isotattici e polimeri a stereoblocchi del propilene. *Chimica e Industria Milan* 39:275. ISSN:0009-4315
78. Turner-Jones A (1971) Development of the γ -crystal form in random copolymers of propylene and their analysis by differential scanning calorimetry and X-ray methods. *Polymer* 12:487. [https://doi.org/10.1016/0032-3861\(71\)90031-0](https://doi.org/10.1016/0032-3861(71)90031-0)
79. Mezghani K, Phillips PJ (1995) γ -Phase in propylene copolymers at atmospheric pressure. *Polymer* 36:2407-411. [https://doi.org/10.1016/0032-3861\(95\)97341-C](https://doi.org/10.1016/0032-3861(95)97341-C)
80. Resconi L, Cavallo L, Fait A et al (2000) Selectivity in propene polymerization with metallocene catalysts. *Chem Rev* 100:1253. <https://doi.org/10.1021/cr9804691>
81. Fischer D, Mülhaupt R (1994) The influence of regio- and stereoirregularities on the crystallization behavior of isotactic poly(propylene)s prepared with homogeneous group IVa metallocene/methylaluminoxane Ziegler-Natta catalysts. *Macromol Chem Phys* 195:1433-41. <https://doi.org/10.1002/macp.1994.021950426>
82. Thomann R, Wang C, Kressler J et al (1996) On the γ -phase of isotactic polypropylene. *Macromolecules* 29:8425. <https://doi.org/10.1021/ma951885f>
83. Alamo RG, Kim MH, Galante MJ et al (1999) Structural and kinetic factors governing the formation of the γ polymorph of isotactic polypropylene. *Macromolecules* 32:4050. <https://doi.org/10.1021/ma981849r>
84. VanderHart DL, Alamo RG, Nyden MR et al (2000) Observation of resonances associated with stereo and regio defects in the crystalline regions of isotactic polypropylene: toward a determination of morphological partitioning. *Macromolecules* 33:6078. <https://doi.org/10.1021/ma992041p>

85. Thomann R, Semke H, Maier RD et al (2001) Influence of stereoirregularities on the formation of the γ -phase in isotactic polypropylene. *Polymer* 42:4597. [https://doi.org/10.1016/S0032-3861\(00\)00675-3](https://doi.org/10.1016/S0032-3861(00)00675-3)
86. Auriemma F, De Rosa C, Boscato T et al (2001) The oriented γ form of isotactic polypropylene. *Macromolecules* 34:4815. <https://doi.org/10.1021/ma0100504>
87. Auriemma F, De Rosa C (2002) Crystallization of metallocene-made isotactic polypropylene: disordered modifications intermediate between the α and γ forms. *Macromolecules* 35:9057. <https://doi.org/10.1021/ma020648r>
88. De Rosa C, Auriemma F, Circelli T et al (2002) Crystallization of the α and γ forms of isotactic polypropylene as a tool to test the degree of segregation of defects in the polymer chains. *Macromolecules* 35:3622. <https://doi.org/10.1021/ma0116248>
89. De Rosa C, Auriemma F, Circelli T et al (2003) Stereoblock polypropylene from a metallocene catalyst with a hapto-flexible naphthyl-indenyl ligand. *Macromolecules* 36:3465. <https://doi.org/10.1021/ma021684t>
90. De Rosa C, Auriemma F, Di Capua A et al (2004) Structure—property correlations in polypropylene from metallocene catalysts: stereodeficient, regioregular isotactic polypropylene. *J Am Chem Soc* 126:17040. <https://doi.org/10.1021/ja045684f>
91. De Rosa C, Auriemma F, Perretta C (2004) Structure and properties of elastomeric polypropylene from C2 and C2v-symmetric zirconocenes. The origin of crystallinity and elastic properties in poorly isotactic polypropylene. *Macromolecules* 37:6843. <https://doi.org/10.1021/ma0493372>
92. De Rosa C, Auriemma F, De Lucia G et al (2005) From stiff plastic to elastic polypropylene: polymorphic transformations during plastic deformation of metallocene-made isotactic polypropylene. *Polymer* 46:9461. <https://doi.org/10.1016/j.polymer.2005.07.028>
93. De Rosa C, Auriemma F, Paolillo M et al (2005) Crystallization behavior and mechanical properties of regiodefective, highly stereoregular isotactic polypropylene: effect of regiodefects versus stereodeficient and influence of the molecular mass. *Macromolecules* 38:9143. <https://doi.org/10.1021/ma051004x>
94. De Rosa C, Auriemma F (2006) Structural—mechanical phase diagram of isotactic polypropylene. *J Am Chem Soc* 128:11024. <https://doi.org/10.1021/ja063464r>
95. De Rosa C, Auriemma F (2007) Stress-induced phase transitions in metallocene-made isotactic polypropylene. *Lect Not Phys* 714:345. https://doi.org/10.1007/3-540-47307-6_17
96. Auriemma F, De Rosa C (2006) Stretching isotactic polypropylene: from “cross- β ” to crosshatches, from γ Form to α form. *Macromolecules* 39:7635. <https://doi.org/10.1021/ma0609127>
97. Auriemma F, De Rosa C, Corradi M (2007) Stereoblock polypropylene as a prototype example of elasticity via a flip-flop reorientation of crystals in a compliant matrix. *Adv Mat* 19:871. <https://doi.org/10.1002/adma.200601296>
98. De Rosa C, Auriemma F, Spera C et al (2004) Comparison between polymorphic behaviors of Ziegler-Natta and metallocene-made isotactic polypropylene: the role of the distribution of defects in the polymer chains. *Macromolecules* 37:1441. <https://doi.org/10.1021/ma035295q>
99. De Rosa C, Auriemma F, Spera C (2004) Comparison between polymorphic behaviors of Ziegler-Natta and metallocene-made isotactic polypropylene: the role of the chain microstructure. *Macromol Symp* 218:113. <https://doi.org/10.1002/masy.200451412>
100. De Rosa C, Auriemma F, Spera C et al (2004) Crystallization properties of elastomeric polypropylene from alumina-supported tetraalkyl zirconium catalysts. *Polymer* 45:5875–5888. <https://doi.org/10.1016/j.polymer.2004.06.037>
101. Lotz B, Wittmann J-C (1986) The molecular origin of lamellar branching in the α (monoclinic) form of isotactic polypropylene. *J Polym Sci, Part B: Polym Phys* 24:1541. <https://doi.org/10.1002/polb.1986.090240712>
102. Stocker W, Maganov SN, Cantow H-J et al (1993) Contact faces of epitaxially crystallized α - and γ -phase isotactic polypropylene observed by atomic force microscopy. *Macromolecules* 26:5915. <https://doi.org/10.1021/ma00074a013>

103. Wittmann J-C, Lotz B (1990) Epitaxial crystallization of polymers on organic and polymeric substrates. *Prog Polym Sci* 15:909. [https://doi.org/10.1016/0079-6700\(90\)90025-V](https://doi.org/10.1016/0079-6700(90)90025-V)
104. De Rosa C, Auriemma F, Resconi L (2005) Influence of chain microstructure on the crystallization kinetics of metallocene-made isotactic polypropylene. *Macromolecules* 38:10080. <https://doi.org/10.1021/ma0510845>
105. Ferro DR, Brückner S, Meille SV et al (1992) Energy calculations for isotactic polypropylene: a comparison between models of the α and γ crystalline structures. *Macromolecules* 25:5231. <https://doi.org/10.1021/ma00046a019>
106. Crissman JM (1969) Mechanical relaxation in polypropylene as a function of polymorphism, degree of lamella orientation. *J Polym Sci A* 2(7):389–404. <https://doi.org/10.1002/pol.1969.160070210>
107. Lovinger AJ, Chua JO, Gryte CC (1977) Studies on the α - and β -forms of isotactic polypropylene by crystallization in temperature gradient. *J Polym Sci Polym Phys Ed* 15:641–656. <https://doi.org/10.1002/pol.1977.180150405>
108. Devaux E, Chabert B (1991) Nature and origin of the transcrystalline interphase of polypropylene glass fibre composites after a shear stress. *Polym Commun* 32:464–468. CODEN:POCOEF, ISSN:0263-6476
109. Varga J, Karger-Kocsis J (1996) Rules of supermolecular structure formation in sheared isotactic polypropylene melts. *J Polym Sci Part B: Polym Phys Ed* 34:657–670. [https://doi.org/10.1002/\(SICI\)1099-0488\(199603\)34:4%3c657:AID-POLB6%3e3.0.CO;2-N](https://doi.org/10.1002/(SICI)1099-0488(199603)34:4%3c657:AID-POLB6%3e3.0.CO;2-N)
110. Varga J, Ehrenstein GW (1996) Formation of β -modification in its late stage of crystallization. *Polymer* 37:5959–5963. [https://doi.org/10.1016/S0032-3861\(96\)00565-4](https://doi.org/10.1016/S0032-3861(96)00565-4)
111. Morrow DR (1969) Polymorphism in isotactic polypropylene. *J Macromol Sci, Phys B* 3:53–65. <https://doi.org/10.1080/00222346908217088>
112. Varga J (1995) Crystallization, melting and supermolecular structure of isotactic polypropylene in polypropylene. In: Karger-Kocsis J (ed) *Structure, blends and composites*, vol 1. Chapman & Hall, London, pp 56–115. <https://doi.org/10.1023/a:1025870111612>
113. Varga J (2002) β -modification of isotactic polypropylene: preparation, structure, processing, properties, and application. *J Macromol Sci Part B* 41:1121–1171. <https://doi.org/10.1081/MB-120013089>
114. Leugering HJ (1967) Einfluss der Kristallstruktur und Überstruktur auf einige Eigenschaften von Polypropylen. *Makromol Chem* 109:204–216. <https://doi.org/10.1002/macp.1967.021090118>
115. Binsbergen FL, de Lange BGM (1968) Morphology of polypropylene crystallized from melt. *Polymer* 9:23–40. [https://doi.org/10.1016/0032-3861\(68\)90006-2](https://doi.org/10.1016/0032-3861(68)90006-2)
116. Shi G, Zhang J, Jin H (1986) α -Kristallines isotaktischen Polypropylen, Verfahren zu seiner Herstellung und daraus hergestellte Körper. German Patent DE 3,610,644, 10 Feb 1986
117. De Rosa C, Auriemma F, Tarallo O et al (2017) The “Nodular” α form of isotactic polypropylene: stiff and strong polypropylene with high deformability. *Macromolecules* 50:5434–5446. <https://doi.org/10.1021/acs.macromol.7b00787>
118. De Rosa C, Auriemma F, Tarallo O et al (2017) Tailoring the properties of polypropylene in the polymerization reactor using polymeric nucleating agents as prepolymers on the Ziegler-Natta catalyst granule. *Polymer Chem* 8:655–660. <https://doi.org/10.1039/C6PY01950A>
119. Shi G, Huang B, Zhang J (1984) Enthalpy of fusion and equilibrium melting point of the β -form of polypropylene. *Makromol Chem Rapid Commun* 5:573–578. <https://doi.org/10.1002/marc.1984.030050915>
120. Ullmann W, Wendorff JH (1979) Studies on the monoclinic and hexagonal modifications of isotactic polypropylene. *Prog Colloid Polym Sci* 66:25–33. <https://doi.org/10.1007/BFb0117332>
121. Lotz B, Fillon B, Therry A et al (1991) Low T transition in isotactic polypropylene: β to α and α to smectic. *Polym Bull* 25:101–105. <https://doi.org/10.1007/BF00338906>
122. Lotz B, Witmann J-C (1992) Isotactic polypropylene: growth transition and crystal polymorphism. *Prog Colloid Polym Sci* 87:2–7. <https://doi.org/10.1007/BFb0115565>

123. Fillon B, Thierry A, Wittmann J-C et al (1993) Self-nucleation and recrystallization of polymers. isotactic polypropylene, β phase: β - α conversion and β - α growth transition. *J Polym Sci Polym Phys* 31:1407–1427. <https://doi.org/10.1002/polb.1993.090311015>
124. Lotz B (1998) Alpha and beta phases of isotactic polypropylene: a case of growth kinetics phase reentrancy in polymer crystallization. *Polymer* 39:4561–4567. <https://doi.org/10.1016/S0032-3861>
125. Varga J, Fujiwara Y, Ille A (1990) $\alpha\beta$ -bifurcation of growth during the spherulitic crystallization of polypropylene. *Period Polytech Chem Eng* 34:255–271
126. Varga J (1992) Supermolecular structure of isotactic polypropylene. *J Mater Sci* 27:2557–2579. <https://doi.org/10.1007/BF00540671>
127. Varga J (1982) Modification change during spherulitic growth of polypropylene. *Angew Makromol Chem* 104:79–87. <https://doi.org/10.1002/apmc.1982.051040107>
128. Padden FJ, Keith HD (1959) Spherulitic crystallization in polypropylene. *J Appl Phys* 30:1479–1484. <https://doi.org/10.1063/1.1713606>
129. Duswalt A, Cox WW (1970) Thermal study of β -form polypropylene. *Am Chem Soc Div Org Coat* 30:93–96. ISSN:0096-512X
130. Duswalt AA, Cox WWA (1971) Thermal study of β -form polypropylene. In: Craver CD (ed) *Polymer characterization, interdisciplinary approaches*. Plenum Press, New York, pp 147–155
131. Varga J (1986) Melting memory effect of the β -modification of polypropylene. *J Therm Anal* 31:165–172. <https://doi.org/10.1007/BF01913897>
132. Varga J, Garzó G, Ille A (1986) Kristallisation, Umkristallisation und Schmelzen der β -Modifikation des Polypropylenes. *Angew Makromol Chem* 142:171–181. <https://doi.org/10.1002/apmc.1986.051420115>
133. Varga J (1989) β -modification of polypropylene and its two-component systems. *J Therm Anal* 35:1891–1912. https://doi.org/10.1007/978-94-011-1950-4_63
134. Keith HD, Padden FJ Jr, Walter NM et al (1959) Evidence for a second crystal form of polypropylene. *J Appl Phys* 30:1485–1488. <https://doi.org/10.1063/1.1734986>
135. Turner-Jones A, Cobbold AJ (1968) The β crystalline form of isotactic polypropylene. *J Polym Sci Part B* 6:539–546. <https://doi.org/10.1002/pol.1968.110060802>
136. Miller RL (1960) Existence of near-range order in isotactic polypropylenes. *Polymer* 1:135. [https://doi.org/10.1016/0032-3861\(60\)90021-5](https://doi.org/10.1016/0032-3861(60)90021-5)
137. Hsu CC, Geil PH, Miyaji H et al (1986) Structure and properties of polypropylene crystallized from the glassy state. *J Polym Sci Polym Phys* 24:2379. <https://doi.org/10.1002/polb.1986.090241018>
138. Piccarolo S, Alessi S, Brucato V et al (1993) Crystallization behavior at high cooling rates of two polypropylenes. In: Dosiere M (ed) *Crystallization of polymers*. Kluwer Academics, Berlin, p 475. ISSN: 0258-2023
139. Coccorullo I, Pantani R, Titomanlio G (2003) Crystallization kinetics and solidified structure in iPP under high cooling rates. *Polymer* 44:307. [https://doi.org/10.1016/S0032-3861\(02\)00762-0](https://doi.org/10.1016/S0032-3861(02)00762-0)
140. Caldas V, Brown GR, Nohr RS et al (1994) The structure of the mesomorphic phase of quenched isotactic polypropylene. *Polymer* 35:899. [https://doi.org/10.1016/0032-3861\(94\)90931-8](https://doi.org/10.1016/0032-3861(94)90931-8)
141. Piccarolo S (1992) Morphological changes in isotactic polypropylene as a function of cooling rate. *J Macromol Sci Phys B* 31:501. <https://doi.org/10.1080/00222349208215467>
142. Miyamoto Y, Fukao K, Yoshida T et al (2000) Structure formation of isotactic polypropylene from the glass. *J Phys Soc Jpn* 69:1735. <https://doi.org/10.1143/JPSJ.69.1735>
143. Wang ZG, Hsiao BS, Srinivas S et al (2001) Phase transformation in quenched mesomorphic isotactic polypropylene. *Polymer* 42:7561. [https://doi.org/10.1016/S0032-3861\(01\)00286-5](https://doi.org/10.1016/S0032-3861(01)00286-5)
144. Minami S, Tsurutani N, Miyaji H et al (2004) SAXS study on structure formation from the uniaxially oriented glass in isotactic polypropylene. *Polymer* 45:1429. <https://doi.org/10.1016/j.polymer.2003.12.062>

145. Martorana A, Piccarolo S, Scichilone F (1997) The X-ray determination of the amounts of phases in isotactic polypropylene samples quenched from the melt at different cooling rates. *Macromol Chem Phys* 198:597. <https://doi.org/10.1002/macp.1997.021980231>
146. Konishi T, Nishida K, Kanaya T et al (2005) Effect of isotacticity on formation of mesomorphic phase of isotactic polypropylene. *Macromolecules* 38:8749. <https://doi.org/10.1021/ma050908f>
147. De Rosa C, Auriemma F (2012) The deformability of polymers: the role of disordered mesomorphic crystals and stress-induced phase transformations. *Ang Chem Int Ed* 51:1207. <https://doi.org/10.1002/anie.201105289>
148. De Santis F, Adamovsky S, Titomanlio G et al (2006) scanning nanocalorimetry at high cooling rate of isotactic polypropylene. *Macromolecules* 39:2562. <https://doi.org/10.1021/ma052525n>
149. Grady A, Sajkiewicz P, Minakov AA et al (2005) Crystallization of polypropylene at various cooling rates. *Mater Sci Eng A* 413:44. <https://doi.org/10.1016/j.msea.2005.08.167>
150. Wyckoff HQ (1962) X-ray and related studies of quenched, drawn, and annealed polypropylene. *J Polym Sci* 62:83. <https://doi.org/10.1002/pol.1962.1206217307>
151. Martorana A, Piccarolo S, Sapoundjieva D (1999) SAXS/WAXS study of the annealing process in quenched samples of isotactic poly(propylene). *Macromol Chem Phys* 200:531. [https://doi.org/10.1002/\(SICI\)1521-3935\(19990301\)200:3%3c531:AID-MACP531%3e3.0.CO;2-K](https://doi.org/10.1002/(SICI)1521-3935(19990301)200:3%3c531:AID-MACP531%3e3.0.CO;2-K)
152. Zhao J, Wang Z, Niu Y et al (2012) Phase transitions in prequenched mesomorphic isotactic polypropylene during heating and annealing processes as revealed by simultaneous synchrotron SAXS and WAXD technique. *J Phys Chem B* 116:147. <https://doi.org/10.1021/jp210499d>
153. Ferrero A, Ferracini E, Mazzavillani A et al (2000) A new X-ray study of the quenched isotactic polypropylene transition by annealing. *Macromol Sci Phys B* 39:109. <https://doi.org/10.1081/MB-100100375>
154. Konishi T, Nishida K, Kanaya T (2006) Crystallization of isotactic polypropylene from prequenched mesomorphic phase. *Macromolecules* 39:8035. <https://doi.org/10.1021/ma060191b>
155. Mileva D, Androsch R, Zhuravlev E et al (2009) Temperature of melting of the mesophase of isotactic polypropylene. *Macromolecules* 42:7275. <https://doi.org/10.1021/ma901797b>
156. Silvestre C, Cimmino S, Duraccio D et al (2007) Isothermal crystallization of isotactic poly(propylene) studied by superfast calorimetry. *Macromol Rapid Commun* 28:875. <https://doi.org/10.1002/marc.200600844>
157. De Rosa C, Auriemma F, Di Girolamo R et al (2013) Morphology and mechanical properties of the mesomorphic form of isotactic polypropylene in stereodeficient polypropylene. *Macromolecules* 46:5202–5214. <https://doi.org/10.1021/ma400570k>
158. Zia Q, Radosch H-J, Androsch R (2007) Direct analysis of annealing of nodular crystals in isotactic polypropylene by atomic force microscopy, and its correlation with calorimetric data. *Polymer* 48:3504. <https://doi.org/10.1016/j.polymer.2007.04.012>
159. Zia Q, Androsch R, Radosch H-J et al (2006) Morphology, reorganization and stability of mesomorphic nanocrystals in isotactic polypropylene. *Polymer* 47:8163. <https://doi.org/10.1016/j.polymer.2006.09.038>
160. Androsch R (2008) In situ atomic force microscopy of the mesomorphic-monoclinic phase transition in isotactic polypropylene. *Macromolecules* 41:533. <https://doi.org/10.1021/ma702334q>
161. Gezovich DM, Geil PH (1968) Morphology of quenched polypropylene. *Polym Eng Sci* 8:202. <https://doi.org/10.1002/pen.760080305>
162. Grubb DT, Yoon DY (1986) Morphology of quenched and annealed isotactic polypropylene. *Polym Commun* 27:84. ISSN:0263-6476
163. Ogawa T, Miyami H, Asai K (1985) Nodular structure of polypropylene. *J Phys Soc Jpn* 54:3668. <https://doi.org/10.1143/JPSJ.54.3668>

164. Zia Q, Androsch R, Radusch H-J et al (2008) Crystal morphology of rapidly cooled isotactic polypropylene: a comparative study by TEM and AFM. *Polym Bull* 60:791. <https://doi.org/10.1007/s00289-008-0908-8>
165. Vittoria V (1989) Effect of annealing on the structure of quenched isotactic polypropylene. *J Macromol Sci Phys B* 28:489–502. <https://doi.org/10.1080/00222348908215238>
166. Zannetti R, Celotti G, Fichera A et al (1969) The structural effects of annealing time and temperature on the paracrystal-crystal transition in isotactic polypropylene. *Die Makromol Chem* 128:137–142. <https://doi.org/10.1002/macp.1969.021280111>
167. De Rosa C, Auriemma F, Di Girolamo R et al (2014) Crystallization of the mesomorphic form and control of the molecular structure for tailoring the mechanical properties of isotactic polypropylene. *J Polym Sci Part B: Polym Phys* 52:677. <https://doi.org/10.1002/polb.23473>
168. Ran S, Zong X, Fang D et al (2001) Structural and morphological studies of isotactic polypropylene fibers during heat/draw deformation by in-situ synchrotron SAXS/WAXD. *Macromolecules* 34:2569. <https://doi.org/10.1021/ma0016477>
169. De Rosa C, Auriemma F, Ruiz de Ballesteros O *et al.* (2009) Stress-induced polymorphic transformations and mechanical properties of isotactic propylene-hexene copolymers. *Cryst Growth Des* 9:165. <https://doi.org/10.1021/cg800102f>
170. De Rosa C, Auriemma F, Ruiz de Ballesteros O et al (2007) Tailoring the physical properties of isotactic polypropylene through incorporation of comonomers and the precise control of stereo- and regioregularity by metallocene catalysts. *Chem Mater* 19:5122. <https://doi.org/10.1021/cm071502f>
171. Poon B, Rogunova M, Hiltner A et al (2005) Chum S.P, Galeski A., Piorowska E., Structure and properties of homogeneous copolymers of propylene with hexene. *Macromolecules* 38:1232. <https://doi.org/10.1021/ma048813l>
172. Natta G, Corradini P, Ganis P (1960) Chain conformation of polypropylene having a regular structure. *Makromol Chem* 39:238. <https://doi.org/10.1002/macp.1960.020390118>
173. Natta G, Corradini P, Ganis P (1962) Prediction of the conformation of the chain in the crystalline state of tactic polymer. *J Polym Sci* 58:1191. <https://doi.org/10.1002/pol.1962.1205816675>
174. Pirozzi B, Napolitano R (1992) Conformational analysis of the polymorphic forms of syndiotactic polypropylene in the crystalline field. *Eur Polym J* 28:703. [https://doi.org/10.1016/0014-3057\(92\)90047-6](https://doi.org/10.1016/0014-3057(92)90047-6)
175. Corradini P, Napolitano R, Petraccone V et al (1982) Conformational analysis of syndiotactic polymer chains in the crystalline state: polypropylene and 1,2-poly(1,3-butadiene). *Macromolecules* 15:1207. <https://doi.org/10.1021/ma00232a053>
176. Napolitano R, Pirozzi B (1997) Analysis of modes of packing of the most stable form of syndiotactic polypropylene. *Polymer* 38:4847. [https://doi.org/10.1016/S0032-3861\(97\)00007-4](https://doi.org/10.1016/S0032-3861(97)00007-4)
177. Lotz B, Lovinger AJ, Cais RE (1988) Crystal structure and morphology of syndiotactic polypropylene single crystals. *Macromolecules* 21:2375. <https://doi.org/10.1021/ma00186a013>
178. Lovinger AJ, Lotz B, Davis DD (1990) Interchain packing and unit cell of syndiotactic polypropylene. *Polymer* 31:2253. [https://doi.org/10.1016/0032-3861\(90\)90310-U](https://doi.org/10.1016/0032-3861(90)90310-U)
179. Lovinger AJ, Davis DD, Lotz B (1991) Temperature dependence of structure and morphology of syndiotactic polypropylene and epitaxial relationships with isotactic polypropylene. *Macromolecules* 24:552. <https://doi.org/10.1021/ma00002a>
180. Lovinger AJ, Lotz B, Davis DD et al (1993) Structure and defects in fully syndiotactic polypropylene. *Macromolecules* 26:3494. <https://doi.org/10.1021/ma00066a006>
181. Lovinger AJ, Lotz B, Davis DD (1992) Electron- and x-ray diffraction investigation of the structure of syndiotactic polypropylene. *Polym Prepr Am Chem Soc* 33:270. ISSN:0032-3934

182. Lovinger AJ, Lotz B, Davis DD et al (1994) Morphology and thermal properties of fully syndiotactic polypropylene. *Macromolecules* 27:6603. <https://doi.org/10.1021/ma00100a053>
183. Stocker W, Schumacher M, Graff S et al (1994) Direct observation of right and left helical hands of syndiotactic polypropylene by atomic force microscopy. *Macromolecules* 27:6948. <https://doi.org/10.1021/ma00101a036>
184. Schumacher M, Lovinger AJ, Agarwal P et al (1994) Heteroepitaxy of syndiotactic polypropylene with polyethylene and homoepitaxy. *Macromolecules* 27:6956. <https://doi.org/10.1021/ma00101a037>
185. Lotz B, Wittmann J-C, Lovinger AJ (1996) Structure and morphology of poly(propylenes): a molecular analysis. *Polymer* 37:4979. [https://doi.org/10.1016/0032-3861\(96\)00370-9](https://doi.org/10.1016/0032-3861(96)00370-9)
186. Lovinger AJ, Lotz B (1997) Structural analysis of minimized models for syndiotactic polypropylene. *J Polym Sci Polym Phys Ed* 35:2523. [https://doi.org/10.1002/\(SICI\)1099-0488\(19971115\)35:15%3c2523:AID-POLB14%3e3.0.CO;2-7](https://doi.org/10.1002/(SICI)1099-0488(19971115)35:15%3c2523:AID-POLB14%3e3.0.CO;2-7)
187. Zhang J, Yang D, Thierry A et al (2001) Isochiral form II of syndiotactic polypropylene produced by epitaxial crystallization. *Macromolecules* 34:6261. <https://doi.org/10.1021/ma010758i>
188. De Rosa C, Auriemma F, Corradini P (1996) Crystal structure of form I of syndiotactic polypropylene. *Macromolecules* 29:7452. <https://doi.org/10.1021/ma9601326>
189. De Rosa C, Auriemma F, Vinti V (1997) Disordered polymorphic modifications of form I of syndiotactic polypropylene. *Macromolecules* 30:4137. <https://doi.org/10.1021/ma961691f>
190. De Rosa C, Auriemma F, Vinti V (1998) On the form II of syndiotactic polypropylene. *Macromolecules* 31:7430. <https://doi.org/10.1021/ma980789m>
191. De Rosa C, Auriemma F, Vinti V et al (1998) Equilibrium melting temperature of syndiotactic polypropylene. *Macromolecules* 31:6206. <https://doi.org/10.1021/ma9805248>
192. Sozzani P, Simonutti R, Galimberti M (1993) MAS NMR characterization of syndiotactic polypropylene: crystal structure and amorphous phase conformation. *Macromolecules* 26:5782. <https://doi.org/10.1021/ma00073a036>
193. Sozzani P, Simonutti R, Comotti A (1994) Phase structure and polymorphism of highly syndiotactic polypropylene. *Magn Reson Chem* 32:S45. <https://doi.org/10.1002/mrc.1260321311>
194. Lacks DJ, Rutledge GC (1995) Molecular Basis for the anisotropic transverse thermal expansion of syndiotactic polypropylene. *Macromolecules* 28:5789. <https://doi.org/10.1021/ma00121a014>
195. Palmo K, Krimm S (1996) Energetics analysis of syndiotactic polypropylene crystal structure. *Macromolecules* 29:8549. <https://doi.org/10.1021/ma961125k>
196. Palmo K, Krimm S (2002) Energetics analysis of forms I–IV syndiotactic polypropylene crystal structures. *Macromolecules* 35:394. <https://doi.org/10.1021/ma011230g>
197. De Rosa C, Auriemma F, Di Girolamo R et al (2010) Helical mesophase of syndiotactic polypropylene in copolymers with 1-hexene and 1-octene. *Macromolecules* 43:9802. <https://doi.org/10.1021/ma1021709>
198. Auriemma F, De Rosa C, Corradini P (1993) Fenomeni di disordine nel polipropilene sindiotattico cristallino *Rend. Fis. Acc. Lincei* 4:287. <https://doi.org/10.1007/BF03001190>
199. De Rosa C, Auriemma F, Fanelli E et al (2003) Structure of copolymers of syndiotactic polypropylene with ethylene. *Macromolecules* 36:1850. <https://doi.org/10.1021/ma020981v>
200. Zambelli A, Tosi C (1974) Stereochemistry of propylene polymerization. *Adv Polym Sci* 15:32. https://doi.org/10.1007/3-540-06910-0_2
201. Auriemma F, Ruiz de Ballesteros O, De Rosa C (2001) Origin of the elastic behavior of syndiotactic polypropylene. *Macromolecules* 34:4485. <https://doi.org/10.1021/ma002021j>
202. De Rosa C, Gargiulo MC, Auriemma F et al (2002) Elastic properties and polymorphic behavior of fibers of syndiotactic polypropylene at different temperatures. *Macromolecules* 35:9083. <https://doi.org/10.1021/ma020394+>

203. Auriemma F, De Rosa C (2003) New concepts in thermoplastic elastomers: the case of syndiotactic polypropylene, an unconventional elastomer with high crystallinity and large modulus. *J Am Chem Soc* 125:13143. <https://doi.org/10.1021/ja036282v>
204. Auriemma F, De Rosa C (2003) Time-resolved study of the martensitic phase transition in syndiotactic polypropylene. *Macromolecules* 36:9396. <https://doi.org/10.1021/ma0350718>
205. Rastogi S, La Camera D, van der Burgt F et al (2001) Polymorphism in syndiotactic polypropylene: thermodynamic stable regions for form i and form ii in pressure-temperature phase diagram. *Macromolecules* 34:7730. <https://doi.org/10.1021/ma0109119>
206. Auriemma F, Born R, Spiess HW et al (1995) Solid-state ^{13}C -NMR investigation of the disorder in crystalline syndiotactic polypropylene. *Macromolecules* 28:6902. <https://doi.org/10.1021/ma00124a028>
207. Auriemma F, Lewis RH, Spiess HW et al (1995) Phase transition from a C-centered to a B-centered orthorhombic crystalline form of syndiotactic polypropylene. *Macromol Chem Phys* 196:4011. <https://doi.org/10.1002/macp.1995.021961212>
208. Auriemma F, De Rosa C, Ruiz de Ballesteros O et al (1997) Kink bands in form II of syndiotactic polypropylene. *Macromolecules* 30:6586. <https://doi.org/10.1021/ma970284g>
209. Bunn A, Cudby EA, Harris RK et al (1981) Solid-state high-resolution carbon-13 NMR spectra of polypropene *J Chem Soc Chem Commun* 15. <https://doi.org/10.1039/c39810000015>
210. Auriemma F, De Rosa C, Esposito S et al (2007) Polymorphic superelasticity in semicrystalline polymers. *Ang Chem Inter Ed* 46:4325. <https://doi.org/10.1002/anie.200605021>
211. Nakaoki T, Ohira Y, Hayashi H et al (1998) Spontaneous crystallization of the planar zigzag form of syndiotactic polypropylene at 0 °C. *Macromolecules* 31:2705. <https://doi.org/10.1021/ma980032v>
212. Ohira Y, Horii F, Nakaoki T (2000) Spontaneous crystallization process of the planar zigzag form at 0 °C from the melt for syndiotactic polypropylene. *Macromolecules* 33:1801. <https://doi.org/10.1021/ma991476+>
213. Nakaoki T, Yamanaka T, Ohira Y et al (2000) Dynamic FT-IR analysis of the crystallization to the planar zigzag form for syndiotactic polypropylene. *Macromolecules* 33:2718. <https://doi.org/10.1021/ma9915428>
214. Ohira Y, Horii F, Nakaoki T (2000) Crystal transformation behavior and structural changes of the planar zigzag form for syndiotactic polypropylene. *Macromolecules* 33:5566. <https://doi.org/10.1021/ma000357n>
215. Ohira Y, Horii F, Nakaoki T (2001) Conformational changes of the noncrystalline chains for syndiotactic polypropylene as a function of temperature: correlations with the crystallizations of form i and form III. *Macromolecules* 34:1655. <https://doi.org/10.1021/ma0014564>
216. Nakaoki T, Ohira Y, Horii F (2001) Investigation of the crystallization process of syndiotactic polypropylene quenched at 0 °C from the melt or concentrated solutions by solid-state ^{13}C NMR spectroscopy. *Polymer* 42:4555. [https://doi.org/10.1016/S0032-3861\(00\)00840-5](https://doi.org/10.1016/S0032-3861(00)00840-5)
217. Vittoria V, Guadagno L, Comotti A et al (2000) Mesomorphic form of syndiotactic polypropylene. *Macromolecules* 33:6200. <https://doi.org/10.1021/ma000373k>
218. De Rosa C, Auriemma F, Ruiz de Ballesteros O (2001) Influence of the stereoregularity on the crystallization of the trans planar mesomorphic form of syndiotactic polypropylene. *Polymer* 42:9729. [https://doi.org/10.1016/S0032-3861\(01\)00487-6](https://doi.org/10.1016/S0032-3861(01)00487-6)
219. De Rosa C, Ruiz de Ballesteros O, Santoro M et al (2003) Influence of the quenching temperature on the crystallization of the trans-planar mesomorphic form of syndiotactic polypropylene. *Polymer* 44:6267. [https://doi.org/10.1016/S0032-3861\(03\)00569-X](https://doi.org/10.1016/S0032-3861(03)00569-X)
220. De Rosa C, Ruiz de Ballesteros O, Santoro M et al (2004) Structural transitions of the trans-planar mesomorphic form and crystalline form III of syndiotactic polypropylene in stretched and stress-relaxed fibers: a memory effect. *Macromolecules* 37:1816. <https://doi.org/10.1021/ma035104j>

221. De Rosa C, Ruiz de Ballesteros O, Auriemma F (2004) Mechanical properties of helical and mesomorphic forms of syndiotactic polypropylene at different temperatures. *Macromolecules* 37:7724. <https://doi.org/10.1021/ma049214h>
222. Sozzani P, Galimberti M, Balbontin G (1992) Syndiotactic polypropylene after drawing: the effect of stretching polymer chains on magic angle spinning NMR. *Makromol Chem Rapid Commun* 13:305. <https://doi.org/10.1002/marc.1992.030130602>
223. Suter UW, Flory PJ (1975) Conformational energy and configurational statistics of polypropylene. *Macromolecules* 8:765. <https://doi.org/10.1021/ma60048a018>
224. Guadagno L, D'Aniello C et al (2002) Elasticity of the oriented mesomorphic form of syndiotactic polypropylene. *Macromolecules* 35:3921. <https://doi.org/10.1021/ma011825b>
225. De Rosa C, Auriemma F, Ruiz de Ballesteros O et al (2003) Synthesis and characterization of high-molecular-weight syndiotactic amorphous polypropylene. *J Am Chem Soc* 125:10913. <https://doi.org/10.1021/ja035911y>
226. De Rosa C, Auriemma F, Ruiz de Ballesteros O (2006) The role of crystals in the elasticity of semicrystalline thermoplastic elastomers. *Chem Mater* 18:3523. <https://doi.org/10.1021/cm060398j>
227. De Rosa C, Auriemma F, Ruiz de Ballesteros O (2003) Mechanical properties and elastic behavior of high-molecular-weight poorly syndiotactic polypropylene. *Macromolecules* 36:7607. <https://doi.org/10.1021/ma034829k>
228. De Rosa C, Auriemma F, Ruiz de Ballesteros O (2004) Structure and polymorphic behavior of high molecular weight poorly syndiotactic polypropylene. *Macromolecules* 37:1422. <https://doi.org/10.1021/ma034805d>
229. Grasruck M, Strobl G (2003) Crystallization of s-polypropylene from the glassy state: indications for a multistage process. *Macromolecules* 36:86. <https://doi.org/10.1021/ma021074t>
230. Strobl G (2009) Colloquium: laws controlling crystallization and melting in bulk polymers. *Rev Mod Phys* 81:1287. <https://doi.org/10.1103/RevModPhys.81.1287>
231. Strobl G (2007) A multiphase model describing polymer crystallization and melting. *Lect Notes Phys* 714:481. https://doi.org/10.1007/3-540-47307-6_23
232. Strobl G (2006) Crystallization and melting of bulk polymers: New observations, conclusions and a thermodynamic scheme. *Prog Polym Sci* 31:398. <https://doi.org/10.1016/j.progpolymsci.2006.01.001>
233. De Rosa C, Auriemma F (2005) From entropic to enthalpic elasticity: novel thermoplastic elastomers from syndiotactic propylene-ethylene copolymers. *Adv Mat* 17:1503. <https://doi.org/10.1002/adma.200401968>
234. De Rosa C, Auriemma F (2006) Structure of syndiotactic propylene-ethylene copolymers: effect of the presence of ethylene units on the structural transitions during plastic deformation and annealing of syndiotactic polypropylene. *Polymer* 47:2179. <https://doi.org/10.1016/j.polymer.2006.01.055>
235. De Rosa C, Auriemma F (2006) Mechanical properties of syndiotactic propylene-ethylene copolymers. *Macromolecules* 39:249. <https://doi.org/10.1021/ma051228f>

Chapter 3

Polypropylene Nucleation



Flóra Horváth, János Molnár and Alfréd Menyhárd

Contents

3.1	Introduction.....	122
3.2	Crystallization Process.....	124
3.3	Nucleation, the Targeted Manipulation of Crystalline Structure	131
3.3.1	Basic Characterization of Nucleating Agents	131
3.3.2	“Conventional” Heterogeneous Nucleating Agents.....	134
3.3.3	Soluble Nucleating Agents, Organogelators and Clarifiers for α -iPP.....	140
3.3.4	Crystallization of iPP in the Presence of Soluble Organogelators.....	145
3.3.5	Estimation of Solubility Limit of Organogelators	150
3.3.6	Supermolecular Structure Formed in the Presence of Organogelators	154
3.3.7	Nucleating Agent Based on Trisamides of Trimesic Acid.....	159
3.3.8	Soluble Nucleating Agents for β -iPP.....	160
3.4	Structure-Property Case Studies.....	166
3.4.1	Prediction of Tensile Modulus from Crystalline Parameters	166
3.4.2	Obtaining Balanced Properties by Efficient Nucleation	167
3.4.3	Improvement of Optical Properties by Efficient Nucleation	170
3.5	Summary.....	173
	References	174

Abstract This chapter aims to summarize the most important details of nucleation in polypropylene. The details of crystallization as well as the most important ways of targeted manipulation of crystalline structure in polypropylene are also discussed. The basic techniques like calorimetry (DSC), thermo-optical and scanning electron microscopy (TOM and SEM) and wide angle X-ray scattering (WAXS) are introduced together with some rarely used technique—like rheology for example—for characterization of nucleating effect. The nucleating agents are classified into two main groups. The first group is the “conventional” heterogeneous nucleating agents and the second class is the “soluble” nucleating agents. The structure that

F. Horváth · J. Molnár · A. Menyhárd (✉)

Department of Physical Chemistry and Materials Science, Faculty of Chemical Technology and Biotechnology, Budapest University of Technology and Economics, Műegyetem rakpart 3 H/1, Budapest 1111, Hungary
e-mail: amenyhard@mail.bme.hu

develops in the presence of both nucleating agent groups is presented in details. Moreover, the correlation between the crystalline structure and the properties is also demonstrated. An empirical equation is also described, which links the crystalline structure to the tensile stiffness quantitatively. The most important structural parameters, which influence the optical properties of the polymer are also introduced, but the quantitative correlation cannot be provided.

3.1 Introduction

Isotactic polypropylene (iPP) is one of the commodity polymers, which is used in the largest amount nowadays [1]. It is a semicrystalline material and its properties can be varied within a wide range throughout the modification of its crystalline structure [2–7]. This flexible property manipulation is the key to the success of iPP based materials. Special additives called as *nucleating agents* are used for alteration of crystalline structure in the industrial practice and in laboratory scale as well [7–13]. These additives assist the crystallization process, because they are present as heterogeneous surfaces during the crystallization of polypropylene. Usually, the crystallization process is faster in their presence and shifts to the higher temperature range in every kind of polypropylene grades, however, the effect of nucleating agents depends slightly on the molecular structure of the iPP grade [14–16]. In the industrial practice propylene is copolymerized together with a smaller amount of ethylene in order to increase the toughness and cold resistance of iPP [17, 18]. Depending on the distribution of ethylene co-monomers random and block iPP grades can be differentiated and nucleating agents are used in all copolymer and homopolymer grades as well nowadays [7, 19, 20].

Before the effect of nucleating agents is discussed, the basic terms of melting and crystallization process will be discussed shortly. iPP grades melt in the range of 100 and 180 °C depending on their molecular structure [6, 21]. The melting and crystallization curves of non-nucleated iPP homopolymer, random and block copolymer grades are presented in Fig. 3.1.

It is clearly discernible that the random iPP copolymer melts at a lower temperature, because its chain regularity is significantly smaller [17, 20, 22–26]. Accordingly, the lamella thickness is proportionally smaller in random iPP compared to that of homopolymer and block copolymer. The lower melting temperature in the case of random iPP copolymer is caused by the lower crystallization temperature, because the smaller chain regularity requires larger supercooling for crystallization. In addition, the random distribution of ethylene decreases the chain regularity and consequently the crystallinity, thus the enthalpy of fusion and crystallization of random copolymers is significantly smaller than that of the block and homopolymers [20, 25, 27, 28].

iPP is a polymorphic polymer, which has four crystalline modifications [2, 21, 29–33]. The α -form is the thermodynamically stable one and it is formed under conventional industrial conditions [34]. The β -modification forms under special thermal conditions or in the presence of special nucleating agents [35]. The γ - and

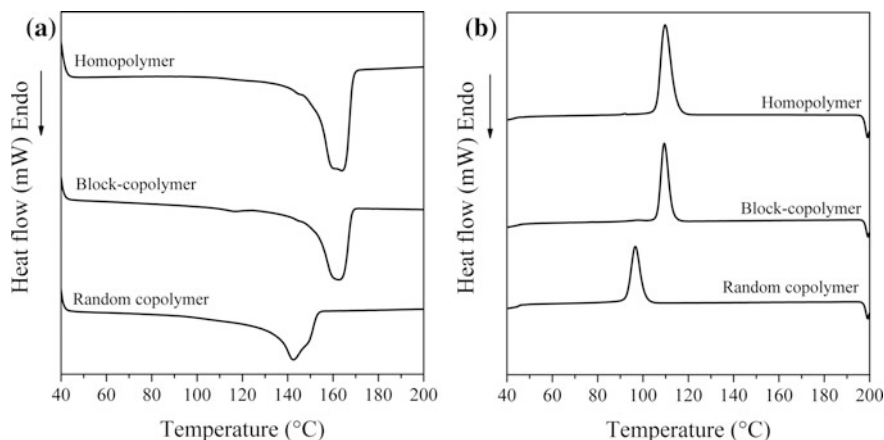


Fig. 3.1 Melting (a) and crystallization curves (b) of iPP homopolymer, random and block copolymer recorded by calorimetry at standard 10 °C/min of heating and cooling rates

ε -forms do not have industrial importance, since they are not produced in the industrial practice in large amounts, however, their presence influences the properties of the polymer slightly [33, 36–41]. The melting and crystallization of the β -modification had been investigated by Varga et al. [6, 35, 42–48] and they revealed that this crystalline form has a special “melting memory” effect [48], which interesting melting behavior is presented in Fig. 3.2.

As it can be seen in Fig. 3.2 the melting temperature of β -modification is lower compared to the α -modification in all iPP grades presented in Fig. 3.1. It should be pointed out that the melting behavior depends on the recooling temperature as it

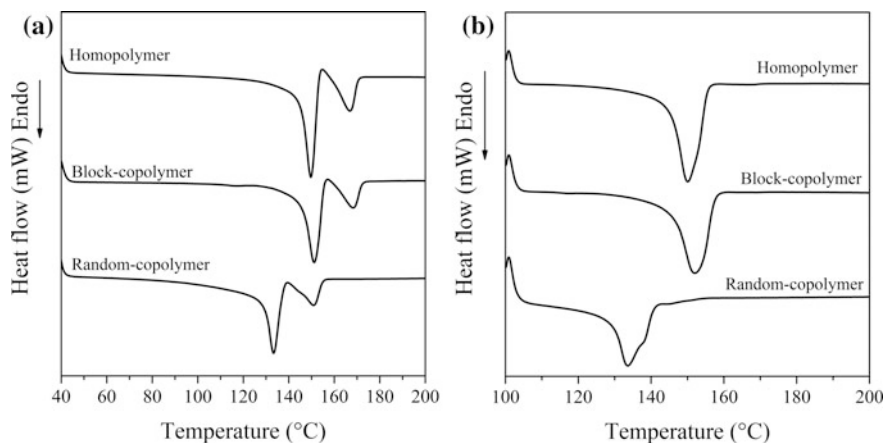


Fig. 3.2 Melting curves of β -nucleated iPP homopolymer, random and block copolymer recorded during heating from 25 °C (a) and 100 °C (b), at standard 10 °C/min of heating rate

was demonstrated in the early work of Varga et al. [45, 48] and this effect was discussed later in details. It was clearly proved that β -modification forms only in a limited temperature range between the $T(\alpha\beta)$ at 100 °C and $T(\beta\alpha)$ at 140 °C [34, 45] and this unique behavior leads to the melting memory effect. As it is presented in Fig. 3.2a, the melting profile depends on the recooling temperature, because a single melting peak can be recorded if the sample is not cooled below 100 °C. However, a complex melting peak appears during the heating of samples cooled below $T(\alpha\beta)$, because a small amount of α -nuclei form during cooling below 100 °C. These α -nuclei, formed during secondary crystallization, act as strong α -nucleating centers during heating and consequently a pronounced $\beta\alpha$ -recrystallization process superponates on the melting process. Accordingly, three processes, melting of β -phase, $\beta\alpha$ -recrystallization and melting of α -form take place during the complex process.

3.2 Crystallization Process

Crystallization is the process in which the crystalline phase forms throughout the organization of polymer chains into folded lamellas. Although, the main goal of this chapter is not the discussion of the detailed phenomenon of crystallization, the basics of the process should be explained in nutshell. A more detailed description can be found in several books [13, 49, 50]. The crystallization process can be divided into two major stages. The first stage is the primary crystallization, which covers the major part of the process and it is usually defined until the 90% of conversion is reached. The conversion is defined as the ratio between the enthalpy of crystallization at a certain temperature ($\Delta H_{c,t}$) and the enthalpy of the entire crystallization process at an infinite time ($\Delta H_{c,\infty}$) according to Eq. 3.1.

$$X_t = \frac{\Delta H_{c,t}}{\Delta H_{c,\infty}} \cdot 100 \quad (3.1)$$

Secondary crystallization takes place above 90% of conversion. This process is usually much slower than the primary crystallization and it consists of post ordering of the crystalline phase with low perfection. Since the nucleating agents influence primary crystallization, this process will be discussed in the following section.

Two elementary processes—nucleation and growth—take place during primary crystallization. Nucleation can be either homogeneous or heterogeneous [13, 51]. Homogeneous nucleation occurs in pure polymer melt, in which the intense thermal motion and fluctuation of the macromolecules results in the random formation of ordered clusters. The formation of these ordered primary clusters becomes more and more pronounced with decreasing temperature. We have to note that these ordered clusters form and disappear continuously in the melt. If the supercooling is large enough, the size of the ordered clusters may exceed a critical value and they can become stable and start to grow. Consequently, they are called stable *nuclei*.

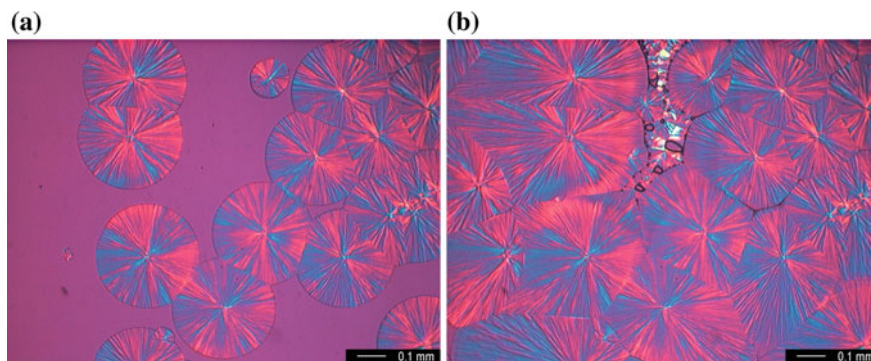


Fig. 3.3 Crystallization of iPP homopolymer (Borealis HB120FB) at 130 °C for **a** 60 min and **b** 130 min

In the case of homogeneous nucleation the formation of stable nuclei is a completely random process thus they can form at any time during primary crystallization at any location in the melt. Consequently, the structure of the sample is rather inhomogeneous, because spherulites with significantly different size develop in the sample. The crystallization process in the case of homogeneous nucleation is presented in Fig. 3.3. The formation of new nuclei is clearly visible in the figure, because the size of the growing spherulites is significantly different. The small spherulites formed later during the crystallization process.

It is known that the shape of the spherulites formed during crystallization throughout homogeneous nucleation is characteristic for the formation time. The straight spherulite boundary in Fig. 3.3 forms in the case of two spherulites formed at the same time. However, the spherulite boundary will be curved (in fact a hyperbola) if the spherulites formed at different time. The exact description of the possible geometry of spherulites was provided by Varga et al. [43, 45, 52] more than twenty years ago. Accordingly, the nucleation process can be divided into two categories: athermal nucleation, where the number of nuclei is constant and thermal nucleation, where the number of nuclei changes in time [13]. The decision of thermal or athermal kind of nucleation is easy based on the shape of spherulite boundaries on optical micrographs. If the number of nuclei is constant the nuclei are formed at the early stage of crystallization. Consequently, they are formed at the same time thus the boundaries between them will be a straight line. This nucleation process is called *instantaneous nucleation* [13, 53–57]. If the neighboring nuclei form at different time the boundary between them will be a curved line with the shape of a hyperbola [43]. We have to note that homogeneous nucleation can be either thermal or athermal depending on the conditions of the crystallization. Usually, nucleation is thermal at small supercooling, i.e. at high temperature and athermal (instantaneous) nucleation occurs at large supercooling.

In the case of heterogeneous nucleation, the primary nuclei are formed on a heterogeneous surface, which is present in the material. We have to note that almost

every heterogeneity has stronger or weaker nucleating efficiency in iPP [12]. The most important requirements for nucleating agents are listed below:

- should have larger surface energy than that of iPP, thus the polymer will wet the surface of the nucleating agents,
- should be present as heterogeneous surface during crystallization,
- have to be stable thermally at the temperature of the processing,
- should have a higher melting point than that of iPP.

The effect of a heterogeneous nucleating agent on the crystallization of iPP is demonstrated in Fig. 3.4. It is clearly visible in the figure that the overall rate of crystallization is much faster in the presence of the nucleating agent, because the larger nucleus density at the same growth rate results in faster process overall. Since the presence of nucleating agents promotes nucleation, this process can be handled as athermal and instantaneous nucleation [53, 55–58].

Although heterogeneous nucleating agents have been used for five decades, the explanation of nucleating was given only in the '90-ies. The first trial of explaining the nucleation efficiency was done by Binsbergen et al. [59, 60] who tried to link the chemical structure of the molecules to their nucleating efficiency. Despite their tremendous work, clear explanation for the nucleation effect could not be presented in their work. Later Alcazar et al. [61, 62] presented a simple approach, in which they explained the nucleating effect with the structural matching between the unit lattice sizes of the heterogeneous surface and the crystalline phase of the iPP. They used this theory to explain the nucleating effect of poly(vinyl cyclohexane) (PVCH), which polymer has a strong nucleating effect in iPP, because the (110) plane of iPP and the (100) contact plane of PVCH have similar dimensions. In addition, besides the dimensional matching, there is also a topographic matching, because of the common orientation of the contact planes (Fig. 3.5).

Later this theory has been used for explaining of the nucleating effect of several additives [63]. Other polymers, like PVDF for example, have strong nucleating

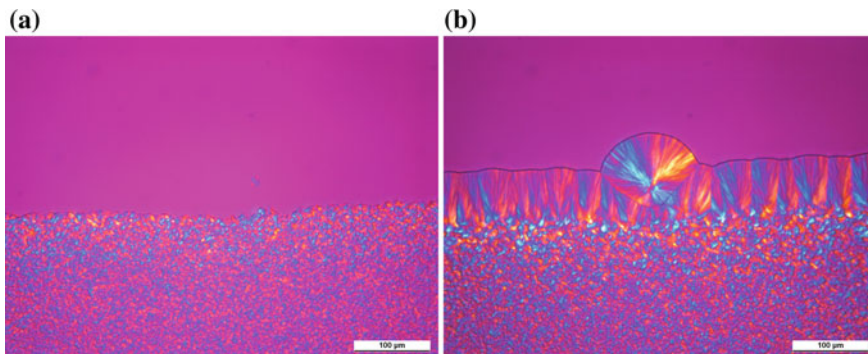
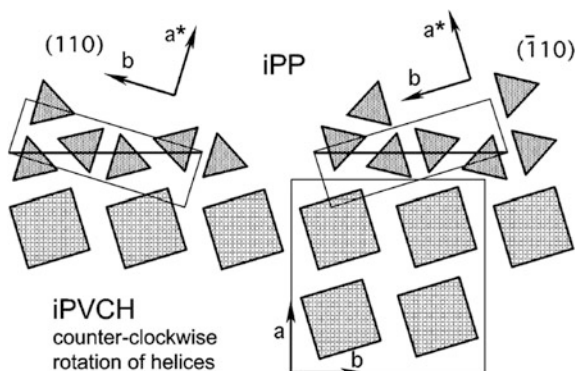


Fig. 3.4 Crystallization of nucleated iPP homopolymer at 140 °C for **a** 14 min and **b** 145 min (lower part is nucleated with 2000 ppm NA-21E)

Fig. 3.5 Schematic view of structural matching between iPP and PVCH [62]



effect on iPP, which is demonstrated in Fig. 3.6 [64]. The nucleating polymer should have a higher crystallization temperature compared to that of iPP matrix in order to perform efficient nucleating effect. According to the literature data, heterogeneous nucleating agents assist crystallization process, thus the crystallization peak shifts to the higher temperatures compared to non-nucleated samples. Consequently, thicker lamellas develop during crystallization and the crystallinity can increase as well in the presence of nucleating agents. These structural changes result in different mechanical and optical properties, thus these additives are used for manipulating the properties within a wide range.

Last but not least a third nucleation mechanism, the self-nucleation or self-seeding, should be discussed [13, 65–70]. Although this form of nucleation does not have practical relevance it is very important from the theoretical point of view. Self-nucleation occurs in polymers which are not heated far above their melting temperature, so the ordered macromolecules keep their conformation above

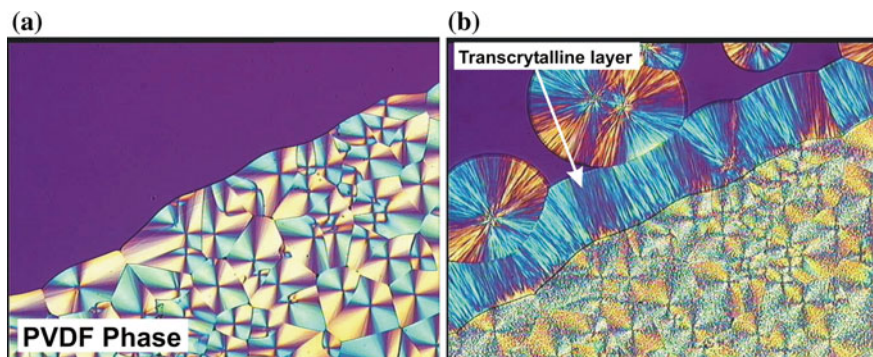


Fig. 3.6 Crystallization of iPP (MOL Petrochemical Tipplén H781) and PVDF (Solway SOLEF 6010) blend at 130 °C for **a** $t_c = 0$ min and **b** $t_c = 20$ min [64]

the melting point for a certain time. Although at a higher temperature the time needed for the elimination of the ordered conformation decreases due to the pronounced thermal motion of the molecules. According to literature data and to our earlier experiences as well, the ordered conformation of the macromolecules, which is also called as thermal prehistory, can be eliminated by annealing at 220 °C for 5 min [6, 48, 63, 71–75]. If the ordered structure of the molecules remains it behaves as a nucleating agent and induces crystallization. Since its structure is exactly the same as that of the crystalline phase, this is the most efficient nucleating agent at all and also athermal and instantaneous nucleation occurs in this process.

The other elementary process of crystallization is the growth of the crystalline phase. The mechanism of growth can be described by the secondary nucleation mechanisms according to the theory of Hoffmann et al. [54, 76, 77]. Three regimes of crystallization can be differentiated according to this theory and these regimes differ in the extent of supercooling. At high temperatures, under small supercooling, a secondary nucleus is formed on the surface then the entire surface is covered by a single layer of crystals. This structure is very regular and develops slowly and it is called regime I. Under larger supercooling at lower temperatures tertiary and further nuclei are formed as well, thus the structure developed is less regular and contains more defects, however, the growth rate is much faster as well. These are the regimes II and III. In practice the crystallization takes place at large supercooling in regime III. The schematic representation of Hoffman's regimes is given in Fig. 3.7.

In order to describe the crystallization process quantitatively different kinetic models are used in the literature [51, 56, 57, 78]. The kinetics of crystallization process is difficult to handle, because the nucleation and growth should be considered simultaneously. The first and most known crystallization model is the Avrami model [56, 57], which was applied successfully for the description of crystallization in polymers under isothermal conditions. The Avrami model handles the spherulites as sporadically forming and growing spheres, which fill up the volume during the crystallization. Mathematically it is a simple S-type Eq., which is given in Eq. 3.2.

$$(1 - X_t) = e^{-kt^n} \quad (3.2)$$

X_t is the conversion of crystallization, which equals to the ratio between the crystallinity at t time and the crystallinity at the end of the process at an infinite time. The k is the overall rate constant of crystallization and n is the Avrami constant. In most cases, the linearized form of the Avrami equation (Eq. 3.3) is used for evaluation.

$$\ln(-\ln(1 - X_t)) = \ln(k) + n \ln(t) \quad (3.3)$$

The linearized form of Eq. 3.3 is mathematically a straight line with the slope of the Avrami exponent (n) and intersect of $\ln(k)$. The polymers can be categorized into different classes according to the Avrami model:

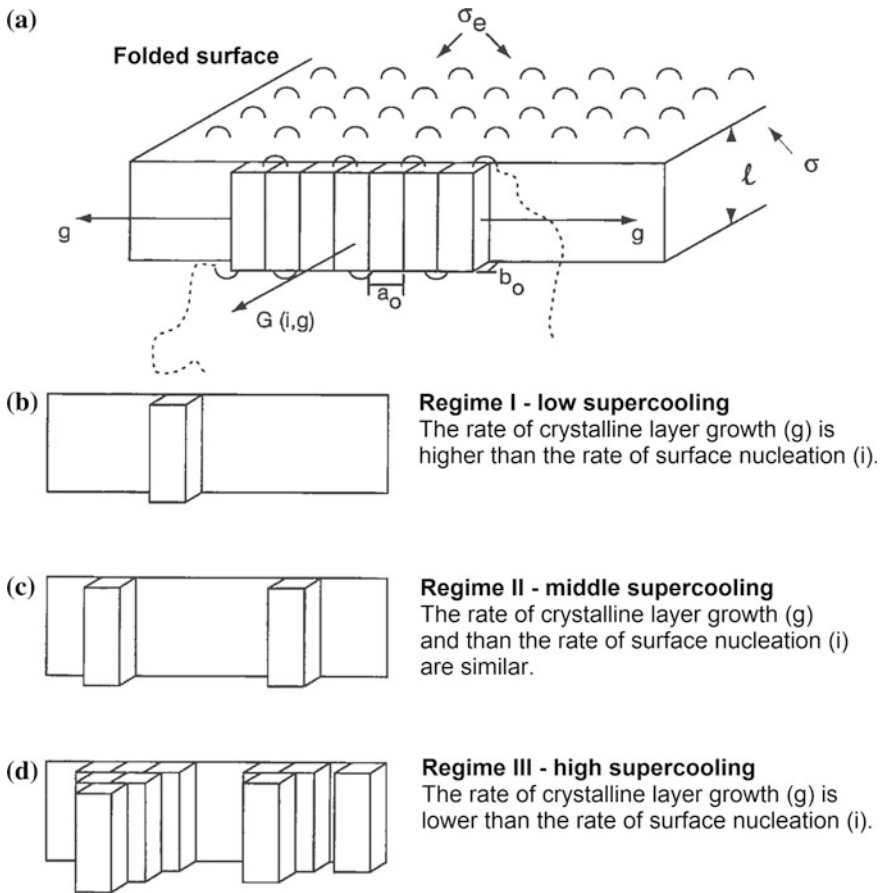


Fig. 3.7 The schematic view of Hoffmann's regimes: **a** secondary nucleation, **b** regime I, **c** regime II and **d** regime III

- The crystallization process can be linearized using Avrami equation and n is an integer between 1 and 4.
- The crystallization process can be linearized using Avrami equation, but n is not an integer between 1 and 4.
- The crystallization process cannot be linearized by Avrami equation.

Although the evaluation of Eq. 3.3 is easy, we have to mention that the method has drawbacks as well. The most difficult part is the estimation of the initial point of crystallization on the conversion curve, because this data influences the kinetic constants (n and k) of crystallization. In addition, the post-crystallization part at larger conversions cannot be linearized by Eq. 3.3, thus the range of evaluation should be determined in every single case. The linearized form of Avrami equation

has been used worldwide frequently for the description of crystallization process for seven decades at least [44, 79–87]. However, nowadays in the age of modern computers the linearized form of Avrami equation is not necessary for evaluation of crystallization data, because the fitting of Eq. 3.2 directly to the conversion curve of crystallization is also a very easy routine work. The two evaluation methods are presented in Fig. 3.8. It is clearly discernible that both evaluation methods result in the same kinetic constants. The advantage of fitting Eq. 3.2 to the conversion curve of crystallization is that the estimation of the initial point of crystallization is not necessary at all, thus the reliability of the results is better. The study of crystallization kinetics under isothermal conditions has large importance despite the fact that these conditions have no practical relevance, because several basic phenomenon of crystallization can be explained based on kinetic results. We have to point out that both techniques result in the same Avrami exponent ($n = 3$), but the value of the overall rate constant may be different, because it is affected by the fitting range of the linearized form.

A more realistic kinetic evaluation is when the crystallization process is investigated under non-isothermal conditions, but in this case, the overall reaction rate is changing with temperature. Accordingly, the equations used for isothermal crystallization cannot be used even if mathematically Avrami equation can be fitted also to conversion curves recorded under non-isothermal conditions. Unfortunately, this mistake can be found in the literature even nowadays. The kinetic evaluation of the non-isothermal crystallization process was solved by Ozawa in 1971 [55, 88]. Several other techniques have appeared in the literature for evaluation of crystallization curves recorded under dynamic cooling condition since the pioneering work of Ozawa. A thorough comparative study on these methods was published by di Lorenzo et al. [88]. The detailed introduction of the kinetic evaluation is not the aim of this chapter, thus these techniques are not listed here in details.

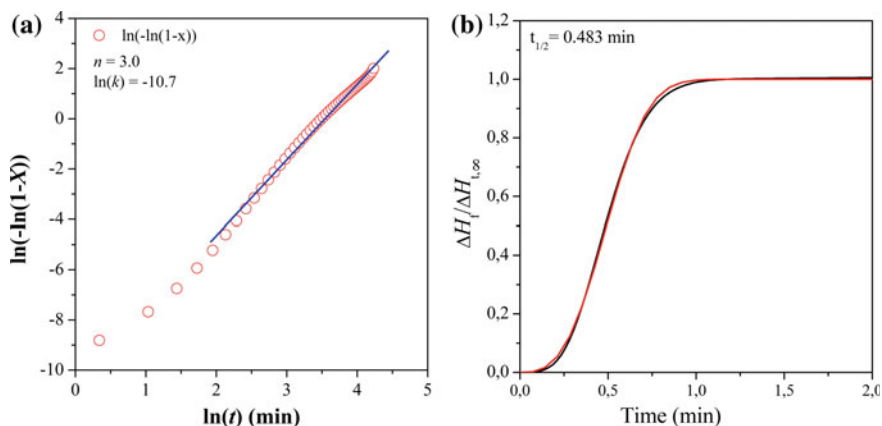


Fig. 3.8 Avrami evaluation of isothermal kinetic data using linearized Eq. 3.3 (a) and the original Avrami equation (b). The crystallization isotherm was recorded at 126 °C using a polypropylene homopolymer (Borealis HB120FR) and 2000 ppm NA21E was used as nucleating agent

3.3 Nucleation, the Targeted Manipulation of Crystalline Structure

3.3.1 Basic Characterization of Nucleating Agents

As it was mentioned earlier the presence of nucleating agents changes the entire crystallization process [8, 10–12, 75, 89–98]. In fact, the presence of nucleating agents decrease the activation energy and the rate of nucleation, because the formation of a heterogeneous nucleus is more favorable on a heterogeneous surface than in the bulk polymer melts. Consequently, significantly more nuclei are formed in the presence of a nucleating agent and the final structure will consist of small supermolecular units with relatively narrow size distribution. In addition, the temperature range of crystallization shifts to higher temperatures, thus more perfect lamellas are formed during the crystallization [13, 51]. Accordingly, the presence of nucleating agents changes the crystalline structure at both lamellar and supermolecular levels. Figure 3.9 represents the structure of the nucleated iPP compared to the non-nucleated structure. The difference between the nucleated and non-nucleated fields is self-explanatory. The modified crystalline structure leads to different properties as well, therefore the goal of the application of nucleating agents is always the targeted manipulation of properties. The basic terms and properties of the nucleating agents will be discussed in details in the following section.

The application of nucleating agents shifts the crystallization temperature toward the higher temperatures. This effect is presented in Fig. 3.10, where three different nucleating agents are compared [63]. One of them is poly(vinyl cyclohexane) (PVCH), which is a very effective nucleating agent polymer in iPP [62]. The second is NA-21E, which is a phosphate derivative and is used in large quantity in the industrial practice [99–101]. The third type is 1,3:2,4-bis(dimethylbenzylidene) sorbitol (DMDBS), which is an organic sorbitol derivative and also a commercial nucleating agent [102–105].

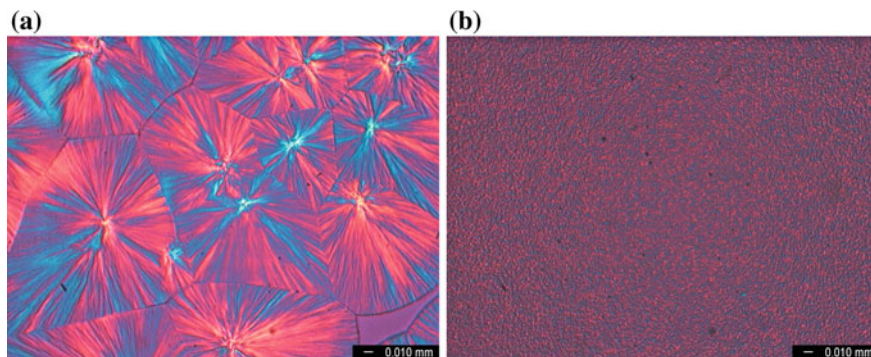
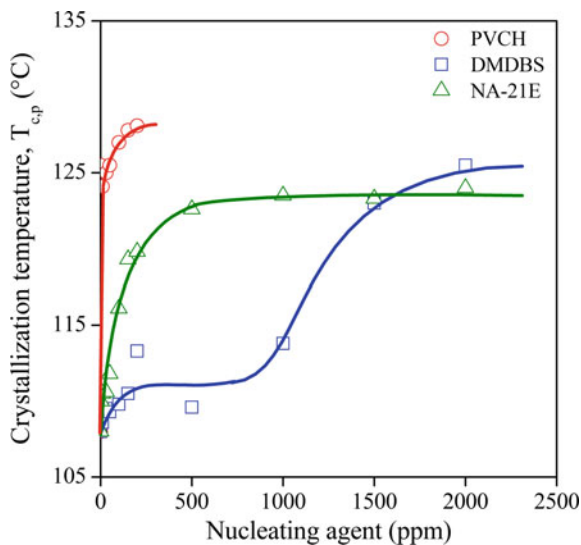


Fig. 3.9 Optical microscopic views of **a** non-nucleated iPP (Borealis HB120FB) crystallized at 130 °C for 70 min and **b** nucleated with PVCH (200 ppm)

Fig. 3.10 Efficiency of PVCH, NA-21E and Millad 3988i



It can be clearly seen that the effects of the three nucleating agents is different. The change in the peak temperature of crystallization (T_{cp}) represents the difference reliably, thus this value is used for the characterization of the efficiency of the nucleating agents.

The only problem with T_{cp} is that the crystallization temperature is dependent on the polymer grade as well, thus the shift in T_{cp} is a relative measure of efficiency only. Thierry et al. [11] introduced a reliable method for comparison of nucleating agents. They suggested preparing a self-seeded sample from the polymer and estimating the peak temperature of crystallization during self-seeding (T_{cpss}). The nucleating efficiency then can be determined as Eq. (3.4):

$$NAE(\%) = \frac{T_{cp} - T_{cpr}}{T_{cpss} - T_{cpr}} * 100 \quad (3.4)$$

NAE is the efficiency factor of the nucleating agent in percentage. T_{cp} is the actual peak temperature of crystallization in the nucleated sample. T_{cpr} and T_{cpss} are the peak temperatures of crystallization in the non-nucleated or in the self-seeded samples respectively. The use of NAE is a little complicated, but it makes possible to compare the nucleating efficiency of a nucleating agent in different iPP polymers. Since this method is more complicated and time-consuming than a standard DSC measurement, only the T_{cp} is used for relative characterization of efficiency in general. A list of nucleating agents according to their efficiency factors (NAE) is given in Table 3.1. The data were taken from the publication of Thierry et al. [11, 69, 70].

The nucleating agents have to be present as heterogeneous surfaces in the polymer melt during crystallization. Their effect depends strongly on their homogeneous distribution in the polymer. Nucleating agents are diverse materials.

Table 3.1 Efficiency scale of additives used as nucleating agents in iPP (based on [11, 69, 70])

Additive name	Concentration (%)	T_{cp} (°C)	NAE (%)
4-biphenyl carboxylic acid	2.0	128.8	66
2-naphtic acid	1.0	127.8	62
2,4-dihydroxy, 5-methylpyrimidine	1.0	125.3	50
1,3:2,4-dibenzylidene D-glucitol	0.4	123.2	41
4-pyridinecarboxylic acid (isonicotinic acid)	1.0	123.0	39
Sodium benzoate	1.0	121.2	31
4-tertobutyl benzoic acid	1.0	120.7	29
2,3-pyridine dicarboxylic acid	1.0	117.3	13

They can be either inorganic particles like talc [75], or organic molecules, like sorbitol derivatives or polymers like PVCH and PVDF [62, 64] for example. As it was pointed out earlier the most important requirement for nucleating effect is the structural matching between the lattice parameters of the crystalline phase of the nucleating agent and iPP. In addition, the presence of heterogeneous surfaces and homogeneous distribution are essential, but the homogeneous distribution of the nucleating agent is difficult to achieve. In order to solve the problem of poor homogeneity soluble nucleating agents were developed in the past decades [8–10, 12, 91, 102, 104–108]. These additives are partially soluble in iPP melt. If they are introduced to iPP in the usual amount between 1000 and 5000 ppm, they can dissolve at the conventional processing temperatures around 230–250 °C and their homogeneity will be excellent in the iPP melt. In order to achieve good efficiency, the nucleating agent has to fall out during cooling of the melt. Falling out should take place at a higher temperature than the crystallization of the polymer and in this case very fine particles will be formed homogeneously and will induce crystallization effectively. The sorbitol derivatives are the most well-known soluble nucleating agents for iPP and they are used in a large amounts in the industrial practice [72, 91, 93, 103–112]. It should be noted that soluble nucleating agents usually have a threshold concentration and below this content they cannot act as nucleating agent, because they cannot fallout from the melt. Accordingly, these additives are applied usually in larger amounts.

iPP is a polymorphic polymer and most nucleating agents induce the formation of the conventional α -modification [9], but there are numerous additives, which promote the formation of the β -modification of iPP [8, 72, 74, 93, 97, 113–139]. The β -nucleating agents are organic molecules and some of them are soluble in the iPP melt. The first β -nucleating agent, the linear trans γ -quinacridone was found by Leugering et al. [140]. This additive is a red pigment, thus its application is limited due to the intense color. During the pioneering research of β -nucleating agents, Varga et al. [74] revealed the supreme efficiency of the Ca-salt of pimelic and suberic acids. In addition, Shi et al. [141] studied the β -nucleating efficiency of the two component systems of pimelic acid and Ca-stearate. Ikeda introduced the N,N'-dicyclohexyl-terephthalamide (NJS) as a soluble and efficient β -nucleating agent

[142]. In the past few decades, several novel β -nucleating agents were found and published in the literature. Some of them are soluble in the iPP melt and many other are similar to the conventional heterogeneous nucleating agents [46, 113, 114, 117, 119, 120, 143–153]. In the case of β -nucleating agents, selectivity has crucial importance, because the lattice parameters of β - and α -iPP are very close to each other. Accordingly, most of the β -nucleating agents induce the crystallization of both modifications and selectivity relates to the relative efficiency for the different modifications. According to the recent state-of-the-art, Ca-pimelate and Ca-suberate prepared by Varga et al. [74, 154] are completely selective to the β -form. The other β -nucleators usually promote the crystallization of the α -form as well, thus a minor amount of α -iPP is always formed in their presence and a mixed polymorph structure is developed. Varga et al. designated this effect as dual nucleating ability [90, 136, 155, 156].

As it was demonstrated above the nucleating agents are diverse materials and they can be differentiated based on their solubility and selectivity, thus the nucleating agents will be discussed in details using this grouping.

3.3.2 “Conventional” Heterogeneous Nucleating Agents

Many materials have nucleating effect in iPP, but those additives, which have industrial or laboratory relevance were collected by Fairgrieve [9, 157]. He gave a substantial description about the nucleating agents available commercially for iPP up to 2005, thus the ordering of these additives is out of the scope of this chapter. In his report, he also tried to collect as much laboratory scale nucleating agents as possible. The most important nucleating agents are presented in Table 3.2 and discussed in this chapter as well. Talc is one of the most frequently used heterogeneous nucleating agents in iPP [75]. It consists of anisotropic needle-like or lamellar crystals. Its efficiency in iPP homopolymer is presented in Fig. 3.11 and it can be seen that T_{cp} changes according to the characteristic curve of heterogeneous nucleating agents. T_{cp} increases steeply at low concentration and reaches saturation below 1000 ppm. The supermolecular structure changes also because the larger nucleus density results in smaller spherulite size. The supermolecular structure in the presence of talc is shown in Fig. 3.12. The size of the spherulites is in the range of few microns, thus the supermolecular structure formed in the presence of heterogeneous nucleating agents is designated as “microspherulitic” structure [63, 158]. As it can be seen in Fig. 3.9, the efficiency of talc does not change significantly over 1000 ppm additive content, but talc is also used as filler in composite materials [159].

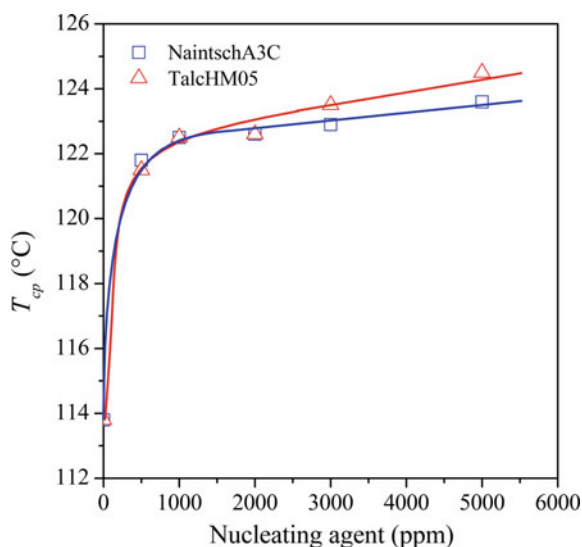
Several other nucleating agents, like sodium-benzoate or NA-11, NA-21E are used in a large amount in the industrial practice [9]. Their efficiency is close to each other, but it has to be noted that the efficiency of a nucleating agent depends on the molecular structure of the polymer itself. Most of these studies are focused on the effect of molecular mass on the crystallization process and only few works discuss the influence of chain regularity [15, 164–166]. Earlier studies revealed that the

Table 3.2 Most frequently used heterogeneous conventional nucleating agents for iPP

Nucleating agent type	Designation	References
Talc	Talc	[75, 160, 161]
Sodium benzoate	NaB	[98, 162]
Sodium-2,2'-methylene-bis(4,6-di-t-butylphenyl) phosphate	NA-11	[101]
2,2'-methylene-bis(4,6-di-t-butylphenyl) phosphate (Al complex)	NA-21E	[100, 101]
Bicyclo [1, 2] heptane-2,3-dicarboxylic acid, disodium salt	HPN-68	[8, 163]
Ca-pimelate ^a	Ca-pim	[74, 154]
Ca-suberate ^a	Ca-sub	[74, 154]

^aPromotes the formation of β -iPP

Fig. 3.11 Nucleating efficiency of different talc types in iPP homopolymer (MOL Petrochemicals, Tipplen H304)



larger chain regularity is accompanied by slightly better efficiency of nucleating agents, because the crystallization is easier in the case of more regular chain structure [110, 167–169].

The primary goal of the introduction of heterogeneous nucleating agents is to improve mechanical properties. Especially the tensile modulus of iPP can be increased in the presence of nucleating agents. As it was demonstrated earlier, the modulus is determined predominantly by crystallinity and lamella thickness [170–172]. The enhancement of modulus in the presence of heterogeneous nucleating agents is presented in Fig. 3.13. It is clearly visible, that the improvement of the properties is strongly dependent on the type of nucleating agents. Conventional heterogeneous nucleating agents have a similar effect as NA-21E in iPP and modulus increases about 20–50%. However, there are superefficient nucleating agents like PVCH, which increases the modulus steeply. The large increase in

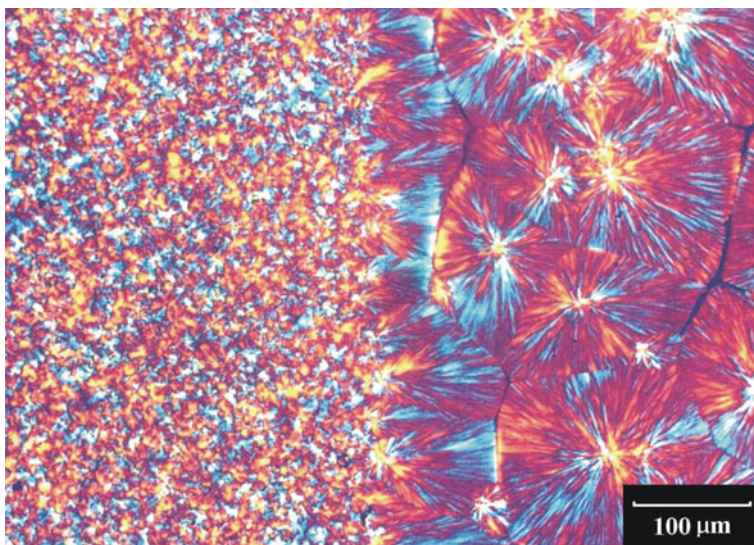
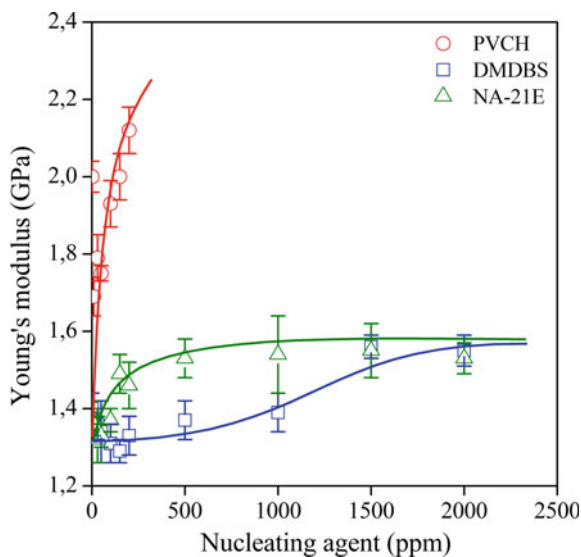


Fig. 3.12 iPP nucleated with talc (left-hand side) and non-nucleated reference polymer at the right-hand side

modulus in the presence of PVCH can be explained by its superior efficiency. It elevates T_{cp} above 130 °C and the crystallinity is also larger by 60% and this unique crystal structure contains very thick lamellas leading to the superior mechanical properties. It should be noted that the large improvement of stiffness is usually accompanied by the proportional decrease of impact resistance.

Fig. 3.13 Effect of nucleating agents on the tensile modulus [63]



As it was described before the presence of nucleating agents changes the crystalline structure at the lamellar level and the crystallinity is also larger usually. However, it was represented in our earlier works that these two factors are not necessarily dependent on each other. Accordingly, they should be handled as independent parameters. For example, in random iPP copolymers, the crystallinity does not change significantly in the presence of efficient nucleating agents, but the T_{cp} increases significantly. Consequently, the structure changes mainly on the lamellar level.

In addition to the change of lamellar thickness, the spherulitic structure also changes in the presence of nucleating agents. The spherulites become smaller and their size distribution becomes more homogeneous [63], thus this structure is designated as “microspherulitic”. Although the change in the spherulitic structure is obvious, the quantitative characterization is not easy. The simplest way is the counting of spherulites on optical micrographs, but we have to remark that this method is notoriously imprecise [173]. A more sophisticated method is the calculation of nucleus density from the kinetic equation of crystallization. Several methods exist in the literature, which derive the nucleus density based on isothermal measurements, but these methods are far from the realistic experimental conditions [53, 58, 173–176]. Our recently published evaluation method makes it possible to calculate nucleus density from a single crystallization curve recorded by calorimetry under isothermal or dynamic conditions as well [173]. Unfortunately, the calculation is a time-consuming procedure, but the nucleus density values represent the effect of nucleating agents clearly (see Fig. 3.14).

The presented nucleus density (N) changes more than four orders of magnitude at least, thus the optical appearance is changing proportionally. Haze, the intensity of scattered light related to the total transparency, is used as the most sensitive measure of optical properties [63, 173]. It is known in the literature that the

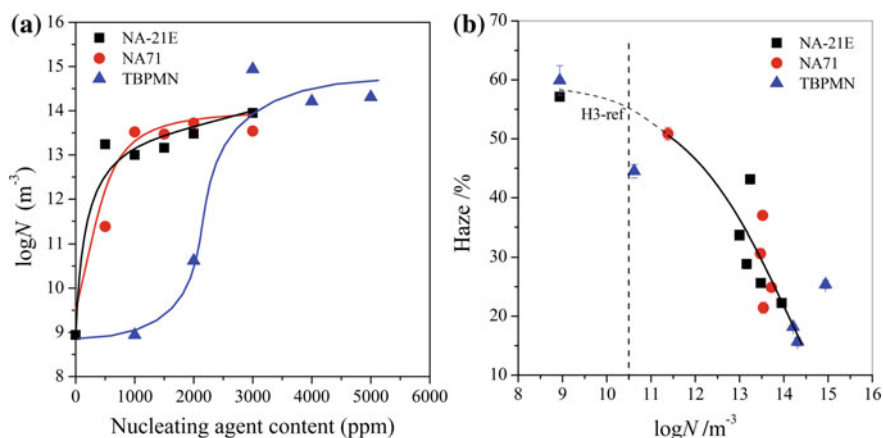
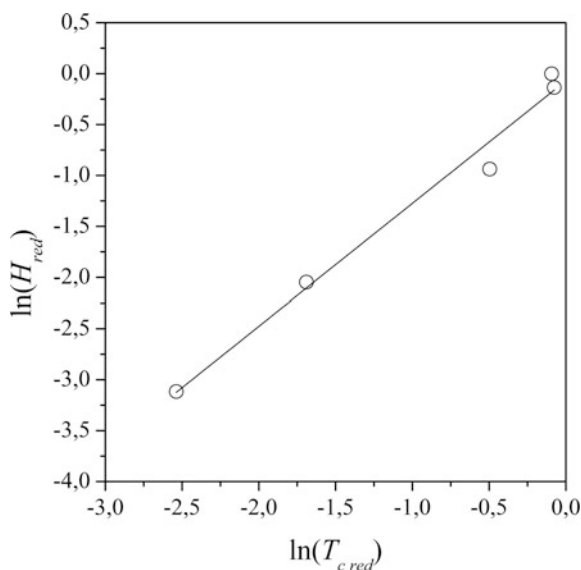


Fig. 3.14 The change in **a** nucleus density as a function of nucleating agent content and **b** haze as a function of nucleus density [173]

introduction of heterogeneous nucleating agents results in a microspherulitic structure, which has lower haze than the non-nucleated iPP, however, the improvement of haze in the presence of conventional heterogeneous nucleating agents is moderate only [63]. Since the spherulitic structure is changing with the efficiency of nucleating agents, the haze value is also dependent on T_{cp} , but the correlation is complicated [16]. In order to represent this correlation an empirical description was presented earlier (see Fig. 3.15) and a reduced haze and efficiency were determined. It was found that the correlation is reasonably good [16], but this simplified model does not explain the nature of light scattering at all.

The nucleating agents may be used for manipulation of crystal modification in iPP. As it was described earlier β -modification of iPP has also industrial relevance, thus there are nucleating agents, which induce the formation of this modification. The selectivity of these additives is significantly different [154]. Ca-pimelate and Ca-suberate are β -nucleating agents, which are insoluble in the iPP melt, thus their effect is similar to the “conventional heterogeneous” nucleating agents. As it can be seen in Fig. 3.16a, these nucleating agents are highly efficient, because the increase in T_{cp} is reasonably large in their presence. The selectivity of these nucleating agents is clearly proved by the polymorphic composition. In general, the selectivity of a β -nucleating agent can be characterized by the β -content of the sample. If β -content is larger the selectivity of the nucleating agent is better. The β -content can be evaluated from the melting curve recorded by calorimetry, after the elimination of the melting memory (see Fig. 3.2). The β -content of mostly known nucleating agents is presented in Fig. 3.16b, where the differences in selectivity can be clearly seen. In fact, literature data hint that only Ca-pimelate and Ca-suberate are completely selective to the β -modification and all other β -nucleating agents promote the

Fig. 3.15 The correlation between reduced haze and efficiency [16]



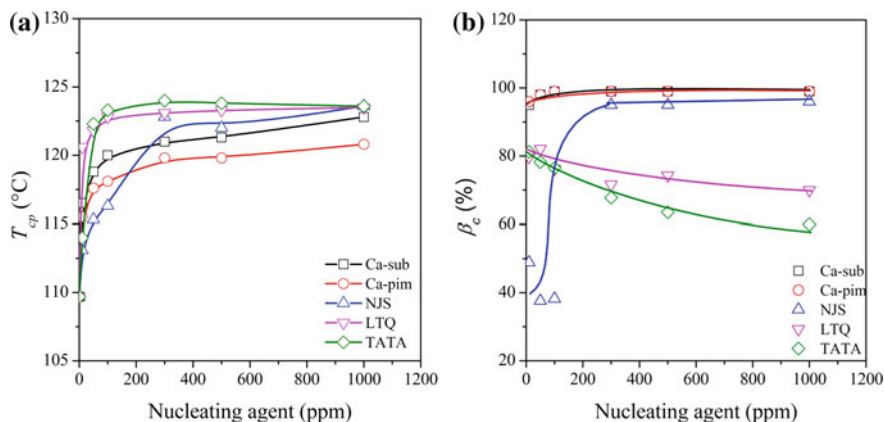


Fig. 3.16 Efficiency (a) and selectivity (b) of β -nucleating agent

crystallization of the α -form as well. The nucleating of two polymorphic modifications at the same time is designated as the dual nucleating ability in our earlier work [71, 90].

The data presented in Fig. 3.16a indicate clearly that the efficiency of β -nucleating agents is similar to that of the α -nucleators and the peak temperatures of crystallization are also in the same range. Accordingly, it is impossible to identify the β -nucleating agents from the crystallization curves. However, the melting profile in the presence of β -nucleators is significantly different as it was demonstrated in Fig. 3.2. The exact polymorphic composition (β_c) of iPP can be determined from the melting curve recorded during heating the sample from 100 °C [35, 154] due to the melting memory effect of β -iPP (Fig. 3.16b). It is clearly visible that β -nucleating agents can be divided into three categories. The introduction of completely selective nucleating agents, like Ca-suberate and Ca-pimelate, results in the formation of pure β -iPP in the entire effective concentration range [154]. However, the presence of nucleating agents with dual nucleating ability results in mixed polymorphic composition. Such nucleating agents are linear trans- γ -quinacridone (LTQ) [140, 154], or tris-2,3-dimethyl-hexylamide of trimesic acid (TATA) [72]. These additives with dual nucleating ability induce larger β -content at small concentration and β_c decreases with their increasing amount. This can be explained easily, because the β -iPP grows faster in the conventional temperature range of crystallization than the α -modification and only a small amount of α -iPP forms if the nucleating agent content is small [80, 154, 177]. The growth of the small amount of α -iPP stops quickly, because β -iPP overgrows it. With increasing the amount of the nucleating agent the ratio of α -iPP increases as well, in addition, nucleus density increases significantly, thus the growth of the individual supermolecular units stops earlier due to the impingements. We have to remark here that NJS in Fig. 3.16 (N,N'-dicyclohexyl-2,6-naphthalene dicarboxamide) is soluble in iPP melt, thus it does not show any efficiency and selectivity in the small concentration range [154].

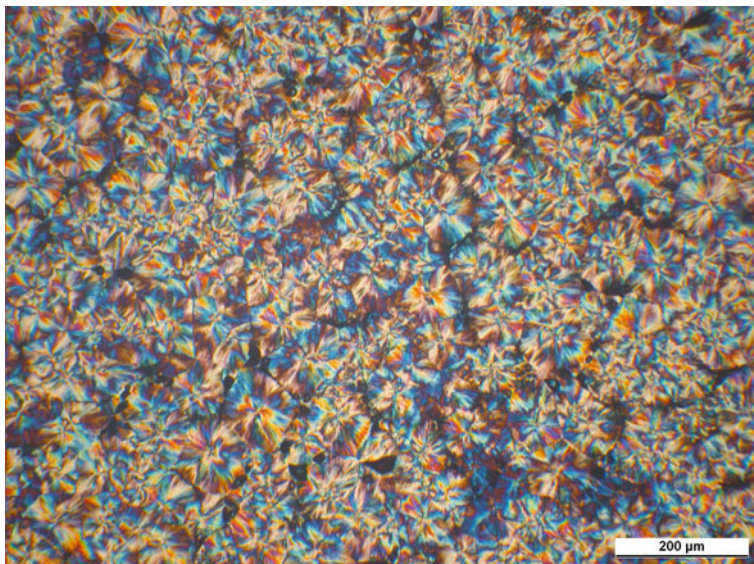


Fig. 3.17 Supermolecular structure of β -nucleated iPP in the presence of 50 ppm Ca-sub after complete crystallization at 130 °C

As it was studied by Varga et al. earlier [6, 35, 42, 43, 178, 179], the supermolecular structure of β -iPP is different compared to the α -form. The microscopic view of β -nucleated iPP is presented in Fig. 3.17. The birefringence of the β -iPP is much stronger, thus it can be differentiated from the α -form easily. The supermolecular structure of β -iPP is demonstrated at low nucleating agent content in order to make the appearance of individual spherulites visible. At larger nucleating agent content microspherulitic structure forms, in which the observation of individual β -spherulites is not possible at all. We have to note that the structure presented in Fig. 3.17 can be prepared using a completely selective β -nucleating agent in a small amount.

3.3.3 Soluble Nucleating Agents, Organogelators and Clarifiers for α -iPP

As it was mentioned in Sect. 3.3.1, the main idea behind the soluble nucleating agents is to solve the problem of homogenization. Sorbitol derivatives were the first soluble nucleating agents for iPP and they are still used even nowadays. The history of sorbitol derivatives goes back in the '70-s [9], when it was discovered that some of them possessed nucleating effect in polyolefins, particularly in PP. The most well-known representative of this type of nucleating agents is the 1,3:2,4-dibenzylidene sorbitol

(usually abbreviated as DBS) (see Fig. 3.18), which was the main object of several researches in the last decades. At the beginning it was developed as a gelling agent in liquids, and was applied in cosmetics and pharmaceuticals. The potential use as a nucleating agent in polymers was observed later. The most important members of this family of nucleating agents are shown in Fig. 3.18.

These compounds are formed in the reaction of sugar alcohols, such as sorbitol and substituted benzaldehydes. In these reactions mono-, di- or triacetals can be synthesized [102]. A schematic representation of the multiple step reaction is demonstrated in Fig. 3.19. In the first step an aldehyde reacts with an alcohol and an intermediate product is formed, which reacts in the next step with another alcohol molecule in order to form the final product. The reaction is reversible, if the pH of the media decreases the balance shifts towards the starting compounds.

The first representative of sorbitol based clarifiers is DBS, which has reasonably good efficiency in iPP, but its use is accompanied by intense odor, which limits its application fields. Intensive researches began to generate the substituted analogues of it, in order to achieve further improvement in its performance, decrease the odor and increase its efficiency. The second and third generation of this nucleating agent family represents clearly this development:

- Reaction of sorbitol and substituted benzaldehyde, where substituents can be alkyl-, alkoxy-, ester-, amide-, halogen-groups. Examples: 1,3:2,4-bis(4-methylbenzylidene) sorbitol (MDBS), 1,3:2,4-bis(3,4-dimethylbenzylidene) sorbitol (DMDBS)

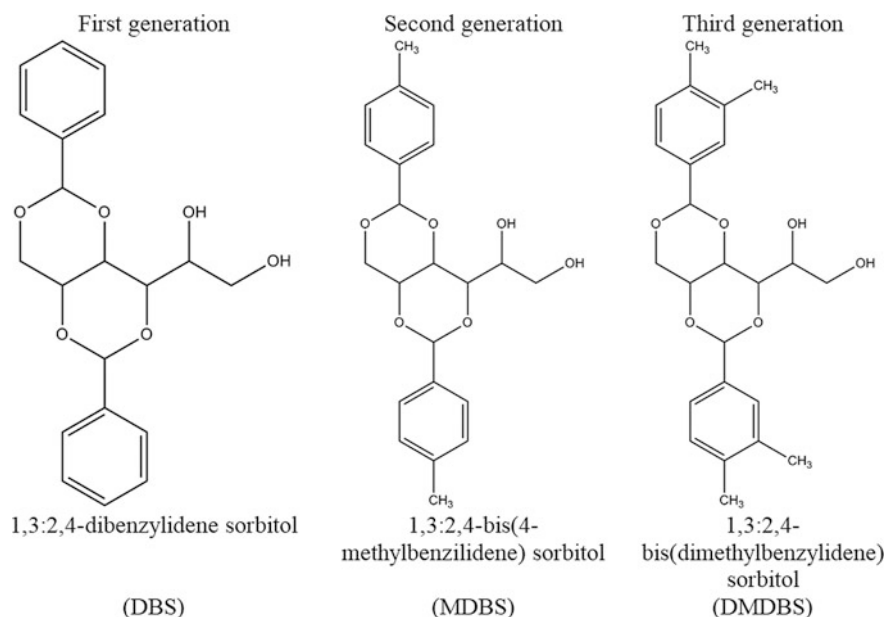


Fig. 3.18 Chemical structure of sorbitol derivatives marketed in the last four decades

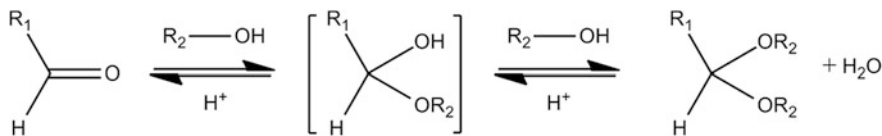


Fig. 3.19 Schematic view of the synthesis route of sorbitol based nucleating agents

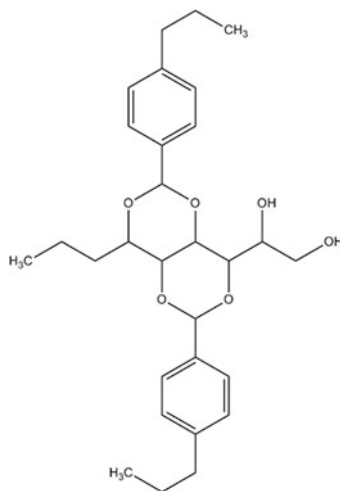
sorbitol (DMDBS). These compounds are used frequently in the industrial practice.

- Dibenzylidene xylonates can be considered to be modified sorbitols, in which the $-\text{CH}_2(\text{OH})-\text{CH}_2-\text{OH}$ part of DBS is changed to another substituent, e.g. carboxyl-group, ester, amide.
- Reaction of isocyanate and the hydroxyl-groups of DBS (or modified DBS).
- Reaction of modified sorbitol (e.g. 1-allylsorbitol) with benzaldehyde.
- Both sorbitol and benzaldehyde can be modified.

Recently, nonitol or its derivatives can be applied instead of sorbitol. A nonitol derivative, 1,2,3-trideoxy-4,6:5,7-bis-O-[(4-propylphenyl)-methylene]-nonitol (TBPMN) (Fig. 3.20) provides superior optical properties, but its price is relatively high. In addition, as its solubility is better than that of DBS, it has to be introduced into the polymer in a much larger amount. Recently, this is called as the fourth generation of sorbitol derivatives [180].

Although the soluble nucleating agents can dissolve at high temperature in the iPP melt, they should recrystallize before the iPP starts to crystallize. Consequently, they form heterogeneous surfaces in the melt, which act as effective nucleating sites. Accordingly, the mechanism of crystallization is similar to that in the presence of conventional heterogeneous nucleating agents, but the distribution and particle size of the nucleating agent and the surface area of the recrystallized nucleating units are significantly different. DBS was the first widely used and investigated sorbitol type nucleating agent. Since this additive has been studied for the longest time, most of the experimental results relate to this compound [91, 105, 108]. An interesting gelling effect was observed and the high nucleating efficiency was explained by this gelation property. It should be noted that the general findings stand for the derivatives of DBS as well. It is necessary to study the structure of the molecules of DBS to understand its unique gelling properties [11, 105]. Due to their special, “butterfly-like” shape (Fig. 3.21a) molecules of DBS form up a physical gel in non-polar media [11]. The benzene rings represent the non-polar “wings” of the molecule, which make it possible to disperse the additive homogeneously in liquids or in the iPP melt. On the other hand, the aliphatic chain (the sorbitol part) corresponds to the “body” and has a polar character because of the hydroxyl-groups attached to the carbons 5 and 6 of the sorbitol part. These polar moieties enable the

Fig. 3.20 Chemical structure of 1,2,3-trideoxy-4,6:5,7-bis-O-[(4-propylphenyl)methylene]-nonitol



formation of intra- and intermolecular bonds (hydrogen bond) between the molecules, but at the same time phenyl interactions of the benzene rings are also present [7]. Several molecules connected to each other in this way build up stable, nearly infinitely long fiber-like structures, with around 10 nm diameter and around 400 m²/g specific area. In non-polar media, e.g. in organic solvents these twisted fibers create an open network (Fig. 3.21b), and because of this behavior these types of nucleating agents are referred as *organogelators*.

In the case of the sorbitol derivative DMDBS TEM micrographs of PP containing 0.4 wt% of the nucleating agent (Fig. 3.22) were taken by Lipp et al. [103], in which a hierarchical structure of the fibers can be observed. Thicker fibers with diameter around 60–80 nm are built up by the thinner, 10 nm thick fibrils, which is in close similarity with the above mentioned observations of Thierry et al. [11].

Since the fibrillary structure introduced above has crucial importance from the point of view of nucleating efficiency, the preconditions of this process should be discussed in details. Molecules having structure presented in Fig. 3.21 can build up a fibrillary structure in most cases. However, there are some exceptions, because the chirality of the molecule can affect the tendency of fibril formation [7]. Helical fibers can be built up only by chiral amphiphilic molecules and a racemic mixture is not capable to form fibrillary aggregates and precipitates in solution. Even in the case of clear enantiomers there can be a difference in the efficiency of the two forms. Smith et al. [102] prepared a trisubstituted sorbitol derivative in the reaction of D-sorbitol and 1-naphthaldehyde in order to demonstrate the role of chirality of the molecules in the fibril formation. In the reaction both the “R” and “S” diastereomers of trinaphthylidene sorbitol were formed (Fig. 3.23).

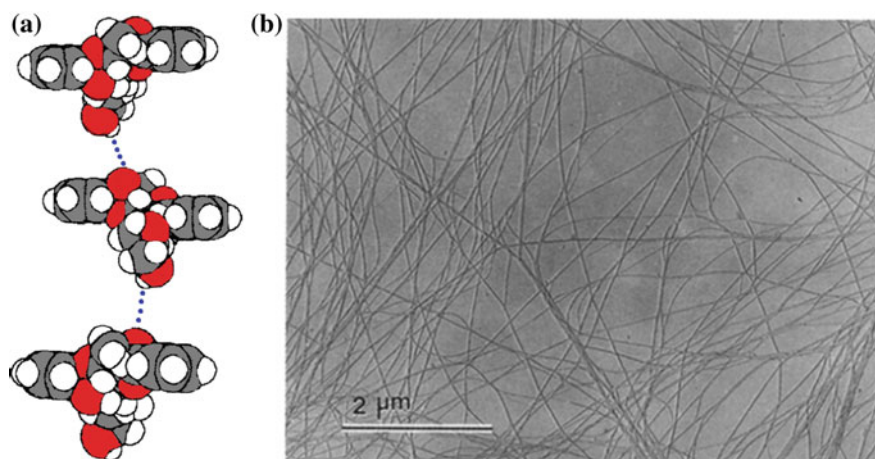


Fig. 3.21 The proposed molecular architecture (a) and fibrillar structure crystallized from tetrahydrofuran (THF) (b) of DBS [7, 11]

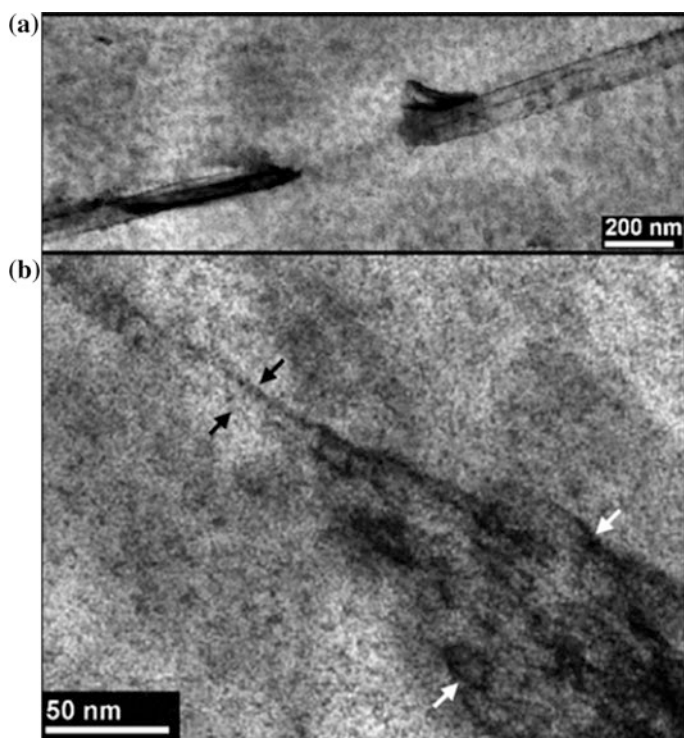


Fig. 3.22 TEM micrograph of DMDBS fibrils formed in iPP [103]

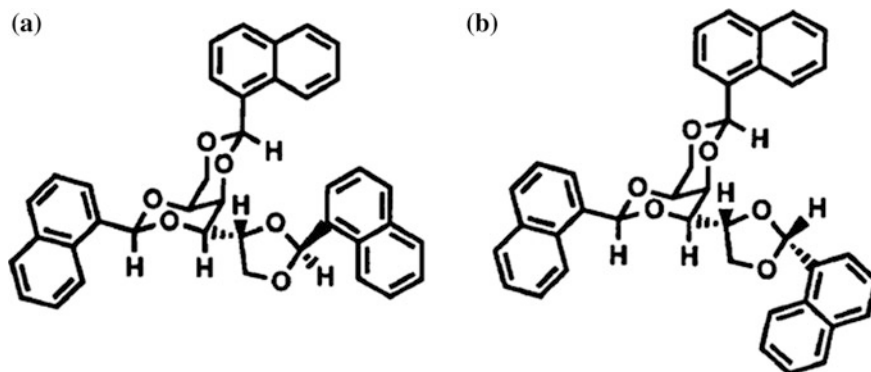


Fig. 3.23 R (a) and S (b) isomers of trinaphthylidene sorbitol synthesized by Smith et al. [102]

The two molecules differ only at the methine carbon attached to the oxygens on carbons 5 and 6 of the sorbitol unit, however, the “S” form is active as a nucleating agent, while the “R” form is inactive, moreover, renders the previously mentioned form ineffective. This nucleating agent (along with the other sorbitol derivatives) is synthesized in a multiple step reversible reaction, which was demonstrated schematically in Fig. 3.19. In the case of trinaphthalidene sorbitol a monoacetal forms first, which in the next step reacts with a naphthaldehyde molecule to form a diacetal. This latter quickly reacts with another naphthaldehyde molecule forming a triacetal, i.e. the “S” form of the product. Because of the reversibility of the reaction, the product can revert to the intermediate products. However, under further heating the “R” diastereomers start to form and its ratio increases with temperature.

3.3.4 Crystallization of *iPP* in the Presence of Soluble Organogelators

As it was mentioned before the crystallization process in the presence of organogelators is different than in the non-nucleated polymer [11, 181]. Large number of nucleating sites is formed and they are finely dispersed in the melt resulting large surface area. When the organogelator is present, the first step is the agglomeration of its molecules and the formation of a three-dimensional homogeneous microfibrillar network, a thermoreversible gel. In the course of cooling these fibrils recrystallize first, having a large specific area and thus providing a huge number of nucleation sites for the polymer. After further cooling, at a lower temperature the polymer crystallizes on the surface of the fibers, forming a

microcrystalline structure with epitaxial growth on the surface. The epitaxial mechanism is possible because of a geometrical matching between the crystalline phase of the polymer and the nucleating agent. In addition the fibrillary structure formed is very efficient at the network points of the fibrils, because there are two heterogeneous surfaces located very close to each other, which is thermodynamically favorable for crystallization. A schematic view is presented in Fig. 3.24.

Unfortunately, organogelators are not able to form large single crystals, thus geometrical matching cannot be checked directly and the verification of the above-proposed mechanism is difficult. The crystallization process and the epitaxial crystal growth were investigated by Thierry et al. [62, 181] using the so-called polymer decoration method, which can be considered an indirect method. In their experiments vacuum cracked polyethylene (PE) was vaporized on the surface of the fibrils of 1,3:2,4-bis(3,4-dimethylbenzylidene)sorbitol (DMDBS). The results indicated that lamellas developed by condensation of PE were randomly oriented upon non-interacting substrates (e.g. glass slide) and were preferably oriented in the case of epitaxial growth indicating the nucleation efficiency of the fibrils (Fig. 3.25). Although this experiment proved the nucleating efficiency and the presumed mechanism i.e. epitaxial growth, it must be considered that the experimental conditions are far from realistic ones prevailing during the crystallization of iPP melt.

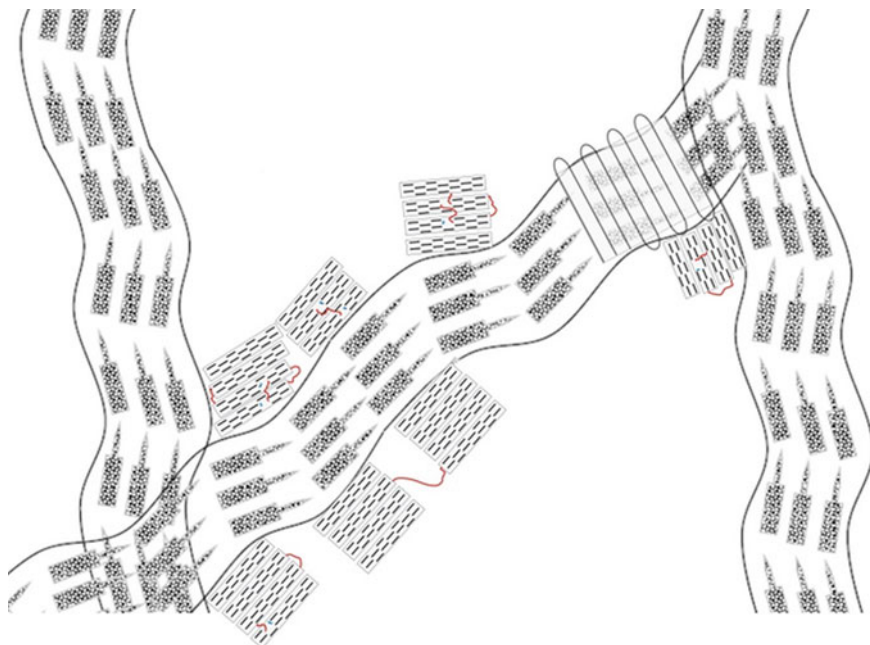


Fig. 3.24 Schematic representation of organogelator fibrils and epitaxial crystallization of iPP on the surface and at the crossing points

The crystallization process is usually studied by calorimetry, but the heat effect of the fibril formation is not detectable at all unfortunately, thus network formation remains invisible for most researchers who measures only DSC curves in order to characterize the crystallization process. The formation of the fibrillary network can be monitored by rheological measurements. In order to study the gelation effect, the crystallization process should be followed by the measurement of the storage modulus as a function of the temperature, in the linear shear deformation range (Fig. 3.26) [7, 181]. Figure 3.26 presents data of a DMDBS-nucleated ethylene-propylene random copolymer, but the tendencies are valid for other iPP polymers containing organogelators as well. In the case of the non-nucleated polymer (labeled with black circles) storage modulus slightly increases with the temperature-decrease, but at a certain temperature (T_2) a sudden increase can be observed, which can be attributed to the initial point of the crystallization. However, in the case of the nucleated polymer (labelled with white squares), the change of the storage modulus is different compared to the non-nucleated system. In the course of cooling a stepwise increase of the modulus can be observed at a higher temperature (T_1), which is originated from the formation of a network structure of the organogelator. In other words, the step belongs to the beginning of the formation of the physical gel of the nucleating agent, and the gelation process ends between T_1 and T_2 . The pronounced crystallization starts around T_2 in the case of nucleated iPP, but the start of steep increase is located at a higher temperature in the nucleated sample.

A similar experiment was carried out by Lipp et al. [103] and DMDBS was used also in their investigations. DSC and rheological measurements were performed, in which the heat flow and the complex viscosity were registered as a function of the temperature during both cooling and heating. The measured data are demonstrated in Fig. 3.27. It can be seen on the DSC curves that adding a little amount of DMDBS elevates the crystallization temperature by 10–15 °C, from 106 to 119 °C.

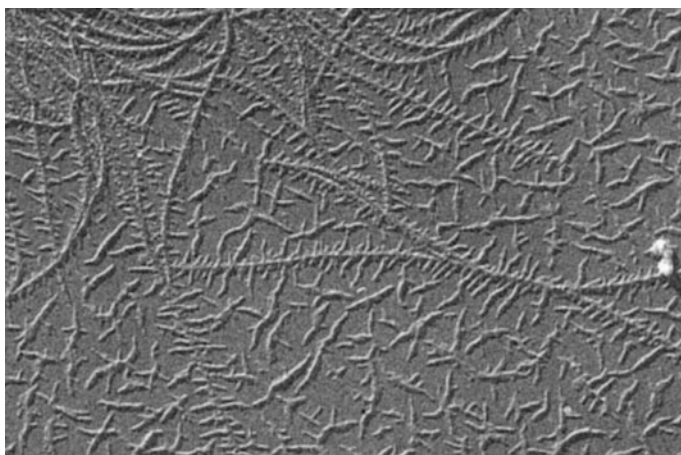
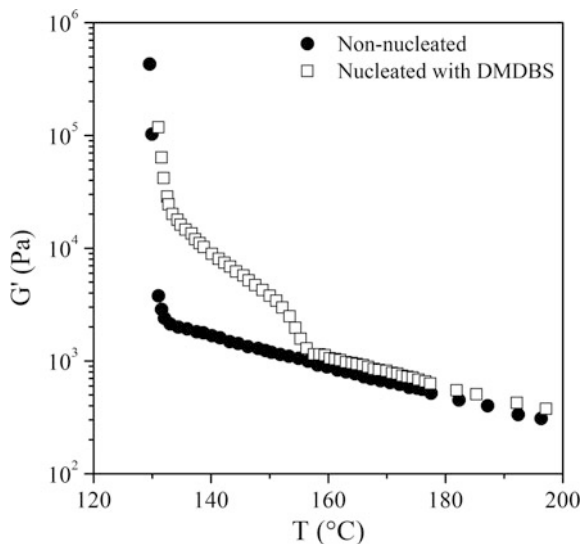


Fig. 3.25 Epitaxial growth on the lateral surface of the organogelator fibrils [181]

Fig. 3.26 Storage modulus of iPP random copolymer (2.5 wt% ethylene content) and its nucleated version as a function of temperature. Cooling rate is 5 °C/min and the frequency is 1 rad/s (the data were mined from the work of Gahleitner et al. [7])



This temperature remains constant by further increasing DMDBS-content. It can be concluded that this compound is an efficient nucleating agent. The shape of the viscosity curves is different in the two cases. If the polymer contains no nucleating agent, the change in complex viscosity in cooling and heating runs is nearly the same (Fig. 3.27a). In contrast to that, the presence of DMDBS causes a stepwise change with a pronounced hysteresis in the viscosity curves (Fig. 3.27b). In the course of cooling, at higher temperatures the shape of the curve is quite similar to that of the neat PP, however, around 160 °C the slope of the curve steeply increases, which can be attributed to the formation of the network of DMDBS fibrils. During heating, the slope of the viscosity curve changes around 192 °C because of the melting of the fibrillar structure.

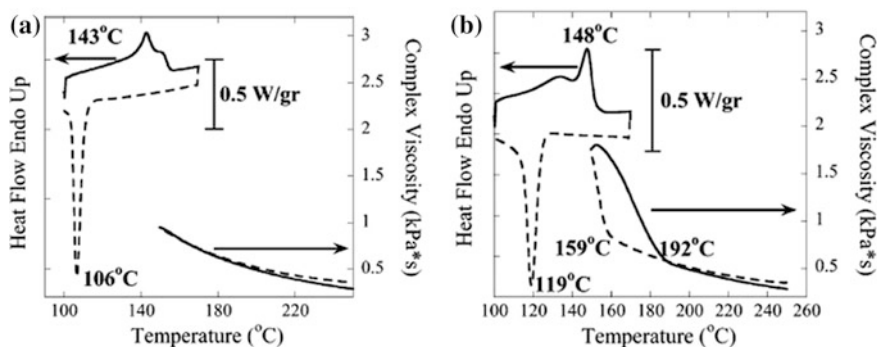
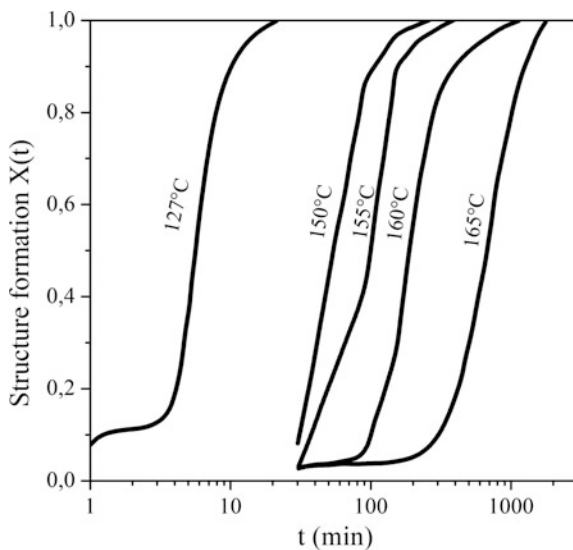


Fig. 3.27 Calorimetric and rheological measurement of crystallization and melting in neat iPP (a) and in iPP nucleated by DMDBS (b) [103]

SAXS measurements were also performed in order to follow and prove the formation of the DMDBS network in the function of time at different temperatures and nucleating contents. From the results it was concluded that at a certain temperature crystallization rate increases with the increase of the DMDBS-content, thus the thermodynamic phase transition temperature (i.e. temperature where the network structure forms) increases with the concentration. When the nucleating agent content is constant, increase in temperature decreases the rate of the network formation, because the thermodynamic driving force (i.e. the undercooling) is smaller. These results corroborate the theory that the mechanism of the structure formation is nucleation and growth, rather than spinodal decomposition. This theory was checked with calculations as well. Lipp et al. [103] calculated the conversion curve of the formation of the network structure, which result is given in Fig. 3.28. Since the formation of the network structure is very fast at low temperature, the measurement at 127 °C had to be carried out using synchrotron radiation. These results revealed that the formation of the fibrillar network can be either very fast or slow depending on the temperature. In fact it is very fast in the temperature range of 120–130 °C, which is practically the temperature range of crystallization of nucleated iPP polymers. Accordingly, the fibril formation is much faster than the crystallization of the polymer so the “organogelation” can take place usually.

According to the above mentioned processes, the formation of the fibrillar network is essential for the efficient nucleation of organogelators. Based on these characteristics the minimum amount of an organogelator is a content where the network can be formed. Consequently, organogelators has a threshold concentration in the practice and below this concentration the nucleating agent is not effective. This threshold concentration depends on the solubility of the organogelator. If the solubility is too large the fibril formation does not happen because the

Fig. 3.28 Conversion curves of fibrillar network formation in iPP registered by SAXS scattering (the temperatures are increasing from left to the right as 127, 150, 155, 160, and 165 °C respectively) [103]



recrystallization of the organogelator does not take place. The optimum amount can be determined by all techniques, which are available to follow the crystallization process like calorimetry, optical microscopy, rheology and X-ray diffraction. For example, increasing the amount of the additive the crystallization process shifts towards higher temperatures, but at a certain concentration of the organogelator the temperature does not increase further. The organogelator content is called optimum amount, where the saturation of the characteristic temperature is reached. This saturation concentration is obviously different for each nucleating agent, and depends on their solubility in the polymer. It is stated to be around 1000 ppm for DBS [182], 1500–1700 ppm MDBS [183], 1700–2000 ppm for DMDBS [104] and 4000 ppm for 1,2,3-desoxy-4,6:5,7-bis(4-propylbenzylidene) nonitol [180, 184].

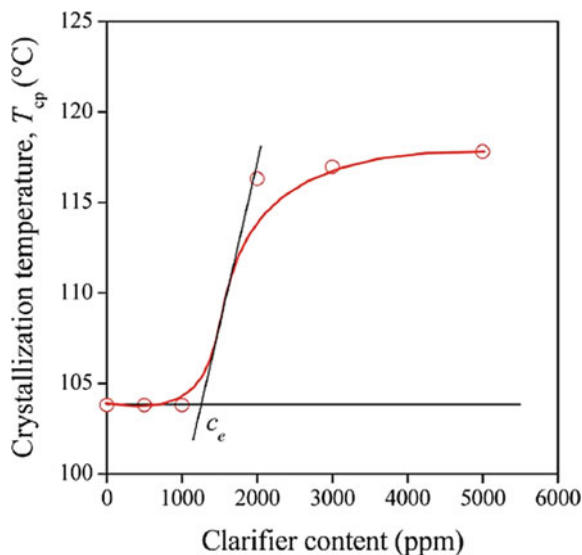
3.3.5 Estimation of Solubility Limit of Organogelators

Since the threshold concentration, as well as the optimum amount, depends on the solubility of the organogelator, the estimation of these points allows us to characterize the solubility of the additive in an indirect way. An experimental solubility value can be determined for example from the peak temperature of crystallization data as the function of the nucleating agent content, as demonstrated in Fig. 3.29 [106]. If the nucleating agent content is increased, until a certain concentration there is no considerable change in the value of the crystallization temperature. However, above a threshold concentration a sudden increase in the crystallization temperature is observable, then it reaches a plateau. The experimental solubility (c_e) is a few thousand ppm, and the exact value depends on the structure of the molecule.

The investigation of the solubility of sorbitols was extended to a wider nucleating agent concentration range by Kristiansen et al. [104] in order to create the experimental phase diagram of the binary system of iPP and DMDBS. Different investigation methods (measurement of haze and clarity, differential scanning calorimetry, rheology and optical microscopy) were used in the study. Using the obtained data, crystallization and melting temperature vs. composition diagrams were constructed. A schematic monotectic phase diagram was also proposed, and the structures developing in the different parts of the diagram were described (Fig. 3.30).

The diagram is divided into four regimes according to the concentration of DMDBS. Regimes I and II are the ranges usually investigated in the practice. In regime I, at very low (up to 1000 ppm) DMDBS content poor efficiency of the additive was observed. Previous studies explained it with the destruction of DMDBS by residues of catalysts or stabilizers, or with its complete dissolution in the iPP melt [185]. However, Kristiansen et al. [104] came up with a new explanation. They claimed that under cooling the polymer crystallizes first, and the presence of the nucleating agent has no effect on the process of crystallization, but it slightly decreases the temperature of it. They explained that the formation of fibrils

Fig. 3.29 Peak temperatures of crystallization as a function of organogelator (DMDBS) content [106]



does not take place, because the organogelator does not exist as a heterogeneous fibrillar network before the crystallization starts.

Regime II covers the concentration range between 1000 and 20,000 ppm approximately. In this case at higher temperatures homogeneous liquid of the melt polymer and nucleating agent exist. In the course of cooling the nucleating agent crystallizes first in the form of fibrils, without prior liquid-liquid phase separation. The fibrillary crystals provide a large surface area of active nucleation sites for the crystallization of the polymer and “organogelation” takes place. The mechanism was described in details in the chapter before.

In regime III no homogeneous liquid phase exists, but liquid-liquid phase separation occurs. Under cooling the additive crystallizes first in the form of large crystals that can be observed even in the optical microscope. Because of the light scattering of these large crystals of the additive the sample is not transparent. The process in regime IV is similar, but there is no phase separation prior to the crystallization of DMDBS.

It must be considered that in systems containing polymers it is almost impossible to reach the equilibrium state. In the study of Kristiansen et al. [104, 105, 186] the kinetics of crystallization as well as the effect of cooling rate was also investigated and significant effect of the cooling rate on properties was demonstrated. Samples prepared at different cooling rates are presented in Fig. 3.31, which contain the same amount of DMDBS, but the cooling rate decreased from left to right. It should be noted that the optical clarity of the sample at the right-hand side could be significantly improved if it was re-melted at 240 °C and re-cooled quickly.

The importance of phase diagram presented in Fig. 3.30 is essential from the point of view of application, because it reveals that organogelators have to be applied in a relatively narrow concentration range (regime II), in addition the

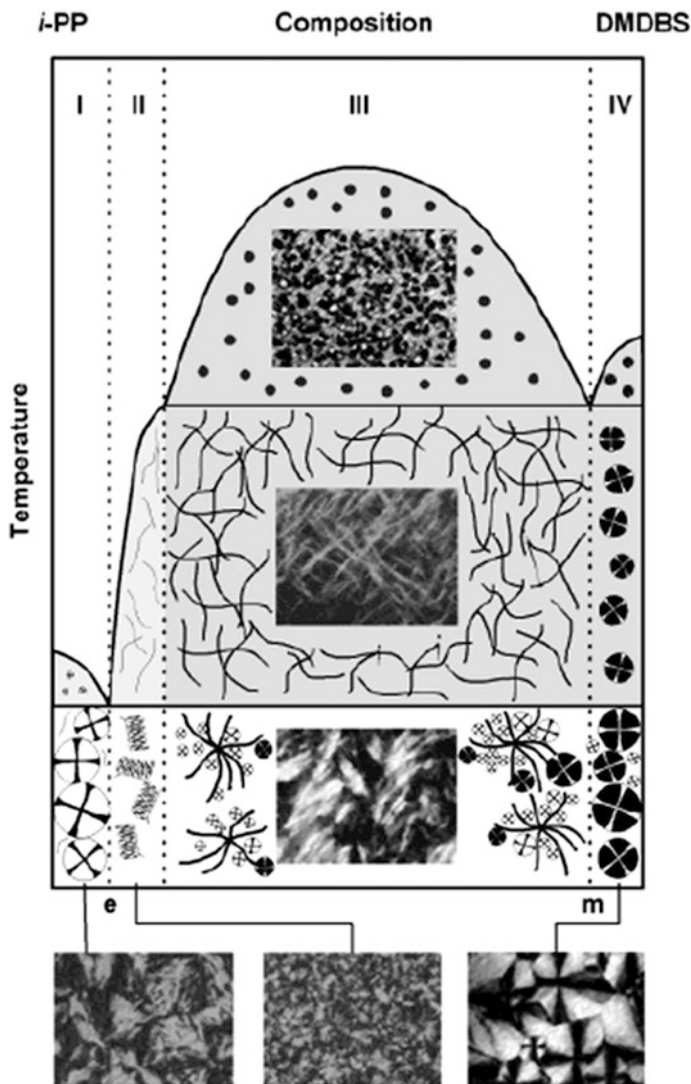


Fig. 3.30 Binary phase diagram of iPP and DMDBS proposed by Kristiansen et al. [104]

processing temperature as well as the cooling conditions have also crucial importance. This makes them significantly different from the conventional nucleating agents, because those are much less sensitive to these parameters. Consequently, the unique optical properties are achievable only in the presence of organogelators and these polymer grades require careful design of the additive package and processing conditions as well. It should be noted, however, that regime II indicated in Fig. 3.31

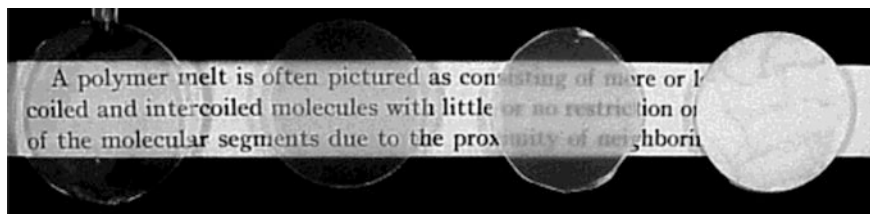


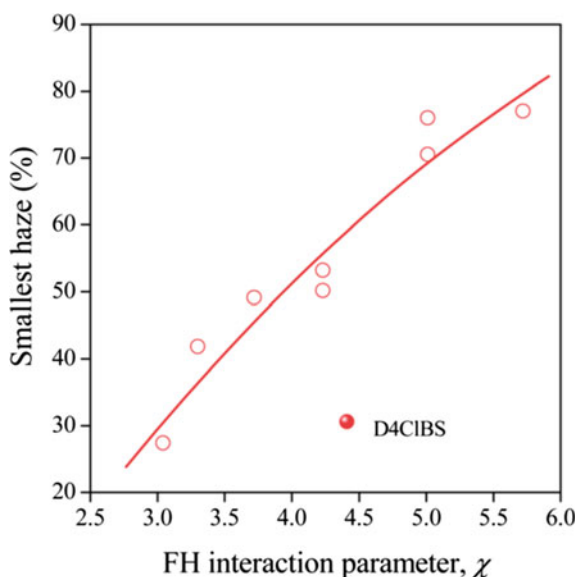
Fig. 3.31 Optical clarity of samples containing 1 wt% DMDBS prepared under different cooling rates (from left to right: injection molded, quenched, 10 °C/min, 10 °C/h) [104]

is between 0 and 2 wt% of DMDBS content, which is one order of magnitude larger than the saturation concentration (2000 ppm or 0.2 wt%) presented in Fig. 3.29.

Horváth et al. [106] made model calculations for the estimation of solubility of several sorbitol derivatives in iPP using thermodynamic equations. They calculated the free energy of mixing using a lattice model and found that the critical concentration of solubility is much smaller compared to the prediction of Kristiansen et al. In addition Horváth et al. [106] found correlation between the experimental solubility (c_e) and the predicted solubility values. Moreover, they have pointed out that the Flory-Huggins interaction parameter between sorbitol derivatives and iPP (calculated using the Hildebrand's solubility parameters [106, 187]) strongly correlates to the optical properties of the samples. The correlation is presented in Fig. 3.32.

Horváth et al. made also interesting observations during heating of sorbitol derivatives in optical microscope (Fig. 3.33). At the beginning the compound was

Fig. 3.32 Smallest haze of samples nucleated with different sorbitol derivatives as a function of Flory-Huggins interaction parameters [106]



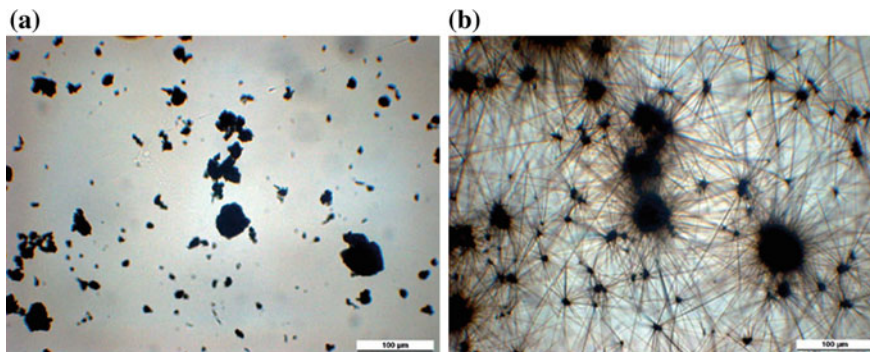


Fig. 3.33 Interesting transition observed on MDBS during heating below their melting points: **a** before and **b** after the transition [106]

in the form of a fine powder (see on Fig. 3.33a), as it formed in the synthesis reaction. At a certain temperature during heating, the structure of the compound changed, and fine needle-like crystals formed (Fig. 3.33b). This interesting effect was observed on all the eight derivatives studied. XRD measurements were performed in order to check the crystalline modification of the compounds before and after the observed transition. It was proved that the crystal modification did not change, thus the phenomenon was explained by the perfection of the crystals, which resulted in an increase in crystallinity. Interestingly, it was found that all of them showed this behavior at a temperature lower than their melting points. According to Horváth et al. this transition is also an important factor from the point of view of nucleating efficiency, because the morphology influences the nucleating effect significantly. On the one hand, the presence of larger and more perfect crystals results in an increase in the melting point. On the other hand, owing to this change in morphology the specific area increases, which aids and accelerates melting or dissolution. This thermally induced transformation has a significant role in the process, which is corroborated by the fact that often a processing temperature lower than the melting point of the nucleating agent is enough, and results in the improvement in properties, mainly in haze.

3.3.6 *Supramolecular Structure Formed in the Presence of Organogelators*

Since the organogelators have special gelation effect in the polymer, the crystalline structure formed in their presence is different compared to that develop during the application of conventional heterogeneous nucleating agents. As it was demonstrated in Sect. 3.3.2 the heterogeneous nucleating agents enhance the nucleus density, consequently the size of the spherulites decreases and a “microspherulitic”

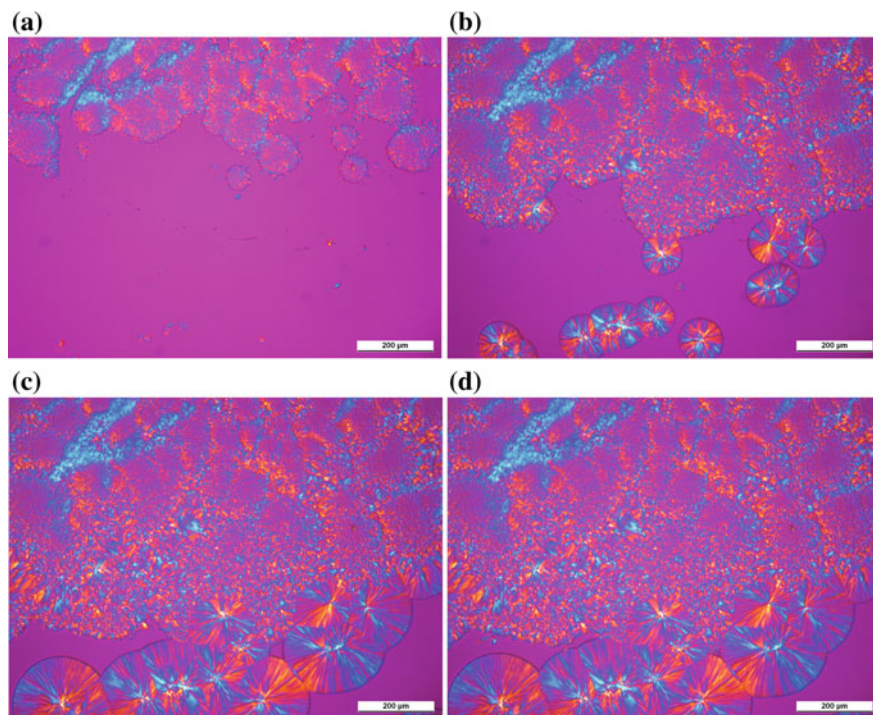


Fig. 3.34 Crystallization of twin slice sample of non-nucleated (lower part) and iPP (Borealis HB120BF) containing 2000 ppm DMDBS (upper part) at 135 °C for **a** $t_c = 6$ min; **b** $t_c = 45$ min; **c** $t_c = 90$ min and **d** $t_c = 100$ min

structure develops. However, the active surface area of the organogelators is much larger due to the formation of fibrillar network, thus the nucleus density is also significantly larger in their presence [16, 63]. In fact spherulitic structure cannot form in the presence of organogelators because the large nucleus density does not allow the free development of spherulites. The impingements occur in the early stage of crystallization and growth stops before the nuclei are transformed into spherulites. Consequently, this structure was designated as “microcrystalline” in our earlier publication [63] in order to differentiate clearly from the microspherulitic structure. The supermolecular structure of iPP nucleated with organogelators is presented in Fig. 3.34.

Comparing Figs. 3.4 and 3.34 it can be established that the front of the nucleated part is different. It is constant in the case of the heterogeneous nucleating agents and it is moving if iPP is nucleated with a soluble organogelator. The moving front between the nucleated and non-nucleated field proves the dissolution and diffusion of the dissolved nucleating agent in the iPP melt. The concentration of the nucleating agent decreases with the distance from the nucleated part of the sample. In the transition zone large spherulites and microcrystalline fields are forming

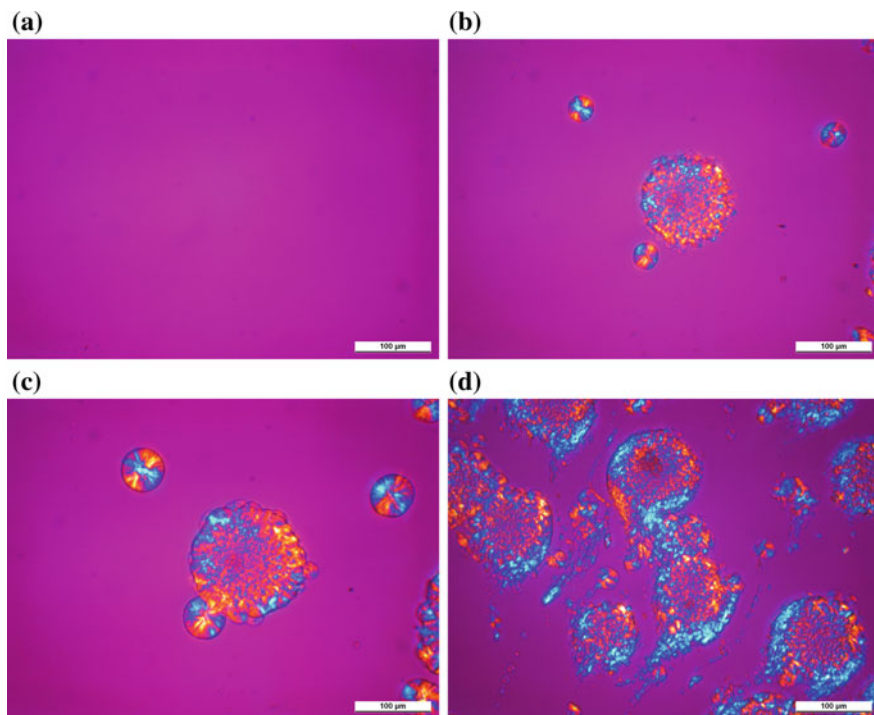


Fig. 3.35 Crystallization of iPP homopolymer (Borealis HB120BF) nucleated with 1000 ppm DMDBS at 140 °C for **a** $t_c = 0$ min; **b** $t_c = 35$ min; **c** $t_c = 90$ min; **d** $t_c = 37$ min other location

simultaneously. The structure of the transition zone can be demonstrated more thoroughly in a sample, which contains 1000 ppm DMDBS. This concentration is around the experimental solubility (c_e), thus it is below the saturation of efficiency. The crystallization process is presented in Fig. 3.35 at high temperature in order to follow the simultaneous development of microcrystalline structures and individual spherulites.

It should be noted that the structure is not homogeneous, which is proved clearly by Fig. 3.35d, which micrograph was taken from a different location of the same sample. Interestingly, the microcrystalline fields have a tail, which consist of small supermolecular units as well and it proves that the dissolution and fall-out is a dynamic process. Consequently, the location of microcrystalline fields may change during the crystallization.

As it was described earlier the properties of the polymer can be changed within a wide range. Since organogelators are efficient nucleating agents, their effect is similar to the heterogeneous nucleating agents, so crystallization temperature shifts to the higher temperatures in their presence. Consequently, thick lamellas are formed and mechanical properties increase as it can be seen in Fig. 3.13. The mechanical properties are usually improved by using conventional heterogeneous

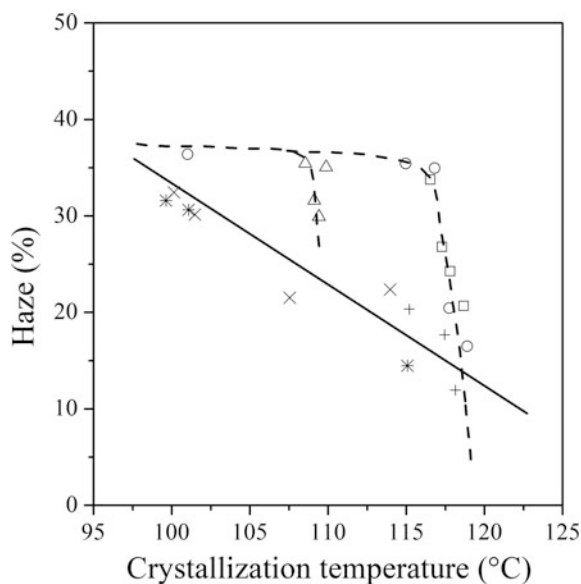
nucleating agents like talc for example, which is significantly cheaper solution than organogelators. Organogelators are used mainly for the improvement of optical properties, because large nucleus density form in their presence is accompanied by small haze and good optical properties as it was also demonstrated in Figs. 3.14, 3.15 and 3.36. In order to differentiate these additives from the conventional nucleating agents, they are called “clarifiers”.

The change in the optical properties, i.e. haze and clarity as a function of the clarifier content is also interesting. Optical properties were investigated in a wide concentration range by Kristiansen et al. In their work DMDBS was used in iPP. Figure 3.37 shows clearly the changes in optical properties as a function of the DMDBS concentration.

In lower concentration ranges optical properties, i.e. haze and clarity are improved with increasing clarifier content, however, the advantageous effect is limited by the solubility of the additive. Above a certain concentration optical properties deteriorate due to the aggregation of the clarifier-fibrils, thus optimal amounts of the clarifiers exist. DBS is effective in a narrow concentration range: up to ca. 0.3 wt% an open network of the DBS fibers form, which creates a perfect opportunity to iPP to crystallize, thus the haze decreases. However, above ca. 0.5 wt% nucleating effect shows a rapid level off, due to the agglomeration of DBS fibers. Therefore, finding the optimal concentration of the nucleating agent is a crucial point to consider.

In brief, optical properties can be improved by the introduction of both traditional nucleating agents and clarifiers (or organogelators), but the superior haze and clarity can be achieved only with the use of clarifiers.

Fig. 3.36 Haze in nucleated iPP as a function of efficiency characterized by crystallization temperature [188]



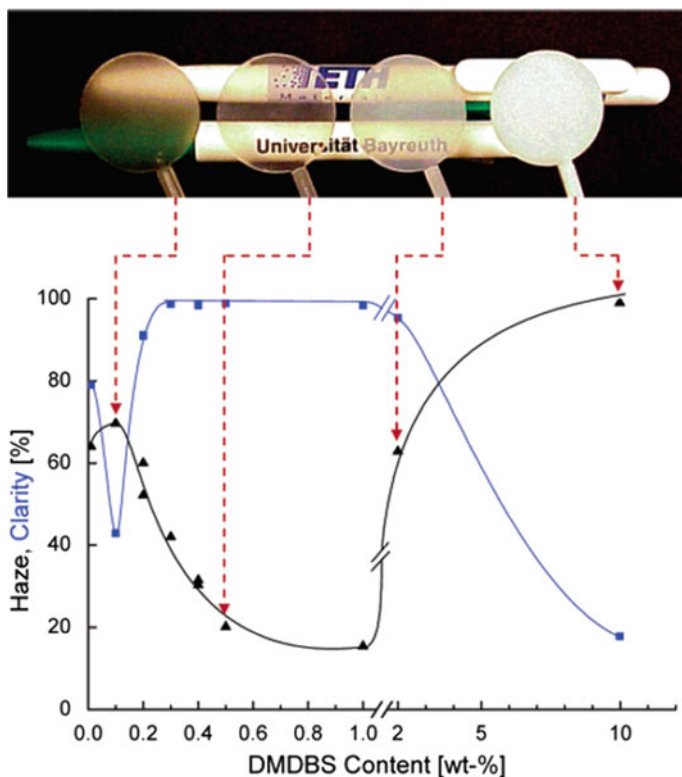


Fig. 3.37 Optical properties of iPP nucleated with DMDBS in a wide concentration range [104]

Unfortunately, in spite of their several advantages, DBS-type nucleating agents have some drawbacks as well. The thermal stability of DBS and of some of its derivatives is not sufficient and the thermal decomposition of the molecules can lead to yellowing of the polymer thus reducing the quality of the product. Moreover, the odor and taste tainting caused by the aldehyde by-products can hinder the applicability of the product in food-industry. Several possibilities exist to improve stability and thus to overcome this problem, for example the use of metal deactivators, acid scavengers, antioxidants and stabilizers. The sensitivity of DBS to the thermal conditions implies difficult processing of the material as it is efficient only in a narrow concentration range, because its morphology undergoes a change by the alteration of temperature.

Difficulties may appear with the dispersion of DBS. This disadvantage can be overcome by adding of surfactants, such as fatty acids and sulfonic acids, or their derivatives (e.g. stearic acid, dioctylsulfosuccinate sodium salt), ethylene oxide polymers (e.g. polyethylene glycol) or oligomers [9, 102].

3.3.7 Nucleating Agent Based on Trisamides of Trimesic Acid

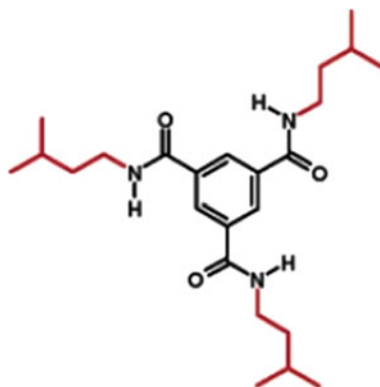
A novel class of nucleating agents was introduced approximately a decade ago [93]. Trisamides of 1,3,5-benzenetricarboxylic acid and analogous compounds belong to this family. The common in the members of this group is that they are designed to possess these three functional parts:

- a central core, e.g. a benzene ring (A),
- groups that can get into hydrogen bonds (X), and
- non-polar peripheral groups (R).

These molecules can be described with a generic structure $A-(X-R)_3$, which trisamide structure is represented in Fig. 3.38.

Owing to the presence of the amide groups these molecules are thermally and chemically stable which is the main advantage in contrast to the sorbitol derivatives [93]. Amide groups also promote one-dimensional crystal growth thus increasing the specific area of the crystals. Moreover, these functional groups together with benzene rings make possible the formation of intermolecular bonds, i.e. hydrogen bonds and phenyl interactions, thus several molecules with their benzene rings oriented parallel can build up larger units, supermolecular structures (self-assembly). An important role of peripheral groups is to increase the non-polar character of the whole molecule thus increasing the solubility in the non-polar melt of iPP. Moreover, peripheral groups have a significant impact on the forming supermolecular structure. In their thorough experimental work Blomenhofer et al. [93] screened 18 possible molecule, which were different only in the peripheral groups (R). One of them (R = *n*-propyl) did not prove to be efficient as the increase in the crystallization peak temperature was not significant. Other molecules

Fig. 3.38 Generic structure of trisamide based nucleating agents [93]



(e.g. R = 2,3-dimethylcyclohexyl) increased haze instead of reducing it so much that they are called “whiteners”.

It is clear that ‘R’ group has much impact on properties of nucleated iPP, which creates an opportunity to control the properties by the application of the proper structure of the nucleating agent. The size, shape and mobility of the ‘R’ group determine the distance of the benzene rings in the forming supermolecular structures [7]. In addition, with the increasing flexibility of substituent ‘R’ the crystallization and dissolution temperatures increase [93].

The role of the direction of the amide groups was also investigated by Blomenhofer et al. [93] and their results are worthy to mention. In general the optical properties were characterized by the haze value, because haze harmonizes the best to the visible change in the optical properties. As it can be seen in Fig. 3.39 the clarity values do not change significantly in the samples studied by Blomenhofer et al. [93]. With an increasing number of “reversed” amide groups (labelled with red in Fig. 3.39), the value of the minimum haze decreases. According to the authors this effect originates in slight changes in the crystal unit cell, which lead to enhanced epitaxial matching with the crystalline phase of the polymer. These results prove clearly that the trisamide derivatives can be applied as clarifiers according to Blomenhofer et al. [93], however, the haze is always larger in their presence compared to that of the effect of sorbitol clarifiers.

If the ‘R’ group is 2,3-Dimethylcyclohexyl then the derivative is a non-selective β -nucleating agent, which is soluble in the iPP melt. In this case the crystallization of the nucleating agent should be at a higher temperature compared to that of the polymer. The supermolecular structure formed in the presence of 1000 ppm TATA is demonstrated in Fig. 3.40. It is clearly visible that the sample crystallized mainly in β -modification, but a considerable amount of α -iPP remained after partial melting of β -iPP. According to the results of Varga et al. the β -content of this sample is 70%.

3.3.8 Soluble Nucleating Agents for β -iPP

The supermolecular structure in the presence of soluble nucleating agents with dual nucleating ability will be discussed in details in this chapter. The dual nucleating ability of a soluble β -nucleating agent was observed during our earlier study [90]. In this particular case a schematic view of crystallization process is shown in Fig. 3.41 in the early and the later stages of crystallization. The two polymorphic modifications are formed simultaneously on the surface of the nucleating agent.

Both modifications can form on the surface, but usually the nucleation density of the different modifications is different, because the nucleating agent is not similarly efficient for the modifications. The nucleation density of a polymorphic modification is proportional to the efficiency of the nucleating agent to that form. Accordingly, the final structure will be dependent on the nucleating agent type and the growth rates of the modifications. Practically, if the growth rate (G) of that

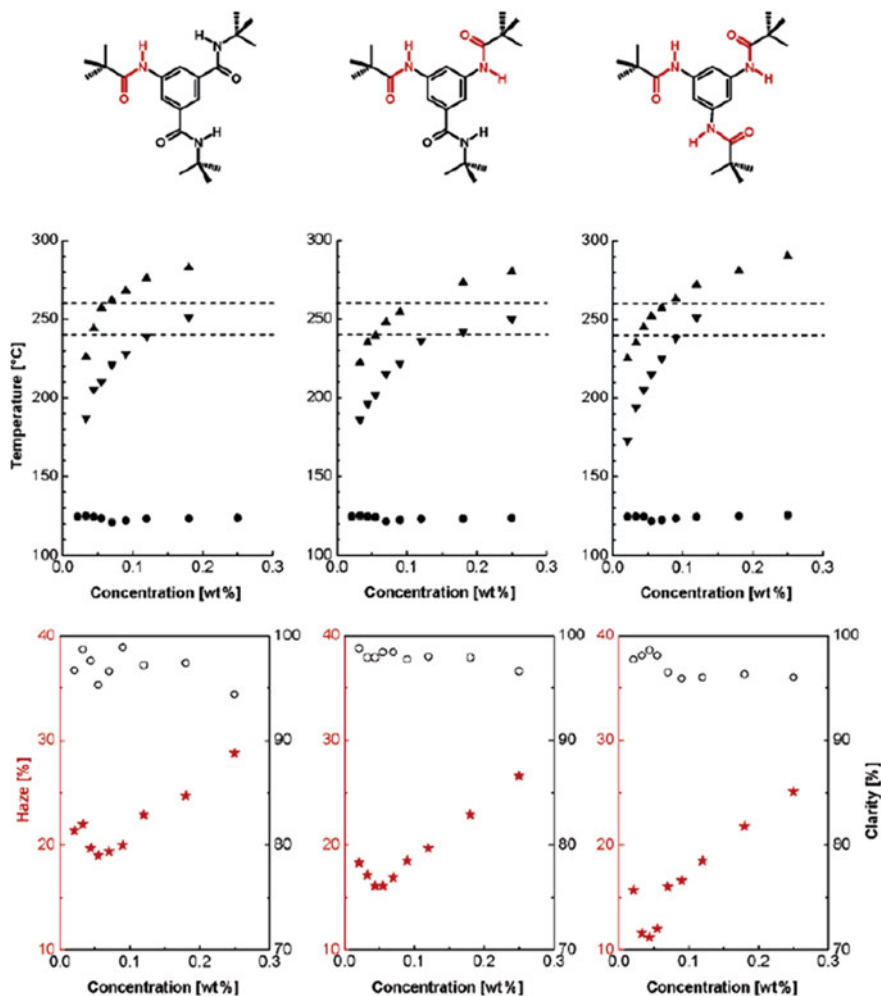


Fig. 3.39 Efficiency and optical properties of iPP nucleated with this benzene trisamide derivatives [93]

modification, in which more nuclei are induced, is equal or faster than the G of the other forms, only that modification will develop despite the fact that other nuclei may form simultaneously during the crystallization. In our example, it means that pure α -iPP will form below $100\text{ }^{\circ}\text{C}$ ($T_{\alpha\beta}$) and above $140\text{ }^{\circ}\text{C}$ ($T_{\beta\alpha}$), because in these temperature ranges the thermodynamically stable α -modification has the fastest growth rate [34, 45]. If the conditions of crystallization are favorable for the β -form (if the temperature is between $T_{\alpha\beta}$ and $T_{\beta\alpha}$), the development of the less stable form is also possible as it is shown in Fig. 3.40. The fan-like formation will overgrow the slower modification resulting in small occluded crystals in the near of the

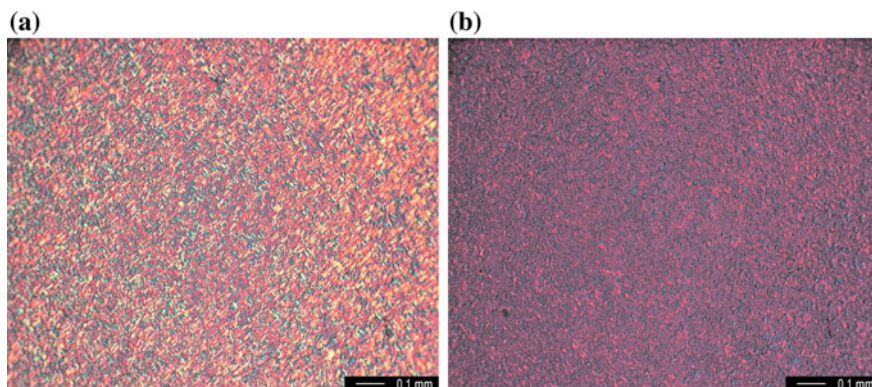


Fig. 3.40 Supermolecular structure of iPP (MOL Petrochemical, Tipplen H890) nucleated with 1000 ppm TATA **a** crystallized at a constant cooling rate of 10 °C/min and **b** the structure after partial melting of β -phase at 155 °C

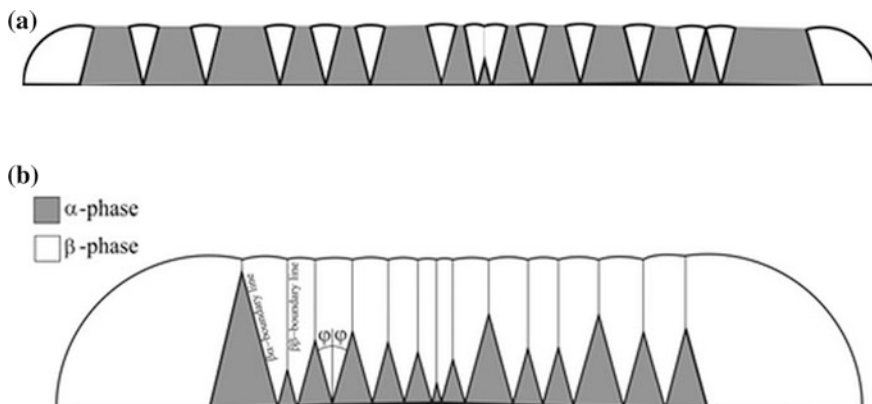


Fig. 3.41 Simultaneous crystallization of two polymorphic modifications on the surface of a non-selective nucleating agent. **a** Early stage of crystallization and **b** overgrown slower modification in the later stage

nucleating surface. The size and the shape of these small crystals as well as the width of the fan-like formations are dependent of the ratio of the growth rates (R) and can be tuned by varying the temperature of crystallization (Eq. 3.5).

$$R = \frac{G_{\beta}}{G_{\alpha}} \quad (3.5)$$

In Eq. 3.6 R should be calculated by dividing the faster growth rate with the slower one. Accordingly, R is always larger than 1. The shape of the fan-like slices can be accurately calculated using Eq. 3.6, because it describes the correlation

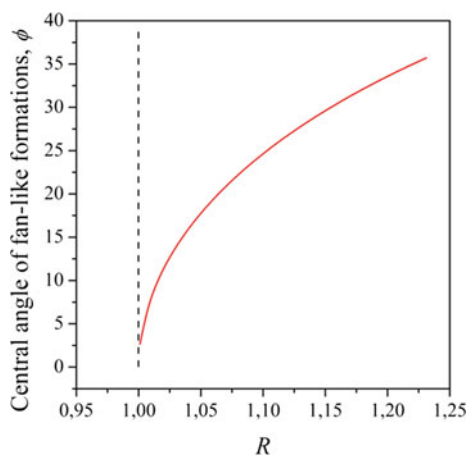
between the ratio of growth rates and the central angle of fan-like formations (φ in Fig. 3.41b).

$$\varphi = \arctan \left[\pm \sqrt{R^2 - 1} \right] \quad (3.6)$$

Figure 3.42 represents the φ angle as a function of R in the case of iPP, because the growth rates of α - and β -modifications were measured earlier [45]. We may note here that the data presented in Varga's work are not valid for all PP grades, because the molecular structure of the polymer influences also the growth rate slightly. However, the ratio of the growth rates might be less influenced by the polymer grade than the primary G data.

As it was demonstrated in Fig. 3.42 the φ angle increases monotonously with increasing R indicating that the larger is the difference in the growth rates, the wider are the fan-like structures. In practice, this is demonstrated by the microscopic view of a crystallization process on the surface of a non-selective nucleating agent needle. The sample contains 500 ppm NJS and was heated to 240 °C before crystallization in order to dissolve NJS completely. The structure formed on the lateral surface of a nucleating agent is demonstrated in Fig. 3.43. NJS is soluble in iPP melt at high temperatures and it recrystallizes in the form of relatively large needles around 170 °C according to our earlier studies [90] in case of slow cooling. This behavior allows us to prepare structures demonstrating the validity of our proposed model. The value of R ratio at 135 °C can be obtained from the work of Varga et al. [45] and its value is 1.178. Using this R value the predicted φ angle is 22.2°, while the measured value from Fig. 3.43d is $22.0 \pm 2.65^\circ$ which is in excellent agreement despite the fact that R value taken from the literature [45] and the structure presented in Fig. 3.43 were made in different polymers. The scattering of the measured angle originates from the inaccurate measuring of the internal angle of the fan-like formations.

Fig. 3.42 Simulation of the central angle (φ) obtained from Eq. 3.6 as a function of R



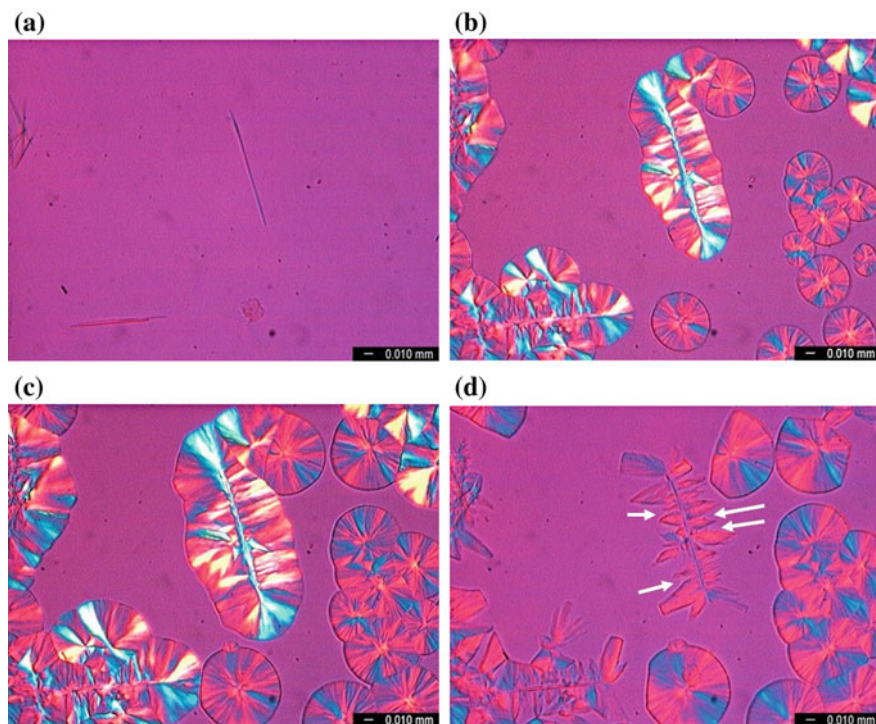


Fig. 3.43 Formation of **a** NJS needle during slow cooling at 170 °C and crystallization on the surface of the NJS needle at 135 °C for **b** 15 min, **c** 30 min and **d** the structure after the partial melting of β -iPP at 156 °C. The well discernable angles, where φ was measured are designated by arrows in the Figure

Under faster cooling, the formation of the nucleating agent needles cannot occur and the recrystallization of NJS results in finely dispersed small crystals in the polymer melt. However, the rules of crystallization on the surface of these small crystals are the same as it was proposed above. In order to demonstrate this process, NJS was added to the polymer in a very small amount (50 ppm) and was cooled “fast” to the crystallization temperature in the optical microscope. In this case the recrystallization and self-organization of the nucleating agent and the crystallization of the polymer take place simultaneously and the process is similar to the real industrial conditions, where the cooling rate is even faster, but the nucleating agent content is larger. The structure formed is shown in Fig. 3.44. An interesting supermolecular structure developed at the center of the micrograph, which consist of β -iPP matrix and overgrown small α -crystals. The nucleating agent is not visible at all, but the small α -crystals can be visualized after the partial melting of the β -phase at 156 °C. This structure becomes homogeneous at larger NJS content.

Similar dual nucleating ability was observed in the presence of dicyclohexylterephthalamide (DCHT), however, the recrystallization of DCHT is different

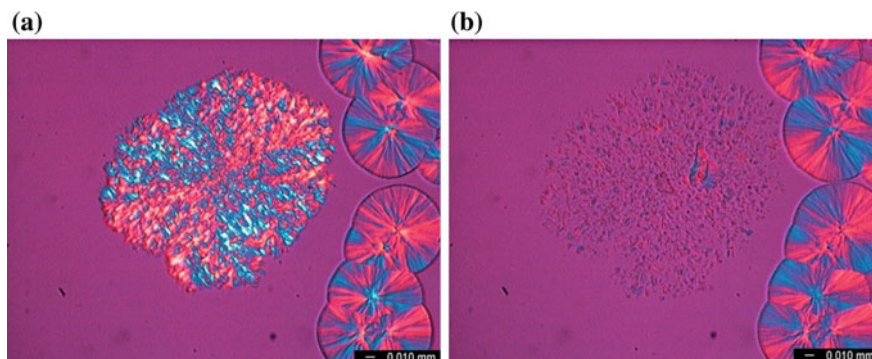


Fig. 3.44 Crystalline structure formed in the presence of 50 ppm NJS **a** at 135 °C and **b** the residual small α -crystals after the partial melting of β -iPP at 156 °C. The sample was heated to 240 °C in order to dissolve the NA and then was cooled directly to the crystallization temperature

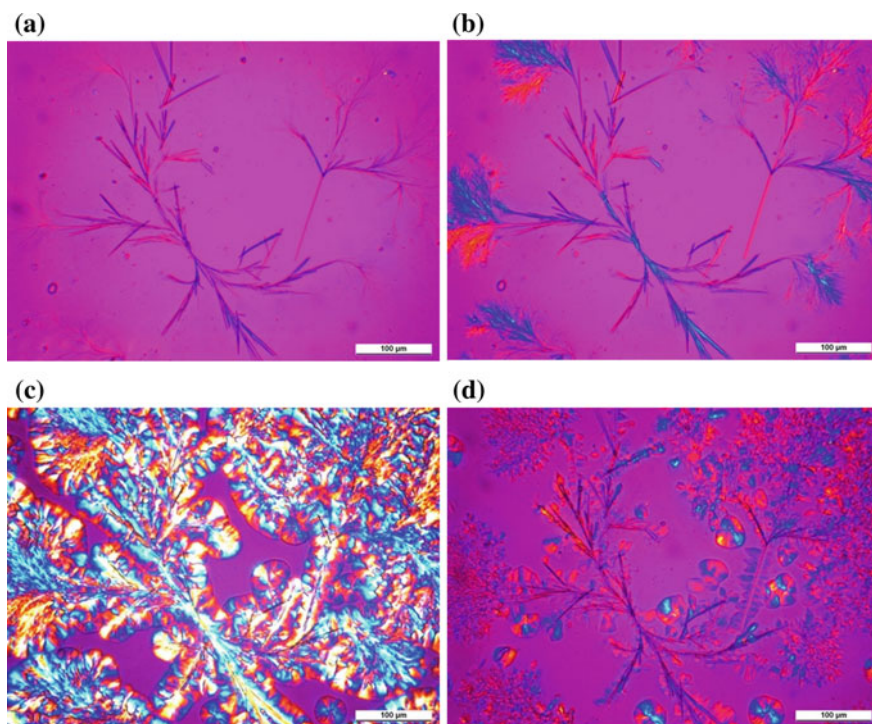


Fig. 3.45 Crystallization process of sample containing 10,000 ppm DCHT. The melt was heated up to 250 °C and held there for 3 min. **a** Cooling run $T = 180$ °C; **b** $T = 135$ °C and $t_c = 1$ min; **c** $t_c = 15$ min; **d** reheating run $T = 158$ °C

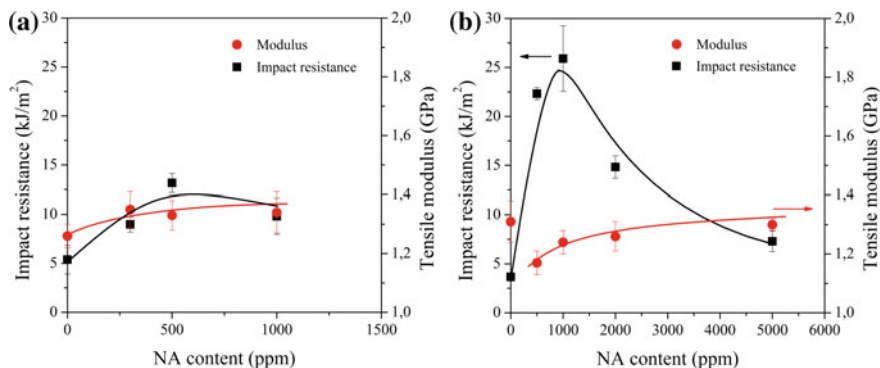


Fig. 3.46 Mechanical properties of iPP nucleated by **a** NJS and **b** DCHT processed under conventional processing conditions [71]

compared to that of NJS [71]. The results indicate that DCHT recrystallizes in fibrillar form as it is presented in Fig. 3.45.

The structure presented in Figs. 3.44 and 3.45 influences the mechanical properties as well. The finely distributed α -crystals have a reinforcing effect on the β -matrix, which has larger impact resistance. Accordingly, the mechanical properties, the stiffness and the impact resistance are presented in Fig. 3.46.

The results indicate clearly the simultaneous improvement of modulus and impact resistance, what is usually not possible in the presence of conventional nucleating agents or clarifiers. Although, the modulus increase is not considerable, the large improvement of impact resistance without a decrease in the modulus is a remarkable result [71].

3.4 Structure-Property Case Studies

3.4.1 Prediction of Tensile Modulus from Crystalline Parameters

As it was described already the introduction of an additive, e.g. a nucleating agent into the polymer results in changes in the crystalline structure and consequently in mechanical properties. The presence of a nucleating agent (or an organogelator) on the one hand increases the ratio of the crystalline phase, and on the other hand increases the lamella thickness throughout the higher crystallization temperature range. Both effects result in modulus increase, which can be calculated with the empirical correlation presented by Pukánszky et al. [170] (Eq. 3.7).

$$E = 0.014 T_{cp} + 0.018 \Delta H_c - 1.77 \quad (3.7)$$

Even though it is not valid in the whole crystallinity range, it gives values very close to the measured ones in a wide range, thus the Eq. has a huge practical importance. We published a novel approach, which is capable to calculate the tensile modulus in the entire crystallinity range [171, 172] (Eq. 3.8).

$$E = E_a + (E_c - E_a) e^{-\left(\left(\frac{1-X}{\bar{l}}\right)^\alpha + \left(\frac{1}{\bar{l}}\right)^\beta\right)^\gamma} \quad (3.8)$$

E_a and E_c are the tensile moduli of amorphous and completely crystalline polymer respectively. X is the crystallinity, \bar{l} is the average lamella thickness and α , β , γ are iterative empirical constants. Equation 3.8 can be used for the description of modulus in general, but its applicability is questionable, because the estimation of average lamellar thickness from the melting curve is time-consuming and difficult. Consequently, the average lamellar thickness was replaced by an average melting temperature (T_{av}), which can be directly and easily obtained from the calorimetric melting curves and Eq. 3.8 was modified as Eq. (3.9):

$$E = E_a + (E_c - E_a) e^{-\left(\left(\frac{1-X}{\bar{l}}\right)^\alpha + \left(\frac{T_m^0 - T_{av}}{T_m^0}\right)^\beta\right)^\gamma} \quad (3.9)$$

The T_{av} value can be calculated from the melting curve directly using Eq. 3.10:

$$T_{av} = \frac{\int \dot{Q} \cdot T dT}{\int \dot{Q} dT} \quad (3.10)$$

Equation 3.9 was used for calculation of the tensile stiffness of several nucleated iPP homopolymers, random copolymers and the agreement between the predicted and measured values is reasonable good. For the calculation the iterative constants α , β and γ in Eq. 3.9 were estimated in our earlier work and they are 0.32, 0.51 and 2.43, respectively [171]. It should be noted that that the correlation presented is valid for other semicrystalline polymers like PA6 (see Fig. 3.47).

3.4.2 Obtaining Balanced Properties by Efficient Nucleation

It was revealed that the best performance of a nucleating agent depends on the molecular structure of the polymer matrix as well [16, 189]. The main goal of most developments today is to produce materials with balanced properties. Usually, large stiffness and fracture resistance are required for structural applications and often the optical properties of the material are also of importance. If optical properties and impact resistance are important properties from the point of view of application, usually random copolymers are used as iPP and sorbitol type clarifiers are applied

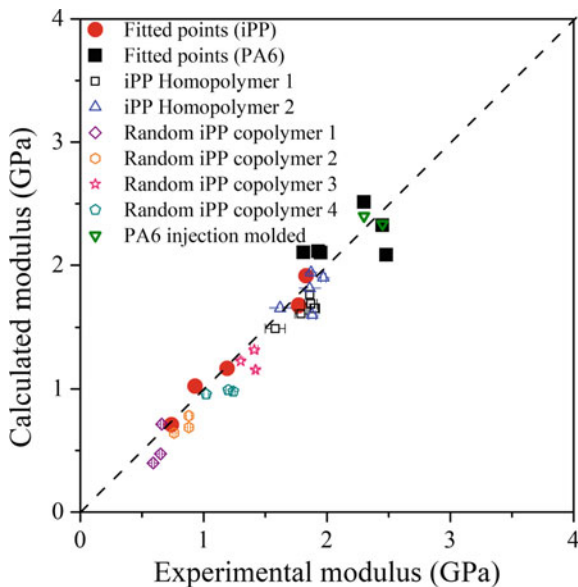


Fig. 3.47 Correlation between the calculated and measured modulus values (calculated modulus was obtained using Eq. 3.9 [171])

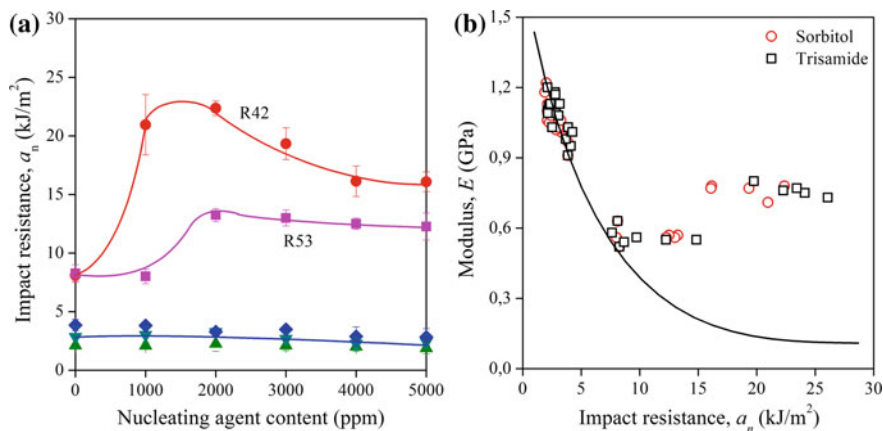
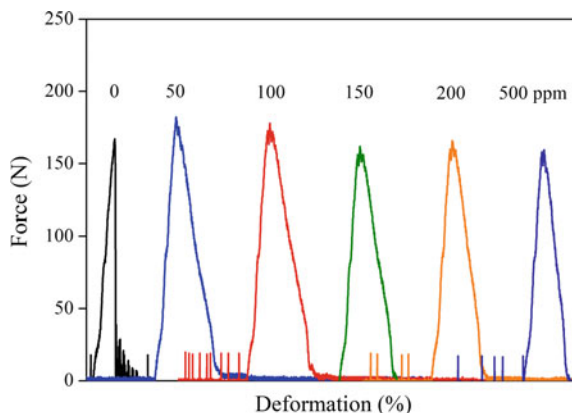


Fig. 3.48 Impact resistance of **a** iPP random copolymers nucleated with TBPMN and **b** correlation between modulus and impact resistance of random copolymers nucleated with TBPMN and trisamide derivative [189]

as nucleating agents in the industrial practice. As it was pointed out in Sect. 3.3.3 the haze of the nucleated iPP grades depends on the chemical structure of the nucleating agents [106].

Fig. 3.49 Effect of nucleation on the fracture of notched specimens prepared from the R42 PP copolymer. Nucleating agent: trisamide [189]



Five iPP random copolymer grades were used in our earlier work in order to obtain the best balanced properties in the presence of soluble clarifiers. The polymers were mainly different in their ethylene content which is represented as R42 or R53 in Fig. 3.48. The code means that samples R42 and R53 contain 4.2 and 5.3 wt % of ethylene. The detailed description of the samples can be found in our earlier work [189].

It was found that the random copolymers with lower ethylene content (lower than 4 wt%) behave according to the general expectations, because their modulus increased and impact resistance decreased with efficient nucleation, but the two types with large ethylene content showed a very unexpected behavior. The modulus of these types increased simultaneously with the significant improvement of the impact resistance as it is demonstrated in Fig. 3.48b. This advantageous effect was observed in the presence of TBPMN and trisamide based nucleating agents as well. The large improvement of impact resistance is resulted in by hindered crack propagation during fracture tests, which was confirmed by instrumented impact tests (Fig. 3.49).

As it can be seen in Fig. 3.49, the maximum force at crack initiation indicates only a slight increase compared to the non-nucleated sample, but this increase cannot explain the large improvement in impact resistance. On the other hand local rearrangement of morphology induced by the nucleating agent and the increase of lamella thickness confirmed by SEM analysis (Fig. 3.50) and also increased crystal orientation, formation of shish-kebab structures in the core of the injection molded specimens all together lead to the hindered crack propagation. A small increase in the γ -phase content of PP was also observed in wide angle X-ray measurements (Fig. 3.51). These changes increased crack propagation energy considerably leading to the large improvement observed in impact resistance.

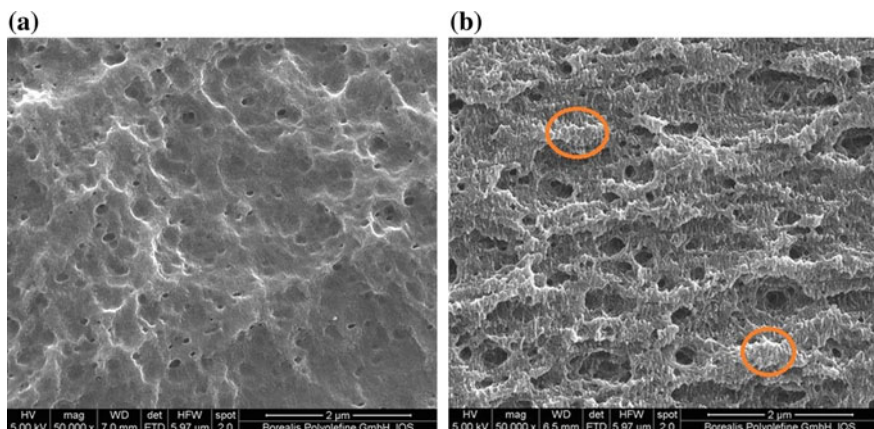
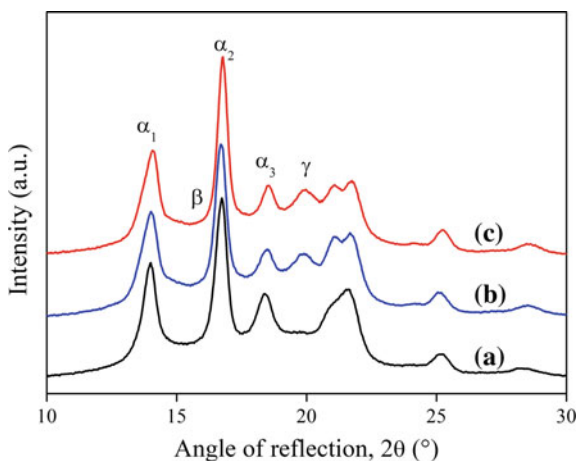


Fig. 3.50 SEM micrographs taken from the etched cryo-cut surface of samples taken from the core area of selected PP specimens. **a** Neat R42 polymer without nucleating agent, **b** R42, 4000 ppm TBPMN [189]

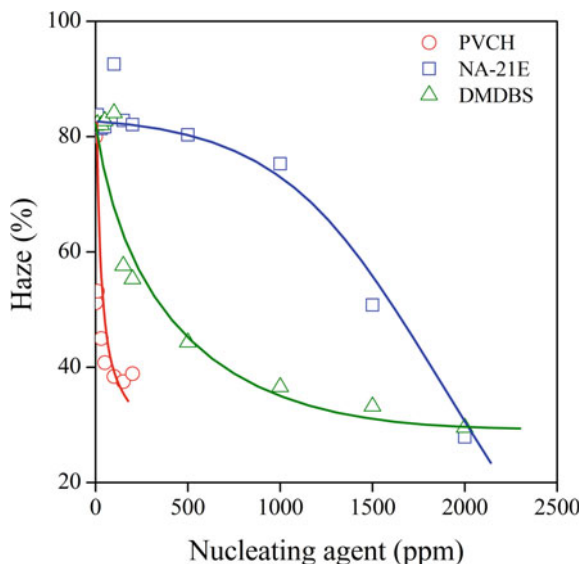
Fig. 3.51 Effect of nucleation on morphology. Increase in the amount of the γ -modification of PP upon nucleation. R42 copolymers; curve **a** neat, **b** 2000 ppm, **c** 4000 ppm sorbitol nucleating agent [189]



3.4.3 Improvement of Optical Properties by Efficient Nucleation

It was mentioned several times that the application of efficient nucleating agents increases the nucleus density, thus the size of the supermolecular units decreases proportionally. Consequently, the haze of the iPP samples decreases as well. The effect of different nucleating agents on the optical properties is compared in our earlier work [16, 63]. It was found that microcrystalline structure has the best optical properties (Fig. 3.52). PVCH and NA-21E are insoluble conventional

Fig. 3.52 The haze of 2 mm thick injection molded iPP (Borealis HB120BF) plates nucleated by different type of nucleating agents [63]



nucleating agents, thus microspherulitic structure formed in their presence. The haze decreases monotonously with their increasing content. The best haze obtained using these additive is 30%, which is the saturation limit, thus further improvement is not probable. DMDBS clarifier is not efficient below 1000 ppm due to its solubility, but the haze value decreases steeply if the organogelation effect appears.

The supermolecular structure formed in the presence of different nucleating agent is presented in Fig. 3.53. The structure formed in the presence of efficient nucleation cannot be studied by optical microscope, thus scanning electron microscope (SEM) was used to characterize the morphology of the nucleated samples. Etching was performed by following the procedure of Olley et al. [190, 191] for one day at room temperature.

The results prove clearly that fine structure formed in the presence of DMDBS and a relatively rough structure was induced by PVCH. After careful analysis of the crystallization kinetics the nucleus density was calculated according to the method of Lamberti et al. [175]. It was clearly demonstrated that the difference in optical properties are caused by the significantly different nucleation density in the presence of different nucleating agents. DMDBS induced the formation of large nucleus density thus the final structure is smooth and the size of supermolecular units is too small to scatter the visible light. Accordingly, the haze will be small. If the nucleus density is smaller the size of the supermolecular units is proportionally larger and consequently, haze is larger as well. The nucleus density values and the correlation of nucleus density with haze are presented in Fig. 3.54.

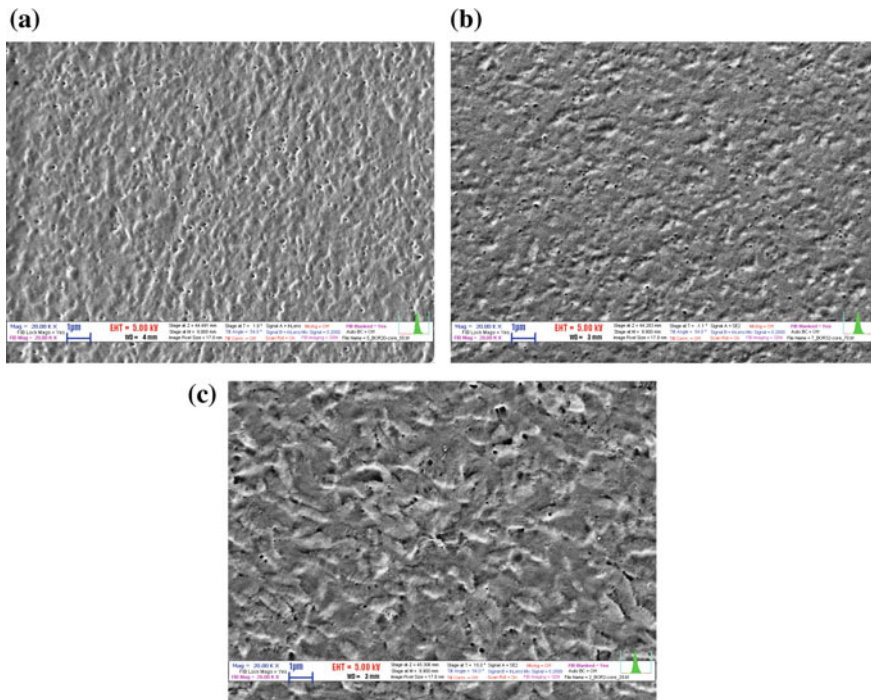


Fig. 3.53 Structure of the core of 2 mm thick injection molded plates containing the nucleating agents studied. SEM micrographs taken from etched fracture surfaces: **a** M3988, 2000 ppm; **b** NA21E, 2000 ppm; **c** PVCH, 2 ppm [63]

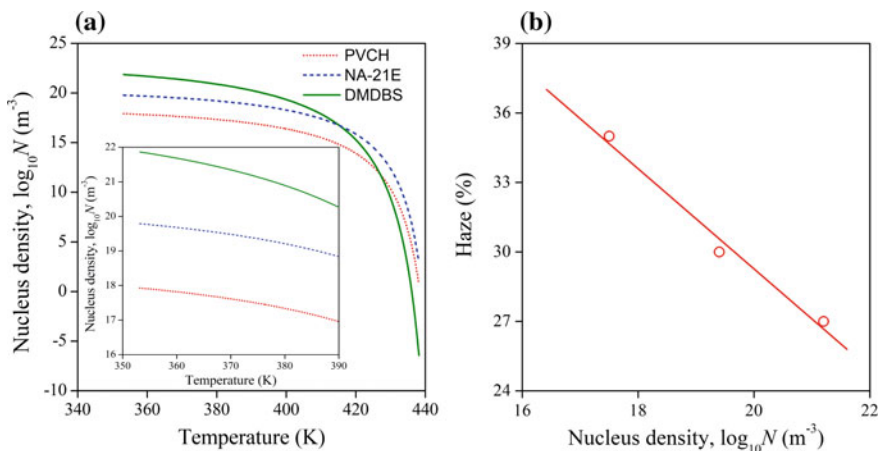


Fig. 3.54 The estimated nucleus density as a function of temperature (a) and the correlation between the nucleus density and haze (b) [63]

These results that the nucleus density and consequently the optical properties are superior in the presence of sorbitol based clarifiers were supported by many other research groups as well [16, 63].

3.5 Summary

The aim of this book chapter is to introduce the most important characteristics of nucleating agents used in iPP polymer. In order to discuss the effect of these additives, the basics of the crystallization process were discussed in nutshell first and the basic characterization of nucleating agents is introduced subsequently. The most probable explanation of nucleating effect on iPP, the “matching lattice size theory” is also discussed. As it was described the efficiency of the nucleating agents is characterized by the peak temperature of crystallization in their presence in the everyday practice. It was pointed out that this characterization is difficult to use if the efficiency of a nucleating agent is studied in different iPP grades. A relative efficiency scale can be also used for characterization of the nucleating agents, but the estimation of NAE value is more difficult than the estimation of T_{cp} .

The mechanism of nucleation is also discussed and the nucleating agents are differentiated based on their nucleation effect. The non-soluble so called “heterogeneous” nucleating agents are discussed first, since they are the first nucleating agents used in the industrial practice. Their effect on the crystalline structure and consequently on the properties is introduced in detail. As it was demonstrated the presence of these additives increases the temperature of crystallization thus lamella thickness and crystallinity increase in their presence. Consequently, the mechanical properties especially the tensile modulus improve, which is the main reason for their application. The number of active nuclei increases in the presence of nucleating agents; thus the optical properties are also improving. The large nucleus density induces the formation of a “microspherulitic” structure in the case of efficient nucleation. In addition, the most frequently used heterogeneous β -nucleating agents are introduced as well.

Recently, the soluble nucleating agents dominate the industrial use, because the homogeneous distribution of these additives in the polymer is easy. In addition, some of them show an interesting gelation effect, which was also discussed in detail. The formation of the fibrillar network structure in the presence of sorbitol derivatives results in a so called microcrystalline structure, where no spherulites can form. This structure is significantly different from the microspherulitic structure developing in the presence of non-soluble conventional nucleating agents. It was demonstrated that the microcrystalline structure has superior optical properties thus these soluble nucleating agents are also called clarifiers. The formation of the supermolecular structure depends always strongly on the conditions of crystallization. The details of the formation of supermolecular structure in the presence of soluble β -nucleating agents are presented also. The presented data indicate that the

soluble β -nucleating agents are not selective to the β -modification. It was demonstrated that mixed polymorph morphology develops in their presence and the rules of the formation of the mixed morphology was described as well. The results presented demonstrate clearly that α - and β -modifications form simultaneously and the faster β -form overgrows the slower α -phase and a special morphology develops in which α -phase reinforces the β -matrix. Consequently, the stiffness and toughness of the sample improve simultaneously.

Few case studies are presented also in order to demonstrate how versatile technique is the nucleation of iPP. In these examples the focus was the modification of tensile modulus, impact resistance and optical properties. As it was demonstrated the improvement of a single property is possible in most cases, however, the main goals of these developments are the development of a material with balanced properties, thus the advantageous property combinations are the most important directions. It was also reported that nucleus density is the key factor of optical properties in nucleated samples, thus the larger is the nucleus density the lower is the haze of the sample.

Acknowledgements One of the authors (Flóra Horváth) is grateful to Gedeon Richter's Talentum Foundation (H-1103 Budapest, Gyömrői út 19-21.) and Pro Progressio Foundation (H-1111 Budapest, Műegyetem rkp. 3.) for their financial support. This work was supported by the ÚNKP-17-4-III, ÚNKP-17-3-I and ÚNKP-18-4 New National Excellence program of the Ministry of Human Capacities. In addition one of the Authors (Alfréd Menyhárd) would like to express his indebtedness for the financial support of János Bolyai Scholarship of the Hungarian Academy of Sciences. The Authors would like to express their gratitude for the permission from the Royal Society of Chemistry for figures reproduced from Ref. [104].

References

1. Moore EP (ed) (1996) Polypropylene handbook: polymerization, characterization, properties, processing, applications. Hanser-Gardner Publications, Cincinnati
2. Padden F Jr, Keith HD (1959) Spherulitic crystallization in polypropylene. *J Appl Phys* 30 (10):1479–1484. <https://doi.org/10.1063/1.1734985>
3. van der Ven S (1990) Polypropylene and other polyolefins. *Studies in Polymer Science*. Elsevier Science Ltd.
4. Vittoria V (1990) Properties of isotactic polypropylene. In: *Handbook of polymer science and technology. Composites and Speciality Applications*, vol 4. Marcell Dekker, New York, Basel, pp 507–555. ISBN 0-8247-8021-3
5. Simonazzi T, Cecchin G, Mazzullo S (1991) An outlook on progress in polypropylene-based polymer technology. *Prog Polym Sci* 16(2–3):303–329. [https://doi.org/10.1016/0079-6700\(91\)90021-c](https://doi.org/10.1016/0079-6700(91)90021-c)
6. Varga J (1995) Crystallization, melting and supermolecular structure of isotactic polypropylene. In: Karger-Kocsis J (ed) *Polypropylene: structure, blends and composites*, vol 1. Chapman & Hall, London, pp 56–115. ISBN 978-0-412-58430-5
7. Gahleitner M, Grein C, Kheirandish S et al (2011) Nucleation of polypropylene homo- and copolymers. *Int Polym Proc* 26(1):2–20. <https://doi.org/10.3139/217.2411>
8. Libster D, Aserin A, Garti N (2007) Advanced nucleating agents for polypropylene. *Polym Adv Technol* 18(9). <https://doi.org/10.1002/pat.970>

9. Fairgrieve S (2005) Nucleating agents. *Rapra Rev Rep* 16(7):1–132 ISSN: 0889-3144
10. Mitsubishi K (1996) Polypropylene, nucleating agents. In: Salamone JC (ed) *The polymeric materials encyclopedia*, vol 9. CRC Press, Boca Raton, FL, pp 6602–6609. ISBN 13: 9780849324703
11. Thierry A, Fillon B, Straupé C et al (1992) Polymer nucleating agents: efficiency scale and impact of physical gelation. *Progr Colloid Polym Sci* 87:28–31. <https://doi.org/10.1007/BFb0115569>
12. Beck HN (1967) Heterogeneous nucleating agents for polypropylene crystallization. *J Appl Polym Sci* 11(5):673–685. <https://doi.org/10.1002/app.1967.070110505>
13. Wunderlich B (1979) *Crystal nucleation, growth, annealing*, vol 2. Macromolecular Physics. Academic Press, London
14. Zheng H, Zeng FXY, Chen ZF et al (2017) Exploring the roles of molecular structure on the beta-crystallization of polypropylene random copolymer. *J Polym Res* 24(12):1–12. <https://doi.org/10.1007/s10965-017-1358-5>
15. Zhou S, Wang W, Xin Z et al (2016) Relationship between molecular structure, crystallization behavior, and mechanical properties of long chain branching polypropylene. *J Mater Sci* 51(12):5598–5608. <https://doi.org/10.1007/s10853-016-9856-0>
16. Horváth Z, Menyhárd A, Doshev P et al (2014) Effect of the molecular structure of the polymer and nucleation on the optical properties of polypropylene homo- and copolymers. *ACS Appl Mater Interfaces* 6(10):7456–7463. <https://doi.org/10.1021/am5008535>
17. Galli P, Haylock JC, Simonazzi T (1995) Manufacturing and properties of polypropylene copolymers. In: Karger-Kocsis J (ed) *Polypropylene: structure, blends and composites*, vol 2. Chapman & Hall, London, pp 1–24. ISBN 978-94-011-0521-7
18. Galli P, Simonazzi T, Delduca D (1988) New frontiers in polymer blends—the synthesis alloys. *Acta Polym* 39(1–2):81–90. <https://doi.org/10.1002/actp.1988.010390116>
19. Albizzati E, Giannini U, Collina G et al (1996) Catalysts and polymerizations. In: Moore EP (ed) *Polypropylene handbook*. Hanser/Gardner Publications, Cincinnati, pp 11–98. ISBN-13: 978-1569902080
20. Doshev P, Kheirandish S, Pukánszky B et al (2011) High-impact EP random copolymers with specific nucleation. *Eur. App. No.* 10151444.6
21. Phillips P. J., Mezghani K (1996) Polypropylene, isotactic (polymorphism). In: Salamone JC (ed) *The polymeric materials encyclopedia*, vol 9. CRC Press, Boca Raton, FL, pp 6637–6649. ISBN 13: 9780849324703
22. van Reenen AJ, Basson NC (2012) Molecular composition and properties of impact propylene copolymers. *Express Polym Lett* 6(5):427–436. <https://doi.org/10.3144/expresspolymlett.2012.45>
23. Chai Z, Guo S, Feng J et al (2006) Advances in modification of ethylene propylene random copolymer. *Petrochem Technol* 35(5):499–504
24. Paulik CE, Neissl W, Soc Plast E (1998) Phase structure and morphology: designing a new class of heterophasic PP copolymers, vol 44. In: *Conference proceedings at Antec '98: plastics on my mind*, vols I-3: vol i; processing, vol II; special areas, Vol III; materials
25. Sterzynski T, Lambla M, Crozier H et al (1994) Structure and properties of nucleated random and block-copolymers of propylene. *Adv Polym Technol* 13(1):25–36. <https://doi.org/10.1002/adv.1994.060130102>
26. Monasse B, Haudin JM (1988) Effect of random copolymerization on growth transition and morphology change in polypropylene. *Colloid Polym Sci* 266(8):679–687. <https://doi.org/10.1007/BF01410276>
27. Gahleitner M, Jääskeläinen P, Ratajski E et al (2005) Propylene-ethylene random copolymers: comonomer effects on crystallinity and application properties. *J Appl Polym Sci* 95(5):1073–1081. <https://doi.org/10.1002/app.21308>
28. Juhász P, Belina K (2001) Crystallization and morphology of propylene/pentene random copolymers. *J Reinf Plast Compos* 20(1):2–11. <https://doi.org/10.1106/A7N4-7YFW-YG88-NDP8>

29. Lotz B (2014) A new ϵ crystal modification found in stereodeficient isotactic polypropylene samples. *Macromolecules* 47(21):7612–7624. <https://doi.org/10.1021/ma5009868>
30. Dorset DL, McCourt MP, Kopp S et al (1998) Isotactic polypropylene, beta-phase: a study in frustration. *Polymer* 39(25):6331–6337. [https://doi.org/10.1016/S0032-3861\(97\)10160-4](https://doi.org/10.1016/S0032-3861(97)10160-4)
31. Lotz B, Wittmann JJ, Lovinger AJ (1996) Structure and morphology of poly(propylenes): a molecular analysis. *Polymer* 37:4979–4992. [https://doi.org/10.1016/0032-3861\(96\)00370-9](https://doi.org/10.1016/0032-3861(96)00370-9)
32. Lotz B, Wittmann JC (1992) Isotactic polypropylene: growth transition and crystal polymorphism. *Progr Colloid Polym Sci* 87:3–7. <https://doi.org/10.1007/BFb0115565>
33. Lotz B, Graff S, Wittmann JC (1986) Crystal morphology of the gamma-(triclinic) phase of isotactic polypropylene and its relation to the alpha-phase. *J Polym Sci Pt B-Polym Phys* 24(9):2017–2032. <https://doi.org/10.1002/polb.1986.090240909>
34. Monasse B, Haudin JM (1985) Growth transition and morphology change in polypropylene. *Colloid Polym Sci* 263(10):822–831. <https://doi.org/10.1007/BF01412960>
35. Varga J (2002) Beta-modification of isotactic polypropylene: preparation, structure, processing, properties, and application. *J Macromol Sci Part B-Phys* B41(4–6):1121–1171. <https://doi.org/10.1081/MB-120013089>
36. Wang Y, Zhao J, Qu MJ et al (2018) An unusual promotion of gamma-crystals in metallocene-made isotactic polypropylene from orientational relaxation and favorable temperature window induced by shear. *Polymer* 134:196–203. <https://doi.org/10.1016/j.polymer.2017.11.040>
37. Wang Y, Chen C, Xu JZ et al (2012) Suppressing of gamma-crystal formation in metallocene-based isotactic polypropylene during isothermal crystallization under shear flow. *J Phys Chem B* 116(16):5056–5063. <https://doi.org/10.1021/jp3003068>
38. Krache R, Benavente R, Lopez-Majada JM et al (2007) Competition between alpha, beta, and gamma polymorphs in beta-nucleated metallocenic isotactic polypropylene. *Macromolecules* 40(19):6871–6878. <https://doi.org/10.1021/ma0710636>
39. Busse K, Kressler J, Maier RD et al (2000) Tailoring of the alpha-, beta-, and gamma-modification in isotactic polypropylene and propene/ethene random copolymers. *Macromolecules* 33(23):8775–8780. <https://doi.org/10.1021/ma000719r>
40. Campbell RA, Phillips PJ, Lin JS (1993) The gamma phase of high-molecular-weight polypropylene: 1. Morphological aspects. *Polymer* 34(23):4809–4816. [https://doi.org/10.1016/0032-3861\(93\)90002-R](https://doi.org/10.1016/0032-3861(93)90002-R)
41. Nedkov E, Kretev V (1990) Mixed spherulites of alpha-phase and gamma-phase in gamma-irradiated and thermal-treated isotactic polypropylene. *Colloid Polym Sci* 268(11):1028–1035. <https://doi.org/10.1007/BF01410591>
42. Varga J, Mudra I, Ehrenstein GW (1999) Crystallization and melting of beta-nucleated isotactic polypropylene. *J Therm Anal Calorim* 56(3):1047–1057. <https://doi.org/10.1023/A:1010132306934>
43. Varga J (1992) Supermolecular structure of isotactic polypropylene. *J Mater Sci* 27(10):2557–2579. <https://doi.org/10.1007/BF00540671>
44. Varga J, Garzó G (1991) Isothermal crystallization of the beta-modification of polypropylene. *Acta Chim Hung* 128:303–317
45. Varga J, Fujiwara Y, Ille A (1990) Beta-alpha-bifurcation of growths during the spherulitic crystallization of polypropylene. *Period Polytech Chem Eng* 34(4):255–271
46. Varga J (1989) Beta-modification of polypropylene and its two component systems. *J Therm Anal* 35:1891–1912. <https://doi.org/10.1007/BF01911675>
47. Varga J, Schulek-Tóth F (1986) Annealing of the beta-modification of polypropylene. *Makromolekulare Chemie-Macromolecular Symposia* 5:213–223. <https://doi.org/10.1002/masy.19860050120>
48. Varga J (1986) Melting memory effect of the beta-modification of polypropylene. *J Therm Anal* 31(1):165–172. <https://doi.org/10.1007/BF01913897>
49. Billmeyer FW (1984) *Textbook of polymer science*. Wiley, New York
50. Gedde UW (1999) *Polymer physics*. Kluwer Academic Publisher, Dordrecht
51. Wunderlich B (2005) *Thermal analysis of polymeric materials*. Springer, Berlin

52. Varga J (1983) Shape of spherulitic boundaries. *Die Angewandte Makromolekulare Chemie* 112(1):161–172. <https://doi.org/10.1002/apmc.1983.051120111>
53. Martins JA, Pinto JJCC (2000) Non-isothermal crystallisation kinetics with instantaneous nucleation. *Polymer* 41(18):6875–6884. [https://doi.org/10.1016/S0032-3861\(00\)00035-5](https://doi.org/10.1016/S0032-3861(00)00035-5)
54. Hoffman JD, Miller RL (1997) Kinetics of crystallization from the melt and chain folding in polyethylene fractions revisited: theory and experiment. *Polymer* 38(13):3151–3212. [https://doi.org/10.1016/S0032-3861\(97\)00071-2](https://doi.org/10.1016/S0032-3861(97)00071-2)
55. Ozawa T (1971) Kinetics of non-isothermal crystallization. *Polymer* 12:150–158. [https://doi.org/10.1016/0032-3861\(71\)90041-3](https://doi.org/10.1016/0032-3861(71)90041-3)
56. Avrami M (1940) Kinetics of phase change II. Transformation-time relations for random distribution of nuclei. *J Chem Phys* 8:212. <https://doi.org/10.1063/1.1750631>
57. Avrami M (1939) Kinetics of phase change I. General theory. *J Chem Phys* 7:1103. <https://doi.org/10.1063/1.1750380>
58. Martins JA, Pinto JJCC (2000) The nonisothermal crystallization kinetics of polypropylene after DSC calibration on cooling. *J Macromol Sci Part B-Phys* B39(5–6):711–722. <https://doi.org/10.1081/MB-100102482>
59. Binsbergen FL (1973) Heterogeneous nucleation in the crystallization of polyolefins. III. Theory and mechanism. *J Polym Sci: Polym Phys Ed* 11(1):117–135. <https://doi.org/10.1002/pol.1973.180110112>
60. Binsbergen FL (1970) Heterogeneous nucleation in the crystallization of polyolefins: part I. Chemical and physical nature of nucleating agents. *Polymer* 11(5):253–267. [https://doi.org/10.1016/0032-3861\(70\)90036-4](https://doi.org/10.1016/0032-3861(70)90036-4)
61. Alcazar D, Ruan JR, Thierry A et al (2006) Polysynthetic twinning in poly (vinylcyclohexane) single crystals and “fractional” secondary nucleation in polymer crystal growth. *Macromolecules* 39(3):1008–1019. <https://doi.org/10.1021/ma0523217>
62. Alcazar D, Ruan J, Thierry A et al (2006) Structural matching between the polymeric nucleating agent isotactic poly(vinylcyclohexane) and isotactic polypropylene. *Macromolecules* 39(8):2832–2840. <https://doi.org/10.1021/ma052651r>
63. Menyhárd A, Gahleitner M, Varga J et al (2009) The influence of nucleus density on optical properties in nucleated isotactic polypropylene. *Eur Polym J* 45(11):3138–3148. <https://doi.org/10.1016/j.eurpolymj.2009.08.006>
64. Varga J, Menyhárd A (2003) Crystallization, melting and structure of polypropylene/poly (vinylidene-fluoride) blends. *J Therm Anal Calorim* 73(3):735–743. <https://doi.org/10.1023/A:1025870111612>
65. Vaezi J, Nekoomanesh M, Khonakdar HA et al (2017) Thermal analysis and successive self-nucleation and annealing (SSA) treatment of synthesized bimodal polypropylene (BPP) reactor blends using homogeneous binary metallocene catalyst. *J Therm Anal Calorim* 130(2):985–995. <https://doi.org/10.1007/s10973-017-6415-0>
66. Müller AJ, Michell RM, Perez RA et al (2015) Successive self-nucleation and annealing (SSA): correct design of thermal protocol and applications. *Eur Polym J* 65:132–154. <https://doi.org/10.1016/j.eurpolymj.2015.01.015>
67. Balzano L, Rastogi S, Peters G (2011) Self-nucleation of polymers with flow: the case of bimodal polyethylene. *Macromolecules* 44(8):2926–2933. <https://doi.org/10.1021/ma102662p>
68. Bassett DC (2004) Polymer morphology: a guide to macromolecular self-organization. *Macromol Symp* 214:5–15. <https://doi.org/10.1002/masy.200451002>
69. Fillon B, Wittmann JC, Lotz B et al (1993) Self-nucleation and recrystallization of isotactic polypropylene (alpha-phase) investigated by differential scanning calorimetry. *J Polym Sci Pt B-Polym Phys* 31(10):1383–1393. <https://doi.org/10.1002/polb.1993.090311013>
70. Fillon B, Lotz B, Thierry A et al (1993) Self-nucleation and enhanced nucleation of polymers—definition of a convenient calorimetric efficiency scale and evaluation of nucleating additives in isotactic polypropylene (alpha-phase). *J Polym Sci Pt B-Polym Phys* 31(10):1395–1405. <https://doi.org/10.1002/polb.1993.090311014>

71. Horváth F, Gombár T, Varga J et al (2017) Crystallization, melting, supermolecular structure and properties of isotactic polypropylene nucleated with dicyclohexyl-terephthalamide. *J Therm Anal Calorim* 128(2):925–935. <https://doi.org/10.1007/s10973-016-6057-7>
72. Varga J, Stoll K, Menyhárd A et al (2011) Crystallization of isotactic polypropylene in the presence of a beta-nucleating agent based on a trisamide of trimesic acid. *J Appl Polym Sci* 121:1469–1480. <https://doi.org/10.1002/app.33685>
73. Menyhárd A, Varga J (2006) The effect of compatibilizers on the crystallisation, melting and polymorphic composition of beta-nucleated isotactic polypropylene and polyamide 6 blends. *Eur Polym J* 42(12):3257–3268. <https://doi.org/10.1016/j.eurpolymj.2006.09.003>
74. Varga J, Mudra I, Ehrenstein GW (1999) Highly active thermally stable beta-nucleating agents for isotactic polypropylene. *J Appl Polym Sci* 74(10):2357–2368. [https://doi.org/10.1002/\(SICI\)1097-4628\(19991205\)74:10%3c2357:AIDAPP3%3e3.0.CO;2-2](https://doi.org/10.1002/(SICI)1097-4628(19991205)74:10%3c2357:AIDAPP3%3e3.0.CO;2-2)
75. Menczel J, Varga J (1983) Influence of nucleating-agents on crystallization of polypropylene. 1. Talc as a nucleating-agent. *J Thermal Anal* 28(1):161–174. <https://doi.org/10.1007/BF02105288>
76. Hoffman JD, Davis GT, Lauritzen JI (1976) In: Hannay NB (ed) *Treatise on solid state chemistry*, vol 3. Plenum Press, New York, pp 497–614. https://doi.org/10.1007/978-1-4684-2664-9_7
77. Clark EJ, Hoffman JD (1984) Regime-III crystallization in polypropylene. *Macromolecules* 17(4):878–885. <https://doi.org/10.1021/ma00134a058>
78. Turi EA (ed) (1981) *Thermal characterization of polymeric materials*. Academic Press Inc., New York
79. Zhang YF, Chen H, Liu BB et al (2014) Isothermal and non-isothermal crystallization of isotactic polypropylene nucleated with 1,3,5-benzenetricarboxylic acid tris(cyclohexylamide). *Thermochim Acta* 590:226–231. <https://doi.org/10.1016/j.tca.2014.07.007>
80. Menyhárd A, Dora G, Horváth Z et al (2012) Kinetics of competitive crystallization of beta- and alpha-modifications in beta-nucleated iPP studied by isothermal stepwise crystallization technique. *J Therm Anal Calorim* 108(2):613–620. <https://doi.org/10.1007/s10973-011-1900-3>
81. Zhang Y-F, Xin Z (2007) Isothermal crystallization behaviors of isotactic polypropylene nucleated with α/β compounding nucleating agents. *J Polym Sci, Part B: Polym Phys* 45(5):590–596. <https://doi.org/10.1002/polb.21072>
82. De Santis F, Adamovsky S, Titomanlio G et al (2007) Isothermal nanocalorimetry of isotactic polypropylene. *Macromolecules* 40(25):9026–9031. <https://doi.org/10.1021/ma071491b>
83. Chen JH, Chang YL (2007) Isothermal crystallization kinetics and morphology development of isotactic polypropylene blends with atactic polypropylene. *J Appl Polym Sci* 103(2):1093–1104. <https://doi.org/10.1002/app.25354>
84. Yu J, He JS (1999) The isothermal crystallization behavior of maleic anhydride graft polypropylene and its ionomers. *Acta Polym Sin* 1:87–92
85. Caze C, Devaux E, Crespy A et al (1997) A new method to determine the Avrami exponent by DSC studies of non-isothermal crystallization from the Molten state. *Polymer* 38(3):497–502. [https://doi.org/10.1016/S0032-3861\(96\)00552-6](https://doi.org/10.1016/S0032-3861(96)00552-6)
86. Atanassov AM (1987) Linear isothermal crystal-growth rate of I-polypropylene by differential scanning calorimetry. *Polym Bull* 17(5):445–451. <https://doi.org/10.1007/BF00255617>
87. Wlochowicz A, Eder M (1984) Distribution of Lamella thicknesses in isothermally crystallized polypropylene and polyethylene by differential scanning calorimetry. *Polymer* 25(9):1268–1270. [https://doi.org/10.1016/0032-3861\(84\)90374-4](https://doi.org/10.1016/0032-3861(84)90374-4)
88. Di Lorenzo ML, Silvestre C (1999) Non-isothermal crystallization of polymers. *Prog Polym Sci* 24(6):917–950. [https://doi.org/10.1016/S0079-6700\(99\)00019-2](https://doi.org/10.1016/S0079-6700(99)00019-2)
89. Fanegas N, Gomez MA, Jimenez I et al (2008) Optimizing the balance between impact strength and stiffness in polypropylene/elastomer blends by incorporation of a nucleating agent. *Polym Eng Sci* 48(1):80–87. <https://doi.org/10.1002/pen.20886>

90. Varga J, Menyhárd A (2007) Effect of solubility and nucleating duality of N, N'-dicyclohexyl-2,6-naphthalenedicarboxamide on the supermolecular structure of isotactic polypropylene. *Macromolecules* 40(7):2422–2431. <https://doi.org/10.1021/ma062815j>
91. Jin Y, Hiltner A, Baer E (2007) Effect of a sorbitol nucleating agent on fractionated crystallization of polypropylene droplets. *J Polym Sci Pt B-Polym Phys* 45(14):1788–1797. <https://doi.org/10.1002/polb.21195>
92. Borysiak S (2007) Determination of nucleating ability of wood for non-isothermal crystallisation of polypropylene. *J Therm Anal Calorim* 88(2):455–462. <https://doi.org/10.1007/s10973-006-8077-1>
93. Blomenhofer M, Ganzleben S, Hanft D et al (2005) “Designer” nucleating agents for polypropylene. *Macromolecules* 38(9):3688–3695. <https://doi.org/10.1021/ma0473317>
94. Menyhárd A, Pukanszky B, Varga J et al (2003) The influence of transparency by different types of highly active nucleating agents in polypropylene systems. *Period Polytech: Chem Eng* 47(1):76–77
95. Gui Q, Zhong X, Zhu W et al (2003) Effects of an organic phosphorus nucleating agent on crystallization behaviors and mechanical properties of poly(propylene). *J Appl Polym Sci* 88(2):297–301. <https://doi.org/10.1002/app.11708>
96. Marco C, Gómez MA, Ellis G et al (2002) Highly efficient nucleating additive for isotactic polypropylene studied by differential scanning calorimetry. *J Appl Polym Sci* 84(9):1669–1679. <https://doi.org/10.1002/app.10546>
97. Marco C, Gomez MA, Ellis G et al (2002) Activity of a beta-nucleating agent for isotactic polypropylene and its influence on polymorphic transitions. *J Appl Polym Sci* 86(3):531–539. <https://doi.org/10.1002/app.10811>
98. Jang GS, Cho WJ, Ha CS (2001) Crystallization behavior of polypropylene with or without sodium benzoate as a nucleating agent. *J Polym Sci Pt B-Polym Phys* 39(10):1001–1016. <https://doi.org/10.1002/polb.1077>
99. Kikkawa K (2003) Novel organophosphate salt based nucleating/clarifying agent for polypropylene. *Pop Plastics Packag* 48(2):155–160
100. Kefeng W, Kancheng M, Zhiwu H et al (2001) Interaction of self-nucleation and the addition of a nucleating agent on the crystallization behavior of isotactic polypropylene. *J Appl Polym Sci* 81(1):78–84. <https://doi.org/10.1002/app.1415>
101. Zhang Y-F, Xin Z (2006) Effects of substituted aromatic heterocyclic phosphate salts on properties, crystallization, and melting behaviors of isotactic polypropylene. *J Appl Polym Sci* 100(6):4868–4874. <https://doi.org/10.1002/app.23209>
102. Smith TL, Masilamani D, Bui LK et al (1994) Acetals as nucleating-agents for polypropylene. *J Appl Polym Sci* 52(5):591–596. <https://doi.org/10.1002/app.1994.070520502>
103. Lipp J, Shuster M, Terry AE et al (2006) Fibril formation of 1,3: 2,4-di(3,4-dimethylbenzylidene) sorbitol in a polypropylene melt. *Langmuir* 22(14):6398–6402. <https://doi.org/10.1021/la060490u>
104. Kristiansen M, Werner M, Tervoort T et al (2003) The binary system isotactic polypropylene/bis(3,4-dimethylbenzylidene)sorbitol: phase behavior, nucleation, and optical properties. *Macromolecules* 36(14):5150–5156. <https://doi.org/10.1021/ma030146t>
105. Kristiansen M, Tervoort T, Smith P (2003) Synergistic gelation of solutions of isotactic polypropylene and bis-(3,4-dimethyl benzylidene) sorbitol and its use in gel-processing. *Polymer* 44(19):5885–5891. [https://doi.org/10.1016/S0032-3861\(03\)00538-X](https://doi.org/10.1016/S0032-3861(03)00538-X)
106. Horváth Z, Gyarmati B, Menyhárd A et al (2014) The role of solubility and critical temperatures for the efficiency of sorbitol clarifiers in polypropylene. *RSC Adv* 4(38):19737–19745. <https://doi.org/10.1039/c4ra01917b>
107. Liu T, Meng H, Sheng XY et al (2011) Effect of 1,3-2,4-di(p-hydroxyl) benzylidene sorbitol on mechanical properties of isotactic polypropylene. *Polym—Plast Technol Eng* 50(11):1165–1169. <https://doi.org/10.1080/03602559.2011.574669>

108. Marco C, Ellis G, Gomez MA et al (2002) Comparative study of the nucleation activity of third-generation sorbitol-based nucleating agents for isotactic polypropylene. *J Appl Polym Sci* 84(13):2440–2450. <https://doi.org/10.1002/app.10533>
109. Kersch M, Pischke L, Schmidt HW et al (2014) Influence of trisamide-based additives on the morphological and mechanical properties of isotactic polypropylene. *Polymer* 55(15):3227–3233. <https://doi.org/10.1016/j.polymer.2014.05.030>
110. Kluge D, Singer JC, Neubauer JW et al (2012) Influence of the molecular structure and morphology of self-assembled 1,3,5-benzenetrisamide nanofibers on their mechanical properties. *Small* 8(16):2563–2570. <https://doi.org/10.1002/smll.201200259>
111. Abraham F, Ganzleben S, Hanft D et al (2010) Synthesis and structure-efficiency relations of 1,3,5-benzenetrisamides as nucleating agents and clarifiers for isotactic poly(propylene). *Macromol Chem Phys* 211(2):171–181. <https://doi.org/10.1002/macp.200900409>
112. Wang JB, Dou QA, Chen XA et al (2008) Crystal structure and morphologies of polypropylene homopolymer and propylene-ethylene random copolymer: effect of the substituted 1,3,5-benzenetrisamides. *J Polym Sci Pt B-Polym Phys* 46(11):1067–1078. <https://doi.org/10.1002/polb.21440>
113. Yu KS, Jiang HC, Zhou HF et al (2018) Evolution of double crystal melting peak in polypropylene foam assisted by beta-nucleating agent and supercritical CO₂. *J Appl Polym Sci* 135(12): Article Number: 46007. <https://doi.org/10.1002/app.46007>
114. Liu YM, Tong ZZ, Xu JT et al (2014) A highly efficient beta-nucleating agent for impact-resistant polypropylene copolymer. *J Appl Polym Sci* 131(18). <https://doi.org/10.1002/app.40753>
115. Wang C, Zhang Z, Ding Q et al (2013) β -crystallization of isotactic polypropylene in the presence of β -nucleating agent and different crystallinity poly(ethylene terephthalate). *Thermochim Acta* 559:17–22. <https://doi.org/10.1016/j.tca.2013.02.021>
116. Sun J, Li Q, Yao XJ et al (2013) A nematic liquid crystalline polymer as highly active novel beta-nucleating agent for isotactic polypropylene. *J Mater Sci* 48(11):4032–4040. <https://doi.org/10.1007/s10853-013-7215-y>
117. Ma YJ, Xin ML, Xu K et al (2013) A novel beta-nucleating agent for isotactic polypropylene. *Polym Int* 62(5):744–750. <https://doi.org/10.1002/pi.4357>
118. Dai X, Zhang ZS, Wang CG et al (2013) A novel montmorillonite with beta-nucleating surface for enhancing beta-crystallization of isotactic polypropylene. *Compos Pt A-Appl Sci Manuf* 49:1–8. <https://doi.org/10.1016/j.compositesa.2013.01.016>
119. Zhao SC, Xu N, Xin Z et al (2012) A novel highly efficient beta-nucleating agent for isotactic polypropylene. *J Appl Polym Sci* 123(1):108–117. <https://doi.org/10.1002/app.34441>
120. Zhang ZS, Wang CG, Zhang JP et al (2012) The beta-nucleation of polypropylene random copolymer filled by nano-CaCO₃ supported beta-nucleating agent. *J Therm Anal Calorim* 109(3):1587–1596. <https://doi.org/10.1007/s10973-011-2092-6>
121. Zhan K-J, Yang W, Yue L et al (2012) MWCNTs supported N, N'-dicyclohexyl-1,5-diamino-2,6-naphthalenedicarboxamide: a novel beta-nucleating agent for polypropylene. *J Macromol Sci Part B-Phys* 51(12):2412–2427. <https://doi.org/10.1080/00222348.2012.676366>
122. Wang C, Chu Y-L, Wu Y-J (2012) Electrospun isotactic polystyrene nanofibers as a novel β -nucleating agent for isotactic polypropylene. *Polymer* 53(23):5404–5412. <https://doi.org/10.1016/j.polymer.2012.09.036>
123. Lv RH, Li ZJ, Na B et al (2012) Cooperative effect of molecular orientation and beta-form on toughening injection-molded isotactic polypropylene with beta-nucleating agent. *J Appl Polym Sci* 125(4):2764–2770. <https://doi.org/10.1002/app.36622>
124. Zhang ZS, Chen CY, Wang CG et al (2011) Nonisothermal crystallization kinetics of isotactic polypropylene nucleated with a novel supported beta-nucleating agent. *J Therm Anal Calorim* 103(1):311–318. <https://doi.org/10.1007/s10973-010-0946-y>

125. Li J, Wang SW, Yang W et al (2011) Mechanical and thermal characteristics and morphology of polyamide 6/isotactic polypropylene blends in the presence of a beta-nucleating agent. *J Appl Polym Sci* 121(1):554–562. <https://doi.org/10.1002/app.33620>
126. Dong M, Guo Z, Su Z et al (2011) The effects of crystallization condition on the microstructure and thermal stability of isotactic polypropylene nucleated by beta-form nucleating agent. *J Appl Polym Sci* 119(3):1374–1382. <https://doi.org/10.1002/app.32487>
127. Xu LL, Zhang XJ, Xu K et al (2010) Variation of non-isothermal crystallization behavior of isotactic polypropylene with varying beta-nucleating agent content. *Polym Int* 59(10):1441–1450. <https://doi.org/10.1002/pi.2891>
128. Wang SW, Yang W, Bao RY et al (2010) The enhanced nucleating ability of carbon nanotube-supported beta-nucleating agent in isotactic polypropylene. *Colloid Polym Sci* 288(6):681–688. <https://doi.org/10.1007/s00396-010-2194-x>
129. Xu LL, Xu K, Chen DH et al (2009) Thermal behavior of isotactic polypropylene in different content of beta-nucleating agent. *J Therm Anal Calorim* 96(3):733–740. <https://doi.org/10.1007/s10973-009-0022-7>
130. Liu MX, Guo BC, Du ML et al (2009) Halloysite nanotubes as a novel beta-nucleating agent for isotactic polypropylene. *Polymer* 50(13):3022–3030. <https://doi.org/10.1016/j.polymer.2009.04.052>
131. Guo X, Zhao S, Xin Z (2009) Efficiency of a novel rare earth compound as beta nucleating agent of isotactic polypropylene. *Shiyou Huagong/Petrochem Technol* 38(6):662–667
132. Bai H, Wang Y, Zhang Z et al (2009) Influence of annealing on microstructure and mechanical properties of isotactic polypropylene with beta-phase nucleating agent. *Macromolecules* 42(17):6647–6655. <https://doi.org/10.1021/ma9001269>
133. Zhao S, Cai Z, Xin Z (2008) A highly active novel beta-nucleating agent for isotactic polypropylene. *Polymer* 49(11):2745–2754. <https://doi.org/10.1016/j.polymer.2008.04.012>
134. Zhang Z, Wang C, Yang Z et al (2008) Crystallization behavior and melting characteristics of pp nucleated by a novel supported beta-nucleating agent. *Polymer* 49(23):5137–5145. <https://doi.org/10.1016/j.polymer.2008.09.009>
135. Zhang Z, Tao Y, Yang Z et al (2008) Preparation and Characteristics Of Nano-CaCO₃ supported beta-nucleating agent of polypropylene. *Eur Polym J* 44(7):1955–1961. <https://doi.org/10.1016/j.eurpolymj.2008.04.022>
136. Na B, Lv RH, Xu WF et al (2008) Effect of nucleating duality on the formation of gamma-phase in a beta-nucleated isotactic polypropylene copolymer. *Polym Int* 57(10):1128–1133. <https://doi.org/10.1002/pi.2454>
137. Dong M, Guo Z, Yu J et al (2008) Crystallization behavior and morphological development of isotactic polypropylene with an aryl amide derivative as beta-form nucleating agent. *J Polym Sci, Part B: Polym Phys* 46(16):1725–1733. <https://doi.org/10.1002/polb.21508>
138. Juhász P, Varga J, Belina K et al (2002) Efficiency of beta-nucleating agents in propylene/alpha-olefin copolymers. *J Macromol Sci Part B-Phys* B41(4–6):1173–1189. <https://doi.org/10.1081/MB-120013090>
139. Radhakrishnan S, Tapale M, Shah N et al (1997) Effect of beta-phase nucleating additives on structure and properties of blow extruded polypropylene. *J Appl Polym Sci* 64(7):1247–1253. [https://doi.org/10.1002/\(SICI\)1097-4628\(19970516\)64:7%3c1247:AID-APP1%3e3.0.CO;2-J](https://doi.org/10.1002/(SICI)1097-4628(19970516)64:7%3c1247:AID-APP1%3e3.0.CO;2-J)
140. Leugering HJ (1967) Einfluss der Kristallstruktur und Überstruktur auf einige Eigenschaften von Polypropylen. *J Macromol Chem* 109:204–216. <https://doi.org/10.1002/macp.1967.021090118>
141. Shi GY, Huang B, Zhang JY (1984) Enthalpy of fusion and equilibrium melting-point of the beta-form of polypropylene. *Makromolekulare Chemie-Rapid Commun* 5(9):573–578. <https://doi.org/10.1002/marc.1984.030050915>
142. Ikeda N, Kobayashi T, Killough L (1996) Novel beta-nucleator for polypropylene. In: *Polypropylene '96*. World congress, Zürich, Switzerland, 18–20 Sept 1996

143. Zhao SC, Liu KH, Zhou S et al (2017) A novel self-dispersed beta nucleating agent for isotactic polypropylene and its unique nucleation behavior and mechanism. *Polymer* 132:69–78. <https://doi.org/10.1016/j.polymer.2017.10.024>
144. Yin C, Wang ZC, Chen JY et al (2017) Influences of isotactic poly(4-methylpentene-1) on the crystallization and morphology of the beta-nucleated isotactic polypropylene. *Soft Mater* 15(1):1–12. <https://doi.org/10.1080/1539445x.2016.1232734>
145. Li YJ, Wen XY, Nie M et al (2017) Toward subtle manipulation of fine dendritic beta-nucleating agent in polypropylene. *ACS Omega* 2(10):7230–7238. <https://doi.org/10.1021/acsomega.7b01036>
146. Li YJ, Li ME, Nie M et al (2017) Reinforcement for polypropylene via self-assembly of beta-form nucleating agent: new insight on the perpendicular orientation of lamellae. *J Mater Sci* 52(2):981–992. <https://doi.org/10.1007/s10853-016-0393-7>
147. Barczewski M, Dobrzynska-Mizera M, Dutkiewicz M et al (2016) Novel polypropylene beta-nucleating agent with polyhedral oligomeric silsesquioxane core: synthesis and application. *Polym Int* 65(9):1080–1088. <https://doi.org/10.1002/pi.5158>
148. Sun J, Jia YG, Tong CC et al (2014) Synthesis of a new liquid crystalline polymer as a highly active beta-nucleator and its effect on melting and crystallization behaviors of isotactic polypropylene. *Int J Polym Anal Charact* 19(6):562–569. <https://doi.org/10.1080/1023666x.2014.932523>
149. Kang J, Gai JG, Li JP et al (2013) Dynamic crystallization and melting behavior of beta-nucleated isotactic polypropylene polymerized with different ziegler-natta catalysts. *J Polym Res* 20(2):70. <https://doi.org/10.1007/s10965-012-0070-8>
150. Ding Q, Zhang ZS, Wang CG et al (2013) The beta-nucleating effect of wollastonite-filled isotactic polypropylene composites. *Polym Bull* 70(3):919–938. <https://doi.org/10.1007/s00289-012-0896-6>
151. Shi Y, Dou Q (2011) Structure and properties of beta-polypropylene. *Hecheng Shuzhi Ji Suliao/China Synthetic Resin and Plastics* 28(2):58–62
152. Zhang ZS, Chen CY, Wang CG et al (2010) A novel highly efficient beta-nucleating agent for polypropylene using nano-CaCO₃ as a support. *Polym Int* 59(9):1199–1204. <https://doi.org/10.1002/pi.2847>
153. Vychnopova J, Cermak R, Obadal M et al (2009) Effect of beta-nucleation on crystallization of photodegraded polypropylene. *J Therm Anal Calorim* 95(1):215–220. <https://doi.org/10.1007/s10973-008-8892-7>
154. Menyhárd A, Varga J, Molnár G (2006) Comparison of different beta-nucleators for isotactic polypropylene, characterisation by DSC and temperature-modulated DSC (TMDSC) measurements. *J Therm Anal Calorim* 83(3):625–630. <https://doi.org/10.1007/s10973-005-7498-6>
155. Kang J, Wang B, Peng HM et al (2014) Investigation on the dynamic crystallization and melting behavior of beta-nucleated isotactic polypropylene with different stereo-defect distribution-the role of dual-selective beta-nucleation agent. *Polym Adv Technol* 25(1):97–107. <https://doi.org/10.1002/pat.3210>
156. Wei ZY, Zhang WX, Chen GY et al (2010) Crystallization and melting behavior of isotactic polypropylene nucleated with individual and compound nucleating agents. *J Therm Anal Calorim* 102(2):775–783. <https://doi.org/10.1007/s10973-010-0725-9>
157. Wypych G (ed) (2016) *Handbook of nucleating agents*, 1st edn. ChemTec Publishing, Toronto, Canada
158. Varga J, Menyhárd A (2012) Thermo-optical microscopy (TOM) for the investigation of the crystallisation, melting and supermolecular structure of polypropylene and their multicomponent systems. In: Méndez-Vilas A (ed) *Current microscopy contributions to advances in science and technology*, vol 2. Microscopy Book Series Formatex Research Center, Badajoz, Spain, pp 1025–1035
159. Pukánszky B (1995) Particulate filled polypropylene: structure and properties. In: Karger-Kocsis J (ed) *Polypropylene: structure, blends and composites*, vol 3. Chapman & Hall, London, pp 1–70. https://doi.org/10.1007/978-94-011-0523-1_1

160. Ferrage E, Martin F, Boudet A et al (2002) Talc as nucleating agent of polypropylene: morphology induced by lamellar particles addition and interface mineral-matrix modelization. *J Mater Sci* 37(8):1561–1573. <https://doi.org/10.1023/a:1014929121367>
161. McGenity PM, Hooper JJ, Paynter CD et al (1992) Nucleation and crystallization of polypropylene by mineral fillers: relationship to impact strength. *Polymer* 33(24):5215–5224. [https://doi.org/10.1016/0032-3861\(92\)90804-6](https://doi.org/10.1016/0032-3861(92)90804-6)
162. Dong M, Guo ZX, Su ZQ et al (2008) Study of the crystallization behaviors of isotactic polypropylene with sodium benzoate as a specific versatile nucleating agent. *J Polym Sci Pt B-Polym Phys* 46(12):1183–1192. <https://doi.org/10.1002/polb.21451>
163. Libster D, Aserin A, Garti N (2006) A novel dispersion method comprising a nucleating agent solubilized in a microemulsion, in polymeric matrix: I. dispersion method and polymer characterization. *J Colloid Interface Sci* 299(1):172–181. <https://doi.org/10.1016/j.jcis.2006.01.064>
164. Wamuo O, Wu Y, Hsu SL et al (2017) Effects of chain configuration on the crystallization behavior of polypropylene based copolymers. *Polymer* 116:342–349. <https://doi.org/10.1016/j.polymer.2017.01.031>
165. Horváth Z, Menyhárd A, Doshev P et al (2014) Chain regularity of isotactic polypropylene determined by different thermal fractionation methods. *J Therm Anal Calorim* 118(1):235–245. <https://doi.org/10.1007/s10973-014-3999-5>
166. Klimke K, Doshev P, Filipe S et al (2009) Heterophasic polypropylene resin with long chain branching. Austria Patent EP 2 319 885 A1
167. Garcia RA, Coto B, Exposito MT et al (2011) Molecular characterization of polypropylene heterophasic copolymers by fractionation techniques. *Macromol Res* 19(8):778–788. <https://doi.org/10.1007/s13233-011-0811-2>
168. Horváth Z, Sajó IE, Klaus S et al (2010) The effect of molecular mass on the polymorphism and crystalline structure of isotactic polypropylene. *Express Polym Lett* 4(2):101–114. <https://doi.org/10.3144/expresspolymlett.2010.15>
169. Chvatalova L, Vychopnova J, Cermak R et al (2008) The role of molecular parameters of PP in the sensitivity to specific nucleation. In: ANTEC, 2008. pp 100–104. ISBN: 9781605603209
170. Pukánszky B, Mudra I, Staniek P (1997) Relation of crystalline structure and mechanical properties of nucleated polypropylene. *J Vinyl Add Tech* 3(1):53–57. <https://doi.org/10.1002/vnl.10165>
171. Molnár J, Jelinek A, Maloveczky A et al (2018) Prediction of tensile modulus of semicrystalline polymers from a single melting curve recorded by calorimetry. *J Therm Anal Calorim* 134(1):401–408. <https://doi.org/10.1007/s10973-018-7487-1>
172. Menyhárd A, Suba P, László Z et al (2015) Direct correlation between modulus and the crystalline structure in isotactic polypropylene. *Express Polym Lett* 9(3):308–320. <https://doi.org/10.3144/expresspolymlett.2015.28>
173. Menyhárd A, Bredács M, Simon G et al (2015) Determination of nucleus density in semicrystalline polymers from nonisothermal crystallization curves. *Macromolecules* 48(8):2561–2569. <https://doi.org/10.1021/acs.macromol.5b00275>
174. Santis F, Pantani R (2013) Nucleation density and growth rate of polypropylene measured by calorimetric experiments. *J Therm Anal Calorim* 112(3):1481–1488. <https://doi.org/10.1007/s10973-012-2732-5>
175. Lamberti G (2004) A direct way to determine iPP density nucleation from DSC isothermal measurements. *Polym Bull* 52(6):443–449. <https://doi.org/10.1007/s00289-004-0304-y>
176. Zhang YF, Hou HH, Guo LH (2018) Effects of cyclic carboxylate nucleating agents on nucleus density and crystallization behavior of isotactic polypropylene. *J Therm Anal Calorim* 131(2):1483–1490. <https://doi.org/10.1007/s10973-017-6669-6>
177. Molnár J, Menyhárd A (2016) Separation of simultaneously developing polymorphic modifications by stepwise crystallization technique in non-isothermal calorimetric experiments. *J Therm Anal Calorim* 124(3):1463–1469. <https://doi.org/10.1007/s10973-016-5271-7>

178. Vancso GJ, Beekmans LGM, Trifonova D et al (1999) Hedritic crystallization in polymers studied by atomic force microscopy. *Abstr Pap Am Chem Soc* 218:U631–U632
179. Varga J, Mudra I, Ehrenstein GW (1998) Morphology and properties of beta-nucleated injection molded isotactic polypropylene. *SPE. Tech Pap* 44(3):3492–3496
180. Bernland K, Tervoort T, Smith P (2009) Phase behavior and optical- and mechanical properties of the binary system isotactic polypropylene and the nucleating/clarifying agent 1,2,3-trideoxy-4,6:5,7-bis-O-[(4-propylphenyl) methylene]-nonitol. *Polymer* 50(11):2460–2464. <https://doi.org/10.1016/j.polymer.2009.03.010>
181. Thierry A, Straupe C, Wittmann JC et al (2006) Organogelators and polymer crystallisation. *Macromol Symp* 241:103–110. <https://doi.org/10.1002/masy.200650915>
182. Wang K, Zhou C, Tang C et al (2009) Rheologically determined negative influence of increasing nucleating agent content on the crystallization of isotactic polypropylene. *Polymer* 50(2):696–706. <https://doi.org/10.1016/j.polymer.2008.11.019>
183. Shepard TA, Delsorbo CR, Louth RM et al (1997) Self-organization and polyolefin nucleation efficacy of 1,3:2,4-di-p-methylbenzylidene sorbitol. *J Polym Sci, Part B: Polym Phys* 35(16):2617–2628. [https://doi.org/10.1002/\(SICI\)1099-0488\(19971130\)35:16%3c2617:AID-POLB5%3e3.0.CO;2-M](https://doi.org/10.1002/(SICI)1099-0488(19971130)35:16%3c2617:AID-POLB5%3e3.0.CO;2-M)
184. Bernland K, Goossens JGP, Smith P et al (2016) On clarification of haze in polypropylene. *J Polym Sci Pt B-Polym Phys* 54(9):865–874. <https://doi.org/10.1002/polb.23992>
185. Kristiansen P (2004) Nucleation and clarification of semi-crystalline polymers. <https://doi.org/10.13140/rg.2.1.2653.3369>
186. Kristiansen PM, Gress A, Smith P et al (2006) Phase behavior, nucleation and optical properties of the binary system isotactic polypropylene/N, N', N''-tris-isopentyl-1,3,5-benzene-tricarboxamide. *Polymer* 47(1):249–253. <https://doi.org/10.1016/j.polymer.2005.08.053>
187. van Krevelen DV, Nijenhuis KT (2009) *Properties of polymers*. Elsevier, Amsterdam
188. Pukánszky B (1999) Optical clarity of polypropylene products. In: Karger-Kocsis J (ed) *Polypropylene: An A-Z reference*. Springer Netherlands, Dordrecht, pp 554–560. https://doi.org/10.1007/978-94-011-4421-6_75
189. Horváth Z, Menyhár A, Doshev P et al (2016) Improvement of the impact strength of ethylene-propylene random copolymers by nucleation. *J Appl Polym Sci* 133(34):43823. <https://doi.org/10.1002/app.43823>
190. Olley RH (1986) Selective etching of polymeric materials. *Sci Prog* 70(277):17–43
191. Olley RH, Bassett DC (1982) An improved permanganic etchant for polyolefines. *Polymer* 23(12):1707–1710. [https://doi.org/10.1016/0032-3861\(82\)90110-0](https://doi.org/10.1016/0032-3861(82)90110-0)

Chapter 4

Crystallization of Polypropylene



Andrzej Pawlak and Andrzej Galeski

Contents

4.1	Introduction (Overview).....	186
4.2	Methods of Crystallization Studies.....	188
4.3	Polymorphism.....	194
4.4	Nucleation and Crystal Growth in General.....	199
4.5	Structure of Single Crystal.....	201
4.6	Structure of Spherulite.....	204
4.7	Shish-Kebabs.....	209
4.8	Nucleation Theories.....	210
4.9	Formation of Spherulitic Structure.....	217
4.10	Crystallization of PP in Specific Conditions.....	225
4.11	The Nucleating Agents.....	229
4.12	Melting of Polypropylene.....	230
	References.....	233

Abstract Various aspects of polypropylene (PP) crystallization are discussed. The methods of studying the crystallization process and formed crystalline structure are presented. The polymorphism of crystals of polypropylene is presented and discussed. The general aspects of crystal nucleation and growth are recalled and typical structures crystallizing in polypropylene are characterized: single crystals, spherulites, shish-kebabs. The main elements of the nucleation theory are presented and the formation of spherulitic structure is discussed in more details. The crystallization of PP under special conditions has been reviewed. Nucleants for crystallization of polypropylene are briefly reviewed. The melting of polypropylene is described.

A. Pawlak (✉) · A. Galeski
Centre of Molecular and Macromolecular Studies, Polish Academy of Sciences,
90-363 Lodz, Poland
e-mail: apawlak@cbmm.lodz.pl

A. Galeski
e-mail: andgal@cbmm.lodz.pl

4.1 Introduction (Overview)

Polymers, among them polypropylene, are able to crystallize when have a regular architecture of macromolecules. In a linear polymer chain the pendant groups can be arranged into ordered configurations or they can be completely random. The steric order is called tacticity. If all chiral centers have the same configuration, the arrangement of the side groups is called isotactic (iPP), and if every other chiral center has the same arrangement, it is called syndiotactic (sPP), whereas a random arrangement of the side groups is called atactic polypropylene (aPP) (see Fig. 4.1). The atactic polymer is amorphous, isotactic and syndiotactic can crystallize. The degree of tacticity of a polymer is usually described by the stereotactic pentad content. The ability of polypropylenes to crystallize depends strongly on the degree of tacticity.

Polypropylene (isotactic and syndiotactic) is a semi-crystalline polymer, which means that in solid state an amorphous phase co-exists with crystalline phase [1]. A semi crystallinity is a consequence of long-chain nature of macromolecules, leading to chain entanglements. Besides non-regularity of structure (tacticity) it decreases the melting temperature and finally may prevent crystallization [2]. Figure 4.1 presents the simplest case of macromolecular structure when CH_3 side groups are bonded directly to main chains. If in a polymer branches exist, i.e. shorter or longer side chains, they limit further the ability to crystallization.

Polypropylene can crystallize from solution or melt, however, most industrial processes and laboratory studies is based on crystallization from melt, which avoids the use of solvent. In contrast to low molecular weight substances or metals the

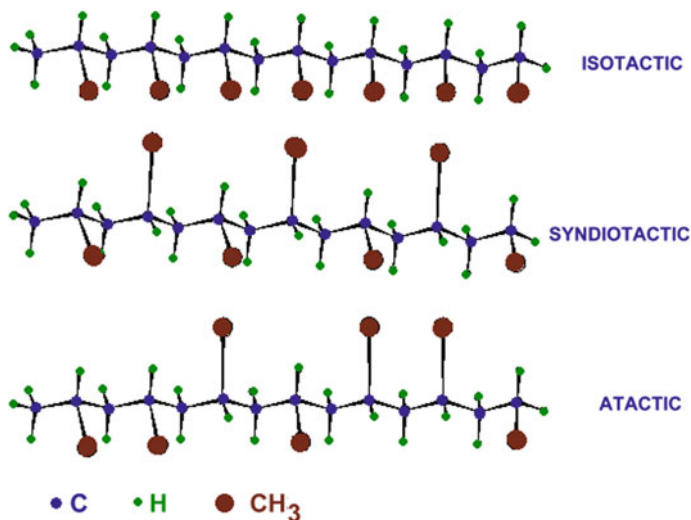


Fig. 4.1 Schematics of stereo-regular arrangements of mers in polypropylene

crystallization of polymers from melt proceeds at large undercooling, i.e. crystallization temperature is well below the melting temperature (10–20 °C and more). The supercooling arises from the extra free energy required to align chain segments. As the temperature is lowered from the melting temperature the energy of formation of a nucleus of critical size is decreased and the crystal growth becomes possible.

There are two steps of crystallization process: nucleation and growth of crystal. Every crystallization in polypropylene is induced by the crystallization nuclei. The growth of crystals occurs on primary nuclei by a series of secondary nucleation events. In this type of event a new crystalline layer is formed on an existing crystal face. The layer grows along the crystal face, process of secondary nucleation is repeated and new crystalline layer begins to expand, after finishing of previous layer or even during this process, depending on the crystallization conditions. The growing crystals usually have regular shapes, often are elongated and have a form of plates, known as lamella. Single polypropylene crystals can be obtained from dilute solutions or from melt when the special procedure is applied.

Crystals of PP are chain folded, i.e. fragment of a macromolecule becomes aligned in a growth layer and continues the attachment to crystal layer by folding and reversing the alignment. Such changes occur many times in the same layer or in a subsequent layer. Because of helical conformation of polypropylene macromolecules the adjacent reversing is not possible for certain crystallographic forms because of chain conformation chirality [3]. Then the reversing occurs in an adjacent subsequent layer [4]. During crystallization from the melt lamellae radiate from the central primary nuclei and by sufficiently frequent branching and so-called cross-hatching (specific for polypropylene) form crystalline aggregates called spherulites. In bulk the spherulites expand by crystal growth filling the available space. PP like other polymers is not fully crystalline. Typical crystallinity for PP is 30–60%. There is an amorphous phase between lamellae in spherulites and amorphous phase between spherulites. The spherulites are most common, but not only possible form of crystalline aggregates. Under certain conditions of sample forming and temperature other forms are created: axialities or hedrities. Recently more and more attention is devoted to shish-kebab structures, growing in polypropylene usually in oriented melt [5].

Both phases existing in a solidified polymer are interconnected by fragments of macromolecules. A single macromolecule may participate in the structure of two or more neighboring lamellae, passing through amorphous phase (so-called tie molecules). The flexible macromolecules entangle in melt together and these entanglements are preserved in amorphous phase of solidified polymers. Both tie molecules and entanglements are able to transfer stresses between lamellar crystals, so to a large extent they determine mechanical properties of polypropylene. A typical density of entanglements for isotactic polypropylene is characterized by molecular mass between entanglement knots and from rheological studies it was estimated at the level of 6900 g/mol [6]. The mechanical properties of amorphous phase depend strongly on the temperature. The characteristic temperature of glass

transition T_g is for iPP $-10\text{ }^\circ\text{C}$, while for sPP $0\text{ }^\circ\text{C}$ [7]. Supaphol and Spruiell [8] reported for syndiotactic PP $T_g = -6.1\text{ }^\circ\text{C}$, but $T_g = 0\text{ }^\circ\text{C}$ was also postulated for sPP by Miller and Seeley [9]. The scatter of these data result from different methods used for determination.

Quenching of molten isotactic polypropylene leads to a phase known as smectic or mesomorphic and exhibiting intermediate order of macromolecules, i.e. between crystalline and amorphous phases.

Light microscopy, X-ray and electron diffraction show that polypropylene can crystallize in different crystallographic forms. For isotactic polypropylene there are three main and they were named as α , β and γ in order of frequency of occurrence. Later the polymorphism of syndiotactic polypropylene was also discovered.

iPP has been polymerized in 1950s applying newly developed Ziegler–Natta process. The tacticity of Ziegler–Natta iPP chains can be varied within a wide range, thus influencing crystallinity and mechanical properties of the product. However, the molar mass distribution (MMD) is always rather wide ($M_w/M_n > 5$) in the case of Ziegler–Natta products and narrow MMD types are only accessible via degradation (controlled rheology process). With the rise of ‘metallocene revolution’, iPP produced by using this new family of catalysts shows more homogeneous properties (narrow molar mass distribution, constant and high tacticity, or purely random insertion of co-monomers), resulting from single active polymerization site [10].

4.2 Methods of Crystallization Studies

There are many methods useful for characterization of crystallization, melting processes and formed crystalline structure. Some of those methods show how the crystallization or melting process proceeds, i.e. what are temperatures of transitions, how the fraction of crystalline phase (crystallinity degree) changes with time. Other methods allow to examine the structures which are formed in situ during growth or later after finishing of crystallization. The most important research methods are briefly described below.

The growth of spherulites and spherulitic structure may be studied using **polarizing light microscopy** (PLM). A light microscope may provide resolution of $0.3\text{ }\mu\text{m}$, limited by the wavelength of light. The observations may be done in transmission or reflection, but usually the crystallization of polymers is observed in the transmission mode. If the microscope is connected with a hot stage, with programmable profile of temperature, it is possible to observe directly the growth of crystalline structures and conversion of melt into solidified polymer. Example of the use of PLM for studies of polypropylene is the determination of spherulitic/crystal growth rate G as a function of crystallization temperature T_c [11]. The microscope equipped with hot stage may be used also for examination of the PP melting progression. The other application of light microscope is the examination of structure after the crystallization (see Fig. 4.2). Specimens for such studies are

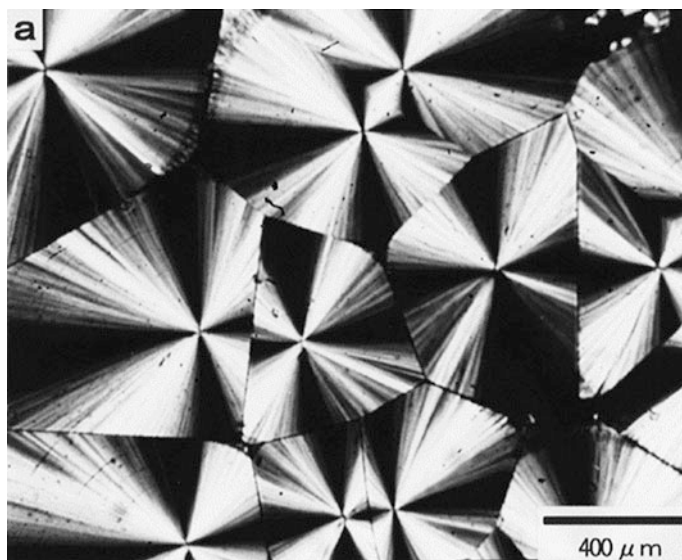


Fig. 4.2 Typical spherulitic morphology of iPP observed by polarizing light microscopy. iPP was crystallized isothermally at $T_c = 150$ °C. Maltese crosses in spherulites are clearly visible. From [12], reprinted with permission by Elsevier, 1998

prepared by sectioning a thin layer from bulk crystallized sample or by observing simply a thin film of polymer that has been melt-pressed or cast from solution. The thickness of observed materials should be appreciably less than the spherulite diameter, to avoid multiple structures being viewed along the light path.

Scanning electron microscopy (SEM) is a technique in which 10–20 keV energy electrons impinge on the surface of a thick sample. The electrons are focused into a narrow beam that scans the surface of a specimen. Elastically backscattered electrons come from a micrometer size layer of the surface and are detected as a function of beam position to provide a representation of surface topography, the signal being more intense from protrusions and less intense from recessed regions.

Secondary electrons are also produced due to reaction of the scanning beam with matter, but only those formed within a few nanometers of the surface can escape and be detected. Resolution of SEM depends on the instrument, beam size and other factors, the resolution can fall somewhere between 1 and 20 nm, for secondary electrons. SEM reveals surface structure (see Fig. 4.3) and, with X-ray detection unit (energy dispersive X-ray analysis, EDAX), chemical composition of sample surface. To prevent electrical charging a polypropylene surface is coated with a metal before studies [11].

For the studies of crystal's details at higher magnification **transmission electron microscopy (TEM)** is used (see Fig. 4.4). The small wavelength of electrons

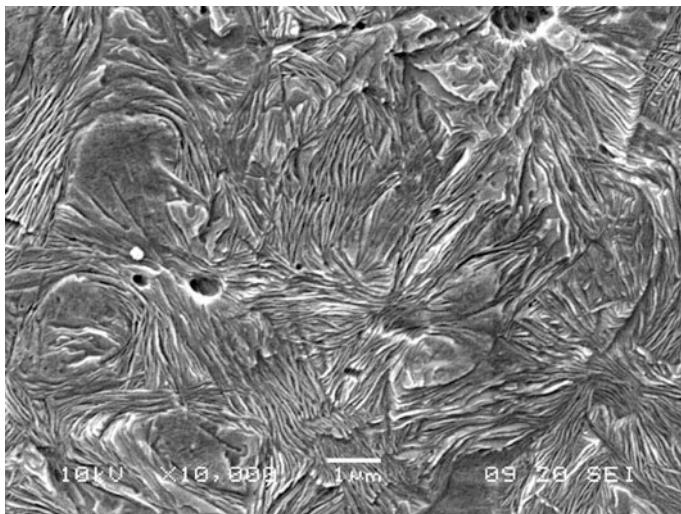
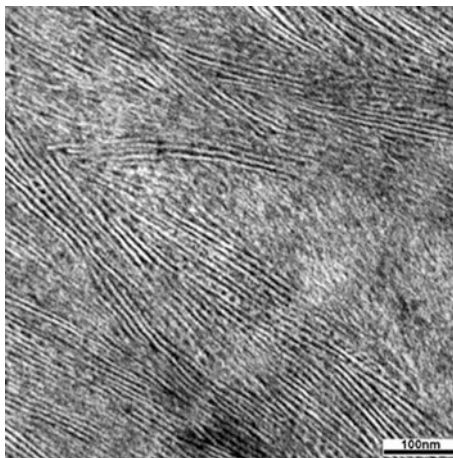


Fig. 4.3 Scanning electron micrograph of raw β form iPP sample. From [13], reprinted with permission by Elsevier, 2006

Fig. 4.4 TEM micrographs of ultrathin section of isotactic polypropylene. The arrangement of lamellar structure is visible. From [14], reprinted with permission by American Chemical Society, 2015



imparts a theoretical resolution of 0.1 nm, about four orders of magnitude better than light microscopy. The image is formed by detection of electrons that pass through the sample.

Electron microscopes require the observations in a high vacuum. The most significant drawback in the use of the TEM in polymer research is the damage caused by the energetic electron beam, which can crosslink, melt, or degrade the polymer. A second problem in transmission electron microscopy is that the

electrons are essentially fully scattered or absorbed within a penetration range of 10–100 nm. One is therefore limited to using thin films for direct observation [11].

The **light scattering** is a tool for detection of small (micrometer) spherulites (Fig. 4.5) and provide a measure of their average size. The largest structures dominate the scattering, and the average radius for a distribution of three-dimensional spherulites is (Eq. 4.1):

$$\langle R_s \rangle = 4.09\lambda / (4\pi \sin(\theta^*/2)) \quad (4.1)$$

where λ is wavelength of light, θ^* is the angle of maximum scattering.

An example of application SALS for the study of spherulitic crystallization of isotactic polypropylene (iPP) is the work of Okada et al. [16].

The crystalline forms of iPP can be clearly distinguished by X-ray diffraction. **Wide angle X-ray scattering (WAXS)** is a technique which may be used for identification of a polymer, determination of its crystallinity, determination of crystal size (“length”), determination of crystalline phase orientation. The identification of a polymer is usually conducted on the basis of positions of peaks representing scattering from different crystallographic planes (Fig. 4.6).

Crystallinity is determined from the scattering from the crystalline phase (area of peaks) and the amorphous phase (halo), after deconvolution of components in entire scattering. The dimension characteristic for lamellar crystal, often defined as length, can be calculated from the width of a diffraction peak. In the case of samples containing β -PP WAXS is also used for determining of β crystals contents in total crystallinity. The relative content of β -form may be calculated using Eq. 4.2 [17]:

$$\varphi = A(300) / [A(300) + A(110) + A(040) + A(130)] \quad (4.2)$$

where $A(110)$, $A(040)$, and $A(130)$ are the areas under the three α -form peaks (110), (040), and (130), while $A(300)$ is the area under the β -form peak (300).

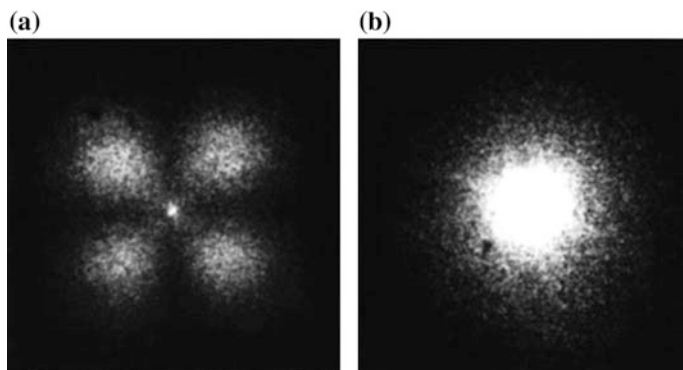


Fig. 4.5 Scattering patterns from PP containing 5% of CaCO_3 0.07 μm particles: **a** H_v pattern; **b** V_v pattern. From [15], reprinted with permission by Springer Nature, 1990

Fig. 4.6 X-ray diffractograms for polymorphic forms of isotactic polypropylene

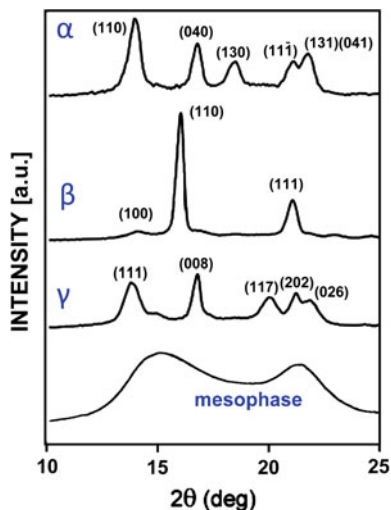
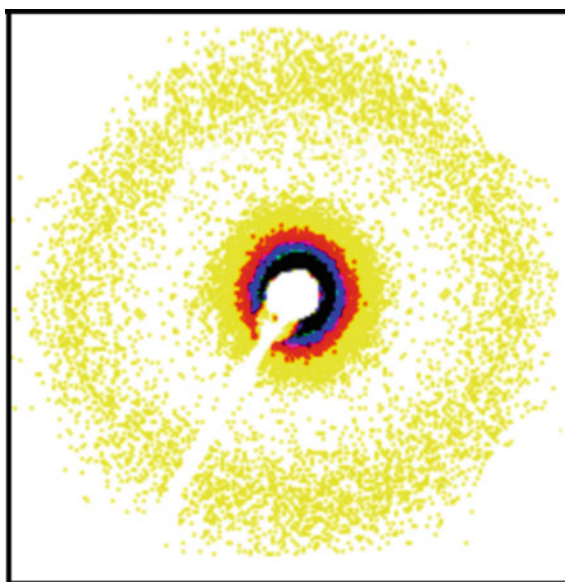


Fig. 4.7 Small angle X-ray scattering pattern from isotactic polypropylene. The ring results from scattering on the periodic lamellar structure. *Authors' own data*



Small angle X-ray scattering (SAXS) is another X-ray technique. The radiation is scattered when passing through the sample and the form of scattering patterns depends on the morphology of polypropylene (Fig. 4.7).

Usually a long period of lamellar stacks, thickness of amorphous and crystalline components in stack (from a correlation function), orientation of lamellar stacks can be determined by this method. Although SAXS and WAXS techniques are typically used for the studies of solidified specimens, but when a source of strong

synchrotron X-ray radiation is available it is possible to examine in situ structure changes during crystallization or melting.

The important technique for the studies of crystallization is **differential scanning calorimetry (DSC)**. Using it is possible to determine peak temperatures of melting and crystallization, crystallinity (from heat of fusion, determined from area under peak), progress of solidification during crystallization (Fig. 4.8).

Since nineties of 20th century an **atomic force microscopy (AFM)** has become one of the tools used for studying polymer crystallization. The combination of high resolution, minimized sample preparation and the non-destructive imaging has allowed visualization of crystallization, melting and re-ordering processes at a lamellar and sub-lamellar scale (i.e. below 10 nm).

AFM method has some drawbacks. First it is a surface technique only. The images are usually obtained slowly, so it is hard to obtain good sample statistics, and not always are possible in situ observations, because the rapid kinetics of crystallization or melting may be incompatible with the slow imaging rates. There are many different modes of operation but the two most commonly used are ‘contact mode’ and ‘tapping mode’ [18]. Application of AFM for studies of iPP morphology is illustrated in Fig. 4.9 and can be found in other various papers [19–21].

Other techniques, such as **infrared (IR)** [23] and **Raman spectroscopies** [24] can also be used to some extent for the detection of crystalline forms. Infrared spectra of semi crystalline polymers include crystallization sensitive bands. The intensities of these bands vary with the degree of crystallinity and have been used as a measure of crystallinity. By measuring the polarized infrared spectra of oriented semicrystalline polymers, information about both the molecular and crystal structure can be obtained. Since the selection rules for Raman and infrared spectra are

Fig. 4.8 Typical DSC scan for metallocene-iPP solid samples. *Authors own data*

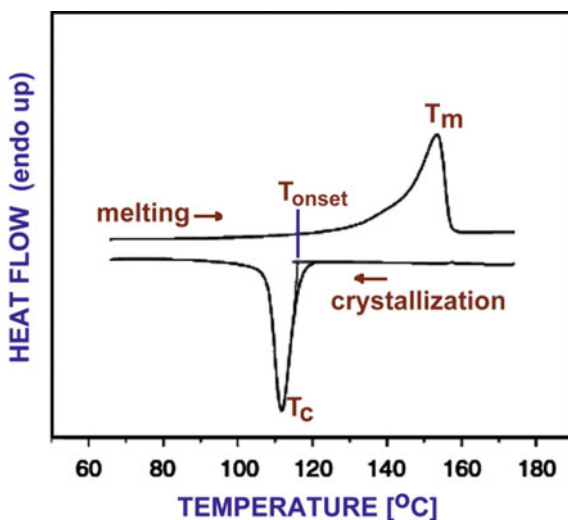
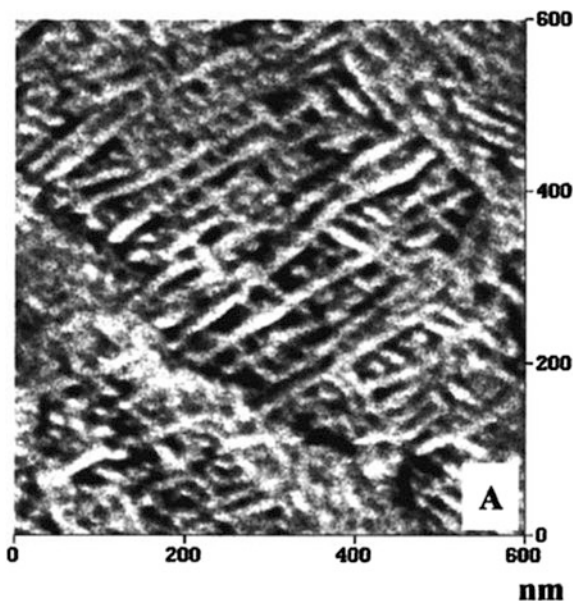


Fig. 4.9 AFM micrographs of slowly cooled iPP showing cross-hatched lamellar structure. From [22], reprinted with permission by American Chemical Society, 2001



different, Raman spectra yield information complementary to the infrared spectra. The Raman spectrum is a scattering phenomenon, whereas the infrared methods depend on transmission, then small bulk, powdered, or turbid samples can be employed [2].

The **density measurements**, with the use for example a gradient column, may be useful for calculations of crystalline phase contents, when as for polypropylene the densities of amorphous and crystalline components are known.

4.3 Polymorphism

Isotactic and syndiotactic polypropylenes can crystallize in many crystallographic forms, which is known as polymorphism. Chapter 2 in this book describes in details the phenomenon, so only the most important for crystallinity studies information are shown here.

Several crystal modifications were observed for **isotactic PP**, including monoclinic α -phase, the trigonal β -phase, the orthorhombic γ -phase, and above mentioned smectic mesophase. All of them share the same 3-fold helix conformation but the spatial arrangements of iPP chains in the crystal lattice varies. A thermodynamically stable phase, predominating under typical processing conditions, is the monoclinic **α -phase**. In the α phase (α -iPP) four different layers are packed along the b-axis. They differ by the helix chirality, up-down orientation (cliniticity), and azimuthal setting. Occasionally, a stacking mistake brings two layers

made of isochiral helices in contact with the helix axes 80° apart (through the vehicle of an epitaxial registry or a rotation twin), which induces a lamellar branching—the only well-documented example of this type in polymer crystallography [25]. The branching of α crystals at the angle of approx. 80° leads to the formation of two populations of lamellae of radial (mother) and tangential (daughter) orientations in spherulitic growth [12, 26] and results in the so-called ‘cross-hatched’ lamellar morphology within spherulites.

The thermodynamically metastable **β -phase** is less frequently observed in commercial grades of iPP products at higher undercooling. The crystal structure of β -modification was established independently by Meille et al. [27] and Lotz et al. [28] as trigonal with unit cell parameters $a = b = 11.01 \text{ \AA}$, $c = 6.5 \text{ \AA}$, $\alpha = \beta = 90^\circ$ and $\gamma = 60^\circ$, containing three isochiral 3_1 helices, which is in contrast to the alternating helical handedness found in α crystal form [13, 25, 29].

The presence of β -form iPP was identified first time by Keith and Padden in 1959 [30]. It was noted that the formation of β -PP was favored by rapidly quenching the polypropylene melt to below 128°C [31]. The β -iPP form usually crystallizes together with the other crystalline phases of iPP and it often exhibits, similar to the α -phase, two melting endotherms in differential scanning calorimetry (DSC). The higher contents of this form can be obtained by crystallization from the melt with the aid of nucleating agents. The other possibilities are: crystallization from melt subjected to shear [32] or crystallization in temperature gradient during zone solidification [33], although no such effect was observed in PP in a constant steady-state temperature gradient [34]. Moreover, the intense nucleation of β -spherulites was observed after cavitation in pockets of melts between spherulites, where negative pressure developed because of density change.

The presence of pure β -PP phase at room temperature was not reported for long time [31], although pure β -PP was observed in the crystallizing polymer between the upper and lower critical temperatures [35, 36], but some α -crystals would form due to conversion of the growth pattern from β to α when the sample was cooled below the lower critical temperature [37]. In 1999 Li et al. [31] doped iPP with 1% of pimelic acid/calcium stearate and crystallized in a two-step isothermal process, first at 130°C and then at 95°C , and finally cooled at the rate of $0.5^\circ \text{C min}^{-1}$. The specimens could be considered as pure β -PP. The heat of fusion of the β -crystal was found to be 168.5 J/g (method: crystallinity calculated from density and DSC data). In comparison, the heat of fusion of the α -crystal in the undoped resin was slightly higher, 177.0 J/g [31].

Because the β -form is metastable with respect to the monoclinic α -form, then it tends to convert to the α -form when the sample is subjected to appropriate thermal treatment [32]. DSC and wide-angle X-ray scattering (WAXS) measurements pointed out that the β - α transition during heating essentially consists of the melting of the β -form and the successive recrystallization in the α -form. DSC measurements, at different heating rates, allowed to confirm that the multiple melting endotherms behavior of the β -phase is correlated to a melting–recrystallization–melting mechanism [32].

The orthorhombic γ -form of PP has a unique structure with nonparallel chain alignment. The lamellae of the γ -phase consist of bi-layers; in adjacent bi-layers chain axis is tilted by approximately 80° against each other, and is inclined by 40° with respect to the lamellar normal [38]. Crystallization of PP in the orthorhombic γ -phase strongly depends upon specific aspects such as molecular structure and crystallization conditions that is pressure and temperature. The γ -phase was observed in very low molecular weight PP [39, 40], in propylene copolymers with small amount of 1-olefine co-units and in the presence of chain irregularities, stereo- or regio-, as those in high molecular weight PP polymerized with metallocene catalysts [41].

The γ -phase content strongly increases with increasing chain irregularity [19, 41], although it also depends on the defect distribution [41]. At fixed defect concentration the dependence of the γ -form content on T passes through a maximum [41–43], which is connected with the temperature dependence of critical sequence length for crystallization; the formation of the γ -polymorph is related to crystallization of relatively short isotactic sequences in extended form enforced by associated chain defects [43]. The occurrence of the maximum was also explained as a result of competing kinetic and thermodynamic effects, the latter related to higher thermodynamic stability of the γ -form and its tolerance of stereo-defects in the cell. According to [42] the effects, which impede the chain-folding in lamellae, enhance the formation of the γ -form because the tilt of chain axis in this form reduces the necessity of chain folding. The γ -phase crystallization is favored under elevated pressure [38, 44, 45], even in highly isotactic PP, independently of molar mass, although it requires also high crystallization temperature, that is a low supercooling [29]. See Fig. 4.10 for comparison.

In addition Lotz et al. [38] observed that tilted γ lamellae can branch from flat-on α -phase crystals.

A few years ago Lotz [47] found a new ε crystal modification of isotactic polypropylene. This form was obtained with a stereodeficient or ‘an-isotactic’ iPP produced with a zirconene catalyst by Rieger et al. [48]. In thin films, most of the PP crystallized as crystals made of α phase backbones with γ phase overgrowths. The new ε form was nucleated by a crystal–crystal growth transition on parent α phase crystals. It was most probably produced with only the highly stereodeficient part of the material. The single crystals of new form were similar to the α form elongated laths, but did not display any of their overgrowths (i.e. $\alpha - \alpha$ lamellar branching or $\alpha - \gamma$ epitaxial relationship). The electron diffraction evidence indicated an orthorhombic unit cell with following parameters: $a = 12.50 \text{ \AA}$, $b = 24.60 \text{ \AA}$, $c = 6.5 \text{ \AA}$, that houses eight stems (space group: Pccn). The chain conformation of this form is the archetypical 3_1 helix of the α , β , and γ forms, but arranged in a near-double-tetragonal packing.

Smectic mesophase or conformational disorder phase is a phase with an extent of order intermediate between the crystalline and amorphous phase [49]. Rapid cooling supports formation of this phase [50, 51] (Fig. 4.11).

The basic crystallographic parameters of main crystallizing forms of PP are presented in Table 4.1 [7].

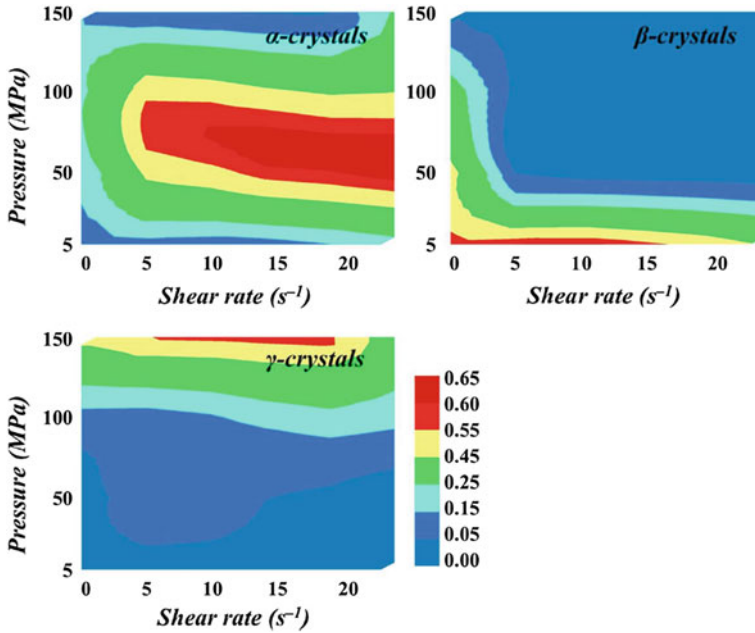


Fig. 4.10 Crystallinities of iPP mixed with β -nucleating agent crystallized at various shear rates ($0\text{--}24\text{ s}^{-1}$) and different pressures (5, 50, 100, and 150 MPa). The crystallinities of α -, β -, and γ -crystals are duplicated with color gradation, where the color change from blue to red indicates the increase in crystallinity. From [46], reprinted with permission by American Chemical Society, 2017

Fig. 4.11 Apparent heat capacity of iPP as a function of temperature, measured on cooling at different rates by fast scanning calorimetry. C-crystalline phase, M-mesophase. From [52], reprinted with permission by Elsevier, 2012

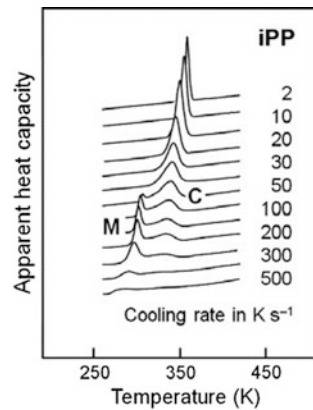


Table 4.1 Basic crystallographic parameters of main crystallizing forms of PP

Form	iPP α	iPP β	sPP
Chain conformation	3_1 helix	3_1 helix	Two fold helix $s(2/1)2$
Unit cell parameters	Monoclinic	Hexagonal	Orthorhombic
Space group	C_{2R}^6-C2/c	$D_3^4-P3_121$	$C 222_1, Ibca$
a	0.665 nm	1.274 nm	1.46, 1.45 nm
b	2.095 nm	1.274 nm	1.56, 1.12 nm
c	0.650 nm	0.635 nm	0.74, 0.74 nm
β	99.3°	120°	90°
The main growth direction	(010)	(300)	
a_o	0.549 nm	0.636 nm	
b_o	0.626 nm	0.551 nm	

Comment In the literature can be found for iPP α also the following values: $b = 2.096$ and $\beta = 99.8^\circ$ [13]

Syndiotactic polypropylene (sPP) was first obtained by Natta [53] as a minor product of the synthesis of isotactic polypropylene with heterogeneous Ziegler–Natta catalyst. For many years sPP was not considered by industry as interesting material because of its poor physical and chemical properties due to the low stereo- and regio-regularities of the macromolecules, low crystallinity and low melting temperature [54]. After the discovery of single center metallocene catalysts in the 1980s the new type of syndiotactic polypropylene, highly stereoregular and regioregular, has been produced. This sPP shows high crystallinity and high melting temperature and some unique elastomeric mechanical behavior.

Syndiotactic polypropylene shows polymorphism. Four different crystalline forms, called I, II, III and IV and a mesomorphic form have been found so far (Table 4.2). Form I, found by Lotz et al. [55], is the stable form of sPP obtained under the most common conditions of crystallization. Form I and metastable form II (discovered earlier) are characterized by chains in $s(2/1)2$ helical conformation packed in different orthorhombic crystalline lattices. Form II has been obtained first

Table 4.2 Crystallographic parameters of syndiotactic PP forms

	I	II	III	IV
Chain conformation	Helical $s(2/1)2$	Helical $s(2/1)2$	Trans-planar	Helical
Unit cell	Orthorhombic $a = 14.5 \text{ \AA}$, $b = 11.2 \text{ \AA}$, $c = 7.4 \text{ \AA}$	Orthorhombic $a = 14.5 \text{ \AA}$, $b = 5.60 \text{ \AA}$, $c = 7.4 \text{ \AA}$	Orthorhombic $a = 5.22 \text{ \AA}$, $b = 11.17 \text{ \AA}$, $c = 5.06 \text{ \AA}$	Monoclinic ^a $a = 14.17 \text{ \AA}$, $b = 5.72 \text{ \AA}$, $c = 11.60 \text{ \AA}$, $\beta = 108.88^\circ$

Based on [54]

^aOriginally [60] proposed the triclinic cell with $a = 5.72 \text{ \AA}$, $b = 7.64 \text{ \AA}$, $c = 11.60 \text{ \AA}$, $\alpha = 73.18^\circ$, $\beta = 88.88^\circ$ $\gamma = 112.08^\circ$. The monoclinic form was proposed by Auriemma et al. [61]

time in oriented fibers from sPP prepared with Ziegler–Natta catalysts [53] and later by removing the tension in fibers initially in the trans-planar form III stretched from highly stereoregular sPP samples. Some years ago the form II sPP has also been obtained in powder samples by crystallization from the melt at 200 bar pressure [56]. Finally, form II has also been obtained by epitaxial crystallization from the melt of single crystals in ultrathin films on the surface of crystals of a low molecular weight substance (2-quinoxalinol) [57]. Forms III and IV are the less stable forms and are observed only in oriented fibers. Form III is obtained by stretching at room temperature and at high deformations of films of metallocene catalyzed sPP. Crystals of the most stable helical form I can transform by stretching into the trans-planar form III [58]. In turn form III transforms into the stable helical forms by annealing the stretched fibers at temperatures above 100 °C and keeping the fibers under tension [59]. Moreover, form III is stable only in the stretched state and transforms into the helical form II by releasing the tension. Form IV was obtained by Chatani et al. [60] by exposing stretched fiber of sPP originally in the trans planar form III to organic solvents. Form IV has been found only in oriented fiber. It transforms into the twofold helical forms by annealing above 50 °C.

4.4 Nucleation and Crystal Growth in General

The process of polypropylene crystallization consists several steps, based on the scheme of nucleation and growth events. The first step is the formation of primary nuclei. Those nuclei may be homogenous, i.e. formed from locally organized polypropylene chains, heterogeneous, when the crystal will grow on the foreign body present in polymer and self-seeded type, when the arrangements of molecules after melting of crystal is not yet fully destroyed and these molecules form a new nucleus during cooling. When the nucleus has the size larger than the critical one it is stable. The growth of crystals occurs on such primary nuclei by a series of secondary nucleation events and spreading of a new crystalline layer on the growth face.

Polypropylene can crystallize from melt (most often) or from solution. Depending on the crystallization conditions single crystals or assemblies of crystals may grow. When PP crystallize from the melt numerous observations confirm that crystal growth rate does not change with time if the temperature is constant and the flow of the melt is not restricted. Some experimental observations for single crystals and spherulites are presented in the next sections, followed by theoretical consideration about the nucleation and crystal growth.

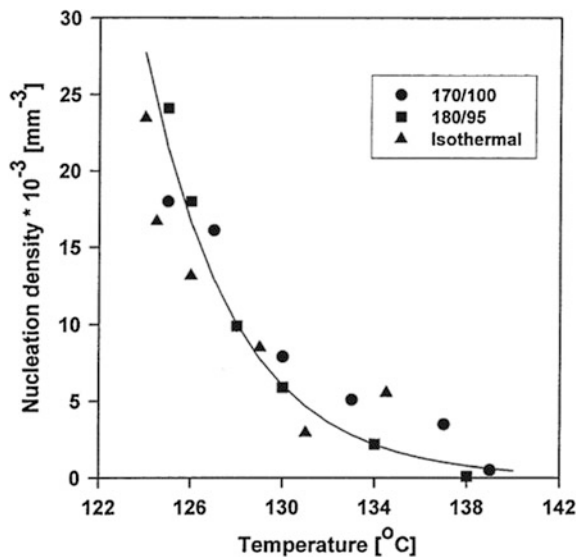
Nucleation of crystals in an undercooled melt, i.e. **primary nucleation**, must overcome a free energy barrier, since the positive surface energy of very small crystals outweighs the negative driving force of crystallization. A **homogeneous** primary nucleation means the creation of a crystal in a pure melt. The kinetics of this nucleation is the product of the probability of the occurrence of a critically sized nucleus and the rate at which the next fragment of molecule (mer) will join the stable nucleus. The homogeneous primary nucleation is rare for crystallization from

the melt or solution, because of the large undercoolings required to achieve a critical nucleus. Experiments to study homogeneous nucleation are best performed by dispersing the melt or solution into near-micron size droplets, many of which are free from impurities that trigger heterogeneous nucleation [62, 63].

Usually the primary nucleation is **heterogeneous**, being controlled by solid impurities (e.g., dust particles, low molecular weight additives) that provide surfaces upon which nucleation can occur easier and faster than by the homogeneous mechanism (Fig. 4.12). The reason for the faster rate is a lower surface energy provided by the impurity, resulting in a reduced size for a critical nucleus. An interesting sort of nucleation is termed **self-seeding** [64]. If the crystalline macromolecular arrangement is not yet completely destroyed after melting, then these ordered fragments of previous crystals may act as heterogeneous elements supporting primary nucleation.

The growth of crystals occurs on primary nuclei by a series of **secondary nucleation** events and spreading of a new crystalline layer on the growth face. Primary nucleation is necessary for initiation of crystallization, however, the controlling factor of the crystal growth is the secondary nucleation of new crystalline layers on an existing crystal. So, the observable crystal growth is the result of two processes, the first being the nucleation of initiating stems on the surface of the crystal, and the second being the coverage of the surface by new stems beginning at the initial stem. The crystal grows macroscopically in the direction normal to its surface while on the molecular level the elementary growth mechanism is the growth along the crystal surface. After completion of a layer on the surface of the crystal a new surface secondary nucleus must be created. After the formation of a stable secondary nucleus, the layer is completed with new stems by the

Fig. 4.12 Nucleation density in iPP crystallized isothermally and in temperature gradients. Determined from microscopic observations of growing spherulites. From [34], reprinted with permission by Springer Nature, 2001



attachment-detachment mechanism. The completion rate, as the layer spreads in the direction parallel to the surface of the crystal, expressed as a difference of attachment and detachment rates of stems to the nucleus on the surface of the substrate, is not a strongly dependent function of temperature.

The kinetic nucleation theory with chain folding now provides the best general tool for understanding the nucleation and the growth of polymer crystals at isothermal conditions from unstrained melt [65]. The important element of crystallization is the movement of molecules toward crystallization site. Widely accepted description of chain motion and transport in the melt is by the reptation concept [66].

4.5 Structure of Single Crystal

The study of the growth of polymer single crystals historically was initiated first for polymers crystallized from dilute solution, with the use of transmission electron microscopy, electron diffraction and X-ray diffraction for examining growing structures. More recently also other techniques such as optical microscopy and AFM are used for morphology characterization.

Polymer **crystallization from very dilute solutions** (i.e. <0.1 wt%) produces crystals which are thin in the chain-axis direction and have faceted, more or less equi-axed shapes (rhombus, hexagon, rectangle, square) normal to the chain axis. These habits reflect the symmetry of the underlying crystal lattice, as is usual for growth under near-equilibrium conditions. As the polymer concentration is increased, the lateral shape changes to produce at first less regular facets, and then extended and ultimately ribbon like crystals [11]. Polymer lamellae commonly create new lateral layers by a spiral growth mechanism. The presence giant screw dislocations, i.e. those with Burgers vectors of magnitude equal to the lamellar thickness, are frequent in polymer crystals grown from solution, especially at higher undercooling. The screw dislocation presents two steps, one on each side of the crystal, to which molecules may add without creating new surface nuclei [67].

The solvents used in polymer solutions are usually organic compounds with small molar volume. Polypropylene is the polymer which in principle can be dissolved only using hot solvents. The major added variable in crystallization from solution is the concentration [68, 69], however, the particular solvent can have a pronounced effect on morphology. It was observed that more concentrated solutions give rise to complex aggregates of multiple lamellar crystals such as axialities [67].

Isotactic polypropylene crystals were grown from dilute (0.001–0.004% by weight) solutions in α -chloronaphthalene. The best shape crystals have been obtained for PP with sharp fraction ($M_w/M_n < 1.05$) [70]. Using similar solution Kojima [71] obtained lath-shaped lamellar crystals when PP had $M_w = 600,000$ or $240,000$ g/mol, but not for samples with $M_w = 82,000$ or $44,000$ g/mol. Crystallization process was here isothermal at 130°C with time of 20 h.

Wittmann and Lotz [3] obtained lamellar single crystals of iPP from dilute solution in α -chloronaphthalene. Monoclinic α -isotactic polypropylene monolayers grow preferentially along the a^* direction. When were cracked perpendicular to a^* , fibrils were pulled out revealing that folding was within the long (010) planes, not in the narrower (100) growth faces [40]. Kojima [71, 72] used carbitol solution (0.005 mass%) for similar experiments. The single crystals were also grown in thin molten film [73] or thin uniform films grown in solution [74]. The degree of stereoregularity is a factor determining the structure of crystals growing isothermally from α -chloronaphthalene solution. Electron micrographs show that with decreasing fraction of isotactic pentads the perfect rectangular shape of the single crystal is lost and the presence of more complex morphologies is observed.

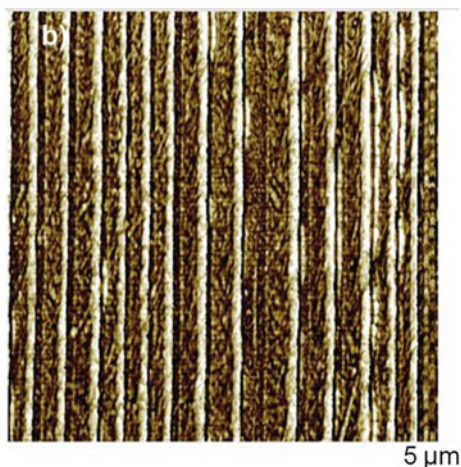
The equilibrium melting temperature T_m° of crystals also depends greatly upon the isotactic pentad concentration. For 100% concentration the extrapolated value of T_m° was 181 °C. T_m° decreased about 1 °C per 1% decrease in the isotactic pentad population [75]. The earlier studies of single crystals were conducted for polypropylene synthesized using Ziegler-Natta catalysts. Xiao and Sun [69] examined metallocene iPP ($M_w = 250,000$ g/mol, $M_w/M_n = 2.3$, 95% tacticity, $T_m = 145$ °C) dissolved in *n*-cyclododecene at 160 °C to reach a concentration of 10 mass%. The solution was then maintained at a temperature within the range of 120–140 °C for 30 min up to 1 h and was subsequently cooled to room temperature at a rate of approximately 2 °C/min. Thin monoclinic crystals of size 0.6×0.4 μm were grown. It has been demonstrated that metallocene iPP exhibits the faster crystallization rate in the very dilute solution than in the concentrated solution (effect of entangling) [68, 69].

Isolated single **crystals of isotactic polypropylene grown from the melt** were studied by light microscopy and atomic force microscopy [76]. Usually the growth of single crystals from melt is conducted in a very thin film [67]. When a polymer is confined in very thin film the spherulitic growth is not possible, only the crystals may growth.

Because of spatial confinement and specific interaction at interfaces, characteristic features of the crystallization process (e.g., crystallization kinetics and the resulting crystal morphology) in thin films are often different from what is found in bulk [77] (see Fig. 4.13). In particular, in the study of thin films much attention has been paid to diffusion-controlled crystal morphologies. Typically, when polymers crystallize in a thin film, crystals with various structures, including faceted, dendritic, seaweed, and finger-like patterns, are observed. The evolution of those morphologies is typically related to a gradient field at crystal growth front formed in thin films [78].

Growth spirals occur in polymer single crystals grown from the melt, but these are easily observed only at low undercooling. An assembly of faceted lamellae is called a hedrite, which is fundamentally the same as the multilayer crystal grown from solution, although the basal fold surfaces are more disordered. Hedrites belong to axialites [11].

Fig. 4.13 AFM phase image of partial cross-sections of 65-layer 1/2 skin polypropylene/polycarbonate (75/25) 25 μm film. Lamellar crystals are clearly seen. From [79], reprinted with permission by Elsevier, 2014



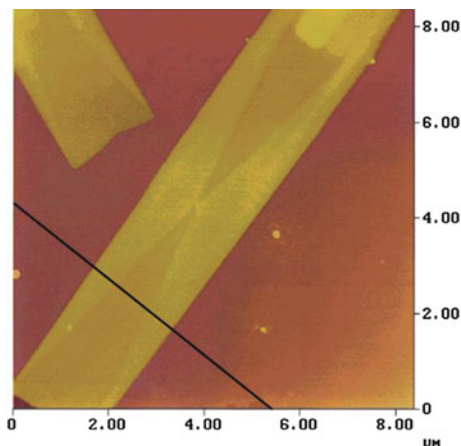
Investigations of the morphology of iPP lamellar crystals grown in thin films can be traced back to the 1960s. [73]. The single crystals of PP obtained by Yamada et al. [76] had a rectangular shapes when were crystallized at high temperatures ($T_c > 155$ °C). The width of crystals increased with decreasing T_c , and their shape became hexagonal in temperature below 130 °C. The single crystals had sectors differing in thickness. The growth rate along the a^* axis (G_{a^*}) agreed with the growth rate of spherulites. The rate had two inflection points on the plots versus $(\Delta T)^{-1}$. The inflection at lower temperature corresponded to the transition between regimes II and III, and the second one was accompanied by an inflection of the growth rate in b-axis direction, G_b . The obtained crystals were surrounded with flat surfaces. In AFM images were not recognized the kinetic roughening in the regime III. The inflections of G_{a^*} and G_b caused a complicated shape change of the aspect ratio, having a minimum at around 135 °C [76].

Thin film of iPP (12 nm thick) can be also prepared by spin coating of 0.25 wt% xylene solution on silicon wafer [78]. Single crystals of the rare γ phase of iPP have been produced by the growth in thin film of melt [38].

In the past few decades, single crystals of syndiotactic polypropylene grown from a thin film, with two pairs of (010) and (100) sectors, which have boundaries along the diagonals of the rectangular shape crystals, were studied in details [54, 55, 80–82] (see Fig. 4.14).

The early studies showed that single crystals grown from solutions of irregular sPP were narrow and elongated, with ill-defined edges. Samples of lowest stereoregularity exhibited dendritic-like structure. Chain axis was nearly perpendicular to the fold surface of crystals [83]. Lotz and Lovinger [55] grew single crystals from melt and these crystals were larger and have more regular habit (rectangular) than crystals from solution. The electron microscopy showed that the crystallographic b axis is parallel to the long axis of the crystals (grown from both solution and melt). The same authors also showed that the morphology of crystals/growing structures

Fig. 4.14 AFM image of syndiotactic PP lamellar single crystal with sectors grown from the melt at temperature of 130 °C. From [82], reprinted with permission by American Chemical Society, 2000



depends on the crystallization temperature: from very large rectangular crystals at highest temperature (105 °C) through axialitic to spherulitic (at 70 °C) [84]. The morphology of crystals growth at high temperature was observed by transmission electron microscopy and atomic force microscopy and it was visible a typical highly faceted regular lath-shaped crystal structure, with micro sectors on the top surface [81, 82].

4.6 Structure of Spherulite

The spherulites are most common form of crystalline aggregates formed during solidification of PP from melt or solution in conditions of a large undercooling. Their name is from a spherical symmetry of ideal spherulite. Below the main features of a single spherulite are described, the discussion about formation of full spherulitic structure is presented later in this chapter.

During cooling from melt, the first structure that forms by primary nucleation is the single crystal creating of the spherulite core [11]. Primary nucleation at usual undercooling occurs on heterogeneous solid particles. Heterogeneous nuclei are usually unknown impurities [85], but they may be stable polymer crystals that are generated by self-seeding [67, 86]. The initial crystal rapidly degenerate into sheaf-like structures during the early stages of the growth of polymer spherulites [87]. These transitional, multilayered structures represent an intermediate stage in the formation of spherulites. Creation of the spherulite core is followed by the radial growth of lamellar crystals at a constant rate at constant temperature. Macromolecular chains are lying parallel to the smallest thickness of the growing crystals with folding of those chains. This is the direction of *c*-axis of the crystals which is normal to the radial growth direction of the spherulites and perpendicular to the lamellae flat surfaces. It shows the resemblance to single-crystal structures [2].

The thickness of lamellae in the chain direction is order of 10–20 nm. In microscopic scale the lamellae are locally nearly parallel and uniformly thick, which is the reason that lamellar stacks give characteristic reflection when scatter X-ray radiation.

The crystals in spherulites when grow at constant temperature have a constant cross section, however, there are one or more processes generating new, laterally adjacent fibrils. Those phenomena cause to fill the space of a spherulite uniformly assuming spherical shape. Possibilities for doing so include non-crystallographic branching (most often), heterogeneous nucleation on existing fibrils, and growth about a giant screw dislocation (with the magnitude of the Burgers vector equal to the crystal thickness; observed for polyethylene) [11]. The spherulite growth proceeds with a few dominant lamellae advancing first into the melt, creating templates for subsequent crystallization in the form of subsidiary, or infilling, lamellae [88]. Usually the new lamellae, initiated at low-angle branch points on the old lamellae, tend to keep the spacing between the crystallites constant. Keith and Padden emphasized [89] that branching in spherulites is irregular and occurs at small, non-crystallographic angles, as opposed to regular branching in dendrites. The remaining space between lamellae contains uncrystallized, amorphous material or voids [11].

Details of lamellar arrangement in spherulites were disclosed by electron microscopy and atomic force microscopy (AFM) of etched samples. PP crystals in spherulites grow with certain crystallographic faces depending of the thermodynamic parameters. The (110) plane of monoclinic α crystals is the growth face at low undercooling while at higher undercooling also other planes are possible, including the most probable (010) plane.

At a temperature below 155 °C in the spherulitic crystallization of α form iPP, in addition to the long radial lamellae (R-lamellae), the short tangential lamellae (T-lamellae) at an angle of 80° grow epitaxially on the lateral (010) planes of R-lamellae. This crystallographic branching leads to the **cross-hatching** phenomenon [26]. Cross-hatched texture is unique for α form and has not been observed in other crystalline modifications of isotactic polypropylene. The cross-hatching density decreases with increasing crystallization temperature. At low temperature, the tangential lamellae develop at almost the same time as the radial lamellae. The thicknesses of radial and tangential lamellae are thus similar. At high temperature, the cross-hatched lamellae grow later than the radial lamellae, and therefore, are thinner. Radial lamellae are then about 40 nm thick, while the tangential lamellae are only 25–30 nm thick [7]. The thicknesses of radial and tangential lamellae depend also on the molecular mass of iPP (see Fig. 4.15).

It was observed that the cross-hatching density decreases with decreasing isotacticity. The reason for it is increasing irregularity of basal (010) planes of radial lamellae. However, the thickness of radial and tangential lamellae increases with decreasing isotacticity. In β crystalline modification of iPP where the cross-hatching does not exist lamellae thickness ranges from 21 to 30 nm [7].

The radially growing lamellae form crystallization front, representing the assembly of growing faces of crystals. A spherulite growth rate measurements is

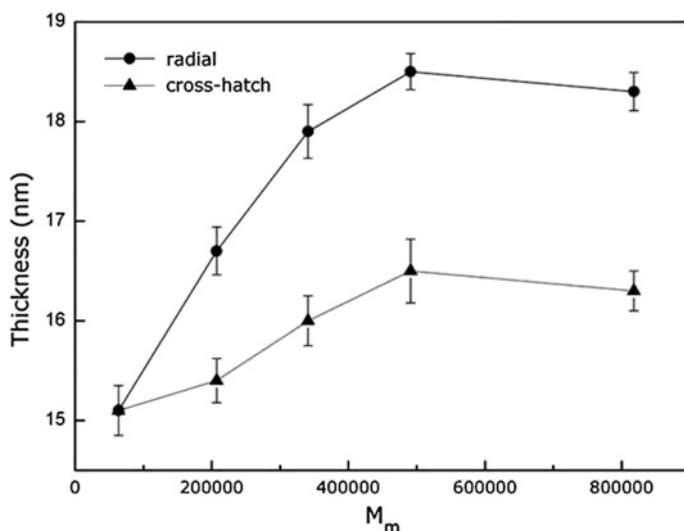


Fig. 4.15 Lamellar thickness as a function of molecular mass (M_m) for crystallization of α -form iPP at 140 °C. Upper curve—radial lamellae, lower curve—cross-hatching lamellae. From [90], reprinted with permission by Elsevier, 2009

based on the determination of the position of crystallization front in successive time intervals [91]. Because the lamellae grow in radial direction then the spherulite growth rate is equivalent to crystal growth rate. Under isothermal conditions the spherulite growth rate tends to assume constant level, so the radius of isolated spherulites increases linearly with time until the growth is limited by the presence of other spherulites. Usually the polypropylene spherulites have diameter in the range of 5–100 μm .

Because the spherulites are assemblies of crystalline, birefringence elements they are easily visible and analyzed using polarized light microscopy. When the spherulites are examined with polarized light microscope an extinction cross is observed, sometimes called a *Maltese cross*. This extinction is centered at the origin of the spherulite, and the arms of the cross are oriented parallel to the vibration directions of the light microscope polarizer and analyzer [2]. The Maltese cross observed in polarized light microscopy is invariant under rotation of the spherulite about the optical path. The decrease of cross-hatching in α spherulites with the elevation of crystallization temperature is reflected in the spherulite birefringence changing from positive to negative [26] (typical images shown in Fig. 4.16).

Padden and Keith [30, 93] were first which classified spherulites according to their birefringence, showing that the growing structures depend on crystallization temperature (Table 4.3).

In addition to the Maltese cross, spherulites may exhibit regularly spaced concentric rings when formed under certain conditions [11]. Such spherulites are called **banded spherulites**. Concentric light–dark rings in polarized light micro-graphs

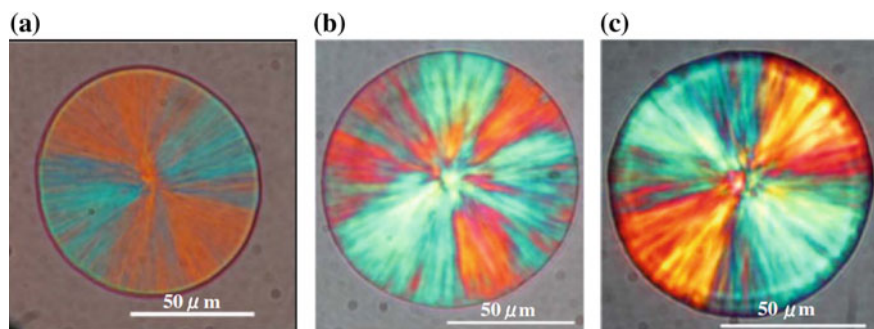


Fig. 4.16 Optical micrographs of a iPP sample crystallized at **a** 120 °C positive spherulite, **b** 130 °C mixed spherulite and **c** 150 °C negative spherulite. From [92], with the permission of Springer Nature, 2008

Table 4.3 Types of iPP spherulites

Spherulite type	Banding	Birefringence (Δn)	Crystallization temperature (°C)
α_I	No	0.003	<134
α_{II}	No	-0.002	>138
α_{III}	No		134–138
β_{III}	No	-0.013	<128
β_{IV}	Yes	-0.023 (bright) and -0.002 (dark)	128–132

were the first experimental indication that the radial growth of polymer spherulites proceeds with twisting of the ribbon-like crystals. The pitch of this twist is constant for isothermal growth and, most remarkably, essentially in phase for all radial directions [11]. The banding is not observed in α -form iPP spherulites, but at some conditions it may be visible in β form spherulites [26].

Two types of β -iPP spherulites can form: the radial and the ringed spherulites, both with strong negative birefringence. Negatively birefringent β form spherulites, composed of R-lamellae only, were observed in iPP samples crystallized below 140 °C (see Fig. 4.17).

The β phase exhibits banded spherulites, over a small range of T_c near 130 °C (Fig. 4.18) [11, 26]. The spacing of bands varies from 75 μm at 125 °C to 90 μm at 133 °C. Curiously, these spacing passed through a minimum of 60 μm at 128 °C (values for polymer of molecular weight 178,000 g/mol) [95].

When the undercooling is relatively low, the trigonal β -polymorph of iPP crystallized at 135–140 °C with a specific nucleating agent creates many objects known as hedrites [21, 97]. Such low birefringent polyhedral aggregates was named by Geil in 1958 [67]. Hedrites exhibit regular polygonal forms.

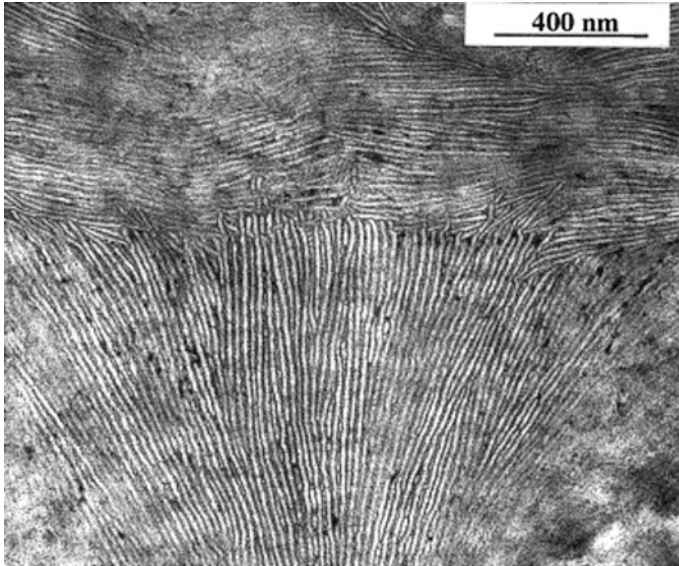
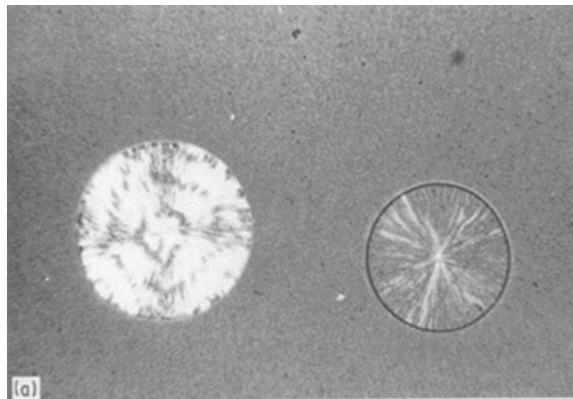


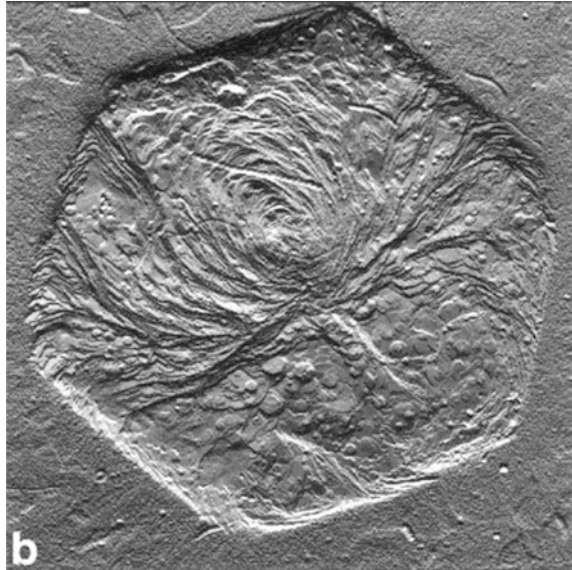
Fig. 4.17 Structure of β -iPP spherulite boundary; lamellae of the neighboring spherulites are perpendicular. From [94], reprinted with permission by John Wiley and Sons, 1999

Fig. 4.18 Structure and melting feature of α and β spherulites grown by stepwise crystallization. Spherulite formed at the first temperature step ($T_d = 135^\circ\text{C}$). From [96], reprinted with permission by Springer Nature, 1992



The appearance of the hedrites depends remarkably on the direction of view and the maturity of the structure (Fig. 4.19). Several forms have been recognized. They are mainly: (i) hexagonites in hexagonal shape with weak birefringence, (ii) axialites with strong negative birefringence, (iii) ovalites in oval form developed from the axialites in later stage of crystallization, and (iv) quasi-spherulites developed either from hexagonites or axialites [49]. These hedrites are regarded as the precursors of β -spherulites since transformation of them into spherulites generally takes place at later stages of the growth [98].

Fig. 4.19 Deflection AFM image showing a hedrite crystallized at 140 °C. From [21], reprinted with permission by John Wiley and Sons, 2000



Mezghani and Phillips [45] showed that iPP crystallizes under elevated pressure in the γ -form positively birefringent spherulites, composed of feather-like structures radiating from spherulites centers. The individual γ lamellae inclined at an angle of 70° to the radial direction are supposed to grow epitaxially on earlier formed γ lamellae or on α radial lamellae.

The spherulitic structures were observed in syndiotactic polypropylene by polarized light microscopy at relatively low crystallization temperatures, whereas single lamellar crystals were observed at higher temperatures [99]. Rodriguez-Arnold et al. [99] carefully checked that in the case of sPP no morphological changes (which occur for some polymers) and no change of the crystal growth front plane occur during the regime II/III transition. Electron diffraction experiments have, indeed, indicated that the growth direction of spherulites is always along the b axis, both below and above the regime transition temperature.

4.7 Shish-Kebabs

The so-called shish-kebab morphology is a familiar feature of polymers crystallized under flow conditions [49, 100]. Shish-kebabs structures grow from melt both in α [100] and β form [101]. During process of melt flow, because of the large orientation and stretch molecules change the random coil conformation and form dense fibrillar aggregates. These aggregates (bundles of molecules) are the precursors of shish-kebab. Literature data indicate that the lifetime of these precursors is much longer than the rheological time scale even when the temperature is above the

melting point of the material. The evolution of fibrillar precursors is very sensitive to external conditions. At sufficiently large undercooling, obtained by lowering the temperature or by increasing the pressure, they rapidly crystallize, following a pathway dictated by the highly anisotropic molecular conformation, and transform into shish.

The final morphology of shish generated in isotactic polypropylene (iPP) at very high shear rates was investigated already in the early 1980s by Schultz et al. [102] and Petermann et al. [103] using a combination of TEM and SAXS. They demonstrated that shish are semicrystalline aggregates where high density (crystalline) domains alternate with low density (disordered) domains in the longitudinal direction and that this density modulation is characterized by a periodicity of ~ 10 nm. The origin of the density modulation is attributed to the initially defected nature of shish in combination with the collective alignment of molecules along the shish backbone [104].

When the stretched molecular chains are formed into extended chain 'shish' crystals, the overgrowth of folded chain 'kebab' crystals is initiated [49]. The extended chains of 'shish' act as row nuclei [105]. Chain folded lamellae, oriented, to a first approximation, perpendicular to the shear flow direction, are produced by epitaxial nucleation on the surfaces of 'shish' structures [106].

The adjacent lamellae are generally parallel to each other, but being separated by a well-defined interval of a few nm [100]. This is an inherent feature which is also found, though with larger separation dimension of 100 nm, in shish-kebabs grown from perturbed solutions [88]. The morphology of shish-kebabs depends on the shear stress. Under low stress the distance of kebabs is large (16 nm) and the thickness of kebabs is lower than shish structure. With increasing shear stress, the kebabs are packed more densely. The relaxation time determines the length of shish crystals. When it is longer the shish structure shortens through fracturing into several parts. The melting experiment showed that non-oriented lamellae of PP (e.g. in spherulites) melt at 167 °C, while kebabs melt at 174 °C and shish at 180 °C [49].

4.8 Nucleation Theories

The most widely accepted theory of nucleation and crystallization is the kinetic theory by Hoffman and Lauritzen [107–109] based on the assumption that chain folding and lamellar formation are kinetically controlled and due to this the growing crystals are not in equilibrium.

The idea of primary nucleation is based on the assumption that thermal fluctuations in an undercooled melt can overcome the barrier caused by the surface free energy of crystals. At a constant volume and energy, the probability that a nucleus of a given size exists is a function of the entropic change, which is proportional to $\exp(\Delta S/k)$ (where k is the Boltzmann constant). At constant temperature and pressure, the probability that a nucleus of given size exists is proportional to $\exp[-\Delta G/(kT)]$.

Turnbull and Fisher [110] derived an equation for the rate of nucleation, i , based on the crystal model, and this equation is dominated by two opposing factors: the free energy of the nucleation barrier ΔG and the free energy of activation ΔG_η (Eq. 4.3):

$$i = (NkT/h) \exp[-(\Delta G + \Delta G_\eta)/(kT)] \quad (4.3)$$

where h is the Planck constant, N number of uncrystallized elements that act as single units which participate in the nucleation process. The above dependence has also application to heterogeneous secondary nucleation [111].

The sketch of chain folded crystal according to [107] is shown in Fig. 4.20.

On this picture σ_e is the fold surface interfacial free energy, σ is the lateral surface interfacial free energy, a single chain making up the entire crystal, l and x are crystal dimensions. It is assumed that rectangular crystal is formed by one long macromolecule and that surroundings is the melt. A free energy of formation of a single crystal is (Eq. 4.4):

$$\Delta G_{cr} = 4xl\sigma + 2x^2\sigma_e - x^2l\Delta f \quad (4.4)$$

where Δf is bulk free energy of fusion, which can be estimated from the entropy of fusion ΔS with assumption of independence of heat fusion Δh of the temperature (Eq. 4.5):

$$\Delta f = \Delta h - T\Delta S = \Delta h - T_m\Delta h/T_m^\circ = \Delta h(T_m^\circ - T_m)/T_m^\circ \quad (4.5)$$

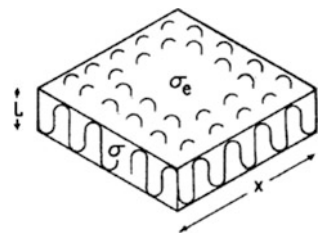
T_m is here a melting temperature, T_m° equilibrium melting temperature, i.e. melting temperature of ideal, infinite size crystal. Because at melting temperature $\Delta G_{cr} = 0$ the Eqs. 4.4 and 4.5 give (Eq. 4.6):

$$4xl\sigma + 2x^2\sigma_e = x^2l\Delta h(T_m^\circ - T_m)/T_m^\circ \quad (4.6)$$

It may be assumed that $x \gg l$ then the first term of Eq. 4.3 can be neglected and (Eq. 4.7):

$$T_m = T_m^\circ [1 - 2\sigma_e/(\Delta hl)] \quad (4.7)$$

Fig. 4.20 The sketch of chain folded crystal, redrawn according to [108]



Equation 4.7 is known as Thomson-Gibbs and is often used for calculation of the crystal thickness l , from melting temperature data. It also may be used for calculations of σ_e , if the thickness of crystal and equilibrium melting temperature are known [2].

The temperature dependence of the secondary nucleation rate at high and moderate crystallization temperatures is determined by the free enthalpy of formation of critical size nucleus on the crystal face. This enthalpy is proportional to $T_m^\circ/(T\Delta T)$. The expression for the secondary nucleation process predicted by the kinetic nucleation theory is as follows (Eq. 4.8):

$$I = (N_o \beta_g p_i) / (a_o n_s) \exp[-4b_o \sigma_e T_m^\circ / (\Delta T \Delta_h f k T)] \quad (4.8)$$

where N_o is the number of reacting species at the growth front, $\beta_g = (K/n)(kT/h) \exp[-Q_D^*/RT]$, n is the number of macromolecule segments in the melt, n_s is the number of stems of width a_o , h is the Planck constant, and Q_D^* is the activation energy for reptation. K is a constant usually of the order of unity as determined from the experiments. T is the temperature of crystallization and ΔT is the undercooling.

The Hoffman's theory describes the secondary nucleation process on an existing surface (primary nucleus) and further crystal growth [112–115]. The starting point was the observation that fold surface interfacial free energy σ_e may be determined from Thomson-Gibbs equation if only the dependence $T_m = f(1/l)$ is known and the heat of fusion is known [107]. According to this theory (see Fig. 4.21a) at high crystallization temperature one surface nucleus is deposited (with time rate i) on the substrate and the growth occurs by completion of layer thickness b on the surface of substrate.

The surface nucleus originates by a polymer segment or set of segments from melt or solution attaching itself to the crystal surface (or substrate) and then coming into crystallographic register with the substrate forming the first stem at the cost of $2bl\sigma$. The molecule then folds and start to crystallize at the position adjacent to the first stem (most probable due to energy reason). By repeating the addition of stems a surface nucleus attains the stability and spreads in the direction g (see Fig. 4.21a). Not only one but many molecules can participate in completing the surface strip to the substrate length L [107].

In Fig. 4.21 G is the growth rate, g is the substrate completion rate, a and b are the molecular width and layer thickness, respectively. The quantity l refers to the initial fold thickness of the lamellae. The portion of chain occupying the length l is called a stem. The molecules forming new layer are pulled out from melt or solution and this process is characterized by reptation rate $r = (l/a)g$. The free energy of the formation of surface nucleus has a maximum when the first stem is attached and with increasing number of stems it assumes the stability.

The free energy of crystallizing chain folded surface nucleus, i.e. v stems and v_f folds ($v_f = v - 1$), is (Eqs. 4.9 and 4.10):

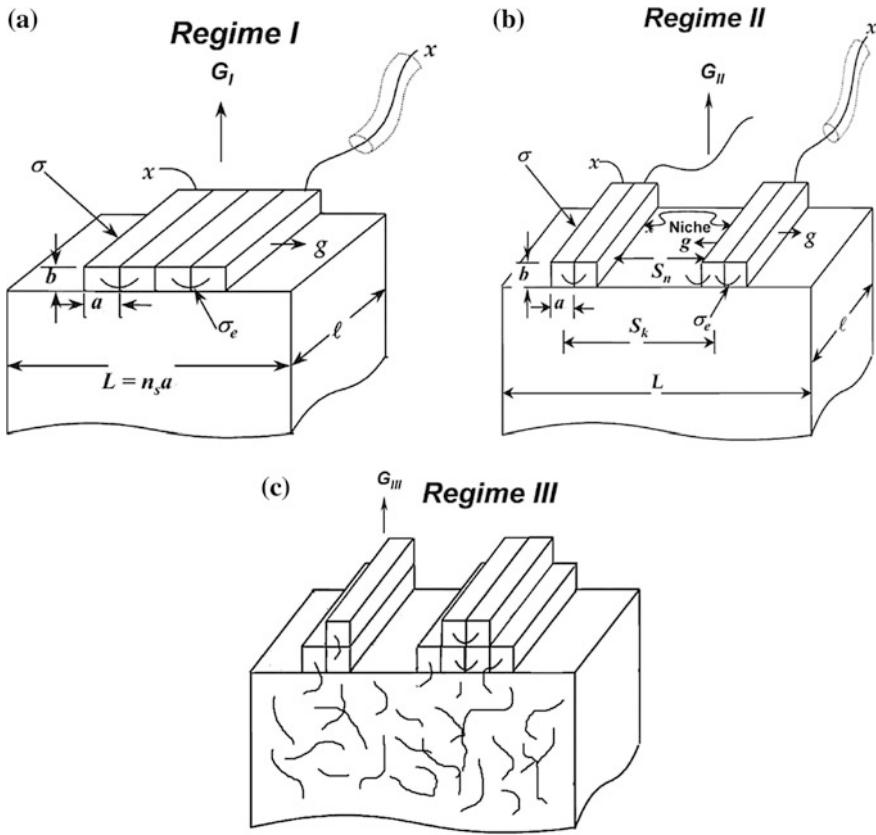


Fig. 4.21 Schematic drawings of how polymer crystal growth takes place in three regimes: **a** regime I; **b** regime II; and **c** regime III. The ‘x’ represents chain ends. **(a)** and **(b)** reprinted from [108, 116] with permissions of Elsevier, 1982 and 1983

$$\Delta G_v = 2bl\sigma + 2v_f ab\sigma_e - vabl\Delta f, \tag{4.9}$$

where for large number of stems $v_f = v$ and

$$\Delta G_v = 2bl\sigma + vab(2\sigma_e - l\Delta f). \tag{4.10}$$

According to Hoffman the overall growth rate during secondary nucleation and crystallization is given by (Eq. 4.11):

$$G = biL = bian_s \tag{4.11}$$

where n_s represents number of stems filling the surface, i is the rate of deposition of surface nuclei.

The above derivation was conducted with the assumption that new secondary nucleation on the surface of crystal (substrate) is possible only after filling the growing layer by stems. This occurs at low undercooling and that range of temperatures is known as regime I of crystallization. When the undercooling is higher it is possible that multiple surface nuclei may occur in time of layer filling on the same crystallizing surface (Fig. 4.21b). It is because the rate of nucleation is larger than the crystallization rate of each molecule.

The rate of lamellae growth G is different when the crystallization of new layer proceeds with more nucleation acts. It occurs at higher undercooling of melt and the corresponding range of temperature is known as regime II. Growth rate of lamellae at this regime, G_{II} is (Eq. 4.12):

$$G_{II} = b(2ig)^{1/2}, \quad (4.12)$$

where g is the completion rate of a layer and could be identified in terms of the nucleation process $g = a(A - B)$, where A and B being attachment and detachment rates, respectively.

The number of nucleation sites per centimeter in regime II is given by Eq. 4.13:

$$N = (i/2g)^{1/2}. \quad (4.13)$$

Later the existence of regime III at lower crystallization temperatures was discovered. In this regime the nucleation on the surface of growing crystal is so intensive that a new layer on crystal surface may be initiated before completion of the previous one. In regime III the chains do not undergo repeated adjacent reentry into the lamellae but have only a few folds before re-entering the amorphous phase. Then they are free to re-enter the same lamella, or go on to the another lamella. The crystal growth rate in this regime G_{III} is given by (Eq. 4.14):

$$G_{III} = biL' = bi'n'_s a, \quad (4.14)$$

where n'_s is the mean number of stems laid down in the niche adjacent to newly nucleated stem, i' is the nucleation rate, L' is the effective substrate length ($\sim(2-3)$ a) [65], i.e. is the effective length of a niche between neighboring secondary nuclei on the growth face. In general L' is considerably smaller than L [7].

Since the Hoffman-Lauritzen theory was originally proposed, it has undergone modifications to accommodate new experimental findings. The one change was in response to the “ δl catastrophe” [111, 114]. Based on the first version of the H-L theory, one expects that the lamellar thickness goes to infinity at $\Delta g_f = 2\gamma/a_0$, where g_f is the bulk free energy density, γ is the lateral surface free energy density, a_0 is the stem width. This can be overcome by introducing a parameter ψ that divide the free energy of crystallization to the free energy of stem attachment, and the remainder which is released during subsequent rearrangement of the attached stem [111].

It is obvious that the radial growth rate of lamellae forming spherulites is dependent on the difference between the crystallization temperature T and equilibrium melting temperature T_m^0 , so it can be described by the Eq. 4.15:

$$G = G_0 \exp[-U^*/R(T - T_{oo})] \exp[-K_g/T(T_m^0 - T)] \quad (4.15)$$

where R is the gas constant, U^* is the activation energy for diffusion of macromolecule segment across the melt-crystal surface, T_{oo} is the temperature at which the molecular motion ceases, $T_{oo} = (T_g - 30 \text{ K})$.

The observable growth rate G is a function of the degree of undercooling and depends on the basic relationship between the nucleation rate i and rate of layer crystallization g . It means that constant K_g depends on the regime of crystallization (Eqs. 4.16–4.18):

– in regime I:

$$K_{gI} = 4b\sigma\sigma_e T_m^0 / (\Delta hk) \quad (4.16)$$

– in regime II:

$$K_{gII} = 2b\sigma\sigma_e T_m^0 / (\Delta hk) \quad (4.17)$$

– in regime III:

$$K_{gIII} = 4b\sigma\sigma_e T_m^0 / (\Delta hk) \quad (4.18)$$

where k is the Boltzmann's constant. Taking the log of Eq. 4.15, one obtains

$$\log G = \log G_0 - U^*/[2.303R(T - T_{oo})] - K_g/[2.303T(T_m^0 - T)] \quad (4.19)$$

The overall features of crystallization regimes is well illustrated by a plot of $\log G + U^*/[2.303R(T - T_{oo})]$ against $1/[2.303T(T_m^0 - T)]$ [65].

Microscopic observations of isothermal crystallization showed that in isotactic α -form PP all three regimes can be distinguished (see Fig. 4.22). Macromolecules are reeled out of the melt mainly in regime I and regime II of crystallization which is connected with the completion of layer on the crystal face in a chain folded manner.

In regime III the chains are displaced only for short distances as required by the number of chain folds in secondary nuclei. Crystallization in regime III of PP is preferred for improved mechanical strength because of many chain links between neighboring crystals and cilia. Since the regime transition is controlled by the relative rates of secondary nucleation and layer completion, any factor (e.g. crosslinking, grafting) that affects either of these rates will alter the temperature at which the transition occurs. iPP in α -form shows the transition temperatures: regime III/II around 137–138 °C and regime II/I shows up around 155 °C only for

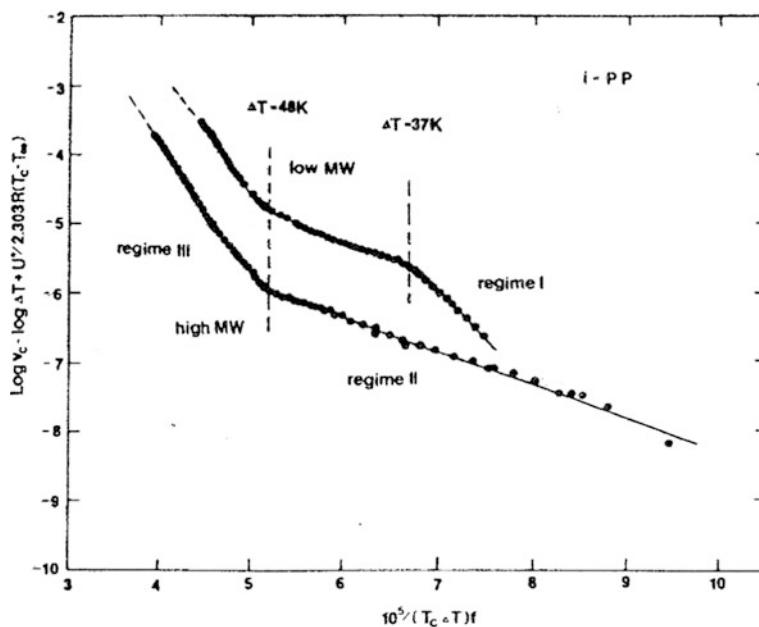


Fig. 4.22 Plot of $\log v_c + V^*/[2.303R(T_C - T_{\infty})] - \log(\Delta T)$ versus $1/[T(\Delta T)f]$ for both low and high molecular mass iPP fractions. The low molecular mass fraction ($M_n = 15,000$ g/mol) shows three regimes, and the high one, ($M_n = 300,000$ g/mol), two regimes. From [117], reprinted with permission by American Chemical Society, 1990

low-molecular fractions of PP. Crystals of β form show the change between regime II and III in the temperature range of 123–129.5 °C [7].

The description of crystallization of PP from melt requires consideration of movements of macromolecules in a molten polymer. The long polymer chains are entangled in the melt. The displacements of macromolecules called ‘reptation’ are possible along a virtual tube circumscribed around a macromolecular chain. Other movements are more difficult since they require extensive cooperation of other chains in the vicinity. The entanglements with neighboring chains, beside the friction of chains against the tube, are additional impediments for the chain movements. Entanglement knots constitute a hindrance for chain transport in the course of crystallization. The chain displacement during crystallization is enforced by crystallization forces after the secondary nucleation event. Calculations showed that in the case of the disentangled chains, the crystallization forces easily overcome the chain friction against the tube. The reptation motions of other macromolecules are so slow in this time scale that the chains can be considered as motionless [7]. The values of free energy were determined for iPP and sPP (Table 4.4).

Miller and Seeley [9] measured spherulitic growth rate of Ziegler–Natta catalysts sPP, and assuming that sPP crystallizes in regime II, and $\Delta H_m^0 = 3.14$ kJ/mol they found the values of the lateral and fold surface free energies, $\sigma = 4.4 \times 10^{-3}$ J/m²

Table 4.4 Temperatures of transitions and energies for iPP and sPP [7]

Properties	iPP α form	iPP β form	sPP
Equilibrium melting point	208 \pm 8 $^{\circ}$ C	176 $^{\circ}$ C	158–161 $^{\circ}$ C
Glass transition	–10 $^{\circ}$ C	–10 $^{\circ}$ C	0 $^{\circ}$ C
Enthalpy of fusion	209.3 \pm 29.9 J/g	177 J/cm ³	190 J/g
Regime I/II transition	155 $^{\circ}$ C		
Regime II/III transition	137 $^{\circ}$ C	123–129.5 $^{\circ}$ C	110 $^{\circ}$ C
L in regime I	0.11 μ m		
L in regime II	0.91 nm		
Fold surface energy, σ_e	122 $\times 10^{-3}$ J/m ² ^s	48–55 $\times 10^{-3}$ J/m ²	49.9 $\times 10^{-3}$ J/m ²
Work of chain folding, q	27.61 kJ/mol		24.27 kJ/mol
Lateral surface free energy, σ	9.2–11.5 $\times 10^{-3}$ J/m ²		11–12 $\times 10^{-3}$ J/m ²
Activation energy for reptation	6.276 kJ/mol		

^sDetermined by Monasse and Haudin 166

and $\sigma_e = 47 \times 10^{-3}$ J/m², respectively, and the average work of chain folding $q = 23.43$ kJ/mol of folds. The Miller and Seeley results were reexamined by Clark and Hoffman [65] and they obtained values $\sigma_e = 49.9 \times 10^{-3}$ J/m², and $q = 24.27$ kJ/mol of fold, using the same value of $T_m^{\circ} = 161$ $^{\circ}$ C.

Polymerized with metallocene catalyst, more stereoregular sPP (85–86% rrrr pentad content) was examined by Rodriguez-Arnold et al. [99]. Based on the value of the equilibrium melting enthalpy $\Delta H_m^{\circ} = 8.0$ kJ/mol, evaluated from extrapolation of heat of fusion at different crystallinities to 100% crystallinity [118], and the glass transition temperature $T_g = 0$ $^{\circ}$ C, they found values of the lateral surface free energy $\sigma = 11.2 \times 10^{-3}$ J/m², of fold surface free energy $\sigma_e = 42$ – 47×10^{-3} J/m² and work of chain folding q in the range between 20.50 and 23.43 kJ/mol of fold.

4.9 Formation of Spherulitic Structure

The architecture of single spherulite was discussed in the above subchapter. In reality during crystallization, specially from melt, individual separated spherulites exist only at the beginning of crystallization. When the spherulite is isolated its growth rate is constant, dependent on the temperature (see Fig. 4.23). With the advance of crystallization spherulites impinge forming the contacts between spherulites and as a result spherulitic structure is formed. Below a formation of spherulitic structure in isothermal conditions is discussed.

Usually the spherulites are really spherical only during the initial stages of crystallization. During the later stages of crystallization spherulites impinge with their neighbors, forming boundaries. When all spherulites are nucleated

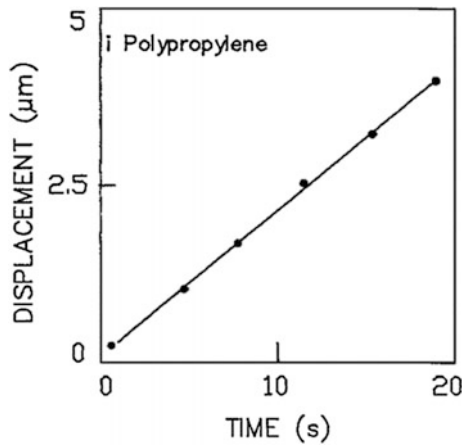


Fig. 4.23 Displacement of boundary of single isolated iPP spherulite. From [91], reprinted with permission by John Wiley and Sons, 1990

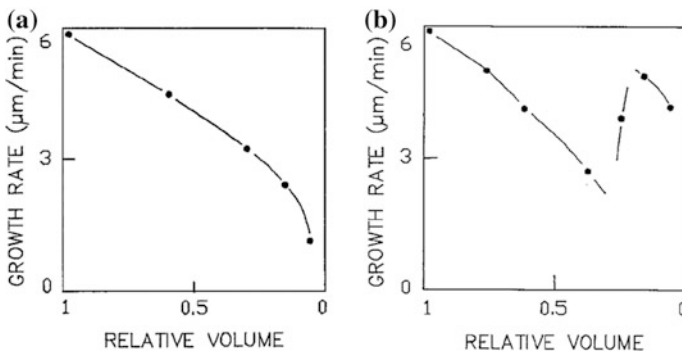


Fig. 4.24 **a** Growth rate of spherulites inside weak spots not showing cavitation versus decreasing relative uncrystallized volume for iPP crystallized at 127 °C; **b** as in **a** but leading to cavitation. From [91], reprinted with permission by John Wiley and Sons, 1990

simultaneously, the boundaries between them are straight (thin films) or planar (bulk materials). However, when spherulites have been nucleated at different times, so that they are different in size when impinging, their boundaries form hyperbolas. In the course of crystallization some pockets of melt may be occluded by impinging spherulites. Crystallization in those pockets is accompanied by the buildup of a negative pressure due to higher density of a solidified phase than of melt [119]. The increasing of pressure in pockets results in slower growth of spherulites (see Fig. 4.24).

The negative pressure can grow to the limit, beyond which the melt fractures, which results in cavities, preferably present near multiple boundary points inside a spherulitic structure [119–123] (Fig. 4.25). The holes or local stresses existing



Fig. 4.25 Scanning electron micrograph of fracture surface of iPP thick plate crystallized isothermally at 134 °C; large cavities between spherulites are visible. *Authors own micrograph*

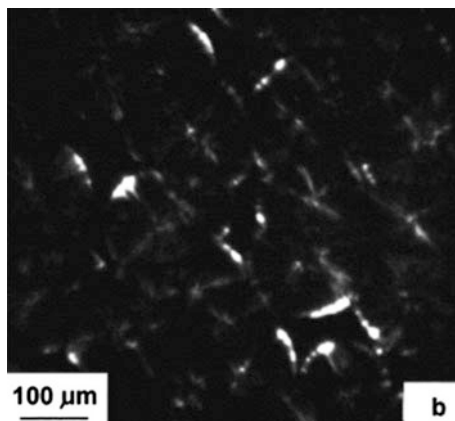
around those pockets weaken a polymer, hence, the regions occluded during crystallization constitute ‘weak spots’ of spherulitic structure. It was shown that cavitation in films of isotactic polypropylene occurs preferably at solid–liquid interface [19, 124]. In thin films the negative pressure arises only during crystallization of a polymer layer between two plates, while in films crystallized with free surface only the thinning of a sample within a weak spot occurs.

The negative pressure in weak spots lowers the equilibrium melting temperature, T_m^0 , hence, decreases the undercooling. The local decrease of undercooling results in the crystallization of thicker lamellae. If after crystallization the negative pressure is released by removing a cover glass from thin film or microtoming of a bulk sample, then the lamellae in weak spots exhibit higher melting temperature, T_m . The increase of melting temperature, ΔT_m , of lamellae in weak spots was observed in isotactic polypropylene. The elevation of melting temperature and the negative pressure buildup depend on the crystallization temperature. For iPP ΔT_m was observed for isothermal crystallization at temperatures below 136 °C and maximum values was 2.7 °C for crystallization at 128 °C [119] (Fig. 4.26).

The increasing negative pressure make more difficult the transport of macromolecules to the growing spherulite and by this the growth rate is significantly reduced. The breaking of melt, with formation of voids and release of pressure lead to recovery to initial growth rate [91, 119].

The other reason of decreasing growth rate of isolated spherulites is the presence of impurities and additives. If during crystallization the concentration of impurities or low molecular weight fractions ahead of crystallization front increases, because of rejection from spherulite, the growth rate decreases.

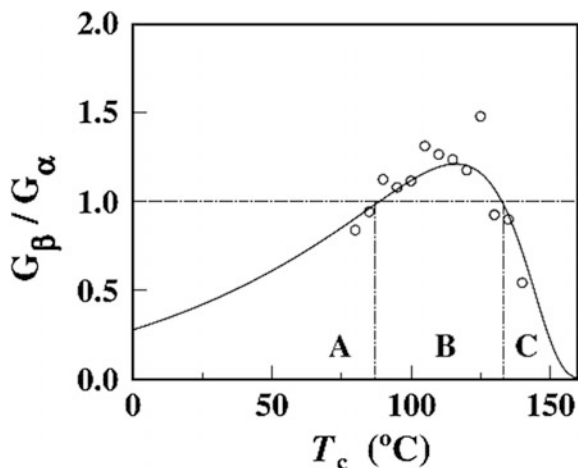
Fig. 4.26 The micrograph of weak spot and its surrounding in iPP thin film crystallized between glass plates at 128 °C. Photograph shows partial melting at 165.5 °C. From [119], reprinted with permission by John Wiley and Sons, 1999



There is also a third reason of changing the growth rate of spherulites with a progress of crystallization. Crystallization of PP is accompanied by the release of latent heat of fusion of nearly 210 J/g. The release of this heat increases the temperature and slows the crystal growth, due to insufficient heat subtraction from the thick sample, limited by thermal conductivity of PP, which is low. A non-isothermal crystallization with the cooling rate 5000 °C/min showed that the release of heat of fusion maintained the growth rate of spherulites at the level of 8–9 μm/s, with constant temperature at the interface of growth [7]. The growth rate of isotactic polypropylene depends on the growing crystalline form. The growth rate of β form is faster in the temperature range 90–133 °C (see Fig. 4.27).

Miller and Seeley [9] measured spherulitic growth rate of Ziegler–Natta catalysts syndiotactic polypropylene, crystallized isothermally at the temperature between 97 and 137 °C. Syndiotactic PP synthesized with the use of metallocene catalyst (having 85–86% rrrrr pentad content) was examined by Rodriguez-Arnold et al. [99].

Fig. 4.27 Ratio of spherulite growth rates of α and β forms (G_β/G_α) for isotactic polypropylene. From [92], reprinted with the permission from of Springer Nature, 2008



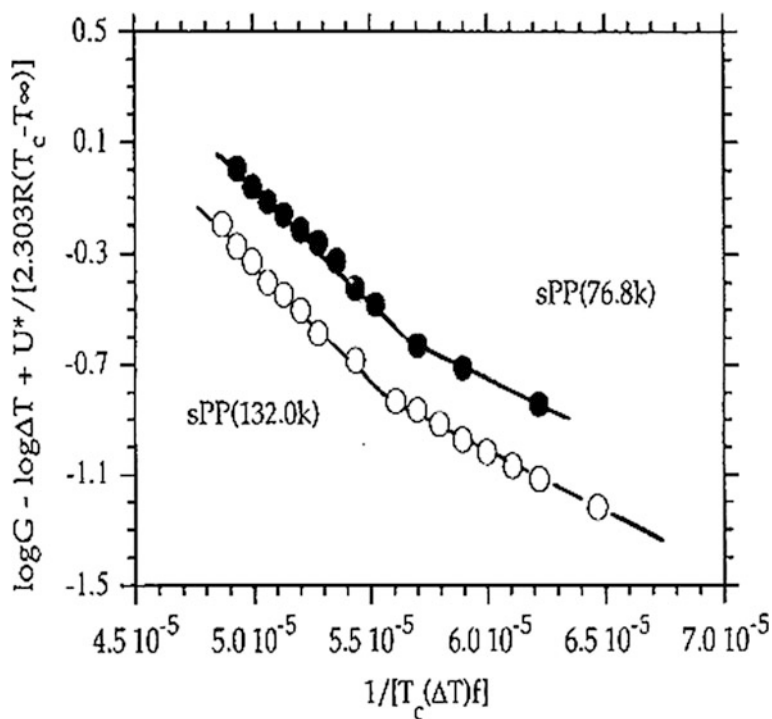
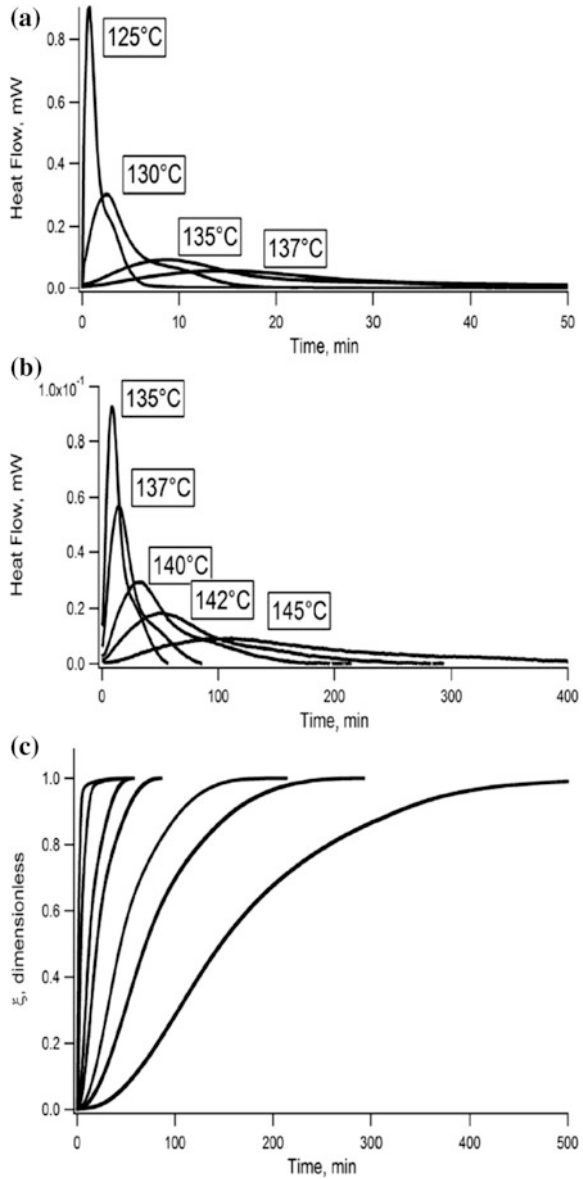


Fig. 4.28 Nucleation theory treatment of the linear growth rate data for two syndiotactic PP fractions. From [99], reprinted with permission by Elsevier, 1994

The effect of the molecular mass on the crystallization kinetics (growth rate) has been studied. They found a change in the growth rate data at crystallization temperature of 110 °C, associated with a regime II/regime III transition (Fig. 4.28). The transition temperature 110 °C was confirmed for sPP by Supaphol and Spruiell [8, 125].

The **overall crystallization rate** is used to follow the course of solidification of PP. The data for description of the process are usually taken from differential scanning calorimetry (see Fig. 4.29), in situ X-ray diffraction or light depolarization microscopy. The overall crystallization rate of polypropylene and formation of spherulitic structure depend on the nucleation rate, $I(t)$ and the growth rate of spherulites, $G(t)$. The conversion of melt to spherulites in the most general case of non-isothermal crystallization is described by the Avrami Equation (Eqs. 4.20 and 4.21):

Fig. 4.29 a, b Thermograms obtained during isothermal crystallization at various temperatures. c Relative degree of space filling during isothermal crystallization at 125, 130, 135, 137, 140, 142, 145 °C (from left to right). From [126], reprinted with permission by John Wiley and Sons, 2015



$$\alpha(t) = 1 - \exp \left\{ -\pi \int_0^t I(T) \left[\int_T^t G(s) ds \right]^2 dT \right\} \tag{4.20}$$

for films and

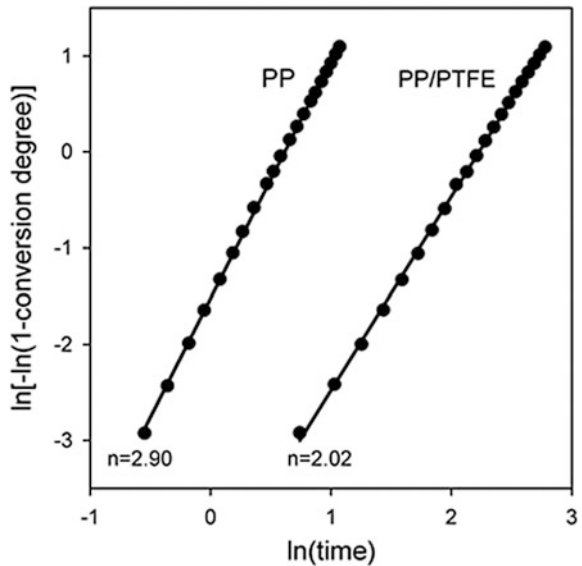
$$\alpha(t) = 1 - \exp \left\{ -(4\pi/3) \int_0^t I(T) \left[\int_T^t G(s) ds \right]^3 dT \right\} \tag{4.21}$$

for bulk samples.

The analysis of the above equations is often applied for obtaining the nucleation data from isothermal and non-isothermal crystallization experiments. Several simplifications of the equations are developed and used for isothermal crystallization (with instantaneous or spontaneous nucleations only) and non-isothermal processes with a constant cooling rate. It was found that the crystallization of PP follows the dependence $\log[1 - \alpha(t)] \sim t^n$ where n is around three for relatively low undercooling and bulk materials which indicates instantaneous character of primary nucleation (Fig. 4.30).

The crystallization in non-isothermal conditions, especially during fast cooling depends on the cooling rate. The decrease of temperature of crystallization peak is observed (see Fig. 4.31) and also change of crystallinity and growing forms (see Fig. 4.32).

Fig. 4.30 The Avrami plots for isothermal crystallization of neat PP and PP/PTFE nanofibers at 128 and 145 °C, respectively. Symbols (●) experimental data, lines (—) linear regression; conversion degree from the range of 0.05–0.95. Time in min. From [127], reprinted with permission by Elsevier, 2016



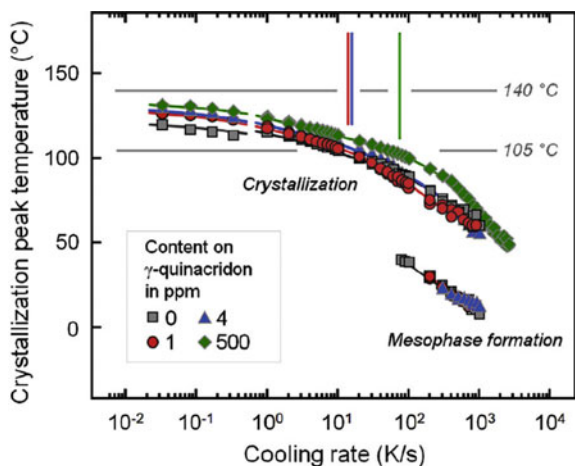
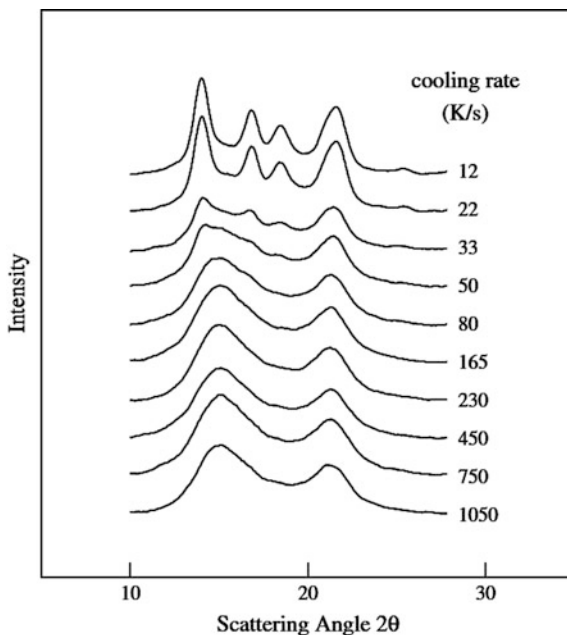


Fig. 4.31 Crystallization peak temperature of iPP containing 0, 1, 4, and 500 ppm γ -quinacridone β -nucleant as a function of the cooling rate. The two horizontal gray lines at 105 and 140 °C indicate the temperature range at which β -crystals grow faster than α -crystals. Data points at rates lower than 1 K/s were collected by DSC, otherwise FSC has been employed for the measurements. From [128], reprinted with permission by Elsevier, 2016

Fig. 4.32 WAXS of iPP crystallized at different rates of cooling from the melt. From [129], reprinted with permission by Elsevier, 2006



To characterize the spherulitic nucleation during non-isothermal crystallization, the Ozawa equation is applied, which could be obtained by integrating twice by parts the Avrami equation and assuming cooling at the constant rate, a . The slope of the plot $\ln\{-\ln[1 - \alpha(T)]\}$ versus $\ln(a)$ equals two or three for instantaneous nucleation, three or four for nucleation prolonged in time, in two- and three-dimensional crystallization, respectively. The values from three to four, depending on the temperature range were obtained for iPP from DSC non-isothermal crystallization [125].

The statistical approach was developed [130, 131] for the description of the kinetics of conversion of melt to spherulites and the kinetics of formation of spherulitic pattern during both, isothermal and non-isothermal crystallizations. The final spherulitic pattern can also be described. The rates of formation of spherulitic interiors and boundaries (boundary lines, surfaces and points) as well as their final amounts could be predicted if spherulites growth and nucleation rates are known. Applied to iPP crystallized during cooling with various rates, the approach allowed for the predictions of tendencies in the kinetics of formation of spherulitic structure and its final form.

The overall crystallization kinetics of sPP have been studied by various authors, using for description the Avrami equation. Balbontin et al. [132] have found that the Avrami exponent n is substantially invariant with the crystallization temperature but depends on the stereoregularity ($n = 1.8\text{--}3.7$). The kinetic constant K was between 0.16×10^{-3} and 4.77×10^{-3} , again depending on the stereoregularity. Similar values of n (1.9–3.0) were found by Rodriguez-Arnold et al. [118] for samples having similar stereoregularity (rrrrr pentad content of 85–86%) but different molecular masses.

4.10 Crystallization of PP in Specific Conditions

Crystallization of PP in specific conditions was a subject of interest in the past. Those conditions can be divided into two groups: flow of melt leading to orientation of macromolecules and non-uniform temperature profile inside the sample during crystallization.

Shear induced crystallization from melt is an important issue, because it occurs at conditions similar to real existing in industrial processing of polypropylene. In most polymer processing operations such as injection molding, film blowing, and fiber spinning, the molten polymer chains are subjected to shear or/and elongation flow fields [49, 105, 133, 134]. The crystallization was studied either during melt flow or after cessation of flow and it was observed that the crystallization process and formed structure are related to the temperature, applied shear rate, total strain and shear strain history. Depending on the conditions the growing structures were varying from spherulites to row-nucleated and shish-kebab morphologies [135, 136] (Fig. 4.33).

One of the factor influencing crystallization is shear rate, the other one is shear strain (equivalent to shearing time for a constant shear rate). Early studies of

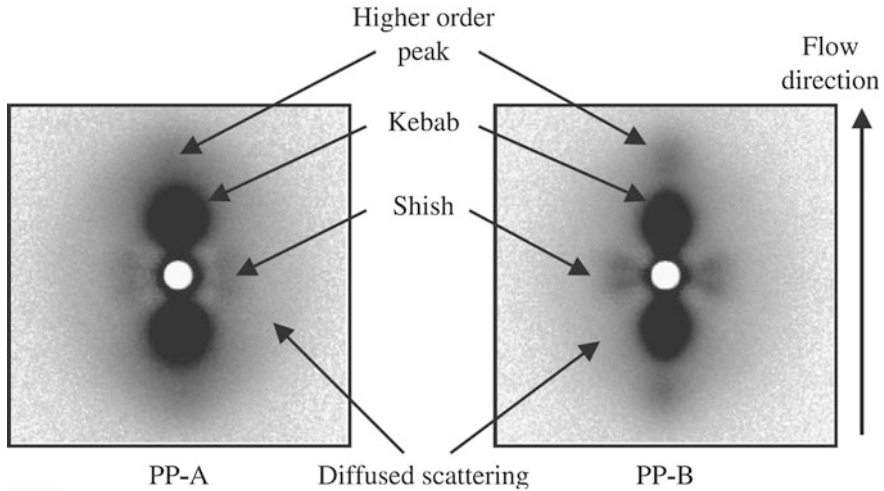


Fig. 4.33 SAXS images of two sheared isotactic polypropylenes measured at room temperature. Sheared melt was kept at 155 °C for 30 min after cessation of shear, and then cooled to room temperature. From [139], reprinted with permission by Elsevier, 2006

crystallization kinetics showed that enhancement in the overall crystallization kinetics occurs whenever crystallization takes place during shear or even after shear. The shear accelerates the nucleation rate and, to less extent, the spherulite growth rate [49, 137, 138].

From the studies of Somani et al. [139] it follows that during deformation the segments of macromolecular chains aligned along the flow direction can undergo an abrupt coil-stretch-like transition, while other segments remain coiled. So, the observed increase in nucleation is caused by orientation of polymer chains in the melt.

For a constant shear rate, a higher shear strain results in a larger increase in the crystallization kinetics, even though the effect of shear strain (or shear time) is limited at low shear rates [49]. If for iPP crystallized at 141 °C the half crystallization time is for quiescent crystallization of order of hours, then it decreases by approximately 2 orders of magnitude upon shearing the melt for 4 s. With the increase of shearing time at constant shear rate the crystallization time first decreases rapidly and then reaches a plateau at a shearing time of about 5 s [49, 134].

Janeschitz-Kriegl [140, 141] and coworkers have isolated the effects of flow from thermal effects and separated simultaneously the nucleation and crystal growth events by counting the formed nuclei. The results have demonstrated that the influence of flow on the nucleus density is overwhelming; especially at high temperatures when the number density of nuclei in quiescent melt is extremely small. Moreover, it was found that the number of nuclei increases continuously with increasing duration of the shearing. Because at high shear rate thread-like structures form and it is impossible to count the nuclei, then the characterization is most

frequently based on crystallization half-time, which is suggested to be inversely proportional to nucleation.

A significant influence of molecular weight on shear-induced crystallization was observed [138]. Haudin et al. [142] performed fiber pullout experiments in isothermal conditions and found that the crystallization rate exponentially increased with molecular mass. Their studies included Ziegler-Natta based and metallocene based homopolymers, and ethylene-propylene copolymers. The role of high molecular weight tail in enhancement of crystallization after shear was showed by Vleeshouwers and Meijer [143]. The importance of molecular weight distribution was also shown by Nogales et al. [105], which performed in situ WAXS and SAXS studies of undercooled melt at 150 °C subjected to a high shear strain (1428%) at a shear rate of 57 s⁻¹ and found the presence of oriented lamellae. The crystallization kinetics strongly depended on the molecular weight distribution. The introduction of a small amount of high molecular weight chains (4%) was sufficient to induce drastic changes in the kinetics, because only polymer chains above some critical molecular weight were sufficiently oriented at a given shear rate. As a consequence, a small amount of high molecular weight tail leads to an absolutely faster crystallization of a sheared iPP melt [49]. The large increase of the flow induced crystallization under the same shear rate was observed with the increase of molecular mass by Jerschow et al. [144].

It was observed that for polymorphic polymers, like PP, shear-flow can also influence the crystal structure. Sheared or strained iPP melt encourages the formation of β form crystals rather than thermodynamically stable α crystals [49]. Crystallization in the shear stress field and in a temperature gradient supports the formation of β phase crystals [98].

The flow-induced orientation decays slower for long chains than for short chains. A two-step mechanism for an explanation of the kinetics of the formation of highly oriented structures was proposed [140, 145], consisting of the sporadic formation of primary nuclei followed by the growth of thread-like precursors, starting from these primary nuclei.

The orientation of molecules and crystals precursor explain formation of shish-kebab structures. The formation of anisotropic morphology is a two-step process. Deformation first forms flow-induced precursors (shish) in the melt, from which lamellae grow epitaxially out from the center when quenched. Kimata et al. [146] identified that these lamellae consist predominately of short chains. After shearing polypropylene samples with deuterium labeled low molecular weight chains, they performed small-angle neutron scattering (SANS) experiments. Results showed that the concentration of low molecular weight chains in lamellae is higher compared to the remaining amorphous region. Since short chains have higher mobility in the melt, their crystalline growth rate is higher compared to longer chains. The longest and slowest relaxing chains in a melt are the easiest to orient and stretch, suggesting that long chains are particularly important in flow-induced crystallization. Nonetheless, Kimata et al. [146] found using their SANS experiments that long chains are not overrepresented in flow-induced precursors. Instead, the concentration of deuterated long chains in shish structure is the same as in the

remaining material. Even though long chains are not overrepresented in flow induced precursors, their slow stretch relaxation appears to be essential for forming precursors [136].

Forty years ago the first investigations of spherulite growth and morphology formed during **zone solidification** (passage of a sample at constant rate through a step temperature gradient sufficient for melting) were conducted for iPP. The anisotropy of spherulite growth, the quasi parabolic shapes of interspherulitic boundaries and the change in the orientation of lamellae towards the direction of motion of the crystallizing front were observed. The final polymer structure was composed of highly elongated spherulites with parallel lamellar fibrils [33, 147]. The crystallization of iPP films in constant unidirectional temperature gradients were studied by Pawlak and Piorkowska [34] by means of light microscopy (see Fig. 4.34) and AFM structure studies. Temperature gradient (35 °C/mm) speeds up significantly the crystallization in films above 130 °C although no enhancement of the spherulite nucleation was found. The spherulites assumed anisotropic shapes. The growth directions of the lamellae bend towards the hotter side of a sample, while being perpendicular to the crystallizing front.

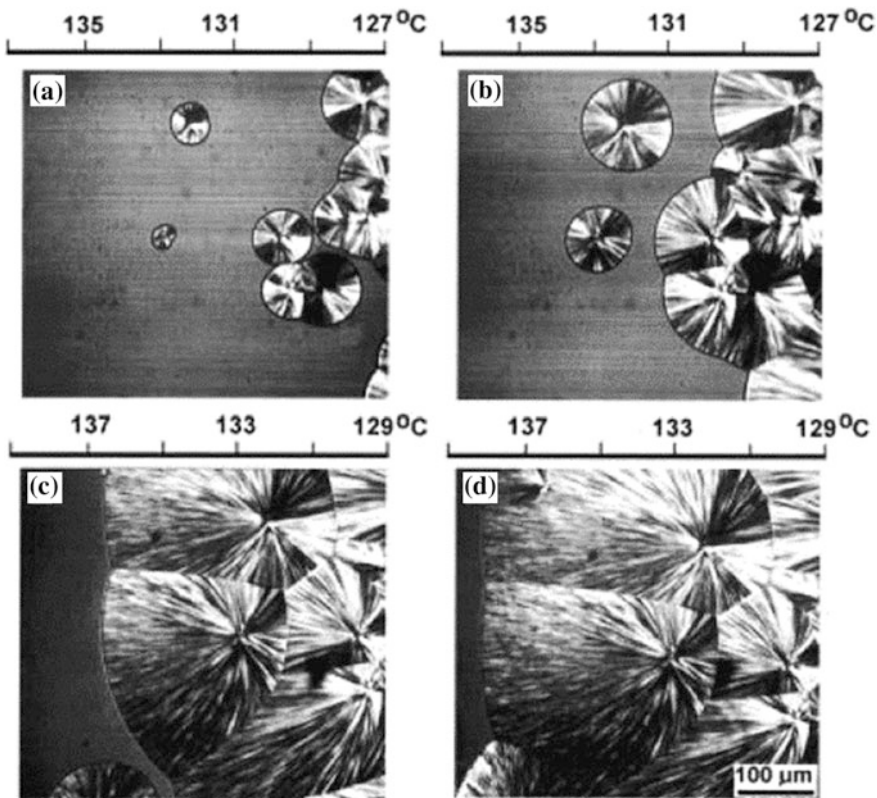


Fig. 4.34 Polarized light micrographs of subsequent stages of crystallization of the iPP in a temperature gradient of 20 °C/mm. From [34], reprinted with permission by Springer Nature 2001

4.11 The Nucleating Agents

Nucleation and nucleants are the subject of Chap. 3 of this book, so only some remarks are presented here. iPP can be nucleated by a wide variety of mineral and organic compounds (Fig. 4.35).

The nucleants may be versatile, or specific for ‘producing’ specific crystallographic form. Many of nucleating agents induce the α phase, fewer nucleating agents induce β phase of iPP. The lack of specificity for some nucleants has been explained by the fact that various substrate/ α -iPP epitaxies are possible, namely, the substrates can interact with two different crystal planes of α -iPP. For example, it is known that nucleating agents with an 6.5 Å lattice parameter induced the α phase, but a 6.5 Å periodicity is also involved in the nucleating agents for the β phase of iPP. The similarity in substrate periodicities suggests that some nucleating agents may induce either the α or β phase under different crystallization conditions.

4-Fluorobenzoic acid is an example of α -phase nucleant, dicyclohexylterephthalamide (DCHT) is an example of β -iPP nucleants, γ -quinacridone (trade name E3B) induces either the α phase or the β phase, depending on T_c : α phase is nucleated for T_c 's higher than 140 °C, β phase for the temperature lower than 140 °C. The same crystal face of γ -quinacridone can induce either α or β -iPP but with two different chain orientations of the polymer on the substrate [149].

The addition of β -nucleating agents can lead to the formation of pure or nearly pure β -modification of isotactic polypropylene. The most popular highly active β -nucleating agent is above mentioned γ -quinacridone. The drawback of the use of γ -quinacridone is its intense red color and its polymorphic nature which may lead to a decrease of nucleating activity. A certain salts of aliphatic dicarboxylic acids are also effective β -nucleating agents. The most beneficial selectivity and activity were found for calcium salts of pimelic (Ca-Pim) and suberic (Ca-Sub) acids [150]. The β -nucleating agent, *N,N'*-dicyclohexyl-2,6-naphthalenedi carboxamide (NJ-StarTR NU100) may exhibit various morphologies in iPP matrix (spherulites or shish-kebabs) at different concentrations and depending on the processing conditions [151, 152].

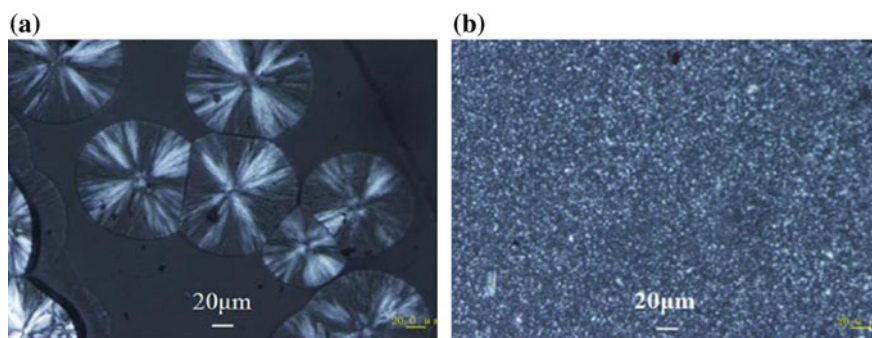


Fig. 4.35 Polarized optical micrographs of pure iPP (a) and iPP nucleated with HHPA-Na (b) under isothermal crystallization at 140 °C. From [148], reprinted with permission by Springer Nature 2017

4.12 Melting of Polypropylene

Equilibrium melting temperature, i.e. temperature of melting of an ideal crystal with infinite size in three dimensions (T_m^0), is one of the main thermodynamic parameters characterizing crystallization and melting behavior of polymers. It is important because crystallization phenomenon, such as lateral growth and nucleation are controlled by supercooling ΔT , defined as $\Delta T = (T_m^0 - T_c)$, where T_c is the crystallization temperature [153].

Traditionally, researchers used two ways to determine T_m^0 : Gibbs-Thomson and Hoffman-Weeks routes. One approach is by using the **Gibbs–Thomson** equation, which reflects the dependence of the surface-to-volume ratio of the crystal and presents the melting temperature versus the reciprocal lamellar thickness [107]. This representation implicitly assumes that the lateral size of crystalline lamellae is much larger than the lamellar thickness. Therefore, a linear extrapolation to an infinitely thick lamellar crystals yields the value of T_m^0 [136, 154, 155]. The melting temperature of lamellar crystal with lateral sizes a and b and thickness l according to Gibbs-Thomson equation is (Eq. 4.22):

$$T_m(l) = T_m^0 \left[1 - \frac{2}{\Delta h} \left(\frac{\sigma}{a} + \frac{\sigma}{b} + \frac{\sigma_e}{l} \right) \right] \quad (4.22)$$

where σ is the surface free energy and Δh is the heat of fusion [156]. In polymers usually $a > l$, $b > l$ and σ_e is the surface free energy of the basal plane of crystalline lamellae, so the Eq. 4.22 can be shown in a more simple form:

$$T_m(l) \cong T_m^0 - \frac{C}{l} \quad (4.23)$$

where

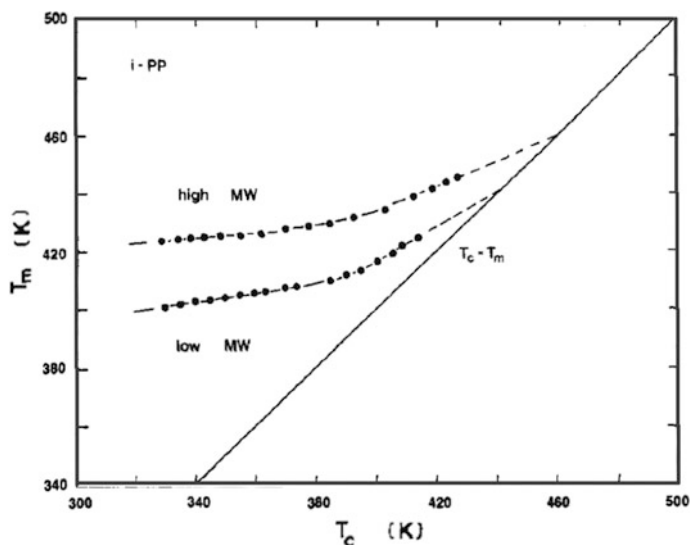
$$C = \frac{2\sigma_e T_m^0}{\Delta h} \quad (4.24)$$

Yamada et al. [153] proposed a new method to determine the corrected Gibbs-Thomson plot. In their method, the heating rate dependence of T_m was omitted by applying the theory of the ‘melting kinetics’, and the effect of lamellar thickening during melting on T_m was also omitted by observing thick lamellae. A reliable Gibbs-Thomson plot and $T_m^0 = 186.2$ °C were obtained for a fraction of isotactic polypropylene (iPP) with high tacticity ([mmmm] = 99.6%, $M_n = 64 \times 10^3$ g/mol and $M_w/M_n = 2.4$). Table 4.5 shows T_m^0 values determined from Gibbs-Thomson equation [153].

The second possibility of determining T_m^0 is by the use of so-called **Hoffman–Weeks** (H–W) line traces T_m as a function of T_c [157]. There, a linear extrapolation to the intersection point of the H–W line with the line of $T_m = T_c$ also is expected to yield T_m^0 [159] (see Fig. 4.36). This H–W plot requires only the measurement of

Table 4.5 T_m^0 of iPP estimated by Gibbs-Thomson plots in the literature [153]

Authors	T_m^0 (°C)	Method		M_w of sample
		T_m	l	
Mezghani and Philips [157]	186.1	Optical	SAXS	151×10^3
Cheng et al. [158]	184.4	DSC, onset	SAXS	202×10^3
	183.2	DSC, onset	SAXS	159×10^3
	180.5	DSC, onset	SAXS	189×10^3
Cheng et al. [117]	180.7	DSC, onset	SAXS	25×10^3
	185.0	DSC, onset	SAXS	600×10^3

**Fig. 4.36** Relationship between the melting temperature and isothermal crystallization temperature of iPP. The extrapolation based on Hoffman and Weeks indicates an equilibrium melting temperature (443.2 and 458.2 K, depending on the molecular weight). From [117], reprinted with permission by American Chemical Society, 1990

peak melting temperatures of samples, which were isothermally crystallized at various temperatures. Thus, it has been frequently adopted for determining T_m^0 . However, most of the times, the values of T_m^0 , which were determined along these two ways, i.e. based on the Gibbs–Thomson equation and derived from the H–W plot, are not the same [155].

The establishment of the equilibrium melting temperature, T_m^0 of iPP has been an elusive and controversial matter for some time. The reported values of T_m^0 have ranged from about 185–220 °C [157, 160–162]. There were proposed several reasons for the wide range in T_m^0 . One, common to many polymers, involves inherent problems in the extrapolations. Other possibilities, specific to iPP, involve

the accurate determination of the structural regularity, interpretation of multiple endothermic peaks that are invariably exhibited during the fusion of PP, use of sufficiently high M_w samples, various heating rates etc. [163].

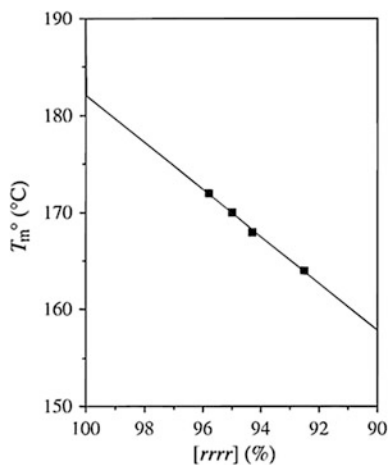
Extending the crystallization and melting lines until they cross gives the Hoffman–Weeks temperature [159, 164, 165]. For isotactic polypropylene, $T_m^0 = 187 \pm 2 \text{ }^\circ\text{C}$ and $T_{\text{HW}} = 208 \pm 8 \text{ }^\circ\text{C}$. Note that since T_{HW} is greater than T_m^0 , the Hoffman–Weeks temperature corresponds to a negative (unphysical) value of $1/l$ at which $T_m(l) = T_c(l)$ [136].

From the isothermal crystallization data the thermodynamic equilibrium properties of sPP were determined [99]. The Hoffman–Weeks extrapolation method and the Thomson–Gibbs equation (by plotting T_m versus the reciprocal of the lamellar thickness l , evaluated from SAXS diffraction experiments) have given a value of equilibrium melting temperature $T_m^0 = 160 \text{ }^\circ\text{C}$. This value is probably too low, due to relatively low stereoregularity of examined polymer. Higher value of $168.7 \text{ }^\circ\text{C}$ was reported by Supaphol and Spruiell [125] for a polymer with 100% syndiotacticity (see Fig. 4.37).

Because in isotactic polypropylene of α form may co-exist radial and tangential lamellae than during examination of melting with DSC are often observed two endothermic peaks in thermograms. The low-temperature endotherm results from a cooperative melting of branched or tangential lamella. The high-temperature one corresponds to the melting of the primary radial lamellae. A microscopic view of melting the iPP spherulites is shown in Fig. 4.38.

The overall birefringence of the spherulites formed at relatively high crystallization temperatures ($T_c > 145 \text{ }^\circ\text{C}$) changes during fusion from a mixed type character to preferentially negative at temperatures corresponding to the peak of the low endotherm. Thus most of the thinner tangential lamellae melt at this temperature. The crystallites formed at temperatures less than about $142 \text{ }^\circ\text{C}$ show melt-recrystallization during fusion. On melting, the initial mixed-type overall

Fig. 4.37 Extrapolated melting temperatures T_m^0 of the sPP samples as a function of the fully syndiotactic pentad content $[\text{rrrr}]$. From [166], reprinted with permission by American Chemical Society, 1998



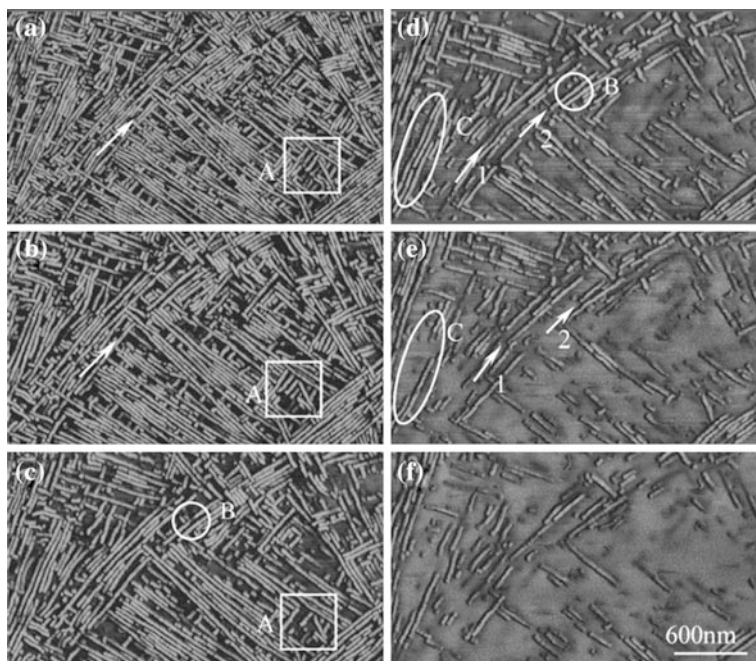


Fig. 4.38 Melting of crosshatched lamellae formed at 146 °C for about 60 min; **a** 146 °C, **b** 163 °C, **c** 164 °C, **d** 165 °C, **e** 166 °C and **f** 167 °C. The time interval between two consecutive images is about 30 min. From [167], reprinted with permission of Springer Nature, 2007

birefringence remains unchanged until complete melting. This indicates that the melting of radial and tangential lamellae, which have approximately the same thickness at this range of crystallization temperatures [168, 169] occurs simultaneously [163, 168]. Epitaxial crystallization and the formation of lamellae branching (crosshatching) are observed at all crystallization temperatures, including 160 °C and greater [163].

References

1. Wunderlich B (1973) *Macromolecular physics. Crystal structure, morphology, defects*, vol 1. Academic Press, New York, p 435
2. Sperling LH (2005) The crystalline state. In: *Introduction to physical polymer science*, pp 239–323. <https://doi.org/10.1002/0471757128.ch6>
3. Wittmann JC, Lotz B (1985) Polymer decoration: the orientation of polymer folds as revealed by the crystallization of polymer vapors. *J. Polym. Sci. Polym. Phys. Ed.* 23 (1):205–226. <https://doi.org/10.1002/pol.1985.180230119>

4. Auriemma F, de Ballesteros OR, De Rosa C et al (2000) Structural disorder in the alpha form of isotactic polypropylene. *Macromolecules* 33(23):8764–8774. <https://doi.org/10.1021/ma0002895>
5. Zhu P-w, Edward G (2004) Distribution of Shish-Kebab structure of isotactic polypropylene under shear in the presence of nucleating agent. *Macromolecules* 37(7):2658–2660. <https://doi.org/10.1021/ma0358374>
6. Eckstein A, Suhm J, Friedrich C, Maier RD, Sassmannshausen J, Bochmann M, Mulhaupt R (1998) Determination of plateau moduli and entanglement molecular weights of isotactic, syndiotactic, and atactic polypropylenes synthesized with metallocene catalysts. *Macromolecules* 31(4):1335–1340. <https://doi.org/10.1021/ma971270d>
7. Galeski A (1994) Nucleation in polypropylene. In: J. Karger-Kocsis (ed) *Polypropylene: structures, properties and blends*. Chapman & Hall, London, pp 25–49
8. Supaphol P, Spruiell JE (2000) Thermal properties and isothermal crystallization of syndiotactic polypropylenes: Differential scanning calorimetry and overall crystallization kinetics. *J Appl Polym Sci* 75(1):44–59. [https://doi.org/10.1002/\(sici\)1097-4628\(20000103\)75:1%3c44:Aid-app6%3e3.0.Co;2-1](https://doi.org/10.1002/(sici)1097-4628(20000103)75:1%3c44:Aid-app6%3e3.0.Co;2-1)
9. Miller RL, Seeley EG (1982) Crystallization kinetics of syndiotactic polypropylene. *J Polym Sci Part B Polym Phys* 20(12):2297–2307. <https://doi.org/10.1002/pol.1982.180201210>
10. Kaminsky W (1998) Highly active metallocene catalysts for olefin polymerization. *J Chem Soc, Dalton Trans* 9:1413–1418. <https://doi.org/10.1039/A800056E>
11. Crist B, Schultz JM (2016) Polymer spherulites: a critical review. *Prog Polym Sci* 56:1–63. <https://doi.org/10.1016/j.progpolymsci.2015.11.006>
12. Yamada K, Matsumoto S, Tagashira K, Hikosaka M (1998) Isotacticity dependence of spherulitic morphology of isotactic polypropylene. *Polymer* 39:5327–5333. [https://doi.org/10.1016/S0032-3861\(97\)10208-7](https://doi.org/10.1016/S0032-3861(97)10208-7)
13. Lezak E, Bartczak Z, Galeski A (2006) Plastic deformation behavior of beta-phase isotactic polypropylene in plane-strain compression at room temperature. *Polymer* 47(26):8562–8574. <https://doi.org/10.1016/j.polymer.2006.10.016>
14. Rozanski A, Galeski A (2015) Crystalline lamellae fragmentation during drawing of polypropylene. *Macromolecules* 48(15):5310–5322. <https://doi.org/10.1021/acs.macromol.5b01180>
15. Suetsugu Y, Kikutani T, Kyu T et al (1990) An experimental technique for characterizing dispersion in compounds of particulates in thermoplastics using small-angle light scattering. *Colloid Polym Sci* 268(2):118–131. <https://doi.org/10.1007/bf01513190>
16. Okada T, Saito H, Inoue T (1992) Time resolved light scattering studies on the early stages of crystallization in isotactic polypropylene. *Macromolecules* 25:1908–1911
17. Jones AT, Aizlewood JM, Beckett DR (1964) Crystalline forms of isotactic polypropylene. *Makromol Chem* 75:134–158
18. Hobbs JK, Farrance OE, Kailas L (2009) How atomic force microscopy has contributed to our understanding of polymer crystallization. *Polymer* 50(18):4281–4292. <https://doi.org/10.1016/j.polymer.2009.06.021>
19. Thomann R, Wang C, Kressler J et al (1996) On the phase of isotactic polypropylene. *Macromolecules* 29:8425–8434. <https://doi.org/10.1021/ma951885f>
20. Vancso GJ, Beekmans LGM, Pearce R et al (1999) From microns to nanometers: morphology development in semicrystalline polymers by scanning force microscopy. *J Macromol Sci Phys B38(5–6):491–503*. <https://doi.org/10.1080/00222349908248115>
21. Trifonova-van Haerigan D, Varga J, Ehrenstein GW, Vancso GJ (2000) Features of the hedritic morphology of beta-isotactic polypropylene studied by atomic force microscopy. *J Polym Sci B Polym Phys* 38:672–681. [https://doi.org/10.1002/\(SICI\)1099-0488\(20000301\)38:5%3c672:AID-POLB4%3e3.0.CO;2-P](https://doi.org/10.1002/(SICI)1099-0488(20000301)38:5%3c672:AID-POLB4%3e3.0.CO;2-P)
22. Androsch R, Wunderlich B (2001) Reversible crystallization and melting at the lateral surface of isotactic polypropylene crystals. *Macromolecules* 34(17):5950–5960. <https://doi.org/10.1021/ma010260g>

23. Beckett DR, Chalmers JM, Mackenzie MW et al (1985) the far-infra-red spectra of crystalline isotactic polypropylene polymorphs. *Eur Polymer J* 21(10):849–852. [https://doi.org/10.1016/0014-3057\(85\)90162-4](https://doi.org/10.1016/0014-3057(85)90162-4)
24. Chalmers JM, Edwards HGM, Lees JS et al (1991) Raman-spectra of polymorphs of isotactic polypropylene. *J Raman Spectrosc* 22(11):613–618. <https://doi.org/10.1002/jrs.1250221104>
25. Lotz B (2014) A new ϵ crystal modification found in stereodeficient isotactic polypropylene samples. *Macromolecules* 47:7612–7624. <https://doi.org/10.1021/ma5009868>
26. Norton DR, Keller A (1985) The spherulitic and lamellar morphology of melt-crystallized isotactic polypropylene. *Polymer* 26:704–716. [https://doi.org/10.1016/0032-3861\(85\)90108-9](https://doi.org/10.1016/0032-3861(85)90108-9)
27. Meille SV, Ferro DR, Bruckner S, Lovinger AJ, Padden FJ (1994) Structure of beta-isotactic polypropylene—a long-standing structural puzzle. *Macromolecules* 27:2615–2622. <https://doi.org/10.1021/ma00087a034>
28. Lotz B, Kopp S, Dorset D (1994) An original crystal-structure of polymers with ternary helices. *C R Acad Sci Ser II* 319(2):187–192
29. Sowinski P, Piorkowska E, Boyer SAE et al (2016) Nucleation of crystallization of isotactic polypropylene in the gamma form under high pressure in nonisothermal conditions. *Eur Polymer J* 85:564–574. <https://doi.org/10.1016/j.eurpolymj.2016.10.055>
30. Keith HD, Padden FJ, Walter NM et al (1959) Evidence for a second crystal form of polypropylene. *J Appl Phys* 30(10):1485–1488. <https://doi.org/10.1063/1.1734986>
31. Li JX, Cheung WL, Jia DM (1999) A study on the heat of fusion of beta-polypropylene. *Polymer* 40(5):1219–1222. [https://doi.org/10.1016/s0032-3861\(98\)00345-0](https://doi.org/10.1016/s0032-3861(98)00345-0)
32. Marigo A, Marega C, Causin V et al (2004) Influence of thermal treatments, molecular weight, and molecular weight distribution on the crystallization of beta-isotactic polypropylene. *J Appl Polym Sci* 91(2):1008–1012. <https://doi.org/10.1002/app.13260>
33. Lovinger AJ, Chua JO, Gryte CC (1977) Studies on alpha and beta forms of isotactic polypropylene by crystallization in a temperature-gradient. *J Polym Sci Part B Polym Phys* 15(4):641–656. <https://doi.org/10.1002/pol.1977.180150405>
34. Pawlak A, Piorkowska E (2001) Crystallization of isotactic polypropylene in a temperature gradient. *Colloid Polym Sci* 279(10):939–946. <https://doi.org/10.1007/s003960100519>
35. Varga J (1986) Melting memory effect of the beta-modification of polypropylene. *J Therm Anal* 31(1):165–172. <https://doi.org/10.1007/bf01913897>
36. Varga J (1989) Beta-modification of polypropylene and its 2-component systems. *J Therm Anal* 35(6):1891–1912. <https://doi.org/10.1007/bf01911675>
37. Lotz B, Fillon B, Thierry A et al (1991) Low T_c growth transitions in isotactic polypropylene—beta to alpha and alpha to smectic phases. *Polym Bull* 25(1):101–105
38. Lotz B, Graff S, Straupe C et al (1991) Single-crystals of gamma-phase isotactic polypropylene—combined diffraction and morphological support for a structure with nonparallel chains. *Polymer* 32(16):2902–2910. [https://doi.org/10.1016/0032-3861\(91\)90185-1](https://doi.org/10.1016/0032-3861(91)90185-1)
39. Lotz B, Graff S, Wittmann JC (1986) Crystal morphology of the gamma-(triclinic) phase of isotactic polypropylene and its relation to the alpha-phase. *J Polym Sci Part B Polym Phys* 24(9):2017–2032. <https://doi.org/10.1002/polb.1986.090240909>
40. Morrow DR, Newman BA (1968) Crystallization of low-molecular-weight polypropylene fractions. *J Appl Phys* 39(11):4944–4950. <https://doi.org/10.1063/1.1655891>
41. Alamo RG, Kim MH, Galante MJ et al (1999) Structural and kinetic factors governing the formation of the gamma polymorph of isotactic polypropylene. *Macromolecules* 32(12):4050–4064. <https://doi.org/10.1021/ma981849r>
42. Thomann R, Semke H, Maier RD et al (2001) Influence of stereoirregularities on the formation of the gamma-phase in isotactic polypropene. *Polymer* 42(10):4597–4603. [https://doi.org/10.1016/s0032-3861\(00\)00675-3](https://doi.org/10.1016/s0032-3861(00)00675-3)

43. De Rosa C, Auriemma F, Circelli T et al (2002) Crystallization of the alpha and gamma forms of isotactic polypropylene as a tool to test the degree of segregation of defects in the polymer chains. *Macromolecules* 35(9):3622–3629. <https://doi.org/10.1021/ma0116248>
44. Mezghani K, Phillips PJ (1998) The gamma-phase of high molecular weight isotactic polypropylene: III. The equilibrium melting point and the phase diagram. *Polymer* 39(16):3735–3744. [https://doi.org/10.1016/s0032-3861\(97\)10121-5](https://doi.org/10.1016/s0032-3861(97)10121-5)
45. Mezghani K, Phillips PJ (1997) The gamma-phase of high molecular weight isotactic polypropylene. 2. The morphology of the gamma-form crystallized at 200 MPa. *Polymer* 38(23):5725–5733. [https://doi.org/10.1016/s0032-3861\(97\)00131-6](https://doi.org/10.1016/s0032-3861(97)00131-6)
46. Yang SG, Chen YH, Deng BW et al (2017) Window of pressure and flow to produce beta-crystals in Isotactic polypropylene mixed with beta-nucleating agent. *Macromolecules* 50(12):4807–4816. <https://doi.org/10.1021/acs.macromol.7b00041>
47. Lotz B (2014) A new epsilon crystal modification found in stereodeficient isotactic polypropylene samples. *Macromolecules* 47(21):7612–7624. <https://doi.org/10.1021/ma5009868>
48. Rieger B, Mu X, Mallin DT et al (1990) Degree of stereochemical control of rac-Et ind 2ZrCl₂ MAO catalyst and properties of anisotactic polypropylenes. *Macromolecules* 23(15):3559–3568. <https://doi.org/10.1021/ma00217a005>
49. Liu Q, Sun XL, Li HH et al (2013) Orientation-induced crystallization of isotactic polypropylene. *Polymer* 54(17):4404–4421. <https://doi.org/10.1016/j.polymer.2013.04.066>
50. Piccarolo S, Saiu M, Brucato V et al (1992) Crystallization of polymer melts under fast cooling. 2. High-purity IPP. *J Appl Polym Sci* 46(4):625–634. <https://doi.org/10.1002/app.1992.070460409>
51. Saraf R, Porter RS (1985) Considerations on the structure of smectic polypropylene. *Mol Cryst Liq Cryst* 2(3–4):85–93
52. Mileva D, Androsch R, Cavallo D et al (2012) Structure formation of random isotactic copolymers of propylene and 1-hexene or 1-octene at rapid cooling. *Eur Polymer J* 48(6):1082–1092. <https://doi.org/10.1016/j.eurpolymj.2012.03.009>
53. Natta G (1960) Alti polimeri lineari del propilene aventi struttura sindiotattica. *Accad Naz Lincei Rend Sci Fis Mat Nat XXVIII* 5:539–544
54. De Rosa C, Auriemma F (2006) Structure and physical properties of syndiotactic polypropylene: a highly crystalline thermoplastic elastomer. *Prog Polym Sci* 31(2):145–237. <https://doi.org/10.1016/j.progpolymsci.2005.11.002>
55. Lotz B, Lovinger AJ, Cais RE (1988) Crystal-structure and morphology of syndiotactic polypropylene single-crystals. *Macromolecules* 21(8):2375–2382. <https://doi.org/10.1021/ma00186a013>
56. Rastogi S, La Camera D, van der Burgt F et al (2001) Polymorphism in syndiotactic polypropylene: thermodynamic stable regions for form I and form II in pressure-temperature phase diagram. *Macromolecules* 34(22):7730–7736. <https://doi.org/10.1021/ma0109119>
57. Zhang J, Yang D, Thierry A et al (2001) Isochiral form II of syndiotactic polypropylene produced by epitaxial crystallization. *Macromolecules* 34(18):6261–6267. <https://doi.org/10.1021/ma010758i>
58. De Rosa C, Corradini P (1993) Crystal-structure of syndiotactic polypropylene. *Macromolecules* 26(21):5711–5718. <https://doi.org/10.1021/ma00073a028>
59. De Rosa C, Auriemma F, Vinti V (1998) On the form II of syndiotactic polypropylene. *Macromolecules* 31(21):7430–7435. <https://doi.org/10.1021/ma980789m>
60. Chatani Y, Maruyama H, Asanuma T et al (1991) Structure of a new crystalline phase of syndiotactic polypropylene. *J Polym Sci Part B Polym Phys* 29(13):1649–1652. <https://doi.org/10.1002/polb.1991.090291310>
61. Auriemma F, De Rosa C, De Ballesteros OR et al (1998) On the form IV of syndiotactic polypropylene. *J Polym Sci Part B Polym Phys* 36(3):395–402. [https://doi.org/10.1002/\(sici\)1099-0488\(199802\)36:3<395:Aid-polb1%3e3.0.Co;2-r](https://doi.org/10.1002/(sici)1099-0488(199802)36:3<395:Aid-polb1%3e3.0.Co;2-r)
62. Burns JR, Turnbull D (1966) Kinetics of crystal nucleation in molten isotactic polypropylene. *J Appl Phys* 37(11):4021–4026. <https://doi.org/10.1063/1.1707969>

63. Koutsky JA, Walton AG, Baer E (1967) Nucleation of polymer droplets. *J Appl Phys* 38 (4):1832–1839. <https://doi.org/10.1063/1.1709769>
64. Fillon B, Wittmann JC, Lotz B et al (1993) Self-nucleation and recrystallization of isotactic polypropylene (alpha-phase) investigated by differential scanning calorimetry. *J Polym Sci Part B Polym Phys* 31(10):1383–1393. <https://doi.org/10.1002/polb.1993.090311013>
65. Clark EJ, Hoffman JD (1984) Regime-III crystallization in polypropylene. *Macromolecules* 17(4):878–885. <https://doi.org/10.1021/ma00134a058>
66. Hoffman JD, Miller RL (1988) Test of the reptation concept—crystal-growth rate as a function of molecular-weight in polyethylene crystallized from the melt. *Macromolecules* 21 (10):3038–3051. <https://doi.org/10.1021/ma00188a024>
67. Crist B (2013) Structure of polycrystalline aggregates. In: Piorowska R, Routledge G (ed) *Handbook of polymer crystallization*. Wiley, New Jersey, pp 73–124
68. Xiao ZG, Sun Q, Xue G et al (2003) Thermal behavior of isotactic polypropylene freeze-extracted from solutions with varying concentrations. *Eur Polymer J* 39(5):927–931. [https://doi.org/10.1016/s0014-3057\(02\)00313-0](https://doi.org/10.1016/s0014-3057(02)00313-0)
69. Xiao ZG, Sun N (2016) Crystallization behavior for metallocene-catalyzed isotactic polypropylene in alkane solvents of various molecular sizes. *J Therm Anal Calorim* 124 (1):295–303. <https://doi.org/10.1007/s10973-015-5146-3>
70. Morrow DR, Sauer JA, Woodward AE (1965) Dilute solution-grown polypropylene single crystals. *J Polym Sci Part B Polym Lett* 3(6):463–466. <https://doi.org/10.1002/pol.1965.110030608>
71. Kojima M (1967) Morphology of polypropylene crystals. I. Dilute solution-grown lamellar crystals. *J Polym Sci Part A-2 Polym Phys* 5(3):597–613. <https://doi.org/10.1002/pol.1967.160050316>
72. Kojima M (1967) Solution-grown lamellar crystals of thermally decomposed isotactic polypropylene. *J Polym Sci Part B Polym Lett* 5(3):245–250. <https://doi.org/10.1002/pol.1967.110050307>
73. Padden FJ, Keith HD (1966) Crystallization in thin films of isotactic polypropylene. *J Appl Phys* 37(11):4013–4020. <https://doi.org/10.1063/1.1707968>
74. Patel GN, Patel RD (1970) Single crystals of high polymers by film formation. *J Polym Sci Part A-2 Polym Phys* 8(1):47–59. <https://doi.org/10.1002/pol.1970.160080104>
75. Martuscelli E, Pracella M, Zambelli A (1980) Properties of solution-grown crystals of fractions of isotactic polypropylene with different degrees of stereoregularity. *J Polym Sci Part B Polym Phys* 18(3):619–636. <https://doi.org/10.1002/pol.1980.180180320>
76. Yamada K, Kajioka H, Nozaki K et al (2011) Morphology and growth of single crystals of isotactic polypropylene from the melt. *J Macromol Sci Part B Phys* 50(2):236–247. <https://doi.org/10.1080/00222341003648847>
77. Prud'homme RE (2016) Crystallization and morphology of ultrathin films of homopolymers and polymer blends. *Prog Polym Sci* 54–55:214–231. <https://doi.org/10.1016/j.progpolymsci.2015.11.001>
78. Zhang B, Chen JJ, Liu BC et al (2017) Morphological changes of isotactic polypropylene crystals grown in thin films. *Macromolecules* 50(16):6210–6217. <https://doi.org/10.1021/acs.macromol.7b01381>
79. Zhang GJ, Lee PC, Jenkins S et al (2014) The effect of confined spherulite morphology of high-density polyethylene and polypropylene on their gas barrier properties in multilayered film systems. *Polymer* 55(17):4521–4530. <https://doi.org/10.1016/j.polymer.2014.07.009>
80. Tsukruk VV, Reneker DH (1995) Surface morphology of syndiotactic polypropylene single crystals observed by atomic force microscopy. *Macromolecules* 28(5):1370–1376. <https://doi.org/10.1021/ma00109a007>
81. Bu ZZ, Yoon Y, Ho RM et al (1996) Crystallization, melting, and morphology of syndiotactic polypropylene fractions. 3. Lamellar single crystals and chain folding. *Macromolecules* 29(20):6575–6581. <https://doi.org/10.1021/ma9603793>

82. Zhou W, Cheng SZD, Putthanarat S et al (2000) Crystallization, melting and morphology of syndiotactic polypropylene fractions. 4. In situ lamellar single crystal growth and melting in different sectors. *Macromolecules* 33(18):6861–6868. <https://doi.org/10.1021/ma000802e>
83. Marchetti A, Martuscelli E (1974) Effect of chain defects on morphology and thermal-behavior of solution-grown single-crystals of syndiotactic polypropylene. *J Polym Sci Part B Polym Phys* 12(8):1649–1666. <https://doi.org/10.1002/pol.1974.180120812>
84. Lovinger AJ, Davis DD, Lotz B (1991) Temperature-dependence of structure and morphology of syndiotactic polypropylene and epitaxial relationships with isotactic polypropylene. *Macromolecules* 24(2):552–560. <https://doi.org/10.1021/ma00002a033>
85. Hoffman JD, Frolen LJ, Ross GS et al (1975) Growth-rate of spherulites and axialites from melt in polyethylene fractions—regime-1 and regime-2 crystallization. *J Res Nat Bur Stan Sect A Phys Chem* 79(6):671–699. <https://doi.org/10.6028/jres.079A.026>
86. Kovacs AJ, Gonthier A (1972) Crystallization and fusion of self-seeded polymers. 2. Growth-rate, morphology and isothermal thickening of single-crystals of low molecular-weight poly(ethylene-oxide) fractions. *Kolloid Z Z Polym* 250(5):530–552. <https://doi.org/10.1007/bf01507524>
87. Khoury F, Passaglia E (1976). In: Hannay NB (ed) *Treatise on solid state chemistry. Crystalline and noncrystalline solids*, vol 3. Plenum, New York
88. Bassett DC (1981) *Principles of polymer morphology*. Cambridge University Press, New York
89. Keith HD, Padden FJ (1963) A phenomenological theory of spherulitic crystallization. *J Appl Phys* 34(8):2409–2421. <https://doi.org/10.1063/1.1702757>
90. White HM, Bassett DC, Jaaskelainen P (2009) A quantitative electron-microscopic investigation of alpha-phase lamellae in isotactic polypropylene fractions. *Polymer* 50(23):5559–5564. <https://doi.org/10.1016/j.polymer.2009.09.038>
91. Pawlak A, Galeski A (1990) Stability of spherulite growth-rate. *J Polym Sci Part B Polym Phys* 28(10):1813–1821. <https://doi.org/10.1002/polb.1990.090281012>
92. Nakamura K, Shimizu S, Umemoto S et al (2008) Temperature dependence of crystal growth rate for alpha and beta forms of isotactic polypropylene. *Polym J* 40(9):915–922. <https://doi.org/10.1295/polymj.PJ2007231>
93. Padden FJ, Keith HD (1959) Spherulitic crystallization in polypropylene. *J Appl Phys* 30(10):1479–1484. <https://doi.org/10.1063/1.1734985>
94. Li JX, Cheung WL (1999) RuO₄ staining and lamellar structure of alpha- and beta-PP. *J Appl Polym Sci* 72(12):1529–1538. [https://doi.org/10.1002/\(sici\)1097-4628\(19990620\)72:12%3c1529:Aid-app4%3e3.0.Co;2-u](https://doi.org/10.1002/(sici)1097-4628(19990620)72:12%3c1529:Aid-app4%3e3.0.Co;2-u)
95. Keith HD, Padden FJ (1996) Banding in polyethylene and other spherulites. *Macromolecules* 29(24):7776–7786. <https://doi.org/10.1021/ma960634j>
96. Varga J (1992) Supermolecular structure of isotactic polypropylene. *J Mater Sci* 27(10):2557–2579. <https://doi.org/10.1007/bf00540671>
97. Varga J, Ehrenstein GW (1997) High-temperature hedritic crystallization of the beta-modification of isotactic polypropylene. *Colloid Polym Sci* 275(6):511–519. <https://doi.org/10.1007/s003960050113>
98. Bai HW, Wang Y, Zhang ZJ et al (2009) Influence of annealing on microstructure and mechanical properties of isotactic polypropylene with beta-phase nucleating agent. *Macromolecules* 42(17):6647–6655. <https://doi.org/10.1021/ma9001269>
99. Rodriguez-Arnold J, Bu ZZ, Cheng SZD et al (1994) Crystallization, melting and morphology of syndiotactic polypropylene fractions. 2. Linear crystal-growth rate and crystal morphology. *Polymer* 35(24):5194–5201. [https://doi.org/10.1016/0032-3861\(94\)90469-3](https://doi.org/10.1016/0032-3861(94)90469-3)
100. Monks AW, White HM, Bassett DC (1996) On shish-kebab morphologies in crystalline polymers. *Polymer* 37(26):5933–5936. [https://doi.org/10.1016/s0032-3861\(96\)00626-x](https://doi.org/10.1016/s0032-3861(96)00626-x)

101. Han R, Nie M, Wang Q (2015) Control over beta-form hybrid shish-kebab crystals in polypropylene pipe via coupled effect of self-assembly beta nucleating agent and rotation extrusion. *J Taiwan Inst Chem Eng* 52:158–164. <https://doi.org/10.1016/j.jtice.2015.02.002>
102. Schultz JM, Lin JS, Hendricks RW et al (1981) Annealing of polypropylene films crystallized from a highly extended melt. *J Polym Sci Part B Polym Phys* 19(4):609–620. <https://doi.org/10.1002/pol.1981.180190405>
103. Petermann J, Gohil RM, Schultz JM et al (1982) The kinetics of defect clustering in fibrillar polypropylene crystals. *J Polym Sci Part B Polym Phys* 20(3):523–534. <https://doi.org/10.1002/pol.1982.180200313>
104. Balzano L, Ma Z, Cavallo D et al (2016) Molecular aspects of the formation of shish-kebab in isotactic polypropylene. *Macromolecules* 49(10):3799–3809. <https://doi.org/10.1021/acs.macromol.6b00428>
105. Nogales A, Hsiao BS, Somani RH et al (2001) Shear-induced crystallization of isotactic polypropylene with different molecular weight distributions: in situ small- and wide-angle X-ray scattering studies. *Polymer* 42(12):5247–5256. [https://doi.org/10.1016/s0032-3861\(00\)00919-8](https://doi.org/10.1016/s0032-3861(00)00919-8)
106. Ania F, Rueda DR, Balta-Calleja FJ et al (2000) Time resolved USAXS study of the shish-kebab structure in PE: annealing and melt crystallization. *J Mater Sci* 35(20):5199–5205. <https://doi.org/10.1023/a:1004864606257>
107. Hoffman JD, Davis GT, Lauritzen JI (1976) Crystalline and noncrystalline solids. In: Hannay NB (ed) *Treatise on solid state chemistry*, vol 3. Plenum, New York
108. Hoffman JD (1983) Regime-III crystallization in melt-crystallized polymers—the variable cluster model of chain folding. *Polymer* 24(1):3–26. [https://doi.org/10.1016/0032-3861\(83\)90074-5](https://doi.org/10.1016/0032-3861(83)90074-5)
109. DiMarzio EA, Guttman CM, Hoffman JD (1979) Is crystallization from the melt controlled by melt viscosity and entanglement effects. *Faraday Discuss* 68:210–217. <https://doi.org/10.1039/dc9796800210>
110. Turnbull D, Fisher JC (1949) Rate of nucleation in condensed systems. *J Chem Phys* 17(1):71–73. <https://doi.org/10.1063/1.1747055>
111. Cheng SZD, Lotz B (2005) Enthalpic and entropic origins of nucleation barriers during polymer crystallization: the Hoffman-Lauritzen theory and beyond. *Polymer* 46(20):8662–8681. <https://doi.org/10.1016/j.polymer.2005.03.125>
112. Lauritzen JI, Hoffman JD (1960) Theory of formation of polymer crystals with folded chains in dilute solution. *J Res Natl Bur Stand Sect A Phys Chem* 64(1):73–102. <https://doi.org/10.6028/jres.064A.007>
113. Hoffman JD, Lauritzen JI (1961) Crystallization of bulk polymers with chain folding—theory of growth of lamellar spherulites. *J Res Natl Bur Stand A* 65(4):297+. <https://doi.org/10.6028/jres.065a.035>
114. Lauritzen JI, Hoffman JD (1973) Extension of theory of growth of chain-folded polymer crystals to large undercoolings. *J Appl Phys* 44(10):4340–4352. <https://doi.org/10.1063/1.1661962>
115. Hoffman JD, Miller RL (1997) Kinetics of crystallization from the melt and chain folding in polyethylene fractions revisited: theory and experiment. *Polymer* 38(13):3151–3212. [https://doi.org/10.1016/s0032-3861\(97\)00071-2](https://doi.org/10.1016/s0032-3861(97)00071-2)
116. Hoffman JD (1982) Role of reptation in the rate of crystallization of polyethylene fractions from the melt. *Polymer* 23(5):656–670. [https://doi.org/10.1016/0032-3861\(82\)90048-9](https://doi.org/10.1016/0032-3861(82)90048-9)
117. Cheng SZD, Janimak JJ, Zhang A et al (1990) Regime transitions in fractions of isotactic polypropylene. *Macromolecules* 23(1):298–303. <https://doi.org/10.1021/ma00203a051>
118. Rodriguez-Arnold J, Zhang AQ, Cheng SZD et al (1994) Crystallization, melting and morphology of syndiotactic polypropylene fractions. 1. Thermodynamic properties, overall crystallization and melting. *Polymer* 35(9):1884–1895. [https://doi.org/10.1016/0032-3861\(94\)90978-4](https://doi.org/10.1016/0032-3861(94)90978-4)

119. Pawlak A, Piorkowska E (1999) Effect of negative pressure on melting behavior of spherulites in thin films of several crystalline polymers. *J Appl Polym Sci* 74(6):1380–1385. [https://doi.org/10.1002/\(sici\)1097-4628\(19991107\)74:6%3c1380:Aid-app9%3e3.0.Co;2-m](https://doi.org/10.1002/(sici)1097-4628(19991107)74:6%3c1380:Aid-app9%3e3.0.Co;2-m)
120. Galeski A, Koenczoel L, Piorkowska E et al (1987) Acoustic-emission during polymer crystallization. *Nature* 325(6099):40–41. <https://doi.org/10.1038/325040a0>
121. Galeski A, Piorkowska E, Koenczoel L et al (1990) Acoustic-emission during crystallization of polymers. *J Polym Sci Part B Polym Phys* 28(7):1171–1186. <https://doi.org/10.1002/polb.1990.090280714>
122. Schultz JM (1984) Microstructural aspects of failure in semicrystalline polymers. *Polym Eng Sci* 24(10):770–785. <https://doi.org/10.1002/pen.760241007>
123. Monasse B, Haudin JM (1986) Thermal-dependence of nucleation and growth-rate in polypropylene by non isothermal calorimetry. *Colloid Polym Sci* 264(2):117–122. <https://doi.org/10.1007/bf01414836>
124. Nowacki R, Kolasinska J, Piorkowska E (2001) Cavitation during isothermal crystallization of isotactic polypropylene. *J Appl Polym Sci* 79(13):2439–2448. [https://doi.org/10.1002/1097-4628\(20010328\)79:13%3c2439:Aid-app1051%3e3.0.Co;2-%23](https://doi.org/10.1002/1097-4628(20010328)79:13%3c2439:Aid-app1051%3e3.0.Co;2-%23)
125. Supaphol P, Spruiell JE (2000) Regime crystallization in syndiotactic polypropylenes: re-evaluation of the literature data. *Polymer* 41(3):1205–1216. [https://doi.org/10.1016/s0032-3861\(99\)00254-2](https://doi.org/10.1016/s0032-3861(99)00254-2)
126. Tranchida D, Mileva D, Resconi L et al (2015) Molecular and thermal characterization of a nearly perfect isotactic poly(propylene). *Macromol Chem Phys* 216(22):2171–2178. <https://doi.org/10.1002/macp.201500189>
127. Galeski S, Piorkowska E, Rozanski A et al (2016) Crystallization kinetics of polymer fibrous nanocomposites. *Eur Polymer J* 83:181–201. <https://doi.org/10.1016/j.eurpolymj.2016.08.002>
128. Rhoades AM, Wonderling N, Gohn A et al (2016) Effect of cooling rate on crystal polymorphism in beta-nucleated isotactic polypropylene as revealed by a combined WAXS/FSC analysis. *Polymer* 90:67–75. <https://doi.org/10.1016/j.polymer.2016.02.047>
129. Zia Q, Androsch R, Radosch HJ et al (2006) Morphology, reorganization and stability of mesomorphic nanocrystals in isotactic polypropylene. *Polymer* 47(24):8163–8172. <https://doi.org/10.1016/j.polymer.2006.09.038>
130. Piorkowska E (1995) Nonisothermal crystallization of polymers. 1. The background of the mathematical-description of spherulitic pattern-formation. *J Phys Chem* 99(38):14007–14015. <https://doi.org/10.1021/j100038a036>
131. Piorkowska E, Galeski A, Haudin JM (2006) Critical assessment of overall crystallization kinetics theories and predictions. *Prog Polym Sci* 31(6):549–575. <https://doi.org/10.1016/j.progpolymsci.2006.05.001>
132. Balbontin G, Dainelli D, Galimberti M et al (1992) Thermal-behavior of highly stereoregular syndiotactic polypropene from homogeneous catalysts. *Makromol Chem Macromol Chem Phys* 193(3):693–703
133. Rozanski A, Monasse B, Szkudlarek E et al (2009) Shear-induced crystallization of isotactic polypropylene based nanocomposites with montmorillonite. *Eur Polymer J* 45(1):88–101. <https://doi.org/10.1016/j.eurpolymj.2008.10.011>
134. Kumaraswamy G, Issaian AM, Kornfield JA (1999) Shear-enhanced crystallization in isotactic polypropylene. 1. Correspondence between in situ rheo-optics and ex situ structure determination. *Macromolecules* 32(22):7537–7547. <https://doi.org/10.1021/ma990772j>
135. Hayashi Y, Matsuba G, Zhao YF et al (2009) Precursor of shish-kebab in isotactic polystyrene under shear flow. *Polymer* 50(9):2095–2103. <https://doi.org/10.1016/j.polymer.2009.03.008>
136. Hamad FG, Colby RH, Milner ST (2015) Lifetime of flow-induced precursors in isotactic polypropylene. *Macromolecules* 48(19):7286–7299. <https://doi.org/10.1021/acs.macromol.5b01408>

137. Tribout C, Monasse B, Haudin JM (1996) Experimental study of shear-induced crystallization of an impact polypropylene copolymer. *Colloid Polym Sci* 274(3):197–208. <https://doi.org/10.1007/bf00665636>
138. Jay F, Haudin JM, Monasse B (1999) Shear-induced crystallization of polypropylenes: effect of molecular weight. *J Mater Sci* 34(9):2089–2102. <https://doi.org/10.1023/a:1004563827491>
139. Somani RH, Yang L, Hsiao BS (2006) Effects of high molecular weight species on shear-induced orientation and crystallization of isotactic polypropylene. *Polymer* 47(15):5657–5668. <https://doi.org/10.1016/j.polymer.2004.12.066>
140. Janeschitz-Kriegl H, Ratajski E, Stadlbauer M (2003) Flow as an effective promotor of nucleation in polymer melts: a quantitative evaluation. *Rheol Acta* 42(4):355–364. <https://doi.org/10.1007/s00397-002-0247-x>
141. Eder G, Janeschitz-Kriegl H, Liedauer S (1990) Crystallization processes in quiescent and moving polymer melts under heat-transfer conditions. *Prog Polym Sci* 15(4):629–714. [https://doi.org/10.1016/0079-6700\(90\)90008-o](https://doi.org/10.1016/0079-6700(90)90008-o)
142. Haudin JM, Duplay C, Monasse B et al (2002) Shear-induced crystallization of polypropylene. Growth enhancement and rheology in the crystallization range. *Macromol Symp* 185:119–133. [https://doi.org/10.1002/1521-3900\(200208\)185:1%3c119:Aid-masy119%3e3.0.Co;2-k](https://doi.org/10.1002/1521-3900(200208)185:1%3c119:Aid-masy119%3e3.0.Co;2-k)
143. Vleeshouwers S, Meijer HEH (1996) A rheological study of shear induced crystallization. *Rheol Acta* 35(5):391–399. <https://doi.org/10.1007/bf00368990>
144. Jerschow P, Janeschitz-Kriegl H (1997) The role of long molecules and nucleating agents in shear induced crystallization of isotactic polypropylenes. *Int Polym Process* 12(1):72–77. <https://doi.org/10.3139/217.970072>
145. Liedauer S, Eder G, Janeschitz-Kriegl H et al (1993) On the kinetics of shear-induced crystallization in polypropylene. *Int Polym Process* 8(3):236–244. <https://doi.org/10.3139/217.930236>
146. Kimata S, Sakurai T, Nozue Y et al (2007) Molecular basis of the shish-kebab morphology in polymer crystallization. *Science* 316(5827):1014–1017. <https://doi.org/10.1126/science.1140132>
147. Smith P, Pennings AJ (1976) Unidirectional solidification of isotactic polypropylene. *Eur Polymer J* 12(11):781–784. [https://doi.org/10.1016/0014-3057\(76\)90070-7](https://doi.org/10.1016/0014-3057(76)90070-7)
148. Zhang YF, Li D, Chen QJ (2017) Preparation and nucleation effects of nucleating agent hexahydrophthalic acid metal salts for isotactic polypropylene. *Colloid Polym Sci* 295(10):1973–1982. <https://doi.org/10.1007/s00396-017-4176-8>
149. Mathieu C, Thierry A, Wittmann JC et al (2002) Specificity and versatility of nucleating agents toward isotactic polypropylene crystal phases. *J Polym Sci Part B Polym Phys* 40(22):2504–2515. <https://doi.org/10.1002/polb.10309>
150. Varga J, Mudra I, Ehrenstein GW (1999) Highly active thermally stable beta-nucleating agents for isotactic polypropylene. *J Appl Polym Sci* 74(10):2357–2368. [https://doi.org/10.1002/\(sici\)1097-4628\(19991205\)74:10%3c2357:Aid-app3%3e3.0.Co;2-2](https://doi.org/10.1002/(sici)1097-4628(19991205)74:10%3c2357:Aid-app3%3e3.0.Co;2-2)
151. Chen J, Schneider K, Kretschmar B et al (2014) Nucleation and growth behavior of beta-nucleated iPP during shear induced crystallization investigated by in-situ synchrotron WAXS and SAXS. *Polymer* 55(21):5477–5487. <https://doi.org/10.1016/j.polymer.2014.07.058>
152. Chen J, Schneider K, Gao S et al (2015) In-situ synchrotron X-ray studies of crystallization of beta-nucleated iPP subjected to a wide range of shear rates and shear temperatures. *Polymer* 76:182–190. <https://doi.org/10.1016/j.polymer.2015.08.042>
153. Yamada K, Hikosaka M, Toda A et al (2003) Equilibrium melting temperature of isotactic polypropylene with high tacticity: 1. Determination by differential scanning calorimetry. *Macromolecules* 36(13):4790–4801. <https://doi.org/10.1021/ma021206i>
154. Iijima M, Strobl G (2000) Isothermal crystallization and melting of isotactic polypropylene analyzed by time- and temperature-dependent small-angle X-ray scattering experiments. *Macromolecules* 33(14):5204–5214. <https://doi.org/10.1021/ma000019m>

155. Xu J, Heck B, Ye HM et al (2016) Stabilization of nuclei of lamellar polymer crystals: insights from a comparison of the Hoffman-Weeks line with the crystallization line. *Macromolecules* 49(6):2206–2215. <https://doi.org/10.1021/acs.macromol.5b02123>
156. Wunderlich B (1980) *Macromolecular physics. Crystal melting*, vol 3. Academic Press, New York
157. Mezghani K, Phillips PJ (1994) Equilibrium melting-point of deuterated polypropylene. *Macromolecules* 27(21):6145–6146. <https://doi.org/10.1021/ma00099a032>
158. Cheng SZD, Janimak JJ, Zhang AQ et al (1991) Isotacticity effect on crystallization and melting in polypropylene fractions. 1. Crystalline-structures and thermodynamic property changes. *Polymer* 32(4):648–655. [https://doi.org/10.1016/0032-3861\(91\)90477-z](https://doi.org/10.1016/0032-3861(91)90477-z)
159. Hoffman JD, Weeks JJ (1962) Melting process and equilibrium melting temperature of polychlorotrifluoroethylene. *J Res Natl Bur Stand Sect A-Phys Chem* 66(JAN-F):13–+. <https://doi.org/10.6028/jres.066a.003>
160. Philips RA, Wolkowicz MD (1996) In: Moore EP Jr (ed) *Polypropylene handbook*. Hanser Verlag, Munich
161. Xu JN, Srinivas S, Marand H et al (1998) Equilibrium melting temperature and undercooling dependence of the spherulitic growth rate of isotactic polypropylene. *Macromolecules* 31(23):8230–8242. <https://doi.org/10.1021/ma980748q>
162. Mezghani K, Campbell RA, Phillips PJ (1994) Lamellar thickening and the equilibrium melting-point of polypropylene. *Macromolecules* 27(4):997–1002. <https://doi.org/10.1021/ma00082a017>
163. Huang TW, Alamo RG, Mandelkern L (1999) Fusion of isotactic poly(propylene). *Macromolecules* 32(19):6374–6376. <https://doi.org/10.1021/ma990092g>
164. Marand H, Xu JN, Srinivas S (1998) Determination of the equilibrium melting temperature of polymer crystals: linear and nonlinear Hoffman-Weeks extrapolations. *Macromolecules* 31(23):8219–8229. <https://doi.org/10.1021/ma980747y>
165. Monasse B, Haudin JM (1985) Growth transition and morphology change in polypropylene. *Colloid Polym Sci* 263(10):822–831. <https://doi.org/10.1007/bf01412960>
166. De Rosa C, Auriemma F, Vinti V, Galimberti M (1998) Equilibrium melting temperature of syndiotactic polypropylene. *Macromolecules* 31(18):6206–6210. <https://doi.org/10.1021/ma9805248>
167. Wang X, Hou WM, Zhou JJ et al (2007) Melting behavior of lamellae of isotactic polypropylene studied using hot-stage atomic force microscopy. *Colloid Polym Sci* 285(4):449–455. <https://doi.org/10.1007/s00396-006-1586-4>
168. Alamo RG, Brown GM, Mandelkern L et al (1999) A morphological study of a highly structurally regular isotactic poly(propylene) fraction. *Polymer* 40(14):3933–3944. [https://doi.org/10.1016/s0032-3861\(98\)00613-2](https://doi.org/10.1016/s0032-3861(98)00613-2)
169. White HM, Bassett DC (1997) On variable nucleation geometry and segregation in isotactic polypropylene. *Polymer* 38(22):5515–5520. [https://doi.org/10.1016/s0032-3861\(97\)00110-9](https://doi.org/10.1016/s0032-3861(97)00110-9)

Chapter 5

Morphology Development and Control



Roberto Pantani, Felice De Santis and Vito Speranza

Contents

5.1	Introduction.....	244
5.1.1	Characteristics of Polypropylene.....	245
5.1.2	Processing of PP.....	246
5.2	Crystallization Kinetics of PP.....	246
5.2.1	Effect of Temperature.....	246
5.2.2	Effect of Pressure.....	249
5.2.3	Effect of Flow.....	252
5.2.4	Effect of Nucleating Agents.....	253
5.2.5	Effect of Stereo-Defects.....	256
5.3	Crystallization Kinetics Models.....	257
5.3.1	Quiescent Crystallization Kinetics.....	257
5.3.2	Flow-Induced Crystallization Kinetics.....	259
5.4	Injection Molding.....	261
5.4.1	Morphology of Injection Molded PP.....	261
5.4.2	Morphology of Micro-Injection-Molded PP.....	264
5.4.3	Advanced Methods to Control Morphology of Injection Molded Parts.....	266
5.5	Modeling Morphology in Injection Molded Parts.....	274
5.5.1	Fibrillar Morphology.....	274
5.5.2	Distribution of Spherulite Diameters.....	276
5.5.3	Simulation of Morphology Development in Injection Molded IPP: A Case Study.....	277
5.6	Other Processing Techniques.....	285
5.6.1	Compression Molding.....	285
5.6.2	Extrusion-Related Techniques.....	286
	References.....	287

R. Pantani (✉) · V. Speranza

Department of Industrial Engineering, University of Salerno, Fisciano, SA, Italy
e-mail: rpantani@unisa.it

V. Speranza

e-mail: vsperanza@unisa.it

F. De Santis

Borealis Polyolefine GmbH, Linz, Austria
e-mail: fedesantis@unisa.it

© Springer Nature Switzerland AG 2019

J. Karger-Kocsis and T. Bárány (eds.), *Polypropylene Handbook*,
https://doi.org/10.1007/978-3-030-12903-3_5

243

Abstract When referred to polymers, the word morphology is adopted to indicate: crystallinity, which is the relative volume occupied by each of the crystalline phases, including mesophases; dimensions, shape, distribution, and orientation of the crystallites. In this chapter, we describe the morphology of isotactic polypropylene in function of the main variables: temperature, pressure, and flow. This description is carried out not only under the phenomenological point of view but also considering the models which describe the effects of these variables. The chapter describes then the morphology development during injection molding, which is taken as an example of a complex process in which fast cooling rates, high pressures and strong flow fields are involved. A case study in which the simulation of the behavior of polypropylene during injection molding tests is eventually reported.

5.1 Introduction

The properties of polypropylene (PP) depend on the molecular weight and molecular weight distribution, crystallinity, type and proportion of comonomer (if used) and the isotacticity. In isotactic polypropylene, for example, the methyl groups are oriented on one side of the carbon backbone. This arrangement creates a greater degree of crystallinity, of about 60%, and results in a stiffer material that is more resistant to creep than both atactic polypropylene and polyethylene.

Most commercial and important polypropylene is isotactic, and thus in this chapter from here on it will be referred to polypropylene without mentioning “isotactic”.

This chapter will deal in particular with the morphology of polypropylene. The term *morphology* means “the study of the form” where form stands for the shape and arrangement of parts of the object. When referred to polymers, the word morphology is adopted to indicate the following:

- crystallinity, which is the relative volume occupied by each of the crystalline phases, including mesophases;
- dimensions, shape, distribution, and orientation of the crystallites.

The variety of plastic characteristics (mechanical, optical, electrical, transport, and chemical) derives not only from the chemical structure of molecules but also from the microstructure and morphology. For instance, crystallinity has a pronounced effect on the mechanical properties of the bulk material because crystals are generally stiffer than amorphous material, and also orientation induces anisotropy and other changes in mechanical properties. Molecular orientation, or simply orientation, arises in injection molding and may have desirable or undesirable consequences. It refers to the preferential alignment of macromolecules in the product. Tensile strength in the orientation direction is basically that of the carbon–carbon (or other covalent bonds) in the polymer backbone. In the transverse direction, the strength is provided by the secondary intramolecular bonds. Hence, uniaxially oriented materials will be much stronger and stiffer in one direction than in another.

The production of high quality polymeric parts, which is a sector in great expansion, requires the capacity of being able to predict and control these morphological features.

In this chapter, the state of the art on the effect of the main processing variables on the formation of the crystalline phases and on the morphology of isotactic polypropylene is carried out, with particular reference to injection molding. This particular process is taken as a reference in this chapter because in injection molding the contemporary effects of high pressures, strong flow fields, and fast cooling rates allow the development of several crystalline phases and structures, unique in all the polymer transformation techniques. The effect of other processing techniques on morphology evolution are briefly outlined at the end of the chapter.

5.1.1 Characteristics of Polypropylene

Isotactic polypropylene can crystallize in different phases. The most common phase is α [1], which is formed at low pressures and at low cooling rates [2]. In the presence of specific nucleating agents, or of specific flow conditions, β -phase can develop [3]. At high pressures and temperatures, γ -phase is formed [4] (see Chap. 2 of this book). A mesomorphic phase is formed at cooling rates higher than 100 K/s [5]. The presence of each of these phases induces different properties to the parts made of polypropylene. The α phase makes polypropylene rigid and strong. In contrast, β phase induces a lower modulus and yield stress, but higher tensile strength and strain, impact strength and toughness [6]. The γ phase has been reported to induce higher elastic modulus and yield stress with respect to α phase, but a slightly lower ultimate strain [7]. A large amount of mesophase makes the material ductile and flexible [8], and also reduces the density [2].

Apart from the phases, polypropylene can crystallize in different shapes. Spherulitic structures appear when the material crystallizes in quiescent conditions, as a result of nucleation and growth phenomena. The size of the spherulites affects the mechanical [9] and optical properties [10] with a general increase of impact strength and transparency on decreasing the spherulite size. In samples containing both phases, β spherulites are usually larger than α spherulites. Under flow conditions, polymer chains are oriented in the melt and can crystallize differently from quiescent conditions. For example, by the effect of flow, the so-called “shish-kebabs” can be formed [11] (see Chap. 4 of this book). In these structures a highly oriented core composed of extended chains (“shish”) forms, on which oriented chain folded lamellae (“kebabs”) grow. These structures usually induce larger moduli and strain at break if deformed in the direction of main orientation [12].

What stated above provides a clear indication that the properties of an object made of polypropylene depends upon the particular crystalline phase and on the structures obtained. The prediction of the final morphology in function of the processing conditions and, above all, the control of the morphological features, is a strategic issue for the polymer processing industry.

5.1.2 Processing of PP

About 40% of polypropylene consumption is processed by injection molding. A lower amount (about 30%) is processed for obtaining fibers by means of fiber spinning. About 20% is the quota used for films. Other processes, like blow molding, represent minor transformation techniques for this material.

As far as morphology development is concerned, cooling rates, deformation fields, and pressure levels play a role during processing [13]. Under this aspect, the main differences between injection molding and other processes like fiber spinning or film blowing rely: on the type of deformation, which is basically due to shear in injection molding (except in narrow sections in which elongational flow can be significant), whereas it is uniaxial in fiber spinning and biaxial in film blowing; on the effect of pressure, since in injection molding the pressure can reach several hundreds of bar, whereas pressure is atmospheric in other processes.

It is evident that injection molding is the processing technique which presents the most complete set of conditions under which morphology development takes place. This is the reason why in the following we refer mainly to this process for the description of morphology evolution of polypropylene in processing conditions.

5.2 Crystallization Kinetics of PP

Traditional studies of polymer crystallization kinetics started from idealized conditions in which all parameters of state (temperature, pressure, etc.) are constants. The importance of crystallization kinetics of polypropylene during industrial processing obviously led to investigate the influence of variable external conditions.

5.2.1 Effect of Temperature

The early models of crystallization in variable conditions concerned only variation of temperature. Standard calorimetric characterization (adopting both isothermal and non-isothermal tests) was performed by means of a Differential Scanning Calorimetry (DSC) apparatus. The thermal inertia of the standard calorimetric cells limited the exploration range for isotactic polypropylene to heating/cooling rate of less than 1 K/s. In fact, PP is considered a fast crystallizing polymer, because of the simple macromolecular chain,

Furthermore, some corrections were proposed to take into account the low heat transfer coefficient of the polymer, according to the procedure illustrated by Eder and Janeschitz-Kriegl [13].

For the same reason, the explored range using DSC in isothermal conditions is limited by the maximum attainable cooling rate, able to prevail crystallization before reaching isothermal test temperature.

In order to describe PP crystallinity evolution under high cooling rates, usually experienced in processing conditions, many efforts have been spent along this direction. In particular, the effect of high cooling rates was analyzed in a series of works conducted by Piccarolo et al. [14] and Coccorullo et al. [2], in which the morphology of samples solidified under high cooling rates (hundreds of K/s) was investigated, observing the formation of a mesophase. Magill [15] and Ding et al. [16] measured crystallinity evolution during cooling at moderate cooling rates (up to about 3 K/s) by means of optical methods. This approach was extended by Titomanlio and co-workers to higher cooling rates (30 K/s) [17, 18].

Modulus, ductility, and strength can be modulated through the crystallization of α phase or the mesophase. Different morphologies are observed depending on the stereoregularity and conditions of crystallization [5]. Crystals of the mesomorphic form always exhibit a nodular morphology, accounting for the similar good deformability of all quenched samples. The mesophase transforms by thermal treatments (annealing at elevated temperature) into the α form preserving the nodular morphology, with an increase of strength while maintaining the ductility typical of the mesophase as shown in Fig. 5.1. Annealing of the mesophase permits

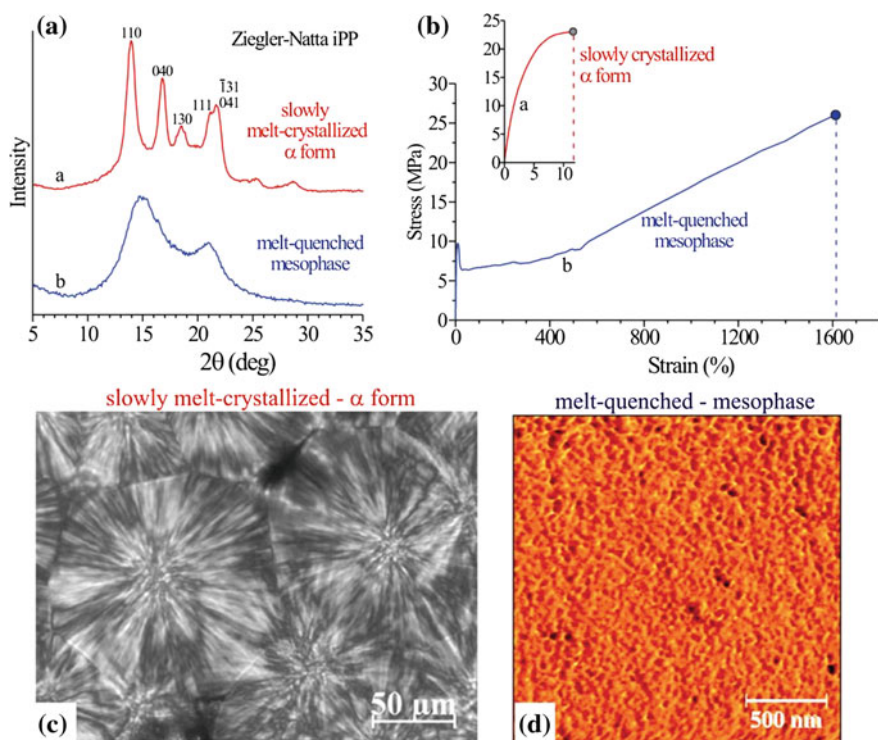


Fig. 5.1 X-ray powder diffraction profiles (a), stress-strain curves (b) and optical microscopy (c) and AFM (d) images of samples of highly stereoregular iPP slowly crystallized from the melt in the α form (a) and crystallized in the mesophase by quenching the melt at 0 °C (b). Reproduced from [5]

a precise adjustment of crystallinity and size of nodular crystals offering additional options to modify the mechanical properties.

More recently the introduction of nanocalorimetry performed with Flash DSC [19] opened the possibility to further explore the crystallization kinetics of PP. In particular, a wide set of cooling scans and subsequent melting behavior of PP were investigated using Flash DSC at very high cooling rate. This technique offered the possibility to perform calorimetric measurements at rates of more than 1000 K/s, both in cooling and in heating, to characterize the crystallization. As shown in Fig. 5.2, when the iPP sample was solidified with cooling rate larger than 160 K/s, a novel enthalpic process was observed that was related to the mesomorphic phase formation [20]. Furthermore, at cooling rates higher than 1000 K/s, the PP sample did not crystallize in the α or in the mesomorphic form. The subsequent heating scan starting from $-15\text{ }^{\circ}\text{C}$ showed an exothermic event, between 0 and $30\text{ }^{\circ}\text{C}$, attributed to the mesophase cold crystallization [20].

Therefore a wide set of crystallization isotherms and the subsequent melting behavior of isotactic polypropylene were investigated using Flash DSC with a very high rate in the cooling step [21]. Isothermal crystallization experiments were carried at any temperature in between the glass transition and melting, as the test temperature can be reached at a cooling rate of 1000 K/s, thus, preventing crystallization during the cooling step. Isothermal tests after such fast cooling were performed at intervals of 5 K within the temperature range $-15\text{--}90\text{ }^{\circ}\text{C}$, and a local exothermal overheating was observed, as shown in Fig. 5.3.

In particular, for each isotherm, the observed peaks were fitted using the Kolmogorov – Johnson – Mehl – Avrami model. The plot of the crystallization kinetics constant as a function of temperature gives clear evidence of two kinetic processes [21], related to α and mesomorphic phases. The subsequent heating scan

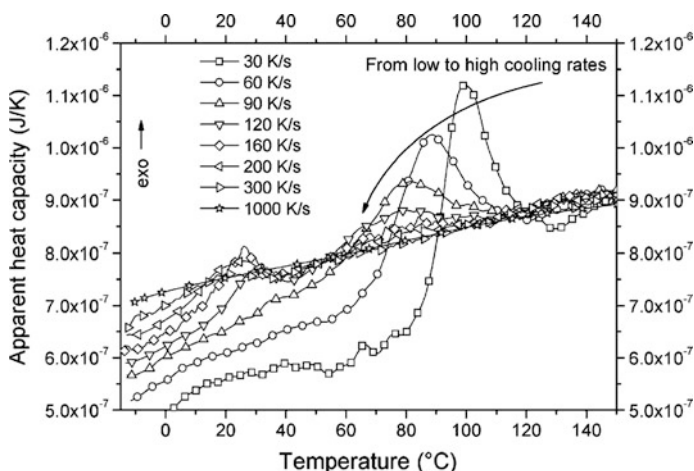
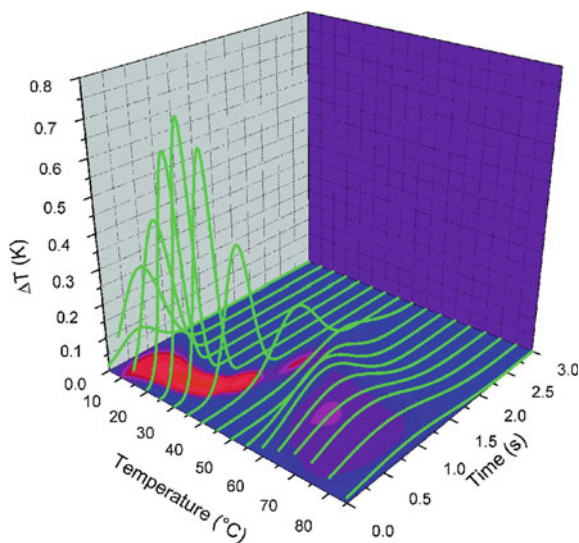


Fig. 5.2 Thermograms of iPP sample at selected cooling rates (30, 60, 90, 120, 160, 200, 300, and 1000 K/s). Reproduced from [20]

Fig. 5.3 Temperature increase evolution versus time for each isothermal test. Reproduced from [21].



performed starting from $-15\text{ }^{\circ}\text{C}$ showed an exothermic event, between 0 and $30\text{ }^{\circ}\text{C}$, due to the mesophase cold crystallization, for isotherms at a temperature lower than $20\text{ }^{\circ}\text{C}$.

The result of the kinetic analysis, i.e. the reciprocal crystallization rate constant k , proportional to crystallization half-time, is reported in Fig. 5.4. The same plot also shows a large number of kinetic data available in the literature concerning the isothermal crystallization of iPP [21], obtained from experiments collected with various methods. Despite the scatter due to the experiments performed on different iPP resins, the results, plotted in Fig. 5.4, clearly indicate a focused band from $110\text{--}160\text{ }^{\circ}\text{C}$. The kinetic data, obtained by interpreting nanocalorimetry isothermal results [21], covered a range of temperatures from $5\text{--}85\text{ }^{\circ}\text{C}$, mostly unexplored previously. In Fig. 5.4, it is evident that at temperatures lower than $45\text{ }^{\circ}\text{C}$, there is a variation in the kinetic behavior: the mesophase is formed by homogeneous nucleation (Avrami index $n = 4$) and above $45\text{ }^{\circ}\text{C}$, the α phase prevails due to heterogeneous nucleation (Avrami index $n = 3$) [21].

5.2.2 Effect of Pressure

During industrial processing, melt polymers are subjected to high pressure, that has an important influence on the material flowing, solidification, and the final properties. At atmospheric pressure, the γ phase of isotactic polypropylene appears under various conditions, for instance when the polymer chains are short [22] or in the case of a ethylene-propylene copolymer with a small amount of ethylene [23, 24]. However, the main way to obtain γ structure for a high molecular weight

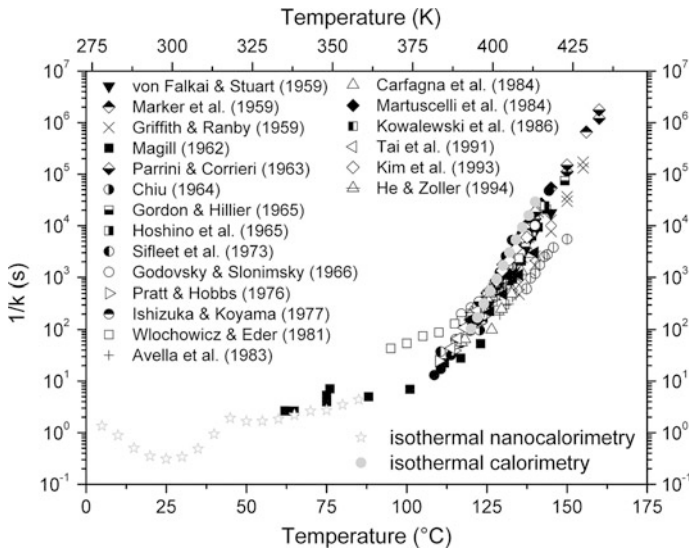


Fig. 5.4 Cumulative data of the isothermal crystallization of iPP: variation of the reciprocal crystallization rate constant k as a function of crystallization temperature. Black symbols: literature data reported in [21]. Isothermal nanocalorimetry and isothermal calorimetry as gray stars and circles, respectively. Reproduced from [21]

homopolymer is to perform crystallization under high pressure [25, 26]. This structure usually become dominant at pressures higher than 200 MPa [27, 28]. The γ form of isotactic polypropylene is certainly the most peculiar considering the nonparallel chain axes, coexisting in the orthorhombic unit cell which was first proposed by Brückner and Meille [25, 29]. Even if, about 50 years ago, it was established that the ratio between the γ -iPP and the α -iPP polymorphs grows with increasing pressure, the solidification process under this conditions still needs to be properly described and quantified [4].

Experimental data, performed in isothermal experiments varying pressure, on the dependence of the specific volume on temperature and pressure, up to 200 MPa, were reported thanks to the High-pressure Dilatometer developed by Zoller [30, 31], as shown in Fig. 5.5.

The specific volume is smaller with increasing pressure, at the same temperature, and the melting transition is evident in Fig. 5.5 with a sharp transition. The melting point rises with pressure. Thus PP can be crystallized at much higher temperatures when pressure is applied. The crystallization under these conditions of high pressures and temperatures has been studied. Zoller et al. [32] explored the pressure effect on crystallization kinetics performing isobaric measurements at constant heating and cooling rate of 2.5 K/min, as shown in Fig. 5.6.

For PP in the semicrystalline region, the volumes in cooling runs are higher than those in heating runs. The volume difference apparently increases with pressure. This indicates that the high pressure crystallization produces samples of lower

Fig. 5.5 Cross-plotted isobars, obtained from isothermal PVT measurements taken in order of increasing temperature. Data reproduced from [31]

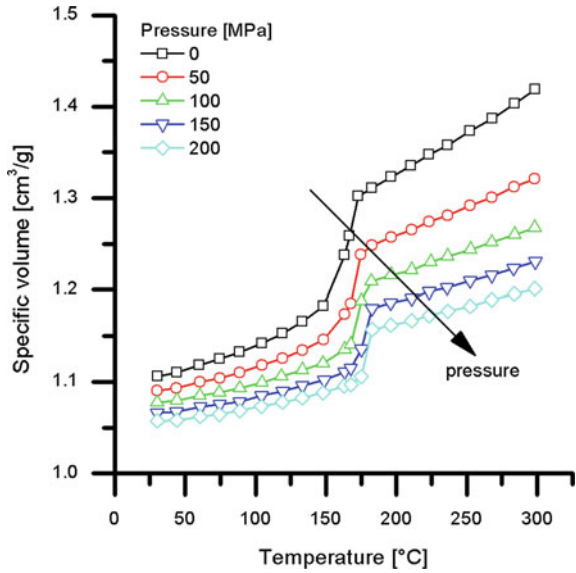
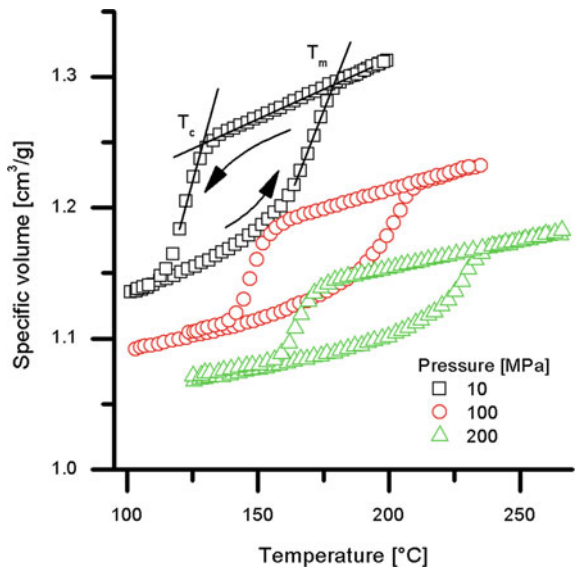


Fig. 5.6 Melting and crystallization isobars of polypropylene at various pressures, with heating and cooling rates: 2.5 K/min. Data reproduced from [32]



density than the low pressure crystallization [32]. The melting and solidification curves are indicated in Fig. 5.6. For all the solidification pressure values, the specific volume in the solid phase at the end of the solidification curve is systematically higher than the one measured at the beginning of the melting curve. This behavior demonstrates that during solidification under pressure some structural transformations occur that can justify the final lower value of density [33].

In particular, He and Zoller [32] explained the reduction of density with the formation of the γ phase, which is less dense than the α phase.

5.2.3 Effect of Flow

In the most commonly adopted polymer processes such as extrusion, injection molding, and film blowing, the molten polymer is subjected to intense shear and elongational flow fields. Process conditions deeply affect the resulting microstructure: crystallization kinetics, morphology (size, shape, orientation of crystallites) and presence of different crystalline phases can be dramatically different with respect to reference isothermal, quiescent, and low-pressure conditions, and this can have a strong influence on the final physical properties.

Recent developments in flow-induced crystallization (FIC) have demonstrated the existence of three stages [34] which, for the same polymer at the same temperature and pressure, take place on increasing the flow intensity: (i) the effect of flow upon final morphologies and upon crystallization kinetics is negligible, (ii) the flow causes a strong enhancement of crystallization kinetics but the spherulitic morphology is kept, although the average spherulitic dimension decreases, (iii) the flow deeply influences both morphology and kinetics by causing formation of fibrillar structures in the polymer melt.

The transition from the stage *i* and the stage *ii* takes place on increasing the Weissenberg number, namely the dimensionless product of relaxation time and shear rate. In the stage *ii*, it is generally well accepted that flow affects the crystallization kinetics by increasing the crystallization temperature [35–37]. This enhances the growth rate and the nucleation rate, since at each given temperature the apparent undercooling increases. It was also found [35] that the formation of γ -phase under flow is also due to the increase of undercooling.

A phenomenon which appears in the stage *ii*, not present in stage *i* at least for polypropylene, is the nucleation rate. In fact, nucleation density under quiescent conditions was found constant at a constant temperature, a nucleation rate was observed and measured under steady shear conditions [37]. The nucleation rate was found to increase on increasing the deformation rate (Fig. 5.7a).

Also the growth rate increases on increasing the deformation rate. This phenomenon was ascribed to the apparent undercooling increase due to the increase in the melting temperature. A quantification of the increase in the melting temperature was carried out in the literature [37], as shown in Fig. 5.7b [36], where data of growth rates, collected at 140 °C are reported at different shear rates.

In Fig. 5.7b, the lines passing through the different points refer to a prediction of growth rate carried out by considering the increase of melting temperature (indicated near to each line) in the Hoffman-Lauritzen equation adopted to describe the growth rate.

The transition from the stage *ii* to the stage *iii* takes place with a complete change of structures, with the appearance of so-called shish-kebab. The “shish” are

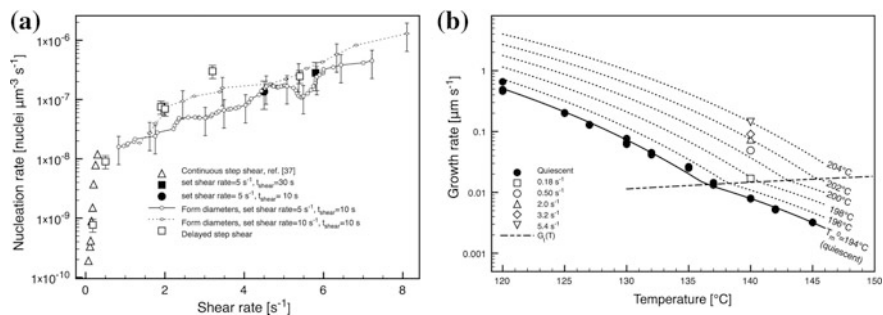


Fig. 5.7 **a** nucleation rate measured from different experiments vs. shear rate; **b** results of growth rate in quiescent conditions (filled circles) and during shear flow. The dashed line identifies the change of growth regime. Predictions of growth rate obtained with different melting temperature are reported as dotted lines. Data reproduced from [36]

fibrillary crystals, whereas the kebabs are radially growing lamellae which nucleate on the shish. Experimental evidence shows that, at each deformation rate, the time required to obtain highly oriented structures decreases with increasing of the deformation rate itself (Fig. 5.8).

The parameter governing this transition is still under debate, with two main hypotheses: a threshold based on a critical Weissenberg number [35], and a threshold based on a critical value of specific work [39, 40]. A more recent approach (described below) proposes a combination of the two criteria.

The shish-kebab morphology presents a complex morphology: kebabs are normally in the stable α -phase, and on their surface, some daughters lamellae can nucleate [41]. These lamellae are still in α -phase and grow at a different angle (40°) with respect to the kebabs. In the presence of pressure, kebab can provide nucleation sites for γ -daughters morphologies [42].

5.2.4 Effect of Nucleating Agents

Nucleating agents provide higher polymer crystallization temperatures, creating a larger number of smaller spherulites. The size reduction of spherulites positively affects the optical properties, reducing haze, and may improve flexural modulus and rigidity [43]. The faster crystallization kinetics of nucleated polypropylene also reduces solidification, and thus processing, times. The effects of some nucleating agents on the properties of iPP samples are reported in Fig. 5.9.

Obviously, in order to achieve an optimal efficiency of a nucleating agent, a good dispersion is required. This means that the dispersion techniques are particularly significant.

For polypropylene, nucleating agents can also be used to promote the formation of a specific crystalline phase. A review of advanced nucleating agents can be found

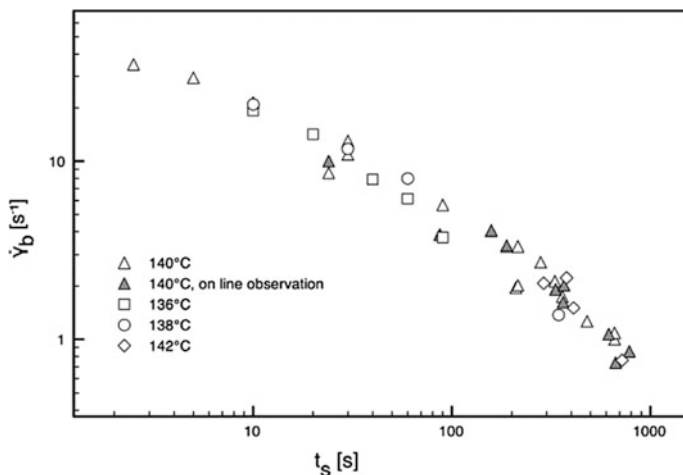


Fig. 5.8 Plot of the critical shear rate at which the oriented structures develop, versus shear time. The temperature at which the tests were conducted is reported. Data reproduced from [38]

in the literature [45]. In Table 5.1 we recall some of the most efficient nucleating agents for the formation of a specific phase in iPP.

It is interesting to notice that the addition of a β -nucleating agent does not affect the rate of mesophase formation at high cooling rates [46], which supports the idea that at high undercooling homogeneous nucleation is the controlling mechanism for ordering.

The efficiency of a nucleating agent is generally estimated by finding the parameter NE% according to the method proposed Fillon et al. [52] (Eq. 5.1):

$$NE\% = 100 \frac{T_c - T_{c1}}{T_{c2} - T_{c1}}, \quad (5.1)$$

where T_c , T_{c1} and T_{c2} are peak crystallization temperatures of the nucleated, non-nucleated and self-nucleated polymer, respectively.

The method relies from the assumption that the procedure to determine T_{c2} allows obtaining the highest achievable crystallization temperature. This procedure is based on the following steps, carried out by a DSC apparatus:

- heating the sample to a temperature higher than melting value and maintaining this temperature for 5 min;
- cooling the polymer at a constant cooling rate to room temperature and (during this step the temperature T_{c1} is obtained);
- heating the sample to a temperature at which melting starts, and holding this temperature for 5 min;
- cooling the sample at the same cooling rate that was applied during the second step (during this step the temperature T_{c2} is obtained).

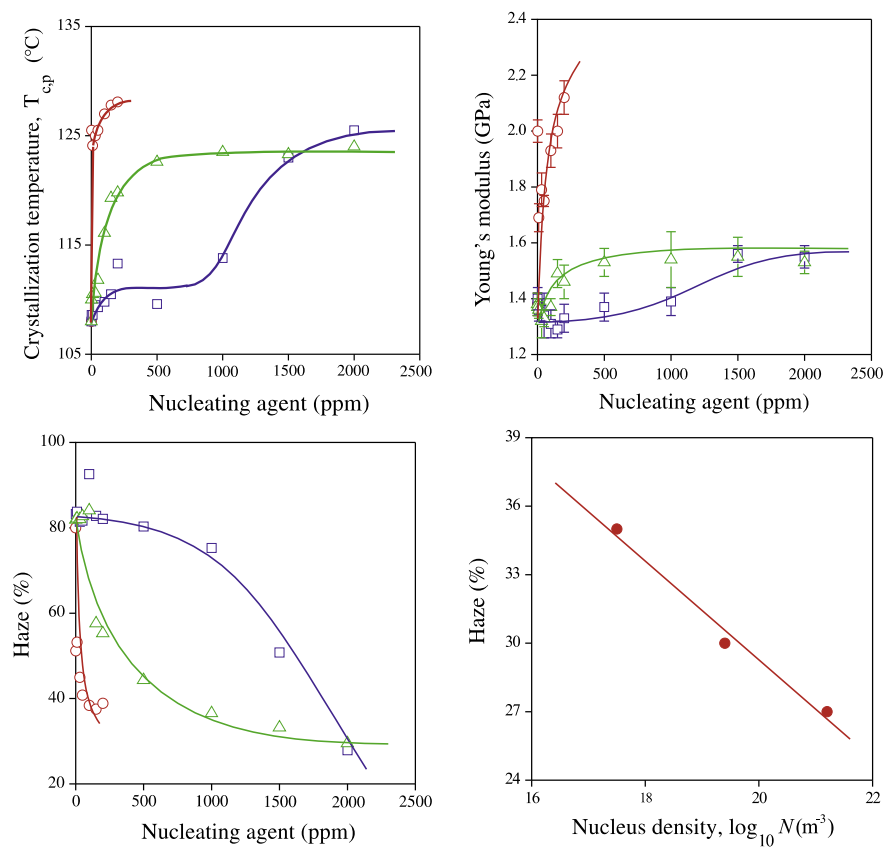


Fig. 5.9 Effect of nucleating agents on the properties of iPP. Circles refer to PVCH, triangles to NA-11, squares to NA21E. Data reproduced from [44]

Table 5.1 Nucleating agents for the formation of a specific phase in iPP

Nucleating agent	Phase	References
PVCH (poly(vinyl cyclohexane))	α	[44]
Na-11 (sodium 2,2'-methylene bis-(4,6-di-tert-butylphenyl)phosphate)	α	[47]
DMDBS (1,3:2,4-bis(3,4-dimethylbenzylidene)-sorbitol)	α	[48]
Linear Trans Quinacridone	β	[49]
Ca-salt of suberic and pimelic acid	β	[49]
N,N'-dicyclohexyl-2,6-naphthalene dicarboxamide	β	[50]
Bicyclo[2.2.1]heptane dicarboxylate salt	γ	[51]

Obviously, much better methods rely on the assessing the crystallization kinetics of the nucleated material [53].

5.2.5 Effect of Stereo-Defects

The concentration of stereo-defects, which can be controlled by suitable catalysts, has been found to be able to control the properties of iPP, making it rigid or flexible [5] by inducing the formation of α or γ phases.

In particular, bundle-like elongated crystalline entities and needle-like crystals of γ phase are observed for stereo-irregular samples slowly crystallized from the melt, whereas α phases develops in the same conditions in highly isotactic samples. Stereo-defective samples of iPP crystallize in the mesomorphic phase, regardless of stereoregularity at very high cooling rates. Mesomorphic phase always exhibit a nodular morphology and absence of lamellar spherulitic superstructures, independent of the stereoregularity. This morphology accounts for the similar good deformability of the mesomorphic samples, whatever the concentration of stereo-defects. The mesophase transforms into α phase without affecting the external habit of the crystals, producing α phase with nodular morphology with increase of strength while maintaining the ductility typical of the mesophase [5].

A scheme of the possibilities to tailor ultimate properties of iPP by means of stereo-defects is shown in Fig. 5.10.

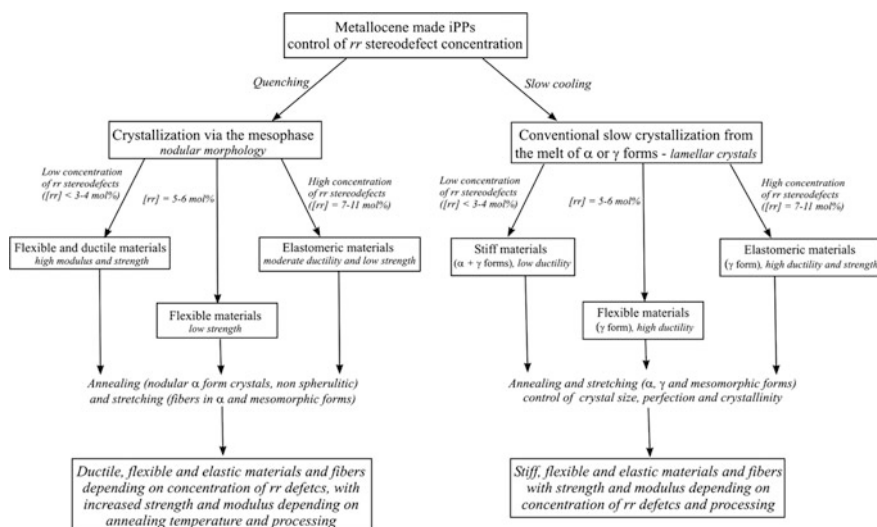


Fig. 5.10 Tailoring of properties of iPP through the control of the concentration of rr stereodefects using metallocene catalysts and the crystallization via the mesophase. Reproduced from [5]

5.3 Crystallization Kinetics Models

5.3.1 Quiescent Crystallization Kinetics

The evolution of crystallinity in a multiphase polymer can be described by Eq. 5.2 [54]:

$$\frac{d\xi_i}{dt} = (1 - \xi) \frac{dk_i}{dt}, \quad (5.2)$$

where the subscript “i” stands for α or mesomorphic phase, k_i is the evolution of the undisturbed volume of i-phase, ξ_i is the relative crystallinity degree of i-phase and ξ is the overall relative crystallinity (i.e. the overall volume fraction occupied by crystalline structures and the sum of all the ξ_i).

In the absence of morphological information (such as nucleation and growth rates) the so-called Avrami-Evans-Nakamura kinetic equation (Eq. 5.3) can be used to describe the evolution of the undisturbed volume:

$$k = \ln 2 \left[\int_0^t K(s) ds \right]^n, \quad (5.3)$$

and the dependence on temperature for the kinetic constant can be described by a simple Gaussian curve (Eq. 5.4):

$$K(T(t)) = K_0 \exp \left(-4 \ln 2 \frac{(T - T_{\max})^2}{D^2} \right). \quad (5.4)$$

The effect of pressure can be taken into account by considering a linear dependence of T_{\max} on pressure (Eq. 5.5):

$$T_{\max} = T_{\max,0} + \alpha_{\max} P. \quad (5.5)$$

This model permits to follow the evolution of the volume occupied by the crystalline structure but does not give details of structure formation, which would, in turn, ignore the effects of the microstructure.

A more detailed model can be used, considering the crystallization kinetics as a sequence of nucleation and growth mechanisms. In this case, Kolmogorov equation can be adopted to describe the evolution of the undisturbed volume (Eq. 5.6).

$$k = \frac{4\pi}{3} \int_0^t \frac{dN(s)}{ds} \left[\int_s^t G(u) du \right]^3 ds \quad (5.6)$$

$G(T(t))$ is the crystal linear growth rate; and $N(T(t))$ is the nucleation density.

The linear growth rate of crystals can be represented by the Hoffman–Lauritzen expression (Eq. 5.7):

$$G(T(t)) = G_0 \exp\left(-\frac{U}{R(T - T_\infty)}\right) \exp\left(-\frac{K_g(T + T_m)}{2T^2(T_m - T)}\right), \quad (5.7)$$

where G_0 and K_g are parameters and have different values corresponding to different crystallization regimes. Very often the crystallization occurs during the process at lower temperature and therefore only one regime (namely Regime III) has to be considered in the modeling.

The model for describing the nucleation density assumed heterogeneous nucleation, with a number of nuclei depending on temperature according to the Eq. 5.8.

$$N(T(t)) = \frac{N_0}{(1 + A_n \exp(B_n(T - T_m)))} \quad (5.8)$$

The effect of pressure on N and G can be also considered through the change in the characteristic temperatures, as described in Eq. 5.9.

$$\begin{aligned} T_m &= T_{m,0} + \alpha_m P \\ T_\infty &= T_{\infty,0} + \alpha_\infty P \end{aligned} \quad (5.9)$$

As stated above with Kolmogorov's model, it is possible to describe evolutions of microstructures. In particular, the number of active nuclei at the end of crystallization process can be calculated as (Eq. 5.10):

$$N_{a,final} = \int_a^{t_{final}} \frac{dN[T(s)]}{ds} (1 - \zeta(s)) ds, \quad (5.10)$$

and the average dimension, \bar{D} , of crystalline structures can be calculated by geometrical considerations as (Eq. 5.11):

$$\bar{D} = \sqrt[3]{\frac{6\zeta_{a,final}}{\pi N_{a,final}}}. \quad (5.11)$$

The radial growth rate, combined with the rate constant, can be used to evaluate the nuclei density as a function of temperature [55]. If crystal growth is assumed to be three-dimensionally spherulitic, the Avrami exponent is $n = 3$ and the nuclei density, N , at a given temperature, takes the form [55, 56] (Eq. 5.12):

$$N(T) = \frac{3 \ln(2)\zeta_\infty}{4\pi} \left[\frac{K(T)}{G(T)}\right]^3, \quad (5.12)$$

in which ζ_∞ is the final volume fraction occupied by spherulitic structures.

5.3.2 Flow-Induced Crystallization Kinetics

As mentioned above, the deformation induced by flow influences the rate of crystallization and thus final morphology of molded products. In order to consider the effect of flow, it is therefore mandatory to model the molecular orientation. A model which resulted to be effective and simple enough to be implemented in simulation software is a nonlinear formulation of the elastic dumbbell model. If \tilde{R} is the end-to-end vector of a molecular chain and the symbol $\langle \rangle$ is the average over the configuration space, a fractional “deformation” of the population of dumbbell sub-chains with respect to the equilibrium conformation can be defined as Eq. 5.13:

$$\tilde{A} = \frac{3}{\langle R_0^2 \rangle} \left[\langle \tilde{R} \tilde{R} \rangle - \langle \tilde{R} \tilde{R} \rangle_0 \right]. \quad (5.13)$$

The evolution of the conformation tensor \tilde{A} describing the sub-chain population was obtained by a Maxwell-type equation [54] with a single dominant relaxation time (Eq. 5.14):

$$\frac{D}{Dt} \tilde{A} - \left(\nabla v \right)^T \times \tilde{A} - \tilde{A} \times \left(\nabla v \right) = -\frac{1}{\lambda} \tilde{A} + \left(\nabla v \right)^T + \left(\nabla v \right). \quad (5.14)$$

The relaxation time, λ , is allowed to vary with shear rate and temperature (Eq. 5.15):

$$\lambda(T, P, \chi, \Delta) = \frac{\lambda_0 \cdot \alpha(T, P, \chi)}{1 + (a\Delta)^b}. \quad (5.15)$$

A shift factor, α , due to temperature, pressure and crystallinity, χ , is also considered; it is expressed by the modified WLF relationship (Eq. 5.16):

$$\alpha(T, P, \chi) = 10^{\frac{-c_1(T-T_0-c_3P)}{c_2+T-T_0}} \cdot \delta(\chi). \quad (5.16)$$

The difference, Δ , between the two main eigenvalues of the tensor \tilde{A} is taken as an appropriate measure of the molecular stretch [57].

In the spherulitic regime, the growth rate could be always described by Eq. 5.7, in which only the melting temperature changed by effect of flow. By considering that under steady shear the shear rate can be directly associated to the molecular stretch Δ , in Fig. 5.11 the melting temperatures are reported as function of the molecular stretch parameter.

Once the melting temperature is calculated, the growth rate can be calculated according to Eq. 5.7. In order to complete the morphology development in the stage *ii*, the nucleation rate needs to be evaluated. For polypropylene, a correlation

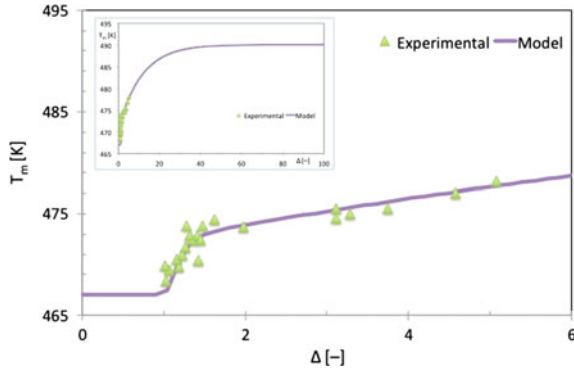


Fig. 5.11 Melting temperature (green triangle symbols) evaluated from steady shear experiments as function of molecular stretch, Δ . Data reproduced from [57]

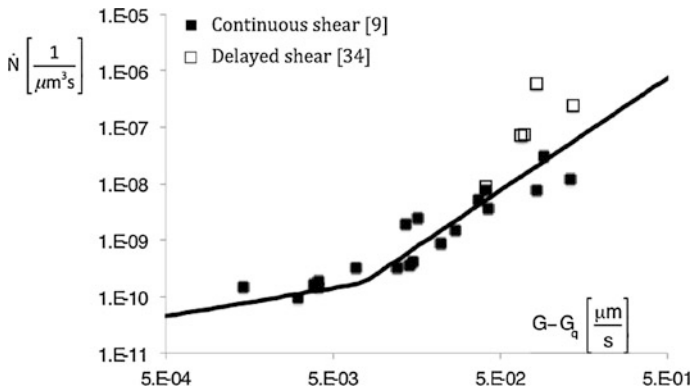


Fig. 5.12 Experimental values of nucleation rate versus excess growth rate under several shear rate conditions (reported as symbols). Data reproduced from [57]

between the excess of growth rate (with respect to quiescent conditions) and the nucleation rate under the same conditions (of shear rate and temperature) was identified in the literature [36, 57]. The existence of such a correlation between growth rate and nucleation rate is consistent with the fact that also nucleation rate is usually described by Hoffman and Lauritzen equation [58, 59]. The correlation adopted between the nucleation rate and the excess growth rate (namely the difference between the growth rate measured under flow and in quiescent conditions at the same temperature) is reported in Fig. 5.12. By adopting the excess growth rate as independent variable, both vertical and horizontal axes are zero in quiescent conditions.

On the basis of this correlation, the nucleation rate can be calculated once the growth rate is known both in quiescent and in flow conditions.

5.4 Injection Molding

5.4.1 Morphology of Injection Molded PP

The morphology distribution inside an injection molded semicrystalline part is made by several layers moving from the surface toward the midplane: a skin layer, where (due to the high cooling rates) the material is quenched and a poorly structured material is found; a shear layer, where due to the strong flow fields highly oriented fibrillar structures are found; a core layer, where spherulitical structures are found, whose dimensions normally increase on increasing the distance from the surface [54, 60–62]. An example of this morphological organization, referred as skin-core morphology [57] is reported in Fig. 5.13. In particular, a thin skin layer composed by globular elements can be found at the sample surface (Fig. 5.13a). A fibrillar layer (sometimes referred to as shear layer) characterized by highly oriented fibrillar structures was found close to the sample surface (Fig. 5.13b). The presence of a transitional region with a gradual change from fibrillar to spherulitical is observed. The presence of spherulitic structures with different dimension in the core region is shown in Fig. 5.13c–e. When the morphology is observed by Polarized Optical Microscopy (POM), a dark band at the midplane can be present. This feature is reported in many literature papers referring to the injection molding of polypropylene [54, 63–67], whereas in some other papers, also reporting full width images of the samples, the phenomenon was not present [60, 68].

In a recent paper [57] it was found that in the dark band smaller spherulites are present with respect to the adjacent layers.

The composition of the morphology is responsible for the end-use properties of a plastic part. A local measure of elastic modulus conducted by Indentation and HarmoniX AFM tests [69] revealed that higher values of the modulus are found in the shear layer, intermediate values in the core spherulitic layer and minimum values in the skin layer. As a result, parts with a thick oriented shear layer show higher impact strength, a poorer dimensional stability [70], and a larger yield stress [71]. In contrast, samples with a larger core layer tend to be brittle (Fig. 5.14).

The thickness of each of the layers depends on the processing conditions. In order to elucidate this point, we refer to some injection molding tests reported in the literature [73]. In particular, the tests were carried out with the iPP T30G supplied by Basell. All the details on geometry and experimental procedures are available in the literature [2, 54, 74].

The test conditions are reported in Table 5.2, and each of them differs from the condition named “standard” for the value of just one of the main processing parameters: flow rate during filling, mold temperature and holding pressure.

The effect of molding conditions on the multilayer morphology of injection molded part is evidenced in Fig. 5.15, where pictures of the samples taken in crossed polarized light are shown. The pictures refer to slices taken in a central position in cavity namely P3, and report just one half of the sample width, with the sample surface at the top, and the midplane at the bottom of the images. The

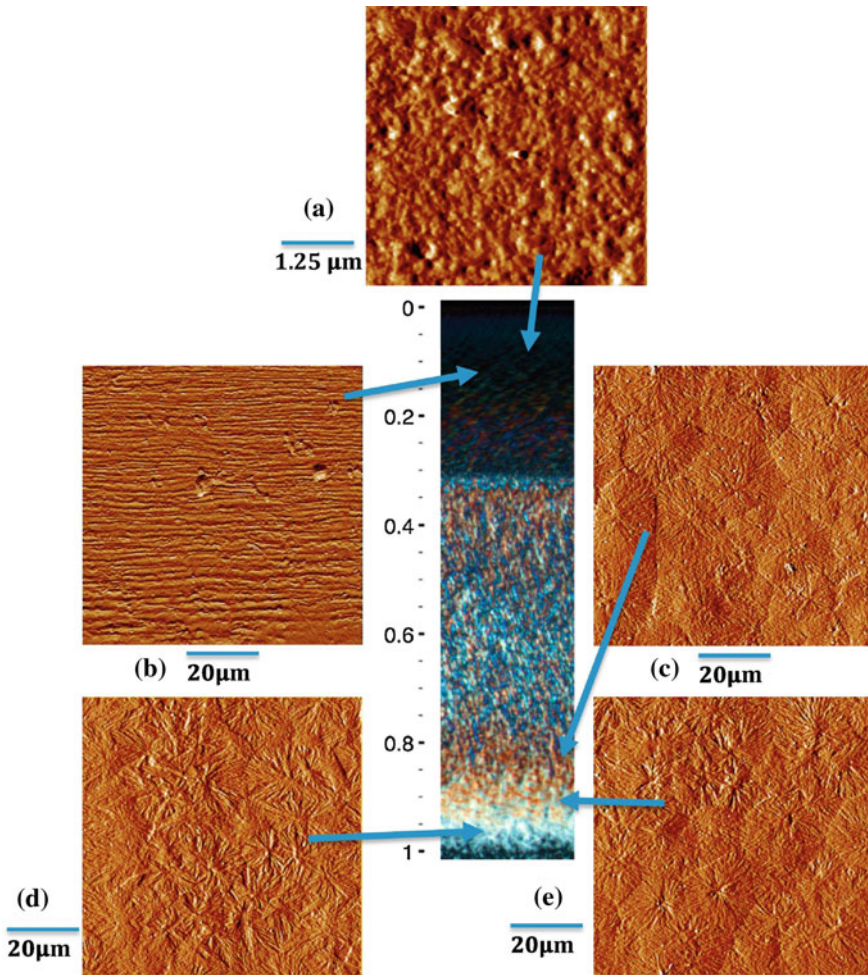


Fig. 5.13 The optical micrograph and AFM amplitude error images of sample “standard” in position P3 (central in cavity). AFM images show details of the morphology along the half-thickness: **a** in skin layer, **b** in the shear layer and **c–e** in the core region. Different scan size was adopted for the AFM images. Reproduced from [57]

thicknesses of the shear layers and of the skin layer in position P3 of those moldings are reported in Table 5.3.

In all cases, the flow is parallel to the plane of the slices. In order to clearly identify the position of the layers, beside each optical micrograph a bar reporting the thickness of the skin layer (black in the bar), the shear layer (grey in the bar) and the spherulitic layer (white in the bar) is shown. The skin layer is clearly evident in all cases except for the High T condition. It is worth mentioning that, according to a detailed characterization of the samples [54], when present, the skin layer is

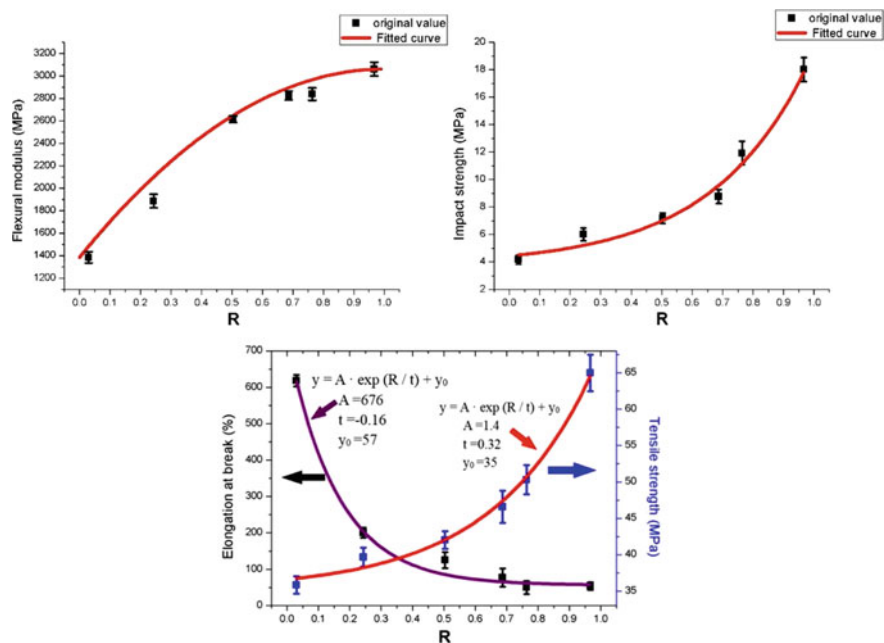


Fig. 5.14 Mechanical properties of different samples of polypropylene versus R (thickness ratio of shear layer to whole sample). Reproduced from [72]

Table 5.2 Processing conditions

	Standard	Slow	High T	High P
Flow rate [cm^3/s]	15	5	15	15
Mold temperature [$^{\circ}\text{C}$]	30	30	70	30
Holding pressure [bar]	400	400	400	700

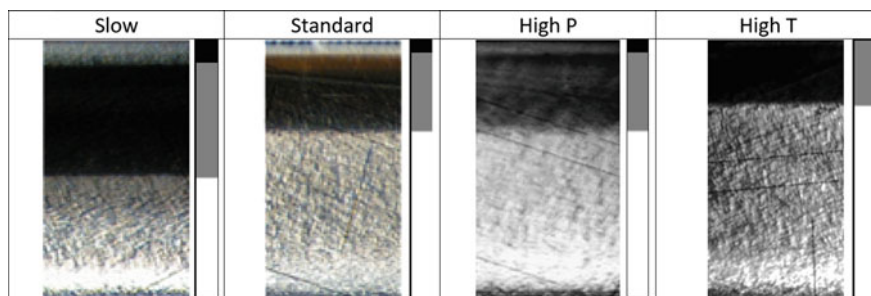


Fig. 5.15 Optical images, in cross polarized light, of the half thickness of the sample in position P3 for all the conditions reported in Table 5.2. The sample surface at the top, and the midplane at the bottom of the images. The thicknesses of the shear layers and of the skin layer in position P3 of those moldings are reported in Table 5.3 [73]

Table 5.3 Thickness of skin and of shear layer for all the conditions considered as measured from optical images reported in Fig. 5.15

	Standard	Slow	High T	High P
Skin layer thickness [μm]	50	80	Not detectable	50
Shear layer thickness [μm]	290	430	250	290

significantly crystalline with a predominance of α phase with few percent of mesomorphic phase. The shear layer appears as the darkest part of the pictures; the core layer, that is formed by spherulitic structures with different dimensions, is instead the lightest one. At the midplane, a darker layer is shown in the optical micrograph of all samples considered in this work.

The morphology developed along the sample thickness is due to the balancing between two phenomena: the molecular stretch which takes place mainly during the filling stage and the cooling rate that determines the solidification. Since the structuring is a kinetic process, when the cooling rate through solidification is very high the material does not have time to achieve a complete structuring. This happens close to the sample surface and determines the formation of a poorly structured skin layer. The thickness of the skin layer is expected to decrease as surface cooling rate decreases, as shown in Fig. 5.15, this happens in the sample sequence conditions slow, standard—high P, high T. The surface cooling rate is expected to be the highest for the slow condition because in that case the both convection and viscous generation, being smaller at any temperature, are less effective to delay the cooling rate through solidification.

5.4.2 Morphology of Micro-Injection-Molded PP

In recent years, plastic molding techniques such as injection molding, which is a suitable process for medium and large-scale fabrication, have been adapted for the necessities of microcomponents fabrication [75], when downscaling systems, products, and their components, the limits of conventional manufacturing techniques are reached. This initiated the improvement of conventional techniques and the further development of new ones, as in the case of the micro-injection molding process. Lateral dimensions in the micrometer range, structural details in the sub-micrometer dimensional level and high aspect ratio (aspect ratio = depth/width) of 10 and above are achieved.

On reducing the thickness of the injection molded parts (having a typical dimension of 1–3 mm) to thin-wall injection molding (typical thickness 300–500 μm), the morphology along thickness tends to maintain the same configuration [76]. The shear layer increases its relative dimension due to the increase of the shear stresses and cooling rates [66]. Moving toward micro-injection molding, with characteristic dimensions of the order of 100 μm , the shear layer extends towards the center of the molding, sometimes resulting in a so called “core-free” part [65], namely the complete absence of spherulitic morphology.

Due to the miniature characteristics of the molded parts, however, a special molding machine and/or auxiliary equipment are required to perform tasks such as shot volume control, process parameters control, injection, packaging of molded parts.

In particular, the rapid control of cavity surface temperature is essential for obtaining a micro-thickness iPP part with an acceptable cycle time [77]. As expected also the resulting morphology, and thus the final properties, could be controlled by the local surface temperature of the mold, as shown in Fig. 5.16.

Furthermore the temperature control of the cavity surface is essential for the replication of micro and nano-features on iPP parts by injection molding [78].

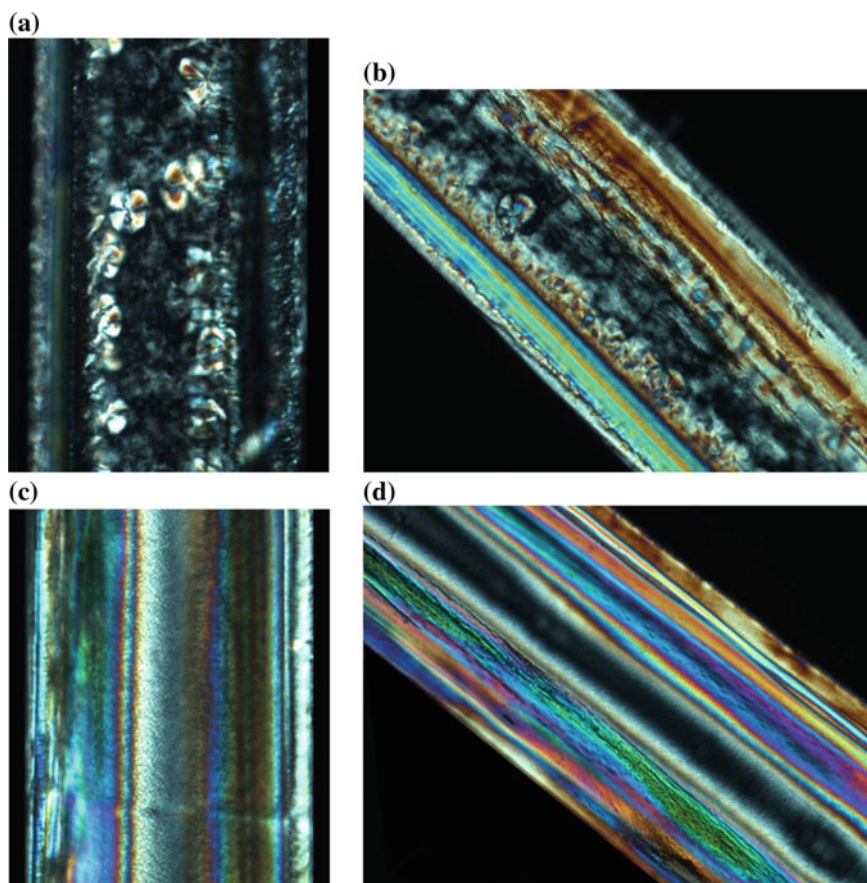


Fig. 5.16 Microtomed slices of molded samples in polarized light. The thickness of the samples is 200 μm . The holding pressure is 200 bar. **a** mold surface 120 $^{\circ}\text{C}$. **b** same sample as in **a**, after a 45 $^{\circ}$ rotation; **c** mold surface 25 $^{\circ}\text{C}$, **d** same sample as in **c**, after a 45 $^{\circ}$ rotation. Data reproduced from [77]

5.4.3 *Advanced Methods to Control Morphology of Injection Molded Parts*

Fast Cavity Surface Heating Technique

The morphology developed in the molded parts is strongly influenced by processing parameters. Molecular stretch distribution at solidification depends on the injection conditions and, therefore, also mold surface temperature. This latter is a key parameter in controlling molecular stretching: if temperature is kept high starting from the filling for a few seconds, the relaxation of the molecular stretching can be calibrated before cooling [79, 80]. At present, the fastest evolution of mold temperature can be obtained by heating devices located just below the cavity surface [77]. Liparoti et al. [69] reported the effect of induced asymmetrical fast surface temperature evolution on the morphology of injection molded isotactic polypropylene (iPP) samples.

An example of cross-section morphology obtained by the optical micrograph of the sample prepared by conventional injection molding (CIM), namely without temperature control (i.e. T_{off}), is shown at the top of Fig. 5.17. The other morphologies reported in Fig. 5.17 refer to the samples obtained keeping one of the the cavity surfaces (the left one, in the Fig. 5.17) at the temperature of 120 °C for 0.5, 8 and 18 s. The different layers developed along the sample thickness are strongly influenced by the temperature of the cavity surface. In particular, the shear layer moves toward the sample surface and its thickness decreases by increasing the heating time. The skin layer disappears for longer heating times, while with a heating time of 0.5 s the presence of the skin layer is not clearly evidenced from the polarized optical micrograph. Figure 5.17 shows that a heating time of the order of the filling time (0.5 s) is sufficient to lose the symmetric morphology of the sample.

The morphology of the samples has a direct effect on the distribution of mechanical properties along the sample thickness (Fig. 5.18).

The maximum value of the modulus is located in the shear layers. The skin layer shows the lowest moduli and the spherulitic core has intermediate modulus values.

Shear Controlled Orientation Techniques

The first technologies developed to modify the morphology of the molded parts, were based on the application of a suitable shear or elongational flow field to the solidifying melt that facilitates and enhances molecular alignment. To fabricate polymer products with high performance the shear controlled orientation injection molding (SCORIM) techniques was developed by Allan and Bevis [81, 82]. Successive shear could increase the degree of orientation of melt as much as possible, thus allowing a high possibility of forming shish kebabs in the moldings. The SCORIM equipment consists of a device that is attached to the injection nozzle and is composed of a hot runner circuit that divides the melt stream into two channels where two hydraulically actuated pistons are operated during the holding pressure stage. The SCORIM double live-feed is shown in Fig. 5.19. Compared to CIM, where the molten material solidifies under the influence of an almost static pressure, in SCORIM, the polymer melt is continuously displaced inside the mold

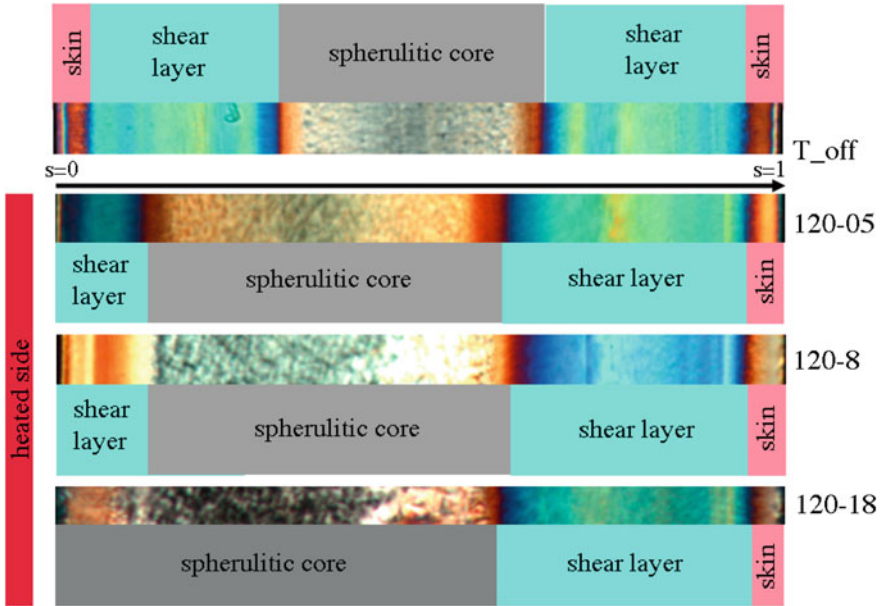
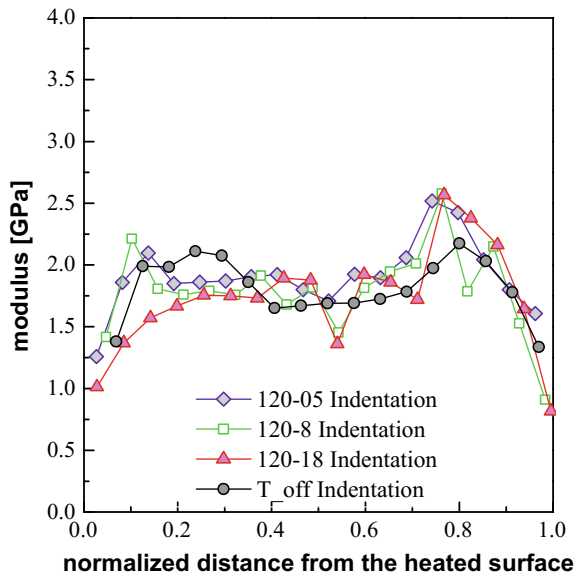


Fig. 5.17 Optical micrographs of the samples from test runs T_{off}, 120-05, 120-8 and 120-18. The heated side is reported on the left most of the figure. Data reproduced from [69]

Fig. 5.18 Elastic modulus distributions (obtained from indentation analyses) along the sample thickness for the samples T_{off}, 120-05, 120-8 and 120-18. Data reproduced from [69]



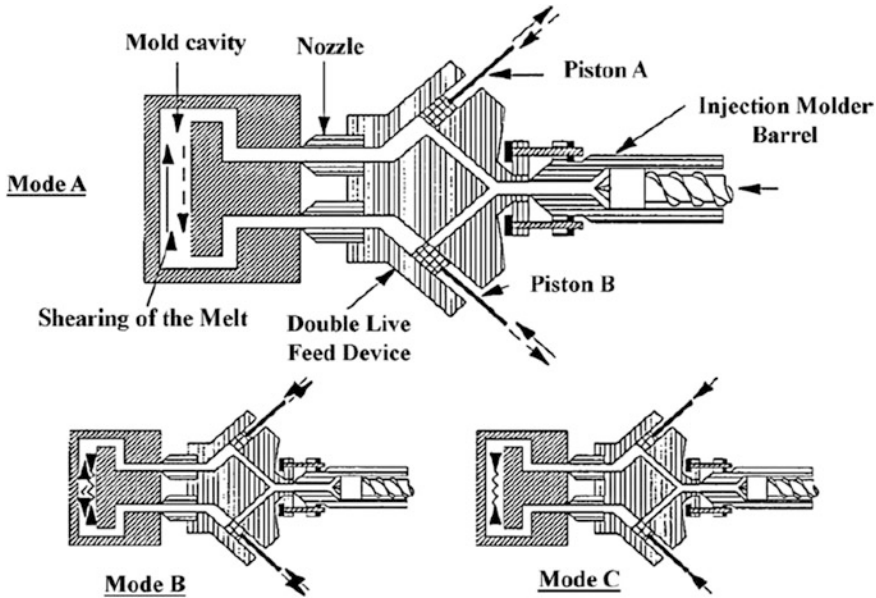


Fig. 5.19 Scheme of the function of the SCORIM procedure along with the three basic modes of operations (A, B and C)—Mode A: the pistons are activated 180° out of phase; Mode B: the pistons are activated in phase; Mode C: the pistons are held down at a constant pressure. Data reproduced from [81]

cavity by the action of the hydraulic pistons. This causes, as the solidification takes place progressively from the skin to core regions, a continuous shear imposed to the melt. This effect is accomplished using the SCORIM Mode A of operation that corresponds to the out-of-phase oscillation of the pistons. Other possible modes include Mode B (in phase oscillation of the pistons) and Mode C (compression of the pistons at a constant pressure). These operational modes can be combined sequentially in several stages during processing to lead to a different shear field at melt/solid interface.

The γ -phase was found to form in highly oriented SCORIM iPP samples [83], with a marked enhancement of the preferred orientation of the α -phase and percentage crystallinity when compared with CIM iPP. Compared with CIM, SCORIM technique results in more pronounced molecular orientation, leading to the substantial increase in Young's modulus of SCORIM moldings [84]. By controlling the processing parameters, it is possible to enhance the stiffness without loss of tensile strength for SCORIM moldings: the moldings prepared by SCORIM exhibit an increase in impact strength of up to four times, as well as gaining remarkable increase in Young's modulus.

A comparison of failure surfaces of CIM and SCORIM moldings are shown in Fig. 5.20 [71]. It can be seen that almost all CIM moldings exhibit four distinct layers: the skin, the oriented zone, the layered core region, and the central core

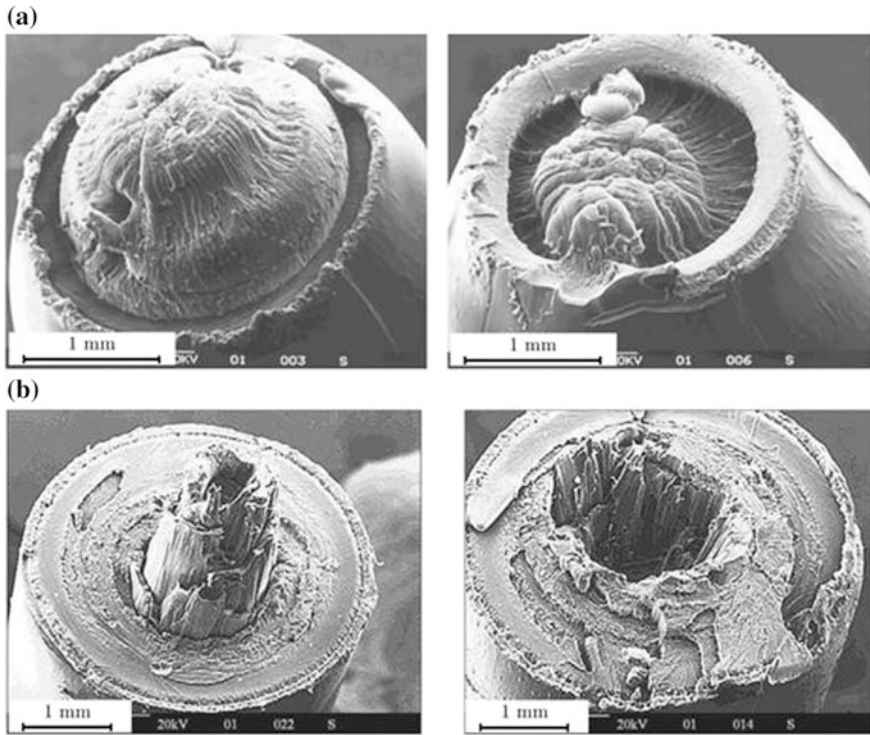


Fig. 5.20 Two opposite tensile failure surfaces of: **a** CIM moldings; **b** the majority of SCORIM moldings. Data reproduced from [71]

region. While the major SCORIM moldings exhibit five distinctive layers: the skin; the sub-skin; the oriented zone; the transition zone between the oriented zone and the core; and the core region. The core region is ductile, so there is a pit in the center of a tensile failure surface.

The results of microstructure investigation indicate that there exists γ -phase of SCORIM iPP moldings with pronounced molecular orientation. So, the common view that iPP has only α - and β -phases in commercially produced moldings is challenged. The presence of γ -phase in injection moldings is indicative of enhanced Young's modulus and tensile strength, and it is consistent with the results of mechanical characterization. Another reason for the substantial increase in Young's modulus of moldings produced by SCORIM is the more pronounced molecular orientation compared to CIM samples. The calculated results from DSC and WAXD show that SCORIM moldings contain less β -phase and exhibit greater overall crystallinity than CIM moldings. The difference in the relative proportions of α -, β -, and γ -phases is marked and depends on processing conditions and the molding method.

The OPIM technique (oscillating packing injection molding), also called dynamic packing injection molding (DPIM) or oscillatory shear injection molding

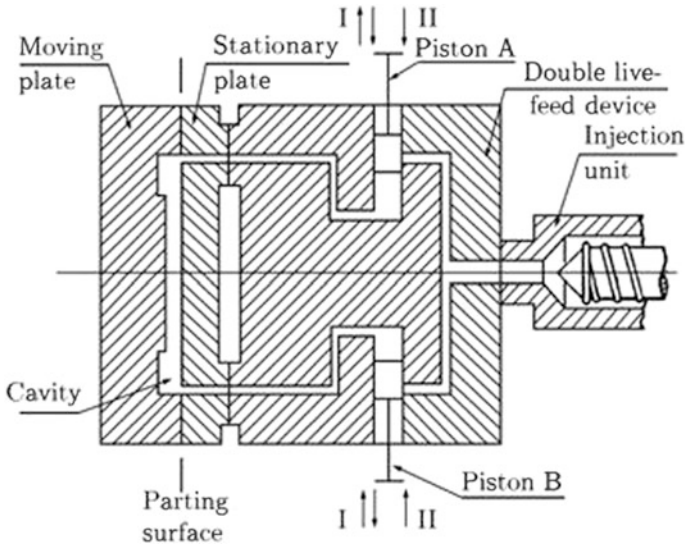


Fig. 5.21 Device for DPIM (I: two pistons reciprocate with a difference of 180°) and SPIM (II: two pistons push forward simultaneously) moldings. Data reproduced from [85]

(OSIM) in some articles, was developed by Shen's group based on SCORIM [85]. The scheme of the OPIM device is shown in Fig. 5.21. Similarly, to the SCORIM technique, there are three movement modes for the two hydraulically actuated pistons to generate a corresponding shear stress field during the cooling solidification of melt in cavity, thus different morphologies in moldings. Contrasting to SCORIM where the multi-piston oscillating packing unit was an independent device, OPIM adopted hot runner system, and combined double live-feed device to injection molding machine, which greatly improved and streamlined the SCORIM device.

The mechanical properties of iPP can be greatly enhanced using OPIM under low pressure [86]. Samples prepared by OPIM under elongational test exhibit a brittle tensile failure, whereas the samples prepared by CIM are ductile. The increase in mechanical properties is mainly attributed to perfect spherulites, the shear-induced shish kebab structure (also confirmed by the high temperature peak of double peaks in DSC curves), and the enhanced orientation of molecular chains. The holding mode has strong influence on the mechanical performance of self-reinforced iPP, while the other processing variables such as oscillating frequency, oscillating pressure, melt temperature and holding time, have little influence on the mechanical properties of OPIM iPP moldings.

The OPIM moldings are anisotropic [87], the stress-strain curves show typical brittle failure in the TD and relative ductile failure in MD as also confirmed in Fig. 5.22 were the SEM micrographs of tensile fracture surfaces are reported.

In Fig. 5.22a the tensile fracture surface of the outer shear region in MD is shown, and it exhibits a very rough and uneven failure surface with voids and

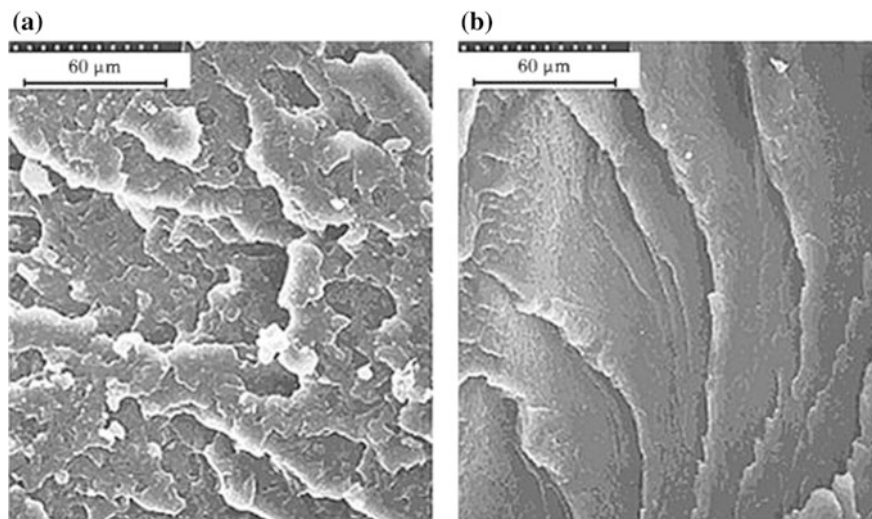


Fig. 5.22 SEM micrographs of the tensile fracture surface of OPIM moldings in **a** MD, and **b** TD. Data reproduced from [87]

crazes. In Fig. 5.22b the tensile fracture surface in TD exhibits a relatively planar failure surface but with delamination. The mechanical property is consistent with the microstructure observed. iPP samples processed by OPIM exhibit interlocking shish kebab structure within the outer shear region and a much smaller spherulitic core region with respect to the CIM samples. Moreover, the OPIM moldings contain both α and β crystalline phases (also contained in CIM samples) and γ crystallites. The OPIM moldings exhibit the highest α -phase orientation and largest proportion of β -phase content in the outer shear region.

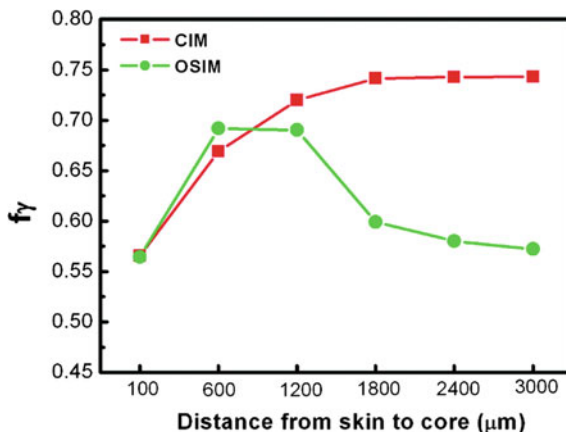
Analysis by 2D-WAXD OSIM show that OSIM samples present, at a given depth, higher degree of molecular orientation and that the α - and γ -crystals appear at different depths of the samples. Moreover, estimation of the overall crystallinity shows that, due to the stronger shear imposed, higher level of crystallinity are reached in the OSIM samples with respect to the CIM samples [88].

The fraction of γ -crystal, f_γ , with respect to α -crystal in samples, was calculated and the distribution of f_γ through the depth of samples was shown in Fig. 5.23.

From the distribution curves of f_γ , it can be seen that the spatial distribution of γ -crystal is different for CIM and OSIM samples. The f_γ of CIM samples increased monotonously in outer regions along the direction from skin to core. However, OSIM samples have almost the same minimal f_γ (~ 0.57) in the skin and core regions, and a maximum in the intermediate regions. The phenomenon of less γ -crystals in the inner regions of OSIM samples contradicts the widely accepted point of view that f_γ should be high when the cooling rate is low caused by shear heating.

OSIM is reported [89, 90] as a successful method for controlling the structure and morphology formation of iPP and tuning its mechanical properties. The competition of shear-induced crystallization and β -nucleant results in the hierarchic

Fig. 5.23 Fraction of γ -crystal with respect to α -crystal, f_γ , evaluated from the X-ray diffraction profiles from skin to core region of CIM and OSIM samples. Data reproduced from [88]



structure of the OSIM β -iPP sample, which is like that of bamboo, which has a tight and fibrillar outer layer, as well as a soft and loose inner layer. In the outer layers (skin and intermediate layers) highly oriented α -form crystals (shish kebabs) are present, while in the core layer high-proportion β -form spherulites are present. In the skin layer, the orientation should be ascribed to the shear imposed on the melt before the gate of mold freezes. In the core layer, as the gate of the mold freezes, iPP is still in melt state, so that the molecular chains have enough time to relax. In this case, the β -nucleating agent takes effect, leading to the formation of β -crystals.

Vibration-assisted Injection Molding

It is quite well known that the external force field can affect the rheological properties of polymer melt. By introducing a vibration field to the polymer melt, it is not only able to depress the shrinkage of molded products in injection molding and improve the surface quality of extrudates [91, 92], but also to substantially increase the orientation potential of polymers by reducing the amount of relaxation [93], therefore achieving control of microstructure and morphology, and enhancement of mechanical performances of the final products. The most important parameters in vibration-assisted injection molding/extrusion are vibration frequency and amplitude. According to the vibration frequency, vibration field can be divided into mechanical vibration and ultrasonic vibration. The frequency of ultrasonic vibration is in the range of 20 kHz and more, while the frequency of mechanical vibration is much lower than that of ultrasonic vibration, which is always within 0–100 Hz. Also, mechanical vibration can be divided into pressure vibration and shear vibration. In the pressure vibration processes, polymer melt is periodically compressed and released, while in the shear vibration processes, a periodical oscillating shear field is imposed on polymer melt.

Li et al. studied the effects of vibration injection molding (VIM) on the morphological structure and mechanical properties of PP [94, 95] by superimposing a pulse pressure on polymer melt during the injection and holding pressure stages. The device and working principle are depicted in Fig. 5.24.

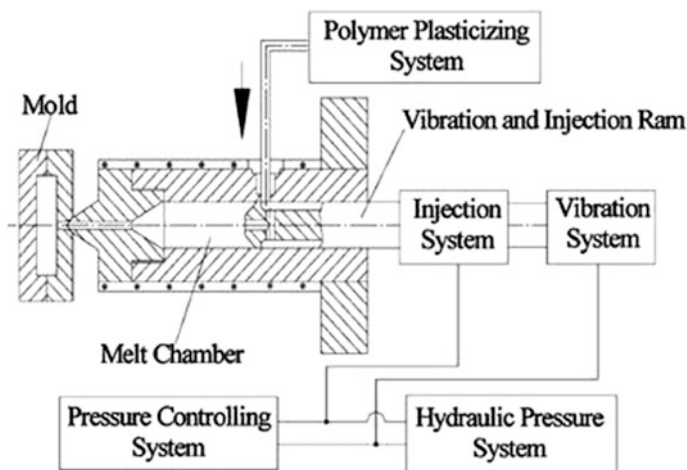


Fig. 5.24 Schematic diagram of the pressure vibration injection molding (VIM). Data reproduced from [95]

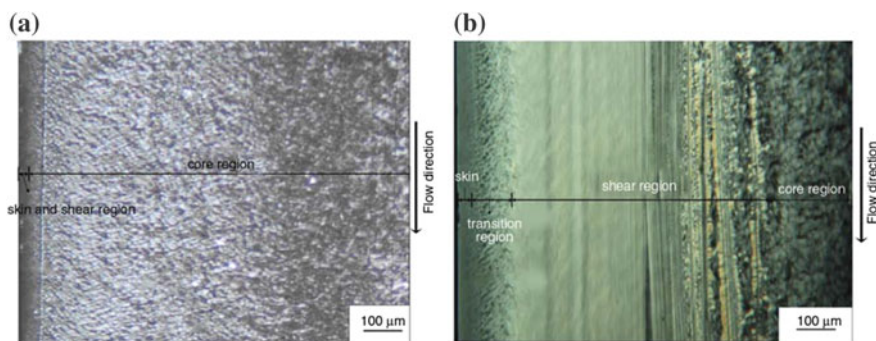


Fig. 5.25 Effect of vibration on the morphology of an injection molded PP sample. **a** CIM, **b** Vibration injection molding. Reproduced from [96]

The ram itself is a part of both the injection and vibration systems. The main processing parameters are vibration frequency and vibration pressure amplitude, which is in the range of 0–2.5 Hz and 0–75 MPa, respectively.

The samples prepared via VIM showed that with the increase of vibration frequency, the yield strength, Young's modulus and impact strength steeply rose firstly, afterwards, remained at a plateau, while the elongation at break decreased firstly and then ramped up. The yield strength and impact strength increased monotonously while the elongation at break decreased remarkably with increasing vibration pressure amplitude. As for morphology, the random distribution of spherulites, obtained by CIM, was changed into parallel lamella perpendicular to the melt flow direction for the VIM-produced samples (Fig. 5.25).

It is believed that the effect of melt vibration on the morphology was to orientate the structure unit along the melt flow direction, especially under the processing conditions with high vibration pressure amplitude. The results also showed that, for VIM, accompanied with higher crystallinity, the melting peaks shifted to higher temperature, meaning more perfect crystalline existed.

5.5 Modeling Morphology in Injection Molded Parts

In the injection molding, polymers are processed under severe conditions (high cooling rates and pressures, strong and complex flow field) and this complex thermomechanical history experienced by the polymer induces a local order of macromolecules. For semi-crystalline materials, highly oriented lamellar crystallite microstructures are detected near to the molding surface, namely in the shear layer where the shear stress levels are high, whereas isotropic spherulitic structures are detected far from the wall, i.e. in the core layer where the shear stress decreasing to very small values. The level of the order reached locally by the macromolecules and thus the structure formation is the result of the competition between the shear deformation, i.e. the flow characteristic time, and the cooling rate, which determines thermomechanical and crystallinity histories and thus the relaxation time.

5.5.1 Fibrillar Morphology

Depending to the processing conditions adopted, sometimes an additional layer, namely a skin layer, is found on the molding surface, before the shear layer, characterized by less oriented crystalline structure. In this layer due to the very high cooling rates, the macromolecules are quenched does not have enough time to organize themselves in highly oriented structures as in the deeper shear layer. It is noteworthy that along the molding thickness some transitional layers are recognized between the skin-shear-core layer structure previously depicted. Experimental investigations have confirmed that in presence of flow under certain threshold the morphology evolution maintains its quiescent characteristic and above a second threshold morphology evolution is modified and oriented structures (shish kebabs) are formed in the crystallizing polymer.

One of the first attempts to model the development of crystallinity and morphology in the injection moldings of iPP was conducted by Isayev et al. [97, 98]. They proposed a unified crystallization model in which the effect of flow on the crystallization kinetics is accounted for. The model, that adopts the “competing mechanisms” of crystallization in terms of the induction time indices, was able to distinguish between the highly oriented skin layer and spherulitic core in the moldings. In particular, they assumed that the polymer solidified in different morphologies depending upon the competition between the degree of supercooling and the molecular orientation caused by the thermomechanical history.

A few years later, at the beginning of the 2000s, Zuidema et al. [99] implemented a model which considered the process of spherulitical nucleation and crystal growth combined with flow-induced crystallization process described by modified version of the model presented by Eder et al. [56, 100]. The Eder's model was adopted for flow-induced crystallization being able to describe the formation of thread-like nuclei (shish) on which lamellae grow mainly perpendicularly (kebabs). In particular, the modification proposed consider the second invariant of the elastic tensor as the driving force for flow-induced nucleation and crystallization instead of the shear rate. To consider flow-induced orientation and stretch of molecules the viscoelastic behavior of polymer is described with a Leonov model [101, 102].

Kennedy and Zheng [103] also modeled the effect of flow on crystallization kinetics and on morphological changes. They considered an effect of flow on nucleation rate related to the excess of free energy and an Avrami index as a function of the second invariant of the second order orientation tensor depending. With the adopted relationship, the Avrami index equals to 3 at a random orientation state, corresponding to spherical growth; and equals to 1 at the perfectly aligned orientation state, corresponding to rod-like growth. For the semicrystalline phase the orientation evolution is described with the rigid dumbbell model.

In the past decade, it was demonstrated that the formation of shish kebabs can be observed at high flow rates. In particular, the chains with a longer relaxation time in the polymer ensemble have to be stretched by flow and thus the shear rates exerted on the chains have to be higher than a critical value that is the inverse of the Rouse time. On the other hands, clear criteria to be adopted to describe the transition from spherulites to the oriented morphologies of shish kebabs was not found. Recent developments [40, 104] have demonstrated that the parameter responsible for the onset of the oriented morphology is the mechanical work; if a polymer has experienced more than a threshold value of the mechanical work oriented shish kebab morphology can be formed. It is important to notice that the threshold work performed at shear rate not above the critical value it is not sufficient to form oriented shish kebab structure. Thus, both the two conditions have to be respected to form oriented shish kebab structure: the threshold work has to be performed above the critical value of the shear rate.

More recently for the injection molding a modification of the above work criterion was developed [73]. The model for fibrillar crystallization mentioned above is adopted with the following additional simultaneity criterion: the whole amount of work has to be done while the molecular stretch is above a critical value; furthermore, if the molecular stretch is let to relax below that critical value, all previous work has to be cancelled in the accounting for the critical work. The criterion that the work performed before the stretch reaches its critical value is not relevant to the purpose of achieving fibrillar crystallization appears physically grounded. In many processing conditions, the polymer melt is oriented first and then has the time to (partially) relax before being oriented again. If the relaxation were complete, it is obvious that the whole previous history does not have any effect of what happens next. This would mean that the time integral of the work alone is not a suitable criterion for describing the phenomenon in complex flow conditions.

The “simultaneity” criterion is consistent with the results of the experiments conducted in literature and reported in [37, 40, 104] that consider an isothermal constant rotating parallel-plate flow, under steady shear rate conditions, if transient flow is negligible. In all the proposed experiments for the radii of the plate in which the fibrillary morphologies formation is observed, the most of the viscous work was actually performed when the steady critical shear rate (molecular stretch) was already achieved and thus the simultaneity criterion is automatically assured.

Comparisons were conducted between experimental results of shear layer thickness observed in different injection molding conditions and prediction obtained on the basis of criteria founded on a critical (shear rate) stretch value and on a critical work value. From the experimental observation was found that, starting from the sample surface, the presence of a skin layer, a shear layer and a spherulitic core layer. The molding conditions that were adopted strongly influenced the thicknesses and the positions of the different layers. From the integral of the viscous work and the final stretch distributions together, predictions of the shear layer thickness and its position was obtained considering all the points presenting both values higher than the chosen threshold (critical values). It was observed that a reasonable comparison with the thicknesses and the positions of the shear layers observed cannot be obtained whatever realistic choice would be done for the two critical values.

Considering the “simultaneity” criterion, the fibrillar crystalline structures can form when the time integral of the viscous work, calculated when the molecular stretch is constantly larger than its critical value, reaches a work threshold. If the stretch relaxes below the its critical value, the work is set to zero again. By plotting the final distribution along the moldings thickness of the time integral of the viscous work it was found that the work threshold mainly influences the thickness of the skin layer whereas the critical value of the stretch substantially affects the time integral of the work close to the midplane, where the molecular stretch is low. It was shown that the simultaneity criterion is suitable to satisfactory describe both the skin and the shear layer thickness for all the considered molding conditions if appropriate values of critical stretch and work threshold are selected.

5.5.2 Distribution of Spherulite Diameters

The final distribution of the spherulite distribution in the gapwise direction is strongly dependent on the thermal and flow histories experienced by the polymer. At the location where cooling rate are higher, i.e. from the core region toward the skin, the diameter of the spherulites become smaller because spherulite growth has smaller time to proceed, nucleation density becomes large and final spherulite dimensions remain small, because they are limited by impingement. The effect of flow on the final distribution of spherulite diameters depends on the competition of two mechanisms. The final dimensions of the spherulites are controlled by the number of active nuclei which are depending not only on the nucleation rate, but

also on the evolution of crystallinity that depends on the nucleation and growth rate. It is well known that flow induces an enhancement of nucleation and of crystallinity. Thus if the effect of flow on the nucleation rate is prevalent, the spherulites diameter decreases by effect of flow induced crystallization. If the effect of flow on the crystallization is prevalent the spherulites diameter increases by effect of flow induced crystallization. In fact, the growth rate is considered in the evolution of the crystallinity with a power 3. This implies that any nucleus quickly occupies a large portion of the space, thus impeding to other nuclei to fall into amorphous regions and to generate other spherulites. Micrographs of slices were taken by a polarized optical microscope (POM) along the gapwise direction [57]. The skin-core morphology of the samples was evident, with a not oriented skin layer about 50–100 μm thick at the sample surface, an oriented fibrillar layer closer to the sample surface (the so-called shear layer) and a spherulitic core. Furthermore, a dark band at the midplane was found. The same phenomenon was reported in some literature papers referring to the injection molding of polypropylene [63–67] without any comment, whereas in some other papers, also reporting full width images of the samples, the phenomenon was not present [60, 68]. The nature of the dark band is difficult to understand. In the literature, it was reported that the thickness of this band increases on increasing the distance from the gate [54], and tends to disappear on increasing the mold surface temperature [54, 69]. Deeper investigation of this dark band showed an unexpected behavior, i.e. a reduction of the spherulite diameters in the region close to the sample half-thickness.

5.5.3 *Simulation of Morphology Development in Injection Molded IPP: A Case Study*

An accurate prediction of morphology distribution inside injection molded parts of semicrystalline polymers is surely a key issue in polymer processing. Indeed, many of the properties of the solid molded parts depend heavily on the distribution of morphological parameters [12, 105] such as for instance spherulite size distribution [106] or the presence of oriented layer induces anisotropy and other changes in mechanical properties [107]. Therefore, the production of high quality polymeric parts in injection molding, which is a sector in great expansion, requires the capacity of being able to predict not only the thermomechanical histories experienced by polymer during the processing but also these morphological features.

A reliable description of morphological evolution in crystalline materials during injection molding process should, therefore, necessarily account for all major crystallization process and capture the main features of melt morphology evolution under both quiescent and processing conditions (various shear and cooling rates), as well as the complicated interaction between crystallinity and flow.

The major challenging problems on this topic include the following:

- modeling of crystallization phenomena under non-isothermal, quiescent and flow conditions;
- understanding of the mechanisms governing crystallization-induced microstructure development;
- study of physical properties of the polymer before and after the crystallization.

The task is particularly challenging, since during injection molding crystallization, and thus morphology evolution, takes place under severe thermomechanical histories, namely high pressure, fast cooling rates. All these effects must therefore be taken into account in the quiescent model describing the crystallization kinetics. Moreover, the effect of flow on the crystallization process has to be accounted for.

When external flow is applied, for example, during molding processes, molecular chains will orient along preferential directions by the flow. This orientation of macromolecules can cause different properties of crystals in different directions. Therefore, one of the biggest challenges concerns the reliable prediction of molecular orientation during processing.

Furthermore, since polymer properties (above all rheology and density) are function of crystallinity, the thermomechanical history which determines crystallinity is in its turn depending on crystallization. This means that for a correct prediction of final morphology in injection molded parts a suitable model for crystallization kinetics in processing conditions (which is already a quite challenging task) is not enough: it is also necessary to use a software which describes the evolution of the main variables during processing and can keep into account, through specific sub-models, the effect of crystallinity on the relevant material properties [108]. Just for sake of clarity, an incorrect description of crystallization kinetics gives rise not only to a wrong prediction of final morphology, but also to an inaccurate calculation of the pressure evolution inside the cavity, which is normally considered as a primary goal of simulation.

As last remark, it should be clear that predictions for injection molding process are obtained extrapolating all the constitutive equations and model identified to describe the polymer behavior well beyond the experimental ranges, within which each model and equation had been identified.

Numerical simulations of the molding tests described in the Sect. 5.4.1 were conducted adopting the UNISA code that considers the one-dimension laminar flow of a viscous non-Newtonian fluid in non-isothermal conditions. The wall slip phenomena is not taken into account. The process is considered symmetric with respect to the midplane. In the energy balance, the convective term along the flow direction, the conductive term along the sample thickness, the crystallization latent heat and the viscous generation are considered. A surface heat transfer coefficient is assigned. The geometry is schematized as a series of rectangular or cylindrical elements.

The process is simulated into two stages: filling and packing/cooling. During the filling stage the material is considered incompressible and the flow rate is imposed. The fountain flow is not implemented but the variables at the flow front are

averaged on the basis of velocity (i.e. cup-mixing variables are considered at the front). During the packing stage, the material is considered compressible and the flow rate, at each position, is determined by the downstream densification. During the cooling stage the velocity field is annulled and pressure evolution is evaluated on the basis of the pVT behavior of the material accounting of crystallization kinetics. The field equations adopted for the numerical simulation are reported in [109, 110].

Details of the constitutive equation adopted (including the values of the constants) are reported in [111]. All the constitutive equations of that iPP resin (T30G) were recently revised [57] on the basis of data published after the publication of the paper which analyzed those injection molding tests for the first time [2, 54].

The effect of flow on crystallization kinetics is accounted through a stretching parameter, as specified elsewhere [57]; the equations for the evolution of the stretch parameter are summarized in the Sect. 5.2.3. The effects of crystallinity on viscosity and density are taken into account. Consistently, the UNISA code adopts a solidification criterion based on the crystallinity. At last, effect of pressure on viscosity, density and crystallinity are considered. The effect of mold deformation can be accounted for [110].

Predictions obtained with the software UNISA has been compared with experimental pressure data acquired during the injection molding process and with experimental morphological distribution (in terms of final crystallinity and spherulite diameters distribution along the gapwise direction and thicknesses and positions of the shear layer).

Predicted pressure evolutions are compared in Fig. 5.26 with the experimental evolutions collected in the five positions along the flow path during the process. In particular diagrams reported on the top (a and b) refer to the condition “standard”, those at the bottom (c and d) refer the condition “slow” as reported in Table 5.2. Comparison of the rightmost diagrams with the leftmost ones allows to identify the relevance of FIC in the predictions of the thermomechanical histories. Although the predictions obtained with and without FIC seem quite similar, at a closer look some significant differences are detected. For both the conditions, the predictions carried out considering the quiescent crystallization present an overestimation of the gate sealing time which is evidenced by a slower decreasing trend of all the predicted pressure curves in the cavity at times longer than about 10 s. A better description of gate sealing time and of the pressure evolutions is instead achieved considering the FIC in the process simulation. The improvement is significant, even if an underestimation of the pressure drop across the gate remains the main difference between data and simulations.

Comparison of predicted and measured final crystallinity distributions close the sample wall are reported in Fig. 5.27. In particular, considering the “standard” test, in Fig. 5.27 are reported distribution of measured α and mesophase and overall crystallinity compared with the predicted distributions obtained considering a quiescent crystallization model (on the left) and the effect of the FIC (on the right).

The measured IR overall crystallinity distribution shows lower value in a layer close to the sample wall (up to 30 μm from the sample wall) where the polymer

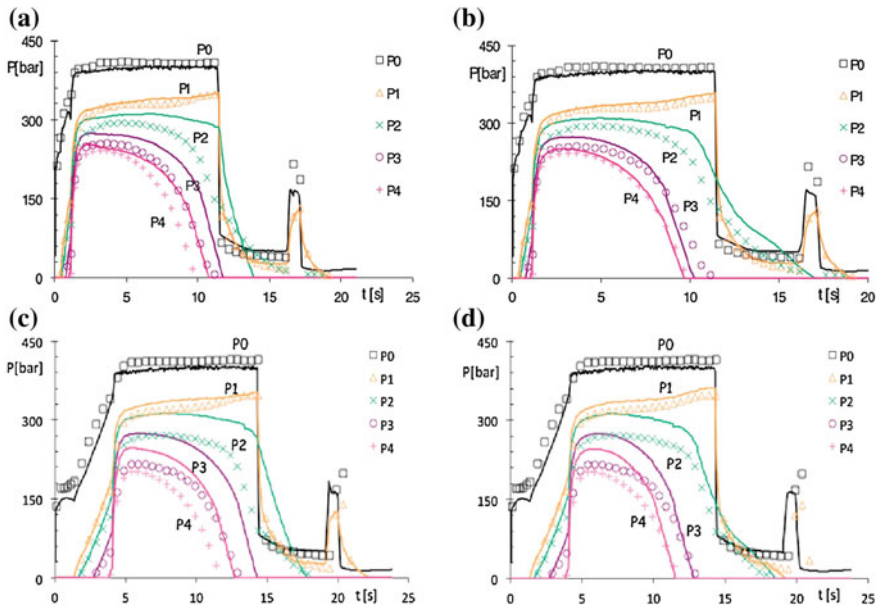


Fig. 5.26 Comparison of pressure evolutions, acquired in the five positions along the flow path during the process, both in “standard” and “slow” condition, with the predicted ones. In particular, for the “standard” condition, predictions are obtained neglecting (a) and considering the FIC (b); for the “slow” condition, predictions are obtained neglecting (c) and considering the FIC (d). Data reproduced from [57]

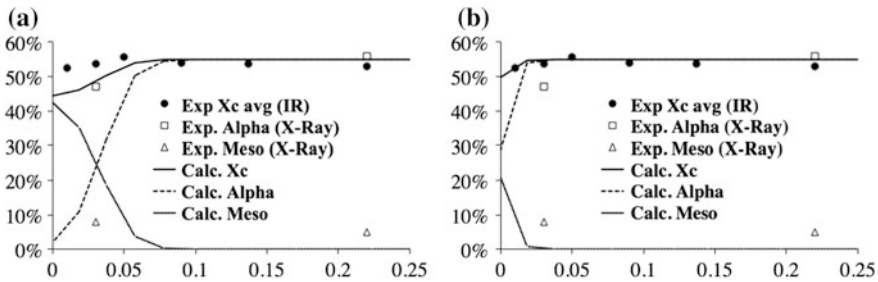


Fig. 5.27 Comparison of the measured final distributions of overall crystallinity, α and mesomorphic phase along the distance d , measured in mm, for the “standard” condition, with the predicted ones. In particular, predictions are obtained neglecting (a) and considering the FIC (b). Data reproduced from [57]

experienced a very high cooling rate; in the remaining thickness of the sample the crystallinity is constant and equal to the equilibrium value of α phase (namely 55%). The mesophase content is about 10% only close to the sample wall whereas α phase content is prevalent as the distance from the sample wall increase. The effect on the predictions obtained considering the FIC is evident. The thickness of

the quenched zone close to the sample wall is sensibly reduced (about halved) with respect to the simulations conducted neglecting the FIC. Therefore, the predicted overall crystallinity distribution tightly describes the experimental data. Furthermore, the α phase distribution predicted has recovered the intense effect of the cooling rate close to the sample wall and now correctly a prevalence of the α phase content is predicted along the whole sample thickness as shown by the performed X-ray analysis.

Comparison of final distribution of crystallinity with predictions obtained considering FIC for all the other tests considered are reported in Fig. 5.28. Predictions of the overall crystallinity in the core and the two phases content correctly describe the measured data. The effect of the processing conditions on the quenching zone thickness is very well predicted. In the “High T” test due to the high mold temperature the cooling rate does not have quenching effect on the material that completely crystallizes to its equilibrium value also near to the sample wall. In the “slow” test due to a lower flow rate the FIC effect on the α crystallization kinetic is not adequate to compensate the effect of the high cooling and therefore the thickness of the quenching zone increase. Only in a thinner zone of about 10 μm the mesomorphic phase content prevails on the α phase content. In the “High P” test, the higher packing pressure effect (that tends to reduce the α phase kinetic at the crystallization temperature in the zone close to sample wall) is coupled with the cooling rate effect; together they counteract the FIC effect more efficiently close to the sample wall with respect the “standard” test and an increase of the quenching zone thickness is predicted.

A comparison between experimental and predicted spherulite diameters is shown in Fig. 5.29 for “standard” and “slow” sample. The predicted spherulite diameters were obtained neglecting and considering FIC. Close to the sample wall the presence of the shear zone, characterized by the presence of fibrillary structures, was observed; in this region, no spherulites are detected. The thickness of this region, measured by the analysis of the images reported in Table 5.3, is marked by a vertical line in the diagrams of Fig. 5.29.

For Fig. 5.29, the left diagrams refer to the predictions carried out by considering the quiescent crystallization kinetics. It can be noticed (Fig. 5.29a, c) that, also neglecting the FIC, the measured distribution of spherulitic dimensions is satisfactorily described by the predictions. The diameters increase as the distance from the sample wall increase due to the decrease of the cooling rate. However, the decrease of the dimensions at the midplane is not captured by quiescent simulations.

If FIC is considered (Figs. 5.29b, d), some significant improvements are observed.

First, in the core spherulitic region, far from the sample midplane, spherulites predicted considering FIC have larger diameters with respect to those predicted by using the quiescent kinetics. Due to FIC the crystallization takes place at higher temperature with respect to the quiescent predictions and both the nucleation rate and the growth rate are enhanced by flow. With the specific correlation between growth rate and nucleation rate adopted, the spherulites generated, due to the flow enhanced growth rate, quickly occupy all the space available for the crystalline α

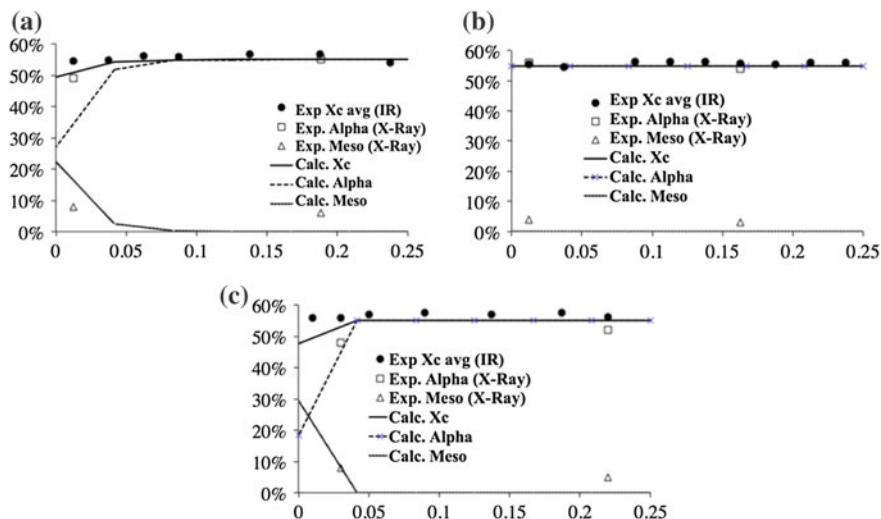


Fig. 5.28 Comparison of the measured final distributions of overall crystallinity, α and mesomorphic phase along the distance d , measured in mm, and the predicted ones (obtained considering FIC) for the “High P” condition (a), for the “High T” condition (b) and “slow” condition (c). Data reproduced from [57]

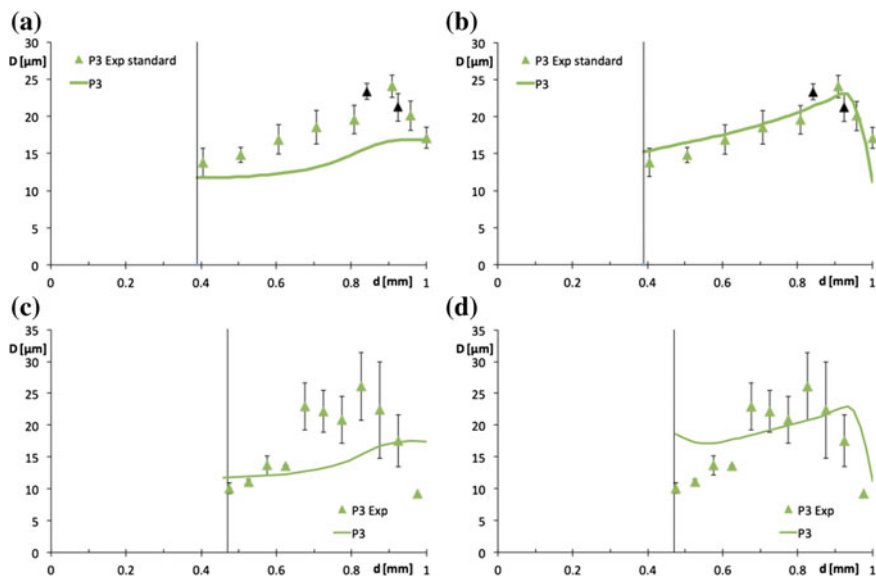


Fig. 5.29 Comparison of spherulite diameters, evaluated from AFM images both in “standard” and “slow” condition in position P3 along the flow path, with the predicted ones. In particular, for the “standard” condition predictions are obtained neglecting (a) and considering the FIC (b); for the “slow” condition, predictions are obtained neglecting (c) and considering the FIC (d). Data reproduced from [57]

phase and thus the formation of other nuclei is prevented giving rise to a larger spherulite diameters. A different correlation with a larger slope would give rise to a decrease of spherulites diameter by effect of FIC.

Second, closer to the midplane a decrease of diameters is correctly predicted when FIC is considered (the phenomenon is not reproduced when a quiescent crystallization kinetics is assumed). As stated above spherulite diameters increase by the effect of flow and approaching the midplane (where the effects of flow induced crystallization are lower) the diameters of the spherulites become smaller. Furthermore, the latent heat of crystallization keeps the region close to the sample midplane at higher temperatures and thus the crystallization at the midplane is delayed occurring at lower temperatures and thus giving rise to smaller spherulites (because the number of heterogeneous nuclei increases when the temperature decreases).

The mechanisms of formation of spherulitic and fibrillary layers are different. In particular, from experimental observation was found that fibrillary morphology develops when stretch and work are sufficiently high to form cylindrical rather spherical growth. As a consequence, predictions on the shear layer developed during the injection molding process can be obtained once a critical (shear rate) stretch value and a critical work value are identified. The thickness and the position of the shear layer are given by all the points presenting both calculated stretch parameter and viscous work higher than the chosen thresholds (critical values). By adopting this criterion, prediction of the shear layer position and thickness observed in the “standard” condition, can be obtained considering the calculated final distribution of the stretch parameter and viscous work reported in Fig. 5.30.

It can be noticed that, whatever realistic choice would be done for the two critical values, it would not sort a reasonable comparison with the thickness and the

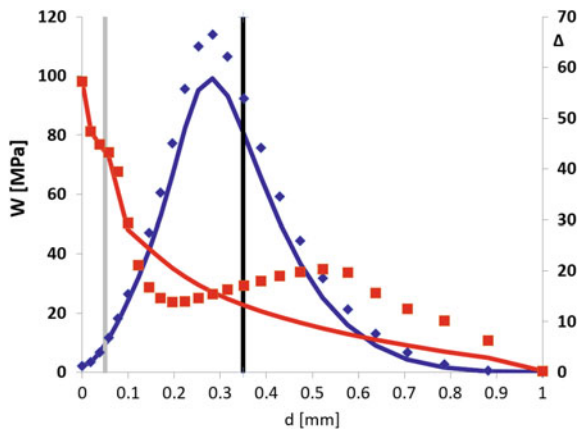


Fig. 5.30 Integral of the viscous work density (right axis) and molecular stretch parameter Δ (left axis), as function of the distance from the surface as calculated for the “standard” condition. The distribution of both variables at the end of the filling stage (lines) and at the end of the process (symbols) are reported. The thicknesses of the skin and shear layer are indicated as a vertical grey and black line respectively [73]

position of the skin and shear layers observed in the “standard” conditions. Similar conclusion was found for all the remaining conditions considered.

A realistic identification of the thicknesses and the position, within the molded samples cross sections, of the shear layers can be achieved by considering the following additional simultaneity criterion: the whole amount of work has to be done while the molecular stretch is above a critical value; furthermore, if the molecular stretch is let to relax below that critical value, all previous work has to be cancelled in the accounting for the critical work. This criterion appears physically grounded. In many processing conditions, the polymer melt is oriented first and then has the time to (partially) relax before being oriented again. If the relaxation were complete, it is obvious that the whole previous history does not have any effect of what happens next. This would mean that the time integral of the work alone is not a suitable criterion for describing the phenomenon in complex flow conditions and it is a sufficient condition whereas the integral of the viscous work and the final stretch distributions together can be considered a necessary criterion for fibrillar morphology of the polymer. The injection molding process seems specifically designed to verify the simultaneity criterion clarified above, since soon after filling the polymer not yet solidified relaxes considerable part of its stretch and after a short (but relevant) time it undergoes further stretching with lower shear rate but under higher viscosity due to the temperature decrease and eventually pressure increase. Furthermore, the *simultaneity* criterion is automatically respected in all the experiments conducted in literature that consider isothermal flow, under steady shear rate conditions.

In Fig. 5.31, the predictions of the position and thickness of the layers across the sample thickness, for all the conditions considered, are reported; results are obtained applying the *simultaneity* criterion and the same threshold values for

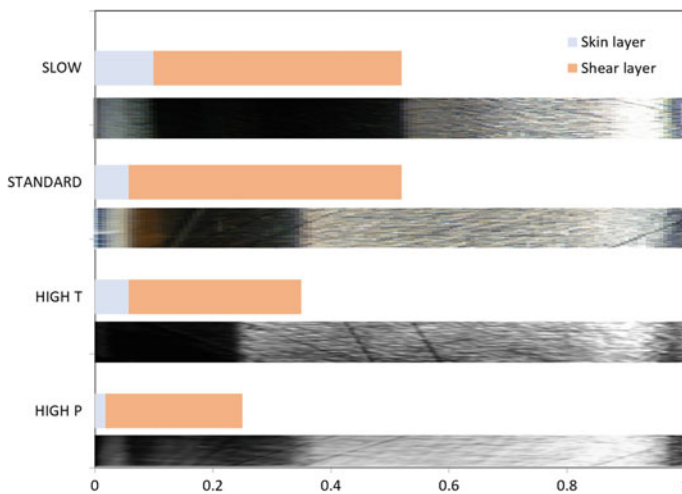


Fig. 5.31 Comparison between measured and predicted thickness and position of the layers across the sample thickness [73]

stretch parameter and critical work. The images of the samples are reported for a visual comparison of the results. It can be noticed that the thicknesses of the skin and of the shear layers are correctly described for all the samples molded with lower packing pressure (namely the standard, high T and slow conditions). An overestimation of the thickness of the shear layer for the sample molded with a pressure of 70 MPa (High P) is found. The reasons of this discrepancy can be found in the effect of pressure on viscosity (and on relaxation time) which obviously becomes extremely significant when the pressure levels increase.

5.6 Other Processing Techniques

5.6.1 *Compression Molding*

Compression molding is a process, commonly adopted for thermosets, in which the material, generally preheated, is first placed in an open, heated mold cavity. The mold is closed with a top force or plug member, pressure is applied to force the material into contact with all mold areas, while heat and pressure are maintained. Advanced PP composite can also be compression molded with unidirectional tapes, woven fabrics, randomly oriented fiber mat or chopped strand. The advantage of compression molding for thermoplastics is its ability to mold large, fairly intricate parts while injection molding could not be used. Therefore, the simplest way to produce isotropic plaques with different thicknesses is compression molding. Although crystallization occurs under a high pressure and temperature gradient, the melt flow and solid-state deformation are slight, so that the molded part possesses a relatively uniform texture (composed of spherulites). Transcrystals form sometimes at the mold surface. Compression-molded PP items are composed of spherulites and exhibit a random crystal orientation [112].

The lamellar thickness, spherulite size and crystallinity are the smaller, the larger the supercooling (defined as the difference between the melting point and crystallization temperature) is. High melting and cooling (mold) temperatures lead to a slow cooling and hence to a high crystallization temperature. This enhances both lamellar thickness spherulite size and crystallinity. The addition of nucleating agents increases the lamellar thickness and crystallinity and decreases the spherulite size. A high pressure has the same effect as the incorporation of nucleants [113].

While the tensile elongation decreases with increasing spherulite size, the yield strength and ultimate tensile strength scarcely depend on it. The tensile modulus, yield strength and hardness increase linearly with increasing crystallinity in contrast to the impact strength.

5.6.2 Extrusion-Related Techniques

Extruders (single screw or twin screw) are commonly used to produce tubes, profiles, films, and sheets, and to coat wires.

The geometry of a single screw extruder is usually constituted of a hopper which is used to feed the system with pellets (or sometimes with powder), a heated barrel (in fact successive zones with different controlled temperatures may be observed along the barrel), and a rotating screw whose core geometry generally increases from the hopper to the die.

For general extrusion of polypropylene, the temperature range from feed throat to front is 200–230 °C, with the die at the same temperature as the front barrel zone. Cast film, fibers, and yarns require higher temperatures; the rear at 220–250 °C and the front, adaptor, and die at 250 °C. Reverse profiles have been used where more mixing is required for pigment or fillers dispersion or melt uniformity.

Sheet and Pipe Extrusions

An extruded PP sheet shows a similar skin-core structure to that developed in injection molding. The skin layer is featureless and the core layer is composed of spherulites. The spherulite size increases toward the interior where the cooling is slower. A high draw ratio, creating high stresses, contributes to the initiation of crystal nuclei and thus to the formation of small spherulites [112]. The α crystallinity is low at the sheet surface and increases toward the interior. The α phase is almost replaced by the mesophase on the surface, with a slight intensification of the amorphous phase. A high draw ratio and short air gap, accompanied with a high melt orientation, initiates orientation crystallization and hence increases the crystallinity.

Film Casting

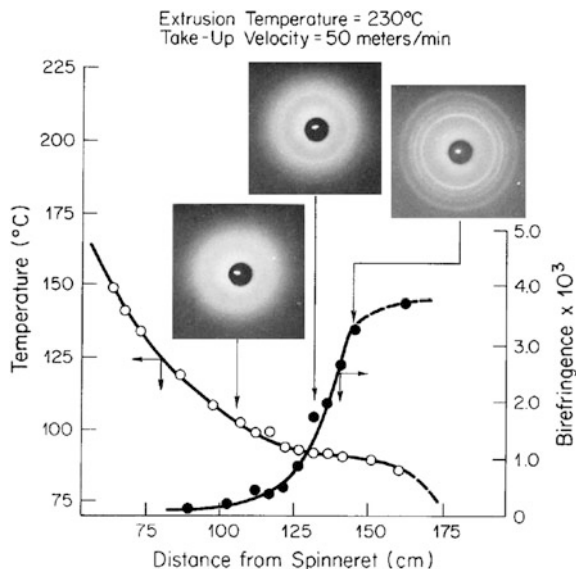
A cast film can be regarded as a thin sheet. While a sheet is composed mostly of the α -form crystals, in the case of the cast film, the cooling effect by the chill roll is so high that the α -crystals change gradually to the mesomorphic form. This modification is triggered by decreasing chill roll temperature. A PP with higher melt flow index (MFI) crystallizes more easily in the smectic form than a lower MFI resin. The spherulite size increases with increasing film thickness and chill roll temperature and decreases with increasing draw ratio and die temperature [114].

The molecular orientation increases with increasing draw ratio and take-up speed and with decreasing cylinder temperature. Crystallization during film casting is also the object of simulation work [115]. The tensile yield strength is higher and the ultimate elongation and strength are lower when the spherulite size becomes larger [114]. The tensile modulus increases linearly with increasing crystallinity. The heat sealing strength decreases with increase in the crystallinity.

Fiber Spinning

In melt spinning, the diameter of a filament extruded from a spinneret gradually decreases and approaches a constant value at the point of crystallization initiation (where crystallization and molecular orientation start). Because the melt-spun PP

Fig. 5.32 On-line WAXS patterns, temperature and birefringence profiles for melt-spun polypropylene filament. Reproduced from [116]



fiber crystallizes under stresses, it is composed of a kind of shish-kebab structure [116].

Depending on the cooling rates, the spun filaments of polypropylene were either mesomorphic or highly crystalline. The mesomorphic form occurs only when rapid cooling rates were achieved by quenching the molten threadline into water.

For filaments spun into ambient air, crystallization to the α monoclinic form occurs in the threadline, as shown with on-line measurements in Fig. 5.32 [116]. The WAXD patterns made on a running filament at different distances from the spinneret are shown in relation to a temperature and birefringence profile for the same run. A hold in the temperature profile occurs as crystallization begins due to the release of the latent heat of crystallization. During crystallization the birefringence rises rapidly, eventually approaching the birefringence of the as-spun filament [116].

References

1. Natta G, Corradini P (1960) Structure and properties of isotactic polypropylene. *Il Nuovo Cimento* (1955–1965) 15(1):40–51. <https://doi.org/10.1007/bf02731859>
2. Coccorullo I, Pantani R, Titomanlio G (2003) Crystallization kinetics and solidified structure in iPP under high cooling rates. *Polymer* 44(1):307–318. [https://doi.org/10.1016/S0032-3861\(02\)00762-0](https://doi.org/10.1016/S0032-3861(02)00762-0)
3. Dorset D, McCourt M, Kopp S et al (1998) Isotactic polypropylene, β -phase: a study in frustration. *Polymer* 39(25):6331–6337. [https://doi.org/10.1016/S0032-3861\(97\)10160-4](https://doi.org/10.1016/S0032-3861(97)10160-4)

4. Angeloz C, Fulchiron R, Douillard A et al (2000) Crystallization of isotactic polypropylene under high pressure (γ phase). *Macromolecules* 33(11):4138–4145. <https://doi.org/10.1021/ma991813e>
5. De Rosa C, Auriemma F, Girolamo R et al (2014) Crystallization of the mesomorphic form and control of the molecular structure for tailoring the mechanical properties of isotactic polypropylene. *J Polym Sci, Part B: Polym Phys* 52(10):677–699. <https://doi.org/10.1002/polb.23473>
6. Varga J (2002) β -modification of isotactic polypropylene: preparation, structure, processing, properties, and application. *J Macromol. Sci, Part B* 41(4–6):1121–1171. <https://doi.org/10.1081/MB-120013089>
7. Lezak E, Bartczak Z, Galeski A (2006) Plastic deformation of the γ phase in isotactic polypropylene in plane-strain compression. *Macromolecules* 39(14):4811–4819. <https://doi.org/10.1021/ma0605907>
8. De Rosa C, Auriemma F, Di Girolamo R et al (2013) Morphology and mechanical properties of the mesomorphic form of isotactic polypropylene in stereodeficient polypropylene. *Macromolecules* 46(13):5202–5214. <https://doi.org/10.1021/ma400570k>
9. Viana JC, Cunha A, Billon N (2001) The effect of the skin thickness and spherulite size on the mechanical properties of injection mouldings. *J Mater Sci* 36(18):4411–4418. <https://doi.org/10.1023/A:1017970416968>
10. Kristiansen M, Werner M, Tervoort T et al (2003) The binary system isotactic polypropylene/bis (3, 4-dimethylbenzylidene) sorbitol: phase behavior, nucleation, and optical properties. *Macromolecules* 36(14):5150–5156. <https://doi.org/10.1021/ma030146t>
11. Phillips AW, Bhatia A, Pw Zhu et al (2013) Polymorphism in sheared isotactic polypropylene containing nucleant particles. *Macromol Mater Eng* 298(9):991–1003. <https://doi.org/10.1002/mame.201200199>
12. Housmans J-W, Gahleitner M, Peters GW et al (2009) Structure–property relations in molded, nucleated isotactic polypropylene. *Polymer* 50(10):2304–2319. <https://doi.org/10.1016/j.polymer.2009.02.050>
13. Janeschitz-Kriegl H (2009) Crystallization modalities in polymer melt processing: fundamental aspects of structure formation. Springer Science & Business Media. <https://doi.org/10.1007/978-3-211-87627-5>
14. Piccarolo S, Saiu M, Brucato V et al. (1992) Crystallization of polymer melts under fast cooling. II. High-purity iPP. *J Appl Polym Sci* 46(4):625–634. <https://doi.org/10.1002/app.1992.070460409>
15. Magill J (1962) A new technique for following rapid rates of crystallization II isotactic polypropylene. *Polymer* 3:35–42. [https://doi.org/10.1016/0032-3861\(62\)90064-2](https://doi.org/10.1016/0032-3861(62)90064-2)
16. Ding Z, Spruiell JE (1996) An experimental method for studying nonisothermal crystallization of polymers at very high cooling rates. *J Polym Sci, Part B: Polym Phys* 34(16):2783–2804. [https://doi.org/10.1002/\(SICI\)1099-0488\(19961130\)34:16%3c2783:AID-POLB12%3e3.0.CO;2-6](https://doi.org/10.1002/(SICI)1099-0488(19961130)34:16%3c2783:AID-POLB12%3e3.0.CO;2-6)
17. Brucato V, De Santis F, Giannattasio A et al (2002) Crystallization during fast cooling experiments, a novel apparatus for real time monitoring. *Macromol Symp* 185:181–196. [https://doi.org/10.1002/1521-3900\(200208\)185:1%3c181:AID-MASY181%3e3.0.CO;2-O](https://doi.org/10.1002/1521-3900(200208)185:1%3c181:AID-MASY181%3e3.0.CO;2-O)
18. De Santis F, Lamberti G, Peters GW et al (2005) Improved experimental characterization of crystallization kinetics. *Eur Polymer J* 41(10):2297–2302. <https://doi.org/10.1016/j.eurpolymj.2005.04.032>
19. Adamovsky S, Schick C (2004) Ultra-fast isothermal calorimetry using thin film sensors. *Thermochim Acta* 415(1–2):1–7. <https://doi.org/10.1016/j.tca.2003.07.015>
20. De Santis F, Adamovsky S, Titomanlio G et al (2006) Scanning nanocalorimetry at high cooling rate of isotactic polypropylene. *Macromolecules* 39(7):2562–2567. <https://doi.org/10.1021/ma052525n>
21. De Santis F, Adamovsky S, Titomanlio G et al (2007) Isothermal nanocalorimetry of isotactic polypropylene. *Macromolecules* 40(25):9026–9031. <https://doi.org/10.1021/ma071491b>

22. Morrow D, Newman B (1968) Crystallization of low-molecular-weight polypropylene fractions. *J Appl Phys* 39(11):4944–4950. <https://doi.org/10.1063/1.1655891>
23. Turner-Jones A (1971) Development of the γ -crystal form in random copolymers of propylene and their analysis by DSC and X-ray methods. *Polymer* 12(8):487–508. [https://doi.org/10.1016/0032-3861\(71\)90031-0](https://doi.org/10.1016/0032-3861(71)90031-0)
24. Mezghani K, Phillips PJ (1995) γ -Phase in propylene copolymers at atmospheric pressure. *Polymer* 36(12):2407–2411. [https://doi.org/10.1016/0032-3861\(95\)97341-C](https://doi.org/10.1016/0032-3861(95)97341-C)
25. Meille SV, Bruckner S, Porzio W (1990) γ -Isotactic polypropylene. A structure with nonparallel chain axes. *Macromolecules* 23(18):4114–4121. <https://doi.org/10.1021/ma00220a014>
26. Sauer J, Pae K (1968) Structure and Thermal Behavior of Pressure-Crystallized Polypropylene. *J Appl Phys* 39(11):4959–4968. <https://doi.org/10.1063/1.1655893>
27. Nakafuku C (1981) High pressure dta study on the melting and crystallization of isotactic polypropylene. *Polymer* 22(12):1673–1676. [https://doi.org/10.1016/0032-3861\(81\)90384-0](https://doi.org/10.1016/0032-3861(81)90384-0)
28. Campbell RA, Phillips PJ, Lin J (1993) The gamma phase of high-molecular-weight polypropylene: 1. Morphological aspects. *Polymer* 34(23):4809–4816. [https://doi.org/10.1016/0032-3861\(93\)90002-R](https://doi.org/10.1016/0032-3861(93)90002-R)
29. Meille SV, Brückner S (1989) Non-parallel chains in crystalline γ -isotactic polypropylene. *Nature* 340(6233):455–457. <https://doi.org/10.1038/340455a0>
30. Zoller P, Bolli P, Pahud V et al (1976) Apparatus for measuring pressure–volume–temperature relationships of polymers to 350 C and 2200 kg/cm². *Rev Sci Instrum* 47(8):948–952. <https://doi.org/10.1063/1.1134779>
31. Zoller P (1979) Pressure–volume–temperature relationships of solid and molten polypropylene and poly (butene-1). *J Appl Polym Sci* 23(4):1057–1061. <https://doi.org/10.1002/app.1979.070230411>
32. He J, Zoller P (1994) Crystallization of polypropylene, nylon-66 and poly (ethylene terephthalate) at pressures to 200 MPa: Kinetics and characterization of products. *J Polym Sci, Part B: Polym Phys* 32(6):1049–1067. <https://doi.org/10.1002/polb.1994.090320610>
33. La Carrubba V, Brucato V, Piccarolo S (2002) Phenomenological approach to compare the crystallization kinetics of isotactic polypropylene and polyamide-6 under pressure. *J Polym Sci, Part B: Polym Phys* 40(1):153–175. <https://doi.org/10.1002/polb.10075>
34. Pantani R, Nappo V, De Santis F et al (2014) Fibrillar Morphology in Shear-Induced Crystallization of Polypropylene. *Macromol Mater Eng* 299(12):1465–1473. <https://doi.org/10.1002/mame.201400131>
35. van Erp TB, Balzano L, Spoelstra AB et al (2012) Quantification of non-isothermal, multi-phase crystallization of isotactic polypropylene: The influence of shear and pressure. *Polymer* 53(25):5896–5908. <https://doi.org/10.1016/j.polymer.2012.10.027>
36. De Santis F, Pantani R, Titomanlio G (2016) Effect of shear flow on spherulitic growth and nucleation rates of polypropylene. *Polymer* 90:102–110. <https://doi.org/10.1016/j.polymer.2016.02.059>
37. Pantani R, Coccoorullo I, Volpe V et al (2010) Shear-induced nucleation and growth in isotactic polypropylene. *Macromolecules* 43(21):9030–9038. <https://doi.org/10.1021/ma101775h>
38. Pantani R, Nappo V, De Santis F et al (2014) Fibrillar morphology formation in a sheared polypropylene melt. *AIP Conf Proc* 1593:76–79. <https://doi.org/10.1063/1.4873738>
39. Janeschitz-Kriegl H, Ratajski E, Stadlbauer M (2003) Flow as an effective promotor of nucleation in polymer melts: a quantitative evaluation. *Rheol Acta* 42(4):355–364. <https://doi.org/10.1007/s00397-002-0247-x>
40. Mykhaylyk OO, Chambon P, Graham RS et al (2008) The specific work of flow as a criterion for orientation in polymer crystallization. *Macromolecules* 41(6):1901–1904. <https://doi.org/10.1021/ma702603v>
41. Troisi E, Arntz S, Roozmond P et al (2017) Application of a multi-phase multi-morphology crystallization model to isotactic polypropylenes with different molecular weight distributions. *Eur Polymer J* 97:397–408. <https://doi.org/10.1016/j.eurpolymj.2017.09.042>

42. van Erp TB, Balzano L, Peters GW (2012) Oriented gamma phase in isotactic polypropylene homopolymer. *ACS Macro Letters* 1(5):618–622. <https://doi.org/10.1021/mz3000978>
43. Gahleitner M, Mileva D, Androsch R et al (2016) Crystallinity-based product design: Utilizing the polymorphism of isotactic PP homo-and copolymers. *Int Polym Proc* 31 (5):618–627. <https://doi.org/10.3139/217.3242>
44. Menyhárd A, Gahleitner M, Varga J et al (2009) The influence of nucleus density on optical properties in nucleated isotactic polypropylene. *Eur Polymer J* 45(11):3138–3148. <https://doi.org/10.1016/j.eurpolymj.2009.08.006>
45. Libster D, Aserin A, Garti N (2007) Advanced nucleating agents for polypropylene. *Polym Adv Technol* 18(9):685–695. <https://doi.org/10.1002/pat.970>
46. Karger-Kocsis J, Varga J, Ehrenstein G (1997) Comparison of the fracture and failure behavior of injection-molded α - and β -polypropylene in high-speed three-point bending tests. *J Appl Polym Sci* 64(11):2057–2066. [https://doi.org/10.1002/\(SICI\)1097-4628\(19970613\)64:11%3c2057:AID-APP1%3e3.0.CO;2-I](https://doi.org/10.1002/(SICI)1097-4628(19970613)64:11%3c2057:AID-APP1%3e3.0.CO;2-I)
47. Yoshimoto S, Ueda T, Yamanaka K et al (2001) Epitaxial act of sodium 2, 2'-methylene-bis-(4, 6-di-*t*-butylphenylene) phosphate on isotactic polypropylene. *Polymer* 42(23):9627–9631. [https://doi.org/10.1016/S0032-3861\(01\)00510-9](https://doi.org/10.1016/S0032-3861(01)00510-9)
48. Liu H, Huo H (2013) Competitive growth of α - and β -crystals in isotactic polypropylene with versatile nucleating agents under shear flow. *Colloid Polym Sci* 291(8):1913–1925. <https://doi.org/10.1007/s00396-013-2922-0>
49. Menyhárd A, Varga J, Molnár G (2006) Comparison of different-nucleators for isotactic polypropylene, characterisation by DSC and temperature-modulated DSC (TMDSC) measurements. *J Therm Anal Calorim* 83(3):625–630. <https://doi.org/10.1007/s10973-005-7498-6>
50. Výchopňová J, Habrová V, Obadal M et al (2006) Crystallization of polypropylenewith a minute amount of β -nucleator. *J Therm Anal Calorim* 86(3):687–691. <https://doi.org/10.1007/s10973-006-7894-6>
51. Libster D, Aserin A, Garti N (2006) A novel dispersion method comprising a nucleating agent solubilized in a microemulsion, in polymeric matrix: II. Microemulsion characterization. *J. colloid interface sci* 302 (1):322–329. <https://doi.org/10.1016/j.jcis.2006.06.060>
52. Fillon B, Lotz B, Thierry A et al. (1993) Self-nucleation and enhanced nucleation of polymers. Definition of a convenient calorimetric “efficiency scale” and evaluation of nucleating additives in isotactic polypropylene (α phase). *J Polym Sci Part B: Polym Phys* 31 (10):1395–1405. <https://doi.org/10.1002/polb.1993.090311014>
53. Nagasawa S, Fujimori A, Masuko T et al (2005) Crystallisation of polypropylene containing nucleators. *Polymer* 46(14):5241–5250. <https://doi.org/10.1016/j.polymer.2005.03.099>
54. Pantani R, Coccorullo I, Speranza V et al (2005) Modeling of morphology evolution in the injection molding process of thermoplastic polymers. *Prog Polym Sci* 30(12):1185–1222. <https://doi.org/10.1016/j.progpolymsci.2005.09.001>
55. Isayev A, Catignani B (1997) Crystallization and microstructure in quenched slabs of various molecular weight polypropylenes. *Polym Eng Sci* 37(9):1526–1539. <https://doi.org/10.1002/pen.11801>
56. Eder G, Janeschitz-Kriegl H, Liedauer S (1990) Crystallization processes in quiescent and moving polymer melts under heat transfer conditions. *Prog Polym Sci* 15(4):629–714. [https://doi.org/10.1016/0079-6700\(90\)90008-O](https://doi.org/10.1016/0079-6700(90)90008-O)
57. Pantani R, Speranza V, Titomanlio G (2017) Effect of Flow-Induced Crystallization on the distribution of spherulite dimensions along cross section of injection molded parts. *Eur Polymer J* 97:220–229. <https://doi.org/10.1016/j.eurpolymj.2017.10.012>
58. Hoffman JD, Lauritzen J (1961) Crystallization of bulk polymers with chain folding-Theory of growth of lamellar spherulites. *J Res National Bureau Standards* 4:297–336. <https://doi.org/10.6028/jres.065A.035>
59. Hoffman J, Lauritzen J, Passaglia E et al (1969) Kinetics of polymer crystallization from solution and the melt. *Kolloid-Zeitschrift und Zeitschrift für Polymere* 231(1–2):564–592. <https://doi.org/10.1007/BF01500015>

60. Roozmond PC, van Drongelen M, Peters GW (2016) Modeling flow-induced crystallization. In: Auriemma F, AG, de Rosa C (ed) *Polymer Crystallization II*. Springer, pp 243–294. https://doi.org/10.1007/12_2016_35
61. Karger-Kocsis J, Csikai I (1987) Skin-core morphology and failure of injection-molded specimens of impact-modified polypropylene blends. *Polym Eng Sci* 27(4):241–253. <https://doi.org/10.1002/pen.760270403>
62. Balzano L, Rastogi S, Peters GW (2008) Flow induced crystallization in isotactic polypropylene – 1, 3: 2, 4-bis (3, 4-dimethylbenzylidene) sorbitol blends: implications on morphology of shear and phase separation. *Macromolecules* 41(2):399–408. <https://doi.org/10.1021/ma071460g>
63. Laschet G, Spekowius M, Spina R et al (2017) Multiscale simulation to predict microstructure dependent effective elastic properties of an injection molded polypropylene component. *Mech Mater* 105:123–137. <https://doi.org/10.1016/j.mechmat.2016.10.009>
64. Liu F, Guo C, Wu X et al (2012) Morphological comparison of isotactic polypropylene parts prepared by micro-injection molding and conventional injection molding. *Polym Adv Technol* 23(3):686–694. <https://doi.org/10.1002/pat.1946>
65. Giboz J, Copponnex T, Mélé P (2009) Microinjection molding of thermoplastic polymers: morphological comparison with conventional injection molding. *J Micromech Microeng* 19(2):025023. <https://doi.org/10.1088/0960-1317/19/2/025023>
66. Giboz J, Spoelstra AB, Portale G et al (2011) On the origin of the “core-free” morphology in microinjection-molded HDPE. *J Polym Sci, Part B: Polym Phys* 49(20):1470–1478. <https://doi.org/10.1002/polb.22332>
67. Wang S, Wang Z, Zhao N et al (2015) A novel morphology development of micro-injection molded isotactic polypropylene. *RSC Advances* 5(52):41608–41610. <https://doi.org/10.1039/C5RA04626B>
68. Jerschow P, Janeschitz-Kriegl H (1996) On the development of oblong particles as precursors for polymer crystallization from shear flow: origin of the so-called fine grained layers. *Rheol Acta* 35(2):127–133. <https://doi.org/10.1007/BF00396039>
69. Liparoti S, Speranza V, Sorrentino A et al (2017) Mechanical properties distribution within polypropylene injection molded samples: effect of mold temperature under uneven thermal conditions. *Polymers* 9(11):585. <https://doi.org/10.3390/polym9110585>
70. Kantz M, Newman H, Stigale F (1972) The skin-core morphology and structure–property relationships in injection-molded polypropylene. *J Appl Polym Sci* 16(5):1249–1260. <https://doi.org/10.1002/app.1972.070160516>
71. Kalay G, Bevis MJ (1997) Processing and physical property relationships in injection-molded isotactic polypropylene. 2. Morphology and crystallinity. *J Polym Sci Part B: Polym Phys* 35(2):265–291. [https://doi.org/10.1002/\(sici\)1099-0488\(19970130\)35:2%3c265::aid-polb6%3e3.0.co;2-r](https://doi.org/10.1002/(sici)1099-0488(19970130)35:2%3c265::aid-polb6%3e3.0.co;2-r)
72. Mi D, Xia C, Jin M et al (2016) Quantification of the effect of shish-kebab structure on the mechanical properties of polypropylene samples by controlling shear layer thickness. *Macromolecules* 49(12):4571–4578. <https://doi.org/10.1021/acs.macromol.6b00822>
73. Pantani R, Speranza V, Titomanlio G (2018) A criterion for the formation of fibrillar layers in injection molded parts. *Int Polym Process*. in press
74. Speranza V, Vietri U, Pantani R (2011) Monitoring of injection molding of thermoplastics: Average solidification pressure as a key parameter for quality control. *Macromol Res* 19(6):542. <https://doi.org/10.1007/s13233-011-0610-9>
75. Tosello G, Hansen HN (2010) *Micro injection molding*. In: *Micro-manufacturing engineering and technology*. Elsevier Science, pp 90–113. <https://doi.org/10.1016/b978-0-323-31149-6.00009-8>
76. Ito H, Yagisawa Y, SAITO T et al (2005) Fundamental study on structure development of thin-wall injection molded products. *Theor Appl Mech Jpn* 54:263–268. <https://doi.org/10.11345/nctam.54.263>

77. De Santis F, Pantani R (2016) Development of a rapid surface temperature variation system and application to micro-injection molding. *J Mater Process Technol* 237:1–11. <https://doi.org/10.1016/j.jmatprotec.2016.05.023>
78. Speranza V, Liparoti S, Calao M et al (2017) Replication of micro and nano-features on iPP by injection molding with fast cavity surface temperature evolution. *Mater Des* 133:559–569. <https://doi.org/10.1016/j.matdes.2017.08.016>
79. Liparoti S, Titomanlio G, Sorrentino A (2016) Analysis of asymmetric morphology evolutions in iPP molded samples induced by uneven temperature field. *AIChE J* 62(8):2699–2712. <https://doi.org/10.1002/aic.15241>
80. Wang G, Zhao G, Wang X (2014) Development and evaluation of a new rapid mold heating and cooling method for rapid heat cycle molding. *Int J Heat Mass Transf* 78:99–111. <https://doi.org/10.1016/j.ijheatmasstransfer.2014.06.062>
81. Kmetty Á, Bárány T, Karger-Kocsis J (2010) Self-reinforced polymeric materials: a review. *Prog Polym Sci* 35(10):1288–1310
82. Allan P, Bevis M (1987) Multiple live-feed injection moulding. *Plastics and rubber processing and applications* 7(1):3–10
83. Kalay G, Allan P, Bevis MJ (1994) γ Phase in injection moulded isotactic polypropylene. *Polymer* 35(12):2480–2482. [https://doi.org/10.1016/0032-3861\(94\)90366-2](https://doi.org/10.1016/0032-3861(94)90366-2)
84. Kalay G, Bevis MJ (1997) Processing and physical property relationships in injection-molded isotactic polypropylene. 1. Mechanical properties. *J Polym Sci Part B: Polym Phys* 35(2):241–263. [https://doi.org/10.1002/\(sici\)1099-0488\(19970130\)35:2%3c241::aid-polb5%3e3.0.co;2-v](https://doi.org/10.1002/(sici)1099-0488(19970130)35:2%3c241::aid-polb5%3e3.0.co;2-v)
85. Lei J, Jiang C, Shen K (2004) Biaxially self-reinforced high-density polyethylene prepared by dynamic packing injection molding. I. Processing parameters and mechanical properties. *J Appl Polym Sci* 93(4):1584–1590
86. Guan Q, Zhu X, Chiu D et al (1996) Self-reinforcement of polypropylene by oscillating packing injection molding under low pressure. *J Appl Polym Sci* 62(5):755–762. [https://doi.org/10.1002/\(SICI\)1097-4628\(19961031\)62:5%3c755::AID-APP6%3e3.0.CO;2-V](https://doi.org/10.1002/(SICI)1097-4628(19961031)62:5%3c755::AID-APP6%3e3.0.CO;2-V)
87. Chen LM, Shen K (2000) Biaxial self-reinforcement of isotactic polypropylene prepared in uniaxial oscillating stress field by injection molding. I. Processing conditions and mechanical properties. *J Appl Polym Sci* 78(11):1906–1910. [https://doi.org/10.1002/1097-4628\(20001209\)78:11%3c1906::aid-app80%3e3.0.co;2-1](https://doi.org/10.1002/1097-4628(20001209)78:11%3c1906::aid-app80%3e3.0.co;2-1)
88. Wang Y, Pan J-L, Mao Y et al (2010) Spatial distribution of γ -crystals in metallocene-made isotactic polypropylene crystallized under combined thermal and flow fields. *J Phys Chem B* 114(20):6806–6816. <https://doi.org/10.1021/jp1002484>
89. Chen Y-H, Zhong G-J, Wang Y et al (2009) Unusual tuning of mechanical properties of isotactic polypropylene using counteraction of shear flow and β -nucleating agent on β -form nucleation. *Macromolecules* 42(12):4343–4348. <https://doi.org/10.1021/ma900411f>
90. Su R, Zhang Z, Gao X et al (2010) Polypropylene injection molded part with novel macroscopic bamboo-like bionic structure. *J Phys Chem B* 114(31):9994–10001. <https://doi.org/10.1021/jp1020802>
91. Sato A, Ito H, Koyama K (2009) Study of application of ultrasonic wave to injection molding. *Polym Eng Sci* 49(4):768–773. <https://doi.org/10.1002/pen.21268>
92. Peng B, Wu H, Guo S et al (2007) Effects of ultrasonic oscillations on rheological behavior and mechanical properties of novel propylene-based plastomers. *J Appl Polym Sci* 106(3):1725–1732. <https://doi.org/10.1002/app.26765>
93. Ibar J (1998) Control of polymer properties by melt vibration technology: a review. *Polym Eng Sci* 38(1):1–20. <https://doi.org/10.1002/pen.10161>
94. Li Y, Shen K (2008) Improving the mechanical properties of polypropylene via melt vibration. *J Appl Polym Sci* 109(1):90–96. <https://doi.org/10.1002/app.27412>
95. Youbing L, Jing C, Kaizhi S (2008) Self-reinforced isotactic polypropylene prepared by melt vibration injection molding. *Polym Plast Technol Eng* 47(7):673–677. <https://doi.org/10.1080/03602550802129551>

96. Liu K, Zhang J, Liu H et al. (2013) A multi-layer bioinspired design with evolution of shish-kebab structures induced by controlled periodical shear field. *Express Polym Lett* 7(4). <https://doi.org/10.3144/expresspolymlett.2013.32>
97. Guo X, Isayev A, Guo L (1999) Crystallinity and microstructure in injection moldings of isotactic polypropylenes. Part I: A new approach to modeling and model parameters. *Polym Eng Sci* 39(10):2096–2114. <https://doi.org/10.1002/pen.11601>
98. Guo X, Isayev A, Demiray M (1999) Crystallinity and microstructure in injection moldings of isotactic polypropylenes. Part II: Simulation and experiment. *Polym Eng Sci* 39(11):2132–2149. <https://doi.org/10.1002/pen.11603>
99. Zuidema H, Peters GW, Meijer HE (2001) Development and validation of a recoverable strain-based model for flow-induced crystallization of polymers. *Macromol Theory Simul* 10(5):447–460. [https://doi.org/10.1002/1521-3919\(20010601\)10:5%3c447:AID-MATS447%3e3.0.CO;2-C](https://doi.org/10.1002/1521-3919(20010601)10:5%3c447:AID-MATS447%3e3.0.CO;2-C)
100. Eder G, Janeschitz-Kriegl H (1997) Crystallization. In: Meijer H (ed) *Materials science and technology: processing of polymers*, vol 18. Wiley-VCH. <https://doi.org/10.1002/9783527603978.mst0211>
101. Baaijens F (1991) Calculation of residual stresses in injection molded products. *Rheol Acta* 30(3):284–299. <https://doi.org/10.1007/BF00366642>
102. Leonov A (1987) On a class of constitutive equations for viscoelastic liquids. *J Nonnewton Fluid Mech* 25(1):1–59. [https://doi.org/10.1016/0377-0257\(87\)85012-7](https://doi.org/10.1016/0377-0257(87)85012-7)
103. Zheng R, Kennedy P (2004) A model for post-flow induced crystallization: General equations and predictions. *J Rheol* 48(4):823–842. <https://doi.org/10.1122/1.1763944>
104. Mykhaylyk OO, Chambon P, Impradice C et al (2010) Control of structural morphology in shear-induced crystallization of polymers. *Macromolecules* 43(5):2389–2405. <https://doi.org/10.1021/ma902495z>
105. Gahleitner M, Wolfschwenger J, Bachner C et al (1996) Crystallinity and mechanical properties of PP-homopolymers as influenced by molecular structure and nucleation. *J Appl Polym Sci* 61(4):649–657. [https://doi.org/10.1002/\(SICI\)1097-4628\(19960725\)61:4%3c649:AID-APP8%3e3.0.CO;2-L](https://doi.org/10.1002/(SICI)1097-4628(19960725)61:4%3c649:AID-APP8%3e3.0.CO;2-L)
106. Salazar A, Rico A, Rodriguez S et al (2012) Relating fracture behavior to spherulite size in controlled-rheology polypropylenes. *Polym Eng Sci* 52(4):805–813. <https://doi.org/10.1002/pen.22145>
107. Pantani R, Sorrentino A, Speranza V et al (2004) Molecular orientation in injection molding: experiments and analysis. *Rheol Acta* 43(2):109–118. <https://doi.org/10.1007/s00397-003-0325-8>
108. Pantani R, Speranza V, Titomanlio G (2016) Thirty years of modeling of injection molding. a brief review of the contribution of UNISA code to the field. *Int Polym Process* 31(5):655–663. <https://doi.org/10.3139/217.3249>
109. Titomanlio G, Speranza V, Brucato V (1997) On the simulation of thermoplastic injection moulding process: II relevance of interaction between flow and crystallization. *Int Polym Proc* 12(1):45–53. <https://doi.org/10.3139/217.970045>
110. Pantani R, Speranza V, Titomanlio G (2001) Relevance of mold-induced thermal boundary conditions and cavity deformation in the simulation of injection molding. *Polym Eng Sci* 41(11):2022–2035. <https://doi.org/10.1002/pen.10898>
111. Pantani R, De Meo A, Speranza V et al (2015) Effect of crystallinity on the viscosity of an isotactic polypropylene. *AIP Conf Proc* 1695:020065. <https://doi.org/10.1063/1.4873738>
112. Karger-Kocsis J (2012) *Polypropylene: an AZ reference*, vol 2. Springer Science & Business Media. <https://doi.org/10.1007/978-94-011-4421-6>
113. Reinshagen J, Dunlap R (1975) The effects of melt history, crystallization pressure, and crystallization temperature on the crystallization and resultant structure of bulk isotactic polypropylene. *J Appl Polym Sci* 19(4):1037–1060. <https://doi.org/10.1002/app.1975.070190413>

114. Akay M (1989) Influence of total processing history on polypropylene structure and properties. *Polym Int* 21(4):285–293. <https://doi.org/10.1002/pi.4980210402>
115. Titomanlio G, Lamberti G (2004) Modeling flow induced crystallization in film casting of polypropylene. *Rheol Acta* 43(2):146–158. <https://doi.org/10.1007/s00397-003-0329-4>
116. Nadella HP, Henson HM, Spruiell JE et al (1977) Melt spinning of isotactic polypropylene: Structure development and relationship to mechanical properties. *J Appl Polym Sci* 21 (11):3003–3022. <https://doi.org/10.1002/app.1977.070211115>

Chapter 6

Polypropylene Copolymers



Markus Gahleitner, Cornelia Tranninger and Petar Doshev

Contents

6.1 History of PP Copolymers	296
6.2 Homogeneous Random Copolymers.....	298
6.2.1 Ethylene/Propylene Random Copolymers	298
6.2.2 Propylene Random Co- and Terpolymers with Higher α -Olefins	307
6.3 Heterophasic Copolymers.....	315
6.3.1 Matrix Design.....	322
6.3.2 Elastomer Design.....	325
6.3.3 Modification of Heterophasic Copolymers	335
6.4 Application of PP Copolymers	340
References	345

Abstract The wide variety of copolymers of polypropylene (PP) is one of the key reasons for the technical and commercial success of this polymer. While historically compounds with elastomers came before reactor-based compositions, the latter now dominate the market. This is the result of developments on both the catalyst and the process side of production. Two main classes are distinguished, homogeneous random copolymer with either ethylene or higher α -olefins (like butene or hexene, both of which can also be combined with ethylene to give terpolymers), and heterophasic copolymers. While the former are single-phase materials, even in case of bimodality in molecular weight and/or comonomer distribution, the latter feature a complex multi-phase structure. Design variations are possible for both the crystalline matrix and the elastomeric inclusions here, allowing a wide variety of property combinations. Applications of PP copolymers are defined by their respective properties and range from advanced packaging solutions through pipe and medical applications to components for the automotive industry.

M. Gahleitner (✉) · C. Tranninger · P. Doshev
Borealis Polyolefine GmbH, Innovation Headquarters,
St. Peterstrasse 25, 4021 Linz, Austria
e-mail: markus.gahleitner@borealisgroup.com

© Springer Nature Switzerland AG 2019
J. Karger-Kocsis and T. Bárány (eds.), *Polypropylene Handbook*,
https://doi.org/10.1007/978-3-030-12903-3_6

6.1 History of PP Copolymers

The success of isotactic polypropylene (iPP) which made it one of the most widely used polymers is directly connected to the development of copolymers. While Karl Ziegler's original patent for low-pressure, high density polyethylene (HDPE) based on titanium-centered catalysts [1] is exclusively focused on ethylene as monomer, Giulio Natta's counterpart [2] already lists a whole class of possible monomers and co-monomers. It is undisputed that Natta's work is largely based on Ziegler's findings on the catalyst side [3], the merit for developing a first understanding of the new polymer's crystalline nature clearly goes to Natta and Corradini [4]. Not only did they resolve the crystal structure of the α -phase and the mesomorphic phase of iPP, including the helical nature of its chain in such crystals, they also established the connection between isotacticity and crystallinity. Later on, these developments became the foundation of understanding crystal structures of many other stereoregular polymers like poly-1-butene and even isotactic polystyrene.

Already in the basic characterization of the new polymer it became clear that (in comparison to HDPE) the higher melting point of ~ 165 °C came associated with a glass transition temperature at ~ 0 °C [5], limiting the polymer's applicability in the low temperature range. The question of toughness and impact resistance had also appeared for HDPE where random copolymerization with higher α -olefins like 1-butene or 1-hexene resulted in the desired improvement [6], even if it should take many years until a polymerization process capable of handling high co-monomer amounts was developed by moving to gas phase.

For iPP, a first but different approach was the addition of certain amounts of an elastomeric component by melt-mixing in extruders. A disperse phase structure of crystalline iPP matrix and elastomeric particles proved capable of adding a whole set of new design parameters to iPP development [7]. Important modifiers, developed just in time for using them for the still new polymers, were ethylene-propylene rubber (EPR), as patented by Natta for Montecatini [8] and ethylene-propylene-norbornadiene rubber (EPDM). The latter offered the advantage but also the risk of being crosslinkable by peroxides as well as by sulfur compounds; it was patented first by Dunlop in 1964. Until today, a wide range of further modifiers have been developed and implemented, from styrene elastomers (e.g. hydrogenated styrene-butadiene block copolymers, SEBS) to PE plastomers [9].

Reactor-based copolymers became available only later, as the original polymerization technologies using hydrocarbon diluents (slurry-type) limited the production of random copolymers to rather low amounts of comonomer and prohibited the production of amorphous EPR components due to their solubility in the diluent. A route to circumvent this problem was the production of ethylene-rich and largely crystalline copolymer fractions, basically C3-LLDPEs. Such grades were, however, rather limited in their low temperature impact performance [10]. The earliest technology to give more flexibility to copolymer design was the Novolen Gas phase process with two sequential reactors allowing the combination of a homopolymer and EPR component in one process [11]. It took, however, several further steps in catalyst and process

design to unlock the full composition design range available today. Highly porous 4th generation Ziegler-Natta (ZN) type catalysts and modern hybrid processes like the Spheripol® technology of LyondellBasell with up to 4 reactors in total enabled a wide range of matrix and elastomer phase design for heterophasic copolymers which will be discussed in detail below. Figure 6.1 schematically shows the development of polymer particles for such PP impact copolymers based on the morphology of the catalyst as presented by Cecchin et al. [12].

In parallel to that, random copolymers with ethylene but also with higher α -olefins like butene or hexene as comonomers were developed. The focus of

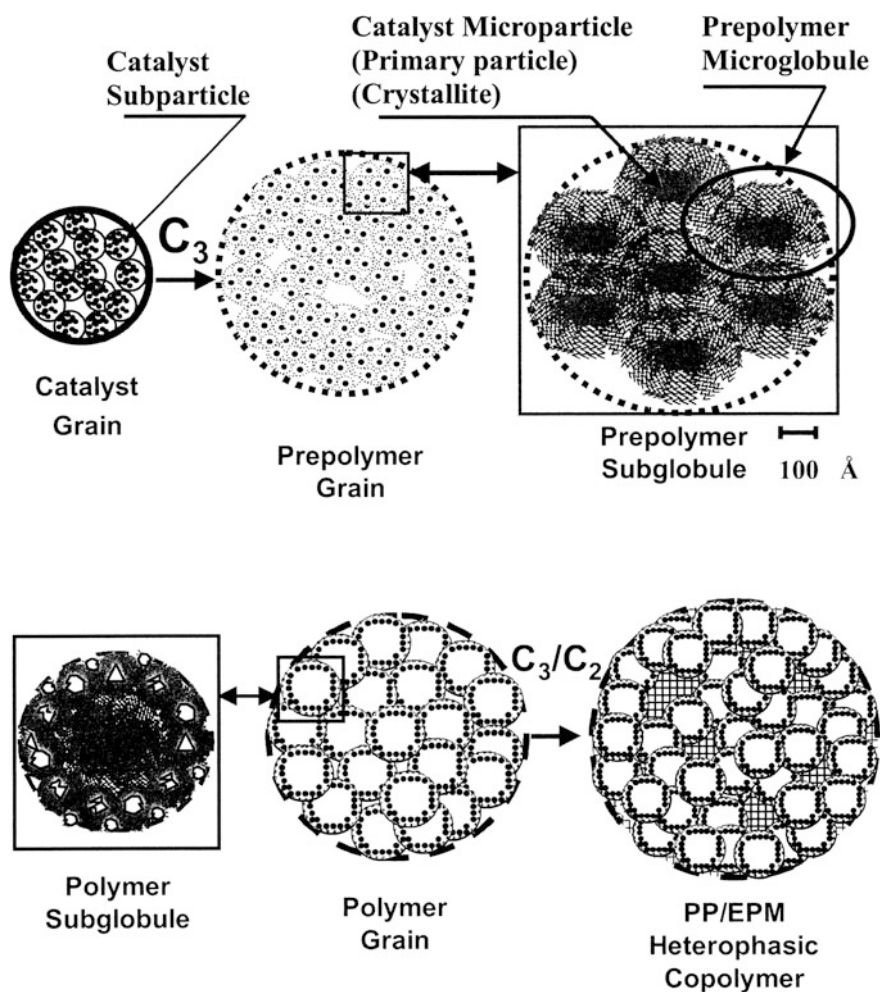


Fig. 6.1 Powder particle growth mechanism for PP impact copolymer over spherical $MgCl_2/TiCl_4$ catalyst: prepolymerization, matrix polymerization and ethylene/propylene copolymerization (from [12]; reprint with permission of Wiley, 2018)

development was less on excellent impact strength here, but more on softness and transparency, their crystallinity reduction going parallel with a reduction of melting and glass transition temperature [13]. While heterophasic copolymers established a leading position in technical uses of injection molded parts like in the automotive industry, random copolymers became indispensable for film and pipe applications.

Both the catalyst and process development have progressed further. Newer ZN types, especially with diethers as internal donors, allow polymerization with or without external donor [14, 15], the nature of catalytic centers being related to the crystallization behavior. The selection of external silane donors also became wider over time, affecting next to isotacticity also hydrogen and comonomer response, but also catalyst lifetime [16].

The introduction of metallocene (MC) catalysts finally allowed reaching very high isotacticities (<99%), additional regio-defects resulting from head-to-head/tail-to-tail monomer insertions reducing the isotactic block length mostly limit the melting point to <160 °C [17]. For heterophasic EP-copolymers (EP-HECOs), the elastomer phase design is facilitated by more isolated ethylene insertion. This enables a remarkably different phase morphology compared to ZN-based products with better phase coupling to the matrix PP and the absence of crystallizable polyethylene in C2-rich copolymers. While similarities exist, the difference in elastomer composition and, consequently, phase morphology, increases with increasing comonomer content in the EPR phase [18].

For single-phase random copolymers (RACOs), the consequences of moving from traditional ZN to MC catalysts are even more interesting. In case of PP with ethylene as comonomer the tendency to a blocky insertion normally sets a limit at ~5 wt% C2 for ZN-based RACOs, while MC-based types can go much higher and allow more flexibility in multimodal comonomer distributions [19, 20]. Moreover, these catalysts allow the efficient incorporation of higher α -olefins like butene or hexene, contributing to the complex polymorphism of iPP [21].

On the process side, the Catalloy process of LyondellBasell and the Borstar® PP technology of Borealis can be seen as further developments of the gas phase and hybrid concept [22], with an increased number of gas phase reactors (GPRs) allowing more flexible copolymer design. The Spherizone or “multizone circulating reactor” (MZCR) process [23] appears to offer more advantages for homogeneous copolymers like random types, requiring one or more additional GPR(s) for producing heterophasic systems.

6.2 Homogeneous Random Copolymers

6.2.1 Ethylene/Propylene Random Copolymers

An efficient approach for enhancing the toughness, transparency and sealing performance of iPP is the copolymerization with ethylene or other higher α -olefins. The advantages of the resulting propylene random copolymer (RACO) are mainly

due to their unique crystalline structure, where the comonomer is acting as molecular defect disturbing the crystalline structure of the polypropylene backbone.

It is known that an insight into the copolymer microstructure and the copolymerization mechanism can be derived from the product of the reactivity ratios of the monomer and comonomer respectively ($r_1 * r_2$). An apparent $r_1 * r_2 \approx 1$ would indicate a random structure with narrow composition distribution, $r_1 * r_2 > 1$ a blocky structure and $r_1 * r_2 < 1$ a copolymer with an alternating structure. The $r_1 * r_2$ of a certain copolymer is a complex function of the intrinsic reactivity of the monomers, their weight fraction as well as of the type of catalyst system. Thus, copolymers produced by means of Ziegler-Natta catalysts although homogeneous as regards the intramolecular sequence distribution exhibit most commonly heterogeneity as far as the intermolecular distribution is concerned [24–26]. Such heterogeneity arises from the multiple types of active sites coexisting in these catalyst systems. On the other hand, copolymers made with metallocene and post-metallocene catalysts are characterized with both uniform inter- and intramolecular comonomer distribution [27, 28]. Further on, such copolymers make it possible to investigate the influence of type and concentration of defects (comonomer and stereo and regio types) on the thermodynamic behavior, the kinetics of phase transformation and the formation of specific crystal polymorphs in crystalline polypropylene [29–32].

Copolymerizing ethylene by means of Ziegler-Natta catalysts is by far the industrially most relevant approach for manufacturing polypropylene copolymers. The so-produced propylene-ethylene copolymers are considered single-phase systems up to ca. 5 wt% of ethylene and are industrially known as PP random copolymers, abbreviated as EP-RACOs. The chain structure and the randomness of the comonomer distribution has been the subject of numerous publications [25–30]. Solution state ^{13}C nuclear magnetic resonance (NMR) spectroscopy offers a direct insight into the sequence distribution of propylene-ethylene copolymers.

Vestberg et al. [25] used this technique to calculate the randomness of ethylene incorporation, based on the amount of isolated ethylene units [PEP] and the total amount of ethylene units [E] using the relationship: $[\text{PEP}]/[\text{E}]$. The same group demonstrated an approach for evaluating randomness using infrared spectroscopy. For this purpose the peak height of the band at 733 cm^{-1} (baseline $690\text{--}780\text{ cm}^{-1}$) and the reference band at 809 cm^{-1} (baseline $750\text{--}890\text{ cm}^{-1}$) were used. Calibration based on ^{13}C -NMR results is required as a prerequisite. As shown in Fig. 6.2, the randomness of ethylene incorporation as defined by FTIR is generally decreasing with increasing comonomer content. The extent of this decrease was found to depend strongly on the type of catalyst. It was shown that differentiation in terms of comonomer incorporation can be achieved also within the traditional ZN catalyst systems by using a specific emulsion-based catalyst preparation technology having narrower distribution in active sites types.

The most even comonomer distribution is, however, achieved using metallocene catalyst. This is reflected by significantly lower values of the reactivity ratio's product (in the range 0.8 to 2.0) compared to those of copolymers synthesized with Ziegler-Natta catalysts [27]. A further advantage of the solution state ^{13}C -NMR is that it enables a

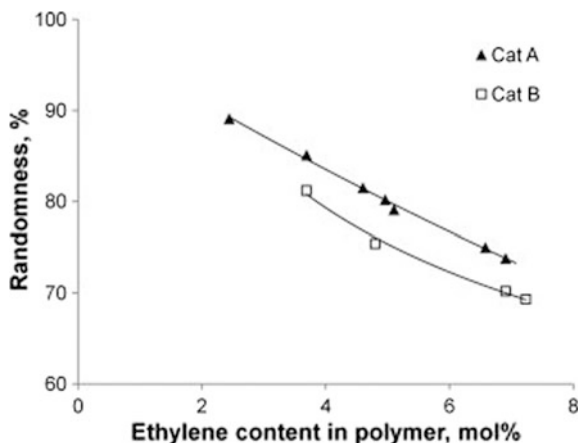
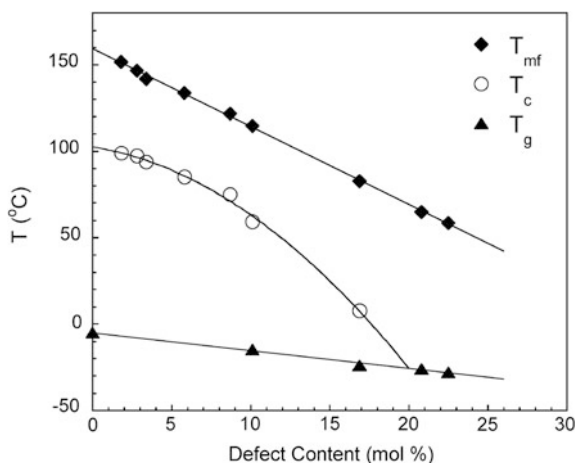


Fig. 6.2 Correlation of randomness by IR as a function of ethylene content for propylene-ethylene copolymers produced with (open square) traditional ZN catalyst systems and with (filled triangle) emulsion based ZN catalyst systems; re-drawn from original data in Ref. [25]

differentiation between the amounts of stereo and/or regio defects along the polypropylene chain typically present in metallocene catalysed polypropylene copolymers and the amount of comonomer units. Those amounts, however, always have to be seen as an average for the whole material. In other words, NMR may not properly reflect the multimodality of comonomer distribution in case the material consists of several fractions having different comonomer content. In order to compensate for this a combination of NMR and various thermal fractionation techniques like Temperature Rising Elution Fractionation (TREF), Stepwise Isothermal Segregation Technique (SIST), Crystallization Analysis Fractionation (Crystaf) or Successive Self-nucleation and Annealing (SSA) has been demonstrated in the literature [13, 33, 34]. By applying these techniques, it is possible to qualitatively or quantitatively fractionate the material based on its crystallizability and derive the lamellae thickness distribution, which is an indirect measure of the comonomer distribution.

As mentioned before, the comonomer acts as defect and disturbs the crystallization of iPP sequences resulting in reduced lamellae thickness. This reduction is reflected by melting point depression whereas the degree of depression is governed primarily by the total amount of comonomer and/or in case of metallocene based copolymers by the total amount of defects. Further on, incorporation of comonomer alters the crystallization kinetics of the polypropylene copolymers. As seen from Fig. 6.3, the crystallization temperature decreases in non-linear manner with increasing comonomer content and after certain comonomer content starts to approach the glass transition temperature of the copolymer. This changes the crystallization regime from nucleation driven to diffusion driven and in combination with the shorter crystallizable sequences influences the competition between formation of alpha and gamma crystallographic polymorphs of isotactic polypropylene.

Fig. 6.3 Final melting (T_{mf}), crystallization (T_c) and glass transition temperatures (T_g) as a function of total chain defects; from [27], reprint with permission of American Chemical Society, 2018

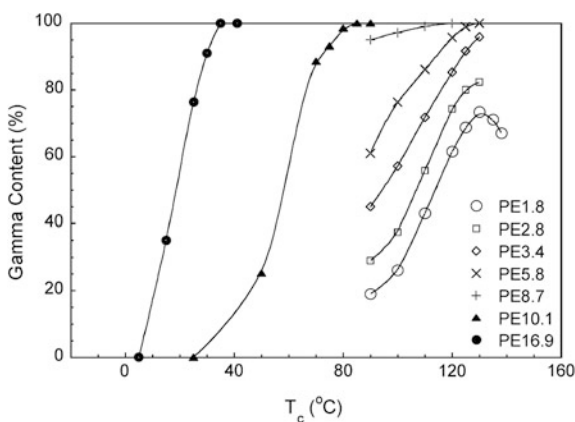


In addition to overall crystallinity, defects also affect the polymorphism. As can be seen in Fig. 6.4, the γ -phase formation is preferred at high crystallization temperatures and high comonomer contents [27–32].

One aspect in explaining the origin of the comonomer effect is the partitioning of the comonomer between the crystalline and amorphous regions of polypropylene. This has been studied in detail by several research groups by means of diverse X-ray scattering techniques as well as solid-state NMR [26, 30, 31, 35]. The current state of the art of knowledge suggests that all comonomer types are partially included in the polypropylene crystalline lattice. The extent of inclusion is strongly dependent on comonomer type, with 1-butene being mostly included, while higher α -olefins such as 1-octene and 1-hexene are mostly excluded.

Ethylene units are suggested to be partially included in the crystal, however, the majority is rejected from the crystal. This is also supported by the strong decrease of the melting temperature with increasing ethylene content. The fact that ethylene is

Fig. 6.4 Percentage of γ -polymorph as a function of crystallization temperature for propylene-ethylene copolymers; from [27], reprint with permission of American Chemical Society, 2018



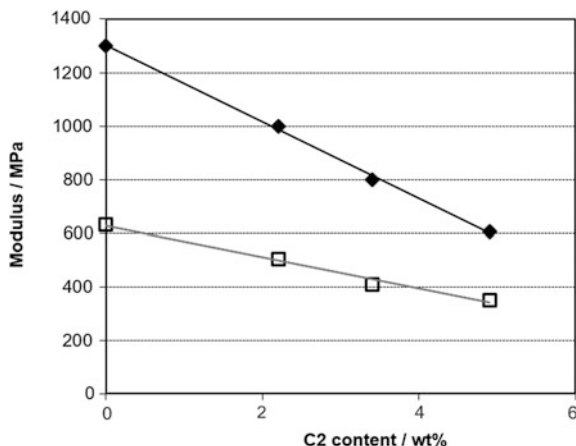


Fig. 6.5 Correlation between modulus of elasticity and total ethylene content for propylene-ethylene copolymers. The (filled diamond) represent flexural modulus from injection molded specimens, whereas (open square) represent tensile modulus from cast film specimen (data from [13])

acting as a defect hindering the crystal growth and resulting in thinner lamellae is also in line with the linear decrease of the modulus of elasticity as a function of ethylene content (see Fig. 6.5).

The extent of the decrease depends on the comonomer type and is essentially in-line with the degree of inclusion (exclusion). Comonomers, such as ethylene, which are predominantly excluded from the crystal and residing in the amorphous fractions between the crystalline lamellae, are more efficient in terms of reducing the modulus. This is in accordance with the fact that modulus of elasticity is mainly governed by the molecular mobility of the amorphous fraction. An in depth analysis of the stress-strain curves of propylene random copolymers in relation to the appearance of the yield point was investigated in the literature [26, 36]. The yield stress was shown to decrease with increasing ethylene content, increasing temperature and decreasing strain rate (see Fig. 6.6). This is attributed to the decreasing lamellae thickness, increasing molecular mobility in the amorphous phase and lowering the barrier for intra- and interlamellar slip.

On the other hand, the reduced lamellae thickness and better quenchability of EP-RACOs into the mesomorphic state, makes them materials of choice for highly transparent cast films. Depending on the processing parameters (e.g. throughput, chill roll temperature etc.) the crystal structure originally generated during the film extrusion process is a mixture of α -crystalline and mesomorphic phase as shown in Fig. 6.7 [37, 38].

Such a structure gives room for post-crystallization into the α -crystalline phase of iPP under the right circumstances. This becomes especially evident in applications involving thermal post-treatment of the films like steam sterilization. Exposure to steam sterilization triggers post-crystallization and lamellae thickening process [39, 40], which in turn influences both mechanical and optical performance.

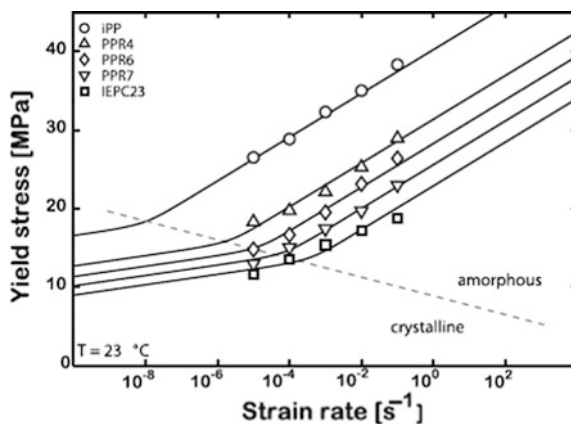


Fig. 6.6 Rate dependence of the yield stress of propylene-ethylene copolymers with increasing ethylene concentration; from [26], reprint with permission of Elsevier, 2018

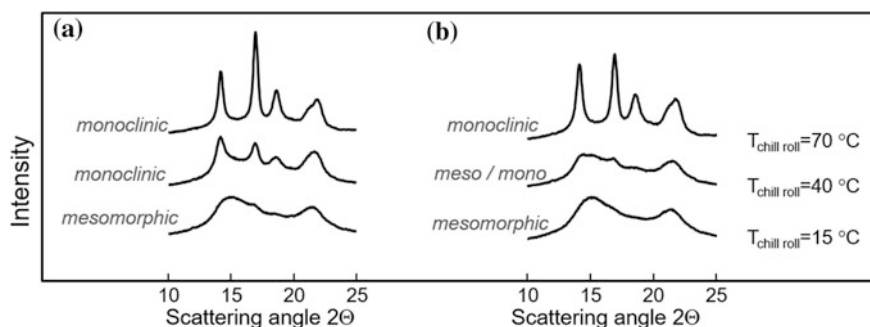


Fig. 6.7 Structure formation during cast film extrusion of propylene-ethylene copolymer as a function of chill roll temperature and line throughput **a** 120 kg/h and **b** 60 kg/h; wide-angle X-ray diffractograms from films with a thickness of 50 μm (unpublished data)

As expected, the modulus of elasticity of the propylene copolymers increases and the toughness decreases with increasing temperature and time of thermal post treatment [41]. Coarsening of the crystal structure leads also to deterioration of the optical properties. The combination of homogeneous comonomer distribution and alpha-nucleation can partly inhibit this process, allowing the preservation of the high transparency also after heat treatment.

Incorporating comonomer along the polypropylene backbone is also broadening its melting range. This is beneficial for the sealing behavior, which is in-line with the melting behavior of the sealant materials. Results demonstrated that seal initiation temperature of propylene copolymers correlates well with the temperature at which $\sim 40\%$ of the polymer is molten, as determined by thermal fractionation [42, 43]. Consequentially, a reduction of seal initiation temperature can be observed with increasing comonomer amount and improved randomness of comonomer distribution.

Additional important parameters influencing the sealing behavior and sealing strength of propylene copolymers are the molecular weight, molecular weight distribution (MWD) and the degree of molecular orientation. This is related to the fact that the heat sealing process involves interdiffusion and entanglement of the polymer chains across the sealing interface. In case of a material with broad MWD, the different fractions will participate in the diffusion flux on different time scales. The low molecular weight chains will easily diffuse, but they would not be sufficient for good adhesion. Thus, the diffusion of the longer chains will be the rate-determining step. Consequentially, increasing molecular weight is leading to an increased seal strength. In case of molecular orientation, the reports are scarcer. The degree of orientation in the films is mainly controlled by the processing parameters (e.g. draw down ratio, blow up ratio, take off speed etc.). It is reported that increasing degree of orientation increases the melting temperature [44–46], which in turn could lead to higher seal initiation temperature. However, there is no systematic study found in the literature, which demonstrates this. In addition, heat sealing of highly oriented samples could result in non-uniform shrinkage of the seal due to relaxation of molecules [46].

Although copolymerization of ethylene is leading to an improved transparency per se, this may not be sufficient for certain applications. This is especially valid for molding applications with wall thickness above 0.5 mm and when “glass-like” transparency is required. In such cases, nucleating agents or clarifiers are added to further improve the optical properties of the propylene copolymers [47]. Especially the so-called clarifiers, being in most of the cases sorbitol-derivatives, improve haze considerably by generating a microcrystalline structure through dissolution and recrystallization. As shown in Fig. 6.8, haze is exponentially decreasing with increasing nucleating agent concentration. The haze value of a highly transparent product must be below 10% (for 1 mm thick specimen); thus, the Fig. amply demonstrates the reason for using random copolymers for clarified products.

The efficiency of a clarifier in improving optical performance was found to be mainly a function of nucleus density and the size of the supermolecular units. Chain regularity, comonomer content and distribution determine the supermolecular structure and thus the dependence of optical properties on nucleation. Beyond its effect on optical performance, nucleation is an important tool for tuning the mechanical properties and processability of polypropylene copolymers. The addition of nucleating agents is known to increase the stiffness of propylene-ethylene copolymers, which is attributed mainly to the increased lamellae thickness. The efficiency of the nucleating agents in increasing stiffness generally deteriorates with increasing comonomer content as the relative amount of crystallizable material reduces. In case of the impact performance, the relationship is more complex, and as shown in Fig. 6.9 the molecular weight plays an at least as important role as the comonomer content and the comonomer distribution.

In the common case of α -nucleation, the impact performance of the propylene-ethylene copolymers remains unaffected or slightly reduced. A clear deviation from this rule is reported by Horváth et al. [48]. They observed a considerable increase of the impact strength in a specific concentration range of the nucleating agent (see Fig. 6.10). Further on, the increase depended strongly on the

Fig. 6.8 Effect of nucleating agent (sorbitol derivative) concentration on the haze (turbidity) of (open circle) propylene-ethylene random copolymer and (open square) polypropylene homopolymer as measured on injection molded plaques (from [180], reprint with permission of American Chemical Society, 2018)

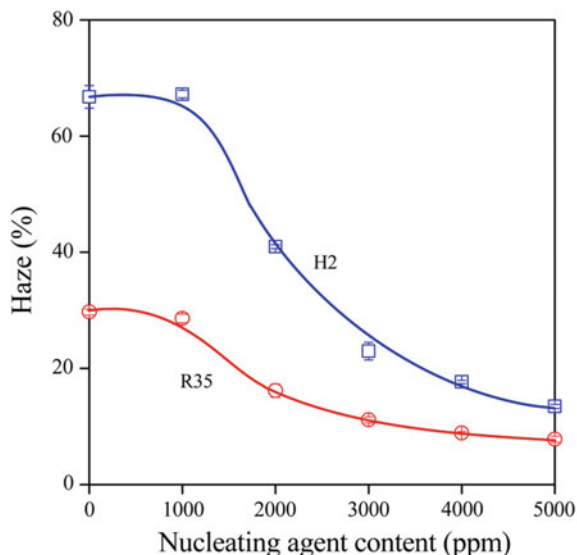
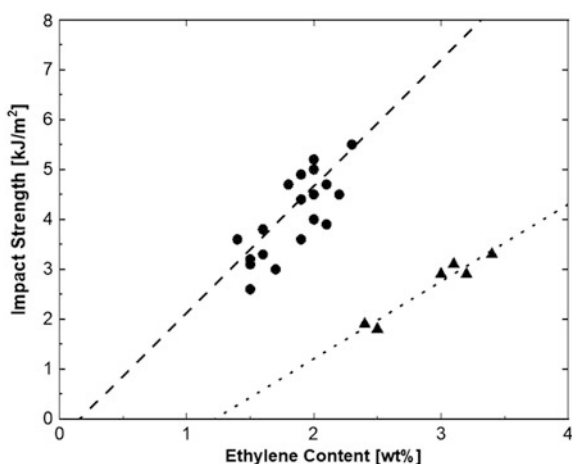


Fig. 6.9 Notched impact strength of propylene-ethylene copolymers as a function of ethylene content for materials with (filled circle) melt flow rate in the range 15–25 g/10 min and (filled triangle) melt flow rate in the range 90–120 g/10 min (2.16 kg/230 °C) (unpublished data)



molecular characteristics of the propylene-ethylene copolymer and could be observed only above a certain ethylene content and molecular weight. It seems that this specific molecular structure has a predisposition for both increase of lamella thickness, and increased crystal orientation as response to nucleation. In addition, formation of shish-kebab structures has been detected in the core of the injection molded specimens. These changes were suggested to increase crack propagation energy considerably leading to the large improvement observed in impact resistance.

Another specific case where an interplay between molecular structure and nucleation leads to improved impact resistance is the case of β -nucleated polypropylene [49, 50]. As demonstrated in Fig. 6.11, the molecular weight of

Fig. 6.10 Effect of nucleation on the impact resistance of PP random copolymers with different molecular characteristics. R42 (C2 content 4.2 wt%, MFR 1.5 g/10 min), R53 (C2 content 5.3 wt%, MFR 12 g/10 min). The other materials have C2 < 3 wt% and MFR in the range 8–15 g/min (data from [48])

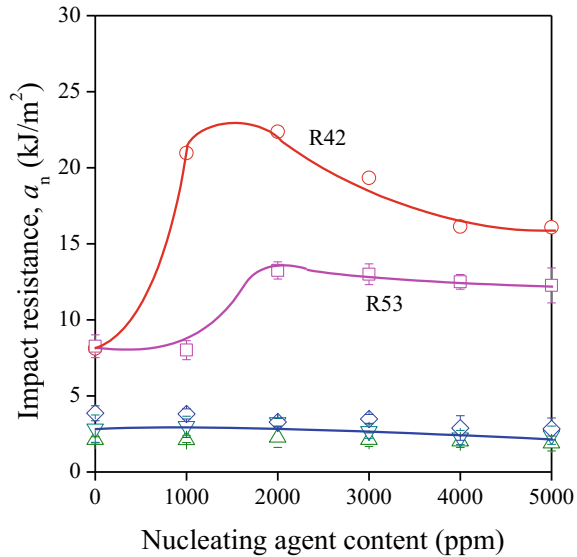
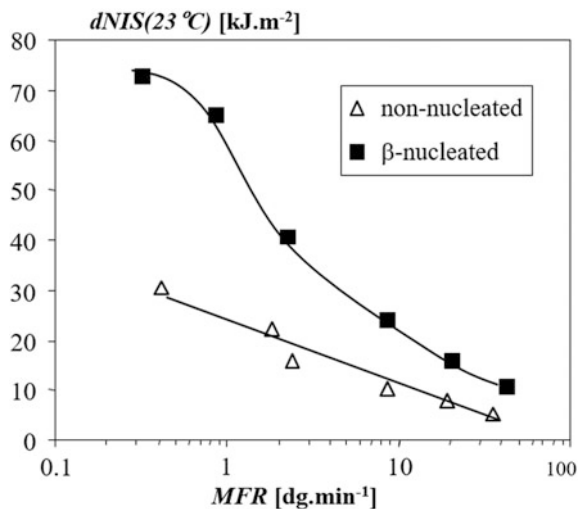


Fig. 6.11 Double notched impact strength of β -nucleated and non-nucleated iPP homopolymer grades of different molecular weight between MFR 0.3 and 40 g/10 min tested at room temperature (data from [49])



the material is the predominant factor determining the extent of toughness increase upon addition of β -nucleating agent, whereas the biggest effect is observed at high molecular weights. The effect results from the development of a specific crystalline structure comprised of lamellae arranged as stacks rather than cross-hatching, which in turn facilitates cavitation and stress-absorbance. Besides the molecular weight, the formation of such structure depends on the processing condition and amount of comonomer. Increasing both, the cooling rate and the comonomer content attenuate the β -crystallization and reduces the amount of β -modification.

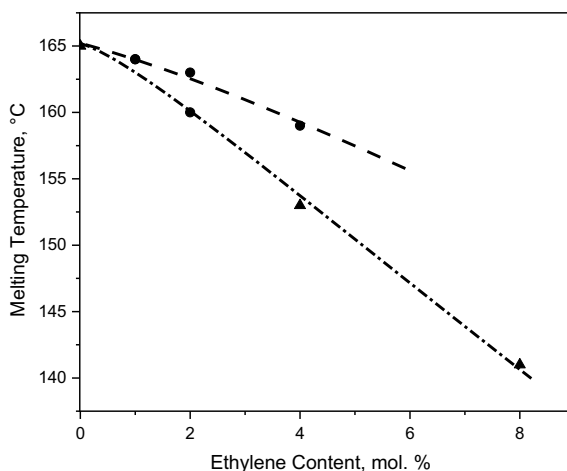
Nevertheless, β -modified propylene-ethylene copolymers find industrial application as piping material for hot and cold water installations. The specific crystal structure of this type of material results in clear improvement of the internal pressure resistance and thus allows wall-thickness reduction of the pipes made thereof [51].

Finally, it can be concluded that a correlation of a particular feature of the polymer structure to a particular end-use property exists in many cases. Nevertheless, the main challenge in developing novel material solutions is the combination of multiple and often antagonistic properties in a single material. This requires breaking classical interdependencies by utilizing more comprehensive polymer design concepts. One example is the development of multimodal materials consisting of several fractions having different molecular characteristics, intimately mixed with each other in e.g. a cascade of polymerization reactors. As shown in Fig. 6.12, propylene-ethylene copolymers with multimodal comonomer distribution demonstrate higher melting temperature for the same comonomer content and comparable mechanical performance. This would be beneficial for applications requiring post thermal treatment without compromising on transparency and mechanical performance.

6.2.2 Propylene Random Co- and Terpolymers with Higher α -Olefins

Contrary to ethylene-propylene random copolymers, which present an important and irreplaceable sector of industrial relevant polyolefins, copolymers of propylene with higher α -olefins like butene, hexene or octene are—apart from ethylene-propylene-butene terpolymers—only used for niche-applications in industry. Ethylene-propylene-butene terpolymers are produced for sealing layer materials or

Fig. 6.12 Melting point of ethylene-propylene copolymers as a function of the total ethylene content for materials having (filled triangle) unimodal and (filled circle) multimodal comonomer distribution (unpublished data)



thermoplastic elastomers. An example for the use of hexene as comonomer in commercial PP grades is the Hostalen PP-XN grade from LyondellBasell, which is used for hot and cold water pipe applications. This material shows a good creep performance and when comparing the morphology of these copolymers to ethylene propylene random copolymers one finds that the hexene containing materials are not showing the cross-hatching typical for α -PP [52].

Compared to ethylene random copolymers the production of copolymer grades with higher α -olefins in industrial processes contains several challenges due to lower reactivity of the heavier comonomers leading to the need for an excess of comonomer during the production. This is followed by the necessity to remove non-reacted comonomer and subsequently sending the monomer to the flare. A way to improve the production of such materials is the use of advanced Ziegler Natta catalysts combined with process technologies having multiple reactors in series or multiple reaction zones like the Spherizone Process of LyondellBasell. Another strategy, namely the use of metallocene catalysts, which show an increased reactivity towards higher alpha-olefins, is applied by Mitsui to produce their Tafmer C3C4-grades [53]. The Borseal grades of Borealis (propylene terpolymer with C2 and C4 comonomer) are produced in a multi-step process with a Ziegler Natta catalyst.

Despite their limited commercial importance, this group of materials is well described and discussed in literature, especially in combination with the possibilities arising from the use of different metallocene catalysts which allow a precise control of micro-structure and show good reactivity towards higher α -olefins [54, 55]. The effect of copolymerizing propene with higher α -olefins on the crystallinity as well as the partitioning of the comonomer are quite extensively—and in the case of hexene also controversially-discussed in literature. However, despite the arising possibilities for product design originating from these copolymerizations a relatively small number of research work is dealing with real application related aspects such as processing behavior or optical properties.

Among the higher α -olefins, 1-butene and 1-hexene are the most used and studied comonomers for being copolymerized with propene. Propylene Butene (C3C4) copolymers show a similar melting point as their ethylene analogues but are superior in stiffness and have a lower content of xylene cold soluble (XCS) fraction. If hexene is copolymerized with propene a rare combination of high clarity, relatively high melting temperature and high flexibility is found. Copolymers of propene and octene are not well investigated and there are only superficial indications that such materials may be useful as elastomers or barrier films. Generally, one can say that copolymers of propene with α -olefins of 6-10 carbon atoms exhibit properties of thermoplastic elastomers. In blends with iPP, these materials will be compatible.

The properties of the resulting materials are dominated by the type and concentration of the comonomer incorporated into the polymer backbone. Including comonomers leads to a targeted disturbance of the chain regularity and thus affects the crystallinity and might also affect the crystal structures formed [29, 30, 32, 56–59].

The structure and crystallization behavior of propylene butene random copolymers is well studied and it is found that they have a unique structure property profile when compared to other propylene α -olefin copolymers. Whereas for the other common propylene α -olefin copolymers the crystallinity decreases with increasing comonomer content, isotactic propylene butene copolymers crystallize in the entire range of compositions up to 100% butene. Depending on the amount of comonomer, these polymers crystallize either in the α - or γ -modification of isotactic polypropylene or in the stable form I of isotactic Poly-1-butene (iPB-1) or in mixtures thereof [21]. The crystallinity of these copolymers is also rather high with values of between 40 and 50% crystallinity. This is again depending on the concentration of the comonomer and shows its minimum at approximately 50% comonomer content.

For copolymers of same total error content, the effect of 1-hexene and 1-octene in hindering the crystallization is more pronounced with respect to ethylene and butene. The crystallization temperature also decreases with increasing comonomer content [32, 56, 57] (see Fig. 6.13a). Thus, the crystallization becomes more difficult when the comonomer length and/or the steric hindrance (length of the n-alkyl branches) increases.

Comparing the melting behavior of different copolymers of propylene and α -olefins one finds that at comparable amount of comonomer, the melting temperature and the melting enthalpy decrease on increasing comonomer bulkiness [56, 57, 59]. The longer the side chains formed by the incorporated comonomer are, the stronger this effect becomes and the steeper is the slope of the curve (see Fig. 6.13b).

However, Arnold et al. [54] found that this holds true if butene and hexene copolymers are compared, but hardly any difference was found for the melting temperatures of a C3C6 and C3C16 copolymer. It might be that the very long side chains are folded and thus there is no linear increase of the effect with increasing

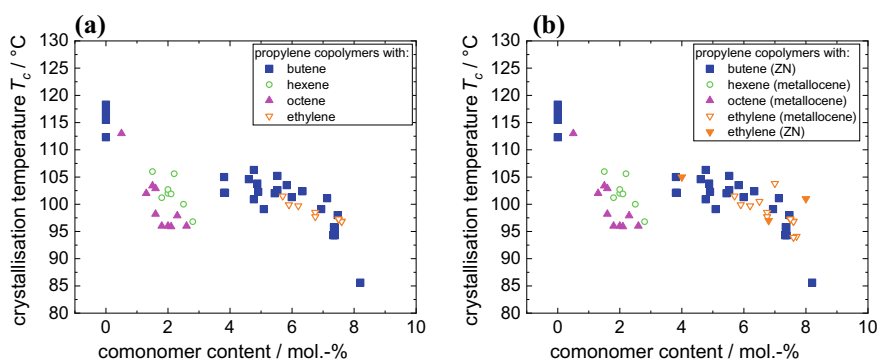


Fig. 6.13 Effect of comonomer insertion on the melting and crystallization behavior of propylene— α -olefin copolymers produced with either a Ziegler Natta catalyst (ZN) or a metallocene catalyst (metallocene): **a** Melting temperature as a function of the comonomer content and **b** crystallisation temperature as a function of the comonomer content (unpublished data)

comonomer length. Comparable data are reported by van Reenen [60], who found similar melting points for copolymers of propene with C8, C10, C12 and C18. Increasing the comonomer content leads to a further decrease of the melting temperature.

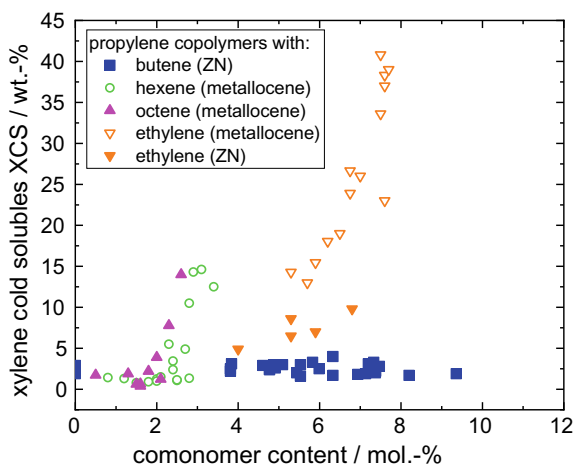
The higher melting point of butene copolymers compared to hexene and/or octene analogues can be explained by the higher probability of 1-butene units to enter the crystalline lattice and the therefrom-resulting longer average crystallizable sequence length. At a similar total concentration of comonomers, the average crystallizable sequence length of propylene copolymers with ethylene and butene is higher than for those with hexene or octene.

The extent of the melting point reduction does not only depend on the comonomer content or type, but also on the catalyst system used for the production of the materials. Ziegler-Natta catalysts produce copolymers with a gradient distribution of comonomer, whereas metallocene catalysts lead to a random incorporation of the comonomer resulting in shorter and thinner lamellae and therefore reduced melting temperatures [58, 61]. Another possibility to design random copolymers with high melting temperatures is the use of a multimodal approach with respect to comonomer content. This means that by utilizing the single reactors of a reactor cascade differently, one can produce in-reactor polymer blends consisting of a fraction with low or no comonomer content and another fraction with higher comonomer content. The advantage of such a complex design is based on the fact that the low comonomer fraction will deliver a high melting point, but the optical and sealing properties are determined by the overall comonomer content. The disadvantage of such a multimodal approach compared to unimodal is, that for a fixed number of available reactors the total achievable comonomer content is lower for the multimodal design.

When increasing the ethylene amount in propylene copolymers, one finds an exponential growth of the xylene cold soluble fraction with increasing comonomer content. This happens due to the formation of a second, non-crystallizable, ethylene-rich fraction. Consequently, the material type changes from the so-called random copolymer to a heterophasic copolymer (see Fig. 6.14). The same sharp increase is found for hexene and octene copolymers, but at lower comonomer contents. For butene copolymers, the amount of xylene cold solubles stay at a constant and low level, independent of the comonomer content. This is possible, due to the possibility of butene comonomers to be incorporated into the PP crystal lattice. Having a low level of extractables is of special importance if a material is targeted at the use in food packaging applications. This industry segment requires materials fulfilling very strict limits for extractables in various solvents. Thus, a possible use of ethylene-butene copolymer is the food packaging market. Dlubek et al. [62] could also show that the local free volume and the amount of amorphous phase increases with increasing comonomer content (except for C4).

While it is generally accepted that 1-butene is readily incorporated into the structure of PP and 1-octene is rejected, there were quite some scientific discussions on the effect and partitioning of 1-hexene. Jeon et al. [29] concluded out of a deep and detailed study based on WAXS, calorimetry and solid state NMR

Fig. 6.14 Amount of xylene cold soluble fraction XCS as a function of the comonomer content for propylene copolymers with higher α -olefins produced with Ziegler Natta and metallocene catalysts (unpublished data)



measurements that 1-hexene is totally excluded from the crystal lattice for comonomer contents up to 13 mol%. He defined a ranking according to the participation of the co-units in the crystals which is reflected in the crystallization rate as: C4 > C2 > C6 = C8. De Rosa's group concluded based on expansion of the unit cell and polymorphism studies that hexene copolymers with low amount of comonomer can be included partially into the crystal lattice [58].

For concentrations of hexene higher than 13 mol% a special behavior of the copolymers is found. Whereas the crystallinity of octene copolymers decreases steadily with increasing comonomer content, hexene copolymers show a flattening of the curve for comonomer contents between 20 and 25 mol% (see Fig. 6.15a). Consequently, materials with this composition show higher levels of crystallinity than that anticipated for a comonomer which is completely excluded from the crystal lattice as it is true for octene. Consequently, it was concluded that at higher hexene contents (>13 mol%) a partial inclusion of hexene into the crystal lattice takes place.

Poon and coworkers described this new crystallographic form of PP containing hexene in at least a part of the chain segments in copolymers with higher hexene contents for the first time in 2005 [63]. This group still proposed an orthorhombic symmetry of the unit cell with eight chains. Later on, after a re-evaluation of the refraction data, it was found that this so-called δ -modification of PP has a trigonal unit cell containing six 3-fold helices [64]. In this way, the polypropylene 3-fold helix confirmation can be kept, but more space is available for the side chains. However, the crystallization of these materials is very slow. An incubation period is needed in order to allow primary nucleation. Then, long fibrous lamellae are formed around the nucleus (see Fig. 6.15b). These materials show a relatively sharp melting peak at approximately 40 °C with relatively constant heat of melting [63]. The same crystal modification is found in C3C5-copolymers and C3/C5/C6-terpolymers [65]. The pentene copolymers melt at a 20 °C higher melting temperature as their hexene analogues, indicating that at high concentration of

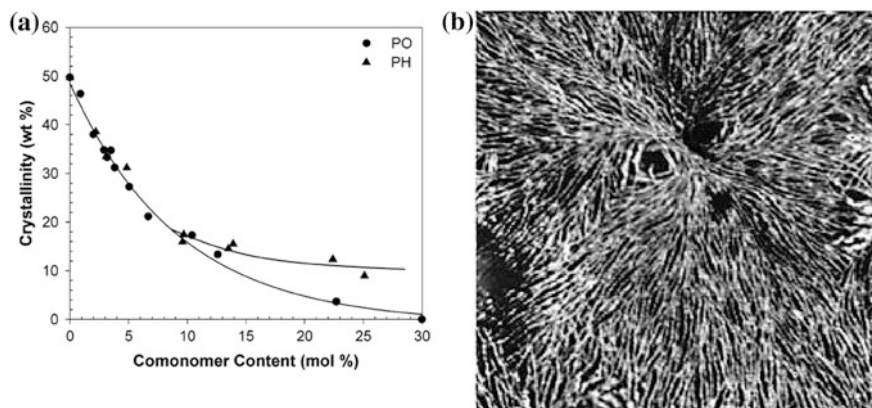


Fig. 6.15 **a** Crystallinity from DSC of hexene (PH) and octene copolymers (PO) as function of the comonomer content and **b** Atomic Force Microscopy (AFM) light image of free surface of a hexene propylene copolymer with 22.4 mol% comonomer content showing the lamellar size scale (image size 2 μm); from [63], reprint with permission of American Chemical Society, 2018

comonomer the incorporation of units resulting in longer side chains destabilize the ordered phase. A faster crystallization rate decrease found for hexene copolymers compared to pentene copolymers also indicated that pentene is incorporated into the crystal lattice more easily.

The different effects of the higher α -olefins on the crystal structure of the materials result in different viscoelastic and mechanical behavior. Studying the results from dynamic-mechanical thermal analysis (DMTA) of these materials allows gaining knowledge on the stiffness of the materials on the one side, but also gives insights to the phase structure. Comparing the storage modulus from different PP copolymers, one finds that the modulus is decreasing with increasing comonomer content due to the incorporation of defects. However, the slope of this curve becomes steeper for hexene and octene copolymers compared to butene or ethylene ones (see Fig. 6.16a). The steeper negative slope means that the same drop in modulus is achieved with much less comonomer in comparison to ethylene copolymers. Upon incorporation of a comonomer, the α -transition related to motions within the polymers' crystalline phase is shifted to lower temperatures as the comonomer content increases (see Fig. 6.16b) [57, 59, 66]. This can be explained by a reduction in crystallinity and crystal size.

The transition around 0 $^{\circ}\text{C}$ (β -transition or glass transition, T_g) is ascribed to motions of the long chain segments. When the comonomer content increases, the amount of amorphous fraction increases and thus the β -transition shifts down to lower temperatures. With increasing length of the comonomer lateral chains, the free volume will further increase leading to a more pronounced effect on the β -transition [59, 67]. Dlubek et al. [62] investigated the effect of different length of the n-alkyl branches in polypropylene copolymers on the free volume using positron annihilation lifetime spectroscopy. The decrease of T_g and the increase of the

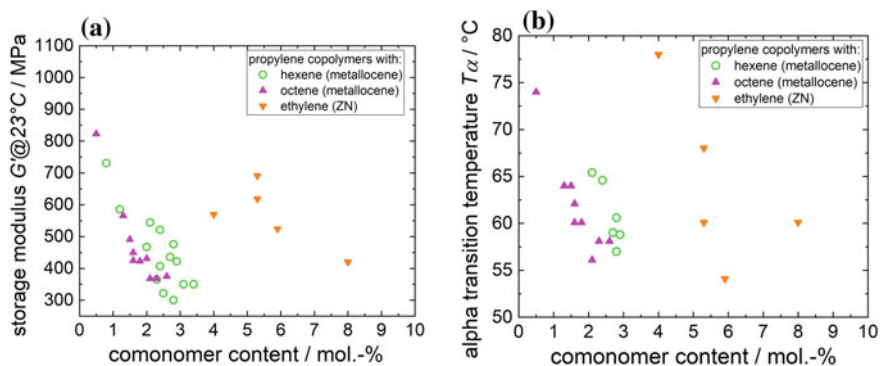


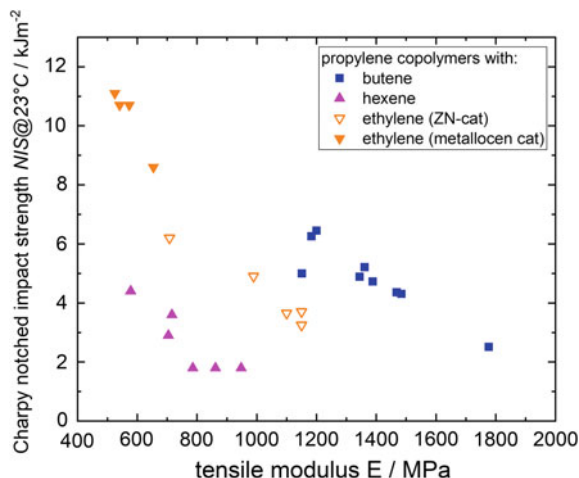
Fig. 6.16 Data from DMTA for propylene copolymers with ethylene and higher α -olefins produced with Ziegler Natta (ZN) and metallocene catalysts: **a** Storage modulus, G' at 23 °C as function of the comonomer content and **b** Alpha transition temperature as a function of the comonomer content (unpublished data)

free volume is found to be linear with the number and length of n-alkyl branches. Only propylene-butene copolymers deviate from this relation. A comparison of hexene and octene copolymers shows that much less octene is needed in order to significantly lower the glass transition temperature and induce rubbery behavior of the material [67]. However, if ethylene and hexene copolymers are compared one finds a similar effect of the comonomer insertion on the glass transition temperature. This indicates that the difference in ability to be included into the crystal lattice does not affect the mobility of the amorphous phase, which is described by the glass transition temperature [59]. Additionally, the less perfect and smaller crystallites of hexene copolymers eases motions in the amorphous phase leading to increased intensity of the β -relaxation.

Since the area under the loss tangent curve ($\tan(\delta)$ -area) can be used to estimate the impact behavior of polypropylene copolymers [62, 67, 68], this indicates that incorporation of hexene improves the impact resistance of polypropylene at low temperatures. If the effect of increase of the $\tan(\delta)$ area in hexene copolymers is compared to that achievable in standard heterophasic PP copolymers or isotactic PP, both toughened with a plastomer, it was found that the increase is stronger for the hexene copolymers [66]. This points out the potential use of hexene copolymers as impact modifier for PP. However, this increase in impact properties is accompanied by a significant decrease of the materials' rigidity and modulus.

Comparing mechanical performance of the copolymers a decrease of the tensile modulus with increasing amount of comonomer and increasing comonomer length is found. The reason for these observations is again based on the variations in crystalline structure, originating from the different comonomers. Also, the deformation mechanisms are strongly dependent on the used comonomer and the composition of the copolymers [57, 59, 63]. Comparing butene and hexene copolymers to the ethylene analogues at a given comonomer content, one finds the butene containing materials to be the stiffest ones and the hexene copolymers to be

Fig. 6.17 Impact/stiffness balance of propylene random copolymers with ethylene and hexene (unpublished data)



the softest ones. In agreement with the higher softness of the materials, also the stress at yield decreases for the hexene copolymers with increasing comonomer content. The Charpy notched impact strength is highest for the hexene containing materials, followed by the ethylene ones. The butene-copolymers behave very similar to PP homopolymers in terms of impact strength (see Fig. 6.17). Considering the impact stiffness balance of the materials mentioned above, which is a very important parameter when it comes to commercial use of polyolefins, one has to say, that this is in favor of ethylene containing materials (at least in the investigated MFR range typical for injection molding applications).

The composition of the materials also affects the deformation mechanism. The longer the comonomer is and the higher the comonomer content is, the less pronounced is the for PP typical necking deformation process. It changes to a ductile and more elastomeric-like mechanism. The lower crystallinity and the associated increase in flexibility in the copolymers are the reasons for the change of the deformation mechanism. This change is accompanied by a parallel decrease of the elastic modulus and yield stress. The only exception from this observation are hexene copolymers with a comonomer content of 10–25 mol% which can crystallize in the δ -modification. They exhibit thermoplastic behavior with the formation of a diffuse neck at relatively low yield stress [63]. It is also shown in literature that during tensile tests, there is no change in the crystalline structure upon drawing of hexene or pentene copolymers showing the δ -modification which is preserved up to breakage [65].

Overall, one can summarize that propylene-butene random copolymers are relatively stiff materials, with good optical properties, low xylene solubles but rather poor impact strength. Propylene-hexene copolymers with comonomer contents up to about 10 mol% show very good optical properties and have a property profile very similar to that of propylene ethylene random copolymers, but at lower comonomer content.

6.3 Heterophasic Copolymers

Heterophasic copolymers of propylene with ethylene and—so far in very rare cases—higher α -olefins are multi-phase compositions comprising a matrix phase and one or more types of dispersed particles [69]. The phase structure is in the micrometer range. Particle size and structure are primarily defined by (a) the composition of both phases defining compatibility and (b) their respective molecular weights defining the viscosity ratio of the components. To a lesser extent the structure is affected by the mixing history.

These polymers mostly resulting from a polymerization technology with at least two stages (subsequent homopolymer & elastomer production) are often still referred to as “block copolymers”. The correct term, however, is “heterophasic copolymers” (EP-HECOs) or “PP impact copolymers” (ICPs). The structure of these reactor blends has been shown to be rather complex: Besides the PP matrix and the amorphous ethylene-propylene rubber (EPR), they can also comprise crystalline copolymers having both PP and PE crystallizable segments, and even neat high density PE (HDPE). Figure 6.18 shows the typical morphology of a standard EP-HECO type for molding applications with core-shell structure defined by the compatibility ranking between the three components, in direct comparison to two compounds of the same polymer modified with different PE types (see Sect. 6.3.3 for details). Elastomer particle size and density increases for both modifications, but the HDPE addition results in a stronger change of the internal particle structure through the formation of massive crystalline PE cores.

The most relevant parameters for the property profile of an EP-HECO are the overall molecular weight, represented for example by the melt flow rate (MFR), and the relative amount of elastomer phase, represented for example by the xylene cold soluble (XCS) fraction [70]. Only a more detailed fractionation, ideally in combination with a phase structure analysis by TEM as in Fig. 6.18 or by atomic force

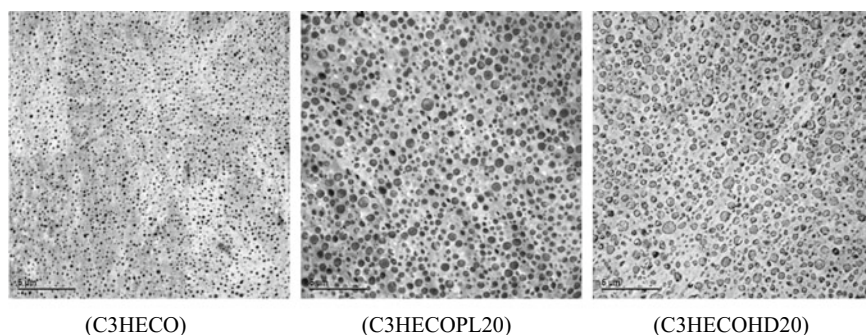


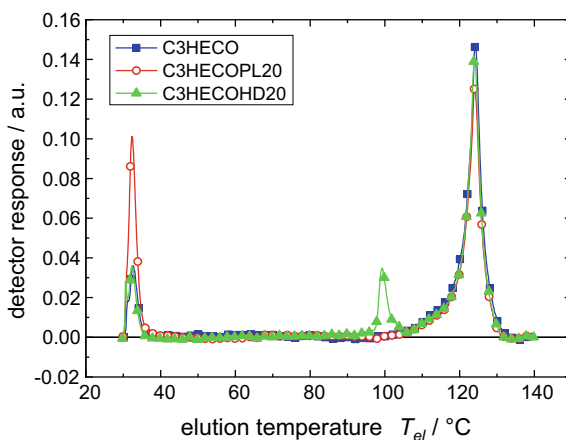
Fig. 6.18 Transmission electron microscopy (TEM, after contrasting with RuO_4) pictures of the morphology of (C3HECO) commercial high impact EP-copolymer with ~ 20 wt% C3-rich EPR, (C3HECOPL20) compound of (C3HECO) with 20 wt% of an ethylene-octene plastomer, (C3HECOHD20) compound of (C3HECO) with 20 wt% of HDPE (from [164], scale bar 5 μm)

microscopy (AFM), can yield a realistic impression of the elastomer phase content, as the XCS will necessarily include parts of the matrix phase while the crystalline (XCI) fraction also contains crystalline PE components.

A number of research groups have dealt over time with this problem [71–73], mostly by combining Temperature Rising Elution Fractionation in a preparative mode with follow-up analysis of fractions and relating the resulting composition data to morphology information. The effect of elastomer/PE phase composition on the morphology, which ultimately defines mechanics and especially the impact performance and will be discussed in detail in Sect. 6.3.2, can be recognized nicely in comparisons as done in the group of Alamo [73]. As an example, Fig. 6.19 shows the analytical TREF curves of the compositions for which the morphology is shown in Fig. 6.18: The base polymer with its rather amorphous elastomer phase as well as the compound with the low-melting point plastomer equally show two elution peaks (cold elution and 105–130 °C) of different weighting. In contrast to that, the HDPE used for the second compound turns up as a separate elution peak at ~ 100 °C.

Why in industrial practice the classical XCS/CXI fractionation is still used rather than a TREF analysis, capable of yielding far more information, can be easily understood from the time requirement of such procedures. It can be combined with some follow-up analysis of the XCS and—if necessary—XCI fraction like a spectroscopic (FTIR or NMR) determination of the comonomer content or a rough evaluation of the molecular weight via the intrinsic viscosity (IV) [74]. This standard procedure is well capable of serving both the needs of quality control in production and of routine analysis in development. Only rather recently, automatized setups for routine fractionation have become available. One example is the CRYSTEX instrument [75] from PolymerChar combining a fractionation by sequential crystallization in a negative temperature gradient (CRYSTAF principle [33]) with the measurement of IV and ethylene (C2) content of the complete solution as well as the crystalline (CF) and soluble (SF) fractions. While not being

Fig. 6.19 Analytical TREF curves of compositions shown in Fig. 6.18; (C3HECOPL20) compound of (C3HECO) with 20 wt% of an ethylene-octene plastomer, (C3HECOHD20) compound of (C3HECO) with 20 wt% of HDPE (from [164])



identical to an XCS/XCI split in most cases, the results from this method are available more quickly and in a more controlled way.

The effect of elastomer particles in improving impact strength results from a change in the deformation and failure mechanism of the composition, which has been studied by numerous research groups. Exemplary is the work of Kim and Michler [76, 77] who studied the failure mechanism at particle level, identifying internal cavitation between the amorphous EPR and crystalline PE components as one of the most important energy absorption mechanisms. Internal particle structure becomes, next to particle size and interparticle distance, thus a further very important parameter for the toughness enhancement. Figure 6.20 presents the failure mechanisms on particle level identified by Kim for ‘core-shell’ (single-core) and ‘salami-type’ (multi-core) elastomer particles, both structures being found in EP-HECOs.

In practice, the particle structure of course has to be considered in combination with size distribution and interparticle distance, both being interrelated through the concentration, i.e. the volume fraction, of the elastomer particles. A significant advantage of reactor-based impact copolymers over mechanical blends is that an intimate mixing of the components can be obtained in a wide range of molecular weight (i.e. viscosity ratio).

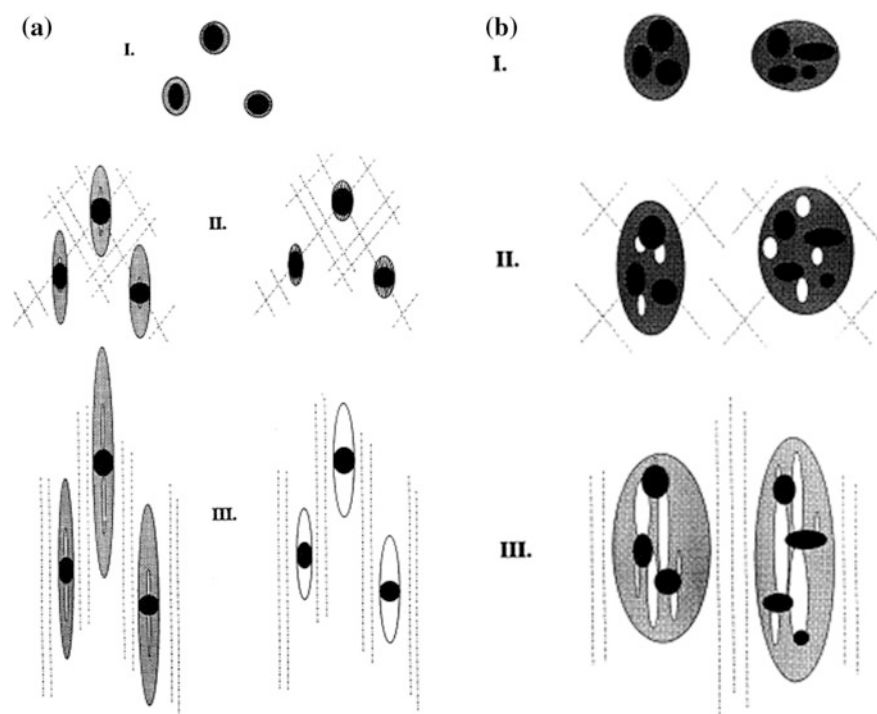


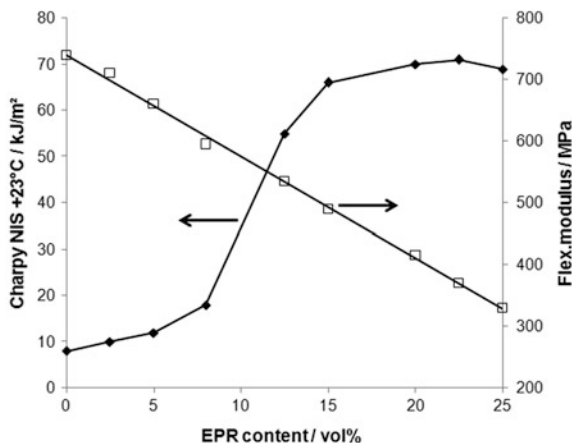
Fig. 6.20 Single (a) and multiple (b) cavitation processes in ternary blend systems like PP/EPR/PE (from [77], reprint with permission of Elsevier, 2018)

A relatively fine dispersion (weight average particle diameter D_W of 0.9–2.0 μm) is observed in these copolymers at phase viscosity ratios (μ) between 3 and 25 [78]. The optimum particle size in terms of impact strength depends on the dominant deformation mechanism of the matrix, which in turn is influenced by the test conditions, i.e. temperature and deformation rate. In PP, both crazing and shear yielding have been observed depending on test temperature and deformation rate. At constant particle size, a step-wise brittle-to-tough transition is observed as a function of EPR concentration, combined with linear reduction of tensile modulus [79, 80]. Figure 6.21 presents the respective correlation for the material series of Starke et al. [79], generated by dilution of a reactor grade having the highest EPR content of 25 wt% with increasing amounts of matrix polymer. The blend concentration where this transition occurs is defined by the chemical composition of matrix and dispersed phase as well as their viscosity ratio, but it should be noted that this concentration still depends on the geometry and test conditions. For PP/EPR compositions, the phase transition and the respective development of the mechanical performance is comprehensively discussed by Kotter et al. [80].

The delocalization of stresses at the failure front or crack tip is not only an important energy absorption process in impact-modified polymer systems in general, but also the source of stress whitening in these polymers. This is not only relevant in terms of optical damage appearing long before failure, even before crack development in plastic parts [81], but also as an instrument for understanding the failure mechanism. Stress whitening traces on crack surfaces after fracture testing [78] are a clear indication of slow crack growth and energy absorption.

A certain contribution of the matrix properties needs to be considered here, however: α -nucleation causing modulus increase of the matrix has been shown to enhance stress whitening [82], while a less stiff random copolymer matrix can eliminate the phenomenon largely. The reason for these effects is very likely the modulus difference between matrix and elastomer phase, confirmed by the fact that an increase of particle modulus by higher crystalline PE content is also capable of reducing stress whitening [83].

Fig. 6.21 EPR concentration effect on stiffness (flexural modulus, ISO 178) and toughness (Charpy notched impact strength, ISO 179 1eA) at 23 °C for a series of random-heterophasic copolymers with constant matrix and EPR composition (data from [79])



A more detailed look at the fracture development as necessary for an in-depth understanding of the failure mechanism of EP-HECOs [84] has, however, revealed that both craze formation and stress delocalization occurs at stresses significantly below the yield stress already. This means that the idea of linearity and reversibility of a deformation in the whole linear region of a stress-strain curve is quite certainly wrong, at least for polymers with a semi-crystalline matrix. Recently published work on 3D-reconstruction of crack development [85] in injection-molded specimens of different copolymer and model blend materials have revealed a number of interesting facts: Surface-to-surface interparticle distance distribution is one of the major factors governing the start and progress of the fracturing process. The crazes were found to follow inhomogeneities in the elastomer particle distribution, meaning that crazes emerged predominantly between particles with short interparticle distance in PP/EPR systems. Propagation in the plastomer (LLDPE) modified PP occurred when debonding of the particles from the PP matrix took place, the damage being restricted to sheet-like volumes perpendicular to the applied force (see Fig. 6.22). Only in pure PP homopolymer samples a change from ductile to semi-brittle behavior could be observed around the yield force [86].

One also has to be aware that, at least for injection molded specimens, superstructures exist. In terms of crystallinity, one normally differentiates between the oriented skin layer being more crystalline and oriented, and the bulk region with less and more isotropic crystal structure. Parallel to that, particle orientation in molding can cause the phase morphology in the skin layer to be different from the one in bulk. This causes also the fracture mechanisms to change in the transition region between both [87]. Thus, in all considerations relating composition and morphology of EP-HECOs to their mechanical performance the effect of processing on the actual structure in the final part must be taken into account.

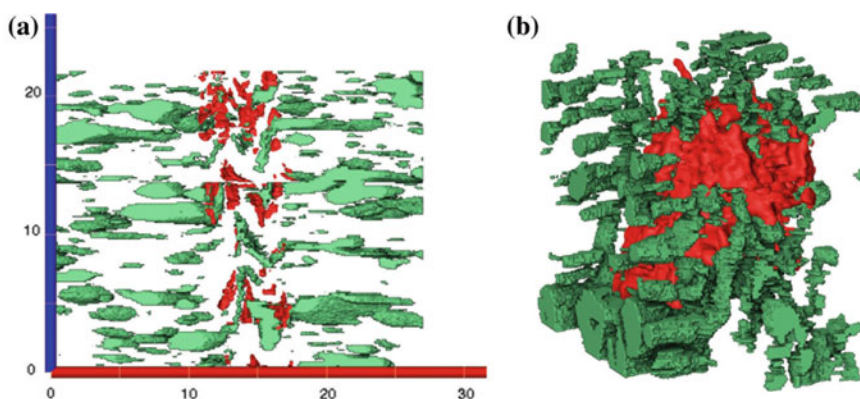


Fig. 6.22 3D reconstruction of part of the damaged region of PP/plastomer blend (tensile test stopped at 50% yield); plastomer particles in green and voids in red. **a** small cross sectional volume, showing the bending of the LLDPE particles in the damaged zones. **b** 3D reconstruction of a void with surrounding particles. Adapted from data used also in [86]

The morphology of an impact-modified PP composition, be it a blend with external elastomers or a reactor-based EP-HECO, is always subject to change as a consequence of deformation in flow. Aggregation of elastomer particles may even occur under quiescent conditions, i.e. in the absence of any flow, as shown already rather early by Mirabella [88]. The ‘phase coarsening’ process was studied here based on an artificially created ‘ideal’ mixture and found to still continue after one hour, but it can become practically relevant also for example in the quiescent melt reservoir of an injection molding machine. When processed, particle orientation and sometimes even breakup i.e. dispersion will occur, generating a stratified structure of elastomer particles with different shape and orientation throughout the resulting part.

An excellent example of the resulting structure is given in the work of Moffitt et al. [89], where a blend of an iPP homopolymer with 25 wt% ethylene-butene rubber (EBR) containing a fluorescent tracer was studied under model conditions. A combination of laser scanning confocal fluorescence microscopy (LSCFM, for EBR particle size and shape) and polarizing light microscopy (PLM, for crystalline PP structures) was applied. Figure 6.23 shows the result of both microscopy techniques and a schematic drawing of particle shape in relation to the crystalline skin-core structure typical for injection molded PP parts.

Depending on the part geometry, the molding process and the material composition, the resulting morphology will vary significantly. The actual degree of deformation and orientation of elastomer particles will largely depend on the viscosity ratio to the matrix, meaning that for a given crystalline PP matrix the stretching and flow alignment of the particles will decrease with increasing molecular weight resp. νV of the disperse phase [78]. For a fixed material

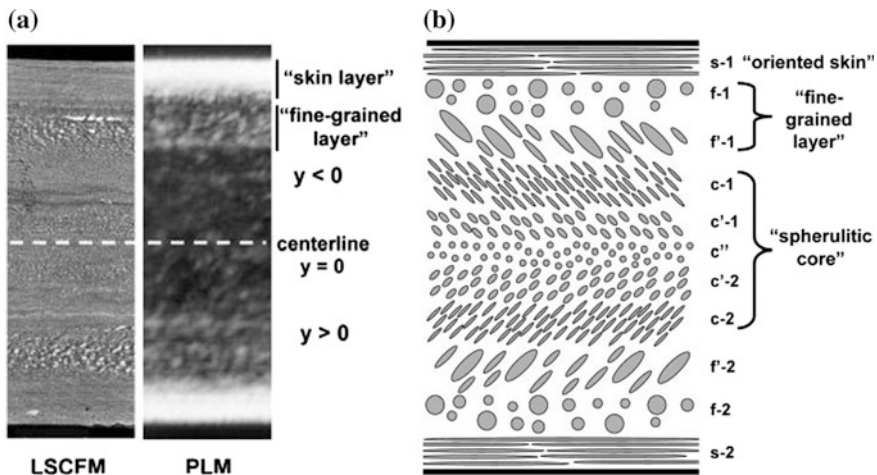


Fig. 6.23 a Stratified morphology of a PP/EBR blend as analyzed by LSCFM and PLM and b in a schematic representation based on the microscopy results (from [89], reprint with permission of Wiley, 2018)

composition, this may result in significant property variations even within one part [90], all that on top of the variations resulting from the crystalline superstructure. Mechanical anisotropy due to particle as well as crystal orientation [91] is normal in such cases, but rather extreme effects can occur e.g. in hinges, stagnation zones or on weld lines [92]. Toughness reduction on weld lines, but also welding factors of e.g. pipes from PP/elastomer compositions may thus be significantly higher than for single-phase materials.

Mechanical effects are, however, not the only consequence of phase structure variation by flow. Surface defects in injection-molded parts like the well-known “tiger stripe” phenomenon, an alternating pattern of dull and glossy stripes perpendicular to the flow direction, has generally been observed more frequently in multi-phase compositions like blends or acrylonitrile-butadiene-styrene (ABS) terpolymers. For PP-based compositions, the effect is highly relevant in automotive components with profiled surfaces. While flow instabilities certainly play an important role in their formation [93], elastomer particle orientation has been found to be critical for local surface gloss and may vary due to these instabilities [94], especially for low viscosity ratios (μ) between elastomer and matrix.

Other processing and application problems are related to phase structure in EP-HECOs and similar PP/elastomer systems as well. One further example is shrinkage and its anisotropy, frequently also linked to thermal expansion (CLTE, coefficient of linear thermal expansion), which may be critical design factor in polymer/metal combinations like car exterior elements. The interaction between matrix polymer and elastomer properties defines both factors in a series of constant elastomer content as shown by Grestenberger et al. [95], where again viscosity ratio is critical. Particle orientation in the skin layer was found to generate disk-like structures in the skin layer, improving dimensional stability for the ideal compositions (see Fig. 6.24). In both cases, nucleation of the matrix phase defining the solidification process in molding plays an additional role. Optimizing dimensional

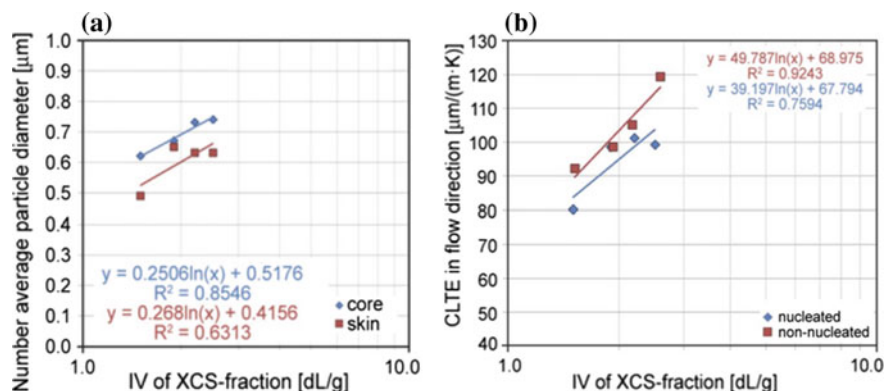


Fig. 6.24 Effect of elastomer molecular weight (IV) on **a** particle aspect ratio and **b** CLTE for PP/EPR compositions with ~30 wt% elastomer content (from [95])

stability in combination with mechanical performance is consequently a rather complex task.

Crystallization in heterophasic systems can also be affected by the dispersed particles, even if their interface to the matrix is largely amorphous. Such effects have been demonstrated in the past for both extruder blends [96] and reactor-based copolymers [97], the composition and inherent crystallinity of the disperse phase being decisive in both cases. As shown for example recently by Van Drongelen et al. [98], particle deformation and epitaxial crystallization at the interface may play an important role here as well.

6.3.1 Matrix Design

The crystalline PP matrix of a heterophasic copolymer provides the basic stiffness for the final composition, as at least the addition of any kind of elastomer or PE will only reduce the modulus, and increase the deformation and creep tendency. Normally, one will therefore try to have the matrix as stiff and crystalline as possible while providing at the same time the base for the necessary processability.

As the elastomer phase needs a certain molecular weight for being able to deliver the necessary toughness (see following Sect. 3.2 for details) and will therefore have higher viscosity, high overall flowability resp. melt flow rate (MFR) of the composition can only be achieved with a high MFR matrix, indirectly also limiting the disperse phase selection. Interconversions between MFR, IV and weight average molecular weight (M_w) can help in establishing the necessary ratios, but for the elastomer phase the comonomer content needs to be considered for such calculations [99].

Three main routes have been established for increasing the stiffness, i.e. the modulus of PP homopolymers:

- High isotacticity giving fast crystallization and high lamellar thickness,
- Broad and/or multimodal molecular weight distribution comprising high molecular weight fractions capable of nucleation under flow, and
- Nucleation (preferably selective for the α -modification).

An advantage of these three approaches is the possibility to combine them.

For Ziegler/Natta (ZN) catalyst based PP the increase in isotacticity, i.e. the first route to higher modulus, is achieved by advanced catalyst/donor combinations [14, 15, 100]. Even if the overall crystallinity of isotactic PP is not increased significantly for pentad regularities ($\langle mmmm \rangle$ as determined by ^{13}C -NMR [17]) above 90%, the crystal growth rate and in parallel the lamellar thickness increase clearly improves the stiffness [101, 102]. At comparable MWD broadness (polydispersity), a higher MFR resp. lower M_w also causes higher stiffness, as short polymer chains crystallize faster. In this case, however, the ‘base toughness’ contribution of the matrix is reduced significantly due to the reduced number of tie molecules connecting the crystal lamellae [103]. While it is difficult to separate different structural

effects, the brittle–ductile transition temperature is shifted to higher temperatures with increasing crystallinity of the polypropylene [104]. Metallocene catalyst (MC) based matrix polymers are mostly limited in crystallinity by regiodefects [105], but also the lower polydispersity is rather negative for achieving high stiffness due to the absence of high molecular weight fractions enhancing crystallization especially under deformation.

Homopolymers based on standard ZN catalysts ($\text{MgCl}_2/\text{TiCl}_4$) from a single-step reaction have a polydispersity (M_w/M_n) of 4–6, while with older catalyst types (TiCl_3 , used in diluents based slurry processes) M_w/M_n could be up to 8. Broad or bimodal MWDs are achieved by multi-stage polymerization with varying hydrogen feed and/or temperature. The resulting higher polydispersities deliver higher crystal orientation through flow-induced crystallization [106] especially in injection molding, resulting in higher stiffness and heat resistance. Figure 6.25 shows the morphology consequence of a polydispersity increase in a model experiment by Pantani et al. [107]; in standard injection these two polymers deliver a modulus difference of ~ 400 MPa. Patent examples show that in presence of ~ 10 wt% elastomer phase still about 15% modulus increase can be gained when moving from a monomodal to a trimodal matrix polymer [108]. At the same time the sensitivity of such materials to variations in processing parameters like melt and mold temperatures, but also flow speeds and shear rates is, however, increased.

Nucleation is the third way of increasing stiffness as well as improving other properties of PP, with a wide range of different types of nucleating agents available

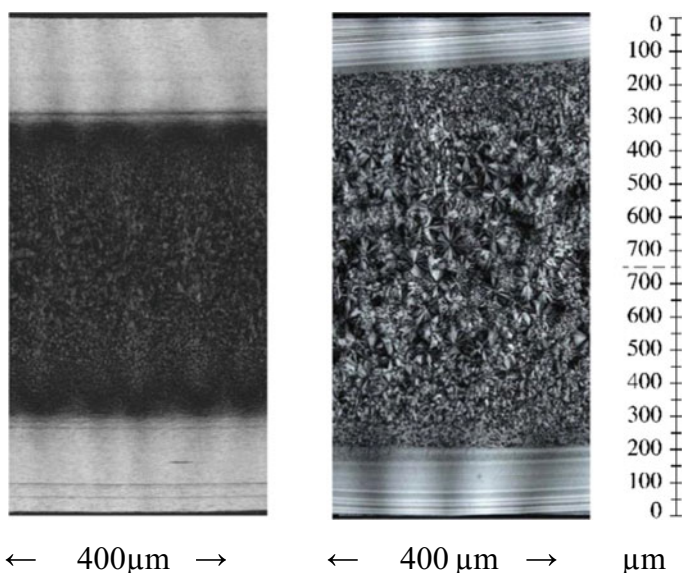


Fig. 6.25 Polydispersity effect on flow induced skin layer and nucleation in core of model specimens (shear rate 100 mm/s for 0.375 s, polarized light microscopy); M_w/M_n 7.5 at 165 °C left versus 5.2 at 145 °C right (based on original images provided by the authors of [107])

[47]. Nucleation of the α -phase is giving higher stiffness. For maximizing the modulus, particulate organophosphate types with their high particle anisotropy and the resulting orientation are suited best [109], which have also been found to maximize the relative thickness of highly oriented skin layers dominated by shish-kebab crystal structures. In contrast, optimizing optical performance is achieved better with soluble nucleating agents of the sorbitol- or trisamide-type [110], where more homogeneous crystal structures (i.e. less skin layers) are achieved in molding.

In any case, the effect of nucleation on impact strength, one of the key parameters for EP-HECOs, needs to be considered as well. For homopolymers and single-phase random copolymers, α -nucleation will normally reduce toughness except at rather high molecular weights [103], but for compositions with elastomer particles the structural effects are more complex [111]. While complete data are not available, both molecular weight and comonomer content of the elastomer affect the impact strength response to α -nucleation, while β -nucleation will always improve the material's toughness [112]. As Fig. 6.26 shows, a positive toughness effect including a shift of the brittle-to-ductile transition temperature is achieved for both types of nucleation with a lower elastomer molecular weight (resulting in smaller particles), but only for β -nucleation with a higher elastomer molecular weight (resulting in bigger particles).

For achieving the opposite effect of reducing the material's stiffness, the PP homopolymer matrix is substituted by a random copolymer, preferably again with ethylene as comonomer. The resulting random-heterophasic propylene copolymers (RAHECOs) are complex materials drawing their property combination from the presence random propylene copolymer (RACO) matrix and the dispersed elastomeric phase (EPR). For designing the properties of such a composition there are a number of possible variation parameters, many of which are intrinsically linked to each other. In an early phase of RAHECO development [113] it was found, that the overall modulus can be related mostly to the comonomer content of the matrix phase and the EPR content (see Fig. 6.27). The toughness and the optical performance of such compositions, however, depends not just upon these parameters but also upon details of the phases' composition and their respective molecular weight.

The concept of RAHECO compositions was developed in the early 1990s [114] and also applied for improving the understanding of fracture mechanics [79], as the better phase compatibility between the RACO matrix and the EPR phase allowed generating very small ($<1 \mu\text{m}$) EPR particles even for less favorable viscosity ratios. This effect, which could also be shown for extruder blends [71], is decisive for the transparency as light scatter inside the polymer will be dominated by matrix/particle interfaces in absence of coarse crystalline structures. At the same time, a high degree of flexibility can be achieved with limited elastomer amount already, making such compositions suitable for production in normal PP production units without the risk of plugging in the last reactor or in the 'dry end' of the plant.

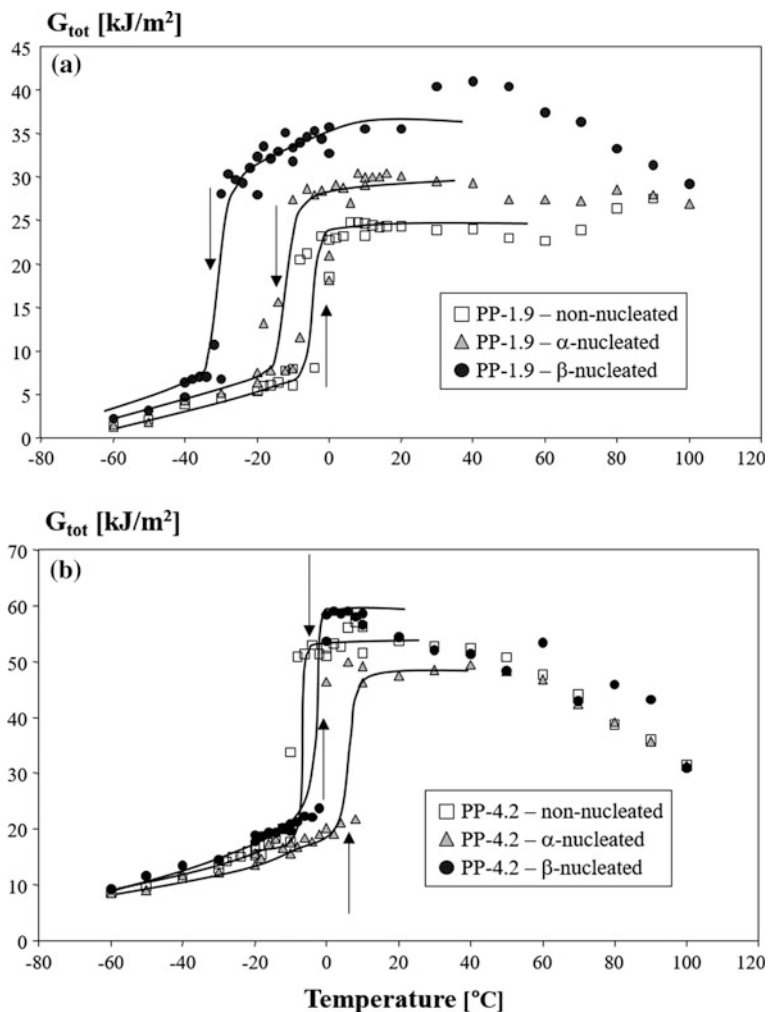
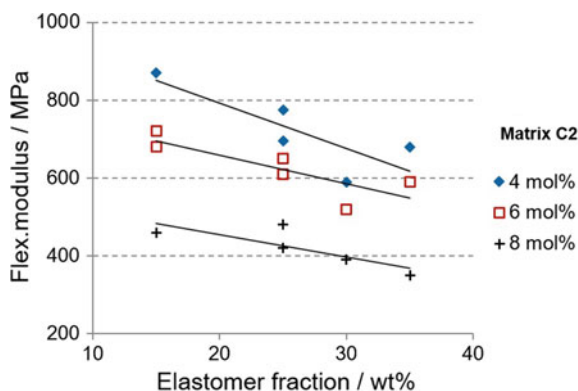


Fig. 6.26 Brittle-to-ductile transition curves as function of temperature for two EE/EPR compositions with 32 wt% of elastomer content (XCS fraction) and a matrix MFR of about 60 g/10 min including α - and β -nucleated versions; **a** low molecular weight elastomer, IV(XCS) 1.9 dl/g; **b** high molecular weight elastomer, IV(XCS) 4.2 dl/g (from [112])

6.3.2 Elastomer Design

Most of the impact strength of a heterophasic copolymer results from the elastomer phase which is present as disperse particles of (rarely) homogeneous, core-shell or ‘salami-type’ (multi-core) structure in the material (see Fig. 6.18). Next to truly amorphous EPR, these particles can also comprise crystalline copolymers having both PP and PE crystallizable segments, and even neat high density PE (HDPE).

Fig. 6.27 Flexural modulus of random-heterophasic ethylene-propylene copolymers (RAHECOs) with different matrix composition and EPR content (C2 of EPR ~45 mol% C2, data from [113])



A detailed analysis of this complex structure is inherently difficult, but progress has been made by combining cross-fractionation with various thermal, spectroscopy and chromatography techniques correlating the molecular structure to the performance of these materials [71, 72, 115, 116]. The experimental effort for this type of analysis significant, and it is necessary to consider molecular weight as well as composition effects. Still it must be clear that while a separation of fractions with different crystallinity is comparatively easy, the same cannot be said for elastomer fractions differing only by comonomer content but being all completely amorphous, i.e. soluble in common fractionation solvents at ambient temperature. Interaction liquid chromatography (ILC) applying special activated surfaces appears to be a viable alternative, achieving both a reduction of time demand and an improved separation [117, 118].

The composition heterogeneity of PP impact copolymers (EP-HECOs) strongly influences the phase behavior and interfacial adhesion between the matrix and the dispersed phase, with the composition of both phases playing a decisive role. For the matrix part this has been discussed in the previous chapter [113, 119] while the effect of elastomer composition will be discussed below. The aspects of molecular weight or rather its ratio between the matrix and the disperse phase [78, 99], as well as of melt-mixing processes after polymerization [120] must not be disregarded here. Heterophasic PP copolymers can consequently be regarded as both mechanically and physically compatibilized systems rather than simple blends.

Before discussing the various options for designing the elastomer phase composition, the basic one is to vary its amount. This relatively simple approach to improve toughness by reducing—assuming constant particle size—the inter-particle distance of elastomer inclusions and increasing the energy absorption capacity has been analyzed for elastomer-modified systems in general before by Wu [121]. The concept of stress overlap affected by a combination of particle size, distance and adhesion between particle and matrix is generally correct but misses upon some aspects of relevance for heterophasic PP compositions. When varying the concentration of EPR particles of constant composition and dimension, a step-wise brittle-to-tough transition in notched impact strength is indeed observed as a

function of concentration, together with a rather linear modulus reduction [79, 80, 122] (see Fig. 6.21).

In detail, however, the structure of both matrix and particle will affect the position and intensity of this transition. The key factors are the modulus ratio (as discussed before for stress whitening) and the internal structure of the elastomer. In fact, the work of Grein [78, 80] and Kotter [80] demonstrates that at least two types of transition can occur in elastomer-modified PP systems. Next to the normal brittle-to-tough transition (BTT) a second tough-to-high-impact-toughness transition (THT) can be observed, the temperatures for both are depending on elastomer concentration and composition (see Fig. 6.28). In terms of crack propagation and failure mode, this corresponds to transitions from unstable through semi-stable to stable crack growth. It should be noted that even when considering testing parameters like geometry and test speed, the actual toughness performance of a component will also depend upon its own geometry and processing effects determining actual particle geometry and orientation (see also Fig. 6.23).

The maximum achievable amount of EPR component for a reactor-based composition is in turn determined by the applied polymerization technology and catalyst. As already discussed in Sect. 6.1, highest elastomer amounts are normally produced in multiple gas phase reactors (GPRs), in which the original porous matrix polymer particles are filled up and possibly expanded by largely amorphous copolymer phase [12, 123–126]. Nearly equally important for this purpose is a polymerization catalyst of long lifetime, as the overall residence times in the reactor cascade can easily exceed 2 h.

The resulting phase structure of the final powder particles is quite different from the one observed in granules after compounding (or even just melting) as shown in Fig. 6.29. A combination of ‘veins’ and ‘aggregates’ of copolymer dominates the

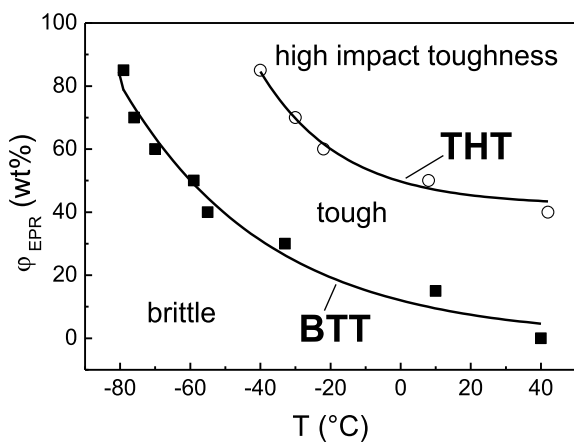


Fig. 6.28 Brittle-to-tough transition (BTT) temperatures and tough-to-high-impact-toughness transition (THT) temperatures versus the EPR content (ϕ_{EPR}) (from [80], reprinted with permission of Wiley, 2018)

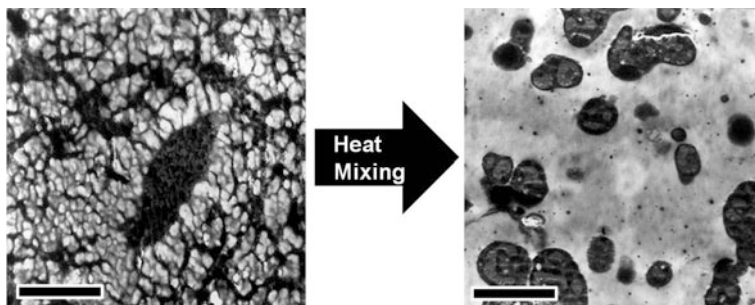


Fig. 6.29 Relation between powder morphology (left) and granule morphology (right), RuO₄-contrasted transmission electron microscopy (TEM); high-impact EP copolymer type with 26 wt% ethylene and 22 wt% elastomer (EPR; xylene soluble fraction); EPR is dark because of lower crystallinity, PP matrix and PE inclusions in particles are light, scale bars 2 μm

powder structure, depending strongly on the catalyst and particle formation in matrix polymer production [123, 127] and elastomer incorporation. In contrast to that, the phase structure with disperse particles, formed already upon simple melting (like in compounding), depends on composition and molecular weight ratios.

In the industrial production of heterophasic copolymers, the critical factor for stable operation is absence of inter-particle stickiness as well as particle-wall adhesion. This must be achieved in the polymerization reactor(s), but also in the vessels and transportation tubes of the downstream section, where catalyst deactivation and powder purging takes place.

In principle, the morphology of the produced polymer particles replicates the morphology of the employed catalyst particles. The spherical aggregates of microcrystalline MgCl₂ presently mostly used as support material for the TiCl₄ in ZN-catalysts [126, 127] offer a porous structure with large surface area. This porosity of the catalyst particle was long considered as key factor for the amount of EPR which can be accommodated in the polymer granule without causing stickiness. Investigations on an apparently (at least initially) non-porous ZN-catalyst from an emulsion process [25], however, already demonstrated that this single factor explanation is obviously too simple. In fact, the powder porosity and structure of the (normally homopolymer) matrix, possibly in combination with reactivity and accessibility of active catalyst particles, appears to be far more relevant for the maximum EPR content achievable in practice.

Especially the structural investigations in the group of Kosek [125, 128, 129] have been important for improving the detail understanding of the formation of copolymer powder particles with higher amounts of elastomer phase. As the overall size of these particles (2–4 mm) is much bigger than their finest structural features (0.1–0.5 μm), only a combination of different structural investigation tools, like X-ray tomography and AFM [129], is capable of delivering all the necessary information. A factor not to be neglected is the mobility of the elastomer phase, which depends on molecular weight (i.e. viscosity) and ethylene content (i.e. PE-like crystallinity), adding to the complexity by being capable of moving from

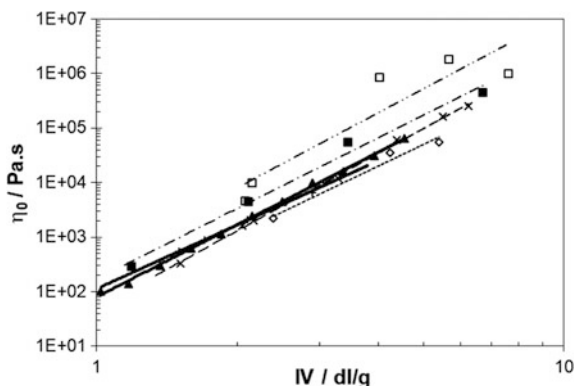
the interior to the surface of the particles both during and after polymerization. Long residence time and high temperature in the GPR will contribute to this ‘migration process’. Given the complexity of the overall process, it is quite certain that significant optimization potential remains here.

With the two parameters of molecular weight and ethylene content, the most important possibilities of varying structure and properties of the elastomer phase have already been mentioned in the previous paragraph. The former one has to be considered in turn from two aspects [78, 99, 130]: First, the absolute molecular weight will, especially for fully or largely amorphous EPR types, define its energy absorption capacity through the presence of a sufficient entanglement density, meaning that higher molecular weights give higher toughness (very much like for amorphous polymers in general). Second, a variation of the viscosity ratio between dispersed phase and matrix will also have a strong influence on the elastomer particle size [78, 99]. The optimum particle size depends on the dominant deformation mechanism of the matrix, which in turn is influenced by the test conditions, i.e. temperature, deformation rate and loading mode (uniaxial or biaxial). While the general situation is similar to the one in simple extruder blends, with mixing quality depending on compatibility and viscosity ratio [7, 131], an intimate mixing of the components can be obtained in a wide range of molecular weight for reactor-based systems.

Two remarks are necessary here, the first one relating to the determination of the average particle size as well as the particle size distribution, which is not without its own inherent problems. High resolution microscopy techniques like scanning (SEM) or transmission electron microscopy (TEM) [132], alternatively also atomic force microscopy (AFM) [133] are the techniques of choice, but sample preparation should be done carefully. Contrast enhancement with ruthenium tetroxide (RuO_4) is preferred over solvent or oxidative etching, as the latter may cause uncertainties about the actual particle dimension. Even then, annealing steps prior to cutting as proposed by Mirabella [88] are advisable to generate relaxed and at least roughly spherical particles in the sample, and the evaluation needs to account for the difference between projection dimensions (2D) and particle dimensions (3D) [133], and the calculated average should be representative (like the weight average particle size D_w). An investigation of fracture surfaces, while certainly helpful for understanding the failure process [78], is completely unsuitable for determining particle size distributions.

The second remark relates to the way of determining viscosity ratios between matrix and elastomer phase for reactor-based compositions. In industrial practice, the molecular weight of fractions or phases is commonly determined via the intrinsic viscosity measured in tetralin (tetrahydronaphthalene) or decalin (decahydronaphthalene) at 130–135 °C [74]. This method is used because it is both fast and simple, and it can be used easily for production control. Correlations to the molecular weight (e.g. M_w , the weight average of the MWD) are possible, but both the composition of the fraction [99] and, to a lesser extent, MWD broadness and shape need to be considered. As M_w correlates nicely to the zero shear viscosity (η_0) of a polymer, solution and melt viscosity are connected nicely. As Fig. 6.30,

Fig. 6.30 Zero shear viscosity as a function of the intrinsic viscosity (decalin 130 °C) for pure polymers and XCS fractions (black triangle pure PE; XCS fractions with C3 of XCS: white square 38 wt%; black square 48 wt%; ×69 wt%; white diamond 75 wt%; +pure PP; from [99], reprint with permission of Springer Nature, 2018



calculated from a study of different PP copolymers with varying elastomer composition and molecular weight shows, at a given IV the melt viscosity of a fraction will depend significantly upon its composition. The IV ratio between elastomer and matrix fraction or, commonly simplified, xylene cold soluble (XCS) and xylene cold insoluble (XCI) fraction, is thus a good approximation of the melt viscosity ratio. Correlations to the melt flow rate (MFR) are somewhat more complex and have to be considered carefully, especially when trying to draw conclusions for polymers based on different catalysts or processes.

The study of Grein et al. [78] presents a variation of elastomer molecular weight in reactor-based PP/EPR copolymers, corresponding to an IV range of 1.6–6.0 at constant matrix molecular weight (~ 250 kg/mol or MFR 230 °C/2.16 kg of 40 g/10 min), rather constant elastomer amount (XCS 21.4–23.1 wt%) and composition ($C_2(\text{XCS}) \sim 40$ wt%). The viscosity ratio μ between the viscosities of the dispersed phase (η_d) and continuous or matrix phase (η_m) was thus varied and found to control morphology. In principle, μ should control the rate of phase separation by coalescence and distribution during compounding. For constant phase composition and elastomer amount, fine dispersion is expected both for (a) low molecular weight of the rubber compared to the matrix, as the mechanical deformation of the dispersed phase and consequently breakup is stronger and (b) high molecular weight of the rubber compared to the matrix because agglomeration of particles is reduced. Covering a range of μ from 3.5 to 23.3 in this study, a plateau with maximum average particle size $D_w \sim 1.9$ μm was found for μ of 7–10 respectively an IV (XCS) of 2.7–3.5, while the smallest particles ($D_w \sim 0.9$ μm) were found for the lowest elastomer molecular weight. Figure 6.31 demonstrates that standard impact tests are dominated by the $M_w(\text{EPR})$ with a roughly linear increase of fracture energy at both ambient and sub-zero temperatures on a logarithmic IV scale, while the ductile-brittle transition temperature shows a certain saturation above an IV (EPR) of 3. The latter phenomenon suggests a strong effect of the particle morphology.

The second main variation relates to the EPR composition, mostly to its ethylene content, which will again affect both particle size and elastomer properties.

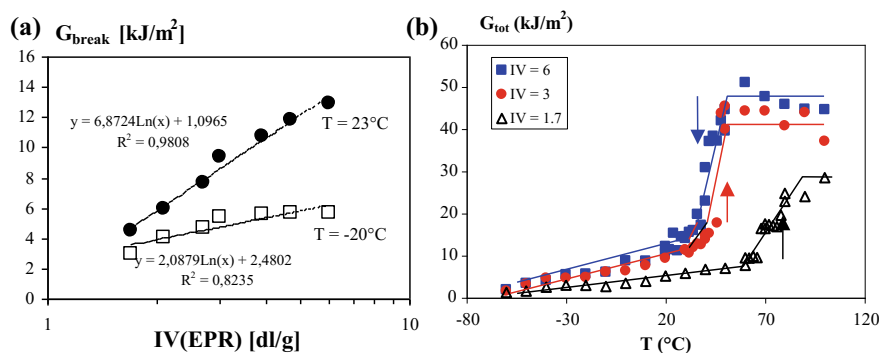


Fig. 6.31 **a** Standard notched Charpy fracture energy, G_{break} at 23 and -20°C , plotted versus the logarithm of the IV of the elastomer phase (resp. XCS fraction). **b** Specific energy to break G_{tot} as function of test temperature in instrumented Charpy tests ($v = 1.5$ m/s), arrows indicating ductile-brittle transition temperature (from [78], reprint with permission of Wiley, 2018)

Propylene-rich EPR (low C_2 content) results in a reduced interfacial tension against the PP matrix, quite like the effect achieved for changing from a homopolymer to a random copolymer matrix described in the previous chapter. A fine particle dispersion with low average size can be achieved by this [99, 134, 135], the respective materials showing very good impact properties at ambient temperatures both under plain strain and plain stress conditions [136]. Like their random-heterophasic counterparts [113, 114] they also exhibit rather good transparency, low shrinkage and high morphology stability during further processing and post-processing steps like sterilization [137]. Next to the good chemical affinity between PP matrix and dispersed phase, the effect is also ascribed to a partial dissolution of a certain amount of the propylene-rich EPR in the amorphous region between the PP lamellae [119]. Low ethylene content also causes a shift of the glass transition temperature (T_g) of the EPR towards higher temperatures, while the T_g of the PP was found to be somewhat reduced. Together this has a significant effect on the stiffness (modulus and yield stress, see Fig. 6.32). Because of the rather high glass transition temperature of the elastomer phase, such systems are less suitable for use at very low temperatures (i.e. $< -10^\circ\text{C}$) [138].

Heterophasic copolymers with a higher ethylene content in the EPR phase comprise a crystalline PE fraction, incorporated as inclusions in the amorphous EPR domains, forming core-shell (single inclusion) and „salami-like” (multiple inclusions) structures [77, 99, 138]. Such copolymers with ethylene-rich disperse phase have very good low temperature toughness, exhibit benefits in scratch and stress-whitening resistance. Similar effects can, however, also be achieved by adding HDPE to a PP copolymer in compounding [83, 139]. The drawback of such EPR structures is its tendency towards agglomeration [140], resulting in coarse particle structures and rather high brittle-to-ductile transition temperatures.

Figure 6.33 gives an overview of the EPR composition effect in terms of phase morphology: The crystalline PE lamellae clearly visible for the higher comonomer

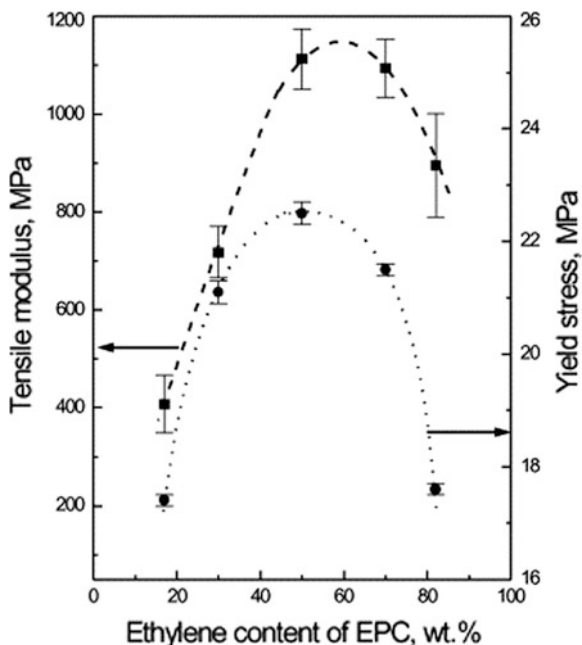


Fig. 6.32 Tensile modulus and yield stress at 23 °C as function of the EPR composition for PP impact copolymers with constant matrix and EPR content (from [136], reprint with permission of Elsevier, 2018)

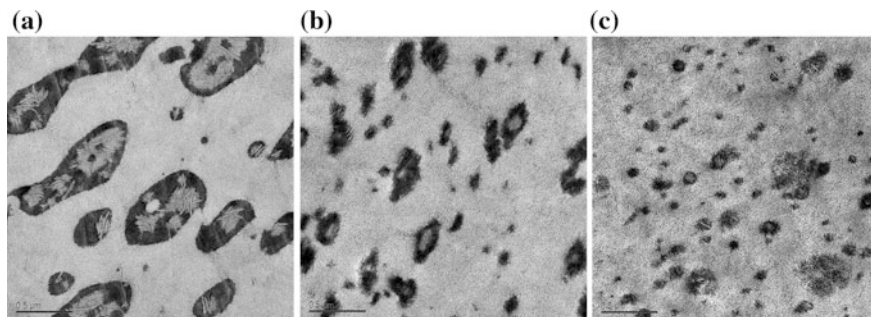


Fig. 6.33 Phase morphology of EP impact copolymers with constant molecular weight of the elastomer phase, $IV(XCS) = 2.1$ dl/g (C2 of XCS: **a** 62 wt%, **b** 31 wt% and **c** 25 wt%; TEM images after RuO_4 contrasting, scale bar size 500 nm; materials from [99])

content disappear gradually with its reduction, the phase boundary gets “fuzzy” and the particle size is reduced, both phenomena indicating better compatibility. In term of mechanical properties, the optimum composition rendering an EPR phase sufficiently immiscible with the matrix to maintain a phase separation and adequately miscible to assure proper matrix/dispersed phase adhesion is generally assumed to

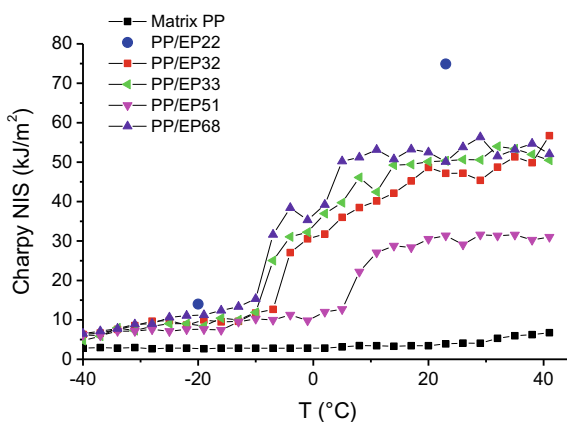
be in the range of 35–45 wt% ethylene [99, 138, 141]. Compositions optimized for different application areas requiring different property combinations will, however, also require respectively adapted elastomer design.

Specific EPR composition effects may not only be achieved by varying the process conditions, but also by selecting specific catalysts [18, 25, 142, 143]. While the variability of elastomer design achieved with Ziegler-Natta (ZN) systems depending on catalyst and donor type may still be limited, massive changes especially in terms of EPR composition are seen when either combining ZN types with metallocene (MC) or in general single-site catalysts (SSC) [142] or using SSC alone for multi-stage copolymerization [18, 143].

In a recent study a series of EP-HECO compositions with identical homopolymer matrix and different composition of EPR phase were produced in bench scale polymerization with an SSC, keeping the amount of EPR phase constant [18]. Extensive characterization of these materials allowed establishing some essential structure-property relations as compared to ZN-based products. When varying the C2 content of the elastomer phase between 32 and 68 wt%, NMR investigations showed a systematic shift from propylene rich EPR with randomly distributed ethylene units to ethylene rich EPR with isolated propylene units. A remarkably different phase morphology compared to ZN-based copolymers with good phase coupling to the matrix PP and the absence of crystallizable polyethylene in the C2-rich copolymers (confirmed by DSC and TEM) resulted from this. Overall, many of the materials showed an interesting stiffness–toughness balance with a rather similar impact behaviour in a broad range of EPR composition. The rather low brittle-to-ductile transition (BDT) temperature (see Fig. 6.34) is remarkable when comparing it to the results of earlier work (see Fig. 6.31 from [78]).

Another option for optimizing property combinations is the development of PP systems containing multiple disperse phases. Here, the design concept is to choose the minor components in such a way that the advantages of the one to compensate the deficiencies of the other. The benefits of using two different elastomers as impact modifiers have also been pointed out in the literature both for PP [144] and

Fig. 6.34 Brittle-to-ductile transition curves (Charpy NIS) of matrix PP and a series of heterophasic SSC-copolymers with varying elastomer composition (numbers next to ‘EP’ indicate C2 content of EPR; from [18])



for glassy polymers [145], accounted to both interfacial adhesion and particle size effects. In case of a semi-crystalline matrix polymers, particle size bimodality is expected to have even stronger influence, because the main deformation mechanism depends on temperature. As the optimum particle size for toughening of polypropylene decreases with increasing temperature, a bimodality of the dispersed phase size could be a promising approach for ensuring toughness over a wide temperature range. Such toughness optimization has for example been shown for a combination of PP with EPR and a metallocene-based plastomer [146].

Advantages of PP based reactor blends with bimodal particle size distribution are suggested in several papers [12, 145] and patents [147–149]. Respective compositions can be produced directly in polymerization units including at least two gas-phase reactors for EPR production, like the Borstar PP or the Spheripol process. In this way, two elastomer fractions differing in composition (ethylene/propylene ratio) and/or molecular weight can be incorporated in the PP matrix. Based on theories considering compatibility [150, 151], three main types of morphology may exist for the PP/EPR1/EPR2 materials (see Fig. 6.35). If the chemical composition of the two elastomers is similar enough for them to be miscible, the morphology (Type I) resembles conventional heterophasic copolymers (Fig. 6.35a). Increasing the gradient in composition and molecular weight between the two EPRs deteriorates compatibility, resulting in two separate disperse phases. Two limiting cases can be expected: Either EPR1 encapsulates EPR2 acting as compatibilizing agent (Type II morphology, Fig. 6.35b) resulting in smaller domains than expected for conventional copolymers with ethylene-rich EPR while retaining their internal structure. Or both EPR phases disperse in discrete domains (Type III, Fig. 6.35c), one of these present in significantly smaller domains without internal structure and the other one in larger „core-shell” or „salami-like” particles. A broader or a bimodal particle size distribution is found in case of Type II and Type III morphology.

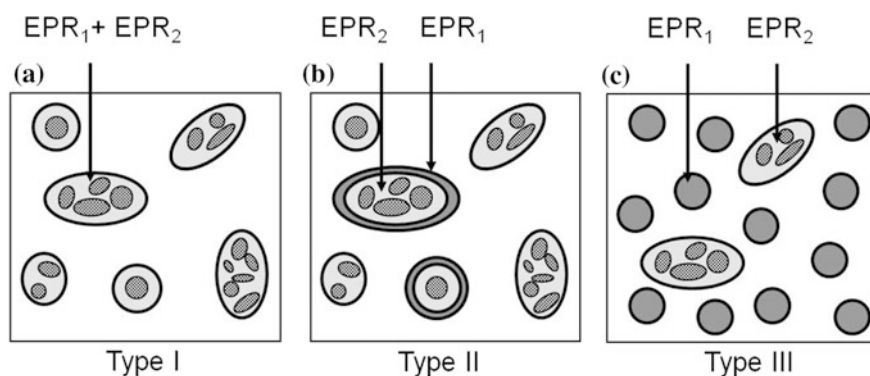


Fig. 6.35 Proposed morphology types of heterophasic copolymers containing two EPR phases: **a** Type I—EPR1 and EPR2 interpenetrate each other. **b** Type II—EPR1 encapsulates EPR2. **c** Type III—discrete dispersion of EPR1 and EPR2 (from [69], reprint with permission of Wiley, 2018)

6.3.3 Modification of Heterophasic Copolymers

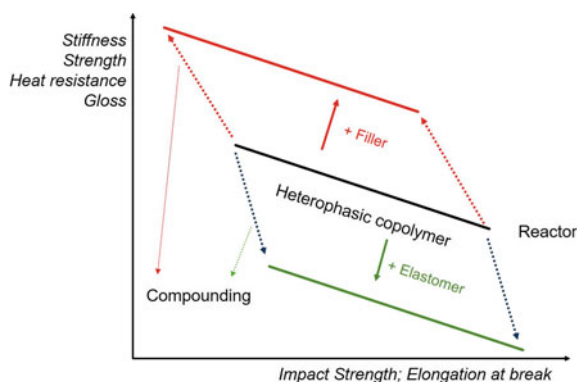
Due to their interesting property balance, heterophasic copolymers (EP-HECOs) are also an ideal starting point for post-reactor modification. Increasing property requirements for polymers in industrial applications, especially when targeting the replacement of the metal or other technical plastics by polyolefins, frequently require such modifications beyond the limitations of in-reactor design as discussed before. The target will mostly be an improvement of the stiffness/impact balance as sketched in Fig. 6.36, frequently combined with higher temperature resistance. It can also be quite the opposite, like improving flexibility and transparency, like for medical applications [152], but even improved surface properties [94], less processing sensitivity [140] or better dimensional stability [95] are relevant targets.

The structural nature of EP-HECOs, a multi-component system in which the constituents are not miscible thus forming two or more separate phases (see previous chapters), forms the base for such modifications. Post-reactor modification may concern the crystalline matrix (like the nucleation options discussed in Sect. 6.3.1 [103, 111, 112]), the disperse elastomer phase(s) or the interaction and adhesion between both.

An industrially widely used approach to improve the mechanical performance of heterophasic copolymers is the addition of inorganic fillers like talc, chalk, mica, kaolin or wollastonite [153–155] as well as different fibers ranging from glass through natural to carbon types [156–158]. The rigidity of the inorganic modifiers will significantly improve the stiffness and the thermomechanical properties of the materials. The further addition of external impact modifiers, plastomers or elastomers, may be needed to limit the resulting drop in impact strength while further improving the toughness at low temperatures (see Fig. 6.36).

The change in properties resulting from the addition of (mostly inorganic) fillers and fibers is primarily related to the filler/matrix interaction. Talc is the most widely used mineral for a number of reasons: It has a low polarity and rather hydrophobic nature, facilitating compounding but also reducing water uptake and agglomerate

Fig. 6.36 Schematic presentation of shifts in the stiffness/impact balance due to the combination of EP-HECOs with fillers and/or external elastomers

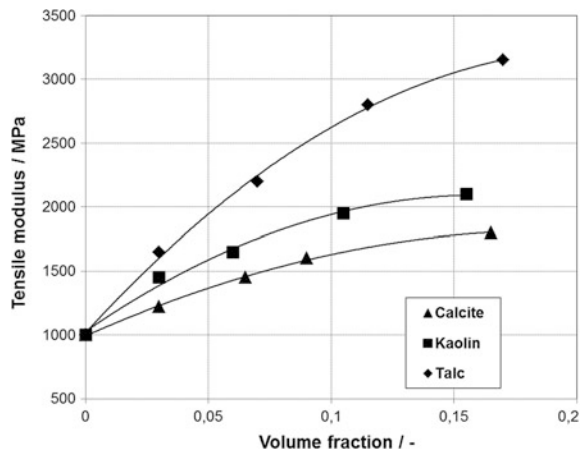


formation. In addition, it is a nucleating agent for the α -phase of PP, maximizing the stiffness increase and making it superior to other minerals in this respect as shown in Fig. 6.37 [47, 153]. Its platelet structure is further beneficial for equilibrating post-processing shrinkage and thermal expansion towards a more isotropic behavior [95]. The limited interfacial adhesion between filler and polymer, however, results in debonding under stress. This causes not only a reduction of the impact strength but also increased stress whitening and more visible scratches on the surface of the materials (see details below).

Next to an increase of the elastomer fraction, one option to compensate for the loss in impact strength is β -nucleation as discussed before for unfilled systems [39, 49]. This approach is only possible for minerals not showing pronounced nucleation activity themselves, like calcium carbonate (chalk) [39, 159]. The other negative phenomenon, increased scratch sensitivity, can be countered by modifying the elastomer composition by addition of high density polyethylene (HDPE) [160], again demonstrating the close relation between scratch visibility and stress whitening [83, 160].

A general principle in modifying the elastomer phase is the compatibility of practically all olefin-based modifiers like ethylene-propylene rubber (EPR), ethylene-propylene-diene rubber (EPDM) and the various polyethylenes ranging in decreasing crystallinity from HDPE to ethylene- α -olefin plastomers, are more compatible to the reactor-made elastomer phase than to the matrix. They will consequently mix and become part of the disperse phase, the resulting morphology depending on the structure of the modifier (see Figs. 6.18 and 6.38). HDPE, for example, becomes part of the core of the original particles and co-crystallizes with the ethylene-copolymer of the original elastomer phase, thus strengthening this phase and improving the scratch resistance (see Fig. 6.38c). Impact strength may be affected positively as well, but elongated particle structures in HDPE modified HECOs should be avoided by selecting a modifier with a proper molecular weight in order to maintain this positive effect [7, 160].

Fig. 6.37 Effect of filler type and concentration on stiffness of composites based on a PP homopolymer (data from [154])



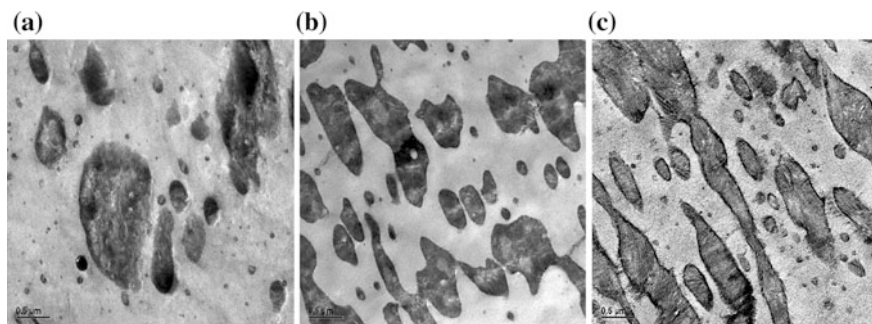


Fig. 6.38 Transmission electron microscopy (TEM, after contrasting with RuO_4) pictures of the morphology of **a** (C3HECO) commercial high impact EP-copolymer with ~ 20 wt% C3-rich EPR, **b** (C3HECOPL20) compound of (C3HECO) with 20 wt% of an ethylene-octene plastomer, and **c** (C3HECOHD20) compound of (C3HECO) with 20 wt% of HDPE (materials as in Fig. 6.18 from [164], scale bar $0.5 \mu\text{m}$)

Other types of PE offer different advantages in EP-HECO modification: Using clarifiers [111] in heterophasic copolymers in order to achieve better transparency has normally a very limited effect. These additives support better transparency of the matrix, but will not solve the issue of light scattering at the interface between matrix and disperse phase. One possibility to develop more transparent materials is the addition of a polymer which is compatible with the dispersed phase while adjusting the density and thus the refractive index of the dispersed phase in a way to become more similar to that of the matrix. High-pressure process based low density PE (LDPE) has been found suitable for this. In this way, the light scattering is reduced and the material becomes more transparent while maintaining high impact strength [161, 162].

Another approach to obtain a heterophasic propylene copolymer combining good low temperature impact strength with transparency is the addition of styrene-butadiene-styrene triblock copolymers (SEBS). Adding this polymer leads to the formation of a ternary system comprising the PP matrix, the ethylene-propylene-rubber and the SEBS. It could be shown that by changing the type of the SEBS (styrene rich versus butadiene-rich type) the resulting morphology as well as the mechanical and optical performance of the compound can be tailor-made [163].

If increased impact strength in a wide temperature range (especially extending far into the sub-zero range) is the main target of modification, then PE plastomers are the modifier of choice. Figure 6.38b shows the rather homogeneous elastomer particle structure resulting from such a modification, and the resulting property improvements have been demonstrated in several studies [147, 163, 164]. Ethylene-hexene- and ethylene-octene plastomers are available in a wide range of molecular weight resp. MFR, enabling also the modification of high flowability copolymers.

Combinations of fillers and external elastomers for modification of EP-HECOs is a standard route for property design. The use of external elastomers with increased polarity, like EPR grafted with maleic anhydride (EPR-g-MAH) or ethylene-vinyl

acetate (EVA) copolymers, offers the additional option of controlling the position of the filler particles in relation to the matrix/elastomer system [165, 166]. For the case of calcium carbonate (chalk), Fig. 6.39 gives two examples of a ternary matrix/elastomer/filler system with (a) separate dispersion when using an ethylene-octene plastomer (EOC) and (b) predominant encapsulation of the filler when using EVA copolymer. This was found to result in higher stiffness for the former but higher impact strength for the latter case [166].

Glass fiber (GF) reinforcement, a generally widely applied technique for achieving very high levels of both modulus and temperature resistance of PP composites, presents a special case. In contrast to mineral filler particles, GF are both thicker and especially longer than the elastomer particles present in an EP-HECO, adding a different structural level to the resulting compositions. Systematic work in this area is so far rather limited, probably because of the anyway present toughening effect in PP/GF systems with sufficient interfacial adhesion. Nevertheless, some examples of positive interaction can be found [157, 167]. More logical appears the use of elastomer modification for PP compounds with natural fibers, which normally suffer from unsatisfactory impact strength [158].

Next to the conventional compounding approach, where several components are mixed together in an extruder without any chemical modification of the constituents, reactive modification of heterophasic copolymers with or without additional components is possible. The simplest reactive process used for PP is peroxide-induced degradation, usually called ‘visbreaking’, for achieving lower molecular weights (i.e. higher MFRs) and narrower MWDs (i.e. lower polydispersities) [168]. When this process using radicals generated by the peroxide is

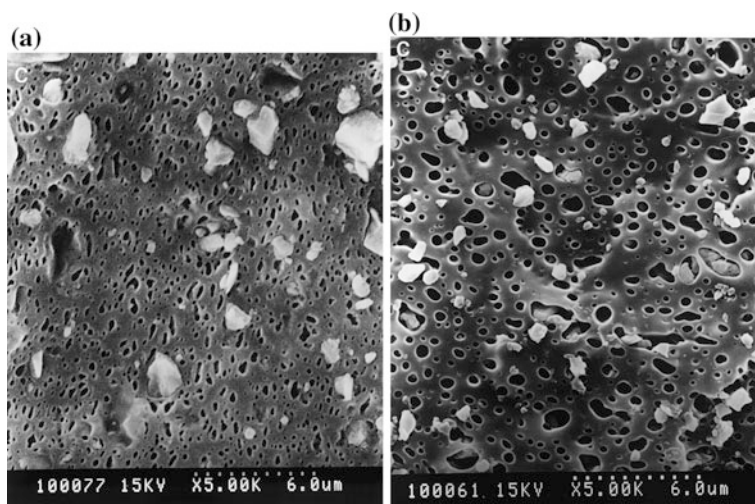


Fig. 6.39 Phase structure images (SEM on cryogenic fractured and heptane vapor etched surfaces) of ternary PP/elastomer/ CaCO_3 composites in the composition 60/30/10 wt%; **a** separate dispersion for EOR, **b** predominant encapsulation of the filler for EVA (from [166], reprint with permission of Elsevier, 2018)

applied for EP-HECOs, problems result from the different reaction of the PP matrix and the elastomer. While in case of PP the radicals predominantly cause chain breakage, the EPR reacts more like PE, i.e. by buildup or even crosslinking. For multiphase copolymers this results in a shift of the viscosity ratio μ and an often significant increase of the particle size, possibly causing problems in mechanical and optical performance [169].

The consequences are quite opposite when a combination of peroxide and bifunctional monomers is used [170] in a modification process originally developed for the production of long-chain branched (high melt strength, HMS) PP homopolymer [171]. In this approach, the formation of ethylene-propylene copolymer grafted to polypropylene is caused by the addition of the free radical initiator (peroxide) and the co-agent (e.g. polybutadiene). The ethylene-propylene copolymer grafted to the polypropylene strengthens the interface between the PP matrix and the EPR particles, reducing the tendency of forming bigger inclusions, like normally in visbreaking. The overall effect on impact strength is positive, while the processability improves as well. Figure 6.40 presents both the morphology evolution and the effect on the brittle-to-ductile transition temperature for a modification series starting from a conventional impact copolymer comprising ~ 28 wt%

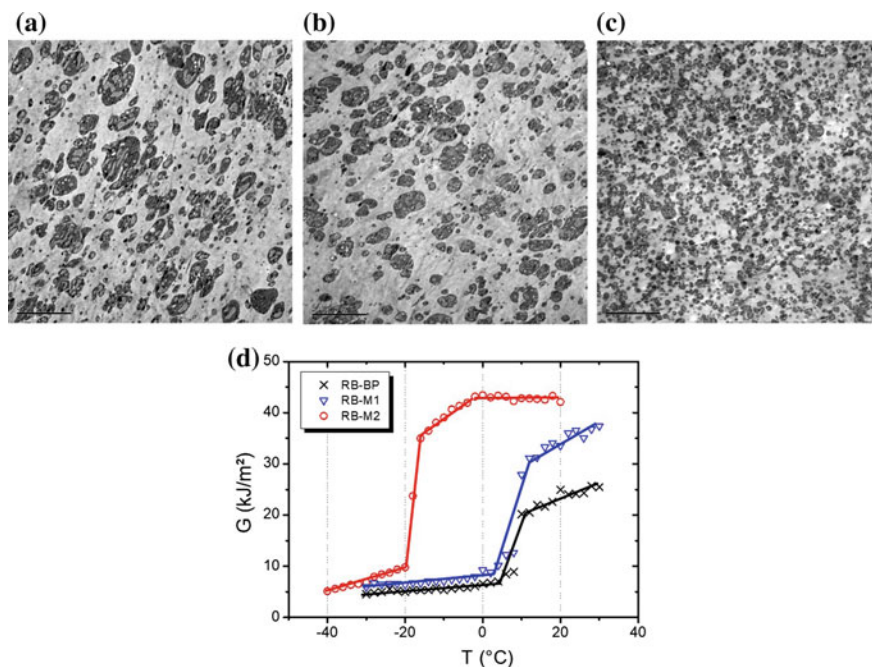


Fig. 6.40 Effect of reactive modification on morphology and Charpy notched impact strength of an EP-HECO; TEM images of **a** base polymer, **b** weakly and **c** strongly modified product (MFR 12 g/10 min in all cases); **d** Shift of brittle/ductile transition to lower temperature by reactive modification (BP—base polymer, M1—weakly modified, M2—strongly modified)

of EPR with an IV of ~ 2 dl/g and having an MFR of 12 g/10 min. Limitations for this process combining peroxide and co-agent arise from the need for good organoleptic properties, as decompositions are unavoidable. Additionally, the concept has been found to cause anisotropic shrinkage and warpage in some cases.

An alternative route for radical-based modification, also developed originally for producing HMS-PP homopolymers [172], is electron beam irradiation. The mechanism appears to be similar and has to be tested so far for PP homopolymer blends with 2.5–50 wt% of ethylene-octene plastomer (EOC), performing the e-beam irradiation either in a kneading chamber [173] or in a continuous setup [174] at intensities up to 12 kGy. The characterization revealed significant crosslinking of the EOC into particles of ~ 1 μm diameter, combined with improved interfacial adhesion as a result of co-grafting to matrix polymer, resulting in higher impact strength. This concept should be applicable for EP-HECOs as well.

6.4 Application of PP Copolymers

As already mentioned in Sect. 6.1, copolymers have been elementary in entering the wide range of applications in which polypropylene is present today. Figure 6.41 presents a look at the global as well as the European application distribution for PP in general. The global production of polypropylene was about 56 million tons per year in 2016, at a cumulative average growth rate of about 5% per year, but with significant regional differences (e.g. only 1.4% per year in Europe). The split between the extrusion segments—films and fibers, but also coating and pipe extrusion—and the combined segments of injection and blow molding is around 50/50%. In detail, it depends on the degree of differentiation in the different world regions.

Random copolymers (RACOs), heterophasic copolymers (HECOs) and filled resp. reinforced compounds based on PP have significantly different application areas with limited overlap. While many applications have a long history already, some have only been enabled by more recent technological developments [175] as well as an improved understanding of structure-property relations and modelling possibilities [176].

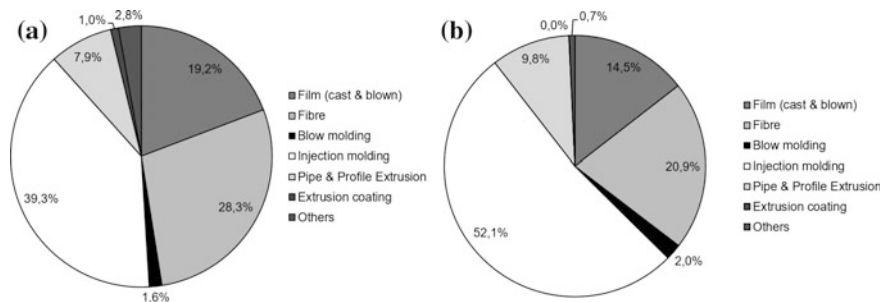


Fig. 6.41 Application segments of PP worldwide (a) and in Western Europe (b). Data from [193]

RACOs with ethylene as well as co- and terpolymers with butene or hexene have a dominant position in applications requiring high transparency resp. low haze. The lower crystallization speed of these polymers allows both for finer crystal structures of the α - or γ -crystal phase [13] and easier quenching into the mesomorphic phase [177], which has an even higher transparency. In PP cast films, ethylene-propylene RACOs are applied both as single-layer materials and for sealing layers, where terpolymers can achieve even lower sealing initiation temperature (SIT). Variations of the processing conditions can affect the property expressions significantly [40, 177], with both film crystallinity and surface structure playing a role in determining especially the optical performance. With higher molecular weight, also blown films can be produced, where multilayer films with polyethylenes are rather common [178]. Uses for RACO films range from pouches, bags and lid films in packaging to office organization and technical films.

Similar molecular weights corresponding to a melt flow rate (MFR 230 °C/2.16 kg) of $\sim 1\text{--}3$ g/10 min are also applicable for extrusion blow molded bottles which are significantly more transparent than comparable articles from PE while also having good stress crack resistance. The use of long-chain branched PP (HMS-PP) as modifier has been shown to improve both processability and optics [179]. Even for the production of injection stretch blow molded bottles RACOs are suitable, preferably in combination with nucleating agents.

Nucleation, especially with soluble α -nucleants like sorbitols [180] is also preferable for RACO types for injection molding covering an MFR (230 °C/2.16 kg) range of 8–100 g/10 min depending on part dimension. Thin-wall packaging articles with high requirements in terms of transparency require higher processability, but with appropriate nucleation leading to a high degree of γ -modification can still assure sufficient toughness [181]. The good stability of such materials in film hinges makes them also suitable candidates for closures in the soft drink and cosmetics segment (see Fig. 6.42).

The highest molecular weight random copolymers, corresponding to an MFR (230 °C/2.16 kg) of 0.2–0.6 g/10 min, are applied for hot water and other pressure pipes [182]. Both the shape of the MWD and the distribution of the comonomer are very important especially for the combination of impact strength and long-term pressure resistance [183]. β -nucleation has been found to be especially advantageous for crack growth resistance in such pipes (as in comparable homopolymers), even if processing effects need to be considered [51]. Only recently, random copolymers with hexene have been presented as possible alternative by one supplier [52].

Non-pressure pipes and especially sewage pipes, including even bigger infrastructural elements of wastewater disposal, can be produced efficiently from high stiffness heterophasic copolymers with high molecular weight matrix [182] and even improved with efficient nucleation systems [180]. Double wall constructions with corrugated structures in the outer wall improve the stability against compression and deformation by external loads like below roads, shown for example in Fig. 6.43. Next to excellent abrasion resistance and flexibility under shock loads, such sewage solutions are also characterized by their low weight reducing installation cost when compared to traditional materials like concrete.



Fig. 6.42 Sports drink bottle closures from nucleated high-flow C2C3 random copolymers (Borealis AG, Austria)



Fig. 6.43 Single- and double-wall sewage pipes with smooth and corrugated structures from high crystallinity EP-HECO grades (Borealis AG, Austria)

In food and non-food packaging, HECOs are applied for both film and injection molding applications. Numerous special grades have been developed in recent years, like sterilizable grades with high transparency combining a high crystallinity matrix with small elastomer particles for microwaveable stand-up pouches or high-flow grades with good performance at $-20\text{ }^{\circ}\text{C}$ for injection molded thin-wall deep-freeze and ice cream containers [184]. High-impact copolymers are also widely used for transport packaging systems like foldable fruit crates, re-usable boxes, trays and pails. In all these cases, next to cost and mechanical performance also sustainability factors are increasingly relevant for actual material selection [185].

In the appliance industry, and even more so in the automotive industry, high-impact HECOs sometimes also termed “reactor-based thermoplastic olefin elastomers” (RTPOs), are essential elements for compounds. Especially in the automotive industry, where PP is the biggest contributor to the polymeric materials in cars, these materials are mostly used in combination with fillers or reinforcements, like talc or glass fibers as outlined in Sect. 6.3.3 [186]. One type of parts showing the development of PP-based compounds since the market introduction in an excellent way are bumpers of passenger cars [187]. This application, which is also volume-wise highly relevant, started with the first use on a FIAT 127 in 1978. Through a combination of reactor-based copolymer development and advanced compounding, the performance as well as the variability of suitable PP grades has been enhanced continuously. Next to several steps in mechanical performance and processability, a number of problems generated by design novelties and increasing customer expectations had to be solved along the way: Shrinkage and dimensional stability [95], UV and thermal resistance, surface quality and paintability [188].

From there, the extension to body panels or even whole bodies of passenger cars but also very large parts in the exterior of trucks and busses has been a logical development. Figure 6.44 presents a recent example for the Smart ForTwo, where all parts of the body—with integrated bumpers—have been realized with an in-mold colored PP compound. In the automotive interior, ABS and other less satisfying material combinations, including the notorious plasticized PVC of the 1970s, have been replaced by PP-based materials. These are applied for dashboards, door claddings, consoles and other elements. An important success factor here is improved scratch resistance, requiring insight into the mechanisms responsible for scratch visibility [189]. Modifications with highly crystalline HDPE were found to be effective here, pointing at mechanistic similarities to stress whitening.

Soft copolymers like the aforementioned Catalloy grades [22] and RAHECOs [113] have also expanded the application range of PP copolymers. In the construction area, roofing membranes generally called “TPO membranes” are a rapidly growing class of compounds based on crosslinked ethylene-propylene-diene (EPDM) copolymers or soft PP copolymers [190] combining ease of installation (the thermoplastic version can be hot-welded) with longevity.

Flexibility in combination with transparency and maintenance of the same in steam sterilization is a typical set of requirements for medical articles and pharmaceutical packaging like pouches and bottles for infusions. Plasticized PVC and LDPE have been dominant materials here for a long time, the former suffering from



Fig. 6.44 Body of the Smart ForTwo produced from colored PP Daplen EF150HP (Borealis AG)



Fig. 6.45 Blow-fill-seal (BFS) bottles from soft copolymer Bormed SB815MO for infusion solutions (Borealis AG)

health and environmental concerns and the latter from limited thermal stability. RAHECO-based constructions can be applied both for pouches [152] and blow-fill-seal bottles (see Fig. 6.45). Here as well compounds with elastomeric

modifiers may be applied. One highly relevant type are styrene elastomers like SEBS, which have also been evaluated as modifiers for pure PP homopolymers [191]. In compounds with soft heterophasic copolymers the overall performance is, however, still better while the system cost can be reduced as well [192].

References

1. Ziegler K, Breil H, Holzkamp E et al (1953) High molecular polyethylenes. DE 973626, 18 Nov 1953
2. Natta G, Pino P, Mazzanti G (1954) Regular linear head-to-tail polymerizates of certain unsaturated hydrocarbons and filaments comprising said polymerizates. DE 1094985, 8 June 1954
3. Sivaram S (2017) Giulio Natta and the origins of stereoregular polymers. *Resonance* 11:1007–1023. <https://doi.org/10.1007/s12045-017-0568-9>
4. Natta G, Corradini P (1960) Structure and properties of isotactic polypropylene. *Il Nuovo Cimento* 15:40–51. <https://doi.org/10.1007/BF02731859>
5. Grebowicz J, Lau S-F, Wunderlich B (1984) The thermal properties of polypropylene. *J Polym Sci Polym Chem Ed* 22:19–37. <https://doi.org/10.1002/polc.5070710106>
6. Mühlhaupt R (2003) Catalytic polymerization and post polymerization catalysis fifty years after the discovery of Ziegler's catalysts. *Macromol Chem Phys* 204:289–327. <https://doi.org/10.1002/macp.200290085>
7. Gahleitner M, Hauer A, Bernreitner K et al (2002) Polypropylene-based model compounds as tools for the development of high-impact ethylene-propylene copolymers. *Intern Polym Proc* 17:1–7. <https://doi.org/10.3139/217.1709>
8. Natta G, Mazzanti G, Boschi G (1956) Improved process for the production of high molecular weight copolymers. DE 1293453, 22 Dec 1956
9. Chum SP, Swogger KW (2008) Olefin polymer technologies—history and recent progress at the dow chemical company. *Prog Polym Sci* 33:797–819. <https://doi.org/10.1016/j.progpolymsci.2008.05.003>
10. Ramsteiner F, Kanig G, Heckmann W et al (1983) Improved low temperature impact strength of polypropylene by modification with polyethylene. *Polymer* 24:365–370. [https://doi.org/10.1016/0032-3861\(83\)90278-1](https://doi.org/10.1016/0032-3861(83)90278-1)
11. Rümpler K-D, Jaggard JFR, Werner RA (1988) Polypropylen-blockcopolymer mit hohem kautschukgehalt durch polymerisation in der gasphase. *Kunststoffe* 78:602–605
12. Cecchin G, Morini G, Pelliconi G (2001) Polypropylene product innovation by reactor granule technology. *Macromol Symp* 173:195–209. [https://doi.org/10.1002/1521-3900\(200108\)173:1%3c195:aid-masy195%3e3.0.co;2-a](https://doi.org/10.1002/1521-3900(200108)173:1%3c195:aid-masy195%3e3.0.co;2-a)
13. Gahleitner M, Jääskeläinen P, Ratajski E et al (2005) Propylene–ethylene random copolymers: comonomer effects on crystallinity and application properties. *J Appl Polym Sci* 95:1073–1081. <https://doi.org/10.1002/app.21308>
14. Morini G, Albizzati E, Balbontin G et al (1996) Microstructure distribution of polypropylenes obtained in the presence of traditional phthalate/silane and novel diether donors: a tool for understanding the role of electron donors in MgCl₂-supported Ziegler–Natta catalysts. *Macromolecules* 29:5770–5776. <https://doi.org/10.1021/ma960070j>
15. Chadwick JC, van der Burgt FPTJ, Rastogi S et al (2004) Influence of Ziegler–Natta catalyst regioselectivity on polypropylene molecular weight distribution and rheological and crystallization behavior. *Macromolecules* 37:9722–9727. <https://doi.org/10.1021/ma048108c>

16. Wang Q, Murayama N, Liu B et al (2005) Effects of electron donors on active sites distribution of MgCl₂-supported Ziegler-Natta catalysts investigated by multiple active sites model. *Macromol Chem Phys* 206:961–966. <https://doi.org/10.1002/macp.200400502>
17. Busico V, Cipullo R (2001) Microstructure of polypropylene. *Prog Polym Sci* 26:443–533. [https://doi.org/10.1016/S0079-6700\(00\)00046-0](https://doi.org/10.1016/S0079-6700(00)00046-0)
18. Aarnio-Winterhof M, Doshev P, Seppälä J et al (2017) Structure-property relations of heterophasic ethylene-propylene copolymers based on a single-site catalyst. *Express Polym Lett* 11:152–161. <https://doi.org/10.3144/expresspolymlett.2017.16>
19. Fujiyama M, Inata H (2002) Crystallization and melting characteristics of metallocene isotactic polypropylenes. *J Appl Polym Sci* 85:1851–1857. <https://doi.org/10.1002/app.10797>
20. Boragno L, Resconi L, Lilja J et al (2013) Propylene copolymer with high impact properties. WO 2014/154610 A1, 26 Mar 2013
21. De Rosa C, Auriemma F, Vollaro P et al (2011) Crystallization behavior of propylene-butene copolymers: the trigonal form of isotactic polypropylene and form I of isotactic poly(1-butene). *Macromolecules* 44:540–549. <https://doi.org/10.1021/ma102534f>
22. Galli P, Vecellio G (2004) Polyolefins: the most promising large-volume materials for the 21st century. *J Polym Sci A Polym Chem* 42:396–415. <https://doi.org/10.1002/pola.10804>
23. Mei G, Herben P, Cagnani C et al (2006) The spherizone process: a new PP manufacturing platform. *Macromol Symp* 245–246:677–680. <https://doi.org/10.1002/masy.200651395>
24. Albizzati E (1998) In: Moore E.P. (eds.) *Polypropylene handbook*. Carl Hanser, Munich (1998), p 89
25. Vestberg T, Parkinson M, Fonseca I et al (2012) Poly(propylene-co-ethylene) produced with a conventional and a self-supported Ziegler-Natta catalyst: effect of ethylene and hydrogen concentration on activity and polymer structure. *J Appl Polym Sci* 124:4889–4896. <https://doi.org/10.1002/app.35586>
26. Agarwal V, van Erp T, Balzano L, et al (2014) The chemical structure of the amorphous phase of propylene-ethylene random copolymers in relation to their stress-strain properties. *Polymer* 55:896–905. <https://doi.org/10.1016/j.polymer.2013.12.051>
27. Jeon K, Chiari YL, Alamo RG (2008) Maximum rate of crystallization and morphology of random propylene ethylene copolymers as a function of comonomer content up to 21 mol %. *Macromolecules* 41:95–108. <https://doi.org/10.1021/ma070757b>
28. Stephens CH, Poon BC, Ansems P et al (2006) Comparison of propylene/ethylene copolymers prepared with different catalysts. *J Appl Polym Sci* 100:1651–1658. <https://doi.org/10.1002/app.23788>
29. Jeon K, Palza H, Quijada R et al (2009) Effect of comonomer type on the crystallization kinetics and crystalline structure of random isotactic propylene 1-alkene copolymers. *Polymer* 50:832–844. <https://doi.org/10.1016/j.polymer.2008.10.032>
30. De Rosa C, Auriemma F, Ballesteros O et al (2007) Crystallization behavior of isotactic propylene-ethylene and propylene-butene copolymers: effect of comonomers versus stereodefects on crystallization properties of isotactic polypropylene. *Macromolecules* 40:6600–6616. <https://doi.org/10.1021/ma070409+>
31. Alamo RG, VanderHart DL, Nyden Marc R et al (2000) Morphological partitioning of ethylene defects in random propylene-ethylene copolymers. *Macromolecules* 33:6094–6105. <https://doi.org/10.1021/ma000267i>
32. Hosier IL, Alamo RG, Estes P et al (2003) Formation of the α and γ polymorphs in random metallocene-propylene copolymers. Effect of concentration and type of comonomer. *Macromolecules* 36:5623–5636. <https://doi.org/10.1021/ma030157m>
33. Kissin YV, Fruitwala HA (2007) Analysis of polyolefins and olefin copolymers using Crystaf technique: resolution of Crystaf curves. *J Appl Polym Sci* 106:3872–3883. <https://doi.org/10.1002/app.27090>
34. Sangroniz L, Cavallo D, Santamaria A et al (2017) Thermorheologically complex self-seeded melts of propylene-ethylene copolymers. *Macromolecules* 50:642–651. <https://doi.org/10.1021/acs.macromol.6b02392>

35. Hosoda S, Hori H, Yada K et al (2002) Degree of comonomer inclusion into lamella crystal for propylene/olefin copolymers. *Polymer* 43:7451–7460. [https://doi.org/10.1016/S0032-3861\(02\)00680-8](https://doi.org/10.1016/S0032-3861(02)00680-8)
36. Auriemma F, De Rosa C, Di Girolamo R et al (2017) Yield behavior of random copolymers of isotactic polypropylene. *Polymer* 129:235–246. <https://doi.org/10.1016/j.polymer.2017.09.058>
37. Gahleitner M, Mileva D, Gloger D et al (2017) Polymer structure effects on crystallization and properties in polypropylene film casting. *AIP Conf Proc* 1914:130001. <https://doi.org/10.1063/1.5016762>
38. Cavallo D, Portale G, Balzano L et al (2010) Real-time WAXD detection of mesophase development during quenching of propene/ethylene copolymers. *Macromolecules* 43:10208–10212. <https://doi.org/10.1021/ma1022499>
39. Gahleitner M, Grein C, Blell R et al (2011) Sterilization of propylene/ethylene random copolymers: annealing effects on crystalline structure and transparency as influenced by polymer structure and nucleation. *Express Polym Lett* 5:788–798. <https://doi.org/10.3144/expresspolymlett.2011.77>
40. Resch K, Wallner GM, Teichert C et al (2007) Highly transparent polypropylene cast films: relationships between optical properties, additives, and surface structure. *Polym Eng Sci* 47:1021–1032. <https://doi.org/10.1002/pen.20781>
41. Gahleitner M, Fiebig J, Wolfschwenger J et al (2002) Post-crystallization and physical aging of polypropylene: material and processing effects. *J Macromol Sci Phys B* 41:833–849. <https://doi.org/10.1081/MB-120013068>
42. Mazzola N, Cáceres C, França M et al (2012) Correlation between thermal behavior of a sealant and heat sealing of polyolefin films. *Polym Test* 31:870–875. <https://doi.org/10.1016/j.polymertesting.2012.06.013>
43. Stehling F, Meka P (1994) Heat sealing of semicrystalline polymer films. II. Effect of melting distribution on heat-sealing behavior of polyolefins. *J Appl Polym Sci* 51:105–119. <https://doi.org/10.1002/app.1994.070510112>
44. Mirabella FM (1987) Determination of the crystalline and noncrystalline molecular orientation in oriented polypropylene by infrared spectroscopy. *J Polym Sci B Polym Phys* 25:591–602. <https://doi.org/10.1002/polb.1987.090250310>
45. Ibadon AO (1991) Effect of orientation on melting of isotactic polypropylene. *J Appl Polym Sci* 43:567–571. <https://doi.org/10.1002/app.1991.070430318>
46. Tetsuya T, Hashimoto Y, Ishiaku US et al (2006) Effect of heat-sealing temperature on the properties of OPP/PP heat seals. Part II. crystallinity and thermomechanical properties. *J Appl Polym Sci* 99:513–519. <https://doi.org/10.1002/app.22443>
47. Gahleitner M, Grein Kheirandish S et al (2011) Nucleation of polypropylene homo and copolymers. *Intern Polym Proc* 26:2–20. <https://doi.org/10.3139/217.2411>
48. Horváth Z, Menyhárd A, Doshev P et al (2016) Improvement of the impact strength of ethylene-propylene random copolymers by nucleation. *J Appl Polym Sci* 133:43823. <https://doi.org/10.1002/app.43823>
49. Grein C (2005) Toughness of neat, rubber modified and filled β -nucleated polypropylene: from fundamentals to applications. *Adv Polym Sci* 188:43–104. <https://doi.org/10.1007/b136972>
50. Benavente R, Caveda S, Perez E et al (2012) Influence of β -nucleation on polymorphism and properties in random copolymers and terpolymers of propylene. *Polym Eng Sci* 52:2285–2295. <https://doi.org/10.1002/pen.23322>
51. Boragno L, Braun H, Hartl AM (2017) Polypropylene for pressure pipes—from polymer design to long-term performance. In: Grellmann W, Langer B (eds) *Deformation and fracture behaviour of polymer materials*. Springer series in materials science. vol 247. Springer, Cham
52. LyondellBasell Industries Holdings B.V. (2016) Hostalen PP “XN” series pipe, leading the way. Information Brochure

53. Spalding MA, Chatterjee AM (eds) (2007) Handbook of industrial polyethylene and technology. Scrivener Publishing, Wiley, USA
54. Arnold M, Henschke O, Knorr J (1996) Copolymerization of propene and higher alpha-olefins with the metallocene catalyst Et[Ind]2HfCl₂/methylaluminoxane. *Macromol Chem Phys* 197:563–573. <https://doi.org/10.1002/macp.1996.021970212>
55. Quijada R, Guevara JL, Galland GB et al (2005) Synthesis and properties coming from the copolymerization of propene with alpha-olefins using different metallocene catalysts. *Polymer* 46:1567–1574. <https://doi.org/10.1016/j.polymer.2004.11.115>
56. Stagnaro P, Costa G, Trefiletti V et al (2004) Thermal behavior, structure and morphology of propene/higher 1-olefin copolymers. *Macromol Chem Phys* 207:2128–2141. <https://doi.org/10.1002/macp.200600288>
57. Palza H, Lopez-Majada JM, Quijada R et al (2008) Comonomer length influence on the structure and mechanical response of metallocenic polypropylenic materials. *Macromol Chem Phys* 209:2259–2267. <https://doi.org/10.1002/macp.200800294>
58. De Rosa C, Auriemma F, Ballesteros OR et al (2008) The double role of comonomers on the crystallization behavior of isotactic polypropylene: propylene-hexene copolymers. *Macromolecules* 41:2172–2177. <https://doi.org/10.1021/ma071753+>
59. Arranz-Andrés J, Suárez I, Pena B et al (2007) Metallocenic isotactic poly(propylene) and its copolymers with 1-hexene and ethylene. *Macromol Chem Phys* 208:1510–1521. <https://doi.org/10.1002/macp.200700115>
60. Van Reenen AJ (2003) Propene copolymers: an overview of recent research. *Macromol Symp* 193:57–70. <https://doi.org/10.1002/masy.200390064>
61. Locatelli P, Sacchi MC, Tritto I et al (1988) Propene/1-butene copolymerization with a heterogeneous Ziegler-Natta catalyst: inhomogeneity of isotactic active sites. *Macromol Chem Rapid Commun* 9:575–580. <https://doi.org/10.1002/marc.1988.030090812>
62. Dlubek G, Bamford D, Rodriguez-Gonzalez A et al (2002) Free volume, glass transition and degree of branching in metallocene-based propylene/alpha-olefin copolymers: positron lifetime, density, and differential scanning calorimetric studies. *J Polym Sci B Polym Phys* 40:434–453. <https://doi.org/10.1002/polb.10108>
63. Poon B, Rogunova M, Hiltner A et al (2005) Structure and properties of homogenous copolymers of propylene and 1-hexene. *Macromolecules* 38:1232–1243. <https://doi.org/10.1021/ma0488131>
64. Lotz B, Ruan J, Thierry A et al (2007) A structure of copolymers of propene and hexene isomorphous to isotactic poly(1-butene) form I. *Macromolecules* 39:5777–5781. <https://doi.org/10.1021/ma052314i>
65. Boragno L, Stagnaro P, Forlini F et al (2013) The trigonal form of i-PP in random C3/C5/C6 terpolymers. *Polymer* 54:1656–1662. <https://doi.org/10.1016/j.polymer.2013.01.041>
66. Majada-Lopez JM, Palza H, Guevara JL et al (2006) Metallocene copolymers of propene and 1-hexene: the influence of the comonomer content and thermal history on the structure and mechanical properties. *J Polym Sci Phys* 44:1253–1267. <https://doi.org/10.1002/polb.20781>
67. Lovisi H, Tavares MIB, de Silva NM et al (2001) Influence of comonomer content and short branch length on the physical properties of metallocene propylene copolymers. *Polymer* 42:9791–9799. [https://doi.org/10.1016/S0032-3861\(01\)00528-6](https://doi.org/10.1016/S0032-3861(01)00528-6)
68. Grein C, Bernreiter K, Gahleitner M (2004) Potential and limits of dynamic mechanical analysis as a tool for fracture resistance evaluation of isotactic polypropylenes and their polyolefin blends. *J Appl Polym Sci* 93:1854–1867. <https://doi.org/10.1002/app.20606>
69. Gahleitner M, Doshev P, Tranninger C (2013) Heterophasic copolymers of polypropylene—development, design principles and future challenges. *J Appl Polym Sci* 130:3028–3037. <https://doi.org/10.1002/app.39626>
70. ISO 16152:2005, Plastics—determination of xylene-soluble matter in polypropylene
71. Zacur R, Goizueta G, Capiati N (2000) Dispersed phase morphology of impact pp copolymers. Effects of blend composition as determined by TREF. *Polym Eng Sci* 40:1921–1930. <https://doi.org/10.1002/pen.11324>

72. Fernández A, Expósito MT, Peña B et al (2015) Molecular structure and local dynamic in impact polypropylene copolymers studied by preparative TREF, solid state NMR spectroscopy, and SFM microscopy. *Polymer* 61:87–98. <https://doi.org/10.1016/j.polymer.2015.01.079>
73. Santonja-Blasco L, Rungswang W, Alamo RG (2017) Influence of chain microstructure on LLPS and crystallization of dual reactor Ziegler-Natta made impact propylene ethylene copolymers. *Ind Eng Chem Res* 56:3270–3282. <https://doi.org/10.1021/acs.iecr.6b04708>
74. EN ISO 1628-3:2010, Plastics—determination of the viscosity of polymers in dilutesolution using capillary viscometers—part 3: polyethylenes and polypropylenes
75. Romero L, Ortín A, Monrabal B et al (2012) A new calibration method for the accurate determination of ethylene content in ethylene-propylene copolymers by CRYSTEX-IR. *Macromol Symp* 312:157–166. <https://doi.org/10.1002/masy.201100014>
76. Kim G-M, Michler GH (1998) Micromechanical deformation processes in toughened and particle-filled semicrystalline polymers: part 1. Characterization of deformation processes in dependence on phase morphology. *Polymer* 39:5689–5697. [https://doi.org/10.1016/S0032-3861\(98\)00089-5](https://doi.org/10.1016/S0032-3861(98)00089-5)
77. Kim G-M, Michler GH (1998) Micromechanical deformation processes in toughened and particle filled semicrystalline polymers: part 2. Model representation for micromechanical deformation processes. *Polymer* 39:5699–5703. [https://doi.org/10.1016/S0032-3861\(98\)00169-4](https://doi.org/10.1016/S0032-3861(98)00169-4)
78. Grein C, Bernreitner K, Hauer A et al (2003) Impact modified isotactic polypropylene with controlled rubber intrinsic viscosities: some new aspects about morphology and fracture. *J Appl Polym Sci* 87:1702–1712. <https://doi.org/10.1002/app.11696>
79. Starke J-U, Michler GH, Grellmann W et al (1998) Fracture toughness of polypropylene copolymers: influence of interparticle distance and temperature. *Polymer* 39:75–82. [https://doi.org/10.1016/S0032-3861\(97\)00219-X](https://doi.org/10.1016/S0032-3861(97)00219-X)
80. Kotter I, Grellmann W, Koch T et al (2006) Morphology–toughness correlation of polypropylene/ethylene–propylene rubber blends. *J Appl Polym Sci* 100:3364–3371. <https://doi.org/10.1002/app.23708>
81. Kojima M (1981) Stress whitening in crystalline propylene-ethylene block copolymers. *J Macromol Sci Phys B* 19:523–541. <https://doi.org/10.1080/00222348108015316>
82. Bakshi S, Kulshreshtha AK, Singh BP et al (1989) Stress-whitening of polypropylene block copolymer in impact tests and its measurement. *Polym Test* 8:191–199. [https://doi.org/10.1016/0142-9418\(88\)90010-4](https://doi.org/10.1016/0142-9418(88)90010-4)
83. Jang HJ, Kim S-D, Choi W et al (2012) Morphology and stress whitening of heterophasic poly(propylene) copolymer/high density polyethylene blends. *Macromol Symp* 312:34–42. <https://doi.org/10.1002/masy.201100021>
84. Gensler R, Plummer CJG, Grein C et al (2000) Influence of the loading rate on the fracture resistance of isotactic polypropylene and impact modified isotactic polypropylene. *Polymer* 41:3809–3819. [https://doi.org/10.1016/S0032-3861\(99\)00593-5](https://doi.org/10.1016/S0032-3861(99)00593-5)
85. Nachtnebel M, Rastel M, Mayrhofer C et al (2017) The fracture behaviour of particle modified polypropylene—3D reconstructions and interparticle distances. *Polymer* 126:65–73. <https://doi.org/10.1016/j.polymer.2017.08.029>
86. Poelt P, Zankel A, Gahleitner M et al (2010) Tensile tests in the environmental scanning electron microscope (ESEM)—part I: polypropylene homopolymers. *Polymer* 51:3203–3212. <https://doi.org/10.1016/j.polymer.2010.04.068>
87. Karger-Kocsis J, Friedrich K (1989) Effect of skin-core morphology on fatigue crack propagation in injection moulded polypropylene homopolymer. *Int J Fatigue* 11:161–168. [https://doi.org/10.1016/0142-1123\(89\)90435-0](https://doi.org/10.1016/0142-1123(89)90435-0)
88. Mirabella FM (1994) Phase separation and the kinetics of phase coarsening in commercial impact polypropylene copolymers. *J Polym Sci Phys* 32:1205–1216. <https://doi.org/10.1002/polb.1994.090320708>

89. Moffitt M, Rharbi Y, Chen W et al (2002) Stratified morphology of a polypropylene/elastomer blend following channel flow. *J Polym Sci Phys* 40:2842–2859. <https://doi.org/10.1002/polb.10301>
90. Karger-Kocsis J, Mouzakis DE (1999) Effects of injection molding-induced morphology on the work of fracture parameters in rubber-toughened polypropylenes. *Polym Eng Sci* 39:1365–1374. <https://doi.org/10.1002/pen.11525>
91. Housmans JW, Gahleitner M, Peters GWM et al (2009) Structure-property relations in molded, nucleated isotactic polypropylene. *Polymer* 50:2304–2319. <https://doi.org/10.1016/j.polymer.2009.02.050>
92. Zhong G-J, Li Z-M (2005) Injection molding-induced morphology of thermoplastic polymer blends. *Polym Eng Sci* 45:1655–1665. <https://doi.org/10.1002/pen.20448>
93. Grillet AM, Bogaerds ACB, Peters GWM et al (2002) Numerical analysis of flow mark surface defects in injection molding flow. *J Rheol* 46:651. <https://doi.org/10.1122/1.1459419>
94. Patham B, Papworth P, Jayaraman K et al (2005) Flow marks in injection molding of polypropylene and ethylene-propylene elastomer blends: analysis of morphology and rheology. *J Appl Polym Sci* 96:423–434. <https://doi.org/10.1002/app.21459>
95. Grestenberger G, Potter GD, Grein C (2014) Polypropylene/ethylene-propylene rubber (PP/EPR) blends for the automotive industry: basic correlations between EPR-design and shrinkage. *Express Polym Lett* 8:282–292. <https://doi.org/10.3144/expresspolymlett.2014.31>
96. Martuscelli E, Silvestre C, Abate G (1982) Morphology, crystallization and melting behaviour of films of isotactic polypropylene blended with ethylene-propylene copolymers and polyisobutylene. *Polymer* 23:229–237. [https://doi.org/10.1016/0032-3861\(82\)90306-8](https://doi.org/10.1016/0032-3861(82)90306-8)
97. Lin Z, Peng M, Zheng Q (2004) Isothermal crystallization behavior of polypropylene cataloys. *J Appl Polym Sci* 93:877–882. <https://doi.org/10.1002/app.20501>
98. Van Drongelen M, Gahleitner M, Spoelstra AB et al (2015) Flow-induced solidification of high-impact polypropylene copolymer compositions: morphological and mechanical effects. *J Appl Polym Sci* 132:42040. <https://doi.org/10.1002/app.42040>
99. Grein C, Gahleitner M, Knogler B et al (2007) Melt viscosity effects in ethylene-propylene copolymers. *Rheol Acta* 46:1083–1089. <https://doi.org/10.1007/s00397-007-0200-0>
100. Seppälä J, Härkönen M, Luciani L (1989) Effect of the structure of external alkoxyxilane donors on the polymerization of propene with high activity Ziegler-Natta catalysts. *Macromol Chem* 190:2535–2550. <https://doi.org/10.1002/macp.1989.021901019>
101. Gahleitner M, Bachner C, Ratajski E et al (1999) Effects of the catalyst system on the crystallization of polypropylene. *J Appl Polym Sci* 73:2507–2515. [https://doi.org/10.1002/\(SICI\)1097-4628\(19990919\)73:12%3c2507:AID-APP19%3e3.0.CO;2-V](https://doi.org/10.1002/(SICI)1097-4628(19990919)73:12%3c2507:AID-APP19%3e3.0.CO;2-V)
102. Pukánszky B, Mudra I, Staniek P (1997) Relation of crystalline structure and mechanical properties of nucleated polypropylene. *J Vin Add Tech* 3:53–58. <https://doi.org/10.1002/vnl.10165>
103. Gahleitner M, Wolfschwenger J, Bernreitner K et al (1996) Crystallinity and mechanical properties of PP-homopolymers as influenced by molecular structure and nucleation. *J Appl Polym Sci* 61:649–657. [https://doi.org/10.1002/\(SICI\)1097-4628\(19960725\)61:4%3c649:AID-APP8%3e3.0.CO;2-L](https://doi.org/10.1002/(SICI)1097-4628(19960725)61:4%3c649:AID-APP8%3e3.0.CO;2-L)
104. Van der Wal A, Mulder JJ, Oderkerk J, Gaymans RJ (1998) Polypropylene–rubber blends: 1. The effect of the matrix properties on the impact behaviour. *Polymer* 39, 6781–6787. [https://doi.org/10.1016/s0032-3861\(98\)00170-0](https://doi.org/10.1016/s0032-3861(98)00170-0)
105. Van der Meer DW, Varga J, Vancso GJ (2015) The influence of chain defects on the crystallization behaviour of isotactic polypropylene. *Express Polym Lett* 9:233–254. <https://doi.org/10.3144/expresspolymlett.2015.23>
106. Phillips R, Herbert G, News J et al (1994) High modulus polypropylene: effect of polymer and processing variables on morphology and properties. *Polym Eng Sci* 34:1731–1743. <https://doi.org/10.1002/pen.760342304>
107. Pantani R, Balzano L, Peters GMW (2012) Flow-induced morphology of iPP solidified in a shear device. *Macromol Mater Eng* 297:60–67. <https://doi.org/10.1002/mame.201100158>

108. Tranninger C, Doshev P, Potter E (2012) Heterophasic propylene copolymer with excellent impact/stiffness balance. EP 2601260 B1, 6 Aug 2010
109. Nagasawa S, Fujimori A, Masuko T et al (2005) Crystallisation of polypropylene containing nucleators. *Polymer* 46:5241–5250. <https://doi.org/10.1016/j.polymer.2005.03.099>
110. Menyhárd A, Gahleitner M, Varga J et al (2009) The influence of nucleus density on optical properties in nucleated isotactic polypropylene. *Eur Polym J* 45:3138–3148. <https://doi.org/10.1016/j.eurpolymj.2009.08.006>
111. Sun M, Gao D, Zhang H et al (2014) Toughening effects of nucleating agent on impact polypropylene copolymer. *J Appl Polym Sci* 131:40705. <https://doi.org/10.1002/app.40705>
112. Grein C, Gahleitner M (2008) On the influence of nucleation on the toughness of iPP/EPR blends with different rubber molecular architectures. *Express Polym Lett* 2:392–397. <https://doi.org/10.3144/expresspolymlett.2008.47>
113. Paulik C, Gahleitner M, Neißl W (1996) Flexible, tough and resilient PP-copolymers. *Kunstst Plast Eur* 86:16–17
114. Cecchin G, Giuglielmi F (1988) Propylene polymer compositions having good transparency and improved impact resistance. EP 0373660 A2, 14 Dec 1988
115. Cheruthazhekatt S, Pijpers TFJ, Harding GW et al (2012) Multidimensional analysis of the complex composition of impact polypropylene copolymers: combination of TREF, SEC-FTIR-HPer DSC, and high temperature 2D-LC. *Macromolecules* 45:2025–2034. <https://doi.org/10.1021/ma2026989>
116. Cheruthazhekatt S, Pijpers TFJ, Harding GW et al (2012) Compositional analysis of an impact polypropylene copolymer by fast scanning DSC and FTIR of TREF-SEC cross-fractions. *Macromolecules* 45:5866–5880. <https://doi.org/10.1021/ma3008702>
117. Pasch H, Albrecht A, Bruell R et al (2009) High temperature interaction chromatography of olefin copolymers. *Macromol Symp* 282:71–80. <https://doi.org/10.1002/masy.200950808>
118. Macko T, Ginzburg A, Remerie K et al (2012) Separation of high-impact polypropylene using interactive liquid chromatography. *Macromol Chem Phys* 213:937–944. <https://doi.org/10.1002/macp.201200017>
119. Kock C, Gahleitner M, Schausberger A et al (2013) Polypropylene/polyethylene blends as models for high-impact propylene-ethylene copolymers. 1: interaction between rheology and morphology. *J Appl Polym Sci* 128:1484–1496. <https://doi.org/10.1002/app.38289>
120. Tocháček J, Jančár J, Kalfus J et al (2011) Processing stability of polypropylene impact-copolymer during multiple extrusion—effect of polymerization technology. *Polym Deg Stab* 96:491–498. <https://doi.org/10.1016/j.polymdegradstab.2011.01.018>
121. Wu S (1985) Phase structure and adhesion in polymer blends: a criterion for rubber toughening. *Polymer* 26:1855–1863. [https://doi.org/10.1016/0032-3861\(85\)90015-1](https://doi.org/10.1016/0032-3861(85)90015-1)
122. Van der Wal A, Nijhof R, Gaymans RJ (1999) Polypropylene-rubber blends 2: the effect of the rubber content on the deformation and impact behaviour. *Polymer* 40:6031–6044. [https://doi.org/10.1016/S0032-3861\(99\)00213-X](https://doi.org/10.1016/S0032-3861(99)00213-X)
123. Debling JA, Ray WH (2011) Morphological development of impact polypropylene produced in gas phase with a TiCl₄/MgCl₂ catalyst. *J Appl Polym Sci* 81:3085–3106. <https://doi.org/10.1002/app.1761>
124. Kittilsen P, McKenna TF (2001) Study of the kinetics, mass transfer, and particle morphology in the production of high-impact polypropylene. *J Appl Polym Sci* 82:1047–1060. <https://doi.org/10.1002/app.1939>
125. Grof Z, Kosek J, Marek M (2005) Modeling of morphogenesis of growing polyolefin particles. *AIChE J* 51:2048–2067. <https://doi.org/10.1002/aic.10549>
126. Bouzid D, McKenna TFL (2006) Improving impact poly(propylene) morphology and production: selective poisoning of catalyst surface sites and the use of antistatic agents. *Macromol Chem Phys* 207:13–19. <https://doi.org/10.1002/macp.200500379>
127. Bartke M, Kröner S, Wittebrock A et al (2007) Sorption and diffusion of propylene and ethylene in heterophasic polypropylene copolymers. *Macromol Symp* 259:327–336. <https://doi.org/10.1002/masy.200751337>

128. Zubov A, Pechackova L, Seda L et al (2010) Transport and reaction in reconstructed porous polypropylene particles: model validation. *Chem Eng Sci* 65:2361–2372. <https://doi.org/10.1016/j.ces.2009.09.082>
129. Smolná K, Gregor T, Kosek J (2013) Morphological analysis of high-impact polypropylene using X-ray microCT and AFM. *Eur Polym J* 49:3966–3976. <https://doi.org/10.1016/j.eurpolymj.2013.08.030>
130. D’Orazio L, Mancarella C, Martuscelli E et al (1991) Polypropylene/ethylene-co-propylene blends: influence of molecular structure and composition of EPR on melt rheology, morphology and impact properties of injection-moulded samples. *Polymer* 32:1186–1194. [https://doi.org/10.1016/0032-3861\(91\)90220-D](https://doi.org/10.1016/0032-3861(91)90220-D)
131. Kontopoulou M, Wang W, Gopakumar TG et al (2003) Effect of composition and comonomer type on the rheology, morphology and properties of ethylene- α -olefin copolymer/polypropylene blends. *Polymer* 44:7495–7504. <https://doi.org/10.1016/j.polymer.2003.08.043>
132. Poelt P, Ingolic E, Gahleitner M et al (2000) Characterization of modified polypropylene by scanning electron microscopy. *J Appl Polym Sci* 78:1152–1161. [https://doi.org/10.1002/1097-4628\(20001031\)78:5%3c1152::AID-APP250%3e3.0.CO;2-7](https://doi.org/10.1002/1097-4628(20001031)78:5%3c1152::AID-APP250%3e3.0.CO;2-7)
133. Tanem BS, Kamfjord T, Augestad M et al (2003) Sample preparation and AFM analysis of heterophase polypropylene systems. *Polymer* 44:4283–4291. [https://doi.org/10.1016/S0032-3861\(03\)00392-6](https://doi.org/10.1016/S0032-3861(03)00392-6)
134. D’Orazio L, Mancarella C, Martuscelli E et al (1991) Polypropylene/ethylene-co-propylene blends: influence of molecular structure of EPR and composition on phase structure of isothermally crystallized samples. *J Mater Sci* 26:4033–4047. <https://doi.org/10.1007/BF02402944>
135. Nomura T, Nishio T, Fujii T et al (1995) Compatibility and tensile behavior of polypropylene/ethylene-propylene rubber blends. *Polym Eng Sci* 35:1261–1271. <https://doi.org/10.1002/pen.760351602>
136. Doshev P, Lach R, Lohse G et al (2005) Fracture characteristics and deformation behavior of heterophasic ethylene–propylene copolymers as a function of the dispersed phase composition. *Polymer* 46:9411–9422. <https://doi.org/10.1016/j.polymer.2005.07.029>
137. Torgersen U, De Mink P, Bernreiter K (2002) Flat film for thermoforming and process for its manufacturing. *EP* 1572785 B1, 18 Dec 2002
138. Doshev P, Lohse G, Henning S et al (2006) Phase interactions and structure evolution of heterophasic ethylene–propylene copolymers as a function of system composition. *J Appl Polym Sci* 101:2825–2837. <https://doi.org/10.1002/app.22921>
139. Massari P, Ciarafoni M, News J (2004) Polyolefinic compositions having good whitening resistance. *EP* 1828304 B1, 23 Dec 2004
140. Tian Y, Song S, Feng J et al (2012) Phase morphology evolution upon melt annealing treatment and corresponding mechanical performance of impact-resistant polypropylene copolymer. *Mat Chem Phys* 133:893–900. <https://doi.org/10.1016/j.matchemphys.2012.01.113>
141. Fan Z-Q, Zhang Y-Q, Xu J-T et al (2003) Structure and properties of polypropylene/poly(ethylene-co-propylene) in-situ blends synthesized by spherical Ziegler-Natta catalyst. *Eur Polym J* 39:795–804. [https://doi.org/10.1016/S0032-3861\(01\)00062-3](https://doi.org/10.1016/S0032-3861(01)00062-3)
142. Lu L, Fan H, Li B-G et al (2009) Polypropylene and ethylene–propylene copolymer reactor alloys prepared by metallocene/Ziegler–Natta hybrid catalyst. *Ind Eng Chem Res* 48:8349–8355. <https://doi.org/10.1021/ie900579h>
143. Tynys A, Saarinen T, Hakala K et al (2005) Ethylene–propylene copolymerisations: effect of metallocene structure on termination reactions and polymer microstructure. *Macromol Chem Phys* 206:1043–1056. <https://doi.org/10.1002/macp.200400523>
144. Karger-Kocsis J, Kiss L (1987) Dynamic mechanical properties and morphology of polypropylene block copolymers and polypropylene/elastomer blends. *Polym Eng Sci* 27:254–262. <https://doi.org/10.1002/pen.760270404>

145. Okamoto Y, Miyagi H, Kakugo M et al (1991) Impact improvement mechanism of HIPS with bimodal distribution of rubber particle size. *Macromolecules* 24:5639–5644. <https://doi.org/10.1021/ma00020a024>
146. Paul S, Kale DD (2000) Impact modification of polypropylene copolymer with a polyolefinic elastomer. *J Appl Polym Sci* 76:1480–1484. [https://doi.org/10.1002/\(sici\)1097-4628\(20000531\)76:9%3c1480::AID-APP12%3e3.0.CO;2-K](https://doi.org/10.1002/(sici)1097-4628(20000531)76:9%3c1480::AID-APP12%3e3.0.CO;2-K)
147. Massari P, News J, Ciarafoni M (2004) Impact resistant polyolefin compositions. EP 1747249 B1, 21 May 2004
148. Grein C, Bernreitner K, Berger F (2004) Novel polypropylene compositions. EP 1769029 B1, 27 May 2004
149. Grein C, Bernreitner K, Thermoplastic polyolefins with high flowability and excellent surface quality produced by a multistage process. EP 2294129 B1, 16 Jun 2008
150. Hobbs SY, Dekkers MEJ, Watkins VH (1988) Effect of interfacial forces on polymer blend morphologies. *Polymer* 29:1598–1602. [https://doi.org/10.1016/0032-3861\(88\)90269-8](https://doi.org/10.1016/0032-3861(88)90269-8)
151. Luzinov I, Pagnouille C, Jerome R (2000) Ternary polymer blend with core–shell dispersed phases: effect of the core-forming polymer on phase morphology and mechanical properties. *Polymer* 41:7099–7109. [https://doi.org/10.1016/S0032-3861\(00\)00057-4](https://doi.org/10.1016/S0032-3861(00)00057-4)
152. Sandholzer M, Bernreitner K, Klimke K (2016) Polypropylene and polypropylene-elastomer blends for medical packaging. *AIP Conf Proc* 1779:110001. <https://doi.org/10.1063/1.4965575>
153. Leong YW, Abu Bakar MB, Mohd Ishak ZA et al (2004) Comparison of the mechanical properties and interfacial interactions between talc, kaolin, and calcium carbonate filled polypropylene composites. *J Appl Polym Sci* 91:3315–3326. <https://doi.org/10.1002/app.13542>
154. Hadal R, Dasari A, Rohrmann J et al (2004) Susceptibility to scratch surface damage of wollastonite- and talc-containing polypropylene micrometric composites. *Mat Sci Eng A* 380:326–339. <https://doi.org/10.1016/j.msea.2004.03.058>
155. Saw LT, Lan DNU, Abdul Rahim NA (2015) Processing degradation of polypropylene-ethylene copolymer-kaolin composites by a twin-screw extruder. *Polym Deg Stab* 111:32–37. <https://doi.org/10.1016/j.polymdegradstab.2014.10.024>
156. Yu B, Geng C, Zhou M et al (2016) Impact toughness of polypropylene/glass fiber composites: interplay between intrinsic toughening and extrinsic toughening. *Comp B* 92:413–419. [10.1016/j.compositesb.2016.02.040](https://doi.org/10.1016/j.compositesb.2016.02.040)
157. Sudár A, Renner K, Móczó J et al (2016) Fracture resistance of hybrid PP/elastomer/wood composites. *Comp Struct* 141:146–154. <https://doi.org/10.1016/j.compstruct.2016.01.031>
158. Liu Y, Zhang X, Song C et al (2015) An effective surface modification of carbon fiber for improving the interfacial adhesion of polypropylene composites. *Mater Design* 88:810–819. <https://doi.org/10.1016/j.matdes.2015.09.100>
159. Gahleitner M, Grein C, Bernreitner K (2012) Synergistic mechanical effects of calcite micro- and nanoparticles and β -nucleation in polypropylene copolymers. *Eur Polym J* 48:49–59. <https://doi.org/10.1016/j.eurpolymj.2011.10.013>
160. Liu X, Miao X, Guo M et al (2015) Influence of the HDPE molecular weight and content on the morphology and properties of the impact polypropylene copolymer/HDPE blends. *RSC Adv* 5:80297–80306. <https://doi.org/10.1039/C5RA08517A>
161. Wolfschwenger J, Härkönen M (2000) Polyolefin compositions with improved properties. EP 1702956 B1, 29 Nov 2000
162. Wolfschwenger J, Grein C, Bernreitner K (2004) Novel propylene polymer compositions. EP 1833909 B1, 18 Nov 2004
163. Grein C, Gahleitner M, Bernreitner K (2012) Mechanical and optical effects of elastomer interaction in polypropylene modification: ethylene-propylene rubber, poly-(ethylene-co-octene) and styrene-butadiene elastomers. *Express Polym Lett* 6:688–696. <https://doi.org/10.3144/expresspolymlett.2012.74>

164. Kock C (2009) Correlations between molecular structure and mechanical properties of selected ethylene-propylene copolymers. Ph.D. thesis. Johannes Kepler University Linz, Austria
165. Kolařík J, Jančář J (1992) Ternary composites of polypropylene/elastomer/calcium carbonate: effect of functionalized components on phase structure and mechanical properties. *Polymer* 33:4961–4967. [https://doi.org/10.1016/0032-3861\(92\)90046-Y](https://doi.org/10.1016/0032-3861(92)90046-Y)
166. Premphet K, Horanont P (2000) Phase structure of ternary polypropylene/elastomer/ filler composites: effect of elastomer polarity. *Polymer* 41:9283–9290. [https://doi.org/10.1016/S0032-3861\(00\)00303-7](https://doi.org/10.1016/S0032-3861(00)00303-7)
167. Stockreiter W, Schininger R, Kastl J (2007) Improved glass fibre reinforced polypropylene. EP 2212381 B1, 20 Nov 2007
168. Tzoganakis C, Vlachopoulos J, Hamielec AE (1988) Production of controlled-rheology polypropylene resins by peroxide promoted degradation during extrusion. *Polym Eng Sci* 28:170–180. <https://doi.org/10.1002/pen.760280308>
169. Sandholzer M, Knall AC, Gahleitner M et al. (2010) Peroxide-induced degradation of impact PP: the influence of rubber design. Proc Polym Proc Soc. European Meeting. Istanbul, Turkey, 20–23 Oct 2010
170. Pham T, Gahleitner M (2005) Interfacial strengthening of high impact polypropylene compounds by reactive modification. *Compos Interf* 12:707–723. <https://doi.org/10.1163/156855405774984129>
171. Rätzsch M, Bucka H, Hesse A et al (1997) Modified polypropylene having improved processability. EP 0879830 B1, 20 May 1997
172. Krause B, Stephan M, Volkland S et al (2006) Long-chain branching of polypropylene by electron-beam irradiation in the molten state. *J Appl Polym Sci* 99:260–265. <https://doi.org/10.1002/app.22471>
173. Rajeshbabu R, Gohs U, Naskar K et al (2011) Preparation of polypropylene (PP)/ethylene octene copolymer (EOC) thermoplastic vulcanizates (TPVs) by high energy electron reactive processing. *Rad Phys Chem* 80:1398–1405. <https://doi.org/10.1016/j.radphyschem.2011.07.001>
174. Aghjeh MR, Khonakdar HA, Jafari SH et al (2016) Rheological, morphological and mechanical investigations on ethylene octene copolymer toughened polypropylene prepared by continuous electron induced reactive processing. *RSC Adv* 6:24651. <https://doi.org/10.1039/C6RA000359A>
175. Mei G, Beccarini E, Caputo T et al (2009) Recent technical advances in polypropylene. *J Plast Film Sheet* 25:95–113. <https://doi.org/10.1177/8756087909343500>
176. Sedighiamiri A, Van Erp TB, Peters GWM et al (2010) Micromechanical modeling of the elastic properties of semicrystalline polymers: a three-phase approach. *J Polym Sci Phys* 48:2173–2184. <https://doi.org/10.1002/polb.22099>
177. Mileva D, Androsch R, Radosch H-J (2009) Effect of structure on light transmission in isotactic polypropylene and random propylene-1-butene copolymers. *Polym Bull* 62:561–571. <https://doi.org/10.1007/s00289-008-0034-7>
178. Zhang XM, Ajji A (2005) Oriented structure of PP/LLDPE multilayer and blends films. *Polymer* 46:3385–3393. <https://doi.org/10.1016/j.polymer.2005.03.004>
179. Bernreiter K, Doshev P (2010) Polypropylene bottles. WO 2011131578 A1, 20 Apr 2010
180. Horváth Z, Menyhárd A, Doshev P et al (2014) Effect of the molecular structure of the polymer and nucleation on the optical properties of polypropylene homo- and copolymers. *Appl Mater Interf* 10:7456–7463. <https://doi.org/10.1021/am5008535>
181. Gahleitner M, Mileva D, Androsch R et al (2016) Crystallinity-based product design: utilizing the polymorphism of isotactic PP homo- and copolymers. *Intern Polym Proc* 31:618–627. <https://doi.org/10.3139/217.3242>
182. Wassenaar J (2016) Polypropylene materials for sewerage & drainage pipes with reduced energy and carbon footprints. *J Mat Sci Eng B* 6:283–290. <https://doi.org/10.17265/2161-6221/2016.11-12.003>

183. Yu L, Wu T, Chen T et al (2014) Polypropylene random copolymer in pipe application: performance improvement with controlled molecular weight distribution. *Thermochim Acta* 578:43–52. <https://doi.org/10.1016/j.tca.2013.11.009>
184. Braun J, Gahleitner M, Jerabek M et al (2016) Polypropylene (PP). *Kunstst Int* 106:18–26
185. Verghese K, Crossin E, Jollands M (2012) Packaging Materials. In: Verghese K, Lewis H, Fitzpatrick L (eds) *Packaging for sustainability*. Springer, London, pp 211–250
186. Moritomi S, Tsuyoshi Watanabe T, Kanzaki S (2010) Polypropylene compounds for automotive applications, translated from R&D report, “Sumitomo Kagaku”, vol 2010-I. Available online at <http://www.sumitomo-chem.co.jp>
187. Liu GY, Qiu GX (2013) Study on the mechanical and morphological properties of toughened polypropylene blends for automobile bumpers. *Polym Bull* 70:849–857. <https://doi.org/10.1007/s00289-012-0880-1>
188. Ernst E, Reussner J, Poelt P et al (2005) Surface stability of polypropylene compounds and paint adhesion. *J Appl Polym Sci* 97:797–805. <https://doi.org/10.1002/app.21743>
189. Koch T, Machl D (2007) Evaluation of scratch resistance in multiphase PP blends. *Polym Testing* 26:927–936. <https://doi.org/10.1016/j.polymertesting.2007.06.006>
190. Paroli RM, Liu KKY, Simmons TR (1999) Thermoplastic polyolefin roofing membranes, construction technology update no. 30, 1999. Available online from <http://irc.nrc-cnrc.gc.ca>
191. Matsuda Y, Hara M, Mano T et al (2005) The effect of the volume fraction of dispersed phase on toughness of injection molded polypropylene blended with SEBS, SEPS, and SEP. *Polym Eng Sci* 45:1630–1638. <https://doi.org/10.1002/pen.20298>
192. Gahleitner M, Sandholzer M, Bernreitner K (2012) Soft polypropylene with improved optical properties. *EP* 2831169 B1, 29 Mar 2012
193. NexantThinking™, Petrochemical market dynamics—polyolefins, July 2015

Chapter 7

Particulate Filled Polypropylene: Structure and Properties



János Móczó and Béla Pukánszky

Contents

7.1	Introduction.....	358
7.2	Factors Determining the Properties of Particulate Filled Polymers	360
7.3	Filler Characteristics	362
7.3.1	Particle Size and Distribution.....	362
7.3.2	Specific Surface Area, Surface Energy	363
7.3.3	Particle Shape	363
7.3.4	Other Characteristics	364
7.4	Structure.....	365
7.4.1	Crystalline Matrices, Nucleation	365
7.4.2	Segregation, Attrition	367
7.4.3	Aggregation	367
7.4.4	Orientation of Anisotropic Particles.....	369
7.5	Interfacial Interactions, Interphase	370
7.5.1	Type and Strength of Interaction	371
7.5.2	Interphase Formation.....	373
7.6	Surface Modification	377
7.6.1	Non-reactive Treatment	377
7.6.2	Coupling	379
7.6.3	Functional Polymers	380
7.6.4	Soft Interlayer	381

J. Móczó · B. Pukánszky (✉)

Department of Physical Chemistry and Materials Science, Laboratory of Plastics and Rubber Technology, Faculty of Chemical Technology and Biotechnology, Budapest University of Technology and Economics, Budapest 1521 P.O. Box 91 Hungary
e-mail: bpukanszky@mail.bme.hu

J. Móczó

e-mail: jmocz@mail.bme.hu

J. Móczó · B. Pukánszky

Research Centre for Natural Sciences, Institute of Materials and Environmental Chemistry, Hungarian Academy of Sciences, Budapest 1519 P.O. Box 286 Hungary

© Springer Nature Switzerland AG 2019

J. Karger-Kocsis and T. Bárány (eds.), *Polypropylene Handbook*,

https://doi.org/10.1007/978-3-030-12903-3_7

357

7.7	Local Micromechanical Deformations	382
7.7.1	Stress Distribution	382
7.7.2	Debonding	382
7.7.3	Other Deformation Mechanisms	383
7.8	Properties	385
7.8.1	Rheological Properties	386
7.8.2	Stiffness	387
7.8.3	Properties Measured at Large Deformations	388
7.8.4	Fracture and Impact Resistance	390
7.8.5	Flammability	391
7.8.6	Conductivity	391
7.8.7	Other Properties	392
7.9	Special Composites	393
7.9.1	Multicomponent Materials	393
7.9.2	Layered Silicate Nanocomposites	396
7.9.3	Natural Reinforcements (Wood, Lignin)	399
7.10	Conclusions	403
	References	404

Abstract The characteristics of all heterogeneous polymer systems including composites containing either micro or nano fillers are determined by four factors: component properties, composition, structure and interfacial interactions. The most important filler characteristics are particle size, size distribution, specific surface area and particle shape, while the main matrix property is stiffness. Segregation, aggregation and the orientation of anisotropic particles determine structure. Interfacial interactions lead to the formation of a stiff interphase considerably influencing properties. Interactions are changed by surface modification, which must be always system specific and selected according to its goal. Under the effect of external load inhomogeneous stress distribution develops around heterogeneities, which initiate local deformation processes determining the macroscopic properties of the composites. In filled polymers, the dominating deformation mechanism is usually debonding. Particulate filled polypropylene is used in many areas, but development never stops. Natural fiber and wood reinforced polymers, layered silicate nanocomposites and hybrid composites are in the focus of attention in recent times.

7.1 Introduction

Particulate filled polymers are used in very large quantities in all kinds of applications from the building industry [1], through automotive parts [2] and household articles, to sanitary films [3, 4]. The use of fillers is an established technology today, thus research and development is not as much in the center of attention in this field as for example in the area of nanocomposites [5]. However, we must consider the relative amount of particulate fillers used compared to clays and other nanofillers.

Table 7.1 Consumption of particulate fillers in Europe in 2017, Courtesy of Roger Rothon

Filler	Amount (ton)
Carbon black	12,000,000
Natural calcium carbonate	12,000,000
Kaolin	1,750,000
Precipitated silica and fumed silica	1,510,000
Talc	1,000,000
Aluminum hydroxide	950,000
Barium sulphate	350,000
Natural fibers	350,000
Crystalline silica	300,000
Precipitated calcium carbonate	275,000
Calcined kaolin	175,000
Wollastonite	150,000
Others	250,000
Total	3,106,000

The total consumption of fillers in Europe alone is currently estimated around 30 million tons (Table 7.1) [6], while GE used about 270 tons of nanocomposite material in 2004, which included the polymer as well [8]. In spite of the overwhelming interest in nanocomposites, biomaterials and natural fiber reinforced composites, considerable research and development is done also on particulate filled polymers.

The reason for the continuing interest in traditional composites lays, among others, in the changed role of particulate fillers. At the early days, fillers were added to the polymer to reduce price. However, the ever-increasing technical and aesthetic requirements as well as soaring material and compounding costs require the utilization of all possible advantages of fillers. Particulate filled polymers possess numerous advantages over their non-modified counterparts. Fillers increase stiffness and heat deflection temperature, decrease shrinkage and improve the appearance of the composites [7–10]. Productivity can be also increased in most processing technologies through their decreased specific heat and increased heat conductivity [11–13]. Fillers are very often introduced into the polymer to create new functional properties not possessed by the matrix polymer at all, like flame retardance or conductivity, thus creating principally new materials [14, 15]. Another reason for the considerable research activity is the appearance of new fillers and reinforcements like layered silicates [5, 16–22], wood flour [30–37], sepiolite [23–26], halloysite [17, 27–29], carbon nanotubes [30–34], graphite and graphene [33, 35–37], etc. which have not been used as fillers at all or only in small quantities earlier.

The properties of all heterogeneous polymer systems are determined by the same four factors: component properties, composition, structure and interfacial interactions [7, 38]. Although certain fillers and reinforcements like layered silicates, other nanofillers, or natural fibers possess special characteristics, the effect of these four

factors are universal and valid for all particulate filled materials. Consequently, in this chapter we focus our attention on them and discuss the most important theoretical and practical aspects of composite preparation and use. Because, unlike many others, we believe that the general rules of heterogeneous materials apply also for nano- and wood reinforced composites, they are also included in this paper, but we point out differences and special questions related to them.

Polypropylene is one of the leading commodity material used in increasing quantities in all fields of life. Its growth rate is one of the largest, if not the largest, among all polymers. Its success is due to its excellent properties, versatility and advantageous price. Soft and flexible products and stiff engineering materials can all be prepared from PP with the appropriate modification of its structure and composition. Further extension of its property profile is possible with fillers and reinforcements. Relatively large amount of a wide range of fillers are used in PP from CaCO_3 and talc through wood and natural fibers to long carbon fibers. Although the variety of fillers and reinforcements is large, the factors and rules determining the properties of PP composites are universal, as pointed out above. Accordingly, we cite references also for other polymers in this chapter, but focus specifically on PP and its copolymers.

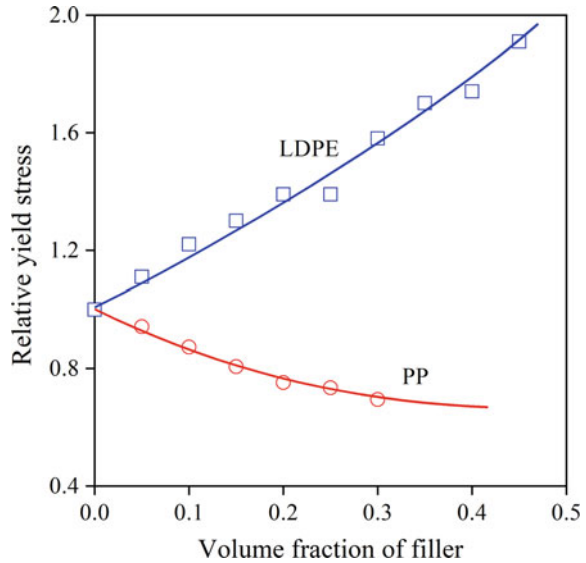
7.2 Factors Determining the Properties of Particulate Filled Polymers

All four factors mentioned in the previous section are equally important in the determination of composite properties and they must be adjusted to achieve optimum performance and economics.

Component properties. The characteristics of the matrix strongly influence the effect of the filler on composite properties; reinforcing effect increases with decreasing matrix stiffness. True reinforcement takes place in elastomers, both stiffness and strength increase [39, 40]. This effect is demonstrated well by Fig. 7.1, in which the tensile yield stress of CaCO_3 composites is plotted against composition for two different matrices. LDPE is reinforced by the filler, while the yield stress of PP containing the same filler decreases continuously with increasing filler content [41, 42]. For the sake of easier comparison, the data were plotted on a relative scale, related to the yield stress of the matrix. The direction of the change in yield stress or strength is determined by the relative load bearing capacity of the components [43, 44]. In weak matrices, the filler carries a significant part of the load; it reinforces the polymer.

Composition. Composition, i.e. the filler content of composites may change in a wide range. The effect of changing composition on composite properties is clearly seen in Fig. 7.1. The interrelation of various factors determining composite

Fig. 7.1 Effect of matrix properties on the tensile yield stress of particulate filled composites. Particle size of CaCO_3 , $R = 1.8 \mu\text{m}$. Symbols: (open circle) PP, (open square) LDPE



properties is also demonstrated by the Fig. 7.1, the same property may change in a different direction as a function of matrix characteristics, or interfacial adhesion. The goal of the use of fillers is either to decrease cost or to improve properties, e.g. stiffness, dimensional stability, etc. These goals require the introduction of the largest possible amount of filler into the polymer, but the improvement of the targeted property may be accompanied by the deterioration of others. Since various properties depend in a different way on filler content, composite properties must be always studied as a function of composition.

Structure. The structure of particulate filled polymers seems to be simple, the homogeneous distribution of particles in the polymer matrix is assumed in most cases. This, however, rarely occurs and often special, particle related structures develop in the composites. The most important of these are aggregation and the orientation of anisotropic filler particles.

Interfacial interactions. Particle/particle interactions induce aggregation, while matrix/filler interactions lead to the development of an interphase with properties different from those of both components. Secondary, van der Waals forces play a crucial role in the development of both kinds of interactions. They are usually modified by the surface treatment of the filler. Reactive treatment, i.e. coupling, is also used occasionally, although its importance is smaller in thermo-plastics than in thermoset matrices.

7.3 Filler Characteristics

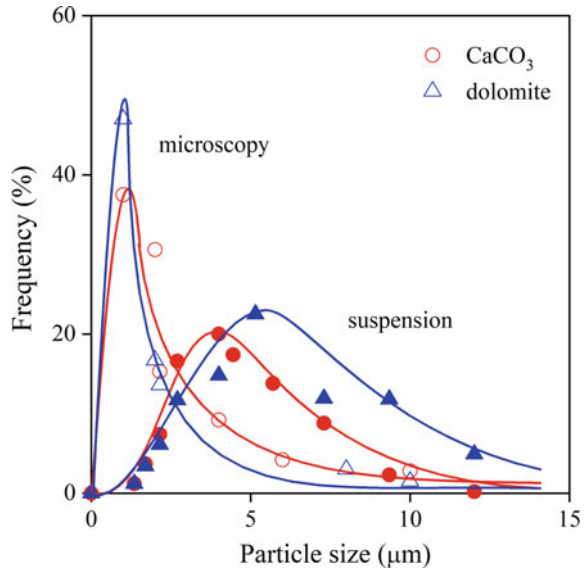
The chemical composition of fillers, which is usually supplied by the producer as relevant information, is not sufficient for their characterization [7], further physical, mostly particle characteristics are needed to forecast their performance in a composite for any application [7]. A large variety of materials are used as fillers in composites. Besides CaCO_3 and carbon black (see Table 7.1) a large number of other materials like talc [45–47], mica [48, 49], short [50, 51] and long glass fibers [52, 53], glass beads [54–56], sepiolite [23, 24, 57], magnesium and aluminum hydroxide [58–62], wood flour and cellulose [63–68], wollastonite [69–71], gypsum [72, 73], clay [74–76], metal powders [77–81], steel fibers [82], silicon carbide [83], phenolic microspheres [84] and diverse flame retardants [85, 86] are also mentioned as potential fillers or reinforcements.

7.3.1 Particle Size and Distribution

The mechanical properties of polymer composites containing uncoated fillers are determined mainly by their particle characteristics. One of the basic information supplied by the manufacturer is average particle size. Particle size has a pronounced influence on composite properties [7, 87]. Modulus, sometimes strength increase, deformability and impact resistance usually decrease with decreasing particle size. Particle size itself, however, is not sufficient for the characterization of any filler; the knowledge of the particle size distribution is equally important [7]. Large particles usually deteriorate the deformation and failure characteristics of composites. Large particles easily debond from the matrix under loading often leading to the premature failure of the part. Debonding stress decreases with increasing particle size [88, 89]. The other end of the particle size distribution, i.e. the amount of small particles, is equally important. The aggregation tendency of fillers increases with decreasing particle size [90]. Extensive aggregation leads to insufficient homogeneity, rigidity and low impact strength as aggregated filler particles act as crack initiation sites [90–92].

The particle size distribution of fillers is usually determined in dispersion by light scattering. This, however, can be very misleading. The particle size distribution of two fillers is presented in Fig. 7.2. Both fillers have a tendency for aggregation, since they contain a fraction of small particles, and the particle size distributions determined by scattering and microscopy differ significantly from each other. These differences appear also in the properties of the composites.

Fig. 7.2 Particle size distributions of fillers showing a tendency for agglomeration. Dependence of distribution on the method of determination. Symbols: (open circle) CaCO₃, (open triangle) dolomite; empty: microscopy, full: suspension



7.3.2 Specific Surface Area, Surface Energy

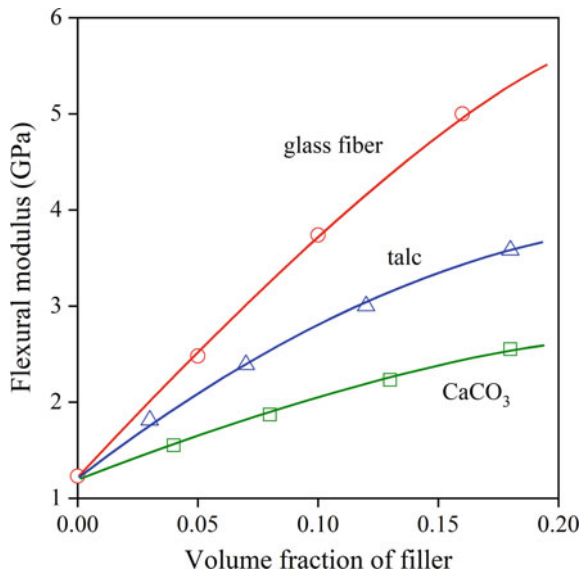
The specific surface area of fillers is closely related to their particle size distribution and it has a direct impact on composite properties. The adsorption of small molecular weight additives, but also that of the polymer is proportional to the area of the matrix/filler interface [7]. The adsorption of additives may change stability, while matrix/filler interaction significantly influences mechanical properties, first of all yield stress, tensile strength and impact resistance [43, 44].

The surface energy of fillers determines both matrix/filler and particle/particle interactions. The former has a pronounced effect on the mechanical properties of the composite; the latter determines aggregation [7, 93]. Both interactions can be modified by surface treatment. Non-reactive treatment leads to improved dispersion, but to decreased matrix/filler interaction [93], while chemical or physical coupling results in improved strength [94, 95]. Some fillers and reinforcements are supplied with surface coating. The amount and character of the coating must be known for the successful application of the filler.

7.3.3 Particle Shape

The shape of the particles influences the reinforcing effect of the filler, which increases with the anisotropy of the particle. Fillers and reinforcements are very often differentiated by their degree of anisotropy (aspect ratio). Fillers with plate-like geometry like talc, mica, or layered silicates reinforce polymers more than

Fig. 7.3 Effect of filler anisotropy on the flexural modulus of PP composites ([101], [102]). Symbols: (open circle) glass fiber, (open triangle) talc, (open square) CaCO_3



spherical fillers and the influence of glass fibers is expected to be even stronger (see Fig. 7.3) [7]. However, based on published papers, it is difficult to obtain a clear picture about the effect of particle characteristics on composite properties for anisotropic fillers. Modulus seems to increase with aspect ratio [96, 97], although Parrinello [98] found the stiffness of short glass fiber filled PP to be independent both of the length and the diameter of the fibers. According to Riley [99], impact resistance increases with decreasing particle size, since large particles act as flaws, while large aspect ratio is claimed to result in increased stress concentration. Tensile strength is said to decrease with increasing particle size, although Trotignon [100] did not observe any change in strength as a function of this characteristic. In spite of these contradictions, or just because of them, it is clear that the aspect ratio and its distribution also must be considered in the application of anisotropic fillers. Anisotropic fillers orientate during processing and they reinforce the polymer only if their orientation is parallel to the direction of the load. Since orientation is often not determined, the real effect of aspect ratio or particle characteristics in general is difficult to judge.

7.3.4 Other Characteristics

The *chemical composition* and especially the *purity* of fillers have both direct and indirect effect on their application possibilities and performance. Traces of heavy metal contamination decrease the stability of polyolefins [7] and lead to the discoloration of the product. Fillers are surface coated in most applications; coupling

agents must be chosen according to the chemical characteristics of both the filler and the polymer matrix. The *hardness* of the filler has a strong effect on the wear of the processing equipment [7], but the size and shape of the particles, composition, viscosity, the rate of processing also influence wear [7]. The *thermal properties* of fillers usually have beneficiary effect on productivity and processing. Decreased heat capacity and increased heat conductivity decrease cooling time [7]. Changing overall thermal properties result in the modification of the skin/core morphology of crystalline polymers and the properties of injection-molded parts. On the other hand, large differences in the thermal properties of the components may lead to the development of thermal stresses [103, 104], which might be detrimental to properties.

Fillers are frequently added to polymers to achieve *functional properties* not possessed by the matrix polymer itself, like flame retardance and conductivity [105–107]. The particle characteristics and physical properties of these additives have the same influence on the properties of composites as those of simple fillers. The characteristics of these modifiers must be optimized in order to achieve the desired goal, i.e. to produce composites with a given functional property, but acceptable mechanical characteristics and aesthetics at the same time.

7.4 Structure

Although the structure of particulate filled polymers is usually thought to be very simple, often structure related phenomena determine their properties. Structure is strongly influenced by the particle characteristics of the filler, composition and the processing technology used. The most important structure related phenomena are homogeneity, the attrition of the filler or reinforcement, aggregation, and the orientation of anisotropic particles. Occasionally fillers might modify the structure of crystalline polymers as well. All structure related effects must be controlled in order to prepare products of high quality.

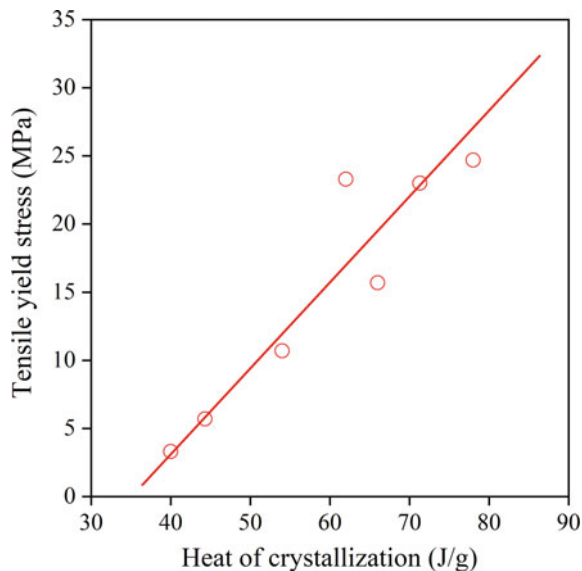
7.4.1 Crystalline Matrices, Nucleation

The properties of crystalline polymers are determined by the relative amount of the amorphous and crystalline phases, crystal modification, the size and perfection of crystallites, the dimensions of spherulites, and by the number of tie molecules [108]. The most important effect of particulate fillers is their ability to act as nucleating agents. The very strong nucleating effect of talc in PP was proved many times [47, 109]. Similarly to talc, layered silicates, and especially montmorillonite (MMT), were shown to nucleate polypropylene quite strongly [110–112]. The influence of other fillers and reinforcements is not so clear. Many fillers have shown weak nucleation effect in PP [113], while some others none [86]. A closer scrutiny

of literature information and experimental data indicate that mostly physical and especially topological factors determine the nucleation effect of fillers. Fillers may influence also the crystal modification of the matrix. Introduction of talc into the β modification of PP resulted in a complete change of crystalline structure, the higher crystallization temperature of the α modification prevented the formation of the β form [114]. Similarly, in the presence of montmorillonite polyamide was shown to crystallize mainly in the γ form [91, 115] irrespectively of the presence and/or type of organophilization [116].

Occasionally strong correlation is claimed between the crystalline structure of the matrix and composite properties. Hutley and Darlington [117] found a more or less linear correlation between the crystallization temperature and the falling weight impact strength of particulate filled PP, while Maiti [118] observed an even better, linear correlation between the crystallinity and tensile characteristics of PP filled with CaCO_3 (Fig. 7.4). However, the similar effect of the filler on two or more composite characteristics might lead to the linear correlation between tensile yield stress and crystallinity as observed by Maiti [118] and often to erroneous conclusions. The detailed analysis of experimental results obtained on PP composites containing different fillers indicated that the effect of changes in crystalline structure may be neglected especially at large filler contents [119]. A very efficient nucleating agent may change the modulus of PP from 1.4 to 1.9 GPa [120], while the introduction of 30 vol% talc results in a composite with a stiffness of almost 8 GPa [119].

Fig. 7.4 Correlation between the heat of crystallization and yield stress of PP/ CaCO_3 composites [118]



7.4.2 Segregation, Attrition

The segregation of a second phase during processing was observed in some heterogeneous polymer systems [121, 122]. Kubát and Szalánczi [121] investigated the separation of phases during the injection molding of polyethylene and polyamide using the spiral test. The two polymers contained large glass spheres of 50–100 μm size and extremely long flow paths up to 1.6 m. They found that considerable segregation took place along the flow path; the glass content of a composite containing 25 wt% filler exceeded 40% locally at the end of the mold. Segregation was observed also across the cross-section of the sample; the amount of filler was larger in the core than at the walls. Segregation depended on filler content and it became more pronounced with increasing size of the particles. The possible segregation of talc particles dispersed in a PP matrix was investigated under more practical conditions in injection molded specimens of $4 \times 10 \times 150$ mm dimensions. No differences were detected in filler content as a function of position; the particles were homogeneously distributed in the PP matrix independently of average filler content. Under practical conditions (small particles, relatively high filler content, normal flow path) segregation is of secondary importance, usually the filler is homogeneously distributed in the matrix polymer.

Another structure related phenomenon is the change of particle dimensions during processing. The attrition of fibers, i.e. the change of fiber length and length distribution, is an intensively studied question in short fiber reinforced composites [123]. Attrition may occur also in composites filled with anisotropic particles with plate like geometry, e.g. mica and talc. The cleavage of these fillers is relatively easy and considerable delamination may take place during processing, especially in injection molding at the very high shear stresses developing [124]. Delamination of mica particles was shown to improve most properties, but decreasing particle size may lead to aggregation [96]. Contrary to traditional fillers, delamination or exfoliation would be very advantageous in layered silicate nanocomposites.

7.4.3 Aggregation

Aggregation is a well-known phenomenon in particulate filled composites. Experience has shown that the probability of aggregation increases with decreasing particle size of the filler. The occurrence and extent of aggregation is determined by the relative magnitude of the forces, which hold together the particles, on the one hand, or try to separate them, on the other. Particulate filled polymers are prepared by the melt mixing of the components, thus the major attractive and separating forces must be considered under these conditions.

When two bodies enter into contact, they are attracted to each other. The strength of adhesion between two particles is determined by their size and surface energy [125, 126] (Eq. 7.1):

$$F_a = \frac{3}{2}\pi W_{AB}R_a, \quad (7.1)$$

where F_a is the adhesive force between the particles, W_{AB} is the reversible work of adhesion and $R_a = R_1R_2/(R_1 + R_2)$, an effective radius for particles of different size. In the presence of fluids, i.e. in suspensions, but also in the polymer melt during homogenization, further forces act among the particles. Depending on the extent of particle wetting, Adam and Edmondson [125] specify two attractive forces. When wetting is complete, viscous force (F_v) acts between particles separating them from each other with a constant rate. F_v depends on the viscosity of the fluid, on separation rate and on the initial distance of the particles. The viscous force might have some importance during the homogenization of composites. If the particles are wetted only partially by the fluid (melt), liquid bridges form and capillary forces develop among them. Four main types of electrostatic forces can hold charged particles together: Coulomb, image charge, space charge and dipole forces [127]. The magnitude of all four is around 10^{-7} – 10^{-8} N, they are significantly smaller than other forces acting among filler particles.

The number of forces separating the particles is smaller. Repulsive forces may act between particles with the same electrostatic charge. The mixing of fluids leads to the development of shear forces, which try to separate the particles. The maximum hydrodynamic force (F_h) acting on spheres in a uniform shear field can be expressed as [125] (Eq. 7.2):

$$F_h = -6.12\pi\eta R^2\dot{\gamma}, \quad (7.2)$$

where η is melt viscosity and $\dot{\gamma}$ is shear rate.

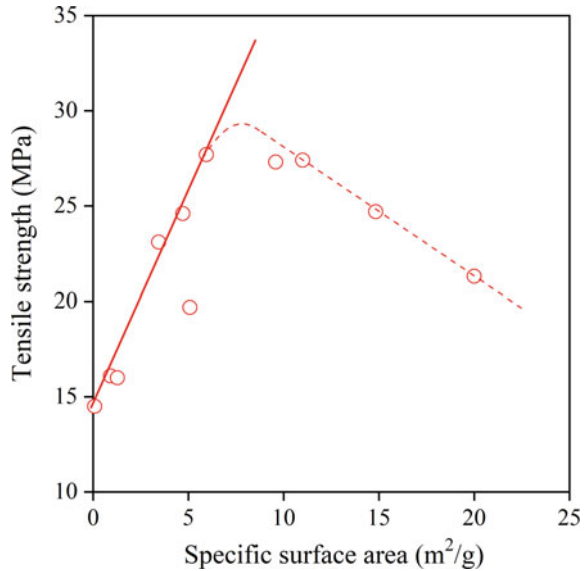
Both adhesive and hydrodynamic forces depend on the size of the particles. The estimation of the two forces by Eqs. 7.1 and 7.2 shows that below a certain particle size adhesion exceeds shear forces and the particles aggregate in the melt. Since commercial fillers have a relatively broad particle size distribution, most fillers aggregate in some extent and the exact determination of the critical particle size, or any other filler characteristic at which aggregation appears is difficult.

Since the relative magnitude of adhesive and shear forces determine the occurrence and extent of aggregation in a composite, the ratio of the two forces gives information about the possibilities to avoid or decrease it (Eq. 7.3):

$$\frac{F_a}{F_h} = k \frac{W_{AB}}{\eta\dot{\gamma}R}, \quad (7.3)$$

where k includes all constants of Eqs. 7.1 and 7.2. Increasing shear rate and particle size will result in decreased aggregation. Naturally both can be changed only in a limited range since excessive shear leads to degradation, while large particles easily debond from the matrix under the effect of external load leading to inferior composite properties. According to Eq. 7.3, smaller reversible work of adhesion also improves homogeneity. Non-reactive surface treatment invariably leads to the

Fig. 7.5 Tensile strength of PP/CaCO₃ composites plotted as a function of the specific surface area of the filler-effect of aggregation



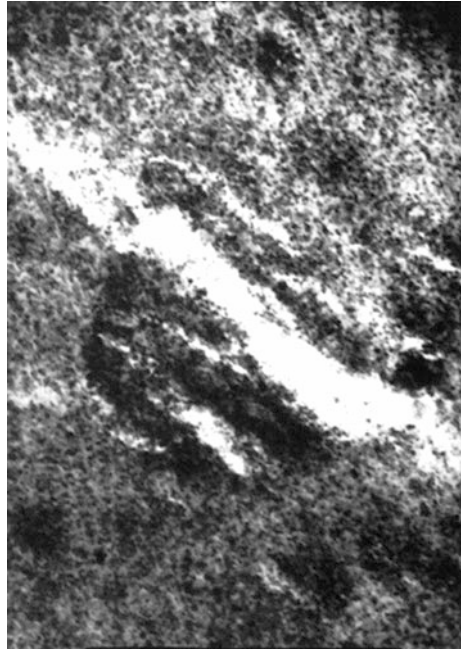
decrease of surface tension and W_{AB} (see Sect. 7.6.1), thus to decreased aggregation, improved processability and mechanical properties.

The presence of aggregates is practically always detrimental to the properties of composites as shown in Fig. 7.5. The strength of PP/CaCO₃ composites initially increases with increasing specific surface area of the filler, but it strongly decreases when aggregation takes place at small particle sizes. The effect is even more pronounced for impact properties, the fracture resistance of composites containing aggregated particles drastically decreases with increasing number of aggregates [99]. Aggregates may act as fracture initiation sites and depending on aggregate strength [90, 92] they may break under the effect of external load, which results in the failure of the product. The phenomenon is demonstrated by Fig. 7.6 showing the initiation and propagation of a crack through an aggregate in a PP/CaCO₃ composite containing small particles.

7.4.4 Orientation of Anisotropic Particles

Another processing induced structural phenomenon is the orientation of anisotropic particles. Both the phenomenon and the resulting structure are similar in short fiber reinforced and particulate filled composites. Plate like, planar reinforcements, however, have some advantages over fibers; the orientation dependent shrinkage of particulate filled composites is significantly smaller than that of the fiber reinforced ones [7]. Orientation and orientation distribution strongly influence property distribution and the overall performance of the product [128].

Fig. 7.6 Initiation and propagation of a crack through an aggregate of CaCO_3 particles in a PP composite



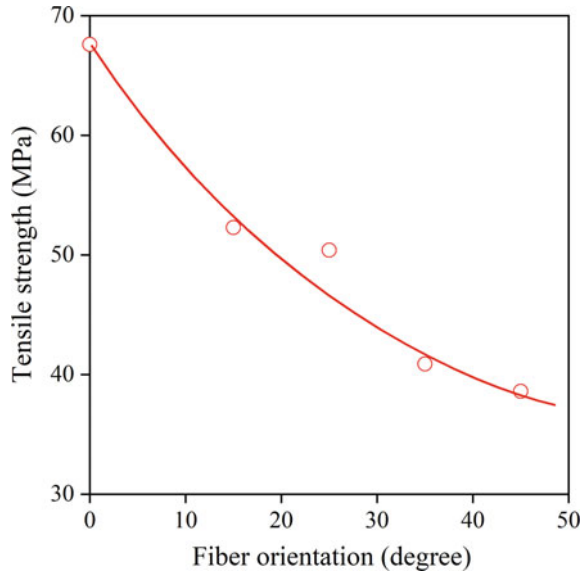
The orientation distribution of fibers and anisotropic particles is determined by the flow pattern and shear forces developing during processing [129]. Orientation is observed both in extrusion [130] and in injection molding, and even the relatively mild shearing conditions of compression molding may induce the orientation of filler particles [130]. In injection molded PP/talc composites parallel orientation was observed at the wall, while more random distribution in the middle of the plates. Average orientation shows significant composition dependence [130]. The average orientation of particles relative to the direction of the external load determines properties. Increasing alignment results in increased reinforcement, i.e. larger modulus, stress and impact strength [131] (see Fig. 7.7).

The orientation of anisotropic filler particles has an especially pronounced effect on the strength of injection molded parts containing weld lines. Fountain flow in the mold leads to the orientation of particles parallel with the melt front resulting in decreased weld line strength [132]. Increasing particle size and filler content result in a decrease of the weld line strength [132], which can be improved by changing particle characteristics (size, treatment, aspect ratio) [132, 133] and mold construction.

7.5 Interfacial Interactions, Interphase

Interfacial interactions play a decisive role in the determination of the mechanical properties of particulate filled polymers, but they strongly influence other characteristics like processability or aesthetics as well.

Fig. 7.7 Effect of fiber orientation (alignment to external stress) on the strength of short glass fiber reinforced PP composites [131]



7.5.1 Type and Strength of Interaction

Both the polymers used as matrices in particulate filled composites and the fillers or reinforcements have the most diverse physical and chemical structures, thus a wide variety of interactions may form between them. Two boundary cases of interactions can be distinguished: covalent bonds, which rarely form spontaneously, but can be created by special surface treatments, and zero interaction, which does not exist in reality, since at least secondary, van der Waals forces always act between the components. In practice the strength of the interaction is somewhere between the two boundary cases.

The theory of adsorption interaction is applied the most widely for the description of interactions in particulate filled or reinforced polymers. The approach is based on the theory of contact wetting, in which interfacial adhesion is created by secondary forces. Accordingly, the strength of the adhesive bond is assumed proportional to the reversible work of adhesion (W_{AB}), which is necessary to separate two phases with the creation of new surfaces. The Dupré equation relates W_{AB} to the surface (γ_A and γ_B) and interfacial (γ_{AB}) tension of the components in the following way (Eq. 7.4):

$$W_{AB} = \gamma_A + \gamma_B - \gamma_{AB}. \quad (7.4)$$

Unfortunately, interfacial tension cannot be measured directly; it is usually derived from thermodynamic calculations. Fowkes [134] assumed that surface tension can be divided into components, which can be determined separately.

The theory can be applied relatively easily for apolar interactions when only dispersion forces act between surfaces. Its generalization for polar interactions is more complicated and the geometric mean approximation gained the widest acceptance. This considers only the dispersion and a polar component of surface tension, but the latter includes all polar interactions [135]. According to the approach interfacial tension can be calculated as (Eq. 7.5):

$$\gamma_{AB} = \gamma_A + \gamma_B - 2(\gamma_A^d \gamma_B^d)^{1/2} - 2(\gamma_A^p \gamma_B^p)^{1/2}, \quad (7.5)$$

where superscripts *d* and *p* indicate the dispersion and polar components of surface tension for components *A* and *B*.

The surface tension of two thermoplastics and six fillers are listed in Table 7.2. Large differences can be observed both in the dispersion, but especially in the polar component. The surface tension of the majority of polymers is in the same range as shown in Table 7.2, in fact between that of PP and PMMA. The examples listed in the table represent the most important particulate fillers and reinforcements used in practice, since clean glass fibers possess similar surface tensions as SiO₂.

Although Eq. 7.5 tries to take into account the effect of the polarity of the surfaces in some extent, the role of acid-base interactions in adhesion became clear and theories describing them are increasingly accepted. Fowkes [136] suggested that the reversible work of adhesion should be defined as (Eq. 7.6):

$$W_{AB} = W_{AB}^d + W_{AB}^{ab} + W_{AB}^p, \quad (7.6)$$

where W_{AB}^{ab} is the part of the reversible work of adhesion created by acid-base interactions. According to Fowkes the polar component can be neglected, i.e. $W_{AB}^p \sim 0$, thus W_{AB} can be expressed as (Eq. 7.7):

$$W_{AB} = 2(\gamma_A^d \gamma_B^d)^{1/2} + nf \Delta H^{ab}, \quad (7.7)$$

Table 7.2 Surface tension of selected polymers and fillers; dispersion (γ^d) and polar (γ^p) components

Material	Surface tension (mJ/m ²)		
	γ^d	γ^p	γ
PP ^a	32.5	0.9	33.4
PMMA ^a	34.3	5.8	40.1
CaCO ₃ ^b	54.5	153.4	207.9
Talc ^c	49.3	90.1	139.4
SiO ₂ ^c	94.7	163.0	257.7
Zeolite ^b	181.9	260.4	442.3
Layered silicate ^b	291.0	500.0	791.0
Wood ^a	45.0	28.8	73.8

^aContact angle, ^binverse gas chromatography (IGC), ^cgravimetric measurement

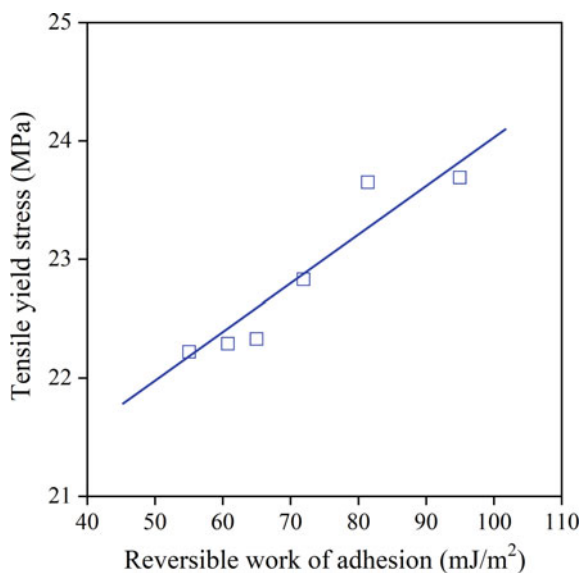
where ΔH^{ab} is the change in free enthalpy due to acid-base interactions, n is the number of moles interacting with a unit surface and f is a conversion factor, which takes into account the difference between free energy and free enthalpy ($f \sim 1$) [136]. The enthalpy of acid-base interaction, ΔH^{ab} , necessary for the determination of the specific component of the reversible work of adhesion, can be calculated from the acid-base constants of the interacting phases by using the theory of Drago [137] or Guttman [138].

In most cases the strength of the adhesive bond is characterized acceptably by the reversible work of adhesion values calculated by the above theory. Often, especially in apolar systems, a close correlation exists between W_{AB} and the macroscopic properties of the composite (Fig. 7.8). In spite of the imperfections of the approach, the reversible work of adhesion can be used for the characterization of matrix/filler interactions in particulate filled polymers. The quantities necessary for the calculation of W_{AB} can be determined by inverse gas chromatography [139], while parameters related to interfacial adhesion can be derived from appropriate models [44, 140].

7.5.2 Interphase Formation

As Table 7.2 shows, non-treated fillers and reinforcements have high-energy surfaces. During the almost exclusively used melt mixing procedure, the forces discussed in the previous section lead to the adsorption of polymer chains onto the active sites of the filler surface. The adsorption of polymer molecules results in the

Fig. 7.8 Effect of interfacial adhesion on the tensile yield stress of PP/CaCO₃ composites; filler: CaCO₃, $\phi_f = 0.1$, $R = 0.9 \mu\text{m}$



development of a layer which has properties different from those of the matrix polymer [141–143]. Although the character, thickness and properties of this interlayer or interphase are much-discussed topics, its existence is an accepted fact now.

The overall properties of the interphase, however, are not completely clear. Based on model calculations the formation of a soft interphase is claimed [144], while in most cases the increased stiffness of composites is explained at least partly with the presence of a stiff interphase [44, 145]. The contradiction obviously stems from two opposing effects. The imperfection of the crystallites and decreased crystallinity of the interphase should lead to smaller modulus and strength, as well as to larger deformability in crystalline polymers [142]. Adhesion and hindered mobility of adsorbed polymer chains, on the other hand, decrease deformability and increase the strength of the interlayer.

The thickness of the interphase is a similarly intriguing and contradictory question. It depends on the type and strength of the interaction and values from 10 Å to several microns have been reported in the literature for the most diverse systems [41, 109, 146–151]. Since interphase thickness is calculated or deduced indirectly from measured quantities, it depends also on the method of determination. Table 7.3 presents some data for different particulate filled polymers. Thermodynamic considerations and extraction experiments yield interphase thicknesses, which are not influenced by the extent of deformation. In mechanical measurements, however, the material is always deformed even during the determination of modulus. The role and effect of immobilized chain ends increase with increasing deformation and the determined interphase thickness increases as well, which proves that chains are attached to the surface of the filler indeed (see Table 7.3).

Table 7.3 Interphase thickness in particulate filled polymers determined by different techniques

Matrix polymer	Filler	Method of determination	Thickness (μm)	Reference
HDPE	SiO ₂	Extraction	0.0036	[147]
HDPE	SiO ₂	Extraction	0.0036	[148]
PP	SiO ₂	Extraction	0.0041	[148]
PP	Graphite	Model calc.	0.001	[150]
PS	Mica	Dyn. mech. meas.	0.06	[146]
PMMA	Glass	Dyn. mech. meas.	1.4	[146]
PP	CaCO ₃	Young's modulus	0.012	[149]
PP	CaCO ₃	Tensile strength	0.15	[149]
PP	CaCO ₃	Tensile yield stress	0.16	[149]
PP	CaCO ₃	Tensile yield stress	0.12	[151]
LDPE	CaCO ₃	Tensile yield stress	0.11	[151]
PMMA	CaCO ₃	Tensile yield stress	0.18	[151]
PVC	CaCO ₃	Tensile yield stress	0.23	[151]

The thickness of the interphase depends on the strength of the interaction. Interphase thicknesses derived from mechanical measurements are plotted as a function of W_{AB} in Fig. 7.9 for CaCO_3 composites prepared with four different matrices: PVC, PMMA, PP and LDPE. Acid-base interactions were also considered in the calculation of W_{AB} [151]. The thickness of the interphase changes linearly with increasing adhesion. The figure proves several of the points mentioned above. The reversible work of adhesion adequately describes the strength of the interactions created mostly by secondary forces and the thickness of the interphase is closely related to the strength of interaction.

The amount of polymer bonded in the interphase depends on the thickness of the interlayer and on the size of the contact area between the filler and the polymer. Interface area is related to the specific surface area of the filler (A_f), which is inversely proportional to particle size. Modulus shows only a very weak dependence on the specific surface area of the filler [152]. Properties measured at larger deformations, e.g. tensile yield stress or tensile strength, depend much stronger on A_f than modulus does [152]. Figure 7.10 shows that yield stresses larger than the corresponding value of the matrix can be achieved, i.e. even spherical fillers can reinforce polymers [44]. If adhesion is strong, yielding should be initiated at the matrix value and no reinforcement would be possible. The reinforcing effect of spherical particles can be explained only with the presence of a hard interphase having properties somewhere between those of the polymer and the filler [44].

Fig. 7.9 Effect of interfacial interactions on the thickness of the interlayer formed spontaneously in polymer/ CaCO_3 composites

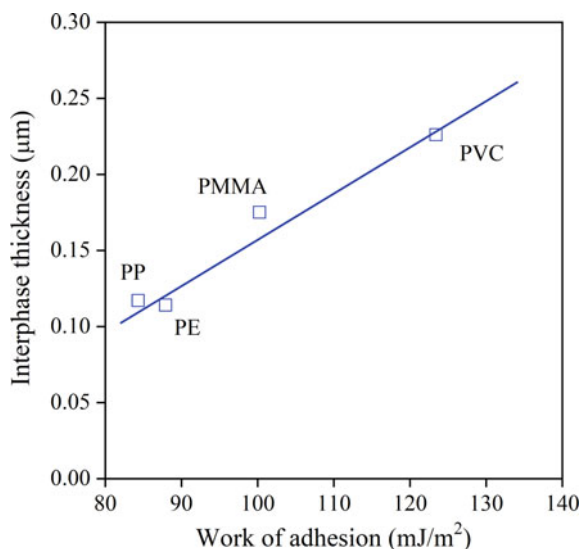
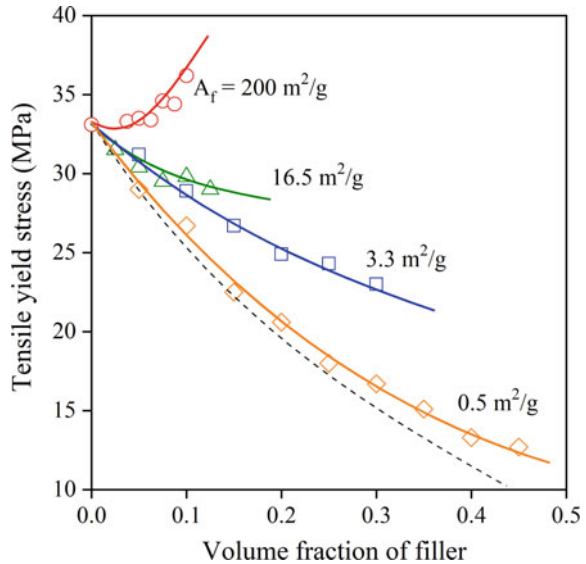


Fig. 7.10 Effect of the size of the interfacial area (A_f) on the yield stress of PP/CaCO₃ composites. Specific surface area: (open circle) 200, (open triangle) 16.5, (open square) 3.3, (open diamond) 0.5 m²/g, -theoretical minimum for zero interaction calculated from Eq. 7.16



7.5.2.1 Wetting

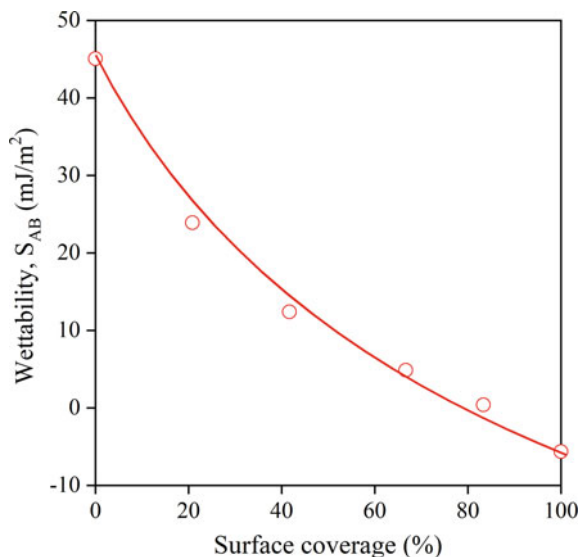
The maximum performance of a composite can be achieved only if the wetting of the filler or reinforcement by the polymer is perfect [153, 154]. The non-reactive treatment of fillers with surfactants is claimed to improve wettability due to changing polarity. The improvement in mechanical properties as an effect of coating is often falsely interpreted as the result of better wetting and interaction. However, according to Fox [155] the wetting of a high-energy solid by a low surface tension fluid is always complete. This condition is completely satisfied by polymers, including apolar ones like PP or PE, and all inorganic fillers (see Table 7.2). If wettability (S_{AB}) is characterized by the thermodynamic quantity (Eq. 7.8):

$$S_{AB} = \gamma_A - \gamma_B - \gamma_{AB}, \quad (7.8)$$

where $\gamma_A > \gamma_B$, wettability decreases on surface treatment due to the drastic decrease of the surface tension (γ_s) of the filler. The correlation is demonstrated by Fig. 7.11 where S_{AB} is plotted against the surface coverage of a CaCO₃ filler with stearic acid [93].

The larger is S_{AB} the better is wettability and in the case of negative values definite contact angle develops (partial wetting). Consequently, wetting becomes poorer on surface coating, but it results in weaker interactions at the same time, which lead to a considerable decrease in aggregation, to better dispersion and homogeneity, easier processing, good mechanical properties and appearance. However, wetting has also kinetic conditions, which depend on the viscosity of the

Fig. 7.11 Wettability of CaCO_3 by PP and its dependence on the surface coverage of the filler with stearic acid



polymer, processing technology and particle characteristics, which might not always be optimal during composite preparation. However, particle related problems (debonding, aggregation) and insufficient homogenization usually create more problems than wetting.

7.6 Surface Modification

The easiest way to change interfacial interactions is the surface coating of fillers. Surface modification is often regarded as magic, which solves all problems of processing technology and product quality, but it works only if the compound used for the treatment (coupling agent, surfactant, etc.) is selected according to the characteristics of the components and the goal of the modification. Surface treatment modifies both particle/particle and matrix/filler interactions, and the properties of the composite are determined by the combined effect of the two. Besides its type, also the amount of the surfactant or coupling agent must be optimized from both the technical and the economical point of view.

7.6.1 Non-reactive Treatment

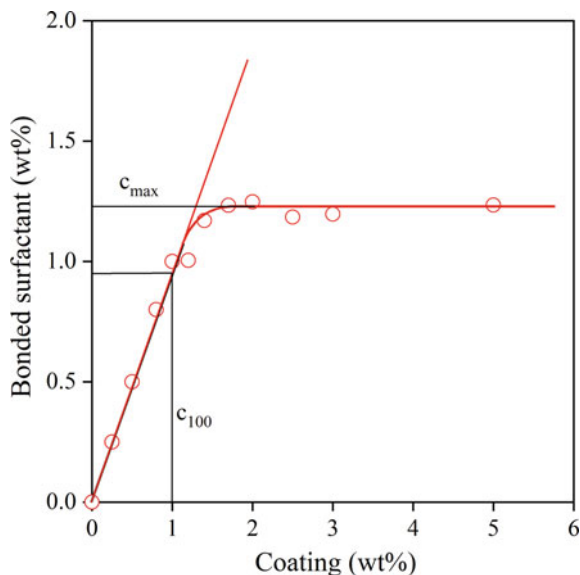
The oldest and most often used modification of fillers is the coverage of their surface with a small molecular weight organic compound [139, 151, 156]. Usually

amphoteric surfactants are used which have one or more polar groups and a long aliphatic tail. Typical example is the surface treatment of CaCO_3 with stearic acid [139, 151, 156]. The principle of the treatment is the preferential adsorption of the surfactant onto the surface of the filler. The high-energy surfaces of inorganic fillers (see Table 7.2) can often enter into special interactions with the polar group of the surfactant. Preferential adsorption is promoted in a large extent by the formation of ionic bonds between stearic acid and the surface of CaCO_3 [157], but in other cases hydrogen or even covalent bonds may also form. Surfactants diffuse to the surface of the filler even from the polymer melt, which is a further proof for preferential adsorption [158].

One of the crucial questions of non-reactive treatment, which, however, is very often neglected, is the amount of surfactant to use. It depends on the type of the interaction, the surface area occupied by the coating molecule, its alignment to the surface, on the specific surface area of the filler and on some other factors. The determination of the optimum amount of surfactant is essential for efficient treatment. An insufficient amount does not achieve the desired effect, while excessive quantities lead to processing problems as well as to the deterioration of the mechanical properties and appearance of the product [157]. The amount of bonded surfactant can be determined by simple techniques. A dissolution method proved to be very convenient for the optimization of non-reactive surface treatment and for the characterization of the efficiency of the coating technology as well [157]. First, the surface of the filler is covered with increasing amounts of surfactant, and then the non-bonded part is dissolved with a solvent. The technique is demonstrated in Fig. 7.12, which presents a dissolution curve showing the adsorption of stearic acid on CaCO_3 . Surface coating is preferably carried out with the irreversibly bonded surfactant (c_{100}); at this composition, the total amount of surfactant used for the treatment is bonded to the filler surface. The filler can adsorb more surfactant (c_{max}), but a part of it can be removed from the surface during compounding and might deteriorate properties. The specific surface area of the filler is an important factor, which must be taken into consideration during surface treatment. The irreversibly bonded surfactant depends linearly on it [157].

As a result of the treatment, the surface free energy of the filler decreases drastically [93, 139, 156]. Smaller surface tension means decreased wetting (see Fig. 7.11), interfacial tension and reversible work of adhesion [151, 157]. Such changes in the thermodynamic quantities result in a decrease of both particle/particle and matrix/particle interaction. One of the main goals, major reason and benefit of non-reactive surface treatment is the first effect, i.e. to change interactions between the particles of fillers and reinforcements. As an effect of non-reactive treatment not only particle/particle, but also matrix/filler interaction decreases. The consequence of this change is reduced yield stress and strength as well as improved deformability [93, 159]. Strong interaction, however, is not always necessary or advantageous for the preparation of composites with desired properties; the plastic deformation of the matrix is the main energy absorbing process in impact, which increases with decreasing strength of adhesion [140, 160].

Fig. 7.12 Dissolution curve used for the determination of surfactant adsorption on a filler. CaCO_3 /stearic acid



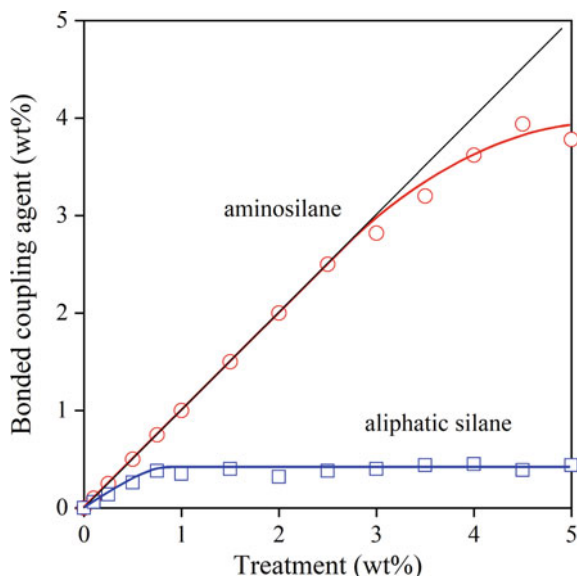
7.6.2 Coupling

Successful reactive treatment assumes that the coupling agent reacts and forms covalent bonds with both components. Silane coupling agents are successfully applied for fillers and reinforcements, which have reactive $-\text{OH}$ groups on their surface, e.g. glass fibers, glass flakes and beads, mica and other silica fillers [100, 161]. The use of silanes with fillers like CaCO_3 , $\text{Mg}(\text{OH})_2$, wood flour, etc. were tried, but often proved to be unsuccessful [162, 163], sometimes contradictory results were obtained even with glass and other siliceous fillers [164]. Acidic groups are preferable for CaCO_3 , $\text{Mg}(\text{OH})_2$, $\text{Al}(\text{OH})_3$ and BaSO_4 . Talc cannot be treated successfully either with reactive or non-reactive agents because of its inactive surface; only broken surfaces contain a few active $-\text{OH}$ groups.

The adsorption of organofunctional silanes is usually accompanied by their polycondensation. The adsorbed amount of coupling agent, the structure, properties and adhesion of the polysiloxane layer depend very much on the chemical composition of the organofunctional group of the silane. This is obvious if we compare the dissolution curve of two silanes, an aliphatic and an aminosilane, respectively, on CaCO_3 (Fig. 7.13). The different chemical structure of the silanes leads to considerably different adsorption isotherms. The figure shows also that the simple dissolution technique can be advantageously applied for the study of reactive coupling agents as well [165].

Although the chemistry of silane modification of reactive silica fillers is well documented, much less is known about the interaction of silanes with polymers. Thermoplastics rarely contain reactive groups, thus they cannot react chemically

Fig. 7.13 Effect of the chemical structure of silane coupling agents on their adsorption on the surface of a CaCO_3 filler. Particle size $1.25 \mu\text{m}$. Symbols: (open circle) aminosilane, (open square) aliphatic silane



with silanes. Polycondensation polymers are the most reactive and literature sources offer sufficient evidence of reactive coupling, indeed. The strength of polyamide and polycarbonate composites increases on aminosilane treatment [166, 167] (Sadler and Vecere 1995, Zolotnitsky and Steinmetz 1995). Reactive treatment is the most difficult in polyolefins, since they do not contain any reactive groups. Some results indicate that polypropylene oxidizes during processing even in the presence of stabilizers and the formed acidic groups react with aminosilanes resulting in reactive coupling [168].

Considering the complexity of the chemistry involved, it is not surprising that the amount of coupling agent and surface coverage have an optimum here too, similarly to surfactants in non-reactive surface treatment. The optimization of the type and amount of coupling agent is crucial also in reactive treatment and although “proprietary” coatings might lead to some improvement in properties, they are not necessarily optimal or cost effective. The improper choice of coupling agent may result in insufficient or even deteriorating effects. In some cases, hardly any change is observed in properties, or the effect can be attributed unambiguously to the decrease of surface tension due to the coverage of the filler surface by an organic substance, i.e. to non-reactive treatment [169].

7.6.3 Functional Polymers

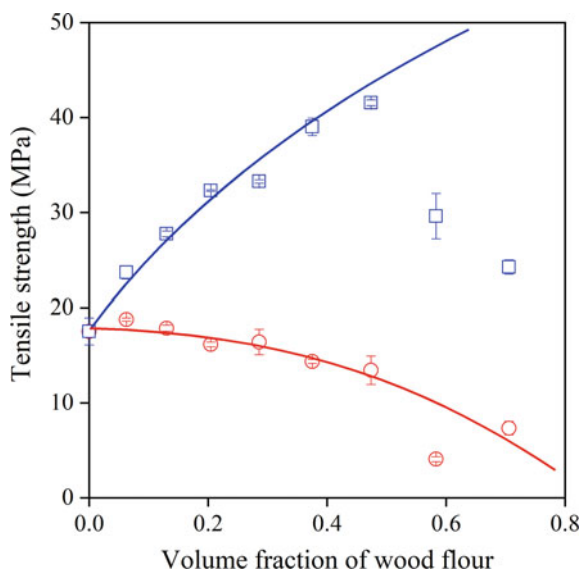
The coverage of filler surface with a polymer layer, which is capable of interdiffusion with the matrix, proved to be very effective both in stress transfer and in

forming a thick diffuse interphase with acceptable deformability. In this treatment, the filler is usually covered by a functionalized polymer, preferably with the same chemical structure as the matrix. The functionalized polymer is attached to the surface of the filler by secondary, hydrogen, ionic and sometimes by covalent bonds. The polymer layer interdiffuses with the matrix, entanglements form and strong adhesion is created. Because of their polarity, in some cases reactivity, maleic anhydride or acrylic acid modified polymers are often used for this purpose. The coupling agent adsorbs onto the surface of most polar fillers even from the melt. This treatment is frequently used in polyolefin composites, in which other treatments usually fail. Often very small amounts of the modified polymer (1–3 wt%) are sufficient to achieve significant improvement in stress transfer [170]. The maximum effect of functionalized PP was found with fillers of high energy surfaces [171] or with those capable for specific interactions, e.g. ionic bond with CaCO_3 [159, 172] or chemical reaction with wood flour, kraft lignin or cellulose [65, 154, 170]. Figure 7.14 demonstrates the successful use of a functionalized polymer in PP composites modified with wood flour.

7.6.4 Soft Interlayer

The introduction of hard particles into the polymer matrix creates stress concentration, which induces local deformation processes around the particles. Occasionally these might be advantageous for increasing plastic deformation and impact resistance, but they usually deteriorate the properties of the composite. The encapsulation of the filler

Fig. 7.14 Dependence of the tensile strength of PP/wood flour (average size (d): 210 μm) composites on wood content and adhesion. Symbols: (open circle) poor adhesion (no MAPP), (open square) good adhesion (MAPP)



particles by an elastomer layer changes the stress distribution around the particles and modifies local deformation processes. Encapsulation can take place spontaneously; it can be promoted by the use of functionalized elastomers or the filler can be treated in advance. Such a surface modification is rarely done directly by covering the filler with a soft layer, but forms spontaneously during the preparation of multicomponent polymer/filler/elastomer composites [173].

7.7 Local Micromechanical Deformations

The introduction of fillers or reinforcements into a polymer matrix results in a heterogeneous system. Under the effect of external load, heterogeneities induce stress concentration, the magnitude of which depends on the geometry of the inclusions, the elastic properties of the components and interfacial adhesion [174]. Heterogeneous stress distribution and local stress maxima initiate local micromechanical deformations, which determine the deformation and failure behavior, as well as the overall performance of the composites.

7.7.1 *Stress Distribution*

Stress concentration and local stress distribution can be estimated by the use of theoretical models or by finite element analysis [175, 176]. The interacting stress fields of neighboring particles are very complicated and change with composition. The most often used approach is the analysis of stresses around a single particle embedded in an infinite matrix, which was first proposed by Goodier [174]. According to his model, radial stress has a maximum at the pole, where it exceeds almost twice the external stress, when a hard particle is embedded into a soft matrix. Micromechanical deformation processes initiated by local stress maxima around the particles are influenced also by thermal stresses induced by the different thermal expansion coefficients of the components, crystallization, or shrinkage during the curing of thermoset matrices [103, 104]. Although the importance of inhomogeneous stress distribution developing in particulate filled composites is pointed out in numerous publications, the exact role of stress concentration is not completely clear and contradictory information is published claiming either beneficial [177] neutral [178] or detrimental effect on the properties [99, 145].

7.7.2 *Debonding*

In particulate filled polymers, the dominating micromechanical deformation process is debonding. The stress necessary to initiate debonding, the number of debonded

particles and the size of the voids formed all influence the macroscopic properties of composites. Several models exist for the prediction of debonding stress including the one below (Eq. 7.9) [175]:

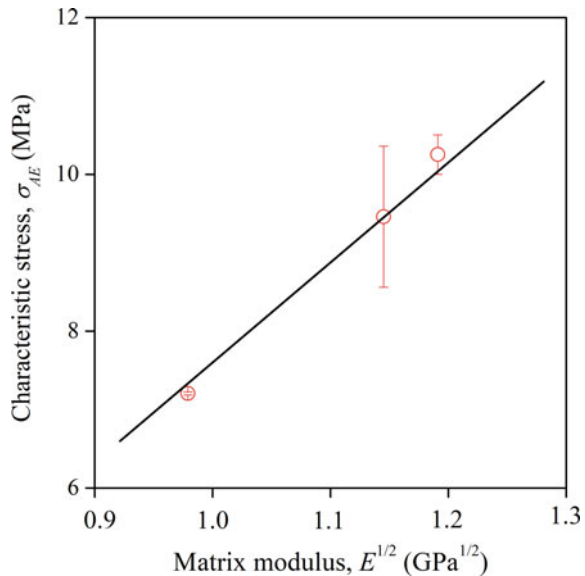
$$\sigma^D = -C_1\sigma^T + C_2\left(\frac{W_{AB}E}{R}\right)^{1/2} \quad (7.9)$$

where σ^D and σ^T are debonding and thermal stresses, respectively, W_{AB} is the reversible work of adhesion and R the radius of the particle. C_1 and C_2 are constants, which depend on the geometry of the debonding process. The validity of the model was checked in various particulate filled composites. Initiation stress determined in PP/wood flour composites from acoustic emission measurements is plotted against the stiffness of the matrix in Fig. 7.15 in the representation predicted by the model [179]. The correlation is close and corresponds to the prediction. Similarly good correlations can be obtained in PP/CaCO₃ composites if we plot debonding stress against the reversible work of adhesion or the particle size of the filler [89] (see Eq. 7.9).

7.7.3 Other Deformation Mechanisms

Micromechanical deformations are competitive processes and the dominating one depends on material properties and loading conditions. Several fiber-related processes, like fiber breakage, pull out, buckling, etc. may take place in short and long

Fig. 7.15 Dependence of debonding stress derived from acoustic emission measurements on the stiffness of the matrix (see Eq. 7.9). Filler content: 20 vol%



fiber reinforced composites. Quite a few of these can be observed in wood fiber reinforced polymers or layered silicate nanocomposites as well. The complexity of deformation and failure in such materials is demonstrated well by the number of processes detected in wood flour reinforced PP composites [67]. The stress versus strain correlation of a PP composite containing 20 wt% unmodified wood flour is presented in Fig. 7.16 together with the acoustic signals detected during deformation.

Since the adhesion between wood and PP is poor and the particles are large (see Eq. 7.9), the majority of the signals is emitted by the debonding of the wood particles. The cumulative number of acoustic events versus elongation plot clearly indicates that at least two processes occur in this composite shown by the two steps in the correlation. The application of a coupling agent, which improves interfacial adhesion between the components changes the mechanism of deformation completely, strength increases considerably, but the number of acoustic events is also larger and their amplitude is higher in this case. Under these conditions, the fracture of the fibers is the dominating local process. The analysis of a large number of results showed that at least four processes take place during the deformation of PP/wood composites. The PP matrix deforms mainly by shear yielding, debonding and fiber pull out dominates when the adhesion is poor, while mainly fiber fracture takes place in the presence of MAPP coupling agent, which creates strong bond between the matrix and the wood particles [67, 180, 181]. The fracture and the fibrillation of a particle are shown in Fig. 7.17 in order to support the analysis.

The importance of local deformations is strongly corroborated by Fig. 7.18 in which composites strength is plotted against the initiation stress of the dominating process of a large number of PP and PLA composites reinforced with wood. It is obvious that micromechanical processes initiated by local stress maxima determine the final properties of particulate filled and reinforced composites and only the

Fig. 7.16 Acoustic emission testing of a PP composite containing 20 wt% wood without MAPP (poor adhesion). Small circles indicate individual acoustic events. Stress versus strain and cumulative number of signal versus strain traces

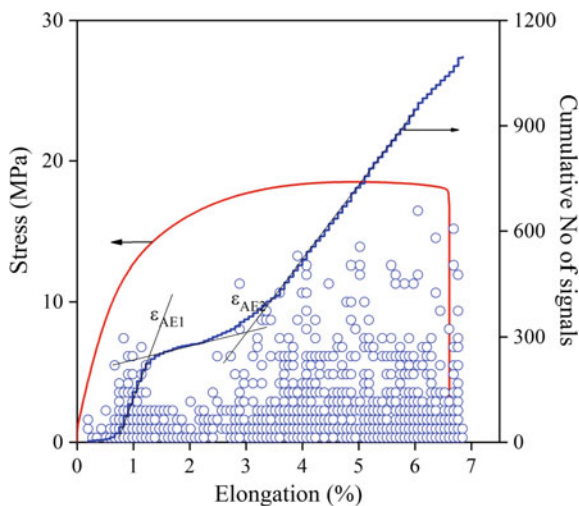


Fig. 7.17 SEM micrograph showing the fracture of a wood particle during the deformation of PP/wood composites. Good adhesion of the components was achieved by the use of functionalized PP (MAPP)

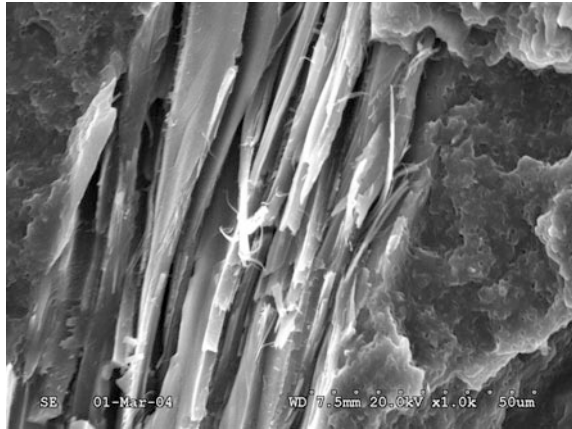
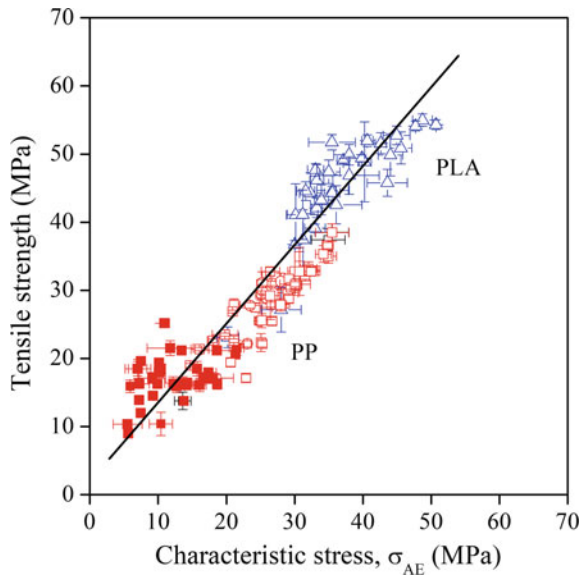


Fig. 7.18 Close correlation between the initiation stress of the dominating deformation process and the strength of the composite. Symbols: (open square) PP/wood, (open triangle) PLA/wood. Full symbols: poor adhesion, empty symbols: good adhesion



analysis of the resulting processes can help the development of stronger and better materials.

7.8 Properties

As mentioned earlier, fillers are not added to the polymer to reduce price any more, but to gain technical advantages. Compounding cost increases price considerably, which is compensated only by improved or new, even functional properties. The

main goals of the addition of fillers are the increase of stiffness, but also strength and heat deflection temperature may be improved by the proper selection of the filler, interaction, and composition. Occasionally other, special properties can be improved or even created. Gas and vapor permeability decreases upon the addition of fillers, while conductivity or flame retardance can be achieved with filler like additives. The properties of particulate filled thermoplastics depend strongly and usually non-linearly on composition; linear composition dependence frequently claimed in the literature usually occurs by chance, or it is observed because the range of compositions used is too narrow. Theoretical models are useful for the prediction of composition dependence, but relatively few models exist and the majority is empirical.

7.8.1 Rheological Properties

The introduction of fillers or reinforcements changes practically all properties of the polymer including its rheological characteristics. Viscosity usually increases with filler content, while melt elasticity decreases at the same time [182]. These changes depend very much on the particle characteristics of the filler although unambiguous correlations are not known. Matrix/filler interactions lead to the formation of an interphase, which has the same effect as that of increasing filler content [141].

The composition dependence of rheological properties is modeled only in surprisingly few cases. Quite a few models are derived from Einstein's equation, which predicts the composition dependence of the viscosity of suspensions containing spherical particles. The original equation is valid only at infinite dilution, or at least at very small, 1–2%, concentrations [183] and in real composites the equation must be modified. Usually additional terms and parameters are introduced into the model most often in the form of a power series [183]. The Mooney equation represents a more practical and useful approach, which contains adjustable parameters accommodating both the effect of interactions and particle anisotropy (Eq. 7.10) [184]:

$$\ln \frac{\eta}{\eta_0} = \frac{k_E \varphi_f}{1 - \varphi_f / \varphi_f^{\max}}, \quad (7.10)$$

where η and η_0 are the viscosity of the composite and the matrix, respectively, φ the volume fraction of the filler, while k_E is an adjustable parameter related to the shape of the particles. φ_f^{\max} is the maximum amount of filler, which can be introduced into the composite, i.e. maximum packing fraction, and it is claimed to depend solely on the spatial arrangement of the particles. The study of PP/CaCO₃ composites proved that interfacial interactions and the formation of a stiff interface influences its value more than spatial arrangement and the maximum amount of filler, which can be introduced into the polymer decreases with increasing specific surface area of the filler.

7.8.2 Stiffness

Modulus is one of the basic properties of composites and the goal of using particulate fillers is often to increase it [86]. Modulus is not only the most frequently measured, but also the most often modeled composite property. A large number of models exist which predict the composition dependence of stiffness or give at least some bounds for its value. The abundance of models is relatively easy to explain: modulus is determined at very low deformations thus the theory of linear viscoelasticity can be used in model equations. The large number of accessible data also helps both the development and the verification of models. Model equations developed for heterogeneous polymer systems can be classified in different ways [185–187]. Ignoring completely empirical correlations, we distinguish four groups here:

1. Phenomenological equations, which are similar to the spring and dashpot models, used for the description of the viscoelastic properties of polymers [186].
2. Bounds. These are usually exact mathematical solutions which do not contain any or only very limited assumptions about the structure of the composite [188].
3. Self-consistent models. The mechanical response of a composite structure is calculated, in which the dispersed particle is assumed to be embedded into the continuous phase. A well-known model of this type, frequently used also for particulate filled composites, is the Kerner equation [186]. Although it was much criticized because of the incorrect elastic solution used [189], the model gained wide use and acceptance.
4. Semiempirical models. In spite of the effort of the self-consistent models to take into account the influence of microstructure, they very often fail to predict correctly the composition dependence of composite modulus, thus additional, adjustable parameters are introduced in order to improve their performance. The most often applied equation of this type is the Nielsen (also called Lewis-Nielsen or modified Kerner) model (Eqs. 7.11–7.14) [87]:

$$G = G_m \frac{1 - AB\phi_f}{1 - B\Psi\phi_f}, \quad (7.11)$$

$$A = \frac{7 - 5\nu_m}{8 - 10\nu_m}, \quad (7.12)$$

$$B = \frac{G_f/G_m - 1}{G_f/G_m + A}, \quad (7.13)$$

$$\Psi = 1 + \left(\frac{1 - \phi_f^{\max}}{\phi_f^{\max^2}} \right) \phi_f, \quad (7.14)$$

where G , G_m and G_f are the shear moduli of the composite, the matrix and the filler, respectively, ν_m is the Poisson's ratio of the matrix and ϕ_f is filler content.

The equations contain two structure related or adjustable parameters (A , Ψ). The two parameters, however, are not very well defined. A can be related to filler anisotropy, through the relation $A = k_E - 1$, where k_E is Einstein's coefficient, but the relation has not been thoroughly investigated and verified. Ψ depends on maximum packing fraction. ϕ_f^{max} is related to anisotropy, but it is influenced also by the formation of an interphase which was not taken into consideration in the original treatment [87]. Its experimental determination is difficult. McGee and McCullogh proposed a different form for Ψ , which is supposed to be based on a more rigorous treatment [185].

In spite of these uncertainties, the model is quite frequently used in all kinds of particulate filled composites for the prediction of the composition dependence of modulus. In some cases, merely the existence of a good fit is established, in others conclusions are drawn from the results about the structure of the composite. However, the attention must be called here to some problems of the application of these equations or any other theoretical model. The uncertainty of input parameters might bias the results considerably. Poisson's ratios between 0.25 and 0.30, as well as moduli between 19.5 and 50.0 GPa have been reported for CaCO_3 [190, 191]. Such changes in component properties may lead to differences in the final prediction, which exceed the standard deviation of the measurement. Maximum packing fraction influences predicted moduli especially strongly, but its value is usually not known. A certain packing of the particles may be assumed, but this approach neglects the effect of particle size distribution and interactions. At the moment, the best solution is the fitting of the equation to the experimental data and the determination of A and ϕ_f^{max} . The model is very useful for the estimation of the amount of embedded filler in polymer/elastomer/filler composites, but otherwise its value is limited.

7.8.3 *Properties Measured at Large Deformations*

The fact that modulus is determined at very small deformations simplifies both measurements and modeling. On the other hand, yield properties are measured at larger deformations making predictions much more difficult. The composition dependence of yield strain is described assuming that at the considerable deformations (5–10%) of yielding only the polymer matrix deforms and the rigid filler does not. This strain magnification of the matrix increases with increasing filler content. One of the equations based on this principle was derived by Nielsen (Nielsen 1974). Occasionally the same approach is used for the prediction of the composition dependence of elongation at break [87, 145].

More attempts are made to predict and analyze yield stress. The most often applied correlation is attributed to Nicolais and Narkis [192], although the equation

of Ishai and Cohen [193] is practically the same. Nicolais and Narkis [192] assumed that the filler decreases the effective cross-section of the matrix, which carries the load during deformation. Assuming a certain arrangement of the particles, they calculated this cross-section and from that the dependence of yield stress on composition (Eq. 7.15):

$$\sigma_y = \sigma_{y0} \left(1 - 1.21 \varphi_f^{2/3} \right), \quad (7.15)$$

where σ_y and σ_{y0} are composite and matrix yield stress, respectively. The approach, however, results in a matrix cross-section assuming zero value at $\varphi_f < 1$, which is naturally incorrect. The model assumes zero interaction and ignores all other factors influencing yield stress. Because of these simplifications, deviations from the prediction occur very often. Consequently, the model is frequently modified to accommodate the effect of different arrangements of the particles [87], interactions, stress concentration [145], or other effects. Usually the two constants, i.e. 1.21 and 2/3, are treated as adjustable parameters, but in such cases they lose their physical meaning and the entire approach becomes invalid.

Another model [44] takes into account at least some of the factors neglected by Nicolais and Narkis [192]. The model applies a different expression for the effective load-bearing cross-section [194] and takes into account also the influence of interfacial interactions and interphase formation (Eq. 7.16) [43]:

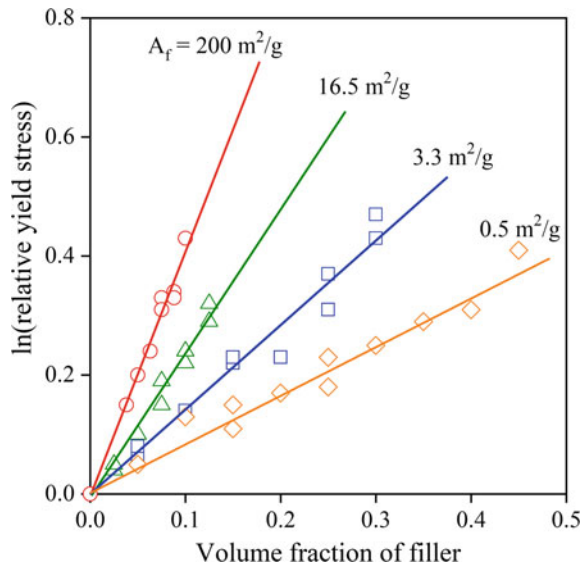
$$\sigma_y = \sigma_{y0} \frac{1 - \varphi_f}{1 + 2.5\varphi_f} \exp(B\varphi_f), \quad (7.16)$$

where B is related to the relative load-bearing capacity of the components, i.e. to interaction. A detailed analysis has shown that B accounts both for changes in interfacial area and for the strength of interaction through the expression (Eq. 7.17):

$$B = \left(1 + A_f \rho_f \ell \right) \ln \frac{\sigma_{yi}}{\sigma_{y0}}, \quad (7.17)$$

where A_f and ρ_f are the specific surface area and density of the filler, while ℓ and σ_{yi} are the thickness of the interphase and its yield stress, respectively. The correlation proved to be valid for most particulate filled systems [67, 93, 149]. The rearrangement of Eq. 7.16 eliminates the effect of changing matrix cross-section and if the natural logarithm of relative yield stress, i.e. $\sigma_{yrel} = \sigma_y(1 + 2.5\varphi_f)/\sigma_{y0}(1 - \varphi_f)$ is plotted against the volume fraction of the filler, straight lines should be obtained. The validity of the approach is proved by Fig. 7.19, in which the relative yield stress of the PP/CaCO₃ composites of Fig. 7.10 is plotted in the linear form. The change in the slope of the straight line indicates the effect of interfacial area (A_f), which increases with decreasing particle size, i.e. with increasing amount of interphase formed (see Eq. 7.17). Parameter B measures quantitatively changes in the strength of interactions achieved by surface modification.

Fig. 7.19 Relative tensile yield stress of the PP/CaCO₃ composites presented in Fig. 7.10 plotted against composition in the linear representation of Eq. 7.16. Specific surface area: (open circle) 200, (open triangle) 16.5, (open square) 3.3, (open diamond) 0.5 m²/g



The composition dependence of ultimate tensile properties, i.e. tensile strength and elongation at break is very similar to that of the yield characteristics. Usually both elongation and strength decrease with increasing filler content, although occasionally some reinforcement can be observed, too. However, changes in elongation with filler content make the prediction of strength difficult; the cross-section of the specimen decreases at large elongations, while the orientation of the matrix results in strain hardening. The modification of Eq. 7.16 successfully copes with these problems, i.e. (Eq. 7.18) [44]:

$$\sigma_T = \sigma_{T0} \lambda^n \frac{1 - \varphi_f}{1 + 2.5\varphi_f} \exp(B\varphi_f), \quad (7.18)$$

where true tensile strength ($\sigma_T = \sigma\lambda$, $\lambda = L/L_0$, relative elongation) accounts for the change in specimen cross-section and λ^n for strain hardening. n characterizes the strain hardening tendency of the polymer and can be determined from matrix properties [44]. B is defined by a correlation similar to Eq. 7.17, but its value is naturally different from that determined from the composition dependence of yield stress.

7.8.4 Fracture and Impact Resistance

Fracture and especially impact resistance are crucial properties of all materials used in engineering applications. Similarly to yield stress, the fracture toughness of

particulate filled polymers is assumed to decrease with filler content, which is not necessarily true. Fracture and impact resistance often increases or goes through a maximum as a function of filler content both in thermoplastic and thermoset matrices [195–198]. Several local deformation processes take place during the deformation and fracture of heterogeneous polymer systems. New deformation processes initiated by heterogeneities always consume energy resulting in an increase of fracture resistance. The various deformation mechanisms consume different amounts of energy, thus the change of properties and composition dependence may also vary according to the actual processes taking place during deformation. Deformation mechanisms leading to the increased plastic deformation of the matrix are the most efficient in improving fracture and impact resistance. Because of the effect of a large number of factors influencing fracture resistance and due to the increased role of micromechanical deformation processes, the modeling of this property is even more difficult than that of other composite characteristics. Nevertheless, a relatively large number of models have been published up to now [199–204], but very few of them gained wide acceptance. The semiempirical model applied for the description of the composition dependence of other mechanical properties (see Eqs. 7.16–7.18) can be extended also to fracture and impact resistance [140]. The model could be used successfully for a large number of composites both with thermoplastic and thermoset matrices.

7.8.5 *Flammability*

The inherent flammability of plastics is one of their major drawbacks and the use of flame-retardants is required today in most applications, especially in construction or transportation. Traditional halogen/antimony flame-retardants are very efficient, but the use of some of their representatives is banned already, because of environmental and health considerations. One of the alternatives is the use of hydrated mineral fillers, like aluminum or magnesium hydroxides. These can provide acceptable levels of flame retardance without the formation of smoke or corrosive and toxic gases. Unfortunately, these minerals must be used in large quantities in order to achieve the necessary effect, which deteriorates other properties, like processability, strength and especially impact resistance. Appropriate surface modification must be used in order to overcome the negative effect of large filler content.

7.8.6 *Conductivity*

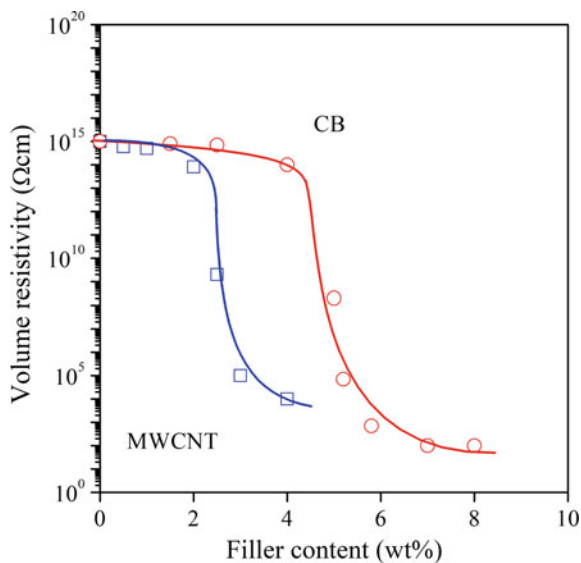
Polymers are insulators with surface resistivity of around 10^{14} – 10^{18} Ω cm. Applications exist which require a certain conductivity, like air ducts in mines, pipes for solvent transport, EMI shielding and some other areas. Conductivity is usually achieved by the introduction of conductive fillers. Traditionally special conductive

carbon blacks or metal fillers, particles or flakes, are used in such applications, but recently intensive research is going on to use carbon nanofibers or nanotubes for this purpose [205–207]. Conductivity increases stepwise at a certain additive content, and the percolation threshold is claimed to be much smaller, around several tenth of a weight percent [205], for nanofillers than for traditional fillers. This claim is strongly supported by the results of Wen et al. [208] presented in Fig. 7.20. The percolation threshold of the special conducting carbon black is around 5 wt% in polypropylene, while that of single walled nanotube is around 2 wt% in the same polymer, indeed. Such behavior can be described and the composition dependence of conductivity can be modeled with percolation theories [209].

7.8.7 Other Properties

Particulate filled and reinforced polymers are frequently used in structural applications and the main goal of modification is often the improvement of stiffness. Nevertheless, occasionally other properties can be at least as important as modulus, while special characteristics are needed in some specific applications. The *heat deflection temperature* (HDT) of particulate filled and reinforced composites is closely related to stiffness and changes with composition in a similar way. Larger reinforcement usually leads to higher HDT, thus anisotropic particles and fibers are more efficient in improving this property than spherical fillers. The introduction of fillers may change the *appearance* of the product (color, surface) or influence the stability of the compound. Some fillers are added to the polymer to improve surface

Fig. 7.20 Comparison of the effect of carbon black and carbon nanotubes on the conductivity of polycarbonate composites. Symbols: (open circle) carbon black, (open square) multiwalled carbon nanotubes



quality (smoothness, shine) or scratch resistance. *Stability* might be influenced quite strongly by the filler. Polyolefins, like PE and PP, are especially sensitive to the presence of heavy metal contaminations, which may accelerate oxidative degradation. Special attention must be called here to layered silicate nanocomposites, both the silicate itself and the functionalized polymer coupling agent was shown to decrease stability in PP nanocomposites [109]. The dissimilar *heat capacity and heat conductivity* of fillers usually have a beneficial effect on processing; shorter cooling times may increase productivity significantly. The *shrinkage* of the polymer also changes advantageously upon the addition of fillers, shrinkage decreases considerably with increasing filler content. Shrinkage of composites containing anisotropic fillers or reinforcements, however, depends on direction that might lead to warpage. The extent of the effect is determined by the orientation of the reinforcement and increases with aspect ratio. Occasionally hybrids, a combination of fillers and fibers are used to compensate the stronger direction dependence of fiber-reinforced composites. Fillers influence the *barrier properties of polymers*, the permeation of gases and vapors decreases with increasing filler content. Platelet like particle geometry is more efficient in decreasing permeability, but the claimed advantage of layered silicates often is not manifested because of the insufficient exfoliation of the clay. Models exist for the description of this phenomenon [110, 111], which take into account the tortuosity of the diffusion path. *Cost* is an important attribute of every engineering material and it usually decreases with increasing filler content. However, decreasing polymer prices and increasing compounding costs make particulate filled polymers competitive only if their technical benefits are utilized in their full extent.

7.9 Special Composites

The introduction of a filler or reinforcement improves some of the properties of the polymer, but influences disadvantageously others. Consequently, many attempts are made to find new ways to achieve desired properties without any sacrifice in others. One way to do this is to combine the effect of two or more different additives. Such combinations result in hybrids with a range of structures and properties. The other approach is to introduce new fillers. Recently much effort was put into the application of nanosized fillers and reinforcements and many attempts are made to use also natural fillers and reinforcements in a wide range of polymers including PP. This section gives a brief survey about these classes of materials.

7.9.1 Multicomponent Materials

One of the main classes of multicomponent polymer systems is formed by composites consisting of a crystalline or glassy matrix, an elastomer and a filler at the

same time. Polypropylene has poor low temperature impact strength, which is frequently improved by the introduction of elastomers [176, 210, 211]. Improvement in impact strength, however, is accompanied by a simultaneous decrease of modulus, which cannot be accepted in certain applications; a filler or reinforcement is added to compensate the effect. Theoretically, two boundary structures may develop in such composites the separate distribution of the components [212–214] and the encapsulation of the filler by the elastomer [213–218]. Surprisingly enough both boundary structures can be observed in practice as shown by Fig. 7.21.

Holes represent the elastomer in the micrographs, since it was etched away to enhance contrast. Separate dispersion is presented in Fig. 7.21a. The holes cover about 20% of the surface of the micrograph, which is in accordance with the volume fraction of the elastomer. Elastomer content is the same in the material shown in Fig. 7.21b, but the area covered by the holes seems to be smaller. Closer scrutiny reveals that a considerable fraction of the voids is located around the filler particles; the elastomer encapsulated the filler. Naturally, the two structures are not exclusive, besides a certain extent of encapsulation, separately dispersed filler and elastomer particles can be also found in the composites.

Although the structures observed agree well with the theoretical possibilities, their occurrence and the reason for it are not evident. A large number of measurements and thermodynamic analysis have shown that the dominating structure is determined by the combined effect of thermodynamic and kinetic factors, by the relative magnitude of adhesion and shear forces prevailing during the homogenization of the composites [219–221]. Thermodynamics always favors embedding, because the surplus energy needed for the formation of new surfaces is smaller in this case. However, if shear forces exceed interfacial interactions, the elastomer layer is sheared off the surface of the filler and separately distributed structure evolves. Adhesive forces depend on interfacial interactions and the particle size of the filler, while shear forces on viscosity and on the rate of mixing. Consequently,

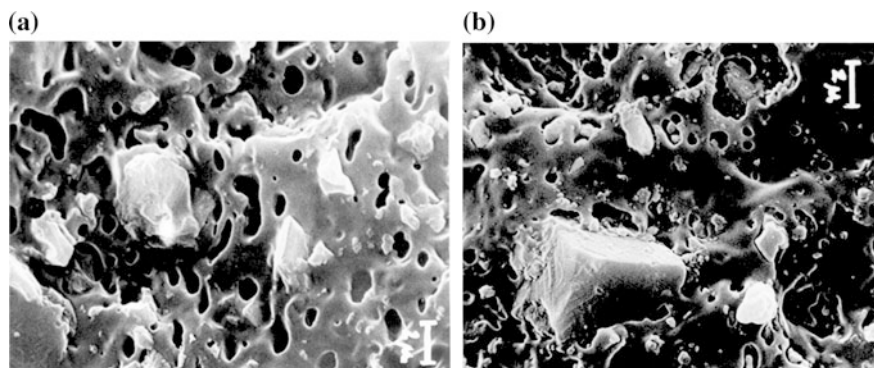


Fig. 7.21 SEM micrographs showing typical structures developing in three-component PP/elastomer (20 vol%)/filler (30 vol%) composites. **a** separate dispersion, **b** embedding of the filler in the elastomer

low surface tension resulting from non-reactive coating, large particles and high shear lead to the separate dispersion of the components. The analysis proved the primary importance of interfacial adhesion in structure formation. Numerous attempts have been made to prepare composites with exclusive structure, i.e. complete coverage or separate distribution. In most cases PP or elastomer modified with maleic anhydride or acrylic acid was used to enhance adhesion between selected components; separate dispersion in the case of MAPP, embedding with MAEPDM [171, 222, 223]. Although the desired effect was observed in almost each case, the exclusiveness could not be proved.

The two structures result in completely different properties mainly due to dissimilar stress distribution and stress concentration around the particles. The effect of embedding is clearly demonstrated by Fig. 7.22, in which the stiffness of the two kinds of composites with different structures is plotted against filler content at 20 vol% elastomer content. We can see that in the composites with the embedded structure stiffness does not increase as expected, but decreases with increasing filler content.

Multicomponent PP composites are extensively used in the automotive industry for the production of bumpers. These materials are expected to have large stiffness and impact resistance simultaneously. Unfortunately, this requirement cannot be easily met, since the two properties are inversely proportional to each other, i.e. an increase in stiffness is usually accompanied by a decrease of impact resistance. This relationship is clearly demonstrated in Fig. 7.23 in which the impact strength and stiffness of three-component PP/elastomer/filler composites are plotted against each other. Most of the composites correspond to the rule mentioned, but a few points are located above the general correlation, i.e. shifted into the desired direction towards larger stiffness and impact resistance. The deviation is obviously related to

Fig. 7.22 Dependence of stiffness on filler content in PP/EPDM/CaCO₃ composites. Elastomer content: 20 vol%. Symbols: (open square) separate dispersion, (open circle) embedding

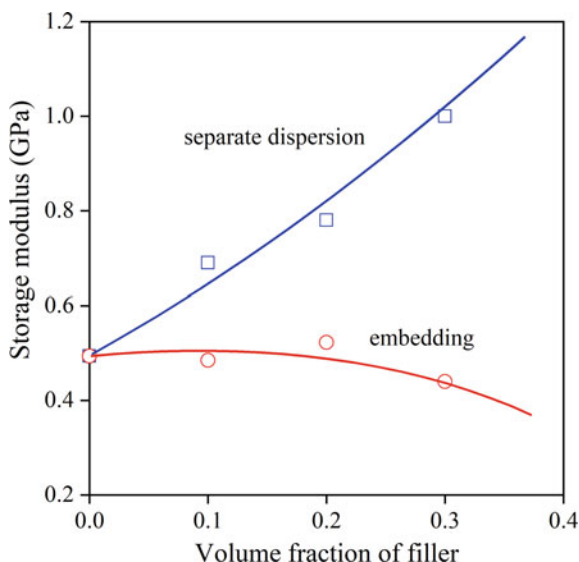
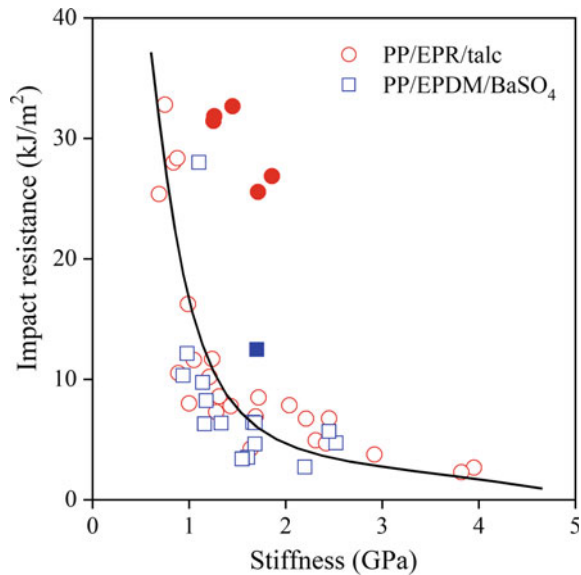


Fig. 7.23 Correlation between the stiffness and toughness of three-component PP/elastomer/filler composites. Influence of changing structure. Symbols: (open circle) PP/EPR/talc, (open square) PP/EPDM/BaSO₄; full symbols: deviation from the general tendency, improved property combination



the structure of the composites, but unfortunately, neither the prediction nor the design of properties is possible at the moment. Further study and analysis are required in order to determine structure-property correlations quantitatively; new materials are developed empirically until then.

7.9.2 Layered Silicate Nanocomposites

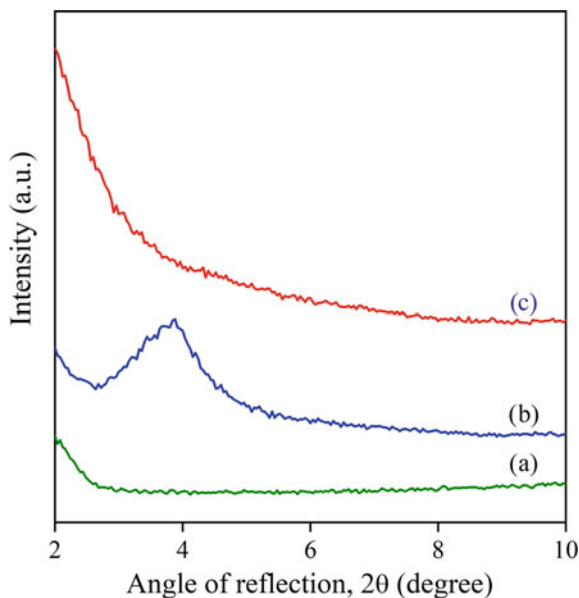
The interest in nanotechnology has been increasing continuously in recent years and it includes all kinds of polymer composites containing nanosized fillers or reinforcements [5]. Layered silicate nanocomposites are one class of these materials containing finely dispersed silicate particles [5, 16, 18, 19, 224]. Extensive exfoliation, i.e. the dispersion of individual silicate layers in the polymer matrix, is a primary condition of the preparation of layered silicate nanocomposites with acceptable properties [225–230]. However, the kinetics and extent of exfoliation depend on many factors and the structure formed in the process is usually much more complicated than that of the traditional particulate filled microcomposites. The presence of original silicate particles, gallery structure, exfoliation and the formation of a silicate network must be considered in nanocomposites, but some of these structural formations are completely neglected in most studies.

The existence of original clay particles, either uncoated sodium montmorillonite (NaMMT), or organophilized silicate, is hardly ever mentioned in studies on nanocomposites. One may deduce from this fact that particles are not present in the composites; i.e. they break down to smaller units, into intercalated stacks or to

individual platelets during mixing. This is not very surprising since mostly XRD and transmission electron microscopy (TEM) are used for the characterization of the composites and those do not necessarily detect the presence of large particles. The problem regarding the use of XRD is illustrated by Fig. 7.24, in which the lower 2θ range of the XRD trace of three PP composites is presented. Trace a) was recorded on a PP/MAPP blend with 20 vol% MAPP content. Naturally, it does not exhibit any silicate reflection. The presence of the silicate is shown clearly in the XRD trace of a PP/OMMT (Nanofil 848, stearylamine, 25 wt%) composite of 2 vol% silicate content and without MAPP (trace b). The incorporation of 20 vol% MAPP into the same composite leads to the complete disappearance of the silicate reflection (trace c) thus one could claim that the original particles disappeared and the silicate is completely exfoliated.

Figure 7.25 completely contradicts the above conclusion regarding trace c). SEM micrographs taken from the etched surfaces of PP/OMMT (Fig. 7.25a) and PP/OMMT/MAPP (Fig. 7.25b) composites show distinct particulate structure in both cases. Large particles are dispersed in PP in the PP/OMMT composite not containing any functionalized polymer. The presence of MAPP clearly changes the morphology. The number of large particles decreases drastically, but a very large amount of smaller particles appear together with one or two larger ones in the 5–10 μm range. Although structure changes considerably, we can safely state that in spite of the absence of the silicate reflection in the corresponding XRD pattern (trace c in Fig. 7.24), completely exfoliated structure has not been achieved, and clay particles in the length scale of microns are present in the composite as well. Their amount and size must strongly influence all properties.

Fig. 7.24 XRD traces of a PP/OMMT blend and PP composites containing 2 vol% silicate; b PP/OMMT, c PP/OMMT/MAPP (20 vol%)



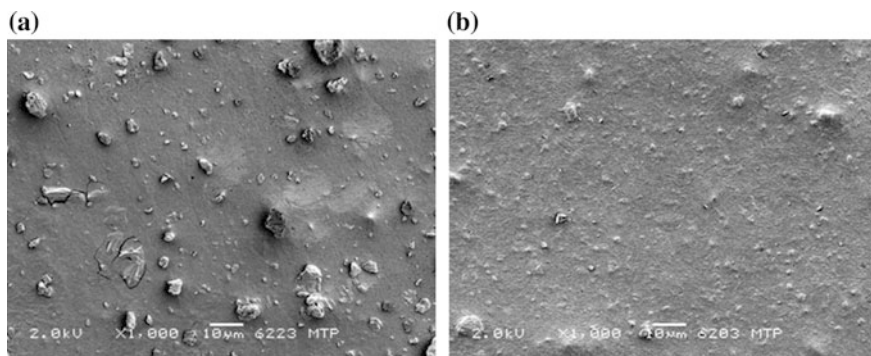


Fig. 7.25 SEM micrographs taken from the etched surface of PP nanocomposites containing 2 vol% organophilic clay. **a** PP/OMMT, **b** PP/OMMT/MAPP (20 vol%)

In the process of nanofiller preparation, solvated inorganic cations located in the galleries of layered silicates are exchanged to organic cations of long chain amines in order to separate the layers. Increased gallery distance and decreased surface energy should lead to easier exfoliation. Consequently, the amount of surfactants located in the galleries and the orientation of the molecules should influence significantly the structure and properties of layered silicate/polymer nanocomposites [231]. The gallery structure of organophilic silicate depends on the chemical structure and amount of the surfactant used for treatment and on the ion exchange capacity of the clay. Fornes et al. [232] claimed that surfactants with two long tails are less advantageous than those with a single aliphatic chain attached to the nitrogen atom; smaller head groups lead to increased exfoliation compared to large ammonium cations, and excess surfactant is disadvantageous for exfoliation, structure development and properties. On the other hand, Vaia [233] found that head groups do not influence intercalation and two long aliphatic chains are more advantageous than one. These contradictions clearly prove that unambiguous, general correlations have not been established yet among the gallery structure of the silicate, interactions and composite properties.

The extent of exfoliation is usually studied by TEM, which is able to detect also individual silicate layers [234, 235]. However, usually intercalated stacks or particles with a range of gallery distances form in the composites and such particles appear in the micrographs. “Very good” composites with a high degree of dispersion may contain stacks of silicates with 3–10 layers [225, 236], but this can be achieved only with the proper selection of components and processing conditions. Unfortunately, structures observed in TEM micrographs depend on composition, but also on sampling, i.e. on the choice of location from which the slice is taken thus it is rather dangerous to draw general conclusions about the extent of exfoliation from them.

At large silicate content and large extent of exfoliation silicate platelets may interact with each other. Face-to-face interaction leads to aggregation, while edge-to-face orientation results in the formation of a silicate network structure. Although quite a few papers mention the formation and existence of such a network as a possibility [229, 230, 237–241], relatively few focus on the determination of the conditions, which would yield such structures or on the characterization of the network itself [229, 239]. The formation of the network is usually detected by TEM [229, 230, 241] or by the analysis of rheological measurements [238, 242]. TEM micrographs published are usually not very convincing, but changes in the low frequency range of complex viscosity or G' , as well as the appearance of a yield stress clearly indicate considerable changes in the structure of the melt, and in all probability refer to the formation of a silicate network [243]. The conditions of network formation and the effect of the network on composite properties are not known presently.

One of the main benefits of layered silicate nanocomposites is claimed to be strong reinforcement at extremely small filler content. The basic conditions for reinforcement are a large extent of exfoliation and good interfacial adhesion between the components. Unfortunately, both the extent of exfoliation and reinforcement are difficult to determine quantitatively and they are rarely discussed in publications. The simple model developed for the prediction of the tensile yield stress and strength of particulate filled polymers (see Eqs. 7.16–7.18 in Sect. 7.8.3) seems to be appropriate for the determination of reinforcement, since parameter B measures the load carried by the filler. Some assumptions make possible also the estimation of the degree of exfoliation. The detailed analysis of a large number of data published in the literature showed that a relatively low level of exfoliation, approximately 12%, is achieved even in the best case and stacks containing approximately 10 silicate layers form in the average [112]. This result agrees well with the experience that complete exfoliation is very difficult to achieve and nanocomposites always contain different structural formations including individual silicate platelets, intercalated stacks, but sometimes even large particles.

7.9.3 *Natural Reinforcements (Wood, Lignin)*

The preparation and use of polymers containing natural fillers or reinforcements is not new in the plastic industry, but these materials went through a revival in recent years all over the world. Mainly commodity thermoplastic polymers are used as matrix materials in wood/plastic composites (WPC) [244, 245]. One of their main advantages is that products can be manufactured with traditional thermoplastic processing technologies for a wide range of applications. Floor or wall coverages and fences are usually prepared from PE, while PVC is mostly used for the production of window or door profiles [246]. Internal panels in cars are produced from polypropylene or polyurethane reinforced with natural fibers [247].

Natural reinforcements possess numerous advantages. They are produced and available in large quantities [248]. Their price is low compared to traditional reinforcements; it competes even with that of mineral fillers. They have large stiffness and strength, as well as low density. They are produced from renewable resources, often as byproducts. They can degrade biologically and the waste can be handled easily. On the other hand, they have a few disadvantages as well. These reinforcements are sensitive to humidity and heat, they have poor transverse strength, and very poor adhesion to the matrix due to their low surface energy. The use of natural fibers and wood flour is a mature technology now; lignin is an emerging raw material with great potential. Intensive research is going on in both areas, i.e. wood and lignin, and the matrix polymer is often PP in these composites and blends.

The properties of PP blends and composites containing natural reinforcements and lignin are determined by the same factors as other composites, but several of these factors have special significance in this case. The particle characteristics of natural reinforcements differ considerably from those of mineral fillers or nano-reinforcements. The size of the particles is usually quite large, wood particles can be several hundred micron large. Most of the particles have anisotropic particle geometry, thus they orientate during processing. The surface energy of natural materials is low; it is in the range of 40–50 mJ/m². Accordingly, the interaction between the polymer and the reinforcement is weak and the large particle size further facilitates debonding. In addition, the inherent strength of the reinforcement is very important; often it determines the ultimate strength of the composites.

The blends and composites always have heterogeneous structure. Structural phenomena also occur and play a role in the determination of composite properties, touching of particles from simple geometrical reason and limited aggregation can take place at large wood content. The orientation of anisotropic particles depends on their aspect ratio and on processing technology. Lignin particles are dispersed as droplets in the polymer matrix; their size depends on interfacial interactions and on the presence or absence of a coupling agent.

Interfacial interactions play a crucial role in the determination of composite properties. The comparison of four surface modification techniques in PP/wood flour composites showed that all four influence the various properties of the composites dissimilarly [118]. Interfacial adhesion and reinforcement improved upon the addition of a maleated polymer (MAPP). Non-reactive surface modification by the use of stearic acid or cellulose palmitate led to a moderate decrease of interaction, while chemical modification, benzylation decreased interfacial adhesion quite considerably. MAPP did not influence any other property of interest; homogeneity, viscosity and water absorption remained unchanged independently of the amount of coupling agent used. Surfactants improved homogeneity and processability, while the chemical modification of wood by benzylation decreased water absorption significantly. The results clearly proved that the proper selection of the approach and the level of surface modification may lead to considerable improvement in targeted properties, on the one hand, and properties must be optimized for good overall performance, on the other. Reactive coupling is also

often used in natural fiber reinforced polymers, silanes, izocyanates, and other coupling agents are often applied to improve properties. The use of functionalized polymers, i.e. maleated PP is the most frequent and efficient approach used in polypropylene as demonstrated by Fig. 7.26 for PP/lignin blends (see also Fig. 7.14 for wood). The strength of the blends not containing the coupling agent decreases drastically with increasing lignin content, while it remains at an acceptable level in its presence. The size of dispersed lignin particles also decreases considerably and homogeneity improves as well when the coupling agent is added.

The properties of composites containing natural reinforcements cover a very wide range. Stiffness usually increases considerably with increasing amount of natural filler, either wood or lignin. On the other hand, strength may increase or decrease depending on the characteristics of the components and interfacial adhesion as Figs. 7.14 and 7.26 show. The tensile strength of PP composites containing various natural reinforcements (wood, corncob) is plotted against composition in Fig. 7.27.

Strength decreases invariably in the case of poor adhesion, but increases significantly, if a MAPP coupling agent is added. The improvement depends also on the particle characteristics of the reinforcement (size, aspect ratio). Unfortunately, deformability decreases drastically with increasing filler content practically always. An even further disadvantage of natural reinforcements is that the impact resistance of their composites is small and it is very difficult or almost impossible to improve. Even the principles discussed in Sect. 7.9.1 for multicomponent materials cannot be applied in their case. Figure 7.28 presents the correlation of notched Charpy impact resistance and stiffness for a wide variety of composites containing various amounts of wood flour and elastomer. The latter is added specifically to improve fracture

Fig. 7.26 Tensile strength of PP/lignin blends plotted as a function of lignin content. Symbols: (open square) no coupling, (open circle) MAPP

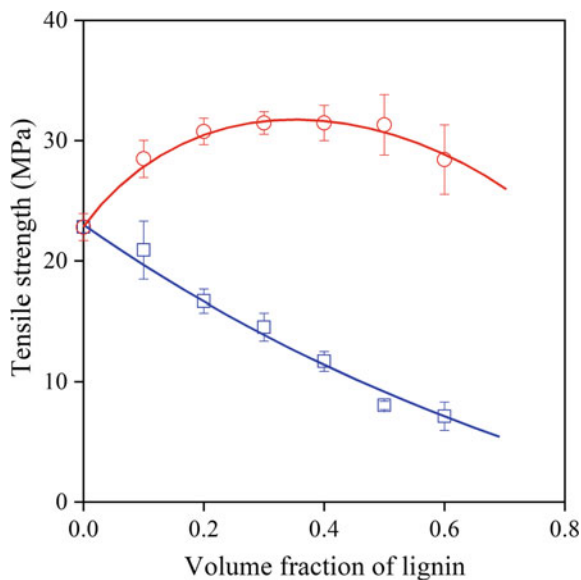


Fig. 7.27 Tensile strength of PP composites reinforced with natural fibers; effect of particle characteristics and adhesion. Full symbols indicate composites prepared without MAPP, while empty symbols show materials with good adhesion (MAPP); (open circle) corncob, aspect ratio (AR): 2.3, (open inverted triangle) wood, AR: 3.5, (open triangle) wood, AR: 6.8, (open square) wood, AR: 12.6

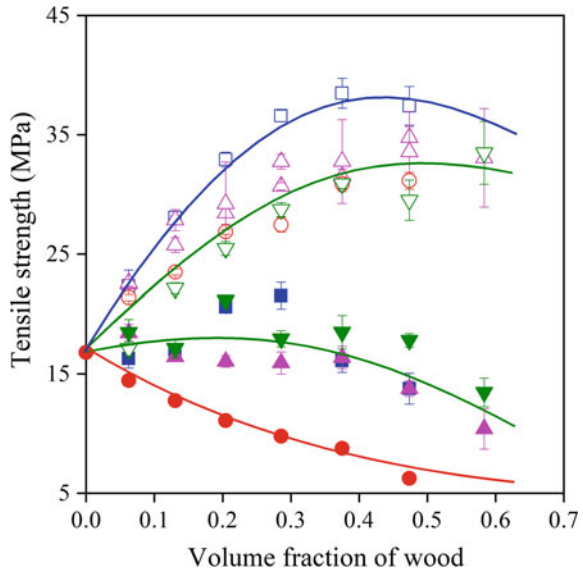
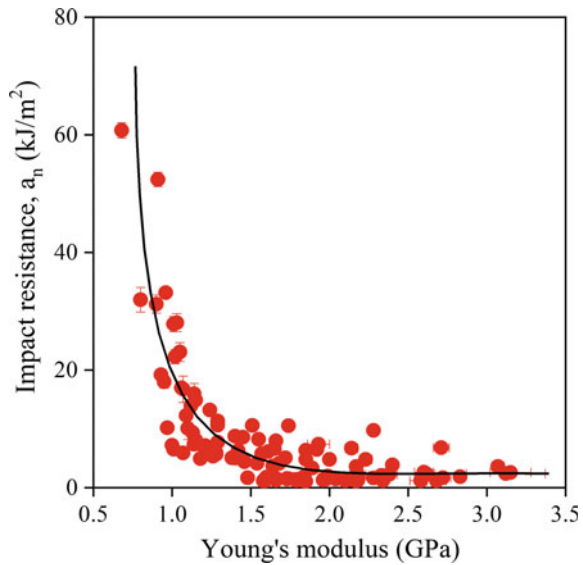


Fig. 7.28 Close correlation between the notched Charpy impact resistance and the stiffness of the composites



resistance. No improvement can be achieved even with the addition of the elastomer (see Fig. 7.23 as comparison), since the inherent strength of the fibers is small and their fracture leads to the catastrophic failure of the composite. Increasing stiffness due to the reinforcing effect of the wood particles further decreases the ability of the matrix to deform plastically and consume energy.

The optimization of the properties of blends and composites containing natural reinforcements is further complicated by the fact that numerous local deformation processes take place in them during deformation (see Sect. 7.7.3). Besides the shear yielding of the matrix and debonding, the usual deformation processes in particulate filled polymer, various fiber related processes also may take place in these materials. The importance of local processes is demonstrated by the correlation of characteristic stress and the tensile strength of composites reinforced with ligno-cellulosic fibers. The correlation is very close and valid irrespectively of the actual mechanism, the type of the matrix polymer or the characteristics of the fibers showing that the failure and ultimate strength are determined by local processes (see Fig. 7.18).

PP composites reinforced with wood, natural fibers or lignin can be produced by thermoplastic processing technologies using equipment adjusted to the materials. The largest amounts are processed by extrusion, but injection molded parts are also prepared in increasing quantities and even thermoformed products appeared on the market lately. Products containing large amounts of wood often require the use of special lubricants or processing aids to improve processability and surface quality. The largest application area of these products are the building and automotive industry, but interior and garden furniture, office appliances and other products are also prepared in increasing numbers. The potential of these composites is large and further growth is expected in the future.

7.10 Conclusions

Although particulate filled polymer composites are mature materials with a long history of application, their structure-property correlations are more complicated than usually assumed. The characteristics of all heterogeneous polymer systems including composites containing micro or nano fillers are determined by four factors: component properties, composition, structure and interfacial interactions. Several filler characteristics influence composite properties, but the most important ones are particle size, size distribution, specific surface area, particle shape and in the case of natural reinforcements the inherent strength of the particles. The main matrix property is stiffness. Composite properties usually depend non-linearly on composition, thus they must be always determined as a function of filler content. The structure of particulate filled polymers is often more complicated than expected, segregation, aggregation and the orientation of anisotropic particles may take place. Interfacial interactions invariably develop in composites; they lead to the formation of a stiff interphase considerably influencing properties. Interactions can be modified by surface treatment, which must be always system specific and selected according to the goal of modification. Particulate filled polymers are heterogeneous materials in which inhomogeneous stress distribution and stress concentration develop under the effect of external load. These initiate local micromechanical deformation processes, which determine the macroscopic

properties of the composites. The dominating deformation mechanism is usually debonding in filled polymers, but quite a few other processes can also take place especially in natural fiber reinforced composites. The number of reliable models to predict properties is relatively small, but they offer valuable information about structure and interactions. Although the modification of polypropylene is an accepted approach and mature technology now, research is going on and further development is expected in the future.

Acknowledgements The research on heterogeneous polymer systems has been financed by the National Scientific Research Fund of Hungary (OTKA Grant No. K 120039).

References

1. Agarwal S, Gupta RK (2017) Plastics in Buildings and Construction. In: Kutz M (ed) Applied plastics engineering handbook, 2nd edn. William Andrew Publishing, pp 635–649. <https://doi.org/10.1016/B978-0-323-39040-8.00030-4>
2. Stewart R (2010) Automotive composites offer lighter solutions. *Rein Plast* 54:22–28. [https://doi.org/10.1016/S0034-3617\(10\)70061-8](https://doi.org/10.1016/S0034-3617(10)70061-8)
3. Maier C, Calafut T (1998) 11—Applications. In: Polypropylene—the definitive user’s guide and databook. William Andrew Publishing, Norwich, NY, pp 87–107. <https://doi.org/10.1016/B978-188420758-7.50016-3>
4. Rother R (2003) Particulate-filled polymer composites. Rapra Technology, Shrewsbury
5. Alexandre M, Dubois P (2000) Polymer-layered silicate nanocomposites: preparation, properties and uses of a new class of materials. *Mater Sci Eng R-Rep* 28(1–2):1–63. [https://doi.org/10.1016/S0927-796X\(00\)00012-7](https://doi.org/10.1016/S0927-796X(00)00012-7)
6. Rother R (2007) The high performance fillers market and the position of precipitated calcium carbonate and silica. In: High performance fillers. Smithers Rapra Ltd., Hamburg, Germany, pp Paper 1 (1–4)
7. Pukánszky B (1995) Particulate filled polypropylene: structure and properties. In: Karger-Kocsis J (ed) Polypropylene: structure, blends and composites—composites, vol 3. Chapman and Hall, London, pp 1–70
8. Pukánszky B (1999) Fillers for polypropylene. In: Karger-Kocsis J (ed) Polypropylene: an A-Z reference. Kluwer Academic, Dordrecht, pp 240–246
9. Pukánszky B (1999) Particulate filled polypropylene composites. In: Karger-Kocsis J (ed) Polypropylene: an A-Z reference. Springer Netherlands, Dordrecht, pp 574–580. https://doi.org/10.1007/978-94-011-4421-6_78
10. Katz HS, Milevski JV (1978) Handbook of fillers and reinforcements for plastics. Van Nostrand, New York
11. Weidenfeller B, Kirchberg S (2016) Thermal and mechanical properties of polypropylene-iron-diamond composites. *Compos B Eng* 92:133–141. <https://doi.org/10.1016/j.compositesb.2016.02.011>
12. Weidenfeller B, Hofer M, Schilling FR (2005) Cooling behaviour of particle filled polypropylene during injection moulding process. *Compos Pt A-Appl Sci Manuf* 36(3):345–351. <https://doi.org/10.1016/j.compositesa.2004.07.002>
13. Weidenfeller B, Hofer M, Schilling FR (2004) Thermal conductivity, thermal diffusivity, and specific heat capacity of particle filled polypropylene. *Compos Pt A-Appl Sci Manuf* 35 (4):423–429. <https://doi.org/10.1016/j.compositesa.2003.11.005>

14. Wang M, Zeng X-F, Chen J-Y et al (2017) Magnesium hydroxide nanodispersion for polypropylene nanocomposites with high transparency and excellent fire-retardant properties. *Polym Degrad Stabil* 146:327–333. <https://doi.org/10.1016/j.polymdegradstab.2017.10.016>
15. Hu P, Yang H (2013) Polypropylene filled with kaolinite-based conductive powders. *Appl Clay Sci* 83–84:122–128. <https://doi.org/10.1016/j.clay.2013.08.025>
16. Ray SS, Okamoto M (2003) Polymer/layered silicate nanocomposites: a review from preparation to processing. *Prog Polym Sci* 28(11):1539–1641. <https://doi.org/10.1016/j.progpolymsci.2003.08.002>
17. Kotal M, Bhowmick AK (2015) Polymer nanocomposites from modified clays: recent advances and challenges. *Prog Polym Sci* 51:127–187. <https://doi.org/10.1016/j.progpolymsci.2015.10.001>
18. Pinnavaia TJ, Beall GW (2001) *Polymer-clay nanocomposites*. Wiley, New York
19. LeBaron PC, Wang Z, Pinnavaia TJ (1999) Polymer-layered silicate nanocomposites: an overview. *Appl Clay Sci* 15(1–2):11–29. [https://doi.org/10.1016/S0169-1317\(99\)00017-4](https://doi.org/10.1016/S0169-1317(99)00017-4)
20. Al-Malaika S, Sheena H, Fischer D et al (2013) Influence of processing and clay type on nanostructure and stability of polypropylene-clay nanocomposites. *Polym Degrad Stabil* 98(12):2400–2410. <https://doi.org/10.1016/j.polymdegradstab.2013.10.009>
21. Kawasumi M, Hasegawa N, Kato M et al (1997) Preparation and mechanical properties of polypropylene-clay hybrids. *Macromolecules* 30(20):6333–6338. <https://doi.org/10.1021/ma961786h>
22. Garcia-Lopez D, Picazo O, Merino JC et al (2003) Polypropylene-clay nanocomposites: effect of compatibilizing agents on clay dispersion. *Eur Polym J* 39(5):945–950. [https://doi.org/10.1016/s0014-3057\(02\)00333-6](https://doi.org/10.1016/s0014-3057(02)00333-6)
23. Ma J, Bilotti E, Peijs T et al (2007) Preparation of polypropylene/sepiolite nanocomposites using supercritical CO₂ assisted mixing. *Eur Polym J* 43(12):4931–4939. <https://doi.org/10.1016/j.eurpolymj.2007.09.010>
24. Bilotti E, Fischer HR, Peijs T (2008) Polymer nanocomposites based on needle-like sepiolite clays: effect of functionalized polymers on the dispersion of nanofiller, crystallinity, and mechanical properties. *J Appl Polym Sci* 107(2):1116–1123. <https://doi.org/10.1002/app.25395>
25. Manchanda B, Kottiyath VK, Kapur GS et al (2017) Morphological studies and thermo-mechanical behavior of polypropylene/sepiolite nanocomposites. *Polym Compos* 38:E285–E294. <https://doi.org/10.1002/pc.23800>
26. Manchanda B, Vimal KK, Kapur GS et al (2016) Effect of sepiolite on nonisothermal crystallization kinetics of polypropylene. *J Mater Sci* 51(21):9535–9550. <https://doi.org/10.1007/s10853-016-0210-3>
27. Prashantha K, Lacrampe MF, Krawczak P (2011) Processing and characterization of halloysite nanotubes filled polypropylene nanocomposites based on a masterbatch route: effect of halloysites treatment on structural and mechanical properties. *Express Polym Lett* 5(4):295–307. <https://doi.org/10.3144/expresspolymlett.2011.30>
28. Khunova V, Kristof J, Kelnar I et al (2013) The effect of halloysite modification combined with in situ matrix modifications on the structure and properties of polypropylene/halloysite nanocomposites. *Express Polym Lett* 7(5):471–479. <https://doi.org/10.3144/expresspolymlett.2013.43>
29. Wang B, Huang HX (2013) Effects of halloysite nanotube orientation on crystallization and thermal stability of polypropylene nanocomposites. *Polym Degrad Stabil* 98(9):1601–1608. <https://doi.org/10.1016/j.polymdegradstab.2013.06.022>
30. Bhattacharyya AR, Sreekumar TV, Liu T et al (2003) Crystallization and orientation studies in polypropylene/single wall carbon nanotube composite. *Polymer* 44(8):2373–2377. [https://doi.org/10.1016/s0032-3861\(03\)00073-9](https://doi.org/10.1016/s0032-3861(03)00073-9)
31. Assouline E, Lustiger A, Barber AH et al (2003) Nucleation ability of multiwall carbon nanotubes in polypropylene composites. *J Polym Sci Pt B-Polym Phys* 41(5):520–527. <https://doi.org/10.1002/polb.10394>

32. Alig I, Lellinger D, Dudkin SM et al (2007) Conductivity spectroscopy on melt processed polypropylene-multiwalled carbon nanotube composites: recovery after shear and crystallization. *Polymer* 48(4):1020–1029. <https://doi.org/10.1016/j.polymer.2006.12.035>
33. Dittrich B, Wartig KA, Hofmann D et al (2013) Flame retardancy through carbon nanomaterials: carbon black, multiwall nanotubes, expanded graphite, multi-layer graphene and graphene in polypropylene. *Polym Degrad Stabil* 98(8):1495–1505. <https://doi.org/10.1016/j.polymdegradstab.2013.04.009>
34. Bikiaris D (2010) Microstructure and properties of polypropylene/carbon nanotube nanocomposites. *Materials* 3(4):2884–2946. <https://doi.org/10.3390/ma3042884>
35. Song PG, Cao ZH, Cai YZ et al (2011) Fabrication of exfoliated graphene-based polypropylene nanocomposites with enhanced mechanical and thermal properties. *Polymer* 52(18):4001–4010. <https://doi.org/10.1016/j.polymer.2011.06.045>
36. Xu JZ, Chen C, Wang Y et al (2011) Graphene nanosheets and shear flow induced crystallization in isotactic polypropylene nanocomposites. *Macromolecules* 44(8):2808–2818. <https://doi.org/10.1021/ma1028104>
37. Huang GB, Wang SQ, Song PA et al (2014) Combination effect of carbon nanotubes with graphene on intumescent flame-retardant polypropylene nanocomposites. *Compos Pt A-Appl Sci Manuf* 59:18–25. <https://doi.org/10.1016/j.compositesa.2013.12.010>
38. Pukánszky B (2000) Polyolefin composites: interfacial phenomena and properties. In: Vasile C (ed) *Handbook of polyolefins*. Marcel Dekker, New York, pp 689–722
39. Donnet J-B, Custodero E (2005) 8—Reinforcement of elastomers by particulate fillers (A2—Mark, James E). In: Erman B, Eirich FR (eds) *Science and technology of rubber*, 3rd edn. Academic Press, Burlington, pp 367–400. <https://doi.org/10.1016/B978-012464786-2/50011-0>
40. Krysztafkiewicz A (1988) Surface-modified fillers for reinforcing elastomers. *Surf Coat Technol* 35(1–2):151–170. [https://doi.org/10.1016/0257-8972\(88\)90065-5](https://doi.org/10.1016/0257-8972(88)90065-5)
41. Vörös G, Fekete E, Pukánszky B (1997) An interphase with changing properties and the mechanism of deformation in particulate-filled polymers. *J Adhes* 64(1–4):229–250
42. Pukánszky B, Vörös G (1996) Stress distribution around inclusions, interaction, and mechanical properties of particulate-filled composites. *Polym Compos* 17(3):384–392. <https://doi.org/10.1002/pc.10625>
43. Pukánszky B, Turcsányi B, Tüdös F (1988) Effect of interfacial interaction on the tensile yield stress of polymer composites. In: Ishida H (ed) *Interfaces in polymer, ceramic, and metal matrix composites*. Elsevier, New York, pp 467–477
44. Pukánszky B (1990) Influence of interface interaction on the ultimate tensile properties of polymer composites. *Composites* 21(3):255–262. [https://doi.org/10.1016/0010-4361\(90\)90240-W](https://doi.org/10.1016/0010-4361(90)90240-W)
45. Leong YW, Abu Bakar MB, Ishak ZAM et al (2004) Comparison of the mechanical properties and interfacial interactions between talc, kaolin, and calcium carbonate filled polypropylene composites. *J Appl Polym Sci* 91(5):3315–3326. <https://doi.org/10.1002/app.13542>
46. Premalal HGB, Ismail H, Baharin A (2002) Comparison of the mechanical properties of rice husk powder filled polypropylene composites with talc filled polypropylene composites. *Polym Test* 21(7):833–839. [https://doi.org/10.1016/S0142-9418\(02\)00018-1](https://doi.org/10.1016/S0142-9418(02)00018-1)
47. Menczel J, Varga J (1983) Influence of nucleating agents on crystallization of polypropylene. *J Therm Anal* 28(1):161–174. <https://doi.org/10.1007/BF02105288>
48. Verbeek J, Christopher M (2012) Mica-Reinforced Polymer Composites. In: Thomas S, Kuruvilla J, Malhotra SK, Goda K, Sreekala MS (eds) *Polymer Composites*. Wiley, Weinheim, pp 673–713
49. Jahani Y (2011) Comparison of the effect of mica and talc and chemical coupling on the rheology, morphology, and mechanical properties of polypropylene composites. *Polym Adv Technol* 22(6):942–950. <https://doi.org/10.1002/pat.1600>

50. Hartl AM, Jerabek M, Freudenthaler P et al (2015) Orientation-dependent compression/tension asymmetry of short glass fiber reinforced polypropylene: deformation, damage and failure. *Compos A Appl Sci Manuf* 79:14–22. <https://doi.org/10.1016/j.compositesa.2015.08.021>
51. Schoßig M, Zankel A, Bierögel C et al (2011) ESEM investigations for assessment of damage kinetics of short glass fibre reinforced thermoplastics—results of in situ tensile tests coupled with acoustic emission analysis. *Compos Sci Technol* 71(3):257–265. <https://doi.org/10.1016/j.compscitech.2010.12.004>
52. Hartikainen J, Hine P, Szabó JS et al (2005) Polypropylene hybrid composites reinforced with long glass fibres and particulate filler. *Compos Sci Technol* 65(2):257–267. <https://doi.org/10.1016/j.compscitech.2004.07.010>
53. Fu S-Y, Lauke B, Mäder E et al (2000) Tensile properties of short-glass-fiber- and short-carbon-fiber-reinforced polypropylene composites. *Compos A Appl Sci Manuf* 31(10):1117–1125. [https://doi.org/10.1016/S1359-835X\(00\)00068-3](https://doi.org/10.1016/S1359-835X(00)00068-3)
54. Liang JZ, Wu CB (2012) Effects of the glass bead content and the surface treatment on the mechanical properties of polypropylene composites. *J Appl Polym Sci* 123(5):3054–3063. <https://doi.org/10.1002/app.34850>
55. Jerabek M, Major Z, Renner K et al (2010) Filler/matrix-debonding and micro-mechanisms of deformation in particulate filled polypropylene composites under tension. *Polymer* 51(9):2040–2048
56. Yang K, Yang Q, Li G et al (2008) Mechanical properties and morphologies of polypropylene with different sizes of glass bead particles. *Polym Compos* 29(9):992–997. <https://doi.org/10.1002/pc.20476>
57. Manchanda B, Kottiyath VK, Kapur GS et al (2017) Morphological studies and thermo-mechanical behavior of polypropylene/sepiolite nanocomposites. *Polym Compos* 38(S1):E285–E294. <https://doi.org/10.1002/pc.23800>
58. Velasco JI, Morhain C, Martínez AB *et al.* (2002) The effect of filler type, morphology and coating on the anisotropy and microstructure heterogeneity of injection-moulded discs of polypropylene filled with aluminium and magnesium hydroxides. Part 2. Thermal and dynamic mechanical properties. *Polymer* 43(25):6813–6819. [https://doi.org/10.1016/S0032-3861\(02\)00669-9](https://doi.org/10.1016/S0032-3861(02)00669-9)
59. Velasco JI, Morhain C, Martínez AB *et al.* (2002) The effect of filler type, morphology and coating on the anisotropy and microstructure heterogeneity of injection-moulded discs of polypropylene filled with aluminium and magnesium hydroxides. Part 1. A wide-angle X-ray diffraction study. *Polymer* 43 (25):6805–6811. [https://doi.org/10.1016/S0032-3861\(02\)00668-7](https://doi.org/10.1016/S0032-3861(02)00668-7)
60. Velasco JI, Morhain C, Arencon D et al (1998) Low-rate fracture behaviour of magnesium hydroxide filled polypropylene block copolymer. *Polym Bull* 41(5):615–622
61. Liauw CM, Lees GC, Hurst SJ et al (1996) The effect of surface modification of aluminium hydroxide on the crystallisation behaviour of aluminium hydroxide filled polypropylenes. *Die Angewandte Makromolekulare Chemie* 235(1):193–203. <https://doi.org/10.1002/apmc.1996.052350116>
62. Liauw CM, Khunova V, Lees GC et al (2001) Interphase structure development in impact modified PP/Mg(OH)₂ composites reactively processed with 1,3-phenylene dimaleimide. *Macromol Symp* 170(1):205–212
63. Bledzki AK, Gassan J (1999) Composites reinforced with cellulose based fibres. *Prog Polym Sci* 24(2):221–274. [https://doi.org/10.1016/S0079-6700\(98\)00018-5](https://doi.org/10.1016/S0079-6700(98)00018-5)
64. Bledzki AK, Sperber VE, Faruk O (2002) Natural and wood fibre reinforcement in polymers, vol 13(8). *Rapra Technology*, Shawbury
65. Dányádi L, Renner K, Szabó Z et al (2006) Wood flour filled PP composites: adhesion, deformation, failure. *Polym Adv Technol* 17(11–12):967–974. <https://doi.org/10.1002/pat.838>

66. Dányádi L, Janecska T, Szabó Z et al (2007) Wood flour filled PP composites: compatibilization and adhesion. *Compos Sci Technol* 67(13):2838–2846. <https://doi.org/10.1016/j.compscitech.2007.01.024>
67. Dányádi L, Renner K, Móczó J et al (2007) Wood flour filled polypropylene composites: Interfacial adhesion and micromechanical deformations. *Polym Eng Sci* 47(8):1246–1255. <https://doi.org/10.1002/pen.20768>
68. Renner K, Móczó J, Pukánszky B (2011) Polymer/wood composites. In: Nicolais L, Borzacchiello A (eds) *Wiley encyclopedia of composites*. Wiley, pp 1–19
69. Liang JZ, Li B, Ruan JQ (2015) Crystallization properties and thermal stability of polypropylene composites filled with wollastonite. *Polym Test* 42:185–191. <https://doi.org/10.1016/j.polymertesting.2015.01.017>
70. Hadal RS, Dasari A, Rohrmann J et al (2004) Effect of wollastonite and talc on the micromechanisms of tensile deformation in polypropylene composites. *Mater Sci Eng A-Struct Mater Prop Microstruct Process* 372(1–2):296–315. <https://doi.org/10.1016/j.msea.2004.01.003>
71. Švab I, Musil V, Šmit I et al (2007) Mechanical properties of wollastonite-reinforced polypropylene composites modified with SEBS and SEBS-g-MA elastomers. *Polym Eng Sci* 47(11):1873–1880. <https://doi.org/10.1002/pen.20897>
72. Essabir H, Nekhlaoui S, Bensalah MO et al (2017) phosphogypsum waste used as reinforcing fillers in polypropylene based composites: structural, mechanical and thermal properties. *J Polym Environ* 25(3):658–666. <https://doi.org/10.1007/s10924-016-0853-9>
73. Dong F, Liu J, Tan H et al (2017) Preparation of calcium sulfate hemihydrate and application in polypropylene composites. *J Nanosci Nanotechnol* 17(9):6970–6975. <https://doi.org/10.1166/jnn.2017.14413>
74. Nekhlaoui S, Essabir H, Kunal D et al (2015) Comparative study for the talc and two kinds of moroccan clay as reinforcements in polypropylene-SEBS-g-MA matrix. *Polym Compos* 36(4):675–684. <https://doi.org/10.1002/pc.22986>
75. Ábrányi Á, Százdi L, Pukánszky B et al (2006) Formation and detection of clay network structure in poly(propylene)/layered silicate nanocomposites. *Macromol Rapid Commun* 27(2):132–135. <https://doi.org/10.1002/marc.200500687>
76. Al-Malaika S, Sheena H, Fischer D et al (2013) Influence of processing and clay type on nanostructure and stability of polypropylene–clay nanocomposites. *Polym Degrad Stabil* 98(12):2400–2410. <https://doi.org/10.1016/j.polymdegradstab.2013.10.009>
77. Maiti SN, Mahapatro PK (1989) Crystallization of PP in PP/Ni composites and its correlation with tensile properties. *J Appl Polym Sci* 37(7):1889–1899. <https://doi.org/10.1002/app.1989.070370712>
78. Gúldas A, Altuğ M, Temel S (2017) Mechanical properties of aluminum powder reinforced polypropylene. *Mater Test* 59(1):86–93. <https://doi.org/10.3139/120.110970>
79. Maiti SN, Mahapatro PK (1990) Thermal properties of nickel powder filled polypropylene composites. *Polym Compos* 11(4):223–228. <https://doi.org/10.1002/pc.750110405>
80. Maiti SN, Mahapatro PK (1988) Melt rheological properties of nickel powder filled polypropylene composites. *Polym Compos* 9(4):291–296. <https://doi.org/10.1002/pc.750090408>
81. Chen XL, Jiao CM, Wang Y (2009) Synergistic effects of iron powder on intumescent flame retardant polypropylene system. *Express Polym Lett* 3:359–365. <https://doi.org/10.3144/expresspolymlett.2009.45>
82. Callens MG, De Cuyper P, Gorbatikh L et al (2015) Effect of fibre architecture on the tensile and impact behaviour of ductile stainless steel fibre polypropylene composites. *Compos Struct* 119:528–533. <https://doi.org/10.1016/j.compstruct.2014.09.028>
83. Bigg DM (1987) Mechanical properties of particulate filled polymers. *Polym Compos* 8(2):115–122. <https://doi.org/10.1002/pc.750080208>
84. Zuchowska D, Hlavata D (1991) Some physical properties of polypropylene-phenolic microsphere blends. *Eur Polym J* 27(4–5):355–357. [https://doi.org/10.1016/0014-3057\(91\)90187-S](https://doi.org/10.1016/0014-3057(91)90187-S)

85. Hamzah M, Hidayah I, Mariatti M et al (2014) Dielectric and thermal properties of flame retardant fillers in polypropylene/ethylene propylene diene monomer composites. *J Reinf Plast Compos* 33(21):1931–1940. <https://doi.org/10.1177/0731684414553381>
86. Bajaj P, Jha NK, Maurya PL et al (1987) Flame retardation of polypropylene: Effect of organoantimony compounds on the structural and mechanical properties. *J Appl Polym Sci* 34(5):1785–1801. <https://doi.org/10.1002/app.1987.070340502>
87. Nielsen LE (1974) *Mechanical properties of polymers and composites*. Marcel Dekker, New York
88. Vollenberg P, Heikens D, Ladan HCB (1988) Experimental determination of thermal and adhesion stress in particle filled thermoplasts. *Polym Compos* 9(6):382–388. <https://doi.org/10.1002/pc.750090603>
89. Pukánszky B, van Ess M, Maurer FHJ et al (1994) Micromechanical deformations in particulate filled thermoplastics—volume strain-measurements. *J Mater Sci* 29(9):2350–2358. <https://doi.org/10.1007/BF00363426>
90. Móczó J, Fekete E, László K et al (2003) Aggregation of particulate fillers: factors, determination, properties. *Macromol Symp* 194:111–124. <https://doi.org/10.1002/masy.200390071>
91. Miltner HE, Van Assche G, Pozsgay A et al (2006) Restricted chain segment mobility in poly(amide) 6/clay nanocomposites evidenced by quasi-isothermal crystallization. *Polymer* 47(3):826–835. <https://doi.org/10.1016/j.polymer.2005.12.014>
92. Fekete E, Molnár S, Kim GM et al (1999) Aggregation, fracture initiation, and strength of PP/CaCO₃ composites. *J Macromol Sci-Phys B38*(5–6):885–899. <https://doi.org/10.1080/00222349908248146>
93. Pukánszky B, Fekete E, Tüdös F (1989) Surface tension and mechanical properties in polyolefin composites. *Makromol Chem-Macromol Symp* 28:165–186. <https://doi.org/10.1002/masy.19890280112>
94. Liauw CM, Lees GC, Rothern RN et al (2006) Evolution of reactive unsaturated interfacial modifiers for polyolefin based composites. *Compos Interfaces* 13(8–9):717–736. <https://doi.org/10.1163/156855406779366750>
95. Iraola-Arregui I, Potgieter H, Liauw CM (2011) Evaluation of coupling agents in poly(propylene)/fly ash composites: effect on processing and mechanical properties. *Macromol Mater Eng* 296(9):810–819. <https://doi.org/10.1002/mame.201000413>
96. Busigin C, Lahtinen R, Martinez GM et al (1984) The properties of mica-filled polypropylenes. *Polym Eng Sci* 24(3):169–174. <https://doi.org/10.1002/pen.760240303>
97. Mitsubishi K, Kodama S, Kawasaki H (1987) Effect of filler properties on the modulus of oriented polypropylene filled with flake-like fillers. *J Macromol Sci B* 26(4):479–494. <https://doi.org/10.1080/00222348708223949>
98. Parrinello LM (1991) Fibre geometry effects on physical properties of chopped fibre composites. *Tappi J* 74(1):85–88
99. Riley AM, Paynter CD, McGenity PM et al (1990) Factors affecting the impact properties of mineral filled polypropylene. *Plast Rub Proc Appl* 14(2):85–93
100. Trotignon JP, Verdu J, De Boissard R et al (1986) Polypropylene-mica composites. In: Sedláček B (ed) *Polymer composites*. Walter de Gruyter, Berlin, pp 191–198
101. Schlumpf HP (1983) Fillers and reinforcing materials in plastics—physicochemical aspects for the processor. *Kunststoffe-German Plastics* 73(9):511–515
102. Ramsteiner F, Theysohn R (1984) On the tensile behaviour of filled composites. *Composites* 15(2):121–128. [https://doi.org/10.1016/0010-4361\(84\)90723-7](https://doi.org/10.1016/0010-4361(84)90723-7)
103. Stoklasa K, Tomis F, Navratil Z (1985) Investigation of polymer systems using thermomechanical analysis. *Thermochim Acta* 93 (SEP):221–224. [http://doi.org/10.1016/0040-6031\(85\)85057-7](http://doi.org/10.1016/0040-6031(85)85057-7)
104. Kerch GM, Irgen LA (1985) Thermal-analysis of the interaction between components in polypropylene and polyethylene blends. *Thermochim Acta* 93 (SEP):155–157. [http://doi.org/10.1016/0040-6031\(85\)85040-1](http://doi.org/10.1016/0040-6031(85)85040-1)

105. Bar M, Alagirusamy R, Das A (2015) Flame retardant polymer composites. *Fiber Polym* 16 (4):705–717. <http://doi.org/10.1007/s12221-015-0705-6>
106. Balakrishnan H, Hassan A, Isitman NA et al (2012) On the use of magnesium hydroxide towards halogen-free flame-retarded polyamide-6/polypropylene blends. *Polym Degrad Stabil* 97(8):1447–1457. <https://doi.org/10.1016/j.polyimdegradstab.2012.05.011>
107. Ma H, Li Z, Tian X et al (2018) Silver flakes and silver dendrites for hybrid electrically conductive adhesives with enhanced conductivity. *J Electron Mater* 47(5):2929–2939. <https://doi.org/10.1007/s11664-018-6145-5>
108. Samuels RJ (1974) *Structured polymer properties, the identification, interpretation, and application of crystalline polymer structure*. Wiley, New York
109. Masahiro N, Yasuharu F, Takenobu M et al (2001) The effect of talc on the crystallization of isotactic polypropylene. *J Appl Polym Sci* 79(9):1693–1703. [https://doi.org/10.1002/1097-4628\(20010228\)79:9%3c1693::AID-APP190%3e3.0.CO;2-P](https://doi.org/10.1002/1097-4628(20010228)79:9%3c1693::AID-APP190%3e3.0.CO;2-P)
110. Maiti P, Nam PH, Okamoto M et al (2002) Influence of crystallization on intercalation, morphology, and mechanical properties of polypropylene/clay nanocomposites. *Macromolecules* 35(6):2042–2049. <https://doi.org/10.1021/ma010852z>
111. Pozsgay A, Frater T, Papp L et al (2002) Nucleating effect of montmorillonite nanoparticles in polypropylene. *J Macromol Sci-Phys B* 41(4–6):1249–1265. <https://doi.org/10.1081/MB-120013095>
112. Százdí L, Pozsgay A, Pukánszky B (2007) Factors and processes influencing the reinforcing effect of layered silicates in polymer nanocomposites. *Eur Polym J* 43(2):345–359. <https://doi.org/10.1016/j.eurpolymj.2006.11.005>
113. Avella M, Cosco S, Di Lorenzo ML et al (2006) Nucleation activity of nanosized CaCO₃ on crystallization of isotactic polypropylene, in dependence on crystal modification, particle shape, and coating. *Eur Polym J* 42(7):1548–1557. <https://doi.org/10.1016/j.eurpolymj.2006.01.009>
114. Varga J, Toth FS (1991) Filled compounds of the β -modification of polypropylene. *Angew Makromol Chem* 188:11–25. <https://doi.org/10.1002/apmc.1991.051880102>
115. Lincoln DM, Vaia RA, Wang ZG et al (2001) Temperature dependence of polymer crystalline morphology in nylon 6/montmorillonite nanocomposites. *Polymer* 42(25):9975–9985. [https://doi.org/10.1016/S0032-3861\(01\)00542-0](https://doi.org/10.1016/S0032-3861(01)00542-0)
116. Choi JS, Lim ST, Choi HJ et al (2006) Effect of interfacial interaction on the structure and rheological properties of polyamide-6/clay nanocomposites. *Compos Interfaces* 13(8–9):773–782. <https://doi.org/10.1163/156855406779366705>
117. Hutley TJ, Darlington MW (1984) Impact strength DSC correlation in mineral-filled polypropylene. *Polym Commun* 25(8):226–228
118. Maiti SN, Mahapatro PK (1990) Crystallization of i-PP/CaCO₃ composites and its correlation with tensile properties. *Int J Polym Mater* 14(3–4):205–222. <https://doi.org/10.1080/00914039008031514>
119. Pukánszky B, Belina K, Rockenbauer A et al (1994) Effect of nucleation, filler anisotropy and orientation on the properties of PP composites. *Composites* 25(3):205–214. [https://doi.org/10.1016/0010-4361\(94\)90018-3](https://doi.org/10.1016/0010-4361(94)90018-3)
120. Pukánszky B, Mudra I, Staniek P (1997) Relation of crystalline structure and mechanical properties of nucleated polypropylene. *J Vinyl Addit Technol* 3(1):53–57. [https://doi.org/10.1016/0010-4361\(94\)90018-3](https://doi.org/10.1016/0010-4361(94)90018-3)
121. Kubát J, Szalánczi A (1974) Polymer-glass separation in the spiral mold test. *Polym Eng Sci* 14(12):873–877. <https://doi.org/10.1002/pen.760141211>
122. Karger-Kocsis J, Csikai I (1987) Skin-core morphology and failure of injection-molded specimens of impact-modified polypropylene blends. *Polym Eng Sci* 27(4):241–253. <https://doi.org/10.1002/pen.760270403>
123. Gupta VB, Mittal RK, Sharma PK *et al.* (1989) Some studies on glass fiber-reinforced polypropylene. Part I: reduction in fiber length during processing. *Polym Compos* 10(1):8–15. <https://doi.org/10.1002/pc.750100103>

124. Tausz SE, Chaffey CE (1982) Ultrasonically de-laminated and coarse mica particles as reinforcements for polypropylene. *J Appl Polym Sci* 27(11):4493–4500. <https://doi.org/10.1002/app.1982.070271136>
125. Adams JM, Edmondson B (1987) Forces between particles in continuous and discrete liquid media. In: Briscoe BJ, Adams JM (eds) *Tribology in particulate technology*. Adam Hilger, Bristol, pp 154–172
126. Adams JM, Mullier MA, Seville JPK (1987) Agglomeration. In: Briscoe BJ, Adams JM (eds) *Tribology in particulate technology*. Adam Hilger, Bristol, pp 375–389
127. Balachandran W (1987) Electrostatic effects in the adhesion of particles to solid surfaces. In: Briscoe BJ, Adams JM (eds) *Tribology in particulate technology*. Adam Hilger, Bristol, pp 135–153
128. Kamal MR, Song L, Singh P (1986) Measurement of fiber and matrix orientations in fiber reinforced composites. *Polym Compos* 7(5):323–329. <https://doi.org/10.1002/pc.750070509>
129. Sanou M, Chung B, Cohen C (1985) Glass fiber-filled thermoplastics. II. Cavity filling and fiber orientation in injection molding. *Polym Eng Sci* 25 (16):1008–1016. <https://doi.org/10.1002/pen.760251604>
130. Rockenbauer A, Jókay L, Pukánszky B et al (1985) Electron-paramagnetic resonance investigation of orientation produced by mechanical processing in the fillers of polymer composites. *Macromolecules* 18(5):918–923. <https://doi.org/10.1021/ma00147a017>
131. Mittal RK, Gupta VB, Sharma P (1987) The effect of fiber orientation on the interfacial shear-stress in short fiber-reinforced polypropylene. *J Mater Sci* 22(6):1949–1955. <https://doi.org/10.1007/BF01132922>
132. Christie M (1986) Toughening weld lines of mica-reinforced PP parts. *Plast Eng* 42(7): 41–45
133. Fisa B, Dufour J, Vukhanh T (1987) Weldline integrity of reinforced-plastics—effect of filler shape. *Polym Compos* 8(6):408–418. <https://doi.org/10.1002/pc.750080607>
134. Fowkes FM (1964) Attractive forces at interfaces. *Ind Eng Chem* 56(12):40–52. <https://doi.org/10.1021/ie50660a008>
135. Wu S (1974) Interfacial and surface tensions of polymers. *J Macromol Sci C* 10(1):1–73. <https://doi.org/10.1080/15321797408080004>
136. Fowkes FM (1981) Acid-base interactions in polymer adhesion. In: Mittal RK (ed) *Physicochemical aspects of polymer surfaces*. Plenum, New York, pp 583–603
137. Drago RS, Vogel GC, Needham TE (1971) Four-parameter equation for predicting enthalpies of adduct formation. *J Am Chem Soc* 93(23):6014–6026. <https://doi.org/10.1021/ja00752a010>
138. Gutmann V (1978) *The donor-acceptor approach to molecular interactions*, 1st edn. Plenum Press, New York
139. Fekete E, Móczó J, Pukánszky B (2004) Determination of the surface characteristics of particulate fillers by inverse gas chromatography at infinite dilution: a critical approach. *J Colloid Interface Sci* 269(1):143–152. [https://doi.org/10.1016/S0021-9797\(03\)00719-7](https://doi.org/10.1016/S0021-9797(03)00719-7)
140. Pukánszky B, Maurer FHJ (1995) Composition dependence of the fracture toughness of heterogeneous polymer systems. *Polymer* 36(8):1617–1625. [https://doi.org/10.1016/0032-3861\(95\)99007-H](https://doi.org/10.1016/0032-3861(95)99007-H)
141. Stamhuis JE, Loppe JPA (1982) Rheological determination of polymer-filler affinity. *Rheol Acta* 21(1):103–105. <https://doi.org/10.1007/BF01520711>
142. Maurer FHJ, Kosfeld R, Uhlenbroich T (1985) Interfacial interaction in kaolin-filled polyethylene composites. *Colloid Polym Sci* 263(8):624–630. <https://doi.org/10.1007/BF01419886>
143. Vollenberg PHT, Heikens D (1989) Particle size dependence of the Young's modulus of filled polymers: I. Preliminary experiments. *Polymer* 30(9):1656–1662. [https://doi.org/10.1016/0032-3861\(89\)90326-1](https://doi.org/10.1016/0032-3861(89)90326-1)
144. Maurer FHJ (1986) Interphase effects on viscoelastic properties of polymer composites. In: Sedláček B (ed) *Polymer composites*. Walter de Gruyter, Berlin, pp 399–411

145. Maiti SN, Mahapatro PK (1991) Mechanical-properties of i-PP/CaCO₃ composites. *J Appl Polym Sci* 42(12):3101–3110. <https://doi.org/10.1002/app.1991.070421204>
146. Iisaka K, Shibayama K (1978) Mechanical alfa-dispersion and interaction in filled polystyrene and polymethylmethacrylate. *J Appl Polym Sci* 22(11):3135–3143. <https://doi.org/10.1002/app.1978.070221109>
147. Maurer FHJ, Schoffeleers HM, Kosfeld R et al (1982) Analysis of polymer-filler interaction in filled polyethylene. In: Hayashi T, Kawata K, Umekawa S (eds) *Progress in science and engineering of composites*. ICCM-IV, Tokyo, pp 803–809
148. Akay G (1990) Flow induced polymer-filler interactions: bound polymer properties and bound polymer-free polymer phase separation and subsequent phase inversion during mixing. *Polym Eng Sci* 30(21):1361–1372. <https://doi.org/10.1002/pen.760302106>
149. Pukánszky B, Tüdös F (1990) Indirect determination of interphase thickness from the mechanical properties of particulate filled polymers. In: Ishida H (ed) *Controlled interphases in composite materials*. Elsevier Science Publishing Co., Inc., New York, pp 691–700. https://doi.org/10.1007/978-94-011-7816-7_64
150. Mansfield KF, Theodorou DN (1991) Atomistic simulation of a glassy polymer/graphite interface. *Macromolecules* 24(15):4295–4309. <https://doi.org/10.1021/ma00015a011>
151. Móczó J, Fekete E, Pukánszky B (2002) Acid-base interactions and interphase formation in particulate-filled polymers. *J Adhes* 78(10):861–875. <https://doi.org/10.1080/00218460214099>
152. Pukánszky B (1992) Effect of interfacial interactions on the deformation and failure properties of PP/CaCO₃ composites. *New Polym Mat* 3:205–217
153. Gutowski W (1990) Effect of fiber-matrix adhesion on mechanical-properties of composites. In: Ishida H (ed) *Controlled interphases in composite materials*. Elsevier, New York, pp 505–520
154. Felix JM, Gatenholm P (1991) The nature of adhesion in composites of modified cellulose fibers and polypropylene. *J Appl Polym Sci* 42(3):609–620. <https://doi.org/10.1002/app.1991.070420307>
155. Fox HW, Hare EF, Zisman WA (1955) Wetting properties of organic liquids on high-energy surfaces. *J Phys Chem* 59(10):1097–1106. <https://doi.org/10.1021/j150532a027>
156. Móczó J, Fekete E, Pukánszky B (2004) Adsorption of surfactants on CaCO₃ and its effect on surface free energy. In: *From colloids to nanotechnology*, vol 125. *Progress in colloid and polymer science*, pp 134–141. https://doi.org/10.1007/978-3-540-45119-8_22
157. Fekete E, Pukánszky B, Tóth A et al (1990) Surface modification and characterization of particulate mineral fillers. *J Colloid Interface Sci* 135(1):200–208. [https://doi.org/10.1016/0021-9797\(90\)90300-D](https://doi.org/10.1016/0021-9797(90)90300-D)
158. Marosi G, Bertalan G, Ruzsákné I et al (1989) Role of interfacial layers in the properties of particle-filled polyolefin systems. *Colloids Surf* 23(3):185–198. [https://doi.org/10.1016/0166-6622\(89\)80334-8](https://doi.org/10.1016/0166-6622(89)80334-8)
159. Jancár J, Kucera J (1990) Yield behavior of polypropylene filled with CaCO₃ and Mg(OH)₂. I: “zero” interfacial adhesion. *Polym Eng Sci* 30(12):707–713. <https://doi.org/10.1002/pen.760301203>
160. Allard RC, Vukhanh T, Chalifoux JP (1989) Fatigue crack propagation in mica-filled polyolefins. *Polym Compos* 10(1):62–68. <https://doi.org/10.1002/pc.750100110>
161. Matienzo LJ, Shah TK (1986) Surface treatment of phlogopite particles for composite applications: XPS and DRIFT studies. *Surf Interface Anal* 8(2):53–59. <https://doi.org/10.1002/sia.740080203>
162. Vollenberg PHT, Heikens D (1990) The mechanical properties of chalk-filled polypropylene: a preliminary investigation. *J Mater Sci* 25(7):3089–3095. <https://doi.org/10.1007/BF00587655>
163. Raj RG, Kokta BV, Daneault C (1989) Polypropylene-wood fiber composites: effect of fiber treatment on mechanical properties. *Int J Polym Mater* 12(3):239–250. <https://doi.org/10.1080/00914038908031503>

164. Mäder E, Freitag K-H (1990) Interface properties and their influence on short fibre composites. *Composites* 21(5):397–402. [https://doi.org/10.1016/0010-4361\(90\)90437-2](https://doi.org/10.1016/0010-4361(90)90437-2)
165. Demjén Z, Pukánszky B, Földes E et al (1997) Interaction of silane coupling agents with CaCO_3 . *J Colloid Interface Sci* 190(2):427–436. <https://doi.org/10.1006/jcis.1997.4894>
166. Sadler EJ, Vecere AC (1995) Silane treatment of mineral fillers—practical aspects. *Plast Rubber Compos Process Appl* 24(5):271–275
167. Zolotnitsky M, Steinmetz JR (1995) Comparative study of organofunctional water-borne silanes as couplants in nylon-66 composites. *J Vinyl Technol* 1(2):109–113. <https://doi.org/10.1002/vnl.730010213.n>
168. Demjén Z, Pukánszky B, Nagy J (1999) Possible coupling reactions of functional silanes and polypropylene. *Polymer* 40(7):1763–1773. [https://doi.org/10.1016/S0032-3861\(98\)00396-6](https://doi.org/10.1016/S0032-3861(98)00396-6)
169. Bajaj P, Jha NK, Jha RK (1989) Effect of titanate coupling agents on mechanical properties of mica-filled polypropylene. *Polym Eng Sci* 29(8):557–563. <https://doi.org/10.1002/pen.760290810>
170. Takase S, Shiraishi N (1989) Studies on composites from wood and polypropylenes. II. *J Appl Polym Sci* 37(3):645–659. <https://doi.org/10.1002/app.1989.070370305>
171. Chiang WY, Yang WD (1988) Polypropylene composites. I. Studies of the effect of grafting of acrylic-acid and silane coupling agent on the performance of polypropylene mica composites. *J Appl Polym Sci* 35(3):807–823. <https://doi.org/10.1002/app.1988.070350320>
172. Renner K, Móczó J, Vörös G et al (2010) Quantitative determination of interfacial adhesion in composites with strong bonding. *Eur Polym J* 46(10):2000–2004. <https://doi.org/10.1016/j.eurpolymj.2010.07.008>
173. Vörös G, Pukánszky B (2001) Effect of a soft interlayer with changing properties on the stress distribution around inclusions and yielding of composites. *Compos Pt A-Appl Sci Manuf* 32(3–4):343–352. [https://doi.org/10.1016/S1359-835X\(00\)00125-1](https://doi.org/10.1016/S1359-835X(00)00125-1)
174. Goodier JN (1933) Concentration of stress around spherical and cylindrical inclusions and flaws. *J Appl Mech* 55:39–44
175. Pukánszky B, Vörös G (1993) Mechanism of interfacial interactions in particulate filled composites. *Compos Interfaces* 1(5):411–427. <https://doi.org/10.1163/156855493X00266>
176. Bucknall CB (1977) Toughened plastics. Applied Sci. Publ, London
177. Nakagawa H, Sano H Improvement of impact resistance of calcium carbonate filled polypropylene and poly-ethylene block copolymer. In: M. CB (ed) Polymer preprints division of polymer chemistry American chemical society, Chicago, IL, USA, 1985. Papers presented at the Chicago, Illinois Meeting, vol 2. Washington, DC, USA. ACS, Div of polymer chemistry, pp 249–250
178. Trantina GG (1984) Fatigue life prediction of filled polypropylene based on creep-rupture. *Polym Eng Sci* 24(15):1180–1184. <https://doi.org/10.1002/pen.760241507>
179. Renner K, Móczó J, Suba P et al (2010) Micromechanical deformations in PP/lignocellulosic filler composites: Effect of matrix properties. *Compos Sci Technol* 70(7):1141–1147. <https://doi.org/10.1016/j.compscitech.2010.02.029>
180. Renner K, Kenyó C, Móczó J et al (2010) Micromechanical deformation processes in PP/wood composites: Particle characteristics, adhesion, mechanisms. *Compos Pt A-Appl Sci Manuf* 41(11):1653–1661. <https://doi.org/10.1016/j.compositesa.2010.08.001>
181. Renner K, Móczó J, Pukánszky B (2009) Deformation and failure of PP composites reinforced with lignocellulosic fibers: effect of inherent strength of the particles. *Compos Sci Technol* 69(10):1653–1659. <https://doi.org/10.1016/j.compscitech.2009.03.015>
182. Faulkner DL, Schmidt LR (1977) Glass bead-filled polypropylene part I: rheological and mechanical properties. *Polym Eng Sci* 17(9):657–665. <https://doi.org/10.1002/pen.760170902>
183. Jeffrey DJ, Acrivos A (1976) Rheological properties of suspensions of rigid particles. *AIChE J* 22(3):417–432. <https://doi.org/10.1002/aic.690220303>
184. Mooney M (1951) The viscosity of a concentrated suspension of spherical particles. *J Colloid Sci* 6(2):162–170. [https://doi.org/10.1016/0095-8522\(51\)90036-0](https://doi.org/10.1016/0095-8522(51)90036-0)

185. McGee S, McGullough RL (1981) Combining rules for predicting the thermoelastic properties of particulate filled polymers, polymers, polyblends, and foams. *Polym Compos* 2 (4):149–161. <https://doi.org/10.1002/pc.750020403>
186. Dickie RA (1978) Mechanical properties (small deformations) of multiphase polymer blends. In: Paul DR (ed) *Polymer blends*. Academic Press, New York, pp 353–391
187. Ahmed S, Jones FR (1990) A review of particulate reinforcement theories for polymer composites. *J Mater Sci* 25(12):4933–4942. <https://doi.org/10.1007/BF00580110>
188. Halpin JC, Kardos JL (1972) Moduli of crystalline polymers employing composite theory. *J Appl Phys* 43(5):2235–2241. <https://doi.org/10.1063/1.1661482>
189. Christensen RM, Lo KH (1979) Solutions for effective shear properties in three phase sphere and cylinder models. *J Mech Phys Solids* 27(4):315–330. [https://doi.org/10.1016/0022-5096\(79\)90032-2](https://doi.org/10.1016/0022-5096(79)90032-2)
190. Cv P, Kf E, Fr J (1982) Dynamic mechanical behavior of filled polyethylenes and model composites. *Polym Eng Sci* 22(15):968–974. <https://doi.org/10.1002/pen.760221511>
191. Vollenberg P (1987) The mechanical behaviour of particle filled thermoplastics, Ph. D. Thesis, Eindhoven University of Technology, Eindhoven
192. Nicolais L, Narkis M (1971) Stress-strain behavior of styrene-acrylonitrile/glass bead composites in the glassy region. *Polym Eng Sci* 11(3):194–199. <https://doi.org/10.1002/pen.760110305>
193. Ishai O, Cohen LJ (1968) Effect of fillers and voids on compressive yield of epoxy composites. *J Compos Mater* 2(3):302–315. <https://doi.org/10.1177/002199836800200303>
194. Turcsányi B, Pukánszky B, Tüdös F (1988) Composition dependence of tensile yield stress in filled polymers. *J Mater Sci Lett* 7(2):160–162. <https://doi.org/10.1007/BF01730605>
195. Liang J-Z, Li RKY (1999) Brittle–ductile transition in polypropylene filled with glass beads. *Polymer* 40(11):3191–3195. [https://doi.org/10.1016/S0032-3861\(98\)00532-1](https://doi.org/10.1016/S0032-3861(98)00532-1)
196. Liang J-Z (2007) Impact fracture toughness of hollow glass bead-filled polypropylene composites. *J Mater Sci* 42(3):841–846. <https://doi.org/10.1007/s10853-006-0074-z>
197. Brown SK (1980) Mechanisms of fracture in filled thermosetting resins. *Br Polym J* 12 (1):24–30. <https://doi.org/10.1002/pi.4980120106>
198. Sung KH (2007) Fracture surface morphology in thermosets modified with hollow microspheres. *J Appl Polym Sci* 105(6):3287–3294. <https://doi.org/10.1002/app.26596>
199. Friedrich K, Karsch UA (1983) Failure processes in particulate filled polypropylene. *Fibre Sci Technol* 18(1):37–52. [https://doi.org/10.1016/0015-0568\(83\)90049-0](https://doi.org/10.1016/0015-0568(83)90049-0)
200. Evans AG, Williams S, Beaumont PWR (1985) On the toughness of particulate filled polymers. *J Mater Sci* 20(10):3668–3674. <https://doi.org/10.1007/BF01113774>
201. Jancár J, Dibenedetto AT, Dianselmo A (1993) Effect of adhesion on the fracture toughness of calcium carbonate-filled polypropylene. *Polym Eng Sci* 33(9):559–563. <https://doi.org/10.1002/pen.760330908>
202. Kendall K (1978) Fracture of particulate filled polymers. *Br Polym J* 10(1):35–38. <https://doi.org/10.1002/pi.4980100107>
203. J. D, T. VK (1988) Role of morphology and coupling agent in fracture performance of glass-filled polypropylene. *Polym Compos* 9(5):360–367. <https://doi.org/10.1002/pc.750090509>
204. Lange FF (1970) The interaction of a crack front with a second-phase dispersion. *The Philosophical Magazine: J Theor Exp Appl Phys* 22(179):0983–0992. <https://doi.org/10.1080/14786437008221068>
205. Potschke P, Kretschmar B, Janke A (2007) Use of carbon nanotube filled polycarbonate in blends with montmorillonite filled polypropylene. *Compos Sci Technol* 67(5):855–860. <https://doi.org/10.1016/j.compscitech.2006.02.034>
206. Panamoottil SM, Potschke P, Lin RJT et al (2013) Conductivity of microfibrillar polymer-polymer composites with CNT-loaded microfibrils or compatibilizer: a comparative study. *Express Polym Lett* 7:607–620. <https://doi.org/10.3144/expresspolymlett.2013.58>
207. Pötschke P, Bhattacharyya AR, Janke A et al (2005) Melt mixing as method to disperse carbon nanotubes into thermoplastic polymers. *Fullerenes, Nanotubes, Carbon Nanostruct* 13(sup1):211–224. <https://doi.org/10.1081/FST-200039267>

208. Wen M, Sun X, Su L et al (2012) The electrical conductivity of carbon nanotube/carbon black/polypropylene composites prepared through multistage stretching extrusion. *Polymer* 53(7):1602–1610. <https://doi.org/10.1016/j.polymer.2012.02.003>
209. Barrau S, Demont P, Peigney A et al (2003) DC and AC conductivity of carbon nanotubes-polyepoxy composites. *Macromolecules* 36(14):5187–5194. <https://doi.org/10.1021/ma021263b>
210. Karger-kocsis J, Kallo A, Kuleznev VN (1984) Phase structure of impact-modified polypropylene blends. *Polymer* 25(2):279–286. [https://doi.org/10.1016/0032-3861\(84\)90337-9](https://doi.org/10.1016/0032-3861(84)90337-9)
211. Karger-Kocsis J, Harmia T, Czigány T (1995) Comparison of the fracture and failure behavior of polypropylene composites reinforced by long glass fibers and by glass mats. *Compos Sci Technol* 54(3):287–298. [https://doi.org/10.1016/0266-3538\(95\)00068-2](https://doi.org/10.1016/0266-3538(95)00068-2)
212. Kolarik J, Lednický F (1986) Structure of polypropylene/EPDM elastomer/calcium carbonate composites. In: Sedláček B (ed) *Polymer composites*. Walter de Gruyter, Berlin, pp 537–544
213. Hornsby PR, Premphet K (1998) Influence of phase microstructure on the mechanical properties of ternary phase polypropylene composites. *J Appl Polym Sci* 70(3):587–597. [https://doi.org/10.1002/\(SICI\)1097-4628\(19981017\)70:3%3c587:AID-APP21%3e3.0.CO;2-X](https://doi.org/10.1002/(SICI)1097-4628(19981017)70:3%3c587:AID-APP21%3e3.0.CO;2-X)
214. Premphet K, Horanont P (1999) Influence of stearic acid treatment of filler particles on the structure and properties of ternary-phase polypropylene composites. *J Appl Polym Sci* 74(14):3445–3454
215. Pukánszky B, Kolárik J, Lednický F (1986) Mechanical properties of three-component polypropylene composites. In: Sedláček B (ed) *Polymer composites*. Walter de Gruyter, Berlin, pp 553–560
216. Stamhuis JE (1984) Mechanical properties and morphology of polypropylene composites. Talc-filled, elastomer-modified polypropylene. *Polym Compos* 5(3):202–207. <https://doi.org/10.1002/pc.750050308>
217. Stamhuis JE (1988) Mechanical properties and morphology of polypropylene composites. III. Short glass fiber reinforced elastomer modified polypropylene. *Polym Compos* 9(4):280–284. <https://doi.org/10.1002/pc.750090406>
218. Stamhuis JE (1988) Mechanical-properties and morphology of polypropylene composites. II. Effect of polar components in talc-filled polypropylene. *Polym Compos* 9(1):72–77. <https://doi.org/10.1002/pc.750090110>
219. Molnár S, Pukánszky B, Hammer CO et al (2000) Impact fracture study of multicomponent polypropylene composites. *Polymer* 41(4):1529–1539. [https://doi.org/10.1016/S0032-3861\(99\)00305-5](https://doi.org/10.1016/S0032-3861(99)00305-5)
220. Hammer CO, Maurer FHJ, Molnár S et al (1999) Control of the structure and properties of barium sulphate-filled blends of polypropylene and ethylene propylene copolymers. *J Mater Sci* 34(23):5911–5918. <https://doi.org/10.1023/A:1004799327190>
221. Pukánszky B, Tüdös F, Kolárik J et al (1990) Ternary composites of polypropylene, elastomer, and filler: analysis of phase structure formation. *Polym Compos* 11(2):98–104. <https://doi.org/10.1002/pc.750110205>
222. Kelnar I (1991) The effect of PP and EPR grafted with acrylic acid on the properties and phase structure of polypropylene/elastomer/short glass fibre composites. *Angew Makromol Chem* 189:207–218. <https://doi.org/10.1002/apmc.1991.051890119>
223. Chiang WY, Yang WD, Pukánszky B (1992) Polypropylene composites. II: structure-property relationships in two- and three-component polypropylene composites. *Polym Eng Sci* 32(10):641–648. <https://doi.org/10.1002/pen.760321002>
224. Giannelis EP (1998) Polymer-layered silicate nanocomposites: synthesis, properties and applications. *Appl Organomet Chem* 12(10–11):675–680. [https://doi.org/10.1002/\(SICI\)1099-0739\(199810/11\)12:10/11%3c675:AID-AOC779%3e3.0.CO;2-V](https://doi.org/10.1002/(SICI)1099-0739(199810/11)12:10/11%3c675:AID-AOC779%3e3.0.CO;2-V)
225. Hua W, Changchun Z, Mark E et al (2001) Processing and properties of polymeric nano-composites. *Polym Eng Sci* 41(11):2036–2046. <https://doi.org/10.1002/pen.10899>

226. Osman MA, Rupp JEP, Suter UW (2005) Tensile properties of polyethylene-layered silicate nanocomposites. *Polymer* 46(5):1653–1660. <https://doi.org/10.1016/j.polymer.2004.11.112>
227. Ellis TS, D'Angelo JS (2003) Thermal and mechanical properties of a polypropylene nanocomposite. *J Appl Polym Sci* 90(6):1639–1647. <https://doi.org/10.1002/app.12830>
228. Oya A, Kurokawa Y, Yasuda H (2000) Factors controlling mechanical properties of clay mineral/polypropylene nanocomposites. *J Mater Sci* 35(5):1045–1050. <https://doi.org/10.1023/A:1004773222849>
229. Okamoto M, Nam PH, Maiti P et al (2001) A house of cards structure in polypropylene/clay nanocomposites under elongational flow. *Nano Lett* 1(6):295–298. <https://doi.org/10.1021/nl0100163>
230. Reichert P, Nitz H, Klinke S et al (2000) Poly(propylene)/organoclay nanocomposite formation: influence of compatibilizer functionality and organoclay modification. *Macromol Mater Eng* 275(2):8–17. [https://doi.org/10.1002/\(SICI\)1439-2054\(20000201\)275:1%3c8:AID-MAME8%3e3.0.CO;2-6](https://doi.org/10.1002/(SICI)1439-2054(20000201)275:1%3c8:AID-MAME8%3e3.0.CO;2-6)
231. Hyun YH, Lim ST, Choi HJ et al (2001) Rheology of Poly(ethylene oxide)/Organoclay Nanocomposites. *Macromolecules* 34(23):8084–8093. <https://doi.org/10.1021/ma002191w>
232. Fornes TD, Paul DR (2003) Modeling properties of nylon 6/clay nanocomposites using composite theories. *Polymer* 44(17):4993–5013. [https://doi.org/10.1016/S0032-3861\(03\)00471-3](https://doi.org/10.1016/S0032-3861(03)00471-3)
233. Vaia RA, Giannelis EP (1997) Lattice model of polymer melt intercalation in organically-modified layered silicates. *Macromolecules* 30(25):7990–7999. <https://doi.org/10.1021/ma9514333>
234. Lim ST, Hyun YH, Choi HJ et al (2002) Synthetic biodegradable aliphatic polyester/montmorillonite nanocomposites. *Chem Mat* 14(4):1839–1844. <https://doi.org/10.1021/cm010377j>
235. Monticelli O, Musina Z, Russo S et al (2007) On the use of TEM in the characterization of nanocomposites. *Mater Lett* 61(16):3446–3450. <https://doi.org/10.1016/j.matlet.2006.11.086>
236. Manias E, Touny A, Wu L et al. (2001) Polypropylene/montmorillonite nanocomposites. Review of the synthetic routes and materials properties. *Chem Mater* 13(10):3516–3523. <https://doi.org/10.1021/cm0110627>
237. Kaempfer D, Thomann R, Mühlaupt R (2002) Melt compounding of syndiotactic polypropylene nanocomposites containing organophilic layered silicates and in situ formed core/shell nanoparticles. *Polymer* 43(10):2909–2916. [https://doi.org/10.1016/S0032-3861\(02\)00113-1](https://doi.org/10.1016/S0032-3861(02)00113-1)
238. Wagener R, Reisinger TJG (2003) A rheological method to compare the degree of exfoliation of nanocomposites. *Polymer* 44(24):7513–7518. <https://doi.org/10.1016/j.polymer.2003.01.001>
239. Varghese S, Karger-Kocsis J (2003) Natural rubber-based nanocomposites by latex compounding with layered silicates. *Polymer* 44(17):4921–4927. [https://doi.org/10.1016/S0032-3861\(03\)00480-4](https://doi.org/10.1016/S0032-3861(03)00480-4)
240. Moussaif N, Groeninckx G (2003) Nanocomposites based on layered silicate and miscible PVDF/PMMA blends: melt preparation, nanophase morphology and rheological behaviour. *Polymer* 44(26):7899–7906. <https://doi.org/10.1016/j.polymer.2003.10.053>
241. Nam PH, Maiti P, Okamoto M et al (2001) A hierarchical structure and properties of intercalated polypropylene/clay nanocomposites. *Polymer* 42(23):9633–9640. [https://doi.org/10.1016/S0032-3861\(01\)00512-2](https://doi.org/10.1016/S0032-3861(01)00512-2)
242. Peter R, Botho H, Thorsten B et al (2001) Morphological stability of poly(propylene) nanocomposites. *Macromol Rapid Commun* 22(7):519–523. [https://doi.org/10.1002/1521-3927\(20010401\)22:7%3c519:AID-MARC519%3e3.0.CO;2-W](https://doi.org/10.1002/1521-3927(20010401)22:7%3c519:AID-MARC519%3e3.0.CO;2-W)
243. Lertwimolnun W, Vergnes B (2005) Influence of compatibilizer and processing conditions on the dispersion of nanoclay in a polypropylene matrix. *Polymer* 46(10):3462–3471. <https://doi.org/10.1016/j.polymer.2005.02.018>

244. Markarian J (2002) Additive developments aid growth in wood-plastic composites. *Plast Add Compd* 4(11):18–21
245. Bledzki AK, Gassan J, Theis S (1998) Wood-filled thermoplastic composites. *Mech Compos Mater* 34(6):563–568. <https://doi.org/10.1007/BF02254666>
246. De Vetter L, Depraetere G, Janssen C et al (2008) Methodology to assess both the efficacy and ecotoxicology of preservative-treated and modified wood. *Ann Sci* 65(5):504
247. Ashori A (2008) Wood–plastic composites as promising green-composites for automotive industries! *Bioresour Technol* 99(11):4661–4667. <https://doi.org/10.1016/j.biortech.2007.09.043>
248. Suddell BC, Evans WJ (2005) Natural fiber composites in automotive applications. In: Mohanty AK, Mishra M, Drzal LT (eds) *Natural fibers, biopolymers, and biocomposites*. CRC Press, Boca Raton, pp 231–259

Chapter 8

Polypropylene Blends: Properties Control by Design



Wen Shyang Chow

Contents

8.1	Introduction.....	420
8.2	Basic Principles of Polymer Blends.....	421
8.3	PP Binary Blends	424
8.3.1	PP/Thermoplastic Blends.....	424
8.3.2	PP Thermoplastic Elastomer	427
8.3.3	PP/Thermoset Blends	431
8.3.4	All-PP Blends	433
8.4	Recycled PP Blends	434
8.4.1	Recycled PP/Other Polymer Blends.....	434
8.4.2	PP/Recycled Polymer Blends.....	435
8.5	PP Ternary Blends.....	437
8.6	Manufacturing of PP Blends	438
8.6.1	Melt Blending.....	438
8.6.2	Fiber Spinning (Microfibril and Nanofibril)	441
8.6.3	Blown Film.....	441
8.6.4	Microlayer Co-extrusion.....	442
8.6.5	Microporous Membranes and Barrier Film Processing.....	442
8.6.6	Electron Beam Irradiation	443
8.6.7	Foaming	444
8.6.8	Water-Assisted Injection Molding	445
8.6.9	Rotational Molding.....	445
8.6.10	In Situ Polymerization.....	446
8.6.11	Microcellular Injection Molding and Dynamic Packing Injection Molding...	446
8.7	Structure-Property Relationship	446
8.7.1	Impact Modification and Toughening.....	446
8.7.2	Crystallization	451
8.7.3	Rheology.....	455
8.7.4	Other Properties.....	457

W. S. Chow (✉)

School of Materials and Mineral Resources Engineering, Universiti Sains Malaysia,
Engineering Campus, 14300 Nibong Tebal, Penang, Malaysia

e-mail: shyang@usm.my

© Springer Nature Switzerland AG 2019

J. Karger-Kocsis and T. Bárány (eds.), *Polypropylene Handbook*,

https://doi.org/10.1007/978-3-030-12903-3_8

419

8.8	Compatibilization of PP Blends.....	459
8.8.1	Physical Compatibilization.....	459
8.8.2	Reactive Compatibilization.....	463
8.8.3	Compatibilization Using Nanofiller.....	467
8.9	Optimization, Modeling and Simulation.....	468
8.9.1	Optimization.....	468
8.9.2	Modeling of Flow-Induced Crystallization.....	469
8.9.3	Molecular Simulation.....	470
8.10	Conclusion and Future Prospective.....	470
	References.....	471

Abstract This chapter focused on the structure-property-processing relationship of polypropylene blends (PP binary and ternary blends). The topics covers PP/thermoplastic, PP/elastomer, PP/thermoset, PP/recycled polymer and all-PP blends. The toughening, crystallization and compatibilization strategies for PP blends are summarized. The processing techniques and properties (e.g. rheology, foamability, dyeability, etc.) of PP blends are discussed. Some of the ways of properties optimization, modeling of flow behavior and molecular simulation are documented. This chapter ends with a future trend and prospective of the PP blends based materials.

8.1 Introduction

Polypropylene (PP) is widely used in automotive and packaging applications. It is undoubtedly that PP is a versatile commodity plastic, which offers outstanding chemical and moisture resistance, low density, good processability and relatively low cost [1]. However, one of the limitations of PP is its poor impact toughness, especially at low temperature. One of the conventional approaches for overcoming this drawback is blending PP with elastomer and olefinic copolymer [2]. Polymer blending is an important technique in industrial practice, because it is an economically viable and versatile way of modifying some basic properties of existing polymers. The usual impact modifiers for the PP are olefinic copolymers based on ethylene and propylene, as well as styrenic rubber block copolymers [3]. The automotive application of polymers blends and reinforced polymers is a very rapidly increasing area. In the last decade the importance of PP and its blends have been increasing especially in bumpers, seating, dashboard, car interior and exterior trim and lighting applications. Development of mat-reinforced PP will profit from the availability of new metallocene-type PP resins [4]. Growing demand from end-use industries such as packaging, automotive and consumer products are expected to drive the market of PP blends.

PP is a polymorphic material which has at least three crystalline forms: α , β and γ . Commercial grades of PP crystallize essentially into the α -crystalline form under the usual industrial thermal conditions. The β -form can be obtained with the help of

a selective β -nucleating agent. The β -crystalline form has many performance characteristics, such as improved impact strength, in comparison with the traditional α -crystalline form. Hence, the research and development of β -PP-based blends would bring the benefits to improve the mechanical properties of PP [5].

Most of the PP blends (e.g. PP/thermoplastic, PP/elastomer, PP/thermoset) are incompatible, and thus they need suitable compatibilizer to stabilize their morphology and to strengthen their properties. Accordingly, some good examples of compatibilization system are discussed in the following section. In this chapter, the PP blends is mostly focus on PP as major matrix, so we can get a clearer picture to improve the properties of PP and its blends.

8.2 Basic Principles of Polymer Blends

Polymer blends offer a balance in mechanical and thermodynamical properties which are both unique and attractive for many industrial applications. They represent one of the most rapidly growing areas in polymer material science. Application of polymer blends in numerous fields such as automotive and packaging, designs of composite and biocompatible materials requires a fundamental understanding of the structure, phase state and composition of blends in the vicinity of interacting surfaces [6]. Polymer blends are either homogeneous or heterogeneous. In homogeneous blends, the final properties are often an arithmetic average of the properties of the blend components. In heterogeneous blends, the properties of all blend components are present. In general, practical use requires polymer blends which are partially or completely miscible.

Homogeneous miscibility in polymer blends requires a negative free energy of mixing that is $\Delta G_{mix} < 0$ (Eq. 8.1).

$$\Delta G_{mix} = \Delta H_{mix} - T \cdot \Delta S_{mix}, \quad (8.1)$$

where ΔH_{mix} is the enthalpy of mixing, ΔS_{mix} is the entropy of mixing, T is the temperature.

However, if two high molecular weight polymers are blended, the gain in entropy, ΔS_{mix} is negligible, and the free energy of mixing can only be negative if the heat of mixing, ΔH_{mix} is negative. In other words, the mixing must be exothermic, which requires specific interactions between the blend components. These interactions may range from strongly ionic to weak and nonbonding interactions, such as hydrogen bonding, ion-dipole, dipole-dipole and donor acceptor interactions. Usually, only van der Waals interactions occur, which explains why polymer miscibility is the exception rather than the rule. Examples of fully immiscible blends are PP/polyamide (PA), PA/acrylonitrile butadiene styrene (ABS), PA/ethylene-propylene-diene monomer (EPDM). All of these blends have become commercially successful, but only after being efficiently compatibilized [7].

The first and simplest, statistical thermodynamics model of polymer blends was developed by Flory and Huggins. The entropy of mixing, ΔS_{mix} , is assumed to be purely combinatorial and is calculated by enumerating the number of arrangements of the molecules on a lattice. The enthalpy, ΔH_{mix} , is simply the van der Waals energy of contact, and the difference between like and unlike pairs is summarized into a single term, the Flory–Huggins interaction parameter, χ , which varies linearly with inverse temperature so long as the interaction energy itself is temperature independent [8].

According to Flory–Huggins equation (Eq. 8.2):

$$\Delta G_{mix}/RT = \varphi_1 \ln(\varphi_1)/N_1 + \varphi_2 \ln(\varphi_2)/N_2 + \chi_{12}\varphi_1\varphi_2, \quad (8.2)$$

where ΔG_{mix} is the change of free energy on mixing two polymers, R is the gas constant, T is the temperature, φ_1 and φ_2 are the volume fractions and N_1 and N_2 are the segment numbers of the two blend components, respectively, and χ_{12} is the Flory–Huggins interaction parameter. When two high molecular weight polymers are blended, the gain in entropy, $\varphi_1 \ln(\varphi_1)/N_1 + \varphi_2 \ln(\varphi_2)/N_2$, is quite small, and the free energy of mixing, ΔG_{mix} , can be negative only if the heat of mixing is near zero or negative, $\chi_{12} < \sim 0.002$ [9].

In general, three different types of blends can be distinguished. In a completely miscible blend, for which $\chi_{12} < \sim 0.002$, it exhibits only one glass transition temperature (T_g), between the T_g values of the blend components, and in a close relation to the blend composition. In a partially miscible blend, a part of one component is dissolved in the other. As a result, two phases are observed, one phase rich in one component and the other phase rich in the other component. Each phase exhibits a T_g , which is between the T_g values of the pure components. In this case, the interphase is wide and interfacial adhesion is good. This type of blend is often referred to as compatible which exhibits satisfactory properties. By far most blends are fully immiscible. They demonstrate coarse phase morphology, with a sharp interphase, and the adhesion between the phases is poor, each components exhibit the T_g of the pure components [9].

One of the approaches for the quantitative estimation of interactions is the measurement of solvent absorption in the components and the blends [10]. The Flory–Huggins interaction parameter can be calculated from equilibrium solvent uptake by Eq. 8.3.

$$\ln a_1 = \ln \varphi_1 + (1 - \varphi_1) + (\chi_{12}\varphi_2 + \chi_{13}\varphi_3)(1 - \varphi_1) - \chi'_{23}\varphi_2\varphi_3, \quad (8.3)$$

where a_1 is the activity of the solvent, φ_1 is volume fraction in the blend at equilibrium, while χ_{12} and χ_{13} are the interaction parameters of the two-component solvent/polymer systems. χ'_{23} is related to the polymer/polymer interaction parameter by Eq. 8.4.

$$\chi'_{23} = \chi_{23}(V_1/V_2), \quad (8.4)$$

where V_1 and V_2 are the molar volumes of the solvent and polymer 2, respectively.

According to Imre et al. [10], the interactions and miscibility are closely related to structure and mechanical properties. A model developed earlier first for particulate filled polymers then adapted to blends allows the determination of a parameter associated to interaction. According to the model the composition dependence of tensile strength can be expressed as shown by Eq. 8.5.

$$\sigma_T = \sigma_{T_0} \lambda^n [(1 - \varphi_d)/(1 + 2.5\varphi_d)] \exp(B_T \varphi_d), \quad (8.5)$$

where σ_T and σ_{T_0} are the true tensile strength ($\sigma_T = \sigma \lambda$, $\lambda = L/L_0$) of the heterogeneous polymeric system (blend or composite) and the matrix respectively, n is a parameter expressing the strain hardening characteristics of the matrix, and B is related to the load bearing capacity of the dispersed phase. This latter is determined by interactions as well as by the inherent properties of the components as expressed by Eq. 8.6.

$$B = \ln[C(\sigma_{Td}/\sigma_{T_0})], \quad (8.6)$$

where σ_{Td} is the strength of the dispersed phase, while C is related to stress transfer between the phases, i.e. interactions, and was found to correlate inversely with the Flory–Huggins interaction parameter. According to the model, plotting a natural logarithm of reduced tensile strength [$\sigma_{Tred} = \sigma_T(1 + 2.5\varphi)/\lambda^n(1-\varphi)$] against composition should obtain a straight line, the slope of which is parameter B and from that parameter C can be calculated.

Nanoblend is one of the future directions in designing polymer blending. Nanostructured polymer blends (referred to as polymer nanoblends) are polymeric systems in which the dispersed-phase domains exhibit length scales of 100 nm or less. Nanoblends have been developed to be applied in electronic, membrane, sensing probes and optical applications. There are several approaches to obtain nanoblends, e.g. reactive extrusion, in situ polymerization, solution casting and melt blending. Polymer nanoblends can be designed by two approaches, one considering thermodynamics aspects and the other one considering micro-rheology basis. In terms of the thermodynamics aspects, the interaction energy density parameter can be used to predict polymer blends phase separation with disperse domains. The interaction energy density parameter is related to the Flory–Huggins interaction parameter and depends on the polymers solubility parameters. Nanostructured blends can be obtained by choosing adequate micro-rheological parameters for the blend such as: disperse and matrix phases viscosity ratio; shear and extensional flow conditions and interfacial tension or energy. All those parameters affect the final particle size of the blend disperse phase. In addition, sometimes compatibilization is necessary to reduce the interfacial tension and to prevent the coalescence for higher disperse phase content in the polymer blend [11]. One of main rheological parameters is the viscosity ratio between the liquids, which can be determined by Eq. 8.7.

$$\eta_r = \eta_d / \eta_m, \quad (8.7)$$

where η_d and η_m are the viscosity values for the disperse and matrix phase at the mixing temperature, respectively. For simple shear flow at small Newtonian liquid deformations, the particle diameter D , due to the drop breakup, can be determined by balancing interfacial tension (Γ) and shear forces ($\dot{\gamma}\eta_m$), as shown in Eq. 8.8:

$$D = 4\Gamma(\eta_r + 1) / [\dot{\gamma}\eta_m((19/4)\eta_r + 4)], \quad (8.8)$$

where $\dot{\gamma}$ is the shear rate and η_m is the matrix phase viscosity.

According to Costa et al. [11], the Eq. 8.8 has been further modified to represent drop breakup in polymer blends, together with the consideration of viscoelastic effects. It was established a critical capillary number value, C_{acrit} , above which drop breakup for polymer blends will occur leading to disperse particle diameter size D , estimated by Eq. 8.9:

$$D > (2\Gamma C_{\text{acrit}} / [\eta_m \dot{\gamma} - N_1]), \quad (8.9)$$

where, N_1 represents the first normal stress difference due to the elastic forces during polymer mixing. C_{acrit} can be estimated as approximately 0.5 for $0.1 < \eta_r < 1$. By optimizing shear and extensional flow conditions and reducing as much as possible the interfacial energy, Γ , it is possible to obtain disperse particle size in the range of nanoscale. In addition, it is necessary to prevent as much as possible the particles coalescence, which can be done through compatibilization and for lower contents of the disperse phase component.

There are several strategies can be used to improve the interaction and compatibility of the polymer blends, for example, addition of premade grafted and block copolymers, addition of reactive polymers, interchange reactions, addition of ionomers, reactive compatibilization and etc. Recently, it was also reported that nanoparticles can act as compatibilizers provided that they can ensure a strong interfacial adhesion between two incompatible polymers [12].

8.3 PP Binary Blends

8.3.1 PP/Thermoplastic Blends

PP has been blended with other thermoplastic to obtain desired properties, with the aim to combine the advantages of the individual polymers in the blends. Plenty of PP blends are reported, for example, PP/polyamide (PA), PP/polystyrene (PS), PP/polycarbonate (PC), PP/poly(methyl methacrylate) (PMMA), PP/polyethylene (PE), PP/poly(ethylene terephthalate) (PET), PP/liquid crystalline polymer (LCP) and so on. In this chapter, a few examples of the PP/thermoplastics blends are discussed.

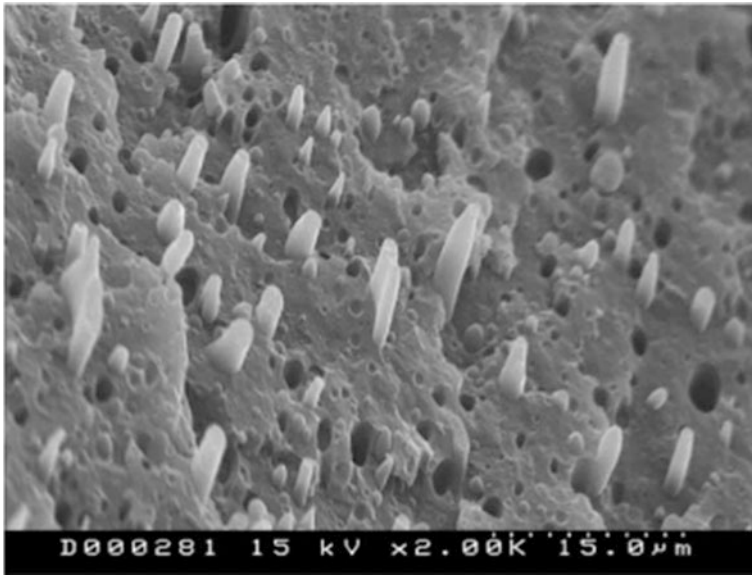


Fig. 8.1 SEM micrograph of PP/PA12 (75/25) blends taken with incidence angle of 40°. Adapted from Aranburu and Eguiazábal [14], with the permission of Hindawi Publishing Corporation

8.3.1.1 PP/PA Blends

Polyamide 6 and PP blending has been attempted to achieve improvement in mechanical properties, paintability and barrier properties, where PA6 contribute mechanical and thermal properties, while PP ensures good processability and insensitivity to moisture [13]. Aranburu and Eguiazábal [14] studied the mechanical and morphological properties of PP/PA12 blends. Figure 8.1 shows the SEM micrograph of PP/PA12 (75/25) blends taken with incidence angle of 40°. It was found that the PA12 particles are elongated in a direction parallel to the injection molding flow direction.

8.3.1.2 PP/PS Blends

PP blends with styrene polymers or copolymers attract much attention. To increase the rigidity of PP and improve toughness and solvent resistance of PS, the physical and mechanical properties, morphologies of PP/PS blends and compatibilized blends have been widely studied [15].

8.3.1.3 PP/Polyethylene Co-octene (POE)

Modified atmosphere packaging (MAP) is a passive way to create an appropriate gas composition around the product, which is typically packaged in plastic bags during shipping, storage and marketing. Blends of PP/polyethylene co-octene (POE) make them very attractive to be used for MAP of fresh products such as apple, blueberry and mushroom. For the maximum POE concentration used (40%), the oxygen permeability increased up to $\sim 100\%$ from that of neat PP. The addition of POE to PP was an effective way to prepare PP-based blends with enhanced oxygen and water vapour permeability [16].

8.3.1.4 PP/PET

PP/PET blend could be expected to combine the barrier properties of both components, since PET has a much lower permeability to gases and a higher permeability to water than PP. These two polymers are also complementary in their resistance to solvent and chemical attack. Since all these properties are of critical importance in packaging, this could be a potential application for these blends [17].

8.3.1.5 PP/LCP

Main chain liquid crystalline polymers (LCPs) have been used in thermoplastic blends to enhance processability (reduce viscosity) and to provide in situ reinforcement. This arises due to the tendency of low-viscosity main chain LCPs to readily fibrillate, particularly when deformed in an extensional flow field [18]. The modulus and tensile strength of PP/thermotropic LCP blends increased with draw ratio and the LCP content. This reinforcement was associated to their morphological transformation from spherical droplets to oriented and elongated microfibrils [19].

8.3.1.6 PP/Polysulfone

Polysulfone (PSU) and PP-based polymers are commercially used for ultrafiltration and microfiltration (polysulfone supported on a PP backing) applications such as extraction of insulin, polymer synthesis and effluent water recovery [20].

8.3.1.7 PP/PS Nanoblend

Nanoblends, in which dispersed-phase domains exhibit length scales of order 100 nm or less, are of growing interest attributed to the potential for enhanced properties. The use of a divinylbenzene (DVB) crosslinking agent and styrene (St) comonomer in the preparation of PP/PS nanoblends by diffusion and

polymerization of St in isotactic polypropylene (iPP) pellets is an effective way to stabilize the initial nanoscopic morphology of the PP/PS blends during subsequent melt processing. With relatively high amounts of benzoyl peroxide (BPO) and DVB, the nanosized PS domains almost kept their shape and size, and only simple aggregates of a few PS particles with an average size of 130 nm were observed after melt mixing of the PP/PS blends [21].

8.3.2 *PP Thermoplastic Elastomer*

Thermoplastic elastomers (TPEs) prepared from polymer blends may be categorized into two types based on rubber vulcanization, i.e. thermoplastic olefins (TPOs) and thermoplastic vulcanizates (TPVs). TPOs often refer to the blends without rubber vulcanization and plastics normally used are polyolefins, i.e. PP and PE. Vulcanization in the rubber phase of TPVs has to occur during melt blending between plastic and rubber through dynamic vulcanization.

8.3.2.1 TPO and PP/Rubber Blends

Öksüz and Eroğlu [22] had investigated the effects of the elastomers, i.e. ethylene-propylene-diene monomer (EPDM), ethylene vinyl acetate (EVA) and styrene-butadiene-styrene (SBS) on the mechanical properties of isotactic polypropylene (iPP). The impact strength increases as the elastomer content increases from 3 to 15 wt%. EPDM is the most effective elastomer for higher toughness values and is followed by EVA and SBS. The higher toughness values obtained for EPDM is due to two factors: (1) good adhesion between EPDM and iPP, and (2) the structure of EPDM is much more flexible than EVA and SBS.

The presence of even a small amount of ionic groups exerts a significant effect on the physical properties of the polymer. The ionic groups present in the polymers interact to form strong intermolecular ionic aggregates, which increase the adhesion of plastic and form the interlocked network structure in rubber/plastic blends. Su et al. [23] studied the mechanical properties and morphological structures of blends based on Zn^{2+} neutralized low degree sulfated ethylene propylene diene monomer rubber (Zn-SEPDm) ionomer and PP. It was found that Zn^{2+} neutralized low degree sulfated EPDM ionomer and PP blends, which are new thermoplastic elastomeric materials, have better mechanical properties than those of PP/EPDM blend. Scanning electron microscopy (SEM) results confirmed that the finer dispersed phase sizes and the smaller interparticle distances are the main reasons for the improvement of the mechanical properties of PP/EPDM blends.

Chakraborty et al. [24] prepared a series of TPE from a binary blend of EPDM and iPP using different types of phase modifiers. The influence of sulphonated EPDM, maleated EPDM, styrene-ethylene-cobutylene-styrene block copolymer, maleated PP, and acrylated PP as phase modifiers showed improved

physico-mechanical properties (e.g. maximum stress, elongation at break, moduli and tension set).

Ma et al. [25] investigated the structure and morphology of partly compatible binary blends of PP with poly(*cis*-butadiene) rubber using SEM. Within the region of compositions from 50 to 70 wt% iPP, the blends show a co-continuous morphology, and the phase-inversion occurs in this region. Hristov et al. [26] studied the fracture toughness of PP/poly(styrene-*ran*-butadiene) rubber (SBR) blends as a function of concentration of maleic anhydride (MA) in the maleated polypropylene (MAPP) compatibilizer under uniaxial static and impact loading conditions. The addition of MAPP to the unmodified PP/rubber blend enhanced the tensile modulus and yield stress as well as the Charpy impact strength. The compatibilized materials deformed uniformly within the gauge length by intensive stress whitening during the uniaxial loading. Salmah et al. [27] prepared PP/chloroprene rubber (CR) blends and it was found that the elongation at break of the blends of PP was increased by the incorporation of CR.

8.3.2.2 TPV

Thermoplastic vulcanizates (TPVs) belong to the family of thermoplastic rubbers. They are (re)processed as thermoplastic resins but exhibits properties similar to those of traditional rubbers. TPVs that combine the processing advantages of thermoplastics with the functional performances of vulcanized rubber are a specific class of polymeric materials, prepared by high shear blending of in situ dynamically vulcanized rubber with a molten thermoplastic. The resulting blend has small, uniform, and finely distributed crosslinked rubber particle matrices. TPV grades are replacing rubbers in increasing amount in various applications, for example, automotive (e.g., windshield blades, glass sealing profiles, shock absorbers, expansion bellows, grips, handles and internal covers) attributed to the recyclability and reprocessability of TPV [28, 29]. PP/EPDM TPVs are available commercially, and have been recognized for their unique physical and mechanical properties as well as excellent weathering resistance over a range of blend combinations [30].

Karger-Kocsis et al. [31] conducted morphological study of PP/EPDM and PP/polyolefin thermoplastic vulcanizate blends. The differences in melt viscosities of the blended components were characterized by the phase viscosity ratio (μ). High degree of dispersion of the impact modifier can be achieved if melt viscosities of the blended components are very closely matched (when $\mu \approx 1$). It was concluded from SEM results that, below an impact modifier content of 20 wt%, the modifier formed the dispersed phase in the continuous PP matrix. In blends containing 50 wt% of impact modifier, the latter may also form continuous phase depending on its type and μ value beside the still continuous PP phase (co-continuous network structure).

In numerous applications the TPV parts are exposed to service conditions where scratch and wear resistances are of great importance. Karger-Kocsis et al. [28] studied the friction, sliding and rolling wear characteristics of PP/EPDM TPV (Santoprene[®] grades) against steel counterparts in dry condition. The wear

performance of the TPVs was investigated in different tribotests, viz. pin-on-plate (POP), cylinder-on-plate (fretting) and rolling ball-on-plate (RBOP), whereby plate was always the rubber. It was established that increasing hardness caused by increasing amount of PP, is usually accompanied with reduced coefficient of friction (COF) and specific wear rate. Both of these proved to be highly dependent on the configuration and parameters of the related tribotests.

Jain et al. [32] examined the deformation and fracture behavior of several PP/EPDM TPV (EPDM; 10–40 wt%) and compared with those of uncrosslinked blends of PP/EPDM. The impact strength of the dynamic vulcanized PP/EPDM TPV blends is higher values compared with uncrosslinked blends. The nucleation effect of the crosslinked particles and the decrease of crystallinity of the EPDM rubber were considered as a contributing factor to the improvement in the impact strength.

Gupta et al. [33] prepared blends of PP/EPDM by dynamic vulcanization using dimethylol phenolic resin. A change in morphology from dispersed phase to co-continuous phase takes place in composition range of 30–40 wt% in unvulcanized blends and in composition range of 20–30 wt% in vulcanized blends. The dynamic vulcanization improved the plastic deformation and tensile properties significantly. The increase of interfacial adhesion caused by the three-dimensional network is considered to be the most important factor in the improvement.

Dynamic vulcanisation by electron induced reactive processing is a potential alternative to prepare TPV. Electron induced reactive processing is a novel technique where chemical reactions are induced by spatial and temporal precise energy input via high energy electrons under dynamic conditions of melt mixing. Naskar et al. [34] prepared TPV by dynamic vulcanisation with 50:50 blend ratio of PP and EPDM using novel electron induced reactive processing under various conditions as an alternative to conventional phenolic resin and peroxide cross-linking systems. Figure 8.2 shows schematic representation of the set-up for the coupling of an electron accelerator with an internal mixer. Their results indicated that in situ compatibilization of PP and EPDM, as well as crosslinking in the EPDM phase are occurring simultaneously, which contributing to the enhancement in the mechanical properties.

Tanrattanakul et al. [29] characterized TPE from PP and natural rubber (NR) with and without phenolic resin as a vulcanizing agent. The unvulcanized thermoplastic natural rubber (uTPNR) illustrated co-continuous phase morphology, whereas the vulcanized thermoplastic natural rubber (vTPNR) displayed dispersed phase of vulcanized natural rubber. Dynamic vulcanization improved tensile strength, elongation at break, tension set and degree of swelling of the TPEs. The vTPNR exhibited higher ozone resistance and swelling resistance than the uTPNR.

Nakason et al. [35] prepared TPV based on epoxidized natural rubber (ENR)/PP blends by dynamic vulcanization. It was found that the TPV prepared from ENR/PP with phenolic modified PP (Ph-PP) as a compatibilizer gave the highest mechanical properties. Another study from Nakason et al. [36] demonstrated that mixing torque, apparent shear stress, apparent shear viscosity, tensile strength, and hardness properties of ENR/PP TPV (with Ph-PP compatibilizer) increased with increasing

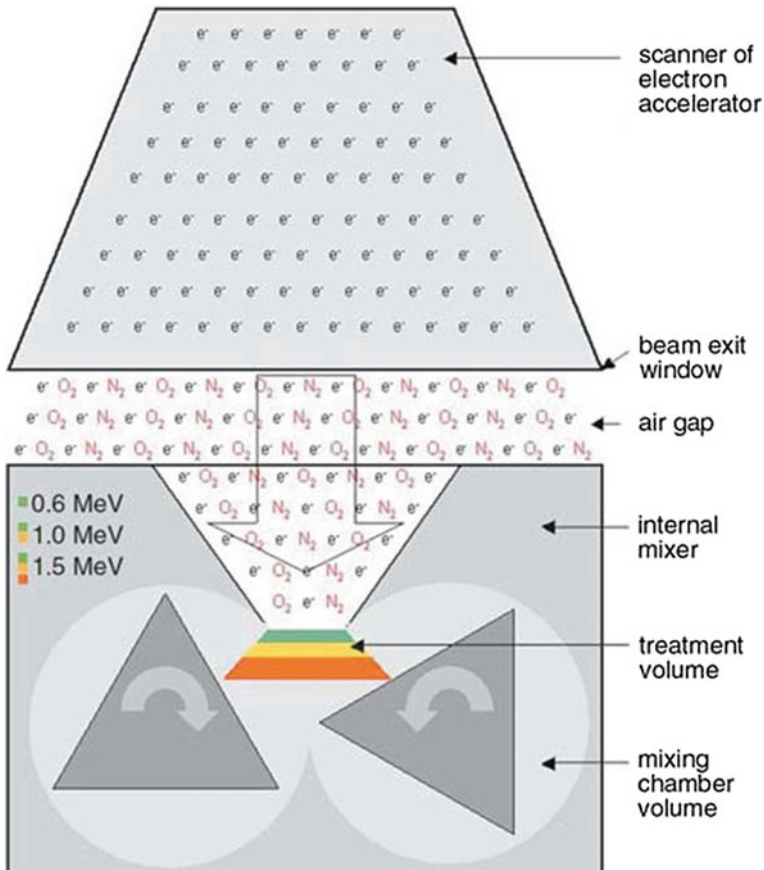


Fig. 8.2 Schematic representation of the set-up: coupling of an electron accelerator with an internal mixer. Adapted from Naskar et al. [34], with the permission of BME-PT

levels of epoxide groups in the ENR. This is attributed to increasing level of chemical interaction between the methylol groups of the Ph-PP and polar functional groups of the ENR.

A TPV composed of PP and EVA, was crosslinked by tetrapropoxysilane (TPOS) as crosslinking agent in the presence of dibutyl tin oxide (DBTO) as catalyst. The crosslinking reaction was carried out through a transesterification reaction between the ester groups of EVA and the alkoxy silane groups of TPOS. This chemistry is non-radical, and thus prevents the degradation of PP in comparison with crosslinking reactions using peroxides as initiator. From the gel content and morphology analysis, it was showed that the correlation between the evolution of the two phase blend morphology and the crosslinking reaction conversion was almost the same for the preparing of the TPV in the internal mixer and

twin-screw extruder. The phase inversion seems to take place at a gel content of around 60% [37].

TPE prepared by blending thermoplastic with nitrile rubber (NBR) has been received a lot of interest because of the combination of the oil-resistant property, the excellent mechanical properties and processing behavior. Soares et al. [38] investigated the efficiency of dicumyl peroxide (DCP) in combination with N,N'-m-phenylene-bismaleimide (BMI) as a crosslinking system for the PP/NBR TPV in the presence of compatibilizing agents (i.e., maleic anhydride-grafted-PP (PP-g-MA)/amino compound and glycidyl methacrylate-grafted-PP (PP-g-GMA) with or without amino compound). The compatibilization with PP-g-MA and XNBR as the coreactive functional groups was performed in the presence of a small amount of triethylene-tetramine (TETA) to impart the adhesion. The PP-g-MA/TETA/XNBR, PP-g-GMA/TETA/XNBR, and PP-g-GMA/XNBR are efficient compatibilizing systems, since they promote an improved tensile properties and compression set when compared with un-compatibilized blend. Van Dyke et al. [39] applied dynamic vulcanization to prepare thermoplastic elastomer blends of PP with chlorobutyl (CIIR) and NBR rubbers. The ultimate tensile strength and hardness values increase as the proportion of PP is increased, in the range of 0–50 wt% PP.

Different TPV were prepared from elastomeric chlorosulfonated polyethylene (CSM) and PP by applying dynamic vulcanization technique. It was revealed that CSM/PP TPV show substantial improvement in stress at ultimate tensile strength, hardness and thermal stabilities with the incorporation of PP [40].

Babu et al. [41] studied the influence of the three structurally different coagents, namely triallyl cyanurate (TAC), trimethylol propane triacrylate (TMPTA) and N,N'-m-phenylene dimaleimide (MPDM) on the thermal and rheological properties of TPV based on the PP and ethylene octene copolymer (EOC). Coagent assisted peroxide cured system affects the crystallizing behavior due to the various types of reactions taking place simultaneously. Generally, increase in dynamic functions is attributed to the improved crosslinking in the EOC phase and immobilization of the interface by compatibilizing efficiency of coagent. It can be concluded that the dual role of MPDM i.e. as a booster for peroxide and as a reactive compatibilizer assist to improve the properties in the solid as well as in the melt state.

8.3.3 *PP/Thermoset Blends*

Some of the PP/thermoset blends are worth mentioning. The introduction of thermoset improves the properties of PP and it widens the application window of PP blends. Many thermoplastic vulcanizate have been attributed to the dynamic vulcanization of elastomer in the molten thermoplastic. By using the same concept dynamic vulcanization have been applied to the preparation of thermoplastic/thermoset blends.

8.3.3.1 PP/Unsaturated Polyester Blends

Wan et al. [42] prepared melt blending of PP with a low molecular weight (MW) crosslinkable unsaturated polyester (UP) resin using a batch mixer and a twin-screw extruder in the presence of peroxide free radical initiator. The blends are also characterized by FTIR which strongly suggests that the presence of block or graft PP-UP structures that may enhance phase interaction and promote compatibility in the reacted PP/UP blends. Such blends are considered as suitable compatibilizers of PP/high MW thermoplastic polyester blends and as modifiers for low density extrusion foaming of similar blends. The different rheological properties of PP and UP can be adjusted by a peroxide initiated reaction during reactive melt blending to produce a finer and more uniform morphology containing crosslinked UP particles in a low viscosity PP matrix. Mixing efficiency, protocol of addition and residence time in the batch and continuous mixers was shown to affect the morphology and rheology of the blends, some of which showed suspension-like behavior, typical of thermoplastic vulcanizates.

8.3.3.2 PP/Epoxy Blends

Jiang et al. [43] used dynamic vulcanization process to prepare PP/epoxy blends. The blends had crosslinked epoxy resin particles finely dispersed in the PP matrix. Maleic anhydride grafted polypropylene (PP-g-MAH) was used as a compatibilizer. The increase in the torque at equilibrium for the PP/PP-g-MAH/epoxy blends indicated the reaction between maleic anhydride (MA) groups of PP-g-MAH and the epoxy resin. The torque at equilibrium of the dynamically cured PP/epoxy blends increased with increasing epoxy resin content. The PP/epoxy blends compatibilized with MAH-g-PP have finer domains than the PP/epoxy blends. The dynamically cured PP/epoxy blends (PP/PP-g-MAH/epoxy/2-ethylene-4-methanimidazole curing agent (EMI-2,4)) exhibited higher flexural modulus than the PP/epoxy and PP/PP-g-MAH/epoxy blends.

8.3.3.3 PP/Novolac Blends

Dynamically cured PP/novolac blends were prepared in a mixing chamber (190 °C and 50 rpm) in the presence of hexamethylenetetramine (HMTA) curing agent and PP-g-MAH. The PP/novolac blends exhibited shear-thinning behavior. It was found that the compatibilization together with the dynamic cure could increase the viscosity and modulus because of the formation of a grafting polymer between the PP-g-MAH and the curing novolac resin [44].

8.3.4 All-PP Blends

In this section, the “all-PP blends” defined as the blending of PP with different tacticity (i.e., effects of stereochemistry), blending PP with functionalized PP (e.g. grafted PP), blending PP with bimodal molecular weight distribution, blending PP with linear and branched chain.

8.3.4.1 PP Blends with Different Tacticity

The stereochemistry of PP strongly influences its final properties through a variety of morphological factors such as crystallinity, lamellar structure, spherulitic macrostructure, and melting behavior. Blends of atactic PP (aPP) with either isotactic polypropylene (iPP) or syndiotactic PP (sPP) homopolymer can exhibit some unique mechanical properties, with the aPP acting as a softening agent. Phillips [45] examined the morphology of iPP/aPP and iPP/sPP blends by using optical microscopy. Comparisons of constant molecular weight iPP/aPP and iPP/sPP mixtures show that the iPP/aPP blend pair exhibits greater miscibility than the iPP/sPP pair.

8.3.4.2 PP/Functional PP Blends

In the study of Flores-Gallardo et al. [46], PP was functionalized with acrylic acid (AA) and styrene as a co-monomer by means of a radical-initiated melt-grafting reaction. The formation of polypropylene grafted with acrylic acid (PP-g-AA) and polypropylene grafted with acrylic acid and styrene (PP-g-AAst) was confirmed. Blends of PP with 0–100 wt% of PP-g-AA were prepared by melt mixing. The contact angles of water on cast-film surfaces of PP/PP-g-AA blends decreases with increasing modified polymer content and decreasing PP-g-AA molecular weight. Using styrene as a second monomer produced a noticeable increase in grafting degree with no significant change in melt index. An increase in crystallization temperature of PP was observed when AA monomers were grafted into PP and with increasing PP-g-AA content in the blend, probably caused by a nucleation effect of AA monomers that would improve the crystallization capability of PP.

Saffar et al. [47] investigated miscibility of a binary blend consisting of PP and PP-g-AA (with an acrylic acid content of 6 wt%). It was found that by using atomic force microscopy (AFM) and time-of-flight secondary-ion mass spectrometry (ToF-SIMS) chemical imaging, an accurate quantitative evaluation of the phases in the polymer blends can be obtained. AFM data effectively detected dispersed-phase domains corresponding to the PP-g-AA rich phase. The size of the domains increased from around 50 nm up to around 250 nm as the PP-g-AA content increased from 5 to 20 wt%.

8.3.4.3 Bimodal PP Blends

Bimodal polypropylene was prepared using three metallocene catalysts: $\text{rac-Me}_2\text{Si}(\text{Ind})_2\text{ZrCl}_2$ (CAT-1), $\text{rac-Et}(\text{Ind})_2\text{ZrCl}_2$ (CAT-2) and $\text{rac-Me}_2\text{Si}(2\text{-Me-benzoin})_2\text{ZrCl}_2$ (CAT-3). The $\text{rac-Et}(\text{Ind})_2\text{ZrCl}_2$ (CAT-2) and $\text{rac-Me}_2\text{Si}(2\text{-Me-benzoin})_2\text{ZrCl}_2$ (CAT-3) were combined in different proportions (wt%/wt%) of (CAT-2/CAT-3) for obtaining a new PP with a bimodal molecular weight distribution. The polymers obtained were compared with those coming from melt mixing of two PP with different molecular weights in an extruder. Both methods allow obtaining bimodal PP, but polymer melt blending shows partial miscibility effects and less crystallinity while binary catalytic systems have several advantages such as intimate mixing of high and low molecular weight components (improved product quality), less process complexity, and higher cost effectiveness [48].

8.3.4.4 Linear and Branched PP Blends

Fang et al. [49] investigated the effect of blending a long-chain branched PP (LCB-PP) with a linear PP (L-PP) on the processability and properties of blown films. Adding an LCB-PP significantly improved the melt strength which leads to strain-hardening behaviour. From bubble stability tests, it was found that area in the stability map increased with LCB-PP content. However, the addition of LCB-PP reduced the mechanical strength of the blown films with a more pronounced impact on the mechanical strength in transverse direction (TD). The addition of long branches created a row nucleated lamellar structure for the blend films, which favoured orientation of the crystals blocks along machine direction (MD).

8.4 Recycled PP Blends

For the benefits of sustainable development, plastic recycling is one of the alternatives to extend the self-life of polymers and thus it can help to reduce carbon footprint. In this section, both of the recycled PP/other polymer blends and recycled polymer/PP blends are discussed.

8.4.1 Recycled PP/Other Polymer Blends

Miskolczi et al. [50] prepared blends of waste PP (from automotive and packaging sector) and polyamide (from automotive sector) in the presence of compatibilizer (polyalkenyl-poly-maleic-anhydride-amide, polyalkenyl-poly-maleic-anhydride-ester, and maleic-anhydride (MA)-grafted-low-polymer). The tensile and flexural

strength and modulus was improved by the using of compatibilizer. This evidences a possible approach to minimize the plastic waste and contribute to the sustainable development of the plastic industry. Garcia et al. [51] investigated the deformation behavior of a recycled PP/partially devulcanized rubber (85 wt%/15 wt%) using morphological analysis (2D via scanning electron microscopy while 3D via X-ray microtomography). It was established that blend composed by the dispersed rubbery phase with the highest devulcanization level presented the most refined morphology. Figures 8.3 and 8.4 shows the 3D microstructures of recycled PP/devulcanized rubber (85/15) sample and recycled PP/vulcanized rubber (85/15) sample respectively. It was found that the dispersed phase of the recycled PP/devulcanized rubber blend is finer compared to that of recycled PP/vulcanized rubber. This indicates that the devulcanization process facilitates the breakup of the rubber particles during the mixing.

8.4.2 PP/Recycled Polymer Blends

Blending of recycled polyethylene terephthalate (RPET) from waste bottles with PP was performed in an attempt to enhance the processability of RPET. This could recycle PET bottles together with their PP-based caps (RPET/PP ratio was varied at 95/5 and 90/10). The specimens containing low molecular weight PP were found to remain homogeneous regardless of compatibilizer and PP content in the RPET/PP blends [52].

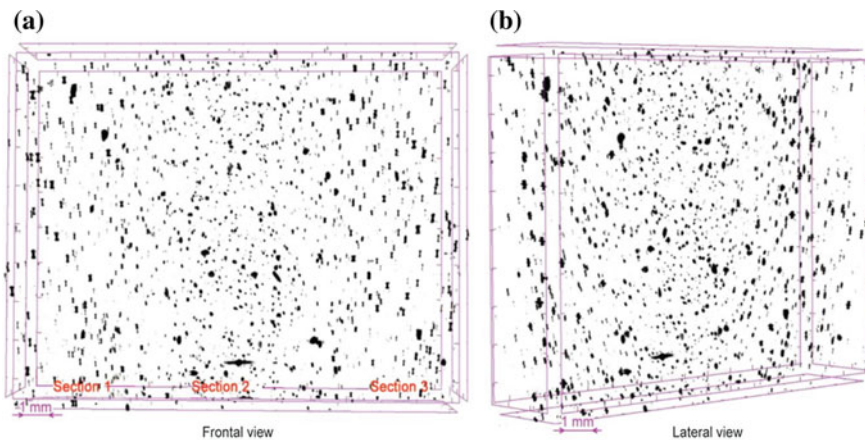


Fig. 8.3 3D images of the recycled PP/devulcanized rubber (85/15) sample using X-ray microtomography. Adapted from Garcia et al. [51], with permission of BME-PT. *Note* Devulcanized rubber prepared from vulcanized ground tire rubber treated in microwave for 6 min

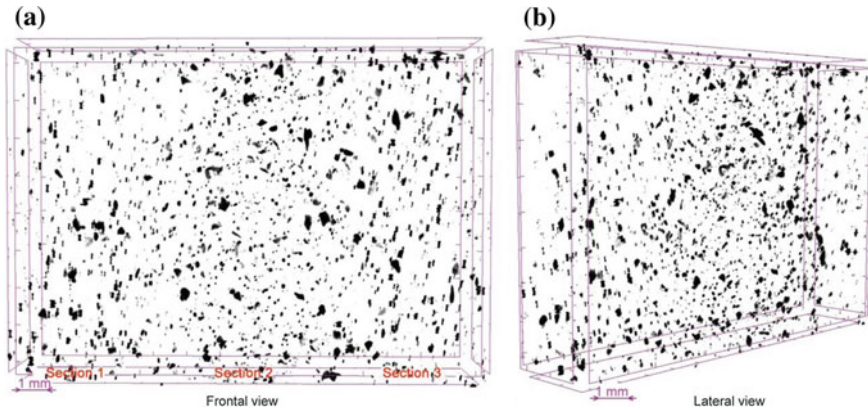


Fig. 8.4 3D images of the recycled PP/vulcanized rubber (85/15) sample using X-ray microtomography. Adapted from Garcia et al. [51], with permission of BME-PT

Polybutylene terephthalate (PBT) is extensively used for automotive and electronics applications. Mechanical recycling of this engineering plastics waste can be realized by blending polyolefins such as the PP. Potential advantages expected from blending the two components are as follows: low absorption of humidity, better processability, good thermal resistance, and dimensional stability. However, PP is neither miscible nor compatible with PBT due to a great difference in polarity. Compatibilization of polyester/polyolefin blends can be achieved by using suitable compatibilizers. Barhoumi et al. [53] prepared blends of recycled PBT parts obtained from scrapped cars (which are used in the electronic application, i.e. connector), and virgin PP by using twin-screw extruder at different compositions. Selected compositions were also prepared with the presence of ethylene-co-glycidyl methacrylate copolymer (E-GMA) and ethylene/methyl acrylate/glycidyl methacrylate terpolymer (E-MA-GMA) compatibilizers. Addition of E-GMA and E-MA-GMA to the PP/PBT blend exhibited a significant change in morphology and improved ductility because of interfacial reactions between PBT end chains and epoxy groups of GMA that generate EG-g-PBT copolymer. Moreover, thermal and viscoelastic study indicated that the miscibility of PP and PBT has been improved. The significant increase of the elongation at break of the PP/PBT/E-MA-GMA blends should be considered as a beneficial aspect.

Binary and ternary blends of the high viscosity recycled high-density polyethylene (reHDPE) from milk bottles, containing either homopolymer PP or copolymer PP, were developed in an effort to reduce viscosity and encourage ease of processing by injection molding, without a significant loss in mechanical properties [54]. Kazemi et al. [55] had reported that the addition of ethylene-octane copolymer (EOC) compatibilizer had improved deformability of recycled PP/PE blends.

Blending of PP with polyamide 6 (PA6) industrial wastes is an important way of valorization. In the presence of PP-g-MA compatibilizer, the interfacial adhesion

was improved, as a result of the creation of an interphase that was formed by the interaction between the PP-g-PA6 copolymer in situ and both phases. This interphase induced an improvement in tensile properties. From an application point of view, 20 wt% PA6 can be blended with PP without affecting Young's modulus and yield stress, however, reduction of elongation at break should be concerned [56].

8.5 PP Ternary Blends

PP ternary blends referring to the PP blends with (at least) another two polymers, for example, PP/PE/EPDM, PP/PA6/ABS, PP/PA/PS, PP/PET/PE and so on. In this section, a few examples of PP ternary blends are discussed.

Tchomakov et al. [57] investigated the ternary blends of high-density polyethylene (HDPE), EPDM and PP. It was found that the modulus, tensile strength and impact resistance can be improved by HDPE addition if the HDPE is localized within the EPDM phase. The use of a two-step mixing procedure where EPDM and PE were mixed together before their incorporation in the PP matrix resulted in finely dispersed droplets. This resulted in an additional 50% increase in Izod impact strength and more than a two-fold increase in elongation when compared to the standard one-step mixing. According to Vranjes and Rek [58] the PP/HDPE blend revealed poor adhesion between PP and HDPE phases. Finer morphology was obtained by incorporation of EPDM in PP/HDPE blends and better interfacial adhesion was observed. The EPDM addition increased the percentage of crystallization (χ_c) of PP in PP/HDPE blends.

Panda et al. [59] studied the morphology and dielectric relaxation of ternary blends of PP/PA6/acrylonitrile butadiene styrene copolymer (ABS). It was found that the PP/PA6/ABS (80/10/10) blends exhibited core-shell morphology. A significant reduction in the domain size of the dispersed phase is observed in the presence of PP-g-MAH compatibilizer. The observed shift in α -relaxation peak of PA6 phase is higher in the presence of PP-g-MA as compared to styrene-maleic anhydride copolymer (SMA; with 8% MA content) in PP/PA6/ABS (80/10/10) ternary blends, indicating the higher extent of interfacial reaction between amine end groups of PA6 and maleic anhydride moiety of PP-g-MA.

Lima et al. [60] investigated the effect of ground tire rubber (GTR) and a novel metallocene-based ethylene-propylene copolymer (EPR; with 15 wt% ethylene content) on the morphology and mechanical behavior of ternary polymer blends based on a highly flowable PP homopolymer (MFI of 35 g 10 min⁻¹; 230 °C, 2.16 kg). The incorporation of EPR in the rubber phase of thermoplastic elastomeric blends (TPE) based on GTR and PP (TPE-GTR) has a positive effect on their mechanical performance, attributed to the toughness enhancement of the PP matrix and to the establishment of shell-core morphology between the rubber phases. The mechanical properties of the ternary blends reveal that TPE-GTR blends allow the recycling of this GTR material by injection molding technologies.

This could contribute toward a sustainable approach on the development of TPE-GTR with high processability for the injection molding industry.

Debolt and Robertson [61] investigated the impact strength of ternary blends of PP, polyamide 66 (PA66), and PS. When the ionomer (a copolymer of PE (80%) and poly(methacrylic acid-co-isobutyl acrylate) (20%) neutralized (ca. 70%) with zinc) and block copolymer styrene-ethylene-butylene-styrene (SEBS) were added together to PP/PA66/PS, the impact strength increased nearly as the sum of the impact strengths from PP/PA66/ionomer and PP/PS/SEBS, as if each compatibilized particle acted as an energy-absorbing center.

Ternary iPP/atactic polystyrene (aPS)/SBS blends with iPP/aPS weight ratio of 50/50 exhibit co-continuous morphology. Poly(styrene-butadiene-styrene) (SBS) block copolymer acts as a compatibilizer in iPP/aPS immiscible blends and forms an interfacial layer between iPP matrix and dispersed aPS/SBS particles. The SBS strongly interacts with iPP and aPS and it significantly changes their phase morphologies as well as crystallization process in iPP [62].

Jazani et al. [63] investigated the mechanical and morphological properties for PP/PC/SEBS ternary polymer blends. When maleic anhydride grafted styrene-ethylene-butylene-styrene (SEBS-g-MAH) was incorporated into the blend, the type of morphology changed from core-shell composite particles to a mixed of core-shell composite particles, individual particles and rod-like composite particles. The change in dispersed phase morphology promoted by adding the SEBS-g-MAH has generated a range of PP ternary blends with higher impact strength and modulus compared with PP matrix.

Chand et al. [64] modified PP and PET blend by incorporating ultrahigh molecular weight polyethylene (UHMWPE) ranging from 1 to 5 phr. Addition of 2 and 5 phr UHMWPE improved the wear resistance of PP/PET blends at different loads, which has been explained on the basis of improved bonding as compared with pure PP/PET blend as well as the enhancement in hardness by UHMWPE. The wear mechanism of PP/PET/UHMWPE blend is attributed to microcutting, microplowing, and debris formation.

8.6 Manufacturing of PP Blends

The final properties of PP blends are not merely controlled by the formulation design. The desired properties of PP blends are governed by the processing method as well. This section will highlight a number of techniques to produce PP blends.

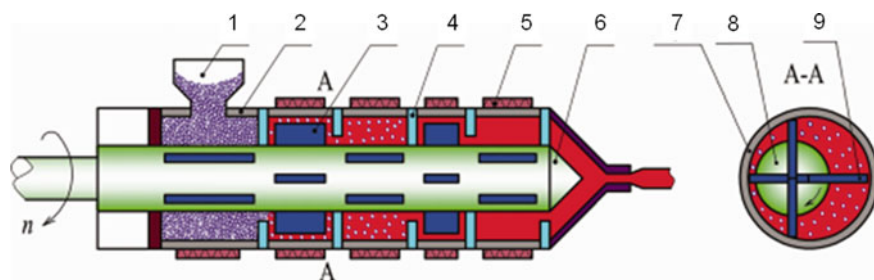
8.6.1 Melt Blending

Considerable evidence has been accumulated to demonstrate that type of flow is an important factor on morphology development and final particle size of polymer. In

polymer processing, the elongation flow is more effective than the shear flow. Elongational flow generates exponential stretching, while simple shear flow just gives linear stretching, which results that the dispersed phase droplets of blends are broken more efficiently in elongational flow than in shear flow. Moreover, compared to shear deformation field, elongational deformation field consumes less energy to generate the same deformation of polymer. Some attempts have been performed to generate elongation flow based on converging channels, but most of these elongation flows are local and fixed. Yang et al. [65] designed a non-screw plasticizing processing tool known as the vane extruder (VE), which consists of certain groups of vane plasticizing units and can generate higher stress and dynamic elongation flow. The elongation flow is more effective possibly because the positive displacement-type flow dominates the solid conveying mechanism of VE. The vane extruder is a novel polymer processing equipment with a structure completely different from that of the traditional twin screw extruder. The VE consists of a number of vane plasticizing and conveying units (VPCU), which are shown in Fig. 8.5 [66]. Compared with screw extruder, VE showed better mechanical properties and finer dispersed particles because of the positive displacement-type characteristics of solids conveying. A super-tough PP/SBS blend with enhanced tensile strength and thermal stability was obtained via this reactive compatibilization method using VE.

Qu et al. [67] studied the morphology development of PP/PS (70/30) blend in a VE. The result shows that the solid pellets of PP/PS blend are melted quickly in the first five vane plasticizing and conveying units (VPCUs), indicating the strong melting ability and short melting length of the VE. Besides, the blend is elongated in both circumferential and axial direction, and the strong elongational deformation field makes the dispersed phase change from stretched striations to droplets rapidly and mix uniformly finally. The results reveal that the droplet size of dispersed phase in blends prepared by VE is smaller than that prepared by twin-screw extruder, indicating VE has better mixing ability than twin-screw extruder.

Shon et al. [68] made an investigation of the development of phase morphology of an immiscible blend PP/PA6 (75/25) in several different commercial mixing



1. hopper; 2. stator; 3. vane; 4. baffle; 5. heater; 6. rotor; 7. stator; 8. rotor; 9. vane

Fig. 8.5 Structural diagram of vane extruder. Adapted from Jia et al. [66], with permission of John Wiley & Sons

machines, i.e. a Buss Kneader, an intermeshing co-rotating twin screw extruder, an intermeshing counter-rotating twin screw extruder, and a continuous mixer. It was found that the intermeshing counter-rotating machine gives the finest dispersed morphologies. According to Polaskova et al. [69] extrusion of immiscible polymers under special conditions can lead to creation of microfibrillar-phase morphology, ensuring significant increase of mechanical properties of polymer profiles.

It has been found that vibration affects diffusion and rate-sensitive processes such as crystallization dynamics and blending. In polymer processing, many prospective vibration technologies such as ultrasonic vibration or mechanical vibration have been used. Wang et al. [70] developed a vibration internal mixer to prepare PP/UHMWPE blends with two additional adjustable processing parameters (vibration frequency and vibration amplitude) as compared with those prepared in the steady mode. Blending PP with UHMWPE, in an oscillatory shear parallelly superposed on a steady shear in the internal mixer, exhibited the different torque vs. time curves possibly embodying energy-saving and higher efficiency compared with blending in the steady shear mode. Vibration can enhance diffusion and dispersion causing different blending effects and forming the corresponding internal structure and better product properties. The forced vibration also increased the interpenetration of two phases. Subsequently, the formed crystals of two components are possibly connected and there is epitaxy of PP and UHMWPE crystals. The larger amount of the small crystals, especially the β -form in the bulk α -form PP together with the co-continuous phase morphology contributes to the higher mechanical properties of PP/UHMWPE.

A reactive extrusion process employing peroxide derived free radicals will significantly affect crystallizable PP chains. Melt-grafted chains have been shown to increase the crystallization temperature of PP. Tortorella and Beatty [71] prepared iPP with an ethylene-octene copolymer using reactive blending. Free radical polymerization of styrene and a multifunctional acrylate during melt extrusion has resulted in the formation of unique features in both amorphous and crystalline phases. Reactive extrusion has significantly altered the size, shape, and distribution of lamellar crystals in PP. It was found that grafting leads to significant changes in the α -crystalline phase of PP and promotes the formation of the β -phase.

Teng et al. [72] prepared compatibilized PP/PA6 blends with PP, ϵ -caprolactam and PP-g-MAH (MA content 0.5 wt%) via in situ polymerization and in situ compatibilization in a batch mixer. It was found that a PP/PA6 blend containing near uniform distribution of PA6 domain sizes with a mean size of 64 nm can be prepared using the reactive blending method. This very fine dispersion of PA6 component in the continuous PP matrix is expected to provide desirable properties such as thermodynamically stable polymer blends structured on sub-micrometer length scales, improved material transparency, creep and solvent resistance, and favorable rheological properties.

8.6.2 *Fiber Spinning (Microfibril and Nanofibril)*

Bicomponent fibers offer several advantages over monocomponent fibers. In a core–sheath configuration a bicomponent fiber can display both the surface properties of the sheath material and the mechanical properties of the core material. The two most commonly used materials in carpeting applications are polyamide (PA6 and PA66) and PP. PP carpets are considered to have wear resistant inferior to those of PA. An ideal carpet fiber would combine the best properties of these polymers. Thus, a melt-pigmented PP sheath, PA6 core fiber would be an improvement over conventional monocomponent PA or PP fibers. Godshall et al. [73] produced a bicomponent fiber consisting of iPP sheath and PA6 core that would be suitable for use in a pigmented carpeting application by using fiber spinning technique. In the study of Fallahi et al. [74], blends of PP, PA6 and PP-g-MAH compatibilizer were spun into continuous filaments by an extruder. The fibrils have diameter less than one micrometer. Further, the diameter of the fibrils was decreased by cold drawing. The PA6 matrix can transfer the applied stresses to the fibrils in the longitudinal direction and elongate the PP fibrils during the blend filament drawing.

An electrically conductive or semiconductive network is one of the key aspects of smart and technical textiles. Melt-blending of a common fiber-forming polymer with an intrinsically conductive polymers (ICP) and then melt-spinning the mixture into fibers provides an interesting approach. Soroudi and Skrifvars [75] prepared melt spun drawn fibers using a ternary blend of PP/PA6/PANI (polyaniline) complex. When the ternary blend fibers were compared to the PP/PANI binary fibers, the formers were able to combine better conductivity (of an order of 10^{-3} S cm⁻¹) with a greater tensile strength only at a draw ratio of 5. The results indicated that the draw ratio was a more critical factor for the ternary blend fibers, as both conductivity and tensile strength depended on the formation of fibrils from the core-shell droplets of the PA6/PANI-complex.

8.6.3 *Blown Film*

Auinger and Stadlbauer [76] investigated the process stability of the blown film from different PP and high melt strength (HMS)-PP blends. Three commercial PP grades were dry-blended with two different HMS-PP grades with varying weight content in the range of 5, 10, and 20 wt%. The maximum stable output could be enhanced up to 50 wt% due to the addition of HMS-PP in accordance to neat PP-grades. The main reason for increasing the output rate is the increase of the strain hardening index (SHI) by the addition of HMS-PP.

8.6.4 *Microlayer Co-extrusion*

Homogeneous dispersion of a high barrier polymer in a polyolefin matrix does not produce the desired barrier enhancement. Generally, the barrier properties follow those of the continuous matrix. Lamellar morphology of the dispersed barrier phase is paramount to achieve good barrier properties. Nanolayer and microlayer coextrusion is a method for combining two or three polymers as hundreds or thousands of alternating layers with individual layers as thin as tens of nanometers. The possibility for utilizing microlayer coextrusion as a tool for creating microplatelets of high aspect ratio was explored by Jarus et al. [77]. PP was combined with PA66 in microlayers, in the presence of PP-g-MAH compatibilizer. A high volume fraction of PA66 microplatelets dispersed in PP was achieved by injection molding the microlayered materials at a temperature intermediate between the melting points of the two constituents. The difference in melting temperatures provided a broad processing window of about 60 °C in which the PP layers melted to form the matrix whereas the PA66 layers remained in the solid state as dispersed microplatelets of high aspect ratio. An enhancement of 4–5 times over the barrier of the conventional melt blend resulted from increased tortuosity of the diffusion pathway. Despite the large difference in melt viscosities, it was possible to combine PP and PA66 as microlayers with more than 2000 layers and nominal layer thicknesses as small as 0.5 μm. Retention of the layered PA66 structure during subsequent injection molding proved this to be a viable route to produce parts containing dispersed microplatelets and nanoplatelets.

8.6.5 *Microporous Membranes and Barrier Film Processing*

Microporous flat films with possible use as membranes were produced via melt processing and post-extrusion drawing from immiscible PP/PS blends containing a compatibilizing copolymer. The blends were first compounded in a co-rotating twin screw extruder and subsequently extruded through a sheet die to obtain the precursor films. These were uniaxially drawn (up to 500%) with respect to the original dimensions to induce porosity and then post-treated at elevated temperatures to stabilize the resultant structure, which consisted of uniform micro-cracks in the order of a few nanometers in width. Comparison of some of the novel microporous structures of this work with commercial membranes prepared by solvent-based phase inversion processes suggests comparable pore size and porosity ranges, with narrower pore size distribution [78]. The employed melt processing method has several potential advantages over other membrane fabrication processes, especially for solvent-resistant membranes: (1) membrane structure can be tailored by adjusting blend components and/or process parameters, (2) high production rates resulting in lower production cost, and (3) a wide variety of polymer systems having different physical and chemical properties can be used as starting materials.

Polymer membranes are increasingly employed for separation processes. They are relatively economic and cover a broad range of applications from microfiltration to reverse osmosis. Sadeghi et al. [79] investigated a polymer blend of branched and linear PP, to develop microporous membranes through melt extrusion (cast film process) followed by film stretching. Adding a small amount of branched PP into linear PP significantly increased the amount of entanglements in the melt state resulting in strain hardening. The early formation of entanglements during melt stretching created a specific crystalline structure for the blend upon crystallization in the precursor film, which favored orientation of the crystals blocks and also improved the tensile strength in the machine direction. The larger amount of pores and porosity are the result of such structure developed under stretching. The permeability of the samples to water vapor and N₂ was significantly enhanced (more than twice) for the blend system.

Polymer blending by extrusion followed by stretching the extruded film at the exit of the die was found to impart the obtained film with barrier properties. Ethylene vinyl alcohol (EVOH) is usually combined with PP in multilayer structures by co-extrusion process. The effects of different functionalized PP and diethyl maleate (DEM) combined with SEBS on various properties of extruded-stretched films of PP/EVOH blends were studied. Melt blending was done in a co-rotating twin-screw extruder through a flat film die. The stretched films of the original PP/EVOH blends and those of the PP-g-DEM and SEBS-g-DEM modified blends showed lamellar-type morphology, whereas PP-g-MAH and SEBS-g-MAH compatibilized PP/EVOH showed fibrillar morphology. Such peculiar morphology resulted in a dramatic decrease of oxygen permeability as compared with the unmodified or MAH modified PP/EVOH blends. The permeability of PP/EVOH (83.5/16.5) nonstretched film and stretched film (at draw ratio 5) is 61.4 and 20.6 mm cm³/(m² day atm), respectively. At draw ratio of 5, the permeability of PP/EVOH/SEBS-g-MAH (81.5/16.5/2) and PP/EVOH/SEBS-g-DEM (81.5/16.5/2) is 32.1 and 0.007 mm cm³/(m² day atm), respectively. It was found that shape factor has a slightly more important effect on permeability than interfacial adhesion [80].

Mohanraj et al. [81] reported the solid-state die-drawing of PP and blends of PP with a polyethylene elastomer to produce highly oriented products with enhanced mechanical properties. The blends showed an improvement in the drawability compared to the PP homopolymer. The addition of elastomer modifier particles (i.e., ethylene octane copolymer containing 25% octane) reduced the draw stress significantly, and allowing the blend to be easily oriented at low draw temperatures.

8.6.6 Electron Beam Irradiation

High energy electrons have been used to induce chemical crosslinking in 50/50 blend of PP and NR. The variation of absorbed dose (150–350 kGy) at fixed electron energy (1.5 meV) brings a dramatic change in the properties of the polymer blend. Polyfunctional monomers (PFMs) are used as co-agent during the

electron beam crosslinking of polymers. Dipropylene glycol diacrylate (DPGDA) was added during melt mixing for samples containing the PFM. The use of a PFM resulted in an increased tensile property at a reduced dose level and helped in generating higher graft-linkage at the interface of PP and NR [82].

Modification of polymers and polymer blends in the presence of high-energy irradiation is a potential method for the development of materials with superior properties. Radiation-crosslinked polyolefins are widely used as heat-shrinkable materials because they can store elastic memory that can be recovered upon application of heat. The phenomenon is referred to as memory effect or elastic memory. Polyfunctional monomers, such as multifunctional acrylate, methacrylate, and allylic reactive molecules, blended with the base polymers help achieve crosslinking at a reduced radiation level without a significant deterioration of the base polymers. Ali et al. [83] prepared PP/PE blends in the presence of trimethylol propane trimethacrylate (TMPTMA) monomer. The prepared polymeric samples were cured using an electron beam accelerator at different irradiation doses ranging from 5 to 50 kGy. Incorporation of TMPTMA monomer was found to positively influence the gel content of all samples. The mechanical strength increases on increasing the irradiation dose and attains its highest value at 20 kGy; a more pronounced effect was observed due to incorporation of TMPTMA into iPP than LDPE samples at low irradiation doses.

8.6.7 *Foaming*

PP foam products are widely used in cosmetics and in the packaging of food and electronics. Therefore, PP foam serves as an alternative to PS foam in the packaging industry. Compared with PS and PE, the foaming process for PP is difficult to control. The poor foamability of PP is because of its high crystallinity and low melt strength. Wang et al. [84] investigated the effect of polydimethylsiloxane (PDMS) on the foaming properties of block-copolymerized polypropylene (B-PP) by blending different contents of PDMS with B-PP in the extrusion process using supercritical CO₂ as the blowing agent. The experimental results indicate that the addition of PDMS greatly increased the expansion ratio of the foamed samples. At the same time, the cell population density of foams obtained from the blends also increased to a certain degree and provided a new perspective on improving B-PP's foaming performance. The maximum expansion ratio of the foam samples obtained from the PP matrix was just seven-fold, whereas the maximum expansion ratio of foams from the PP/PP-g-MAH/PDMS blends with a weight ratio of 98/1/1 was almost 14-fold. This is due to the fact that PDMS has high CO₂ solubility and high CO₂ infiltration capacity.

In general, to produce foam products successfully, PP had to be modified. The crystallinity and melt strength had great effect on the microcellular foamability. The blend with lower crystallinity and higher melt strength had better cellular structure and broader temperature range suited for microcellular foaming. Zhang et al. [85]

prepared PP/PE blends by using microcellular foaming. The relationship between crystallinity, melt strength, and cellular structure was studied. At PE content of 30%, the melt strength and PP melting point were highest and the PP crystallinity was least. The blend with lower PP crystallinity and higher melt strength had better cellular structure and broader microcellular foaming temperature range. It was established that the blend with higher melt strength can be microcellular foamed in a broader range of foaming temperature.

In the study of Spitael and Macosko [86], several PP and their blends were foamed in a continuous twin-screw coextrusion foaming line with carbon dioxide as the blowing agent. Blends of low concentrations of branched polymer in the linear PP show significant strain hardening. Strain hardening is expected to prevent cell coalescence and lead to higher cell concentrations. It was found that even small amounts of branched PP blended in linear PP can improve the foaming process.

8.6.8 Water-Assisted Injection Molding

The obtaining high contents of β -form crystals during processing are of practical importance to enhance the toughness of iPP products. The idea of reinforcing and toughening the iPP via the in situ microfibrillation of a high strength polymeric β -nucleating agent is more attractive and of more practical importance. Wang et al. [87] investigated the phase and crystal morphologies of iPP/acrylonitrile–styrene copolymer (SAN; as β -nucleating agent) blend part molded via water-assisted injection molding (WAIM). Comprehensive analysis of both experimental and simulated results showed that not only the shear flow field but also elongational flow field occurring during the WAIM was responsible for the formation of SAN micro-fibers and unique crystal morphology distribution in the WAIM iPP/SAN blend part.

8.6.9 Rotational Molding

Polymer blends can address the growing needs of the rotational molding industry by providing new tailored materials with good balances of properties. PP has seen growing interest in rotational molding, because of its high stiffness and good performance at high temperatures. Wang and Kontopoulou [88] had investigated the performance of PP/ultra low density ethylene- α -olefin copolymer (or polyolefin plastomer, POP) blends in rotational molding. The sinter melting curves of these blends exhibited bimodality, due to the wide melting point difference between the two polymers. Increasing POP content resulted in higher sintering and densification rates. Blends of PP with polyolefin plastomers can be rotomolded successfully, yielding products with good ductility and impact properties compared to pure PP. It was also established that using components with lower viscosity results in better sintering and densification characteristics attributed to the enhanced flow properties.

8.6.10 *In Situ Polymerization*

The versatility of polymerization processes made possible the production of blends in situ directly in the reactor. Blends of iPP, EPR, and ethylene-propylene crystalline copolymer (EPC) can be produced through in situ polymerization processes directly in the reactor and blends with different structure and composition can be obtained. Pires et al. [89] studied the structure of reactor-made blends of PP, EPR, and EPC produced by a Ziegler-Natta catalyst system. For higher ethylene concentration in the feed, rich ethylene rubber was formed, as well as a higher amount of EPC.

8.6.11 *Microcellular Injection Molding and Dynamic Packing Injection Molding*

Microcellular injection molding is a very effective method to produce excellent dimensional stability parts with lower injection pressure, shorter cycle time, and less material. Polymer blending could provide a new way to prepare microcellular foams with much higher cell density and smaller cell size in microcellular injection molding [90].

The properties of polymer blends depend strongly on processing, for the phase morphology and crystalline structure can be controlled by the stress and temperature field existing in processing. To realize in-process morphology control, generally a prolonged oscillating shear field is imposed on the polymer melt during the packing stage of injection molding, leading to a high orientation of molecular chains and an anisotropic morphology. It is possible to control the phase morphology and crystalline structure of polyolefin blends according to the concept of in-process morphology control by dynamic packing injection molding (DPIM) technique [91].

8.7 Structure-Property Relationship

8.7.1 *Impact Modification and Toughening*

PP exhibited low fracture toughness at low temperature range under its glass transition temperature. The high notch sensitivity of PP at room temperature often limits its industrial applications. It is known that elastomer-toughened PP blends are one of the strategies to obtain PP with higher toughness. Some of the recommended elastomers and polymers for PP toughening are ethylene-propylene copolymer (EPR), ethylene-propylene diene monomer (EPDM), ethylene vinyl acetate copolymer, styrene-butadiene-styrene (SBS), styrene-ethylene-butadiene-styrene copolymers (SEBS) and poly(ethylene-octene) (POE).

It is well known that toughening in PP/rubber blends is due to crazing and shear yielding of the matrix. The impact modifier particles act as stress concentrators initiating plastic deformation of matrix strands between the rubber particles. Moreover, cavitation inside the particles or at the interface has to be induced as an important precondition for effective toughening. The toughening efficiency depends greatly upon the type of rubber, the loading of rubber, the rubber particle size and distribution, the interparticle distance, and the test conditions [26].

Tang et al. [92] studied the influence of ethylene/styrene interpolymer (ESI) impact modifier on the toughening of PP random copolymer (RC-PP). The ESI have substantially random incorporation of styrene except successive head-to-tail styrene chain insertions. ESI shows excellent compatibility and good toughening effect to styrenic polymers, polyolefins, and a wide variety of other thermoplastics due to their inherent combination of olefinic and styrenic functionality in the backbone of polymer chains. ESI is an effective impact modifier for RC-PP and super-toughened polymer blends are achieved with low amount of ESI (ca. 5 wt%). RC-PP/ESI blends exhibit significant enhancement in toughness and ductility, but shows slightly reduction in tensile strength and elastic modulus with the addition of ESI. SEM observations reveal that the improved impact strength of RC-PP/ESI blends is attributed to cavitation and shear yielding of matrix RC-PP.

Polymer blends of RC-PP and poly(ethylene-octene) (POE) were prepared by melt-blending process using a co-rotating twin-screw extruder. The POE content was varied up to 35 wt%. RC-PP/POE blends exhibited significant enhancement in toughness and ductility. Super-toughened RC-PP/POE blends (Izod impact strength more than 500 J/m) can be readily achieved with only 10 wt% of POE [93].

Poly(ethylene oxide) (PEO) was used as impact modifier to tailor the toughness of iPP. An optimum performance was achieved at a medium PEO content of 15 wt % where the toughness was enhanced by 300%, while the strength only decreased slightly. When the PEO content is less than 15 wt%, it is well dispersed in the iPP matrix, and the addition of PEO also induces moderate amounts of β -form PP. The dispersed PEO could not crystallize and these numerous non-crystallized PEO microspheres are embedded in iPP spherulites, which is mainly responsible for the toughening in the iPP/PEO blends. Nevertheless, when the PEO content is greater than 15 wt%, the PEO phase becomes crystallized and phase segregation takes place, resulting in a drastic deterioration in mechanical properties [94].

Zhang et al. [2] prepared a blend of PP with a toughening master batch (TMB). The TMB were synthesized in a low-viscosity reaction system by using dynamic vulcanization technique starting from PP as matrix resin and ethylene-propylene or butadiene-styrene elastomer as toughening agent through polymer-bridge conjunction derived from a bridging agent monomer containing a carbonate group in the presence of a free radical initiator. In most of the TMB, over half the elastomers existed in a network form, and some of the PP was also connected with elastomers through the polymer bridging or branched chain of bridging agent. The TMB have given the toughened PP similar structural characteristics as with ABS and high

impact polystyrene (HIPS), while an excellent toughness with good rigidity remained.

According to Kakkar and Maiti [95] the impact strength of iPP can be increased by adding 0.32 volume fraction of ethylene vinyl acetate copolymer (EVA). The enhanced impact strength may be attributed to the flexibility effect of EVA, which, along with the amorphous chains, cushions the spherulites of iPP, which enabling the absorption of high impact energy.

Premphet and Paecharoenchai [96] investigated blends of PP and metallocene produced ethylene–octene copolymer (EOR) with a bimodal particle size distribution. The EOR characteristics such as molecular weight (MW), molecular weight distribution (MWD) and octane content showed a strong influence on impact property only when the concentration of EOR in the blends was higher than 10 wt%. High impact strength was achieved by the use of EOR with high octene content and high molecular weight. The critical ligament thickness of approximately 0.3–0.4 μm was observed for the PP/EOR blends. The impact strength increased dramatically with decreasing the ligament thickness below this critical value. Above this critical value, the characteristics of rubber showed no role on toughening efficiency.

The propylene-co-poly(ethylene-propylene) copolymer is one of the polymers that can be used for the rubber toughening of PP. Thanyapruksanon et al. [97] synthesized polypropylene-block-poly(ethylene-propylene) copolymer (PP-co-EP) by varying the feed condition and changing the feed gas in the batch reactor system using Ziegler–Natta catalysts system at a copolymerization temperature of 10 °C. The copolymer obtained can be used for PP toughening. The differential scanning calorimetry (DSC), dynamic mechanical analysis (DMA), and SEM results indicated that the PP-co-EP included in the amorphous region of PP and the polymer blends have lower glass transition temperature (T_g), and higher toughness than commercial-grade PP within the low temperature range.

The development and commercialization of olefin block copolymer (OBC) offer new opportunities for polyolefin blends and create a need for understanding their effectiveness on polymer toughening. Liu et al. [98] had investigated the miscibility and mechanical properties of iPP/OBC blends (70/30). The OBC domain size decreases with increasing the 1-octene content in the soft segment. The impact strength of the blends is greatly increased with increasing the 1-octene content in the OBC soft segment. It is believed that the enhanced mechanical properties were due to the increase in iPP/OBC interfacial bonding as the OBC soft segments 1-octene content increased, resulting in substantially higher iPP/OBC adhesion and smaller particle size in the iPP matrix.

Elastomer-toughening of PP occurs always at the cost of the decrease of tensile strength and modulus because of the poor strength of elastomer and the poor interfacial interaction between matrix and dispersed phase. It is well known that β -form PP crystallites show higher toughness. Bai et al. [99] blended two different nucleating agents (NA), such as α -form nucleating agent 1,3:2,4-bis(3,4-dimethylbenzylidene) sorbitol (DMDBS) and β -form nucleating agent aryl amides compounds (TMB-5) with PP/POE blends. Once nucleating agent and POE are simultaneously added into PP, PP/POE/NA blends show great improvement of

toughness even at low POE content. The addition of nucleating agent and elastomer into PP simultaneously shows an apparent synergistic toughening effect for PP. It is well known that the main mode of energy absorption during the impact process of elastomer toughened PP is shear yielding of matrix. The easier the shear yielding of the matrix, leads to the better impact toughness of the blends. The great improvement of PP/POE/NA blends toughness is mainly attributed to two combination factors: (1) shear yielding induced by POE particle during impact deformation, and (2) the effects of nucleating agent which cause the significant decrease of PP spherulites size and the homogeneous dispersion of the spherulites.

In the study of Fanegas et al. [100], iPP blends were prepared with two different thermoplastic elastomers, SEBS and a metallocenic ethylene-octene copolymer (EO). The addition of a nucleating agent (methylene-bis (4,6-di-tert-butylphenyl) phosphate sodium salt) as a third component exerted a significant effect on the overall properties. The improvement of impact properties found in binary blends was accompanied by a decrease in stiffness. However, the addition of the nucleating agent provided a good balance between impact strength and stiffness, which is due to the fact that the nucleating agent generates smaller spherulites, thus improving the mechanical properties.

Grein and Gahleitner [101] studied the effects of nucleation on the toughness of iPP/ethylene-propylene rubber (EPR) blends with different rubber molecular architectures. Two reactor-made iPP/EPR blends were produced with a high yield 4th generation Ziegler-Natta-catalyst. Both grades contained 32 wt% of xylene cold soluble (XCS, approximated to be the EPR content), had a propylene-rich rubber (C3-XCS of about 55 wt%). The rubbery phase of PP-1.9 had an intrinsic viscosity (IV) of 1.9 dl/g, while the dispersed phase of its counterpart, PP-4.2 had an IV of 4.2 dl/g. Figure 8.6 shows that the particle size of the iPP/EPR blends is dependent of the intrinsic viscosity of their elastomer phase. The PP-1.9 exhibited smaller EPR inclusions than its homologue which had an IV of 4.2. Consequently, the inter-particle distance (ID) of PP-1.9 was smaller to than that of PP-4.2. For blends exhibiting a small inter-particle distance between their EPR phases, toughness was promoted slightly by α -nucleation and to a large extent by β -nucleation as compared to the non-nucleated blends. These findings indicate the significance of relationship between the rubbery phase and the matrix to maximize the fracture resistance of polymer blends.

It is known that brittle-ductile transition behaviors of PP/elastomer blends do not only depend on the dispersed elastomer phase, but also on the matrix properties such as crystalline structure and morphology. The presence of large amounts of β -form crystals in the PP matrix is favorable to the shift of brittle-ductile transition towards lower temperatures. Therefore, a notable decrease in brittle-ductile transition temperature of PP random copolymer matrix with soft rubber phase will be expected if extensive β -form crystals could be formed in the matrix [1]. Adding both impact polypropylene copolymer (IPC) and β -nucleating agent (a rare earth agent composed of hetero-nuclear dimetal complexes of lanthanum and calcium containing some specific ligands) into PP random copolymer has three effects: (1) leading to a significant enhancement in β -crystallization capability of PP

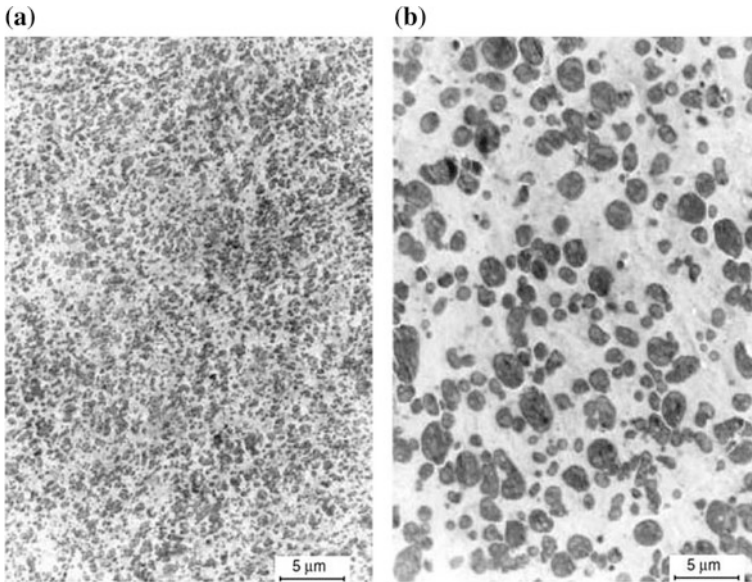


Fig. 8.6 Transmission electron micrograph of ruthenium tetroxide (RuO₄) stained PP-1.9 and PP-4.2. Adapted from Grein and Gahleitner [101], with the permission of BME-PT

random copolymer, (2) contributing to the shift of brittle-ductile transition to lower temperatures, (3) increasing the brittle-ductile transition rate. The reason for these changes can be explained by two phenomena. First, the transition of crystalline structure from α -form to β -form reduces the plastic resistance of PP random copolymer matrix, thus facilitates the initiation of matrix shear yielding during the impact process. Second, the well dispersed rubbery phase in IPC with high molecular mobility at relatively low temperatures is beneficial to the shear yielding of PP random copolymer matrix and thus greater improvement in impact toughness of the ternary blends can be achieved [1].

Jafari and Gupta [102] used two elastomers (EVA and EPDM) as impact modifier for PP. EPDM is found to be a better impact modifier for PP by increasing the impact strength of PP by a factor of up to about 20, whereas the EVA showed only two times the improvement in impact properties of PP. The analysis of dynamic mechanical properties revealed that there is a direct correlation between impact strength and loss peak area, that is, the impact strength of blend increased with the increase of the loss factor. This suggested that the energy of dissipation due to viscoelasticity of the blend is an important mechanism of impact toughening of PP/EVA blend. The energy dissipation due to viscoelastic relaxation is therefore suggested as a mechanism of impact toughening of PP, in addition to the other commonly known mechanisms of toughening (i.e., shear yielding and crazing induced by deformation of rubber-phase domains). Thus, in addition to commonly

known mechanisms of impact toughening, the energy dissipation due to viscoelasticity should be taken into account for designing supertough PP.

8.7.2 Crystallization

The high tendency of iPP to crystallization is due to its regular chain structure. A similar tendency to crystallization is implied in propylene copolymers with relatively low comonomer content (ethylene, olefins), e.g. block copolymers (BC-PP) and random copolymers (RC-PP) [103]. The β -nucleated iPP homopolymers have received considerable interest recently. This interest is mostly due to the peculiar thermal and mechanical performance of the β -crystalline PP [104]. It was well known that β -PP possessed higher toughness and heat distortion temperature than those of α -PP. If β -PP blends with other polymers could be prepared, they could be obtained with higher toughness and heat distortion temperature. In this section, the research findings on how to increase the β -PP content as well as crystallization rate of PP are documented. On the other hand, it is also important to know some of the opposite findings, e.g., inappropriate usage of compatibilizer/additives, inappropriate cooling rate and processing condition (mold temperature, injection speed) can reduce crystallization rate and/or suppress the β -PP nucleation.

It was found that addition of other crystalline polymers gives different effects on the β -nucleation of PP blends. The β -nucleation of PP in the blends depended on the preparation methods and the crystallization temperature and α -nucleation of other crystalline polymers. If the crystallization temperature of other crystalline polymers was lower than that of PP or the α -nucleation of the second component was weak, the second component would not affect the β -nucleation of PP in the blends, e.g. with LDPE. On the other hand, if the crystallization temperature of other crystalline polymers was higher than that of PP, the α -nucleation of the second component could markedly decrease the β -nucleation of PP in the blends, and it was difficult to prepare β -PP blends with high content of β -crystal [15].

According to Zhang and Robert Kwok [5] β -PP can be detected only when the PA6 content is lower than 3 wt%, which indicates that PA6 strongly suppresses the formation of β -PP. Thus, the preparation of PP/PA6 blends with β -PP matrix is very difficult. The reason is that the β -nucleating agent is selectively encapsulated in the polar phase. However, suitable compatibilizers can assist the distribution of the β -nucleating agent between both phases of the blend and promote the formation of a matrix rich in β -PP. It was found that higher β -PP content could be obtained by adding the β -nucleating agent to the PP blends at a temperature below 190 °C.

Zhang et al. [15] prepared β -PP/PS blends with PP, PS, and a novel supported β -nucleating agent or β -nucleated PP and PS. The results indicated that the PP with high content of β -crystal was obtained by addition of calcium carbonate (CaCO_3) supported β -nucleating agent into PP. Nevertheless, the addition of compatibilizers, e.g. PP-g-MA, glycidyl methacrylate-grafted PP (PP-g-GMA), and maleic

anhydride-grafted ethylene vinyl acetate copolymer (EVA-g-MA) slightly decreases the β -nucleation of PP in these blends.

Wang et al. [105] studied the morphology development during isothermal crystallization in equal molecular weight iPP and atactic polypropylene (aPP) blends with time-resolved simultaneous small-angle X-ray scattering (SAXS) and wide-angle X-ray scattering methods with synchrotron radiation. A detailed analysis of the SAXS patterns indicates that aPP disrupts the ordering within the lamellar stacking. The results are generally consistent with predominantly interfibrillar incorporation of the aPP diluent within the microstructure, with only modest interlamellar incorporation dependent on the crystallization temperature.

Finlay et al. [106] studied the properties of slowly cooled iPP/HDPE blends. At slow cooling rates, the HDPE and iPP components in the blends crystallize at lower temperatures than in the pure homopolymers, suggesting that the presence of one component inhibits rather than promotes the crystallization of the other.

Borysiak [107] found that incorporation of poly(styrene-ethylene-butylene-styrene) grafted with maleic anhydride (SEBS-g-MA) block copolymers into iPP/PS blends resulted in a significant decrease in β -content of iPP. It was also found that at a higher temperature mold and lower injection speed, the amount of β -phase of iPP matrix slightly reduced.

Yang and White [108] prepared PP mixed with ethylene butene copolymers (EBM; containing 51.6 mol% butane). The EBM could largely decrease the crystallization rates of the PP phase because the EBM molecules diluted the PP molecule concentration, and thus decreased both the nucleation and crystallization growth rates.

Zhang et al. [109] prepared PP/PS blends modified with reactive monomers, such as maleic anhydride (MAH) and styrene (St), and in situ formed PP/PS blends by melting extrusion. The results indicated that the addition of MAH hardly influenced the crystallization temperature of PP in the blends. However, the addition of MAH and St increased the crystallization temperature of PP in its blends, and made PP form a single peak of melting instead of a shoulder peak of melting. This could be attributed to the heterogeneous nucleation of PP-g-MAH, which was in situ formed in melt mixing.

Yang et al. [110] used a highly efficient nano-CaCO₃-supported β -nucleating agent to obtain iPP/PA6 blends with a high β -iPP content. PP-g-MA, PP-g-GMA, maleic anhydride grafted poly(ethylene octene) (POE-g-MA), and EVA-g-MA elastomers were added to the blends as compatibilizers. PP-g-MA, POE-g-MA, and EVA-g-MA reduced crystallization temperature of iPP and increased the β -iPP content in the β -nucleated iPP/PA6 blends, and this can be attributed to the fact that the compatibilizer improved the dispersion of PA6 in the iPP phase, resulting in a decrease in the crystalline ability and α -nucleating ability of PA6.

The isothermal crystallization kinetics of blends of different PP resins and a liquid crystalline polymer (LCP) after two different melting conditions (200 and 290 °C) were studied by DSC and polarized light optical microscopy. The resins were a homopolymer (hPP), a random copolymer with 3% ethylene (cPP), and a

grafted copolymer with 0.15% of maleic anhydride (gPP). The LCP was Vectra A950, a random copolymer made of 75 mol% of 4-hydroxybenzoic acid and 25 mol% of 2-hydroxy,6-naphthoic acid. It was observed that the overall crystallization rates of all the blends after melting at 200 °C were higher than those after melting at 290 °C. The LCP acted as a nucleating agent for all the PP resins; however, its nucleating effect was stronger for the hPP than for the cPP and gPP resins. All the PP resins formed transcrystallites on the surface of LCP domains [111]. According to Yu et al. [18] isothermal crystallization showed decreased crystallization half-times with the incorporation of LCP, and these were further reduced with compatibilizer (i.e., PP grafted with epoxy via glycidyl methacrylate). It was again proved that the LCP can act as nucleating agent for PP.

Guan et al. [112] investigated the crystallization behaviors of PP homopolymer and its blends with 0–15% functionalized polypropylene (FPP), the backbones of which were grafted with guanidine and diamide polymer chains. There was about 10 wt% of a modifying agent (guanidine and diamide polymers) grafted onto the backbone of PP in FPP. The FPP increased the crystallization rate. The half-time of crystallization for PP/FPP blends was much shorter than that for the PP homopolymer. FPP acts as a nucleation agent and accelerates the crystallization. The crystallization temperature of PP/FPP blends is 10 °C higher than that of PP. However, blending with FPP does not alter the crystal conformation α -phase monoclinic structure.

Wu et al. [113] investigated the crystallization behavior and morphology of nonreactive and reactive melt-mixed blends of PP and polyamide 12 (PA12). It was found that the crystallization behavior and the size of the PA12 particles were dependent on the content of the PP-g-MAH compatibilizer because an in situ reaction occurred between the maleic anhydride groups of the compatibilizer and the amide end groups of PA12. The compatibilized blends showed fractionated crystallization, which depended on compatibilizer content. An increasing amount of compatibilizer caused a large decrease in enthalpy that was associated with the crystallization of PA12, which completely disappeared when the concentration of compatibilizer was more than 4%. These finely dispersed PA12 particles crystallized coincidentally with the PP phase. The in situ formed graft copolymer (PP-MA)-g-PA12 played a role in concurrent crystallization by reducing interfacial tension and increasing the dispersion of PA12.

Random ethylene-propylene copolymer (PP-R) produced by copolymerization of propylene and ethylene is a product of modified PP that has received a great deal of attention in academic and plastic industry. Wang and Gao [114] studied the nonisothermal crystallization behavior and morphology of blends of PP with PP-R. The single peak during the melting and crystallization process indicated that PP and PP-R were very miscible and they are co-crystallizable. The values of the Avrami exponent indicated that the crystallization nucleation of the blends was heterogeneous while the growth of the spherulites was tridimensional. The addition of a minor PP-R phase favored an increase in the overall crystallization rate of PP.

Lin et al. [115] prepared β -nucleated PP, uncompatibilized β -nucleated PP/poly (trimethylene terephthalate) (PTT), β -nucleated PP/PTT blends compatibilized with PP-g-MAH and styrene–ethylene–propylene copolymer. The β -nucleating agent (N,N'-dicyclohexylterephthalamide) was mixed and blended with PP by a twin-screw extruder at temperatures of 170–200 °C to prepare the β -nucleated PP. All of the β -nucleated PP/PTT blends contained β -crystals of PP, and the compatibilizers exhibited synergistic effects with the β -nucleating agent to further increase the content of β -crystals.

Another interesting topic worth to mentioning is the β -transcrystallinity of iPP reinforced by fibers. According to Hao et al. [116] the polyethylene terephthalate (PET) fiber containing higher content of β -nucleating agent (β -NA) has dual nucleation ability, which it has both β - and α -nucleating ability. The β -NA loaded in the PET fiber would lead to dense β -nuclei and enhance the growth of β -transcrystallinity, while the local surface without β -NA of the fiber induce the formation of α -crystallites. The interfacial morphology evolution of iPP reinforced by PET fiber loaded with β -NA and that after being selective melting is schematically shown in Fig. 8.7.

Lima et al. [117] analyzed the effect of ground tyre rubber (GTR), EPDM and EPR on the crystallization of binary and ternary PP blends. Results reveal that GTR has a strong nucleating effect on PP and that its presence leads to higher crystallization rates. The EPDM presence has a slight effect on the PP crystallization

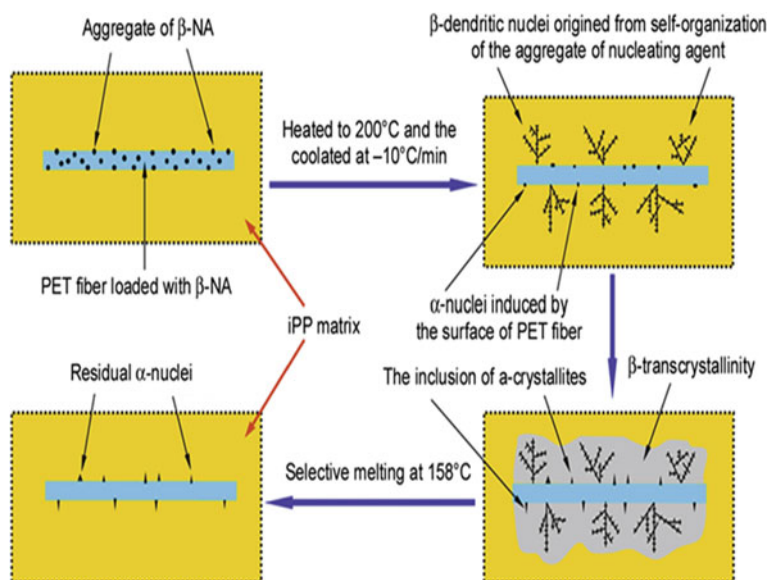


Fig. 8.7 Schematic illustration of the interfacial morphology evolution of iPP reinforced by PET fiber loaded with β -NA and that after being selective melting. Adapted from Hao et al. [116], with the permission of BME-PT

process whereas EPR has no significant effect. A decrease of the half time of crystallization and increase on the rate constant k indicate a significant increase of the overall crystallization rate. The Avrami exponent n values (~ 3) confirm the heterogeneous mechanism and indicate a three-dimensional spherulitic growth.

8.7.3 Rheology

Rheological study of PP blends is an important tool to understand their processability, melt strength, linear viscoelastic behavior, miscibility of the blends component in the melt state, relaxation process as well as phase morphology.

Blends of PP copolymer and a polyolefinic elastomer (POE) were prepared by a melt-blending process at 210 °C and 60 rpm using a counter-rotating twin-screw extruder. The POE content was varied up to 25 wt%. All blend compositions showed well-defined zero shear viscosity and shear thinning behavior. Rheology of PP copolymer/POE blends shows different behavior up to concentrations of POE corresponding to the tough–brittle transition. The linear viscoelastic properties were used to check the miscibility of the two components in the melt state. All blend compositions showed a good degree of miscibility over the range of POE concentrations studied. The PP copolymer/POE system appears to be a miscible blend, at least up to 25 wt% concentration of POE [118].

One of the effective approaches to enhance the melt strength of PP is to add polymers with long chain branches such as ethylene-butene copolymers (PEB). Zhang et al. [119] studied the extensional rheological behavior of PP, PEB and their blends in the melt state. The PEB enhances the strain hardening of the PP. The transient elongational viscosity of the PP/PEB blends with 20 and 40 wt% PEB deviates from the linear viscoelastic envelope at all strain portions, attributed to their morphology evolution during elongation.

It is well known that the representation of the dynamic shear data in Cole–Cole plots (η'' versus η') gives information about the relaxation processes occurring in a multiphase system. This type of representations can also be used to predict the compatibility of polymer blends. It is assumed that when a blend is compatible, a single curve is obtained in this type of plots, independent of the composition of the blend. According to López Manchado et al. [120] plots of η'' versus η' (Cole–Cole plots) show that the PP/EPDM blend with the lower EPDM rubber content (25 wt %) has a certain rheological compatibility with neat PP. A general processing behavior similar to that of PP was observed for blends with low content of EPDM (25 wt%), indicating that the same industrial thermoplastic molding processes used for neat PP can be adopted with evident economic advantages.

Ardakani et al. [121] studied the rheology, morphology and interfacial interaction of PP/polybutene-1 (PB-1) blends. A droplet-matrix morphology was observed for all blends in SEM images. At low concentrations, up to 10 wt% PB-1, the particles size is smaller than 40 nm and homogeneously dispersed in the matrix. By increasing the percentage of PB-1 a non-homogenous morphology is obtained and

the size of the droplets increased. The complex viscosity of samples at various percentages of PB-1 showed the log-additivity mixing rule behavior in low frequencies and positive-negative deviation behavior at high shear rates. The phenomena such as decrease in the sensitivity of storage modulus to shear rate in the terminal region, the deviation of Cole–Cole plots from the semi-circular shape, and the tail in relaxation spectrums at high relaxation times are the evidences of two phase heterogeneous morphology.

Marguerat et al. [122] investigated the relation of morphology to the linear viscoelastic properties PP/EVA and PP/ethylene methyl acrylate (EMA) blends. The rheological properties of the elastomeric phase were modified by crosslinking in presence of an organometallic catalyst. The Palierne model was used to describe the linear viscoelastic behavior of the blends, and to estimate the interfacial tension between the immiscible components. In general, the Palierne model is used to describe the viscoelastic behavior of blends, assuming a monodisperse distribution in size of the inclusions. It was proved that the Palierne model describes relatively well the linear viscoelastic properties of reactive and nonreactive PP/EVA and PP/EMA blends containing 20 wt% or less elastomer.

Shi et al. [123] studied the melt rheological properties of binary uncompatibilized PP/PA6 blends and ternary blends compatibilized with PP-g-MAH using a capillary rheometer. The experimental shear viscosities of the blends were compared with those calculated from Utracki's relation. The value δ represents the difference between the experimental viscosity, $\log \eta$, and the calculated one, $\log \eta'$. The deformation recovery and/or break-up ability of the dispersed droplets greatly affect the final apparent shear viscosity of blends during capillary flow. From the macroscopic point of view, the deviation value δ between the experimental and the theoretical apparent shear viscosity values calculated from Utracki's relation proved to be useful in characterizing the deformation recovery and/or breakup ability of the dispersed droplets in polymer blends. In binary PP/PA6 blends, when the deformation recovery of dispersed droplets plays the dominant role, δ is negative. The higher the dispersed phase content, the more deformed the droplets are and the lower the apparent shear viscosity. Also, the absolute value of δ increased with dispersed phase composition. In ternary PP/PA6/PP-g-MAH blends, when the elongation and break-up of the dispersed droplets play the dominant role, a positive deviation can be found between the experimental and the calculated results. The higher the content of the dispersed phase, the higher the absolute δ values of the ternary blends are and the stronger the positive deviation.

The dynamic rheological behavior is measured by small amplitude oscillatory shear on rotational rheometer for PP/PA6 blends compatibilized by PP-g-MAH. The dynamic rheological measurement shows that when the weight ratio of PP/PP-g-MAH/PA6 increases from 100/6/0 to 100/6/60, the complex viscosity and dynamic modulus at low frequency increase gradually, but when the weight ratio of PP/PP-g-MAH/PA6 continues to increase to 100/6/80 and 100/6/100, the complex viscosity and dynamic modulus decrease. Bousmina's model can fit the data well when the weight ratio of PP/PP-g-MAH/PA6 is 100/6/20 and 100/6/40, respectively. Note that Bousmina's model considers the blend as a three-region system,

that is, spherical droplets surrounded by matrix shells dispersed in a homogeneous matrix. In addition, Bousmina's model considers the flow circulation inside and outside the droplet, hence it can corroborate the experimental data of compatibilized blends [124].

8.7.4 Other Properties

Efforts have been done to solve the limitation or to improve the potential properties of PP, for example, foamability, dyeability and weatherability—in order to widen the applications of PP blends.

8.7.4.1 Foamability

PP has been considered as a substitute for other thermoplastic foam materials. However, some studies have shown that it is not easy to foam PP for three reasons: (1) PP is a semi-crystalline polymer and gases are difficult to dissolve in the crystalline regions, (2) the melt strength of PP is low that the cell walls may not have enough strength to bear the extensional force and may collapse easily during foaming, and (3) the viscosity of PP is dependent on the foaming temperature, that is, even small overheating of the polymer melt leads to a very large drop in viscosity and hence cause the coalescence of bubbles. Thus, the operating temperature interval for PP foaming is quite narrow. Li et al. [125] used polypropylene block (PP-B) copolymer as a modifier to improve the crystallization behaviors and foaming performance of PP homopolymer (HPP). The experimental results indicate that the crystallization temperature and rate of PP-B are higher than those of HPP, so it can be used as the nucleation modifier to improve the HPP/PP-B crystallization behaviors. The higher crystal density and melt strength are advantageous for the improvement of cell structure of the foamed materials. In comparison with pure HPP, the blending of PP-B can make the crystal grain fine dramatically. SEM results show that much more uniform, smaller cells can be obtained for the HPP/PP-B blends. The crystal nuclei formed earlier can act as physical crosslink points, increasing the melt strength and improving dramatically the cell structure and morphology of the HPP/PP-B blends.

Another way to improve the foaming of a linear PP is to incorporate long-chain branches (LCBs). The PPs with LCBs have a pronounced strain hardening, which is closely related to an enhancement of the melt strength. Different methods have been applied to modify PP by LCB. Most of the LCB PP are produced by in situ polymerization and by post-reactor treatment. After the reactor treatment, the LCBs can be formed by reactive extrusion or by electron beam irradiation. Several studies have shown that foaming of LCB PP, either pure branched PP or blended with linear PP, leads to higher expansion ratio and more homogeneous cellular structures. The blends rich in LCB PP show better foamability owing to their higher melt

strength. The balance between the large nucleation of the linear PP and the reduction of the cell coalescence due to the important strain hardening of the LCB PP can lead to a higher cell concentration in the blends of linear and branched PPs than in the neat polymers. While the linear PP does not exhibit strain hardening, the blends of the linear and the HMS PP show pronounced strain hardening, increasing with the concentration of HMS PP. The results demonstrate the importance of the extensional rheological behavior of the base polymers for a better understanding and steering of the cellular structure and properties of the cellular materials [126].

8.7.4.2 Dyeability

As a textile fiber, PP is incapable of being dyed by conventional dyestuffs from an aqueous dye bath because of its nonpolar and highly crystalline structure. These inherent attributes limit the dye receptivity of PP, and this is considered to be the drawback of PP usage in the textile industry. It has been observed that melt blending of PP with PS, PA and polyesters before spinning is an efficient process for enhancing the dyeability of PP fibers. Mirjalili et al. [127] attempted to predict the optimal disperse dye uptake of PP modified with PET and PP-g-MAH compatibilizer without adversely impairing its mechanical properties. For this purpose, the amounts of three independent variables in the blend composition, namely, the weight fractions of PP, PET, and PP-g-MAH, were varied according to a special cubic mixture experimental design. By use of a special cubic experimental design, it was demonstrated that the desired dyeability was attained by the addition of limited amounts (10–15 wt%) of PET. The results indicated that the PP/PET/PP-g-MA blends in which the PET and PP-g-MA contents were in the range 10–15 and 4–5 wt%, respectively, gave maximal dye uptake and desirable tensile properties. On the basis of these results, it was concluded that an optimum PET:PP-g-MAH ratio of 3:1 provided a PP/PET/PP-g-MAH blend with desired dyeability and acceptable mechanical properties.

8.7.4.3 Weatherability

The study of degradation and stabilization of polymers is extremely important from the scientific and industrial point of view, to ensure a long service life of the product. Mouffok and Kaci [128] investigated the degradation of uncompatibilized and compatibilized PP/PA-6 (70/30 wt%) with PP-g-MAH (2 wt%) under accelerated UV light. Fourier transform infrared spectroscopy (FTIR) analysis of the structure of the compatibilized and uncompatibilized blends after exposure to UV light showed the formation of photoproducts corresponding to both components. The overall results suggest that the photooxidation in PP/PA-6 blends starts in PA-6 phase initiating chain oxidation of PP. The photooxidation of the two phases occurs simultaneously due to the interactions between the photoproducts of both

components, increasing the degradation rate of the blend. The compatibilizer acts as a photooxidation promoter in PP/PA-6 blends. Accordingly, to improve the durability of these blends, it is necessary to prevent them against UV degradation by optimizing the quantity and quality of UV stabilizer to be used. In addition, the selection of appropriate compatibilizer for PP/PA6 blends that is more durable in the UV environment should be considered.

8.8 Compatibilization of PP Blends

Most of polymers are immiscible with each other because of the positive Gibbs energy of mixing, which results in phase separation, poor adhesion in interfaces, and deteriorated ultimate properties. Therefore, compatibilization of the immiscible polymer pairs must be taken into full consideration during the design of high-performance polymer blends. Compatibilization of multiphase polymer systems has been reviewed extensively in literature. It is well established that compatibilization can be achieved either by addition of pre-synthesised copolymer (physical compatibilization) or through the in situ generation of graft or block copolymers at the interface between the individual polymers by chemical reactions during processing (reactive compatibilization) [129]. To improve the compatibility of PP blends, suitable compatibilizing agents are often added to the blends to decrease the interfacial tension and achieve more homogeneous dispersion with smaller domain size. Reactive compatibilization is another interesting method from economic and academic points of view in which the compatibilizer is generated during the blending process and preferentially locates at the interface.

8.8.1 Physical Compatibilization

Styrene-butadiene-styrene (SBS), styrene-ethylene-butadiene-styrene (SEBS), styrene-ethylene-propylene (SEP), styrene-isoprene-styrene (SIS), and polypropylene-g-polystyrene copolymer (PP-g-PS) are some of the recommended compatibilizers for PP/PS blends. Among which, PP-g-PS graft copolymer, composed of a PP backbone and PS branches, is an ideal compatibilizer for PP/PS blends due to the good compatibility of PP backbone and PS branches with PP bulk and PS bulk, respectively. Wang et al. [130] evaluated the effects of PP-g-PS on the morphological and rheological properties of PP/PS blends. The results revealed that the addition of PP-g-PS graft copolymers significantly reduced the PS particle size and enhanced the interfacial adhesion between PP and PS phases. According to Li et al. [131] DMA and SEM results illustrated that the PP-g-PS is an efficient compatibilizer for the PP/PS blend. The phase separation decreased when PP-g-PS was added. This phenomenon is much clearer when the PP/PS blend ratio is 75/25.

The presence of PP-g-MAH increases the phase stability of PP/PS (90/10 and 80/20) blends by preventing the coalescence. Hence, finer and more uniform droplets of PS dispersed phases are observed. The compatibilizer induced some improvement in impact strength for the blends. The degree of crystallinity of PP/PS (80/20) blends was increased from 38.8 to 49.2% by the addition of 10 wt% PP-g-MAH [132]. According to Slouf et al. [133] styrene-ethylene-propylene (SEP) can act as an efficient compatibilizer of iPP/atactic PS blends.

Syed Mustafa et al. [134] investigated the use of an aromatic vinyl monomer (AVM)-grafted PP (PPA) as a compatibilizer for PP/PS blend. PPA was prepared by grafting a monofunctional aromatic vinyl monomer onto PP using organic peroxide at 180 °C for 10 min in a Brabender mixer. Results obtained from tensile and impact strength, heat deflection and melt flow index measurements show some improvement in the properties of the blends indicating some compatibilization effects in the blend system.

Mandal and Chakraborty [135] prepared PP blends with thermotropic Vectra B-950 liquid crystalline polymer (LCP; an aromatic copolyesteramide comprising 60 mol%, hydroxy naphthoic acid, 20 mol%, terephthalic acid, and 20 mol% p-aminophenol) in different proportions in presence of 2 wt% of ethylene-acrylic acid copolymer (based on PP) as a compatibilizer. The tensile properties of the compatibilized blends displayed improvements in modulus and ultimate tensile strength of PP matrix with the incorporation of 2–10 wt% of LCP incorporation. The development of fine fibrillar morphology in the compatibilized PP/LCP blends had large influence on the mechanical properties.

Mandal et al. [136] prepared blends of PP and Vectra A950, a thermotropic liquid crystalline polymer (LCP; an aromatic copolyester comprising 25 mol% of 2,6-hydroxynaphthoic acid and 75 mol% of para hydroxybenzoic acid) blends were prepared in a single-screw extruder with the variation in Vectra A950 content in presence of fixed amount (2 wt%, with respect to PP and LCP mixture as a whole) of ethylene-acrylic acid (EAA) copolymer as a compatibilizer. Mechanical analysis of the compatibilized blends within the range of LCP incorporations (2–10 wt%) indicated pronounced improvement in the modulus, ultimate tensile strength and hardness. FTIR results confirmed the existence of strong interaction between the segments of EAA and LCP Vectra A 950 through intermolecular H-bonding in the blends. This investigation demonstrates that the preferential alignment (fibrillar morphology) of Vectra A950 during melt blending as well as the enhanced interfacial adhesion between Vectra A950 and the compatibilizer EAA play the key role in improving the mechanical properties of the blends.

The grafting polymer containing maleic anhydride (e.g. PP-g-MAH) or epoxy glycidyl methacrylate (e.g. PP-g-GMA) groups can potentially react or become involved in hydrogen bonding with hydroxy or carboxy on the LCP polyester and provide compatibilization between the phases. Liquid crystalline polyester was dispersed in PP to provide a coarse two-phase incompatible blend. Glycidyl methacrylate grafted polypropylene was effective as a compatibilizer, and smaller particles of LCP were formed with good interfacial adhesion [18].

Farasogldu et al. [137] used PP-g-MAH to compatibilize PP/LCP blends. Two types of LCP were used, namely Vectra A950 (VA; based on 73% hydroxybenzoic acid and 27% hydroxynaphthoic acid) and Vectra B950 (VB; synthesized from 60% hydroxynaphthoic acid, 20% terephthalic acid and 20% aminophenol). It was found that the greater enhancement in tensile modulus, yield stress, yield strain and thermomechanical behavior is obtained for 5% compatibilizer content in either 10 or 20% per weight LCP phase.

Lee et al. [138] investigated the effects of SEBS-g-MAH on the mechanical and morphological properties of PP/ABS blends. The PP/ABS (70/30) blends containing SEBS-g-MAH showed improved impact strength with minimal tensile strength loss. This result suggests that MAH in SEBS-g-MAH plays an important role as an impact modifier and compatibilizer with the PP/ABS blend, possibly because of dipolar interactions between the MAH group and polar group in ABS.

The polypropylene-graft-cardanol (PP-g-cardanol) was prepared by reactive extrusion with PP and natural renewable cardanol which could increase the interfacial energy of PP and inhibit the degradation of PP during the process of reactive extrusion and usage. Cardanol grafted onto PP could inhibit the light and heat degradation because the natural product of cardanol had the dual effect of electron donating and electron withdrawing due to the $p-\pi$ conjugated system of cardanol. PP-g-cardanol and PP-g-MAH were used as compatibilizers of the PP/ABS blends. From the results of morphological studies, the droplet size of ABS was minimized to 1.93 and 2.01 μm when the content of PP-g-cardanol and PP-g-MAH up to 5 and 7 phr, respectively. The results of mechanical testing showed that the tensile strength, impact strength and flexural strength of PP/ABS (70/30) blends increase with the increasing of PP-g-cardanol content up to 5 phr [139].

Lee and Kim [140] examined the effect of three compatibilizers, i.e. a hybrid compatibilizer composed of PP-g-MAH and polyethylene-glycidyl methacrylate (PE-g-GMA), a single PP-g-MAH compatibilizer, and a single PE-g-GMA compatibilizer on the mechanical, morphological, and rheological properties of a ternary blend of PP, poly(lactic acid) (PLA), and a toughening modifier (Biomax Strong 120). The tensile strength, flexural strength, and impact strength of the ternary blends (PP/PLA/toughening modifier: 60/30/10) with a hybrid compatibilizer content of 3 phr exhibited better material properties than the blend containing only a single compatibilizer.

Dai and Ye [141] investigated a series of compatibilizers, including polypropylene (PP) grafted with 2-tertbutyl-6-(3-tertbutyl-2-hydroxy-5-methylbenzyl)-4-methylphenyl acrylic ester (BPA), glycidyl methacrylate (GMA), GMA/styrene (GMA-st), and 2-allyl bisphenol A for the purpose of improving the compatibility of PP/PC blends. PP-g-BPA shows a remarkable compatibilizing effect on PP/PC blends since it has similar group—benzene ring with PC, and it is a sort of heat-resistant antioxidant in the meantime, which can reduce the molecular degradation of PP during grafting and blending under high temperatures. The blending morphologies change from the cylinder-shaped domains to a spherical shape and more reduced homogeneous size of the dispersed PC particles by addition of PP-g-BPA.

Zhang et al. [142] prepared ternary blends of PP, a polypropylene-grafted acrylic acid copolymer (PP-g-AA), and an ethylene–acrylic acid copolymer (EAA) by melt blending. Scanning electron microscopy observations confirmed that PP-g-AA acted as a compatibilizer and improved the compatibility between PP and EAA in the ternary blends. According to Wang and Ishida [143] the interfacial adhesion of blend of iPP/poly(vinyl methylether) (iPVME) has been improved by the addition of PP-g-AA as a compatibilizing agent. The addition of 2.5 wt% PP-g-AA reduces the PVME domain size greatly and the addition of 5 wt% PP-g-AA results in a homogeneous morphology. The increase of the interfacial adhesion is attributed to the specific intermolecular interaction between the acrylic acid group of PP-g-AA and the ether group of PVME.

Polypropylene–phenol formaldehyde-based compatibilizers, i.e. polypropylene-graft-phenol formaldehyde copolymers (PP-g-PF) were suitable for blends or alloys of PP and engineering polymers having aromatic residues or functionality complementary to hydroxyl. Blends of iPP/PBT and iPP/poly(phenylene ether) (PPE) were compatibilized by PP-g-PF. Impact strength was observed to be the most sensitive response to blend compatibilization. The PP-g-PF compatibilizer was observed to be more efficient in blends of PBT than of PPE. The main reason for that was the availability of reactive end-groups in the case of PBT, making covalent bonding between the compatibilizer and PBT possible [144].

Thermotropic liquid crystalline ionomer (LCI) is a kind of LCP containing ionic groups; they can offer the possibility for promoting intermolecular interaction through ion–dipole association and the improvement of the interfacial adhesion between the phases in blends. Sun et al. [145] used side-chain liquid crystalline ionomer (SLCI) containing sulfonic acid groups with a polymethylhydrosiloxane main-chain to improve the compatibility of PP and PBT. The SLCI containing sulfonate acid groups acted as physical crosslinking agent along the interface, which compatibilized PP/PBT blends. Specific interaction was formed by ion–dipole interaction between the ionic groups of SLCI and the polar groups in PBT. The interaction led to the compatibilization of the SLCI in PP/PBT/SLCI blends. This resulted in much finer dispersion of the minor PBT phase in PP matrices and stronger interfacial adhesion between these phases. The compatibilization effect of 4 wt% SLCI content was better than that of other SLCI contents in the blends.

PP/PA blends were compatibilized with PP modified with vinylsilane or maleic anhydride and ethylene–propylene random (EPR) copolymer modified with maleic anhydride. Tensile strength and elongation at break increased for blends compatibilized with modified PP. It can be seen that blends compatibilized with PP-g-MAH showed the greatest tensile strength among all the blends. They had the highest elongation at break, indicating good adhesion between the phases. The morphology of the blends showed a finer dispersion of the PA minor phase in the PP matrix [146].

Marco et al. [147] investigated the role played by two different interface agents on the basis of atactic PP in the PP/PA6 blends. Two grafted polymers containing either succinic anhydride (a-PP-SA) or both succinyl-fluorescein and succinic anhydride grafted groups (a-PP-SF/SA). Thermo-optical morphological studies

have indicated that the presence of the interface agents improves the degree of compatibilization through a reduction in the size of the PA6 domains dispersed in the PP matrix. The compatibilizing efficiency of a-PP-SA is greater than that of a-PP-SF/SA for the PP/PA6 system. Franzheim et al. [148] studied the effects of PP-g-MAH on the morphology development of PP/PA6 blends. It was observed that compatibilization has a stronger influence on the blend morphology than a variation of process or rheological conditions with physical blends. Furthermore, the compatibilization leads to a concurrent crystallization of the PA6 phase with the PP phase. According to Laredo et al. [149] the inclusion of 10 wt% of PP-g-MAH into the PP/PA6 (70/30) blend has improved the dispersion of the PA6 in the amorphous phase. Also, the sorption of water of the PP-g-MAH compatibilized PP/PA6 blends is lower than that of the unmodified blend.

Lu et al. [150] prepared amine (primary and secondary) functional PP by the melt blending of maleated PP with small diamines, including hexamethylenediamine (primary–primary diamine), p-xylylenediamine (primary–primary diamine) and N-hexylethylenediamine (primary–secondary diamine), at various diamine/anhydride molar ratios in a batch mixer and a twin-screw extruder. It was found that the adhesion between polyurethane (PU) and PP was greatly promoted by the amine-functionalized PP.

Kim et al. [151] investigated the properties of PP/ethylene vinyl alcohol (EVOH) blends compatibilized with polypropylene grafted with itaconic acid (PP-g-IA). It was found that carboxylic acid groups in PP-g-IA and hydroxyl group in EVOH formed strong in situ hydrogen bond in the compatibilized blends, resulting in better morphological and mechanical properties of the compatibilized blends than those of un-compatibilized blends. In the case of PP/EVOH blends with PP-g-IA, the Young's modulus, ultimate tensile strength and elongation at break increased significantly as compared with PP/EVOH blends without PP-g-IA. These results indicated that PP-g-IA led to a good compatibilizing effect between PP and EVOH resin.

Table 8.1 summarizes some of the compatibilizer used for PP blends. It can be concluded that selection of suitable and loading of compatibilizer is an important factor to enhance the compatibility between PP and other polymers (e.g. PA, PS, ABS, PC, LCP).

8.8.2 *Reactive Compatibilization*

In the previous section, it can be seen that block copolymers are successfully employed as good compatibilizers because they are able to locate at the interface and act as emulsifiers to lower the interfacial tension. However, due to their high molecular weight nature, large amount of the block copolymers often prefer to form micelles in either homopolymer phases, rather than residing along the interfaces. This make reactive compatibilization an alternative approach to produce useful polymer blends [152].

Table 8.1 Compatibilizer for PP blends (PP as major matrix)

PP type	Other polymer	Compatibilizer	Findings	Reference
Polypropylene (PP) [MW = 590,000 g/mol]	Liquid crystal polymer (LCP; Rodrun LC3000) [60 mol% hydroxybenzoic acid (HBA) and 40 mol% ethylene terephthalate]	PP-g-GMA (glycidyl methacrylate content of 1.5 wt%); loading 1, 2, 5, and 10 wt%	Adding PP-g-GMA further reduced crystallization half-times	[16]
PP	Liquid crystal polymer (LCP)	PP-g-MAH (less than 1 wt% MAH); loading 5 wt%	Adding PP-g-MAH increased tensile modulus, yield stress, yield strain and thermomechanical behavior of PP/LCP blends	[137]
PP	Liquid crystal polymer (LCP)	Ethylene-acrylic acid (EAA) (comonomer content 6 wt%)	Strong interaction formed between the segments of EAA and LCP Vectra A 950 through intermolecular H-bonding in the blends	[136]
PP	Polystyrene (PS)	PP-g-MAH (8 to 10 wt% MAH); loading 2, 5 and 10 wt%	Adding PP-g-MAH stabilizing the morphology and improving the impact strength	[132]
iPP [MW = 3.07×10^5 g/mol]	Atactic polystyrene (PS) [MW = 3.72×10^5 g/mol]	PP-g-PS	PP-g-PS graft copolymers were effective in reducing the PS particle size and enhancing the interfacial adhesion between PP and PS phases	[130]
PP [MW = 230,000 g/mol]	Acrylonitrile butadiene styrene (ABS) [MW = 160,000 g/mol]	SEBS-g-MAH; loading 1, 3, 5, 7 and 10 phr	Adding SEBS-g-MAH (up to 7 phr) improve impact strength of the blends	[138]
iPP	Acrylonitrile-butadiene-styrene (ABS)	PP-g-cardanol (grafting degree is 3.88%); loading 1, 3, 5, 7, 9 phr	Adding PP-g-cardanol improved tensile strength, impact strength and flexural strength of PP/ABS (70/30) blends	[139]

(continued)

Table 8.1 (continued)

PP type	Other polymer	Compatibilizer	Findings	Reference
PP [MW = 386,648 g/mol]	Polycarbonate (PC)	PP-g-BPA (degree of grafting 5.59 BPA); loading 5 and 15 wt%	Adding PP-g-BPA increased tensile strength and impact strength of PP/PC blends	[141]
PP	Ethylene-acrylic acid copolymer (EAA)	PP-g-AA (grafting degree of acrylic acid is 0.85 wt%)	Adding PP-g-AA improved the compatibility between PP and EAA	[142]
iPP [MW = 250,000 g/mol]	Poly(vinyl methylether) (PVME) [MW = 90,000 g/mol]	PP-g-AA (acrylic acid 6 wt%); loading 2.5 and 5 wt%	The addition of 2.5% PP-g-AA reduces the PVME domain size greatly and the addition of 5% PP-g-AA results in a homogeneous morphology	[143]
PP	Polybutylene terephthalate (PBT)	Side-chain liquid crystalline ionomer (SLCI) containing sulfonic acid groups with a polymethylhydrosiloxane main-chain; loading 2–12 wt%	SLCI resulted in much finer dispersion of the minor PBT phase in PP matrices and stronger interfacial adhesion between these phases	[145]
PP	Polyamide 6 (PA6)	PP-g-MAH (functionalization degree MAH 0.70%); loading 4 and 7 wt%	The yield stress and elongation at break of PP/PA6 blends increased significantly	[146]
iPP [MW = 334,000 g/mol]	PA6 [MW = 25,000 g/mol]	Succinic anhydride grafted atactic polypropylene (a-PP-SA) (containing 3.1 wt% grafted groups)	a-PP-SA improved the degree of compatibilization through a reduction in the size of the PA6 domains dispersed in the PP matrix	[147]
PP [MW = 34,400 g/mol]	Ethylene vinyl alcohol (EVOH) [MW = 41,400 g/mol]	PP-g-IA (graft ratio of 1%); loading 10 phr	The PP-g-IA compatibilized PP/EVOH blends have higher storage modulus, Young's moduli, ultimate tensile strength, and elongation at break than un-compatibilized blends	[151]

Hung et al. [152] attempted to reactively compatibilize the nonreactive PP/PS blend system by physically functionalizing PP and PS with the addition of PP-g-MAH and styrene maleic anhydride random copolymer (SMA), respectively. An epoxy monomer, serving as a coupler and possessing four epoxy groups able to react with the maleic anhydride of PP-g-MA and SMA, was added during melt blending. Observations of the finer PS domain sizes and improved mechanical properties support the potential of reactive compatibilization of this nonreactive PP/PS blend by combining physically functionalized PP and PS with tetra-glycidyl ether of diphenyl diamino methane (TGDDM) in a one-step extrusion process. The tensile strength and flexural modulus of the compatibilized blends are substantially improved compared to non-compatibilized blends. A small quantity of the TGDDM is important to function as a coupler in the PP/PS blend during melt blending.

Kaya et al. [153] synthesized oxazoline-functionalized PP by using the *rac*-Et [1-Ind]₂ZrCl₂/Methylaluminoxan (MAO) catalyst system. To investigate their compatibilization efficiency, copolymers with different oxazoline groups were reactive blended with carboxylic-terminated PS. The copolymer with the oxazoline group containing phenoxy moiety showed the highest compatibilization efficiency. The increase in melt viscosity, melting temperature, and onset temperature of the crystallization indicate a reaction between the oxazoline group of the copolymer and the carboxylic group of the PS, resulting in an amide- and an ester-covalent bond. Li et al. [154] prepared isocyanate- and amine-functionalized PP and PS through grafting and copolymerization method. These compounds are used as precursors for PP-g-PS copolymers and reacted at the matrix interface of PP/PS blends. The addition of the reaction compatibilizer greatly altered the distribution in the matrix such that PS particles became finely dispersed. DMA measurements confirm that the compatibility of PP/PS blends with compatibilizers is better than without compatibilizers.

Yang et al. [65] reported that in situ reactive compatibilization of PP and SBS, was achieved in the presence of an initiator, dicumyl peroxide (DCP). Co-vulcanizing agent triallyl isocyanurate (TAIC) was used to improve the crosslinking efficiency from controlling the degradation reaction, remarkably decrease the probability of PP chains scission during blending. With improved interfacial adhesion, compatibilized blends not only were toughened but also exhibited enhanced tensile strength and thermal stability. Cryofractured surface morphologies of reactive compatibilized blends showed a reduction of dispersed particle sizes and an increment on interfacial adhesion, especially for PP/SBS/DCP/TAIC (50/50/1.5/0.75) blend.

Bohn et al. [155] prepared carboxylated and maleated as reactive compatibilizers for PP/PA66 blends. The PP has been functionalized, via reactive extrusion, with MAH and with asymmetric functional peroxide. In compatibilized blends of PP and PA66, the PP that was functionalized with the asymmetric peroxide is found to be an improved compatibilizer compared to that of PP-g-MAH.

Compatible polymer blends of PP with an amorphous polyamide (aPA) were obtained through reactive compatibilization by adding 20 wt% PP-g-MAH to the blends. The aPA was synthesized from a random copolymer of isophthalic acid,

12-aminododecanoic acid, and bis(4-amino-3-methylcyclohexyl) methane. The addition of the compatibilizer to the blends led to both a significant decrease in the dispersed phase particle size (roughly from 1–2 to 0.2 μm) and an improvement in interfacial adhesion. This was attributed to the formation of PP-g-aPA grafted copolymers by an in situ reaction of the anhydride groups of the PP-g-MAH with the amine end groups of aPA as well as to their location at the interface [156].

In Tortorella and Beatty [157] research work, iPP has been reactively blended with various grades of an ethylene–octane copolymer (EOC) in a twin-screw extruder. Free radical polymerization of styrene and a multifunctional acrylate during melt extrusion has resulted in an enhancement of mechanical properties over the binary blend. The reactive blend (containing 74.3% PP, 18.6% EOC, 6% styrene, 0.3 2,5-dimethyl-2,5-di-(t-butylperoxy) hexane initiator, and 0.8% multifunctional acrylate) exhibits a notched Izod impact strength over 12 times that of pure PP and greater than double the performance of the binary blend.

Another possibility for in situ compatibilization of polyolefin/PS blends is an electrophilic substitution of a proton on the aromatic ring of PS by an alkane or olefin in the presence of a strong Lewis acid, known as Friedel–Crafts (F–C) alkylation reaction. Binary polymer blends of PP/PS (blending ratio: 80/20) were compatibilized by Friedel–Crafts alkylation reaction, catalyzed by a Lewis acid of anhydrous aluminum chloride (AlCl_3). The results showed that the rheological properties (i.e. storage modulus, loss modulus, complex modulus, and complex viscosity) of the in situ compatibilized blends were all obviously influenced by the rheological properties of the matrix and slightly influenced by the rheological properties of the dispersed phase, especially when AlCl_3 content was lower than about 0.10 wt% [158]. Abbasi et al. [159] attempted to study the effect of reactive compatibilization via Friedel–Crafts alkylation reaction, using AlCl_3 as a catalyst, on the rheology, morphology and mechanical properties of PP/PS blends in the presence of an organoclay. Generation of PP-g-PS copolymer was confirmed by using FTIR analysis. During the reactive compatibilization process, the interfacial interaction between the PP matrix and dispersed PS phase increased attributed to the formation of PP-g-PS copolymer, which led to finer and well-distributed PS particles in the PP matrix.

8.8.3 *Compatibilization Using Nanofiller*

The addition of most of the compatibilizers induces a significant loss of blend stiffness. Thus, nanoparticles have then attracted great interest because the nanofiller can play the role of both structural reinforcement and compatibilizer for several types of immiscible polymer blends. It has been proposed that the compatibilizing effect of the nanoparticles on immiscible polymer blends depending on the localisation of the filler in the blend. Yousfi et al. [160] reported that the incorporation of nanoscale talc particles in an immiscible PP/PA6 blends has resulted in remarkable improvements in the morphological structure evidenced by a

dramatic reduction of the dispersed domain size revealed by SEM and transmission electron microscopy (TEM) analysis. The addition of talc nanofillers induces a significant decrease of the size of the PA6 domains.

Graphene oxide (GO) and its derivatives have been employed to compatibilize polymer blends. The π - π stacking effect between graphene (functionalized graphene) and aromatic rings of some polymers can be used to improve the interfacial interaction. A remarkable reduction of interfacial adhesion for an immiscible polymer blend can be achieved by incorporating little amount of graphene. You et al. [161] synthesized polypropylene-graft-reduced graphene oxide (PP-g-rGO) and used as a compatibilizer for PP/PS blends. The PP-g-rGO was prepared by grafting PP-g-MAH chains onto amino functionalized reduced graphene oxide (rGO) nanosheets. SEM observation revealed an obvious reduction of the dispersed PS phase size in PP/PS (70/30 by weight) blends by incorporating only 1.5 wt% of PP-g-rGO. The compatibilization effect of PP-g-rGO lead to the enhancement of the tensile strength and elongation at break of the PP/PS blends. The compatibilizing mechanism is attributed to the fact that PP-g-rGO can adsorb PS chains on their basal planes through π - π stacking, as well as promote intermolecular interactions with PP through the grafted PP chains.

Lin et al. [162] improved the mechanical properties of PP/PET/SEBS-g-MAH blends via selective dispersion of halloysite nanotubes in the blend. The substantially improved mechanical properties in the blends have been correlated to the unique selective dispersion of HNTs in the interfacial region and the changed crystallization behavior. The crystallization of PP in the blend was also facilitated by the selective dispersion of HNTs and the folding surface-free energy was substantially increased.

8.9 Optimization, Modeling and Simulation

8.9.1 Optimization

The optimum condition of processing parameters (mixing temperature, rotor speed, fill factor, and blend ratio) and prediction models for the best key mechanical properties is important to achieve the desired properties of PP blends and suited them for certain application.

Uthaipan et al. [30] investigated the processing and properties EPDM/PP TPV by using the Taguchi's optimization technique and data analysis. The results reveal that all of the processing parameters affected significantly the mechanical properties of the EPDM/PP TPV, but specifically the blend ratio contributed more than 90% in effect size on tensile strength and tension set. It can be summarized that the morphological structure and stress relaxation of the TPVs were strongly governed by the EPDM content in the blend ratio. That is, the higher the EPDM content, the better phase morphology having smaller size of the vulcanized EPDM particles

distributed in the PP matrix and the higher rate of stress relaxation. The influences of processing parameters i.e. mixing temperature, rotor speed, fill factor, and blend ratio on the production of EPDM/PP TPV were statistically investigated, using the Taguchi approach to experiment based optimization. The obtained results suggest that the Taguchi methodology with an L9 orthogonal array as experimental design was successfully used to analyze the effects of processing parameters, and to find optimal sets of parameters for select key mechanical properties of TPVs.

Tucker et al. [163] studied the mechanical and morphological properties of PP/PA6 blends compatibilized with PP-g-MAH and SEBS-g-MAH using a factorial design known as extreme vertices. The effect of PA6/compatibilizer ratio is critical to the optimization of PP/PA6 compatibilized blends irrespective of PA6 amount over the range of compositions studied. The effect is observed in response surfaces of yield stress and modulus for PP-g-MAH compatibilized blends, and SEBS-g-MAH compatibilized blends. The experimental design employed (extreme vertices) is able to effectively use experimental data to model mechanical properties even when very few treatment combinations are used. The quantification of main effects and interactions allows a better understanding of the complex behavior of ternary polymer blends.

8.9.2 Modeling of Flow-Induced Crystallization

Flow-induced crystallization (FIC) is an important experimental phenomenon and is usually observed during polymer processing. FIC leads to specific morphology and mechanical behavior of materials, which are different from those during quiescent crystallization processes. To get an insight into the FIC phenomenon, there has been much work reported concerning the prediction of the crystallization kinetics in a flow field based on different theories. Yu et al. [164] reported the FIC of iPP upon addition of poly(ethylene-co-octene) (PEO) in terms of theoretical modeling. The crystallization of iPP and PEO blends in flow is simulated by a modified FIC model based on the conformation tensor theory. Two kinds of flow fields, shear flow and elongational flow, are considered in the prediction to analyze the influence of flow field on the crystallization kinetics of the polymer. The simulation results show that the elongation flow is much more effective than shear flow in reducing the dimensionless induction time of polymer crystallization. In addition, the induction time of crystallization in the blends is sensitive to the change of shear rate. In comparison with experimental data, the modified model shows its validity for the prediction of the induction time of crystallization of iPP in the blends. The consistency of the experiments and predictions confirmed the validity of the model. The work is helpful to understand the FIC process of iPP in a complex blend system and the rheological properties of iPP/PEO blends.

8.9.3 Molecular Simulation

Molecular simulation has become one of the most important tools to predict or validate structure–property relationship of polyblends, blend compatibility, and phase behavior of polymers. Dai et al. [165] used simulations based on molecular dynamics and MesoDyn theories to investigate the compatibility, morphology evolution of PP/PC blends, and the relationship between the composition and microstructure. The systems of PP/PC (54/46) with larger value of order parameters showed the stronger immiscibility and the faster separation process. The systems of PP/PC (82/18) reached the equilibrium state after a comparatively longer time, and showed less immiscible systems and a slower separation process, which was consistent with the results of free-energy density.

8.10 Conclusion and Future Prospective

This chapter documented the properties and processing of PP blends (e.g. PP/thermoplastic, PP/rubber—TPO and TPV, PP/thermoset, PP/recycled polymers and all-PP blends). The ways to improve the impact toughness and crystallization of PP have been summarized. The compatibility of PP with other polymers can be achieved by using either physical compatibilization or reactive compatibilization. The processing and properties of PP blends should be controlled by design, in order to optimize their performance (e.g. strength, toughness, crystallizability, rheology and morphology). For example, adding compatibilizer may improve the compatibility of the PP blends at the cost of toughness and crystallization; adding elastomer

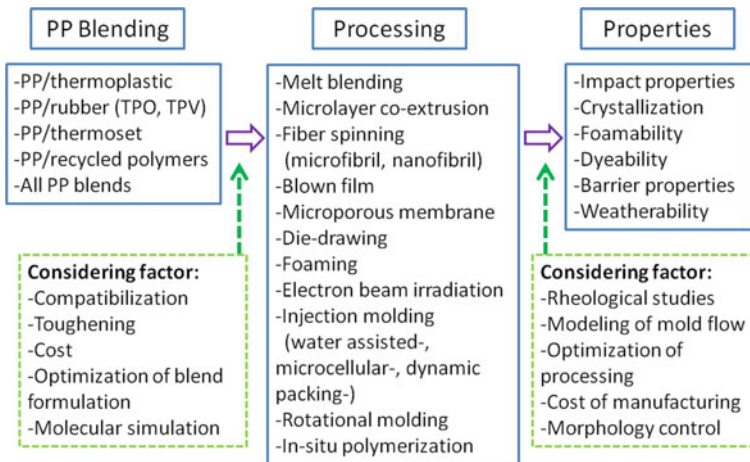


Fig. 8.8 Process and properties control by design for the manufacturing of PP blends

for PP toughening may influencing their compatibility and crystallization behavior; adding “too many” component in PP blends may affecting its rheological behavior and processability. Thus, a proper processing and properties control by design, using advanced modeling and simulation software, together with the strong scientific fundamental background and advanced processing technique should be the way to achieve high performance PP blends. Figure 8.8 shows the process and properties control by design for the manufacturing of PP blends. There are few topics can be considered for the future development of PP blends, these include (1) PP blending with biopolymers using more sustainable processing technique (via green technology), (2) nanoblends based on PP (using nanoscopic morphology stabilization concept), (3) morphology evolution of PP blends via nanofiller compatibilization (through selective dispersion/localization), (4) process-induced phase and crystal morphology development (using nanotechnology), (5) modeling and molecular simulation of the PP blends and (6) in-process morphology control (for example, by using dynamic packing injection molding).

References

1. Zhu Y, Luo F, Bai H et al (2013) Synergistic effects of β -modification and impact polypropylene copolymer on brittle-ductile transition of polypropylene random copolymer. *J Appl Polym Sci* 129:3613–3622. <https://doi.org/10.1002/app.39107>
2. Zhang H, Wang J, Cao S, Shan A (2000) Toughened polypropylene with balanced rigidity (I): preparation and chemical structure of toughening master batch. *Polym Adv Technol* 11:334–341. [https://doi.org/10.1002/1099-1581\(200007\)11:7<334::AID-PAT976>3.0.CO;2-K](https://doi.org/10.1002/1099-1581(200007)11:7<334::AID-PAT976>3.0.CO;2-K)
3. Chow WS, Abu Bakar A, Mohd Ishak ZA et al (2005) Effect of maleic anhydride-grafted ethylene-propylene rubber on the mechanical, rheological and morphological properties of organoclay reinforced polyamide 6/polypropylene nanocomposites. *Eur Polym J* 41:687–696. <https://doi.org/10.1016/j.eurpolymj.2004.10.041>
4. Karger-Kocsis J (2000) Swirl mat- and long discontinuous fiber mat-reinforced polypropylene composites—status and future trends. *Polym Compos* 21:514–522. <https://doi.org/10.1002/pc.10206>
5. Zhang RH, Li RKY (2013) Effect of syndiotactic polystyrene on the crystallization behavior of isotactic polypropylene/syndiotactic polystyrene blends with and without β -nucleating agent. *Polym Int* 62:919–927. <https://doi.org/10.1002/pi.4378>
6. Lipatov YS (2002) Polymer blends and interpenetrating polymer networks at the interface with solids. *Prog Polym Sci* 27:1721–1801. [https://doi.org/10.1016/S0079-6700\(02\)00021-7](https://doi.org/10.1016/S0079-6700(02)00021-7)
7. Koning C, Van Duijn M, Pagnoulle CJR (1998) Strategies for compatibilization of polymer blends. *Prog Polym Sci* 23:707–757. [https://doi.org/10.1016/s0079-6700\(97\)00054-3](https://doi.org/10.1016/s0079-6700(97)00054-3)
8. Higgins JS, Tambasco M, Lipson JEG (2005) Polymer blends; stretching what we can learn through the combination of experiment and theory. *Prog Polym Sci* 30:832–843. <https://doi.org/10.1016/j.progpolymsci.2005.06.001>
9. He Y, Zhu B, Inoue Y (2004) Hydrogen bonds in polymer blends. *Prog Polym Sci* 29:1021–1051. <https://doi.org/10.1016/j.progpolymsci.2004.07.002>
10. Imre B, Renner K, Pukánszky B (2014) Interactions, structure and properties in poly (lactic acid)/thermoplastic polymer blends. *Express Polym Lett* 8:2–14. <https://doi.org/10.3144/expresspolymlett.2014>

11. Costa LC, Neto AT, Hage E (2014) PMMA/SAN and SAN/PBT nanoblends obtained by blending extrusion using thermodynamics and microrheology basis. *Express Polym Lett* 8:164–176. <https://doi.org/10.3144/expresspolymlett.2014.20>
12. Taguet A, Cassagnau P, Lopez-Cuesta J-M (2014) Progress in polymer science structuration, selective dispersion and compatibilizing effect of (nano) fillers in polymer blends. *Prog Polym Sci* 39:1526–1563. <https://doi.org/10.1016/j.progpolymsci.2014.04.002>
13. Chow WS, Mohd Ishak ZA, Karger-Kocsis J et al (2003) Compatibilizing effect of maleated polypropylene on the mechanical properties and morphology of injection molded polyamide 6/polypropylene/organoclay nanocomposites. *Polymer* 44:7427–7440. <https://doi.org/10.1016/j.polymer.2003.09.006>
14. Aranburu N, Eguiazabal JI (2015) Improved mechanical properties of compatibilized polypropylene/polyamide-12 blends. *Int J Polym Sci* 2015:8 pages. <https://doi.org/10.1155/2015/742540>
15. Zhang Z, Wang C, Du Y et al (2013) Preparation and investigation of the β -nucleated polypropylene/polystyrene blends. *J Appl Polym Sci* 127:1114–1121. <https://doi.org/10.1002/app.37560>
16. Acosta MN, Ercoli DR, Goizueta GS et al (2011) Blends of PP/PE co-octene for modified atmosphere packaging applications. *Packag Technol Sci* 24:223–235. <https://doi.org/10.1002/pts.929>
17. Gartner C, Suárez M, López BL (2008) Grafting of maleic anhydride on polypropylene and its effect on blending with poly (ethylene terephthalate). *Polym Eng Sci* 48:1910–1916. <https://doi.org/10.1002/pen.21106>
18. Yu L, Simon G, Shanks RA, Noblle MR (2000) Crystallization and compatibilization of polypropylene-liquid crystalline polyester blends. *J Appl Polym Sci* 77:2229–2236. [https://doi.org/10.1002/1097-4628\(20000906\)77:10%3c2229:AID-APP16%3e3.0.CO;2-Z](https://doi.org/10.1002/1097-4628(20000906)77:10%3c2229:AID-APP16%3e3.0.CO;2-Z)
19. Liang YC, Isayev AI (2002) Self-reinforced polypropylene/lcp extruded strands and their moldings. *Polym Eng Sci* 42:994–1018. <https://doi.org/10.1002/pen.11008>
20. Flaris V, Montero N, Steinberg C (2012) Surface energy of polypropylene/polysulfone compatibilized blends. *J Vinyl Addit Technol* 18:222–227. <https://doi.org/10.1002/vnl.20307>
21. Yao XR, Wang L, Guo ZX, Yu J (2013) Morphology stabilization of the polypropylene/polystyrene nanoblends prepared by diffusion and polymerization of styrene in isotactic polypropylene pellets during melt mixing by the incorporation of divinylbenzene. *J Appl Polym Sci* 127:1092–1097. <https://doi.org/10.1002/app.37951>
22. Öksüz M, Eroğlu M (2005) Effect of the elastomer type on the microstructure and mechanical properties of polypropylene. *J Appl Polym Sci* 98:1445–1450. <https://doi.org/10.1002/app.22271>
23. Su Z, Jiang P, Li Q et al (2004) Mechanical properties and morphological structures relationship of blends based on sulfated EPDM ionomer and polypropylene. *J Appl Polym Sci* 94:1504–1510. <https://doi.org/10.1002/app.21068>
24. Chakraborty P, Ganguly A, Mitra S, Bhowmick AK (2008) Influence of phase modifiers on morphology and properties of thermoplastic elastomers prepared from ethylene propylene diene rubber and isotactic polypropylene. *Polym Eng Sci* 48:477–489. <https://doi.org/10.1002/pen.20984>
25. Ma GQ, Zhao YH, Yan LT et al (2006) Blends of polypropylene with poly(cis-butadiene) rubber. III. Study on the phase structure and morphology of incompatible blends of polypropylene with poly(cis-butadiene) rubber. *J Appl Polym Sci* 100:4900–4909. <https://doi.org/10.1002/app.23499>
26. Hristov V, Lach R, Krumova M, Grellmann W (2005) Fracture toughness of modified polypropylene/poly(styrene-ran-butadiene) blends. *Polym Int* 54:1632–1640. <https://doi.org/10.1002/pi.1894>
27. Salmah H, Azra BN, Yusrina MD, Ismail H (2015) A comparative study of polypropylene/(chloroprene rubber) and (recycled polypropylene)/(chloroprene rubber) blends. *J Vinyl Addit Technol* 21:122–127. <https://doi.org/10.1002/vnl.21390>

28. Karger-Kocsis J, Felhös D, Xu D, Schlarb AK (2008) Unlubricated sliding and rolling wear of thermoplastic dynamic vulcanizates (Santoprene®) against steel. *Wear* 265:292–300. <https://doi.org/10.1016/j.wear.2007.10.010>
29. Tanrattanakul V, Kosonmetee K, Laokijfaaroen P (2009) Polypropylene/natural rubber thermoplastic elastomer: effect of phenolic resin as a vulcanizing agent on mechanical properties and morphology. *J Appl Polym Sci* 112:3267–3275. <https://doi.org/10.1002/app.29816>
30. Uthaiipan N, Junhasavasdikul B, Nakason C (2015) Prediction models for the key mechanical properties of EPDM/PP blends as affected by processing parameters and their correlation with stress relaxation and phase morphologies 26:970–977. <https://doi.org/10.1002/pat.3511>
31. Karger-Kocsis J, Kalló A, Kuleznev VN (1984) Phase structure of impact-modified polypropylene blends. *Polymer* 25:279–286. [https://doi.org/10.1016/0032-3861\(84\)90337-9](https://doi.org/10.1016/0032-3861(84)90337-9)
32. Jain AK, Nagpal AK, Singhal R, Gupta NK (2000) Effect of dynamic crosslinking on impact strength and other mechanical properties of polypropylene/ethylene-propylene-diene rubber blends. *J Appl Polym Sci* 78:2089–2103. [https://doi.org/10.1002/1097-4628\(20001213\)78:12%3c2089:AID-APP50%3e3.0.CO;2-H](https://doi.org/10.1002/1097-4628(20001213)78:12%3c2089:AID-APP50%3e3.0.CO;2-H)
33. Gupta NK, Jain AK, Singhal R, Nagpal AK (2000) Effect of dynamic crosslinking on tensile yield behavior of polypropylene/ethylene-propylene-diene rubber blends. *J Appl Polym Sci* 78:2104–2121. [https://doi.org/10.1002/1097-4628\(20001213\)78:12%3c2104:AID-APP60%3e3.0.CO;2-7](https://doi.org/10.1002/1097-4628(20001213)78:12%3c2104:AID-APP60%3e3.0.CO;2-7)
34. Naskar K, Gohs U, Wagenknecht U, Heinrich G (2009) PP-EPDM thermoplastic vulcanisates (TPVs) by electron induced reactive processing. *Express Polym Lett* 3:677–683. <https://doi.org/10.3144/expresspolymlett.2009.85>
35. Nakason C, Wannavilai P, Kaesaman A (2006) Thermoplastic vulcanizates based on epoxidized natural rubber/polypropylene blends: effect of compatibilizers and reactive blending. *J Appl Polym Sci* 100:4729–4740. <https://doi.org/10.1002/app.23260>
36. Nakason C, Wannavilai P, Kaesaman A (2005) Thermoplastic vulcanizates based on epoxidized natural rubber/polypropylene blends: effect of epoxide levels in ENR molecules. *J Appl Polym Sci* 101:3046–3052. <https://doi.org/10.1002/app.23926>
37. Verbois A, Cassagnau P, Michel A et al (2004) New thermoplastic vulcanizate, composed of polypropylene and ethylene-vinyl acetate copolymer crosslinked by tetrapropoxysilane: evolution of the blend morphology with respect to the crosslinking reaction conversion. *Polym Int* 53:523–535. <https://doi.org/10.1002/pi.1428>
38. Soares BG, De Oliveira M, Meireles D et al (2008) Dynamically vulcanized polypropylene/nitrile rubber blends: the effect of peroxide/bis-maleimide curing system and different compatibilizing systems. *J Appl Polym Sci* 110:3566–3573. <https://doi.org/10.1002/app.28946>
39. Van Dyke JD, Gnatowski M, Burczyk A (2008) Solvent resistance and mechanical properties in thermoplastic elastomer blends prepared by dynamic vulcanization. *J Appl Polym Sci* 109:1535–1546. <https://doi.org/10.1002/app.28149>
40. Mandal AK, Siddhanta SK, Chakraborty D (2013) Chlorosulfonated polyethylene-polypropylene thermoplastic vulcanizate: mechanical, morphological, thermal, and rheological properties. *J Appl Polym Sci* 127:1268–1274. <https://doi.org/10.1002/app.37725>
41. Babu RR, Singha NK, Naskar K (2010) Dynamically vulcanized blends of polypropylene and ethylene octene copolymer: influence of various coagents on thermal and rheological characteristics. *J Appl Polym Sci* 117:1578–1590. <https://doi.org/10.1002/app.32023>
42. Wan C, Patel SH, Xanthos M (2003) Reactive melt modification of polypropylene with a crosslinkable polyester. *Polym Eng Sci* 43:1276–1288. <https://doi.org/10.1002/pen.10108>
43. Jiang X, Huang H, Zhang Y, Zhang Y (2004) Dynamically cured polypropylene/epoxy blends. *J Appl Polym Sci* 92:1437–1448. <https://doi.org/10.1002/app.13700>
44. Cui L, Zhou Z, Zhang Y et al (2007) Rheological behavior of polypropylene/novolac blends. *J Appl Polym Sci* 106:811–816. <https://doi.org/10.1002/app.26515>

45. Phillips RA (2000) Macromorphology of polypropylene homopolymer tacticity mixtures. *J Polym Sci, Part B: Polym Phys* 38:1947–1964. [https://doi.org/10.1002/1099-0488\(20000801\)38:15%3c1947:AID-POLB10%3e3.0.CO;2-M](https://doi.org/10.1002/1099-0488(20000801)38:15%3c1947:AID-POLB10%3e3.0.CO;2-M)
46. Flores-Gallardo SG, Sánchez-Valdes S, Ramos De Valle LF (2001) Polypropylene/polypropylene-grafted acrylic acid blends for multilayer films: preparation and characterization. *J Appl Polym Sci* 79:1497–1505. [https://doi.org/10.1002/1097-4628\(20010222\)79:8%3c1497:AID-APP170%3e3.0.CO;2-3](https://doi.org/10.1002/1097-4628(20010222)79:8%3c1497:AID-APP170%3e3.0.CO;2-3)
47. Saffar A, Jalali Dil E, Carreau PJ et al (2016) Phase behavior of binary blends of PP/PP-g-AA: limitations of the conventional characterization techniques. *Polym Int* 65:508–515. <https://doi.org/10.1002/pi.5082>
48. Moya EL, Van Grieken R, Carrero A, Paredes B (2012) Bimodal poly(propylene) through binary metallocene catalytic systems as an alternative to melt blending. *Macromol Symp* 321–322:46–52. <https://doi.org/10.1002/masy.201251107>
49. Fang Y, Sadeghi F, Fleuret G, Carreau PJ (2008) Properties of blends of linear and branched polypropylenes in film blowing. *Can J Chem Eng* 86:6–14. <https://doi.org/10.1002/cjce.20011>
50. Miskolczi N, Kucharczyk P, Sedlarik V, Szakacs H (2013) Plastic waste minimization: compatibilization of polypropylene/polyamide 6 blends by polyalkenyl-poly-maleic-anhydride-based agents. *J Appl Polym Sci* 129:3028–3037. <https://doi.org/10.1002/app.38724>
51. Garcia PS, Gouveia RF, Maia JM et al (2018) 2D and 3D imaging of the deformation behavior of partially devulcanized rubber/polypropylene blends. *Express Polym Lett* 12:1047–1060. <https://doi.org/10.3144/expresspolymlett.2018.92>
52. Inoya H, Wei Leong Y, Klinklai W et al (2012) Compatibilization of recycled poly(ethylene terephthalate) and polypropylene blends: effect of polypropylene molecular weight on homogeneity and compatibility. *J Appl Polym Sci* 124:3947–3955. <https://doi.org/10.1002/app.34405>
53. Barhouni N, Jaziri M, Massardier V, Cassagnau P (2008) Valorization of poly(butylene terephthalate) wastes by blending with virgin polypropylene: effect of the composition and the compatibilization. *Polym Eng Sci* 48:1592–1599. <https://doi.org/10.1002/pen.21116>
54. Kukaleva N, Simon GP, Kosior E (2003) Binary and ternary blends of recycled high-density polyethylene containing polypropylenes. *Polym Eng Sci* 43:431–443. <https://doi.org/10.1002/pen.10035>
55. Kazemi Y, Ramezani Kakroodi A, Rodrigue D (2015) Compatibilization efficiency in post-consumer recycled polyethylene/polypropylene blends: effect of contamination. *Polym Eng Sci* 55:2368–2376. <https://doi.org/10.1002/pen.24125>
56. Jaziri M, Barhouni N, Massardier V, Mélis F (2008) Blending PP with PA6 industrial wastes: effect of the composition and the compatibilization. *J Appl Polym Sci* 107:3451–3458. <https://doi.org/10.1002/app.27542>
57. Tchomakov KP, Favis BD, Huneault MA et al (2005) Mechanical properties and morphology of ternary PP/EPDM/PE blends. *Can J Chem Eng* 83:300–309. <https://doi.org/10.1002/cjce.5450830216>
58. Vranjes N, Rek V (2007) Effect of EPDM on morphology, mechanical properties, crystallization behavior and viscoelastic properties of iPP + HDPE blends. *Macromol Symp* 258:90–100. <https://doi.org/10.1002/masy.200751210>
59. Panda B, Bhattacharyya AR, Kulkarni AR (2013) Morphology and dielectric relaxation spectroscopy of ternary polymer blends of polyamide6, polypropylene, and acrylonitrile butadiene styrene co-polymer: Influence of compatibilizer and multiwall carbon nanotubes. *J Appl Polym Sci* 127:1433–1445. <https://doi.org/10.1002/app.38074>
60. Lima PS, Oliveira JM, Costa VAF (2015) Partial replacement of EPR by GTR in highly flowable PP/EPR blends: effects on morphology and mechanical properties. *J Appl Polym Sci* 132:42011 (1–9). <https://doi.org/10.1002/app.42011>

61. Debout MA, Robertson RE (2004) Impact strength and elongation-to-break of compatibilized ternary blends of polypropylene, nylon 66, and polystyrene. *Polym Eng Sci* 44:1800–1809. <https://doi.org/10.1002/pen.20182>
62. Šmit I, Radonjić G (2000) Effects of SBS on phase morphology of iPP/aPS blends. *Polym Eng Sci* 40:2144–2160. <https://doi.org/10.1002/pen.11347>
63. Jazani OM, Arefazar A, Jafari SH et al (2011) A study on the effects of SEBS-g-MAH on the phase morphology and mechanical properties of polypropylene/polycarbonate/SEBS ternary polymer blends. *J Appl Polym Sci* 121:2680–2687. <https://doi.org/10.1002/app.33715>
64. Chand N, Naik AM, Khaira HK (2007) Development of UHMWPE modified PP/PET blends and their mechanical and abrasive wear behavior. *Polym Compos* 28:267–272. <https://doi.org/10.1002/pc.20302>
65. Yang L, Huang J, Lu X et al (2015) Influences of dicumyl peroxide on morphology and mechanical properties of polypropylene/poly(styrene-*b*-butadiene-*b*-styrene) blends via vane-extruder. *J Appl Polym Sci* 132:41543 (1–12). <https://doi.org/10.1002/app.41543>
66. Jia S, Qu J, Liu W et al (2014) Thermoplastic polyurethane/polypropylene blends based on novel vane extruder: a study of morphology and mechanical properties. *Polym Eng Sci* 54:716–724. <https://doi.org/10.1002/pen.23598>
67. Qu JP, Chen HZ, Liu SR et al (2013) Morphology study of immiscible polymer blends in a vane extruder. *J Appl Polym Sci* 128:3576–3585. <https://doi.org/10.1002/app.38573>
68. Shon K, Bumm SH, White JL (2008) A comparative study of dispersing a polyamide 6 into a polypropylene melt in a buss kneader, continuous mixer, and modular intermeshing corotating and counter-rotating twin screw extruders. *Polym Eng Sci* 48:755–766. <https://doi.org/10.1002/pen.20941>
69. Polaskova M, Cermak R, Sedlacek T et al (2010) Extrusion of polyethylene/polypropylene blends with microfibrillar-phase morphology. *Polym Compos* 31:1427–1433. <https://doi.org/10.1002/pc.20928>
70. Wang K, Zhou C, Zhang H, Zhao D (2002) Modification of polypropylene by melt vibration blending with ultra high molecular weight polyethylene. *Adv Polym Technol* 21:164–176. <https://doi.org/10.1002/adv.10020>
71. Tortorella N, Beatty CL (2008) Morphology and crystalline properties of impact-modified polypropylene blends. *Polym Eng Sci* 48:1476–1486. <https://doi.org/10.1002/pen.21102>
72. Teng J, Otaigbe JU, Taylor EP (2004) Reactive blending of functionalized polypropylene and polyamide 6: in situ polymerization and in situ compatibilization. *Polym Eng Sci* 44:648–659. <https://doi.org/10.1002/pen.20059>
73. Godshall D, White C, Wilkes GL (2001) Effect of compatibilizer molecular weight and maleic anhydride content on interfacial adhesion of polypropylene-PA6 bicomponent fibers. *J Appl Polym Sci* 80:130–141. [https://doi.org/10.1002/1097-4628\(20010411\)80:2%3c130:AID-APP1081%3e3.0.CO;2-C](https://doi.org/10.1002/1097-4628(20010411)80:2%3c130:AID-APP1081%3e3.0.CO;2-C)
74. Fallahi E, Barmar M, Kish MH (2008) Micro and nano fibrils from polypropylene/nylon 6 blends. *J Appl Polym Sci* 108:1473–1481. <https://doi.org/10.1002/app.27792>
75. Soroudi A, Skrifvars M (2012) Electroconductive polyblend fibers of polyamide-6/polypropylene/ polyaniline: electrical, morphological, and mechanical characteristics. *Polym Eng Sci* 52:1606–1612. <https://doi.org/10.1002/pen.23074>
76. Auinger T, Stadlbauer M (2010) Inter-relationship between processing conditions and mechanical properties of blown film from different polypropylenes and high melt strength polypropylene blends. *J Appl Polym Sci* 117:155–162. <https://doi.org/10.1002/app.31928>
77. Jarus D, Hiltner A, Baer E (2001) Microlayer coextrusion as a route to innovative blend structures. *Polym Eng Sci* 41:2162–2171. <https://doi.org/10.1002/pen.10911>
78. Xanthos M, Chandavasu C, Sirkar KK, Gogos CG (2002) Melt processed microporous films from compatibilized immiscible blends with potential as membranes. *Polym Eng Sci* 42:810–825. <https://doi.org/10.1002/pen.10993>
79. Sadeghi F, Aji A, Carreau PJ (2008) Microporous membranes obtained from polypropylene blends with superior permeability properties. *J Polym Sci, Part B: Polym Phys* 46:148–157. <https://doi.org/10.1002/polb.21350>

80. Ait-Kadi A, Bousmina M, Yousefi AA, Mighri F (2007) High performance structured polymer barrier films obtained from compatibilized polypropylene/ethylene vinyl alcohol blends. *Polym Eng Sci* 47:1114–1121. <https://doi.org/10.1002/pen.20794>
81. Mohanraj J, Chapleau N, Ajji A et al (2003) Production, properties and impact toughness of die-drawn toughened polypropylenes. *Polym Eng Sci* 43:1317–1336. <https://doi.org/10.1002/pen.10112>
82. Mondal M, Gohs U, Wagenknecht U, Heinrich G (2013) Efficiency of high energy electrons to produce polypropylene/natural rubber-based thermoplastic elastomer. *Polym Eng Sci* 53:1696–1705. <https://doi.org/10.1002/pen.23414>
83. Ali ZI, Youssef HA, Said HM, Saleh HH (2006) Influence of electron beam irradiation and polyfunctional monomer loading on the physico-chemical properties of polyethylene/polypropylene blends. *Adv Polym Technol* 25:208–217. <https://doi.org/10.1002/adv.20072>
84. Wang M, Ma J, Chu R et al (2012) Effect of the introduction of polydimethylsiloxane on the foaming behavior of block-copolymerized polypropylene. *J Appl Polym Sci* 123:2726–2732. <https://doi.org/10.1002/app.34854>
85. Zhang P, Zhou NQ, Wu QF et al (2007) Microcellular foaming of PE/PP blends. *J Appl Polym Sci* 104:4149–4159. <https://doi.org/10.1002/app.26071>
86. Spital P, Macosko CW (2004) Strain hardening in polypropylenes and its role in extrusion foaming. *Polym Eng Sci* 44:2090–2100. <https://doi.org/10.1002/pen.20214>
87. Wang B, Huang HX, Wang ZY (2015) Process-induced phase and crystal morphologies in water-assisted injection molded polypropylene/polymeric β -nucleating agent blend parts. *Polym Eng Sci* 55:1698–1705. <https://doi.org/10.1002/pen.24008>
88. Wang WQ, Kontopoulou M (2004) Rotational molding of polypropylene/ultra-low-density ethylene- α -olefin copolymer blends. *Polym Eng Sci* 44:1662–1669. <https://doi.org/10.1002/pen.20165>
89. Pires M, Mauler RS, Liberman SA (2004) Structural characterization of reactor blends of polypropylene and ethylene-propylene rubber. *J Appl Polym Sci* 92:2155–2162. <https://doi.org/10.1002/app.20193>
90. Liu T, Lei Y, Chen Z et al (2015) Effects of processing conditions on foaming behaviors of polyetherimide (PEI) and PEI/polypropylene blends in microcellular injection molding process. *J Appl Polym Sci* 132:41443. <https://doi.org/10.1002/app.41443>
91. Su R, Jiang K, Ge Y et al (2011) Shear-induced fibrillation and resultant mechanical properties of injection-molded polyamide 1010/isotactic polypropylene blends. *Polym Int* 60:1655–1662. <https://doi.org/10.1002/pi.3148>
92. Tang J, Tang W, Yuan H, Jin R (2010) Super-toughed polymer blends derived from polypropylene random copolymer and ethylene/styrene interpolymer. *J Appl Polym Sci* 115:190–197. <https://doi.org/10.1002/app.31035>
93. Tang W, Tang J, Yuan H, Jin R (2011) Crystallization behavior and mechanical properties of polypropylene random copolymer/poly(ethylene-octene) blends. *J Appl Polym Sci* 122:461–468. <https://doi.org/10.1002/app.34162>
94. Li X, Su R, Gao J et al (2011) Toughening of polypropylene with crystallizable poly(ethylene oxide). *Polym Int* 60:781–786. <https://doi.org/10.1002/pi.3015>
95. Kakkar D, Maiti SN (2012) Effect of flexibility of ethylene vinyl acetate and crystallization of polypropylene on the mechanical properties of i-PP/EVA blends. *J Appl Polym Sci* 123:1905–1912. <https://doi.org/10.1002/app.34680>
96. Premphet K, Paecharoenchai W (2002) Polypropylene/metallocene ethylene-octene copolymer blends with a bimodal particle size distribution: mechanical properties and their controlling factors. *J Appl Polym Sci* 85:2412–2418. <https://doi.org/10.1002/app.10886>
97. Thanyaprueksanon S, Thongyai S, Praserttham P (2007) New synthesis methods for polypropylene-co-ethylene-propylene rubber. *J Appl Polym Sci* 103:3609–3616. <https://doi.org/10.1002/app.25392>
98. Liu G, Zhang X, Li X et al (2012) Correlation of miscibility and mechanical properties of polypropylene/olefin block copolymers: effect of chain composition. *J Appl Polym Sci* 125:666–675. <https://doi.org/10.1002/app.36244>

99. Bai H, Wang Y, Song B, Han L (2008) Synergistic toughening effects of nucleating agent and ethylene–octene copolymer on polypropylene. *J Appl Polym Sci* 108:3270–3280. <https://doi.org/10.1002/app>
100. Fanegas N, Gómez MA, Jiménez I et al (2008) Optimizing the balance between impact strength and stiffness in polypropylene/elastomer blends by incorporation of a nucleating agent. *Polym Eng Sci* 48:80–87. <https://doi.org/10.1002/pen.20886>
101. Grein C, Gahleitner M (2008) On the influence of nucleation on the toughness of iPP/EPR blends with different rubber molecular architectures. *Express Polym Lett* 2:392–397. <https://doi.org/10.3144/expresspolymlett.2008.47>
102. Jafari SH, Gupta AK (2000) Impact strength and dynamic mechanical properties correlation in elastomer-modified polypropylene. *J Appl Polym Sci* 78:962–971. [https://doi.org/10.1002/1097-4628\(20001031\)78:5%3c962:AID-APP40%3e3.0.CO;2-5](https://doi.org/10.1002/1097-4628(20001031)78:5%3c962:AID-APP40%3e3.0.CO;2-5)
103. Varga J (1995) Crystallization, melting and supermolecular structure of isotactic polypropylene. *Polypropylene structure, blends and composites*. Springer, Netherlands, Dordrecht, pp 56–115
104. Chen HB, Karger-Kocsis J, Wu JS, Varga J (2002) Fracture toughness of α - and β -phase polypropylene homopolymers and random- and block-copolymers. *Polymer* 43:6505–6514. [https://doi.org/10.1016/S0032-3861\(02\)00590-6](https://doi.org/10.1016/S0032-3861(02)00590-6)
105. Wang ZG, Phillips RA, Hsiao BS (2001) Morphology development during isothermal crystallization. II. Isotactic and syndiotactic polypropylene blends. *J Polym Sci, Part B: Polym Phys* 39:1876–1888. <https://doi.org/10.1002/polb.1162>
106. Finlay J, Hill MJ, Barham PJ et al (2003) Mechanical properties and characterization of slowly cooled isotactic polypropylene/high-density polyethylene blends. *J Polym Sci, Part B: Polym Phys* 41:1384–1392. <https://doi.org/10.1002/polb.10440>
107. Borysiak S (2011) The supermolecular structure of isotactic polypropylene/atactic polystyrene blends. *Polym Eng Sci* 51:2505–2516. <https://doi.org/10.1002/pen.22039>
108. Yang J, White JL (2012) Crystallization behavior of polypropylene/ethylene butene copolymer blends. *J Appl Polym Sci* 126:2049–2058. <https://doi.org/10.1002/app.35184>
109. Zhang Y, Huang Y, Mai K (2005) Crystallization and dynamic mechanical properties of polypropylene/polystyrene blends modified with maleic anhydride and styrene. *J Appl Polym Sci* 96:2038–2045. <https://doi.org/10.1002/app.21658>
110. Yang Z, Zhang Z, Tao Y, Mai K (2009) Preparation, crystallization behavior, and melting characteristics of β -nucleated isotactic polypropylene blends with polyamide. 112:1–8. <https://doi.org/10.1002/app>
111. Marinelli AL, Bretas RES (2002) Blends of polypropylene resins with a liquid crystalline polymer. I. Isothermal crystallization. *J Appl Polym Sci* 87:916–930. <https://doi.org/10.1002/app.11386>
112. Guan Y, Wang S, Zheng A, Xiao H (2003) Crystallization behaviors of polypropylene and functional polypropylene. *J Appl Polym Sci* 88:872–877. <https://doi.org/10.1002/app.11668>
113. Wu Y, Yang Y, Li B, Han Y (2006) Reactive blending of modified polypropylene and polyamide 12: effects of compatibilizer content on crystallization and blend morphology. *J Appl Polym Sci* 100:3187–3192. <https://doi.org/10.1002/app.23572>
114. Wang D, Gao J (2006) Melting, nonisothermal crystallization behavior and morphology of polypropylene/random ethylene-propylene copolymer blends. *J Appl Polym Sci* 99:670–678. <https://doi.org/10.1002/app.22507>
115. Lin Z, Chen C, Li B et al (2012) Compatibility, morphology, and crystallization behavior of compatibilized β -nucleated polypropylene/poly(trimethylene terephthalate) blends. *J Appl Polym Sci* 125:1616–1624. <https://doi.org/10.1002/app.35635>
116. Hao XQ, Zheng GQ, Dai K et al (2011) Facile preparation of rich β -transcrystallinity in PET fiber/iPP composites. *Express Polym Lett* 5:1017–1026. <https://doi.org/10.3144/expresspolymlett.2011.99>
117. Lima PS, Oliveira JM, Costa VAF (2015) Crystallization kinetics of thermoplastic elastomeric blends based on ground tyre rubber. *J Appl Polym Sci* 132:42589 (1–11). <https://doi.org/10.1002/app.42589>

118. Paul S, Kale DD (2002) Rheological study of polypropylene copolymer/polyolefinic elastomer blends. *J Appl Polym Sci* 84:665–671. <https://doi.org/10.1002/app.10376>
119. Zhang XM, Li H, Chen WX, Feng LF (2012) Rheological properties and morphological evolutions of polypropylene/ethylene-butene copolymer blends. *Polym Eng Sci* 52:1740–1748. <https://doi.org/10.1002/pen.23116>
120. López Manchado MA, Biagiotti J, Kenny JM (2001) Rheological behavior and processability of polypropylene blends with rubber ethylene propylene diene terpolymer. *J Appl Polym Sci* 81:1–10. <https://doi.org/10.1002/app.1407>
121. Ardakani F, Jahani Y, Morshedian J (2012) Dynamic viscoelastic behavior of polypropylene/polybutene-1 blends and its correlation with morphology. *J Appl Polym Sci* 125:640–648. <https://doi.org/10.1002/app.36324>
122. Marguerat F, Carreau PJ, Michel A (2002) Morphology and rheological properties of polypropylene/reactive elastomer blends. *Polym Eng Sci* 42:1941–1955. <https://doi.org/10.1002/pen.11087>
123. Shi D, Jiang F, Ke Z et al (2006) Melt rheological properties of polypropylene-polyamide6 blends compatibilized with maleic anhydride-grafted polypropylene. *Polym Int* 55:701–707. <https://doi.org/10.1002/pi.2036>
124. Liao HY, Zheng LY, Hu YB et al (2015) Dynamic rheological behavior of reactively compatibilized polypropylene/polyamide 6 blending melts. *J Appl Polym Sci* 132:42091 (1–8). <https://doi.org/10.1002/app.42091>
125. Li Z, Chen M, Ma W (2016) Promoting effect of crystallization on the foaming behavior in polypropylene homopolymer/polypropylene block copolymer blends. *Polym Eng Sci* 56:1175–1181. <https://doi.org/10.1002/pen.24351>
126. Laguna-Gutierrez E, Van Hooghten R, Moldenaers P, Rodriguez-Perez MA (2015) Understanding the foamability and mechanical properties of foamed polypropylene blends by using extensional rheology. *J Appl Polym Sci* 132:42430 (1–14). <https://doi.org/10.1002/app.42430>
127. Mirjalili F, Moradian S, Ameri F (2011) Attaining optimal dyeability and tensile properties of polypropylene/poly(ethylene terephthalate) blends with a special cubic mixture experimental design. *J Appl Polym Sci* 121:3201–3210. <https://doi.org/10.1002/app.33859>
128. Mouffok S, Kaci M (2015) Artificial weathering effect on the structure and properties of polypropylene/polyamide-6 blends compatibilized with PP-g-MA. *J Appl Polym Sci* 132. <https://doi.org/10.1002/app.41722>
129. Jose S, Francis B, Thomas S, Karger-Kocsis J (2006) Morphology and mechanical properties of polyamide 12/polypropylene blends in presence and absence of reactive compatibiliser. *Polymer* 47:3874–3888. <https://doi.org/10.1016/j.polymer.2006.03.046>
130. Wang L, Tan H, Gong J, Tang T (2014) Relationship between branch length and the compatibilizing effect of polypropylene-g-polystyrene graft copolymer on polypropylene/polystyrene blends. *J Appl Polym Sci* 131:40126 (1–9). <https://doi.org/10.1002/app.40126>
131. Li Z, Ke Y, Hu Y (2004) Study on a new kind of polypropylene-graft-polystyrene: preparation and application. *J Appl Polym Sci* 93:314–322. <https://doi.org/10.1002/app.20472>
132. Parameswaranpillai J, Joseph G, Jose S, Hameed N (2015) Phase morphology, thermomechanical, and crystallization behavior of uncompatibilized and PP-g-MAH compatibilized polypropylene/polystyrene blends. *J Appl Polym Sci* 132:42100 (1–11). <https://doi.org/10.1002/app.42100>
133. Slouf M, Radonjic G, Hlavata D, Sikora A (2006) Compatibilized iPP/aPS blends: the effect of the viscosity ratio of the components on the blends morphology. *J Appl Polym Sci* 101:2236–2249. <https://doi.org/10.1002/app.23571>
134. Syed Mustafa SJ, Azlan MRN, Fuad MYA et al (2001) Polypropylene/polystyrene blends-preliminary studies for compatibilization by aromatic-grafted polypropylene. *J Appl Polym Sci* 82:428–434. <https://doi.org/10.1002/app.1868>
135. Mandal PK, Chakraborty D (2009) Studies on morphology, mechanical, thermal, and dynamic mechanical behavior of extrusion blended polypropylene and thermotropic liquid

- crystalline polymer in presence of compatibilizer. *J Appl Polym Sci* 111:2345–2352. <https://doi.org/10.1002/app.28988>
136. Mandal PK, Siddhanta SK, Chakraborty D (2012) Engineering properties of compatibilized polypropylene/liquid crystalline polymer blends. *J Appl Polym Sci* 124:5279–5285. <https://doi.org/10.1002/app.34277>
 137. Farasoglou P, Kontou E, Spathis G et al (2000) Processing conditions and compatibilizing effects on reinforcement of polypropylene-liquid crystalline polymer blends. *Polym Compos* 21:84–95. <https://doi.org/10.1002/pc.10167>
 138. Lee YK, Lee JB, Park DH, Kim WN (2013) Effects of accelerated aging and compatibilizers on the mechanical and morphological properties of polypropylene and poly (acrylonitrile-butadiene-styrene) blends. *J Appl Polym Sci* 127:1032–1037. <https://doi.org/10.1002/app.37504>
 139. Deng Y, Mao X, Lin J, Chen Q (2015) Compatibilization of polypropylene/poly (acrylonitrile-butadiene-styrene) blends by polypropylene-graft-cardanol. *J Appl Polym Sci* 132:41315 (1–7). <https://doi.org/10.1002/APP.41315>
 140. Lee HS, Kim JD (2012) Effect of a hybrid compatibilizer on the mechanical properties and interfacial tension of a ternary blend with polypropylene, poly(lactic acid), and a toughening modifier. *Polym Compos* 33:1154–1161. <https://doi.org/10.1002/pc.22244>
 141. Dai S, Ye L (2008) Effect of novel compatibilizers on the properties and morphology of PP/PC blends. *Polym Adv Technol* 19:1069–1076. <https://doi.org/10.1002/pat.1080>
 142. Zhang J, Yao Y, Wang XL, Xu JH (2006) Polypropylene/polypropylene-grafted acrylic acid copolymer/ethylene-acrylic acid copolymer ternary blends for hydrophilic polypropylene. *J Appl Polym Sci* 101:436–442. <https://doi.org/10.1002/app.23252>
 143. Wang D, Ishida H (2006) The effect of addition of poly(propylene-g-acrylic acid) on the morphology of poly(vinyl methylether) and isotactic polypropylene blend. *J Appl Polym Sci* 101:4098–4103. <https://doi.org/10.1002/app.23429>
 144. Børve KL, Kotlar HK, Gustafson C-G (2000) Polypropylene-phenol formaldehyde-based compatibilizers. III. Application in PP/PBT and PP/PPE blends. *J Appl Polym Sci* 75:361–370. [https://doi.org/10.1002/\(SICI\)1097-4628\(20000118\)75:3%3c361:AID-APP4%3e3.0.CO;2-A](https://doi.org/10.1002/(SICI)1097-4628(20000118)75:3%3c361:AID-APP4%3e3.0.CO;2-A)
 145. Sun QJ, Zhang BY, Yao DS et al (2009) Miscibility enhancement of PP/PBT blends with a side-chain liquid crystalline ionomer. *J Appl Polym Sci* 112:3007–3015. <https://doi.org/10.1002/app.29874>
 146. Nachtigall SMB, Felix AHO, Mauler RS (2003) Blend compatibilizers based on silane- and maleic anhydride-modified polyolefins. *J Appl Polym Sci* 88:2492–2498. <https://doi.org/10.1002/app.12119>
 147. Marco C, Collar EP, Areso S, García-Martínez JM (2002) Thermal studies on polypropylene/polyamide-6 blends modified by succinic anhydride and succinyl fluorescein grafted polypropylenes. *J Polym Sci B: Polym Phys* 40:1307–1315. <https://doi.org/10.1002/polb.10188>
 148. Franzheim O, Rische T, Stephan M, Macknight WJ (2000) Blending of immiscible polymers in a mixing zone of a twin screw extruder—effects of compatibilization. *Polym Eng Sci* 40:1143–1156. <https://doi.org/10.1002/pen.11242>
 149. Laredo E, Grimau M, Bello A et al (2005) The effect of compatibilization on the dynamic properties of polypropylene/nylon-6 blends studied by broad band dielectric spectroscopy. *J Polym Sci B: Polym Phys* 43:1408–1420. <https://doi.org/10.1002/polb.20421>
 150. Lu QW, Macosko CW, Horrión J (2005) Melt amination of polypropylenes. *J Polym Sci A: Polym Chem* 43:4217–4232. <https://doi.org/10.1002/pola.20899>
 151. Kim JS, Jang JH, Kim JH et al (2016) Morphological, thermal, rheological, and mechanical properties of PP/EVOH blends compatibilized with PP-g-IA. *Polym Eng Sci* 56:1240–1247. <https://doi.org/10.1002/pen.24357>
 152. Hung CJ, Chuang HY, Chang FC (2008) Novel reactive compatibilization strategy on immiscible polypropylene and polystyrene blend. *J Appl Polym Sci* 107:831–839. <https://doi.org/10.1002/app.25201>

153. Kaya A, Pompe G, Schulze U et al (2002) The effect of TIBA on metallocene/MAO catalyzed synthesis of propylene oxazoline copolymers and their use in reactive blending. *J Appl Polym Sci* 86:2174–2181. <https://doi.org/10.1002/app.11161>
154. Li H, Zhang XM, Zhu SY et al (2015) Preparation of polypropylene and polystyrene with -NCO and -NH₂ functional groups and their applications in polypropylene/polystyrene blends. *Polym Eng Sci* 55:614–623. <https://doi.org/10.1002/pen.23927>
155. Bohn CC, Manning SC, Moore RB (2001) Comparison of carboxylated and maleated polypropylene as reactive compatibilizers in polypropylene/polyamide-6,6 blends. *J Appl Polym Sci* 79:2398–2407. [https://doi.org/10.1002/1097-4628\(20010328\)79:13%3c2398:AID-APP1047%3e3.0.CO;2-3](https://doi.org/10.1002/1097-4628(20010328)79:13%3c2398:AID-APP1047%3e3.0.CO;2-3)
156. Aranburu N, Eguiazabal JI (2013) Compatible blends of polypropylene with an amorphous polyamide. *J Appl Polym Sci* 127:5007–5013. <https://doi.org/10.1002/app.38090>
157. Tortorella N, Beatty CL (2008) Morphology and mechanical properties of impact modified polypropylene blends. *Polym Eng Sci* 48:2098–2110. <https://doi.org/10.1002/pen.21089>
158. Li J, Ma G, Sheng J (2010) Linear viscoelastic characteristics of in situ compatibilized binary polymer blends with viscoelastic properties of components variable. *J Polym Sci, Part B: Polym Phys* 48:1349–1362. <https://doi.org/10.1002/polb.22034>
159. Abbasi F, Tavakoli A, Razavi Aghjeh MK (2018) Rheology, morphology, and mechanical properties of reactive compatibilized polypropylene/polystyrene blends via Friedel-Crafts alkylation reaction in the presence of clay. *J Vinyl Addit Technol* 24:18–26. <https://doi.org/10.1002/vnl.21522>
160. Yousfi M, Livi S, Dumas A et al (2014) Compatibilization of polypropylene/polyamide 6 blends using new synthetic nanosized talc fillers: Morphology, thermal, and mechanical properties. *J Appl Polym Sci* 131:40453 (1–12). <https://doi.org/10.1002/app.40453>
161. You F, Wang D, Li X et al (2014) Synthesis of polypropylene-grafted graphene and its compatibilization effect on polypropylene/polystyrene blends. *J Appl Polym Sci* 131:40455 (1–7). <https://doi.org/10.1002/app.40455>
162. Lin T, Zhu L, Chen T, Guo B (2013) Optimization of mechanical performance of compatibilized polypropylene/poly(ethylene terephthalate) blends via selective dispersion of halloysite nanotubes in the blend. *J Appl Polym Sci* 129:47–56. <https://doi.org/10.1002/app.38700>
163. Tucker JD, Lee S, Einsporn RL (2000) Study of the effect of PP-g-MA and SEBS-g-MA on the mechanical and morphological properties of polypropylene/nylon 6 blends. *Polym Eng Sci* 40:2577–2589. <https://doi.org/10.1002/pen.11388>
164. Yu F, Zhang Z, Yu W et al (2012) Modeling of flow-induced crystallization in blends of isotactic polypropylene and poly(ethylene-co-octene). *Polym Int* 61:1389–1393. <https://doi.org/10.1002/pi.4220>
165. Dai S, Ye L, Hu GH (2012) Molecular simulation on relationship between composition and microstructure of PP/PC blend. *J Appl Polym Sci* 126:1165–1173. <https://doi.org/10.1002/app.36977>

Chapter 9

Composites



Tatyana Ageyeva, Tamás Bárány and József Karger-Kocsis

Contents

9.1	Introduction.....	484
9.2	Nanocomposites.....	486
9.2.1	Preparation.....	487
9.2.2	Structure Development and Characterization.....	492
9.2.3	Properties and Their Prediction.....	493
9.2.4	Processing and Applications.....	499
9.3	Discontinuous Fiber-Reinforced Composites.....	499
9.3.1	Manufacturing.....	500
9.3.2	Structure Development and Characterization.....	502
9.3.3	Properties and Their Prediction.....	505
9.3.4	Processing and Applications.....	515
9.4	Mat-Reinforced Composites.....	516
9.4.1	Manufacturing.....	518
9.4.2	Structure Development and Characterization.....	519
9.4.3	Properties and Their Prediction.....	522
9.4.4	Applications.....	526
9.5	Fabric-Reinforced Composites.....	527
9.5.1	Manufacturing.....	528
9.5.2	Structure Development and Characterization.....	532
9.5.3	Properties and Their Prediction.....	534
9.5.4	Processing and Applications.....	544
9.6	Laminate Composites.....	545
9.6.1	Manufacturing.....	546
9.6.2	Structure Development and Characterization.....	549

József Karger-Kocsis is deceased

T. Ageyeva · T. Bárány (✉) · J. Karger-Kocsis
Department of Polymer Engineering, Faculty of Mechanical Engineering, Budapest
University of Technology and Economics, Műegyetem rkp. 3, Budapest 1111, Hungary
e-mail: barany@pt.bme.hu

T. Ageyeva
Bauman Moscow State Technical University, 2nd Baumanskaya Str., 5, 105005 Moscow,
Russia

9.6.3 Properties and Their Prediction.....	553
9.6.4 Processing and Applications	556
9.7 Conclusion and Outlook.....	556
References	557

Abstract The current chapter is dedicated to polypropylene (PP) based composites. The material grouping and presentation in the chapter follows the logic of the reinforcement length gain and covers the areas from nano- to macro-composites. Thus, separate sections are devoted to PP-nanocomposites, discontinuous fiber-reinforced, mat-reinforced, fabric-reinforced and aligned fiber-reinforced composites. Each section describes the aspects of manufacturing techniques, structure development, properties characterization as well as processing and application of the related composites. As PP matrix belongs to the family of fairly unexpensive high-volume thermoplastics and related composites are feasible for semi-structural and structural applications, the chapter is mostly concentrated in PP-composites for automotive application.

Abbreviations and Designations

0D	Zero-dimensional
1D	One-dimensional
2D	Two-dimensional
3D	Three-dimensional
ACN	Addressable conducting network
AFM	Atomic force microscopy
C	Central layers
CAD	Computer aided design
CEC	Cation exchange capacity
CF	Carbon fiber
CMT	Carbon fiber mat thermoplastic
CNT	Carbon nanotubes
CT	Compact tension
DBP	Double-belt press
D-LFT	Directly produced long fiber reinforced thermoplastics
DMTA	Dynamic-mechanical thermal analysis
EMI	Electromagnetic interference
ETC	Extreme temperature conditions
EFW	Essential work of fracture
FCP	Fatigue crack propagation
FDM	Fused deposition modelling
FE	Finite element
FR-PP	Fabric reinforced polypropylene
FTIR	Fourier-transform infrared
GF	Glass fiber

GMT	Glass mat-reinforced thermoplastics
GMT-C	Continuous fiber GMT
GMT-D	Discrete fiber GMT
GO	Graphene oxide
GR	Graphene
HDT	Heat distortion temperature
HDT-B	Heat distortion temperature tested by B-method
HPSC	High pressure stiffness conditions
HRR	Heat release rate
IFR	Intumescent flame retardant
L	Longitudinal
LEFM	Linear elastic fracture mechanics
LGF	Long glass fiber
LOI	Limiting oxygen index
LPSC	Low pressure stamping conditions
LTCE	Linear thermal coefficient of expansion
LWRT	Lightweight reinforced thermoplastics
MAO	Methylaluminoxane
MFD	Mold filling direction
MMT	Sodium montmorillonite
MRT	Mat-reinforced thermoplastics
MWCNT	Multiwall carbon nanotube
NF	Natural fibers
NMT	Natural mat thermoplastic
PA	Polyamide
POSS	Polyhedral oligomeric silsesquioxane
PP-g-MA	Maleic anhydride grafted PP
PP-g-MAA	PP grafted with maleic acid
PYFM	Post-yield fracture mechanics
RC	Reference forming conditions
RT	Room temperature
S	Surface layers
SCC	Slow cooling conditions
SCF	Short carbon fiber
SEM	Scanning electron microscopy
SGF	Short glass fiber
SMC	Sheet molding compound
SR-PP	Self-reinforced PP
T	Transverse
TC	Transcrystalline
TEM	Transmission electron microscopy
TGA	Thermogravimetric analysis
TTSP	Time-temperature superposition principle
UD	Unidirectional

XRD	X-ray diffraction
ZN	Ziegler-Natta
ε	Strain
E	Flexural modulus
E_f	Flexural modulus of the fibers
E_m	Flexural modulus of the matrix
K_Q	Fracture toughness
R	Reinforcing effectiveness term
T_g	Glass transition temperature
T_m	Melting temperature
V_f	Fiber volume fraction
V_m	Matrix volume fraction
ρ	Density
σ	Normal stress
τ	Shear stress
μ	Dynamic viscosity of the resin

9.1 Introduction

Composites are defined as materials consisting of two or more distinct phases (matrix and reinforcing phases) separated by a recognizable interphase. Earlier definition emphasizes that the two phases should be chemically and physically different. This is, however, no more a stringent criterion because the two phases may be of the same polymer, as this is the case with single-polymer composites possessing ultimate recyclability. The polypropylene (PP)-based single-phase composites are termed as to “all-PP” or self-reinforced polypropylene composites, as well. Composite materials exhibit such structural and functional properties which cannot be attained by any of their constituents alone. The reinforcing phase is much stronger and stiffer than that of the matrix. The role of the matrix is to keep in position and protect the reinforcement from environmental attack. For the stress (shear and transverse types) transfer from the “weak” matrix to the “strong” reinforcement, the finite thickness interphase is responsible. The reinforcing (disperse) phase is usually anisometric and thus exhibits a rather large length-to-thickness (aspect) ratio. The length of the reinforcement varies in an extreme large range from nanoscale to practically infinite (in case of endless or continuous fiber reinforcement). The variation in their thickness is more restricted and usually remains under few millimeters. Note that the thickness of carbon (CF) and glass fibers (GF) is in the ranges of 5–10 μm and 10–25 μm , respectively. It is worth of noting that isometric nanoparticles (i.e. having an aspect ratio of 1) may meet the criteria of reinforcement albeit such particles, at least in microscale, belong to the category of fillers. Major effect of fillers is cost-reduction along with some improvements in the non-structural properties.

Composites are classified differently. Considering the matrix phase, the usual classification is ceramic-, metal- and polymer-matrix based systems. Depending on the actual size of the reinforcement, one can speak about nano-, micro- and macrocomposites. From the viewpoint of the reinforcing structures possible categories are for example discontinuous/continuous fiber-reinforced materials, composites with textile architectures, laminate composites. Because of the embedded fiber reinforcements, the composites can be made anisotropic in that their mechanical response depends on the loading direction. This feature is highly desirable and beneficial because during design and manufacturing the composite’s structure can be tailored upon the expected loading condition. Polymer composites are very popular due to their low cost and easy fabrication methods. This note especially holds for PP-based ones as PP belongs to the family of the rather inexpensive high-volume thermoplastics. The PP matrix can be combined with the reinforcement in different ways to prepare a great variety of preforms, semi-finished products, textile fabrics, etc. Their structure and appearance determine the processing alternative to convert them into the final parts. Figure 9.1 shows an overview of the manufacturing alternatives of thermoplastic composites.

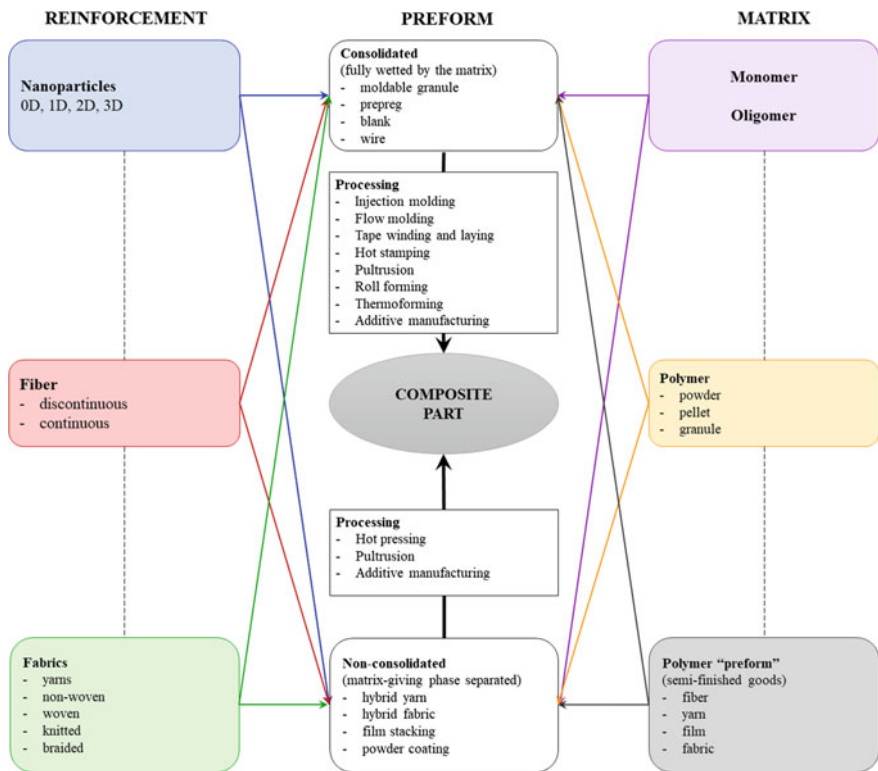


Fig. 9.1 Overview of possible manufacturing routes for thermoplastic matrix-based composite products

Note that the chart in Fig. 9.1 is of general character and valid for all thermoplastic polymer-based composites. In this diagram, consolidated and non-consolidated “preforms” were differentiated. The basic difference between them is whether the reinforcement is fully wetted by the matrix or no intimate contact exist between reinforcement and matrix. In the latter case, the matrix-yielding phase is available in separate forms, usually as fiber or film.

Moreover, Fig. 9.1 serves as guide-line for the present chapter on PP composites. Accordingly, next we shall introduce the structure-property relationships of PP-nanocomposites, discontinuous fiber-reinforced composites, mat-reinforced composites, fabric-reinforced composites and aligned fiber-reinforced laminate composites. Splitting between mat- and fabric-reinforced PP composites, irrespective of the fact that they are listed under “fabrics” in Fig. 9.1, is reasoned by the broad application of mat-reinforced PP composites.

The mechanical properties of PP based composites depend on the numerous factors, such as, reinforcement nature, volume fraction and architecture, quality of impregnation, amount of various defects and fiber-matrix interface quality. Nevertheless, reinforcement architecture plays a crucial role in mechanical response. Thus, mat and short fiber reinforced PPs demonstrates lowest values of strength and modulus, while unidirectional (UD) shows the highest level of mechanical response but only in longitudinal direction (Fig. 9.2).

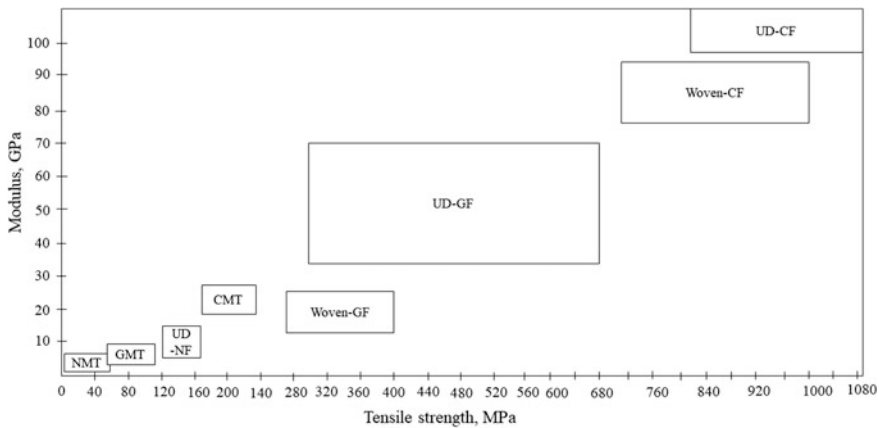


Fig. 9.2 Mechanical properties of different types of PP based composites. Designations: NMT—Natural fiber mat-reinforced thermoplastic; GMT—glass mat thermoplastic; CMT—carbon-mat thermoplastic; NF—natural fibers; woven—woven textile. Note, the matrix materials of the mentioned composites is always PP

9.2 Nanocomposites

Nanoparticle-modified polymer composites (also termed polymeric nanocomposites, inorganic/organic hybrid materials) have attracted great scientific and technological interest owing to their exceptional physico-mechanical, thermal and other

properties achieved at very low nanoparticle content (<5 wt% or <2–3 vol%). Nanoparticle means that the size of the related inorganic or organic filler—at least in one dimension—is on nanometre scale. Although the term nanocomposite sounds as a current one, nanocomposites have been produced industrially more than half century ago. In this respect attention should be drawn to the reinforcement of rubbers by nanometer scale carbon black. In addition, many natural and artificial products can be considered as nanocomposites based on their structural build-up.

Major specific feature of nanofillers and -reinforcements is their huge interfacial surface area, which may be as high as 1000 m²/g. As a consequence, the interphase properties may become the controlling parameters of the macroscopic response of polymer nanocomposites. Unlike the two-dimensional (2D) interface, the interphase (3D) concept considers that the molecular mobility changes from the particle's surface toward the bulk in the range of several nanometers.

A further aspect is that with decreasing mean particle size the average distance between the nanoparticles also decreases when keeping the volume fraction of the filler constant. This may activate filler-filler interactions and result in a peculiar physical network structure.

Nanoparticles may be grouped upon their shape in 0D (spheroid), 1D (e.g. tube, fiber, whisker), 2D (platelet, disk) and 3D (framework). The anisometric nature of fillers is usually characterized by the aspect ratio (length/thickness or length/diameter ratio).

Polymer nanocomposites, including the PP-based ones, are very promising materials for various applications due to improved and novel properties, as shown later.

9.2.1 Preparation

There are numerous ways to produce nanocomposites. In this chapter a distinction between preformed and in situ generated nanoparticles will be made. The corresponding nanocomposites can be produced by different techniques which are usually listed in three major groups: (i) in situ polymerization, (ii) solvent-assisted techniques (including aqueous dispersions) and (iii) melt compounding. There are, however, some other methods, such as a combination of the above methods (e.g. water-assisted melt compounding [1]), ball milling (dry or wet), sol-gel chemistry implemented in one of the above listed techniques, etc.

Among the in situ techniques we may consider also the polymer intercalation in 2D layered structures and 3D frameworks because microscopic particles (>10 μm) are introduced into the polymer or monomer in which the particles disintegrate in nanoscale during processing or polymerization.

To incorporate micron-size preformed inorganic particles into a polymer matrix is a well-known method for improving the modulus, heat distortion temperature (HDT) and to reduce the shrinkage of such composites. This is associated, however, with a pronounced reduction in ductility. By diminishing the particle size (nanoscale) or by enhancing the particle volume fraction, the flexural and the tensile

strength can be enhanced. On the other hand, the fracture toughness and modulus remain fairly independent of the particle size, even when going down to the nanoscale. An increase of the glass transition temperature (T_g) of polymers owing to addition of various preformed nanoparticles reflect a restricted motion of the polymer chains, and thus a good bonding between the particles and the matrix.

9.2.1.1 In Situ Polymerization

In this case the nanofiller is dispersed or swollen in the monomer or oligomer in the presence or absence of additional solvent. A very promising way is to render the surface of the particle catalytic for the subsequent polymerization. In case of 0D particles the related method is termed as polymerization filling, whereas for 2D and 3D additives as intercalative polymerization. The in situ polymerization was explored to produce PP nanocomposites with different fillers with and without catalytic activities for the propylene polymerization. Basic advantage of the in situ polymerization that thermodynamic and kinetic limitations, which are controlling parameters of melt compounding, and partly also for solution blending, are “bypassed”. The polymer grows from the fillers’ surface thereby hampering the agglomeration of 0D particles and causing intergallery expansion (intercalation) or full delamination (exfoliation) in 2D-type nanoreinforcements. Attention should be paid, however, to the fact, that subsequent melt processing of such in situ polymerized PP nanocomposites may result in a pronounced agglomeration, deintercalation phenomena. Zapata and Quijada [2] compared the properties of PP/silica (0D) nanocomposites produced with and without catalytic activity of the silica in metallocene polymerization of propylene. The authors found that the dispersion of the silica nanospheres is better when their surface is catalytically active. PP/fumed silica nanocomposites were prepared by Azinfar et al. [3] using a “bisupported” Ziegler-Natta (ZN) catalyst in which magnesium ethoxide and silica served as conjugate support of the catalyst. In majority of the polymerization works, however, 2D fillers were preferentially used being more suited for catalyst support and offering larger property improvements than 0D versions. Among the 2D nanofillers clays and graphene (GR) versions were tried. Ramazani et al. [4] used pristine clay (sodium montmorillonite, MMT), whereas Cardoso et al. [5] an organophilic clay as ZN catalyst supports for the preparation of PP/clay nanocomposites. In both cases the clay was intercalated and partly exfoliated after the polymerization. Using organophilic clay (introduced later), however, is beneficial with respect of further melt processing for which the in situ polymerized PP/clay nanocomposite may serve as adequate “masterbatch”. GR nanosheets (up to 20 wt %) were successfully dispersed in PP via in situ polymerization using a metallocene complex with methylaluminumoxane (MAO) cocatalyst. GR increased the crystallization and degradation temperatures and resulted in balanced stiffness/ductility performance [6]. Funck and Kaminsky [7] demonstrated that oxidized multiwall carbon nanotube (MWCNT) can be incorporated into PP through polymerization of propylene with a metallocene/MAO catalyst and in situ coating. Huang et al. [8] followed a

similar way and prepared PP/graphene oxide (GO) nanocomposites through in situ ZN polymerization. In this work the surface functional groups ($-\text{OH}$ and $-\text{COOH}$) of GO were converted into Mg/Ti catalyst species prior to polymerization. This work demonstrated that using a GO-supported ZN catalysts even a polar GO can well be dispersed in apolar PP. Unlike 2D layered structures which can be delaminated (exfoliated, intercalated) during polymerization, the 3D frameworks (natural zeolites, synthetic molecular sieves and mesoporous glasses) are stable and thus have to be added as nanofillers.

With respect to the catalysts and in situ propylene polymerization methods in absence and presence of nanofillers, the interested reader is addressed to the book of Kaminsky [9].

9.2.1.2 Solvent-Assisted Techniques

Preparation of nanocomposites via solution dispersion is mostly of academic interest (to study selected structure-property relationships) and especially adapted for polymers soluble only in organic solvents. On the other hand, the properties of polymer nanocomposites prepared by solution mixing can serve as benchmarking for melt compounded ones, as they exhibit the highest available values. That is the reason why works often compared the properties of solution and melt blending produced PP nanocomposites, such those with GR [10]. Solvent-assisted dispersion of clay [11] and cellulose nanowhisker [12] in PP were also topics of investigations.

Considering the fact that some nanoparticles are water-swellaible (e.g. clays) and dispersible (e.g. boehmites [13], oxidized carbonaceous nanofillers), they can be incorporated in their aqueous slurry into the molten polymer during compounding. The beauty of this method is that nanofillers without surface treatment can be used instead of their more expensive organophilic versions. This was explored in different polymers [1], including PP/boehmite [13], and PP/clay [14] nanocomposites. A further advent of this water-mediated method is that rubber latices can also be used and thus rubber-toughened PP nanocomposites can also be produced in line. Note that the mean size of the rubber in the latex matches very well with the size requirements for thermoplastics [15]. PP latex is also available and thus can be combined with water dispersible nanofillers, such as GO, through latex compounding. In a follow-up procedure the GO-containing “masterbatch” (eventually after reduction of GO to GR) can be dispersed in molten PP [16].

9.2.1.3 Melt Compounding

The vast majority of works was dealing with the preparation of PP nanocomposites through melt compounding. This note holds for all types of nanofillers. 0D-type nanoparticles, e.g. SiO_2 [17, 18], TiO_2 [19], CaCO_3 [20], alumina (Al_2O_3 [21], boehmite [13]), polyhedral oligomeric silsesquioxane (POSS) [22] are frequently incorporated into PP by melt compounding techniques. Note that many

nanoparticles are commercially available with and without surface treatments. Among the 1D fillers halloysite [23], carbon nanotube (CNT) variants [24–26], cellulose nanofibers and whiskers [27, 28] should be mentioned.

The commonly used 2D reinforcements are 2:1 layered silicates (phyllosilicates) of natural (e.g. bentonite, MMT—often termed clays) and artificial (e.g. fluorohectorite) origin. They contain two tetrahedral silicate sheets fused to an edge-shared octahedral one resulting in an overall thickness of ca. 1 nm. The lateral dimension of the layered silicates varies in a very broad range from several ten nanometres to several micrometres yielding an aspect ratio of up to 6000 for synthetic versions [29]. Isomorphic substitution of higher valence cations (Al^{3+} and Mg^{2+}) in the silicate framework by lower valence ones (Fe^{2+} , Mg^{2+} and Li^+ , respectively) generated negative charges on the layers, which are counterbalanced usually by alkaline cations (Na^+ , Ca^{2+} —generally in hydrated forms). As a consequence, such layered silicates exhibit a cation exchange capacity (CEC) and the inter-gallery cations can be replaced by suitable organic cationic surfactants. For that ammonium salts are preferentially used. By this cation exchange the hydrophilic silicate is rendered organophilic and at the same time the interlayer spacing (basal or d spacing) increases. The latter is tuned by the chemical build-up of the onium intercalant (often containing a long alkyl chain) the further role of which may be to support the chemical interaction with the matrix [30]. Note that the interlayer spacing should be larger than ca. 1.5 nm in organophilic clay (i.e. the interlamellar distance > 0.5 nm). Since the price of the organophilic silicates is higher (more than threefold) than that of the purified pristine ones which was the driving force for the development of water-assisted techniques [1].

Though the overwhelming majority of the works done in the past were dealing with “cationic” layered silicates, layered silicates with anion exchange capacity (their layers have a positive surface charge which is compensated by intergallery anions) are also available. The corresponding hydrotalcites are incorporated in PP, especially to improve its fire resistance [31, 32]. An excellent review on synthetic layered nanoparticles, covering clays, layered double hydroxides and the like, was compiled by Utracki et al. [29].

Other recently explored 2D nanofillers are GR and its derivatives, such GO, differently reduced GOs. GR is a 2D one atom thick planar sheet composed of sp^2 hybridized C atoms exhibiting outstanding mechanical, thermal and electric properties. This carbon allotrope is the thinnest known material in the universe. Oxidation of GR results in the appearance of polar groups (hydroxyl, carboxyl, epoxy) rendering it more hydrophilic. Reduction of GO, by whatever means, restores in large extent the original sp^2 hybridization along with property improvements. Though GR can be produced via direct synthesis, most of the works followed a “top down” strategy using graphite. It is the right place to underline that the terms used for PP/GR(GO) nanocomposites are rather inconsistent. An excellent review on PP/GR nanocomposites, covering their preparation through in situ polymerization, solution-assisted techniques and melt compounding was published by Tripathi et al. [33].

Melt compounding is a very attractive way to produce commercial nanocomposites. This is owing to: (a) fast dispersion of the nanoparticles in the melt, (b) available industrial melt compounding capacities, and (c) environmental friendly preparation. Similar to solvent intercalation, melt intercalation is also governed by thermodynamic (compatibility) and kinetic (diffusivity) parameters. It is intuitive that polymer molecules densely adhering to 0D particle's surface, intercalating in 2D layers or penetrating in 3D frameworks lose their conformational freedom which is associated with entropy loss. The attributes "nano", "nanoscale" already suggest that the formation of polymer nanocomposites has many similarities with (im)miscible polymer blends and thus the related rules can also be adopted. So, in order to get molecular, i.e. nanoscale, dispersion, the Gibb's free energy must be negative. As entropy loss produces an adverse effect, it has to be "overcompensated". This may occur by entropy gain (e.g. interdiffusion between molecules of the organophilic modifier and PP molecules) and/or by energetically favored interactions (e.g. between molecules of "functionalized" PP and functional groups on the particles. Energetically favored interactions involve acid/base and chemical reactions, H-bonding etc., all of them affecting the term enthalpy of mixing. Effects of possible interactions and kinetics have to be considered when selecting the surface modification and compounding conditions [34, 35]. As far as kinetics of nanostructure formation concerns the effects of locally acting shear and elongational flow fields should be emphasized. As the majority of the experimental work was done by extrusion melt compounding, the related research focused on the effects of shear stresses varied by different ways [36, 37]. Effects of the elongational flow on the morphology development became under spot of interest only recently [38, 39]. Basic outcome of these studies was that the dispersion state of the nanoparticles is governed also by the shear/elongational flow and residence time (i.e. kinetics). It is worth of noting that the above thermodynamical interactions and kinetics (processing-related effects) are often interrelated especially due to the fact that compatibilizers are mostly used, as well.

As most nanoparticles are of polar nature, their incorporation into the apolar PP is a great challenge. Recall that traditional fillers are often "coated" by surfactants (tensides). Their role is to improve the compatibility between the filler and polymer via their long alkyl chains. The same philosophy can be followed for the dispersion of nanofillers. The related polymers, oligomers are called as compatibilizers. They are usually grafted copolymers due to economic reasons. Maleic anhydride grafted PP (PP-g-MA, grafting degree is at about 1 wt%) is the preferred compatibilizer (e.g. [40, 41]). It was reported that lower molecular mass PP-g-MA may favor the organoclay exfoliation in contrast to that of higher molecular mass version [42]. Generally, in the presence of compatibilizer a higher degree of dispersion (intercalation/exfoliation when appropriate) was found than in their absence. This was reflected in improved mechanical properties.

Using PP-containing blends attention should be drawn to the fact that the nanoparticle introduced may be preferentially embedded in one of the blend's components. Moreover, the nanofillers themselves may work for interphase modification, compatibilization [43].

9.2.2 Structure Development and Characterization

The structure of polymer nanocomposites is very complex as it covers the following domains: dispersion state of the nanoparticles, changes on molecular and supermolecular level in the matrix (bulk), interphase formation between the surface of the nanoparticles and bulk material. Moreover, there is a strong interrelation between the above characteristics. As a consequence, it is not an easy task to find those structural parameters which control a given property.

9.2.2.1 Particle Dispersion

It is obvious that nanoscale sensitive experimental techniques have to be used to detect the dispersion state of the nanoparticles. For that purpose, transmission electron microscopy (TEM) is preferred. It should be born in mind, however, that the view field at high magnifications may not represent that of the whole sample. Further, it is essential to describe the dispersion state. Albeit some trials were made to make use of image analysis codes, this issue is not yet solved properly. Another straightforward technique is the atomic force microscopy (AFM). Real breakthrough in the characterization of the dispersion of nanoparticles can be expected from tomographic methods, such as electron, X-ray microcomputed, focused ion beam [44] and optical coherence tomography methods [45].

Polymer intercalation in 2D silicate layers is usually evidenced by X-ray diffraction (XRD) performed at small diffraction angles (2Θ). In XRD pattern intercalation manifests in a shift towards lower scattering angles in the range $2\Theta = 1\text{--}10^\circ$. In contrast to the frequently quoted claim that missing peak in the XRD spectra represents exfoliation, it is not at all correct. In order to get a reliable picture on the silicate dispersion, XRD and TEM results should be compared, and even optical microscopy included (due to the presence of micronscale agglomerates).

9.2.2.2 Matrix Polymer (Bulk)

Changes in the matrix morphology owing to the presence of nanoparticles occur at different levels. Like some micro- and macroscopic fillers and reinforcements, nanoparticles also act as heterogeneous nucleation agents. High nucleation density on the filler surface may generate transcrystalline (TC) growth. TC is caused by dense nuclei on the heterogeneous surface due to which the spherulitic crystallization is laterally hindered. So, growth occurs in one direction, viz. perpendicular to the filler surface. It is believed that the TC layer supports the stress transfer from the weak matrix to the “strong” nano-reinforcement [46]. PP TC, being of epitaxial origin, was observed on the crystalline surfaces of CNT [47] and GR [48].

The heterogeneous nucleating effect of nanoparticles has been demonstrated for many semi-crystalline thermoplastics including PP. It is noteworthy that practically all of them support the crystallization in α -form. Studies devoted to the crystallization (isothermal, non-isothermal) behavior of various PP-based nanocomposites showed that the usual descriptions (Avrami, Ozawa etc.) are valid. Very interesting results were achieved by investigating PP/mesoporous silicate nanocomposites. It was shown that isotactic PP confined in the mesopores does not crystallize [49]. This fact explains the reason of a research trend dealing with the crystallization behavior of polymers under spatial constraints.

9.2.2.3 Interphase

To examine the interactions between nanoparticles and polymers various techniques can be used. Fourier-transform infrared (FTIR) spectroscopy, solid state nuclear magnetic resonance, calorimetry, thermogravimetric analysis (TGA), chromatographic and electrophoretic measurements, all can contribute to get a better insight in structure-property relationships and interphase properties [30]. A rather simple and informative method is the dynamic-mechanical thermal analysis (DMTA). Strong absorption of polymer molecules on nanoparticles possessing very high specific surface area yields a change in the T_g peak (shape alteration, intensity reduction, shift toward higher temperature). A direct evidence for changes in the interphase characteristics may deliver the AFM.

9.2.3 Properties and Their Prediction

It was shown before that the structure of nanocomposites is highly complex and partly of hierarchical nature. Therefore, it is of great challenge to trace those structural parameters which affect the desired property. In respect to the structure-property relationships the basic question we have to give an answer is: do these issues belong to polymer physics or continuum (composite) mechanics? In the former case the bulk and interphase, whereas in the latter reinforcement-related characteristics should govern the properties. Unfortunately, no definite answer can be given to the above question. In certain conditions, grouped in low frequency mechanical tests (creep, fatigue), aspects of polymer physics may dominate. In tests of high frequency loading (dynamic, impact) the use of composite analogies (i.e. continuum mechanics) seems to be straightforward. With other wording, composite rules are more promising to describe the elastic (linear elastic, linear mechanic), whereas polymer physics principles are more suited to assess the relations between structure and viscoelastic (non-linear elastic) properties.

9.2.3.1 Mechanical Response

Stiffness and ultimate tensile properties

The simplest way to predict stiffness (Young's or E -modulus) is to check whether or not the rule of mixtures holds. For macroscopically filled systems the Kerner equation is widely used. The disagreement between the Kerner's prediction and experimental results got for nanocomposites with 0D fillers forced the researchers to consider the interphase. It was treated as an immobilized layer which increased the effective filler volume fraction. Results suggested that the thickness of the immobilized layer may be much larger than the size of the particles [50]. For the prediction of the shear modulus of PP nanocomposites with 0D fillers the Einstein equation and its modifications (Guth, Cohan, Mooney) may work [51], which are well accepted predictions for rubbers. The strength of traditionally filled systems decays according to a power law function. This means that the strength of the composite is always below than that of the neat matrix polymer as the filler does not bear any part of the external load. In contrast, considerable strength increase was measured for nanoparticle reinforced thermoplastic systems. The related functions were treated by empirical models as listed in Ref. [50]. On the other hand, the reinforcing effect of nanoparticle is not fully understood. Behind the strength increase one may surmise some analogy with nanoparticle-reinforced rubbers.

Usual analytical descriptions of the stiffness of PP nanocomposites with 1D and 2D nanoparticles agree with those of conventional composites. Accordingly, the popular models are: Voigt upper bound—Reuss lower bound, Hashin and Shtrikman upper and lower bounds, Halpin-Tsai model, Mori-Tanaka theory, Hui-Shia model [52]. Interested reader may find several papers quoting why one of models was working better than the other(s). Kalaitzidou et al. [53] for example analyzed the flexural and tensile moduli of PP nano (graphite nanoplatelet, vapor-grown carbon nanofiber, carbon black, MMT) and microcomposites (CF) and found that the Halpin-Tsai and Tandon-Weng models worked best, however, only up to a given concentration of the reinforcements. Above a threshold filler loading the models overestimated the experimental values. It is noteworthy, that for modelling the mechanical (elastic) properties of polymer nanocomposites molecular dynamics [54, 55] and finite element (FE) simulations are becoming favored topics [52]. Among the latter multiscale representative volume element modelling seems to be the most promising way [56].

The scenario is far less so clear for the ultimate properties. Exfoliation of 2D nanoparticles raises the stiffness which is accompanied by reduced strain (ductility). So, the nanocomposites are becoming "harder" but more "fragile". The ultimate properties depend not only on the intercalation/exfoliation state, but also on characteristics of the interphase (wetting, adhesion) and the bulk (polymorphism, crystallinity, spherulite size).

Creep and fatigue behavior

Few papers were published on the yield, creep and fatigue behavior of nanocomposites. This is quite surprising as the above long duration tests are very sensitive to changes in the interphase and bulk properties. Studying the temperature

and strain rate sensitivity of the yield strength of organoclay modified polyamide-6 (PA-6) and PP nanocomposites, Mallick and Zhou [57] found that the Eyring equation works well also for these nanocomposites. Based on normalized stress-cycles (S-N) curves, derived from tension-tension fatigue, the authors concluded that the fatigue failure is initiated by re-agglomerated particles [57]. The creep failure of PP and its nanocomposites with and without PP-g-MA was found to occur at a critical strain independent of the stress level applied in the work of Lv et al. [58]. This peculiar critical strain is combined with a time-strain superposition method to predict the creep failure lifetime of PP nanocomposites. Researchers prefer to perform short term creep test at different temperatures and/or stress levels and generate master curves by time-temperature and time-strain superpositions [59]. Drozdov et al. [60] found that reinforcement of PP with 1 wt% of organoclay increased the time to failure by an order of magnitude. The cited authors proposed new constitutive equations considering the viscoelasticity and viscoplasticity of the investigated nanocomposites. Incorporation of clay in PP resulted in reduced fatigue crack growth rates [61]. Note that this is a universal feature of reinforcements [62]. The creep and fatigue performances of polymer nanocomposites were finely surveyed by Pegoretti [63].

Toughness

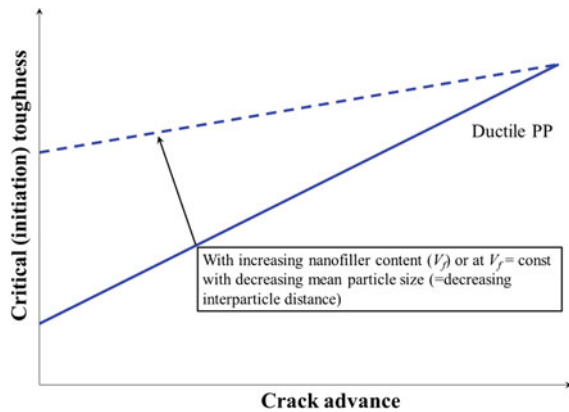
Toughness of nanocomposite deserves a separate treatise owing to highly contradictory findings in the open literature. Usually there is trade-off between stiffness, strength and toughness. Accordingly, nanoparticles with reinforcing effect should result in toughness reduction. In many cases, however, the opposite tendency was found [64]. It should be emphasized here that fracture mechanical studies on polymer composites, especially on PP-based ones are scarce [50, 65–67]. On the other hand, only fracture mechanical methods provide toughness values which can be collated being material parameters (e.g. [68]).

The usual thumb of rule is that at very low nanoparticle content (<2–3 wt%) the toughness does not alter compared to the matrix. At higher nanoparticle content, however, a strong decrease in the toughness can be observed. To explain the toughness improvement first the “percolation theory” of Wu was adopted [69]. It was soon recognized that this theory could not account for the toughness upgrade, as the matrix ligament between the particles is too large to create the necessary stress overlapping. To overcome this problem a double percolation model was proposed [50]. According to the authors’ feeling even this model needs refinement. Specific effects of the interphase (immobilized layer, transcrystallinity, crystalline polymorph, etc.) which affect the matrix deformation have to be considered. Many model explanations lack to give information why and how cavitation occurs in the nanocomposites with intercalated/exfoliated, finely and coarsely dispersed structures. Note that the toughness in rigid particle filled polymers is linked to cavitation which is followed by stretching of the interparticle matrix ligaments [70]. This effect along with the inhomogeneous distribution of rigid spherical particles was considered in the analytical model of Lauke [71] recently.

Resistance curve approaches of ductile fracture mechanics (J-integral and essential work of fracture (EWF) [72, 73] were mostly used to assess the toughness

of PP nanocomposites. For low aspect ratio nanofillers (i.e. 0D type boehmites) it was found that the critical value (specific EWF) went through a maximum whereas the slope of the resistance curve, i.e. specific plastic work, decrease with increasing nanofiller contents [74, 75]. The scenario is more complex for 1D fillers, such as MWCNT, where a ductile-semiductile transition was observed [76] that basically blurs the EWF application. Karger-Kocsis et al. [77] studying the effect of various nanofillers in PP (boehmite, MWCNT, clay, GR, added in 1 wt% each) concluded that the EWF method can only be adapted for low aspect ratio nanofillers. A further finding was that there is an adverse effect between the energy required to crack initiation and propagation, i.e. both of them can hardly be increased at the same (cf. Fig. 9.3).

Fig. 9.3 Schematic toughness resistance curves for PP nanocomposites



Similar results, tendencies were reported for PP/MMT nanocomposites using the J-integral [65] and EWF [78] approaches. Nevertheless, examples for simultaneous improvements in resistances to crack initiation and propagation can also be found [79]. It is noteworthy that the EWF results on PP nanocomposites are often “scattered” due to the fact that the prerequisites of the EWF applications can only be met with very ductile PP copolymers. Problems linked with unstable necking/tearing can be considered by suitable energy partitioning [73, 80] during EWF which is not always followed.

Finally, toughness decrease in nanocomposites is likely the rule and not the exception. This claim is in concert for example with the ultimate (tensile) properties and pressure-volume-temperature diagram data. Recall that the latter technique evidenced a considerable decay in the free volume upon exfoliation [81] which means restricted molecular motion and thus suggests toughness reduction.

9.2.3.2 Rheological Behavior

It was early recognized that the structure of nanocomposites strongly influences the rheological behavior, especially in the low frequency range (linear viscoelasticity)

[82]. In this range the melt viscosity (studied mostly in shear) increases monotonically with increasing nanoparticles' content irrespective to their shape and incorporation method [82, 83]. Polymer nanocomposites with high aspect ratios (1D and 2D versions) usually exhibit higher viscosities than quasi-spherical types (0D) in the linear viscoelastic range. Surprisingly, boehmite, belonging to the 0D particles, causes a very small increase in the shear viscosity of PP both in the linear and non-linear rheology ranges [75]. As known, PP shows shear thinning behavior (non-linear viscosity range), i.e. the melt viscosity decreases with increasing shear rate. Shear thinning may start at lower shear rates than that of the related matrix polymer with anisometric particles due to their alignment into the flow direction. Note that at very high shear rates, characteristic for injection molding operations, only a small difference in the melt viscosities between the parent PP and its nanocomposite can be found. The latter may be even lower than that of the matrix [84]. The complex viscosity of neat PP as a function of the angular frequency shows Newtonian behavior at low frequencies. The Newtonian range may disappear with increasing nanoparticle content and a transition from liquid-to-solid-like behavior takes place (termed as to rheology percolation), as shown by Prasantha et al. [24] on the example of PP/MWCNT nanocomposites. The related "liquid-solid" change is best visualized through the van Gurp-Palmen plots (phase angle vs. absolute value of complex shear modulus) [24, 85].

The relationship between the shear viscosity and shear rate (in the range of 10^{-3} to 2 s^{-1}) could be well described by the Carreau model [84]. Chafidz et al. [86] reported that the complex shear viscosity as a function of angular frequency (shear rate) can well be described by the Carreau-Yasuda equation. For the shear thinning behavior, determined by rheometer, the Oswald-de Waale (power law) function may also work properly [86]. Information derived from dynamic oscillatory shear, steady shear and elongational flow measurements, eventually combined with "superimposed" techniques like transient/intermittent ones) can deliver a deeper insight in the structure of the nanocomposites and its alteration owing to shear and elongational flows [38, 87, 88]. It was shown for example that the morphological stability of nanocomposites can be successfully studied in rheological measurement [89]. Solomon et al. [90] reported that the course of the storage modulus versus frequency in the viscoelastic range reflects well effects of the intercalation of organoclay (caused by amine surfactants of various chemical build-up).

9.2.3.3 Thermal Behavior

For many applications it is of great importance to know the linear thermal coefficient of expansion (LTCE) of nanoparticle-reinforced composites. It is intuitive that the orientation of 1D and 2D particles makes the LTCE direction dependent. Usually, with increasing nanoparticles' content the LTCE is reduced as shown on example of PP/CNT nanocomposites [91]. Using organoclay at 6 wt % loading the LTCE of PP was decreased by 20% [92]. On the other hand, more moderate results can also be found for PP/clay nanocomposites in the literature.

For the estimation of the LTCE of nanocomposites with various nanoparticles (0D, 1, 2D types) the Chow-model may be successfully adapted as shown by Yoon et al. [93].

Another property of engineering relevance is the HDT. Note that HDT is always enhanced by incorporation of nanoparticles. The related change in PP nanocomposites, yielding at about 40 °C enhancement in HDT at 6 wt% clay content, is originated from a better mechanical stability rather than any increase in the crystallinity and related melting interval. Not surprisingly, the HDT improvement with organoclay is less than with pristine ones [94]. Fornes and Paul [95] proved that the HDT-B (HDT tested by B-method) value of nanocomposites can be calculated by adopting the Halpin-Tsai composite theory for the DMTA properties when coupled with the method of Scobbo. The so-predicted HDT-B values and experimentally measured data exhibited a very good agreement, though for PA/clay nanocomposites.

9.2.3.4 Other Properties

Improvement in the transport properties of 2D nanoparticle-reinforced PPs is the major driving force of commercialization of the related nanocomposites at present. Reduction in the permeability is usually attributed to the fact that the diffusing molecules have to bypass the impermeable platelets (“tortuous path”, labyrinth effect) which are more or less well oriented normal to the diffusion direction. It was found that the Nielsen’s model works well to predict the gas barrier properties in such systems [87]. Recently, more advanced theories were developed addressing changes in the alignment, interphase and bulk properties, as well [96, 97]. Recall that the theoretical models generally consider the silicate layers as perfectly aligned and exfoliated showing a large aspect ratio [87]. However, gas permeability measured is usually markedly below the theoretical predictions [98, 99]. Nevertheless, 2D nanoparticles are far more effective with respect to gas permeation than 0D types [100]. Attention should be called to the fact that permeability is a product of the diffusivity (diffusion coefficient) and equilibrium sorption of the penetrant under given conditions. So, the outcome does not represent a “design parameter”. Nevertheless, studying this behavior useful information can be deduced indirectly, even for the structure of the nanocomposites.

Many reports quoted that the thermal stability (usually studied by TGA) of the polymers increased when containing dispersed nanoparticles. The temperature linked to a given mass loss, and the amount of the char residue increased with increasing clay content. The related increase depended on the clay dispersion, which was controlled by the organophilic surfactant of the clays [101]. It is often claimed that the slowdown in the thermal degradation is due to hampered diffusion of the degradation products from the bulk towards the gas phase. It is worth of noting that all inorganic fillers exhibit some flame retardant effect in their composites. Its manifestation, however, depends on the method selected [102]. Limiting oxygen index (LOI) data showed that there is a large difference between fillers as a

function of their dispersion state (micro- or nanoscale) and aspect ratio [103]. Note that in an LOI test the flame spreads from the top of the specimen downwards. So, in this test the char formation has a great influence. Needless to say that a vertical burn test (e.g. according to UL 94 descriptions) may deliver completely different results. Nowadays, the ultimate method to check the fire retardance is the use of cone calorimetry. In the related tests the heat release rate (HRR) and mass loss rate are registered as a function of time. Numerous works using this method indicated that in presence of different nanoparticles (among which layered silicate were preferentially used) the peak HRR is efficiently reduced, however, with some extension in the overall burning time [103–105]. This was traced to the formation of a carbonaceous/silicate char of thermal insulating properties on the specimen surface [104]. To improve the very poor fire resistance of PP the preferred concept is to make use of intumescent coatings [106]. Intumescent formulations are halogen-free and produce a charred cellular layer upon heating. The related layer is acting as a heat shield by protecting the underlying material from the heat flux of the flame. This concept was adopted for polymer nanocomposites due to two effects: (a) char yielding behavior and (b) reinforcing effect of the clay [107]. Note that the reinforcing effect of the nanoclay is of vital importance as the usual intumescent formulations result in materials of poor mechanical performance. Based on the above behavior layered clay containing PP nanocomposites should have improved resistance to ablation, too.

9.2.4 Processing and Applications

The unique combination of some key properties paved already the way for PP nanocomposites for industrial applications (packaging—due to barrier properties [108], automotive—due to high stiffness, high strength, low density, enhanced HDT, improved mar and scratch resistance [109]). The processing, covering all aspects (welding, joining, etc.) of PP nanocomposites follows the rules established for the neat PPs. Albeit PP nanocomposites are commercialized at present mostly as precompounded grades, in ready to use or in masterbatch (to be “diluted” forms), the in situ “polymerization filling” methods may be the winners in the future.

9.3 Discontinuous Fiber-Reinforced Composites

The history of fiber-reinforced thermoplastic polymers began only some decades ago, when industrial production of the reinforcing fibers (glass in 1935, carbon in 1959, aramid in 1971) and adequate matrix polymers (e.g. PA-6.6 in 1938 and polyethylene terephthalate in 1955) was started. Incorporation of discontinuous fibers into thermoplastics generally yields improvements in mechanical and thermal properties, for instance, stiffness, strength, dimensional stability, service

temperature, resistance to creep and fatigue. These improvements are, however, connected with reduced strain (ductility) characteristics and pronounced anisotropy as a result of the structuring of the reinforcement in the molded parts.

Fiber reinforcement is the best way to transfer commodity or high volume thermoplastics, such as PP into engineering thermoplastics. It is noteworthy that the criteria for engineering thermoplastics—namely, continuous service temperature above 100 °C and tensile strength higher than 40 MPa [110]—can also be met by several plastics without reinforcement.

The relative high annual growth rate of fiber-reinforced composites compared to neat plastics is mostly the result of the substitution of metallic and ceramic items by compression-, injection-, and extrusion-molded composite parts manufactured from discontinuous fiber-reinforced polymers.

9.3.1 *Manufacturing*

The production of discontinuous fiber-reinforced PP composites is usually separated from that of the final shaping that occurs generally by injection molding. Accordingly, PP and the fiber (GF, CF and various NFs) are first processed into a granular, pelletized feedstock. For the incorporation of the fiber extrusion compounding is used. In the eldest version, the PP granules and chopped fibers (<10 mm length) are dry blended before feeding into the hopper of a single- or twin-screw extruder. The extruded composite, in filament (“wire”) form, is cooled and subsequently pelletized (diameter: ~3 mm, length: 3–6 mm). This operation results in severe breakage of the reinforcing fibers: the maximum length generally remains below 0.5 mm in the ready-to-mold granules. In a more advanced version, the fiber (either in chopped or in continuous form) is introduced through a suitable decompression port of the extruder in the already plasticized PP. When rovings, tows are added then the extruder screw also overtake the role of the cutter. In this case the fiber attrition is less severe and thus in the final product the fiber length may surpass 1 mm length. This is the right place to call the attention to the distinction between short and long fiber reinforced PPs: the mean fiber length is below 1 mm for short, while it is above this threshold for long fiber-reinforced grades. In many research works this definition is applied for the initial feedstock, whereas in others for the residual fiber length distribution in the molded parts. Recognizing the beneficial effects of long fibers (enhanced strength and impact resistance) various processes (“wire coating”, cross-head extrusion, different pultrusion methods (using powder coating or melt impregnations) were developed for the production of long fiber-reinforced (mostly long glass fiber, LGF) PP composites after the pioneering activity of ICI Ltd. in 1985 (introduction of Vertron™ types) [111]. In these processes continuous GF or yarns (composed of discontinuous fibers, such as NF variants [112]) are impregnated by the PP melt before cutting to ≤ 10 mm length. In long fiber-reinforced composites the wet-out of the fibers by the matrix is less

perfect compared to traditional compounding, and thus bunched, bundled fibers may be present in the molded items.

The development of discontinuous fiber-reinforced thermoplastics is well reflected by a steady increase in the aspect ratio (length to diameter, l/d) of the fibers both in the parent granules and molded parts. The l/d ratio of short fiber-reinforced grades produced by extrusion melt compounding technique was ≈ 20 earlier, nowadays it lies at ≈ 50 . The next milestone was achieved by pultrusion and powder coating techniques, through which granule size fiber length was set. In the related long fiber-reinforced injection and compression moldable grades the initial aspect ratio of the discontinuous reinforcement (usually GF) is ≈ 1000 and ≈ 2500 , respectively.

A further logical step was to avoid the preparation of the pelletized feedstock. This was solved by merging the preparation of the fiber-reinforced composite with that of its molding in line. Several attempts were made into this direction during modification of the injection molding machines. Although the feasibility of this approach was shown [113, 114] industrial breakthrough occurred when the final part was produced in compression molding [115]. As described in the next paragraph, PP-based GMT were substituted by directly produced long fiber reinforced thermoplastics (D-LFT). In the corresponding D-LFT systems the fiber length range is from 10 to as high as 25–50 mm.

There are some novel processing techniques for discontinuous fiber reinforced PPs, such as fused deposition modelling (FDM). In FDM the composite parts are produced by layer to layer deposition of the molten polymer. The reinforcing fibers in the deposited PP filaments, wires may be GF [116], CF and also NF [117].

The overwhelming majority of discontinuous fiber-reinforced PPs is processed by injection molding. Injection molding comprises the plastification of a given charge of the composite before its injection into a mold with cold walls. After cooling, the solidified parts are ejected and the cycle is repeated. By this way, parts of very complex shapes, with high dimensional accuracy can be produced at extreme high productivity (i.e. very short cycle times). The related machines are sophisticated, highly automatized ones. Injection/compression molding is rarely practiced: here first the melt is injected into the mold before it is subjected to the second compression step yielding the final product [118].

It should be born in mind that the mean fiber length and the fiber length distribution may markedly differ between the feedstock granules and the injection-molded items. Compounding and injection molding are accompanied with severe fiber breakage. This prominently reduces the tensile strength and impact properties. Fiber attrition is influenced by both material- (with increasing fiber content the fiber/fiber interaction is increasing) and processing-related factors (locally acting high stresses due to back pressure or injection speed, convergent and divergent flows at the nozzle, gate design, runner system of the mold etc.—all imposing critical stresses and contributing to fiber/“wall” (surface of the screw, barrel and mold) frictions. Fiber attrition due to various processing parameters was already the topic of works, especially in case of LGF-reinforced PPs [119–121]. Since the processing parameters affect mostly the strength and impact data, these

characteristics were considered when evaluating set changes in the processing [122–124]. Based on the experimental findings, Phelps et al. [125] developed a model to predict the breakage rate assuming that breakage is owing to buckling under hydrodynamic compressive stresses and some off-orientation of the fibers with respect to that of the flow.

All-PP composites can also be prepared by injection molding from chopped consolidated preforms of PP copolymer (matrix) and PP multifilament (reinforcement) [126, 127].

9.3.2 *Structure Development and Characterization*

Injection molding induces changes in the molecular orientation and crystallization behavior of neat PP [128]. This is also the case for the matrix polymer of short and long fiber reinforced grades. On the other hand, the effects of the skin-core structured matrix are masked by the molding-induced fiber structuring in the reinforced composites. The layering of the fibers and their orientation in each layer in the molded part is due to the melt flow within the mold. For the flow field consisting of shear and elongational flows, processing conditions are not the only important factors; the mold construction (sprue, runner, gate, and cavity geometry inducing converging and diverging flow during processing) is also relevant.

It is widely accepted that fiber orientation in discontinuous fiber-reinforced thermoplastics can adequately be described by the model of Tadmor [129], which involves the fountain or volcano effect discussed by Rose [130]. According to this model, the fiber orientation pattern produced by injection molding can be approximated by a three-layer laminate structure. This is depicted schematically and as it looks in practice in Fig. 9.4. In the surface (S) layers, fibers are oriented parallel to the mold filling direction (MFD). This is caused by the shear flow of the melt along the quickly solidified layer at the mold wall. In the central (C) layer, fibers adopt an orientation perpendicular to the MFD in the plane of the molded item. This kind of alignment is due to the elongational flow at the midplane of the cavity. Factors contributing to the mid-plane elongational flow are diverging flow at the cavity entrance and the fountain effect. The fiber layering can be even more complicated, since particulate fillers tend to migrate toward the mid plane of the molding, where flow speeds are higher [131]. This change, attributed to normal stress effects, again modifies the flow profile and thus the layering and orientation of the discontinuous reinforcement.

Figure 9.4 illustrates the designation of the compact tension (CT) specimens preferentially used. Note that the designation of the CT specimens considers the loading—notching (longitudinal, L or transverse, T) directions in respect to the MFD.

Results of numerous investigations carried out on injection-molded plaques (film-gate, 3–4 mm thick) indicate that ([132], cf. Fig. 9.5):

- Both the fiber layering and alignment increase with fiber volume fraction (V_f).
- The absolute values of the fiber orientation (see later) are closely matched in the S and C layers, and fiber orientation increases with V_f .
- The processing effects (melt, mold temperature, and injection speed) are of secondary importance compared with V_f .

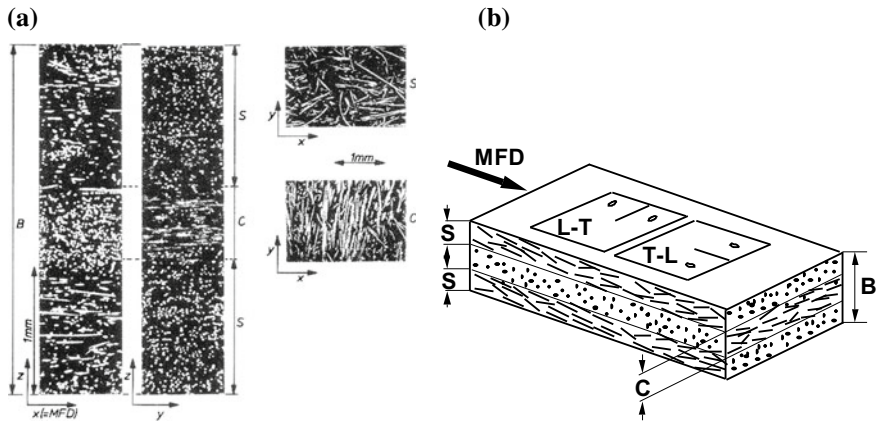


Fig. 9.4 Fiber orientation resulting from injection molding **a** for 40 wt% (=19.4 vol%) long GF reinforced PP; **b** flow induced fiber layering schematically along with specimens (compact tension) preparation. Designations: B—specimen (cavity) thickness, C—central layer thickness, S—surface layer thickness

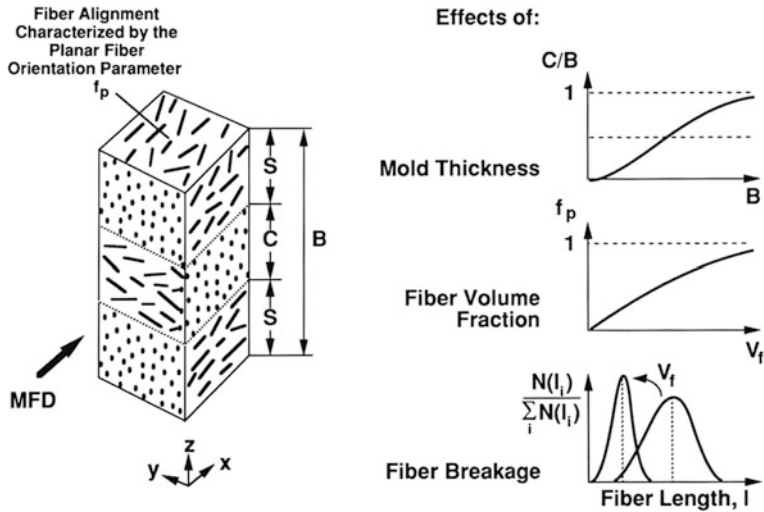


Fig. 9.5 Effects of cavity thickness (B) and V_f on the layering, planar orientation (f_p) and mean fiber length of injection molded discontinuous fiber-reinforced composites

For thinner or thicker items, which in addition involve other gate constructions, these statements are not always valid.

Microstructural investigations carried out on LGF reinforced injection-molded thermoplastics showed significant analogies with short glass fiber (SGF) composites [133–135], namely: (i) the relative thickness of the C layer increases with increasing aspect ratio, and (ii) fiber bending and bunching may occur.

Fiber bunching is connected with the pultrusion pelletizing process used for the production of LGF-reinforced injection moldable composites. Both of the effects of fiber bending and bunching reduce the effective aspect ratio of the reinforcement in the molded part [133, 135].

The aspect ratio of the fibers in the molded item depends on material factors (especially V_f), mold geometry, and processing parameters. Higher fiber loading shifts the aspect ratio distribution curve toward lower values as a result of increased fiber/fiber and fiber/wall interactions causing fiber fracture. This effect is much less pronounced for LGF than for SGF reinforced composites, provided that mold construction for the former system is adequate. It is due to the preliminary orientation of the fibers during manufacturing. The aspect ratio distribution curve of the reinforcement may differ when various layers across the thickness of the molded part are considered [133]. This is mainly due to fiber enrichment in the C layer, differences between bunching and filamentization in the S and C layers, and effects of the flow field on fibers with different aspect ratios.

Distinction between the S and C layers becomes more problematic when in PP composites with compliant NFs or PP fibers, especially at high fiber loading [126, 127].

For the flow features and microstructural development in discontinuous fiber-reinforced thermoplastics, detailed information can be taken from the Ref. [136].

The above treatise makes clear that the microstructural parameters of reinforced injection-molded composites are fiber layering, fiber orientation (they are commonly termed fiber structuring), V_f , effective fiber aspect ratio and its distribution.

For the determination of fiber layering by imaging of polished sections or thin slices via light (reflective or transmission), scanning electron microscopy (SEM), and contact microradiography are preferred. For fiber orientation, microwave, X-ray diffraction, sonic, and thermographic measurements can also be used. A novel powerful technique is the X-ray computed (micro)tomography [137] allowing us to determine both the fiber length and fiber orientation distributions spatially [138–140].

Recall that in Fig. 9.4, a SEM micrographs taken from polished sections along the thickness-MFD ($z-x$) and $y-x$ planes are shown. The evaluation of fiber alignment and mean fiber orientation in a given plane is very time-consuming, as it involves determining the angle distribution under which fibers are aligned. In this respect, image analysis offers the new possibility of getting information about not only in-plane but also spatial orientations [141]. Fiber orientation can be described

either by using mean orientation factors, such as Hermans [142, 143], Krenchel [144], or by vectors [145].

The aspect ratio (since the diameter of the fibers is mainly constant, it can be replaced by fiber length) distribution curves are generally determined from microphotographs of the fibers taken after burning away the matrix. In many cases the matrix polymer can also be removed by solvents.

The above-mentioned microstructural parameters are summarized in a reinforcing effectiveness term (R). This term previously considered the effects of fiber structuring with respect to the loading direction and the fiber loading [146]. This was extended later to include the aspect ratio and aspect ratio distribution [132, 133, 135], and generalized in the form (Eq. 9.1):

$$R = \sum_i T_{rel,i} \cdot f_{p,eff,i} \cdot V_{f,i} \left(\frac{l}{d} \right)_{equ,i} \frac{\left(\frac{l}{d} \right)_{n,i}}{\left(\frac{l}{d} \right)_{m,i}} \quad (9.1)$$

where $T_{rel,i}$ is the relative thickness of the i -th layer normalized to the sample thickness (B), see Figs. 9.4 and 9.5), $f_{p,eff,i}$ is the effective orientation in the i -th layer calculated using the function of planar orientation (f_p) versus $f_{p,eff}$ introduced by Friedrich [146], $V_{f,i}$ is the fiber volume fraction in the i -th layer, $(l/d)_{equ,i}$ is the equivalent aspect ratio in the i -th layer, $(l/d)_{m,i}$ and $(l/d)_{n,i}$ are the mean mass- and number average aspect ratios in the i -th layer, respectively [133].

The reinforcing effectiveness, and the corresponding microstructural efficiency (see later) concepts worked adequately when considering the fracture mechanics-related parameters of discontinuous fiber-reinforced PPs [68, 132, 135]. On the other hand, it can be prophesized that X-ray tomographic inspections along with the related image analysis will give a new impetus to determine or redefine the reinforcing effectiveness parameter.

9.3.3 Properties and Their Prediction

The performance of discontinuous fiber-reinforced composites, including PP-based ones, was already the topic of several books, book chapters and reviews [135, 147–149]. Therefore, next the state of knowledge will be summarized on selected properties thereby considering the molding-induced structuring of the discontinuous reinforcements.

9.3.3.1 Mechanical Response

Tensile tests

The mechanics of discontinuous fiber-reinforced composites is more complex than continuous, aligned fiber containing ones because in the former case the fibers

have different length and spatial orientation. Therefore, the distributions of fiber length and orientation should be considered when modeling the physico-mechanical properties. The “shear lag” theory of Cox [150] assumes that both the fiber and matrix behave as elastic bodies and perfect bonding exist between them along a cylindrical interface. As a consequence, differences in the strain displacements appear in the fiber and matrix along the interface. Though the tensile stress development in the fiber is realistic, the shear strength should fall to zero at the fiber ends instead of showing a maximum according to this model. A further deficiency is that the interface strength is disregarded though it may cause debonding or yielding—associated with subsequent stress redistribution—when the interface or the matrix is weaker. According to the Kelly-Tyson approach [151] the interface strength is balanced by that of the fracture strength of the fiber. The stress builds up from the fiber end toward the middle part is similar to that of the Cox model, but the increase is linear up to a point (stress transfer length) where no strain difference will be between the matrix and fiber. Both models adequately predict the course of the reinforcement efficiency as a function of the fiber aspect ratio. Provided that the fibers are aligned parallel to the applied stress then the E-modulus of the composite (E_c) can be calculated by the modified “rule of mixture” (Eq. 9.2):

$$E_c = \eta_1 E_f V_f + E_m V_m, \quad (9.2)$$

where η_1 is the fiber length efficiency factor representing the average stress in the short divided by the stress in the continuous fiber composite at a similar applied strain [152], E_f, E_m —E-modulus of fibers and matrix respectively; V_f, V_m —volume fraction of fibers and matrix respectively. This equation was refined by Bader and Bowyer [148, 153, 154] who considered that the reinforcing efficiency is a function of the applied strain, as well. Equation (9.2) can be further refined to take the fiber orientation into account:

$$E_c = \eta_0 \eta_1 E_f V_f + E_m V_m \quad (9.3)$$

where η_0 is the mean angle of the fibers to the loading direction. Its value is 1, 0.375 and 0.2 for uniaxial, planar random and spatial random orientations, respectively [148]. Equation (9.3) proved to be useful to estimate the E-modulus of mat-reinforced PP composites [152]. The most popular model to predict the stiffness is credited to Halpin and Tsai (Eqs. 9.4 and 9.5) [155]:

$$E_c = E_m \left(\frac{1 + \xi \eta V_f}{1 - \eta V_f} \right), \quad (9.4)$$

where

$$\eta = \frac{\left(\frac{E_f}{E_m}\right) - 1}{\left(\frac{E_f}{E_m}\right) + \zeta}, \quad (9.5)$$

where η —efficiency factor; ζ —measure of reinforcement geometry which depends on loading conditions.

Its wide use is due to the fact that by suitable choice of the two constants, the Halpin-Tsai equation allows predictions anywhere between the Voigt upper (ζ is infinite) and Reuss lower bound (ζ is zero) rules of mixture equations. Based on the Halpin-Tsai approach Garesci and Fliegner [156] modeled the E -modulus of direct LFT-PP composites whereby considering the V_f , fiber orientation and fiber length distributions. The two latter distributions were assessed in X-ray microtomography and quantified. It is noteworthy that many other equations, already listed for nanocomposites, have been developed and adapted for discontinuous fiber-reinforced PP composites.

The strength prediction is more problematic than that of the stiffness due to the different failure events which may happen even when the fibers are uniaxial aligned (debonding with cavitation, matrix fracture, crazing, plastic flow—all at the fiber ends) [148]. This is the possible reason why for optimization of the tensile strength of discontinuous fiber-reinforced composites experimental methods (design of experiments) are used [157]. Though many approaches have been recommended for aligned short fiber composites, one of the most popular ones is based on the Kelly-Tyson equation [152] that considers that the failure is different for fiber below and above the critical fiber length. Since the critical fiber length (aspect ratio) is linked with the interfacial shear strength, this is the right place to comment how it can be tailored. An interfacial shear strength of 4–6 MPa is fairly typical for the adhesion between unmodified PP and GF without specific sizing [152, 158]. Similar values have been reported also for composites with other fibers than GF [159]. These values are, however, far less than shear strength of the PP (when estimated as the half of the yield strength; 15–16 MPa). Values closely matched with the shear strength of PP can be reportedly reached when to the PP matrix a suitable coupling agent (almost exclusively maleic anhydride grafted PP, PP-g-MA) is added and the GF is sized by an appropriate silane [160]. In case of crystalline fibers, such as CF [161], NF [162] and even PP (in case of all-PP composites [163]) a TC layer may form on their surfaces (Fig. 9.6).

The related one-dimensional spherulitic growth is caused by the fiber surface-induced dense heterogeneous nucleation of the crystallizing PP. The TC layer is often quoted for improved stress transfer which is, however, not always experimentally evidenced [46, 164]. It is worth of noting that various surface

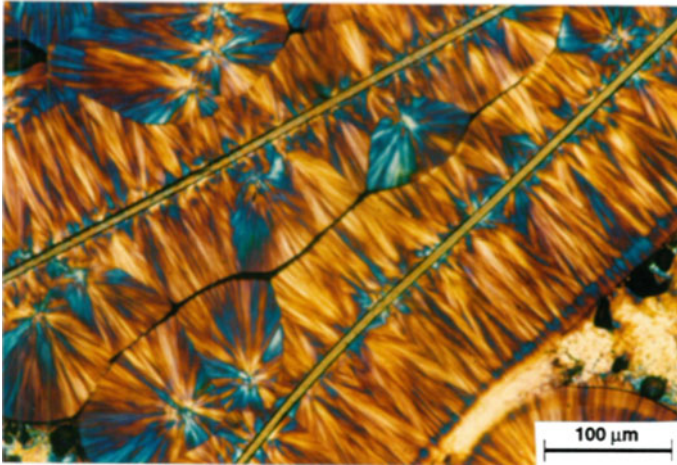


Fig. 9.6 Transcrystalline PP layer formed on the surface of aramide (Kevlar™ 29) fibers. Note: crystallization in quiescent melt at 133 °C

modifications are used for NFs to improve their bonding to PP [165]. Hybridization of fibers is an often practiced tool for property improvements [166]. NFs are hybridized with man-made fibers in order to enhance the strength and reduce its scatter [167]. Nowadays, discontinuous fibers are combined with micron- [168], and especially nanoscale fillers [169, 170] in order to tailor the mechanical and thermal properties of the related composites.

Fracture behavior

Results from standardized toughness testing methods can only be compared when all the specimen- and testing-related conditions are identical. By contrast fracture mechanics may yield toughness which is a material property, i.e. independent of specimen's and testing configurations (but still temperature and frequency dependent). Fundamental aspect of fracture mechanics is that the onset of fracture depends not only on the applied stress but also on intrinsic flaws that act as stress concentrators. Such stress concentration sites are always present in neat and reinforced molded plastics, either as a result of processing or caused by use. The common effects of stress and flaw size are combined in linear elastic fracture mechanics (LEFM) which deals only with bodies that obey the Hookian law, that is, whose deformation is fully elastic. The related terms are the stress intensity factor (K) or fracture toughness and strain energy release rate (G) or fracture energy.

The main criterion of LEFM, namely fully elastic deformation, is very severe for plastics that may undergo pronounced plastic deformation (yielding or tearing) during fracture. In this case, other approaches, are pursued for plastics: J-integral, crack opening displacement, and EWF [171, 172]. These material parameters are included in plastic, elastoplastic, or post-yield fracture mechanics (PYFM). Fracture mechanics methods are aimed at determining that critical parameter at which unstable (LEFM) or stable crack growth (PYFM) takes place.

Fiber reinforcement may affect fracture toughness in different ways. It can be improved, worsened, or held at a constant level by fiber incorporation, depending on the matrix of the composite [132]. The layering and orientation of the fibers in injection-molded items were already shown in connection with Figs. 9.4 and 9.5. On the fracture surface of the specimens, fibers lying parallel or longitudinal to the crack plane (L fibers) can clearly be distinguished from those oriented perpendicularly or transversely to it (T fibers) (Fig. 9.7).

Note that the anisotropic structuring of the fibers yields different fracture mechanical values when specimens with various notch directions (T and L; see Fig. 9.4b) are tested [132, 134, 146]. The load bearing capacity of T fibers aligned in the load direction is considerably higher than that of the L fibers, which have practically no reinforcing effect. Therefore, the fracture mechanical response depends on the relative thickness of the layers containing T and L fibers, respectively.

The degree of fiber orientation in these layers is also important. T fibers completely aligned in the load direction guarantee the best stress transfer and thus the greatest reinforcement. Fiber misalignment along the load direction necessarily reduces the overall reinforcing effect. Friedrich introduced an effective fiber orientation term that takes this fact into account [146].

The influence of fiber aspect ratio on fracture toughness at a given fiber loading depends also on the matrix characteristics. However, with increasing fiber aspect ratio K_c always increases, at least above a given threshold l/d . This is connected with an increase in the performance of the discontinuous-fiber-reinforced composites, since their strength increases with increasing aspect ratio [147].

Recall that all above listed parameters, governing the fracture behavior, were included in the reinforcing effectiveness (R) term. Thus, the fracture mechanics parameters should depend on the R term for discontinuous fiber-reinforced PP composites. This has been proven for both SGF- and LGF-reinforced systems subjected to static [134, 173] and dynamic conditions [174]. Figure 9.8 shows an

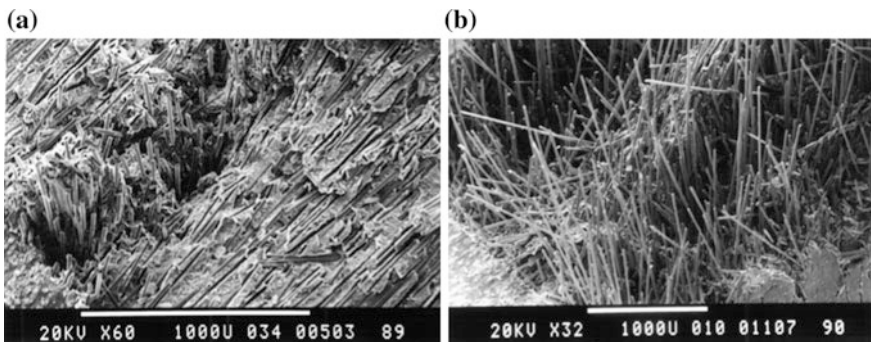
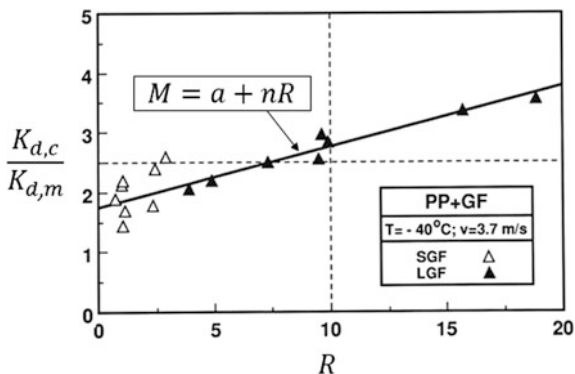


Fig. 9.7 Fracture surface at the razor notch of 40 wt% (=19.4 vol%) SGF (a) and LGF (b) reinforced injection-molded PP. (In this T-L type CT specimen, L fibers can be found on the surface, whereas T fibers in the central layer, as indicated; cf. Fig. 9.4)

Fig. 9.8 Relative dynamic fracture toughness ($\frac{K_{c,d}}{K_{c,m}}$) as a function of the reinforcement efficiency factor R for short and long GF-reinforced PP composites. Notes: V_f content up to 40 wt%; testing conditions: $-40\text{ }^\circ\text{C}$ at 3.7 m/s impact speed (based on [175])



example of high-speed impact tests results that the relative change in the dynamic fracture toughness of the composites compared to the matrix can follows a linear relationship as a function of R (Eq. 9.6):

$$\frac{K_{c,d}}{K_{c,m}} = M = a + nR, \tag{9.6}$$

where M is the microstructural efficiency, a —stress condition factor considering that the matrix fails differently when reinforced than without, n is the energy absorption coefficient, and R is the reinforcement effectiveness.

It is noteworthy that the microstructural efficiency concept worked also properly for the J-integral data of PP composites [173]. It has to be emphasized that dynamic failure mechanisms are the same as those shown and discussed with respect to static loading. Although failure mapping is seldom performed for dynamic measurements, the following effects can be predicted: (i) the frequency embrittlement of the PP matrix promotes brittle matrix cracking, eventually associated with limited craze formation (frequency-dependent T_g), (ii) among the fiber-related failure events, fiber pullout and fracture tend to dominate. Their relative proportions depend not only on the testing conditions but also on the fiber-matrix bonding.

Fatigue

Discontinues fiber-reinforced PP composite parts are widely used in fields in which cyclic subcritical (i.e. fatigue) loading occur. The fatigue performance can be characterized either by the endurance limit (maximum allowed applied stress causing no damage after 10^6 fatigue cycles) or by parameters of the fatigue crack propagation (FCP) curves. The FCP approach is based on the fracture mechanics, i.e. accepting the presence of inherent flaws, inhomogeneity. Such flaws may act as initial cracks and thus the life expectation of the related parts is controlled by the FCP behavior. If the controlling step is, however, the development of crack (or more generally some kind of damage) then the fatigue endurance limit has to be determined via Wöhler curves. To measure the Wöhler curves specimens are subjected to cyclic loading at different maximum stresses at a given loading

configuration. Its modeling is a great challenge because the actual damage mode and sequence should be known and properly parametrized [176].

The fracture mechanics approach can be applied for cycling fatigue of notched specimens. During fatigue slow crack growth occurs under subcritical stress amplitudes; that is, the stress intensity factor amplitude remains below that of the critical value (K_{Ic}). In FCP the crack growth rate per cycle is established as a function of the stress intensity factor amplitude (ΔK). A threshold value ΔK_{th} , which is connected with the onset of fatigue growth, can be read from the FCP curve and may serve for design purpose. After this threshold a stable crack propagation range can be usually found for which the Paris-Erdogan relationship holds (Eq. 9.7):

$$\frac{da}{dN} = A(\Delta K)^m, \tag{9.7}$$

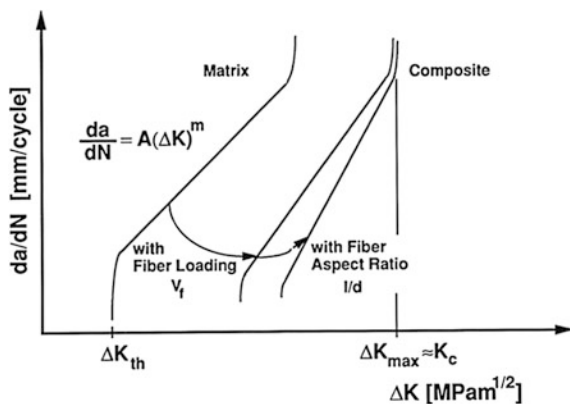
where A is the pre-exponential factor, ΔK is the stress intensity amplitude and m is the exponential term. Note that $\frac{da}{dN}$ can be plotted also as a function of ΔG instead of ΔK [177].

According to the experiments [178–180], the controlling parameters of the FCP behavior are V_f , molding-induced layering (reflected by the notching of the specimens with respect to the MFD) and fiber aspect ratio. Their effects are schematically depicted in Fig. 9.9.

Figure 9.10 makes obvious that LGF extends the damage zone compared to the SGF counterpart thereby improving the resistance to FCP.

Note, however, that all the above parameters are involved in the R -term. Accordingly, there is a good correlation between the crack growth rate and the reinforcing efficiency (R): increasing R results in an improved resistance to FCP. Moreover, it has been shown that $\log(\frac{da}{dN})$ versus $\log M$ data pairs lay on a straight line, also for discontinuous GF-reinforced PP composites [181].

Fig. 9.9 Changes in the stable FCP behavior due to microstructural parameters, schematically. *Note:* Scheme in double logarithmic scaling [181]



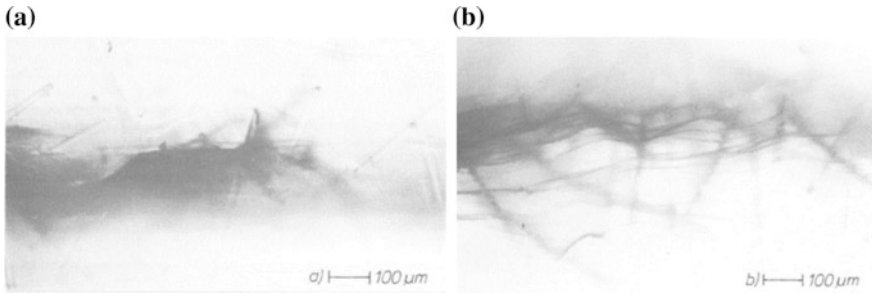


Fig. 9.10 Transmitted light pictures on the crack tip damage zone showing the matrix- (craze bands) and fiber-related (stress concentration at fiber end, debonding, pull-out) failure events in 10 wt% SGF (a) and LGF-reinforced PP (b), respectively [178]

Creep

The long-term creep behavior is of paramount importance since many composite parts have to withstand to a constant load during their lifespan. Different models have been proposed and adapted for thermoplastics like PP [182, 183] and their discontinuous fiber-reinforced composites [184, 185] to describe their creep behavior. Exploiting the viscoelastic feature of polymeric materials, the preferred way is to increase the temperature to accelerate the time dependence of the creep and create master curves based on the time-temperature superposition principle (TTSP). Accordingly, short-term creep experiments, performed at various temperatures, are used to create a master curve, which describes the long-term deformation at a reference temperature. Usually, the Williams-Landel-Ferry [186] or the Arrhenius equation, or a combination of them, are applied to determine the shift factor that is needed for the construction of the long-term master curve (supposing load and time independent shift factor parameters). Based on short term measurements such as tensile ($\varepsilon_2(t_2)$) and creep ($\varepsilon_1(t_1, t_0)$) tests of $t_M = 10$ h performed on PP/GF samples at different load levels ($\sigma(t_0) \rightarrow \varepsilon_0$) Vas and Bakonyi [182, 185] developed a novel statistical phenomenological method for modeling the creep process (ε_1) and assessing the statistical properties of the creep strain (ε_{1B}) and lifetime (t_{1B}) to failure. A kind of load-time superposition principle realized by nonlinear symmetry (R) and variable transformations (S_1, S_2) was used to approximate the mean creep-strength curve ($\varepsilon_{1B}-t_0$ or $\varepsilon_{1B}-t_{1B}$) and the whole mean creep process as a master curve ($\varepsilon_{1B}(t_0): t_0 \leq t_1 \leq t_{1B}$) at arbitrary creep load levels ($0 \leq t_0 \leq t_{2B}$) also outside the measuring range (Fig. 9.11). Weibull based probabilistic approach enabled to estimate the confidence intervals of the curves and the creep failure data. The method can be applied to modeling the stress relaxation process as well.

Fracture mechanics approaches can also be used to study the time dependent crack growth at constant load, termed as to static fatigue (Eq. 9.8):

Computer aided design (CAD) is a technique that has been successfully applied to optimization of mold construction for molded parts. In CAD design of an injection-molded part, the first step is to visualize the weak sites, that is, the weld lines. The next step is to change the position and/or type of runner and gate so that weld lines do not evolve or, if this is impossible, are positioned where low stresses in the part during service can be predicted. The next phase is modelling the flow in the mold, subdivided into FEs, and characterizing the melt flow patterns in these mold segments. For the calculation of the flow patterns, rheological parameters, determined experimentally or estimated by the software, are used. The flow modelling is repeated in several steps until optimized mold filling occurs. The aim is to get the same material flow in all segments of the mold resulting in smooth surfaced, warpage-free products with controlled shrinkage [192].

9.3.3.3 Thermal Properties

As mentioned before, crystalline reinforcing fibers usually work as heterogeneous nucleants and even may promote TC growth. Due to this nucleation, the undercooling (supercooling), meaning the temperature interval between the melting and crystallization of PP, is reduced. As a consequence, injection molded parts may be earlier ejected thereby increasing the productivity. Similar to nanocomposites, incorporation of discontinuous fibers markedly enhances the HDT. Parallel to that also the thermal expansion coefficient is reduced. On the other hand, the thermal expansion coefficient may show a strong direction dependence owing to the fiber local orientation.

To enhance the thermal conductivity, hybridization of GF and NF with CFs and with suitable micro- (such as boron nitride) and nanofillers (CNT, GR, inorganic “fullerenes” [193]) are the preferred strategies. Based on results achieved by PP/CF composites it was reported that the polymer coupling agent (PP-g-MA) does not affect the thermal conductivity [194]. Modeling of the thermal conductivity followed the theories developed for the mechanical behavior of short fiber composites [188, 195, 196]. The byside effect of the fiber/nanofiller hybridization is often an enhanced resistance to thermal degradation. Like to nanocomposites [197], this improvement is traced to the formation of a protective char layer on the burning surface and/or to an enlarged diffusion path of the burnable volatile degradation products from the bulk toward the surface.

PP is an easy burning material due to its high carbon and hydrogen contents. Therefore, flame retardants are incorporated when the specification in the related application field requires a flame retarded PP grade. Though different classifications exist [198], the flame retardants work either in the gaseous or in the condensed phase via various chemical and physical mechanisms interfering with that of the combustion. The flame retarding effect of $\text{Al}(\text{OH})_3$ and $\text{Mg}(\text{OH})_2$ is due to their endothermic degradation whereby water is released which “cools” the flame and dilutes the composition of the burning pyrolysis gas. Unfortunately, their required amount may be as high as 65 wt% in order to meet the V-0 rating of the UL94

classification [199]. This high loading is undesirable having a negative impact on the processability and mechanical properties of the related composite. The nowadays preferred phosphorous containing flame retardants act in the gas, and eventually, also in the condensed phase (char formation). Its amount may be below 5 wt% P-content in a fire-proof PP. Intumescent coatings form a carbonaceous foamed mass when exposed to heat, and work as a heat shield and barrier layer against the diffusion of the evolved degradation products [106]. It is noteworthy that NFs, being combustible themselves, may cause a “candlewick” effect that should be depressed by suitable surface treatments [200]. Vadas et al. [201] investigated the effect of ammonium polyphosphate in an injection-moldable all-PP composites. The LOI was enhanced from 18 to 29.5% and the UL-94 classification changed from HB to V-2 when the composite contained 15 wt% ammonium polyphosphate flame retardant.

9.3.3.4 Other Properties

Some application fields, such as bipolar plate in fuel cells [202], housing of electronic devices (electromagnetic interference (EMI) shielding [203], require electric conductive PP composites. For this purpose, generally PP/SCF (short carbon fiber) composites have been prepared. For high conductivity the requirement is to reach the percolation threshold. The percolation threshold is assigned to a long-range connection of randomly distributed particles. PP/SCF conductive composites showed a conductivity of 10^{-6} S/m when containing more than 3 wt% of CF, and an optimal EMI shielding efficiency of 25 dB when containing 20 wt% of CF [204]. The percolation threshold loading can be reduced when conductive fillers (any kind) with different aspect ratios are simultaneously present. This hybridization strategy is now exhaustively followed. The related development is fueled also by the need of electric conductive filaments for FDM. Krause and Pötschke found for example that electric (and thermal conductive) PP composites can be produced at low SCF/carbonaceous nanofiller (MWCNT or GR) loading (7.5 vol%) [205].

9.3.4 Processing and Applications

Among the guidelines for processing of short and long fiber reinforced thermoplastic, priority is given to processing parameters and mold constructions that contribute to preserving the initial aspect ratio, that is, the fiber length of the reinforcement. Avoiding fiber breakage requires molding at minimal frictional heating. On a given reciprocating injection molding machine this can be achieved by slow screw rotation, low injection speed, low back pressure, and high barrel temperature. Processing of LGF reinforced thermoplastics is very similar to that of SGF composites. It is recommended, however, to choose a 10–20 °C higher barrel temperature and a special “low work” screw. This screw is characterized by a long

feed section with constant root and wide, deep flights. This section is followed by a low gradual compression zone without kneading or mixing elements; the screw ends in a constant-root metering section with flat flights. In addition, certain aspects of mold construction have to be considered (short runners, large film or fan gates).

Service conditions for short fiber reinforced thermoplastic composite parts often require a given well-defined fiber structuring. For injection-molded items, a new technique called multiple live-feed injection molding was developed. In this method, a packing head is inserted between the mold and the head of the injection-molding machine. The melt flow, and thus fiber orientation in the packing stage, can be modified accordingly by a programmable movement of the pistons of the packing head that pressurizes the solidifying melt directly [206]. A similar approach, called dynamic packing injection molding, has been developed recently [207]. In this method oscillatory shear is imposed on the gradually cooled melt during the packing, solidification stage. Albeit this yields some reduction in the mean fiber length, the improved orientation of the fibers and that of the matrix compensate this effect and results in strongly enhanced tensile strength compared to conventional injection molding for both SGF- and LGF-PPs. In injection molded parts the development of weld lines (“cold” and “hot” ones whether the melt streams are opposed or merging side by side) can hardly be avoided. In order to diminish the parallel layering of the fibers in the weld line several processing options, such as “push-pull” injection molding, sequential filling [208] are possible.

The application of short and long fiber-reinforced PP composites is very broad covering practically all sectors. Long fiber-reinforced versions are preferred composites for automotive applications. Nowadays, substantial efforts are made to reinforce PP with recycled discontinuous CF and use them in the automotive sector [209, 210].

9.4 Mat-Reinforced Composites

Mat-reinforced thermoplastics (MRT), belonging to the family of “organosheets”, are usually defined as semi-finished blanks consisting either of continuous or discontinuous (chopped) long fiber mat impregnated with a thermoplastic polymer. Final shaping of these blanks, cut to size, occurs mostly in hot flow (compression) molding for which the blanks are preheated.

MRT sheets were first presented in the 1967 by PPG Industries and Union Carbide under the trademark Azdel[®] as an alternative material to stamped metal for economical production of large parts [211, 212]. Short cycle time (20–60 s), as well as superior mechanical properties together with low weight, allowed MRT to occupy a niche of semi-structural elements in the automotive industry.

Physical and mechanical properties of composites are strongly affected by numerous factors: nature of the reinforcement and matrix, content and architecture

of the reinforcement, adhesion between reinforcement and matrix, etc. Reinforcement in the form of mat delivers MRT mechanical performance that place it between short fiber injection molded and advanced long fiber reinforced composites [213]. Although MRTs are available with various polymeric matrices: poly (butylene terephthalate), poly(ether imide), polycarbonate, PA-6, etc.—the most popular, due to a low price and widespread availability, is PP. Fibers of different nature could be used for MRT—GF, CF, NF, etc.

Traditional and still most popular reinforcement type for MRT is GF mat. The corresponding organosheets are called as GMT. GFs ensure MRTs with a tensile strength in the range of 68–108 MPa, and modulus in the range of 3.9–6.2 GPa. Such level of mechanical performance stipulates typical application of GMT in automotive for semi-structural parts, e.g. undercover, seat back frame, load floor, etc. Mat architectures determine mechanical performance of GMT. For instance, short chopped fibers provide better surface finish as well as filling of deep complex mold cavity, while continuous randomly oriented fiber mat gives high stiffness and impact strength [214]. First serial produced GMT part—front-end for Chevrolet Monza—dated back to 1975 [215]. Since that time GMT has been successfully implemented for decades, and today is commercially produced by a number of companies. The best known tradenames are: Azdel[®], Symalite[®], Isosport[®], Elastopreg[®] and others.

Recently, the focus of research has been shifted toward NFs as prospective reinforcements for ecologically friendly composites. Respective MRTs are named as natural mat thermoplastics (NMTs). Despite of certain advantages of NFs covering wide availability, low cost and density as well as ecofriendly image, the mechanical properties of NFs are generally lower than those with man-made reinforcements. Thus, NMT with hemp, jute or flax fibers exhibits almost half of the tensile strength of GMT. At the same time, the tensile modulus of hemp or flax fiber reinforced NMTs is comparable with that of GMT. Moreover, NFs have more than twice lower density than GF, therefore demonstrating better specific (relative to density) properties. The last fact enables application of NMTs in cars, but restrains it for non-structural parts enduring minimal loads. Possible applications of NMTs could be door panels, sun visors, spare-tire covers, seat foundations, instrumental panels, etc.) [216]. Commercially available NMT sheets are either melt impregnated or semi-finished needle punched mats.

Lack of the examples of carbon mat thermoplastics (CMT) could be explained by the infeasibility to fully implement the superior structural properties of CF in the form of mat. Nonetheless, CMT could be a prospective solution for the application of recycled CFs.

All-PP or “self-reinforced” PP (SR-PP) composites containing mat reinforcements have also been produced [217]. In these cases, the processing window was ensured by using random PP copolymers [218] or beta PP homopolymer matrices [217].

9.4.1 Manufacturing

Manufacturing of MRT sheets originally occurred earlier in two distinct phases: mat production and its impregnation to produce semi-finished blank. However, recently integral solutions combining these two processes have appeared. They are named as ‘direct’ processes which were already introduced in the previous section.

Sheets production techniques could be specified according to the mat placement’s approach—dry-laid or wet-laid (melt impregnation and slurry deposition method respectively) [219]. The *dry-laid* technique implies one step impregnation and lamination of the reinforcement mat in a double-belt press (DBP). The consolidated sheet has a thickness of 2–4 mm. They can be divided into two grades—*stampable* and *hot flowing* (Fig. 9.12). *Stampable* versions contain chemically bonded swirl mat composed of endless fiber rovings. Such mat structure restricts the deformability of the material during stamping. As a consequence, the molded part

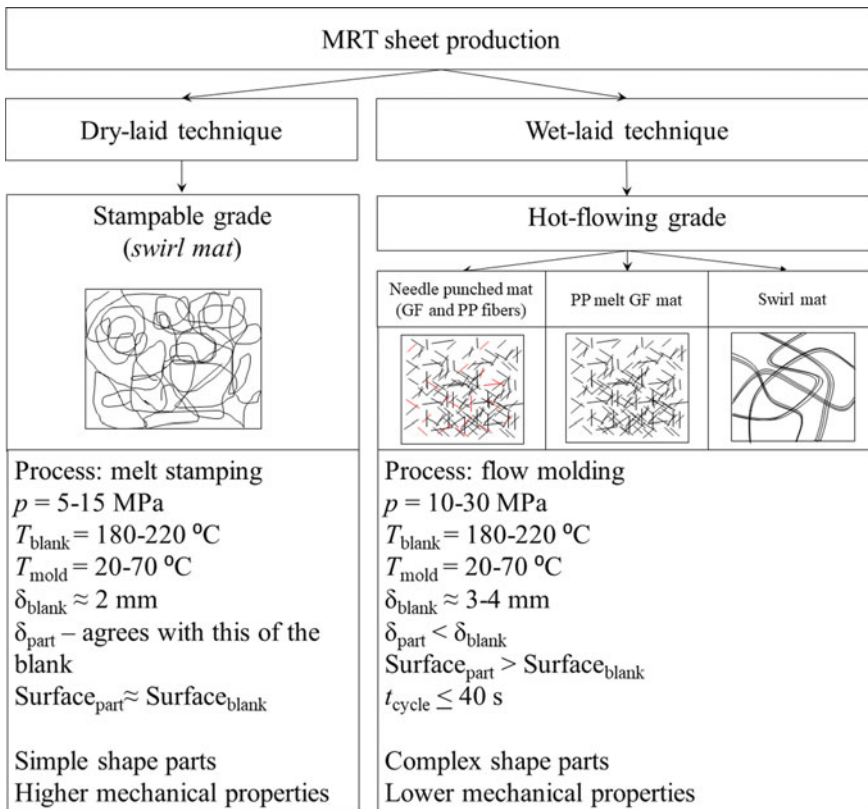


Fig. 9.12 Methods of the production of MRT sheets and its manufacturing technologies: p —pressure; T_{blank} , T_{mold} —temperature of the preheated blanks and the mold, respectively; δ_{blank} , δ_{part} —thickness of the blank and part; t_{cycle} —cycle time

surface area as well as thickness does not strongly differ from those of the blank. In other words, the complexity of the part's shape is limited. *Hot flowing* grade MRTs are formed by needling of discontinuous or continuous fibers. They exhibit good deformability when manufactured to the final parts. Eventually, complex parts containing ribs, thickness alteration and inserts could be molded. Although hot flowing grade MRTs provide lower mechanical performance than stampable ones, they dominate the market. This is due to the offered design freedom and high productivity (very short cycle times).

Wet-laid methods originated from papermaking industry. Among them the *slurry* and *foam deposition* techniques should be noted. Both techniques imply mixing of the PP powder or fiber with chopped reinforcing fibers, water and binder, depositing the corresponding blend on a moving conveyer belt and draining. These steps are followed by drying, heating, cooling, compacting and consolidation of the organosheets. In *slurry deposition* method the raw materials are dispersed in a very large quantity of water. In the resulting MRTs the reinforcing fibers are “fully” impregnated. By contrast, *foam deposition* method involves dispersing of aqueous foam, thus enabling to produce *partially consolidated* MRT. The term ‘*partially consolidated*’ means, essentially, that fibers are impregnated by the polymer only locally. So the resin acts as a binder, bundling the fibers together and forming 3D skeleton structure, that exhibits higher (comparatively to monolithic) specific flexural properties [220]. Partially consolidated GMTs are developed by Hanwha Azdel (SuperLite[®]), Quadrant (SymaLite[®]—product, consisting of GF and thermoplastic fibers) and Owens Corning.

9.4.2 Structure Development and Characterization

Conventional MRT part forming

The manufacturing process of MRT parts comprises blank cutting, its preheating to the melting temperature and compression molding. Preheating of the sheet could be implemented by IR radiation, hot air convection or contact thermal conductivity. Selection of the preheating depends mostly on the type of the reinforcement and mat production's method. For example, GMT as well as melt-impregnated NMT could generally be heated either by IR radiation or by air convection. However, the story is different for needle punched NMT, that needs longer heating time, and, as a consequence, should be heated by conduction [216].

Typical *hot stamping* process parameters, required to form a part with swirl mat MRT, are the following: pressure—5 to 15 MPa, blank temperature—180 to 220 °C, mold temperature—20 to 70 °C. The thickness and surface area of the resulting composite parts conforms those of the blanks [219]. In contrast, *hot-flowing grade* mat require higher pressure, usually 10–30 MPa. The final composite part has lower thickness comparatively to the blank, and higher surface area. The cycle time does not exceed 60 s.

MRT production line comprises the following units: tray for organosheets, preheating oven, feeding unit, press with the mold, removal robot and, optionally, postprocessing unit. Transfer between different line components can be implemented manually, but in most cases is carried out automatically by robots and conveyers.

Partially consolidated MRT

In conventional MRT sheets the reinforcement is well impregnated (though void content may reach several %), while partially consolidated MRT exhibit 3D framework structure. Partially consolidated MRTs are also referred as lightweight reinforced thermoplastics (LWRT) and produced with the areal density as low as 1200 g/m². In contrast, the areal density of traditional MRTs ranges between 2000 and 2500 g/m².

Due to springback effect stipulated by the fiber relaxation during the preheating of LWRT, the thickness of the composite part could be up to six times higher than that of the original organosheet. This issue provides three positive effects:

- Relative to the mechanical performance, higher thickness accompanied with lower density delivers the composite higher specific bending stiffness. This could be easily illustrated by the following expression (Eq. 9.9):

$$\bar{S} = \frac{S}{\rho} = \frac{E}{\rho} \cdot I = \frac{E}{\rho} \cdot \frac{bh^3}{12}, \quad (9.9)$$

where \bar{S} – specific bending stiffness, S – bending stiffness, ρ – density, E – flexural modulus, I – axial moment of inertia, b – part cross section width, h – part cross section height. Note, that expression is written for the rectangular cross section.

- With respect to the manufacturing process a lower pressure (less than 0.5 MPa) than for traditional MRT is required. The related technology is therefore essentially thermoforming, that—besides evident process simplification—permits integration of functional and decoration surfaces in one shot.
- The third benefit belongs to the acoustic performance of the resulting composite. As the increased “voided” thickness represents a greater pass along with multiple reflection and absorption possibilities for the sound, the partially consolidated MRTs exhibit excellent noise reduction. Thus, headliner manufactured from partially consolidated GMT demonstrates doubled sound absorption coefficient at frequencies higher than 2000 Hz than those from polyester or polyurethane reinforced with GF [221].

The mentioned issues make LWRT very attractive materials for automotive interior components, such as door trims, sunshades, headliners, trunk trims, parcel shelves, etc.

Direct Long Fiber Thermoplastics

As mentioned above, originally the manufacturing of the semi-finished thermoplastic sheets and the production of the final parts occurred separately. However, the breakthrough idea to combine these processes has appeared in 1990s, and

become a well-established integrated production technology soon. This technique traced back to GMT and is called as *direct long fiber thermoplastic*. The specific feature of D-LFT is incorporation and impregnation of the reinforcement fibers with the PP matrix directly during the compounding and plastification of the composites. For the first step—compound production—extrusion technology is used.

For the second step two variants are available: compression or injection molding. Accordingly, two types of D-LFT are distinguished: open machine process (compression molding cf. Fig. 9.13) and close machine process (injection molding). Each method has certain pros and cons. Thus, compression molding enables shorter cycle time, higher fiber length and consequently better mechanical properties, but at the same time formed parts have flashes and require post-processing. Whereas injection molding provides parts with an accurate contour and excellent surface quality, allows to integrate various inserts, but require longer cycle time and yields more sever fiber length degradation.

Despite definite increase of the capital costs, D-LFT provides certain benefits to the production, as well as to the structural performance of the composite parts. First of all, the discarded step of additional heating and plastification of the blanks, allows to diminish residual stresses in the composite part. Second, the manufacturer has more freedom in materials' formulation and adoption of the process to demands of the actual part. Third, long GFs (12–50 mm) provide outstanding mechanical properties to the composite. However, a drawback of D-LFT is the alignment of the fibers and resulting anisotropy generated by the flow processing [219].

The initial step of the D-LFT process includes melting and degassing of PP as well as its blending with cut fibers, introduced in form of rovings, by virtue of the extrusion process. Accordingly, the extruder acts as fiber cutter, at the same time cf. Fig. 9.13. It is imperative to maintain the length of the reinforcing fibers, as high as possible, in the molded part. Therefore, fiber-protection screw geometries, non-return valves, shut-off nozzles and runner systems as well as large screw

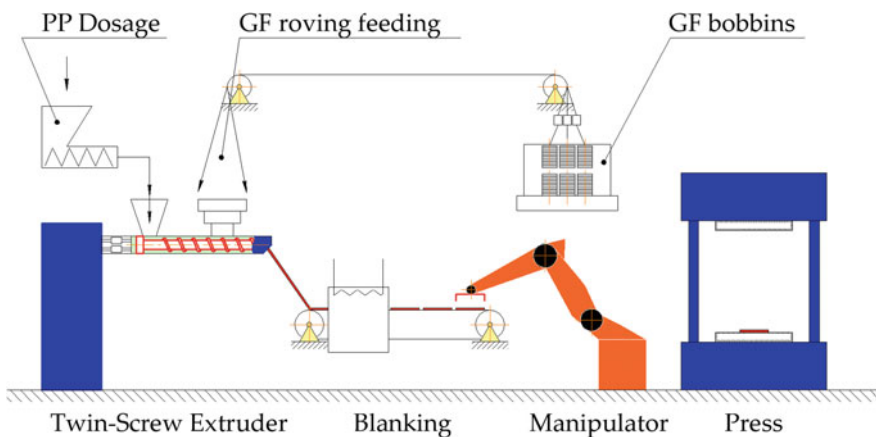


Fig. 9.13 LFT production method schematically

diameters are recommended [222]. Further, the extruded mixture goes through the slit die and applied to the conveyer belt. Next step is either pressing or injection molding.

Composite parts molded from long fiber (12–50 mm) D-LFT compounds show tensile strength and modulus values in the range of 100–125 MPa and 8.2–9.2 GPa, respectively. Their flexural strength, modulus and notched Charpy impact energy are lay in the ranges: 180–200 MPa, 8.2–9.0 GPa and 26–30 kJ/m², respectively. Such mechanical performance predestinates LFT compounds to apply them for semi-structural and structural automobile parts. Typical applications are body panels, seat pans, sound shields, front-end assemblies, structural body parts, truck panels and housings, doors, tailgates and fender sections. The commercially produces LFT PP compounds are Celstran[®] and Stamax[®].

D-LFT foam

Further development step in injection molded D-LFTs has been done in the direction of foaming. Adding of a blowing agent into the LFT compound during the plastification phase allows obtaining LFT foam with compact surface layers and porous structure in the core. D-LFT foam technology approach was introduced by Roch et al. [222, 223] from Fraunhofer ICT as an alternative to MuCell[®] process. The relative D-LFT foam technique utilized nitrogen as a blowing agent at a concentration of 3 wt%. Nitrogen was pre-compressed up to 350 bar and introduced as a supercritical fluid into the melt compound in twin-screw extruder via a gas injector. A ‘breathing mold’ technique was used to obtain integral foam sheets. GF-reinforced PP composites with and without foaming, yielding different thicknesses, were produced and their properties compared. Thus, 5.8 mm samples demonstrated 300% gain in flexural rigidity compared to the unfoamed reference with 3.6 mm thickness. The accompanied weight saving is amounted 35%. Another advantage, provided by foaming, was a diminishing in fiber alignment and in the related mechanical anisotropy. Further benefit of the incorporation of long GFs incorporation into foamed PP was some toughness improvement.

9.4.3 Properties and Their Prediction

9.4.3.1 Mechanical Response

As it was mentioned earlier the mechanical response of MRT are determined by the mat architecture and nature of the fibers. The static mechanical properties of MRT reinforced with NF, GF, and CF are presented in Table 9.1.

Mechanical properties of continuous fiber or swirl mat GMT (GMT-C) outperforms those of the discontinuous fiber GMT (GMT-D). As for tensile and flexural properties, the difference is less distinct, but for the fracture toughness (K_Q) it is essential [228]. The reason of it is explained by the internal structure provided by mat. Thus, swirl mat brings GMT-C mesh-like internal structure (Fig. 9.14a). Deformation and breakage of such structure occur locally, so that stress could be effectively redistributed and transferred on the other fibers in the network before

Table 9.1 Mechanical properties of PP based MRTs. Designations: SMC—Sheet Molding Compound

Reinforcement	Fiber mass fraction (wt%)	Density (kg/m ³)	Tensile		Flexural		Ref.
			σ (MPa)	E (GPa)	σ (MPa)	E (GPa)	
Neat PP	0	900	0.7–1.7	1.9–3.5	–	–	[213]
SR-PP	50	800-900	31–99	2.4–2.7	–	–	[217]
NMT							
Flax	40	1190	57	8.8	81	4.2	[213, 224]
Hemp	40	1190	52	6.9	–	–	[213]
Jute	40	1190	27	3.7	–	–	[213]
Bamboo		1010	30	3.6	–	–	[213]
GMT							
GMT20	20	1070	68.6	3.9	93	3.4	[225, 226]
GMT30	30	1110	78.4	4.4	98	3.9	
GMT40	40	1180	90–108	5.6–6.2	138–160	4.9–6.1	
UD45	45	1270	254	11.8	215	9.8	
CMT	25	1140	~ 175	~ 20	~ 240	~ 16	[227]
SMC	30–40	1700–2300	60–160	10–15	120–250	8–14	[225]
Steel	–	7800	450–650	190–210	–	200	–

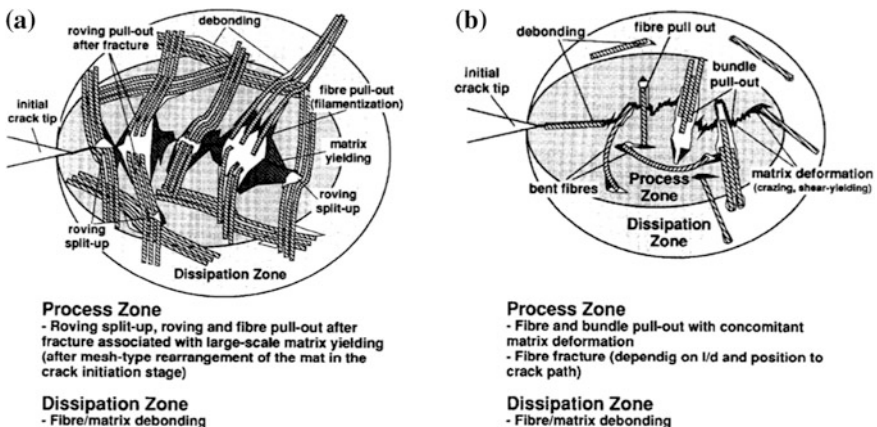


Fig. 9.14 Schematic representation of failure mode in **a** GMT-C and **b** GMT-D [228] ([211] reproduced with the permission of Springer Nature)

failure. This possibility is completely missing for GMT-D structure (Fig. 9.14b), where the failure is immediately stipulated either by ‘fiber-matrix’ debonding, fiber pull-out and fracture, or matrix deformation. As a result, GMT-C demonstrates larger than GMT-D damage zone, that in case of GMT-C, could reach up to 30 mm in diameter [228–231].

The recycling prospective of MRT depends on the fiber type. Thus, Bourmaud et al. [232] studied the degradation of flax-PP and glass-PP nonwoven composites. They found out, that after three compression moulding recycling cycles, the decrease in modulus is about 40% for flax reinforced PP, and only 4% for glass reinforced PP. At the same time both flax- and glass-PP demonstrated significant strength reduction (70 and 75%, respectively).

9.4.3.2 Rheological Behavior

Modern approaches to the process engineering involve wide use of simulation, that provides significant cost and time savings. Consequently, detailed knowledge of the rheological behavior of the material under molding conditions are essential for process modelling. A number of studies are dedicated to experimental investigations and mathematical modelling of GMT stamping rheology [233–238]. The squeeze flow technique is often chosen for rheological testing of GMT, due to its experimental simplicity, suitability for continuous fiber materials and its broad similarity to the pressing process [235].

Two flow models could be used to describe possible flow behavior in a biaxial flow geometry. The first one is ‘shear flow’ model that assumes zero velocity of the fluid at the plate surface. The second one is ‘biaxial extension’ model, where complete slip occurs at the plate surfaces. Both models are described by power-law constitutive equations, that take into account anisotropy and non-Newtonian flow effects (Eqs. 9.10 and 9.11) [239]:

$$\tau = A_s \dot{\gamma}^m, \quad (9.10)$$

$$\sigma = A_e \dot{\varepsilon}^m, \quad (9.11)$$

where τ and σ are shear and strain stresses respectively; A_s and A_e —shear and extensional power law constants; γ and ε —shear and strain rates respectively.

The shear and extensional viscosities (η_s and η_e) at particular strain rate could be given by Eqs. 9.12 and 9.13:

$$\eta_s = A_s \dot{\gamma}^{m-1}, \quad (9.12)$$

$$\eta_e = A_e \dot{\varepsilon}^{m-1}. \quad (9.13)$$

Kotsikov et al. [235] concluded, that squeezing flows of GMT cannot be modelled as pure shear flow without introducing large errors in the prediction of squeezing forces. In contrary, biaxial extension model provides good agreement with the experimental results.

Dweib and Brádaigh [237, 238] considered the constitutive equation for a transversally isotropic power-law fluid (Eq. 9.14):

$$\begin{bmatrix} \sigma_{xx} \\ \sigma_{yy} \\ \sigma_{zz} \end{bmatrix} = \begin{bmatrix} \eta_1 & 0 & 0 \\ 0 & \eta_2 & 0 \\ 0 & 0 & \eta_1 \end{bmatrix} \cdot \begin{bmatrix} \dot{\epsilon}_{xx} \\ \dot{\epsilon}_{yy} \\ \dot{\epsilon}_{zz} \end{bmatrix} - \begin{bmatrix} P \\ P \\ P \end{bmatrix}, \tag{9.14}$$

where σ_{xx} , σ_{yy} , σ_{zz} —normal components of the stress tensor in x , y and z directions; η_1 , η_2 —fluid viscosities; $\dot{\epsilon}_{xx}$, $\dot{\epsilon}_{yy}$, $\dot{\epsilon}_{zz}$ —strain rates in x ; y and z ; P —hydrostatic pressure.

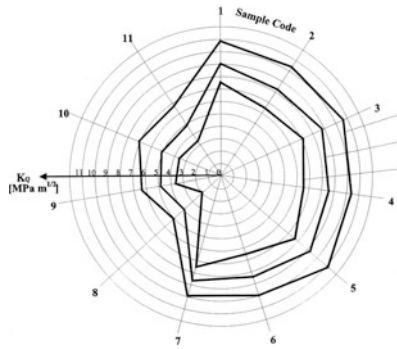
They modelled squeezing flow as a pure extensional flow and also as a combination of shearing and extensional flows. They determined, that the extensional viscosity at 180 °C and constant closing speed of 0.5 mm/s, in x and z directions lied in the range of 0.79–0.85 MPa·s, and in y direction it was slightly higher (0.9–1.2 MPa·s) [238].

9.4.3.3 Thermal Behavior

During the service life semi-structural automotive parts are generally subjected to fairly high mechanical and thermal loads. For instance, in hot climate the temperature of some components can rise up to 80 °C or beyond. So, it is very important to possess information about the behavior of MRT under a combination of thermal and mechanical loads. One of the main parameters that characterize the thermal behavior of composites under the mechanical load is HDT. For GMT the HDT ranges from 145 to 158 °C, while for NMT reinforced with flax—from 140 to 145 °C [219]. However, HDT data only hint for thermal operation limits because the real structures are subjected to loadings highly different from a clear flexure used in HDT determination.

The effect of temperature on the creep behavior of continuous fiber GMT was investigated by Dassapa et al. [240]. Short-term creep tests consisting of 30 min creep followed by 1 h recovery were conducted at five stress levels at the range of 20–60 MPa, and at 14 temperatures at the range of 25–90 °C. The researchers concluded that continuous fiber GMT should not be used at stresses over 60 MPa, particularly when the temperature exceeded 50 °C, due to significant increase of the creep rate.

Czigány et al. [241] studies temperature influence on the fracture behavior of GMT. Diagram in Fig. 9.15 demonstrates the fracture toughness of GMT-C (Index 1–7) and GMT-D (Index 8–11) at various temperatures: –40 °C, room temperature (RT), and +90 °C [241]. The values of fracture toughness of GMT-C was almost twice higher than those of GMT-D at all temperatures. Temperature rise influenced negatively the fracture toughness. The highest value of K_Q is observed at –40 °C, i.e. the temperature below T_g . At RT impact strength of both, GMT-C and GMT-D reduced by almost 20%, at +90 °C by 30–40% (Fig. 9.15).



Sample no.	Fracture toughness (K_{Ic}) (MPa $m^{1/2}$)		
	$T = -40^\circ\text{C}$	$T = \text{RT}$	$T = +90^\circ\text{C}$
1	10.78±0.32	8.99±0.89	7.46±0.54
2	10.41±0.17	8.20±0.33	6.43±0.11
3	10.69±0.71	8.82±0.51	7.13±0.47
4	10.45±0.28	8.60±0.08	6.56±0.05
5	11.02±0.19	9.28±0.39	7.81±0.28
6	10.01±0.71	8.47±0.32	6.56±0.50
7	10.10±0.13	8.71±0.47	7.65±0.42
8	5.07±0.36	3.99±0.21	2.04±0.16
9	6.34±0.20	4.83±0.19	3.53±0.25
10	7.05±0.27	5.06±0.28	3.61±0.42
11	6.72±0.43	4.94±0.17	3.42±0.14

Fig. 9.15 Fracture toughness of swirl mat (Index 1-7) and long fiber (Index 8-11) GMT at different temperatures ([241] reproduced with the permission of Elsevier)

9.4.3.4 Other Properties

As it was mentioned above, the fatigue behavior differs for GMT-C and GMT-D. Thus, the fatigue endurance limit of GMT-C after 10^6 fatigue cycles can be given by 25–30% of the static tensile strength [229]. This issue limits swirl mat thermoplastics application mostly for impact resistant parts, while GMT-Ds are more suitable for long-term loading conditions.

9.4.4 Applications

Some examples of GMT parts application are presented in Table 9.2.

Table 9.2 Examples of MRT composites application

Year	Part	Ref.
1975	Front-end/retainer for Chevrolet Monza	[215]
1977	Front support frame for Pontiac Firebird, Chevrolet Camaro	
1978	Seat pan for Chevrolet Corvette	
1992	Technical front-end VW Golf III	
1993	Battery tray for Suzuki Wagon R	[242]
1997	Hatchback door DC W 168	[215]
1997	Fuel tank cover for Toyota Harrier Hybrid	[242]
2002	Front seat structure for Bentley Continental	
2003	Hatchback door Nissan Murano	[215]
2004	Lightweight underbody systems of the BMW series: E 60/61, E 63/64, E 8x and E 9x	
2009	Battery tray for Mitsubishi i-MiEV	[242]
2014	Front-end for Mercedes S-Class Coupé	

9.5 Fabric-Reinforced Composites

Reinforcement in the form of fabric provides composite with higher strength and stiffness compared to short and long fiber reinforced versions. This is mostly due to different mechanisms of carrying load in the corresponding composite structures. The main structural element in fabric is yarn, that particularly overtakes the mechanical load applied to the structure. Distribution of the load in a textile is carried out by friction forces between fibers, that results in higher critical length of the fibers, and consequently—higher strength of the material. The other aspect is that the fiber content in fabric-reinforced composites is in the range of 45–55 vol%, which is higher than those in discontinuous fiber-reinforced grades (20–35 vol%). This is associated with better mechanical performance *per se*. Another distinct feature of fabric reinforced composites is a certain anisotropy of their properties. This fact allows to create customized structures with tailored properties in the required directions.

Better mechanical properties and possibility of creation structures with tailored properties, provided by the fabric, together with good formability through the thermoplastic matrix, enable the applications of fabric reinforced polypropylene (FR-PP) in structural automotive parts. Fabrics with various weaving styles are currently available. The most popular fabrics are schematically presented at Fig. 9.16.

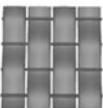
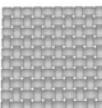
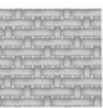
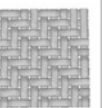
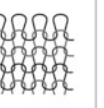
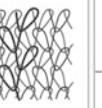
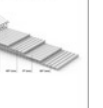
Fabrics						
1D	2D					3D
Unidirectional  Low drapeability/ no crimp <ul style="list-style-type: none"> • Predominant stress and stiffness in one direction • Good handling characteristics 	Plain weave  Low drapeability/ high crimp	Satin weave  Good drapeability/ low crimp	Twill weave  Average drapeability/ average crimp	Wet-knitted  Excellent drapeability/ moderate crimp	Warp-knitted  Excellent drapeability/ moderate crimp	Multiaxial  Average drapeability/ no crimp <ul style="list-style-type: none"> • Strength and stiffness in three directions • Time saving, cost-effective technology
		<ul style="list-style-type: none"> • Strength and stiffness in two directions • Very good handling characteristics • Possibility to 'hybridize' fabric, by mixing fibers of various nature 				

Fig. 9.16 Typical fabrics used as reinforcements in composites

However, despite of certain advantages of FR-PP, their production is associated with definite challenges. The FR-PP manufacturing could be basically divided into two stages: impregnation and consolidation. Consolidation does not expose serious problems, but impregnation of the fabric with the molten PP is not an easy task due to a high viscosity of the PP melt (200–2000 Pas [243]). Traditionally,

the impregnation and consolidation processes are separated. The impregnated product is semi-finished sheet or prepreg (also called as “organosheet”), while the result of the consolidation stage is the composite part. “Direct” processing routes, implying in line fabrication of both semi-finished material and composite parts have appeared two decades ago, and now they represent established manufacturing techniques (Fig. 9.17) [244]. The processing techniques of semi-finished FR-PP sheets production, and composite parts’ forming will be discussed in Sect. 9.6.1.

By compression molding of PP fabrics themselves—called hot compaction method—all-PP composites having identical polymer components can be produced. Hot compaction means that a thin skin of high tenacity polymer fibers or tapes melts and upon cooling this melted material recrystallizes to form the matrix of a self-reinforced composite [245–247]. This composites is commercialized under the name of CURV[®].

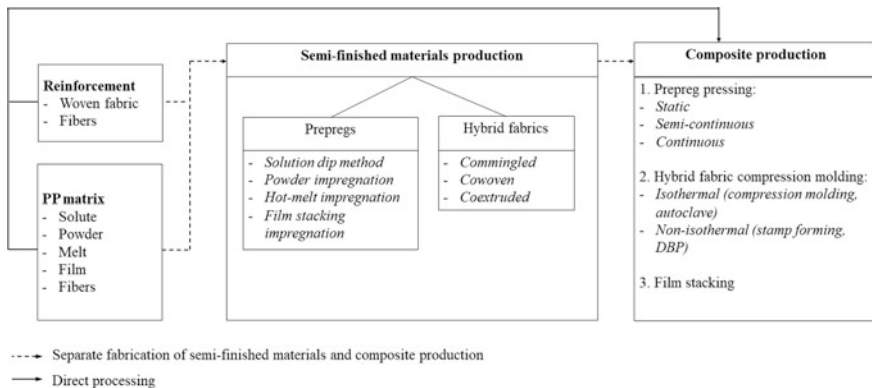


Fig. 9.17 Principal scheme of the production of FR-PP in sequential and direct ways, respectively

9.5.1 Manufacturing

The manufacturing techniques of semi-finished materials could be classified based on the matrix state during combining the fabric with the matrix (Fig. 9.17). Thus, impregnation with the solute PP matches to solution dip method [248, 249], powder—to powder impregnation [250, 251], film—to film stacking [252], melt—to hot-melt impregnation [253, 254]. Combining the reinforcement with PP in the form of fibers termed to as hybrid fabric (commingled and co-woven) technology. Each of these compounding techniques are reviewed below.

Solution dipping

Solution dip impregnation method is probably the earliest thermoplastic prepreg fabrication technique [248, 249]. Its another name is “solvent impregnation”, that illustrates the necessity to use a solvent in order to reduce the viscosity of PP, and therefore facilitate the impregnation. The solution dip method generally assumes two manufacturing steps. The first one is conveyance of the reinforcement textile through the bath with the solute PP. Then, the impregnated fabric goes through a heating chamber, where the solvent is completely evaporated to prevent void formation (Fig. 9.18). The solvent removal is usually the most problematic issue of this technique, because the amount of the diluent required to decrease the high-molecular weight polymer viscosity to an acceptable threshold could reach 85 vol% and more. Beyond that, the semi-crystalline PP can only be dissolved at rather high temperature (>180 °C) due to its excellent resistance to common solvents. Hence, these issues limit the application of solvent impregnation prominently.

Powder impregnation

The aim of the processing by the powder impregnation technique is to bring matrix and fibers to the intimate contact in order to minimize the flowing distance during consolidation [255]. The matrix material should be ground so, that the particles diameter is comparable with that of the fiber diameter. The powder is scattered over the textile, and stick to the fibers via electrostatic attraction. The powder-coated material is then consolidated in a DBP (Fig. 9.18) or interval press to semi-finished products.

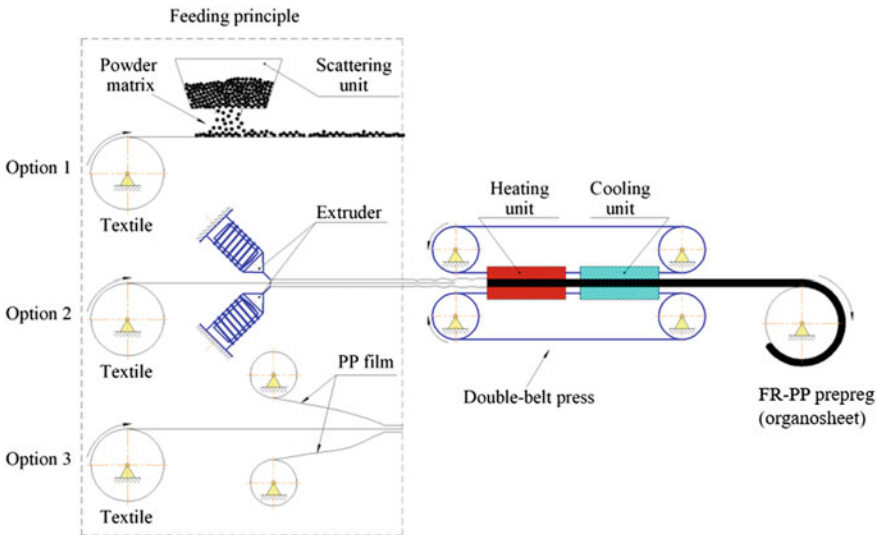


Fig. 9.18 Schematic representations of the continuous powder, hot melt and film stacking impregnation processes using a DBP

The consolidation behavior of FR-PP during powder impregnation process was described by Connor et al. [255]. The proposed model assumes that melt particles form drops, and each drop generates a “bridge” between the adjacent fibers. During the impregnation process every single resin ‘bridge’ spreads along the fibers due to the applied pressure and capillary forces. The bridges distribution pushes out the air from the composite and reduce the inter-fiber spacing.

Powder impregnation technique was first implemented by Price [250, 256] in 1970s for glass roving. However, fabric impregnation is also possible with this process [244], but not really feasible due to economic reasons (substantial loss of powder during handling).

Hot melt and film stacking impregnation

Hot melt impregnation [253] and film stacking are very similar processes which imply either direct extrusion of the matrix material in the molten state onto the textile material or feeding of the matrix in film form on both surfaces of the fabric (cf. Fig. 9.18). Both methods require DBP, that apply constant pressure and heat simultaneously. In case of film-stacking method DBP provides heat and pressure necessary for impregnation, while in case of hot melt process it additionally supports the distribute of the PP melt through/in the fabric [257].

Hot melt impregnation could be considered as a liquid flow through porous media and this process could be mathematically described by Darcy law (Eq. 9.15):

$$\vec{V} = -\frac{\vec{K}}{\mu} \nabla p, \quad (9.15)$$

where \vec{V} —velocity vector; \vec{K} —preform permeability vector; μ —dynamic viscosity of the resin; ∇p —pressure gradient.

The pressure gradient consists of two contributions: (i) mechanical pressure applied to the fluid, and (ii) capillary forces acting between the molten matrix and the reinforcing fibers. The permeability is clearly a key parameter in impregnation modelling and it strongly depends on the fibers architecture. This parameter could be defined either analytically or experimentally [258]. Although experimental techniques are well established, they normally require a large set of carefully controlled tests that are usually rather time-consuming. Analytical approaches are also widely used, but as all predictive techniques, they involve definite assumptions which generally impair the accuracy of the methods. A popular model to predict the permeability is the Kozeny-Carman equation (Eq. 9.16) [259]:

$$K = \frac{r^2}{4k} \cdot \frac{\epsilon^3}{(1 - \epsilon)^2}, \quad (9.16)$$

where r —is the radius of the particles; ϵ —is the porosity; k —is the Kozeny constant.

The Kozeny-Carman equation is based on a capillary model and thus it is inherently a one-dimensional model that works well only for isotropic medium. Gutowsky et al. [260] expanded the application of the Kozeny-Carman equation to describe the permeability of anisotropic preforms. However, Kozeny-Carman and Gutowsky approaches are restricted to a simplified geometry and applicable only for UD fiber architecture (i.e. not working for woven and stitched preforms). Computer modelling approaches help us, however, to investigate complex preform geometries, define pressure and velocity fields, and to calculate the permeability vectors accordingly [258].

Hybrid yarns, fabrics

Hybrid fabrics containing both the matrix and reinforcement fibers, can be principally divided into two groups: commingled and co-woven fabrics. Commingled fabric consists of hybrid yarns in which the matrix and reinforcement are “blended” intimately at the level of the filaments (Fig. 9.19a). Co-woven fabric includes separate PP and reinforcing yarns (GF, CF, NF, etc.) (Fig. 9.19b). The positive effect of such hybridization lies in diminishing of the distance that resin must flow to achieve impregnation [255].

Hybrid yarns can be manufactured by means of various techniques: commingling in an air jet [262], on-line commingling, that utilizes air texturing instead of air jet texturing [263, 264], co-wrapping, core-spinning [262] and stretch-breaking [262]. The last option—stretch-broken commingled fibers—is a prospective opportunity for recycled CF [265]. Hybrid yarns could be later processed to the fabrics using standard weaving techniques.

Both, commingled and co-woven hybrid fabrics are used as drapable preforms and transformed into the shaped final composite parts through the consolidation process applying heat and pressure [266]. A mathematical model of the commingled fabric consolidation was developed by van West et al. [267]. This model utilizes the Darcy’s law to describe the radial flow of the resin across the fiber bundle by considering that the permeability changes with the V_f during the consolidation process.

‘Hybrid’ yarn can also be prepared by coextrusion when PP homopolymer is coated with PP copolymer having lower melting temperature followed by intensive stretching. The woven fabric from the coextruded yarn is the preform of the all-PP composites [268, 269]. This composites is commercialized under the name of PURE[®].

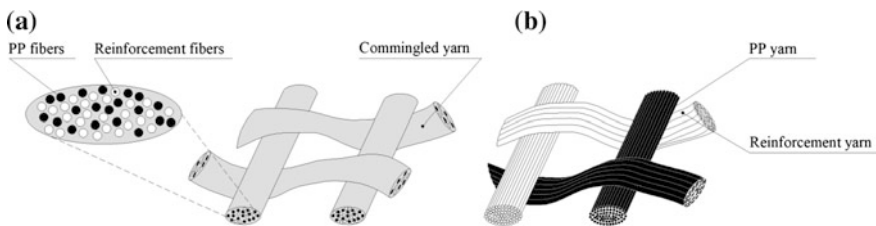


Fig. 9.19 Commingled (a) and co-woven (b) hybrid textile structures [261]

9.5.2 Structure Development and Characterization

Manufacturing techniques for composite parts production from FR-PP could be divided into three groups, namely *prepreg pressing*, *hybrid fabric pressing* and *film stacking*. As mentioned previously, for mass production ‘direct’ processing routes, i.e. in-line production of both the semi-finished impregnated material and composite part, are also feasible.

Prepreg pressing

Pressing of the FR-PP organosheets does not principally differ from that of stampable grade MRT described in Sect. 9.4. The process includes the same manufacturing steps: prepreg preheating, transferring to the mold, pressing and demolding of the part. The distinct feature of FR-PP prepregs is their zero flowability. Therefore, the shaping is restricted by the fabric structure. The usual processing temperature for FR-PP lays in the range of 160–220 °C, pressure—in the range of 5–10 MPa, and processing time—less than 5 min. FR-PP organosheets are produced under the tradenames: Tepex[®], GMTex[®] and others.

Sandwich panels consisting of FR-PP skins and either foam or honeycomb PP core can be also produced by hot pressing. A comprehensive overview in this field is given in Ref. [270]. Sandwich panels with GF FR-PP and PP honeycomb are commercially produced under the tradename MonoPan[®].

Hybrid fabric pressing

As mentioned previously, the main target of the hybridization of the reinforcement fabric with PP is to diminish the matrix flow distance. This distance in a typical commingled material amounts to 20–40 μm [262]. Another advantage of hybrid fabrics over impregnated prepreg sheets resides in better drapability that allows the preform to conform easily to a complex mold surface [266].

To form a composite part from hybrid fabrics it is necessary to melt the matrix fibers, impregnate the reinforcement and consolidate the material. The distinct feature of the described process is that impregnation and consolidation occur in one-shot. Forming techniques for hybrid fabrics could be principally divided into two groups: isothermal and non-isothermal [271]. During the isothermal process the mold and material are thermo-cycled together above the melting temperature of PP [272–274]. Consequently, manufacturing techniques associated with the isothermal consolidation process are compression molding and autoclave forming. These techniques provide perfect consolidation state and excellent performance, but strongly limit the production rate. In contrast, non-isothermal consolidation occurs when the fabric is preheated above the PP melting temperature in an external heating unit and then transferred into the mold maintained at a temperature below the “solidification” of PP [261, 271, 275]. Preheating could be implemented by hot air, IR or contact heating. Nevertheless, non-isothermal technique requires very fast transfer of the preform to the mold in order to avoid significant heat loss. For example, the temperature of four-layer stack of woven GF/PP preform drops from 220 °C to T_m (160–170 °C) within only 20 s [262]. Manufacturing technique utilizing non-isothermal processes for commingled and co-woven fabrics is stamp

forming. A typical stamp forming processing cycle consists of material heating above the melting temperature of PP, applying pressure, and further cooling below the solidification (between the crystallization and glass transition temperature) while maintaining pressure [267]. The pressure necessary to consolidate hybrid fabric is generally lower than that of GMT, as there is no need for fabric structure to move with the flowing matrix in order to fill the mold.

Properties of a composite part produced of commingled or co-woven fabric strongly depend on the processing parameters, such as melting temperature, mold temperature, pressure and holding time. Additionally, impregnation and consolidation time of the hybrid fabrics are dependent on the fabric structure, yarn dimensions and shape, number of fibers per yarn, fiber diameter, and quality of commingling. A number of works were dedicated to the determination of the optimal (from mechanical performance point of view) parameters for both, isothermal and non-isothermal forming. Some results of the research activity in this field are presented in Table 9.3.

Average process parameters for isothermal process are the following: mold temperature—190 to 205 °C, average holding time—5 to 8 min, pressure—0.4 to 4.5 MPa. By contrast, non-isothermal consolidation process exhibit lower holding time (less than 60 s) and lower mold temperature 60–100 °C, while the pressure level is nearly the same (2.3–4.0 MPa).

Commingled fabrics are produced under the tradename Twintex[®], ThermoPly[®], and others.

Film stacking technique

Film stacking manufacturing process is suitable for the laboratory scale production [252, 279]. This technique utilizes a hot press and allows to produce either organosheets or laminates with the sizes limited by the sizes of the mold.

Various processing parameters for film stacking technique are mentioned in the literature. Thus, Kim and Lee [252, 279] produced PP prepregs reinforced with the woven CF fabric and defined the following processing parameters: mold temperature—230 °C, slowly increased pressure—up to 28 MPa, time to pressure rise—10 min. Russo et al. [280] produced laminates from 8 layers of plain weave type glass fabric (204 g/m²) and 2 types PP films (35–40 μm), produced of PPs with difference flow grades—70 g/10 min and 12 g/10 min. For the first one the following processing parameters were used: temperature—190 °C, pressure—2.5 MPa, holding time—45 min. The second one required slightly higher values of temperature and pressure (210 °C and 4 MPa respectively) and same processing time—45 min. Scarponi et al. [281] manufactured hemp FR-PP laminates with the following parameters: temperature—200 °C, pressure—5 MPa, holding time—10 min. Okumura et al. [282] produces CF FR-PP laminate with the following processing parameters: temperature—180 °C, pressure—14.6 MPa, holding time—20 min.

Film-stacking method is widely used for production of self-reinforced PP composites [283, 284]. In this case the matrix (viscosity, type) and the reinforcement (fabric type, content) can be combined in a wide range in order to ensure the necessary processing window and to tailor the properties of the resulting composites.

Table 9.3 Optimal processing parameters for composite manufacturing from commingled fabrics

Process	Fabric parameters	Laminate parameters	Optimal processing parameters				Ref.
			T_0 (°C)	T_{mold} (°C)	t (min)	p (MPa)	
Isothermal	GF/PP warp-knitted fabric 450 g/m ² $v_{GF} = 60$ wt%	12 layers Flat laminate	–	205	8	4.5	[273]
	GF/PP twill $v_{GF} = 60$ wt%	Flat laminate	–	200	5	0.7	[274]
	GF/PP Tubular weft-knits	10 layers	–	200	5	4.0	[276]
	GF/PP twill 745 g/m ² $v_{GF} = 60$ wt%	4 layers	–	200	4	0.4	[277]
	Flax/PP UD fabric (flax—warp, PP—weft)	–	–	190	20	0.5	[278]
Non-isothermal	GF/PP twill 650 g/m ² $v_{GF} = 60$ wt%	8 layers [8 (0/90)] _T Flat laminate	220	60	0.75	2.3	[261]
	GF/PP twill 1485 g/m ² 743 g/m ² $v_{GF} = 60$ wt%	3 layers of 1485 g/m ² and 6 layers of 743 g/m ² Flat laminate	190	100	1	4.0	[275]

9.5.3 Properties and Their Prediction

9.5.3.1 Mechanical Response

FR-PP exhibits higher level of static and dynamic mechanical properties than MRT. Thus, the tensile strength, tensile modulus, flexural strength and flexural modulus of Twintex[®] with 60 wt% of GF are in the range of 300–400 MPa (ISO 527), 14–20 GPa (ISO 527), 280–380 MPa (ISO 14125) and 13–18 GPa (ISO 14125), respectively [285]. The impact strength of Twintex[®] amounts 160–200 kJ/m² (ISO 180). FR-PPs exhibit significant strain rate dependent deformation behavior [286, 287]. Thus, tensile and compression modulus and strength increases with the increasing strain rate, while shear modulus and strength tends to decrease [286]. Compared to GF/PP, woven fabric reinforced all-PP composites demonstrates

lower tensile properties (strength in the range of 55–85 MPa, and Young's modulus in the range 1.7–2.3 GPa [284]) but significantly higher impact strength—250 to 550 kJ/m² [283].

The interfacial strength plays a significant role in the mechanical behavior of FR-PP, as it is responsible for the efficient load transfer. The specific feature of the PP matrix, which influences the adhesion, is its non-polar nature. Due to this reason PP does not adhere well to most of the fibers. In order to improve the interfacial adhesion between PP matrix and reinforcement two basic strategies have been developed. The first one implies fiber surface modifications with coupling agents, plasma treatment, wet oxidation, whiskerization, etc. The purpose of the surface treatment is to increase the surface energy, induce chemically active functional groups or increase the surface roughness of the fiber to enhance the physical bonding with the matrix. The most commonly used and industrially adopted method for GF modification is treatment with the silanes bearing alkoxy silane groups. After hydrolysis, the silanol groups formed react with the hydroxyl groups on the GF surface [288]. Silanes are not effective for untreated CFs as they do not contain –OH group. Nevertheless, hydroxyl groups can be generated on the CF surface by plasma, wet chemical or electrochemical oxidation treatments. As for the NFs, they are also incompatible with PP matrix due to a polar nature of cellulose. One possible treatment for NFs are silanization [289]. The interested reader could find more information on NF modification in Ref. [165].

The second strategy introduces polar functional groups into the PP. The polar groups in PP chains are generated by reactions with species that contain specific functional groups in their structures, such as ester, carboxylic acid or anhydride groups [290]. The most popular interfacial compatibilizers are: PP-g-MA, PP grafted with maleic acid (PP-g-MAA), and styrene butadiene styrene block copolymer grafted with maleic anhydride, etc. However, combination of both strategies is also commonly used to improve the adhesion between fibers and PP matrix.

Some fiber treatments reduce the strength of the individual fibers, but the increased 'fiber-matrix' adhesion leads to a higher interfacial strength and higher mechanical response of the whole composite. Thus, Han et al. [288] investigated the influence of plasma treatment followed by silane application on CFs. They demonstrated, that albeit 1 min plasma treatment together with the silane treatment decreased the filament strength from 3.68 to 3.23 GPa, the interlaminar shear strength (ILSS) showed 48.7% growth.

Okumura et al. [282] investigated the effects of removal of sizing and PP-g-MAA content on the mechanical properties of carbon FR-PP. They reported, that the flexural strength of the samples, containing 1 wt% of PP-g-MAA, reached the value of 453 MPa at about 50 vol% of CF content, that is more than twice higher than for the untreated sample. Removal of the sizing agent increased the flexural strength even more.

Russo et al. [291] studied the effect of the PP-g-MA compatibilizer on the mechanical behavior of plain weave glass FR-PP. Thus, PP-g-MA increased the flexural strength of the composite from 97.9 to 183.0 MPa, and the flexural

modulus from 15.3 up to 17.1 GPa. However, improved adhesion deteriorated the falling weight impact resistance.

Alcock et al. prepared woven fabric reinforced all-PP composites from coextruded tapes (reinforcement content ca. 90%). They concluded that the developed composite's tensile properties outperformed the GMT-PP and remain slightly below the woven glass fiber reinforced PPs [268]. All-PP composites possess excellent falling weight resistance [292], which can be tailored by the consolidation quality of the composite (depends mainly on consolidation temperature and pressure) [284].

9.5.3.2 Rheological Behavior

The rheological behavior of FR-PP is defined by its both constituents—thermoplastic matrix and textile. The predominant flow mechanisms in FR-PP governed by the matrix are resin percolation and transverse squeeze flow (Fig. 9.20). On the other hand, the formability, shaping of FR-PP is controlled by the fabric. The main deformation modes determined by the textile are bending, fiber straightening, yarn buckling, as well as intra- and inter-ply shear (in-plane and out-of-plane shear correspondingly) [293, 294]. Bending mode is characterized by relatively small deformations, and consequently is associated with single curved shapes. At the same time in-plane shear enables higher deformations and is representative to double curved shapes. In fact, in-plane shear behavior is a key deformation mode of textile reinforced composites utilizing GFs and CFs fibers [295]. At the same time, for all-PP composites deformation modes connecting with the fibers plays much more important role [296].

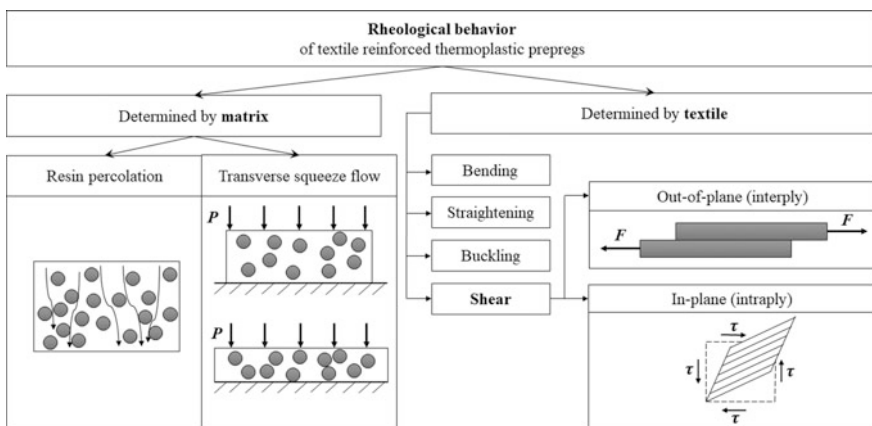


Fig. 9.20 Forming mechanisms of thermoplastic textile reinforced prepregs determined by their constituents (based on Ref. [300])

The rheology of textile composites could be characterized experimentally, by using picture frame and bias extension tests [297–299]. On the other hand, prospective prediction methods have been developed, as well [300].

Numerous works were dedicated to the prediction of the forming behavior of a textile. Four prediction methods are mentioned in literature, namely: kinematic, continuous, semi-discrete and mesoscopic. All the described approaches are based on the different assumptions and have their certain pros and cons [293]. Thus, kinematic approach (also called as fishnet or geometrical mapping algorithm [301]), assumes that yarns are inextensible, warp and weft yarns can freely rotate at the intersections points while slide is prohibited. Modell, based on kinematic approach, is also called as a ‘trellis model’, and consists of a mapping of the fabric geometry from an initial to a final surface with an in-plane shearing as the only deformation mechanism [302]. Major benefit of the fishnet algorithms is that they deliver results very fast, but disregarding mesh deformation possibilities except of shearing. As a consequence, kinematic approach is primary used at the initial design stage. *Continuous* method treats the textile as a continuous medium during forming, moreover the inherent anisotropy can be taken into account. Standard FEs (shell, membrane, 3D) could be used to simulate textile forming with the continuous approach [293, 303]. However, this method does not fully characterize the mechanical behavior of the textile. Semi-discrete approach assumes the textile as a set of woven cells, where one-unit cell is submitted to the loads of its neighboring yarn. Mesoscopic or meso-scale approach is the most accurate one, as it considers the textile as a set of yarns connecting to each other, where each fiber bundle is modelled. The principal difference of the mesoscopic method from the listed above approaches are accounting of the contact of the yarns with friction and possible slipping between them.

Nevertheless, none of the described above predictive methods includes the influence of the viscous matrix, and consequently cannot take into account the influence of processing conditions (i.e. temperature, rate of loading, contact forces, interplay friction, etc.), that appear during thermoforming (Fig. 9.21). Below, we will describe modelling approaches that take into consideration both, matrix and fabric behavior.

Rheological models for the forming behavior of composite materials with one or two families of reinforcing fibers were first presented by Rogers [305]. Rogers’ models are based on the set of material models known as ideal fiber reinforced materials [306, 307]. The specific feature of these models is a kinematic constraint of fibers inextensibility accompanied with the assumption of the material incompressibility and a suitable anisotropic constitutive relationship. Fibers are considered as linear elastic, whereas the matrix—linear viscoelastic material. The relevant constitutive equation for viscoelastic matrix was a simple generalization of the elastic equation, in which algebraic designation of moduli and strains were replaced by relaxation moduli and strain rates.

Johnson [302] extended Rogers’ work and proposed a rheological model for textile reinforced thermoplastic prepregs, which takes into account fabric

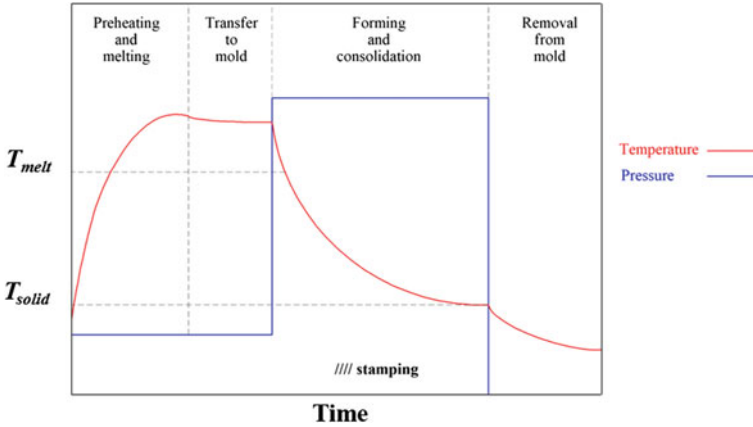


Fig. 9.21 Principle stages of pressure and temperature in the processing of thermoplastic prepregs (based on Ref. [304])

deformation together with the resin viscosity (so called “biphase model”). Johnson’s model assumes textile reinforced thermoplastic sheet to be a continuum with continuously distributed fibers. Each ply comprises an incompressible anisotropic Newtonian viscous fluid and two families of high stiffness inextensible fibers (Eq. 9.17) [300]:

$$\begin{pmatrix} \sigma_{11} \\ \sigma_{22} \\ \sigma_{12} \end{pmatrix} = \underbrace{\begin{pmatrix} 4\eta_1 & 2\eta_1 & 0 \\ 2\eta_1 & 4\eta_1 & 0 \\ 0 & 0 & 2\eta_1 \end{pmatrix} \begin{pmatrix} d_{11} \\ d_{22} \\ d_{12} \end{pmatrix}}_{\text{Viscous part}} + \underbrace{E_1 \begin{pmatrix} \varepsilon_{11} \\ 0 \\ 0 \end{pmatrix} + E_2 \begin{pmatrix} c^4 & c^2s^2 & c^3s \\ c^2s^2 & s & cs^3 \\ c^3s & cs^3 & c^2s^2 \end{pmatrix} \begin{pmatrix} \varepsilon_{11} \\ \varepsilon_{22} \\ \varepsilon_{12} \end{pmatrix}}_{\text{Elastic part}}, \tag{9.17}$$

where σ_{ij} —element stress components, η_1 —viscosity, d_{ij} —the velocity gradient, E_1, E_2 —elasticity modulus, $c = \cos \phi, s = \sin \phi, \varepsilon_{ij}$ —strain components.

The basic assumptions and appropriate equations of the Johnson’s model are listed below:

- (a) *Incompressibility condition* express mathematically, that fluid volumes are preserved (Eq. 9.18):

$$\text{tr}(\mathbf{d}) = 0, \tag{9.18}$$

where tr—trace of a tensor, \mathbf{d} —Eulerian rate of strain tensor.

- (b) *Inextensibility condition* expresses that the strain rate components in the fiber direction are equal to zero (Eqs. 9.19 and 9.20):

$$\text{tr}(\mathbf{A}\mathbf{d}) = \text{tr}(\mathbf{B}\mathbf{d}) = 0, \quad (9.19)$$

$$\mathbf{A} = \mathbf{a} \cdot \mathbf{a}; \mathbf{B} = \mathbf{b} \cdot \mathbf{b}, \quad (9.20)$$

where \mathbf{a} , \mathbf{b} —unit vectors, that denote fiber orientation.

- (c) *Fibers rotation with the fluid* elements during deformation, which leads to Eqs. 9.21 and 9.22 for the orientation vectors:

$$\frac{D\mathbf{a}}{Dt} = \mathbf{a} \cdot \nabla \mathbf{v}, \quad (9.21)$$

$$\frac{D\mathbf{b}}{Dt} = \mathbf{b} \cdot \nabla \mathbf{v}, \quad (9.22)$$

where $\frac{D}{Dt}$ is time derivative defined as (Eq. 9.23):

$$\frac{Dg}{Dt} = \frac{\partial g}{\partial t} + \mathbf{v} \cdot \nabla g, \quad (9.23)$$

where \mathbf{v} —velocity vector.

- (d) *Constitutive equation* for a Newtonian viscous fluid with two families of inextensible fibers (Eqs. 9.24 and 9.25):

$$\boldsymbol{\sigma} = -p\mathbf{I} + S_a\mathbf{A} + S_b\mathbf{B} + 2\eta_1\mathbf{d} + 2\eta_2(\mathbf{A}\mathbf{d} + \mathbf{d}\mathbf{A} + \mathbf{B}\mathbf{d} + \mathbf{d}\mathbf{B}) + 2\eta_3(\mathbf{C}\mathbf{d} + \mathbf{d}\mathbf{C}), \quad (9.24)$$

$$\mathbf{C} = \frac{1}{2}(\mathbf{a}\mathbf{b} + \mathbf{b}\mathbf{a})(\mathbf{a} \cdot \mathbf{b}), \quad (9.25)$$

where $-p\mathbf{I}$ —arbitrary hydrostatic pressure term [305], S_a, S_b —fiber tension stresses, which are the reaction to the inextensibility constraints in the fiber directions, η_1, η_2 —in-plane viscosities related to shear along and transverse to the fibers, η_3 —viscosity, that is related to trellis deformation in the fiber plane where the fabric angle changes.

- (e) *Equilibrium equation* (9.26):

$$\frac{\partial \sigma_{ij}}{\partial x_j} = 0, \quad (9.26)$$

where $\boldsymbol{\sigma}$ —stress.

However, the model proposed by Johnson is idealized as it neither considers fabric weave nor includes any interaction effects between the warp and weft fibers. Interaction between fibers is included through their influence on the viscosity parameters and on the fabric locking angle. The author noted that viscoelastic and thermal effects could be included to the presented model by allowing the viscosity

to be rate and temperature dependent. In his further work Johnson [300] extended the proposed rheological model for temperature-dependent viscoelastic material and implemented it in the explicit FE code PAN-STAMP (originally intended to the metal stamping) to characterize the in-plane behavior of each ply in the laminate media.

Luca et al. [308] simulated textile thermoplastic forming by utilizing ‘biphase model’ in which matrix has a thermo-viscous behavior, while woven fibers are treated as elastic. The out-of-plane shearing between the adjacent layers was handled using viscous-friction and contact constraints. The heat transfer assumed to be predominantly one-dimensional (through-the-thickness), and tool-to-ply and ply-to-ply heat transfer was simulated via the mechanical contact. However, limited in-plane heat transfer was also considered and modelled using conventional anisotropic heat conduction. The proposed simulation technique was verified with the experiment and demonstrated consistent agreement in predicting of ply wrinkling and fiber reorientation.

Nishi et al. [309] simulated the forming behavior of the woven thermoplastic prepreg during the non-isothermal thermoforming process. The modelling process was performed as a complex thermal-mechanical analysis, that took into account the mechanical response of the anisotropic nonlinear textile and temperature dependence of isotropic elasto-plastic matrix. The thermoplastic textile prepreg was simulated as a macroscale model consisting of a layer of fabric and placed around two layers of matrix. The authors proposed the combined shell and membrane model, where the textile was simulated with membrane elements, while matrix—with shell elements. They adapted the micromechanical model proposed by Ivanov et al. [310] to the membrane element in order to describe the in-plane behavior of the prepreg, while shell elements were responsible for the bending stiffness. The authors also considered the heat transfer on the contact surface between prepreg and tool during the non-isothermal forming process. The resulting FE model accurately predicted in-plane shear response and demonstrated a good agreement with the bias-extension experimental measurements. A similar approach was utilized by Gong et al. [311].

Harrison et al. [312] created an analytical constituent-based multi-scale energy model for the prediction of complex rheological behavior of viscous FR-PP prepreg. The developed model took into account the fabric weave architecture, the V_f as well as the PP rheology. The prepreg was modelled as two-phase structure composed of stacked textile and matrix layers. The developed model was not fully predictive, as it did not take into account the meso-scale kinematics. However, the proposed model gave accurate and quick prediction of FR-PP forming behavior at different shear rates and temperatures without recourse to either textile composite characterization experiments or sophisticated FE simulations. In his further work Harrison incorporated the constituent-based multi-scale energy model into the non-orthogonal one [313]. Next, he combined multi-scale energy model with macro-scale and successfully implemented it in FE codes Abaqus Standard and Abaqus Explicit [314]. In a later study [315] he demonstrated the possibility of

modelling of a press forming of 0/90 cross-ply GF-PP using the double-dome geometry by comparison of the obtained numerical results with the experimental.

9.5.3.3 Thermal Behavior

The real life operation conditions of composite structures predominantly involve combined thermo-mechanical loading. For automotive application a typical temperature range is from $-40\text{ }^{\circ}\text{C}$ up to $80\text{ }^{\circ}\text{C}$, thus it is essential to understand the mechanical behavior of FR-PP in this temperature window. With increasing temperature, the stiffness and strength of thermoplastics normally decreases, whereas the failure strain increases. These effects become dramatic when exceeding the polymer's T_g . This is the reason why matrix-dominated properties (shear, transverse stiffness and strength, compression strength) are reduced with the temperature rise. By contrast, the mechanical properties of man-made reinforcement are not essentially influenced by the temperature in a wide temperature range. As a consequence the effect of elevated temperature on the fiber-dominated properties (tensile, bending strength, etc.) is much less significant [316, 317].

Although the recommended operation temperature of semi-crystalline PP is far below its melting temperature, the glass transition region should be taken into account. Thus, if the temperature rises above T_g , the macromolecules motion in the amorphous regions increases, in such a manner enhancing ductile character of PP. The glass transition region of PP matrix ranges from $-10\text{ }^{\circ}\text{C}$ up to $+20\text{ }^{\circ}\text{C}$ [317].

Hufenbach et al. [318] investigated the thermal-mechanical behavior of glass FR-PP produced of a commingled fabric (twill weave Twintex[®]) under static load. The tested samples had a [(0/90)]₄ lay-up and contained 51 vol% of the reinforcement. The authors defined Young's modulus and tensile strength at 23 and $80\text{ }^{\circ}\text{C}$ in 0° , 45° and 90° directions (Table 9.4).

Obviously, the off-axis mechanical properties of woven GF-PP composites are more influenced by the temperature than those in warp- and weft-directions [319], see also Table 9.4.

The compression strength of FR-PP in fiber direction is strongly influenced by the matrix stiffness, as it prevents fibers from kinking. Therefore, glass FR-PP demonstrates almost 70% drop of compression strength between -40 and $80\text{ }^{\circ}\text{C}$

Table 9.4 Mechanical properties of woven GF-PP at 23 and $80\text{ }^{\circ}\text{C}$ [318]

Direction	$T\text{ (}^{\circ}\text{C)}$	$E\text{ (GPa)}$	$\sigma^+\text{ (MPa)}$	Damping values $\tan \delta\text{ (-)}$
0°	23	14.2	299	0.02861
	80	13.8	268	0.04863
45°	23	5.5	115	0.03267
	80	2.9	58	0.05862
90°	23	14.7	280	0.03008
	80	13.3	257	0.04901

(from 256 to 79 MPa) [317]. At T_m the compression strength falls to zero [319]. The in-plane Poisson's ratio is considered to be constant at the mentioned temperature range [317].

However, static properties are not enough for reliable structural design of automotive components. It is necessary to understand cyclic (fatigue) and dynamic (crash and impact) properties under combined thermo-mechanical loading conditions. Bureau and Denault [320] tested woven GF reinforced PP composites under cyclic sinusoidal load at -40 , 23 and 50 °C and compared the obtained results with polyester based composite. The flexural fatigue modulus was reported in terms of 'normalized modulus' (modulus at a given cycle divided by the initial one). The maximum flexural fatigue stresses obtained were 300 MPa at -40 °C, 186 MPa at 23 °C, and 175 MPa at 50 °C that corresponded accordingly to 88, 75 and 121% of the yield stress of FR-PP. However, none of the examined PP based samples failed after 2×10^6 cycles. At 50 °C FR-PP demonstrated slightly higher fatigue resistance than at -40 °C and even significantly better performance has been found at 23 °C, which is very close to T_g of the PP matrix.

Anyway, despite the fact that woven GF PP composites lose their static mechanical properties with the temperature rise, their fatigue performance remains quite high: $2 \dots 3 \times 10^6$ cycles when tested at fatigue levels equivalent to the yield stress, and about 4×10^6 cycles when tested at 84% of its yield stress [320].

Bocz et al. pointed out that for woven fabric reinforced self-reinforced PP composites has been much lower amount of intumescent flame retardant (IFR) can be efficient in PP than for traditional PP and PP composites. V-0 classification in UL-94 test can be achieved with only 9 wt% of IFR additive. It was proved that the significant shrinkage, exhibited by the highly-stretched PP tapes when exposed to heat, is the key factor behind the self-extinguishing behavior of flame retarded SRCs with rather low additive content (only 9 wt% IFR) [321, 322].

9.5.3.4 Other Properties

Due to its relatively low glass transition temperature, PP matrix demonstrates ductility properties even at RT, thus providing its composites considerably improved fatigue performance in comparison with a conventional thermoset composite [272]. Fatigue performance of FR-PP depends on both fiber orientation and load mode. Thus, Ferreira et al. [323] examined the fatigue behavior of glass FR-PP with three different layups: 0 ; $+30/-30/0^\circ$; and $+45/0/-45^\circ$. The authors demonstrated that 0° laminate shows 1.5–1.8 higher fatigue strength than those with the other lay-ups tested (Fig. 9.22).

Three typical stages of stiffness loss could be distinguished during the fatigue damage accumulation. The first one is rather short (do not exceed 5% of loading time) and it demonstrates a progressive stiffness reduction. The second stage corresponds to a gradual stiffness degradation and lasts the majority of all fatigue life (75–85%). The third stage is associated with the stiffness catastrophic drop until failure and lasts 10–20% of the fatigue life [272, 324].

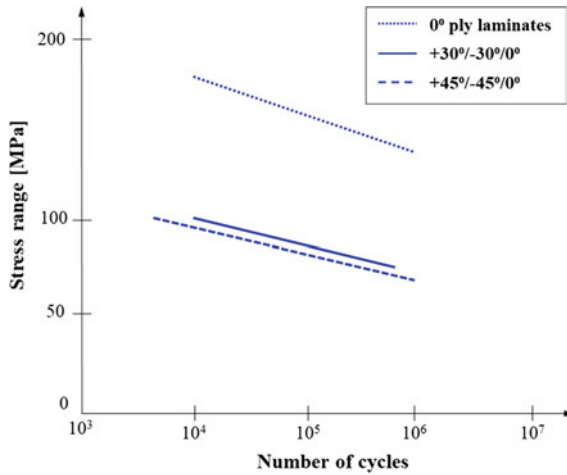


Fig. 9.22 Summary of Wöhler fatigue behavior of woven GF-PP ($V_f = 0.338$) at different layups (based on Ref. [323])

Besides service temperatures the processing conditions could influence significantly the fatigue performance of FR-PP [272]. Thus, low cooling rates, low molding temperatures, low pressures, or short heating cycles obviously leads to poor microstructural characteristics, which consequently negatively affect the fatigue performance (Fig. 9.23). Bureau and Denault [272] examined the fatigue response of the woven GF reinforced PP under various molding conditions: SCC—slow cooling conditions, ETC—extreme temperature conditions, LPSC—low pressure stamping conditions, HPSC—high pressure stiffness conditions and RC—reference forming conditions (Table 9.5).

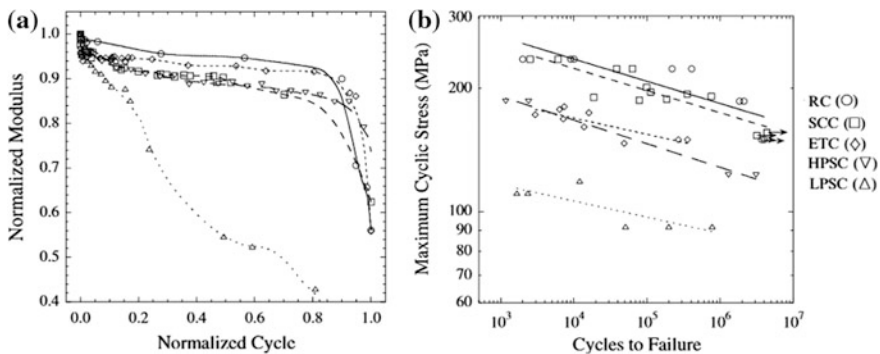


Fig. 9.23 Fatigue performance of woven GF reinforced PP: **a** normalized flexural modulus as a function of number of cycles at a maximum stress level of 75% of the flexural strength for RC, SCC, ETC and LPSC, and 62% for HPSC; **b** maximum cycle stress for various ([272] reproduced with the permission of Elsevier)

Table 9.5 Processing conditions used for the molding of woven GF reinforced PP [272]

Conditions	Temperature (°C)	Holding time (min)	Cooling rate (°C/min)	Pressure (MPa)
RC	200	5	10	0.70
SCC	200	5	1	0.35 ^a
ETC	315	20 ^b	10	0.35 ^a
PSC	160	10	10	0.70
LPSC	200 ^c	— ^d	10	0.11
HPSC	200 ^c	— ^d	10	0.10

^aA lower pressure was used to prevent matrix flow due to the long duration of molten stage

^bA longer time was used to maximize matrix degradation

^cPSC plate is preheated to temperature in an infrared oven and then placed upon a mold prior to stamping

^dUndetermined: stamping was done at constant closing speed until desired pressure was reached

The best fatigue performance from the flexural stiffness point of view was demonstrated by the composites formed under RC and ETC process conditions (Fig. 9.23a). However, composites formed under RC and SCC conditions exhibited “indefinite” fatigue life ($>3-4 \times 10^6$ cycles) at the cyclic stress of 150 MPa (Fig. 9.23b).

Mathieu et al. [325] studied the durability characteristics of glass FR-PP under the influence of the environmental conditions typical for civil engineering constructions. They defined the long-term properties of FR-PP under the influence of tap and 3% salt water at 13, 50 and 70 °C as well as freeze/thaw cycles. The loss of elastic modulus after 168 days in salt solution amounted to 9, 20 and 23% at 23, 50 and 70 °C respectively, while in tap water the loss of modulus was 12, 19 and 20%. The degradation of flexural strength under the same testing conditions amounted to 19, 30 and 44% for immersion in salt solution, and 11, 20 and 24%—for immersion in tap water. Freeze/thaw cycling (800 cycles) resulted in 8 and 32% loss of flexural strength and 0 and 22% loss of elastic modulus for unsaturated and saturated in water samples.

9.5.4 Processing and Applications

Excellent energy absorption capacity and advanced fatigue performance together with high lightweight potential, and high production capacity qualifies FR-PP for crash resistant as well as semi-structural and structural components in automotive application. The typical examples of using FR-PP in automobiles could be: seat pan [326], floor panels [327], A-, B- and C-pillars [92], different protection shields [328] and so on.

9.6 Laminate Composites

Laminated composites consist of several monolayers (plies) containing endless fibers with various orientation angles (Fig. 9.24). Each monolayer comprises the reinforcement in the form of UD fibers (or tapes) embedded in the matrix. Next we refer to such monolayers as UD-PP.

Conceptually, the production of laminated composites from UD-PP does not differ from that of FR-PP, and consists of two basic stages, namely impregnation and consolidation. These steps can be either separated or combined in one production line. For detailed description of these production concepts interested reader is addressed to Sects. 9.4 and 9.5. Although the manufacturing methods of the semi-finished UD-PP does not principally differ from those of FR-PP, the production routes of composite parts involve also techniques typical for UD composites, i.e. pultrusion, filament winding (FW), etc. (Fig. 9.25).

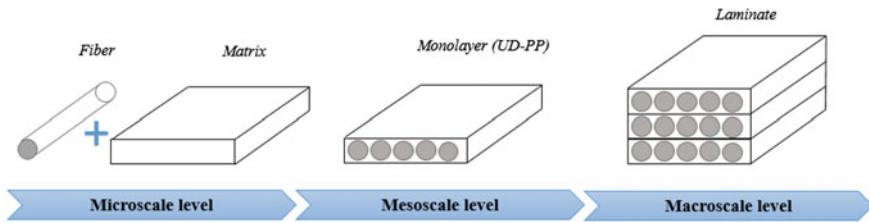


Fig. 9.24 Different structural levels of laminated composites

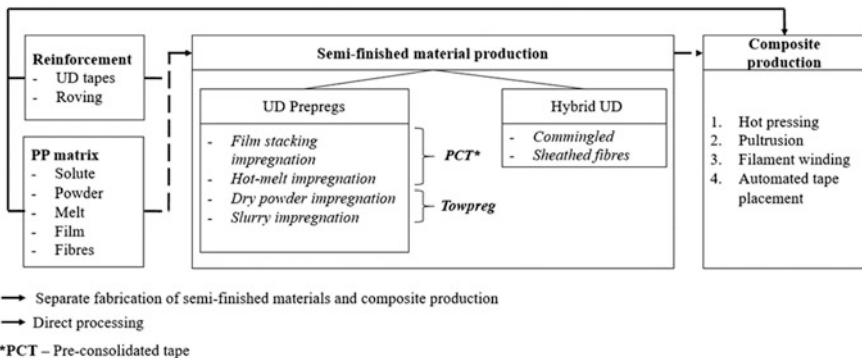


Fig. 9.25 Principal scheme of the UD-PP sequential production

9.6.1 Manufacturing

As it was mentioned before, the manufacturing techniques of UD-PP preregs are very similar to those of FR-PP and already introduced in Sect. 9.5. However, some of the techniques have certain distinguishing features which will be highlighted below.

UD thermoplastic preregs are differently classified. Thus semi-finished materials impregnated with solute, melt or film polymer are called as ‘pre-consolidated tapes’ (PCT), while preregs impregnated with powder are called as ‘towpregs’ (Fig. 9.26). UD-PP towpregs are produced under the tradenames FibrFlex[®], TenCate Cetex[®], PolyStrand[®], and others.

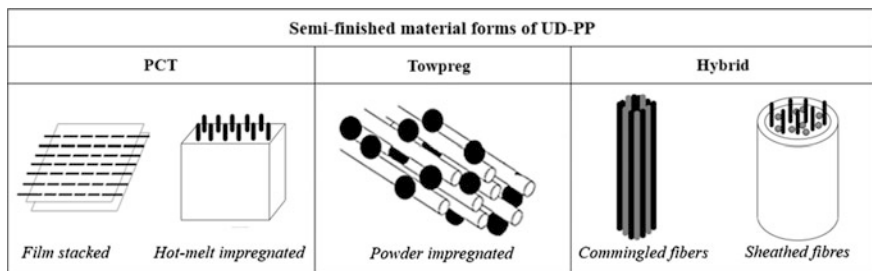


Fig. 9.26 Semi-finished material forms of UD-PP

Hybrid UD reinforcements could be in the form of commingled or sheathed fibers. In the latter case the roving or fibers are mingled with very fine matrix powder and jacketed by a thin polymer sheath [329, 330].

Film stacking is the most widely used method to produce small quantity of the UD-PP, while for the mass production hot melt, *dry powder* or *slurry* methods are far more suitable. A distinct feature of all the mass production techniques of UD-PP is the utilization of ‘pultrusion-like’ equipment. This involves the pulling of a continuous fiber tow through an “impregnation medium”, which is either the polymer melt or dry polymer powder, or a fluid dispersion of polymer powder. This is followed in-line with suitable post-treatments.

Hot melt pultrusion

Basically, hot melt pultrusion lines for UD-PP prepreg production consists of the following units: creel; fibers guidance, spreading, preheating and drying; polymer feeder; impregnation and consolidation cell; cooling chamber, pulling and cutting units (Fig. 9.27).

However, feeding unit could be implemented by different ways. Thus, it could be either an injection [331] or an extrusion equipment [332, 333]. Both variants are currently used. For example, Nunes et al. [332, 334] produced PP-based PCTs with GF and CF reinforcements via a pultrusion line utilizing an extrusion feeder

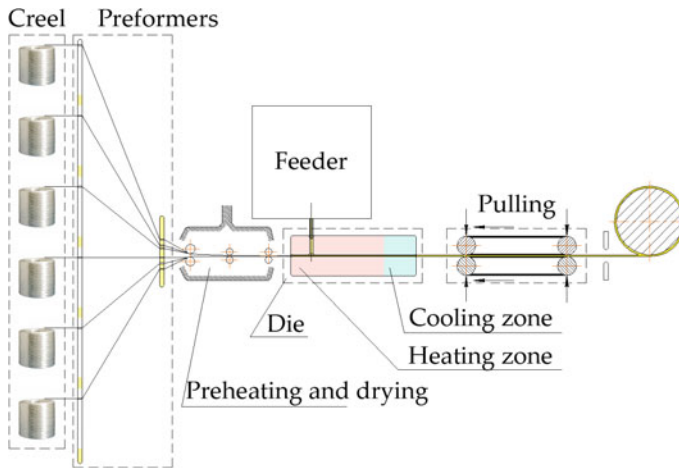


Fig. 9.27 Hot melt thermoplastic pultrusion production line

(cross-head extrusion die). The width of the resulting tape was 25 mm and the fiber content was 45 and 60 wt% for CF and GF, respectively. The same principle is utilized by CompTape B.V. (Delft, Netherlands) [333], that commercially produce PCTs with PP matrix. Poon et al. [335] also adapted an extruder feeding systems for UD-PP prepreg production.

By contrast Thermoplastic Pultrusion Technologies (Yorktown, Virginia, USA) used injection polymer feeder [331]. The major difference between injection and extrusion feeding units is in the polymer supply (intermittent vs. continuous, respectively). Note that an injection feeder requires higher pressures, as well as, stricter process control compared to the extrusion one.

Nunes et al. [336, 337] demonstrated that the impregnation quality of pultruded PCT is better than that of powder impregnated towpreps. However, hot melt pultrusion technique is not free from shortcomings. The main drawbacks of this technology are: (i) impregnation is affected by the matrix viscosity, and (ii) the polymer melt should have high enough thermooxidative stability.

Dry powder processing

Dry powder prepegging method was developed by Price in 1973 [338]. In this technique finely ground PP particles, suspended in dry air, are deposited onto the fiber tow exploiting of aerodynamic, gravitation, van der Waals and electrostatic forces. A typical powder-coating line comprises wind-off block, fibers' spreader, fiber pre-heating and coating sections, consolidation oven and wind-up unit (Fig. 9.28) [339–342]. The coating section could either include a simple powder feeder and a vibrating bath, or a more complicated powder feed hopper creating fluidized bed. There are several methods to create fluidized powder beds which have been surveyed by Padaki and Drzal [343].

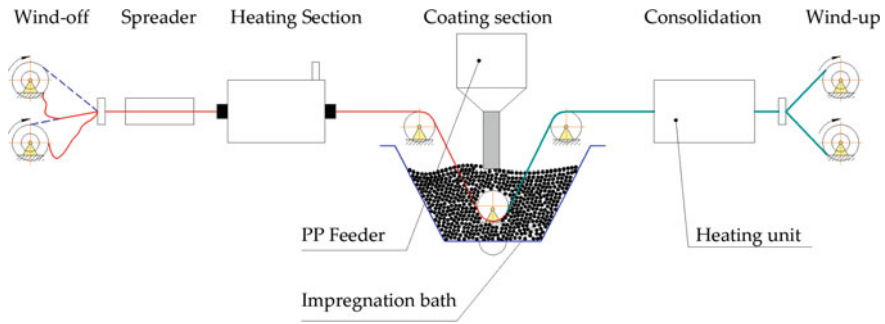


Fig. 9.28 Schematic diagram of the powder-coating line set-up (based on Ref. [340])

A research group in Polytechnic Institute of Leiria (Portugal) [340, 344, 345] conducted a comprehensive research study on the dry powder impregnated towpreg manufacturing. It was reported that particles size is one of the most important processing parameters. Thus, the optimum PP particles size from the point of view of production capacity should be 400 μm , while to guarantee adequate mechanical properties the particle size should not exceed 320 μm [344]. The optimized processing conditions were: linear fiber pulling speed in the range of 1.1–1.2 m/min, coating chamber and consolidation oven temperature at 55 and 280 $^{\circ}\text{C}$, respectively, and relative humidity in the coating chamber at 80%.

Despite of the great advantage of dry powder prepregging, namely independence of the matrix viscosity, it has definite drawbacks. One of them is the high friction between dry fibers and guide rollers that causes fibers damage. Electrostatic forces that stipulate particles deposition on the tows do not guarantee good process control due to the high loss of polymer powder. As a result, it is quite difficult to achieve consistent V_f in towpregs. Moreover, it is practically impossible to attain a uniform powder distribution in the towpreg. The last fact causes the appearance of pores and microvoids in the final product.

Slurry processing (wet impregnation)

Slurry processing implies drawing of the reinforcing fibers through a medium consisting of a liquid carrier with suspended polymer particles [343, 345, 346]. The presence of a liquid phase reduces the friction force between the tow fibers and guide pins, thus minimizing fibers damage. Moreover, capillary forces help the penetration of particles into the tow yielding some interlocking effect [347]. However, wet powder impregnation process requires the removal of the liquid carrier prior to consolidation that decreases the cost efficiency and production capacity [348].

9.6.2 Structure Development and Characterization

Production technologies for laminated composite manufacturing could be roughly divided into two groups—‘continuous’ and ‘discrete’ methods. ‘Continuous’ techniques include pultrusion and filament winding (FW), while ‘discrete’ ones the hot pressing and automated tape placement (ATP).

Pultrusion of UD-PP composites

The very first attempts to produce laminated thermoplastic composite by means of pultrusion process were taken in 1980th [349]. Since that time a great number of investigations were dedicated to the different aspects of the thermoplastic pultrusion technology. Today pultrusion is a well-established manufacturing technique of thermoplastic profiles. A typical thermoplastic pultrusion line includes block of creels with the bobbins of fibers, guiding device, fibers’ preheater, set of two dies, pulling and cutting mechanism (Fig. 9.29).

The main difference of a thermoplastic pultrusion line from thermoset one resides in a presence of two dies working for heating and cooling, respectively. The matrix flow occurs in a heating die that, due to higher viscosity of thermoplastic matrix, is much shorter in length than the thermoset analogue. Moreover, the cavity of the heating die section of thermoplastic pultrusion is tapered over a larger length than the thermoset one. This cavity profile is aimed at generating back flow of the matrix melt in order to achieve the desired impregnation and compaction of the profile [350]. A cooling die is intended for the consolidation of the profile.

Nunes and co-workers [334] defined the optimal processing parameters for production of laminated GF-PP composite profiles using a laboratory scale pultrusion line. This pultrusion processing window was given by the following parameters: pre-heating chamber—170 to 180 °C, consolidation die temperature—280 °C, cooling die temperature—25 °C, and linear pultrusion speed—0.2 to 0.3 m/min. Similar results were obtained for GF-PP by Poon et al. [335], and for

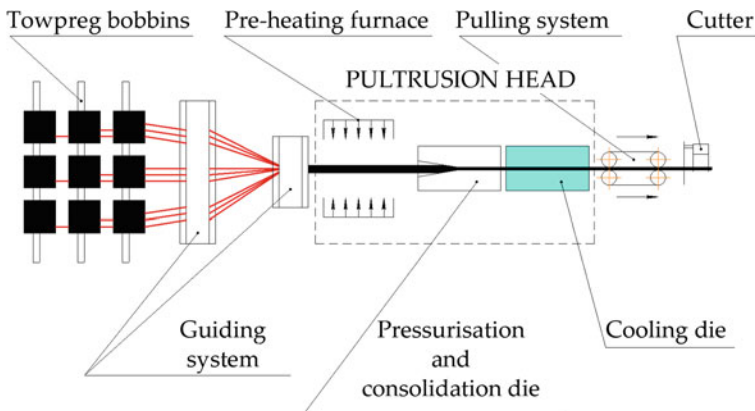


Fig. 9.29 Schematic diagram of thermoplastic pultrusion production line

flax fibers reinforced PP by Angelov et al. [351]. However, a line speed up to 2 m/min was achievable, depending on the section thickness of the profile [352]. Despite of maturity of the thermoplastic pultrusion process, its main drawback is that the angle of the reinforcement with respect of the production is limited. Thus, only UD laminates can be produced by means of pultrusion.

Filament winding

Filament winding (FW) is an automated manufacturing technique that enables to produce axially symmetric shell bodies with continuous fiber reinforcement placed at different angles. However, the reinforcement angles, feasible by FW, are limited for geodesic ones.

By contrast to thermoset the thermoplastic FW offers in situ (on-line) consolidation of composite product, thus enabling to eliminate post-consolidation procedure and, consequently, to attain better economic efficiency and higher production rates. The thermoplastic FW process consist of two steps: (i) heating of the prepreg up to the polymer melting temperature and (ii) applying compaction pressure and consolidation of the prepreg with the substrate laminate at the contact region (Fig. 9.30). A FW production line typically consists of a winding machine, creel, pre-heating and heating units, consolidation roller and mandrel.

The key issue in the successful implementation of thermoplastic FW is the heating that can be achieved by a variety of methods, i.e. direct flame, hot gas, IR radiation, ultrasonic [355] and laser energy. Funk and Neitzel [356, 357] estimated the feasibility of each heating method from the technical and economical positions. They determined, that laser heating enables the highest winding speed (up to 140 m/min) but at the same time is accompanied by high investment and processing costs. IR heating method exhibited lower (compared to laser) expenditures together with lower winding speed (not more than 27 m/min). Direct flame and hot gas

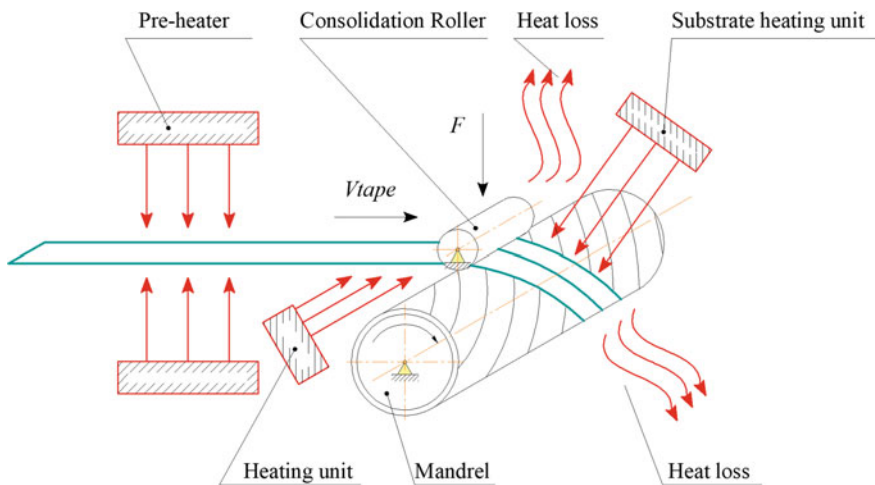


Fig. 9.30 Schematic diagram of thermoplastic FW process (based on Ref. [353, 354])

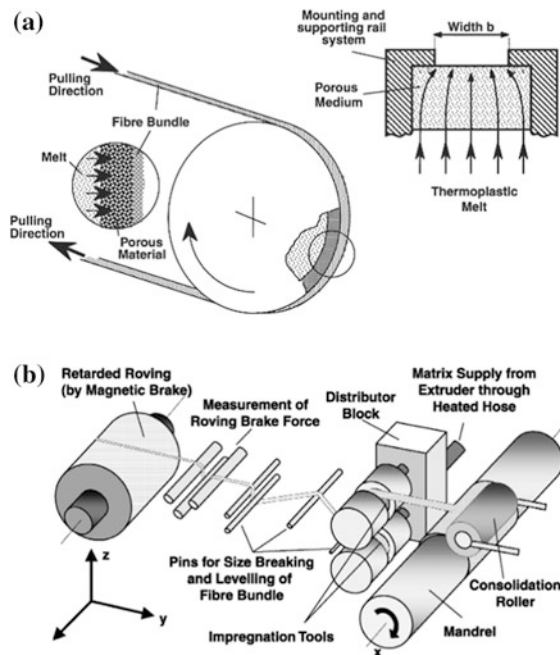
techniques are low-cost options allowing an average winding speed in the range of 18–60 m/min.

Dai and Ye [353] defined the processing window for GF-PP rings produced with a FW technique utilizing hot gas heating and constant compaction line pressure. Optimal processing parameters for composite tubes produced from commingles GF roving were obtained by Dobrzanski et al. [358] by means of Taguchi method.

The feasibility of a direct processing route for FW (D-FW) that involved the fibers' impregnation, winding and consolidation in line, was first demonstrated by Astrom and Pipes in 1990th [359]. For the fiber impregnation the authors have chosen a combination of powder impregnation in an agitated powder bed. The powder-impregnated fibers entered in a small pultrusion die before depositing them onto the mandrel. Besides a very low processing speed (0.7 m/min), for this D-FW other technological restrictions, such as high void content and weak consolidation, had to be taken into account.

Henninger and Friedrich [360, 361] informed about an on-line melt impregnation technique using an 'impregnation wheel'. The working principle of this technique involves an impregnation of a reinforcement tow with the molten polymer squeezed by a pressure through a porous ring (Fig. 9.31a). The supply of polymer melt is provided by a normal single screw extruder and a flexible heated hose. The schematic diagram of D-FW line utilizing 'impregnation wheel' technology is presented in Fig. 9.31b. The maximum achievable winding speed causing no degradation in the mechanical properties was 15 m/min, and the maximum processing temperature was given by 230 °C [361].

Fig. 9.31 D-FW production line: **a** working principle of an 'impregnation wheel' technology; **b** schematic diagram of the D-FW production line ([360, 361] reproduced with the permission of Elsevier)



As it was mentioned before the possible fiber architecture with FW process is limited by geodesic angle. The next discussed technology is free of this restriction.

Automated Tape Placement

Automated tape placement (ATP) is a manufacturing technique, that allows to create large scale flat, single- and even double-curved laminate composite products without any limitation on the reinforcing angle. ATP is a logical extension of a thermoplastic tape placement technology, that becomes possible with the advances in automation/robotics [362]. The ATP process is similar to FW and involves the prepreg's melting (at least locally) and bounding it to the laminate substrate by application of a compaction force exerted by a consolidation roller (Fig. 9.32). During the consolidation procedure the prepreg tapes are cooled to the tool temperature. Possible heating methods for ATP are the same as for FW. However, due to a high production capacity demands, the most effective heat source for ATP is laser [363–366].

The laser-assisted ATP rates could reach 160 m/min [364], thus allowing cost-effective production of fully consolidated load-optimized 3D structural components for automotive, aerospace, sport and other industries. An extensive research in this field was conducted by Fraunhofer Institute for Production Technology (Fraunhofer IPT) [364, 365, 367, 368]. This research group developed a production system for ATP [364] and a multi-material-head for ATP which is able to process thermoplastic and thermoset tapes, as well as dry fiber roving covered with adhesive [367]. Moreover, they demonstrated the feasibility of combining of ATP produced shell parts with 3D-printed thermoplastic structures [369].

Hot pressing manufacturing technique for UD-PP composites does not principally differ from that for FR-PP which is described in details in Sect. 9.5.

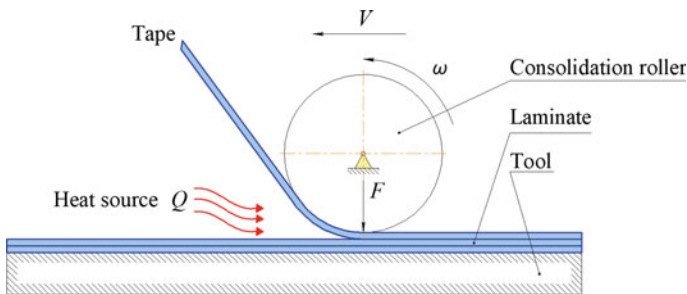


Fig. 9.32 Schematic diagram of ATP technology

9.6.3 Properties and Their Prediction

9.6.3.1 Mechanical Response

Due to their reinforcement architecture UD-PP composites demonstrate the highest level of mechanical response in longitudinal direction when compared with FR-PP, GMT, LFT and other PP based composites (Fig. 9.2).

The static mechanical properties of UD-PP can be defined either experimentally and also well-predicted by theories. Mechanical testing methods for UD composites are well established laboratory techniques that are ruled by a number of standards. Thus, ISO 527-5 is a relevant international standard for tensile testing of UD composites, ASTM D 695, ASTM D 3410, DIN 65 380 and others—for compression testing, ASTM D 790—for flexural testing. However, there are further relevant testing standards summarized in Ref. [172]. Some mechanical testing results of UD-PP are presented in Table 9.6. More information about the properties of UD-PP reinforced with NFs a concerned reader could find in an overview paper of Malkapuram et al. [289].

Table 9.6 Mechanical properties of UD-PP

Reinforcement type (prepreg type)	Production technique	V_f (%)	ρ (kg/m ³)	Tensile		Flexural		Ref.
				σ (MPa)	E (GPa)	σ (MPa)	E (GPa)	
Flax (commingled)	Pultrusion	38	800	145	15.1	101	14.3	[376]
Flax	Hot pressing	17.4–31.8	1000–1070	–	–	89.9–212.4	11–22	[377]
Kenaf (film stacking)	Vacuum bag	≈44	–	120	~ 14	–	–	[378]
Kenaf (film stacking)	Hot pressing	–	–	~ 83–93	~ 5	–	–	[379]
GF (towpreg)	Pultrusion	56.2	–	305	29.9	>117	22.5	[344]
		52.1	1322–1767	>336	33.9	158–241	28.6	[332]
	FW	59	–	431	31	–	–	[344]
GF (commingled)	Pultrusion	37.1	1519	545.9	24.9	595	26.2	[332]
		50	1480	515	33.4	335	28.8	[376]
GF (PCT)	pultrusion	30	–	355	71.3	329	16.8	[332]
GF (PCT) Plytron®	–	35	1480	680	22.5	570	22	[380]
CF	–	40	–	1421	–	750	90	[381]

The mechanical properties of UD-PP can be improved by interphase engineering. The related methods do not differ from those for FR-PP described in Sect. 9.5 [370–374].

The theoretical prediction of the mechanical properties of UD in longitudinal direction is based on the rule of mixture [375]. However, this prediction is rather rough and can be used only for engineering evaluations.

The effective properties of the laminated composites consisting of several UD monolayers are defined by the orientation, thickness, and stacking sequence of the individual layers. The theory that describe the linear elastic behavior of laminated composites subjected to in-plane loads and bending moments is referred as Classical Laminate Theory (CLT) [382, 383]. CLT is a well-known analytical predictive technique widely used by engineers and researchers to determine linear elastic properties of composites. To evaluate the failure response of the laminated composites different failure criteria are considered. In general, fiber reinforced composites exhibit various types of internal failure, namely: fiber breakage, matrix deformation and cracking, fiber debonding, fiber pull-out and delamination. The development of fiber reinforced composites failure criteria has been conducted for more than 30 years by the researchers all over the world. The progress in failure prediction approaches was summarized in a comprehensive review conducted by Orifici et al. [384].

9.6.3.2 Rheological Behavior

The rheological behavior of UD-PP is governed by the same laws as FR-PP and is well described in Sect. 9.5.3.2.

9.6.3.3 Thermal Behavior

Thermal properties of composites are the main parameters that define thermal response, performance and reliability of the related structures. Generally thermal properties of laminated composites depend on a number of variables, i.e. reinforcement type, its content and laying angle, void content, temperature, etc. Consequently, it is highly desirable to control and tailor the composite thermal properties. Apart from traditional experimental methods, a number of predictive methods for thermal conductivity, diffusivity and specific heat determination exist [385, 386]. One of the most widely used methods to predict the thermal conductivity of UD composites is thermal-electrical analogy method. This is based on the similarity of the partial differential equation governing the thermal potential and electric potential distribution. According to this analogue the effective thermal conductivity of a composite could be determined as the equivalent electrical resistance by the Ohm's law [387].

9.6.3.4 Other Properties

Fatigue

The UD-PP composites are mainly developed for long term load-bearing applications, and therefore fatigue response of such composites is of great importance. The UD composite behavior under cyclic load is governed by diffuse damage accumulation. A general concept of UD composites tension-tension fatigue behavior was proposed by Talreja [388]. This concept implies that at low cycle fatigue catastrophic fiber damage is dominant, at intermediate cycle—progressive fiber-bridged matrix cracking and/or interfacial shear failure is prevalent, while for high cycle—failure initiated in the matrix and arrested by the fibers can be considered as typical.

Van den Oever and Peijs [389] examined the fatigue performance of UD-GF-PP with both unmodified and MAH-modified matrices under longitudinal tensile (Fig. 9.33a), transverse and shear (Fig. 9.33b) loads. The authors found only a slight improvement in fatigue performance for the UD-PP with maleic anhydride modified matrix.

The influence of interfacial strength of the UD-PP on the fatigue performance was also studied by Gamstedt et al. [390]. Enhancement of the interfacial strength between fibers and matrix with MAH led to better fatigue resistance and prolonged fatigue life.

Zushi et al. [381] defined the fatigue endurance limit (that can be used for design) for UD-PP reinforced with CFs as 500 MPa, that is one third of the static tensile strength.

Electric conductivity

Damage sensing/location and self-healing are the present hot topics in the field of advanced laminate composites, including PP-matrix based ones, as well. Joo et al. [391] demonstrated that addressable conducting network (ACN) technique is

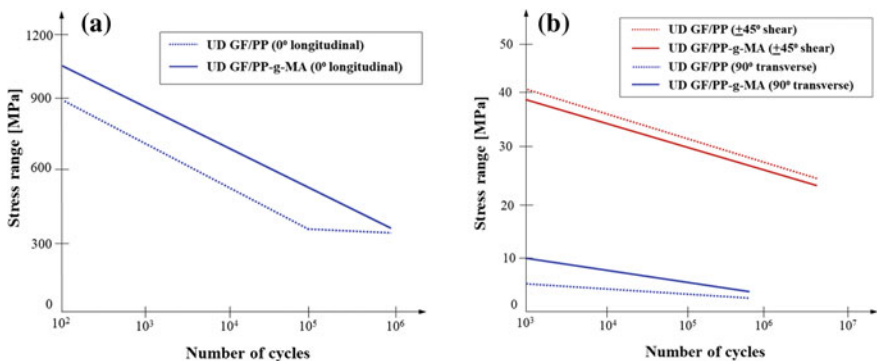


Fig. 9.33 Fatigue performance of UD-PP composites: **a** Longitudinal fatigue data for 0° laminate; **b** transverse and shear fatigue data for 90° off-axis laminates and ±45° angle-ply laminates correspondingly (based of Ref. [389])

promising method for damage sensing of composites. This technique utilizes the electrically conductive network of composite itself as sensor. Structural delamination or matrix cracking can be evaluated through resistance change by interruption of the through-thickness electric current flow. Metallic line electrodes on the top and bottom of the composite laminate, arranged in a grid pattern, serve to detect the change in the resistivity. To set the required through-thickness electric conductivity CNT and the like may be incorporated into the PP matrix or between the UD-CF laminae. It is noteworthy that composites containing both traditional fibrous and nanoscale reinforcements are referred to as hierarchical, multiscale or fuzzy composites. The beauty of this ACN approach is that it may work also for self-healing of the related composites when triggering resistive heating. The cited work showed that damage sensing was possible with high accuracy and the self-healing efficiency, measured in flexural tests, was as high as 96%.

9.6.4 Processing and Applications

UD-PP tapes and towpregs may be the feedstock for a vast variety of laminated composite products. Pultrusion is the preferred technique to produce profiles with various cross sections. FW allows the production of rotary bodies, i.e. pressure vessels, tanks, pipes, etc. ATP enables to create large-scale structures with single and double curvatures for aerospace, automotive and sport industries. However, technological versatility together with the ability to vary the laminate layup provides engineers a certain freedom, when creating laminated PP composite structures.

9.7 Conclusion and Outlook

The good mechanical and thermal properties of PP can be markedly enhanced by incorporation of reinforcements the range of which cover nanoparticles through textile architecture to UD aligned endless fibers. Beside of structural properties, the composites can be ensured with functional ones, such as thermal and electrical conductivities when for example carbonaceous nanofillers are introduced additionally. The latter nanofillers may play a key role in the preparation of smart composites having for example self-sensing and self-healing possibilities.

A general trend in the manufacturing of PP composites is the combination of several steps in-line. In the corresponding direct processes, the preparation and storage of semi-finished parts are avoided. Among the novel in situ preparation methods a bright future can be predicted the additive manufacturing methods, such as fused deposition of PP filaments with endless fiber reinforcement.

In the field of PP nanocomposites the R&D works will focus on using carbonaceous nanofillers to achieve functional properties. Considerable efforts will be

dedicated to model the structure-property relationships in nanocomposites whereby considering the actual dispersion state (agglomeration phenomena) of the nanoadditives.

Hybridization of the reinforcing fibers may drive the development of discontinuous fiber-reinforced injection-moldable composites. Use of recycled CFs in PP matrix may be a viable contribution to circular economy targeting the reuse of discarded composites. Tomographic inspections may result in new definition of the microstructure and its efficiency (i.e. fiber orientation distribution, fiber length alignment, fiber layering) in molded parts. The related works may contribute to more reliable flow modeling, as well. Textile engineering using commingled fibers will likely be the driver for the development of textile-reinforced PP composites. This note holds also for the related all-PP composites. The traditional processing techniques using UD fiber-reinforced PP preforms, such as filament winding, tape laying, may face to sever competition with additive manufacturing versions.

As far as the testing of PP composites concerns the general trend is to assess and describe their long-term performance including creep and fatigue.

References

1. Karger-Kocsis J, Kmetty Á, Lendvai L et al (2015) Water-assisted production of thermoplastic nanocomposites: a review. *Materials* 8(1):72–95. <https://doi.org/10.3390/ma8010072>
2. Zapata P, Quijada R (2012) Polypropylene nanocomposites obtained by in situ polymerization using metallocene catalyst: influence of the nanoparticles on the final polymer morphology. *J Nanomater* 2012:6. <https://doi.org/10.1155/2012/194543>
3. Azinfar B, Ahmad Ramazani SA, Jafariesfad N (2014) In situ preparation and property investigation of polypropylene/fumed silica nanocomposites. *Polym Compos* 35(1):37–44. <https://doi.org/10.1002/pc.22631>
4. Ahmad Ramazani SA, Tavakolzadeh F, Baniasadi H (2010) Synthesis of polypropylene/clay nanocomposites using bisupported Ziegler-Natta catalyst. *J Appl Polym Sci* 115(1):308–314. <https://doi.org/10.1002/app.31102>
5. Cardoso RDS, Oliveira JDS, Ramis LB et al (2018) Ziegler-Natta catalyst based on MgCl₂/clay/ID/TiCl₄ for the synthesis of spherical particles of polypropylene nanocomposites. *J Nanosci Nanotechnol* 18(7):5124–5132. <https://doi.org/10.1166/jnn.2018.15308>
6. Milani MA, González D, Quijada R et al (2013) Polypropylene/graphene nanosheet nanocomposites by in situ polymerization: synthesis, characterization and fundamental properties. *Compos Sci Technol* 84:1–7. <https://doi.org/10.1016/j.compscitech.2013.05.001>
7. Funck A, Kaminsky W (2007) Polypropylene carbon nanotube composites by in situ polymerization. *Compos Sci Technol* 67(5):906–915. <https://doi.org/10.1016/j.compscitech.2006.01.034>
8. Huang Y, Qin Y, Zhou Y et al (2010) Polypropylene/graphene oxide nanocomposites prepared by in situ Ziegler – Natta polymerization. *Chem Mater* 22(13):4096–4102. <https://doi.org/10.1021/cm100998e>
9. Kaminsky W (ed) (2013) Polyolefins: 50 years after Ziegler and Natta II. Polyolefins by metallocenes and other single-site catalyst. *Advances in polymer science*, vol 258. Springer, Heidelberg. <https://doi.org/10.1007/978-3-642-40805-2>

10. Kalaitzidou K, Fukushima H, Drzal LT (2007) A new compounding method for exfoliated graphite–polypropylene nanocomposites with enhanced flexural properties and lower percolation threshold. *Compos Sci Technol* 67(10):2045–2051. <https://doi.org/10.1016/j.compscitech.2006.11.014>
11. Chiu F-C, Chu P-H (2006) Characterization of solution-mixed polypropylene/clay nanocomposites without compatibilizers. *J Polym Res* 13(1):73–78. <https://doi.org/10.1007/s10965-005-9009-7>
12. Ljungberg N, Bonini C, Bortolussi F et al (2005) New nanocomposite materials reinforced with cellulose whiskers in atactic polypropylene: effect of surface and dispersion characteristics. *Biomacromol* 6(5):2732–2739. <https://doi.org/10.1021/bm050222v>
13. Karger-Kocsis J, Lendvai L (2018) Polymer/boehmite nanocomposites: a review. *J Appl Polym Sci* 135(24):45573. <https://doi.org/10.1002/app.45573>
14. Kato M, Matsushita M, Fukumori K (2004) Development of a new production method for a polypropylene-clay nanocomposite. *Polym Eng Sci* 44(7):1205. <https://doi.org/10.1002/pen.20115>
15. Karger-Kocsis J (2000) Reinforced polymer blends. In: Paul DR, Bucknall CB (eds) *Polymer blends*, vol 2. Wiley, New York, pp 395–428
16. Song P, Cao Z, Cai Y et al (2011) Fabrication of exfoliated graphene-based polypropylene nanocomposites with enhanced mechanical and thermal properties. *Polymer* 52(18):4001–4010. <https://doi.org/10.1016/j.polymer.2011.06.045>
17. Bouaziz A, Jaziri M, Dalmas F et al (2014) Nanocomposites of silica reinforced polypropylene: correlation between morphology and properties. *Polym Eng Sci* 54(9):2187–2196. <https://doi.org/10.1002/pen.23768>
18. Dabrowska I, Fambri L, Pegoretti A et al (2015) Spinning, drawing and physical properties of polypropylene nanocomposite fibers with fumed nanosilica. *Express Polym Lett* 9:277–290. <https://doi.org/10.3144/expresspolymlett.2015.25>
19. Zohrevand A, Aji A, Mighri F (2014) Morphology and properties of highly filled iPP/TiO₂ nanocomposites. *Polym Eng Sci* 54(4):874–886. <https://doi.org/10.1002/pen.23625>
20. Lin Y, Chen H, Chan C-M et al (2008) High impact toughness polypropylene/CaCO₃ nanocomposites and the toughening mechanism. *Macromolecules* 41(23):9204–9213. <https://doi.org/10.1021/ma801095d>
21. Zhao H, Li RKY (2005) Crystallization, mechanical, and fracture behaviors of spherical alumina-filled polypropylene nanocomposites. *J Polym Sci, Part B: Polym Phys* 43(24):3652–3664. <https://doi.org/10.1002/polb.20654>
22. Pracella M, Chionna D, Fina A et al (2006) Polypropylene-POSS nanocomposites: morphology and crystallization behaviour. *Macromol Symp* 234(1):59–67. <https://doi.org/10.1002/masy.200650209>
23. Prashantha K, Lacrampe MF, Krawczak P (2011) Processing and characterization of halloysite nanotubes filled polypropylene nanocomposites based on a masterbatch route: effect of halloysites treatment on structural and mechanical properties. *Express Polym Lett* 5(4):295–307. <https://doi.org/10.3144/expresspolymlett.2011.30>
24. Prashantha K, Soulestin J, Lacrampe MF et al (2009) Masterbatch-based multi-walled carbon nanotube filled polypropylene nanocomposites: assessment of rheological and mechanical properties. *Compos Sci Technol* 69(11):1756–1763. <https://doi.org/10.1016/j.compscitech.2008.10.005>
25. Szentes A, Varga C, Horváth G et al (2012) Electrical resistivity and thermal properties of compatibilized multi-walled carbon nanotube/polypropylene composites. *Express Polym Lett* 6(6):494–502. <https://doi.org/10.3144/expresspolymlett.2012.52>
26. Prashantha K, Soulestin J, Lacrampe MF et al (2009) Taguchi analysis of shrinkage and warpage of injection-moulded polypropylene/multiwall carbon nanotubes nanocomposites. *Express Polym Lett* 3(10):630–638. <https://doi.org/10.3144/expresspolymlett.2009.79>
27. Hassan ML, Mathew AP, Hassan EA et al (2014) Improving cellulose/polypropylene nanocomposites properties with chemical modified bagasse nanofibers and maleated polypropylene. *J Reinf Plast Compos* 33(1):26–36. <https://doi.org/10.1177/0731684413509292>

28. Hubbe MA, Rojas OJ, Lucia LA et al (2008) Cellulosic nanocomposites: a review. *BioResources* 3(3):929–980
29. Utracki LA, Sepéhr M, Boccaleri E (2007) Synthetic, layered nanoparticles for polymeric nanocomposites (PNCs). *Polym Adv Technol* 18(1):1–37. <https://doi.org/10.1002/pat.852>
30. Utracki LA, Kamal MR (2002) Clay-containing polymeric nanocomposites. *Arab J Sci Eng* 27(1):43–67
31. Gao Y, Zhang Y, Williams GR et al (2016) Layered double hydroxide-oxidized carbon nanotube hybrids as highly efficient flame retardant nanofillers for polypropylene. *Sci Rep* 6:35502. <https://doi.org/10.1038/srep35502>
32. Nagendra B, Rosely CVS, Leuteritz A et al (2017) Polypropylene/layered double hydroxide nanocomposites: influence of LDH intralayer metal constituents on the properties of polypropylene. *ACS Omega* 2(1):20–31. <https://doi.org/10.1021/acsomega.6b00485>
33. Tripathi SN, Srinivasa Rao GS, Mathur AB et al (2017) Polyolefin/graphene nanocomposites: a review. *RSC Adv* 7(38):23615–23632. <https://doi.org/10.1039/C6RA28392F>
34. Hári J, Horváth F, Móczó J et al (2017) Competitive interactions, structure and properties in polymer/layered silicate nanocomposites. *Express Polym Lett* 11(6):479–492. <https://doi.org/10.3144/expresspolymlett.2017.45>
35. Hári J, Dominkovics Z, Fekete E et al (2009) Kinetics of structure formation in PP/layered silicate nanocomposite. *Express Polym Lett* 3(11):692–702. <https://doi.org/10.3144/expresspolymlett.2009.87>
36. Lee SH, Youn JR (2008) Experimental and theoretical study on shear flow behavior of polypropylene/layered silicate nanocomposites. *Adv Compos Mater* 17(3):191–214. <https://doi.org/10.1163/156855108X345225>
37. He S, Zhang J, Xiao X et al (2017) Study on the morphology development and dispersion mechanism of polypropylene/graphene nanoplatelets composites for different shear field. *Compos Sci Technol* 153:209–221. <https://doi.org/10.1016/j.compscitech.2017.10.024>
38. Battisti M, Perko L, Arunachalam S et al (2018) Influence of elongational flow generating nozzles on material properties of polypropylene nanocomposites. *Polym Eng Sci* 58(1):3–12. <https://doi.org/10.1002/pen.24361>
39. Huang Z-X, Meng C, Zhang G et al (2017) Manufacturing polymer/clay nanocomposites through elongational flow technique. *Mater Manuf Process* 32(12):1409–1415. <https://doi.org/10.1080/10426914.2017.1339316>
40. Reichert P, Nitz H, Klinke S et al (2000) Poly(propylene)/organoclay nanocomposite formation: influence of compatibilizer functionality and organoclay modification. *Macromol Mater Eng* 275(1):8–17. [https://doi.org/10.1002/\(SICI\)1439-2054\(20000201\)275:1%3c8:AID-MAME8%3e3.0.CO;2-6](https://doi.org/10.1002/(SICI)1439-2054(20000201)275:1%3c8:AID-MAME8%3e3.0.CO;2-6)
41. Garcia-López D, Picazo O, Merino JC et al (2003) Polypropylene–clay nanocomposites: effect of compatibilizing agents on clay dispersion. *Eur Polym J* 39(5):945–950. [https://doi.org/10.1016/S0014-3057\(02\)00333-6](https://doi.org/10.1016/S0014-3057(02)00333-6)
42. Koo CM, Kim MJ, Choi MH et al (2003) Mechanical and rheological properties of the maleated polypropylene–layered silicate nanocomposites with different morphology. *J Appl Polym Sci* 88(6):1526–1535. <https://doi.org/10.1002/app.11782>
43. Li W, Karger-Kocsis J, Thomann R (2009) Compatibilization effect of TiO₂ nanoparticles on the phase structure of PET/PP/TiO₂ nanocomposites. *J Polym Sci, Part B: Polym Phys* 47:1616–1624. <https://doi.org/10.1002/polb.21752>
44. Ray SS (2010) A new possibility for microstructural investigation of clay-based polymer nanocomposite by focused ion beam tomography. *Polymer* 51(17):3966–3970. <https://doi.org/10.1016/j.polymer.2010.06.025>
45. Schneider S, Eppler F, Weber M et al (2016) Multiscale dispersion-state characterization of nanocomposites using optical coherence tomography. *Sci Rep* 6:31733. <https://doi.org/10.1038/srep31733>

46. Karger-Kocsis J, Varga J (1999) Interfacial morphology and its effects in polypropylene composites. In: Karger-Kocsis J (ed) *Polypropylene: an A-Z reference*, vol 2. Polymer Science and Technology Series. Springer Netherlands, Dordrecht, Netherlands, pp 348–356. https://doi.org/10.1007/978-94-011-4421-6_50
47. Zhang S, Minus ML, Zhu L et al (2008) Polymer transcrystallinity induced by carbon nanotubes. *Polymer* 49(5):1356–1364. <https://doi.org/10.1016/j.polymer.2008.01.018>
48. Abdou JP, Braggin GA, Luo Y et al (2015) Graphene-induced oriented interfacial microstructures in single fiber polymer composites. *ACS Appl Mater Interfaces* 7(24):13620–13626. <https://doi.org/10.1021/acsami.5b03269>
49. Nakajima H, Yamada K, Iseki Y et al (2003) Preparation and characterization of polypropylene/mesoporous silica nanocomposites with confined polypropylene. *J Polym Sci, Part B: Polym Phys* 41(24):3324–3332. <https://doi.org/10.1002/polb.10700>
50. Zhang MQ, Rong MZ, Friedrich K (2003) Processing and properties of nonlayered nanoparticle reinforced thermoplastic composites. In: Nalwa HS (ed) *Handbook of organic-inorganic hybrid materials and nanocomposites*, vol 2. Nanocomposites. American Scientific Publishers, Los Angeles, pp 113–150
51. Karamipour S, Ebadi-Dehaghani H, Ashouri D et al (2011) Effect of nano-CaCO₃ on rheological and dynamic mechanical properties of polypropylene: experiments and models. *Polym Test* 30(1):110–117. <https://doi.org/10.1016/j.polymertesting.2010.10.009>
52. Hu H, Onyebueke L, Abatan A (2010) Characterizing and modeling mechanical properties of nanocomposites-review and evaluation. *J Miner Mater Charact Eng* 9(4):275–319. <https://doi.org/10.4236/jmmce.2010.94022>
53. Kalaitzidou K, Fukushima H, Miyagawa H et al (2007) Flexural and tensile moduli of polypropylene nanocomposites and comparison of experimental data to Halpin-Tsai and Tandon-Weng models. *Polym Eng Sci* 47(11):1796–1803. <https://doi.org/10.1002/pen.20879>
54. Rouhi S, Alizadeh Y, Ansari R (2016) Molecular dynamics simulations of the interfacial characteristics of polypropylene/single-walled carbon nanotubes. *Proc Inst Mech Eng Part L: J Mater: Des Appl* 230(1):190–205. <https://doi.org/10.1177/1464420714557167>
55. Rezaiean N, Ebadi-Dehaghani H, Khonakdar HA et al (2016) Microstructure and properties of polypropylene/clay nanocomposites. *J Macromol Sci Part B* 55(10):1022–1038. <https://doi.org/10.1080/00222348.2016.1230462>
56. Spencer PE, Sweeney J (2009) Modeling of polymer clay nanocomposites for a multiscale approach. In: Karger-Kocsis J, Fakirov S (eds) *Nano- and micromechanics of polymer blends and composites*. Carl Hanser Verlag GmbH & Co. KG, Munich, pp 545–578
57. Mallick PK, Zhou Y (2003) Yield and fatigue behavior of polypropylene and polyamide-6 nanocomposites. *J Mater Sci* 38(15):3183–3190. <https://doi.org/10.1023/A:1025161215708>
58. Lv Y, Huang Y, Kong M et al (2014) Creep lifetime prediction of polypropylene/clay nanocomposites based on a critical failure strain criterion. *Compos Sci Technol* 96:71–79. <https://doi.org/10.1016/j.compscitech.2014.03.011>
59. Pedrazzoli D, Pegoretti A (2014) Long-term creep behavior of polypropylene/fumed silica nanocomposites estimated by time–temperature and time–strain superposition approaches. *Polym Bull* 71(9):2247–2268. <https://doi.org/10.1007/s00289-014-1185-3>
60. Drozdov AD, Høg Lejre AL, Christiansen Jd (2009) Viscoelasticity, viscoplasticity, and creep failure of polypropylene/clay nanocomposites. *Compos Sci Technol* 69(15):2596–2603. <https://doi.org/10.1016/j.compscitech.2009.07.018>
61. Ramsaroop A, Kanny K, Mohan T (2010) Fracture toughness studies of polypropylene- clay nanocomposites and glass fibre reinforced polypropylene composites. *Mater Sci Appl* 1(5):301–309. <https://doi.org/10.4236/msa.2010.15044>
62. Karger-Kocsis J (1989) Fracture of short-fibre reinforced thermoplastics. In: Friedrich K (ed) *Application of fracture mechanics to composite materials*, vol 6. Composite Materials Series. Elsevier Applied Science, Amsterdam, pp 189–247

63. Pegoretti A (2009) Creep and fatigue behavior of polymer nanocomposites. In: Karger-Kocsis J, Fakirov S (eds) Nano- and micromechanics of polymer blends and composites. Hanser, Munich, pp 301–339. <https://doi.org/10.3139/9783446430129.009>
64. Karger-Kocsis J (2009) On the toughness of “nanomodified” polymers and their traditional polymer composites. In: Karger-Kocsis J, Fakirov S (eds) Nano- and micromechanics of polymer blends and composites. Hanser, Munich, pp 425–470. <https://doi.org/10.3139/9783446430129.012>
65. Chen L, Wong SC, Pisharath S (2003) Fracture properties of nanoclay-filled polypropylene. *J Appl Polym Sci* 88(14):3298–3305. <https://doi.org/10.1002/app.12153>
66. Bureau MN, Perrin-Sarazin F, Ton-That MT (2004) Polyolefin nanocomposites: essential work of fracture analysis. *Polym Eng Sci* 44(6):1142–1151. <https://doi.org/10.1002/pen.20107>
67. Chan C-M, Wu J, Li J-X et al (2002) Polypropylene/calcium carbonate nanocomposites. *Polymer* 43(10):2981–2992. [https://doi.org/10.1016/S0032-3861\(02\)00120-9](https://doi.org/10.1016/S0032-3861(02)00120-9)
68. Karger-Kocsis J (1999) Dependence of the fracture and fatigue performance of polyolefins and related blends and composites on microstructural and molecular characteristics. *Macromol Symp* 143(1):185–205. <https://doi.org/10.1002/masy.19991430115>
69. Ou Y, Yang F, Yu ZZ (1998) A new conception on the toughness of nylon 6/silica nanocomposite prepared via in situ polymerization. *J Polym Sci, Part B: Polym Phys* 36(5):789–795. [https://doi.org/10.1002/\(SICI\)1099-0488\(19980415\)36:5%3c789:AID-POLB6%3e3.0.CO;2-G](https://doi.org/10.1002/(SICI)1099-0488(19980415)36:5%3c789:AID-POLB6%3e3.0.CO;2-G)
70. Argon AS, Cohen RE (2003) Toughenability of polymers. *Polymer* 44(19):6013–6032. [https://doi.org/10.1016/S0032-3861\(03\)00546-9](https://doi.org/10.1016/S0032-3861(03)00546-9)
71. Lauke B (2017) Fracture toughness modelling of polymers filled with inhomogeneously distributed rigid spherical particles. *Express Polym Lett* 11(7):545–554. <https://doi.org/10.3144/expresspolymlett.2017.52>
72. Arencón D, Velasco JI (2009) Fracture toughness of polypropylene-based particulate composites. *Materials* 2(4):2046. <https://doi.org/10.3390/ma2042046>
73. Bárány T, Czigány T, Karger-Kocsis J (2010) Application of the essential work of fracture (EWF) concept for polymers, related blends and composites: a review. *Prog Polym Sci* 35(10):1257–1287. <https://doi.org/10.1016/j.progpolymsci.2010.07.001>
74. Turcsán T, Mészáros L, Khumalo VM et al (2014) Fracture behavior of boehmite-filled polypropylene block copolymer nanocomposites as assessed by the essential work of fracture concept. *J Appl Polym Sci* 131(13). <https://doi.org/10.1002/app.40447>
75. Pedrazzoli D, Tuba F, Khumalo V et al (2014) Mechanical and rheological response of polypropylene/boehmite nanocomposites. *J Reinf Plast Compos* 33(3):252–265. <https://doi.org/10.1177/0731684413505787>
76. Satapathy BK, Ganß M, Weidisch R et al (2007) Ductile-to-semiductile transition in PP-MWNT nanocomposites. *Macromol Rapid Commun* 28(7):834–841. <https://doi.org/10.1002/marc.200600892>
77. Karger-Kocsis J, Khumalo VM, Bárány T et al (2013) On the toughness of thermoplastic polymer nanocomposites as assessed by the essential work of fracture (EWF) approach. *Compos Interfaces* 20(6):395–404. <https://doi.org/10.1080/15685543.2013.807145>
78. Bureau MN, Ton-That M-T, Perrin-Sarazin F (2006) Essential work of fracture and failure mechanisms of polypropylene–clay nanocomposites. *Eng Fract Mech* 73(16):2360–2374. <https://doi.org/10.1016/j.engfracmech.2006.04.012>
79. Saminathan K, Selvakumar P, Bhatnagar N (2008) Fracture studies of polypropylene/nanoclay composite. Part I: effect of loading rates on essential work of fracture. *Polym Test* 27(3):296–307. <https://doi.org/10.1016/j.polymertesting.2007.11.008>
80. Karger-Kocsis J (1996) For what kind of polymer is the toughness assessment by the essential work concept straightforward? *Polym Bull* 37(1):119–126. <https://doi.org/10.1007/bf00313827>

81. Utracki LA, Simha R, Garcia-Rejon A (2003) Pressure – volume – temperature dependence of poly- ϵ -caprolactam/clay nanocomposites. *Macromolecules* 36(6):2114–2121. <https://doi.org/10.1021/ma0215464>
82. Giannelis EP, Krishnamoorti R, Manias E (1999) Polymer-silicate nanocomposites: model systems for confined polymers and polymer brushes. In: Granick S (ed) *Polymers in confined environments*. *Advances in Polymer Science*, vol 138. Springer, Berlin, pp 107–147. https://doi.org/10.1007/3-540-69711-x_3
83. Privalko VP, Shumsky VF, Privalko EG et al (2002) Viscoelasticity and flow behavior of irradiation grafted nano-inorganic particle filled polypropylene composites in the melt state. *Sci Technol Adv Mater* 3(2):111. [https://doi.org/10.1016/S1468-6996\(00\)00011-6](https://doi.org/10.1016/S1468-6996(00)00011-6)
84. Gu SY, Ren J, Wang QF (2004) Rheology of poly(propylene)/clay nanocomposites. *J Appl Polym Sci* 91(4):2427–2434. <https://doi.org/10.1002/app.13403>
85. Trinkle S, Friedrich C (2001) Van Gorp-Palmen-plot: a way to characterize polydispersity of linear polymers. *Rheol Acta* 40(4):322–328. <https://doi.org/10.1007/s003970000137>
86. Chafidz A, Kaaressina M, Al-Zahrani S et al (2014) Multiwall carbon nanotubes filled polypropylene nanocomposites: rheological and electrical properties. *Polym Eng Sci* 54(5):1134–1143. <https://doi.org/10.1002/pen.23647>
87. Sinha Ray S, Okamoto M (2003) Polymer/layered silicate nanocomposites: a review from preparation to processing. *Prog Polym Sci* 28(11):1539–1641. <https://doi.org/10.1016/j.progpolymsci.2003.08.002>
88. Okamoto M, Nam PH, Maiti P et al (2001) A house of cards structure in polypropylene/clay nanocomposites under elongational flow. *Nano Lett* 1(6):295–298. <https://doi.org/10.1021/nl0100163>
89. Reichert P, Hoffmann B, Bock T et al (2001) Morphological stability of poly(propylene) nanocomposites. *Macromol Rapid Commun* 22(7):519–523. [https://doi.org/10.1002/1521-3927\(20010401\)22:7%3c519:AID-MARC519%3e3.0.CO;2-W](https://doi.org/10.1002/1521-3927(20010401)22:7%3c519:AID-MARC519%3e3.0.CO;2-W)
90. Solomon MJ, Almusallam AS, Seefeldt KF et al (2001) Rheology of polypropylene/clay hybrid materials. *Macromolecules* 34(6):1864–1872. <https://doi.org/10.1021/ma001122e>
91. Bikiaris D (2010) Microstructure and properties of polypropylene/carbon nanotube nanocomposites. *Materials* 3(4):2884–2946. <https://doi.org/10.3390/ma3042884>
92. Karian H (ed) (2003) *Handbook of polypropylene and polypropylene composites*. CRC Press, Boca Raton (Revised and Expanded. *Plastics Engineering*)
93. Yoon PJ, Fornes TD, Paul DR (2002) Thermal expansion behavior of nylon 6 nanocomposites. *Polymer* 43(25):6727–6741. [https://doi.org/10.1016/S0032-3861\(02\)00638-9](https://doi.org/10.1016/S0032-3861(02)00638-9)
94. Manias E, Touny A, Wu L et al (2001) Polypropylene/montmorillonite nanocomposites. Review of the synthetic routes and materials properties. *Chem Mater* 13(10):3516–3523. <https://doi.org/10.1021/cm0110627>
95. Fornes TD, Paul DR (2003) Modeling properties of nylon 6/clay nanocomposites using composite theories. *Polymer* 44(17):4993–5013. [https://doi.org/10.1016/S0032-3861\(03\)00471-3](https://doi.org/10.1016/S0032-3861(03)00471-3)
96. Bharadwaj RK (2001) Modeling the barrier properties of polymer-layered silicate nanocomposites. *Macromolecules* 34(26):9189–9192. <https://doi.org/10.1021/ma010780b>
97. Martínez-Hermosilla GA, Mesic B, Bronlund JE (2015) A review of thermoplastic composites vapour permeability models: applicability for barrier dispersion coatings. *Packag Technol Sci* 28(7):565–578. <https://doi.org/10.1002/pts.2125>
98. Ellis TS, D'Angelo JS (2003) Thermal and mechanical properties of a polypropylene nanocomposite. *J Appl Polym Sci* 90(6):1639–1647. <https://doi.org/10.1002/app.12830>
99. Gorrasí G, Tortora M, Vittoria V et al (2003) Transport properties of organic vapors in nanocomposites of organophilic layered silicate and syndiotactic polypropylene. *Polymer* 44(13):3679–3685. [https://doi.org/10.1016/S0032-3861\(03\)00284-2](https://doi.org/10.1016/S0032-3861(03)00284-2)
100. Gómez M, Bracho D, Palza H et al (2015) Effect of morphology on the permeability, mechanical and thermal properties of polypropylene/SiO₂ nanocomposites. *Polym Int* 64(9):1245–1251. <https://doi.org/10.1002/pi.4909>

101. Tang Y, Hu Y, Song L et al (2003) Preparation and thermal stability of polypropylene/montmorillonite nanocomposites. *Polym Degrad Stab* 82(1):127–131. [https://doi.org/10.1016/S0141-3910\(03\)00173-3](https://doi.org/10.1016/S0141-3910(03)00173-3)
102. Wang L, He X, Wilkie CA (2010) The utility of nanocomposites in fire retardancy. *Materials* 3(9):4580–4606. <https://doi.org/10.3390/ma3094580>
103. Wagenknecht U, Kretzschmar B, Reinhardt G (2003) Investigations of fire retardant properties of polypropylene-clay-nanocomposites. *Macromol Symp* 194(1):207–212. <https://doi.org/10.1002/masy.200390084>
104. Gilman JW, Jackson CL, Morgan AB et al (2000) Flammability properties of polymer – layered-silicate nanocomposites. Polypropylene polystyrene nanocomposites. *Chem Mater* 12(7):1866–1873. <https://doi.org/10.1021/cm0001760>
105. Arao Y (2015) Flame retardancy of polymer nanocomposite. In: Visakh PM, Arao Y (eds) *Flame retardants: polymer blends, composites and nanocomposites*. Engineering Materials. Springer International Publishing, Cham, pp 15–44. https://doi.org/10.1007/978-3-319-03467-6_2
106. Le Bras M, Bourbigot S (1999) Intumescent fire retardant polypropylene formulations. In: Karger-Kocsis J (ed) *Polypropylene: an A-Z reference*. Polymer Science and Technology Series, vol 2. Springer Netherlands, Dordrecht, pp 357–365. https://doi.org/10.1007/978-94-011-4421-6_51
107. Tang Y, Hu Y, Wang S et al (2003) Intumescent flame retardant–montmorillonite synergism in polypropylene-layered silicate nanocomposites. *Polym Int* 52(8):1396–1400. <https://doi.org/10.1002/pi.1270>
108. Manikantan MR, Varadharaju N (2011) Preparation and properties of polypropylene-based nanocomposite films for food packaging. *Packag Technol Sci* 24(4):191–209. <https://doi.org/10.1002/pts.925>
109. Garcés JM, Moll DJ, Bicerano J et al (2000) Polymeric nanocomposites for automotive applications. *Adv Mater* 12(23):1835–1839. [https://doi.org/10.1002/1521-4095\(200012\)12:23%3c1835:AID-ADMA1835%3e3.0.CO;2-T](https://doi.org/10.1002/1521-4095(200012)12:23%3c1835:AID-ADMA1835%3e3.0.CO;2-T)
110. Utracki LA (1987) Present and future trends in polymer blends technology. *Int Polym Process* 2(1):3–12. <https://doi.org/10.3139/217.870003>
111. Lutz A, Harmia T (1999) Impregnation techniques for fiber bundles or tows. In: Karger-Kocsis J (ed) *Polypropylene: an A-Z reference*, vol 2. Springer Netherlands, Dordrecht, pp 301–306. https://doi.org/10.1007/978-94-011-4421-6_43
112. Uawongsuwan P, Yang Y, Hamada H (2015) Long jute fiber-reinforced polypropylene composite: effects of jute fiber bundle and glass fiber hybridization. *J Appl Polym Sci* 132(15). <https://doi.org/10.1002/app.41819>
113. Hawley RC, Jones RF (2005) In-line compounding of long-fiber thermoplastics for injection molding. *J Thermoplast Compos Mater* 18(5):459–464. <https://doi.org/10.1177/0892705705054413>
114. Yan X, Shen H, Yu L et al (2017) Polypropylene–glass fiber/basalt fiber hybrid composites fabricated by direct fiber feeding injection molding process. *J Appl Polym Sci* 134(44):45472. <https://doi.org/10.1002/app.45472>
115. Bourban P-E, Manson J-A (1999) Integrated manufacturing. In: Karger-Kocsis J (ed) *Polypropylene: an A-Z reference*, vol 2. Springer Netherlands, Dordrecht, pp 341–347. https://doi.org/10.1007/978-94-011-4421-6_49
116. Carneiro OS, Silva AF, Gomes R (2015) Fused deposition modeling with polypropylene. *Mater Des* 83:768–776. <https://doi.org/10.1016/j.matdes.2015.06.053>
117. Milosevic M, Stoof D, Pickering K (2017) Characterizing the mechanical properties of fused deposition modelling natural fiber recycled polypropylene composites. *J Compos Sci* 1(1):7. <https://doi.org/10.3390/jcs1010007>
118. Yang C, Huang H-X, Li K (2010) Investigation of fiber orientation states in injection-compression molded short-fiber-reinforced thermoplastics. *Polym Compos* 31(11):1899–1908. <https://doi.org/10.1002/pc.20986>

119. Giusti R, Zanini F, Lucchetta G (2018) Automatic glass fiber length measurement for discontinuous fiber-reinforced composites. *Compos Part A: Appl Sci Manuf* 112:263–270. <https://doi.org/10.1016/j.compositesa.2018.06.016>
120. Inoue A, Morita K, Tanaka T et al (2015) Effect of screw design on fiber breakage and dispersion in injection-molded long glass-fiber-reinforced polypropylene. *J Compos Mater* 49(1):75–84. <https://doi.org/10.1177/0021998313514872>
121. Vaxman A, Narkis M, Siegmann A et al (2012) Short-fiber thermoplastics composites: fiber fracture during melt processing. In: Nicolais L (ed) *Wiley encyclopedia of composites*. Wiley, New York. <https://doi.org/10.1002/9781118097298.weoc225>
122. Barbosa SE, Kenny JM (1999) Processing of short fiber reinforced polypropylene. II: statistical study of the effects of processing conditions on the impact strength. *Polym Eng Sci* 39(10):1880–1890. <https://doi.org/10.1002/pen.11581>
123. Puch F, Hopmann C (2015) Experimental investigation of the influence of the compounding process and the composite composition on the mechanical properties of a short flax fiber-reinforced polypropylene composite. *Polym Compos* 36(12):2282–2290. <https://doi.org/10.1002/pc.23141>
124. Nalini R, Kristiina O, Nayak SK et al (2016) Effect of long fiber thermoplastic extrusion process on fiber dispersion and mechanical properties of viscose fiber/polypropylene composites. *Polym Adv Technol* 27(5):685–692. <https://doi.org/10.1002/pat.3742>
125. Phelps JH, Abd El-Rahman AI, Kunc V et al (2013) A model for fiber length attrition in injection-molded long-fiber composites. *Compos Part A: Appl Sci Manuf* 51:11–21. <https://doi.org/10.1016/j.compositesa.2013.04.002>
126. Kmetty Á, Bárány T, Karger-Kocsis J (2012) Injection moulded all-polypropylene composites composed of polypropylene fibre and polypropylene based thermoplastic elastomer. *Compos Sci Technol* 73:72–80. <https://doi.org/10.1016/j.compscitech.2012.09.017>
127. Kmetty Á, Tábi T, Kovács JG et al (2013) Development and characterisation of injection moulded, all-polypropylene composites. *Express Polym Lett* 7(2):134–145. <https://doi.org/10.3144/expresspolymlett.2013.13>
128. Karger-Kocsis J, Friedrich K (1989) Effect of skin-core morphology on fatigue crack propagation in injection moulded polypropylene homopolymer. *Int J Fatigue* 11(3):161–168. [https://doi.org/10.1016/0142-1123\(89\)90435-0](https://doi.org/10.1016/0142-1123(89)90435-0)
129. Tadmor Z (1974) Molecular orientation in injection molding. *J Appl Polym Sci* 18(6):1753–1772. <https://doi.org/10.1002/app.1974.070180614>
130. Rose W (1961) Fluid-fluid interfaces in steady motion. *Nature* 191:242. <https://doi.org/10.1038/191242a0>
131. Hegler RP, Mennig G, Schmauch C (1987) Phase separation effects in processing of glass-bead- and glass-fiber-filled thermoplastics by injection molding. *Adv Polym Technol* 7(1):3–20. <https://doi.org/10.1002/adv.1987.060070102>
132. Karger-Kocsis J (1989) Chapter 6—Microstructure and fracture mechanical performance of short-fibre reinforced thermoplastics. In: Friedrich K (ed) *Composite Materials Series*, vol 6. Elsevier, pp 189–247. <https://doi.org/10.1016/b978-0-444-87286-9.50010-3>
133. Karger-Kocsis J, Friedrich K (1988) Fracture behavior of injection-molded short and long glass fiber—polyamide 6.6 composites. *Compos Sci Technol* 32(4):293–325. [https://doi.org/10.1016/0266-3538\(88\)90067-x](https://doi.org/10.1016/0266-3538(88)90067-x)
134. Spahr DE, Friedrich K, Schultz JM et al (1990) Microstructure and fracture behaviour of short and long fibre-reinforced polypropylene composites. *J Mater Sci* 25(10):4427–4439. <https://doi.org/10.1007/bf00581104>
135. Karger-Kocsis J (1995) Microstructural aspects of fracture in polypropylene and in its filled, chopped fiber and fiber mat reinforced composites. In: Karger-Kocsis J (ed) *Polypropylene structure, blends and composites*, vol 3. Springer Netherlands, Dordrecht, pp 142–201. https://doi.org/10.1007/978-94-011-0523-1_4
136. Clegg DW, Collyer AA (eds) (1986) *Mechanical properties of reinforced thermoplastics*. Springer, Netherlands. <https://doi.org/10.1007/978-94-009-4193-9>

137. Garcea SC, Wang Y, Withers PJ (2018) X-ray computed tomography of polymer composites. *Compos Sci Technol* 156:305–319. <https://doi.org/10.1016/j.compscitech.2017.10.023>
138. Köpplmayr T, Milosavljevic I, Aigner M et al (2013) Influence of fiber orientation and length distribution on the rheological characterization of glass-fiber-filled polypropylene. *Polym Test* 32(3):535–544. <https://doi.org/10.1016/j.polymertesting.2013.02.002>
139. Alemdar A, Zhang H, Sain M et al (2008) Determination of fiber size distributions of injection moulded polypropylene/natural fibers using X-ray microtomography. *Adv Eng Mater* 10(1–2):126–130. <https://doi.org/10.1002/adem.200700232>
140. Hanneschläger C, Revol V, Plank B et al (2015) Fibre structure characterisation of injection moulded short fibre-reinforced polymers by X-ray scatter dark field tomography. *Case Stud Nondestr Test Eval* 3:34–41. <https://doi.org/10.1016/j.cnsdt.2015.04.001>
141. Fischer G, Eyerer P (1988) Measuring spatial orientation of short fiber reinforced thermoplastics by image analysis. *Polym Compos* 9(4):297–304. <https://doi.org/10.1002/pc.750090409>
142. Hermans PH (1946) Contributions to the physics of cellulose fibres. *J Polym Sci.* (Elsevier, New York). <https://doi.org/10.1002/pol.1947.120020321>
143. Pipes BR, McCullough RL, Taggart DG (1982) Behavior of discontinuous fiber composites: fiber orientation. *Polym Compos* 3(1):34–39. <https://doi.org/10.1002/pc.750030107>
144. Krenchel H (1964) Fibre reinforcement: theoretical and practical investigations of the elasticity and strength of fibre-reinforced materials. Akademisk Forlag, Copenhagen
145. Advani SG, Tucker CL (1987) The use of tensors to describe and predict fiber orientation in short fiber composites. *J Rheol* 31(8):751–784. <https://doi.org/10.1122/1.549945>
146. Friedrich K (1985) Microstructural efficiency and fracture toughness of short fiber/thermoplastic matrix composites. *Compos Sci Technol* 22(1):43–74. [https://doi.org/10.1016/0266-3538\(85\)90090-9](https://doi.org/10.1016/0266-3538(85)90090-9)
147. Hull D (1981) An introduction to composite materials. Cambridge University Press, Cambridge
148. Bader MG, Hill AR (1993) Short fiber composites. In: Chou T-W (ed) *Materials science and technology*. VCH, Weinheim, pp 293–338. <https://doi.org/10.1002/maco.19940450218>
149. Fu S-Y, Lauke B, Mai Y-W (2009) Science and engineering of short fibre reinforced polymer composites. CRC Press
150. Cox HL (1952) The elasticity and strength of paper and other fibrous materials. *Br J Appl Phys* 3(3):72. <https://doi.org/10.1088/0508-3443/3/3/302>
151. Kelly A, Tyson WR (1965) Tensile properties of fibre-reinforced metals: copper/tungsten and copper/molybdenum. *J Mech Phys Solids* 13(6):329–336. [https://doi.org/10.1016/0022-5096\(65\)90035-9](https://doi.org/10.1016/0022-5096(65)90035-9)
152. Thomason JL (1999) Mechanical and thermal properties of long glass fiber reinforced polypropylene. In: Karger-Kocsis J (ed) *Polypropylene: an A-Z reference*, vol 2. Springer Netherlands, Dordrecht, pp 407–414. https://doi.org/10.1007/978-94-011-4421-6_57
153. Bowyer WH, Bader MG (1972) On the re-inforcement of thermoplastics by imperfectly aligned discontinuous fibres. *J Mater Sci* 7(11):1315–1321. <https://doi.org/10.1007/bf00550698>
154. Bowyer WH, Bader MG (1972) Reinforcement of thermoplastics using carbon fibres. *Faraday Special Discuss Chem Soc* 2:165–173. <https://doi.org/10.1039/S19720200165>
155. Affdl JCH, Kardos JL (1976) The Halpin-Tsai equations: a review. *Polym Eng Sci* 16(5):344–352. <https://doi.org/10.1002/pen.760160512>
156. Garesci F, Fliegner S (2013) Young's modulus prediction of long fiber reinforced thermoplastics. *Compos Sci Technol* 85:142–147. <https://doi.org/10.1016/j.compscitech.2013.06.009>
157. Yaghoobi H, Fereidoon A (2018) Modeling and optimization of tensile strength and modulus of polypropylene/kenaf fiber biocomposites using Box-Behnken response surface method. *Polym Compos* 39(S1):E463–E479. <https://doi.org/10.1002/pc.24596>

158. Hoecker F, Karger-Kocsis J (1993) Effects of crystallinity and supermolecular formations on the interfacial shear strength and adhesion in GF/PP composites. *Polym Bull* 31(6):707–714. <https://doi.org/10.1007/BF00300131>
159. Etaati A, Pather S, Cardona F et al (2016) Injection molded noil hemp fiber composites: interfacial shear strength, fiber strength, and aspect ratio. *Polym Compos* 37(1):213–220. <https://doi.org/10.1002/pc.23172>
160. Karger-Kocsis J, Czirágy T (1998) Effects of interphase on the fracture and failure behavior of knitted fabric reinforced composites produced from commingled GF/PP yarn. *Compos Part A: Appl Sci Manuf* 29A:1319–1330. [https://doi.org/10.1016/S1359-835X\(98\)00042-6](https://doi.org/10.1016/S1359-835X(98)00042-6)
161. Wu C-M, Chen M, Karger-Kocsis J (1998) Transcrystallization in syndiotactic polypropylene induced by high-modulus carbon fibers. *Polym Bull* 41(2):239–245. <https://doi.org/10.1007/s002890050357>
162. Sanadi AR, Caulfield DF (2000) Transcrystalline interphases in natural fiber-PP composites: effect of coupling agent. *Compos Interfaces* 7(1):31–43. <https://doi.org/10.1163/156855400300183560>
163. Abraham TN, Wanjale SD, Bárány T et al (2009) Tensile mechanical and perforation impact behavior of all-PP composites containing random PP copolymer as matrix and stretched PP homopolymer as reinforcement: effect of β nucleation of the matrix. *Compos Part A: Appl Sci Manuf* 40(5):662–668. <https://doi.org/10.1016/j.compositesa.2009.03.001>
164. Karger-Kocsis J (2000) Interphase with lamellar interlocking and amorphous adherent—a model to explain effects of transcrystallinity. *Adv Compos Lett* 9(2):225–227
165. Pickering KL, Efendy MGA, Le TM (2016) A review of recent developments in natural fibre composites and their mechanical performance. *Compos Part A: Appl Sci Manuf* 83:98–112. <https://doi.org/10.1016/j.compositesa.2015.08.038>
166. Fu S-Y, Lauke B, Mäder E et al (2001) Hybrid effects on tensile properties of hybrid short-glass-fiber-and short-carbon-fiber-reinforced polypropylene composites. *J Mater Sci* 36(5):1243–1251. <https://doi.org/10.1023/a:1004802530253>
167. Ranganathan N, Oksman K, Nayak SK et al (2015) Regenerated cellulose fibers as impact modifier in long jute fiber reinforced polypropylene composites: effect on mechanical properties, morphology, and fiber breakage. *J Appl Polym Sci* 132(3). <https://doi.org/10.1002/app.41301>
168. Hartl AM, Jerabek M, Lang RW (2015) Anisotropy and compression/tension asymmetry of PP containing soft and hard particles and short glass fibers. *Express Polym Lett* 9(7):658–670. <https://doi.org/10.3144/expresspolymlett.2015.61>
169. Diego P, Alessandro P, Kyriaki K (2015) Synergistic effect of graphite nanoplatelets and glass fibers in polypropylene composites. *J Appl Polym Sci* 132(12). <https://doi.org/10.1002/app.41682>
170. Cui-Cui W, Yue-Ying Z, He-Yi G et al (2018) Enhanced mechanical and thermal properties of short carbon fiber reinforced polypropylene composites by graphene oxide. *Polym Compos* 39(2):405–413. <https://doi.org/10.1002/pc.23950>
171. Atkins AG, Mai YW (1988) Elastic and plastic fracture: metals, polymers, ceramics, composites, biological materials. Ellis Horwood, Chichester
172. Gllermann W, Seidler S (eds) (2013) Polymer testing, 2nd edn. Hunser Publishers, Munich
173. Karger-Kocsis J (1993) Microstructure-fracture toughness relationship of short fiber-reinforced PP homopolymer and PP/elastomer blends. *J Polym Eng* 12(1–2):77–108. <https://doi.org/10.1515/POLYENG.1993.12.1-2.77>
174. Karger-Kocsis J (1993) Instrumented impact fracture and related failure behavior in short-and long-glass-fiber-reinforced polypropylene. *Compos Sci Technol* 48(1–4):273–283. [https://doi.org/10.1016/0266-3538\(93\)90144-6](https://doi.org/10.1016/0266-3538(93)90144-6)
175. Karger-Kocsis J (1993) Instrumented impact fracture and related failure behavior in short-and long-glass-fiber-reinforced polypropylene. *Compos Sci Technol* 48(1):273–283. [https://doi.org/10.1016/0266-3538\(93\)90144-6](https://doi.org/10.1016/0266-3538(93)90144-6)

176. Nouri H, Meraghni F, Lory P (2009) Fatigue damage model for injection-molded short glass fibre reinforced thermoplastics. *Int J Fatigue* 31(5):934–942. <https://doi.org/10.1016/j.ijfatigue.2008.10.002>
177. Pegoretti A, Ricco T (1999) Fatigue crack propagation in polypropylene reinforced with short glass fibres. *Compos Sci Technol* 59(7):1055–1062. [https://doi.org/10.1016/S0266-3538\(98\)00143-2](https://doi.org/10.1016/S0266-3538(98)00143-2)
178. Karger-Kocsis J, Friedrich K, Bailey RS (1991) Fatigue and failure behavior of short and long glass fiber reinforced injection-molded polypropylene. *Sci Eng Compos Mater* 2(1):49–68. <https://doi.org/10.1515/SECM.1991.2.1.49>
179. Karger-Kocsis J, Friedrich K, Bailey RS (1991) Fatigue crack propagation in short and long glass fiber reinforced injection-molded polypropylene composites. *Adv Compos Mater* 1(2):103–121. <https://doi.org/10.1163/156855191X00225>
180. Pegoretti A, Ricco T (2000) Fatigue fracture of neat and short glass fiber reinforced polypropylene: effect of frequency and material orientation. *J Compos Mater* 34(12):1009–1027. <https://doi.org/10.1177/002199830003401203>
181. Karger-Kocsis J (2004) In: Moore DR (ed) *the application of fracture mechanics to polymers, adhesive and composites* (European Structural Integrity Society), vol 33, 1st edn. Elsevier, Amsterdam, pp 233–239
182. Vas LM, Bakonyi P (2012) Estimating the creep strain to failure of PP at different load levels based on short term tests and Weibull characterization. *Express Polym Lett* 6:987–996. <https://doi.org/10.3144/expresspolymlett.2012.104>
183. Achereiner F, Engelsing K, Bastian M et al (2013) Accelerated creep testing of polymers using the stepped isothermal method. *Polym Test* 32(3):447–454. <https://doi.org/10.1016/j.polymertesting.2013.01.014>
184. Houshyar S, Shanks RA, Hodzic A (2005) Tensile creep behaviour of polypropylene fibre reinforced polypropylene composites. *Polym Test* 24(2):257–264. <https://doi.org/10.1016/j.polymertesting.2004.07.003>
185. Vas LM, Bakonyi P (2013) Creep failure strain estimation of glass fibre/polypropylene composites based on short-term tests and Weibull characterisation. *J Reinf Plast Compos* 32(1):34–41. <https://doi.org/10.1177/0731684412453513>
186. Williams ML, Landel RF, Ferry JD (1955) The temperature dependence of relaxation mechanisms in amorphous polymers and other glass-forming liquids. *J Am Chem Soc* 77(14):3701–3707. <https://doi.org/10.1021/ja01619a008>
187. Karger-Kocsis J (2012) Structure and fracture mechanics of injection-molded composites. In: Nicolais L (ed) *Wiley encyclopedia of composites*. Wiley, New York, pp 2939–2952
188. Wetherhold RC (2012) Short-fiber-reinforced polymeric composites: structure–property relations. In: Nicolais L (ed) *Wiley encyclopedia of composites*. Wiley, pp 1–8. <https://doi.org/10.1002/9781118097298.weoc224>
189. Advani SG (2012) Molding: short-fiber composites, flow processing. In: Nicolais L (ed) *Wiley encyclopedia of composites*. Wiley, New York, pp 1–12. <https://doi.org/10.1002/9781118097298.weoc154>
190. Wang Z, Smith DE (2018) Rheology effects on predicted fiber orientation and elastic properties in large scale polymer composite additive manufacturing. *J Compos Sci* 2(1):18. <https://doi.org/10.3390/jcs2010010>
191. Ausias G, Agassant J-F, Vincent M et al (1992) Rheology of short glass-fiber reinforced polypropylene. *J Rheol* 36(4):525–542. <https://doi.org/10.1122/1.550362>
192. Matsuoka T (1999) Warpage and its prediction in injection-molded parts. In: Karger-Kocsis J (ed) *Polypropylene: an A-Z reference*, vol 2. Springer Netherlands, Dordrecht, pp 859–865. https://doi.org/10.1007/978-94-011-4421-6_117
193. Diez-Pascual AM, Naffakh M (2013) Polypropylene/glass fiber hierarchical composites incorporating inorganic fullerene-like nanoparticles for advanced technological applications. *ACS Appl Mater Interfaces* 5(19):9691–9700. <https://doi.org/10.1021/am402750t>

194. Djamila K, Ahmed K, Ghezalla T et al (2018) Tensile properties, thermal conductivity, and thermal stability of short carbon fiber reinforced polypropylene composites. *Polym Compos* 39(S2):E664–E670. <https://doi.org/10.1002/pc.24093>
195. Chen C-H, Wang Y-C (1996) Effective thermal conductivity of misoriented short-fiber reinforced thermoplastics. *Mech Mater* 23(3):217–228. [https://doi.org/10.1016/0167-6636\(96\)00010-5](https://doi.org/10.1016/0167-6636(96)00010-5)
196. Kumlutas D, Tavman IH (2006) A numerical and experimental study on thermal conductivity of particle filled polymer composites. *J Thermoplast Compos Mater* 19(4):441–455. <https://doi.org/10.1177/0892705706062203>
197. Vuorinen E, Nhlapo N, Mafa T et al (2013) Thermooxidative degradation of LDPE nanocomposites: effect of surface treatments of fumed silica and boehmite alumina. *Polym Degrad Stab* 98(11):2297–2305. <https://doi.org/10.1016/j.polyimdegradstab.2013.08.011>
198. Bellucci F, Camino G (2012) Flammability of polymer composites. In: Nicolais L (ed) *Wiley encyclopedia of composites*. Wiley, New York, p 17. <https://doi.org/10.1002/9781118097298.weoc091>
199. Bourbigot S, Bras ML, Delobel R (1999) Flame-retardant polypropylene compositions. In: Karger-Kocsis J (ed) *Polypropylene: an A-Z reference*, vol 2. Springer Netherlands, Dordrecht, pp 254–263. https://doi.org/10.1007/978-94-011-4421-6_35
200. S-l Du, X-b Lin, R-k Jian et al (2015) Flame-retardant wrapped ramie fibers towards suppressing “candlewick effect” of polypropylene/ramie fiber composites. *Chin J Polym Sci* 33(1):84–94. <https://doi.org/10.1007/s10118-015-1560-z>
201. Vadas D, Kmetty Á, Bárány T et al (2018) Flame retarded self-reinforced polypropylene composites prepared by injection moulding. *Polym Adv Technol* 29(1):433–441. <https://doi.org/10.1002/pat.4132>
202. Yeetsorn R, Fowler MW, Tzoganakis C (2011) A review of thermoplastic composites for bipolar plate materials in PEM fuel cells In: Cuppoletti J (ed) *Nanocomposites with unique properties and applications in medicine and industry*, InTech, pp 317–344. <https://doi.org/10.5772/19262>
203. Hsieh C-T, Pan Y-J, Lin J-H (2017) Polypropylene/high-density polyethylene/carbon fiber composites: manufacturing techniques, mechanical properties, and electromagnetic interference shielding effectiveness. *Fibers Polym* 18(1):155–161. <https://doi.org/10.1007/s12221-017-6371-0>
204. Huang C-L, Lou C-W, Liu C-F et al (2015) Polypropylene/graphene and polypropylene/carbon fiber conductive composites: mechanical, crystallization and electromagnetic properties. *Appl Sci* 5(4):1196–1210. <https://doi.org/10.3390/app5041196>
205. Krause B, Pötschke P (2015) Electrical and thermal conductivity of polypropylene filled with combinations of carbon fillers. In: *Regional Conference Graz 2015—Polymer Processing Society PPS*, Graz, 21–25 September 2015. AIP Conference Proceedings, pp 040003-040001. <https://doi.org/10.1063/1.4965494>
206. Kalay G, Bevis MJ (1999) Application of shear-controlled orientation in injection molding of isotactic polypropylene. In: Karger-Kocsis J (ed) *Polypropylene: an A-Z reference*, vol 2. Springer Netherlands, Dordrecht, pp 38–46. https://doi.org/10.1007/978-94-011-4421-6_6
207. Wang J, Geng C, Luo F et al (2011) Shear induced fiber orientation, fiber breakage and matrix molecular orientation in long glass fiber reinforced polypropylene composites. *Mater Sci Eng, A* 528(7):3169–3176. <https://doi.org/10.1016/j.msea.2010.12.081>
208. Fisa B, Meddad A (1999) Weldlines. In: Karger-Kocsis J (ed) *Polypropylene: an A-Z reference*, vol 2. Springer Netherlands, Dordrecht, pp 874–881. https://doi.org/10.1007/978-94-011-4421-6_119
209. Tomioka M, Ishikawa T, Okuyama K et al (2017) Recycling of carbon-fiber-reinforced polypropylene prepreg waste based on pelletization process. *J Compos Mater* 51(27):3847–3858. <https://doi.org/10.1177/0021998317694423>
210. Meng F, McKechnie J, Pickering SJ (2018) An assessment of financial viability of recycled carbon fibre in automotive applications. *Compos Part A* 109:207–220. <https://doi.org/10.1016/j.compositesa.2018.03.011>

211. Karger-Kocsis J (1999) Glass mat reinforced thermoplastic polypropylene. In: Karger-Kocsis J (ed) *Polypropylene: an A-Z Reference*. Polymer Science and Technology Series, vol 2. Springer Netherlands, pp 284–290. <https://doi.org/10.1007/978-94-011-4421-6>
212. N/A (1968) Carbide, PPG form G.R.T.L. to make thermoplastic sheet. *Chemical & Engineering News* 46:15. <https://doi.org/10.1021/cen-v046n004.p015>
213. Shah DU (2013) Developing plant fibre composites for structural applications by optimising composite parameters: a critical review. *J Mater Sci* 48:6083–6107. <https://doi.org/10.1007/s10853-013-7458-7>
214. Kurcz M, Baser B, Dittmar H et al (2005) A case for replacing steel with glass-mat thermoplastic composites in spare-wheel well application. <https://doi.org/10.4271/2005-01-1678>
215. Schemme M (2008) LFT—development status and perspectives. *Reinf Plast* 52(32–34):36–39. [https://doi.org/10.1016/S0034-3617\(08\)70036-5](https://doi.org/10.1016/S0034-3617(08)70036-5)
216. Okzman K (2000) Mechanical properties of natural fibre mat reinforced thermoplastic. *Appl Compos Mater* 7(5):403–414. <https://doi.org/10.1023/a:1026546426764>
217. Bárány T, Karger-Kocsis J, Czigány T (2006) Development and characterization of self-reinforced poly(propylene) composites: carded mat reinforcement. *Polym Adv Technol* 17:818–824. <https://doi.org/10.1002/pat.813>
218. Bárány T, Izer A, Czigány T (2006) On consolidation of self-reinforced polypropylene composites. *Plast, Rubber Compos* 35(9):375–379
219. Karger-Kocsis J (2000) Swirl mat- and long discontinuous fiber mat-reinforced polypropylene composites—status and future trends. *Polym Compos* 22(4):514–522. <https://doi.org/10.1002/pc.10206>
220. Benevolenski OI, Karger-Kocsis J, Czigány T et al (2003) Mode I fracture resistance of glass fiber mat-reinforced polypropylene composites at various degree of consolidation. *Compos Part A: Appl Sci Manuf* 34(3):267–273. [https://doi.org/10.1016/S1359-835X\(02\)00045-3](https://doi.org/10.1016/S1359-835X(02)00045-3)
221. Raghavendran V, Haque E (2001) Development of low density GMT headliners with improved acoustic performance. In: *Automotive Composites Conference*, Troy, MI, p 7, 19–20 Sept 2001
222. Roch A, Huber T, Henning F et al (2014) LFT foam—lightweight potential for semi-structural components through the use of long-glass-fiber-reinforced thermoplastic foams. In: Altstädt V, Keller J-H, Fathi A (eds) *29th International Conference of the Polymer Processing Society*, Nuremberg, Germany. AIP Publishing LLC, pp 471–476. <https://doi.org/10.1063/1.4873824>
223. Roch A, Menrath A, Huber T et al (2013) Lightweight potential of fiber-reinforced foams. *Cell Polym* 32(4):213–227
224. Bos HL, Müssig J, van den Oevera MJA (2006) Mechanical properties of short-flax-fibre reinforced compounds. *Compos Part A: Appl Sci Manuf* 37:1591–1604. <https://doi.org/10.1016/j.compositesa.2005.10.011>
225. <http://www.hanwhaus.com/html/gmt.html>. Accessed 27 Mar 2018
226. Knox MP (2001) Continuous fiber reinforced thermoplastic composites in the automotive industry. In: *Automotive Composites Conference*, Troy, MI, p 5, 19–21 Sept 2001
227. Caba AC (2005) Characterization of carbon mat thermoplastic composites: flow and mechanical properties. PhD Thesis. Virginia Polytechnic Institute and State University
228. Karger-Kocsis J, Harmia T, Czigány T (1995) Comparison of the fracture and failure behavior of polypropylene composites reinforced by long glass fibers and by glass mats. *Compos Sci Technol* 54(3):287–298. [https://doi.org/10.1016/0266-3538\(95\)00068-2](https://doi.org/10.1016/0266-3538(95)00068-2)
229. Karger-Kocsis J, Fejes-Kozma ZS (1994) Failure mode and damage zone development in a GMT-PP by acoustic emission and thermography. *J Reinf Plast Compos* 13(9):768–792. <https://doi.org/10.1177/073168449401300901>
230. Karger-Kocsis J (1993) Fracture mechanical characterization and damage zone development in glass fiber mat-reinforced thermoplastics. *Polym Bull* 31(2):235–241. <https://doi.org/10.1007/bf00329971>

231. Benevolenski OI, Karger-Kocsis J (2001) Comparative study of the fracture behavior of flow-molded GMT-PP with random and chopped-fiber mats. *Compos Sci Technol* 61 (16):2413–2423. [https://doi.org/10.1016/S0266-3538\(01\)00160-9](https://doi.org/10.1016/S0266-3538(01)00160-9)
232. Bourmaud A, Fazzini M, Renouard N et al (2018) Innovating routes for the reused of PP-flax and PP-glass non woven composites: a comparative study. *Polym Degrad Stab* 152:259–271. <https://doi.org/10.1016/j.polymdegradstab.2018.05.006>
233. Davies P, Manson J-AE (1993) Rheological properties of stampable thermoplastic composites. *J Thermoplast Compos Mater* 6:239–254. <https://doi.org/10.1177/089270579300600305>
234. Davis SM, Mcalea KP (1990) Stamping rheology of glass mat reinforced thermoplastic composites. *Polym Compos* 11(6):368–378. <https://doi.org/10.1002/pc.750110610>
235. Kotsikos G, Bland JH, Gibson AG (1996) Squeeze flow testing of glass mat thermoplastic material. *Compos Part A* 27 A:1195–1200. [https://doi.org/10.1016/1359-835x\(96\)00077-2](https://doi.org/10.1016/1359-835x(96)00077-2)
236. Kotsikos G, Bland JH, Gibson AG (1999) Rheological characterization of commercial glass mat thermoplastics (GMTs) by squeeze flow testing. *Polym Compos* 20(1):114–123. <https://doi.org/10.1002/pc.10339>
237. Dweib MA, Brádaigh CMÓ (1998) Anisotropic modeling of isothermal squeezing flow of glass-mat reinforced thermoplastics (GMT). *Polym Compos* 19(5):588–599. <https://doi.org/10.1002/pc.10132>
238. Dweib MA, Brádaigh CMÓ (1999) Extensional and shearing flow of a glass-mat-reinforced thermoplastics (GMT) material as a non-Newtonian viscous Fluid. *Compos Sci Technol* 59:1399–1410. [https://doi.org/10.1016/S0266-3538\(98\)00182-1](https://doi.org/10.1016/S0266-3538(98)00182-1)
239. Gibson AG, Kotsikos G, Bland JH et al (1998) Squeeze flow In: Collyer AA, Clegg DW (eds) *Rheological measurement*. Springer, Dordrecht, p 779. <https://doi.org/10.1007/978-94-011-4934-1>
240. Dasappa P, Lee-Sullivan P, Xiao X (2009) Temperature effect on creep behavior of continuous fiber GMT composites. *Compos Part A: Appl Sci Manuf* 40:1071–1081. <https://doi.org/10.1016/j.compositesa.2009.04.026>
241. Czigány T, Marosfalvi J, Karger-Kocsis J (2000) An acoustic emission study of the temperature-dependent fracture behavior of polypropylene composites reinforced by continuous and discontinuous fiber mats. *Compos Sci Technol* 60(8):1203–1212. [https://doi.org/10.1016/S0266-3538\(00\)00059-2](https://doi.org/10.1016/S0266-3538(00)00059-2)
242. Biro DA, Pleizier G, Deslandes Y (1992) Application of the microbond technique. 3. Effects of plasma treatment on the ultra-high modulus polyethylene fiber epoxy interface. *J Mater Sci Lett* 11(10):698–701
243. Vanclooster K, Lomov SV, Vespoest I (2008) Investigation of interply shear in composite forming. In: *The 11th International ESAFORM Conference on Material Forming*, Lyon, France. Springer, Heidelberg, 23–25 April 2008
244. Mitschang P, Blinzler M, Woginger A (2003) Processing technologies for continuous fibre reinforced thermoplastics with novel polymer blends. *Compos Sci Technol* 63:2099–2110. [https://doi.org/10.1016/S0266-3538\(03\)00107-6](https://doi.org/10.1016/S0266-3538(03)00107-6)
245. Hine PJ, Ward IM, Jordan ND et al (2003) The hot compaction behaviour of woven oriented polypropylene fibres and tapes. I. Mechanical properties. *Polymer* 44(4):1117–1131
246. Ward IM, Hine PJ (2004) The science and technology of hot compaction. *Polymer* 45 (5):1413–1427. <https://doi.org/10.1016/j.polymer.2003.11.050>
247. Swolfs Y, Zhang Q, Baets J et al (2014) The influence of process parameters on the properties of hot compacted self-reinforced polypropylene composites. *Compos Pt A-Appl Sci Manuf* 65:38–46. <https://doi.org/10.1016/j.compositesa.2014.05.022>
248. Goodman KE, Loos AC (1990) Thermoplastic prepreg manufacture. *J Thermoplast Compos Mater* 3(1):34–40. <https://doi.org/10.1177/089270579000300104>
249. Turton CN, McAinsh J (1974) Thermoplastic compositions US3785916A Patent US3785916A, 1974-01-15
250. Iyer SR, Drzal LT (1990) Manufacture of powder-impregnated thermoplastic composites. *J Thermoplast Compos Mater* 3:325–355. <https://doi.org/10.1177/089270579000300404>

251. Sharma M, Bijwe J, Mitschang P (2011) Wear performance of PEEK–carbon fabric composites with strengthened fiber–matrix interface. *Wear* 271(9):2261–2268. <https://doi.org/10.1016/j.wear.2010.11.055>
252. Kim JW, Lee JS (2016) The effect of the melt viscosity and impregnation of a film on the mechanical properties of thermoplastic composites. *Materials* 9(6):448. <https://doi.org/10.3390/ma9060448>
253. Gibson AG, Manson J-A (1992) Impregnation technology for thermoplastic matrix composites. *Compos Manuf* 3(4):223–233. [https://doi.org/10.1016/0956-7143\(92\)90110-G](https://doi.org/10.1016/0956-7143(92)90110-G)
254. Hartness T, Husman G, Koenig J et al (2001) The characterization of low cost fiber reinforced thermoplastic composites produced by the DRIFT™ process. *Compos Part A: Appl Sci Manuf* 32(8):1155–1160. [https://doi.org/10.1016/S1359-835X\(01\)00061-6](https://doi.org/10.1016/S1359-835X(01)00061-6)
255. Connor M, Toll S, Manson J-AE et al (1995) A model for the consolidation of aligned thermoplastic powder impregnated composites. *J Thermoplast Compos Mater* 8:138–162. <https://doi.org/10.1177/089270579500800201>
256. Price RV (1970) Production of impregnated rovings. US3742106 Patent US3742106A
257. Astrom BT (1997) Thermoplastic composite sheet forming: materials and manufacturing techniques. In: Bhattacharyya D (ed) *Composite sheet forming*, vol 11. Elsevier, p 530
258. Wong CC, Long AC, Sherburn M et al (2006) Comparisons of novel and efficient approaches for permeability prediction based on the fabric architecture. *Compos Part A: Appl Sci Manuf* 37(6):847–857. <https://doi.org/10.1016/j.compositesa.2005.01.020>
259. Bird RB, Armstrong RC, Hassager O (eds) (1987) *Dynamics of polymeric fluids*, vol 1. Wiley Interscience, New York (Fluid Mechanics)
260. Gutowsky TG, Morigaki T, Cai Z (1987) The consolidation of laminate composites. *J Compos Mater* 21:172–188. <https://doi.org/10.1177/002199838702100207>
261. Wakeman MD, Cain TA, Rudd CD et al (1998) Compression moulding of glass and polypropylene composites for optimised macro- and micro- mechanical properties—I commingled glass and polypropylene. *Compos Sci Technol* 58(12):1879–1898. [https://doi.org/10.1016/S0266-3538\(98\)00011-6](https://doi.org/10.1016/S0266-3538(98)00011-6)
262. Svensson N, Shishoo R, Gilchrist M (1998) Manufacturing of thermoplastic composites from commingled yarns—a review. *J Thermoplast Compos Mater* 11:22–56. <https://doi.org/10.1177/089270579801100102>
263. Mäder E, Rausch J, Schmidt N (2008) Commingled yarns—processing aspects and tailored surfaces of polypropylene/glass composites. *Compos Part A: Appl Sci Manuf* 39(4):612–623. <https://doi.org/10.1016/j.compositesa.2007.07.011>
264. Wiegand N, Mäder E (2017) Commingled yarn spinning for thermoplastic/glass fiber composites. *Fibers* 5(26):1–15. <https://doi.org/10.3390/fib5030026>
265. Akonda MH, Lawrence CA, Weager BM (2012) Recycled carbon fibre-reinforced polypropylene thermoplastic composites. *Compos Part A* 43:79–86. <https://doi.org/10.1016/j.compositesa.2011.09.014>
266. Van West BP, Pipes BR, Keefe M et al (1991) The draping and consolidation of commingled fabrics. *Compos Manuf* 2(1):10–22. [https://doi.org/10.1016/0956-7143\(91\)90154-9](https://doi.org/10.1016/0956-7143(91)90154-9)
267. Van West BP, Pipes BR, Advani SG (1991) The consolidation of commingled thermoplastic fabrics. *Polym Compos* 2(6):417–427. <https://doi.org/10.1002/pc.750120607>
268. Alcock B, Cabrera NO, Barkoula NM et al (2007) The mechanical properties of woven tape all-polypropylene composites. *Compos Pt A-Appl Sci Manuf* 38(1):147–161
269. Peijs T (2003) Composites for recyclability. *Mater Today* 6(4):30–35
270. Grünwald J, Parlevliet P, Altstädt V (2017) Manufacturing of thermoplastic composite sandwich structures: a review of literature. *J Thermoplast Compos Mater* 30(4):437–464. <https://doi.org/10.1177/0892705715604681>
271. Liu D, Ding J, Fan X et al (2014) Non-isothermal forming of glass fiber/polypropylene commingled yarn fabric composites. *Mater Des* 57:608–615. <https://doi.org/10.1016/j.matdes.2014.01.027>

272. Bureau MN, Denault J (2004) Fatigue resistance of continuous glass fiber/polypropylene composites: consolidation dependence. *Compos Sci Technol* 64(12):1785–1794. <https://doi.org/10.1016/j.compscitech.2004.01.016>
273. Bernhardsson J, Shishoo R (2000) Effect of processing parameters on consolidation quality of GF/PP commingled yarn based composites. *J Thermoplast Compos Mater* 13:292–313. <https://doi.org/10.1177/089270570001300403>
274. Youssef Y, Denault J (1998) Thermoformed glass fiber reinforced polypropylene: microstructure, mechanical properties and residual stresses. *Polym Compos* 19(3):301–309. <https://doi.org/10.1002/pc.10103>
275. Trudel-Boucher D, Fisa B, Denault J et al (2006) Experimental investigation of stamp forming of unconsolidated commingled E-glass/polypropylene fabrics. *Compos Sci Technol* 66(3):555–570. <https://doi.org/10.1016/j.compscitech.2005.05.036>
276. Karger-Kocsis J, Czirágy T (1997) Interfacial effects on the dynamic mechanical behavior of weft-knitted glass fiber fabric-reinforced polypropylene composites produced of commingled yarns. Tensile and flexural response. *Appl Compos Mater* 4:209–218. <https://doi.org/10.1007/BF02481390>
277. Zhao N, Rödel H, Herzberg C et al (2009) Stitched glass/PP composite. Part I: tensile and impact properties. *Compos Part A: Appl Sci Manuf* 40(5):635–643. <https://doi.org/10.1016/j.compositesa.2009.02.019>
278. Lu Z, Gu H, Zhen Zhong L (2011) Study on the natural fiber/PP wrap spun yarns reinforced thermoplastic composites. *Adv Mater Res* 194–196:1470–1475. <https://doi.org/10.4028/www.scientific.net/AMR.194-196.1470>
279. Kim JW, Lee JS (2016) Influence of interleaved films on the mechanical properties of carbon fiber fabric/polypropylene thermoplastic composites. *Materials* 9(5):344. <https://doi.org/10.3390/ma9050344>
280. Russo P, Acierno D, Simeoli G et al (2013) Flexural and impact response of woven glass fiber fabric/polypropylene composites. *Compos Part B: Eng* 54:415–421. <https://doi.org/10.1016/j.compositesb.2013.06.016>
281. Scarponi C, Schiavoni E, Sanchez-Saez S et al (2012) Polypropylene/hemp fabric reinforced composites manufacturing and mechanical behavior. *J Biobased Mater Bioenergy* 6(4):361–369. <https://doi.org/10.1166/jbmb.2012.1245>
282. Okumura W, Hasebe H, Kimizu M et al (2013) Development of carbon fiber fabric reinforced polypropylenes. Part 1: effect of content of maleic acid and removal of sizing agent. *Sen'i Gakkaishi* 69(9):177–182. <https://doi.org/10.2115/fiber.69.177>
283. Bárány T, Izer A, Karger-Kocsis J (2009) Impact resistance of all-polypropylene composites composed of alpha and beta modifications. *Polym Test* 28(2):176–182. <https://doi.org/10.1016/j.polymertesting.2008.11.011>
284. Izer A, Bárány T, Varga J (2009) Development of woven fabric reinforced all-polypropylene composites with beta nucleated homo- and copolymer matrices. *Compos Sci Technol* 69(13):2185–2192. <https://doi.org/10.1016/j.compscitech.2009.06.002>
285. TWINTEX® T PP. PP Glass Fabrics. http://www.ocvreinforcements.com/pdf/products/Twintex_TPP_09_2008_Rev0.pdf
286. Brown KA, Brooks R, Warrior NA (2010) The static and high strain rate behaviour of a commingled E-glass/polypropylene woven fabric composite. *Compos Sci Technol* 70(2):272–283. <https://doi.org/10.1016/j.compscitech.2009.10.018>
287. Hufenbach W, Langkamp A, Gude M et al (2013) Characterisation of strain rate dependent material properties of textile reinforced thermoplastics for crash and impact analysis. *Procedia Mater Sci* 2:204–211. <https://doi.org/10.1016/j.mspro.2013.02.025>
288. Han SH, Oh HJ, Kim SS (2014) Evaluation of fiber surface treatment on the interfacial behavior of carbon fiber-reinforced polypropylene composites. *Compos Part B: Eng* 60:98–105. <https://doi.org/10.1016/j.compositesb.2013.12.069>
289. Malkapuram R, Kumar V, Negi YS (2009) Recent development in natural fiber reinforced polypropylene composites. *J Reinf Plast Compos* 28(10):1169–1189. <https://doi.org/10.1177/0731684407087759>

290. Etcheverry M, Barbosa SE (2012) Glass fiber reinforced polypropylene mechanical properties enhancement by adhesion improvement. *Materials* 5:1084–1113. <https://doi.org/10.3390/ma5061084>
291. Simeoli G, Acierno D, Meola C et al (2014) The role of interface strength on the low velocity impact behaviour of PP/glass fibre laminates. *Compos Part B: Eng* 62:88–96. <https://doi.org/10.1016/j.compositesb.2014.02.018>
292. Alcock B, Cabrera NO, Barkoula NM et al (2006) Low velocity impact performance of recyclable all-polypropylene composites. *Compos Sci Technol* 66(11–12):1724–1737
293. Boisse P (2015) Textile composite forming simulation. In: Aliabadi MH (ed) *Computational and experimental methods in structures*, vol 6. Imperial College Press, London, p 241
294. Cherouat A, Borouchaki H, Giraud-Moreau L (2010) Mechanical and geometrical approaches applied to composite fabric forming. *Int J Mater Form* 3(2):1189–1204. <https://doi.org/10.1007/s12289-010-0692-5>
295. Boisse P, Zouari B, Daniel J-L (2006) Importance of in-plane shear rigidity in finite element analyses of woven fabric composite preforming. *Compos Part A: Appl Sci Manuf* 37 (12):2201–2212. <https://doi.org/10.1016/j.compositesa.2005.09.018>
296. Cabrera NO, Reynolds CT, Alcock B et al (2008) Non-isothermal stamp forming of continuous tape reinforced all-polypropylene composite sheet. *Compos Part A: Appl Sci Manuf* 39(9):1455–1466. <https://doi.org/10.1016/j.compositesa.2008.05.014>
297. McGuinness GB, Brádaigh CMÓ (1998) Characterisation of thermoplastic composite melts in rhombus-shear: the picture-frame experiment. *Compos Part A: Appl Sci Manuf* 29 (1):115–132. [https://doi.org/10.1016/S1359-835X\(97\)00061-4](https://doi.org/10.1016/S1359-835X(97)00061-4)
298. Lebrun G, Bureau MN, Denault J (2003) Evaluation of bias-extension and picture-frame test methods for the measurement of intraply shear properties of PP/glass commingled fabrics. *Compos Struct* 61(4):341–352. [https://doi.org/10.1016/S0263-8223\(03\)00057-6](https://doi.org/10.1016/S0263-8223(03)00057-6)
299. Harrison P, Clifford MJ, Long AC (2004) Shear characterisation of viscous woven textile composites: a comparison between picture frame and bias extension experiments. *Compos Sci Technol* 64:1453–1465. <https://doi.org/10.1016/j.compscitech.2003.10.015>
300. Johnson AF, Pickett AK (1996) Numerical simulation of the forming process in long fibre reinforced thermoplastics. In: *CADCOMP '96*, Udine, Italy, pp 233–242, 1–3 July 1996
301. Nishi M, Hirashima T (2013) Approach for dry textile composite forming simulation. In: *The 19th International Conference on Composite Materials-ICCM19*, Montreal, Canada, p 8, 28 July–2 Aug 2013
302. Johnson AF (1995) Rheological model for the forming of fabric-reinforced thermoplastic sheets. *Compos Manuf* 6(3):153–160. [https://doi.org/10.1016/0956-7143\(95\)95006-K](https://doi.org/10.1016/0956-7143(95)95006-K)
303. Boisse P, Hamila N, Helenon B et al (2008) Different approaches for woven composite reinforcement forming simulation. *Int J Mater Form* 1(21–29). <https://doi.org/10.1007/s12289-008-0002-7>
304. Pickett AK, Queckborner T, de Luka P et al (1994) Industrial press forming of continuous fibre reinforced thermoplastic sheets and the development of numerical simulation tools. In: *Flow processes in composite materials 94*, Galway, Republic of Ireland, University College Galway, pp 356–368
305. Rogers TG (1989) Rheological characterization of anisotropic materials. *Composites* 20 (1):21–27. [https://doi.org/10.1016/0010-4361\(89\)90677-0](https://doi.org/10.1016/0010-4361(89)90677-0)
306. Spencer AJM (1972) *Deformation of fibre-reinforced materials*. Oxford University Press, Oxford
307. Spencer AJM (1984) Constitutive theory for strongly anisotropic solids. In: Spencer AJM (ed) *Continuum theory of the mechanics of fibre-reinforced composites*, vol 282. Springer Vienna, Vienna, pp 1–32. https://doi.org/10.1007/978-3-7091-4336-0_1
308. de Luca P, Lefébre P, Pickett AK (1998) Numerical and experimental investigation of some press forming parameters of two fibre reinforced thermoplastics: APC2-AS4 and PEI-CETEX. *Compos Part A: Appl Sci Manuf* 29(1):101–110. [https://doi.org/10.1016/S1359-835X\(97\)00060-2](https://doi.org/10.1016/S1359-835X(97)00060-2)

309. Nishi M, Kaburagi T, Kurose M et al (2014) Forming simulation of thermoplastic pre-impregnated textile composite. *Int J Mater Text Eng* 8:779–787
310. Ivanov I, Tabiei A (2004) Loosely woven fabric model with viscoelastic crimped fibres for ballistic impact simulations. *Int J Numer Methods Eng* 61:1565–1583. <https://doi.org/10.1002/nme.1113>
311. Gong Y, Xu P, Peng X et al (2018) A lamination model for forming simulation of woven fabric reinforced thermoplastic prepregs. *Compos Struct* 196:89–95. <https://doi.org/10.1016/j.compstruct.2018.05.004>
312. Harrison P, Clifford MJ, Long AC et al (2004) A constituent-based predictive approach to modelling the rheology of viscous textile composites. *Compos Part A: Appl Sci Manuf* 35 (7):915–931. <https://doi.org/10.1016/j.compositesa.2004.01.005>
313. Harrison P, Long AC, Yu WR et al (2006) Investigating the performance of two different constitutive models for viscous textile composites In: 8th international conference on textile composites (TEXCOMP), Nottingham, UK, 16–18 October 2006
314. Harrison P, Yu W-R, Long AC (2011) Rate dependent modelling of the forming behaviour of viscous textile composites. *Compos Part A: Appl Sci Manuf* 42(11):1719–1726. <https://doi.org/10.1016/j.compositesa.2011.07.026>
315. Harrison P, Gomes R, Curado-Correia N (2013) Press forming a 0/90 cross-ply advanced thermoplastic composite using the double-dome benchmark geometry. *Compos Part A: Appl Sci Manuf* 54:56–69. <https://doi.org/10.1016/j.compositesa.2013.06.014>
316. Hufenbach WA, Kostka P, Maron B et al (2013) Development and investigation of a textile-reinforced thermoplastic leaf spring with integrated sensor networks. *Procedia Mater Sci* 2:173–180. <https://doi.org/10.1016/j.mspro.2013.02.021>
317. Hufenbach W, Gude M, Böhm R et al (2011) The effect of temperature on mechanical properties and failure behaviour of hybrid yarn textile-reinforced thermoplastics. *Mater Des* 32(8):4278–4288. <https://doi.org/10.1016/j.matdes.2011.04.017>
318. Hufenbach W, Böhm R, Thieme M et al (2011) Polypropylene/glass fibre 3D-textile reinforced composites for automotive applications. *Mater Des* 32(3):1468–1476. <https://doi.org/10.1016/j.matdes.2010.08.049>
319. Gibson AG, Torres MEO, Browne TNA et al (2010) High temperature and fire behaviour of continuous glass fibre/polypropylene laminates. *Compos Part A: Appl Sci Manuf* 41 (9):1219–1231. <https://doi.org/10.1016/j.compositesa.2010.05.004>
320. Bureau MN, Denault J (2004) Fatigue resistance of continuous glass fiber/polypropylene composites: temperature dependence. *Polym Compos* 25(6):622–629. <https://doi.org/10.1002/pc.20057>
321. Bocz K, Bárány T, Toldy A et al (2013) Self-extinguishing polypropylene with a mass fraction of 9% intumescent additive—a new physical way for enhancing the fire retardant efficiency. *Polym Degrad Stab* 98(1):79–86. <https://doi.org/10.1016/j.polymdegradstab.2012.10.029>
322. Bocz K, Igricz T, Domonkos M et al (2013) Self-extinguishing polypropylene with a mass fraction of 9% intumescent additive II—influence of highly oriented fibres. *Polym Degrad Stab* 98:2445–2451. <https://doi.org/10.1016/j.polymdegradstab.2013.06.011>
323. Ferreira JAM, Costa JDM, Reis PNB et al (1999) Analysis of fatigue and damage in glass-fibre-reinforced polypropylene composite materials. *Compos Sci Technol* 59 (10):1461–1467. [https://doi.org/10.1016/S0266-3538\(98\)00185-7](https://doi.org/10.1016/S0266-3538(98)00185-7)
324. Reis PNB, Ferreira JAM, Richardson MOW (2011) Fatigue damage characterization by NDT in polypropylene/glass fibre composites. *Appl Compos Mater* 18(5):409–419. <https://doi.org/10.1007/s10443-010-9172-9>
325. Mathieu R, René R, Brahim B (2010) Environmental effects on glass fiber reinforced polypropylene thermoplastic composite laminate for structural applications. *Polym Compos* 31(4):604–611. <https://doi.org/10.1002/pc.20834>
326. Hufenbach W, Langkamp A, Adam F et al (2011) An integral design and manufacturing concept for crash resistant textile and long-fibre reinforced polypropylene structural components. *Proc Eng* 10:2086–2091. <https://doi.org/10.1016/j.proeng.2011.04.345>

327. Vaidya UK, Samalot F, Pillay S et al (2004) Design and manufacture of woven reinforced glass/polypropylene composites for mass transit floor structure. *J Compos Mater* 38 (21):1949–1971. <https://doi.org/10.1177/0021998304048418>
328. Knox MP (2001) Continuous fiber reinforced thermoplastic composites in the automotive industry. In: *Automotive composites conference*, Troy, Michigan, p 6, 19–20 Sept 2001
329. Ye L, Friedrich K (1995) Processing of thermoplastic composites from powder/sheath-fibre bundles. *J Mater Process Technol* 48(1):317–324. [https://doi.org/10.1016/0924-0136\(94\)01664-M](https://doi.org/10.1016/0924-0136(94)01664-M)
330. Friedrich K, Gogeva T, Fakirov S (1988) Thermoplastic impregnated fiber bundles: manufacturing of laminates and fracture mechanics characterization. *Compos Sci Technol* 33 (2):97–120. [https://doi.org/10.1016/0266-3538\(88\)90013-9](https://doi.org/10.1016/0266-3538(88)90013-9)
331. Maywood W (2003) Thermoplastic pultrusion process unveiled. *Reinf Plast* 47(9):18. [https://doi.org/10.1016/S0034-3617\(03\)00926-3](https://doi.org/10.1016/S0034-3617(03)00926-3)
332. Novo PJ, Silva JF, Nunes JP et al (2016) Pultrusion of fibre reinforced thermoplastic pre-impregnated materials. *Compos Part B: Eng* 89:328–339. <https://doi.org/10.1016/j.compositesb.2015.12.026>
333. COMPTAPE. <http://compositetape.com/>. Accessed 10 June 2018
334. Nunes JP, Silva JF, Santos MS et al (2013) Processing conditions and properties of continuous fiber reinforced GF/PP thermoplastic matrix composites manufactures from different pre-impregnated materials. In: *The 19th international conference on composite materials*, Montreal, Canada, pp 3428–3438, 28 July–2 August 2013
335. Poon WKY, Jin YZ, Li RKY (2001) Pultrusion of glass fibre reinforced/maleated-PP modified/PP matrix composites. In: *13th international conference on composite materials*, Beijing, p 10
336. Novo PJ, Nunes JP, Silva JF et al (2013) Production of thermoplastics matrix preimpregnated materials to manufacture composite pultruded profiles. *Ciência & Tecnologia dos Materiais* 25(2):85–91. <https://doi.org/10.1016/j.ctmat.2014.03.004>
337. Novo P, Silva JF, Nunes JP et al (2012) Development of a new pultrusion equipment to manufacture thermoplastic matrix composite profiles. In: *15th European conference on composite materials*, Venice, Italy, 24–28 June 2012. *European Society for Composite Materials*, pp 1–8
338. Price RV (1973) Production of impregnated rovings. US3742106 Patent 3742106
339. Goud V, Alagirusamy R, Das A et al (2018) Dry electrostatic spray coated towpregs for thermoplastic composites. *Fibers Polym* 19(2):264–374. <https://doi.org/10.1007/s12221-018-7470-7>
340. Silva RF, Silva JF, Nunes JP et al (2008) New powder coating equipment to produce continuous fibre thermoplastic matrix towpregs. *Mater Sci Forum* 587–588:246–250. <https://doi.org/10.4028/www.scientific.net/MSF.587-588.246>
341. Velosa JC, Nunes JP, Silva JF et al (2010) Production of thermoplastic towpregs. *Mat Sci Forum* 636–637:220–225. <https://doi.org/10.4028/www.scientific.net/MSF.636-637.220>
342. Silva JF, Nunes JP, Velosa JC et al (2010) Thermoplastic matrix towpreg production. *Adv Polym Technol* 29(2):80–85. <https://doi.org/10.1002/adv.20174>
343. Padaki S, Drzal LT (1999) A simulation study on the effects of particle size on the consolidation of polymer powder impregnated tapes. *Compos Part A: Appl Sci Manuf* 30 (3):325–337. [https://doi.org/10.1016/S1359-835X\(98\)00115-8](https://doi.org/10.1016/S1359-835X(98)00115-8)
344. Nunes JP, van Hattum FWJ, Bernardo CA et al (2005) Production of thermoplastic Towpregs and Towpreg-based composites. In: Friedrich K, Fakirov S, Zhang Z (eds) *Polymer composites: from nano- to macro-scale*. Springer US, Boston, MA, pp 189–213. https://doi.org/10.1007/0-387-26213-x_11
345. Nunes JP, Silva JF, Marques AT et al (2003) Production of powder-coated towpregs and composites. *J Thermoplast Compos Mater* 16:231–248. <https://doi.org/10.1177/089270503025872>
346. O'Connor JE (1987) Reinforced plastic US4680224 Patent 4,680,224

347. Ho KKC, Shamsuddin S-R, Riaz S et al (2011) Wet impregnation as a route to unidirectional carbon fibre reinforced thermoplastic composites manufacturing. *Plast, Rubber Compos* 40 (2):100–107. <https://doi.org/10.1179/17432891X12988>
348. Vodermayr AM, Kaerger JC, Hinrichsen G (1993) Manufacture of high performance fibre-reinforced thermoplastics by aqueous powder impregnation. *Compos Manuf* 4(3):123–132. [https://doi.org/10.1016/0956-7143\(93\)90096-Q](https://doi.org/10.1016/0956-7143(93)90096-Q)
349. Carlsson A, Astrom BT (1998) Experimental investigation of pultrusion of glass fibre reinforced polypropylene composites. *Compos Part A: Appl Sci Manuf*, 585–593. [https://doi.org/10.1016/s1359-835x\(97\)00115-2](https://doi.org/10.1016/s1359-835x(97)00115-2)
350. Tomas ÅB, Byron PR (1993) A modeling approach to thermoplastic pultrusion. I: Formulation of models. *Polym Compos* 14(3):173–183. <https://doi.org/10.1002/pc.750140302>
351. Angelov I, Wiedmer S, Evstatiev M et al (2007) Pultrusion of a flax/polypropylene yarn. *Compos Part A: Appl Sci Manuf* 38(5):1431–1438. <https://doi.org/10.1016/j.compositesa.2006.01.024>
352. Devlin BJ, Williams MD, Quinn JA et al (1991) Pultrusion of unidirectional composites with thermoplastic matrices. *Compos Manuf* 2(3):203–207. [https://doi.org/10.1016/0956-7143\(91\)90141-3](https://doi.org/10.1016/0956-7143(91)90141-3)
353. Dai S-C, Ye L (2002) GF/PP tape winding with on-line consolidation. *J Reinf Plast Compos* 21(1):71–90. <https://doi.org/10.1106/073168402024283>
354. Schledjewski R, Latrille M (2003) Processing of unidirectional fiber reinforced tapes—fundamentals on the way to a process simulation tool (ProSimFRT). *Compos Sci Technol* 63 (14):2111–2118. [https://doi.org/10.1016/S0266-3538\(03\)00108-8](https://doi.org/10.1016/S0266-3538(03)00108-8)
355. Lionetto F, Dell’Anna R, Montagna F et al (2016) Modeling of continuous ultrasonic impregnation and consolidation of thermoplastic matrix composites. *Compos Part A: Appl Sci Manuf* 82:119–129. <https://doi.org/10.1016/j.compositesa.2015.12.004>
356. Funck R, Neitzel M (1994) Thermoplastic tape winding with high speed and at quasi-axial pattern. In: 3rd International conference on flow processes in composite materials (FPCM-3), Galway, Ireland, pp 237–247, 7–9 July 1994
357. Funck R, Neitzel M (1995) Improved thermoplastic tape winding using laser or direct-flame heating. *Compos Manuf* 6(3):189–192. [https://doi.org/10.1016/0956-7143\(95\)95010-V](https://doi.org/10.1016/0956-7143(95)95010-V)
358. Dobrzanski LA, Domagala J, Silva JF (2007) Application of Taguchi method in the optimisation of filament winding of thermoplastic composites. *Arch Mater Sci Eng* 28 (3):133–140
359. Åstrom BT, Pipes RB (1990) Thermoplastic filament winding with on-line impregnation. *J Thermoplast Compos Mater* 3(4):314–324. <https://doi.org/10.1177/089270579000300403>
360. Henninger F, Friedrich K (2002) Thermoplastic filament winding with online-impregnation. Part A: Process technology and operating efficiency. *Compos Part A: Appl Sci Manuf* 33 (11):1479–1486. [https://doi.org/10.1016/s1359-835x\(02\)00135-5](https://doi.org/10.1016/s1359-835x(02)00135-5)
361. Henninger F, Hoffmann J, Friedrich K (2002) Thermoplastic filament winding with online-impregnation. Part B. Experimental study of processing parameters. *Compos Part A: Appl Sci Manuf* 33(12):1684–1695. [https://doi.org/10.1016/s1359-835x\(02\)00136-7](https://doi.org/10.1016/s1359-835x(02)00136-7)
362. Kim HJ, Kim SK, Lee WI (1996) A study on heat transfer during thermoplastic composite tape lay-up process. *Exp Therm Fluid Sci* 13(4):408–418. [https://doi.org/10.1016/S0894-1777\(96\)00095-7](https://doi.org/10.1016/S0894-1777(96)00095-7)
363. Maurer D, Mitschang P (2015) Laser-powered tape placement process—simulation and optimization. *Adv Manuf Polym Compos Sci* 1(3):129–137. <https://doi.org/10.1179/2055035915Y.0000000005>
364. Brecher C, Stimpfl J, Dubratz M et al (2011) Innovative manufacturing of 3D-lightweight components. *Micro Mater Process* 8(5):36–40. <https://doi.org/10.1002/latj.201190057>
365. Brecher C, Emonts M, Stimpfl J et al (2014) Production of customized hybrid fiber-reinforced thermoplastic composite components using laser-assisted tape placement. In: Denkena B (ed) *New production technologies in aerospace industry. Lecture Notes in Production Engineering*. Springer, Cham, Switzerland, pp 123–129. https://doi.org/10.1008/978-3-319-01964-2_17

366. Parandoush P, Tucker L, Zhou C et al (2017) Laser assisted additive manufacturing of continuous fiber reinforced thermoplastic composites. *Mater Des* 131:186–195. <https://doi.org/10.1016/j.matdes.2017.06.013>
367. Brecher C, Werner D, Emonts M (2015) Multi-material-head. One tool for 3 technologies: laser-assisted thermoplast-tape placement, thermoset-prepreg-placement and dry-fiber-placement. In: 20th international conference on composite materials, Copenhagen, 19–24 July 2015
368. Kukla C, Peters T, Janssen H et al (2017) Joining of thermoplastic tapes with metal alloys utilizing novel laser sources and enhanced process control in a tape placement process. *Proc CIRP* 66:85–90. <https://doi.org/10.1016/j.procir.2017.03.307>
369. Janssen H, Peters T, Brecher C (2017) Efficient production of tailored structural thermoplastic composite parts by combining tape placement and 3D printing. *Proc CIRP* 66:91–95. <https://doi.org/10.1016/j.procir.2017.02.022>
370. Rijdsdijk HA, Contant M, Peijs AAJM (1993) Continuous-glass-fibre-reinforced polypropylene composites: I. Influence of maleic-anhydride-modified polypropylene on mechanical properties. *Compos Sci Technol* 48(1):161–172. [https://doi.org/10.1016/0266-3538\(93\)90132-z](https://doi.org/10.1016/0266-3538(93)90132-z)
371. Hamada H, Fujihara K, Harada A (2000) The influence of sizing conditions on bending properties of continuous glass fiber reinforced polypropylene composites. *Compos Part A: Appl Sci Manuf* 31(9):979–990. [https://doi.org/10.1016/S1359-835X\(00\)00010-5](https://doi.org/10.1016/S1359-835X(00)00010-5)
372. Rausch J, Zhuang RC, Mader E (2010) Systematically varied interfaces of continuously reinforced glass fibre/polypropylene composites: comparative evaluations of relevant interfacial aspects. *Express Polym Lett* 4(8):576–588. <https://doi.org/10.3144/expresspolymlett.2010.72>
373. Yashas Gowda TG, Sanjay MR, Subrahmanya Bhat K et al (2018) Polymer matrix-natural fiber composites: an overview. *Cogent Eng* 5:13. <https://doi.org/10.1080/23311916.2018.1446667>
374. Lariviere D, Krawczak P, Tiberi C et al (2004) Interfacial properties in commingled yarn thermoplastic composites. Part I: characterization of the fiber/matrix adhesion. *Polym Compos* 25(6):577–588. <https://doi.org/10.1002/pc.20052>
375. Liu CR (1998) A step-by-step method of rule-of-mixture of fiber- and particle-reinforced composite materials. *Compos Struct* 40:313–322. [https://doi.org/10.1016/S0263-8223\(98\)00033-6](https://doi.org/10.1016/S0263-8223(98)00033-6)
376. Van de Velde K, Kiekens P (2001) Thermoplastic pultrusion of natural fibre reinforced composites. *Compos Struct* 54(2):355–360. [https://doi.org/10.1016/S0263-8223\(01\)00110-6](https://doi.org/10.1016/S0263-8223(01)00110-6)
377. Van de Velde K, Kiekens P (2003) Effect of material and process parameters on the mechanical properties of unidirectional and multidirectional flax/polypropylene composites. *Compos Struct* 62(3):443–448. <https://doi.org/10.1016/j.compstruct.2003.09.018>
378. Lee S, Shi SQ, Groom LH et al (2010) Properties of unidirectional kenaf fiber–polyolefin laminates. *Polym Compos* 31(6):1067–1074. <https://doi.org/10.1002/pc.20893>
379. Tholibon D, Tharazi I, Bakar A et al (2016) Tensile properties of unidirectional kenaf fiber polypropylene composite. *Jurnal Teknologi (Sci Eng)* 78:101–106. <https://doi.org/10.11113/jt.v78.9153>
380. Okereke MI (2016) Flexural response of polypropylene/E-glass fibre reinforced unidirectional composites. *Compos Part B: Eng* 89:388–396. <https://doi.org/10.1016/j.compositesb.2016.01.007>
381. Zushi H, Ohsawa I, Kanai M et al (2005) Fatigue behaviour of unidirectional carbon fiber reinforced polypropylene. In: The 9th Japan international SAMPE symposium, Tokyo, 29 Nov–2 Dec 2005, pp 26–31
382. Ashton JE, Whitney JM (1970) Theory of laminated plates. In: *Progress in Material Science*, vol 4. Technomic, Stamford, Conn
383. Herakovich CT (1998) *Mechanics of fibrous composites*. Wiley, New York
384. Orifici AC, Herszberg I, Thomson RS (2008) Review of methodologies for composite material modelling incorporating failure. *Compos Struct* 86(1):194–210. <https://doi.org/10.1016/j.compstruct.2008.03.007>

385. Boudenne A, Tlili R, Certes YC (2012) Thermophysical and thermal expansion properties. In: Nicolais L, Borzacchiello A (eds) Wiley Encyclopedia of Composites. Wiley, New York
386. Progelhof RC, Throne JL, Ruetsch RR (1976) Methods for predicting the thermal conductivity of composite systems: a review. *Polym Eng Sci* 16(9):615–625. <https://doi.org/10.1002/pen.760160905>
387. Cho YJ, Youn JR, Kang TJ et al (2005) Prediction of thermal conductivities of fibre reinforced composites using a thermal-electrical analogy. *Polym Polym Compos* 13(6):637–644
388. Talreja R (1981) Fatigue of composite materials: damage mechanisms and fatigue-life diagrams. *Proc R Soc Lond Ser A Math Phys Sci* 378(1775):461–475. <https://doi.org/10.1098/rspa.1981.0163>
389. van den Oever M, Peijs T (1998) Continuous-glass-fibre-reinforced polypropylene composites II. Influence of maleic-anhydride modified polypropylene on fatigue behaviour. *Compos Part A: Appl Sci Manuf* 29(3):227–239. [https://doi.org/10.1016/s1359-835x\(97\)00089-4](https://doi.org/10.1016/s1359-835x(97)00089-4)
390. Gamstedt EK, Berglund LA, Peijs T (1999) Fatigue mechanisms in unidirectional glass-fibre-reinforced polypropylene. *Compos Sci Technol* 59(5):759–768. [https://doi.org/10.1016/S0266-3538\(98\)00119-5](https://doi.org/10.1016/S0266-3538(98)00119-5)
391. Joo S-J, Yu M-H, Kim WS et al (2018) Damage detection and self-healing of carbon fiber polypropylene (CFPP)/carbon nanotube (CNT) nano-composite via addressable conducting network. *Compos Sci Technol* 167:62–70. <https://doi.org/10.1016/j.compscitech.2018.07.035>

Chapter 10

Foams



Tobias Standau and Volker Altstädt

Contents

10.1	Introduction—Basics of Foaming	580
10.1.1	Market Situation	580
10.1.2	Basics of Foaming	580
10.1.3	Foam Morphology and Cell Types	586
10.1.4	Foam Relevant Properties	587
10.1.5	Blowing Agents	591
10.2	Foam Processing	593
10.2.1	Batch Processes	593
10.2.2	Foam Extrusion	595
10.2.3	Bead Foaming	601
10.2.4	Foam Injection Molding	613
10.2.5	Other Methods	621
10.3	PP Foams and Additives	623
10.3.1	Temperature-Insensitive Additives	623
10.3.2	Temperature-Sensitive Additives	630
	References	634

Abstract This chapter deals with polypropylene foams and consist out of 3 parts. Firstly—for a better understanding—the basics of foaming are described. This includes the fundamental physical processes of diffusion, nucleation and cell growth. Furthermore, material properties which are relevant for foaming are explained and typical blowing agents (physical and chemical) are introduced. Secondly, the foaming processes for polypropylene are summarized, beginning with the so-called batch foaming which is mostly relevant for scientific research. More industrial relevant processes for foaming PP are foam extrusion, foam

T. Standau · V. Altstädt (✉)

Department of Polymer Engineering, University of Bayreuth, Universitätsstraße 30,
95447 Bayreuth, Germany

e-mail: altstaedt@uni-bayreuth.de

URL: <https://www.polymer-engineering.de>; <https://www.nmbgmbh.de>

V. Altstädt

Neue Materialien Bayreuth GmbH, Gottlieb-Keim-Straße 60, 95448 Bayreuth, Germany

© Springer Nature Switzerland AG 2019

J. Karger-Kocsis and T. Bárány (eds.), *Polypropylene Handbook*,

https://doi.org/10.1007/978-3-030-12903-3_10

579

injection molding (FIM) and bead foaming. With FIM light-weight parts with good mechanical properties can be produced. This can be achieved with physical and chemical blowing agents and with different methods. Bead foams possess a very low density and can be directly brought into relative complex shapes. Therefore, expanded Polypropylene (EPP) is maybe the most important PP foam at all. Both methods for bead foam production (discontinuous with autoclave and continuous with extrusion process) are described as well as the fusion processes (steam chest molding). The last part of this chapter is designated to the many additives that are used in PP foams (i.e. talc, clay etc.) and their influence on properties like expansion behavior and foam morphology.

10.1 Introduction—Basics of Foaming

10.1.1 Market Situation

The number of commodity goods, which are partially or even completely made of plastics, are continuously increasing. As a result, the polymer market shows high annual increase rates, with an estimated European growth rate of 2.9% by 2022 [1]. In particular, the polymer foam market is expected to show an average annual growth rate of 4.8% by 2019 [2]. Considering only the European market, a total amount of about 57 megatons (Mt) of plastics are produced per year [3]. Based on weight, assuming an average density of 100 kg/m^3 , foams make up only 8% (about 4.5 Mt) but regarding the overall volume the share is 50% [4]. The characteristic properties of foams, compared to compact material, result in the mentioned differences in growth and market share. The most advantageous property of foams is the reduced weight. Consequently, less material is required, compared to a compact part. Most common foaming processes are autoclave foaming, continuous foam extrusion, bead foaming and foam injection molding. Additional advantageous properties, besides weight reduction, are very good thermal and acoustic insulation properties and high energy absorption [5, 6], which has led to a wide range of applications, for example as shock absorbers (e.g. in automotive or sports), insulation boxes (e.g. food transport) or as insulating material in the construction industry [5–8].

10.1.2 Basics of Foaming

The overall foaming process, shown schematically in Fig. 10.1, consists of several steps. First, a gas is mixed into a polymer phase with subsequent homogenization into a single melt phase. Here, the solubility depends on material type, the gas pressure and temperature. Upon addition of the blowing agent (e.g. liquid, supercritical CO_2) to the polymer melt, the fluid molecules are adsorbed at the surface of the polymer phase. The solubility of the blowing agent is dependent on its nature

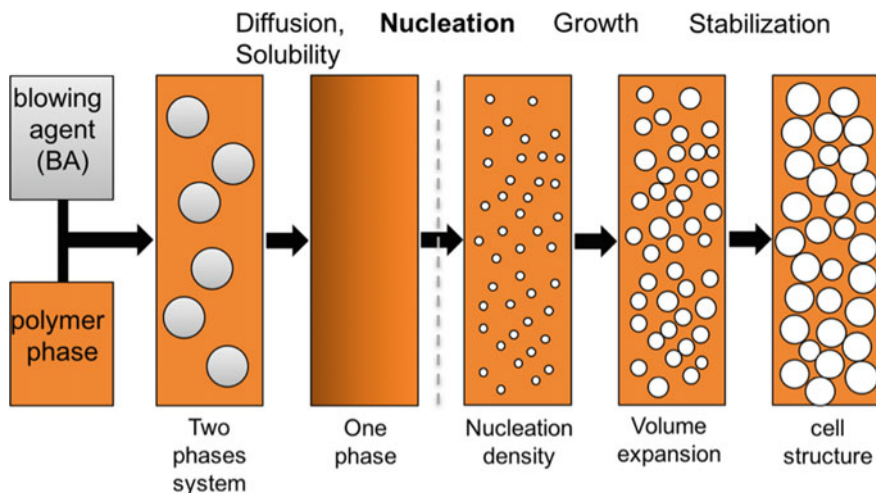


Fig. 10.1 Schematics of the foaming process steps, e.g. during foam extrusion. *Copyright (2018) University of Bayreuth, Department of Polymer Engineering*

(e.g. polarity, molecular size), while the diffusion of the blowing agent molecules in the polymer is affected by partial pressure or concentration gradients [4]. The foaming itself consists of nucleation of the polymer melt, cell growth through expansion and final foam stabilization.

10.1.2.1 Diffusion and Solubility

During the homogenization step of the polymer and the blowing agent, the rate of concentration balance depends on the temperature and the chemical structure of the polymer matrix as well as on the blowing agent. Thus, in a one-dimensional mass transport, the diffusion rate can generally be described by the first Fick's law (Eq. 10.1) [9]:

$$\frac{dm}{dt} = -D \cdot A \cdot \rho \cdot \frac{dc}{dx} \quad (10.1)$$

where:

- m Mass of diffusing material
- D Diffusion coefficient
- A Surface area
- ρ Density
- c Concentration
- x Spatial coordinates

Thus, Fick's law describes the time-dependent mass transport of fluid molecules through a polymer matrix, whereby the diffusion rate depends on the concentration of blowing agent [9]. The temperature-dependent diffusion coefficient (Brownian motion) of the propellant fluid and the polymer can be described by an Arrhenius approach (Eq. 10.2).

$$D = D_0 \cdot e^{\frac{-\Delta E_D}{RT}} \quad (10.2)$$

where:

- D_0 Constant for polymer-blowing agent system
- ΔE_D Activation energy of the diffusion
- R General gas constant
- T Absolute temperature

That elucidates, that the diffusion coefficient is temperature-dependent and also increases with rising temperature. The amount of blowing agent that can be dissolved in the polymer is limited by the saturation limit (polymer dependent). As saturation increases, the local concentration difference and hence the diffusion rate decreases. The saturation limit of a polymer can be described by Henry's Law (Eq. 10.3) [10]:

$$c = S \cdot p \quad (10.3)$$

where:

- c Concentration of solved gas in the polymer
- S Solubility coefficient
- p Partial pressure of the gas

This results in a direct proportionality between the gas concentration in the polymer and the pressure. At high pressures and temperatures, the solubility coefficient can be formulated as a temperature and pressure dependent function. The temperature dependence is described in Eq. 10.4 [11]:

$$S = S_0 \cdot e^{\frac{-E_S}{RT}} \quad (10.4)$$

where:

- S_0 Coefficient
- R General gas constant
- E_S Heat of solution
- T Absolute Temperature

A graphic representation of the temperature and pressure dependence is shown in Fig. 10.2. It illustrates the increase in solubility with higher pressure and a decrease with rising temperature. In addition, the blowing agent acts as a plasticizer

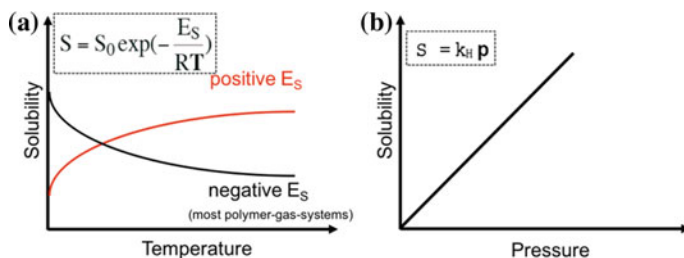


Fig. 10.2 Dependence of the solubility of gases in polymer phase on temperature (a) and pressure (b). Copyright (2018) University of Bayreuth, Department of Polymer Engineering

and significantly reduces polymer viscosity by the attachment of the gas molecules between the polymer chains, resulting in increased mobility [12–15].

10.1.2.2 Nucleation

The process of foam growth begins with nucleation, which can occur either homogeneous, heterogeneous or both. *Homogeneous nucleation* results in cell formation from a homogeneous phase. Due to kinetic inhibition (critical nuclei size), the pure self-nucleation is rather unlikely. Only if the critical nucleus radius r^* , and thus Gibb's free energy barrier ΔG_{Hom}^* , is exceeded, the nucleus is stable and can continue to grow (see Fig. 10.3).

The critical nucleus radius and the Gibb's energy barrier are described as follows:

$$r^* = \frac{2\gamma_{\alpha\beta}}{\Delta p} \quad (10.5)$$

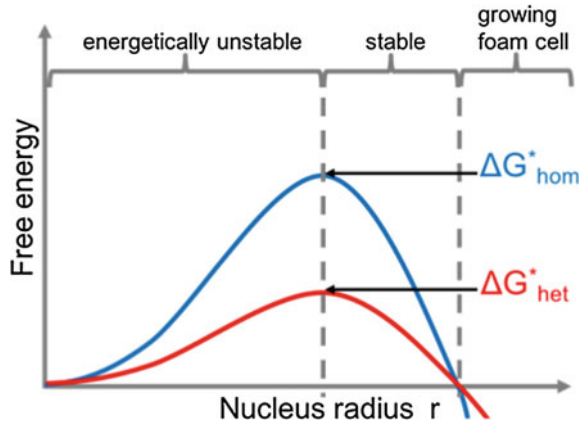
$$\Delta G_{Hom}^* = \frac{16\pi\gamma_{\alpha\beta}^3}{3\Delta p^2} \quad (10.6)$$

where:

- $\gamma_{\alpha\beta}$ Surface energy
- Δp Pressure difference

In the presence of a second phase, the cells can be formed more easily at the interface of the foreign substance or walls. In this case, the foreign substance serves as a nucleating agent (NA) and a *heterogeneous nucleation* occurs. As result, the nucleation is influenced by the shape factor S , which depends on the contact angle θ between the foam cell and the impurity/NA interface, and thus reduces the energy barrier (Eqs. 10.7 and 10.8). The higher the concentration of nucleating agents, such as talc or titanium oxide, the faster nucleation takes place. In addition, high

Fig. 10.3 Energetic hindrance of homogeneous and heterogeneous nucleation depending on nuclei radius. Copyright (2018) University of Bayreuth, Department of Polymer Engineering



nucleation density enables smaller cell sizes, thus influencing foam morphology. Even in processes without additional NA, blowing agent residues (chemical), degraded polymer residues, or foreign substances can initiate heterogeneous nucleation [12–15].

$$S(\theta) = \frac{1}{4}(2 + 3 \cos \theta - \cos^3 \theta) \quad (10.7)$$

$$\Delta G^*_{\text{Het}} = \frac{16\pi\gamma_{\alpha\beta}^3}{3\Delta P^2} S(\theta) \quad (10.8)$$

10.1.2.3 Cell Growth

During this stage the cell structure of the foams is formed. The cell growth can be induced by gas diffusion from the polymer phase into the growing cells, expansion by temperature or density reduction and coalescence of smaller cells. Cell growth continues until an equilibrium is achieved between the energy required for surface expansion and volume work in the growing foam cell. This can be mathematically described as:

$$\gamma \cdot dA = p \cdot dV \quad (10.9)$$

where:

- γ Surface tension
- A Surface of the growing bubble

For a simpler outline, a spherical-shape model is used to describe the geometry of the foam cell. Under this assumption, Eq. 10.9 yields the following term (Eq. 10.10):

$$\gamma \cdot 8\pi r \cdot dr = p_1 \cdot 4\pi r^2 dr \quad (10.10)$$

where:

- p_1 Partial pressure = $2\gamma/r$
 r Growing cell diameter

Due to the free surface energy γ , a system with a small number of large cells is more stable during cell growth than a system with many small ones. The pressure is higher in small foam bubbles and hence gases prefer to diffuse from small into larger growing cells. As a result, the system strives, with sufficient amount of time, to change a fine cell distribution towards a foam with large cells. The rate of diffusion of the gas into an already existing bubble is described by Stoke's law (Eq. 10.11):

$$w = \frac{g \cdot (2r)^2}{18\eta} \Delta\rho \quad (10.11)$$

where:

- w Diffusion rate
 g Acceleration of gravity
 r Growing cell radius
 η Dynamic viscosity
 ρ Density

Thus, decreasing viscosity of the melt and increasing growing cell diameter favors the diffusion rate. Conversely, a reduction in gas loading leads to an increase in viscosity and can be used to stabilize the foam [12–15].

10.1.2.4 Cell Structure and Foam Stabilization

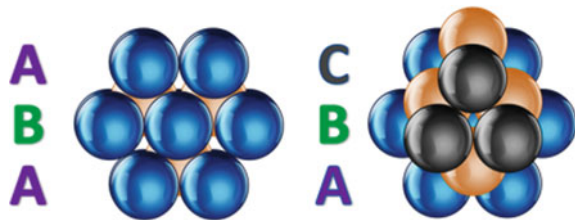
During the foaming process, the polymer is stretched between adjacent cells and forms thin membranes (cell walls). If the cell membranes remain around the cells as growth proceeds, than closed-cell structures are created. If the membrane tears (also known as cell coalescence), the foam becomes partially or completely open-celled. The tearing of the membranes is promoted by strong expansion and the concomitant displacement of the polymer. Excessive rupture of the cell walls before foam stabilization can lead to a foam collapse. The foam cells can be stabilized by increasing the viscosity (e.g. by cooling, molecular weight build-up or strain hardening), reducing the surface tension and by increasing the free energy with rising surface area. If the gas volume is small enough, the spherical shape of the foam cells remains. With increasing volume, the spherical shape can no longer be retained, so that polyhedral shapes are formed. The typical geometry usually exhibited by low density foams are dodecahedra with many four- or five-sided membranes [12–15].

10.1.3 Foam Morphology and Cell Types

The properties and morphology of foamed material are determined by both the size and shape of the cells, as well as the size and configuration of the intercellular space. The interspaces are filled by the polymer matrix and form the walls and framework structures of foams. The morphology of foamed plastics can be described by the theory of close-packing of equal spheres. The spheres are considered to be hollow spheres stacked in layers, and the empty space in-between represents the polymeric framework structure. Basically, two arrangements are possible, the cubic close packed (ccp) (also called faced-centered cubic) and the hexagonal close-packed (hcp) lattice. These differ only in the arrangement of the third layer. The three-dimensional structures are generated by packing the spheres as close as possible, positioned on the gaps of the previous sphere-layer. However, each hollow sphere generates two gaps in the next layer, generating several possibilities for the packing of the third layer. For the ccp, in the third layer the gaps left in the second level are covered (ABC). In the hcp, however, the third layer is packed according the first one (ABA) (see Fig. 10.4) [13, 14].

Despite different symmetry, in both cases the packing density and the space filling are equal to 74.05%. However, since the geometry is not spherical in real systems, hcp can fill more than 95% of the volume [13, 14]. In addition to cell size, cell thickness and density, the cell types also influence the foam properties. In order to obtain good mechanical properties, like foam stiffness, and good thermal insulating characteristics, the foam cell diameters should be reduced while retaining a homogeneous cell morphology. By decreasing the average cell diameter, the thermal insulating properties increase [16]. The foam stiffness and hence the mechanics, on the other hand, depend not only on the cell diameter, but also on the thickness of the framework that can be adjusted by density reduction (higher density results in higher foam stiffness) [17, 18]. Therefore, a lot of research concentrates on microcellular plastic foams. These foams can be usually characterized by an average cell diameter between 1–10 μm , a high cell density ranging of 10^9 – 10^{12} cells/ cm^3 and a weight reduction of 5–95% [19, 20]. By choosing the process and varying the chemical composition of the polymer phase, closed-cell or open-cell structures can be purposely generated (see Fig. 10.5).

Fig. 10.4 Illustration of the close-packing of equal spheres in hcp (left) and ccp (right) lattices. Copyright (2018) University of Bayreuth, Department of Polymer Engineering



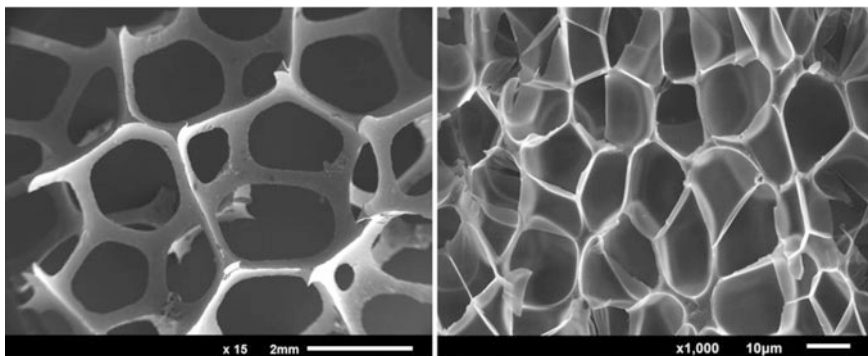


Fig. 10.5 SEM-picture of an open-cell foam structure (left) and close-cell foam structure (right). Copyright (2018) University of Bayreuth, Department of Polymer Engineering

In order to obtain a closed-cell foam, certain requirements must be met. To qualify as a closed-cell foam, not more than two torn cell walls per cell-unit or pore are allowed and the majority of the cell framework must be shared by at least three other structural elements. These differences in structure are the reason for the different properties of foams. Closed-cell foams have good insulating properties. Open-celled foams can absorb more water and moisture compared to the closed-cell structure and damp or absorb sound much better. In addition, they have a higher permeability to gases or steam, but reduced thermal insulation properties and electrical conductivity. By subsequent methods, such as mechanical or thermal treatment, closed-cell materials can be converted into open-cell foams [13, 14].

10.1.4 Foam Relevant Properties

Polypropylene (PP) is an outstanding choice as matrix material for polymeric foams due to its favorable mechanical properties and chemical resistance. However, its complex microstructure and semi-crystalline nature results in unfavorable foaming properties. It is difficult to obtain homogeneous lightweight foams due to its low melt elasticity as well as viscosity and its low temperature dependence of melt viscosity in fully molten state, which makes the control of viscosity by temperature variation highly challenging. Furthermore, crystallization can occur during foaming, which can lead to either shutdowns of the process (e.g. freezing of the die during foam extrusion) or unfavorable foam structures due to cell rupture.

It is concluded, that a good knowledge on the rheology and crystallization properties is essential to adjust the morphology and thereby the elastic modulus, strength [21], impact behavior [22] and thermal conductivity [23] of foamed products.

During foam extrusion (see Sect. 10.2.2), temperature, pressure, and blowing agent affect the flow behavior of the melt and ultimately the foam properties. In addition, the melt behaves differently under shear and elongational flow. The flow patterns in the extruder are dominated by shear deformation. However, the elongational properties become relevant after the melt leaves the die, since in foaming stage the melt is subjected to elongational flow during bubble growth, namely equi-biaxial extension. This section gives a brief overview on the challenges and influences of foaming polypropylene in an extrusion process.

10.1.4.1 Rheology

The rheology of PP is a major challenge in achieving low-density foams. Generally, PP has a comparatively low viscosity in fully molten state compared to amorphous polymers such as polystyrene or polycarbonate.

In extrusion, it is desired to control the melt viscosity by setting an adequate mass temperature. However, this is highly difficult for polypropylene as low temperatures cannot be accessed, which would lead to favorably high viscosity, due to crystallization and thus freezing of the extrusion die. Hence, the temperature window for extrusion foaming of polypropylene is generally very narrow for standard grades.

Furthermore, the elongational properties of the melt are of utmost importance, as they govern the cell growth and influence the rupture of the forming cell walls. The viscoelastic behavior of the melt in elongational deformation is crucial for the formation of the foam morphology [24], as mostly low average cell size, a narrow cell size distribution and low density are required. Polypropylene is well known to possess very disadvantageous elongational properties; both melt strength and drawability are very low for standard grades.

However, PP can be modified in order to improve its foamability. In particular, the effect of strain hardening at large elongational strains is desired to support cell stabilisation. In this frame, strain hardening is highly beneficial for foaming due to the effect of self-healing of cell walls during the expansion of foam cells.

Strain hardening means the rise of the elongational viscosity $\eta_E(t)$ above the zero-rate elongational viscosity $\lim_{\dot{\epsilon} \rightarrow 0} \eta_E(\dot{\epsilon})$. It helps to prevent cell coalescence and to widen the processing window [25], i.e. for the foaming of PP [26]. In terms of chain topology, strain hardening is caused by long chain branching (LCB) [27, 28].

However, LCB-PP has the disadvantage of a lower solubility of CO₂ compared to linear PP [29]. This arises due to the fact that LCB-PP has a lower specific volume compared to linear PP as well as a more pronounced resistance against swelling, which is caused by dissolution of CO₂ [30].

Compared to linear polymers the rheological characterization of LCB polymers is more challenging, since they possess characteristics, which complicate the measurements and analyses. For example, LCB polymers may not obey the Cox-Merz rule [31–33]. Furthermore, it is also difficult to obtain the zero-shear

viscosity of heavily long-chain branched polymers from oscillatory data. Their very long relaxation time would require very low frequencies, which cannot be accessed experimentally without thermal degradation of the material. Hence, creep experiments must be performed to obtain this material's property [34].

A further challenge is thermo-rheological complexity, which was already mentioned above. The time-temperature-superposition (TTS) of many polymers can be described by only one pair of shift factors per temperature, leading to a so-called "master-curve". This behavior is then called thermo-rheologically simple. If it is not possible to obtain a satisfactory master-curve, as a systematic deviation with temperature is observed (e.g. the shift factors are dependent on stress, modulus or relaxation strength), the polymer is called thermo-rheologically complex. In thermo-rheologically complex polymers, two or more relaxation mechanisms do not have the same temperature dependency [35], which leads to time or frequency dependent temperature shift factors. LCB often causes thermo-rheological complexity, which was shown by several authors [36–38]. Although, the determination of thermo-rheological complexity is not straightforward, it can help to widen the temperature processing window. For example, Raps et al. [39] found that long-chain branching leads to an increased temperature sensitivity of the melt viscosity at strain-rates relevant for foaming, which should allow a better process control during foaming.

It was seen, that foaming PP in a continuous process as foam extrusion is highly challenging and requires a tight control of the process conditions due to a narrow processing window. This is due to various reasons. Firstly, a low melt viscosity as well as elasticity, which leads to difficult foam stabilization. Secondly, these are very hard to control by the extrusion temperature as the sensitivity of the melt viscosity on temperature changes is very low in fully molten state. The low melt elasticity and its low temperature sensitivity are less critical for long chain branched polypropylene (also called high melt-strength PP).

10.1.4.2 Crystallization

The crystallization kinetics and crystalline morphology of ready-available semi-crystalline polymers is well known due to its high importance for the manufacturing of polymer products by techniques like fiber-spinning, blow molding and injection molding [40]. In the case of foam and cellular polymeric materials, although to a lesser extent, it is well known that crystallization phenomena play a major role in foaming [41].

Crystallization phenomena at the relevant conditions for gas loaded polymers intended for foaming must be understood to obtain good foam morphologies, to reduce development time and set the lower limit of the processing window of temperature. Many factors change the crystallization behavior of polymer melts. Those factors will be discussed subsequently.

The effect of pressure on the crystallization of various polymers has been discussed in various publications in the past. For example, Kardos et al. found that

with increasing pressure [42] polypropylene tends to crystallize higher amounts of the γ -phase and less α -phase. At approximately 500 MPa all crystals were found to be in the γ -modification. Brückner et al. studied the crystallization of iPP under high pressure with special emphasis on the occurrence of the γ -phase. They proposed that the crystal-amorphous interphase plays a major role in the formation of the respective crystalline phases [43].

Carrubba et al. used a master-curve approach to describe the effect of both pressure and cooling rate [44] for iPP, as well as PA6 and PET, where pressure could be represented as a fictional cooling-rate.

Besides pressure and cooling rate, also molecular structure determines the crystallization-behavior. Especially important is long chain branching (LCB), as discussed before. One effect of LCB on crystallization is an increase of crystallization temperature [45] and the amount of γ -phase [46].

Also, additives, which are often used as nucleating agents, have a profound influence on crystallization. Yuan and Turng [47], who studied the effect of nanoclays on foam injection molding of PA6, found a reduced amount of α -crystals due to the addition of nanoclay, but more γ -phase crystals. However, the total crystallinity was reduced by addition of nanoclay and supercritical blowing agent.

Since gas is solved into the polymer for purpose of foaming, its effect on crystallization must be considered as well. Takada et al. studied the effect of CO₂ on crystallization of iPP [48]. Solved gas increases molecular mobility and free volume, thus leading a decrease of chain-chain interactions. Because of that, motion of chains into the crystal-amorphous boundary is improved, leading to a higher crystallization rate. However, the nucleation rate is decreased. It can be concluded, if crystallization is nucleation-controlled, the overall rate is decreased by incorporation of CO₂, otherwise it is increased. Takada et al. investigated the effect of dissolved CO₂ on the isothermal crystallization of PET in another paper [49]. They found that, if the reduction of the glass transition temperature (T_g) is higher than the melting temperature (T_m), then the crystallization rate is increased. If their reduction is fairly similar, crystallization rate is decreased (nucleation controlled region). They concluded that this rule may be applicable to all semi-crystalline polymers. Moreover, Oda and Saito [50] found that spherulite growth rate reached an optimum at moderate CO₂-pressure thus emphasizing the competition between plasticization effects, which dominate at low concentrations, and exclusion effects pushing CO₂ away from the crystallization front at high CO₂ concentrations. High CO₂-pressure also affects the crystal morphology. The amount of γ -modification increases almost linearly with gas-pressure for LCB-PP, with even higher effect than branching. Also, the fraction of amorphous phase is increased [46]. However, there is also a backside in crystallization: the occurrence of crystals leads to a significant reduction of gas-solubility as well as diffusivity [41].

Furthermore, the timing and kinetics of crystallization is crucial for a well-defined and fine cellular morphology. If crystallization proceeds too quickly and in a very narrow window, the chance of the freezing of the die in foam extrusion process is much more pronounced. Also, if crystallization takes place

during cell growth, the cellular structure might collapse, become very inhomogeneous or partially open-cellular.

Crystallization of PP is a challenge during foaming processes as it can lead to process shutdown (e.g. freeze of the die). Crystallization is highly sensitive towards the process conditions as temperature, pressure and the content of the blowing agent.

10.1.5 Blowing Agents

The blowing agent is a key component for foaming. There are different types of blowing agents (chemical and physical) that differ in possible density reduction. **Chemical blowing agents** (CBA) are compounds that release gases as part of a chemical reaction (even thermal decomposition, mainly releasing CO₂, CO, N₂, NH₃, etc.). CBAs usually achieve lower expansion ratios (process and application dependent), compared to physical propellants, and a solid residue remains in the polymer (see Table 10.1). In principle, the following mechanisms can be distinguished:

- (a) Gas release due to an irreversible reaction



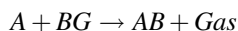
e.g.: Azodicarbonamide (ADC) \Rightarrow CO₂, CO, N₂, NH₃

- (b) Gas release resulting from an equilibrium reaction:



e.g.: Carbonates and bicarbonates of alkaline or alkaline earth metals \Rightarrow CO₂

- (c) Combination of several components, which release gas due to a chemical interaction:



e.g.: Citric acid combined with sodium bicarbonate \Rightarrow CO₂, H₂O

Physical blowing agents, on the other hand, are substances that foam the material through physical processes, such as change of state (liquid to gas), evaporation or desorption, at higher temperatures or under reduced pressure. Generally, propellants have to fulfill certain requirements, such as good solubility, odor neutrality, environmental friendliness and be commercially advantageous. That is also the reason why the chlorofluorocarbons (CFCs) are no longer in use.

Table 10.1 Overview of most used chemical blowing agents according to [4]

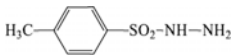
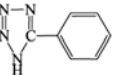
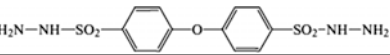
Blowing agent	Formula	Gas release rate (ml/g)
Sodium bicarbonate	NaHCO_3	160–170
Citric acid and derivates	$\text{ROOC-CH}_2\text{-C(OH)(COOR)-CH}_2\text{-COOR}$	90–130
Azodicarbonamide (ADC)	$\text{H}_2\text{N-CO-N}=\text{N-CO-NH}_2$	280–320
Toluenesulfonyl hydrazide (TSH)		120–140
Oxybis(benzenesulfonyl hydrazide) (OBSH)		120–150
5-Phenyltetrazole (5-PT)		120–140

Table 10.2 Overview of most frequently used physical blowing agents according to [4]

Blowing agent	Structural formula	Molecular weight (g/mol)
n-Butane	$\text{CH}_3\text{-CH}_2\text{-CH}_2\text{-CH}_3$	58.1
Isobutane	C_4H_{10}	58.1
n-Pentane	C_5H_{12}	72.2
Isopentane	C_5H_{12}	72.2
Nitrogen	N_2	28.0
Carbondioxide	CO_2	44.0

Even though CFCs are good propellants, they cause catalytic degradation of the ozone layer and have an overall bad carbon footprint. Based on the prerequisites, only a few propellants are relevant for industrial applications, such as summarized in Table 10.2.

For foaming polymers, both volatile solvents can be used, such as ketones or hydrocarbons, as well as gases. The gases are inert substances, such as CO_2 , N_2 or helium, which are added to the polymer melt under high pressure and get dissolved. By a pressure drop, the solubility of the blowing agent is greatly reduced, so that the polymer melt is foamed mechanically (mechanical foaming) or by the gas expansion. The choice of blowing agents can affect morphological and thermal properties (melting peaks) as well as cell homogeneity [14].

10.2 Foam Processing

10.2.1 Batch Processes

Batch foaming is a discontinuous process taking place in an autoclave at certain temperature and pressure. In general, batch process is easy to operate and can produce foams with controllable structure and properties. There are two types of batch foaming processes: temperature and pressure-induced batch foaming.

In *temperature-induced batch foaming* process, as shown in Fig. 10.6, the sample is impregnated with blowing agents in an autoclave. Once saturation reached, pressure is released at a relatively low temperature in order to prevent foaming. Then the supersaturated sample is dipped into a hot oil bath for a specific time period to induce cell nucleation and cell growth. Subsequently the sample is taken out from the hot oil bath and is immersed into a cooling oil/water bath to stabilize the cell structure [15, 41].

Batch foamed PP is mostly produced by *pressure-induced batch foaming* process involving two steps: blowing agents sorption and depressurization, which are illustrated in Fig. 10.7. Firstly, blowing agents are dissolved and diffused into the PP matrix at controlled temperature and pressure. After the sample is saturated by blowing agents for a certain time, pressure is released rapidly to the atmospheric pressure. This pressure drop acts as driving force for cell nucleation and cell growth. In this process, foam cell structure and foam expansion are influenced by many

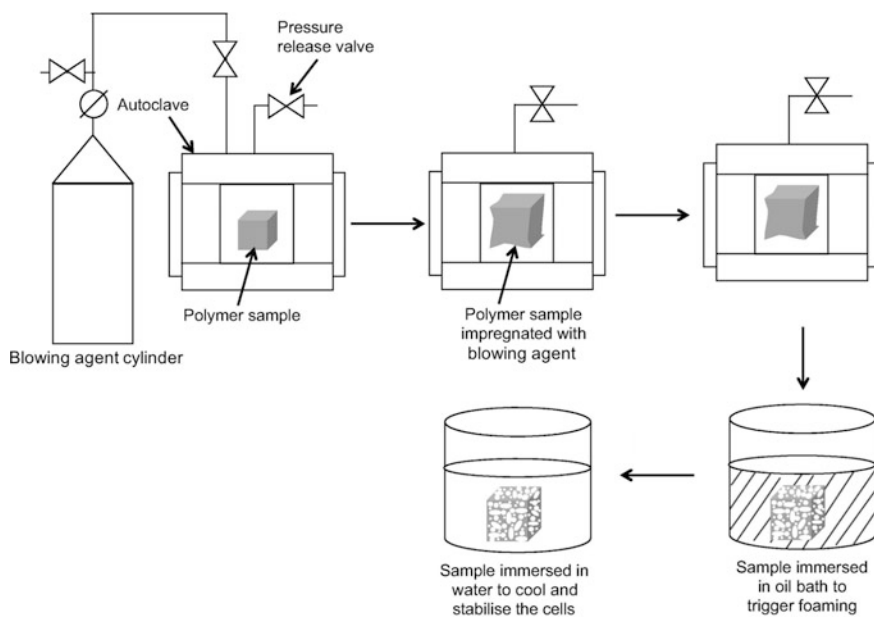


Fig. 10.6 Temperature-induced batch foaming process [15]. Copyright (2018) Elsevier

factors compromising with each other, such as temperature, pressure, type of blowing agent, blowing agent sorption time, pressure drop as well as pressure drop rate. By controlling these processing parameters, PP foams with desired cell morphology can be obtained. In the work of Xu et al., the effects of individual processing parameter on PP foam expansion and foam morphology, including cell size and cell density, were discussed. For instance, at the foaming temperature of 154 °C and the foaming pressure of 25 MPa, cell size could be reduced from 34.3 to 11.2 μm and cell density could be increased from 1.2×10^8 cells/cm³ to 2.2×10^8 cells/cm³ by increasing the depressurization rate from 5 to 25 MPa/s [51]. A higher depressurization rate induces a higher level of supersaturation and a higher driving force for the cell nucleation. On the other hand, an increase in depressurization rate results in a limited time for blowing agent diffusion, therefore, more blowing agent is used for cell nucleation instead of cell growth leading to smaller cell size and larger cell density.

Foaming temperature and pressure are two essential parameters playing a role together on foam cell structure and expansion. They determine the amount of blowing agents dissolved and diffused in PP matrix within a certain time, as the solubility and diffusivity of blowing agents depend on temperature and pressure, according to Sect. 10.1.2.1. It is noteworthy that the effects of temperature and pressure on blowing solubility vary from the types of blowing agent. For instance, with higher pressure, solubilities of both CO₂ and N₂ in PP increase. However, solubility of CO₂ in PP decreases with higher temperature, while solubility of N₂ in PP increases as temperature increases [52]. Furthermore, temperature and pressure also affect the crystal structure of PP, which has a further impact on cell structure. Since PP is a semi-crystalline polymer, blowing agents are only dissolved into the amorphous region, when the crystalline region is intact. Jiang et al. reported that with increasing pressure, interlamellar regions was extended by blowing agent (CO₂) largely, which created more space for cell growth and therefore achieved foams with more homogeneous morphology in both amorphous and crystalline regions [53]. In addition to the combining effects of temperature and pressure, their individual effects are discussed as follows.

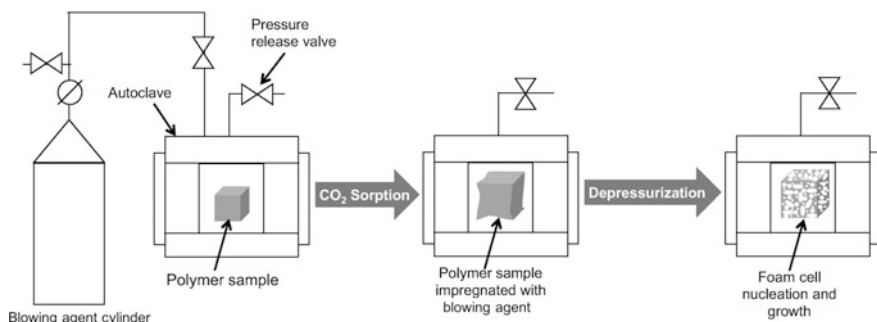


Fig. 10.7 Pressure-induced batch foaming process [15]. Copyright (2018) Elsevier

The *temperature* has a big influence on the foaming result. At low temperature, the high stiffness of PP matrix makes expansion difficult [54]. As the temperature increases, the melt strength of PP decreases and therefore the deformability of PP increases allowing cells to be expanded by blowing agents more “easily”. On the other hand, a higher temperature leads to an increase in blowing agent diffusivity in PP, which favors the cell growth. Nevertheless, when the temperature is too high, blowing agents can escape out rapidly from the PP matrix to the environment instead of contributing to foam expansion [51]. Therefore, an optimum temperature should be selected to achieve the largest expansion, at which PP is soft enough to be expanded and sufficient amount of blowing agents can be retained in PP.

Furthermore, *saturation pressure* and *the pressure drop rate* affect the foaming. Besides the effect on blowing agent solubility, the foaming pressure changes energy barrier as well. According to Eqs. 10.6 and 10.8, a higher foaming pressure, which means a larger pressure drop during the depressurization to atmospheric pressure, reduces the Gibb’s energy barrier to nucleation strongly, therefore promotes cell nucleation [55].

Saturation time, which is the time for blowing agent dissolving and diffusing into PP to reach the equilibrium, is determined by the foaming temperature and pressure. Within a short time, dissolution and diffusion of blowing agents inside the PP are neither complete nor uniform, resulting in a low foam expansion and an inhomogeneous cell structure. Thus, a sufficient absorption of blowing agent over time is required for adequate cell nucleation and growth during the phase of depressurization [56].

10.2.2 Foam Extrusion

The high demand of polymeric foams for lightweight applications, insulation and packaging makes a continuous process favorable wherever possible. The main economical advantage of foam extrusion is resulting from high throughputs. In industry, common top throughput rates are around 900 kg/h, in some cases up to 2800 kg/h are possible with corresponding machines. Additionally, the extrusion process is versatile and easy to control. It is possible to combine multiple functions in one process, as melting, degassing, gas/liquid phase injection, dispersion and homogenization, as well as reactions such as crosslinking can take place. Once the process is set up, it is running continuously without further need of adjustments or interruptions. Since the 1970s, foam extrusion is adopted in industry for the continuous production of polymeric foams in large amounts [57].

In 2017, more than 1300 publications about foam extrusion are listed since 1967. Nowadays, the foam extrusion process is the state of the art process for polymeric foam profiles, pipes, foils and sheets. It is adapted for a broad diversity of polymers such as PE, PS, PET and PVC. Foam extrusion of PP is relatively new as limited research on the production of PP foams was conducted in former times. One of the first patents dealing with PP foam extrusion has been claimed by DOW in the early

1970's [58]. For their experiments, a tandem single screw extrusion line was operated, where the A-Extruder screw was built up of a feed, melt and meter section ($L/D = 24$, diameter 63.5 mm) and the B-Extruder screw was comprised of a feed section and a mixing section of the torpedo type. It is described how different "activating liquids" such as FCKW, pentane or hexane, are dissolved in linear isotactic PP as physical blowing agents. The extruded foam sheets exhibited a closed, polyhedral cell morphology with a median cell diameter of 500 μm and an intermediate density of 300 kg/m^3 . However, the known low melt strength and elasticity, as well as low strain hardening are common issues of neat PP that prevent proper foaming and morphologies. The high crystallinity additionally effects the foaming negatively, as the processing window is small compared to amorphous polymers [59–62]. The development of high melt strength PP types (HMS PP) in the early 1990's [57] and its commercialization, firstly by Montell Company [59], lead to better performance in foaming processes due to long chain branching which improved the rheological properties of PP. This invention and further research regarding nucleating agents, branching and modification of strain hardening and crystallization behavior finally enabled the broad commercial use of PP [59–61, 63]. In literature, common nucleating agents are micro-sized talc [61, 64], nanoclay, e.g. organically modified montmorillonite clay [65–67] and fumed silica [68]. The addition with nucleating agent leads to the formation of smaller cells and improve the homogeneity of the cell structure. As these additives are solid, the crystallization behavior, melt viscosity, strain hardening and consequently expansion behavior is also influenced. The strain hardening and crystallization behavior can be further influenced by either blending linear PP with different molecular weights (broad molecular weight distribution), blending linear with branched or cross-linked PP, as well as by different CO_2 concentrations [69]. A study of Spitael et al. [25] reveals synergistic effects by blending linear and branched PP. For their study, a twin-screw extruder ($L/D = 25$, diameter 16 mm) was operated. It was obtained, that an increased cell concentration of $54.5 \times 10^6 \text{ cells}/\text{cm}^3$ (average cell size 37 μm , 130 kg/m^3) within their 25 wt% branched PP blend system can be reached, compared to the linear PP with $21.2 \times 10^6 \text{ cells}/\text{cm}^3$ (average cell size 63 μm , 120 kg/m^3) and the best performing branched PP with $11.5 \times 10^6 \text{ cells}/\text{cm}^3$ (average cell size 57 μm , 280 kg/m^3). This effect is resulting from an increased amount of cell nuclei in the linear PP combined with the strain hardening increased by the branched PP content. Branched PP can be obtained by reactions of linear PP with peroxides, such as (2,5-dimethyl-2,5-bis-t-butylperoxy) hexane, acting as chain scissors and multifunctional agents, such as trimethylolpropane triacrylate [60], that introduce multiple reactive sites at the split linear PP backbone that recombine randomly and thus form branches. Nam et al. [60] investigated the effect of long chain branches in PP on the density of extruded foam. A linear PP type was modified prior to reactive extrusion step with two different amounts of peroxide and multifunctional monomer in order to compare these three PP types in foam extrusion. For the experiments, a twin-screw extruder setup ($L/D = 18$, diameter 25 mm) with attached static mixer was operated (more about static mixer see below). The extruder setup in this experimental setup makes the use of a static

mixer advantageous due to the use of two chemical blowing agents (CBA) that have to be dispersed properly. Next to the branching, the amount of CBA, die temperature, screw speed and die L/D ratio was varied. An evaluation according to Taguchi's experimental design showed, that the long-chain branching of PP shows the most influence on foam density. Among the PP types investigated, the PP type with the higher branching amount obtained the lowest foam density and most homogeneous morphology. In case of best conditions, the highest branched PP reached 250 kg/m^3 , in contrast the linear PP around 540 kg/m^3 .

Nowadays, there are two common setup variations for foam extrusion established in industry. Depending on the target throughput and polymer recipe, either a single-extruder or a tandem line system with two extruders linked together is run [70].

A single extruder offers a compact setup and is mainly used in research and lower throughput fabrications, as an economical throughput is limited to around 300 kg/h . Here, the residence time is the limiting factor for proper process control and product quality. It is linked directly with the extruder dimensions. This is why additional pre-compounding steps are often used and/or static mixer devices are applied. The static mixer device is a tempered downstream unit attached between extruder and die. It is, in contrast to an extruder, built up with specially arranged static elements that can be screw-like, lamellar or grids. The element design and its arrangement thereby causes a turbulence flow, where the melt flow is divided and recombined several times, whereas radial mixing occurs. This further step leads to a better homogenization and longer residual time, resulting in a better foaming performance as less inhomogeneities occur. In other words, a static mixer enhances and elongates the mixing time and thus contributes to a proper homogenization in a small size setup [60, 71]. However, due to the melt flow behavior in the static mixer, the throughput is again limited. For higher throughputs, the single-extruder design requires dimensions, where costs and space demands overcome the benefits of this setup compared to a tandem extrusion line. Lee et al. [68] investigated different screw configurations of a twin-screw compounding extruder (L/D 40, diameter 30.5 mm) where nanosilica was compounded with a throughput rate fixed to 2.5 kg/h and a barrel temperature of max. $220 \text{ }^\circ\text{C}$ into linear isotactic PP prior to foam extrusion. It is concluded that the dispersion of nanosilica in the PP matrix is best at high shear stress and long residence time, generated by narrow staggered kneading discs and reverse pumping elements. Furthermore, the influence of screw speed on dispersion quality revealed that increased screw speed resulted in a more uniform aggregate size. The optimized dispersion of the nanosilica allowed to enhance its nucleation ability and consequently improved the overall foam structure in the follow up foam extrusion experiments where a single screw extruder with attached static mixer and filament die was operated. Cell size and density was improved from magnitude $500 \text{ }\mu\text{m}$ and $1 \times 10^5 \text{ cells/cm}^3$ to $100 \text{ }\mu\text{m}$ and $1 \times 10^7 \text{ cells/cm}^3$ at optimized parameters when nanoclay was added.

Tandem extrusion lines are applied at a progressive rate in industry, as they separate the extrusion process in two steps and thus facilitate the ability of process control. The typical setup of a tandem extrusion line with two extruders in an in-line

arrangement consists of a co-rotating twin-screw melting A-Extruder and a single screw cooling B-extruder. However, a combination of two single screw extruders is also possible, as the screw configuration can be adapted for specific requirements. The screw can be designed with different elements, such as conveying, reverse, kneading, degassing or blocking elements, each can be built up with different diameters (staging, flight depth and length) and thus influence the apparent shearing, residence time and dispersion performance. However, co-rotating twin-screw extruders own the best performance with regards to the dispersion performance and are the first choice for compounding. Hence, the A-Extruder is responsible for conveying, melting and dispersion. A schematic built up of a tandem extrusion line with a co-rotating twin-screw A-Extruder and single-screw B-Extruder is shown in Fig. 10.8.

At the beginning of the process, the granules and possible additives are fed into the A-Extruder (Fig. 10.8). The rotating screws are transporting the material into the heated barrel, where appearing shear forces generate additional heat. This leads to a plastification of the polymer. The temperatures of the different extruder zones are dependent on the PP type as linear PP types can be processed at lower temperatures compared to branched or cross-linked types. In literature, target temperatures between 130 and 193 °C can be found for the feeding zone. [60, 71–73] The twin-screw setup enables proper conveying and plasticizing combined with homogenization of polymer, additives and blowing-agent [25]. The screw configuration itself allows to control the pressure profile, melt flow and shearing of the material along the barrel [68]. As the material is reaching the plastification zone,

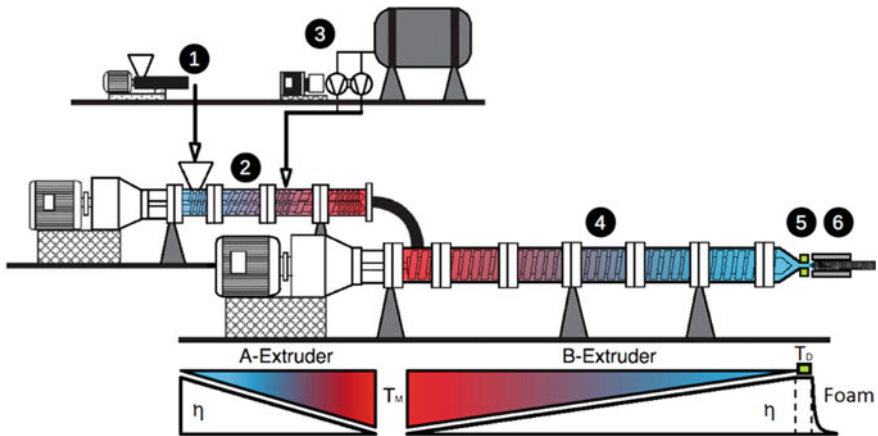


Fig. 10.8 Schematic illustration of a tandem extrusion line with dosing unit for granules and solid additives (e.g. nucleating agents, chemical blowing agents) (1), gaseous or liquid additives (physical blowing agents) (3), a twin-screw A-Extruder (2) linked to a single screw B-Extruder (4), die (5) and downstream unit (6). Additionally, the profiles for melt temperature T_M and melt viscosity η are shown. Copyright (2018) University of Bayreuth, Department of Polymer Engineering

barrel temperatures between 190 and 221 °C are aimed [60, 65, 71]. When the melt is plasticized and a certain pressure is built up in the barrel, the injection of physical blowing agents, such as super critical CO₂ or pentane, is possible. Chemical blowing agents are about to decompose due to the shearing and high temperature along the barrel. A complete decomposition at this point is important to achieve a homogeneous dispersion in the following metering zone. There, at temperatures between 170 and 230 °C [60, 65, 71], the blowing agent is solved and dispersed in the melt for a uniform, single-phase system [57, 70]. A study of Hasan et al. [74] revealed, that the solubility of CO₂ is depending on the PP type. It was found, that linear PP is able to store more CO₂ compared to branched PP, as branches lead to lower free volume and entanglements hinder swelling. Such effects have to be considered as an overload with blowing agents lead to process instabilities due to decomposition of the single phase system resulting in worse product qualities. The high temperature and dissolved blowing agent lead to a significant lowering of the melt viscosity in the metering zone of the extruder (see melt viscosity profile illustrated in Fig. 10.8). Special blocking elements mounted in the extruder screws hinder a reflux of the gas loaded melt to the hopper. While at single-extruder lines the melt now reaches the die or a further downstream unit, the melt is conveyed into the B-Extruder at a tandem extrusion line. In case of a reactive foam extrusion, the extra residual time there enables further reaction and homogenization. Furthermore, an additional regulation of the melt temperature (T_M) enables additional tuning possibilities to the final foam morphology. The cooling of the gas-loaded melt increases the pressure along the barrel as well as the viscosity (see melt viscosity profile illustrated in Fig. 10.8). Additionally, the solubility of the gas is increased while the diffusivity is lowered [70, 73, 74]. Both effects are desired for proper cell growth and stabilization. Depending on the PP system, barrel temperatures between 140 and 190 °C are operated in literature [58, 61, 73]. Another factor influencing the expansion behavior is the crystallization kinetics. Its influence related to T_M was revealed in a study of Tabatabaei et al. [73], where the crystallization behavior of extruded PP with different CO₂ concentrations, processing temperatures and flow rates was investigated. It is shown, that an increased CO₂ content decreases the strain-induced crystallization kinetics and the crystallization temperature is lowered. As a reason, the plasticizing effect of CO₂ is stated. A study of Nofar et al. [69] is resulting in a similar outcome when nanoclay is involved. However, the addition of nanoclay allowed improving the expansion ratio and cell density significantly.

The residence time of the melt in each extruder is depending on the barrel dimensions of the extruder, the screw speed, its screw configuration and the resulting L/D ratio of the screw. L describes the flight length and D the outside diameter. A bigger ratio indicates a longer flight length whereas more shear, homogenization and residence time can be generated. Typical technical scale extruders in research operate with 18D [60, 61, 71, 72]. However, in industry much higher ratios are operated.

The pressure drop after the die finally leads to the expansion of the melt. In general, a high pressure drop is desired. Studies revealed, that the expansion behavior is depending significantly on T_M [69, 73] as well as the die temperature (T_D). T_M is

governing the cell formation in a significant manner, as it provides more impact to the initial foaming temperature compared to T_D . Even at low throughput rates, the residual time of the melt at the die is far lower compared to the residual time in the barrel. Thus, T_M and T_D have to be adjusted separately. While T_M is primarily chosen in dependence of the processing window given by the nature of the respective polymer composition, T_D offers a broad possibility for adjustments as the expansion behavior is linked with the composition, e.g. additives and amount of blowing agent. However, the semi-crystalline nature of PP is resulting in a narrow processing window. Burt states a processing window around 4 °C for proper PP extrusion foams [62]. Figure 10.9 illustrates the effect of T_D on the foam expansion, properly adjusted T_M presupposed.

In case of T_D below the optimum, the crystallization onset is faster than the expansion of the melt. The pressure of the entrapped gas is insufficient to overcome the increased melt strength due to crystallization, causing a freeze of the melt before proper expansion. This can be observed by a small initial expansion rate, defined by the melt opening angle α , and a final diameter d of the extruded foam close to the die dimensions. The foam morphology thereby is irregular with small cells. At T_D above the optimum α is significantly increased due to the lower melt strength. However, the low viscosity also enables a fast diffusion of the blowing agent out of the extrudate, leading to a smaller expansion ratio d at the end. Additionally, the cell size is inhomogeneous with increased cell sizes, as coalescence occurs. The optimum T_D , is found when both effects are balanced and a d_{max} is reached combined with a proper cell morphology [61, 64, 65].

A study of Kaewmesri et al. [64] describes this effect in dependency of different amounts of talc and CO₂. It is shown that especially at high CO₂ concentrations, where the plasticizing effect is stronger, the expansion ratio is significantly depending on die temperature. One sample, with fixed talc content, exhibited with 5% CO₂ an expansion range of 2 fold in worst case, and 14 fold at T_D optimum. Talc mainly supported the cell nucleation thereby and its optimum was found to be depending on CO₂ concentration. Cell densities between 1×10^2 (without talc and low CO₂ content) and 1×10^8 cells/cm³ (with talc and high CO₂ content) and cell sizes between 400 μm and below 10 μm were obtained depending on talc and CO₂ content. As expected, talc lowered the cell size and increased the cell density.

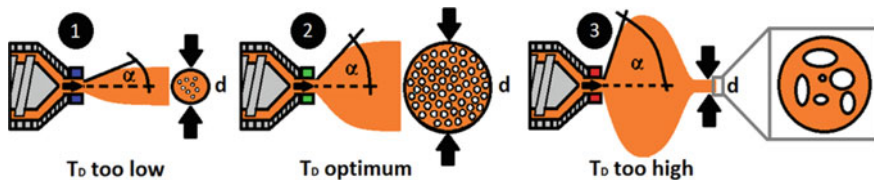


Fig. 10.9 Schematic illustration of the influence of the die temperature (T_D) on expansion after die, characterized by the opening angle α , and the final diameter d at low (1), optimum (2) and high (3) T_D . T_M is supposed to be adjusted properly. Copyright (2018) University of Bayreuth, Department of Polymer Engineering

At increased amounts of talc, above 1.6 wt% respectively, the influence of T_D on cell size was notably lowered due to the increased melt strength at high temperatures.

The die is primary adapted to the final shape requirements, as it shapes the extruded foam in a significant manner. Common dies are rod and slit dies, as well as certain types of profiles. Profile dies are adapted to more complex geometries compared to slit dies. Nonetheless, a proper die design in detail is of importance, as it is known to have impact on pressure drop and cell nucleation density [25, 70]. An example is the continuous production of microcellular and low density PP foams, that can be produced better with filament dies as the pressure drop is higher compared to rod dies [70, 75].

It is further possible to attach additional downstream units after the die in order to provide further shaping or modifications. One example for downstream units are calibrators. They allow forming the extrudate in a defined plate-like shape. Such calibrated PP foam sheets can be used for damping, thermal and sound insulation. Common applications are transport containers and packaging systems, as well as encasements such as insulation components and linings. The light-weight closed cell structure, high stiffness, water and chemical resistance as well as the broad ability of additives (UV stabilization, colors etc.) make PP foams suitable for many applications. Another use for PP foam sheets can be seen as core materials in laminate sandwich structures. An example are light weight PP foam cores with densities in the range of 100 kg/m^3 for wind turbine rotor blades.

Layered sandwich-like products can also be produced in one step by so called coextrusion, where multiple extruder lines with different colors or polymers are coupled and extruded simultaneously together. The foamed sheet can be covered by compact material in order to obtain sandwich structures of enhanced mechanical properties. This coextrusion is used for foamed PP foils and sheets as they can be found in the automotive, building and food packaging industry. Advantageous of coextrusion is the time and cost-saving processing, as further lamination steps are not necessary.

10.2.3 Bead Foaming

Bead foams, also known as particle foams, are a special type of polymer foams. They are molded foam products obtained from a two-step fabrication, where in the first steps small foamed beads are made that are later in a second step usually fused with hot steam in a shape giving cavity to the final part in a sintering-like process (see Fig. 10.10) [6]. In contrast to foam extrusion and foam injection molding bead foam products can be light weight and simultaneously have a complex geometry [57, 76].

In general, based on the polymer and processing method there are two different types of bead foams: expandable and expanded beads. Expandable beads are gas loaded and are foamed in a separated step, whereby expanded beads are already foamed. Only amorphous polymers, like polystyrene, are suitable for expandable

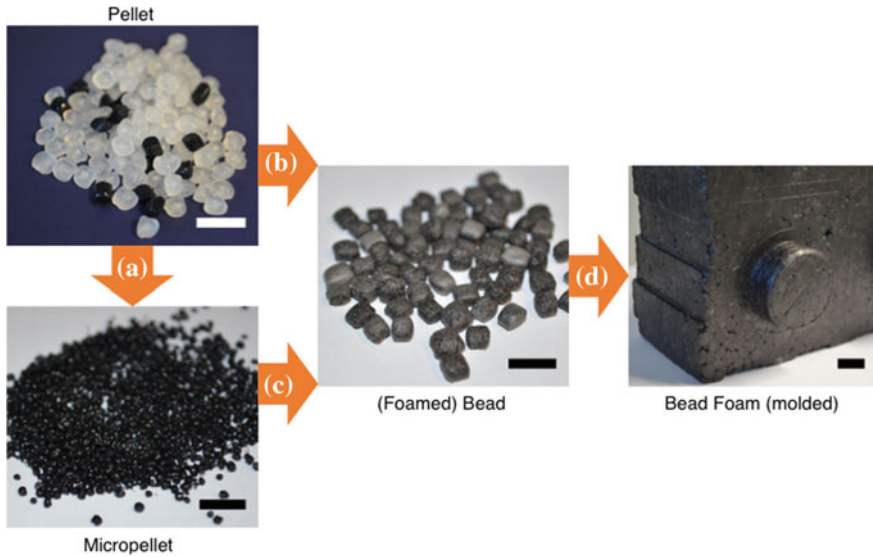


Fig. 10.10 Process chain of bead foams. Scale bar = 1 cm. Pellets with color masterbatch **a** production of micropellets, **b** continuous, **c** batch foaming and **d** molded bead foam. Copyright (2018) University of Bayreuth, Department of Polymer Engineering

beads, since they can store a blowing agent in the solid state over a long period (>6 month) [6]. One big advantage of the expandable beads is the reduced transportation costs in comparison to already expanded beads, caused by the lower volume of the beads. But expandable beads have to be prefoamed in a secondary step at the manufacturing company. However, bead foams from polypropylene cannot be derived as expandable bead foams, as PP is semi-crystalline and thereby has an unfavorable gas sorption behavior.

The most used bead foams on the market are Expandable and Expanded PolyStyrene (EPS), Expanded PolyEthylene (EPE) and PolyPropylene (EPP), which will be described more in detail in the following paragraphs.

The foamed beads for EPP can be produced either in an autoclave (see Sect. 10.2.3.1) or—less common—during a continuous extrusion process with an attached underwater pelletizing system (see Sect. 10.2.3.2) [6, 57, 76, 77]. EPP was developed in the 1980s by the Japanese company JSP with the trade mark ARPRO [59]. Other large-scale producers of EPP bead foams are the German company BASF SE with Neopolen P and the Belgian company Kaneka with the EPP product named EPERAN PP.

EPP bead foams are soft elastic thermoplastic beads with a mainly closed cell foam structure and can be produced in a density range between 15 and 250 kg/m³ [77–79]. EPP parts are commonly used in the area of transportation and in the automotive sector [7]. Typical applications are thermo-insulating boxes for hot food delivery, packaging for higher-value products, e.g. electronics and automotive parts

(sun shields, bumper cores etc.). This is mainly due to the very good mechanical properties, as high specific energy absorption, low energy consumption and multiple compression set without significant property loss compared to the cheaper expanded polystyrene [14].

10.2.3.1 Autoclave Bead Foams

Currently, the EPP production in Europe is around 30.000 tons. Worldwide it is even higher with annual growth rates of over 5% [80]. Almost the whole EPP on the market is produced with the discontinuous autoclave method even though a continuous production is possible (see Sect. 10.2.3.2).

The autoclave method is based on the pressure induced foaming, which is described generally in Sect. 10.2.1. In the autoclave water is used as heat transfer media. A sketch of the process is shown in Fig. 10.11. Several publications are dealing with the procedure of the autoclave method to generate expanded polypropylene (EPP) [81–85].

In the steel autoclave, PP is feed as μ -granules with water. Usually, the μ -granules are made out of random-copolymer with a rather low MFI of around 1–8 g/10 min (ASTM D-1238, at 230 °C and 2.16 kg) [82–85]. In industry, carbon black is used typically as nucleating agent. The μ -granules can be made with an underwater granulator with a special breaker plate in a continuous process. For even sorption behavior in the autoclave and a geometrical shape after expansion that benefits a good filling of the mold (less voids in the final part) the μ -granules should be small and ideally spherical (diameter \sim 1 mm).

The autoclave has a stirrer and is heated to the desired saturation temperature (T_{sat}), which is close to the melting point of the polypropylene ($T_{\text{m},0}$). To avoid sticking of the μ -granules during the heating, special additives—such as tensides are added. CO_2 is added, leading to a consequently high saturation pressure (p_{sat}). The water as well as the PP is taking up the CO_2 during an isothermal saturation time (t_{sat}). Then, the valve at the bottom of the autoclave is opened inducing a pressure drop. The gas-loaded μ -granules immediately leave the stirring autoclave through the modular die in the direction of the lower expansion tank. Due to the pressure drop foaming is initiated. While laboratory pressure vessels are in a range of 1–15 L industrial scale autoclaves have a volume of approximately 300 up to 1000 L.

The distinctive feature of the autoclave method is the formation of a double melting peak, which is important for the later welding in steam chest molding process (SCM) as described in Sect. 10.2.3.5. As stated by Harrison, it is possible for most of the semi-crystalline polymers to create multiple melting peaks [86]. Reasons for a new peak can be either different crystal sizes [87], different crystal structures [42, 88, 89] or rearrangement (so-called perfection) during the heating or isothermal phases, respectively [90]. This double melting peak, as described for PP by Hingmann et al. [91] is in the case of autoclave-EPP a result of the isothermal saturation time under CO_2 atmosphere as stated by Nofar et al. [82]. Interestingly,

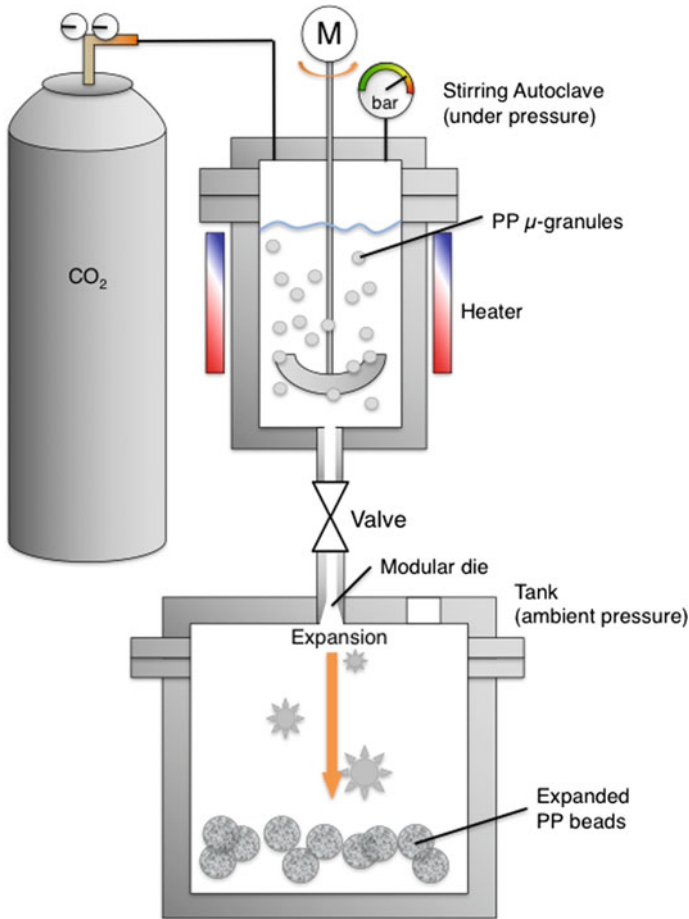


Fig. 10.11 Sketch of the autoclave method to produce EPP. Copyright (2018) University of Bayreuth, Department of Polymer Engineering

it was found that WAXS patterns of PP before and after autoclave treatment are nearly the same, indicating no new crystal phase is formed. However, PP with double melting peaks shows narrower peaks (WAXS) as result of the more ordered crystal phase. Still, the unfoamed and foamed PP only show the alpha phase [82, 83]. As summarized by the schematic first heating curves for unfoamed and foamed PP, as shown in Fig. 10.12, both melting peaks develop in different stages of the autoclave process.

It is assumed, that during the isothermal saturation phase at T_{sat} the less close-packed crystals melt (i.e. below T_{sat}). The more close-packed crystals (i.e. above T_{sat}) do not melt and can form more ordered structures [92] which is attributed to CO_2 induced crystallization [83]. However, this so-called perfection of the crystals [82, 90, 93] leads to a higher melting point $T_{\text{m,high}}$. When foaming

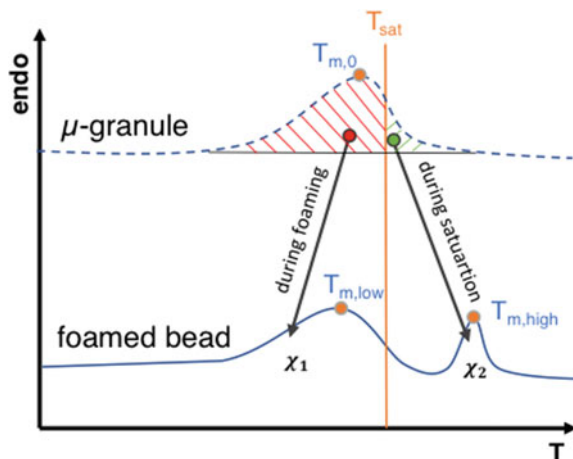


Fig. 10.12 Schematic DSC curve of the polypropylene before and after the autoclave treatment (1st heating). Copyright (2018) University of Bayreuth, Department of Polymer Engineering

(i.e. opening of the bottom valve of the autoclave), the isothermal saturation phase terminates. Due to the induced pressure drop also the temperature decreases (i.e. rapid cooling) and the formerly molten crystal reform, leading to the lower melting peak $T_{m,low}$ (equals to the original melting peak $T_{m,0}$).

The expanded beads have to be collected from the expansion tank and can be further processed. A detailed description of the necessary welding process can be found in Sect. 10.2.3.4. In Fig. 10.13 SEM images of a single bead and a molded part are shown.

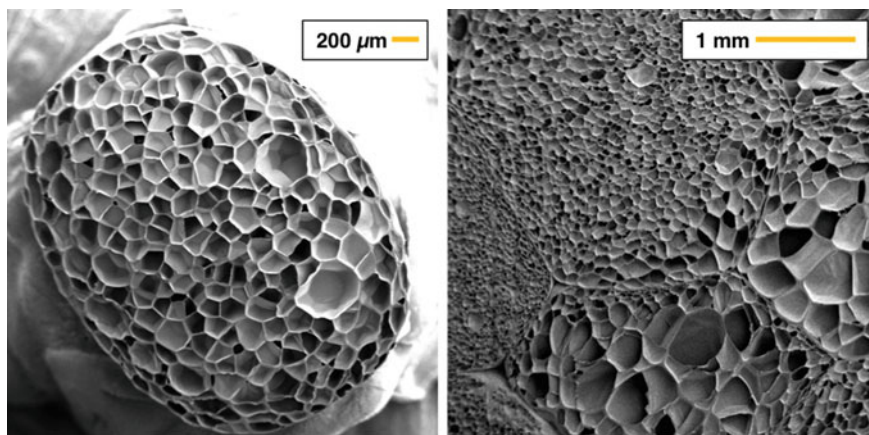


Fig. 10.13 SEM images of single bead (left) and fused part (right). Copyright (2018) Neue Materialien Bayreuth GmbH

Nofar et al. mimic the processes happening in the autoclave by carrying out experiments on a High-Pressure DSC with different polymers such as PP [82] and PLA [94]. So, it is possible to determine the influence of saturation time, -pressure and -temperature on the thermal behavior of the polymer (e.g. peak separation, ratio of peak areas etc.).

The most crucial process parameters of the autoclave method are the saturation time, -pressure and -temperature as they can vary the expansion behavior and the morphology. Furthermore, these parameters affect the thermal behavior.

Influence of saturation temperature

In the study of Guo et al. [83] the saturation temperature was varied from 144 to 150 °C at constant saturation pressure of 50 bar. It was found, that largest cells and expansion can be achieved at highest saturation temperature. However, the melting behavior limits the saturation temperature.

For the thermal properties Nofar et al. [82] showed that especially in terms of the double melting peak creation the temperature is the most sensitive parameter. The higher melting peak $T_{m,high}$ is significantly above the saturation temperature T_{sat} which was set close to the original melting temperature $T_{m,0}$. Depending on T_{sat} a higher or lower portion of unmelted crystals can be perfected leading to a different thermal behavior (i.e. different peak ratios). Furthermore, it has to be noted, that the mobility of the unmelted crystals is enhanced and dissipation energy for rearrangement is lowered with increasing saturation temperature, which is favorable in terms of retraction of the chains to form crystals with an increased degree of perfection.

Influence of saturation time

It can be expected that with a longer saturation time more gas can be solved in the μ -granules, which is beneficial for the expansion (i.e. lower density).

As it can be seen from the study of Nofar et al. [82] a saturation time below 20 min is not sufficient to form the double melting peak. A longer annealing time (i.e. t_{sat}) results in a longer diffusion time for the unmelted crystal molecular rearrangement leading to an increased amount of perfected crystals. Consequently, the amount of the lower melting crystals is decreased. The total crystallization is also enhanced with longer saturation times. So, with increasing saturation time the amount of perfected crystals is increased leading to a higher crystallinity of the second melting peak as the crystals have more time to arrange in a more ordered structure and grow.

Influence of saturation pressure

A higher saturation pressure p_{sat} will lead to a higher amount of gas dissolved in the polymer [74, 95]. Guo et al. [83] varied the saturation pressure from 30 to 50 bar while keeping the saturation temperature constant (at 146 °C). Here it was found, that an increasing p_{sat} leads to a decreased cell size and cell density. Also the cell wall thickness was reduced. The authors also mention that CO₂ molecules can act as a nucleating point.

With increasing saturation pressure (CO_2) the plasticization effect is more pronounced resulting in a decreased saturation temperature required for the generation of $T_{m,\text{high}}$ (i.e. crystal perfection). As a consequence the amount of perfected crystals decreases with increasing p_{sat} as less of the unmelted crystals will remain for perfection [82]. Thus, more low melting crystals ($T_{m,\text{low}}$) are formed. However, it was shown, that the plasticization effect could be compensated with a decreased saturation temperature.

Moreover, the design of the die (outlet) influences the foaming behavior as it affects the pressure drop (rate). Therefore, so-called modular dies are used varying in length and diameter resulting in different expansions of the beads.

Furthermore, the addition of organic solvents in the autoclave acts as a plasticizer. Consequently, the melting temperature can be reduced drastically. The foaming can be carried out at much lower temperatures. However, this hinders the formation of the double melting peak. Though, to create the double melting peak, the addition of an immiscible blend partner is required. This could be polyethylene. Lan et al. [84] showed this in their work. They foamed PP at low temperatures of 92–96 °C with 10 bar of n-pentane achieving beads with expansion rates of 10-50 but with a single melting peak. As comparison, with CO_2 as blowing agent (30 bar) foaming was carried out at 150–153 °C resulting in foams with an expansion ratio of 8:20. By adding polyethylene, they could achieve bead foams blown with pentane with two melting peaks as PP and PE forms an immiscible blend.

10.2.3.2 Continuous Produced Bead Foams

The production of expanded polypropylene and other olefin polymers in a continuous extrusion process was developed by BASF SE and patented in the early 1970s [96]. In the literature this process is described as the “BASF Method” [77]. The extrusion process with attached underwater pelletizing can be sub-divided into two parts as it can be seen in Fig. 10.14. The first part is similar to the foam extrusion, which was described earlier in detail (see Sect. 10.2.2). The under-water pelletizing system is replacing the die in this case.

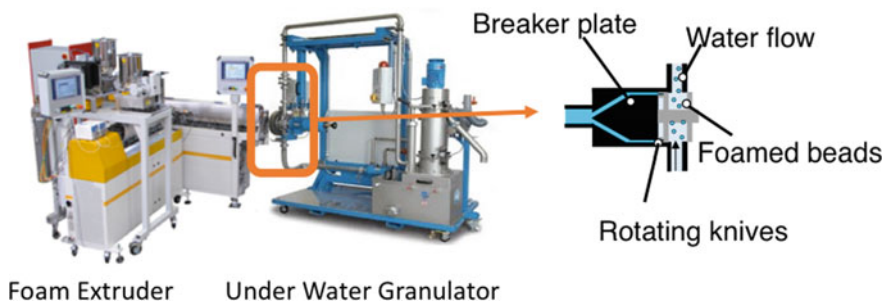


Fig. 10.14 Tandem extrusion line with attached underwater granulator (left) and schematic drawing of the underwater granulator (right). (modified from [6]). *Copyright (2018) Elsevier*

For the production of EPP a high melt strength PP has to be used, which is in general a long chain branched grade [14]. After plasticizing of the polymer, the blowing agent is injected and a homogeneous one-phase system is created. Commonly, super-critical carbon-dioxide is used, but other physical blowing agents such as nitrogen or butane as well as chemical foaming agents like sodium bicarbonate are suitable [14, 59, 77].

In contrast to the foam extrusion process, the gas loaded one-phase system is extruded through a breaker plate, attached at the end of the extruder, into a water flow. The one phase system expands due to the high-pressure drop after the breaker plate. Then, the expanded polymer strand is cut with a rotating knife with several blades into small beads. Since the foaming and cutting of the beads takes place at the same time, the foamed beads have rounded edges (ideally spherical). Water cools and transports the beads to a collection point where they are pre-dried and ejected from the machine.

By changing the parameters of the extruder, like temperature and blowing agent concentration, as well as the underwater pelletizing system parameters, different bead characteristics, like density and shape, can be adjusted. The parameters of the underwater pelletizing system are die diameter and amount of dies as well as water pressure, water temperature and knife speed. Köppl et al. [97] investigated the influence of these parameters on the foam morphology and overall bead shape of expanded PBT, which is a semi-crystalline polymer, too. For example, a higher water pressure of the under-water pelletizer leads to beads with a lower density. At a higher pressure the boiling point of the water is raised and a better cooling of the beads is achieved, which results in a better foam stabilization. An increase in the rotational speed of the knives leads to smaller foamed beads with nearly unchanged bead density.

Compared to the batch foaming process, the continuous processing of PP bead has several advantages. These are most of all the ability of permanent production, but also the possibility of a more precise addition of blowing agent and the adding of additives, like color pigments. However, continuously produced bead foams tend to show a higher open cell content and different foam morphology.

10.2.3.3 Pre-expansion of EPP

As mentioned before, only expanded PP (EPP) beads can be produced. But in an additional optional processing step before molding, it is possible to further reduce the density with the pressure loading method [7, 98, 99]. This processing is specific for PP foams and has two great advantages: First, only few different EPP densities have to be produced, since the customer can set the required density. Secondly, due to the up to five times higher density in comparison to the final part, the shipping is much more (cost-) efficient. The pre-expansion process is shown in Fig. 10.15 schematically. This process is detached of the production and generally conducted at the customer.

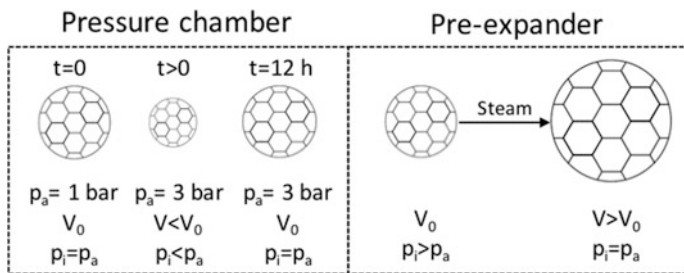


Fig. 10.15 Pre-expansion of EPP with the pressure loading method with the internal bead pressure p_i , the atmospheric pressure p_a and the volume (V) of the beads. *Copyright (2018) University of Bayreuth, Department of Polymer Engineering*

For further expansion and therefore reducing the density, the already foamed beads with an internal bead pressure (p_i) are filled into a pressure chamber. The atmospheric pressure (p_a) is set to about 3 bar of the pressure chamber. Due to the overpressure, the beads are temporary compressed and air diffuses into the foam cells. After several hours (up to 12 h) the beads have returned to their original volume (V_0) and the internal bead pressure and in the set atmospheric pressure are equal. After removing the beads out of the chamber, the internal bead pressure is higher and the beads were expanded in a so-called pre-expander to the targeted density. During the pre-expansion, the beads are heated up with hot steam and the overpressure inside the beads lead to a further expansion [98].

With the optional pre-expansion of EPP a volume increase up to 3.5 times, which gives a resulting density reduction of about 250% [98].

10.2.3.4 Steam-Chest Molding

The expanded beads are finally steam-chest molded, which is a sintering like process, where the single beads were molded to complex shapes. Alternative designations are fusion, welding or molding. The molding process is schematically shown in Fig. 10.16 and can be divided into five steps.

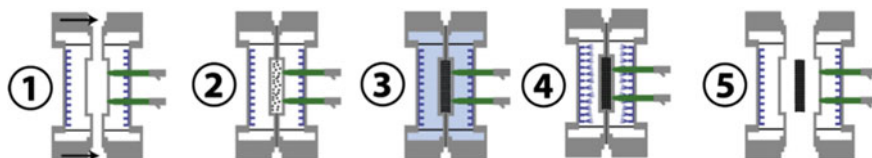


Fig. 10.16 Steam-chest molding process: 1: closing; 2: filling with beads; 3: steaming; 4: cooling; 5: ejection [6]. *Copyright (2018) Elsevier*

1. **Closing:** The mold is first moved by pneumatic pressure whereby the clamp force is applied with a hydraulic or mechanical system.
2. **Filling:** Two different filling methods exist: the pressure filling and the crack filling [6, 99]. In both methods the beads are transported by an applied back pressure [7].

During pressure filling, the beads are compressed with an overpressure of about 3 bar. The compressed beads are then directly injected into the mold. Due to the pressure drop in the mold the beads expand and voids in between them get reduced. During the crack filling, the mold is not completely closed before filling. The EPP beads are filled in and the mold is closed completely afterwards. Consequently, the beads are compressed in one dimension and the contact area between the single beads increases.

3. **Steaming:** The beads are subjected to hot water steam with a steam pressure between 2.5 and 4 bar (steam temperatures between 125 and 145 °C) [7, 14, 99]. The different valve positions and settings during the steaming are shown in Figs. 10.16 and 10.17.

At the beginning of the steam-chest molding process, all valves are opened (A). The steam chambers are flushed with steam. This displaces the air in the steam chambers and heating them up. This is followed by a cross-steaming step (B). The steam valve is first opened on one side and the outlet valve on the other site. The steam flows from one chamber through the mold into the other chamber. The same procedure is then repeated the other way around. Steam pressure and therefore temperature and the duration of deposition determine the degree of welding of the molded part. Subsequently, autoclave steaming takes place. Both steam valves are

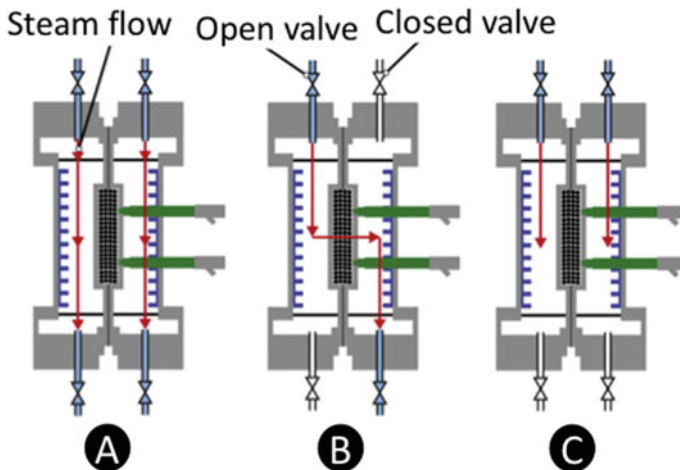


Fig. 10.17 a Purging of the mold, b cross-steaming, c autoclave steaming [6]. Copyright (2018) Elsevier

opened with closed outlet valves (C). Here, the steam pressure and the duration of steaming determine the surface quality of the molded part [6].

4. **Cooling:** The cooling of the molded part is conducted via water spray nozzles behind the mold to prevent a change of shape during ejection. The needed time is depending on the thickness and density of the molded part [99].
5. **Ejecting:** Before demolding, the molded part needs a stabilization time so that the foam pressure drops to an acceptable level (lower than 0.5 bar) [6, 14]. When the mold is opened, the part is pressed out of with mechanically or pneumatically controlled ejectors. In addition, the demolding process can be supported by an air blast from the steam ducts.

After molding the parts have to be stabilized. Therefore, the parts are conditioned for several hours in warm air (about 80 °C). First to remove containing interstitial water and secondly for form stabilization [99]. During molding the steam condensates inside the beads, which leads to local pressure drop [6]. After ejection a local shrinkage could occur. The tempering recovers the original shape.

10.2.3.5 Fusion Process

The fusion process is particularly important for the quality of the molding process and in conclusion for the molded part. The fusion process itself is explained below.

During the molding it has to be ensured that an interfacial contact between the beads is achieved [6, 100–102]. Bead unevenness and bead roughness are smoothed either by an external force or internal pressure of the beads. The importance of a large contact area between the beads has been described and investigated in detail by Anand et al. by the theory of viscoelastic contact [102–106].

The beads are subjected to hot steam, which acts as a heat medium. The hot steam softens or melts the beads surface. Surface wetting and weak physical forces (van der Waals' interactions) occur initially [6, 101]. After further steaming the wetting merges directly into the fusion process, which is generally described as a welding [100, 101] process can be described by the reptation theory by de Gennes [107, 108] to the reptation theory, polymer chains are entangled, which leads to a tube like shape [6, 101, 107]. One polymer chain, enclosed by other chains, can only move by lateral movement [100]. This chain movement is shown in Fig. 10.18.

When observing an individual chain, at the beginning ($t = 0$), the polymer chain is trapped in the original tube-like structure, made of other polymer chains, and can only move by Brownian motion [6, 101]. In the further process, the chain ends, which are now called minor chains, are moving outside the tube (see Fig. 10.18b) and the chain gradually escapes the original tube (see Fig. 10.18c). The time needed to move into a whole new tube is the so called reptation time t_R [6, 101]. The reptation time and the diffusion coefficient of an linear polymer chain depend on its molecular weight (Eqs. 10.12 and 10.13) [101]:

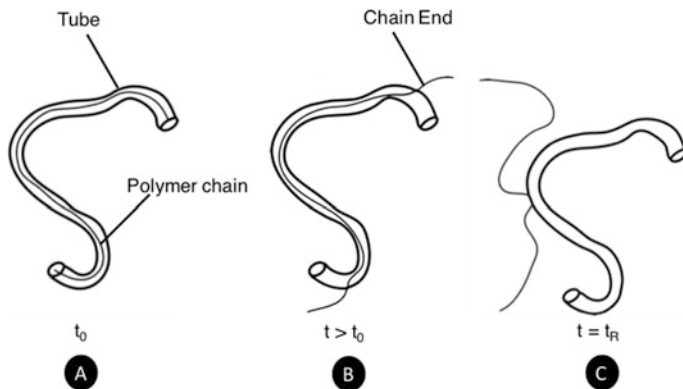


Fig. 10.18 Chain movement from its original tube into a new one [100]. *Copyright (2018) American Chemical Society*

$$t_R \approx M^3 \tag{10.12}$$

$$D \approx M^{-2} \tag{10.13}$$

This theory can be transferred to the steam-chest molding of polymeric beads, which is shown in Fig. 10.19.

Here both bead surfaces are molten by the hot steam and the polymer chains start to move. After inter-diffusion across the bead interface, the polymer chains form new entanglements resulting in a strong physical connection of the beads [109].

During the molding it has to be ensured, that the surface of the beads is molten and inter-diffusion across the bead interface can take place but at the same time the overall foam structure has to be stable during the whole process. Thus, the temperature of the steam is important. Nofar et al. [82] described, that a double crystal melting peak is necessary for good sintering and the geometrical exactness of the final product. As shown in Fig. 2.20, the optimal steam temperature lies between the two crystal peaks obtained in the autoclave process (see Sect. 10.2.3.1).

Fig. 10.19 Reptation movement across bead interfaces. *Copyright (2018) University of Bayreuth, Department of Polymer Engineering*

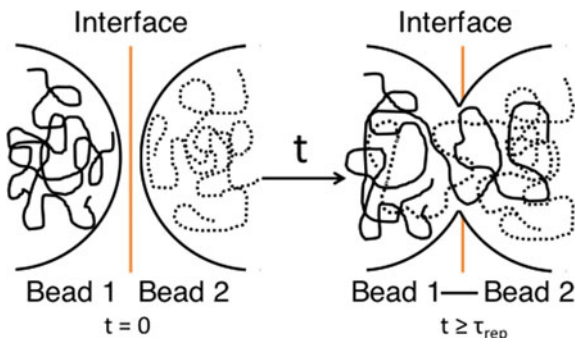
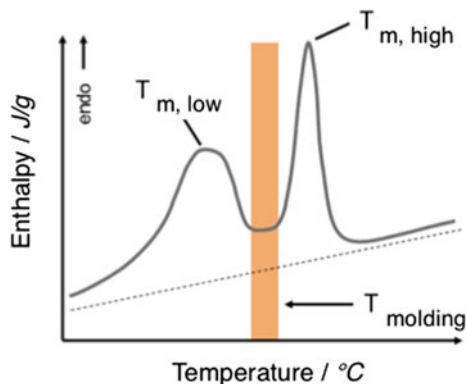


Fig. 10.20 Double crystal melting peak of foamed PP beads measured with DSC. Copyright (2018) University of Bayreuth, Department of Polymer Engineering



The double peak originates either from the bead expansion process, where crystals of varying perfection are built or from a blend of two different polymers. The less perfect crystals represents a melting temperature $T_{m,low}$ and the perfected crystals a melting temperature $T_{m,high}$ [92]. During steam-chest molding at $T_{molding}$, the less perfect crystals are melted and the polymer chains act across the bead interface and fuse the beads together, while the more perfect crystals retain the overall shape [82, 92]. A change of the temperature, either too high or too low, leads to a bad fusion or a deformation of the molded part [6, 82, 110]. Instead of the double melting peak, a wide melting peak has the same effect, which is normally achieved during the continuous EPP extrusion (see Sect. 10.2.3.2).

10.2.4 Foam Injection Molding

Thermoplastic foam injection molding (FIM) is a special injection molding technology, where a porous structure is produced in the center of the part and compact surface on the outside. Due to the formation of this foam core the weight of the part is minimized. To generate the foam a gas is dissolved in the polymer melt in the injection unit of the injection molding machine. As long as the plasticized material in the cylinder is under high pressure (up to 200 bar), the gas stays in solution. As soon as it is injected in the mold an abrupt pressure drop appears, the gas diffuses from the solution and foams the material. This physical effect can be compared with opening a bottle of mineral water.

The formation of the foam morphology is essentially defined by the thermal conditions in the mold. The melt that enters first in the cavity solidifies immediately at the mold wall, which has a considerably lower temperature. Because of the expeditious solidification of the melt, no foam is developed in the skin layer. This compact skin layer isolates the following hot melt stream thermally from the colder mold wall, so the material in the core of the component is longer capable to flow and a foam can be developed. In this so-called low-pressure foam injection molding

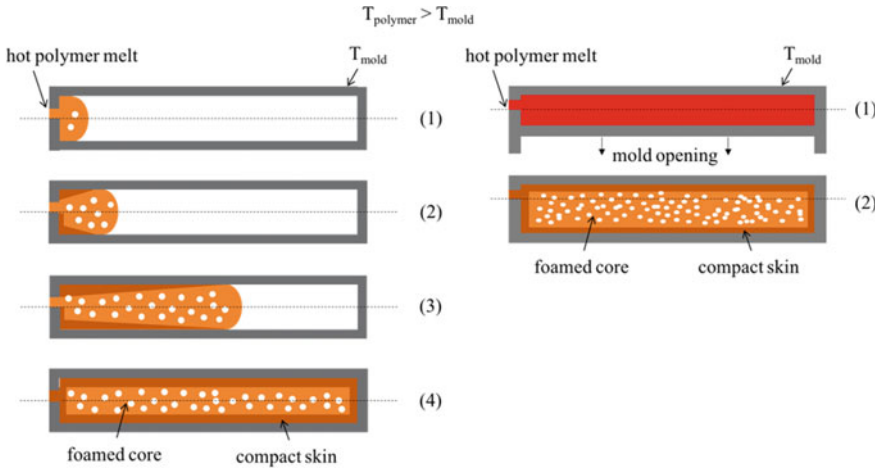


Fig. 10.21 Mold filling and formation of the classical FIM foam morphology. Left: low pressure foam injection molding; right: high-pressure foam injection molding. *Copyright (2018) Neue Materialien Bayreuth GmbH*

processes the cavity is only filled with 80 vol. % gas-loaded polymer melt. Due to the expansion while foaming the polymer melt the cavity is filled totally (see Fig. 2.21 left side). Another possibility is the high-pressure foam injection molding process where the cavity is filled completely under high pressure. Following the mold is opened precise to the desired thickness and the melt foams due to the enlargement of the volume and the resulting pressure drop (see Fig. 2.21 right side). For this precise opening, a so-called breathing mold is necessary.

The resulting morphology, containing compact skin layers and a foamed core, is described as an integral structure and can be seen in Fig. 2.22, where the density is high in the skin layers whereas it is low in the foamed core.

Density reductions from 5 to 50% compared to the compact material can be achieved via foam injection molding. The attainable density is highly influenced by the cavity geometry and thickness, processing conditions and material properties. Figure 10.23 shows the density of foam injection molded parts in comparison to

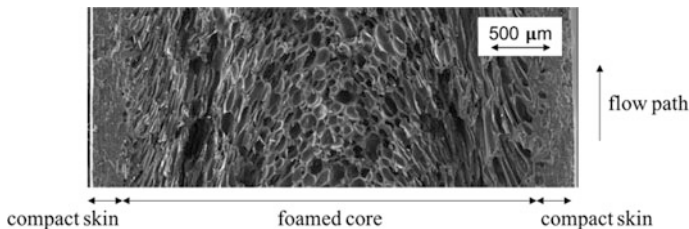


Fig. 10.22 Typical integral structure of foam injection molded parts. *Copyright (2018) Neue Materialien Bayreuth GmbH*

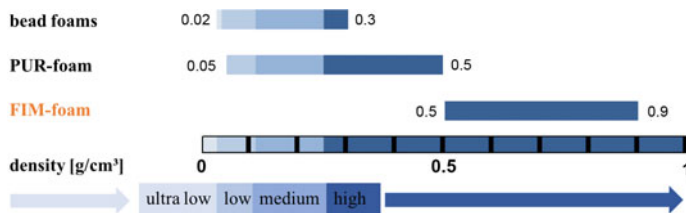


Fig. 10.23 Density of foam injection molded parts in comparison to other established foams. *Copyright (2018) Neue Materialien Bayreuth GmbH*

other established foams. In general bead foams and PUR-foams show a lower density than foam injection molded parts, which are mostly used to reduce the weight of structural elements [111]. Typical examples for foam injection molded parts are instrument boards and gear boxes in the automotive sector.

10.2.4.1 Chemical Foam Injection Molding

The gas can be disposed into the polymer in two main different kinds: physical blowing agents and chemical blowing agents. Latter are solid agents (e.g. sodium bicarbonate) that are mixed with the granules in the hopper, activated by the high temperature while plasticizing the polymer they deliver the gas that is to be solved in the melt (see Sect. 10.1.4). These additives are organic or inorganic substances that decompose above a specific temperature and release a gaseous component. While the blowing agent is heated together with the matrix material in the cylinder of the injection molding machine the activation energy is delivered. The chemical blowing agents are decomposed and the released gases are solved in the matrix material because of the high pressure. The shear forces by the injection molding screw homogenize the mixture. The process of chemical foam injection molding is mostly influenced by the temperature conditions. To achieve the maximum gas yield it is necessary to control the residence time and the pressure. Hence, the chemical blowing agent and the process properties have to be adjusted. The decomposition temperature of the chemical blowing agent should be 10 °C below the melt temperature of the plastic matrix to avoid an incomplete decomposition. Contrariwise a too high processing temperature leads to a decomposition of the blowing agent in the feed section of the screw, which leads to gas losses and process instabilities.

The dosing of chemical blowing agents is uncomplicated and there is no special machinery necessary. Only a closing nozzle or a mold with a hot runner system and closing system is needed to avoid premature foaming of the polymer melt in the cylinder of injection unit.

After the injection of the gas-loaded polymer melt into the mold, due to the pressure drop the gas dissolves from the polymer matrix. For the resulting foam morphology, the nucleation is crucial (see Sect. 10.1.2.2). It can be additionally

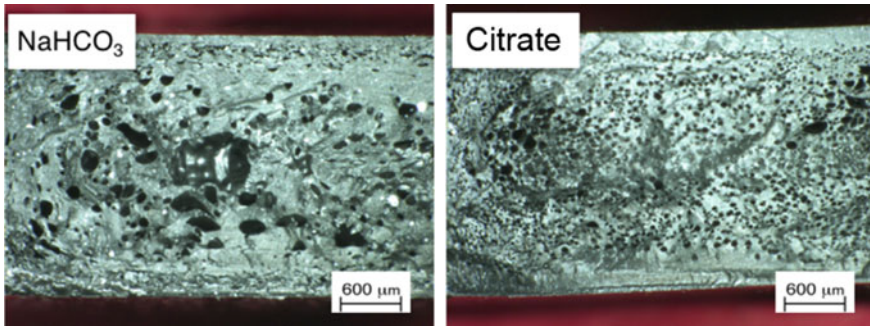


Fig. 10.24 Foamed polypropylene with different chemical blowing agents (density reduction: NaHCO_3 : 25%; citrate: 22%). Copyright (2018) Carl Hanser Verlag GmbH & Co. KG

forced by adding nucleation agents like talcum. After nucleation, the gas cells start to grow until the polymer matrix is solidified. Figure 10.24 shows exemplary foamed polypropylene with different chemical blowing agents (both 1.5% masterbatch).

The highest achieved density reduction with NaHCO_3 was 25% while with citrate only 22% density reduction was reached, due to a lower gas disposal of citrate. Besides the higher achievable density reduction, the higher gas disposal of NaHCO_3 leads to a less uniform foam morphology. For chemical foam injection molding with citrate a defined integral structure was build, which also leads to higher mechanical stability because of thicker compact skin layers.

10.2.4.2 Physical Foam Injection Molding

Physical blowing agents can be processed in different ways: the granules can be charged with physical blowing agent under high pressure before entering the injection unit with a digester or directly in the hopper of the injection unit (ProFoam by Arburg). Another possibility is to inject the physical blowing agent in supercritical state directly into the plasticized melt in the cylinder. For this type of physical foam injection molding, two available technologies are used: CellMould (Battenfeld) and MuCell (Trexel, see Fig. 10.25). While the plasticizing screw of the MuCell-process features two non-return valves, the screw for CellMould-process has one non-return valve and one special barrier geometry. Another difference is the possibility of gas-usage: while for MuCell-process nitrogen and carbon dioxide can be processed, CellMould only allows the usage of nitrogen [112, 113].

In the foam injection molding process the thermal management of the mold as well as the thickness of the cavity are crucial for the stabilization of the foam cells. For small thicknesses and cold molds, the polymer melt solidifies quickly and the growing foam cells are stabilized fast. For bigger thicknesses and higher mold

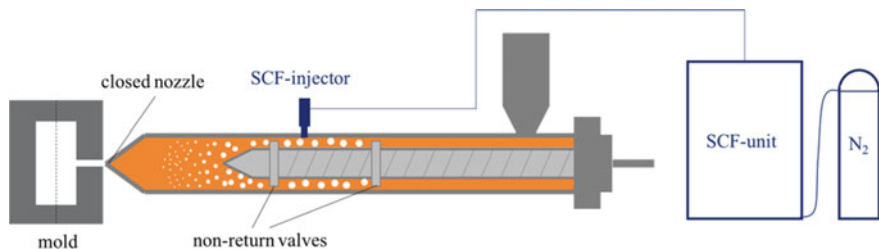


Fig. 10.25 Physical foam injection molding with supercritical fluid (SCF, e.g. N₂; MuCell). Copyright (2018) Neue Materialien Bayreuth GmbH

temperatures the melt in the center of the cavity stays longer molten and leads more often to cell coalescence. Furthermore, a higher melt temperature and a lower injection speed lead to larger cells. And in general, a higher weight reduction results in larger cells [111, 114]. The thickness of the compact layer, as well as the cell size and cell size distribution directly affect the mechanical stability of foam injection molded parts.

10.2.4.3 Mechanical Properties

Components produced by foam injection molding show, as Figs. 10.21 and 10.22 demonstrate, always a so-called sandwich-structure, which can be described as a 3-layer setup. This structure is a mono-material-sandwich and contains a foamed core and compact skin layers at both sides. The mechanical properties are defined by this structure (skin thickness and cell size), the distance of the skin layers and the core density. Applying bending load, the strain rises linear from the center of the part to the outer layers. In compact parts a linear rising strain results, whereas in foam injection molded parts an erratic increase of the strain from foamed core to compact skin layers appears as it is shown in Fig. 10.26.

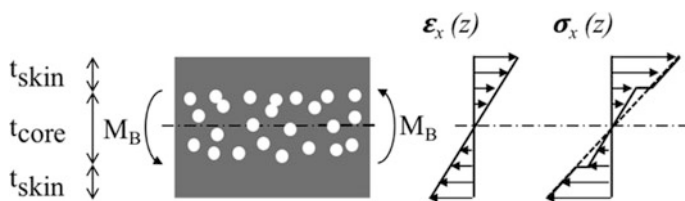


Fig. 10.26 Bending properties of foam injection molded parts. Copyright (2018) Neue Materialien Bayreuth GmbH

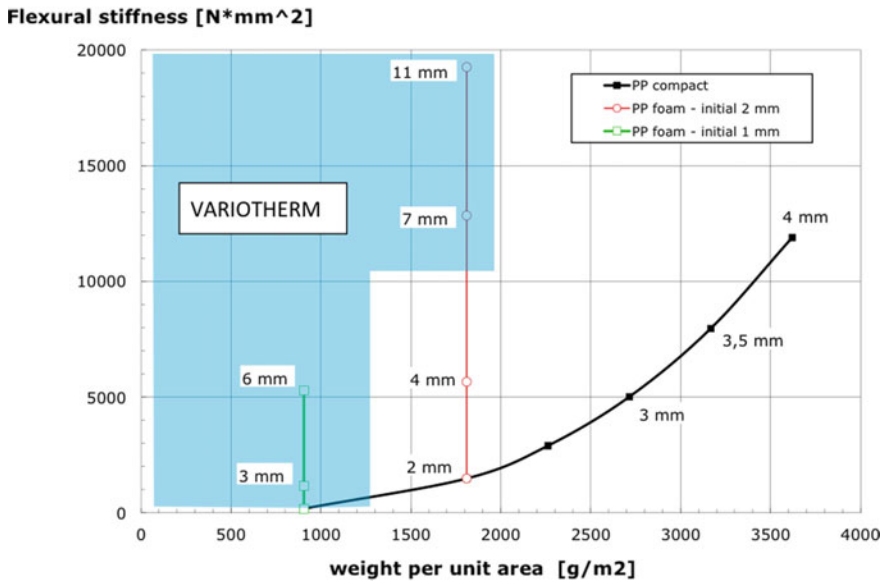
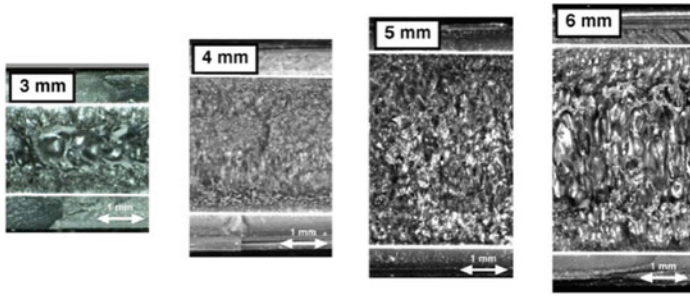


Fig. 10.27 Bending stiffness of foamed parts with different thicknesses in comparison to compact parts. Copyright (2018) Dr. Andreas Spörrer

The bending stiffness increases with increasing distance of compact skin layers to the center axis, due to the rising moment of inertia, and increasing skin thicknesses. The total thickness (and thus the mechanical properties) of foam injection molded parts can be varied in the high-pressure process by changing the precise opening stroke of the mold. Figure 10.27 shows the bending stiffness of compact components made with PP of different thicknesses compared to physically foamed components of different thicknesses and thus, different distances of compact layers. The mass per unit area (g/cm^2) of the foamed parts was kept constant. It can be seen that the bending stiffness of the foamed parts increases significantly as the distance between compact layers increases. This means that for constant part weight a higher bending stiffness can be achieved by applying foam injection molding [115].

10.2.4.4 Advantages and Disadvantages

In the conventional injection molding of compact components, a holding pressure is applied after the filling to compensate the shrinkage of the component during the solidification of the melt and thus to minimize warpage and sink marks. This can be omitted in the foam injection molding process, since the expanding blowing agent operates as an internal holding pressure in the cavity. This very constant, flow path-independent pressure leads to a lower shrinkage and thus too less warpage of the parts compared to compact injection-molded components. In addition to the reduced warpage, also sink marks on the part can be avoided. Beside these advantages, directly related to the component, there are also process advantages. Due to the elimination of the holding pressure, the cycle time decreases. However, the necessary stabilization of the foam cells may require a longer cooling time.

The solution of a blowing agent in the polymer melt leads to a reduction of the viscosity, since the attachment of the fluid molecules in between the macromolecular chains of the polymer leads to an increased mobility of the individual chain segments. The viscosity reduction can be used to achieve longer flow paths with the same thickness. Furthermore, the injection pressure is reduced by the decreased viscosity. The necessary closing force depends directly on the injection pressure. Higher injection pressure leads to a higher closing force of the machine. Therefore, smaller and thus cheaper machines with lower closing forces can be used [116].

One major challenge of foam injection molding is the production of parts with a good optical appearance. Due to the foaming of the polymer at the flow front, foam cells are transported by the displacement flow to the parts surface (see Fig. 10.28). These cells solidify at the surface and are fractured as a result of the flowing melt. This leads to so-called silver streaks [117].

For reducing silver streaks a dynamical mold cooling can be applied. The mold is heated during injection of the material; hence, the material is still formable and the cells that reach the part's surface are smoothed. Afterwards the mold is cooled

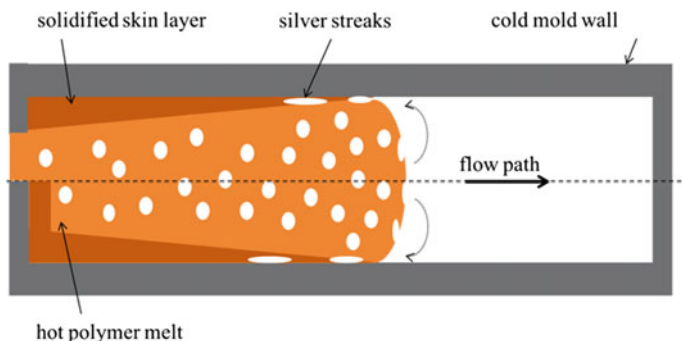


Fig. 10.28 Formation of silver streaks at the surface of foam injection molded parts. *Copyright (2018) Neue Materialien Bayreuth GmbH*

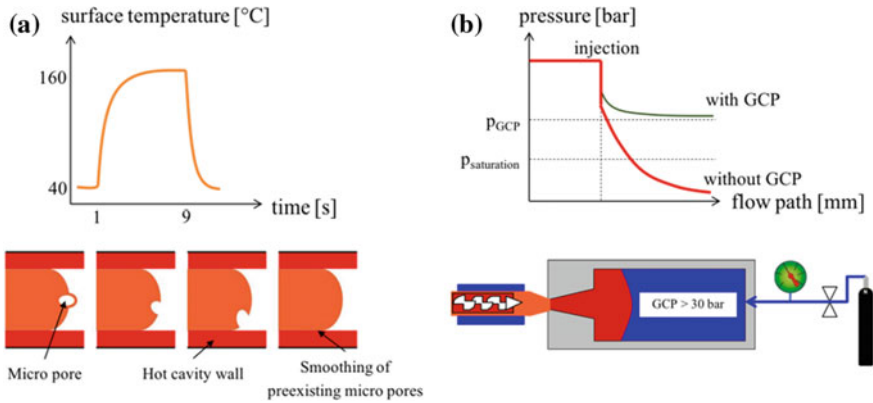
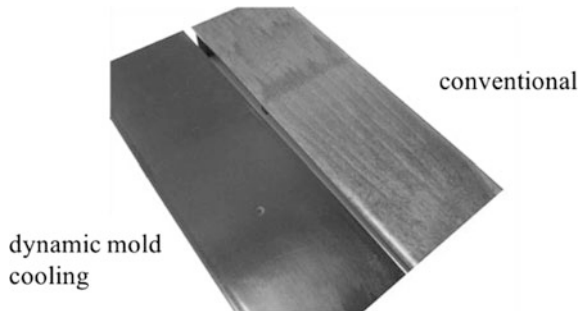


Fig. 10.29 Surface optimization: **a** dynamic mold cooling; **b** gas counter pressure (GCP). Copyright (2018) Neue Materialien Bayreuth GmbH

Fig. 10.30 Surface optimization by dynamic mold cooling. Copyright (2018) Neue Materialien Bayreuth GmbH



abruptly, to reduce the cycle time of the process. Polypropylene is generally injected into a mold with a temperature of 160 °C and cooled afterwards with a mold temperature of 40 °C (see Fig. 10.29a). A second possibility for surface optimization is to apply gas counter pressure in the mold. Due to a high gas pressure (commonly nitrogen with more than 30 bar) applied in the mold (see Fig. 10.29b), foaming at the melt front can be avoided.

In Fig. 10.30 the improvement of the surface of an injection foamed part by using dynamic mold cooling is clearly visible. The effect of the micropores is strongly reduced leading to no silver streaks.

10.2.4.5 Conclusion

With thermoplastic foam injection molding, components with compact skin layers and a foamed core can be realized by using physical and chemical blowing agents. This structure requires a high weight-related bending stiffness, whereby foamed

parts have a high lightweight construction potential. By applying dynamic mold cooling or gas counter pressure, process-related silver streaks on the surface can also be avoided and lightweight visible parts can be produced.

10.2.5 Other Methods

Apart from the methods described previously, several other techniques can be applied to obtain porous materials. These techniques will be presented in the following.

10.2.5.1 Stretching of Films

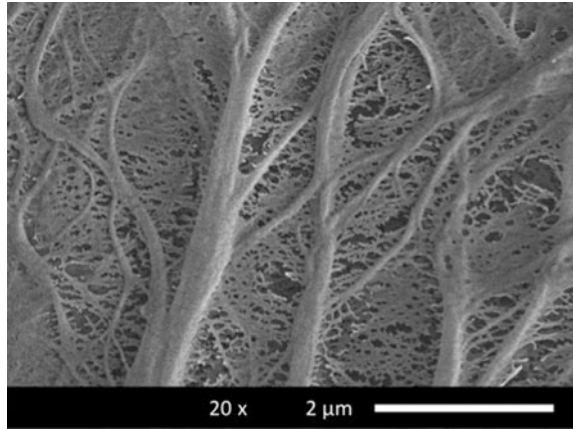
In order to produce micro-porous films, several stretching methods are available. The general approach is in all cases to first extrude a compact polymer film and then to create pores by stretching the film either in one direction or biaxial.

One possibility to achieve this is to incorporate a second, incompatible polymer phase or inorganic fillers into the polyolefin matrix. The second polymer is typically either an amorphous polymer or a semi-crystalline polymer with a glass transition temperature above the one of the matrix polymer. Typical inorganic fillers include calcium carbonate, clay or titanium dioxide. During the stretching process, as a result of the poor compatibility of the two phases and the occurring stresses, voids are formed between filler and matrix [118].

Alternatively, as a second phase, a hydrocarbon liquid or some other low-molecular weight substance can be used. This second phase has to be dispersed in small domains in the polymer matrix and can then be extracted after the extrusion and stretching process with a volatile solvent. This method is used for example to produce battery separator membranes for lithium-ion batteries [119].

Especially for the case of polypropylene, one further method is available to produce micro-porous films. Polypropylene is a so-called polymorphic material, which means it can crystallize in different modifications: a monoclinic alpha modification, a trigonal beta modification, and an orthorhombic gamma modification [120]. Under standard processing conditions, mainly the alpha modification is obtained [119–121], which is the thermodynamically stable modification [121]. The thermodynamically metastable beta modification is usually not found under normal processing conditions, but can be induced by shear [122], temperature gradients [123] or by adding special beta-nucleating agents [124, 125]. One characteristic of the thermodynamically metastable beta phase is the formation of micro voids, if the material is stretched past the yield point. With this method, void contents of more than 50% can be reached and often, open celled structures with interconnected cells are formed. These films (example can be seen in Fig. 10.31) are typically used as breathable garments, roofing membranes or battery separator membranes as water

Fig. 10.31 Scanning electron micrograph of a micro-porous PP film made from biaxial stretching of beta PP according to [126]. *Courtesy of Philip Jacoby, Copyright 2018*



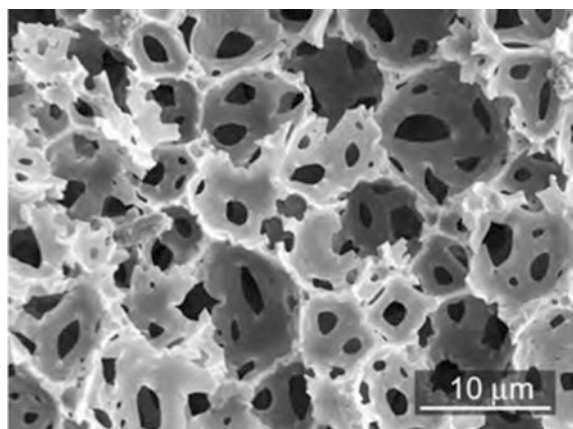
vapor can pass through the films whereas big water drops cannot pass through [126].

10.2.5.2 Templated Porous Polymers

The general concept of creating porous polymers with a templating method is to incorporate a second phase into the polymer and then to remove this phase in order to create porosity as shown in Fig. 10.32.

The second phase can be created by block copolymer templating, where two immiscible polymers are copolymerized. As a result of microphase separation, a very fine two phase morphology is formed. By selective extraction of one of the phases, a porous polymer with a very fine morphology can be obtained [127, 128].

Fig. 10.32 Scanning electron micrograph of a porous structure created by emulsion templating of styrene and divinylbenzene. Reference [130]. *Copyright (2018) Wiley Periodicals, Inc.*



Another way is to create a second phase by colloidal templating. In this case, a biphasic system is created and then the continuous phase is polymerized. The colloidal entities are then removed after polymerization. Depending on the colloidal system, pore sizes in the range from a few nanometers to hundreds of micrometers are obtained [127, 129].

10.3 PP Foams and Additives

It is crucial to achieve fine and uniform cells for PP foams to be used in various application fields. Nevertheless, obtaining foams with a fine cell structure is restricted due to the weak melt strength and melt elasticity of linear PP [131]. Concerning the limitations to achieve fine cell structured foams, previous efforts focused on developing approaches which provide PP with superior melt strength and improved foamability, such as long chain branching [132, 133], crosslinking [134] and a means of reinforcing the entanglement network in the melt. Nevertheless, in regard to high price and difficulties in the preparation of high melt strength PP, the commercial use in the foaming applications is limited [66, 131]. Therefore, the strategy of introducing additives into PP matrix gained attention in the last decades as an alternative to achieve PP foams with improved foam cell morphology. In the literature, one can encounter with mainly two categories of additives, namely temperature-insensitive and temperature-sensitive additives. Temperature-insensitive additives such as talc, clay, carbon fillers and nano-fibers, are mostly inorganic substances which are insoluble in PP melt and their structure and properties do not alter with change in temperature while temperature-sensitive additives such as trisamides (e.g. 1,3,5-benzenetrisamide) are usually organic substances which can be soluble and self-assemble to supramolecular nano-objects with change in temperature [135, 136].

10.3.1 *Temperature-Insensitive Additives*

Concerning the mentioned requirements for improving the foamability and achieving the fine cell structured foams, addition of temperature-insensitive additives such as calcium carbonate (CaCO_3) [137], talc [64, 138], clay [69, 139, 140], graphene [141], carbon nano fibers [142], hollow glass microspheres [143], silica and silicates [68, 144], sodium benzoate [145] and zeolite [146] into PP. The additives, which are insoluble in PP increase the melt strength of the PP, lead to superior foamability and contribute to the mechanical resistance of the cells [139].

10.3.1.1 Foams with CaCO₃

Huang and Wang [137] reported an attempt to improve the foamability of PP by means of introducing nano-CaCO₃ with the concentrations of 5 and 20 wt%. The neat PP foams and with CaCO₃ were produced by microcellular batch foaming with a saturation time of 22 h in a CO₂ atmosphere. The authors claimed that the highest cell density (8.4×10^{11} cells/cm³) was reached only with 5 wt% nano-CaCO₃. It was proposed the smaller cell size and higher cell density depend on the dispersion quality of the nanoparticles. It was observed that 5 wt% nano-CaCO₃ led to better dispersion in the PP matrix and thus much more effective nucleation sites for foaming are available. When the nanoparticle concentration was increased to 20 wt% non-uniform cell size distribution was seen due to the conglomeration of the nanoparticles at a higher nano-CaCO₃ content in which agglomerated nanoparticles led to big bubbles around them compared to the cells nucleated around the finely dispersed particles.

10.3.1.2 Foams with Talc

Kaewmesri et al. [64] used talc to improve the foamability and final extruded foam morphology of PP. The researchers were employed differently a branched, recyclable PP having already high melt strength compared to the linear PP for further foaming in the presence of talc with 0.8, 1.6 and 2.4 wt% by using 5 wt% CO₂ as a blowing agent via small-scale tandem foam extrusion line. It was claimed that already small concentrations of talc (0.8 wt%) led to the higher expansion ratios such as 14-fold and cell densities of up to 10^7 – 10^9 cells/cm³ with cell sizes less than 0.02 mm.

10.3.1.3 Foams with Clay

Okamoto et al. [139] produced PP nanocomposite foams including 4 wt% clay particles by batch foaming process at 134.7 °C and under 10 MPa. They employed supercritical CO₂ as a blowing agent. The authors claimed that the clay particles were aligned along the cell boundary (see Fig. 10.33a) with the effect of the biaxial flow during the foaming. It was proposed that the alignment of the clay particles provide further enhancement in mechanical properties such as modulus of the foam as these particles helps cells withstand the subjected force.

It was shown with the transmission electron microscope images (see Fig. 10.33a) that the clay particles could either turn their face (marked with the arrows (A)) or fix their face orientation (marked with the arrows (B)) and align along the flow direction of the materials during the foaming process. It was also exhibited in Fig. 10.33b that the clay particles were dispersed randomly in the cell struts (marked with the arrows (C)). The authors reported that this random

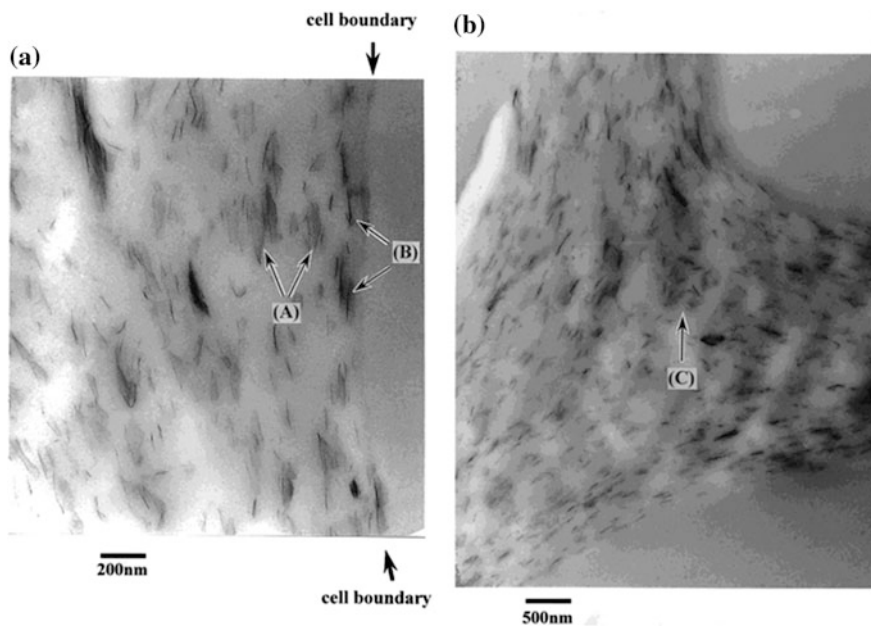


Fig. 10.33 Transmission electron microscope images of the foams **a** one cell wall and **b** one cell strut. Reprinted (adapted) with permission from [139]. Copyright (2018) American Chemical Society

dispersion in the cell strut, which is the region where three contacting cells grow, was resulted by the stagnation flow of the material.

Jiang et al. [140] also prepared PP/clay nanocomposite foams by using batch foaming process at 16.5 MPa and a temperature of 156 °C. Supercritical CO₂ (scCO₂) was employed as a blowing agent and effect of scCO₂ was investigated. Different from the previous work, the scientists used the 0.6 wt% maleic anhydride (MA) as a compatibilizer, which was grafted using scCO₂-assisted solid-state grafting technique. The compatibilized PP (PP-g-MA) compounded with two different types of organoclays, which were film and engineering grades. They were montmorillonites (MMT) having mean dry particle size of 15-25 μm. Surface treatments of the clay were implemented by organic modifiers. The authors found that the blends of PP/PP-g-MA (85/15) exhibited more uniform cell structure with a cell density of 4.8×10^7 cells/cm³ and average cell size of 37.7 μm compared to the pure PP. It was found interesting to observe that both cell size and cell density increased compared to the neat PP, explained with the different crystallinity and microstructure of the blend PP/PP-g-MA caused by the compatibilized PP, PP-g-MA which led to decrease in crystallinity and more defects in the crystals. Thus, the blend of PP/PP-g-MA was selected as a reference material to understand the effect of clay layers on the foaming of the nanocomposites. It was reported that only 0.5 wt% clay of both film and engineering grades was enough to increase the

cell density, however, the increase with the film grade was more significant and was higher than those of engineering grade. Decrease in cell size was remarkable from PP/PP-g-MA blend to the PP with 0.5 wt% both clay types. The authors concluded that the incorporation of clay layers could improve the cell nucleation of the nanocomposites.

Different from the previous study by Jiang et al. [140], Nofar et al. [69] were produced linear PP based microcellular foams by using nano-sized clay (montmorillonite modified with a quaternary ammonium salt) by single-screw extrusion foaming employing supercritical CO₂ (5 wt%) as a blowing agent. A high melt flow coupling agent, namely maleic anhydride—grafted PP, was also used for overcoming the agglomeration problem of the nanoclay and gaining a superior dispersion quality of nanoclay in linear PP homopolymer. Figure 10.34 exhibits the effect of nanoclay having different contents on the morphology of the extruded foams at 115 °C die temperature.

It was claimed that with introducing only small amount of nanoclay (0.5 wt%), the melt strength of the linear PP was dramatically increased and thus a significant improvement in the foam cell density (10^{5-7} cells/cm³) and expansion ratio of 8 was achieved. Higher nanoclay content up to 5 wt% led to further enhancements in the foamability, expansion ratio up to 20, foam cell density up to 10^{8-9} cells/cm³ and a more uniform morphology due to increase of melt strength and cell nucleation sites.

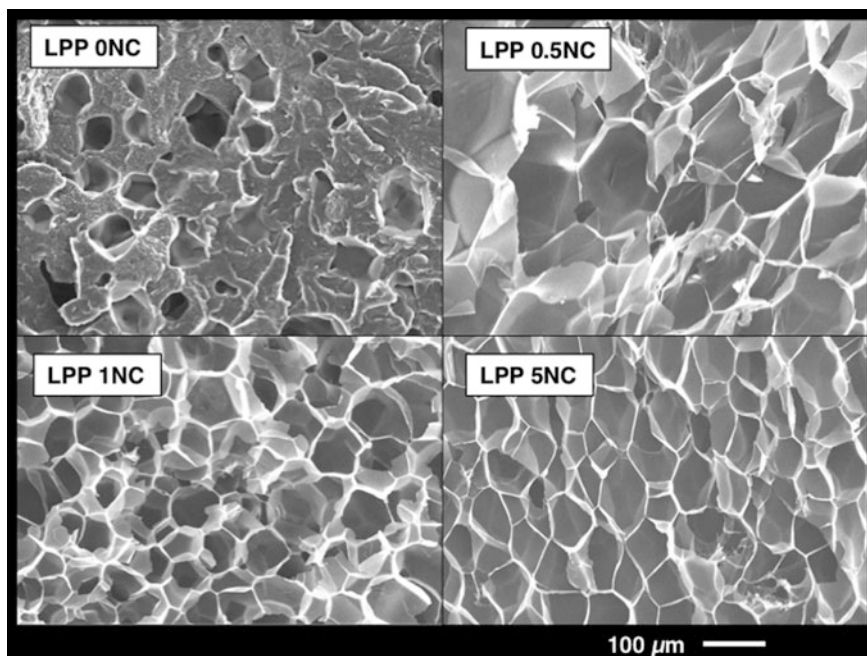


Fig. 10.34 Foam morphologies of linear polypropylene (LPP) and LPP/nanoclay foams at 115 °C die temperature with different clay content (also see [69]). *Courtesy of Mohammadreza Nofar, Copyright 2018*

10.3.1.4 Foams with Carbon Fillers

Besides clay/nanoclay fillers, carbon based fillers such as graphene [141], carbon nanofibers [142] have been also used to improve foamability and increase melt strength of PP so that foams having smaller cell sizes and uniform cell size distribution could be achieved. For gaining these foams having improved morphologies, Antunes et al. [141] manufactured PP foams having the concentrations of 2.5 and 5 wt% of graphene with the form of nanoplatelets, having average thickness of 6–8 nm and diameter of 15 μm , via physical foaming. The researchers inserted the solid precursor namely, neat PP, PP with graphene, to the high-pressure vessel and remained the samples to be saturated with supercritical CO_2 at 155 $^\circ\text{C}$ and 180 bar for 30 min. The CO_2 saturated samples then cooled down to the temperature of 135 $^\circ\text{C}$ via a cooling water system for 5 min. The saturated precursors afterwards were let foaming at 135 $^\circ\text{C}$ (decompression temperature) by decreasing the pressure of the vessel to ambient pressure with a pressure drop rate of 30 bar/s. The authors stated that introduction of 2.5 and 5 wt% graphene provided foams with higher cell densities of 2.31×10^6 and 3.28×10^6 cells/ cm^3 , respectively considering to the neat PP with 1.62×10^6 cells/ cm^3 . They also claimed that the cell nucleation density was increased 42% and cell size was decreased from approximately 75 to 67 μm with increasing graphene concentration from 2.5 to 5 wt%. It was concluded the improved expansion ratio and cell morphology of the PP foams with graphene may lead to the higher orientation of the alpha- monoclinic PP crystals perpendicular to the foam surface and higher exfoliation of the graphene nanoplatelets and thus enhanced mechanical properties. Possessing developed foam morphology and properties makes PP based foams promising products to be used in electromagnetic interference shielding applications in which enhanced foam morphologies are required.

In another study Wang et al. [142] reported an attempt to enhance the foamability of PP with the introduction of short carbon fibers with the concentrations of 5, 15 and 25 wt%. They produced carbon fiber filled PP foams by a batch foaming process at 180 $^\circ\text{C}$ with CO_2 as a blowing agent. The authors claimed that the increasing amount of carbon fibers influences the melt viscosities of PP and thus the blowing agent solubility in PP. A higher filler concentration led to an increase in solubility of CO_2 and thus foams with more homogeneous cell size distribution as well as well-defined closed cell structure. It was found that the foams having 25 wt% carbon fiber concentration had as the lowest foam density of 0.52 g/cm^3 , the most uniform cell size distribution, the most improved cell morphology in which the mean cell diameter was approximately 29 μm and the cell density was 7.99×10^6 cells/ cm^3 as well in comparison with the foams of neat PP and PP with 5 and 15 wt% carbon fibers. Furthermore, the researchers suggested that the increased cell density with higher carbon fiber concentration might be due to heterogeneous mechanism dominated foam cell nucleation with the addition of more carbon fibers. The interface between carbon fibers and PP was energetically favored and played as nucleation sites for foaming due to the weak interaction.

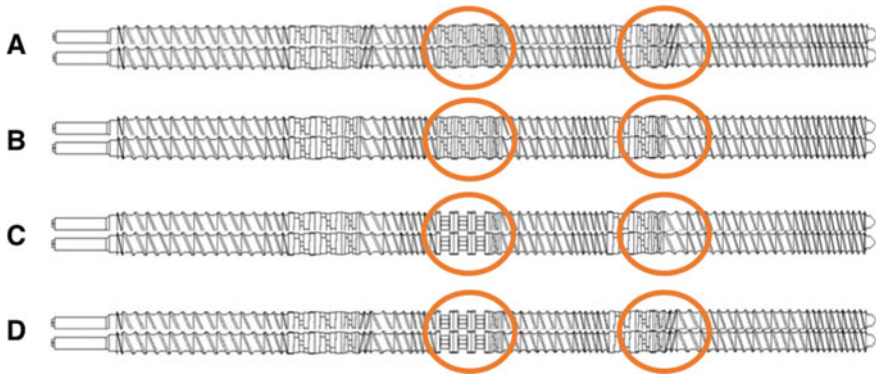
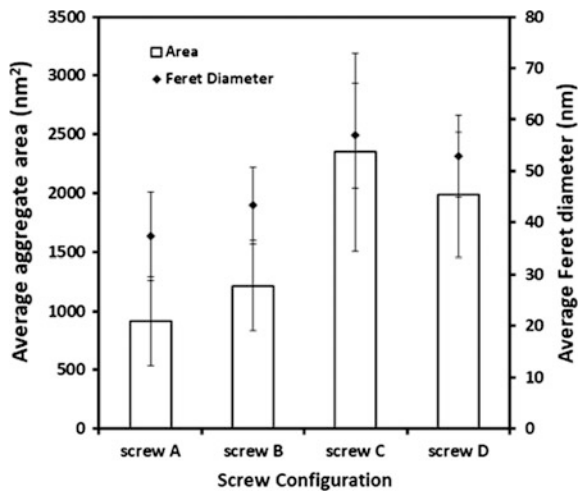


Fig. 10.35 Four screw configurations providing good dispersive mixing (a) and (b); and distributive mixing (c) and (d). Different screw elements were marked. Modified from [68]. Copyright (2018) Carl Hanser Verlag GmbH & Co. KG, Munich

Lee et al. [68] prepared the nanocomposites of isotactic PP foams in the presence of nanosilica particles (12 nm of mean particle size) of 1 phr and maleated PP as compatibilizer by co-rotating twin-screw extruder (L/D = 40). As with nanoclay, the poor dispersability of the additive in the polypropylene matrix may lead to an agglomeration problem and thus enlarge the cell size. To avoid this, four different screw configurations were employed as shown in Fig. 10.35 in order to find optimum screw configuration, which gives the best additive dispersion.

All of the screw configurations were consisted of three kneading block elements. Furthermore, the researchers reported that the first two screw configurations (and b) led to shorter residence time and better dispersive mixing due to the small staggered angle discs while the other configurations (Fig. 10.35c, d) provided longer

Fig. 10.36 Effect of screw configuration on the average silica aggregate (the error bars represent 95% confidence intervals) [68]. Copyright (2018) Carl Hanser Verlag GmbH & Co. KG, Munich



residence time and better distributive mixing with their greater stagger angles of the configurations. The influence of different screw configurations on the dispersion of nanosilica (1 phr) in PP matrix was summarized in Fig. 10.36a.

It was concluded that the screw configuration A, which had narrow staggered kneading discs and additional reverse screw elements, yielded the smallest average aggregate area as well as best dispersion. After the optimization of screw configuration, the researchers produced PP foams with the concentrations of 0.5 and 1 phr nanosilica particles by batch foaming method. It was stated that as with nanoclay, nanosilica also increased the melt strength and led to strain hardening and hence improved foamability with the lower risk of cell coalescence. Introduction nanosilica of 0.5 phr to the PP matrix led the highest cell density of approximately 1.60×10^7 cells/cm³.

10.3.1.5 Foams with Sodium Benzoate

An attempt was made by Colton [145] to improve the nucleation of crystalline structure and foam morphology of PP by means of introduction of 1 wt% sodium benzoate. The author was developed the strategy of achieving microcellular foams by using these sodium benzoate particles possessing the diameter of 0.5 μm and the surface tension of 25 dynes/cm. The PP foams including additive was produced by pressure-induced batch foaming process at 165 °C and 30 min saturation time. It was reported that the addition of sodium benzoate provided enough sites with the appropriate surface energy conditions to significantly aid in the nucleation of microcellular foams. It was added that this additive led to reduction in the overall surface tension of the polymer and hence enhancement in nucleation was observed.

10.3.1.6 Foams with Hollow Glass Microspheres

Barboza and Paoli [143] created foams by introducing the hollow glass microspheres (HGM) trade name of Glass Bubbles[®] possessing diameters in the range of 10–100 μm into PP. The researchers extruded PP with 10 wt% (20 vol%) Glass Bubbles[®] at 210 °C. The researchers claimed that Glass Bubbles[®] led to decrease in density (approximately 6%) without great loss in mechanical properties. They were also claimed that the hollow spaces in PP foams may improve the isotropy of the foam and contribute to decrease the thermal conductivity.

10.3.1.7 Foams with Zeolite

Bertrand [146] invented expanded PP films having a uniform density and improved physical and mechanical properties. The inventor claimed that the manufactured expanded PP films were aimed to possess a high crystallization temperature in the range of 115 and 135 °C. The expanded isotactic PP films including 0.3 wt% of a

mixture of adipic acid and zeolite (ratio of 1:3) were prepared by the blown film technique using 0.5 wt% blowing agent (citric acid and sodium bicarbonate). The inventor reported that the final expanded PP exhibited density of $4.61 \times 10^{-6} \text{ N/mm}^3$, tensile strength at 5 wt% elongation of 11.16 N/mm^2 , tensile strength at break of 11.4 N/mm^2 and elongation at break of 1.76%. Ratio of elastic modulus to density was found as $1.86 \times 10^8 \text{ mm}$.

10.3.1.8 Conclusion

When all of the additives were taken into account, it can be concluded that temperature-insensitive additives provides PP foams with improved morphology in which foam cells have smaller sizes and more uniform size distribution compared to the neat PP foams which might be due to the higher foam nucleation efficiency and melt strength and improved foamability. It is also noteworthy that not only additives but also foam processing type as well as processing parameters such as temperature, pressure, saturation time and blowing agent have a significant influence on the final foam morphology and properties. The most common challenge, which is agglomeration of the additives due to the poor dispersion in PP melt, was attempted to minimize by using compatibilizers and different screw configurations.

10.3.2 Temperature-Sensitive Additives

The group of temperature sensitive additives is relative young compared to temperature insensitive additives. However, it has gained increasing interest over the past years and provides certain advantages compared to conventional additives. Temperature sensitive additives are based on organic molecules, that can be soluble in the polymer melt, thus allowing for easy dispersion, and can self-assemble to supramolecular structures in the polymer melt upon cooling. The self-assembly process is shown in Fig. 10.37 for the example of additives based on 1,3,5-benzenetrisamides. Other examples of additives from this group are benzenebisamides or sorbitol derivatives. Through the formation of H-bonds between

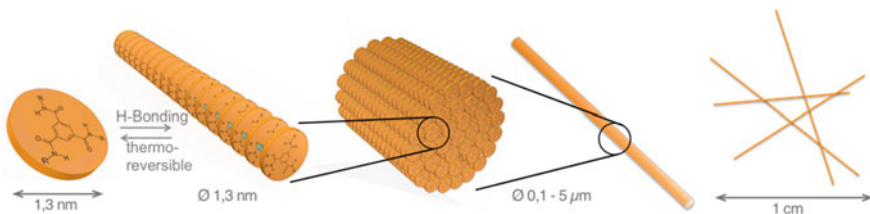
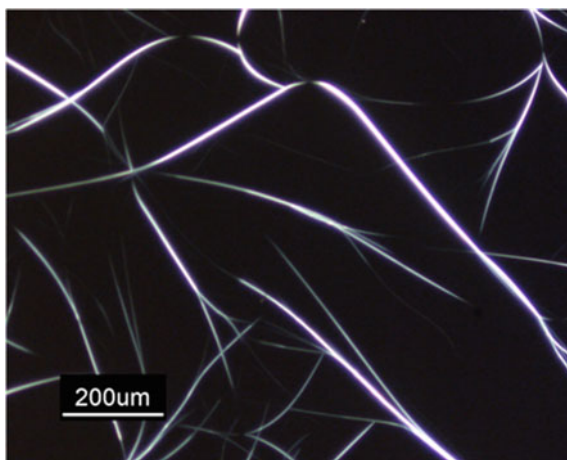


Fig. 10.37 Schematic representation of the self-assembly of temperature sensitive additives in a polymer melt. Copyright (2018) University of Bayreuth, Department of Polymer Engineering

Fig. 10.38 Fibers of a self-assembled temperature sensitive additive in a polypropylene melt viewed through crossed polarizers in a light microscope. *Copyright (2018) University of Bayreuth, Department of Polymer Engineering*



the amide groups, the molecules assemble into columns that form fiber-line structures with thickness in the range of 0.01–5 μm and can reach lengths up to centimeters. Due to their birefringence, these fiber-like structures can be seen in the polymer melt in polarized light microscopy (see Fig. 10.38).

Solubility and self-assembly strongly depend on the chemical structure of additive and polymer, the concentration of the additive, the temperature of the polymer melt and the cooling rate [136, 147, 148].

Most of these additives have mainly been investigated as crystal nucleating agents in compact PP [136, 147]. However, some studies already show the great potential of this class of additives as highly efficient foam nucleating agents. Here, they can be an alternative to conventional foam nucleating agents such as talc, as they are easier to disperse in the polymer melt and provide a higher surface area requiring lower concentrations. Compared to other fiber-like nucleating agents such as fibers made from polymers like PTFE or PET, they do not require an additional processing step, as the additive fibers are formed in situ in the foaming process.

The focus of these studies has been on additives based on 1,3,5-benzenetrisamides [149, 150].

Based on their unique temperature-dependent behavior, they can be tailored to the temperature profile in a foam injection molding or foam extrusion process to where they are first dissolved in the polymer melt for a good dispersion of the additive and then self-assemble before foaming can take place to ensure a high density of nucleation sites for the foam cells. This principle is shown in Figs. 10.39 and 10.40 for foam extrusion as well as foam injection molding including melt temperature and pressure as the two most important parameters for foaming.

In the foam extrusion process (see Fig. 10.39), the additive is dissolved in the polymer melt above the solubility temperature of the additive in the first extruder of the tandem extrusion line and gas is injected in the melt (I + II). In the second extruder, the polymer melt is cooled down to the optimum foaming temperature and

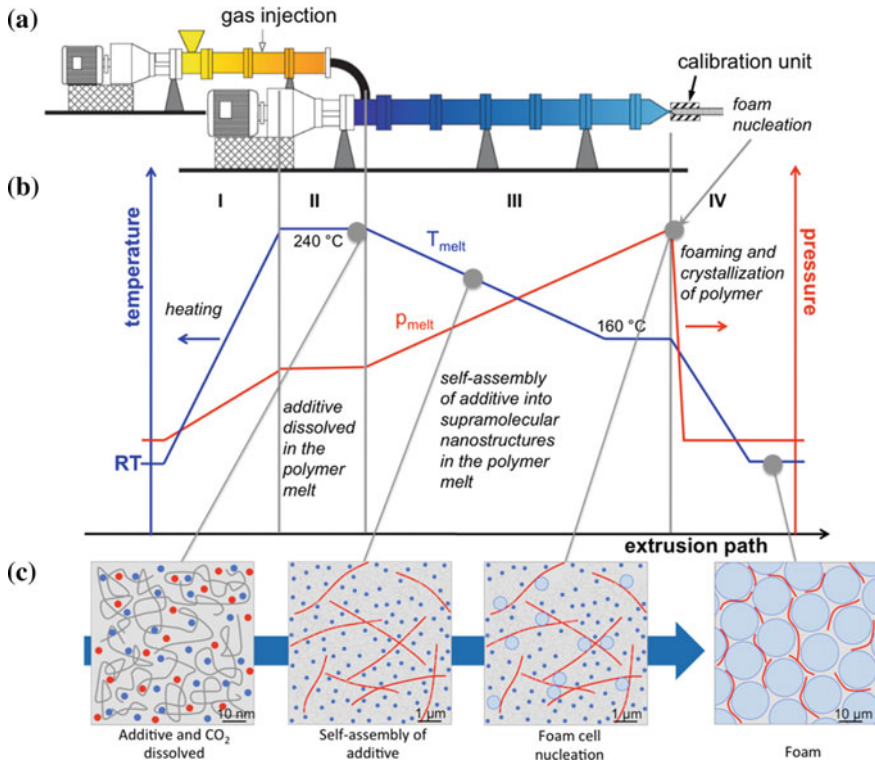


Fig. 10.39 Foam extrusion process with temperature sensitive additives. **a** Experimental setup with tandem extrusion line, **b** processing scheme with steps I-IV, **c** schematic representation of the foam nucleation concept [150]. Copyright (2018) University of Bayreuth, Department of Polymer Engineering

the self-assembly of the additive can take place (III). The pressure drop at the die of the extruder induces foaming. Here the additive can act as a nucleating agent for the foam cells (IV) [150].

In the foam injection molding process the principle is similar as can be seen from Fig. 10.40. The additive is first dissolved in the gas loaded polymer melt in the plastification unit (I). After injection of the melt into the mold, the melt is cooled down below the self-assembly temperature of the additive, but above the crystallization temperature of the polymer (II). Afterwards, the mold is opened partially (breathing mold technology) in order to create a pressure drop and induce foaming where the supramolecular additive acts as nucleation sites for the foam cells (III). In the end, the foamed part can be ejected (IV) [149].

As a direct result of the nucleation, the resulting foam morphology is significantly influenced. Both for foam injection molding, as well as for foam extrusion, a significant decrease of the cell size as well as more homogeneous cell size distribution have been reported (see Fig. 10.41) [149, 150]. This has been most

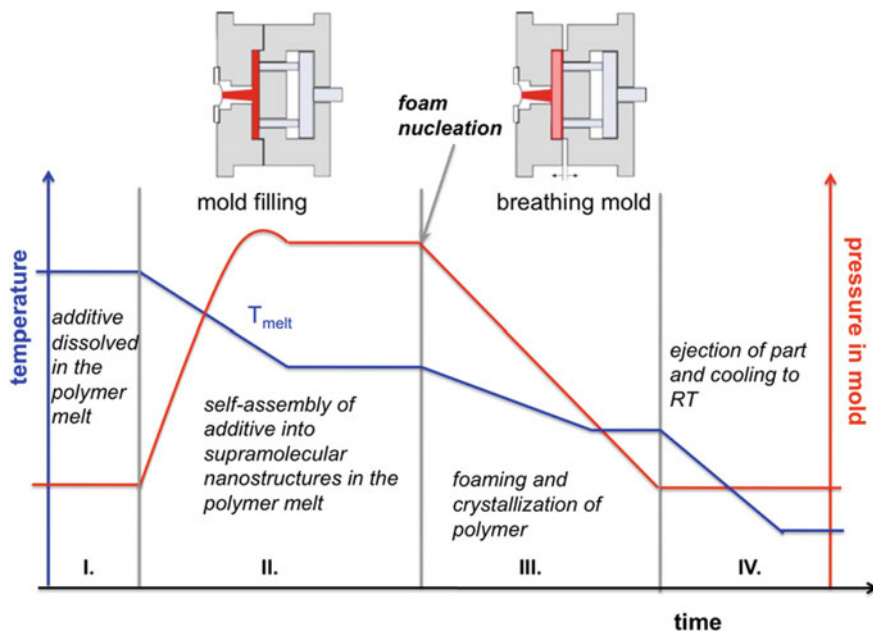


Fig. 10.40 Foam injection molding process with temperature sensitive additives. Modified from [149]. Copyright (2018) University of Bayreuth, Department of Polymer Engineering

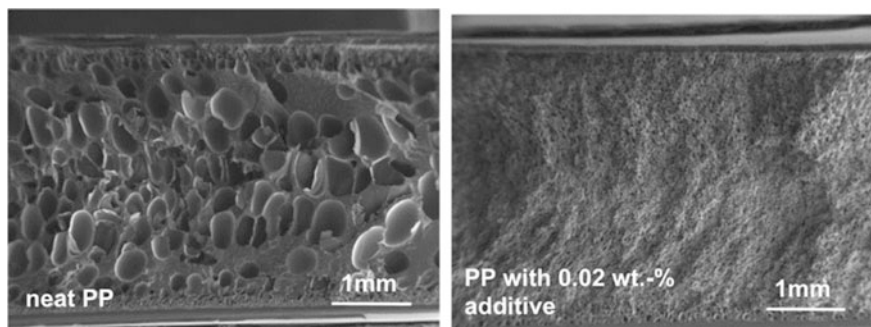


Fig. 10.41 Morphology of injection molded foams from PP without (left) and with 0.02 wt% (right) of a temperature sensitive additive. Reference [149]. Copyright (2018) University of Bayreuth, Department of Polymer Engineering

pronounced in a linear polypropylene type in injection molding where a decrease in average cell size from 120 μm for the neat material to 20 μm for the material with only 0.02 wt% additive have been achieved [149].

Apart from the influence of the temperature sensitive additives on the morphology, a distinct influence on the mechanical properties has been reported. An

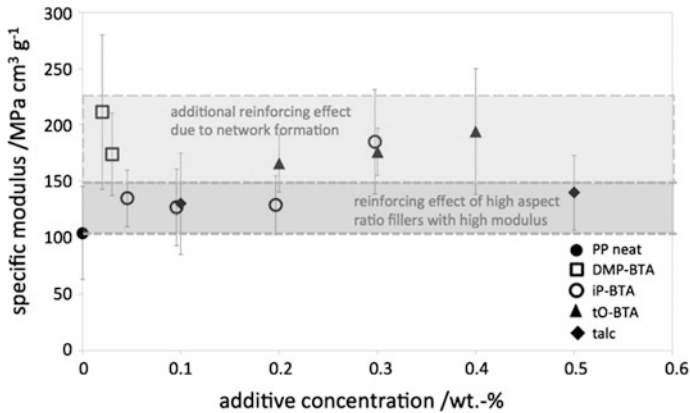


Fig. 10.42 Specific compression moduli of polypropylene foams with different temperature sensitive additives and talc as a reference. Reference [150]. Copyright (2018) University of Bayreuth, Department of Polymer Engineering

increase in impact toughness with the addition of these additives has been attributed to an increase in cell strut thickness [149].

Apart from the indirect influence through changes in the foam morphology, an additional effect of the additive itself as a reinforcing agent has been found for compression behavior. Here, an increase in specific compressive modulus of up to 100% with the addition of only 0.02 wt% of a temperature sensitive additive has been observed (see Fig. 10.42) [150].

Acknowledgements For their contribution to this chapter the following people are acknowledged (in alphabetic order): Merve Aksit, Christian Bethke, Dominic Dörr, Katharina Krause, Michaela Mörl, Daniel Raps, Nick Weingart and Chunjing Zhao.

References

1. Europa K (2015) Marktstudie Kunststoffe - Europa Einleitung Deutschland produziert am meisten Kunststoffe in Europa Wichtigste Absatzmärkte für Kunststoffe. 12–15
2. Smithers Rapra (2014) The future of polymer foams to 2019. 110
3. PlasticsEurope (2015) Plastics—the facts 2014/2015: an analysis of European plastics production, demand and waste data. PlasticsEurope 1–34. <https://doi.org/10.1016/j.marpolbul.2013.01.015>
4. Altstädt V, Mantey A (2010) Thermoplast- Schaumspritzgießen. Carl Hanser Verlag, München
5. Nallagundla Venkata Reddy, Rakesh Lingam JC (2015) Handbook of manufacturing engineering and technology. Springer, London
6. Raps D, Hossieny N, Park CB, Altstädt V (2015) Past and present developments in polymer bead foams and bead foaming technology. Polym (United Kingdom) 56:5–19. <https://doi.org/10.1016/j.polymer.2014.10.078>
7. Eaves D (2004) Handbook of polymer foams. Rapra Technology

8. Viot P, Plougonven E, Bernard D (2008) Microtomography on polypropylene foam under dynamic loading: 3D analysis of bead morphology evolution. *Compos Part A Appl Sci Manuf* 39:1266–1281. <https://doi.org/10.1016/j.compositesa.2007.11.014>
9. Ramesh NS, Malwitz N (1996) Bubble growth dynamics in olefinic foams. *Polym Prepr* 37:783–784
10. Gendron R, Daigneault LE (2003) Continuous extrusion of microcellular polycarbonate. *Polym Eng Sci* 43:1361–1377. <https://doi.org/10.1002/pen.10116>
11. Li P, Chung TS, Paul DR (2014) Temperature dependence of gas sorption and permeation in PIM-1. *J Memb Sci* 450:380–388. <https://doi.org/10.1016/j.memsci.2013.09.030>
12. Baldwin DF (1994) Microcellular polymer processing and the design of a continuous sheet processing system. Ph.D. thesis
13. Shutov F (1983) Foamed polymers. cellular structure and properties. *Adv Polym Sci* 51:155–218. <https://doi.org/10.1007/BFb0017587>
14. Mills NJ (1993) Handbook of polymeric foams and foam technology. *Polymer (Guildf)* 34:2237. [https://doi.org/10.1016/0032-3861\(93\)90758-3](https://doi.org/10.1016/0032-3861(93)90758-3)
15. Okolieocha C, Raps D, Subramaniam K, Altstädt V (2015) Microcellular to nanocellular polymer foams: progress (2004–2015) and future directions—a review. *Eur Polym J* 73:500–519. <https://doi.org/10.1016/j.eurpolymj.2015.11.001>
16. Schellenberg J, Wallis M (2010) Dependence of thermal properties of expandable polystyrene particle foam on cell size and density. *J Cell Plast* 46:209–222. <https://doi.org/10.1177/0021955X09350803>
17. Chen Y, Das R, Battley M (2015) Effects of cell size and cell wall thickness variations on the stiffness of closed-cell foams. *Int J Solids Struct* 52:150–164. <https://doi.org/10.1016/j.ijsolstr.2014.09.022>
18. Ashby MF, Medalist RFM (1983) The mechanical properties of cellular solids. *Metall Trans A* 14:1755–1769. <https://doi.org/10.1007/BF02645546>
19. J.E. Martini, F.A. Waldman NPS (1982) The production and analysis of microcellular thermoplastic foams. *SPE ANTEC Technical Paper* 43:674–676
20. Doroudiani S, Park MTK (1998) Processing and characterization of microcellular foamed high density polyethylene/isotactic polypropylene blends. *Polym Eng Sci* 1205–1215
21. Doroudiani S, Kortschot MT (2003) Polystyrene foams: III. structure-tensile properties relationships. *J Appl Polym Sci* 90:1427–1434. <https://doi.org/10.1002/app.12805>
22. Rachtanapun P, Selke SEM, Matuana LM (2004) Relationship between cell morphology and impact strength of microcellular foamed high-density polyethylene/polypropylene blends. *Polym Eng Sci* 44:1551–1560. <https://doi.org/10.1002/pen.20152>
23. Ferkl P, Pokorný R, Bobák M, Kosek J (2013) Heat transfer in one-dimensional micro- and nano-cellular. *Chem Eng Sci* 97:50–58
24. Köppl T, Raps D, Altstädt V (2014) E-PBT—bead foaming of poly(butylene terephthalate) by underwater pelletizing. *J Cell Plast* 50:475–487. <https://doi.org/10.1177/0021955X14528524>
25. Spital P, Macosko CW (2004) Strain hardening in polypropylenes and its role in extrusion foaming. *Polym Eng Sci* 44:2090–2100. <https://doi.org/10.1002/pen.20214>
26. Borealis (2010) Daploy WB140HMS Daploy WB140HMS
27. Stadler FJ, Piel C, Klimke K et al (2006) Influence of type and content of various comonomers on long-chain branching of ethene/ α -olefin copolymers. *Macromolecules* 39:1474–1482. <https://doi.org/10.1021/ma0514018>
28. Stadler FJ, Nishioka A, Stange J et al (2007) Comparison of the elongational behavior of various polyolefins in uniaxial and equibiaxial flows. *Rheol Acta* 46:1003–1012. <https://doi.org/10.1007/s00397-007-0190-y>
29. Hasan MM, Li YG, Li G et al (2010) Determination of solubilities of CO₂ in linear and branched polypropylene using a magnetic suspension balance and a PVT apparatus. *J Chem Eng Data* 55:4885–4895. <https://doi.org/10.1021/je100488v>

30. Li YG, Park CB (2009) Effects of branching on the pressure–volume–temperature behaviors of PP/CO₂ solutions. *Ind Eng Chem Res* 48:6633–6640. <https://doi.org/10.1021/ie8015279>
31. Ferri D, Lomellini P (1999) Melt rheology of randomly branched polystyrenes. *J Rheol J Rheol* 43:1272–1355. <https://doi.org/10.1122/1.4966040>
32. Venkatraman S, Okano M (1990) Polymer melts : the Cox-Merz rule revisited. *Polym Eng Sci* 30:308–313. <https://doi.org/10.1002/pen.760300508>
33. McCallum TJ, Kontopoulou M, Park CB et al (2007) The rheological and physical properties of linear and branched polypropylene blends. *Polym Eng Sci* 47:1133–1140. <https://doi.org/10.1002/pen.20798>
34. Münstedt H (2011) Rheological properties and molecular structure of polymer melts. *Soft Matter* 7:2273–2283. <https://doi.org/10.1039/C0SM00891E>
35. Brinson HF, Brinson LC (2008) *Polymer engineering science and viscoelasticity*. Springer, US, Boston, MA
36. Carella JM, Gotro JT, Graessley WW (1986) Thermorheological effects of long-chain branching in entangled polymer melts. *Macromolecules* 19:659–667. <https://doi.org/10.1021/ma00157a031>
37. Malmberg A, Liimatta J, Lehtinen A, Löfgren B (1999) Characteristics of long chain branching in ethene polymerization with single site catalysts. *Macromolecules* 32:6687–6696. <https://doi.org/10.1021/ma9907136>
38. Wood-Adams P, Costeux S (2001) Thermorheological behavior of polyethylene: effects of microstructure and long chain branching. *Macromolecules* 34:6281–6290. <https://doi.org/10.1021/ma0017034>
39. Raps D, Köppl T, Heymann L, Altstädt V (2017) Rheological behaviour of a high-melt-strength polypropylene at elevated pressure and gas loading for foaming purposes. *Rheol Acta* 56:95–111. <https://doi.org/10.1007/s00397-016-0988-6>
40. Watanabe K, Suzuki T, Masubuchi Y et al (2003) Crystallization kinetics of polypropylene under high pressure and steady shear flow. *Polymer (Guildf)* 44:5843–5849. [https://doi.org/10.1016/S0032-3861\(03\)00604-9](https://doi.org/10.1016/S0032-3861(03)00604-9)
41. Doroudiani S, Park CB (1996) Effect of the crystallinity and morphology on the microcellular foam structure of semicrystalline polymers. *Polym Eng Sci* 36:2645–2662
42. Kardos JL, Christiansen AW, Baer E (1966) Structure of pressure-crystallized polypropylene. *J Polym Sci Part A-2 Polym Phys* 4:777–788. <https://doi.org/10.1002/pol.1966.160040509>
43. Brückner S, Phillips PJ, Mezghani K, Meille SV (1997) On the crystallization of γ -isotactic polypropylene: a high pressure study. *Macromol Rapid Commun* 18:1–7. <https://doi.org/10.1002/marc.1997.030180101>
44. La Carrubba V, Brucato V, Piccarolo S (2004) The use of master curves to describe the simultaneous effect of cooling rate and pressure on polymer crystallization. *Polym Int* 53:61–68. <https://doi.org/10.1002/pi.1404>
45. Naguib HE, Park CB, Song SW (2005) Effect of supercritical gas on crystallization of linear and branched polypropylene resins with foaming additives. *Ind Eng Chem Res* 44:6685–6691. <https://doi.org/10.1021/ie0489608>
46. Liao R, Yu W, Zhou C et al (2008) The formation of γ -crystal in long-chain branched polypropylene under supercritical carbon dioxide. *J Polym Sci Part B: Polym Phys* 46:441–451. <https://doi.org/10.1002/polb.21372>
47. Yuan M, Turng LS (2005) Microstructure and mechanical properties of microcellular injection molded polyamide-6 nanocomposites. *Polymer (Guildf)* 46:7273–7292. <https://doi.org/10.1016/j.polymer.2005.06.054>
48. Takada M, Tanigaki M, Ohshima M (2001) Effects of CO₂ on crystallization kinetics of polypropylene. *Polym Eng Sci* 41:1938–1946. <https://doi.org/10.1002/pen.10890>
49. Takada M, Ohshima M (2003) Effect of CO₂ on crystallization kinetics of poly(ethylene terephthalate). *Polym Eng Sci* 43:479–489. <https://doi.org/10.1002/pen.10039>

50. Oda T, Saito H (2004) Exclusion effect of carbon dioxide on the crystallization of polypropylene. *J Polym Sci Part B: Polym Phys* 42:1565–1572. <https://doi.org/10.1002/polb.20076>
51. Xu ZM, Jiang XL, Liu T et al (2007) Foaming of polypropylene with supercritical carbon dioxide. *J Supercrit Fluids* 41:299–310. <https://doi.org/10.1016/j.supflu.2006.09.007>
52. Li G, Wang J, Park CB, Altstädt V (2007) Solubility measurements of N₂ and CO₂ in polypropylene and ethene/octene copolymer. *J Applied Polym Sci* 103:2945–2953
53. Jiang XL, Liu T, Xu ZM et al (2009) Effects of crystal structure on the foaming of isotactic polypropylene using supercritical carbon dioxide as a foaming agent. *J Supercrit Fluids* 48:167–175. <https://doi.org/10.1016/j.supflu.2008.10.006>
54. Naguib HE, Park CB, Lee PC (2003) Effect of talc content on the volume expansion ratio of extruded PP Foams. *J Cell Plast* 39:499–511. <https://doi.org/10.1177/002195503039247>
55. Colton JS, Suh NP (1987) Nucleation of microcellular foam: theory and practice. *Polym Eng Sci* 27:500–503. <https://doi.org/10.1002/pen.760270704>
56. Reverchon E, Cardea S (2007) Production of controlled polymeric foams by supercritical CO₂. *J Supercrit Fluids* 40:144–152. <https://doi.org/10.1016/j.supflu.2006.04.013>
57. Lee ST (2000) *Foam extrusion*. CRC Press LLC, Boca Raton
58. Parrish RG (1972) *Microcellular Foam Sheet*. 13
59. Yu L, Zhu Q, Yu T (2013) Development and application of expanded polypropylene foam. *J Wuhan Univ Technol Mater Sci Ed* 28:373–379. <https://doi.org/10.1007/s11595-013-0698-1>
60. Nam GJ, Yoo JH, Lee JW (2005) Effect of long-chain branches of polypropylene on rheological properties and foam-extrusion performances. *J Appl Polym Sci* 96:1793–1800. <https://doi.org/10.1002/app.21619>
61. Naguib HE, Park CB, Reichelt N (2004) Fundamental foaming mechanisms governing the volume expansion of extruded polypropylene foams. *J Appl Polym Sci* 91:2661–2668. <https://doi.org/10.1002/app.13448>
62. Burt JG (1979) The elements of expansion of thermoplastics: part II. *J Cell Plast* 15:158–162. <https://doi.org/10.1177/0021955X7901500305>
63. Mohebbi A, Mighri F, Aji A, Rodrigue D (2015) Current issues and challenges in polypropylene foaming: a review. *Cell Polym* 34:299–337
64. Kaewmesri W (2006) Effects of CO₂ and talc contents on foaming behavior of recyclable high-melt-strength PP. *J Cell Plast* 42:405–428. <https://doi.org/10.1177/0021955X06066995>
65. Chaudhary AK, Jayaraman K (2011) Extrusion of linear polypropylene-clay nanocomposite foams. *Polym Eng Sci* 51:1749–1756. <https://doi.org/10.1002/pen.21961>
66. Zhai W, Kuboki T, Wang L et al (2010) Cell structure evolution and the crystallization behavior of polypropylene/clay nanocomposites foams blown in continuous extrusion. *Ind Eng Chem Res* 49:9834–9845
67. Zheng WG, Lee YH, Park CB (2010) Use of nanoparticles for improving the foaming behaviors of linear PP. *J Appl Polym Sci* 21. <https://doi.org/10.1002/app.32253>
68. Lee SH, Zhang Y, Kontopoulou M et al (2011) Optimization of dispersion of nanosilica particles in a PP matrix and their effect on foaming. *Int Polym Process* 26:388–398. <https://doi.org/10.3139/217.2403>
69. Nofar M, Majithiya K, Kuboki T, Park CB (2012) The foamability of low-melt-strength linear polypropylene with nanoclay and coupling agent. *J Cell Plast* 48:271–287. <https://doi.org/10.1177/0021955X12440271>
70. Lee ST, Ramesh NS (2005) *Thermoplastic foam processing principles and development*. CRC Press LLC, Boca Raton
71. Park CB, Cheung LK (1997) A study of cell nucleation in the extrusion of polypropylene foams. *Polym Eng Sci* 37:1–10. <https://doi.org/10.1002/pen.11639>
72. Behravesh AH, Park CB, Cheung LK, Venter RD (1996) Extrusion of polypropylene foams with hydrocerol and Isopentane. *J Vinyl Addit Technol* 2:349–357

73. Tabatabaei A, Barzegari MR, Mark LH, Park CB (2017) Visualization of polypropylene's strain-induced crystallization under the influence of supercritical CO₂ in extrusion. *Polymer (United Kingdom)* 122:312–322. <https://doi.org/10.1016/j.polymer.2017.06.052>
74. Hasan MM, Li YG, Li G et al (2010) Determination of solubilities of CO₂ in linear and branched polypropylene using a magnetic suspension balance and a PVT apparatus. *J Chem Eng Data* 55:4885–4895. <https://doi.org/10.1021/jc100488v>
75. Xu Z, Xue P, Zhu F, He J (2005) Effects of formulations and processing parameters on foam morphologies in the direct extrusion foaming of polypropylene using a single-screw extruder. *J Cell Plast* 41:169–185. <https://doi.org/10.1177/0021955X05051740>
76. Zhai W, Kim YW, Park CB (2010) Steam-chest molding of expanded polypropylene foams. 1. DSC simulation of bead foam processing. *Ind Eng Chem Res* 49:9822–9829. <https://doi.org/10.1021/ie101085s>
77. Klempner D, Frisch K (2004) *Handbook of polymeric foams and foam technology*. Hanser, München
78. Wörthwein H (2014) Method for the manufacture of EPP moulded parts. 1:1–10
79. BASF SE (2017) Neopolen P—designed for new ideas. Prod Broch
80. Market 2015–2019 (2015) Global expanded polypropylene (EPP) foam (low density, high density & porous PP)
81. Kuninori H, Shimada H (1983) Pre-foamed particles of polypropylene resin and process for production thereof (US Patent US 4379859). 1–4
82. Nofar M, Guo Y, Park CB (2013) Double crystal melting peak generation for expanded polypropylene bead foam manufacturing. *Ind Eng Chem Res* 52:2297–2303. <https://doi.org/10.1021/ie302625e>
83. Guo P, Liu Y, Xu Y et al (2014) Effects of saturation temperature/pressure on melting behavior and cell structure of expanded polypropylene bead. *J Cell Plast* 50:321–335. <https://doi.org/10.1177/0021955X14525798>
84. Lan X, Zhai W, Zheng W (2013) Critical effects of polyethylene addition on the autoclave foaming behavior of polypropylene and the melting behavior of polypropylene foams blown with n-pentane and CO₂. *Ind Eng Chem Res* 52:5655–5665. <https://doi.org/10.1021/ie302899m>
85. Tang L, Zhai W, Zheng W (2011) Autoclave preparation of expanded polypropylene/poly (lactic acid) blend bead foams with a batch foaming process. *J Cell Plast* 47:429–446. <https://doi.org/10.1177/0021955X11406004>
86. Harrison IR (1985) Modelling 'melting' in macromolecules. *Polymer (Guildf)* 26:3–7. [https://doi.org/10.1016/0032-3861\(85\)90050-3](https://doi.org/10.1016/0032-3861(85)90050-3)
87. Samuels RJ (1975) Quantitative structural characterization of the melting behavior of isotactic polypropylene. *J Polym Sci Polym Phys Ed* 13:1417–1446. <https://doi.org/10.1002/pol.1975.180130713>
88. Padden FJ, Keith HD (1959) Spherulitic crystallization in polypropylene. *J Appl Phys* 30:1479–1484. <https://doi.org/10.1063/1.1734985>
89. Pae KD (1968) Solid-solid transition of isotactic polypropylene. *Polymer (Guildf)* 6:657–663. <https://doi.org/10.1002/pol.1968.160060401>
90. Zhang R, Luo X, Wang Q, Ma D (1994) Melting behavior of low ethylene content polypropylene copolymers with and without nucleating agents. *Chin J Polym Sci* 12:246–255
91. Hingmann R, Rieger J, Kersting M (1995) hingmann_1995.pdf. *Macromolecules* 28:3801–3806
92. Choi JB, Chung MJ, Yoon JS (2005) Formation of double melting peak of poly (propylene-co-ethylene-co-1-butene) during the preexpansion process for production of expanded polypropylene. *Ind Eng Chem Res* 44:2776–2780. <https://doi.org/10.1021/ie0401399>
93. Cho K, Li F, Choi J (1999) Crystallization and melting behavior of polypropylene and maleated polypropylene blends. *Polymer (Guildf)* 40:1719–1729. [https://doi.org/10.1016/S0032-3861\(98\)00404-2](https://doi.org/10.1016/S0032-3861(98)00404-2)

94. Nofar M, Ameli A, Park CB (2015) Development of polylactide bead foams with double crystal melting peaks. *Polymer (Guildf)* 69:83–94. <https://doi.org/10.1016/j.polymer.2015.05.048>
95. Li G, Wang J, Park CB, Simha R (2007) Measurement of gas solubility in linear/branched PP melts. *J Polym Sci Part B: Polym Phys* 45:2497–2508. <https://doi.org/10.1002/polb.21229>
96. Stastny F, Gaeth R, Trieschmann HGD (1971) Process of making particulate expanded olefin polymers having high thermal stability. 59–61
97. Köppl T, Raps D, Altstädt V (2014) E-PBT—bead foaming of poly(butylene terephthalate) by underwater pelletizing. *J Cell Plast* 50:475–487. <https://doi.org/10.1177/0021955X14528524>
98. Kurtz GmbH (2017) Technical information EPP pre-expansion. 30
99. BASF SE (2017) Neopolen P—Technical Information. 1–10
100. Yang F, Pitchumani R (2002) Healing of thermoplastic polymers at an interface under nonisothermal conditions. *Macromolecules* 35:3213–3224. <https://doi.org/10.1021/ma010858o>
101. Wool RP, Yuan B-L, McGarel OJ (1989) Welding of polymer interfaces. *Polym Eng Sci* 29:1340–1367. <https://doi.org/10.1002/pen.760291906>
102. Anand JN, Kabam HJ (1969) Interfacial contact and bonding in autohesion: I—contact theory. *J Adhes* 1:16–23. <https://doi.org/10.1080/00218466908077369>
103. Anand JN, Balwinski RZ (1969) Interfacial contact and bonding in autohesion: II—intermolecular forces. *J Adhes* 1:24–30. <https://doi.org/10.1080/00218466908077370>
104. Anand JN (1969) Interfacial contact and bonding in autohesion: III—parallel plate attraction. *J Adhes* 1:31–37. <https://doi.org/10.1080/00218466908077371>
105. Anand JN, Dipzinski L (1970) Interfacial contact and bonding in autohesion: IV—experimental verification of theory. *J Adhes* 2:16–22. <https://doi.org/10.1080/0021846708544575>
106. Anand JN (1970) Interfacial contact and bonding in autohesion: V—bonding of “flat” surfaces. *J Adhes* 2:23–28. <https://doi.org/10.1080/0021846708544576>
107. De Gennes PG (1976) Dynamics of entangled polymer solutions. I. The Rouse model. *Macromolecules* 9:587–593. <https://doi.org/10.1021/ma60052a011>
108. De Gennes PG (1976) Dynamics of Entangled polymer solutions. II. Inclusion of hydrodynamic interactions. *Macromolecules* 9:594–598. <https://doi.org/10.1021/ma60052a012>
109. Bousmina M, Qiu H, Grmela M, Klemberg-Sapieha JE (1998) Diffusion at polymer/polymer interfaces probed by rheological tools. *Macromolecules* 31:8273–8280. <https://doi.org/10.1021/ma980562r>
110. Zhai W, Kim YW, Jung DW, Park CB (2011) Steam-chest molding of expanded polypropylene foams. 2. Mechanism of interbead bonding. *Ind Eng Chem Res* 50:5523–5531. <https://doi.org/10.1021/ie101753w>
111. Guanghong H, Yue W (2012) Microcellular foam injection molding process. Some critical issues inject molding. <https://doi.org/10.5772/34513>
112. Volpe V Foam injection molding with physical blowing agents
113. Ruckdäschel H (2008) Micro- and nanostructured polymer blends—processing, properties and foaming behaviour
114. Shaayegan V, Wang G, Park CB (2016) Effect of foam processing parameters on bubble nucleation and growth dynamics in high-pressure foam injection molding. *Chem Eng Sci* 155:27–37. <https://doi.org/10.1016/j.ces.2016.07.040>
115. Reza M (2009) Structure-flexural modulus relationships in polymeric structural
116. Kramschuster A, Cavitt R, Ermer D et al (2006) Effect of processing conditions on shrinkage and warpage and morphology of injection moulded parts using microcellular injection moulding. *Plast Rubber Compos* 35:198–209. <https://doi.org/10.1179/174328906X128199>

117. Zhang L, Zhao G, Dong G et al (2015) Bubble morphological evolution and surface defect formation mechanism in the microcellular foam injection molding process. *RSC Adv* 5:70032–70050. <https://doi.org/10.1039/C5RA07512B>
118. Wu PC, Jones G et al (2007) Novel microporous films and their composites. *J Eng Fiber Fabr* 2:49–59
119. Arora P, Zhang Z (2004) Battery separators. *Chem Rev* 104:4419–4462. <https://doi.org/10.1021/cr020738u>
120. Bai H, Wang Y, Zhang Z et al (2009) Influence of annealing on microstructure and mechanical properties of isotactic polypropylene with β -phase nucleating agent. *Macromolecules* 42:6647–6655. <https://doi.org/10.1021/ma9001269>
121. Tordjeman P, Robert C, Marin G, Gerard P (2001) The effect of α , β crystalline structure on the mechanical properties of polypropylene. *Eur Phys J E* 4:459–465
122. Varga J, Karger-kocsis J (1993) The occurrence of transcrystallization or row-nucleated cylindrical crystallization as a result of shearing in a glass-fiber-reinforced polypropylene. *Compos Sci Technol* 48:191–198
123. Crissman JM (1969) Mechanical relaxation in polypropylene as a function of polymorphism and degree of lamella orientation. *J Polym Sci* 7:389–404
124. Varga J (2002) B-modification of isotactic polypropylene: preparation, structure, processing, properties, and application. *J Macromol Sci Part B* 41:1121–1171. <https://doi.org/10.1081/MB-120013089>
125. Kersch M, Schmidt HW, Altstädt V (2016) Influence of different beta-nucleating agents on the morphology of isotactic polypropylene and their toughening effectiveness. *Polymer (United Kingdom)* 98:320–326. <https://doi.org/10.1016/j.polymer.2016.06.051>
126. Jacoby P (2014) Beta nucleation of polypropylene—properties, technology and applications. Elsevier, Amsterdam
127. Silverstein MS (2014) PolyHIPEs: recent advances in emulsion-templated porous polymers. *Prog Polym Sci* 39:199–234. <https://doi.org/10.1016/j.progpolymsci.2013.07.003>
128. Nguyen TH, Vayer M, Sinturel C (2018) PS-b-PMMA/PLA blends for nanoporous templates with hierarchical and tunable pore size. *Appl Surf Sci* 427:464–470. <https://doi.org/10.1016/j.apsusc.2017.08.160>
129. Silverstein MS (2014) Emulsion-templated porous polymers: a retrospective perspective. *Polymer (Guildf)* 55:304–320
130. Sergienko AY, Tai H, Narkis M, Silverstein MS (2002) Polymerized high internal-phase emulsions: properties and interaction with water. *J Appl Polym Sci* 84:2018–2027. <https://doi.org/10.1002/app.10555>
131. Wang K, Wu F, Zhai W, Zheng W (2013) Effect of polytetrafluoroethylene on the foaming behaviors of linear polypropylene in continuous extrusion. *J Appl Polym Sci* 129:2226–2253
132. Scheve BJ, Mayfield JW, DeNicola JAJ (1972) US Patent 3
133. Zhang ZJ, Wan D, Xing HP et al (2012) A new grafting monomer for synthesizing long chain branched polypropylene through melt radical reaction. *Polymer (Guildf)* 53
134. Lin W, Shao Z, Jy D, Chung TCM (2009) Cross-linked polypropylene prepared by PP copolymers containing flexible styrene groups. *Macromolecules* 42:3750–3754
135. Schöne J, Kotter I, Grellmann W (2012) Zeitschrift Kunststofftechnik. *J Plast Technol* 8:231–251
136. Blomenhofer M, Ganzleben S, Hanft D et al (2005) “Designer” nucleating agents for polypropylene. *Macromolecules* 38:3688–3695. <https://doi.org/10.1021/ma0473317>
137. Huang H-X, Wang J-K (2007) Improving polypropylene microcellular foaming through blending and the addition of nano-calcium carbonate. *J Appl Polym Sci* 106:505–513. <https://doi.org/10.1002/app.26483>
138. Naiki M, Fukui Y, Matsumura T et al (2001) Effect of talc on the crystallization of isotactic polypropylene. *J Appl Polym Sci* 79:1693–1703. [https://doi.org/10.1002/1097-4628\(20010228\)79:9%3c1693:AID-APP190%3e3.0.CO;2-P](https://doi.org/10.1002/1097-4628(20010228)79:9%3c1693:AID-APP190%3e3.0.CO;2-P)

139. Okamoto M, Nam PH, Maiti P et al (2001) Biaxial flow-induced alignment of silicate layers in polypropylene/clay nanocomposite foam. *Nano Lett* 1:503–505. <https://doi.org/10.1021/nl010051+>
140. Jiang X-L, Bao J-B, Liu T et al (2009) Microcellular foaming of polypropylene/clay nanocomposites with supercritical carbon dioxide. *J Cell Plast* 45:515–538. <https://doi.org/10.1177/0021955X09339470>
141. Antunes M, Gedler G, Velasco JI (2013) Multifunctional nanocomposite foams based on polypropylene with carbon nanofillers. *J Cell Plast* 49:259–279. <https://doi.org/10.1177/0021955X13477433>
142. Wang C, Ying S, Xiao Z (2013) Preparation of short carbon fiber/polypropylene fine-celled foams in supercritical CO₂. *J Cell Plast* 49:65–82. <https://doi.org/10.1177/0021955X12459642>
143. Barboza ACRN, De Paoli M (2002) Polipropileno Carregado com Microesferas Ocas de Vidro (Glass Bubbles™): Obtenção de Espuma Sintética. *Polímeros* 12:130–137. <https://doi.org/10.1590/S0104-14282002000200013>
144. Ss H, Hsu PP (2013) Effects of silica particle size on the structure and properties of polypropylene/silica composites foams. *J Ind Eng Chem* 19:1377–1383
145. Colton JS (1989) The nucleation of microcellular foams in semi-crystalline thermoplastics. *Mater Manuf Process* 4:253–262. <https://doi.org/10.1080/10426918908956288>
146. Bertrand J-N (1986) Expanded polypropylene films and process for preparing them. *EP* 0 178 282 A2
147. Libster D, Aserin A, Garti N (2007) Advanced nucleating agents for polypropylene. *Polym Adv Technol* 18:685–695. <https://doi.org/10.1002/pat.970>
148. Varga J, Menyhárd A (2007) Effect of solubility and nucleating duality of N,N'-dicyclohexyl-2,6-naphthalenedicarboxamide on the supermolecular structure of isotactic polypropylene. *Macromol Theory Simulations* 40:2422–2431
149. Stumpf M, Spörrer A, Schmidt H-W, Altstädt V (2011) Influence of supramolecular additives on foam morphology of injection-molded i-PP. *J Cell Plast* 47:519–534. <https://doi.org/10.1177/0021955X11408769>
150. Mörl M, Steinlein C, Kreger K et al (2017) Improved compression properties of polypropylene extrusion foams by supramolecular additives. *J Cell Plast*. <https://doi.org/10.1177/0021955X17695096>